MARINE 2013
Computational Methods in Marine Engineering V

Hamburg, 29-31 May 2013

Birgitt Brinkmann and Peter Wriggers (Eds.)



Computational Methods in Marine Engineering V
MARINE 2013

Computational Methods in Marine Engineering V

Proceedings of the V International Conference on Computational Methods in Marine Engineering, held in Hamburg, Germany 29-31 May 2013

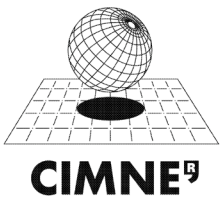
Edited by

Birgitt Brinkmann
Leuphana University, Lüneburg, Germany

Peter Wriggers
Leibniz University, Hannover, Germany

A publication of:

International Center for Numerical Methods in Engineering (CIMNE)
Barcelona, Spain



International Center for Numerical Methods in Engineering (CIMNE)
Gran Capitán s/n, 08034 Barcelona, Spain
www.cimne.com

Computational Methods in Marine Engineering V
Birgitt Brinkmann and Peter Wriggers (Eds.)

First edition, May 2013

© The authors

Printed by: Artes Gráficas Torres S.L., Huelva 9, 08940 Cornellà de Llobregat, Spain

Depósito legal: B-14014-2013

ISBN: 978-84-941407-4-7

PREFACE

This volume contains the full length papers presented at MARINE 2013, the Fifth International Conference on Computational Methods in Marine Engineering, held at Patriotische Gesellschaft, Hamburg, Germany, 29-31 May 2013. The first edition of these series of conferences was held 27-29 June 2005 in Oslo, Norway, the second 5-7 June 2007 in Barcelona, Spain, the third 15-17 June 2009 in Trondheim, Norway and the fourth 28-30 September 2011 in Lisbon, Portugal.

Computational methods are an essential tool in marine applications, such as the maritime and offshore industries and engineering challenges related to the marine environment and renewable energies. Therefore, the overall mission for these events "A meeting place for researchers developing computational methods and scientists and engineers focusing on challenging applications in Marine Engineering" is even more appropriate than when this series of conferences started 8 years ago.

This year's conference contains 7 invited plenary lectures and 134 presentations organized in sessions dedicated e.g. to "Fluid-Structure Interaction", "Fluid-Dynamic Optimization of Ships and Components", "Algorithms for Multidisciplinary Problems in Marine Engineering", "Isogeometric Methods for Marine Engineering", "Advances in Numerical Methods for Marine Engineering", "Safety in Marine Engineering", "Design of Offshore Wind Structures", "Cables", "Structural Analysis of Marine Structures" organized by recognized experts in the respective field. The program extends over three days with 3 parallel sessions.

MARINE 2013 is the fifth international conference on this topic organized in the framework of the Thematic Conferences of the European Community on Computational Methods in Applied Sciences (ECCOMAS). MARINE 2013 is also a Special Interest Conference of the International Association for Computational Mechanics (IACM).

The conference was jointly organized by Institut für Nachhaltigkeitssteuerung of the Leuphana Universität Lüneburg (LUL) and the Institut für Kontinuumsmechanik of the Leibniz Universität Hannover (LUH) and the International Center for Numerical Methods in Engineering (CIMNE) in co-operation with the Technical University of Catalonia (UPC). We would like to show our appreciation to the presenters of the plenary lectures, session organizers and to all authors for their combined effort in making MARINE 2013 an intellectually stimulating conference. We also acknowledge the support from the sponsors listed on the next page. Finally, we express our sincere thanks to Alessio Bazzanella from the Congress Department of CIMNE, Barcelona, Spain, for his dedication and excellent work in the support of the organization of the conference and the publication of this volume.

Hamburg, 1st of May 2013

Birgitt Brinkmann
(Leuphana Universität Lüneburg)

Peter Wriggers
Peter Wriggers
(Leibniz Universität Hannover)

Editors

ACKNOWLEDGEMENTS

The conference organizers acknowledge the support towards the organization of the MARINE 2013 Conference to the following organizations:

European Community on Computational Methods in Applied Sciences (ECCOMAS)

International Association for Computational Mechanics (IACM)

Leuphana University, Lünenburg, Germany

Leibniz University, Hannover, Germany

International Center for Numerical Methods in Engineering (CIMNE), Barcelona, Spain

Norwegian University of Science and Technology, NTNU

Instituto Superior Técnico

Universitat Politècnica de Catalunya, Spain

HOCHTIEF Solutions AG

Springer

SUMMARY

Preface 7
Acknowledgements 9
Contents 13

Invited Sessions

IS - Computational Methods for Fluid-Structure-Interaction 21
Invited Session Organized by ***Bettar Ould el Moctar***

IS - Computational Methods in Offshore Wind energy 35
IS Organized by Peter Schaumann and Raimund Rolfes

IS - Design of Offshore Wind Structures - How to Drive Costs Down? 58
Invited Session organized by Eckard Ritterbach and Stefan Woltering

IS - Fluid-dynamic Optimization of Ships and Components 69
Invited Session organized by Stefan Harries

IS - Green Energy Production from the Oceans 113
Invited Session organized by Francesco Salvatore

IS - Isogeometric Methods for Marine Engineering 144
Invited Session organized by Trond Kvamsdal and Kjell Mathisen

IS - Numerical Modeling and Characterization of Nets for Marine Applications 168
Invited Session organized by Igor Tsukrov

IS - Numerical Simulation of Fluid-structure Interaction: Recent Developments and Applications 202
Invited Session organized by Alexander Düster

IS - Offshore Renewable Energy 309
Invited Session organized by Julio García-Espinosa

Contributes Sessions

Advances in Numerical Methods 320

Advances in Numerical Methods for Marine Engineering 365

Algorithms for Multidisciplinary Problems in Marine Engineering 400

Cables 444

Fluid-Structure Interaction 479

Marine Engineering 512

Modeling and Numerical Methods 587

Offshore Windfarms 634

Safety in Marine Engineering 660

Sea Pipes and Anchoring Systems 677

Ship Hydrodynamics 699

Ships Hydrodynamics and Systems 760

Structural Analysis of Marine Structures 818

CONTENTS

Invited Sessions

IS - Computational Methods for Fluid-Structure-Interaction
*Invited Session Organized by **Bettar Ould el Moctar***

Approximation of the Elastic Deformation of a Body Subject to Large Rigid Body Motions through Truncated Expansion into Generalized Coordinates 21
C. Cabos and M. Kroemer

IS - Computational Methods in Offshore Wind energy
IS Organized by Peter Schaumann and Raimund Rolfes

A Novel Plasticity-Based Fatigue Failure Model for Grouts in Grouted Joints for Offshore Wind Turbines with Monopiles 35
P. Schaumann and S. Lochte-Holtgreven

Determining of Design Loads for Drive Train Components of Wind Turbines using the Multibody-System Simulation.....47
B. Schlecht, T. Rosenlöcher and T. Schulze

IS - Design of Offshore Wind Structures - How to Drive Costs Down?
Invited Session organized by Eckard Ritterbach and Stefan Woltering

Searching for the Silver Bullet in Wind Offshore 58
D. Bartminn and D.J. Quintana

IS - Fluid-dynamic Optimization of Ships and Components
Invited Session organized by Stefan Harries

Optimization Using Viscous Flow Computations for Retrofitting Ships in Operation.....69
M. Brenner, V. Zagkas, S. Harries and T. Stein

Hull Optimization for Operational Profile – The Next Game Level 81
K. Hochkirch, J. Heimann and V. Bertram

Robust Design Optimization of a Monohull for Wave Wash Minimization.....89
D. Peri and M. Diez

Optimisation of a Chemical Tanker and Propeller with CFD 101
A. van der Ploeg and E.J. Foeth

IS - Green Energy Production from the Oceans
Invited Session organized by Francesco Salvatore

Numerical Prediction of the Performance of Axial-flow Hydrokinetic Turbine.....113
P. Chandras, L. Sharma and D. Chatterjee

WaveCat® Wave Energy Converter Modeling by Means of a RANS-VoF Numerical Model 125
H. Fernandez, G. Iglesias, I. Lopez and S. Schimmels

Review of Individual Based Modelling Techniques in a Marine Environment.....137
T. Lake, I. Masters and T.N. Croft

IS - Isogeometric Methods for Marine Engineering
Invited Session organized by Trond Kvamsdal and Kjell Mathisen

A Multi-Objective Optimization Environment for Ship-Hull Design based on a BEM-Isogeometric Solver....144
A. Ginnis, R. Dunigneau, C. Politis, K. Kostas, K. Belibassakis, T. Gerostathis and P.D. Kaklis

Modelling and Simulation of Main engine Excitation on Board Vessels....156
C. Tamm and M. Kurch

IS - Numerical Modeling and Characterization of Nets for Marine Applications
Invited Session organized by Igor Tsukrov

Effect of the Bending Stiffness on the Volumetric Stability of Fish Cages with Copper Alloy Netting....168
J. DeCew, M. Osienski, A. Drach, B. Celikkol and I. Tsukrov

Design and Modeling of Submersible Fish Cages with Copper Netting for Open Ocean Aquaculture....178
A. Drach, I. Tsukrov, J. DeCew, M.R. Swift, B. Celikkol and C. Hurtado

Numerical and Experimental Study of the Flow Field around Fishing Net....190
Y. Zhao, C. Bi, G. Dong, Y. Li and F. Gui

IS - Numerical Simulation of Fluid-structure Interaction: Recent Developments and Applications
Invited Session organized by Alexander Düster

Fast Solvers for Thermal Fluid Structure Interaction....202
P. Birken, T. Gleim, D. Kuhl and A. Meister

Numerical Simulation of Hydroacoustic Fluid-Ship Interaction by Fast BEM & FEM Coupling...213
L. Gaul, D. Brunner and M. Junge

GPGPU-accelerated Simulation of Wave-Ship Interactions using LBM and a Quaternion-based Motion Modeler....229
C. Janßen, H. Nagrelli and T. Rung

A New Turbulent Three-dimensional FSI Benchmark FSI-PfS-3A: Definition and Measurements....241
A. Kalmbach, G. De Nayer and M. Breuer

Development of a Hybrid Approach using Coupled Grid-Based and Grid-Free Methods....255
N. Kornev and G. Jakobi

Unsteady FSI Simulation of Downwind Sails....266
N. Parolini and M. Lombardi

Stochastic Navier-Stokes Equations are a Coupled Problem....278
J. Rang and H.G. Matthies

Concept and Realization of Coupling Software EMPIRE in Multi-Physics Co-Simulation....289
T. Wang, S. Sicklinger, R. Wüchner and K.-U. Bletzinger

Modeling of Water Flow with Free Surface....299
M. Warmowska

IS - Offshore Renewable Energy
Invited Session organized by Julio García-Espinosa

Dynamic modelling of mooring for floating offshore structures....309
J.E. Gutiérrez Romero, B. Zamora Parra, J. García-Espinosa and J.A. Esteve Perez

Contributes Sessions

Advances in Numerical Methods

Vibration analysis of in-plane loaded plates with arbitrary stiffener arrangements using a semi-analytical approach 320
L. Brubak, J. Hellesland and O.J. Hareide

Comparison of Computational Methods for Evaluation of Wave-load Induced Fatigue Damage Accumulation In Ship Structure Details 332
V. Ogeman, W. Mao and J. Ringsberg

Propagation Over a Sloping Bottom of Waves Generated by Ships 344
S. Rodrigues, M.F. Nascimento, N. Fonseca, J.A. Santos and C.F. Neves

Simulation of Moonpool Water Motion 356
H.J.L. van der Heiden, P. van der Plas, A.E.P. Veldman, R. Luppes and R.W.C.P. Verstappen

Advances in Numerical Methods for Marine Engineering

Advances in the Development of a New Cartesian Explicit Solver for Hydrodynamics 265
P. Bigay, C. Leroy, G. Oger, P.M. Guilcher and D. Le Touzé

A Hybrid Particle-Grid Scheme for Computing Hydroelastic Behaviors Caused by Slamming ... 376
H. Mutsuda, S. Baso and Y. Doi

Resolution Refinement Technique in a Smoothed Particle Hydrodynamics Numerical Flume for Coastal Engineering Applications 388
D.R.C.B. Neves, E. Didier, P.R.F. Teixeira and M.G. Neves

Algorithms for Multidisciplinary Problems in Marine Engineering

Numerical Analysis of the Ship Propulsion Control System Effect on the Manoeuvring Characteristics both in Model and Full Scale 400
M. Altosole, M. Figari, M. Martelli, M. Nataletti, S. Vignolo and M. Viviani

Bulbous Bow Shape Optimization 412
L. Blanchard, E. Berrini, R. Duvigneau, Y. Roux, B. Mourrain and E. Jean

Bevel Gear Calculation of a Vessel Drive Train with Azimuthing Thrusters 424
B. Schlecht, C. Bauer and T. Rosenlöcher

Comprehensive Analysis of Thruster Drivetrains to Determine Reliable Load Assumptions 433
B. Schlecht, T. Rosenlöcher and C. Bauer

Cables

Numerical Analysis of Impact of Energy Buoy Anchoring Configurations on its Motion and Efficiency 444
C. Dymarski and P. Dymarski

Simulation of Mooring Cable Dynamics Using a Discontinuous Galerkin Method 455
J. Palm, G. M. Paredes, C. Eskilsson, F. Tavera Pinto and L. Bergdahl

Numerical Simulation of the Behaviour of a Moored Ship Inside an Open Coast Harbour 467
L. Pinheiro, C. Fortes, J.A. Santos and J. Fernandes

Fluid-Structure Interaction

Simulation of a Pendulum with Fluid Interaction and Experimental Validation 479
F. Beck, F. Fleissner and P. Eberhard

Fluid Structure Interaction Analysis of a Hydrofoil 491
C. Lothode, M. Durand, A. Leroyer, M. Visonneau, M. Delaitre, Y. Roux and L. Dorez

Local Grid Refinement for Free-Surface Flow Simulations in Offshore Applications.....502
P. van der Plas, H. van der Heiden, R. Luppes and A. Veldman

Marine Engineering

Testing a Semi-Automated Tool for Full-Scale Marine Propellers Working Behind a Ship 512
S. Berger, M. Druckenbrod, M. Pergande and M. Abdel-Maksoud

Ship Energy Assessment by Numerical Simulation.....530
A. Coraddu, M. Figari and S. Savio

Ship Propulsion Prediction with a Coupled RANSE-BEM Approach 541
G. Deng, P. Queutey, M. Visonneau and F. Salvatore

A Throughflow Method for the Analysis of Mixed Flow Waterjet Pump 552
G. Ricci, C. Costa and A. Satta

Technical-Economical Analysis of Cold-Ironing: Case study of Cruise Terminal of Port of Venice 564
S. Ricci, C. Marinacci, R. Masala and A. Tieri

Mathematical Simulation and Computer System for Pre-processing of Propeller Geometry for CFD Analysis and Production Applications.....575
A. Yakovlev, N. Marinich and A. Senyushkina

Modeling and Numerical Methods

Axisymmetric transient modelling of a wind turbine foundation in cohesionless soil using the Prevost‘s model 587
B. Cerfontaine, S. Levasseur and R. Charlier

The Effect of Different Volume-of-Fluid (VOF) Methods on Energy Dissipation in Simulations of Propagating Waves.....599
B. Duz, R. Huijsmans, A. Veldman, M. Borsboom and P. Wellens

Analysis of the Influence of Complex Material Behaviour on Fusion Welding Simulations 611
J.P. Lefebvre, L. D‘Alvise, N. Poletz, M. Cazuguel, E. Wyart and A. Francois

Computational Modelling of Two-phase Flow around a Savonius Type Wave Energy Converter in a Two-Dimensional Numerical Wave Tank 622
M. Tutar and C. Erdem

Offshore Windfarms

Computational Prediction of Near and Far Field Noise due to Pile Driving for Offshore Wind Farms 634
K. Heitmann, T. Lippert, M. Ruhnau, S. Lippert and O. von Estorff

New Development of Cost-Efficient Multi-Pile Concrete Foundation (MCF) for Offshore Wind Turbine 642
K.D. Kim, A. Manovachirasan and H. Jeon

Quantity and Type Forecasting Tool for Offshore Wind Power Plant Spare Parts 652
R. Rauer, T. Muensterberg and C. Jahn

Safety in Marine Engineering

Fatigue Strength Assessment of HP Stiffener Joints with Fillet-Welded Attachments Using the Peak Stress Method 660
C. Fischer, W. Fricke, G. Meneghetti and C.M. Rizzo

A Preliminary Study on Ultrasonic Non-Destructive Testing of Concrete in Maritime Environment.....670
A. Shah, Y. Ribakov and C. Zhang

Sea Pipes and Anchoring Systems

The Effective Axial Force Concept for Offshore Lined and Clad Pipes. 677
K. Vedeld, H.A. Sollund and O. Fyrileiv

Cnoidal Wave Induced Forces on a Submarine Pipeline 689
X.H. Xia, Y.F. Xu, J.H. Wang and J.J. Chen

Ship Hydrodynamics

Prediction of the Scale Effect for the Hull-Propeller Interaction Factors.....699
D.V. Bagaev, M.P. Lobachev, N.A. Ovchinnikov and A.E. Taranov

Zig-Zag Manoeuver simulation by CFD for a tanker like vessel 711
G. Dubbioso, D. Durante and R. Broglia

Comparison of Different Approaches for the Design and Analysis of Ducted Propellers 723
S. Gaggero, M. Viviani, G. Tani, F. Conti, P. Becchi and F. Valdenazzi

Influence of Propeller Tip Roughness on Tip Vortex Structure 737
C. Krueger, N. Kornev, C. Semlow and M. Paschen

The Design of Turbines for Harnessing Marine Currents 748
J. Moreu, J. Valle, M. Moreu and M. Taboada

Ships Hydrodynamics and Systems

The Thesaurus Project, a long Range AUV for Extended Exploration, Surveillance and Monitoring of Archaeological Sites 760
B. Allotta, L. Pugi, F. Bartolini, J. Gelli, G. Vettori, A. Ridolfi, R. Costanzi, N. Monni, L. Gualdesi and M. Natalini

Non-Stationary Probability of Parametric Roll of Ships in Random Seas.....772
L. Dostal and E. Kreuzer

Numerical Study of two Olympic Racing-Kayaks in Presence of Lateral Wind 781
M. Hamdaoui, Y. Roux, E. Jean, R. Duvigneau, J.C. Gonneau and F. During

Numerical Simulation of Flows around KVLCC2 Hull Form with Ship Motions in Regular Waves 794
K. Ohashi, N. Sakamoto and T. Hino

Analysis and Compensation of Magnetic Anomalies on Vessel´s Flight Decks 806
A. Villalba and A. Álvarez

Structural Analysis of Marine Structures

Mean Load Effects on the Fatigue Life of Offshore Wind Turbine Foundations 818
J. Blasques and A. Natarajan

Dynamic Simulations of an Airplane-Shaped underwater Towed Vehicle 830
A. Cammarata, M. Lacagnina and R. Sinatra

Numerical Investigation of Spudcan Footing Penetration in Layered Soil.....842
P. Gütz, P. Peralta, K. Abdel-Rahman and M. Achmus

Deformation behaviour of reinforced concrete shells for offshore structures 854
W. Krakowski, M. Empelmann and L. Eckfeldt

Programming Methods for Pre-design of Coastal Structures.....868
M. Lima, C. Coelho and P. Cachim

Modelling Flat Ship Plates Using Equivalent Single Layer Theory.....880
J. Romanoff, J. Jelovica, E. Avi and A. Niemelä

A Semi-Analytical Model for Structural Response Calculations of Subsea Pipelines in Interacting Free Spans.....889
H. Sollund and K. Vedeld

Structural Design of a Bulbous Bow with Regard to Collision Safety.....901
I. Tautz, M. Schöttelndreyer, J. Gauerke, E. Lehmann and W. Fricke

A New Composite Material for Fiberglass Boat Construction.....912
A. Wahrhaftig, H.J. Caribe Ribeiro and A. Nascimento

The Pull-out Capacity of Mobile Platform Legs From Saturated Silt 921
X.W Zhang, R. Uzuoka and X.W. Tang

Author Index 932

INVITED SESSIONS

V International Conference on Computational Methods in Marine Engineering
MARINE 2013
B. Brinkmann and P. Wriggers (Eds)

APPROXIMATION OF THE ELASTIC DEFORMATION OF A BODY SUBJECT TO LARGE RIGID BODY MOTIONS THROUGH TRUNCATED EXPANSION INTO GENERALIZED COORDINATES

Christian Cabos*, Matthias Krömer†

* Germanischer Lloyd SE
Brooktorkai 18, 20457 Hamburg, Germany
e-mail: christian.cabos@gl-group.com, web page: http://www.gl-group.com

† Germanischer Lloyd SE
Brooktorkai 18, 20457 Hamburg, Germany
e-mail: matthias.kroemer@gl-group.com, web page: http://www.gl-group.com

Key words: Fluid Structure Interaction, OpenFOAM, Finite Element, Modal, Floating Object

1 INTRODUCTION

An important marine application of fluid structure interaction is the elastic deformation of a ship's hull in waves, which becomes particular significant on resonance either due to periodic waves (springing) or slamming events (whipping). Compared to the hull's dimensions, these elastic deformations are small and can be represented by a linear finite element model of the ship. On the other hand, the total motion of the ship in waves, i. e. the sum of rigid body motion and elastic deformation, may become large, so the rigid body motion has to be treated in a fully nonlinear fashion.

In this paper, a mathematical description of the nonlinear motion and linear structure deformation is derived. It uses generalized coordinates based on decomposition of the ship motion into generalized modes in a body-fixed reference frame. I.e., in this modal approach, structure nodal displacements are approximated by a small number of displacement functions.

A prototypical application of the described solution approach, (coupled to the OpenFOAM fluid solver) to a ship in waves has been published in [3]. Comparison with experimental data and results of an alternative structure approach have been published in [6]. The current paper focuses on numerical verification. To this end, a benchmark setup is proposed and computational results are presented in section 4.

2 STRUCTURAL PART

The principle of virtual work for a body with volume V and surface A equates the work performed by volume loads $p_V - p_{VI} - p_{VD}$ and surface loads $p_S - p_{SD}$ with the work due to internal stresses σ (see e.g. chapter 15 of [1])

$$\int_V \underline{\gamma}^\top \sigma dV = \int_V \underline{u}^\top (p_V - p_{VI} - p_{VD}) dV + \int_A \underline{u}^\top (p_S - p_{SD}) dA. \tag{1}$$

Here $\underline{u}$ are virtual displacements with kinematically compatible strains $\underline{\gamma}$. The volume loads consist of external loads p_V, inertia forces p_{VI} and damping forces p_{VD}. Similarly, the surface loads consist of the external loads p_S and the damping forces P_{SD}. The inertia forces are given by $p_{VI} = \rho \ddot{u}_a$ with the body's mass density ρ and the absolute acceleration $\ddot{u}_a$.

Equation (1) is valid also in moving reference frames. Writing it out, we have

$$\int_V \underline{u}^\top \rho \ddot{u}_a dV + \int_V \underline{u}^\top p_{VD} dV + \int_A \underline{u}^\top p_{SD} dA + \int_V \underline{\gamma}^\top \sigma dV = \int_V \underline{u}^\top p_V dV + \int_A \underline{u}^\top p_S dA \tag{2}$$

where the summands describe the contributions from inertial forces, internal damping, surface damping, elastic forces, external volume forces, and external surface forces, respectively. It is the term $\ddot{u}_a$ which can add complication in the case that the reference frame undergoes acceleration or rotation. In case the reference frame moves with translatory acceleration $\ddot{U}$, angular velocity Ω and angular acceleration $\dot{\Omega}$, the absolute acceleration of a mass point at position x is given by (see [1])

$$\ddot{u}_a = \ddot{u} + 2\Omega \times \dot{u} + \dot{\Omega} \times u + \Omega \times (\Omega \times u) + \ddot{U} + \dot{\Omega} \times x + \Omega \times (\Omega \times x). \tag{3}$$

Here, u denotes the relative displacement in the local, moving coordinate system.

2.1 Discretization

In this paper, the structural displacements of the hull will be approximated by a linear combination of n displacement functions $\phi_i, i = 1, \ldots, n$

$$u(x,t) = \sum_{i=1}^{n} \phi(x)_i r_i(t) = \Phi(x) r(t). \tag{4}$$

The time dependent modal coefficients $r_i, i = 1..n$ are assembled in the vector

$$r = [r_i, ..., r_n]^T \tag{5}$$

and the modes into the matrix

$$\Phi = [\phi_1, ..., \phi_n]. \tag{6}$$

The ϕ_i will be called modes in the following but can be any displacement functions of the body. A possible choice would be free vibration modes, but they can also be any other set of displacements, e.g. reactions from a set of loads experienced in a typical environment of the ship. The modes need not be mutually orthogonal.

While conceptually similar to "generalized" or "principal coodinates" in classical mechanics, we prefer the term "modal coefficients" for the r_i in order to stress the approximation by a small number of modes.

To discretize the equation of motion (2) while considering (3), we now also apply $\phi_j, j = 1, \ldots, n$ as the virtual displacements $\underline{u}$ (and $\underline{\gamma}$ as their corresponding strains). This yields the following time dependent vector equation

$$M\ddot{r} + [C + G(\Omega)]\dot{r} + [K + H(\dot{\Omega}) + Z(\Omega)]r = \int_A \Phi^T p_S dA + \int_V \Phi^T p_V dV - R(\Omega, \dot{\Omega}, \ddot{U}). \quad (7)$$

Here the symbols R, H, Z, G, and M denote

$$R = \int_V \rho\Phi^T[\ddot{U} + (\dot{\Omega} \times x) + \Omega \times (\Omega \times x)]dV, \quad (8)$$

the angular acceleration stiffness

$$H = \int_V \rho\Phi^T(\dot{\Omega} \times \Phi)dV, \quad (9)$$

the centripetal forces

$$Zr = \int_V \rho\Phi^T[\Omega \times (\Omega \times \Phi)]dV\ r, \quad (10)$$

the Coriolis forces

$$G\dot{r} = 2\int_V \rho\Phi^T(\Omega \times \Phi)dV\ \dot{r}, \quad (11)$$

and the mass matrix

$$M = \int_V \rho\Phi^T\Phi dV. \quad (12)$$

The matrix K denotes the stiffness which represents the fourth term in (2), and the damping matrix C contains the contributions from the second and third term in (2). All terms of the equation of motion in the moving coordinate system have been given above for completeness. In ship applications, however, the forces resulting from the terms containing G, H, and Z are typically negligibly small whereas R results in a significant contribution.

In the following, the first six modes $\phi_i, i = 1, \ldots, 6$ will be assumed to represent the rigid body motion of the ship. Since we assume that the ship will undergo large rigid body motions but only small (linear) elastic deformations, these first six modes have

special relevance. In particular, a body fixed reference frame for solving the structural equations of motion will be chosen such that the modal coefficients $r_1, \ldots, r_6$ for the rigid body modes are zero in the body fixed system. Due to the movement of the body fixed coordinate system, additional inertial forces will result. In the following sections, the terms "inertial", "global" resp. "body fixed", "local", "moving" will be used synonymously.

If the modes used for the projection are normalized and orthogonal with respect to the mass matrix, M becomes the unit matrix. In case moreover global vibration eigenmodes are chosen, K is the diagonal matrix of the squared circular eigenfrequencies ω_i^2. Damping is then typically chosen as applied for a global ship vibration analysis, i.e. as a percentage of critical damping applied to the respective mode (see e.g. [2]).

Introducing the abbreviations

$$C^*(\Omega) = C + G(\Omega), \tag{13}$$

$$K^*(\dot{\Omega}, \Omega) = K + H(\dot{\Omega}) + Z(\Omega), \tag{14}$$

$$R^*(t, \dot{\Omega}, \Omega, \ddot{U}) = \int_A \Phi^T p_S dA + \int_V \Phi^T p_V dV - R(\Omega, \dot{\Omega}, \ddot{U}) \tag{15}$$

equation (7) reads

$$M\ddot{r} + C^*(\Omega)\dot{r} + K^*(\dot{\Omega}, \Omega)r = R^*(t, \Omega, \dot{\Omega}, \ddot{U}). \tag{16}$$

Note that the projected matrices can be computed efficiently before the time integration, i.e. no matrix vector products with the full system matrices are required during time integration (see ([7]).

Solution of equation (16) requires a nonlinear solver, because of the constraints $r_i = 0, i = 1, \ldots, 6$ and the fact that $\ddot{U}$, Ω, and $\dot{\Omega}$ are unknown for the specific timestep. The solution procedure is described in section 2.2.

2.2 Solution procedure

Temporal discretization of equation (16) results in an equation system that is linear in the unknown modal coefficients r and non-linear in the unknown rigid body motion parameters $\ddot{U}$, $\dot{\Omega}$, Ω. By observing that the modal coefficients $r_1 \ldots r_6$ representing rigid body modes are zero at all times in the body fixed reference frame, and by relating Ω to $\dot{\Omega}$ via finite difference approximation for closure, a block structure of the equation system can be found that allows to

- first obtain a non-linear solution for the rigid body parameters $\ddot{U}$, and $\dot{\Omega}$ via Newton iteration, and
- then obtain the elastic modal coefficients $r_7 \ldots r_n$ via linear equation solver.

- Then, rigid body degrees of freedom U, Ω are computed via temporal integration, and
- nodal displacements and the rotation matrix required for transformation between global and local reference frames are computed.
- This procedure is applied in each implicit iteration/time step.

For a detailed description of the aforementioned items see [3].

3 FLUID PART

The open source Computational Fluid Dynamics (CFD) solver OpenFOAM 2.1, which is based on the Finite Volume Method, is adopted for the fluid part. OpenFOAM (`www.openfoam.com`) features the computation of the free surface between two media (here, air and water) according to the Volume Of Fluid (VOF) method. This method is based on the solution of a transport equation for the volume fraction of one medium, where the convective term is discretized in a manner that on the one hand maintains a sharp interface between volume fraction one and zero and on the other hand guarantees that the volume fraction is bounded between one and zero. The remaining transport equations (mass conservation, momentum conservation, etc.) are solved for an *effective fluid* whose properties (density, viscosity) result from an volume fraction weighted average of the properties of the individual media.

The coupling between fluid and structure solvers is achieved by transfering of hydrodynamic forces at the fluid boundary face centers to the finite element model nodes, calling the modal solver, and transfering of structure motion/deformation to the fluid boundary vertices. The mapping between the (generally non-matching) fluid and structure representations of the common boundary is described in detail in [4, 3]. The aforementioned sequence is repeated in each time step until convergence is achieved, resulting in an implicit method.

After the boundary vertices of the fluid grid have been moved according to the structure motion/deformation, the interior fluid grid has to be smoothed in order to prevent cell deterioration and to maintain grid quality. Currently, we apply an algorithm provided by OpenFOAM. In the future, grid smoothing based on precomputed grid deformations corresponding to structure modes may be implemented for performance reasons.

4 OpenFOAM'S "floatingObject" TUTORIAL AS A BENCHMARK FOR MARINE FSI

Starting with version 1.7, OpenFOAM provides a fluid structure interaction tutorial "floatingObject", which features free surface capturing, moving grid, and 6 degree of freedom rigid body motion, but no strucure elasticity. We use this tutorial as a benchmark setup, and compare and discuss results obtained with the original OpenFOAM and our modal FSI solver. The following cases have been simulated:

- the original case as provided as the OpenFOAM tutorial (medium grid) (Fig. 4)
- the original case, on coarse and fine grids. Time step size has been adapted to the grid size in order to maintain the Courant number (Fig. 2)
- the original case, with corrected pressure initialization, on coarse, medium, and fine grids (Fig. 1, 3, 7)
- the benchmark setup with our modal solver, using only rigid body modes of a simple finite element model ("1x1x1"), on coarse, medium, and fine fluid grids (Fig. 4, 6, 7)
- the benchmark setup with our modal solver, using additionally the lowest elastic eigenmodes of systematically refined finite element models ("3x3x2", "6x6x4", "12x12x8"), on medium fluid grid (Fig. 8)
- various free surface initalizations, fluid viscosities, etc. for debugging purposes (Fig. 5)

4.1 Brief description of the original tutorial and solver

The "floatingObject" tutorial is based on the well known "breaking dam with obstacle" example which has become a benchmark for free surface capturing, see e. g. [5] (also available in OpenFOAM in the "interFoam" category). Here, the obstacle is a floating body that is moving due to the hydrodynamic forces resulting from the collapsing water column.

From the fluid perspective, the floating body is a moving boundary which has to be accounted for by propagation of the boundary motion into the interior of the fluid domain and by consideration of the contribution of grid motion to convective fluxes. In OpenFOAM, these features are implemented in the "interDyMFoam" (Dynamic Mesh) solver.

From the structure perspective, the total force and moment resulting from fluid boundary forces represent the driving force and moment in the floating body's equation of motion, where the body is characterized in OpenFOAM by its total mass, center of gravity, and tensor of inertia. OpenFOAM provides a 6 degree of freedom rigid body motion solver based on the leapfrog time integration method, and the means for computing total boundary forces and moments, the boundary motion of a rigid body due to translation and rotation of its center of gravity, and the propagation of boundary motion into the interior of the fluid domain (grid smoothing).

In this benchmark case, a floating body (represented by a closed interior wall) is placed at the center of a partially filled tank. Initial conditions for the free surface are such that the body is in static equlibrium (i. e. weight and hydrostatic pressure forces balance), see Fig. 1. Near to the outer wall, the free surface forms a water column. When the water

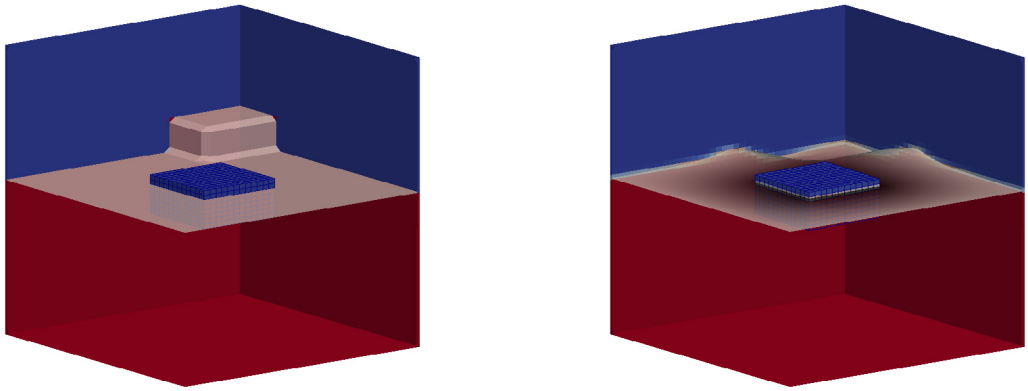


Figure 1: Original setup (with corrected pressure initialization): initial state $t = 0$ (left) and intermediate state $t = 0.30\,\mathrm{s}$ (right)

column is released at the beginning of the simulation, a wave is propagating through the domain, imposing hydrodynamic forces on the body, resulting in body motion. After several reflections from the walls, the free surface gradually comes to rest due to viscous damping, and the floating body assumes a new equilibrium position (provided that the grid deformation has not become to large, such that the computation aborts due to numerical error).

Due to "interDyMFoam" being an explicit solver, the Courant number $U\Delta t/\Delta x$ exposes a stability limit on the time step size Δt. For this reason, the time step size is adjusted during the simulation in order to maintain a Courant number smaller than 0.5.

For the provided grid resolution, typical time step size is 0.009 s. The computed wave period is a little less than 0.9 s. In the original setup, the simulated time is restricted to 6 s, which is not long enough to reach the equilibrium state. Computational time on a single core of a standard PC is approximately 45 min.

In the tutorial case, the water column is placed asymmetrically, such that all 6 rigid body motion degrees of freedom are excited.

4.2 Modal solution

Our FSI solver is also based on "interDyMFoam", with the exception that the high level grid movement routine `mesh.update()`(triggering OpenFOAM's 6dof solver in the original code) is replaced by a coupling code that calls our modal solver. Also, an outer iteration level has been added in order to account for the nonlinear coupling of fluid and structure.

The coupling code, based on the OpenFOAM library, computes modal forces from fluid boundary face forces (which involves mapping, transformation from gobal to local frame, modal decomposition) and fluid node displacements from modal coefficients (which involves modal composition, transformation from local to global frame, inverse mapping).

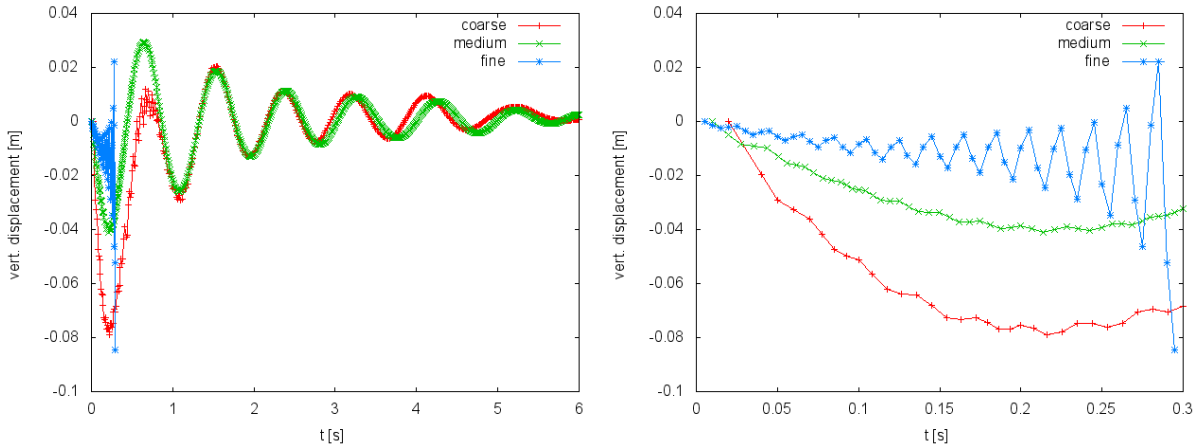


Figure 2: Convergence analysis for the original case: vertical displacement vs. full time range (left) and detail (right), divergence in fine grid solution due to oscillations

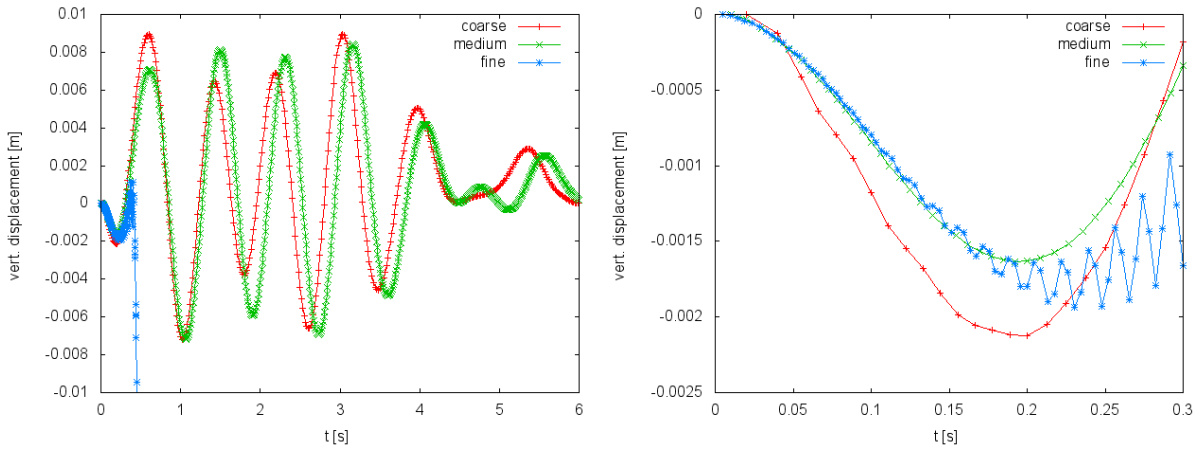


Figure 3: Convergence analysis for the modified original case with corrected pressure initialization: vertical displacement vs. full time range (left) and detail (right), despite corrected initialization, fine grid solution is still diverging due to oscillations

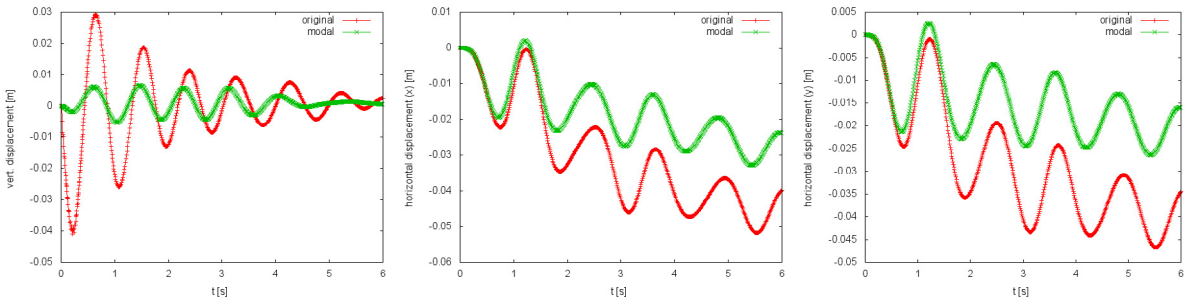


Figure 4: Original vs. Modal solution: vertical displacement (left), horizontal displacement (x) (center), horizontal displacement (y) (right). Large difference in vertical displacement is due to error in original setup, see Fig. 7.

The modal solver has been implemented in a separate library with no dependencies on OpenFOAM in order to allow standalone testing and coupling to other CFD systems. At the core of the modal solver library is the routine "`solve`" which performs one time step according to section 2.2, i. e. computes rigid body motion and modal coefficients updates for supplied modal forces based on variable values of the previous time step.

In addition to the fluid grid, a Finite Element model of the structure is required for the modal solver. For evaluation of the fluid, coupling, and rigid body code the simplest possible model will do (here: 8 nodes, 6 plane stress elements). Computation of structure elasticity requires refined models. Nodal masses are chosen such that total mass, center of gravity, and ideally the tensor of inertia are matched, the latter requires additional nodes/elements which do not lie on the boundary. Modes, mapping, etc. are precomputed in a preprocessing step, see [7].

4.2.1 Comparison of results

In Fig. 4, rigid body motion is compared for the original and the modal solvers. The original solution differs significantly from the modal solution. At first sight, decay of heave amplitude looks more plausible in the original solution, and assuming (wrongly, see below), that the original solution is correct, we started searching for errors in the modal solver, taking the following steps to assess the correctness of the modal implementation:

- In order to test the modal motion library, a stand-alone program (i. e. not depending on OpenFOAM) has been used to compute rigid body motion and modal coefficients based on supplied time series of either modal, FE nodal, or CFD boundary face forces.
- Using the stand-alone program, it has been verified that analytically prescribed FE nodal forces corresponding to pure translation/rotation result in the expected rigid body motion for each degree of freedom.

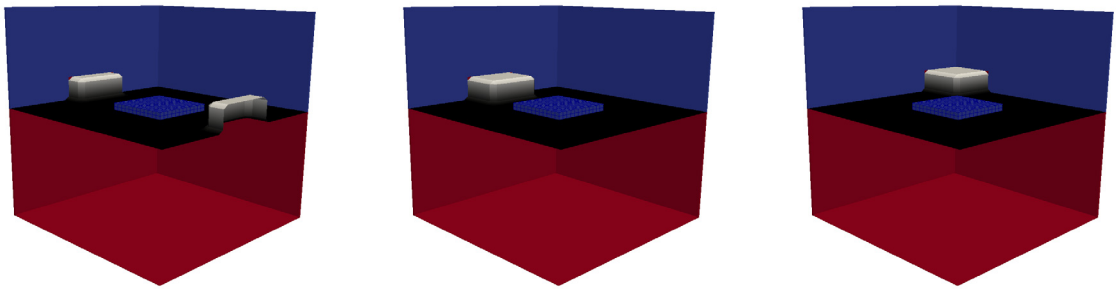


Figure 5: Symmetric setups allow testing of individual rigid body degrees of freedom: heave only (left), one rotational degree of freedom (center), symmetric excitation of sway and surge resp. pitch and roll (right)

- Using exported time series of CFD boundary face forces of the original solver, it has been verified that rigid body motion computed with the modal solver matches the original rigid body motion.
- It has been carefully checked that the resulting total force and moment obtained from the fluid boundary faces (OpenFOAM routine) match the ones obtained from the structure nodal forces.
- In the coupling code, it has been verified that analytically prescribed rigid body motion results in the expected CFD node displacements resp. grid deformation.
- For the coupled procedure, the result for variable time step size has been compared with the result for fixed time step sizes for the minimum and maximum applied time step sizes.
- For the modal solver, it has been verified that symmetric initialization of the water column results (Fig. 5) in the expected motion.
- For the modal solver, the convergence to a grid-independent solution has been verified, see Fig. 6.
- For the modal solver, in order to verify the long-term equilibrium state, the fluid viscosity has been raised, resulting in the expected behavior.

On the other hand, no grid convergence is achieved in the original solution. The explicit method becomes unstable on finer grids although the time step size has been reduced in order to maintain the Courant number limit, see Fig. 2. Observing the large downward motion at the beginning of the simulation (which is not plausible if the floating body has been in hydrostatic equilibrium), we concluded that the original solution is not correct, and started searching for errors in the original setup. We finally found that proper initialization of the pressure (which was missing) is crucial for the explicit original solver

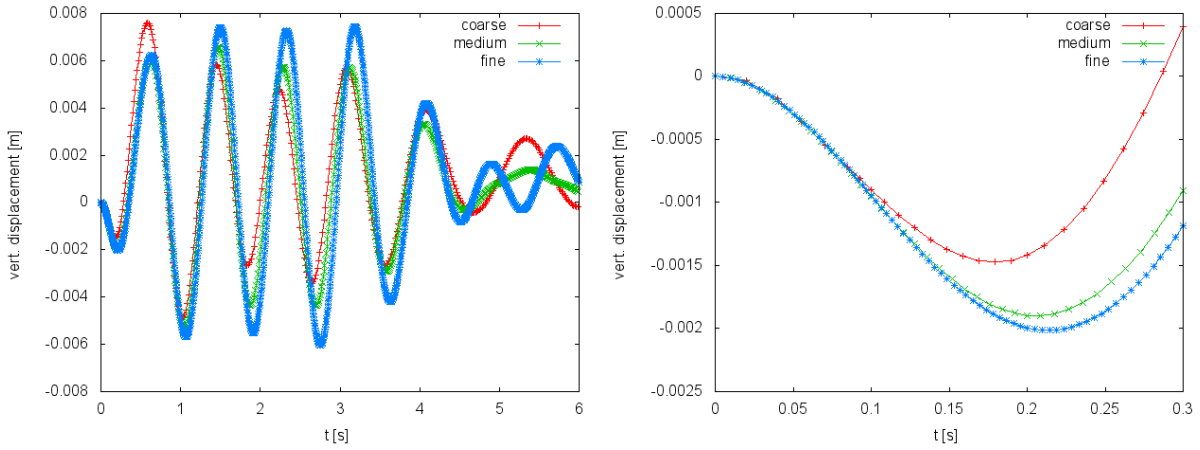


Figure 6: Convergence analysis for the modal solution: vertical displacement vs. full time range (left) and detail (right). Second order convergence is achieved at the beginning of the simulation, convergence deteriorates when the free surface elevation can no longer be adequately resolved on coarse grids.

(our implicit solver computes the correct pressure in the first outer iteration of the first time step). In Fig. 7, the comparison of original and modal solver is much more favorable.

The aforementioned convergence studies also reveiled the following noteworthy observations:

- It has been demonstrated by grid refinement, that surprisingly even the coarse grid solution is "good enough" for quick qualitative tests of e. g. changes to the program code. Systematic refinement in each space direction (and time in order to maintain the Courant number) by a factor of two results in an increase in computing time by a factor of approximately 16, which effectively prohibits testing on a fine grid. In our case, coarse grid computing times were some minutes, medium grid in the order of an hour, fine grid in the order of a day. (The original setup corresponds to the medium grid.)

- It has been observed that the accuracy deteriorates when the wave amplitude becomes smaller. This is in accordance to Schwenkenberg [7], who noticed that higher grid resolution is required for smaller wave height in simulation of a ship's motion in regular waves.

- It has been observed that rigid body degrees of freedom which should be zero at all times due to symmetry, sometimes may become significantly large due to spurious acceleration caused by round-off error. Structure motion damping is achieved through fluid viscosity only, which sometimes is not sufficient to prevent e. g. significant yaw angles, which may even lead to divergence due to grid deformation. For this reason it is common practice to suppress "theoretically" zero degrees of freedom, e. g. yaw angle in seakeeping computations for head waves, see [7].

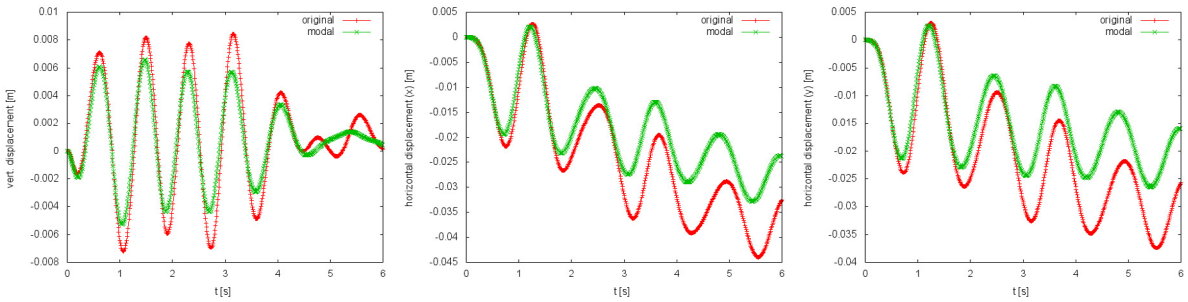


Figure 7: Modified Original (corrected pressure initialization) vs. Modal solution: vertical displacement (left), horizontal displacement (x) (center), horizontal displacement (y) (right). Difference in vertical displacement is much smaller than in the original setup, see Fig. 4.

4.2.2 Effects of structure elasticity

The original benchmark case does not feature structure elasticity. In the preceding section, only the rigid body modes of a simple 8-node/6-element finite element model (denoted "`1x1x1`") have been used in the modal solution for comparison purposes. In order to demonstrate the effect of structure elasticity, simulations with systemactically refined finite element models have been performed on the medium size fluid grid (correspondig to the original setup) with the modal solver. The maximum resolution "`12x12x8`" was chosen to match the medium size fluid grid, because the mapping of structure nodal deformation to fluid boundary vertices requires that each fluid boundary face is mapped to exactly one finite element. i e. the finite element model may be coarser but not finer than the fluid grid. The element thickness was chosen such that the elastic displacement became noticeable, resulting in lowest eigenfrequencies in the order of 10 Hz. In the simulations, 18 elastic modes (plus 6 rigid body modes) have been used. Figure 8 displays elastic and total displacements at the center of the bottom of the structure. Significant elastic deformation is observed at the beginning of the simulation. After some time, the elastic deformation reaches a static but non-zero value. This is due to the fact that the weight forces are concentrated at the boundaries of the finite element model, whereas the buoyancy forces are evenly distributed, resulting in a "hogging" situation. Good convergence with the finite element model resolution is observed. Moreover, observed period of elastic deformation agrees well with the lowest structure eigenfrequency.

5 CONCLUSIONS

A method for the solution of the fluid structure interaction problem in ship design has been presented. It is characterized by the formulation of the equation of motion in a body-fixed reference frame and the approximation of the structural deformation by a number of modes. This approach reduces the number of degrees of freedom of the discretized structural equation system significantly, and at the same time maintains the fully nonlinear rigid body motion.

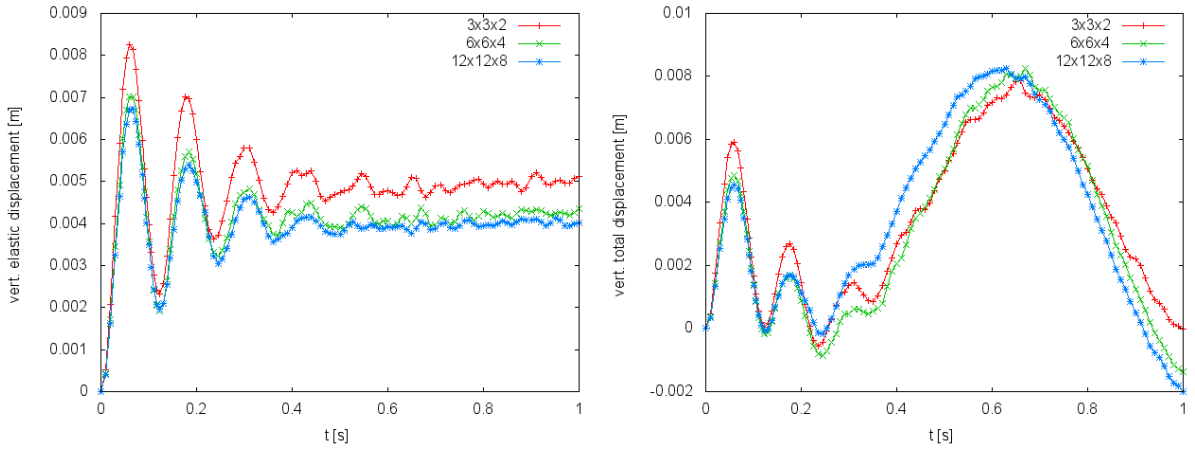


Figure 8: Elastic and total vertical displacement for FE node at bottom center. Static elastic displacement due to "hogging" mass distribution.

The method has been applied to a benchmark setup provided by a case from the OpenFOAM tutorials. This benchmark has proven to be valuable for the following reasons:

- simple geometry: both the fluid domain and the finite element model are represented by structured grids which can easily be refined (in contrast to e. g. boundary-fitted unstructured grids for ships)
- moderate problem size: grid refinement for convergence analysis does not require excessive computing time
- known final state which has to be reached by a long-term simulation
- selective testing of rigid body motion degrees of freedom by suitable symmetric initialization

The emphasis of our study has been on rigid body motion because there is no elastic deformation for comparison in the original benchmark case. Due to the initial discrepancy between original and modal solution, a procedure for verification of the modal solver has been devised, aiming at plausible results in simple setups and convergence to a grid/time step independent solution. The following observations have been made:

- The original OpenFOAM solution setup lacks proper pressure initialization, leading to incorrect rigid body motion and instability.
- The original explicit method becomes unstable on fine grid — "numerical" viscosity (i. e. an discretization error) is required for stability.
- The proposed implicit method is more stable and allows refinement to the grid independent solution.

- The modal solution is in good agreement with the modified original solution with corrected pressure initialization.

This paper presented a derivation of the modal equation of motion as well as numerical verification of the solution procedure for rigid body motion. Furthermore, it has been demonstrated that the modal solver gives plausible results for structure elasticity. Namely, convergence with respect to the finite element model resolution is achieved. Application of the described algorithm to application cases for ships have been presented previously in [3] and [6].

REFERENCES

[1] John Argyris and Hans-Peter Mlejnek. *Die Methode der Finiten Elemente, Band III - Einführung in die Dynamik*. Friedr. Vieweg & Sohn, Braunschweig, 1988.

[2] I. Asmussen, W. Menzel, and H. Mumm. GL Technology, Ship Vibration. Technical report, Germanischer Lloyd, 2001.

[3] C. Cabos, B. Dilba, M. Krömer, and A. Schwenkenberg. Modal Approach to Fluid Structure Interaction Applied to a Ship in Waves. In Guedes Soares & Fricke, editor, *Advances in Marine Structures*. Taylor & Francis, London, 2011.

[4] H. Eisen and C. Cabos. Efficient Generation of CFD-based Loads for the FEM-Analysis of Ship Structures. In *International Conference on Computer Applications in Shipbuilding*, Portsmouth, 2007.

[5] J.H. Ferziger and M. Perić. *Computational Methods for Fluid Dynamics*. Springer Verlag, Berlin Heidelberg New York, 3rd edition, 2002.

[6] J. Oberhagemann, M. Krömer, C. Cabos, and O. el Moctar. A Fluid-Structure Coupling Method Based on Field Methods and a Structural Mode Decomposition. In *6th International Conference on Hydroelasticity in Marine Technology*, Tokyo, 2012.

[7] A. Schwenkenberg. Einfluss der Modenauswahl auf die modale Berechnung der Strukturverformung von Schiffen im Seegang. Diplomarbeit, Technische Universität Hamburg-Harburg, 2011.

V International Conference on Computational Methods in Marine Engineering
MARINE 2013
B. Brinkmann and P. Wriggers (Eds)

A NOVEL PLASTICITY-BASED FAILURE MODEL FOR GROUTS IN GROUTED JOINTS FOR OFFSHORE WIND TURBINES WITH MONOPILES

PETER SCHAUMANN AND STEPHAN LOCHTE-HOLTGREVEN*

* Gottfried Wilhelm Leibniz University Hannover -
ForWind Center for Wind Energy Research
Institute for Steel Construction, 30167 Hannover, Germany
e-mail: stahlbau@stahl.uni-hannover.de, www.stahlbau.uni-hannover.de

Key words: Offshore Wind, Material Modeling, Concrete Plasticity, Fatigue

Abstract. Grouted Joints are exposed to large numbers of dynamic loads and high extreme loads which have to be considered in the numerical based structural design. Besides nonlinear contact and geometry, nonlinear material behavior of steel and especially grout has to be considered. To adopt local stress states in the grout layer the Ottosen failure criterion was adopted and coupled with a multiaxial hardening law. Furthermore, a method is presented which allows the determination of simplified multiaxial S-N-curves. Developed methods are benchmarked against test results and are evaluated.

1 INTRODUCTION

Offshore Wind Turbines are exposed to a large number of load cycles from wind and wave actions during a service life of 20 years. In shallow waters up to 30 m the Monopile foundation is mostly used, see Figure 1 left. The connection between the driven or drilled pile and the tower is realized by grouted joints using a transition piece. The force fit between pile and transition piece is realized by a high performance concrete or grout layer.

The global bearing capacity of grouted joints is influenced by the slenderness of the steel pipes and the overlap length between pile and transition piece, see Figure 1 center. The local bearing capacity at the steel grout interface is dominated by the surface conditions. Under bending moments the bearing capacity of grouted joints with plain steel surface is represented by contact pressure, friction, and surface irregularities. In the past design flaws in offshore codes lead to an overestimation of the axial capacity of grouted joints with plain steel surfaces [1]. By arranging shear keys at the opposing steel surfaces the axial capacity can be increased significantly. As a detriment shear keys have to be treated as local notches inducing high local stresses in steel and grout, see Figure 1 right.

In current design guidelines for offshore wind turbines [2], [3] a numerical based design of steel and grout for substructures under predominant bending is recommended. Therefore, geometric and material nonlinearities have to be taken into account. In contrast to geometric nonlinearities, material nonlinearities under multiaxial compression stress states are not available in Finite Element Codes like ANSYS® or Abaqus®.

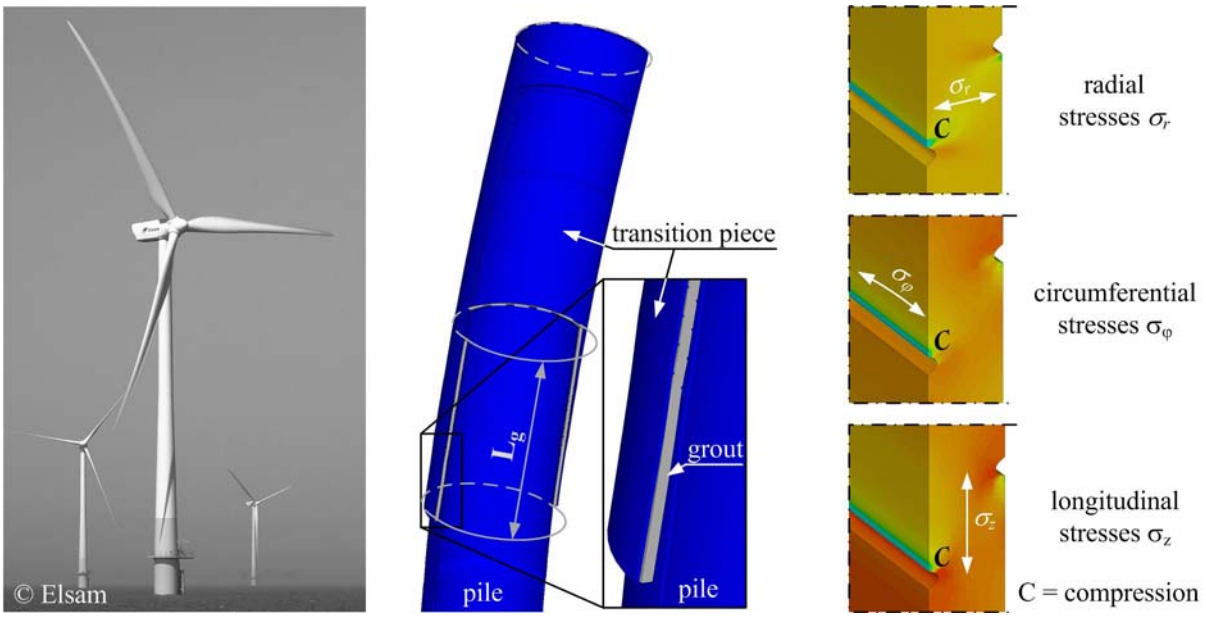


Figure 1: Offshore Wind Turbine with Monopile foundation (left), grouted joint deformation (center) and local stresses (right)

Investigations by Schaumann et al. [4] and Lochte-Holtgreven [5] showed that for grouted joints with plain steel surfaces, comparable simple material models for concrete like the Drucker-Prager-criterion lead to satisfying results. For grouted joints with additional mechanical interlock like shear keys the Drucker-Prager-criterion overestimates the bearing capacity and underestimates plastic strains of the grout layer. Within a national funded research project [6] a multiaxial failure criterion for concrete was coupled with a hardening function and implemented in a Fortran user subroutine for the Finite Element Program ANSYS®. In this paper the developed plasticity-based failure criterion and presents a simplified approach for the determination of simplified multiaxial S-N-curves for normal and high strength concrete is described.

2 FAILURE MODEL FOR HIGH-STRENGTH GROUTS

2.1 Failure Surface

Multiaxial compression stress states in brittle grout or concrete materials are commonly described with multi-parameter failure criterions. The accuracy of the criterion highly depends on the number of shape parameters which influence the shapes of the meridians in the Rendulic and deviatoric stress space. Normal and high strength concretes are commonly described with the failure criterion acc. to Ottosen [7], see Eq. (1).

$$F(I_1,J_2,\theta) = A\cdot\frac{J_2}{f_c^2} + \lambda\cdot\frac{\sqrt{J_2}}{f_c} + B\cdot\frac{I_1}{f_c} - 1 = 0 \tag{1}$$

where A, λ and B are shape parameters of the tensile and compressive meridian, I_1 is the first invariant of the stress tensor, J_2 is the second invariant of the deviatoric stress tensor, and f_c is the uniaxial compressive strength of the grout or concrete material. The general

mathematical formulation of the shape parameters for normal and high strength concrete can be taken from Ottosen [7] or Dahl [8]. For λ equals to zero the Ottosen-criterion can be reduced to a Drucker-Prager-criterion [9]. In case of λ and B being zero, the chosen failure surface is reduced to the von-Mises-criterion. As shown in Figure 2 the yield surface consists of curved meridians in the Rendulic-plane. For small hydrostatic stresses λ the shape parameter λ leads to a triangular yield surface in the Deviatoric-plane. With increasing hydrostatic stresses a circular failure surface is described.

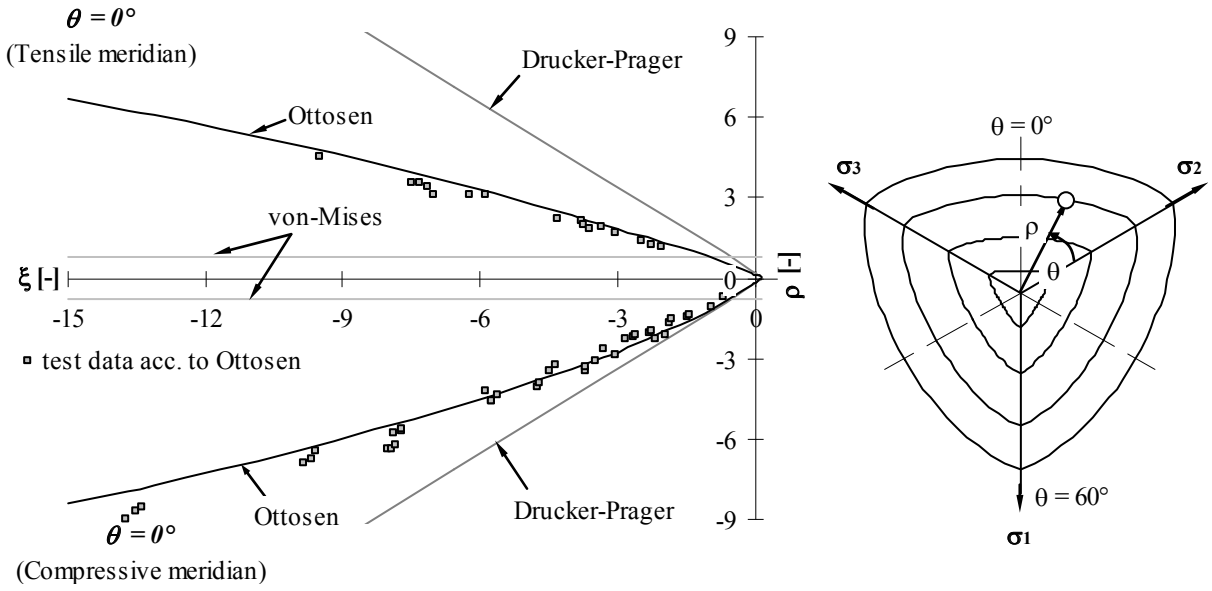


Figure 2: Failure surface of the Ottosen-criterion as Rendulic-Plane (left) and Deviatoric-Plane (right)

Ottosen and Dahl showed that the Ottosen-criterion can be used for normal and high strength concretes under multiaxial stress states. Hence, the revised fib model code 2010 [10] also recommends this failure criterion for numerical modeling of normal and high strength concretes. Due to the pure stress based formulation of the failure criterion, a relationship between multiaxial stresses and strains is not possible.

2.2 Hardening Function

Compared to steel, normal and high strength concretes and grouts have to be considered as anisotropic materials. Even if for small tensile and compressive stresses concrete and grout show a nearly linear elastic material behavior, increasing compression stress states lead to plastic strains which can be drawn back to occurring cracking. If the compressive strength of the material is exceeded, material failure will arise. In case of a strain-driven test, a strain softening of the material can be observed leading to a reduced allowable stress state. Under uniaxial tensile stresses, concretes and grouts show a brittle failure if the uniaxial tensile strength f_{ct} is exceeded. For concretes under uniaxial compression, a stress-strain-relation is proposed in [10], which is defined for concretes up to an uniaxial strength of f_c = 100 MPa. For high strength concretes (f_c > 55 MPa), the softening branch of the mentioned stress-strain-relationship is invalid. Hence, this relationship cannot be used for numerical modeling of

concretes under large strains and displacements. To adopt the material of high strength brittle concretes and grouts, a hardening law *q(κ)* acc. to Grassl et al. [11] can be used, see Eq. 2.

$$q(\kappa) = q_h(\kappa) \cdot q_s(\kappa) \tag{2}$$

By separating the hardening branch $q_h(\kappa)$ and the softening branch $q_s(\kappa)$ of the plastic strain, nearly every type of stress-strain-relation can be adopted, see Figure 3.

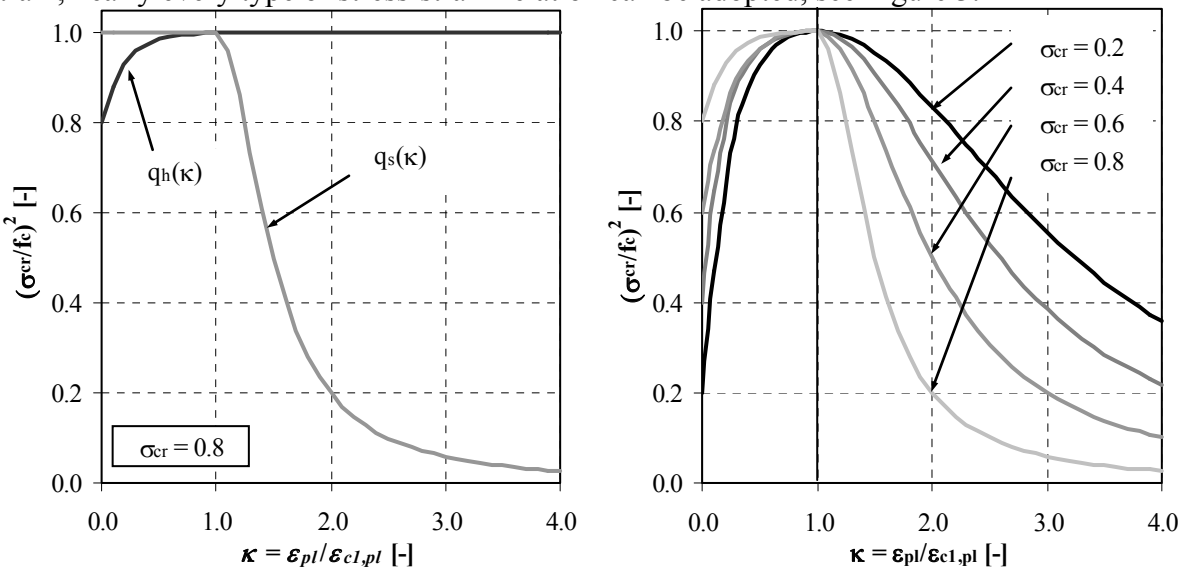


Figure 3: Hardening function acc. to [11] and [12]

Besides ductile low strength concretes also brittle high strength grouts with large hardening and brittle softening branches can be assumed. Mathematical formulations of hardening and softening branches were adopted from [12]. Eq (3) shows the formulation of the hardening branch.

$$q_h(\kappa) = \sigma_{cr} + \frac{(1-\sigma_{cr}) \cdot r \cdot \kappa}{r - 1 + \kappa^r} \tag{3}$$

where σ_{cr} denotes the related stress at which level plastic strains occur, r is the slope of the tangential modulus and κ is the ratio of confined volumetric plastic strain to unconfined volumetric plastic strain. For the hardening regime the value for the softening branch is $q_s(\kappa) = 1$. After exceeding the plastic part of the strain at peak stress ($\kappa = 1$), the hardening branch $q_h(\kappa)$ is 1 and the softening branch can be calculated acc. to Eq. 4.

$$q_s(\kappa) = \frac{C_1 \cdot (\kappa - 1)^2 + C_2 \cdot (\kappa - 1) + C_3}{(\kappa - 1)^2 + C_2 \cdot (\kappa - 1) + C_3} \tag{4}$$

In Eq. 4 C_1 to C_3 denote arbitrary curve fitting parameters.

2.3 Multiaxial Strain Progression

With the hardening function acc. to [11] a multifunctional relation between uniaxial stresses and strains can be established. Under confined stresses, the multiaxial strength as well

as the corresponding strain is increased significantly. Investigations by Candappa et al. [13] showed that the axial strain e_1^u at peak stress under triaxial compression can be extrapolated linearly, see Eq. 5.

$$\frac{\varepsilon_1^u}{\varepsilon_c^u} = 1 + 20\left(\frac{\sigma_3}{f_c}\right) \tag{5}$$

In Eq 5 is ε_c^u the axial strain at peak stress in uniaxial compression, σ_3 the third principal stress and f_c the uniaxial compressive strength of concrete. Results of the best-fit approach and the progression of the simplified linear approximation are shown in Figure 4.

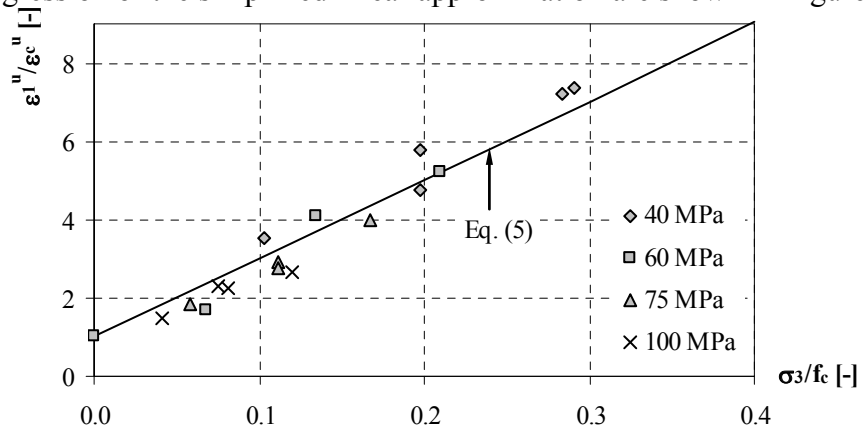


Figure 4: Axial strain at peak stress versus level of confinement acc. to [13]

2.4 Coupling of Failure Surface and Hardening Function

Based on the general formulation of the failure surface, the failure criterion can be linked with the hardening function by using a shape factor as proposed by Chen et al. [14].

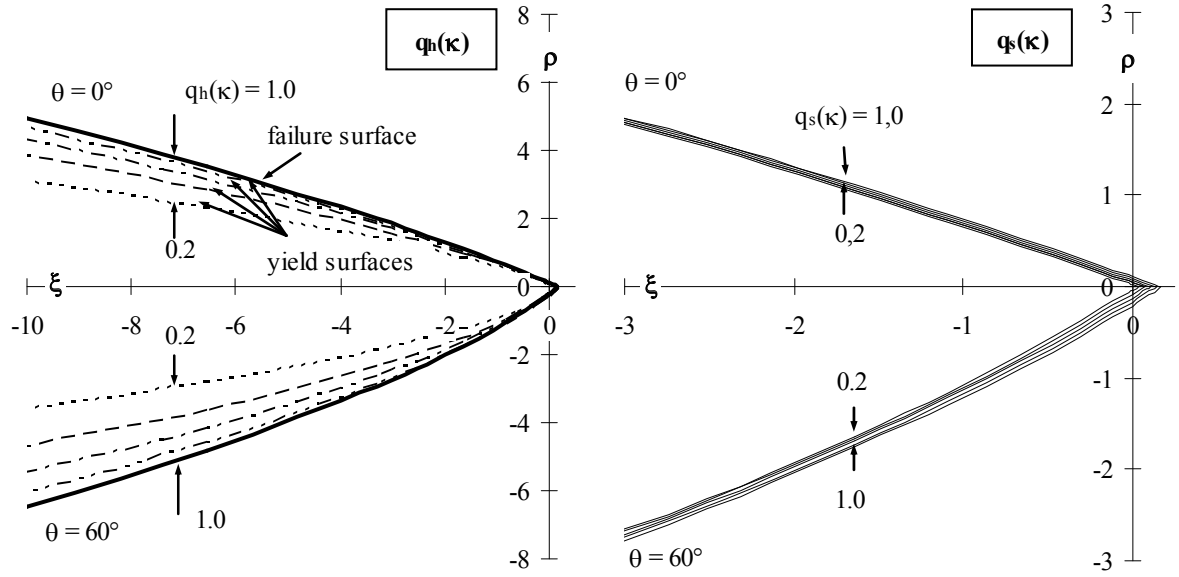


Figure 5: Yield and failure surfaces on the hardening (left) and softening branch (right)

In case of no material failure and the occurrence of material yielding, the failure surface is modified by the hardening function. The yield surface indicating material yielding is displayed in Eq. 6.

$$f(I_1, J_2, \theta, \kappa) = A \cdot \frac{J_2}{f_c^2} + q_h(\kappa) \cdot \left(\lambda \cdot \frac{\sqrt{J_2}}{f_c} + B \cdot \frac{I_1}{f_c} \right) - q_h(\kappa) \cdot q_s(\kappa) = 0 \tag{6}$$

The function describes the yield surface for a given stress - strain state on the hardening branch of the hardening function (Figure 5 left) and the softening branch (Figure 5 right).

3 EXTENSION FOR FATIGUE LOADS

For anisotropic materials like concrete and grout, the mean stress level is decisive for the fatigue performance of the material. In case of fatigue loadings under pure uniaxial compression stresses the number of endurable load cycles is significantly higher than under compression-tension or pure tension stresses. Compared to approaches for normal strength concretes [15], latest developments for high performance concretes show that for pure compression fatigue stresses the fatigue life can be increased significantly [16]. Investigations by Lochte-Holtgreven [5] indicate that 'modern' S-N-curves for high performance concretes can be used for high-performance grouts used in offshore substructures.

3.1 Damage Parameter κ^{fat}

Assuming that the uniaxial S-N-curve under pure compression acc. to [10] is valid for a fatigue failure on the compressive meridian, the yield surface from Eq. 5 can be transferred to a fatigue failure surface. The damage parameter κ_c^{fat} corresponds with the related upper stress level $S_{c,max}$ under multiaxial stresses and the lower stress level. Hence, this implies that the fatigue failure on the compressive meridian complies with a uniaxial fatigue failure under pure compression, see Figure 6 left.

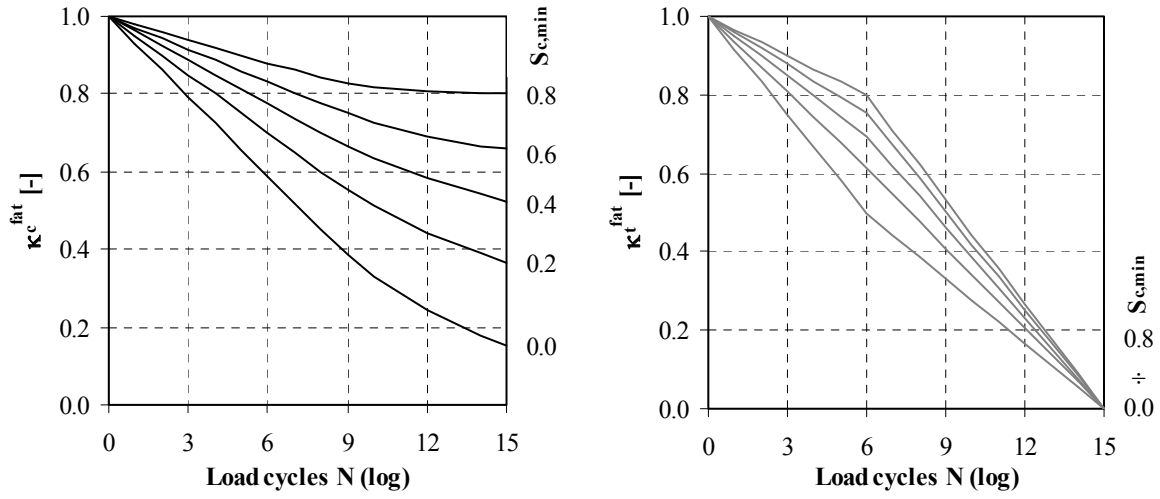


Figure 6: Damage parameters for fatigue on the compressive meridian (left) and tensile meridian (right)

For a fatigue failure on the tensile meridian, Göhlmann [17] showed that for a number of

load cycles less then 10^6, the damage parameter κ_t^{fat} corresponds to a uniaxial fatigue failure under pure compression. For the high cycle fatigue regime, the damage progression on the tensile meridian is similar to the progression of the S-N-curves under pure compression and pure tension, see Figure 6 right.

Based on the boundary conditions mentioned above, the damage parameter κ_c^{fat} for a fatigue failure on the compressive meridian was derived by Lochte-Holtgreven [5] and can be calculated as shown in Eq. 7 and 8.

$$log\ N \leq 8: \qquad \kappa_c^{fat} = \frac{(Y-1)}{8} \cdot log\ N + 1 \tag{7}$$

$$log\ N > 8: \qquad \kappa_c^{fat} = \left(Y - S_{c,min}\right) \cdot 10^{\left[\frac{(log\ N-8)}{8 \cdot ln10} \cdot \frac{(Y-1)}{(Y-S_{c,min})}\right]} + S_{c,min} \tag{8}$$

with:

$$Y = \frac{0.45 + 1.8 \cdot S_{c,min}}{1 + 1.8 \cdot S_{c,min} - 0.3 \cdot S_{c,min}^2} \qquad and \qquad S_{c,min} = \frac{\sigma_{c,min}}{F\left(I_1, J_2, \theta\right)}$$

where log N is the number of load cycles until failure and $S_{c,min}$ is the related minor stress level. For a failure on the tensile meridian reference is made to Göhlmann [17] who derived the damage parameter κ_t^{fat}, see also Eq. 9 and 10.

$$log\ N \leq 6: \qquad \kappa_t^{fat} = 1 - \frac{log\ N}{\left(12 + 16 \cdot S_{c,min} + 8 \cdot S_{c,min}^2\right)} \tag{9}$$

$$log\ N > 6: \qquad \kappa_t^{fat} = \left(1 - \frac{6}{\left(12 + 16 \cdot S_{c,min} + 8 \cdot S_{c,min}^2\right)}\right) \cdot \frac{\left(15 - log\ N\right)}{9} \tag{10}$$

3.2 Modified Fatigue Failure Surface

The shape of the failure surface under static loading conditions is mainly influenced by the shape parameters A, λ and B. In [5], the shape parameters were extended with respect to the damage parameters. Based on this the failure surface from Eq. 1 can be expanded for the fatigue loading conditions, see Eq. 11.

$$F(I_1, J_2, \theta) = A\left(\kappa^{fat}\right) \cdot \frac{J_2}{f_c^2} + \lambda\left(\kappa^{fat}\right) \cdot \frac{\sqrt{J_2}}{f_c} + B\left(\kappa^{fat}\right) \cdot \frac{I_1}{f_c} - 1 = 0 \tag{11}$$

Depending on the confining stress level α_{2c} and α_{3c}, the lower stress level $S_{c,min}$ and number of endurable load cycles N, fatigue failure surfaces can be calculated, see Figure 7.

In doing so, simplified S-N-curves for high performance grouts under multiaxial stress states can be determined. For the determination of the shape parameters $A(\kappa^{fat})$, $\lambda(\kappa^{fat})$, and $B(\kappa^{fat})$ reference is made to Lochte-Holtgreven [5].

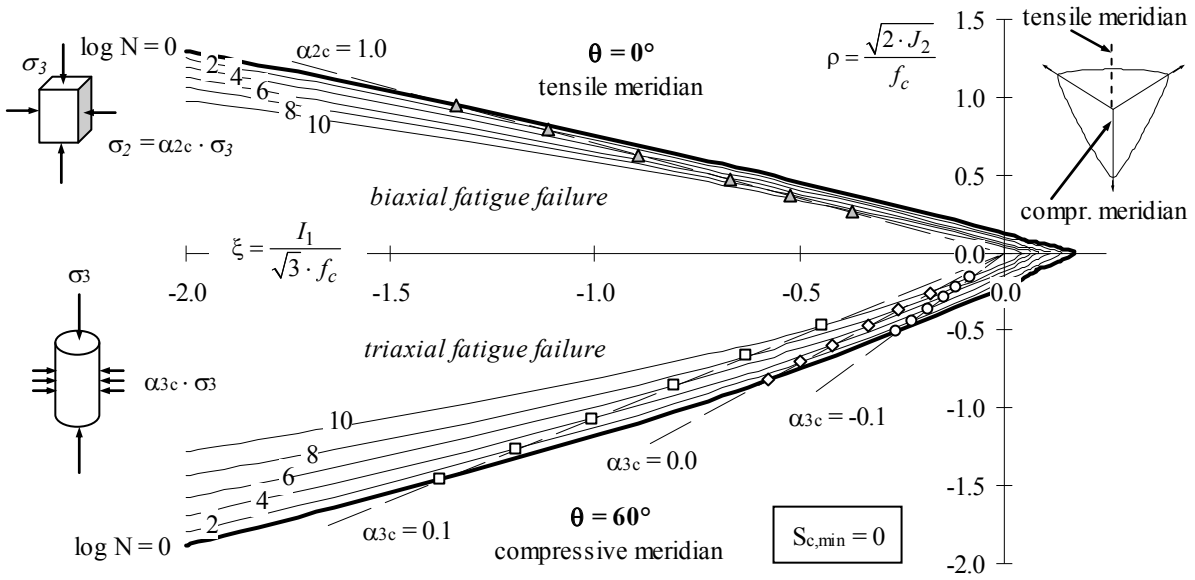


Figure 7: Fatigue failure surfaces in the Rendulic-plane for different number of load cycles

4 VALIDATION

4.1 Static Loading Conditions

The plasticity-based model for high strength grouts was benchmarked on test results under compression. In a first step, stress-strain-relations of normal (NC) and high strength concrete (HSC) under various compression stress states were recalculated. Besides results of experimental investigations by Kupfer et al. [18], test results from Dahl [8] were used. The relevant material parameters and confining stress states can be taken from Table 1. The confinement factors α_{2c} and α_{3c} shown in Figure 7 describes the ratio between confining and axial compression stress and can be calculated acc. to Eq. 12.

$$\alpha_{2c} = \frac{\sigma_2}{\sigma_3 = \sigma_{axial}} \qquad \alpha_{3c} = \frac{\sigma_{lat} = \sigma_1 = \sigma_2}{\sigma_3 = \sigma_{axial}} \tag{12}$$

Table 1. Material parameters of the experimental investigations

concrete grade	compressive strength f_c [MPa]	strain at peak stress ε_{c1} [-]	tensile strength f_t [MPa]	confining stress σ_1	confining stress σ_2	Ref.
normal strength (NC)	32.8	-0.0022	0.09 · f_c	0 f_c 0.52 · f_c	0 0 0	[18]
high strength (HSC)	88.4	-0.003	0.10 · f_c	0.6 · f_c 0.8 · f_c 1.4 · f_c		[8]

The results of compression tests under static loading conditions are depicted in Figure 8. Under consideration of the test results for normal strength concrete according to Kupfer et al. [18], the calculated stress-strain-relations under uni- and biaxial compression stress states show good agreement with the test results, see Figure 8 left. Small deviations of the calculated stress-strain-relations in the high stress regime can be traced back on the formulation of stiffness matrix and Poisson's ratio used by Lochte-Holtgreven [5]. However, for the loading regime until failure the developed failure model seems to be sufficient.

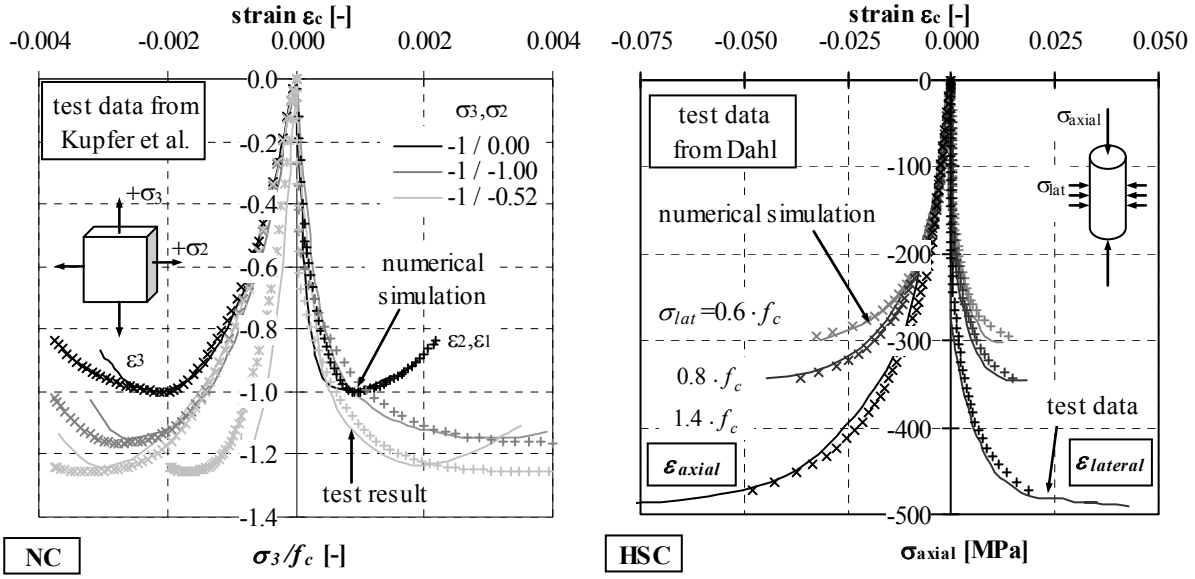


Figure 8: Measured and calclulates σ-ε-relations for normal (left) and high strength concrete (right)

The comparison of the calculated stress-strain-relations with test results on high-strength-concrete cylinders under triaxial compression stresses from Dahl [8] show also satisfying results. It can be concluded that the developed failure model is suitable for the numerical simulation for normal and high strength concrete under multiaxial compression stresses.

4.2 Fatigue Loading Conditions

In contrast to static loading conditions, under an increasing number of load cycles the damage parameters reduce the volume of the fatigue failure surface and so the endurable stress under multiaxial compression stress states. Based on the fatigue failure surface acc. to Eq. 11, the number of endurable load cycles for normal and high strength concrete was calculated. Therefore test results acc. to Su et al. [19] for normal strength concrete (NC) cubes under uni- and biaxial fatigue stresses as well as test results acc. to Grünberg et al. [20] for high strength concrete (HSC) cylinders were used.

In Figure 9 left the calculated S-N-curves are depicted versus the measured load cycles of normal strength concrete cubes. Both uniaxial and biaxial simplified S-N-curves show good agreement with the test results.

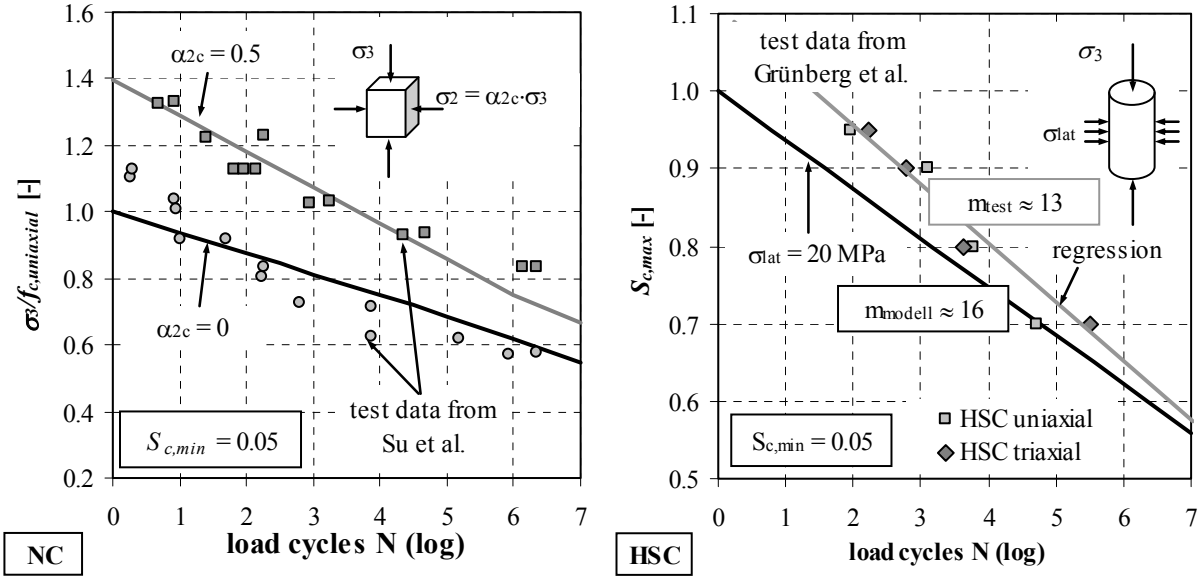


Figure 9: Measured and calculated endurable load cycles for NC (left) and HSC (right)

A similar result can be seen for the calculated S-N-curve for high strength concrete under uni- and trixial compression stresses, see Figure 9 right. Compared to the measured S-N-curve which can be expressed by a logarithmic regression, the slope m of the calculated S-N-curve is slightly larger. On the one hand this can be traced back to the calculated multiaxial strength $F(I_1,J_2,\theta)$ and so the shape parameter of the failure surface. On the other hand the measured number of load cycles acc. to Grünberg et al. [20] has not been normalized on the uni- and multiaxial compressive strength respectively. But, it can be noted that the developed approach leads to sufficient and simplified S-N-curves for normal and high strength concrete under multiaxial compression stress states. A simplified fatigue design for high strength and grouts is possible.

5 CONCLUSION

Local stress states in grouted joints under bending moments are influenced by the surface conditions of the steel tubes. If additional mechanical interlock for increased axial capacities are arranged, local grout stresses are increased significantly. In that case available failure criteria for grout overestimate the real stress states. To realize a sufficient and reliable design a novel plasticity-based failure model for high strength grouts in grouted joints for Offshore Wind Turbines. A typical application is the connection between transition piece and pile of Offshore Wind Turbines with Monopiles. The Ottosen failure criterion was coupled with a hardening law. By this typical hardening and softening branches of uni- and multiaxial stress-strain-curves of normal and high strength concrete can be adopted. In addition, shape parameters of the Ottosen failure criterion were extended for fatigue loading conditions. Both models were benchmarked against test results for uni- and multiaxial static and fatigue loading conditions. It could be shown that the caclulated stress-strain-curves as well as the simplified S-N-curves show very good agreement with test results and that multiaxial stress states of normal and high strength concrete can be assessed sufficiently.

6 ACKNOWLEDGMENT

The research project 'GROW - Grouted Connections for Offshore Wind Turbine structures' (funding code 0327585) at the Institute for Steel Construction, Leibniz Universität Hannover in partnership with the Germanischer Lloyd Industrial Services, Heijmans Oevermann GmbH and the SIAG Anlagenbau Finsterwalde GmbH was funded from 2006-2010 by the German Federal Ministry of Environment, Nature Conservation, and Nuclear Safety (BMU), Germany. The provision of material by all partners and the sponsorship by the BMU are kindly acknowledged.

REFERENCES

[1] Schaumann, P., Lochte-Holtgreven, S., Lohaus, L., Lindschulte, N. Durchrutschende Grout-Verbindungen in OWEA - Tragverhalten, Instandsetzung und Optimierung. *Stahlbau*, Volume 79, Issue 9, pp. 637 - 647, Ernst & Sohn, Berlin, 2010 (in German).

[2] DNV-OS-J101. *Offshore Standard: Design of Offshore Wind Turbine Structures*, Det Norske Veritas, Høvik, Norway, February 2011.

[3] Germanischer Lloyd. *Guideline for the Certification of Offshore Wind Turbines*. Germanischer Lloyd Wind Energie GmbH, Hamburg, June 2005.

[4] Schaumann, P. and Lochte-Holtgreven, S. Schädigungsmodell für hybride Verbindungen in Offshore-Windenergieanlagen. *Stahlbau*. Volume 80, Issue 4, pp. 226 - 232, Verlag Ernst & Sohn, Berlin, 2011 (in German).

[5] Lochte-Holtgreven, S. *Zum Trag- und Ermüdungsverhalten biegebeanspruchter Grouted Joints in Offshore-Windenergieanlagen*. Dissertation, Schriftenreihe des Instituts für Stahlbau, Gottfried Wilhelm Leibniz Universität Hannover, 2013 (in preparation).

[6] Schaumann, P., Lochte-Holtgreven, S., Hausschildt, M., Klose, M., Hülsmann, N., Reisch, A., Schaaf, R., Kaiser, A. *Experimentelle und numerische Untersuchungen zum Tragverhalten von Grout-Strukturen in OWEA (GROW)*. Final Report of the BMU-research project GROW, FKZ: 0327585, Hannover, 2011 (in German).

[7] Ottosen, N.S. A Failure Criterion for Concrete. *Journal of the Engineering Mechanics Division*, Vol. 103, No. 4, pp. 527-535, American Society of Civil Engineers, ISSN 00447951, 1977.

[8] Dahl, K.K.B. *A Failure Criterion for Normal and High Strength Concrete*. Serie R, No 286, Technical University of Denmark, Lyngby, Denmark, 1992.

[9] Drucker, D. C. *A Definition of Stable Inelastic Material*. NorX-362(2o)/2. Technical Report No. 2. Division of Engineering, Brown University. Providence, Rhode Island, U.S.A, 1957.

[10] Walraven J. et al.: *Model Code 2010, First complete draft - Volume 1*, draft model code, Bulletin 55, International Federation for Structural Concrete fib, Lausanne Switzerland, 2010.

[11] Grassl, P., Lundgren, K., Gylltoft, K. Concrete in compression: A plasticity theory with a novel hardening law. *International Journal of Solids and Structures 39*, pp. 5205 - 5223, Pergamon Press, 2002.

[12] Carrezado R.: *Mecanismos de confinamento em pilares de concreto encamisados con polímeros reforçados com fibras submetidos à flexo-compressão*, Dissertation, Escola de Engenharia de São Carlos-Universidade de São Paulo, 2005.

[13] Candappa, D. C., Sanjayan, J. G., Setunge, S. Complete Triaxial Stress-Strain Curves of High-Strength Concrete. *Journal of Materials in Civil Engineering*, Vol. 13, No. 3, pp. 209 - 215 May/June 2001, ASCE, ISSN 0899-1561/01/0003-0215, 2001.

[14] Chen, W. F. and Han, D. J. *Plasticity for Structural Engineers*, Springer Verlag, New York - Berlin - Heidelberg, ISBN 0-387-96711-7, 1988.

[15] CEB/fip Model Code 1990. *Design Codes*, Euro-International Committee for Concrete, Thomas Telford, London, 1993.

[16] Lohaus, L., Wefer, M., Oneschkow, N. High Performance Concrete - How to deal with fatigue?, in: *Proceedings of the fib Symposium Prague 2011*, Session 1-2: New Model Code, S.119 - 122, Prague, Czech Republik, 2011.

[17] Göhlmann J. *Zur Schädigungsberechnung an Betonkonstruktionen von Windenergieanlagen unter mehrstufiger und mehraxialer Ermüdungsbeanspruchung*. Dissertation, Berichte des Instituts für Massivbau der Leibniz, Fraunhofer IRB-Verlag, Hannover, 2009 (in German).

[18] Kupfer H., Hilsdorf, H. K. and Rüsch, H. Behaviour of Concrete under Biaxial Stresses. Title No. 66-52, Vol. 66, No. 8, pp. 656 - 666, *Journal of the ACI*, ISSN 00028061, 1969.

[19] Su E. M. C. and Hsu, T. C. Biaxial Compression Fatigue and Discontinuity of Concrete. Title-No. 85-M22, *ACI Materials Journal*, American Concrete Institute, March - April, 1988.

[20] Grünberg J., Oneschkow, N. *Gründung von Offshore-Windenergieanlagen aus filigranen Betonkonstruktionen unter besonderer Beachtung des Ermüdungsverhaltens von hochfesten Beton*. Final Report of the BMU-Research Project, FKZ: 0327673, Hannover, 2011 (in German).

V International Conference on Computational Methods in Marine Engineering
MARINE 2013
B. Brinkmann and P. Wriggers (Eds)

DETERMINING OF DESIGN LOADS FOR DRIVE TRAIN COMPONENTS OF WIND TURBINES USING THE MULTIBODY-SYSTEM SIMULATION

MARINE 2013

PROF. DR.-ING. B. SCHLECHT, DR.-ING. T. ROSENLÖCHER
DIPL.-ING. T. SCHULZE

Institute of Machine Elements and Machine Design, Chair of Machine Elements
Technische Universität Dresden
01062 Dresden, Germany
e-mail: thomas.rosenloecher@tu-dresden.de, web page: http://www.me.tu-dresden.de

Key words: Multibody System Simulation, Modelling Process, Wind Turbines

Abstract. The analysis of drivetrains operating under high dynamic loads presupposes the assembly of a detailed simulation model which is able to represent the dynamic behaviour of the drivetrain in the frequency and time domain. The assembly of a corresponding model requires a huge amount of parameters and is very time-consuming. By the disassembling of a complex structure in simple substructures an automated modelling process can be used and offers a considerable reduction of modelling time as well as an easy modification of the level of detail for each submodel. Additionally the systematically modelling procedure simplifies the exchange and the validation of models.

1 INTRODUCTION

The intensified efforts to provide alternative and renewable sources of energy led to a world width growing wind turbine industry during the last years. Beside the advantages of this clean energy source and the successive increasing output power rates for on- and offshore wind turbines the occurring damages clarify the demand of a higher reliability. The operation of a non-stiff founded light weight construction under high dynamic stochastic loads was until the erection of the first wind turbines not known and led to new challenges which are not completely solved until today.

2 MOTIVATION

In comparison to the wind turbine design software used by the wind turbine manufacturers the multibody system simulation allows a more precise modelling of the drive train components [1], [8]. Instead of a detailed rotor model and a simple 3-mass torsional vibration model for the gear box and the generator, all components can be represented under consideration of up to six degrees of freedom and the coupling stiffness [5], [9]. The resulting simulation model of the wind turbine allows the determination of the natural frequencies of the complete structure and shows additionally the mode shapes of all drivetrain components. To detect possible ranges of resonances the effects of the rotor, the gear meshing frequencies as well as rotation speeds of the components can be compared to the calculated natural frequencies. Additionally the

simulation in the time domain offers the determination of the torques, forces, displacements, velocities and accelerations for the modelled components and degrees of freedom. The resulting values at the different load conditions can be used for the design of the components, bearings, gearings as well as for the gear box housing and the supporting structure.

3 BASICS OF DRIVETRAIN SIMULATION

The analysis of drivetrains operating under high dynamic loads presupposes the assembly of a detailed simulation model which is able to represent the dynamic behaviour of the drivetrain in the frequency and time domain. Even if high performance computers are available the level of detail of the simulation model has to correspond to the formulated question to ensure a feasible calculation effort. Despite the currently given possibilities of the simulation software the modelling process is very time-consuming. Based on the present data and the experiences of the engineer a discrete simulation model has to be assembled.

To provide a comprehensible model which allows the determination of reliable simulation results a systematically enlargement of the models must occur. Based on a simple torsional vibration model the successive release of the axial, radial and torsional degrees of freedom have to be performed. Additionally flexible components can be implemented so that all relevant influence factors on the dynamic behaviour are considered. For each modification of the model an examination and validation of the results in the frequency and time domain is mandatory. Each enlargement of the model requires additional parameters to describe the mass, the mass moment of inertia, stiffness and damping parameters and to define the joints and constraints. Therewith a detailed modelling of a drivetrain leads finally to a huge amount of parameters. The different work steps to calculate the parameters and to prepare the model can cause failures so that a continuous examination of the model is necessary. Even for a thoroughly modelled system sometimes the troubleshooting requires a higher effort than the actual modelling process.

The aim of the modelling method must be a systematically assembly of a reliable, reproducible and understandable model. Especially a comparable modelling process can additionally improve the exchange of models, the transfer of models to colleagues and customers as well as the discussion about the models. The possibility of an automated modelling process is based on some simple specifications. Generally a standardised naming of all components, variables, forces elements, joints, and constraints should be used and applied to generate simple simulation models which can be classified as shafts, helical and spur gear stages, planetary gear stages, bevel gear stages, rotor and propeller blades (figure 1). These models are assembled to describe the complete construction and the dynamic behaviour of the drivetrain.

The advantages of the modelling process is the usage of simple submodels instead of large models of the complete structure. Furthermore a modularisation allows a comparable modelling process for different kind of applications (wind turbines, crane drives, ship drives …). These models are assembled in one main model so that any complex system can be described by using a small number of standardised submodels. Additionally the substructures can be simplified to subcomponents like shafts, bearings and gearings.

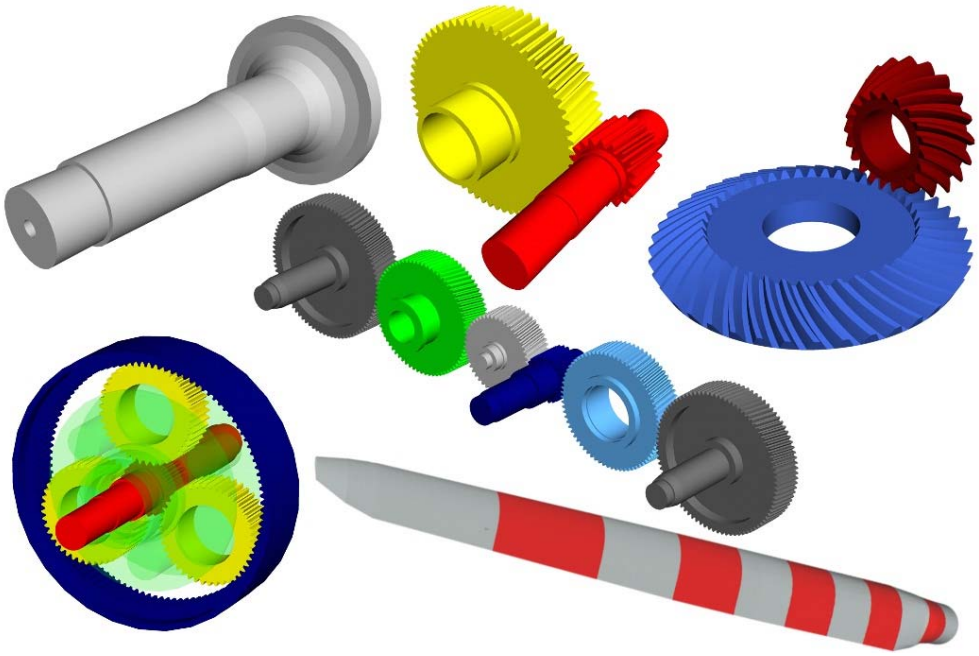


Figure 1: Different kinds of submodels

For the assembly of each substructure one single global reference frame and defined interfaces for the main model are used. The exact positioning of each component is already ensured in the submodel. Additionally the standardisation of the positioning, naming, modelling and defining the intersection points allow the simple replacement of substructures. A different level of detail or degrees of freedom can be adjusted easily in the submodels and implemented in the main model.

The realisation of the automated modelling process presupposes the disassembling of a complex structure in single substructures. According to this approach a simulation model of a common wind turbine consists out of the substructures rotor, mainshaft, coupling, generator and an additionally subdivided gearbox. For the gearbox basically a combination of helical/spur and planetary gear stage substructures are necessary (figure 2). Each substructure consists of model components which can be subdivided into shafts, gear stages, bearings and supporting structures. The description of the single components for the simulation model are done by the geometry in EXCEL spreadsheets using the drawings. These information can be imported to a user interface for the different kinds of possible substructure which have to be defined. Additionally the specification of the used modelling method for shafts (discrete – SIMBEAM), gearings (sliced model, type of planetary gear stage) and bearings as well as the definition of degrees of freedom and the joint connections can occur.

Based on the complete required information the calculation of the mass, mass moment of inertia, centre of gravity, the coupling stiffness and further model data will be performed. Afterwards the full parameterised SIMPACK model files are written automatically for the submodels. Also the assembly of the substructures in a main structure by the definition of the interfaces (spring/damper elements, constraints) can be done automatically. Based on the geometrical information of the drivetrain the complete model can be created without the usage of the actual user interface of the software (figure 3), [11].

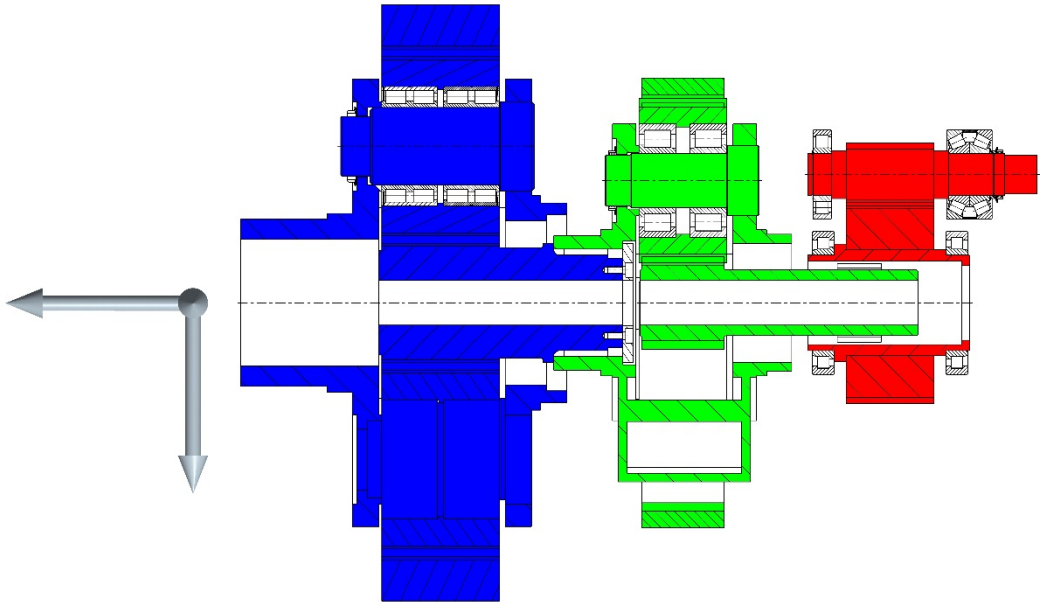


Figure 2: Disassembling of a gearbox

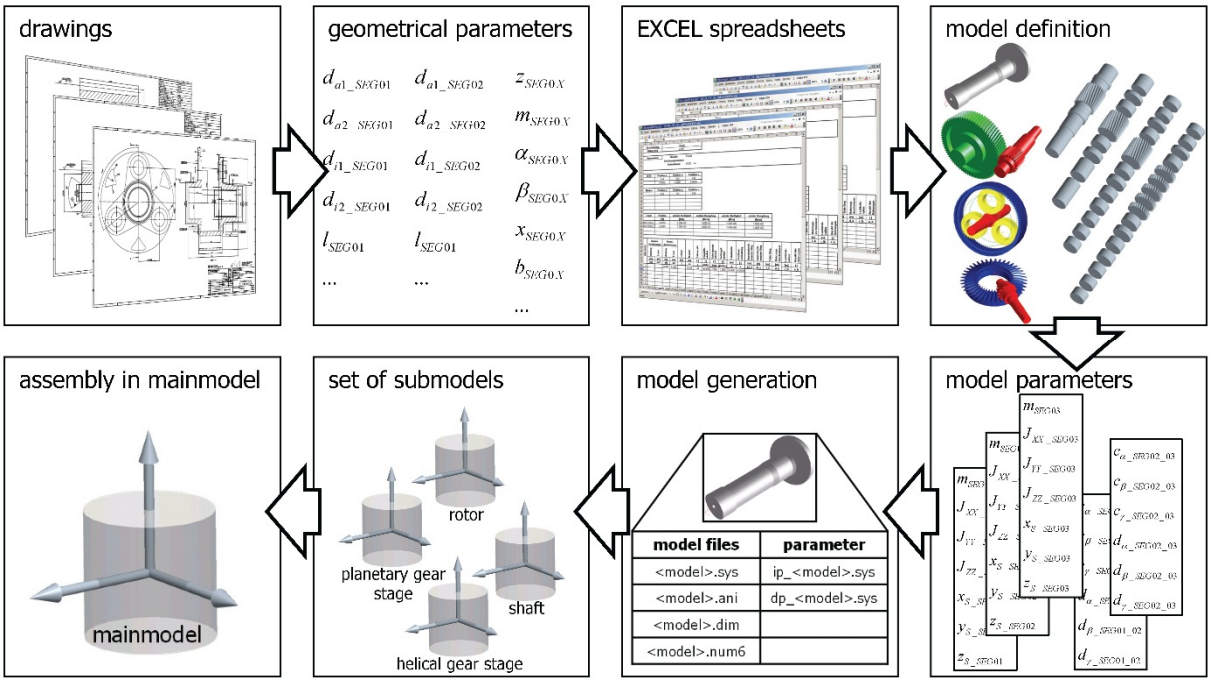


Figure 3: Workflow of an automated modelling process

4 MODELLING OF DRIVETRAIN COMPONENTS

The dynamic behaviour of a drivetrain results from the ratio and the distribution of the mass, mass moment of inertia and stiffness. The determination of the mass parameters is possible by three-dimensional CAD models or by using simple analytical approaches [4], [15]. A higher effort requires the calculation of the relevant stiffness parameters for all drivetrain components.

The torsional stiffness of the drivetrain is mainly characterised by the stiffness of the shafts.

Especially slender shafts have to be considered with their elastic properties. Additionally the bending stiffness of such shafts may have a considerable influence on the dynamic behaviour as well as on the resulting displacements. The required simulation model can be assembled by using the method of discretisation, a beam approach or by implementing modally reduced finite-element models [2], [12], [17].

By the enlargement of the torsional vibration model with the axial and radial degrees of freedom also the properties of the bearings must be represented in the simulation model. Fundamentally the modelling of the bearings is realised by a force element which introduces the reaction forces in axial and radial direction as well as the reaction moments if necessary. The bearing properties can be described by average bearing stiffness, characteristic curves or complex models implemented as DLL's [16].

The transmission ratio between the rotor and the high speed generator is realised by a gear box consisting of a set of planetary and helical gear stages (figure 4). The changing speeds and torques in a gear box as well as the varying gearing stiffness resulting from the total overlap ratio have an important influence on the dynamic behaviour of the drivetrain and must be considered in the simulation model. SIMPACK offers the tool boxes GEAR WHEEL and GEAR PAIR whereby a comfortable modelling of gearing is possible.

An alternative modelling approach offers the mathematical description of the resulting forces in the gearing by user routines. Based on the calculation of the tooth normal force in the ideal pitch point the complete tooth contact is simplified described in one point. The tooth normal force consists of stiffness and damping dependent parts. Information about the displacements and velocities in tangential, radial and axial direction resulting from the difference values between both gears can be determined from the joint states and the corresponding trigonometric relationships [11], [15]. The gearing stiffness can be considered as average contact stiffness according to DIN 3990 and variable gearing stiffness over the path of contact using Fourier coefficients (figure 5).

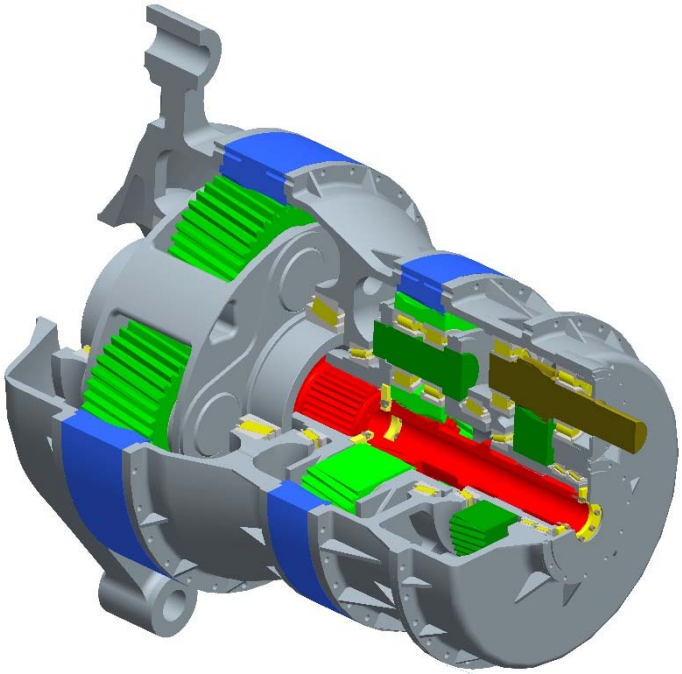


Figure 4: Gear box of a 3 MW wind turbine

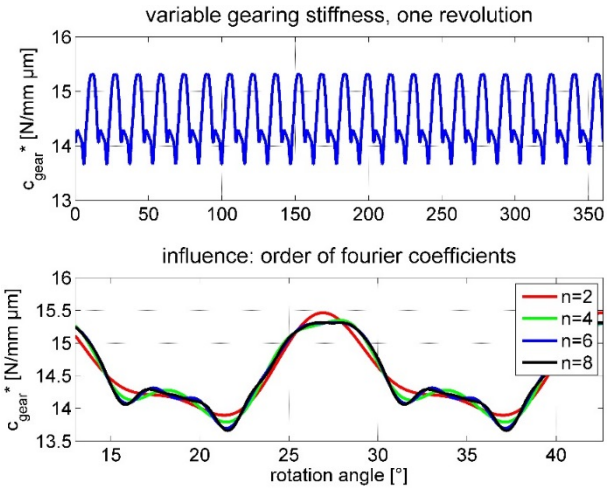


Figure 5: Variable gearing stiffness over the contact path using Fourier coefficients

An enlargement of the drivetrain model requires models of the coupling and the generator using rigid bodies and the coupling stiffness to consider all relevant components of a wind turbine. The most important influence on the dynamic behaviour results from the rotor blades. A simplified approach for the modelling of the rotor blade stiffness can be done on basis of the discretisation. The dividing of a blade into an arbitrary number of masses and the connection of the single masses by spring-damper-elements allows the representation of the bending stiffness (figure 6). Therefore the information of the mass and stiffness distribution as well as the natural frequencies in edge and flap wise direction are sufficient [11]. If additionally the information of every single profile polar are available the rotor blade generation in SIMPACK offers an automatized procedure.

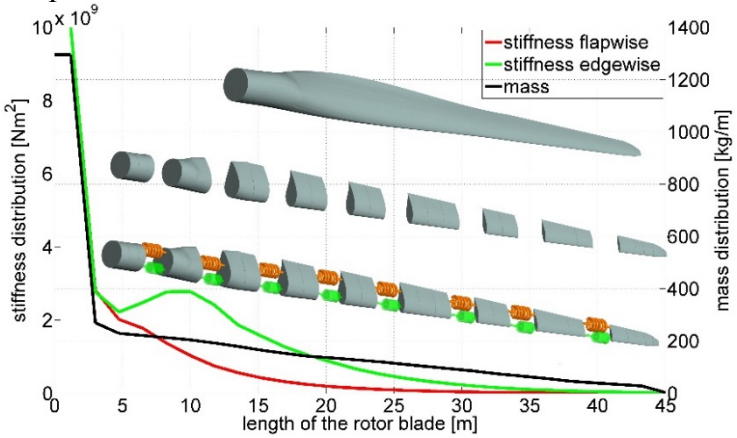


Figure 6: Discretisation of a rotorblade

A detailed modelling of the shafts, bearings, gearings, the coupling, the generator and the rotor allows the representation of the dynamic interaction between the components and the determination of displacements, speeds, accelerations, forces and torques. Even if spring-damper elements are used to support the components, the surrounding structure like the gearbox housing or the main frame are assumed as a stiff coupling to the global reference system. Thereby the influences resulting from the flexible structure of a wind turbine are neglected. The

enlargement of the stiff multibody-system model using modally reduced finite-element structures allows the consideration of these effects.

An implementation of a flexible structure is based on a meshed finite-element model of the component geometry and the definition of material properties. Additionally the connection points to the supporting spring-damper elements have to be modelled by means of multi-point-constrains (MPC). Due to the resulting complexity and degrees of freedom of the FE-models a reduction of the structure is required. The application of the approach according to Craig-Bampton needs the definition of the connection points between the flexible structure and the rigid bodies [3], [6]. Furthermore the information to the mode shapes of natural frequencies are necessary which should be represented by the reduced model and used to determine the deformation under load. The amount of natural frequencies chosen for the modal reduction defines the valid frequency range and the accuracy of the model which is also influenced by the choice of frequency response modes in the SIMPACK toolbox FEMBS. The implementation of flexible structures allows the representation of the flexibility of the supporting structure as well as the consideration of the stiffness of drivetrain components as shafts or planetary carrier with a higher accuracy.

5 ANALYSIS OF NATURAL FREQUENCIES AND EXCITATIONS

The available flexible multibody-system model allows the determination of the natural frequencies under consideration of all degrees of freedom. The resulting frequencies have to be compared to the occurring excitations to determine speed ranges at which resonances can occur. Relevant excitations are the first, second, third, sixth (ninth, twelfth) order of the rotor rotation frequency. Additionally the first and second order of the rotation frequencies of all drivetrain components as well as the meshing frequencies of the gear stages have to be considered. The comparison of natural frequencies and excitations by means of a Campbell diagram shows possible resonance points as intersections. At last only the analysis of the occurring mode shapes allows further statements whether the excitation of a natural frequency can cause critical operation points or not (figure 7).

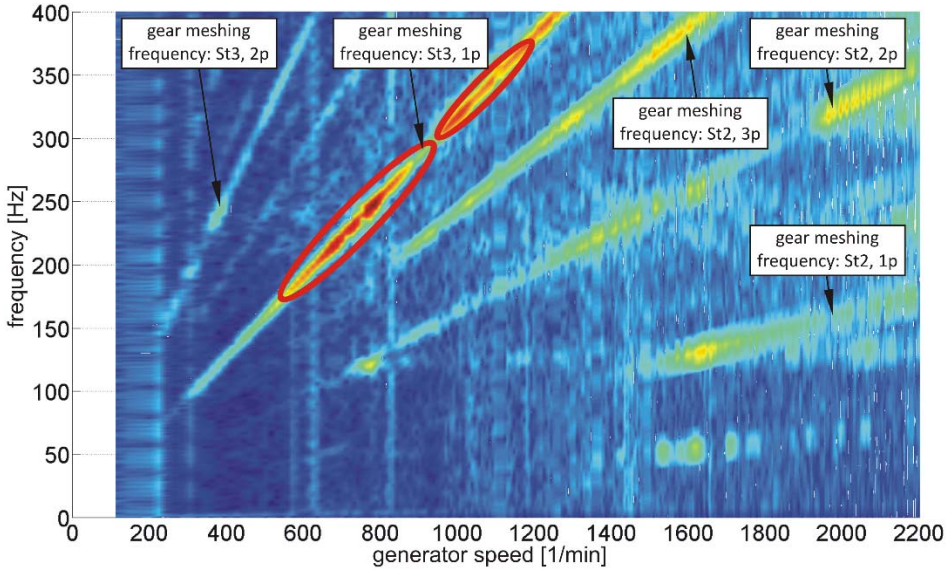


Figure 7: Frequency spectrum of the acceleration of the sun of the low speed gear stage

6 ANALYSIS IN THE TIME DOMAIN

The detailed flexible multibody-system model offers also the possibility to determine the resulting displacements, deformations, speeds, accelerations, forces and torques under the dynamic loads resulting from the stochastic wind field. To model a realistic wind field different approaches are available. Common wind turbine design software like Bladed, Flex5 and AeroDyn are mainly used to define the design loads. Also interfaces between AeroDyn and SIMPACK are available offering the possibility to determine wind loads based on all information to the rotor blades, tower and wind turbine parameters. If not all required information is given different simplified approaches respectively measurement results can be used to determine the force components [7]. Another way would be a wind model based on the information of the wind speed, power coefficients and assumed load distributions over the blade length and the height. Superpositioned with a stochastic wind field the resulting forces for 9 segments over the blade length and each blade under consideration of the tower shadow can be calculated. An enlargement of this approach replaces the assumptions for the wind field and load distribution by measurement results captured as torque and bending moments at the main shaft. An algorithm adjusts the single blade forces to achieve the measured results on the main shaft in the simulation model so that finally the measured states of the wind turbine can be represented by the model. The changing forces at the flexible modelled rotor blades are shown in figure 8 as arrows and scaled deformations.

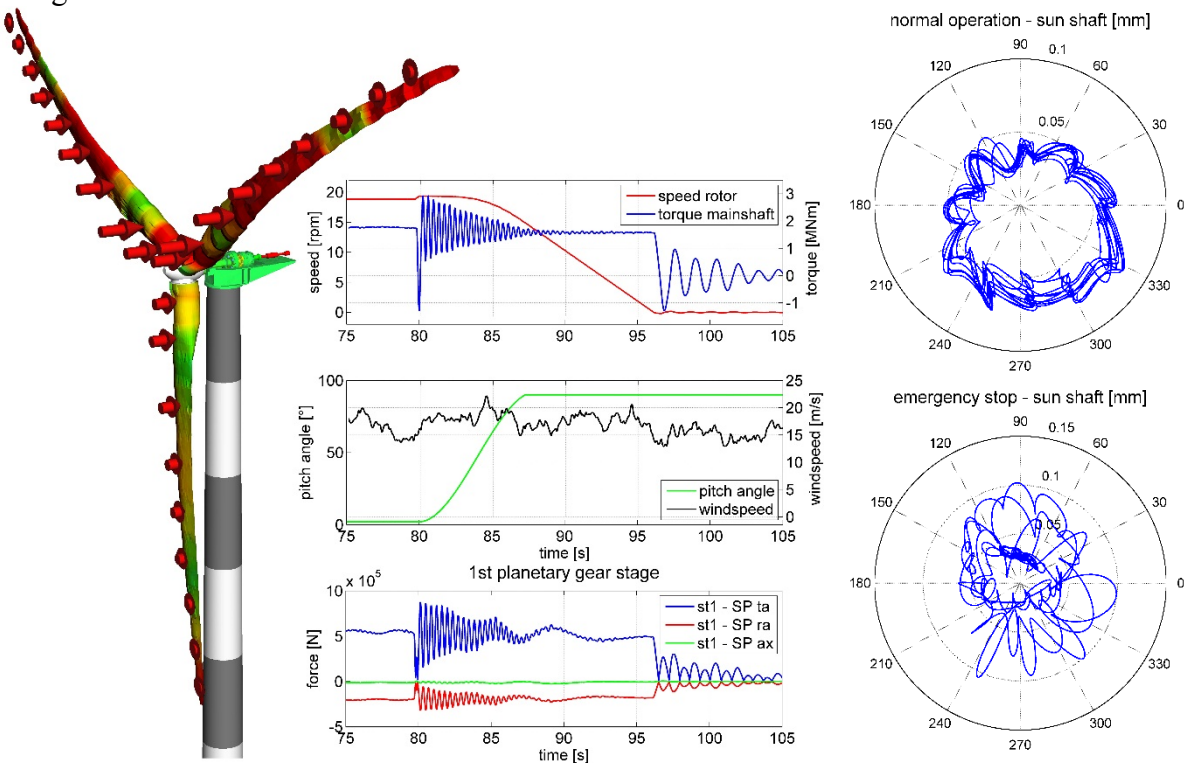


Figure 8: Wind loads on flexible rotor blades, results

Interesting load cases which can be calculated are the operation of the wind turbine under different load conditions and extreme load cases like emergency stops. The resulting speeds, torques, forces in the gearing of the first planetary stage as well as bearing forces are shown in

figure 8. In addition the information to displacements of the main shaft, gearbox and gearbox components like the sun shaft can be taken from the results to get a better understanding of the dynamic behaviour and the occurring loads under different load conditions. Especially for the design of the rotor sided planetary gear stage in addition to the occurring loads also the load distribution is of great importance. The load distribution changes during each rotation of the planet carrier because next to the introduced torque also radial forces and bending moments are influencing the positions of the gearbox components [14]. These additional loads resulting from the dead load of the rotor and the highly variable operating conditions. The detailed simulation models provide the possibility to analyse load distributions in each tooth contact for different modifications and loads as it is exemplarily shown in figure 9.

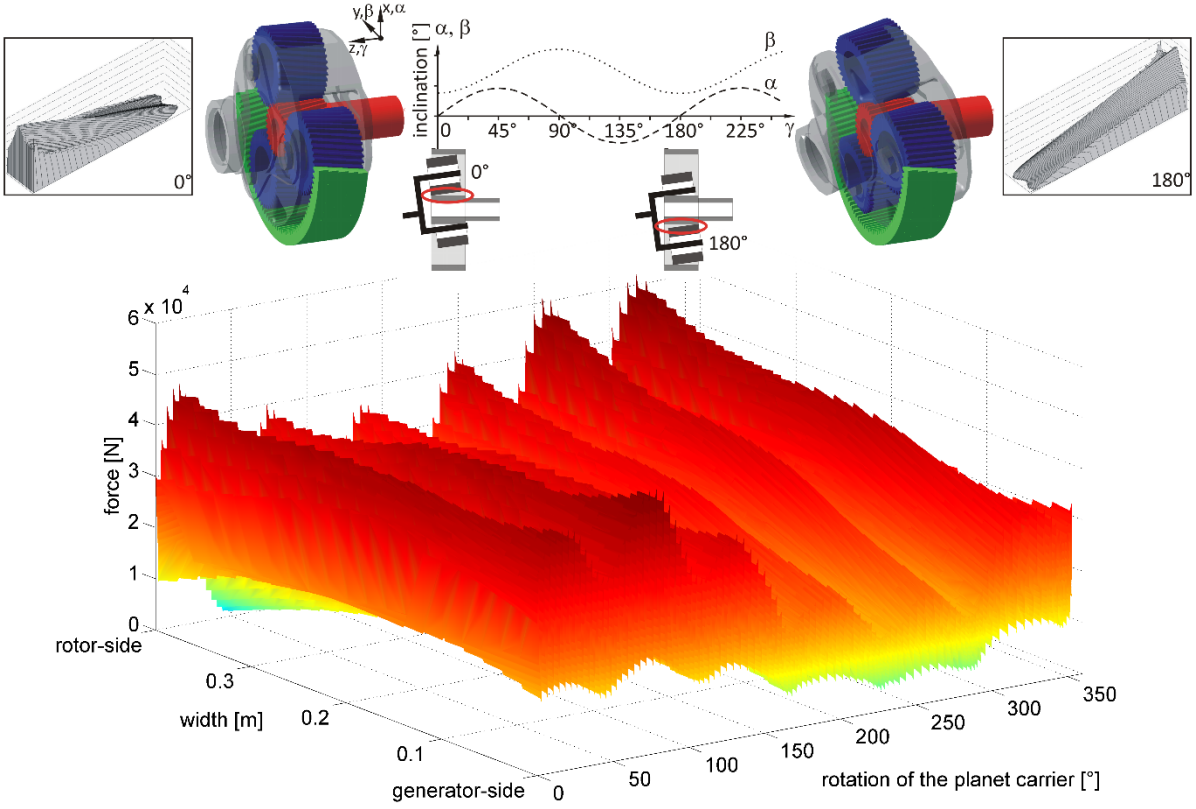


Figure 9: Distributed gearing forces (sun-planet) resulting from the inclination of the planet carrier

7 CONCLUSION

A general problem of the construction and dimensioning of large drive trains is the determination of possible resonances already in an early state of the development process. Due to the complex and high elastic system which is operating under turbulent stochastic load conditions especially wind turbines are systems where such design challenges have to be considered. Comparable conditions can also be found in other fields of application. This leads to the conclusion that it is absolutely necessary to have an exact knowledge to the dynamic behaviour of the entire drive system and its surrounding structure already in the design phase. However, that requires an appropriate method to represent the oscillating system. At first, it seems as if a simple torsional model is enough to determine the first torsional natural

frequencies. But latest if elastic MBS-model are used it can be seen that even this simple mode shape can be superposed by further mode shapes (e.g. bending of the housing). To reach a complete and significant characterisation of the dynamic system it is not enough to perform a torsional vibration analysis for large drive trains with elastic elements. Instead, reduced FEM-models according to the method of Craig-Bampton are integrated in the MBS-environment and analysed as elastic MBS-models [10], [13]. In order to keep the extended and partly complex way of modelling in a manageable scope and industrially usable a modularised model development is required.

Also in the future the modelling will not be automatized entirely, because the skilled eye of the experienced engineer is needed to distinguish between stiff and elastic structure, between bodies with mass and decisive stiffness and between relevant or needless boundary conditions. The Chair of Machine Elements at the Technische Universität Dresden has experience in the development of software independent methods to simulate the dynamic behaviour of large drive trains. Beside the work on the presented examples, the ongoing research on different scopes of application will support the way to a reliable, reproducible and understandable modelling process.

REFERENCES

[1] Bossanyi, E. A.: Bladed for Windows. Bristol: Garrad Hassan and Partners Ltd., 2002

[2] Claeyssen, J. R.; Soder, R. A.: A dynamical basis for computing the modes of Euler-Bernoulli and Timoshenko beams. In: Journal of Sound and Vibration (2003), 259(4), S. 986-990

[3] Craig, R.; Bampton, M.: Coupling of Substructures for Dynamic Analyses. In: AIAA Journal (1968), Vol. 6, No. 7, S. 1313

[4] Dresig, Hans: Schwingungen mechanischer Antriebssysteme. 2. Aufl. Berlin: Springer, 2006

[5] Gasch, Robert; Twele, Jochen: Windkraftanlagen: Grundlagen, Entwurf, Planung und Betrieb. Wiesbaden: Teubner, 2010

[6] Guyan, R. J.: Reduction of Stiffness and Mass Matrices. In: AIAA Journal (1965), Vol. 3, No. 2, S. 380

[7] Hähnel, Thomas: Auslegung von Maschinenelementen dynamisch hochbelasteter Antriebe mittels Messung und Simulation. Dresden, Technische Universität Dresden, Lehrstuhl Maschinenelemente und Maschinenkonstruktion, Dissertation, 2009

[8] Hansen, Morten H.; Hansen, Anca; Larsen, Torben J.; Øye, Stig; Sørensen, Poul; Fuglsang, Peter: Control design for a pitch-regulated, variable speed wind turbine. Risø National Laboratory, Roskilde, Denmark, 2005

[9] Hau, Erich: Windkraftanlagen - Grundlagen, Technik, Einsatz, Wirtschaftlichkeit. 4. Aufl. Berlin: Springer, 2008

[10] Roberson, Robert E.; Schwertassek, Richard: Dynamics of Multibody Systems. Berlin: Springer, 1988

[11] Rosenlöcher, Thomas: Systematisierung des Modellierungsprozesses zur Erstellung elastischer Mehrkörpersystem-Modelle und dynamischen Untersuchung von Großantrieben. Dresden, Technische Universität Dresden, Lehrstuhl Maschinenelemente und Maschinenkonstruktion, Dissertation, 2012

[12] Ruge, P.; Birk, C.: A comparison of infinite Timoshenko and Euler-Bernoulli beam models on Winkler foundation in the frequency- and time-domain. In: Journal of Sound and Vibration (2007), 304, S. 932-947

[13] Schiehlen, Werner; Eberhard, Peter: Technische Dynamik: Modelle für Regelung und Simulation. Stuttgart: Teubner, 2004

[14] Schlecht, Berthold; Senf, Michael; Bauer, Christian, Rosenlöcher, Thomas: Stress Analysis of Gearings within their Elastic Environment under the Influence of its Dynamic Behaviour. International Conference on Gears, München, 2010

[15] Schulze, Tobias: Ganzheitliche dynamische Antriebsstrangbetrachtung von Windenergieanlagen unter Verwendung modularer Simulationsmodelle. Dresden, Technische Universität Dresden, Lehrstuhl Maschinenelemente und Maschinenkonstruktion, Dissertation, 2007

[16] Wiche, E: Radiale Federung von Wälzlagern bei beliebiger Lagerluft. In: Konstruktion 19, Heft 5, S. 184 - 192, 1967

[17] Wünsch, D.; Carcia del Castillo, L.: Experimentelle Modellfindung und modellhafte Ermittlung dynamischer Belastungen torsionsschwingungsfähiger Systeme. Frankfurt am Main: Forschungsvorhaben FVA Nr. 95, Forschungshefte 213 und 214 der Forschungsvereinigung Antriebstechnik e.V., 1986

Searching for the Silver Bullet in Wind Offshore

Dipl.-Ing. Daniel Bartminn CEng MICE*[1], MSc.-Ing. Jesus David Quintana Saavedra*[2]

RWE Innogy Wind Energy Offshore
Design and Analysis Group
Überseering 34
22297 Hamburg, Germany
E-mail: daniel.bartminn@rwe.com - Web page : http: // www.rwe.com

*[2] RWE Innogy Wind Energy Offshore
Design and Analysis Group
Überseering 34
22297 Hamburg, Germany
E-mail: david.quintana@rwe.com - Web page : http: // www.rwe.com

Key words: Wind Offshore, cost reduction, Marine Engineering, optimisation

Abstract. Strategies for cost reduction in the wind offshore industry:
The desire for cost reduction and optimisation of the design of offshore structures supporting wind turbines has to follow the requirement to identify, define and formulate all relevant boundary constraints driving the holistic cost of a design. This paper aims not to just summarize key cost drivers, but also shows examples with real cost saving potential at different stages (design, fabrication, construction, installation) during the development of a wind farm. In order to formulate an optimisation algorithm, the complex context the industry is operating in needs to be understood. However this may be a step to far. The complexity of unknown factors in an emerging and growing wind offshore industry will demonstrate that alongside to computational optimisation and academic problem formulation of individual sub tasks, what will be needed is human intuition, vision, innovation, engineering judgment and the masterminds which influence the outcome of their endeavour in a positive way. Firstly, an overview of cost categories is given ranging from material cost to finance cost. Secondly examples of risks and design obstacles are mapped, both in order to present the backdrop in front of which various strategies for delivery can be chosen.

Examples of structural optimisation taking into account some of the key cost drivers are presented at the heart of the paper, showing how different boundary constraints and design approaches will lead to different design solutions. Further the influence of the choice of risk profiles and the impact on the design with a view of the different project phases is shown. Consequentially the authors attempt to develop new strategies based thereon.

1 INTRODUCTION

The Offshore Wind Energy market is still a relatively young industry. After initial smaller offshore parks which were constructed during the nineties, the first larger offshore wind parks with installed capacities notably larger than 10MW only became operational within the last

ten years, for example Horns Rev 1 Denmark in 2002, North Hoyle UK in 2003, Egmond an Zee NL in 2006 or alpha ventus in Germany in 2009. However with now an increasing number of large wind farms with installed capacities beyond 200MW completed, under construction or nearing FID (Final Investment Decision) it can be said that the market begins to mature, with more than a dozen designers, fabricators and installation contractors specialized in this market. Likewise there are around a dozen European utilities operating offshore wind farms. All of those having more offshore wind parks in the pipeline and with feed in tariffs incrementally reducing over the coming years it is clear that cost pressures will dramatically increase on offshore wind park developments to compete with other form of electricity generation.

The desire for cost reduction and optimisation of the design of offshore structures supporting wind turbines has to follow the requirement to identify, define and formulate all relevant boundary constraints driving the holistic cost of a design.

2 COST DRIVERS AND BOUNDARY CONDITIONS

2.1 General Boundary Conditions

The development of an offshore wind farm can be broadly divided in the following time sequence: development phase; design phase, with varies sub phases from concept to front end engineering design (FEED) basic and detailed design; implementation phase; operating phase and decommissioning phase, where activities of procurement, permit and certification are related within these phases.

As with any small or large scale construction project the developer or eventual operator can follow in principle two distinctively different procurement strategies, which have their own impact on the design.

On the one hand there is the multi contract strategy with front end engineering design (FEED) carried out by the utility or developer itself, given full control over the design, interfaces and individual contracts and on the other hand there is the functional turnkey contract. Both approaches have their advantages and disadvantages and choice depends on many factors such as whether the project developer has a future project pipeline or intends to operate the farm himself, availability of in house resources, ability to learn from mistakes, appetite to carry design risks and liabilities and of course project finance and programme.

2.2 Cost Categories

In order to drive costs down for offshore wind structures it is of course important to understand the various cost drivers or categories and their context within the whole wind farm development. There are two approaches one can classify the cost categories, one is following the function within the wind park, while the other is divides costs in general cost components applicable to each item.

Accordingly a horizontal division would typically be reflected in individual contract lots such as:

I) Wind Turbine Generator (WTG)

II) WTG Foundations

III) Offshore substation platform (OSP)

IV) Interarray cable

V) Met Masts

VI) Harbour and Logistics

VII) Installation

VIII) Onshore works

IX) SCADA

X) Project Management Design, Permits and Certification

XI) Site investigations, UXO clearance

The vertical cost drivers could be classified as :

A) Material cost

B) Fabrication cost

C) Operation and Maintenance

D) Design uncertainties (Risk)

E) Weather

F) Insurance and Finance cost

G) Certification, Inspection and Quality Control

H) Supply chain and market constraints

The interdependency of the vertical and horizontal categories can be also illustrated in a matrix format:

	Material	Fabrication	O&M	Design and Risk	Weather	Ins. & Finan.	Quality	Supply chain
WTG	X	X	X	X	X	X	X	X
WTG Found.	X	X	X	X	X	X	X	X
OSP	X	X	X	X	X	X	X	X
Cable	X	X	X	X	X	X	X	X
Met Mast	X	X	X		X		X	
Harbour			X		X	X		X
Onshore	X	X	X	X		X	X	
SCADA			X	X	X	X		
PM, Design, Permits & Cert	X	X	X	X	X		X	
SI& UXO				X	X	X		
Installation	X	X		X	X	X	X	X

The crosses mark areas of greatest interdependence in terms of cost impact, however to some extent each one category has an impact on any other. Also some categories could be associated with vertical or horizontal structure such as Project management, design and certification tasks are possibly both vertical or horizontal.

The scarcity of resources needs to be distributed to an optimum, this is particular true for materials. Due the bulk character of wind offshore projects, careful material selection with a view to market availability is very important. Fluctuations of material cost could have a significant impact of other design decisions. For example aluminium cables have different installation requirements than copper cables, and not to mention to huge impact the choice for a concrete gravity solution instead of steel monopile foundation would have on installation

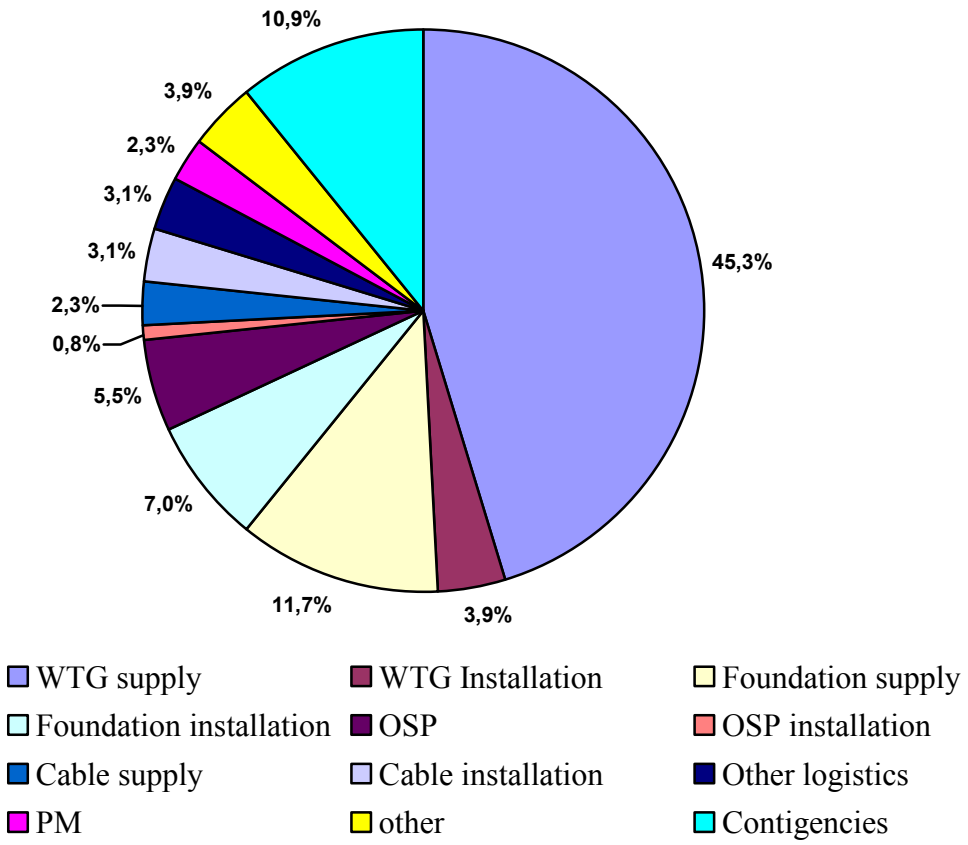
operations or the respective choice of fabrication facilities and in turn the geographical distribution of preferred supplier of foundations of WTGs.

Other vertical cost drivers have to some extent a more gradual influence. As such the choice of acceptable failure probability and fine tuning of safety factors both with regards to actions and resistance lead to changes on a sliding scale, however also certain design parameters for example with regards to water depth, wave heights, wind speeds or soil stiffness, may reach limits which define step changes between design options.

Design uncertainties reflecting the still limited data base of experience, e.g. due to few years operation life time of current offshore projects, are reflected in changing (updating) and improving design standards and/or permit and certification requirements in order to mitigate risk and last but not least on insurance premiums and finance cost, depending on the perceived risk profile. All of which may have direct cost impacts.

Certainly the evolution to ever larger turbines has a constant impact on the demands on the balance of plant, from foundations to installation vessels, and what the optimum in one wind park could be very in another. Naturally the distribution of cost between the various wind farm components should in future more and more balanced towards the WTG package.

A typical cost distribution for an offshore wind farm would be as shown below.



2.3 Risks and Design Obstacles

The limits of technical feasibility, for example of the monopile foundation depending on WTG size and water depth, the impact of project delays on the availability of installation vessels or fabrication facilities are examples of project and design risks which have potential step change or cliff edge effects. They imply a project risk which would have substantial impact on the project profitability. Other risks are related to environmental scenarios such as extreme wave and/or hydrodynamic conditions, unexpected scour development, boat impact, vessel collision, corrosion dependent fatigue issues or variability of soil stiffness and consequent changes to turbine loads or design load cases are by and large better understood with regards to their probabilistic distribution and risk profile and influence of the design, such risks have more uniformly continuous effect on the cost. However also the technical solutions to such influence factors are subject to scrutiny by external finance partners, who are interested whether or not state of the art technology has been applied, or whether innovative solutions are sufficiently mature to present an acceptable risk profile. This leads to a contrasting juxtaposition of the desire for innovation and low risk tried and tested solutions. Application of radical innovation is often hampered by the need for full scale demonstration, which is cost and time consuming, especially in terms of calibration of test results with in-situ conditions.

Other external obstacles to the design might be presented by consent based restrictions for example on piling noise, installation windows or other restrictions related to the marine life. Such obstacles could favour otherwise less economical solutions.

Identification of all foreseeable risks, their continuous mitigation and evaluation in risk registers is also an essential part of the process just as recording of lessons learned from previous projects. Detailed root cause analysis of any identified failures, in terms of design and contract strategies or decision making process is the indispensable basis for any future optimizations. As far as possible this shall include monetary evaluation.

The challenge to the decision maker is find the optimum solution, in spite of lacking a reliable database of all cost factors or fully understanding the interdependence of the various parameters.

Judging market readiness and future development at early project stages, leaving sufficient room for optionality while not losing the focus of the preferred solution, is the task to be investigated and solved during the design process.

Nevertheless an attempt should be made to find the optimum solution both holistically and for the individual items.

3 EXAMPLES FOR COST SAVING POTENTIALS

Experience so far has shown that incremental changes and continuous marginal improvements are currently the greatest contributors to cost reductions. This experience also reflects the developments of the onshore wind industry and other industries. Probably it is also a reflection of market and finance mechanisms and appetite for risk. Even where public funding for demonstrators is available it has not always led to market entry of revolutionary concepts. Still some current examples shall be given below for both global concepts and

measures for marginal improvements.

3.1 Global concepts

Various structural concepts as alternatives to the predominant monopile are currently evaluated by RWE Innogy as part of the tender for innovative foundation demonstration field within the wind park Innogy Nordsee 1. The foundation concepts which were shortlisted based on their technological maturity and future potential, these included:

1) Concrete Gravity base foundation
2) Suction bucket
3) Combined multiple suction bucket and steel frame (SPT concept)
4) Twisted jacket
5) Modified jacket foundations with cast nodes

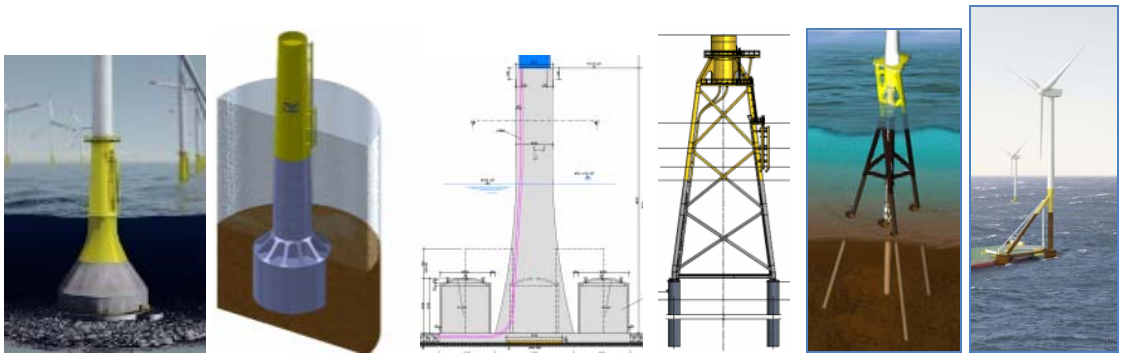


Fig. 3.1 Innovative foundations, MTH, Fred Olson, Max Bögle, Weserwind/tkb, Keystone, twisted jacket, SPT

Although the commercial evaluation process is currently still on-going it is yet to be seen whether or not such radical concepts can challenge the monopile or jacket as the foundation the solution of choice for future projects.

Other global optimization concepts are reliability and risk based system modelling for optimization of design, maintenance and operation. Such system modelling should ideally all components of the wind park.

3.2 Marginal improvements

Since such global optimization approaches for the time being at least lack a reliable database of cost factors the industry focusses on many individual areas, which have potential for future cost saving.

3.2.1 Modified P-Y Curves and understanding of cyclic loading

Determination of lateral resistance of monopiles is based on p-y curves, according to the state-of-the-art methods, which describes development of lateral resistance and stiffness

depending on the loads applied. The basis of these curves stems from test conducted of piles of relatively smaller diameter, as considered in e.g. API rules, and their general accepted limit is around 2m. Large scale tests and new theories are under development to substantiate the design of large diameter monopiles. By now the industry is looking at monopiles with diameters approaching 7m and more, hence it is essential to understand any design uncertainties both as potential to tap into available design margin but also to uncover possible risks.

Likewise under discussion are the criteria used for the embedment length, which are governed by concerns regarding to the cyclic degradation during the life time of the foundation. The potential for recovery particular of sandy soils may be better than currently appreciated. Improved p-y curves are developed with in the Joint Industry Project (JIP) PISA.

3.2.2 Improved S/N Curves

Often the design of the steel components, e.g. monopile foundations, is governed by fatigue loads. However codified S/N curves for marine structures are based on research and test data carried out some decades ago with welding techniques and steel grades, which are not representative (or could not be applicable) of the wind industry of today. It is the aim of the SLIC JIP to develop improved S/N curves.

3.2.3 Risk based design

Some offshore standards already allow for a risk based design approach. It is to be distinguished between manned and unmanned installations, and oil and gas industry has developed design approaches reflecting various levels of risk operating personnel, the environment and the capital investment. The industry as whole has yet to define appropriate risk profiles and the limits for acceptable failure probabilities.

It is however essential to define such levels in order to optimize the system as a whole.

3.3 Fabrication

It is self-evident that any structure should be optimized for the respective fabrication process. Many factors are common to fabrication process, such limits of plate sizes, thickness and common material grades and geometrical limitations and these should be included in the optimization routines, other factors may vary between fabricators such as optimum ratio of plate size thickness and welding procedures, nevertheless the designer should aim to gain a common understanding of the influencing factors as far as reasonable possible.

3.5 Installation

Optimizing the design for installation procedures offshore is paramount to the wind offshore industry. With large number of repeated installation weather windows can become critical. Limits of commonly available installation vessels represent often governing criteria for sensible maximum lift weights and sizes. Reducing the number of offshore operations and heavy lifts is not just a commercial necessity but also an optimum from a health and safety point of view.

3.6 Supply Chain Strategies

The sheer number of influence factors lends itself to introduce some simplification and cost certainty by following supply chain strategies, which enable both risk reduction and cost optimization.

Frame work contracts with material and component suppliers, fabricators or installation companies have the benefit to work within known boundary condition and offer a certain planning certainty for both parties involved.

4 OPTIMISATION ROUTINES

4.1 Computational approaches

Optimization routines have been developed for multi parameter problems, for example stochastic local search methods for highly constrained combinatorial optimization problems, such graph colouring can be applied to defined subsystems of parameters. Other approaches have been used for example is the design optimization of the Beijing Water cube or the famous birds nest, once on design solution was found various parameter were changed to explore the benefits of alternative designs. The weighing of parameters however may for some time still be creative part in the process.



Structural optimisation routines have been applied for other complex task, such as the Bird Nest in Beijing

The combination of various optimisation routines and algorithms of local sub-problem specific optimisation and global dependent combinatorial optimisation, is an approach with is yet to be applied. The databases required to apply such a theory and approach with academic rigour are not publicly available. However for certain projects such data exist could form the basis for applying these concepts in an appropriate research alliance.

Due to the multidisciplinary engineering tasks in the scope of the development and design of foundations for offshore wind turbines the use of different computational approaches are required. Optimisation routines in order to guarantee an sliding interface between the input data, analytical approach and interpretation of results are highly recommended to be integrated in the development phases.

4.2 Strategic approaches

Until such a optimisation routine is established as a closed solution, the design and project team has to derive simplified strategic approaches which follow similar concepts of local search methods where selected parameters are varied more or less randomly. In practice this implies for the designer or analyst searching for the optimum, it would be valid to concentrate optimization efforts on relatively narrow bands. Nevertheless far field searches looking for optimum valleys beyond the ridge of known constraints should be included in mathematical optimization models.

The concept of racing methods for competing algorithms is applied in an abstract way, by optimising sequentially for varying parameters and eliminating unfavourable solutions at earlier stages. The example below shows how the optimum diameter for a monopile was determined by first comparing relatives weights optimised for the eigenfrequency criterion, than for fatigue loads. It can be seen that after the first evaluation out of 15 possible combination 9 were eliminated as not promising, reducing the computation effort for the second loop to 40% of the initial set up. The remaining 40% were than evaluated for fabrication optimised weights, i.e. including waste and welding efforts related to standard plate sizes and industry practice. It is clear that numerous other combination related to platform configuration or corrosion protection concept are possible, and the sequence of eliminating combination is to date based on engineering judgement.

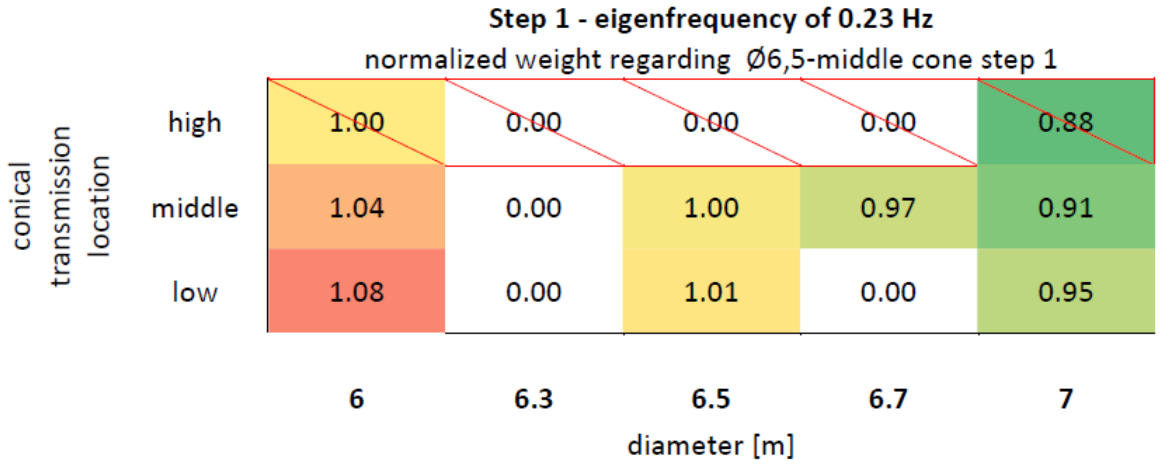


Fig 4.2.1 Evaluation according to Eigenfrequencies

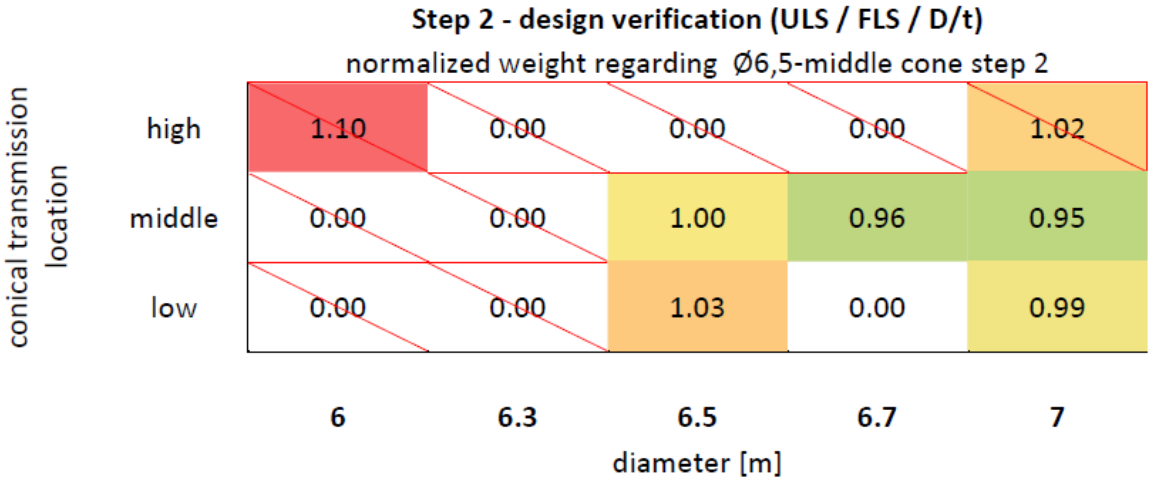


Fig 4.2.2 Evaluation according ULS/FLS design

From the above it can be seen that there is ample room for optimising weights at early stages, which will have follow on effects on fabrication and installation contract. Therefore a multistage process under supervision of and control by the end user seems to date the most favourable approach. However close cooperation and knowledge of the whole supply chain and their open collaboration is needed to achieve meaningful optimisation.

5 CONCLUSIONS

The paper has presented various cost categories relevant to wind offshore projects. Cost drivers were divided into functional elements and general common elements. Global and radical approaches to cost reduction exist next to local specific innovations targeting marginal gains. At the moment these are often unconnected isolated efforts, but as such more promising than the one big solution, the “silver bullet” to drive down cost. Strategies of how local or isolated efforts can be coordinated or formalised to find closed solution optimisation algorithms. The optimisation strategy should be project specifically focused and can be defined through a common understanding between related parties at early project phases. For such tasks reference was made to optimisation techniques know from programing or structural optimisation in a multidisciplinary engineering approach. The techniques can be applied in an more abstract and less formal way to develop approaches which can be applied to whole complex projects in order to achieve reliable results for project decision processes.

REFERENCES

[1] Chiarandini, M.. *Stochastic Local Search Methods for highly constrained combinatorial search problems*. Dissertation TU Darmstadt, (2005).

V International Conference on Computational Methods in Marine Engineering
MARINE 2013
B. Brinkmann and P. Wriggers (Eds)

OPTIMIZATION USING VISCOUS FLOW COMPUTATIONS FOR RETROFITTING SHIPS IN OPERATION

MATTIA BRENNER[*], VASSILIOS ZAGKAS[†], STEFAN HARRIES[*] AND TOBIAS STEIN[*]

[*] FRIENDSHIP SYSTEMS GmbH (FSYS)
Benzstr. 2, 14482 Potsdam, Germany
e-mail: info@friendship-systems.de, www.friendship-systems.com

[†] Naval Architecture Progress (NAP)
80, Kolokotroni Str., 18535 Pireaus, Greece
email: nap@nap.gr, www.nap.gr

Key words: Retrofitting, Optimization, Viscous Flow, Parametric Modeling, Energy Saving

Abstract. Shipping is commonly believed to be the most energy efficient mode of transport. Nonetheless, the shipping industry is required to reduce its environmental impact. The IMO has developed a package of measures for reducing shipping's CO2 emissions within an agreed timetable for adoption (Energy Efficiency Design Index for the design of new ships and the Ship Energy Efficiency Management Plan for the operational phase).

Approximately three-quarters of the vessels are rather young, so most ships in operation need solutions to reduce their pollution. In general, the suitable solutions differ from ship newbuilding, in which hull form optimization and newest machinery technology can be readily employed.

This paper will demonstrate how simulation-driven design using the CAE platform *FRIENDSHIP-Framework*, coupled to the viscous flow CFD solver *SHIPFLOW*, can be used to efficiently develop optimized solutions for the retrofitting of ships in operation. Systematic variation as well as formal optimization is used in the process, coupling automated generation of geometry variants to simulation. The retrofitting solutions that will be covered are measures to decrease the resistance or increase the propulsive efficiency of the ship. Typical examples are energy-saving devices that are added to the ship or replacing parts of the hull or the appendages with new, optimized shapes. The validity of the concept will be demonstrated with the results from case studies that include a motor yacht, as well as a commercial RoPax ship.

1 INTRODUCTION

It is well a well-known fact that shipping is believed to be a more energy efficient mode of transport than transport by land or air, but, especially due to the large overall volume of shipping, that does not excuse the industry from making improvements to prevent climate changes for future generations and generally reduce its environmental impact. To tackle this challenge, the IMO Marine Environment Protection Committee has already developed a package of measures for reducing shipping's CO2 emissions within an agreed timetable for

adoption (Energy Efficiency Design Index for the design phase of new ships (EEDI), and the Ship Energy Efficiency Management Plan (SEEMP) for the operational phase).

Approximately three quarters of the vessels in the world shipping fleet are relatively young (less than 15 years old), so that most of the ships currently in operation need solutions to reduce pollution, e.g. by retrofitting and other suitable measures. In general, these solutions differ substantially from the ones in ship newbuilding, where hull form optimization and newest machinery technology can be readily employed.

A further incentive for retrofitting comes, due to the raising fuel costs, from the increasingly common “slow steaming”. When operating at a different condition than the one it was initially designed for, even if it is saving fuel costs due to the smaller speed, the ship might not operate as efficiently as it could, giving potential for even further savings.

2 SIMULATION-DRIVEN DESIGN

While simulation tools have widely become an integral component of the hydrodynamic design of ships, it is mostly the modeling inside a computer aided design (CAD) system that remains the driver of the process. Since most design decisions are based on simulation results, this type of process can be called simulation-based design. Simulation-driven design goes an extra step. Instead of checking and comparing the performance of a few manually created variants, the idea is to let the simulation tell what the optimal shape should look like, making it the new driver of the design process [1]. Basically, this is the ultimate implementation of the popular saying that "form follows function" [2].

The appended hull of a ship with its relationships to the environment constitutes a very complex system, where the shape of the system is tightly connected to its functional characteristics. To be able to optimize such a system for its prospective mission, the designer has to fully understand its sensitivity and reactions to changes of the defining form parameters from a performance point of view. Knowledge of the system’s behavior within the complete design space enclosed by constraints is needed, so that changes of the properties can be directly related to performance. Evaluating some manual variants, obtained by changing single parameters or manipulating the shape, can only serve to sample the design space and select the best variant. Driven systematic variation in contrast yields a real trend indication. Finally, by using formal optimization, and this is the most consequent implementation of simulation-driven design, the simulation is really used to produce shapes, rather then just evaluating them.

3 DESIGN VS. RETROFIT

During the design phase of a new vessel, especially at the very beginning, the freedom for design decisions has very little limitations. The principal dimensions might already be fixed, as well as some constraints given by the desired cargo capacity of the vessel. Within these constraints the shape of the vessel’s hull can be freely changed in order to optimize the geometry for performance. Typically, the forebody is modified to reduce wave resistance, while the aftbody shape is tuned for a low viscous resistance, high propulsive efficiency and homogeneous wake distribution. In this phase, simulation-driven design can effectively be employed to increase the knowledge about the system and therefore converge to a better solution in a shorter time (see Figure 1).

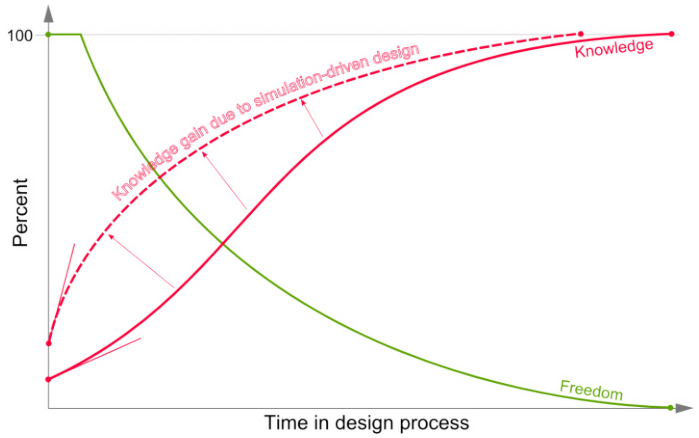


Figure 1: Freedom vs. knowledge in the design process

When tackling the retrofit of an existing vessel in contrast, the freedom for finding suitable design solutions is immensely smaller. Possible solutions include the replacement of parts of the hull by redesigned shapes, typically this can be applied to the bulbous bow and to other rather independent parts of the hull like the skeg, as well as the addition of so-called propulsion improvement devices like wake equalizing ducts, pre and post swirl stators. Various constraints apply to such cases, ranging from physical to regulatory and economical. The accuracy of estimated gains in efficiency is a governing factor in retrofitting ships in operation, considering that such decisions are based on the actual ROI of the retrofitting. The expected accuracy is met with the use of viscous flow computations, both for local optimization and overall performance assessment. Due to the capability to find a truly optimized solution, in the context of retrofitting, simulation-driven design can push the design of the retrofitting solutions from an economically infeasible situation to a result that will yield an ROI time within reasonable bounds.

4 OPTIMIZATION SYSTEM AND PROCEDURE

The optimization platform that was used for the simulation-driven design of retrofitting solutions in the following case studies consisted of the *FRIENDSHIP-Framework* (FFW), a generalized CAE workbench for the design of products with flow related tasks. The FFW supplies a wide range of functionality for simulation-driven design like parametric modeling, interfaces for the coupling of external simulation codes, as well as algorithms for systematic design studies and formal optimization.

SHIPFLOW was used as CFD solver to provide the required feedback about the performance measures for each analyzed variant. *SHIPFLOW* is a CFD suite specifically targeted at the field of naval architecture. It includes different solvers for potential flow, boundary layer analysis and a state-of-the-art viscous flow RANS solver. The different modules can run independently or in a coupled way in a so-called zonal approach.

The typical optimization process starts with an appropriate parameterization of the geometry. Two options can be selected in the FFW: partially and fully parametric modeling. Partially parametric modeling starts from an arbitrary geometry description, e.g. imported surfaces, offsets or meshes, and applies transformations that are defined by parameters. Fully

parametric modeling in contrast starts from a set of parameters and generates the shape by stepwise setting up geometric entities that are connected to the parameters and to each other by dependencies. The most flexible and efficient approach in the case of retrofitting is usually that of a fully parametric model limited to the area of interest. The initial geometry is imported; the parts to be optimized are cut out or removed and finally replaced with a parametric geometry.

An efficient optimization strategy that has proved its validity in many commercial and research project consists of design space exploration with a systematic variation algorithm, followed by a local optimization with a deterministic search method. While the former gives a global overview of the design space, allowing for the identification of areas of interest, the latter will fine-tune the design to the optimal solution within that area.

5 CASE STUDIES

5.1 RoPax vessel

Case description

The contemplated vessel in this first case study is a twin screw RoPax ship with a length of 170 m. It is one of two sister vessels that have passed approximately half of the lifetime estimated by their operator. They were initially designed for a speed of 23 kts, but due to restrictions in fuel consumption, they are currently operated at a slower speed. In the past they had already been retrofitted with CLT propellers. However, the goal was to find economically feasible solutions to further improve the efficiency of the vessel at the new operating speed.

Retrofitting solutions

As mentioned before, changing appendage geometries is a common retrofitting option, considering performance improvements and its investment volume. On a twin screw vessel a natural choice of possible appendages are the shaft brackets [3]. The influence of these struts on the wake field in the propeller plane is substantial. With adjusted struts, flow homogeneity and possibly even pre-swirl can be controlled directly before interacting with the propeller. Therefore, wake quality measures, such as homogeneity and wake fraction can be improved.

The RoPax is outfitted with two straight struts in V-configuration on every shaft. Because of fixed connection points on the shaft surface and the hull, the geometry variations were done by changing two angles per strut: the base angle of attack on the shaft surface, as well as the strut twist angle (see Figure 2).

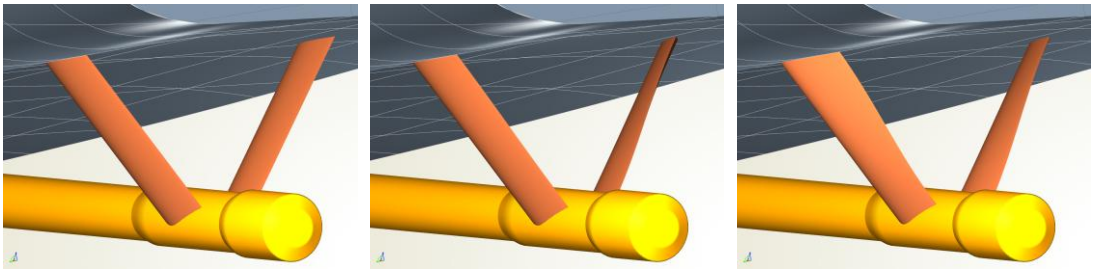


Figure 2: Geometry, f.l.t.r.:baseline, best Pd, best wake variation

SHIPFLOW's viscous flow solver with its overlapping grid technology makes variations in the strut geometry easy because the other component grids remain unaltered, while only the strut grids are modified (see Figure 3).

A strut variation, generating 20 variants with altering angles in the range of -20° to 20° was carried out. Based on the results of the variation, the wake quality could be significantly improved. The design with the best homogeneity decreased the wake variation by about 24%. In this design (Figure 2 right) both struts were twisted considerably in opposite directions, while the base angles remained nearly at the original values. The SVA wake quality criterion [4] (eta_n_SVA) increased by 1,8% (see Table 1).

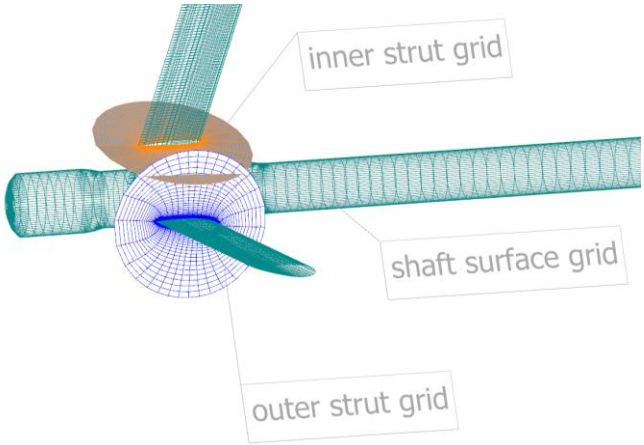


Figure 3: Overlapping component grids on shaft and struts

In this case the wake improvement happened at the expense of the resistance. All created variants showed deterioration in the viscous resistance, possibly due to an increase in the longitudinally projected area of the struts. For the design with the best wake variation, the viscous resistance increased by about 10%.

Table 1: Selected results from the strut variation

Design	wake fraction	wake variation	eta_n_SVA	Rv [kN]
baseline	**0.053**	**0.427**	**0.771**	**602.2**
design_best_wvar	0.058	0.344	0.785	663.2
design_best_RV	0.053	0.423	0.782	602.5
design_best_PD	0.055	0.423	0.766	659.6

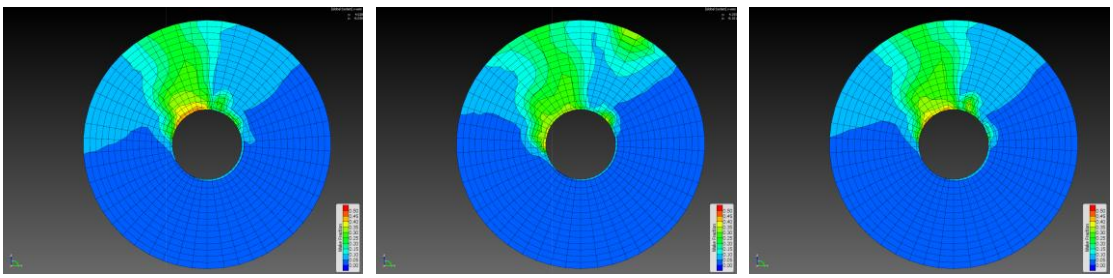


Figure 4: wakefields, f.l.t.r.:baseline, best wake variation, best Rv

This retrofitting investigation is still ongoing and a further variation with self-propulsion computations should demonstrate if the wake field improvements will counteract the loss in viscous resistance by increasing the propulsive efficiency. Additionally, in order to increase the influence on the wakefield and introduce a substantial amount of pre swirl, stator fins will be fitted on the propeller shaft in further investigations

While retrofitting for optimized wake, careful consideration for the effect of altering frequencies and possible propeller hull induced vibrations shall be taken at a later stage.

5.2 Motor yacht

Case description

The vessel in this case study is a modern 50 m long twin screw motor yacht with a hybrid round bilge/chined hull, a bulbous bow and a central skeg. The motor yacht was initially designed to serve the owner's needs. However, new operational parameters and several luxury additions to the yacht had increased its actual design draft. Addressing all the statutory implications coming along with the increased design draft is a usual case, especially with the space/tonnage constrained motor yacht designs. On the other hand, the hydrodynamic implications coming from the increased draft have to be addressed and compensated with a more fundamental approach.

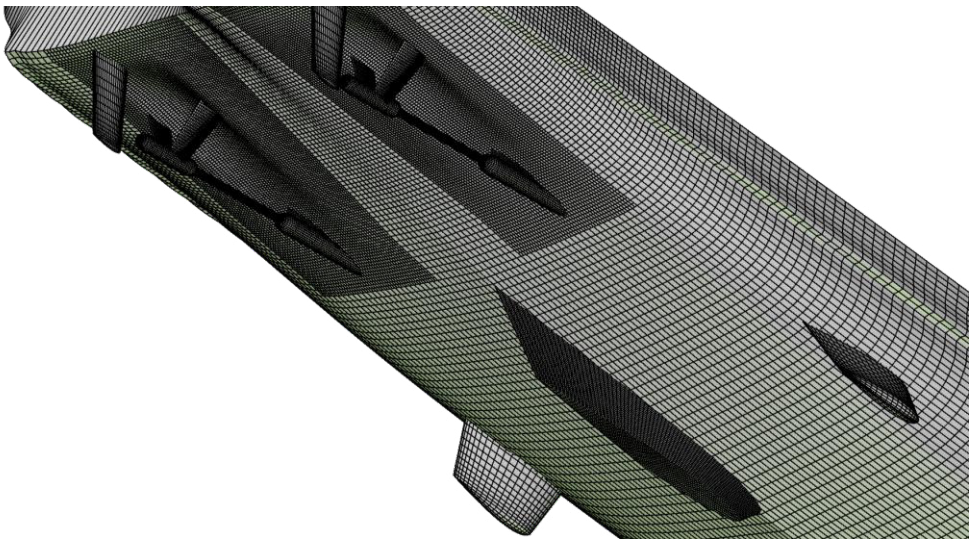


Figure 5: Preparation of hull and appendages mesh

As a first approach the causes for the increased overall resistance were pinpointed to be the increased wetted surface, the submergence of the bulbous bow causing increased wave resistance and a possible overall disturbance of the propeller wake field. While the first cause came from a logical assumption, which can be quite simply determined, the second and third cause needed a deeper investigation. Viscous flow computations were carried out for the previous and current design draft, in order to determine various efficiency parameters.

From the data retrieved by these initial computations it was derived that from a 12.5% increase in draught, the resistance of the vessel had increased by almost 35%. The substantial

increase was found to be mostly due to the increased wetted surface of the vessel (increased by about 23%) and the rest 12% due to the increased wave elevations and the disturbed wake field to the propeller. The maximum wake variation was significantly increased, which means that the uniformity of the wake field had been disturbed. The flow velocity had been reduced as a consequence of the additional sinkage of the hull, therefore increasing the wake fraction. The Taylor wake fraction is an indicator of the flow retardation through viscous effects; increased wake fraction often results in amplified resistance and propeller loading.

Overall, the increased draught had imposed a reduction of about 13% to the top speed and the fuel consumption had increased, imposing also a lower travel range, which is an important factor for motor yachts. All the computational estimations were compared with following sea trials that proved to be in close correlation.

The value of these results did not only stem from the prediction of the speed, which may be biased by assumptions and simplifications, but also from determining the root cause of the increased resistance of the hull and the poor propeller performance. With the aid of the findings from the preliminary viscous flow investigation, it was possible to effectively determine the required changes in order to improve the hydrodynamic performance of the vessel.

Table 2: Self-propulsion results for the different drafts

PROPULSIVE FACTORS:	16kts@Initial Draft	16kts@Increased Draft
KT Thrust coefficient	0.1733	0.1927
KQ Torque coefficient	0.0256	0.0276
JV Advance ratio	0.5484	0.5109
rps	9.38	10.07
Rpm (Propeller)	562.8	604.11
Rpm (Engine)	2286	2453
Q [Nm]	24218.61	30060.2
PD per engine [kW]	1427.365	1901.681
PD total [kW]	2854.731	3803.362

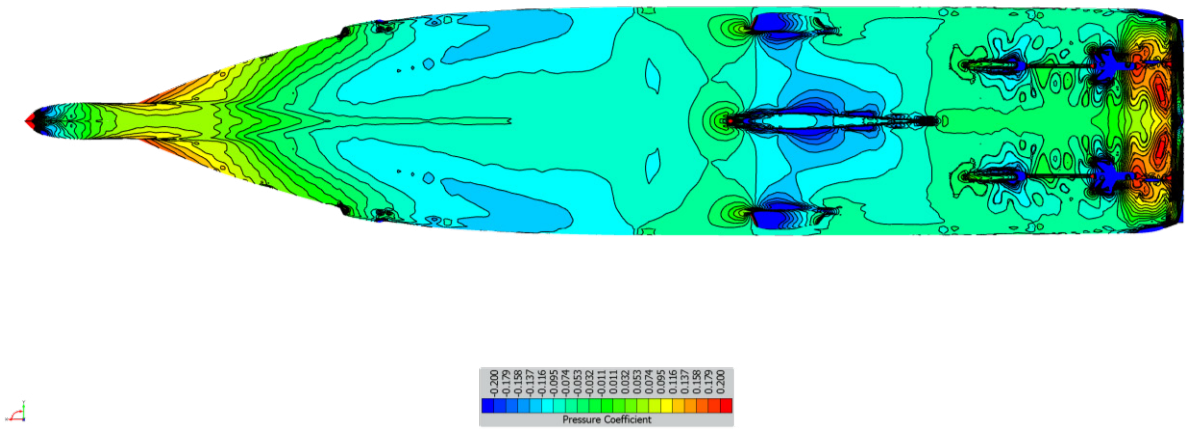


Figure 6: Fish view perspective of pressure distribution on the appended hull for increased draught

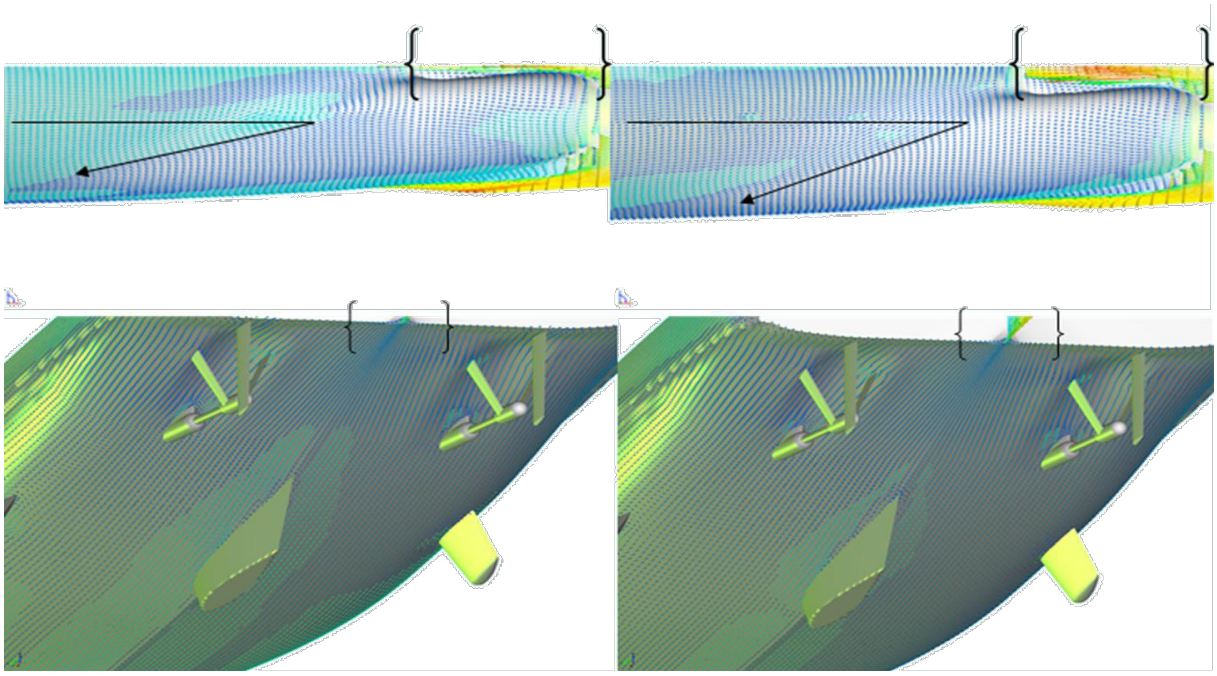


Figure 7: Plot of limiting vectors on bulb and aftbody, initial vs. deeper draught at 16 knots

Retrofitting solutions

Further to the above investigation, an appropriate strategy was determined in order to define the retrofitting optimization process.

Findings	Objectives	Geometry	Tools
- Increased Wetted Surface	- Minimize	- Bulbous Bow	- Potential Flow Optimization
- Increased Wave Resistance	- Minimize	- Skeg	- Viscous Flow Optimization
- Disturbed Wake Field	- Improve Efficiency	- Bulb & Skeg	- Viscous Flow Self-Propulsion Opt.

In this case study a two-step optimization approach was utilized. The first step involved the individual optimization of appendages with appropriate computational methods; while the second step involved the combined optimization of the best selected appendages from step one, with a final viscous numerical self-propulsion test, including a lifting line propeller model. The individual bulbous bow optimization was a trivial procedure involving only a potential flow computation and it won't be described in detail here, while the skeg and the holistic optimization approach were realized using *SHIPFLOW*'s viscous flow module, XCHAP. The relevant objectives and their constraints are described below.

Geometry	Objectives	Constraints
- Bulbous Bow	- ↑Underwater Volume ↓ Rw	- minimum KM, fairness of new geometry relative to existing hull
- Skeg	- ↑Underwater Volume ↓ Rt	- minimum KM, variants shall be adapted to the existing structure
- Bulb & Skeg	- Improve Wake Fraction, η_N,	- existing propellers arrangement, trim, loading conditions

The main constraint in optimizing the skeg and the bulb of a ship in operation comes from the fact that the new geometries shall be structurally feasible and shall blend fairly with the

existing hull-form. In this particular case study the skeg optimization was carried out with the objective of modifying only a minor part of the existing structure.

The shape of the skeg on this vessel was basically that of a wing that intersects the hull surface. From the point of view of modeling, the geometry was generated as ruled surface between parameterized upper and a lower profile sections (see Figure 8).

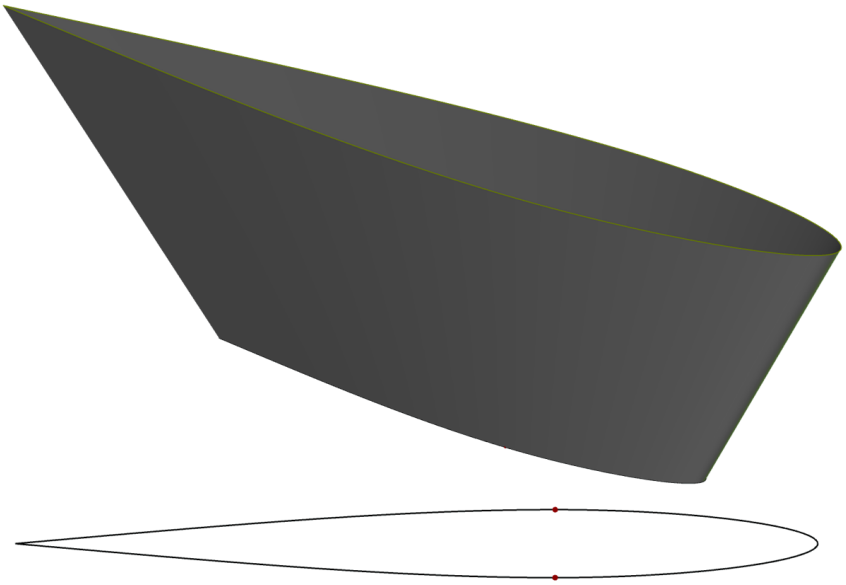


Figure 8: Skeg surface and profile section

The parameters selected to control the skeg shape were:

- Longitudinal position of the leading edge of the lower profile
- Length of the lower profile
- Thickness of the lower profile
- Longitudinal position of the leading edge of the upper profile
- Length of the upper profile
- Thickness of the upper profile
- Relative longitudinal position of the maximum thickness
- Fullness of the after profile part
- Fullness of the forward profile part

The parametrically defined model of the skeg was utilized to optimize it with regards to additional volume, reduced viscous resistance and good quality of the wake field to the propellers. During the optimization process 150 variants were investigated (see Figure 9 for examples). The new skeg geometry was supposed to have enough volume to compensate for the ship's increased draft. The results of the optimization showed that with an increase of the volume, the frictional resistance slightly increased, mostly due to a further increased wetted surface. However, the viscous pressure resistance, that was about twice as large as the frictional resistance, decreased, leading to an overall lower viscous resistance with rising volume (see Figure 10). Additionally, the optimized geometry contributed to a better wake field.

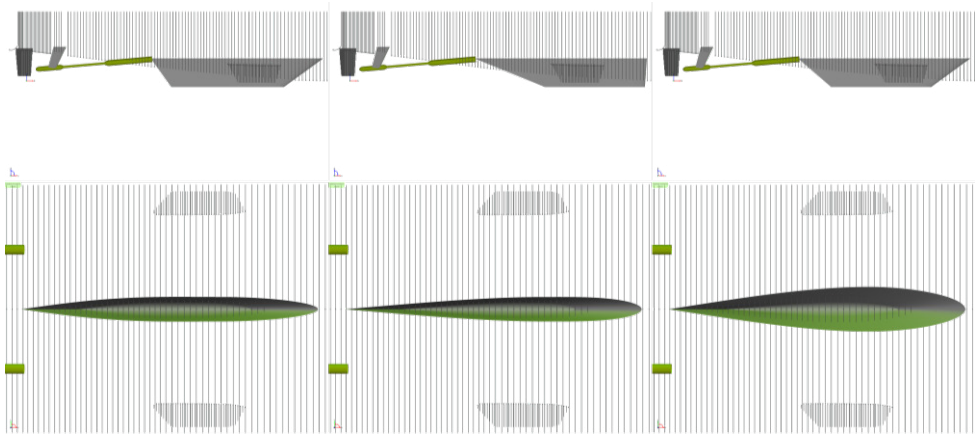


Figure 9: Sample of systematic variation of the skeg parameters

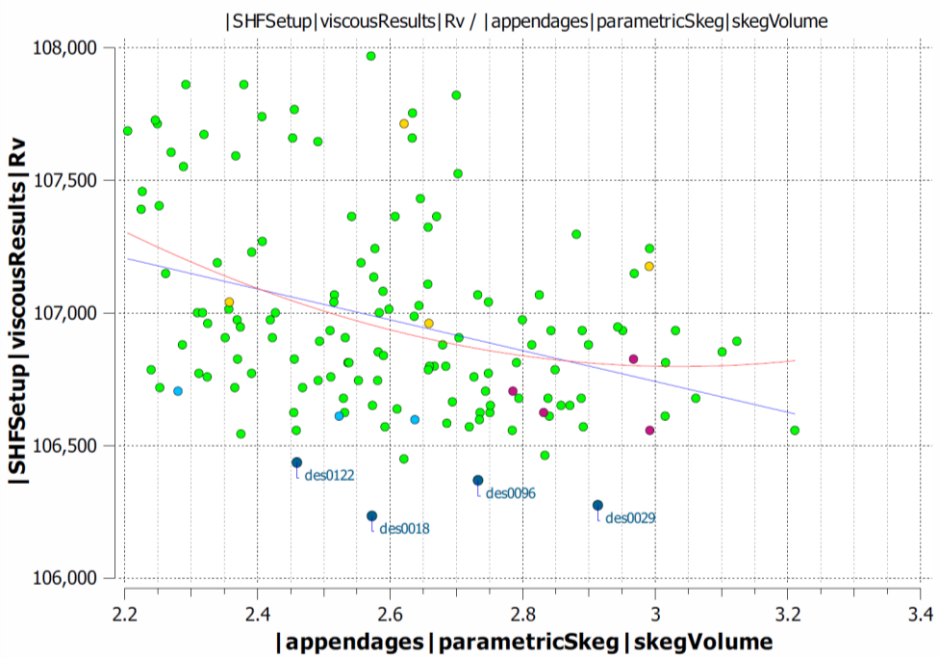


Figure 10: Viscous resistance vs. skeg volume

After the individual optimization of each component, bulb and skeg, the final geometries were incorporated in a final hull-form, fine tuned with a further local optimization and in the end a self-propulsion computation was conducted in order to derive the final performance prediction and the wake field data to be used for evaluating the overall performance and determining the most efficient wake adapted propeller design. The numerical self-propulsion test with the optimized bulb and skeg showed a decrease of about 16% in power requirement. The resistance computations demonstrated a reduction of about 4% in total resistance, an improvement of 13% in the wake fraction, as well as a lowered wake variation (-4%), with just a very slight deterioration of the SVA wake quality criterion. The new optimized skeg and bulb geometries contributed about 4 m³ of underwater volume, thus reducing the wetted surface and optimizing the wake field as far as possible.

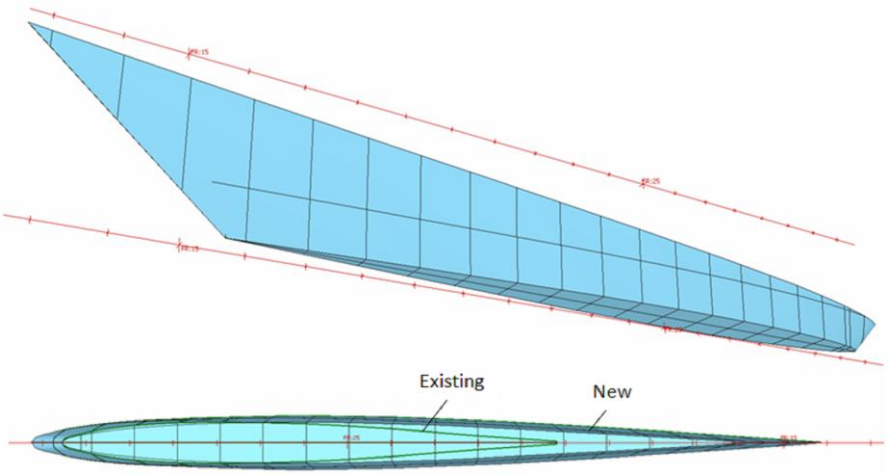


Figure 11: Final optimized and faired skeg geometry

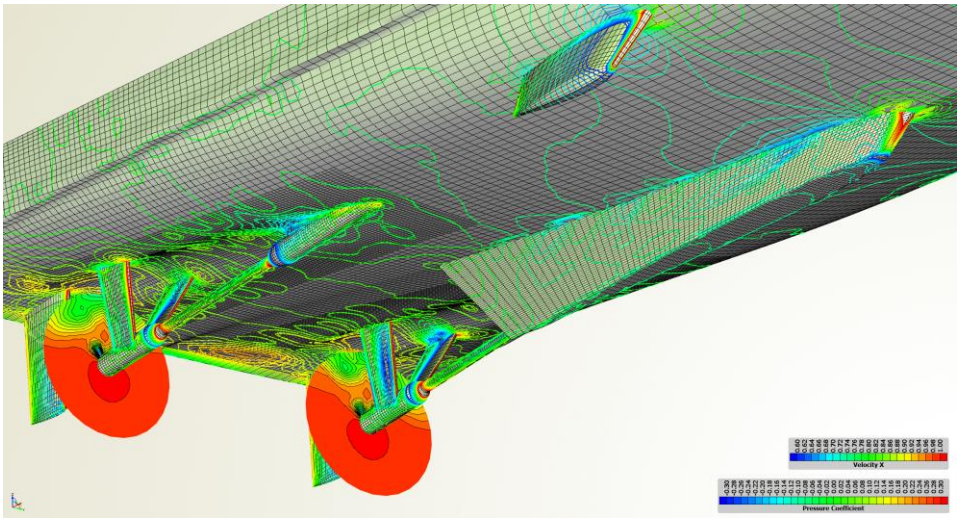


Figure 12: Pressure distribution on hull and wake field of variant with optimized skeg

When optimizing appendages through an enlargement of the volume, careful consideration shall be taken with regards to abrupt changes in the KM hydrostatic value that has a direct effect on the stability of the vessel. Therefore, finally, the selected optimized appendages were structurally modeled (see Figure 11) and their weight and center of gravity properties were estimated. The hydrostatic properties of the hull with the new appendages were calculated and the final loading conditions were derived in order to evaluate the trim and draft that the vessel would have after the retrofitting.

Further to the viscous flow optimization results, a holistic approach on improving the vessel's performance was adopted. The optimum efficiency gain was observed when retrofitting the skeg by an extension to the existing structure, retrofitting the bulb by an external addition to the existing bulb and by selecting new wake adapted propellers. The total fuel consumption gain with the above suggested retrofitting was estimated to be about 16% on the main engines' consumption. Considering the operational range and the vessel's average speed it was estimated that the difference between the optimized and non-optimized design is

~70,000€/10,000 nm, which reflects to something more than a summer month of operations in the Mediterranean Sea for an active motor yacht owner.

Looking at the results from an environmental perspective, the relevant EEOI values were calculated. For a given journey between Piraeus and Nice of about 1260 nm with a constant speed of 15.4 knots, the EEOI value of the current vessel is about 34.8 units, while for the vessel with optimized appendages it is 29.2 units. The EEOI index for the motor-yacht was based on the IMO recommended formula, while the cargo quantity was appropriately replaced by the Gross Tonnage of the vessel.

$$EEOI = \frac{(Fuel \times CO2\ Conversion\ Factor)}{(Cargo\ Quantity \times Distance)}$$

Through a hypothetical operational analysis for a full summer season it was estimated that the use of optimized appendages on such ships in operation can yield a reduction of up to 25% on the EEOI rolling average.

6 CONCLUSIONS

The theoretical considerations in this paper, as well as their practical implementation in the demonstrated case studies, show that viscous flow CFD methods and simulation-driven design comprising systematic variation and formal optimization can be of valuable help in the design of retrofitting solutions for ships in operation. They give an accurate prediction of the expected gains and push the design towards an economically feasible solution.

In the displayed case studies, several performance measures like wake field quality, resistance and required power could be improved and at least in one of the cases this led to a significant improvement in energy efficiency and environmental impact.

Acknowledgement

AKNOWLEDGEMENT

Parts of the work presented here were realized within the research and development project ReFIT, granted within the ERA-NET MARTEC Call 2010, with FRIENDSHIP SYSTEMS being funded by the Federal Ministry of Economics and Technology (BMWi) on the orders of the German Bundestag and PtJ as the conducting agency (FKZ 03SX319).

REFERENCES

[1] Brenner, M., Abt, C., Harries, S. Feature Modelling and Simulation-driven Design for Faster Processes and Greener Products, *Proceedings of International Conference on Computer applications in Shipbuilding (ICCAS)* (2009), Shanghai, China.

[2] Sullivan, L. The Tall Office Building Artistically Considered, *Lippincott's Magazine*, (1896).

[3] Brenner, M. *Integration of CAD and CFD for the Hydrodynamic Design of Appendages in Viscous Flow*, Diploma Thesis, Technical University Berlin, (2009).

[4] Fahrbach, M. *Bewertung der Güte von Nachtromfeldern* (in German), Diploma Thesis, Technical University Hamburg, (2004).

V International Conference on Computational Methods in Marine Engineering
MARINE 2013
B. Brinkmann and P. Wriggers (Eds)

HULL OPTIMIZATION FOR OPERATIONAL PROFILE – THE NEXT GAME LEVEL

KARSTEN HOCHKIRCH*, JUSTUS HEIMANN* AND VOLKER BERTRAM*

* FutureShip
Behlertstr. 3a, D-14467 Potsdam, Germany
e-mail: karsten.hochkirch@GL-group.com, www.futureship.net

Key words: Optimization, Ship Design, Hull Design, Energy Efficiency, Marine Engineering

Abstract. This paper describes an industry project to improve the fuel efficiency of a large containership through formal hull optimization. The ship owner targeted for overall fuel savings in actual operation, rather than being focused solely on a single design point. Combining parametric hull design description, computational fluid dynamics (CFD) and a dedicated optimization shell, a professional baseline was optimized for the operational profile of the existing fleet. The baseline design was designed traditionally by a combination of CFD and model tests for a single design point. Exploring a design space of several thousand designs, a design was found that was superior to the baseline over the whole operational range, resulting in a reduction of 3.7% in fuel consumption. The predicted gain in fuel efficiency was validated in independent ship model tests at Hamburg Ship Model Basin. The main lesson learnt is that state-of-the-art optimization for a realistic operational profile rather than a single design point opens the door to significant further fuel savings.

1 INTRODUCTION

For decades, ships have been designed for much lower fuel costs. Increasing fuel prices and IMO regulations to curb CO_2 (carbon-dioxide) emissions put pressure on ship owners to obtain more fuel efficient ships. As a result, we have seen a multitude of proposals to reduce fuel consumption in ships. More detailed discussion of available options in resistance, propulsion, machinery and operation (with different focus for different ship types), can be found e.g. in [1], [2], [3], and [4].

The largest potential in fuel savings lies in the design stage. Traditional ship designs reflect much lower fuel prices than the industry is facing today and likely to face tomorrow. Consequently, these designs are no longer fit for current market or fit for the future. Various publications, e.g. [5], have identified ship hull optimization as one of the "low-hanging fruits" for significant fuel savings. In fact, hull optimization is applicable and financially attractive for virtually all ship types.

The term "hull optimization" is widely used and in many cases abused. Often the term "improvement" would be more appropriate than "optimization". Our interpretation of "hull optimization" has changed over time. We distinguish here "optimization" from "improvement":

- Simulation-based hull improvement is commonly employed in industry. In this design approach, a few (typically less than 20) hull variants are generated and assessed by computational fluid dynamics (CFD) and/or model tests. This is standard design procedure and employed by many model basins, but frequently we see in our experience that significant improvement beyond this approach is possible.
- (Formal) optimization looks at thousands or even tens of thousands of designs and uses an optimization algorithm to find the best design.

See our COMPIT paper, [6], for an extensive discussion of ship hull optimization and its historical development to the present state of the art. In their outlook for the (near) future, the authors discuss further potential for improvement in current ship hull optimization practice. A key aspect in this respect is the consideration of the ship's actual operational profile instead of just one design (or contract) point. A "point" in this respect is the combination of load condition and speed. Ships are frequently operated at lower speeds or partial drafts (with varying trim angles). The design should then strive for a "best" compromise between these conditions, yielding e.g. the lowest yearly fuel costs (for a given ship size). We will present here a recent industry application which gives insight into how significant the improvements can be following this approach, even when starting from state-of-the-art first-class designs.

The key to unlocking the theoretical potential lies often with the ship owner and the building specifications. In the presented case, the Hamburg based ship owner Hamburg-Süd followed its long tradition of using avant-garde technology to maintain a highly competitive fleet; the company was among the first to see the potential in having its ships optimized for the actual operational profile. The final significantly higher fuel efficiency of the new designs was the result of a fruitful cooperation between ship owner, shipyard and FutureShip as service provider in ship optimization.

2 OPTIMIZATION OF A LARGE CONTAINERSHIP

2.1 Challenging starting point

Hamburg-Süd wanted to improve on its fleet of large container vessels operating between Europe and South America. The envisioned new vessel was designed for 9600 TEU capacity and a service speed of 21 knots. The ships were to be built at a major Korean shipyard, but as fuel efficiency had become a key issue for survival in fierce market competition, Hamburg-Süd wanted the new design optimized for fuel consumption, not for an artificial contract point, but for the actual operational profile on the trade.

2.2 Global optimization process

The starting point of the optimization was a parametric hull description using the FRIENDFSHIP-Framework. The containership hull was described using 86 free form parameters (44 for the forebody and bulb, 39 for the aftbody and skeg, 3 for the bilge shape) for hull form variation, Fig.1. The form parameters defined, for example:

- Shape of basic curves (centre plane curve, flat of bottom, transom edge, etc.)
- Length overall, length between perpendiculars
- Flare angles of surfaces along basic curves
- Bulbous bow shape, length and height
- Stem angle
- Waterline entrance angle
- Parallel midbody length
- Bilge shape
- Transom edge height
- ...

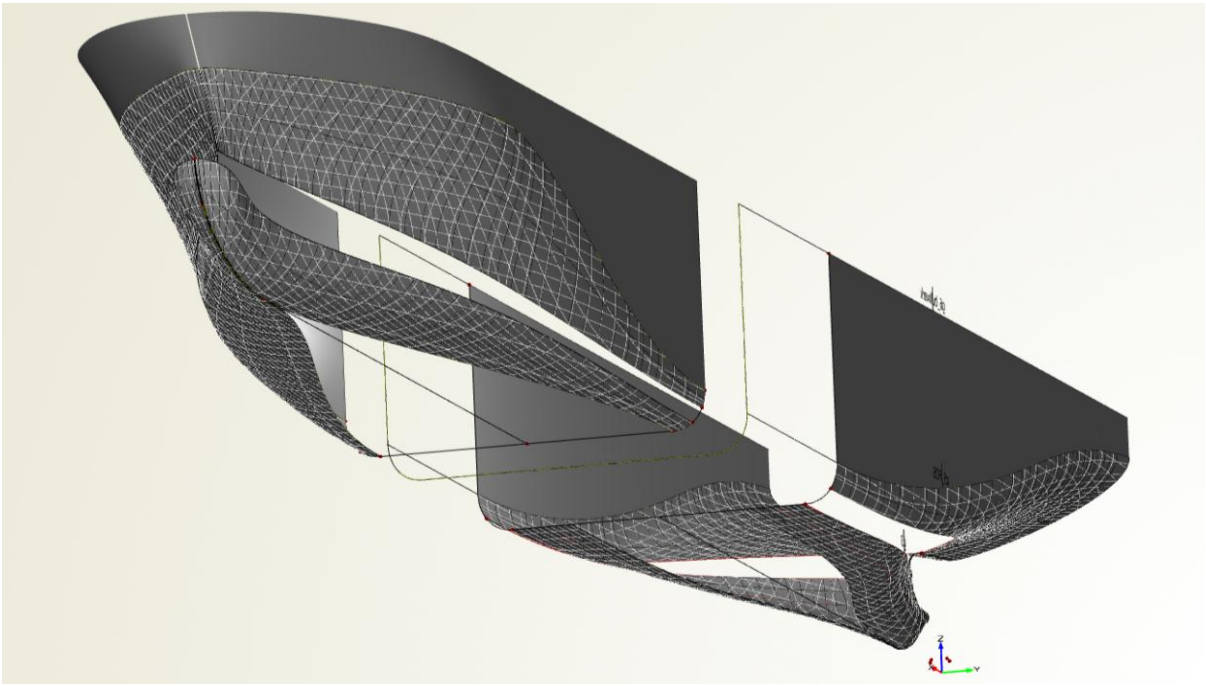


Figure 1: Parametric hull description

Geometrical constraints were specified by the shipyard. These concerned bow flare, clearance for propeller and rudder, and hard points for the engine in the aftbody. In addition, there were indirect geometry constraints: displacement volume and metacentric height should not be lower than in the baseline design.

Hamburg-Süd supplied records of actual operational data for a fleet of seven ships for the whole year 2010. This database of speeds and drafts was condensed to four representative clusters of speed-draft combinations with associated weights ranging between 20 and 30%. The objective was then to reduce the combine fuel consumptions for these four operational states, considering their time share in yearly operation.

A global hull optimization was performed using a fast, simplified hydrodynamic assessment of the generated hull variants. The potential flow solver FS-Flow computed the wave resistance. This fully nonlinear wave resistance code captures the dynamic trim and sinkage iteratively. The viscous resistance was approximated by a semi-empirical friction line, but considering the actual wetted hull surface and local Reynolds numbers, thus capturing directly some of the effects of hull changes on the viscous pressure resistance. The propeller thrust was simulated by a propeller body force model. Such a simplified hydrodynamic model allows exploring a vast number of possible designs. But it also requires an indirect and approximate formulation of the objective function, as a direct estimation of the power (and thus fuel consumption) with reasonable accuracy is not feasible. For the purpose of a first global selection, we then formulate several objectives that address partial aspects of good resistance and propulsion:

- wave pattern resistance
- maximum crest-to-trough wave height along the ship hull
- hydrodynamic fairness parameter along the hull
- wake homogeneity parameter
- wake number

In a refinement of the hull optimization, only the aftbody was modified and the hydrodynamic assessment used a high-fidelity CFD code, solving the Reynolds-averaged Navier-Stokes equations (RANSE), thus capturing viscous effects directly in the simulation.

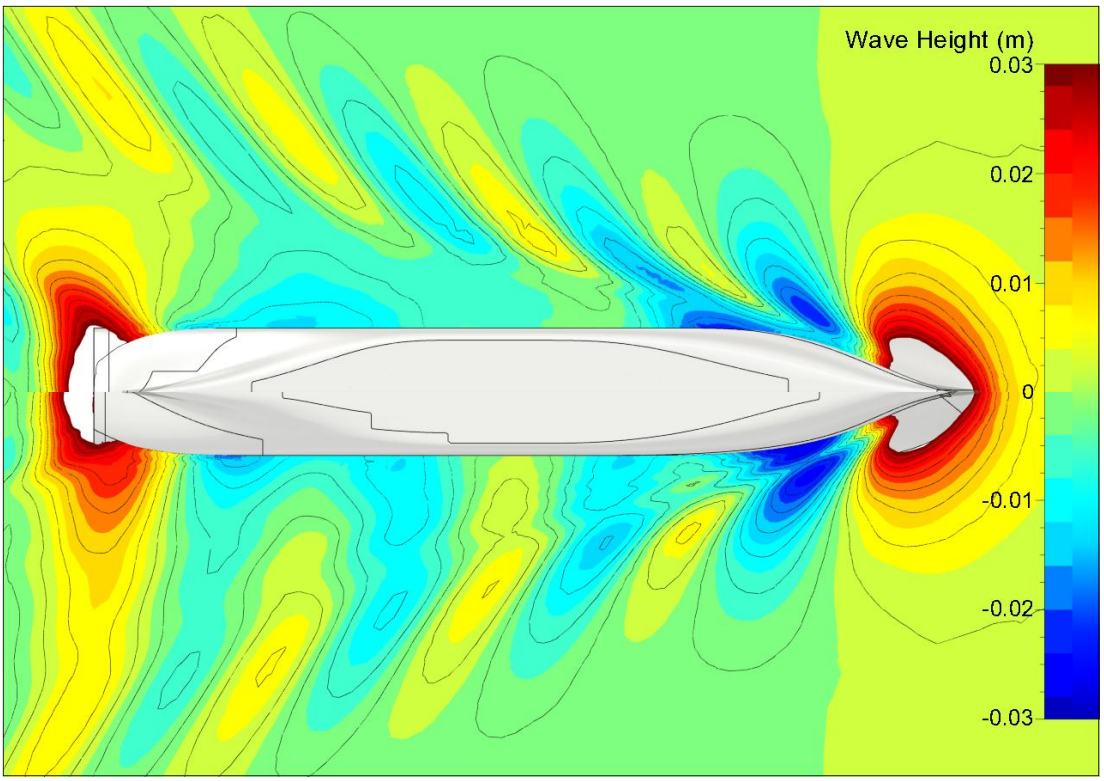


Figure 2: Wave patterns for one operational condition; baseline (top) and optimized design (bottom)

Fig.2 compares for one operational condition the computed wave patterns of the baseline design and our optimized design. Fig.3 gives the corresponding pressure distributions on the hull. The relatively small differences in wave and pressure patterns translate into significant fuel savings. For this particular operational condition, the required power for FutureShip's optimized hull was 6.5% lower than for the baseline.

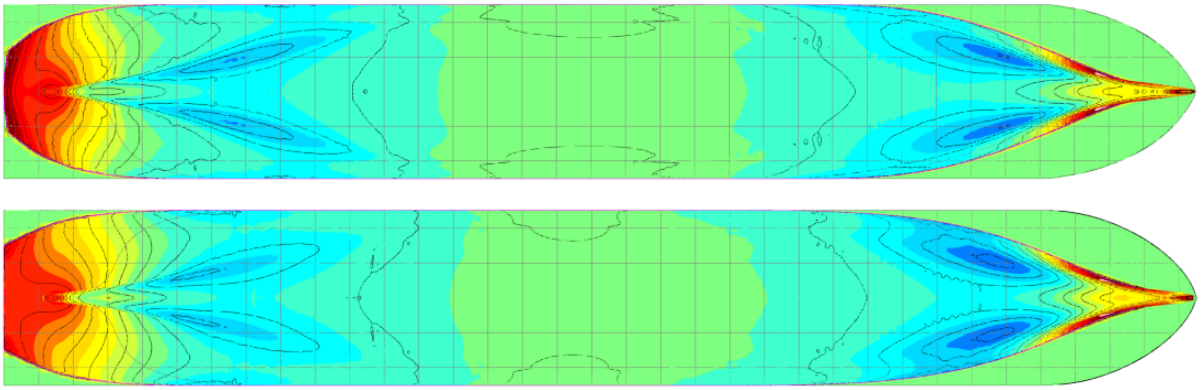


Figure 3: Pressures on hull for one operational condition; baseline (top) and optimized design (bottom)

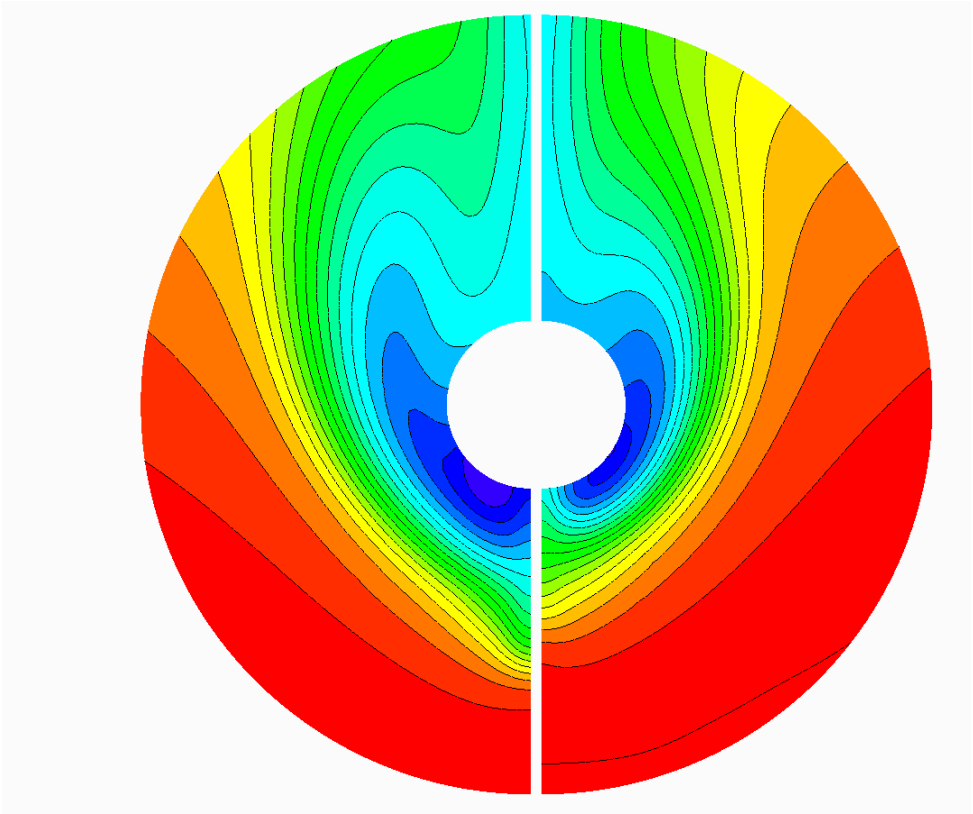


Figure 4: Wake for one operational condition; baseline (left) and optimized (right)

Fig.4 compares the wake distributions of baseline and optimized ship. The optimized wake features a less pronounced hook and a generally more even wake distribution. Correspondingly the wake fraction was reduced from $w = 0.335$ (baseline) to $w = 0.269$ (optimized). The more homogeneous wake distribution will also reduce the risk of cavitation.

2.3 Validation

For final validation, professional model tests were conducted at Hamburg Ship Model Basin, Fig.5. The baseline design and FutureShip's optimized design were tested under same conditions and full-scale predictions followed the general guidelines. The model tests confirmed that FutureShip's design outperformed the baseline design on all conditions of the operational profile. Based on the model tests, the optimized hull design will save 3.7% for the specified mix of operational profiles.



Figure 5: Model tests at HSVA validated the predicted savings

3 KEY SOFTWARE ELEMENTS FOR THE OPTIMIZATION

Formal hull optimization with associated constraints requires suitable tools for assessment, optimization and process control. Below the tools used by FutureShip in this project are briefly described:

- Optimization and process control (FS-Optimizer)

  FS-Optimizer is a generic optimization toolkit for simple set-up of tailored applications, combining a selection of arbitrary analysis programs (needed for objective

functions and constraints), applying a variety of methods for designs space exploration and formal optimization. Constraints can be included and monitored during the optimization. The program has a graphical interface and can also be run in batch mode for time consuming numerical computations on main frame computers. The program can run in unlimited threading mode to make full use of parallel computing environments like HPC (high performance computing) clusters. Advanced users may incorporate own algorithms to control the optimization while still taking advantage of the file and directory handling provided by FS-Optimizer.

- Parametric design modeler (FRIENDSHIP-Framework)

  The FRIENDSHIP-Framework is a Computer Aided Engineering (CAE) system, integrating geometric modeling, simulation, systematic variation, and formal optimization in the design of ships and turbo-machinery. Its parametrically oriented platform conveniently allows modeling complex geometries (e.g. ship hull or propeller) by a selection of high-level shape descriptors. A typical scenario is that longitudinal properties of the sections are modeled by fairness optimized B-spline curves. We employ the FRIENDSHIP framework as standard geometry modeler.

- Fully nonlinear wave resistance code (FS-Flow)

  FS-Flow is a nonlinear wave resistance code, based on a Rankine panel method. The in-house code has special interfaces with the other tools discussed. FS-Flow uses a panel representation of the hull (including lifting surfaces if applicable) and a portion of the free water surface. The source strength on each panel is adjusted to fulfill the various boundary conditions, namely zero normal velocity on the hull and kinematic and dynamic boundary conditions on the water surface. Lifting surfaces like keel, rudder and fins (e.g. in case of sailing yachts or stabilizer systems) are modeled in FS-Flow by lifting patches which carry in addition to the source panels also a dipole distribution, enforcing a Kutta condition at the trailing edge. The ship's dynamic floating position and the wave formation are computed iteratively. After each iteration step, the geometry of the free surface is updated and the sinkage, trim, heel and propeller thrust of the vessel are adjusted. The calculations are considered to be converged when all forces and moments are in balance and all boundary conditions are fulfilled. Having determined the source strengths, the pressure and velocity at each point of the flow field can be calculated. The wave resistance can be either computed by integrating the pressure over wetted surface of the hull or from wave pattern analysis, [7]. FS-Flow is based on potential flow theory. Most viscous effects (such as a recirculation zone at the stern) and breaking waves cannot be modeled correctly.

- Viscous CFD code (FS-Foam)

  FS-Foam solves the (Reynolds averaged) Navier-Stokes equations (RANSE). It is based on the open-source CFD package OpenFOAM. The free-surface modeling is

based on the Volume-of-Fluid (VOF) method (interDyMFoam). The domain is discretized using the Finite Volume Method (FVM). OpenFOAM also provides a solver to integrate the equations of motions for six degrees of freedom (sixDoFsolver). We have combined those features to an integrated solver, which can simulate steady viscous flow around a ship including dynamic trim and sinkage.

- Ship stability software (FS-Equilibrium)

  FS-Equilibrium is a workbench for analysis of equilibrium conditions of floating bodies in six degrees of freedom. Typical applications are all types of hydrostatic analysis. Due to its modular setup, the code is easily adapted to work for a specific design problem. An application programming interface (API) is available for optional user-defined modeling of forces. For the task at hand only a small subset of the functionality was employed to monitor the changes of hydrostatic properties due to the hull shape changes.

4 CONCLUSIONS

A systematic formal optimization for a 9600 TEU container vessel was undertaken, considering a representative spectrum of operational conditions rather than a single design point. The baseline design was a professional Korean shipyard design derived by state-of-the-art simulation-based design and model tests. The optimization analyzed the performance of several thousand design variants striving to minimize the overall (yearly) fuel consumption for actual operational profiles. The optimized design was tested in an independent ship model basin which confirmed significant fuel savings just short of 4%.

REFERENCES

[1] Bertram, V., Fach, K., Sames, P., and Höppner, V. Engineering options to reduce emissions. *10th Int. Marine Design Conf. (IMDC),* Trondheim (2009).

[2] Bertram, V., Höppner, V., and Fach, K. Intelligent engineering options for highly fuel-efficient fishing vessels. *1st Symp. Fishing Vessel Energy Efficiency*, Vigo (2010).

[3] Bertram, V. and Vordokas, H. Reducing fuel consumption in moderately fast displacement ships. *6th Conf. High-Performance Marine Vehicles (HIPER)*, Melbourne (2010).

[4] Hochkirch, K. and Bertram, V. Fluid dynamics options for reducing CO2 emissions. *7th Green Ship Technology Conf.*, Copenhagen (2010).

[5] Buhaug, Ø., Corbett, J.J., Endresen, Ø., Eyring, V., Faber, J., Hanayama, S., Lee, D.S., Lee, D., Lindstad, H., Markowska, A.Z., Mjelde, A., Nelissen, D., Nilsen, J., Pålsson, C., Winebrake, J.J., Wu, W.Q., Yoshida, K. *Second IMO GHG study 2009*. Int. Maritime Organization (IMO). London (2009).

[6] Hochkirch, H. and Bertram, V. Hull Optimization for Fuel Efficiency – Past, Present and Future. *11th Conf. Computer and IT Applications in the Maritime Industries (COMPIT),* Liege (2012). pp.39-49.

[7] Heimann, J., Hutchison, B.L. and Racine, B.J. Application of the free-wave spectrum to minimize and control wake wash, *SNAME Annual Meeting & Expo*, Houston (2008).

V International Conference on Computational Methods in Marine Engineering
MARINE 2013
B. Brinkmann and P. Wriggers (Eds)

ROBUST DESIGN OPTIMIZATION OF A MONOHULL FOR WAVE WASH MINIMIZATION

Daniele Peri*, Matteo Diez*

*CNR-INSEAN - Maritime Research Center
Via di Vallerano, 139 - 00128 Roma, Italy
e-mail: daniele.peri@cnr.it, web page: http://www.insean.cnr.it

Key words: Ship Design Optimization, Robust Design Optimization, Marine Engineering

Abstract. In this paper the robust optimization of a monohull for the reduction of the wave impact on the shoreline is described. Single and multi-objective techniques are considered in order to compare different approaches to the same problem. Robust Design Optimization (RDO) techniques are considered with two different formulations of the problem (deep water and shallow water) in order to give evidence of the importance of the consideration of variable operating conditions of the ship.

1 INTRODUCTION

Great attention is payed nowadays to a number of different implications of the impact of the human activities on the environment. Under this perspective, specific rules are currently under discussion in order to force ship designers in considering strictly some constraints on CO_2 emissions. But there are also some other aspects, not specifically covered by dedicated international rules, that needs to be considered seriously.

One of them is the impact on the seashore of the wave pattern produced by the passage of a ship while traveling in the vicinity of the coastline. The erosion caused by the recursive operation of a ship in proximity of the coast may be great, as illustrated in figure 1, where the effects of the constant passage of a fast ferry are evident. Some local authorities have specific rules, but there is not yet a global agreement on this topic.

In this paper, some numerical optimization studies are presented in order to reduce or eliminate the damages potentially connected with the wave pattern of a monohull traveling in proximity of the seashore. Methodology for the quantification of the potential damage is presented in the next section, together with the numerical methodology adopted for the determination of the far field generated by a ship traveling at constant speed are discussed. Numerical optimization tools are also described, and presentation of results follows.



Figure 1: Effect of the passage of a fast ferry in proximity of the shoreline. **On left:** initial status. **On right:** same location after 6 months after the fast ferry starts its service.

2 QUANTIFICATION OF THE POTENTIAL DAMAGE CAUSED BY A WAVE PATTERN

The first problem to solve in the reduction of the effects of wave wash is related to the methodology for the evaluation of the potential damage. In fact, there is not a clear correlation between the effects and the wave pattern. Towing tanks are typically too small in order to produce dedicated experimental tests, so that the full scale experiments are usually conducted, but isolation of the contribution of a specific source is not easy.

Starting form a large number of experimental campaign, the Danish Maritime Authority has released a criterion to be fulfilled by a ship operating in proximity of the coast along the entire route. The criterion, reported in [6], is formulated as

$$H_h \leq 0.5\sqrt{\frac{4.5}{T_h}} \tag{1}$$

where H_h is the maximum wave height (in meters) of the long-periodic wave, having a time period of T_h (in seconds). Criterion is applicable to a water depth of 3 meters. Complete description of the criteria and reasons for the formulation are also reported in [6].

Other criteria, reported in [7], are expressed in term of radiated energy, and two different criteria are provided for deep and shallow water. In deep water, the criterion is

$$E = \frac{\rho g^2 H^2 T^2}{16\pi} \tag{2}$$

while for shallow water the criterion is

$$E = \frac{\rho g^2 H^2 \lambda}{8} \tag{3}$$

where λ is defined as

$$\lambda = \frac{9T^2}{2\pi}\texttt{tanh}\left(\frac{2\pi H}{L_W}\right) \tag{4}$$

where T is the wave period, L_W is the wave length and H the wave height. Between the two different criteria, the one described in [6] has been applied in the following, since the criteria is specifically developed for high-speed ferries, which is the subject of the following computations.

3 APPROACH

Being the wave pattern the main element to be determined in order to evaluate the impact on the shore using the selected formulation, a potential solver for inviscid flows has been adopted in this case. Same code has been successfully applied on similar problems in [4].

The necessity to evaluate the far field generated by the ship passage implies a really large computational domain to be considered, and this requirement could be not practical also for a simple potential solver, due to the large portion of free surface to be included into the simulation. As a consequence, a far field extrapolation has been obtained starting from the simulation of the near field only. The formulation adopted in the following is described in [10]. Theory is derived for the shallow water problem, and the deep water problem is obtained as a particular case. From the extrapolation of the wave field, a longitudinal wave cut is produced, and the spectrum in the frequency domain is obtained. Wave heights are compared with the limit curve obtained from [6], and the verification of the constraint is checked.

The criterion provides a limit curve that is supposed to include the results from the wave spectrum analysis (upper limit). The area of the portion of the curve exceeding the limit curve is adopted as an indicator of the potential damage associated to the analyzed wave pattern. If the constraint is satisfied, the minimum distance from the limit curve is assumed as indicator: this is in order to give a numerical evaluation of the designs not exceeding the limit curve.

4 SINGLE OBJECTIVE UNCONSTRAINED DETERMINISTIC OPTIMIZATION

In order to obtain some general tendencies, a single objective optimization problem has been set up and solved. No geometrical constraints have been adopted, in order to observe the extreme trends.

First element of the setup of the optimization problem is the determination of a parameterization of the hull geometry. Rather than producing a dedicated parameterization of the selected hull form, a space deformation approach has been adopted. A parallelepiped including the selected geometry has been divided into a selected number of slices, parallel to the three principal planes of a cartesian reference system. Each vertex obtained by the

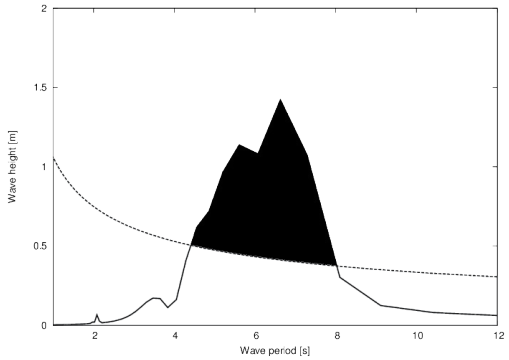


Figure 2: Criterion for the evaluation of the potential damage caused by wave pattern: measure of the black area between the limit curve provided by the criterion reported in [6] and the frequency analysis of the longitudinal wave cut gives the numerical estimate of the wave was indicator.

intersection of the generated planes represents a potential control points for the deformation of the space embedded by the parallelepiped. Some of the control points are fixed, other can move along prescribed directions. The methodology for the deformation of the embedded portion of 3D space is currently referred as Free Form Deformation (FFD), proposed and described in [9]. In figure 3 an example of deformation of the original hull shape adopted in this paper is depicted. 7 design variables have been adopted for the hull deformation. One moves vertically the lower part of the bow, one moves vertically the stern, one is moves longitudinally the central section while 4 other parameters are deforming laterally the hull. Some vertexes are linked together in order to preserve the fairness of the hull.

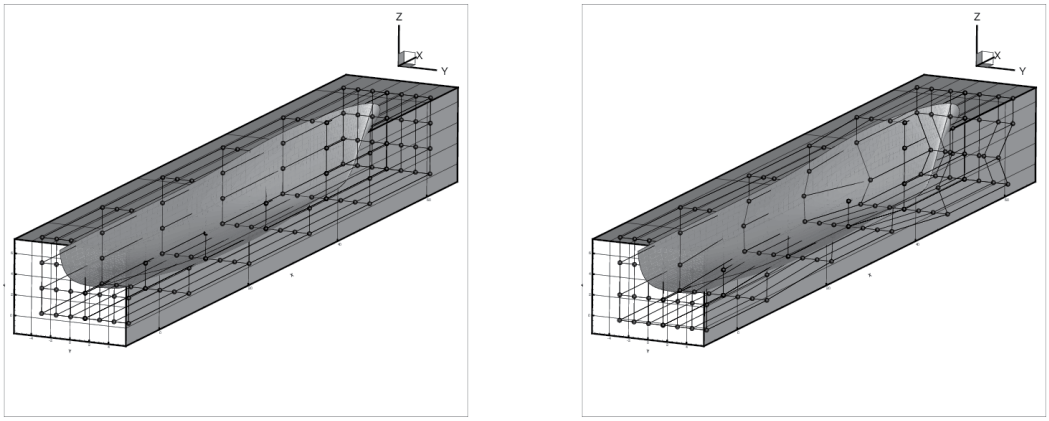


Figure 3: **On left:** FFD parameterization for the original geometry. **On right:** deformation of the original geometry as per the deformation of the FFD net.

A second element is represented by the optimization algorithm. In this first example, the classical non-linear simplex algorithm is adopted [8]. Although a complete global convergence demonstration does not exists, and some counterexamples are well known in literature, the algorithm is pretty efficient and it is also able to naturally manage the small roughness typically connected with numerical simulations, so that the algorithm is rarely trapped into false local minima created artificially by the inaccuracies in the objective function determination. The use of the simplex algorithm has been dictated by the final goal of observing the trends rather than producing the best possible shape. By the way, no geometrical constraint is applied: as a consequence, the final shape could be well away from satisfying criteria of acceptance for construction.

A third element is the set of constraints to be satisfied by the optimal design. As anticipated, in this case the only constraint is the total displacement, fixed to the original value. The prescribed value of the displacement has been obtained by changing the draught of the ship, so that all the configurations considered during the optimization problem solution are feasible.

The last element is the objective function: the optimization has been performed to minimize the measure of the impact of the wave pattern, that has been perviously described and is illustrated in figure 2. We will refer to it in the following as "wave wash indicator". In this case, the objective function is computed for a single speed, that is, Fr=0.5. The extension of the analyzed free surface portion is 2 ship length in lateral and longitudinal direction. Last part of the analyzed wave field is the input for the extrapolation of the far field, and a longitudinal wave cut is obtained at a lateral distance of 3.5 ship length. Extrapolation is produced for a lateral distance on 15 ship lengths and for a lateral distance on 10 ship lengths. This last is also the length of the extrapolated longitudinal wave cut analyzed in order to derive the wave wash indicator.

In figure 4, the solution of the single-objective optimization problem is presented. On left part of figure 4, the limit curve is presented together with the wave spectra of the original and optimized hull shapes. Dotted line is representing the wave spectrum of the original hull shape, while the dashed line is representing the wave spectrum of the optimal hull shape. Limits for the computed and extrapolated free surface portions are also represented in the right part of figure 4 together with the estimated and extrapolated wave patterns. A change in the wave frequencies associated with the wave patterns is evident from the comparison presented in the left part of figure 4, reflected also in the shape of the wave pattern reported in the right part of the same figure. High frequency content is increased, since the criterion is more permissive in that area. The criterion is not completely fulfilled, but the nearly complete elimination of the more dangerous part of the wave pattern is evident.

5 ROBUST OPTIMIZATION

During the design phase, the operative conditions of a ship are typically defined fixing strictly the speed of advance, sometime considering a (limited) number of design speeds.

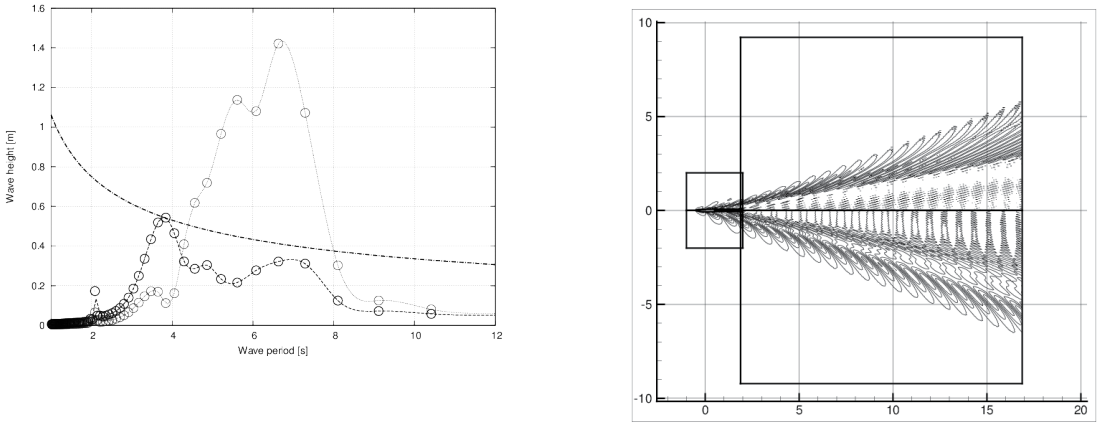


Figure 4: **On left:** Comparison between original and optimal wave field analysis. Optimization is here unconstrained, in order to give perspective on the trends. **On right:** wave field before (bottom) and after (top) the optimization. Computed wave field boundaries and extrapolated wave field boundaries are also reported. Unit length in this last graph is L_{PP}.

As a consequence, the design problem is including one or at least few speeds, so that the more complex case involves the formulation of a multi-objective optimization problem, considering some relevant objectives at the various design speeds. Unfortunately, in real life the ship is traveling in rough seas, with variable loading conditions etc., so that doesn't operate exactly at design speeds. As a consequence, it is more appropriate ti use a formulation in which the optimization is performed for a range of stochastic speeds. This is what is usually done in "Robust Design Optimization" (RDO). Examples for the naval field are reported in [2] and [3], where also a rigorous formulation and definition of RDO is provided.

In RDO, the input is assumed together with its probability density function, and the objective functions are typically some quantities derived from the statistical analysis of the output: this way, a probabilistic scenario for the ship is assumed, and the optimization is taking into account this situation. Commonly the expected value or the variance of the objective functions are optimized, in order to obtain a low value of the output expectation or a small variation of it. If no elements about the probability density function are available, due to the absence of a statistical analysis of the input, some assumptions can be made: if a constant value is assumed, the implicit hypothesis is that all the speeds in the selected interval have the same probability of occurrence during the lifetime of the ship.

In this example, the expected value of the wave wash indicator has beed optimized under the assumption for the Froude number to be uniformly distributed in the interval [0.4:0.6]. As a second objective, the expected value of the total resistance is considered with the same interval of variation of the Froude number and the same probability density function. The expected value is computed though the evaluation of the integral of the

objective function, using the definition

$$\mu = \frac{\int_{0.4}^{0.6} F(Fr) dFr}{\Delta Fr}$$

where $F(Fr)$ can be the total resistance or the wave wash indicator. The integral has been evaluated by using a Gauss quadrature formula with 5 points. Former convergence study for this integral demonstrated that with 5 integration points the integration error, for the original hull configuration, is lower than 1% of the converging value of the integral for both the objective functions.

Due to the multi-objective nature of the optimization problem, a different optimization algorithm is here applied: Particle Swarm Optimization (PSO) has been selected due to their efficiency and effectiveness [1]. It may be noted that, while the standard formulation of PSO adopted in literature uses random coefficients, in [1] a fully deterministic version of the algorithm is introduced. Same parametrization as per the previous deterministic optimization problem has been adopted: 7 design variables are to be optimized in order to find the optimal hull shape. The swarm is composed by 4×NDV elements, where NDV is the number of design variables. Algorithm is stopped after 2800 evaluations of the objective function. A parallel machine with 288 cores has been utilized for the solution of this problem.

In order to produce realistic hull shapes, a further geometrical constraint has been added to the previous formulation, where a single equality constraint on the displacement has been enforced. Constraint is applied to the moving vertexes of the FFD box, whose displacement is limited to 1 meter, in ship scale. As a consequence, the results will be not comparable with the ones of the previous single objective problem.

Two different water depths have been considered in two separate optimization problems: 10 meters of water depth and infinite depth. For those two conditions, two different Pareto fronts have been derived. In order to give visual results, the best for each of the two objective functions have been extracted from each Pareto front. The 4 geometries, two for each optimization problem solution, are reported in figure 5, in comparison with the original geometry, reported with dashed lines. A vertical translation has been applied to the optimal hull shapes in order to compare at the same displacement, since the constraint has been enforced by changing the draught. For all the optimal shapes, a common factor is the change of the bow part of the hull, with an increase of the volumes in the lower front part. This is partly a similitude with the AXE-bow proposed in [5]. A vertical shift at the transom stern is suggested in all the cases: it appears to be larger in the case of the total resistance than for the wave wash. Width of the transom at the waterline is increased accordingly. Another common aspect is the increase of the waterline length, obtained as a side effect of the bow changes, while overall length is unchanged. Beam at the waterline is decreased for all the optimal hulls, with a grater emphasis for the optimal hulls for total resistance. As a consequence, waterline is more straight for the optimal

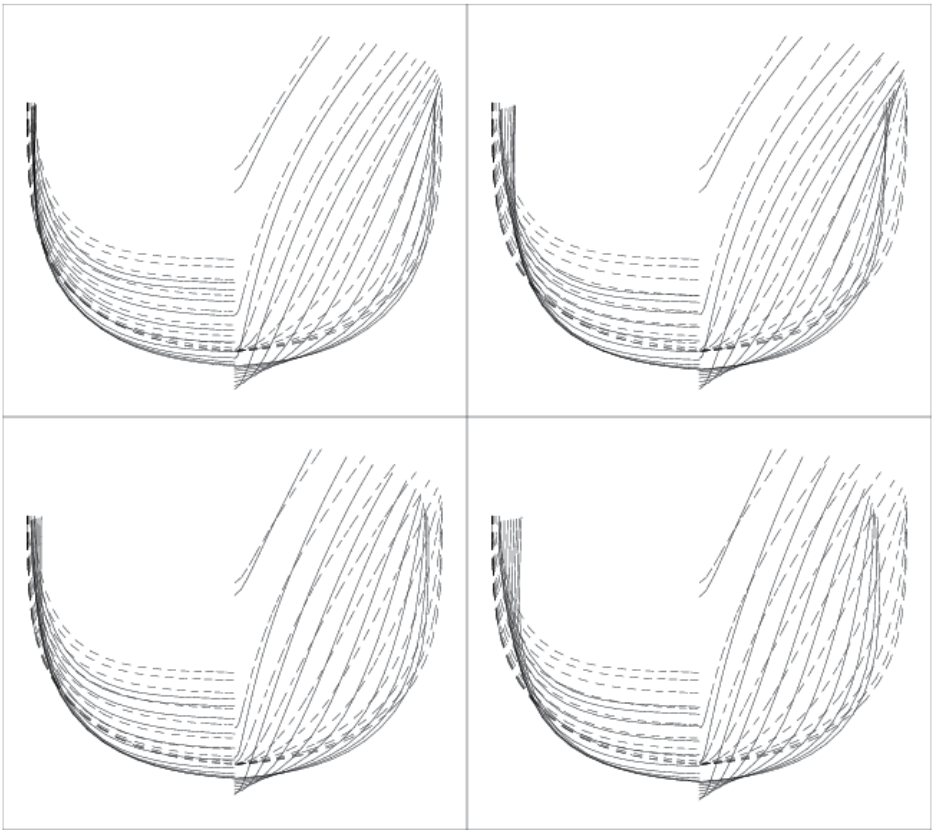


Figure 5: Four different optimal configurations for the two different objectives and for the two different depth. **On the left column:** optimal for the wave wash. **On the right column:** optimal for the total resistance. **On top:** shallow water condition. **On bottom:** deep water condition.

hull for total resistance (reduced beam and increased transom width).

The observation of the Pareto front for both deep water and shallow water conditions reveals how the shallow water condition is much more severe for the total resistance. In fact, while the range of the wave wash indicator is substantially unchanged for the two Pareto fronts, the width of the total resistance axis is greater for the shallow water condition. This indicates a larger increase of the total resistance while the wave pattern impact is reduced.

In figure 7 the variations of the total resistance and the wave wash indicator (the area exceeding the wave wash limit curve, as illustrated in figure 2) over the investigated Froude number interval is reported. It is interesting to observe how the wave wash indicator is increased for hull shape that is optimal for the total resistance in both shallow and deep water conditions, while the total resistance is always improved, also for the hulls that are optimal for the wave wash.

Looking at the deep water condition only, the best hull for total resistance is not the

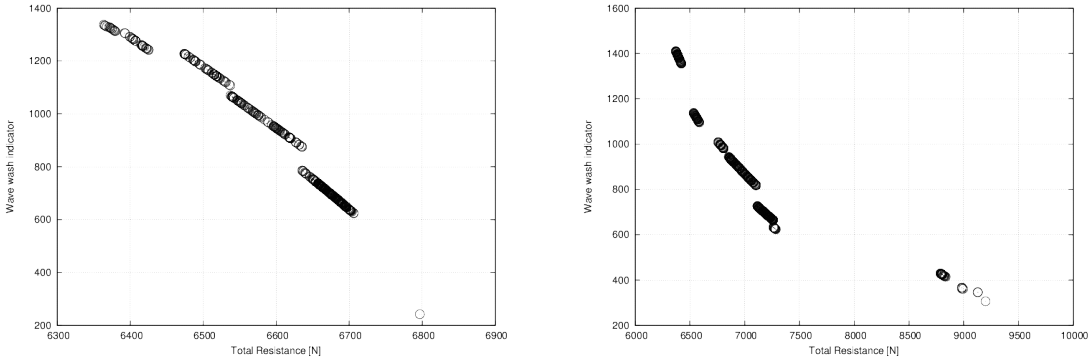


Figure 6: Pareto front for the two different bottom conditions considered. **On left:** deep water condition. **On right:** shallow water condition.

best for this criterion along the entire investigated Froude range, but it is the best on average. Best hull for wave wash is behaving better in the lower Froude number range, but the improvement provided by the optimal hull in the higher Froude number range are larger, so that the performances are on average better. The measure of the improvement is provided by the area under the two curves. In all the other conditions, there is a clear dominance of one hull above the other.

In figure 8 the extrapolated wave patterns are reported for all the four different hull shapes. For all the configurations, wave height is reduced with respect to the original hull for the configurations that are optimal for the wave pattern, while the configurations optimal for the total resistance have a larger wave height. This situation is more evident if the frequency domain analysis of the longitudinal cuts is observed. Results are reported in figure 9. Here the increases of the wave height for the hull shapes providing optimal total resistance values are evident. On the contrary, hull with reduced wave wash have a smaller wave height. A shift of the wave spectrum in the frequency domain is observed, with different characteristics in shallow and deep water conditions. In fact, while for the shallow water conditions there is a clear shift of the spectrum toward the higher frequencies, for the deep water there is an increase of the range of frequencies for which the criterion is not fulfilled, but with a lower peak wave height.

6 CONCLUSIONS

A methodology for the improvement of the hull shape performances in order to reduce the impact of the generated free surface waves has been presented and tested. Results are demonstrating the usefulness of the approach. Further application to more specific and practical design problems will be able to provide more elements for completing the analysis.

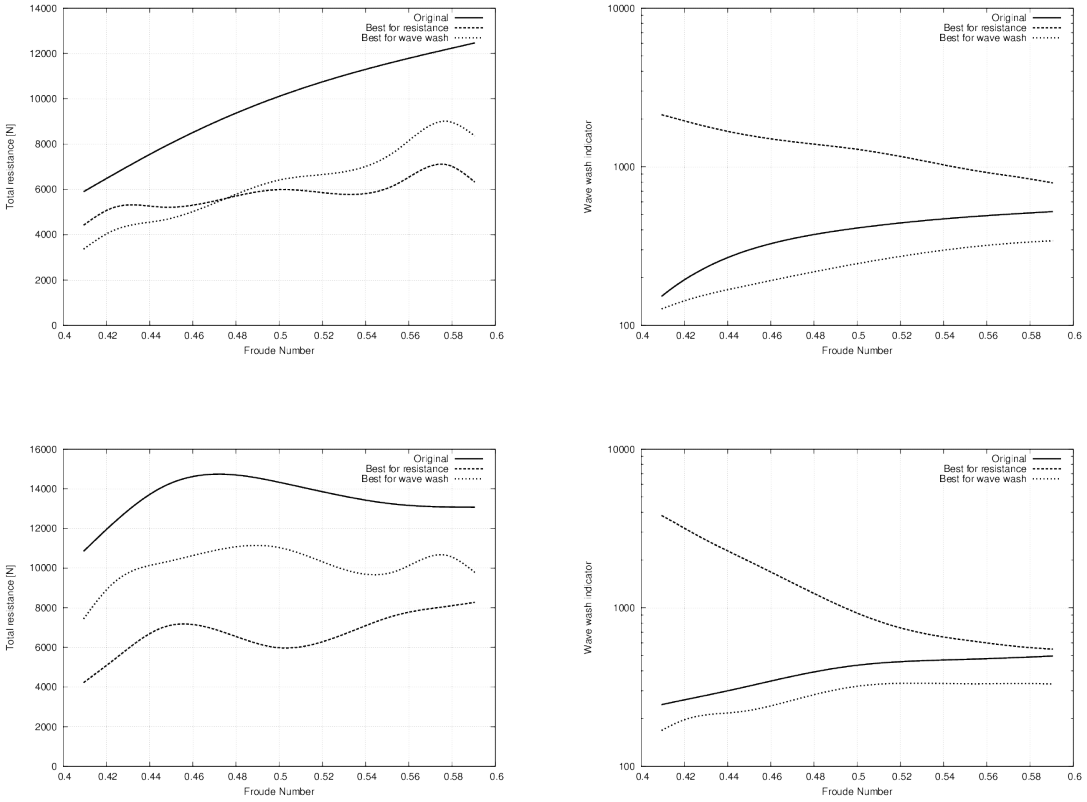


Figure 7: Objective functions for the different optimal conditions considered. **On left:** total resistance in the investigated Froude numbers range. **On right:** wave wash indicator in the investigated Froude numbers range. **On top:** deep water condition. **On bottom:** shallow water condition.

ACKNOWLEDGMENTS

This work has been partly funded by the Flagship Project RITMARE - The Italian Research for the Sea - coordinated by the Italian National Research Council and funded by the Italian Ministry of Education, University and Research within the National Research Program 2011-2013.

REFERENCES

[1] Campana, E.F., Fasano, G., Peri, D., Globally convergent modifications of Particle Swarm Optimization for Unconstrained Optimization, book chapter in *Particle Swarm Optimization: Theory, Techniques and Applications*, Nova Publishers, Series: Advances in Engineering Mechanics (Series Editor: Dr. Bohua Sun), 2012.

[2] Diez, M., Peri, D., Robust optimization for ship conceptual design, *Ocean Engineering*, Volume 37, Issues 11-12, Pages 966-977, August 2010.

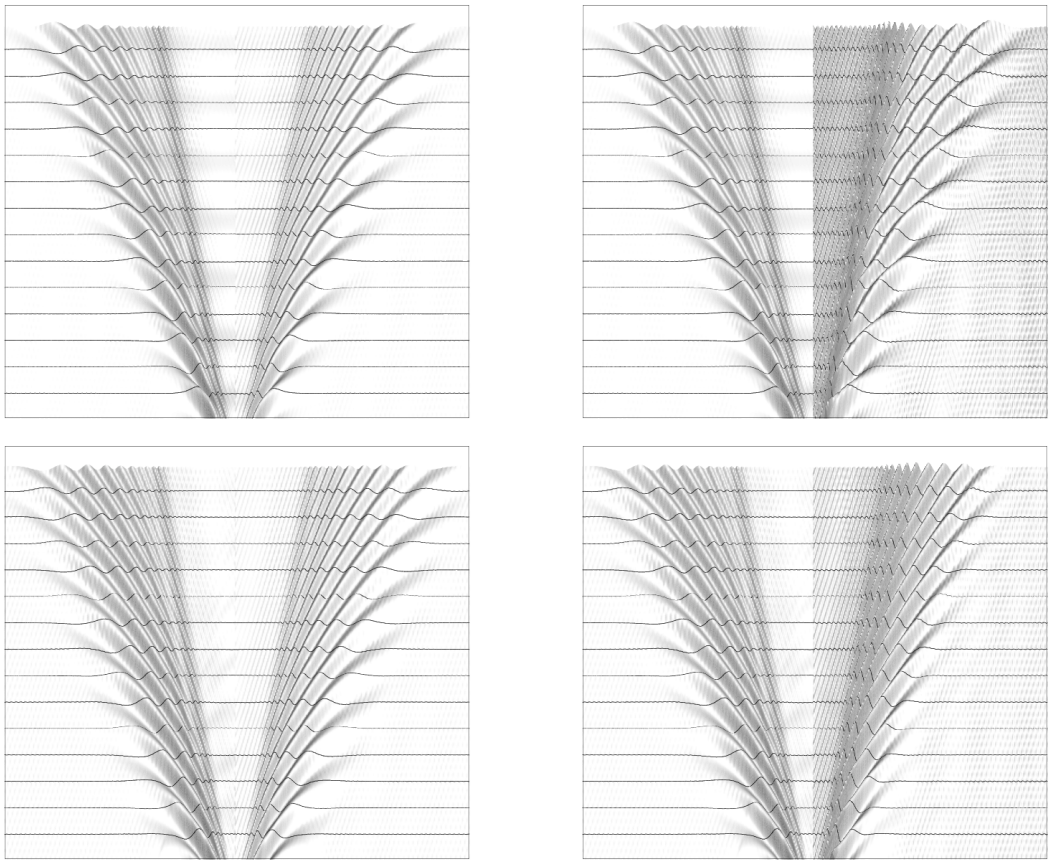


Figure 8: Wave pattern the different optimal conditions considered. For each sub-picture, left part represents the original hull, right part the optimal hull. **On left:** best for wave wash. **On right:** best for total resistance. **On top:** deep water condition. **On bottom:** shallow water condition.

[3] Diez, M., Peri, D., Optimal Hull-Form Design Subject to Epistemic Uncertainty, *Ship Technology Research*, Vol. 59, No. 1, Pages 14-20, January 2012.

[4] Kandasamy, M., S. Ooi, K., Carrica, P., Stern, F., Campana, E.F., Peri, D., Osborne, P., Cote, J., Macdonald, N., de Waal, N., Multi-fidelity optimization of a high-speed foil-assisted semi-planing catamaran for low wake, *Journal of Marine Science and Technology*, vol. 16 (2), pp. 143-156, Springer, 2011.

[5] Keuning, J.A., Pinkster J., Van Walree, F., Further Investigations into the Hydrodynamic Performance of the AXE Bow Concept, In *Proc. of the 6th Symposium on High Speed Marine Vehicles* (WEMT 2002), Castello di Baia, Italy, pp II 25-II 38, 2002.

[6] Kirkegaard, J., Kofoed-Hemsen, H. and Elfrink, B., Wave Wash of High-Speed Craft in Coastal Areas, In *Proceedings of 26th Conference on Coastal Engineering*, Copen-

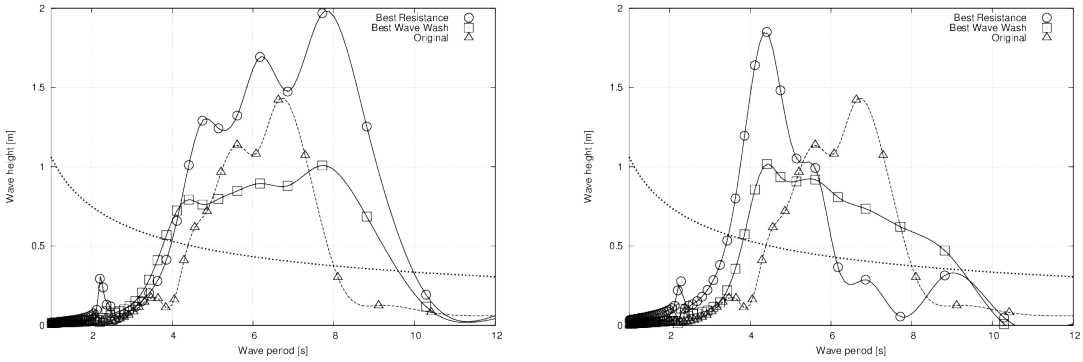


Figure 9: Fequency domain analysis of the longitudinal wave cut for the original and optimized hull shapes. **On left:** deep water condition. **On right:** shallow water condition.

hagen, Denmark, 1998.

[7] Molland, A.F., Turnock, S.R. and Hudson, D.A., Ship Resistance and Propulsion, *Cambridge University Press*, 2011.

[8] Nelder, J. A., R. Mead, A simplex method for function minimization, *Computer Journal*, 7: 308-313, 1965.

[9] Sederberg, T.W., Parry, S.R., Free-form deformation of solid geometric models, In *Proceedings of ACM Siggraph Computer Graphics*, Vol. 20, N. 4, Dallas, USA, August 18-22, 1986.

[10] Soding, H., Far Field Ship Waves, *Ship Technology Research*, V. 53, 138-147, 2006.

V International Conference on Computational Methods in Marine Engineering
MARINE 2013
B. Brinkmann and P. Wriggers (Eds)

OPTIMIZATION OF A CHEMICAL TANKER AND PROPELLER WITH CFD

AUKE VAN DER PLOEG AND EVERT-JAN FOETH

Maritime Research Institute Netherlands (MARIN)
6700 AA Wageningen
a.v.d.ploeg@marin.nl

Key words: Computational Fluid Dynamics, Optimization, Scale Effects.

1 INTRODUCTION

In the 7th-Framework EU project "STREAMLINE" one work package was entirely devoted to the optimization of state-of-the-art propulsion. The hull form of a chemical tanker, referred to as the 'Streamline tanker', together with its propeller was optimized using CFD. The ship speed was 14 knots, Lpp=*94m, B=15.4m*, the draft was *6m* and the block coefficient was *0.786*. The Reynolds numbers at model and full scale were $8.9 \cdot 10^6$ and $6.0 \cdot 10^8$, respectively.
In this paper we describe techniques for optimizing the lines of the aft body using the RANS-code PARNASSOS, together with an optimization of the propeller using the BEM code PROCAL. Sections 2 and 3 give a brief description of the method used for hull form variation and the viscous-flow solver.
The optimization of the lines of the ship was done for zero drift angle and free surface effects were not taken into account. All RANS computations computed the flow around one half of the symmetric ship only and symmetry boundary conditions could be imposed on the (undisturbed) water surface. Since scale effects in the wake field can be quite significant, the optimization should be performed at full scale. Modifications aft of midship were allowed only and the displacement should not decrease. Further, the propeller location as well as the ship's main dimensions were fixed. Constraints to guarantee sufficient room for machinery were that section 2 (the blue line shown in Figure 1) and all sections more upstream should stay outside a box indicated by the red lines in Figure 1.
The choice of object functions is of crucial importance in hull form optimization projects. Minimization of the resistance is not be the best way to reduce fuel consumption, since a decrease of the resistance is usually accompanied by a relatively strong decrease of the nominal wake fraction [7] which can reduce the propulsive efficiency. Therefore, as a first object function we used an estimate of the required power. The second object function was a function that represents the quality of the full-scale wake. The latter can be of interest when noise and vibration on board ships, or the risk of damage to the propeller and rudder due to (erosive) cavitation has to be minimized. In Section 4 we describe the object functions in more detail.
In Section 5 we will describe the results obtained from several systematic variations, together with the scale effects for some candidate hull forms. In Section 6, we discuss the propeller geometry parameterization developed for this optimization, as well as the results that we obtained.

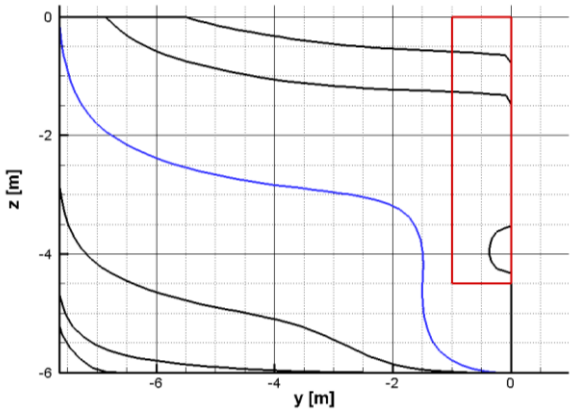


Figure 1 Body plan of the original vessel, together with the box to indicate room for machinery.

2. HULL FORM VARIATIONS

We used the GMS-Merge tool [3] for the parametric deformations of the geometry. GMS-Merge interpolates between some basis hull forms that were created by whatever means (e.g. manually) in our CAD system GMS. These basis hull forms 'span' the design space. It is important here that specific and effective variations of the hull form are chosen, for example based on an analysis of the results from a first CFD computation for the original vessel. Any design experience can be used in the choice of the basis hull forms, but otherwise successive cycles can help to display the dependence of the flow on the hull form and may indicate possibilities for further improvement. If the basis hull forms satisfy the geometric constraints, often all variations in the design space do so, although this is not guaranteed.
Figure 2 illustrates how GMS-Merge can make combinations of the basis hull forms, starting with the original hull and having made five basis hull forms. With all sliders in top position, the original hull form is obtained. With only one of the sliders completely down the basis hull forms are obtained. One can pull several sliders simultaneously to make combinations. The parameters of the hull forms to be evaluated are the percentages of the respective sliders being pulled down. In this example we have a 5-dimensional parameter space so if we use 3 steps to go from one hull form to the next, we have a total of 4^5=1024 variants.
The next step was performing a RANS computation for each variant using an automated grid generator. The parameter range can be narrowed, based on an evaluation of all variations or add new basis hull forms and delete others, etc. The process typically proceeds in a number of consecutive steps, providing large freedom and insights in possibilities for further improvement.

3. RANS COMPUTATIONS

The RANS code used is PARNASSOS, a code developed & applied by MARIN and IST [2]. PARNASSOS computes the steady, turbulent flow around ship hulls by solving the discretised Reynolds-Averaged Navier-Stokes equations for steady, incompressible flow. For the optimization of the Streamline tanker we used the standard $k-\omega$ SST turbulence model without corrections.

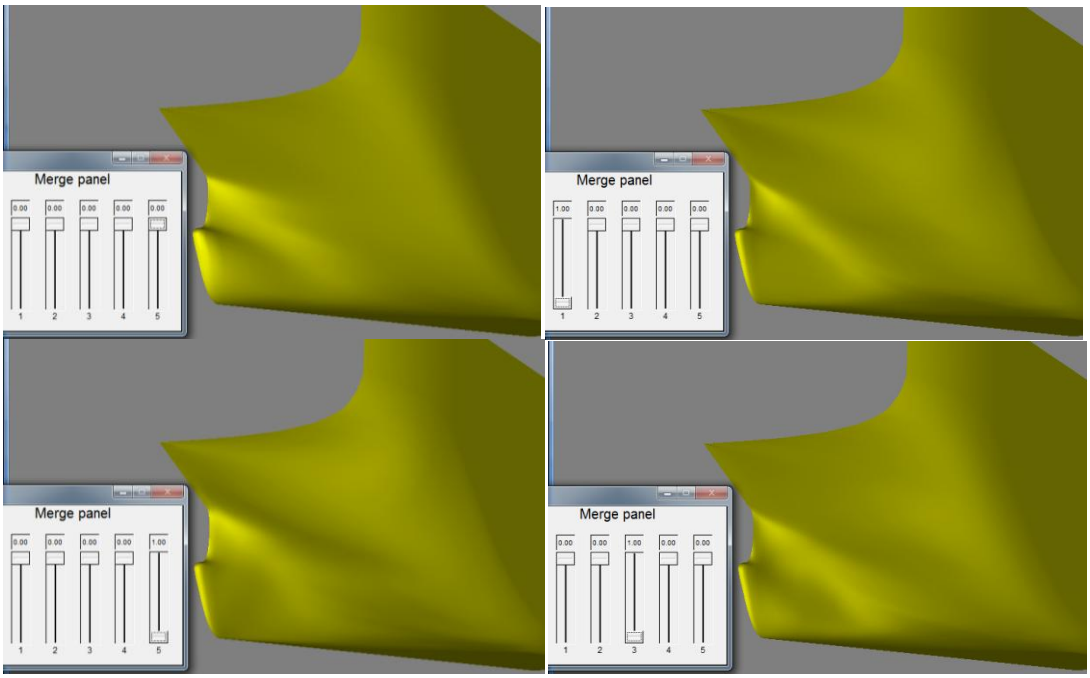


Figure 2 Illustration of GMS, tool for hull form variation.

A finite-difference discretization was used with second and third-order schemes for the various terms. The way in which the resulting system of non-linear equations is solved is very efficient with respect to both CPU-time and memory usage [6], which makes it very well suited for doing systematic variations or in combination with an optimization strategy.
The inflow boundary was located 0.5 L_{pp} in front of the bow and the outflow boundary at 1.5 L_{pp} behind the ship. The lateral outer boundary was a quarter of a cylinder with axis $y=z=0$ and radius 1.0 L_{pp}. At this boundary tangential velocities and pressure found from a potential-flow computation were imposed. Structured grids of H-O topology were used. No wall functions were used; not even for full-scale Reynolds number: all y^+ were below one. The grids had a strong contraction in wall-normal direction towards the hull in order to resolve the viscous sublayer. At full scale the grid consisted of 344 x 140 x 52 cells in the streamwise, wall-normal and girthwise directions, respectively, adding up to a total of 2.5 M cells. A mild stretching towards the bow and the stern in longitudinal direction was used. To give an indication of the grid resolution, Figure 3 shows the wall grid for the original vessel. In previous studies ([7], [8]) it was shown that with this grid density computed trends in the object functions are grid independent.

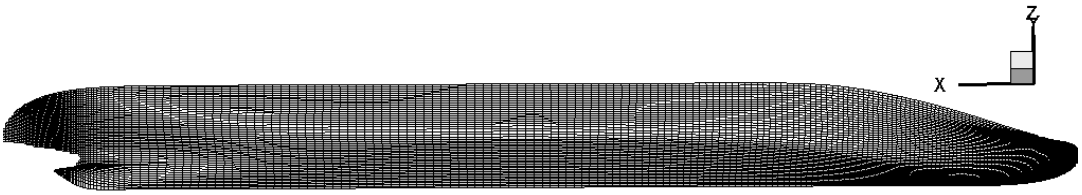


Figure 3 Illustration of the resolution of the wall grid

3.1 Automatic grid generation

Grids need to be generated around each variant, by a fully automatic grid generation procedure. To minimize the effect of discretization errors on the computed trends, these grids have to be as similar as possible. As a first step in the construction of the grid for a hull form variant, the wall grid for the original hull form (Figure 3) is projected on the variant. Next, the 3D-grid is obtained using the usual grid-generation techniques: for this we use in-house developed elliptic grid generation software, which solves a Poisson equation to have maximal orthogonality of the gridlines in the interior of the computational domain. Near the boundaries, orthogonality can be controlled by the user. These settings are chosen the same for all hull forms.

4. OBJECT FUNCTIONS FOR HULL FORM OPTIMIZATION

In [7] and [8] it was found that a decrease of the resistance was usually accompanied by a relatively strong decrease of the nominal wake fraction, changing the point of operation of the propeller. Therefore, the resistance is not a good choice as a first object function if we want to improve the fuel efficiency. Instead, we used an estimate of the power delivered to the propulsor:

$$P_D = \frac{1-w}{1-t}\frac{R_T \cdot V_S}{\eta_R \cdot \eta_O} \tag{1}$$

in which R_T is the towing resistance, w the estimated effective wake fraction, V_S the ship speed, t the thrust deduction coefficient, η_o the propeller efficiency in open water, and η_R the relative rotative efficiency, approximated by 1. The behind efficiency of the propeller is defined as $\eta_B \equiv \eta_O \cdot \eta_R$. It is essential to estimate η_B, as this efficiency can vary significantly between design variations. The behind efficiency could be evaluated by a coupling with a propeller code or by incorporating the propeller in the RANS computation. However, this would mean that one optimizes the hull form for the particular propeller chosen, instead of optimising both in combination. In order to estimate better the achievable performance, η_B is obtained from the B-series of propellers [4].

The thrust, wake fraction, number of blades, propeller diameter and revolution rate were fixed, while the blade area ratio and pitch ratio for each hull form were found from the B-series. The effective wake is estimated from the nominal wake using the NOMEFF tool [1]. NOMEFF calculates the induction velocities and interaction velocities by a force-field method that solves linearised Euler equations for a given force distribution. The interaction velocities were then added to the nominal wake field found from the first RANS computation that was performed for each hull form variant.

To compute the thrust deduction we perform a second RANS computation including a force distribution representing the propeller with an imposed thrust T_0. This imposed thrust is an approximation of the thrust T required for self propulsion, assuming a linear behavior between the force on the hull and T_0. The thrust deduction coefficient can then be computed from $t = (R_0 - R_T)/T_0$ with R_0 the resistance force from the second RANS computation. The self-propulsion thrust $T = R_T/(1-t)$.

4.1 Wake object function for the full-scale wake

In case of danger of erosive cavitation, one would like to prevent strong variations of the wake in circumferential direction, especially in the top half of the propeller plane. We will use the L1-norm of the variation of

$$\beta = \tan^{-1}\left(V_x / \left(\omega \tfrac{r}{R} - V_\theta\right)\right)$$

With V_x and V_θ the V_x and V_θ axial and tangential velocity components respectively, θ the angular position in rad. and ω the propeller rotation rate in rad/s. β is the undisturbed propeller inflow angle and its variation in circumferential direction as the propeller rotates is $\partial\beta/\partial\theta$. The L1-norm is determined from integration in circumferential direction and over a range of radii from the hub to the tip and the propeller radius:

$$WOF \equiv \frac{\int_{r=hub}^{r=tip} \oint_\theta \left|\frac{\partial\beta}{\partial\theta}\right| f(\theta,r)\, d\theta r dr}{\int_{r=hub}^{r=tip} \oint_\theta f(\theta,r)\, d\theta r dr} \tag{2}$$

Herein f is a weighting function that can be used to make the outer region and/or the top region of the propeller more important, here defined as $f(\theta,r) = re^{-2(\theta-\theta_{top})^2}$.

5. RESULTS FROM SYSTEMATIC VARIATIONS OF THE HULL FORM

The results of several systematic variations are shown in Figure 4. Each symbol corresponds with a hull form for which the two full-scale RANS computations were required to obtain the object function values. Separate colours indicate results of separate systematic variations. The aim is to decrease both object functions, hence the more 'optimal' hull forms are closer to the lower-left corner of the chart. As can be seen from the figure, there is a set of hull forms (the Pareto front) that show the best compromise between decreasing the required power (1) and the wake object function (2).

5.1 Scale effects

Table 1 shows computed values of the candidates and original hull form at full scale and in model scale (in brackets). The thrust deduction at model scale corresponds with the thrust required for ship-self propulsion. The decrease of the required power was much stronger at model scale than at full scale. Without optimizing at model scale, we already get a decrease of the first object function of 4.5%. Hence we expect that a further decrease of the required power at model scale is possible when doing the optimization at model scale. The stronger decrease in required power at model scale is mainly due to the stronger increase in the open-water efficiency. The second object function decreases much less (except for cand3) at model scale, but the question is whether it is useful to have a decrease of a wake function evaluated for the model-scale wake. Further, we see a strong decrease of the wake fraction from model to full scale and hardly any scale effect in the thrust deduction, as can be expected. Of course, the resistance coefficients, especially the friction resistance coefficients, are significantly higher for model scale. The viscous resistances relative to the ITTC-57 friction line (the form factor $1+k$) increases clearly from model to ship A similar trend is found in previous computations of many other ships [9].

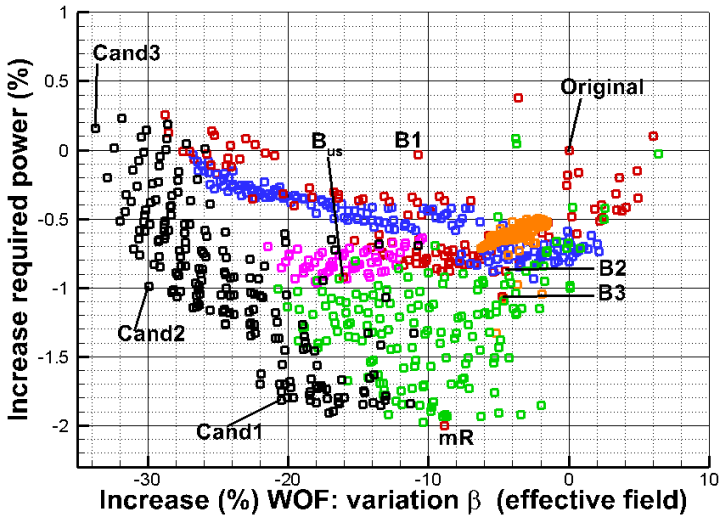


Figure 4 Results of several systematic variations performed for full scale as a function of the object functions

Table 1 Scale effects for candidate hull forms and original vessel. Ship (Model).

	Original		cand3		cand2		cand1	
w	0.208	(0.279)	0.194	(0.264)	0.183	(0.247)	0.171	(0.232)
1000Cvf	1.67	(2.98)	1.67	(2.98)	1.67	(2.98)	1.67	(2.98)
1000Cvp	0.43	(0.66)	0.46	(0.66)	0.44	(0.62)	0.41	(0.58)
1000Ct	2.10	(3.64)	2.13	(3.64)	2.10	(3.59)	2.08	(3.55)
$1+k$ *(ITTC '57)*	1.29	(1.19)	1.30	(1.19)	1.29	(1.17)	1.27	(1.16)
t	0.178	(0.182)	0.158	(0.164)	0.155	(0.159)	0.152	(0.155)
η_o	0.667	(0.550)	0.673	(0.561)	0.678	(0.571)	0.684	(0.579)
			0.9%	(+2%)	+1.6%	(+3.8%)	+2.5%	(+5.3%)
η_H	1.038	(1.136)	1.045	(1.135)	1.034	(1.118)	1.024	(1.100)
			+0.7%	(0%)	-0.3%	(-1.6%)	-1.3%	(-3.8%)
$2000P_D/(\rho V_s^3 S_W)$	3.03	(5.83)	3.03	(5.71)	3.00	(5,62)	2.97	(5.57)
			+0.1%	(-2.1%)	-1%	(-3.6%)	-1.8%	(-4.5%)
WOF	0.072	(0.097)	0.048	(0.066)	0.050	(0.086)	0.057	(0.099)
			-33%	(-32%)	-31%	(-11%)	-21%	(+2%)

Figure 5 compares the scale effects in the nominal wakes. In each picture the wake of a candidate hull form is compared with that of the original hull form. Of course, for each hull form we see a much more pronounced boundary layer at model scale compared to full scale. Both at model and full scale, the Cand3 has less variation of the velocity in the top of the propeller plane, which also results in lower values of the wake object function (Table 1).

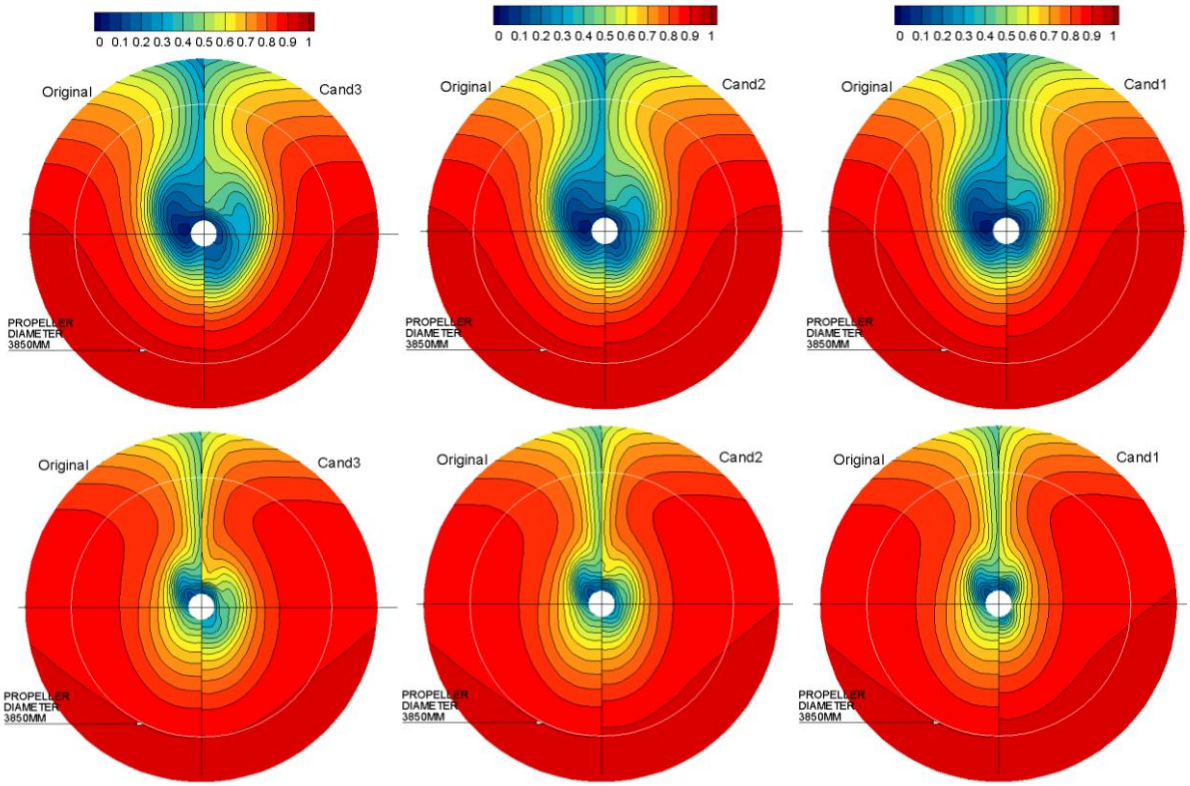


Figure 5 Comparisons of the nominal wakes with that of the original vessel. Top: model, bottom: ship.

6. PROPELLER OPTIMIZATION ROUTINE

The propeller geometry is fully parameterized in its main parameters and its radial distribution functions for pitch, chord, camber, thickness, skew and rake. The distribution functions are replaced by NURBS[1] curves consisting of one or two line segments that are C1-continuous. Each segment is written in its Bézier form whereby the curve is defined along a parameter t as a sum of base functions

$$c(t_j) = \frac{\sum_{i=0}^{n} \beta_i^n(t_j) w_i \cdot p_i}{\sum_{i=0}^{n} \beta_i^n(t_j) w_i}$$

with β_i^n a Bernstein polynomial in the form of $\beta_i^n(t_j) \equiv \binom{n}{i} t_i^i (1-t_j)^{n-i}$.

Each Bernstein polynomial runs from $t_j = 0$ to $t_j = 1$ along each curve interval defined by points p_i that each have a weight w_i. The order n can be selected to be any number but is here chosen to be 3 with (at most) 4 required control points, resulting in a cubic curve

[1] Non-rational uniform basis spline

whereby p_0 and p_3 are the end points of the curve and $p_1 - p_0$ and $p_3 - p_2$ directly specify the derivate at the ends of the curve. Some useful properties of the NURBS curve are that the curve is always enclosed within the convex hull of the points p—i.e., the smallest area containing all points p—provided that $w_i \geq 0$, the x, y coordinates of the curve depend on the respective x, y coordinates of the controls only (i.e., no coupling between the coordinates), and the curves can be evaluated analytically for most of their properties.

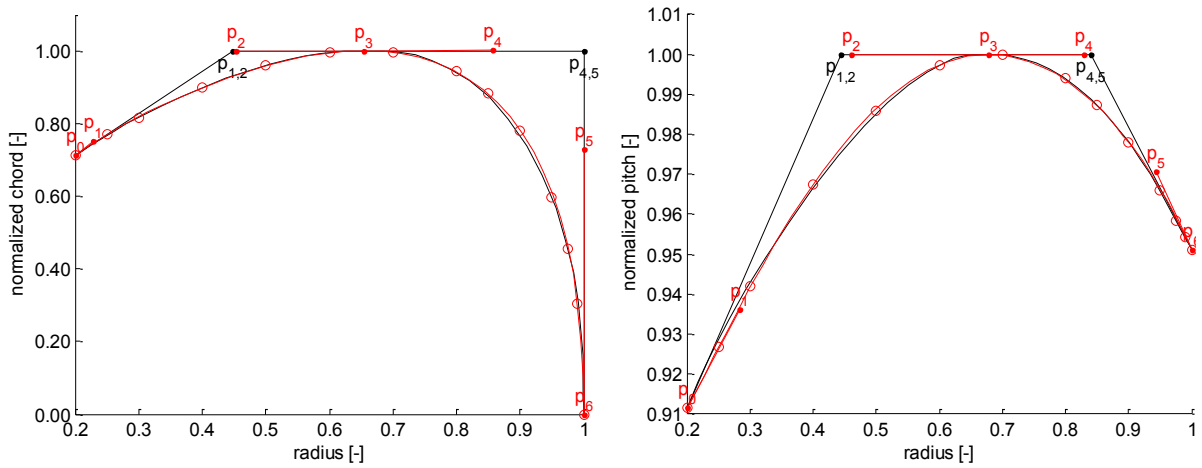


Figure 6 ***Chord (left) and pitch distribution of the Streamline stock propeller showing input data points(○), and best fits of Beziér curves (red) and the parameterization (black), including the control points of both fits. Both fits share*** $p_{0,3,7}$. ***The coindiding points*** $p_{1,2}$, ***and*** $p_{4,5}$, ***effectively reduce the order of the curve (*** $n = 2$***).***

With this simple distribution a series of discrete points for the radial distribution functions can be selected, directly linked to geometrical parameters. For instance, the normalized pitch and chord distribution, see Figure 6, can be fitted well with two cubic segments with seven control points and uniform weights (red curve); the start and end point lie at the hub and tip respectively and the centre point indicates the radial position of the distribution's maximum. For these two example fits, four additional points are required to determine the derivative and curvature at the ends and centre of the curve. For the parameterization the curve is further simplified by positioning the two intermediate points at the intersection along the curve end derivatives. As the centre point is defined as the curve's maximum location, the derivate at the centre is always zero, leaving the derivate at the far ends and all weight factors as remaining degrees of freedom (dof).

In order to estimate and reduce these dofs for the chord and pitch distributions, as well as the other functions, we have analysed the database of propellers at MARIN containing over 1,200 unique propeller designs. A curve-fitting algorithm approximated all the radial distribution functions, returned the quality of the fit, derivative and curvature information and showed that most radial distribution functions could be captured with only one or two curve segments.

Heuristic regression functions were derived to estimate the derivatives in the end points of each curve segment and the weight factors based on the relative position of these end points, in effect reducing the dof to one per curve segment. The best fit of these parameters with the input data is also presented in Figure 6 (black), showing the coinciding points $p_{1,2}$ and $p_{4,5}$ demonstrating that the input data of the stock propeller can be captured by the parameterized chord and pitch functions.

From the database analysis it followed that the majority of the radial distribution functions for skew, pitch, thickness and chord can be described by these simple functions, requiring a small number of parameters. Many propellers have a constant rake angle that can be readily described, but more modern designs using tip rake or CPPs designed for low blade spindle torque will require an extended parameterization to capture the more complex shape. The camber distribution for the propellers showed that over a third of all propellers have a (near) constant camber-to-chord ratio but that the other distributions showed much variation with resulting poorer fits using simple curves. It was observed that the propellers with a constant camber-to-chord ratio were typically the oldest designs, often with sections consisting of a flat face with leading and trailing edge offsets, instead of sections built up from a chord-wise thickness and camber distribution.
The analysis of the propeller database was also used to create probability density functions of each parameter so that value intervals could be specified. These limits can be used to avoid propellers that either are unrealistic (e.g. nearly no chord length at the hub or maximum chord length at the tip) or that challenge the limits of the analysis tool (e.g., extreme pitch reductions at the hub and tip where the tool is less accurate) or simply as set design values (e.g., blade area ratio, minimum skew angle).

The propeller analysis tool used was PROCAL, a Boundary-Element Method (BEM) developed within MARIN's Cooperative Research Ships (CRS) [10], based on Morino's formulation. The propeller and hub were meshed by a routine that used the parameterization directly. Results can be obtained using limited calculation time on a single CPU. Therefore, a large number of geometries can be analysed during an optimization routine.

Each propeller has to meet the required thrust at the set rpm and ship speed, thereby specifying the 'effective' pitch. If not, propellers are obtained that work at a different point of operation and show an illusory efficiency increase; it is a trivial solution to fit a ship with a propeller with a higher pitch working at a lower rpm and attain a higher efficiency. In order to avoid this biased comparison, all propellers must share the (design) effective pitch and generate thrust within 1% accuracy.

A first estimate of the pitch is specified using the concept of virtual pitch; instead of using the pitch angle based on the nose-tail line of a section, the pitch was based on the mean zero angle-of-attack of each propeller section as calculated by thing-wing theory. An automatic pitch correction routine steered each design towards the design point in two steps, multiplying the pitch distribution by a factor until thrust identity was obtained. First, a series of steady calculations was performed using a coarse grid and a circumferentially averaged wake,

typically requiring three calculations and yielding the dependency of propeller thrust on pitch. Second, a series of unsteady calculations using a fine mesh was performed until thrust identity was obtained, using the thrust/pitch relation from the first series for the first pitch adaptation, then using the results of unsteady calculation. Typically convergence was obtained in two or three steps. All designs for which this iteration did not converge were automatically rejected and earmarked for autopsy.

Well over 10,000 propellers could be generated and analysed per day using a 128-processor cluster. The rejection rate was typically below 0.05%, with rejected designs caused by an unfortunate combination of propeller parameters (e.g., self-intersecting propeller blades).

In this first analysis the focus was on an optimum behind efficiency. Cavitation was not included as these calculations are comparatively CPU-intensive and it is hypothesized that a first optimization is required determining the main parameter range before continuing to minimise the cavitation itself. As a second optimization goal was as the minimization of amplitude of the first harmonic of the propeller thrust. As this object function acts directly on the propeller-wake interaction, equivalent to the WOF from the hull optimization (eq. 2) but now for the propeller only. The camber of the sections was set at a constant ratio with the chord at all radial positions and the thickness of the propeller was taken as a constant distribution. Naturally, both settings do not apply for a propeller design whereby cavitation and weight constraints are in play, but these settings do not significantly influence the results from the PROCAL calculation, nor alter the conclusions of this study.
The following parameters were chosen for the analysis

- Diameter 4076mm
- Number of blades 3,4,5
- Blade Area Ratio 0.50 – 0.80
- Chord hub/ max chord 0.30 – 1.00
- Radial position max. chord 0.30 – 0.80
- Chord tip 0
- Pitch hub/ max pitch 0.50 – 1.00
- Radial position max. pitch 0.40 – 0.80
- Pitch hub/ max pitch 0.60 – 1.00
- Rake angle -10 – +10 deg
- Skew angle range 2 – 47 deg
- Mean skew angle -5 – 17.5 deg
- Camber to chord ratio 0.00 – 0.04
- Section thickness NACA66 TMB modified
- Section Camber NACA 0.80 MOD mean line

The remaining parameters for skew, chord, and pitch curvature were chosen from the database probability functions. The results of the analysis for the full-scale wake field of the original hull (see Figure 7) are clustered per blade number. The effect of blade number on efficiency is clearly visible with a preference for more blades; a conclusion that could also be drawn the

from B-series analysis. The optimum diameter of the propeller is smaller for a propeller with more blades; as the currently fitted diameter is below the optimum for all blade numbers, the propeller with more blades is closer to the optimum and performs best. The results for efficiency show a ceiling in efficiency results that is more than one percent above the currently fitted propeller. The results also show that the combination of uncoupled parameters is most proficient at designing ill-performing propeller designs. The effect of blade number and skew angle on the thrust variations can only be obtained from the more detailed analysis and show a decrease in thrust variations as a function of skew angle and, more importantly, blade number.

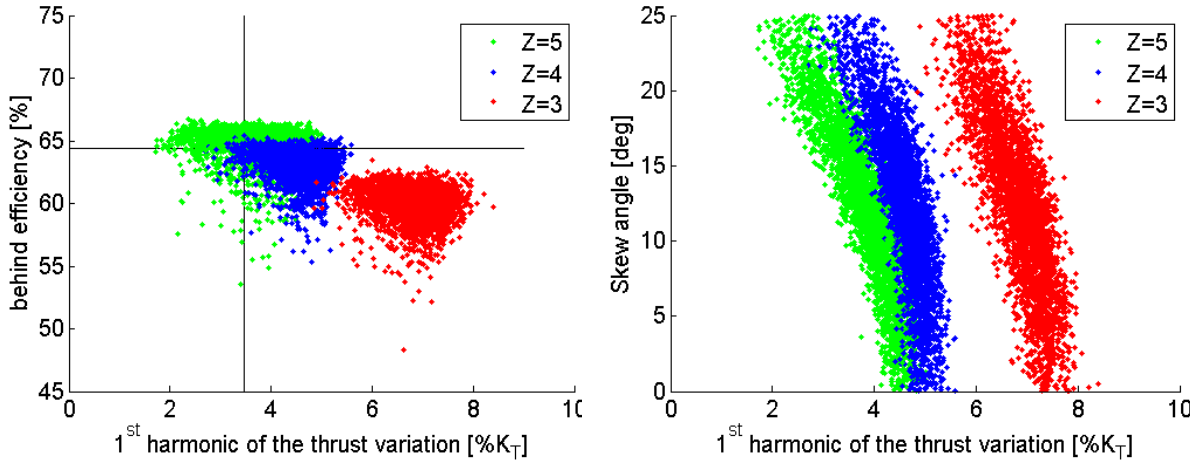


Figure 7 Behind efficiency, skew angle and thrust variation dependency for all analysed propellers.

The 5-bladed propeller selected as the best compromise showed an efficiency of 66.7% compared to the efficiency of 64.4% of the original propeller. When the analysis was repeated for hull from candidate 2, allowing for a larger propeller diameter (5.9%) while maintaining the propeller-hull clearance and without exceeding the hull base line but using the same rpm, a behind efficiency of 71.5% was obtained. A cavitation analysis showed very small cavitation volumes.

7. CONCLUSIONS & DISCUSSION

Multi-objective optimization of the Streamline tanker at full scale has been done in which the first object function is an estimate of required power and the second one is an object function for the full-scale wake: the variation of the angle of attack. Minimizing the power to sustain a given speed is a better goal than minimizing the towing resistance, as a decrease in the resistance is often accompanied by many other effects like a decrease in the nominal wake fraction, which can significantly reduce the hull efficiency.
A combined decrease of both object functions could be obtained. It appears that the decrease of the first object function is much larger at model scale than at full scale. Without doing the actual optimizing at model scale, we already get a decrease of the first object function of

4.5%. Hence it appears that it is much easier to optimize the model than the ship. Nevertheless, for the ship a decrease of 2% in the object function is possible. Some variants allow an increase of the propeller diameter without increasing the propeller clearance. A first exploration of these hull forms combined with an increase of the propeller diameter showed that a further decrease of the required power (3% at full scale) is possible.
The propeller followed from an analysis of parameterized variation aimed at increasing efficiency and reducing blade-rate shaft vibrations. A 2.3% efficiency increase was found while keeping the propeller diameter the same, increasing to 7.1% for a larger propeller fitted in the improved wake field of the optimized hull form, but running at the same rpm.

ACKNOWLEDGEMENT
The research reported in this paper formed part of WP21 and WP35 of the STREAMLINE (STrategic REsearch for innovAtive Marine propulsioN concEpts) project, co-funded by the European Commission within the Seventh Framework Programme. This support is gratefully acknowledged.

References

[1]. GENT W. van and HOEKSTRA M., (March 1985), *Force field approach for propeller-wake interaction*, MARIN Report No. 44303-7-SR.
[2]. HOEKSTRA M., (1999), *Numerical simulation of ship stern flows with a space-marching Navier Stokes method*, Thesis, Technical University of Delft.
[3]. HOEKSTRA M. and RAVEN H.C., (2003), *A practical system for hydrodynamic optimization of ship hull forms*, NAV 2003 Conference, Palermo, Italy.
[4]. KUIPER, G., (1992), *The Wageningen Propeller Series.* MARIN publication 92-001. Published on the occasion of its 60th anniversary.
[5]. PLOEG A. van der, (2011), *A Comparison of Several Strategies to Optimize a Ship's Aft Body*, Journal of Ship Production and Design,Vol. 27, No. 4, pp. 202-211.
[6]. PLOEG A. van der, HOEKSTRA M., and EÇA L., (2000), *Combining accuracy and efficiency with robustness in ship stern flow computation,* Proc. 23rd Symp. Naval Hydrodynamics, Val de Reuil, France.
[7]. PLOEG A. van der and HOEKSTRA M., (2009), *Multi-objective optimization of a tanker after body using PARNASSOS*, Proceedings 12th NuTTs-symposium, Cortona.
[8]. PLOEG A. van der and RAVEN H.C., (2010), *CFD-based Optimization for Minimal Power and Wake Field Quality*, Proceedings 11th International Symposium on Practical Design of Ships and other Floating Structures, Rio de Janeiro, pp. 92-101.
[9]. RAVEN H.C., PLOEG A. van der, STARKE A.R. EÇA L. (2008), Towards a CFD-based Prediction of Ship Performance ---Progress in Predicting Full-Scale Resistance and Scale Effects, RINA MARINE CFD.
[10]. VAZ, G. and BOSSCHERS, J., (2006), *Modelling of three dimensional sheet cavitation on marine propellers using a boundary element method*, *6th int. symp. on cavitation CAV2006*, Wageningen, NL.
[11]. BOSSCHERS J., VAZ, G., STARKE A.R., WIJNGAARDEN E. van, (2008) *Computational analysis of propeller sheet cavitation and propeller-ship interaction*, RINA CFD MARINE CFD, Southampton, UK.,

V International Conference on Computational Methods in Marine Engineering
MARINE 2013
B. Brinkmann and P. Wriggers (Eds)

NUMERICAL PREDICTION OF THE PERFORMANCE OF AXIAL-FLOW HYDROKINETIC TURBINE

PAVAN CHANDRAS[1], LAVEENA SHARMA[2] AND DHIMAN CHATTERJEE[3]

Department of Mechanical Engineering,
Indian Institute of Technology Madras,
Chennai, TamilNadu, INDIA.
1. e-mail: chandraspavan@gmail.com
2. e-mail: sharma.laveena071@gmail.com
3. email: dhiman@iitm.ac.in

Key words: Hydrokinetic Turbine, Numerical Simulation, Performance, Geometry, Free Surface

Abstract. *The present work is focused on the numerical prediction of the performance of axial flow hydrokinetic turbine under practical conditions. The models are designed to produce an electrical power output of 200 W at an incoming water speed of 1 m/s. Three different models of three-bladed turbine, based on swept direction, are designed to study the effect of geometry on the turbine performance while operating under identical conditions. Numerical simulations indicate that a peak turbine power of 480 W at a tip speed ratio of 3.5 is obtained for unswept bladed turbine with sharp trailing edge. Results suggest that forward and backward swept blades perform better than the unswept blade for blunt trailing edge. Simulations are carried out for different nose profiles for hub. It is found that a turbine experiences lesser thrust force with an ellipsoidal nose having ratio of major axis to minor axis of 4. In order to capture a real life scenario effectively, the effect of turbine location inside the water, particularly with respect to the free surface is investigated further. The safe depth for turbine installation is found to be at least 1.4 m from the free surface.*

1 INTRODUCTION

Hydrokinetic turbine, utilizing kinetic energy of flowing water, offers a renewable source of extracting power from rivers and seas. Though this type of "net-zero head" turbine has lower efficiency than conventional dam-dependent hydraulic turbine, yet this is more suited from the perspective of minimum adverse effect on environment and population displacement. Hence, there is a spurt in research activities in studying these turbines [1].

These types of turbines can be axial-flow or cross-flow depending on the disposition of the shaft with respect to the flowing water current. Axial-flow hydrokinetic turbine, the focus of present work, has an axis of shaft parallel to the incoming flow while cross-flow turbine has axis perpendicular to the flow. Former is more efficient than later type of turbines but suffers from lower conversion efficiency in case the incoming flow direction does not match with the shaft direction. In such a scenario, use of properly designed ducts can prove to be beneficial [2, 3].

Practical works on the generation of electric power using axial-flow hydrokinetic turbine was done mainly by different industries [4-6]. However, with passage of time and with improvement in computational resource over the years, more and more papers are published

which predicts performance of these hydrokinetic turbines numerically [7, 8]. This shift towards numerical prediction also took place because numerical methods provide a quicker route to arrive at improved design. Sophisticated mathematical techniques like large eddy simulations to assess role of turbulence on turbine performance and resultant wake flow is used [7]. This approach being computationally resource intensive, many researchers resort to RANS for prediction of performance of hydrokinetic turbine [8]. Hence similar strategy of using RANS is adopted in the present work.

Present work discusses the design aspect of an axial-flow hydrokinetic turbine and its performance capability of the turbine as a function of tip speed ratio, incoming water speed and flow directions, as well as installation parameters like elevation from the river bed and depth from the free surface.

2 TURBINE DESIGN AND MODELLING

An axial-flow hydrokinetic turbine is designed to produce an electrical output power of 200 W. Generator efficiency (η_G) for these turbines running at low rotational speeds is expected to be low and hence it is taken to be 60%. A survey of existing designs indicates that, though Betz's limit is 59.3%, most of the turbines operate with much lower efficiencies. So, as a conservative estimate, turbine efficiency (expressed as power coefficient, C_p) is considered to be 35% in this work. Designing of the turbine is represented here in terms of design of rotor, hub and shaft.

2.1 Design of rotor blades

Electrical output power (P_{elec}) produced by a hydrokinetic turbine is given by the relation [9]:

$$P_{elec} = \frac{1}{2}\rho A V_{\infty}^{3} C_p \eta_G \tag{1}$$

In this equation, V_∞ is freestream (water current) speed much ahead of the turbine inlet and is taken in the present work to be 1 m/s unless specifically mentioned. ρ is the density of water and is taken as 997 kg/m^3. A is the projected area of the turbine. This relation yields tip diameter of the turbine (D_{tip}) to be 0.8 m. Various hub to tip ratios (D_{hub}/D_{tip}) were attempted, starting from high values of 0.35 to values as low values as 0.15. It was seen that higher ratios yielded poor performance while too low ratio may be unusable from stress (due to bending moment of long blades) considerations. Hence, hub diameter (D_{hub}) was taken as 0.3 m.

Based on the suggestion by Anyi and Kirke [10], we have also used S822 aerofoil as blade profile. As reported in that paper, other than improved stall characteristics and high lift to drag ratio it offers resistance against fouling. Figure 1(a) shows a typical S822 profile. Basic simulations were performed with this profile of the blade after choosing a desired angle of incidence of 5° at all locations from hub to tip as the profile shows high lift and low drag-lift ratio at this angle of attack. But from fabrication considerations, sharp trailing edge may not be realized in practice and hence after defining optimum parameters, later simulations to investigate the effect of sweep on blade performance were carried out using modified trailing edge with small but finite radius as shown in Figure 1(b).

The blade consists of nine stations, thicker at the root for greater flexural strength and narrower at the tip for minimum drag. Hence, the chord length of the blade airfoil gradually decreases from root to tip whereas the twist angles increases towards root. The blade is twisted with different twist angles in such a fashion that the relative speed of water (W) at every cross section gives rise to maximum lift by keeping the angle of attack reasonably constant throughout the blade span [10].

2.2 Design of hub

Hub geometry was modeled in Solid Works^{TM} with different nose profiles. Two types of configurations were modeled: hub with hemispherical front and rear, and hub with elliptical front and hemispherical rear (Fig. 2), to study the effect of hub geometry on the wake region as well as on the overall thrust force experienced by the turbine. Various ellipsoids with ratio of major axis to minor axis from 1 to 4 were tried out to check the reduction in thrust force with the ratio. This will be discussed later in the paper with simulated results.

2.3 Design of shaft

The diameter of the output shaft is designed to withstand the torque generated by the turbine at free stream water speed. With appropriate factor of safety and using steel as shaft material, shaft diameter was determined to be 50mm.

2.4 Blade Configurations

In this work, individual blade profiles at different radial locations stacked along their mid-chord, quarter-chord and along the leading edge to investigate the effect of sweep. Nine blade profiles from root to tip stacked along an axis joining the center of the airfoil chords leads to the construction of radial, unswept blades. While the profiles stacked from quarter chord i.e. 1/4th the chord length taken from leading edge results in backward sweep. The third one was stacked along the leading edge exactly like wind turbine blade profiles. This configuration gives rise to forward swept blades. Different blade configurations thus obtained are shown in Fig. 3.

3 GOVERNING EQUATION AND NUMERICAL TECHNIQUES

Turbulent, incompressible flow simulations were carried out using Reynolds-averaged Navier Stokes (RANS) equations based on equations described below [8]:

$$\nabla \bullet \vec{W} = 0$$

$$\rho\left[\frac{\partial \vec{W}}{\partial t} + \nabla \bullet \left(\vec{W}\vec{W}\right) + \left(2\vec{\Omega} \times \vec{W} + \vec{W} \times \vec{W} \times \vec{r}\right)\right] = -\nabla p + \nabla \bullet \tau \tag{2}$$

In this work, k-ω SST (Shear Stress Transport) turbulence model was chosen as it provides a good compromise between computational cost and solution accuracy for flows with swirl [8].

3.1 Numerical strategy

As already mentioned, solid model of the turbine geometry was created in Solid Works^{TM}. Meshing was done in ICEMCFD^{TM} while numerical simulations were carried out using ANSYS CFX^{TM}.

The computational domain consists of far field which is non-rotating, while the rotor domain rotates at the rotational speed of turbine. Inlet condition is specified in terms of freestream velocity (V_∞), outlet boundary is depicted as pressure boundary condition (Fig. 4). Fine structured mesh is created for the rotor using grid generating tool, TurboGrid^{TM}. For simplicity, unstructured mesh is created for far field domain in ICEM CFD. For most of the work reported here, exchange of pressure and velocity data across stationary and rotating frames of references were carried out using frozen rotor method. Though this model cannot capture transient effects at the interface, yet it offers steady state solutions to multiple frames of reference problem. This approach was adopted as it is computationally less expensive. In problems dealing with free-surface, transient analysis was carried out and for those cases only, frozen rotor interaction was replaced by transient rotor-stator interaction. Flowchart indicating sequence of operations adopted is given in Fig. 5 for clarity. Second-order advection schemes were used for numerical simulations in order to minimize numerical diffusion. Convergence control is performed in terms of physical timescale, which in this case is defined as the inverse of rotational speed [rad/s] of rotor.

To establish the credibility of the numerical results, a domain independence study, a grid sensitivity study and a study on rms-residuals was carried out. These are now taken up for discussion.

3.2 Domain independence study

Ideally far-field domain should be made as large as possible. However, too large a computational domain is computationally expensive and may not contribute to accuracy of the predictions. Hence, the study was conducted for three separate far-field domains - small, medium and large on the basis of their volume. The idea here is to choose a domain which can offer result that matches with the ideal trend obeyed by the turbines, and in minimum run time. Table 1 summarizes the effort in this direction and enables us to choose appropriate computational domain. The far field domain is made cylindrical whose diameter is taken as 5 times the diameter of the rotor tip and is extended $3D_{tip}$ upstream and $7D_{tip}$ downstream to negate any undesirable boundary effects thereby offering a good trade-off between reliability of results and computational effort.

3.3 Grid sensitivity study

Grid sensitivity study was carried out to determine the effect of mesh sizes on the predicted turbine performance. It was seen that grid independent solution was obtained for a mesh having 22,09,641 number of nodes in the rotating domain along with 3,86,972 nodes in the stator. Hence this mesh was adopted for the present work.

3.4 Study on RMS residuals

Effect of fixing the convergence level may have significant effect on the performance of

the turbine. For industrial applications, ANSYS CFX recommends a rms convergence level of 10^{-4}. We have tried to ascertain the influence of results obtained with by computing for a rms level of 10^{-5}. Outcome of such study indicates that for present computations 10^{-4} residual level suffices.

Table 1 Comparison between results of various far-field domains

Property	Small	Medium	Large
Volume of far field (x149.158 m^3)	1 (D X L)	3.37 (1.5D X 1.5L)	11.37 (2.25D X 2.25L)
No. of nodes in far field domain	1,90,710	3,86,972	10,88,203
Power coefficient	0.51	0.49	0.49
Percentage difference in results	3.9 %	0.8 %	-
Run time of simulation	3 hr 22min	3hr 39min	7hr 20 min

Thus after having ascertained different parameters that may affect the outcome of numerical prediction, we now present the significant results.

4. RESULTS AND DISCUSSION

Figure 6(a) depicts the variation of static pressure along the flow direction. This plot proves the capability of numerical simulations to capture the essential flow physics. It is observed that the rotor slows the water speed of 1 m/s far upstream to 0.65 m/s at the plane of rotation due to drag which develops from the pressure drop over the rotor. This pressure drop depends on the water density and viscosity, initial water speed, and final water speed at the rotor plane. A small pressure rise is expected upstream of the rotor before a discontinuous pressure drop over the rotor. During the downstream action of the rotor, the pressure returns continuously to the atmospheric level while the flow regains velocity. However, unlike classical actuator disc theory, the rotor imparts a rotational velocity as can be seen from the streamlines in the wake of the turbine (Fig. 6b).

Figure 7 depicts predicted turbine output power for different rotational speeds. It is seen that there is a peak in output power at around 42 rpm corresponding to a tip speed ratio (λ) of 3.5 which is quite close to the selected design condition of λ =4. To understand what happens at lower or higher values of tip speed ratio, Fig. 8 shows streamlines past the blade at mid-span. It shows that at lower tip-speed ratios like 2, there is a large-scale flow separation indicative of stall, resulting in lower lift to drag ratio and hence lower power output. At higher tip-speed ratio of 6, the flow incidence angle is close to zero, resulting in low pressure difference between pressure and suction sides — thereby giving rise to very low lift value.

4.1 Performance at various incoming speed

The incoming flow water speed in river or seas need not remain constant in natural conditions. Hence, similar simulations were conducted to compute the variation of power coefficient (C_p) with tip speed ratio (λ) as a function of incoming water speed. Figure 9(a) shows variation of power coefficient with different tip speed ratios. On the other hand, power output should increase as cubic power of speed of incoming water flow. Figure 9(b) shows the variation and power-law curve fitting indicates that $P_c = 491.5V_\infty^{3.03}$ with $R^2 = 1$.

4.2 Performance at different flow directions

Hydrokinetic turbines, utilizing water currents, are affected by variation in flow directions. It is also known that axial-flow machines are more susceptible to this phenomenon. So, numerical simulations were carried out to determine the variation of power coefficient at different tip speed ratios as a function of incoming flow directions ranging from 0^o to 20^o (Fig. 10). It is seen that, as the flow deviates from the axis, performance deteriorates and for 20^o of deviation, peak power coefficient drops from 0.48 to 0.42 at tip speed ratio of 3. As the angle of approach progresses, the effect of flow separation becomes more pronounced and results in the drop in efficiency of the turbine.

4.3 Effect of hub geometry on turbine performance

The airfoil is designed to offer maximum lift to make the rotor revolve, with minimum drag. Combination of these forces result in tangential force and axial and radial thrust. The tangential force provides necessary torque. The thrust force perpendicular to the plane of rotation is undesirable. Our work suggests that thrust variation could result from the shape of the hub while power coefficient is largely unaffected by changes in hub profile (Fig. 11). The variation of thrust is plotted as a function of nose profile defined by the ratio of major axis to minor axis, ranging from 1 to 4. A reduction in the thrust force with increase in ratio is observed here. It is important to note here, hub nose profile has an impact over thrust but does not show any considerable effect on the power coefficient. This reduction can be explained in terms of pressure gradient across the hub and the expansion of wake in the surrounding region. Out of the designed configurations hub with hemispherical front and rear offers sudden pressure rise while on the other hand, hub with ellipsoidal front displays a smooth rise in pressure throughout the span.

4.4 Performance at various elevations from river bed

The flow speed of water in a river varies from the river bed to free surface. Hence, the performance of the turbine was studied at various elevations from river bed assuming linear variation of water speed of 0 to 2 m/s from bottom to free surface. Assuming depth of river to be 10m, output power and thrust force are plotted against elevations ranging from 2m to 5m (Fig. 12).

It should be noted here that the effect of relative angular position of the blades at different incoming flow directions with different elevations is not accounted here. Transient simulations are needed to plot the torque values as a function of both varying incoming speed and varying incoming flow directions taken together. Therefore, simulations to plot torque

against different angular positions at different elevations were carried out separately, taking identical velocity profile from top to bottom.

Though that numerical analysis indicates that the rate of increase in output power with respect to elevation is significantly higher than that of thrust force, we cannot afford to mount the turbine beyond certain height. This is because, the bending moment of the supporting tower increases at a higher rate, due to the combined effect of height and the thrust force. The height at which turbine should be mounted can be calculated only after fixing the geometrical shape and material of the tower, which is beyond the scope of this study.

4.5 Safe depth below the free surface

Simulations done to determine how the performance of this turbine gets affected in the presence of free surface indicate that if the turbine is not mounted at a safe depth, the free surface may interact with the rotating turbine thereby causing a dip in the free surface due to sudden drop in pressure below the atmospheric pressure as the flow past the rotor.

Furthermore, if the effect of free-surface becomes significant, the usual scaling law of same blade-based Reynolds number and turbomachines relations will not be valid for the existing turbine. Froude number ($Fr = V_{rel,tip} \Big/ \sqrt{gH_{depth}}$) can be used to determine the free surface interaction with the rotating blades. Here, the characteristic velocity of flow is taken as the relative velocity at the tip of the rotating blade which is the maximum speed observed. The characteristic length (H_{depth}) is chosen as the distance from axis of rotation of turbine to the free surface. Taking Froude number as 0.95, for subcritical flow regime, the safe depth at which the turbine may be mounted is calculated as 1.4 m. Figure 13 shows typical contour of vapour fraction of water indicating the location of free surface.

4.6 Effect of blunt trailing edge

Figure 14 indicates the variation of power coefficient with tip-speed ratio for unswept rotor with and without blunt trailing edges. It is clear from Fig. 8 that there is degradation in turbine performance which could be due to the blunt trailing edge that causes flow separation downstream of the trailing edge.

4.7 Effect of blade sweep

Blade sweep, as discussed earlier, was attempted as it is well known that sweeping of turbine blades in turbomachine applications can influence the performance of the machine. It may be noted here that the results shown in Fig. 15 are for these three configurations with blunt trailing edges. Among these unswept blade is the worst in terms of performance though the behaviour is similar. Hence, results discussed so far on unswept blade is expected to be valid for swept blades as well.

5 CONCLUSION

Numerical prediction of hydrokinetic turbine performance was carried out and it was demonstrated that an ellipsoidal hub shape can reduce thrust without compromising on the performance. Different blade sweeps were achieved through stacking of blades along different chord locations and it was seen that the performance of forward swept blade is the best (with

shaft power of 385 W) and unswept blade performs worst (shaft power of 373 W). Blunt trailing edge, necessitated from manufacturing constraints, reduces performance of the turbine when compared with that due to sharp trailing edge. Effect of turbine location inside the water body seems to affect the turbine performance and care must be taken to have appropriate depth below the water-air interface. From the present results, a safe depth of 1.4 m below the free surface for the given turbine configurations was shown to be necessary.

ACKNOWLEDGEMENT

Authors would like to acknowledge the funding received from National Institute of Ocean Technology, Chennai, India.

REFERENCES

[1] Khan M.J., Bhuyan G, Iqbal M.T., Quaicoe J.E. Hydrokinetic energy conversion systems and assessment of horizontal and vertical axis turbines for river and tidal applications: a technology status review. *Applied Energy* (2009) **86**:1823-1835.

[2] Malipeddi, A. R. and Chatterjee, D. Influence of duct geometry on the performance of Darrieus hydroturbine. *Renewable Energy* (2012) **43**, 292-300.

[3] Setoguchi T. Development of two-way diffuser for fluid energy conversion system. *Renewable Energy* (2004) **29(10)**1757-1771.

[4] http://verdantpower.com

[5] http://www.bluenergy.com/Technology.htm

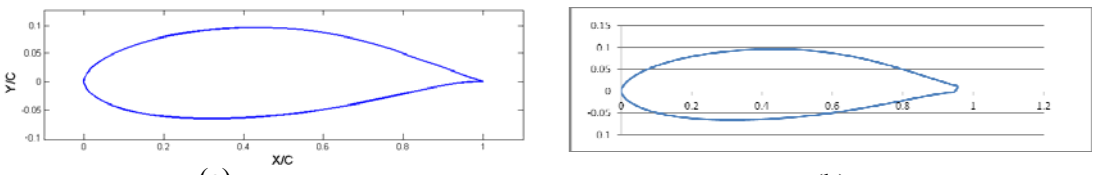
[6] http://www.gcktechnology.com/GCK/pg2.html

[7] Kang, S., Borazjani, I., Jonathan, A.C. and Sotiropoulos, F. Numerical simulation of 3D flow past a real-life marine hydrokinetic turbine. *Adv. Water Res.* (2012) **39**, 33–43.

[8] Mukherji, S. S. Kolekar, N., Banerjee, A. and Mishra, R. Numerical investigation and evaluation of optimum hydrodynamic performance of a horizontal axis hydrokinetic turbine. *J. Renewable Sustainable Energy* (2011) **3**, 063105.

[9] Guney, M. S. and. Kaygusuz, K. Hydrokinetic energy conversion systems: A technology status review. *Renewable and Sustainable Energy Reviews* (2010) **14**, 2996–3004.

[10] Anyi, M. and Kirke, B. Hydrokinetic turbine blades: Design and local construction techniques for remote communities. *Energy for Sustainable Development* (2011) **15**, 223-230.



(a) (b)

Figure 1. Profiles of S822: a) original profile, b) modified profile

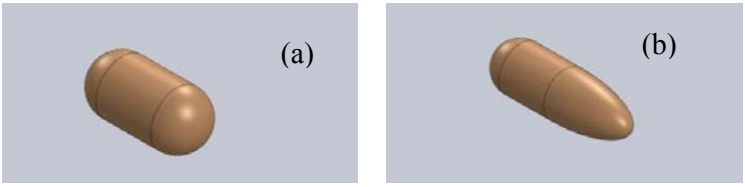


Figure 2. Profiles of hub: a) hemispherical front b) ellipsoidal front

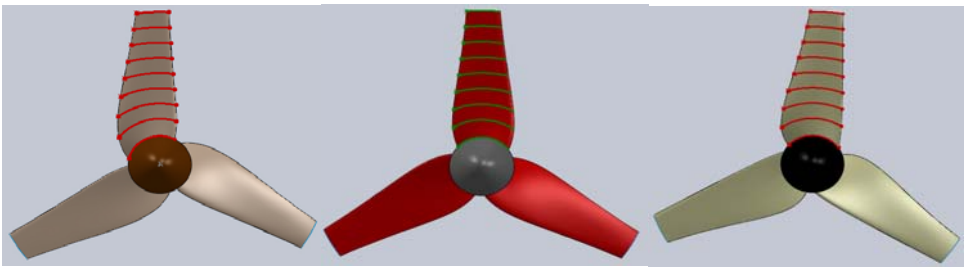


Figure 3. Front views of (a) backward-swept, (b) zero swept, and, (c) forward-swept turbine geometries

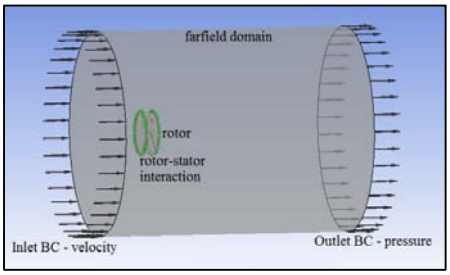


Figure 4. Computational domain along with boundary conditions

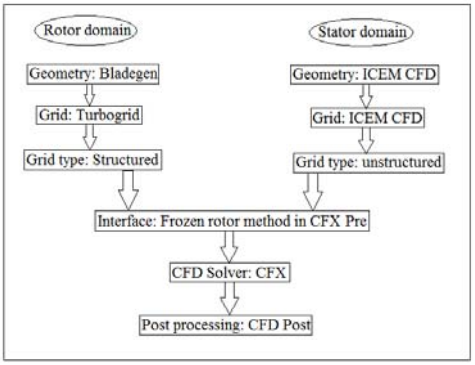


Figure 5. Numerical strategy adopted in predicting hydrokinetic turbine performance

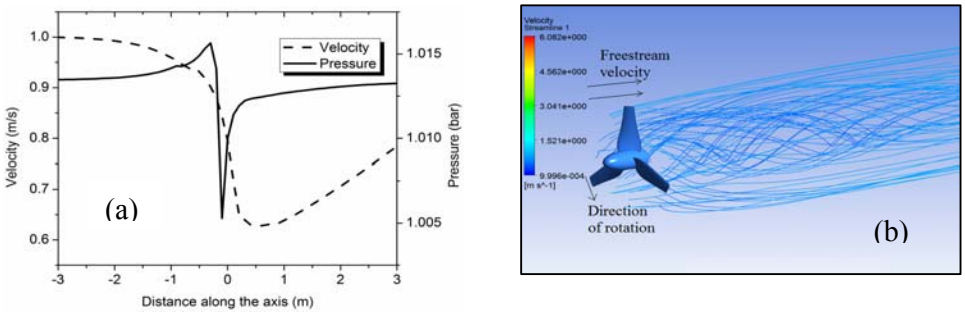


Figure 6. (a) Pressure and velocity variation axial direction, (b) Streamlines in the wake of rotating turbine

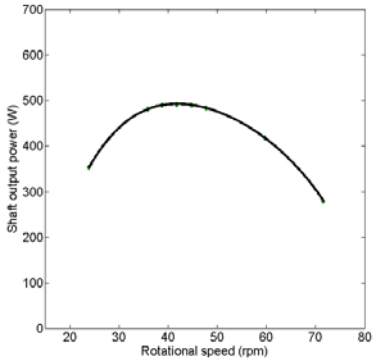


Figure 7. Variation of shaft out power with rotational speed

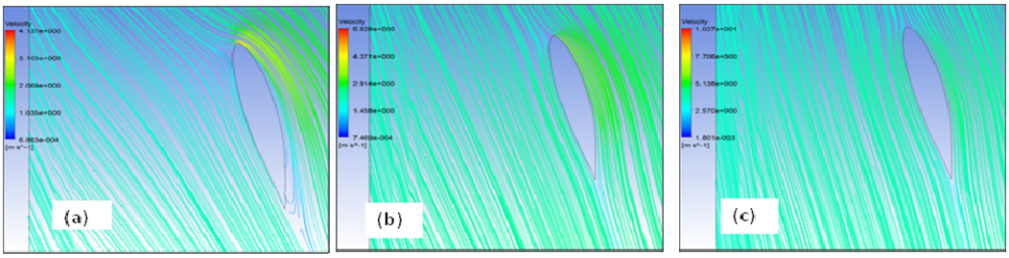


Figure 8. Streamlines depicting relative velocity near a blade at mid-span. (a) λ=2, (b) λ=3.5 and (c) λ=6

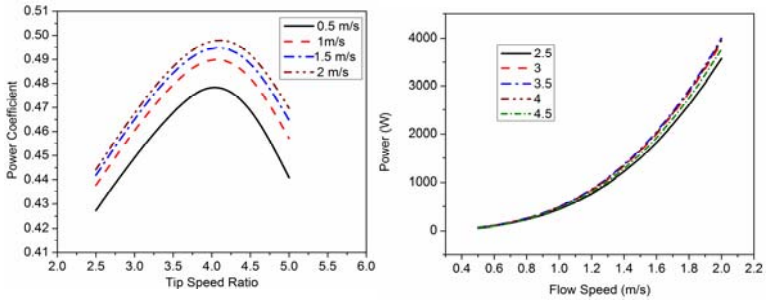


Figure 9. Effect of freestream speed. (a) Variation of power coefficient with tip speed ratio and (b) Variation of maximum output power with freestream speed

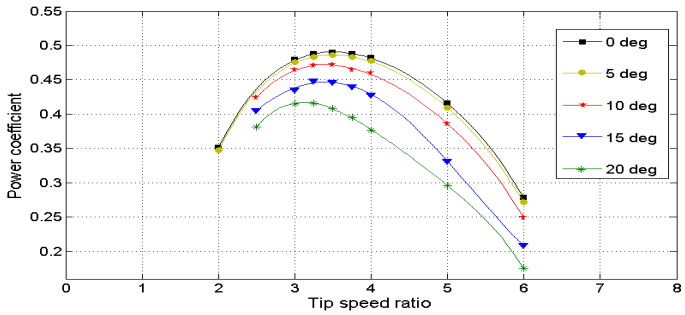


Figure 10. (a) Effect of incoming flow direction on turbine performance

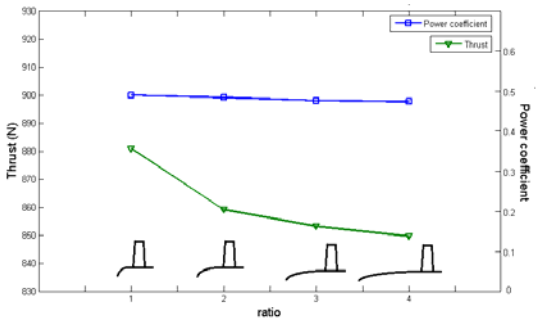


Figure 11. Effect of nose profile on thrust and power coefficient

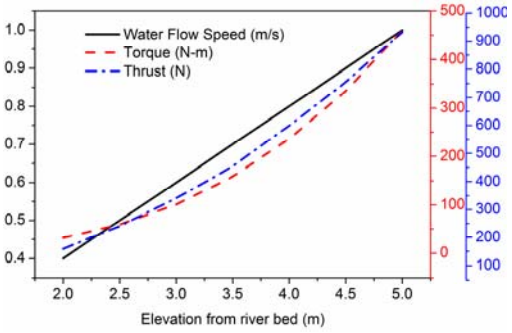


Figure 12. Effect of elevation on turbine performance

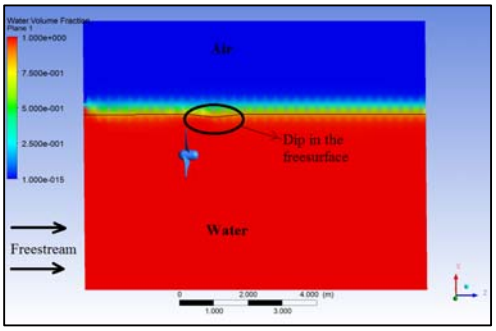


Figure 13. Variation of free surface height due to the placement of turbine near the surface

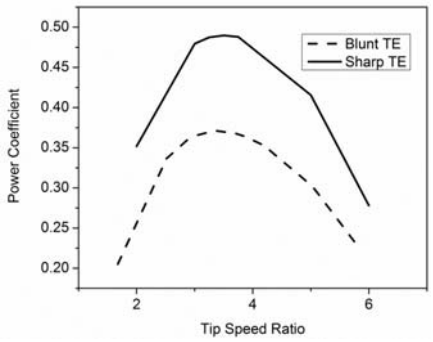


Figure 14. Effect of trailing edge shape on turbine performance

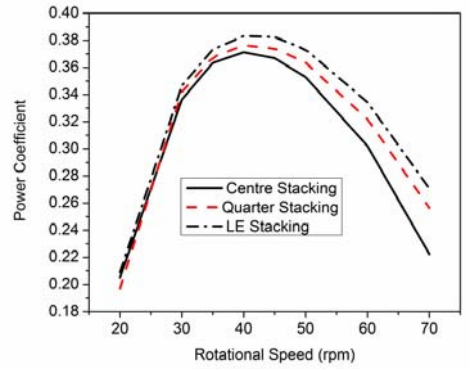


Figure 15. Effect of blade stacking and orientation on turbine performance

V International Conference on Computational Methods in Marine Engineering
MARINE 2013
B. Brinkmann and P. Wriggers (Eds)

WAVECAT® WAVE ENERGY CONVERTER MODELLING BY MEANS OF A RANS-VOF NUMERICAL MODEL

H. FERNÁNDEZ[a], G. IGLESIAS[b], I. LÓPEZ[c] AND S. SCHIMMELS[a]

[a] Forschungszentrum Küste (FZK)
Merkurstrasse 11, D-30419 Hannover, Germany
e-mail: fb@fzk-nth.de, http://www.fzk-nth.de

[b] School of Marine Science and Engineering,
Plymouth University
Drake Circus, PL4 8AA, Plymouth, United Kingdom
email: gregorio.iglesias@plymouth.ac.uk, http://plymouth.ac.uk/staff/giglesias

[c] Group of Civil Engineering and Marine Energies,
University of Santiago de Compostela
Campus Universitario sn, 28002, Lugo, Spain
email: ivan.lopez@usc.es, http://www.usc.es/gicema

Key words: WaveCat, Wave Energy Converter, Wave Overtopping, RANSE-VoF.

Abstract. The WaveCat Wave Energy Converter is a floating structure formed by two hulls (like a catamaran), but unlike a catamaran the hulls are not parallel, they converge from bow towards stern. Its principle of wave energy capturing is wave overtopping, the incident waves are propagating between the wedge formed by the two hulls and they eventually overtop the freeboard, the water is collected in reservoirs placed on deck and the difference between the water level inside the reservoirs and the mean sea level is taken into advantage to propel ultra-low head turbines. Physical model tests were performed in order to validate and develop the basic concept, small and medium scale experiments with a fixed and a floating model respectively. In addition a numerical model was developed, RANS-VoF models were employed; the model solves the RANS (Reynolds Averaged Navier Stokes) equations with a Volume-of-Fluid approach (in order to track the free surface position). The goal of the model is conducting the optimization of the device. In this sense a numerical wave tank as well as a 2D fixed model were validated and both 3D fixed and floating models were implemented. Detailed methodology about the implementation and validation of these models is presented in this paper.

1 INTRODUCTION

For wave energy to become a fully developed source of energy three main aspects should be solved. Initially, the wave energy resource should be further assessed due to the spatial and temporal variations that this resource represents, see [1], thus a more accurate siting for wave

energy farms can be conducted. Secondary, as in the case of other renewables (e.g. wind energy), performing the environmental impact assessment is an important aspect (imposed by law), in order to assess the consequences of converting the energy source into electricity and therefore establishing or not the viability of the wave energy farm; some work of this kind was performed at different locations of the European coast [2, 3]. Finally, reliable, efficient and low impact WECs have to be developed, this is the most challenging aspect, in this sense, intense work was made over the last years to optimize and assess different WEC technologies [4-6]. This work deals with the WaveCat, a recently patented Wave Energy Converter. Different experimental campaigns were conducted with this concept [7] to perform the prove of concept as well as to record data for the validation of numerical models. As a complementary tool in the development of this WEC, the goal of this paper is to present the different numerical RANS-VoF models developed for the WEC optimization. The use of numerical modeling allows a great capability in terms of measurement techniques (i.e. flow velocity fields, pressure distribution, turbulence intensity…) and once the models are validated, an important amount of money and time can be saved with model construction, sensors, calibrations, etc.

2 THE WAVECAT CONCEPT

The WaveCat is a floating WEC intended to work in intermediate water depths (50-100 m), its principle of capturing is wave overtopping. The device is formed by two hulls, the hulls form a wedge in plan view, they are convergent from bow towards stern, Figure 1. The single-point mooring to a catenary-buoy allows the device to be parallel to the incident waves. Waves are propagating between the wedge and their height is enhanced, due to this amplification the amplitude of the incoming waves is bigger than the current freeboard and wave overtopping is occurring at a certain point in the inner hull side. The water is elevated to different reservoirs placed on-deck and its potential energy is used to move ultra-low head turbines located below the reservoirs and the water is returned back to the sea; further information about the concept can be found in [7, 8].

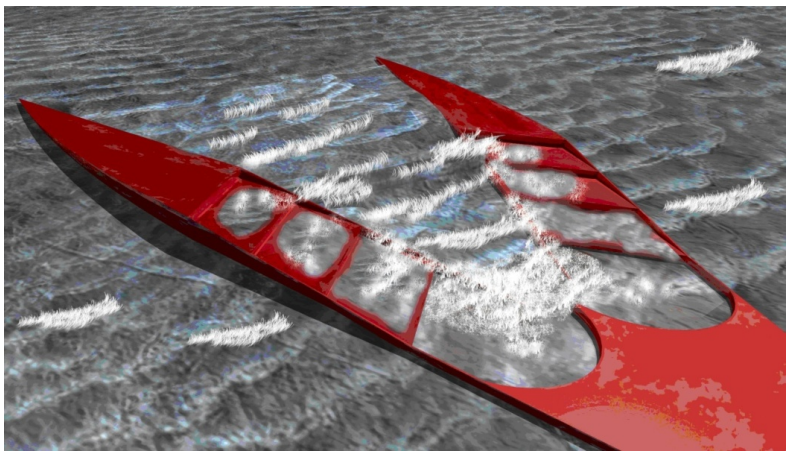


Figure 1: The WaveCat concept

3 WAVECAT NUMERICAL MODELING

3.1 The RANS-VOF model

The model is based on the Navier-Stokes equations, which are non linear equations representing the fluid motion. For a generic case in three dimensions and an incompressible fluid (density is constant in space and time) the equations are the following:

$$\frac{(\partial u)}{\partial x} + \frac{(\partial v)}{\partial y} + \frac{(\partial w)}{\partial z} = 0, \tag{1}$$

$$\frac{(\partial u)}{\partial t} + \frac{(\partial uu)}{\partial x} + \frac{(\partial uv)}{\partial y} + \frac{(\partial uw)}{\partial z} = f_x + \frac{1}{\rho}\frac{(\partial \sigma_{xx})}{\partial x} + \frac{1}{\rho}\frac{(\partial \sigma_{xy})}{\partial y} + \frac{1}{\rho}\frac{(\partial \sigma_{xz})}{\partial z}, \tag{2}$$

$$\frac{(\partial v)}{\partial t} + \frac{(\partial vu)}{\partial x} + \frac{(\partial vv)}{\partial y} + \frac{(\partial vw)}{\partial z} = f_y + \frac{1}{\rho}\frac{(\partial \sigma_{yx})}{\partial x} + \frac{1}{\rho}\frac{(\partial \sigma_{yy})}{\partial y} + \frac{1}{\rho}\frac{(\partial \sigma_{yz})}{\partial z} \text{ and} \tag{3}$$

$$\frac{(\partial w)}{\partial t} + \frac{(\partial wu)}{\partial x} + \frac{(\partial wv)}{\partial y} + \frac{(\partial ww)}{\partial z} = f_z + \frac{1}{\rho}\frac{(\partial \sigma_{zx})}{\partial x} + \frac{1}{\rho}\frac{(\partial \sigma_{zy})}{\partial y} + \frac{1}{\rho}\frac{(\partial \sigma_{zz})}{\partial z}. \tag{4}$$

In the previous system of equations the unknowns are (u,v,w) the field velocities. The vector f of f_i components represents the forces per unit of volume and σ is the tensor of σ_{ij} components representing the forces per unit of surface. The equations presented above represent in differential form the equation of mass conservation and the equation of momentum conservation. Solving these equations with the proper boundary conditions provides the flow characteristics in three dimensions. However the computational requirements and specially the difficulty to deal with turbulence requires introducing a turbulence model simplifying the initial equations.

The model solves the Reynolds Averaged Navier Stokes (RANS) equations by means of applying a finite volume method. These equations are obtained by means of the decomposition of the instant velocity and the pressure field of the Navier-Stokes equations in an average value and in a fluctuant component. The resulting equations are identical to the original ones, except for a new additional term appearing in the transport equation. This term is the Reynolds stress tensor, which is defined as follows:

$$T_t \equiv -\rho\overline{v'v'} = \begin{bmatrix} \overline{u'u'} & \overline{u'v'} & \overline{u'w'} \\ \overline{u'v'} & \overline{v'v'} & \overline{v'w'} \\ \overline{u'w'} & \overline{v'w'} & \overline{w'w'} \end{bmatrix}. \tag{5}$$

In this case an *Eddy* viscosity model was employed using the concept of turbulent viscosity in order to model the Reynolds stress tensor as function of mean flow quantities. A $k - \varepsilon$ model was used in this work, this model offers a good compromise between accuracy, strength and computational requirements. As we are dealing with a free surface problem, i.e. multiphase flow (air and water), a Volume of Fluid (VoF) scheme was employed in this work [9]. By means of this approach, the free surface position between phases is captured, this

scheme was chosen because it is a proper way to simulate free surface flows and the size of the free surface is very small relatively to the rest of the flow, furthermore the VoF method is numerically efficient.

3.2 Numerical wave tank

Firstly, the experimental wave flume of the University of Santiago de Compostela (Spain) is reproduced by means of the numerical model in order to validate wave generation and propagation. The experimental facility is 20 m long, 0.65 m wide and 0.95 m high whereas the analogous numerical wave tank is exactly the same but the absorption system in the wave generator is carried out with a ramp upstream to the position of the wave maker (5.5 m length) and the flume height is slightly smaller (0.7 m for the numerical wave tank) in order to reduce the number of cells and therefore the computational cost, Figure 2. Regarding the width of the tank, as this is a 2D problem, only a longitudinal slice with a width of 0.001 m is considered. The reference system is set as follows: X is parallel to the longitudinal axes of the flume and positive towards the ramp, Z is zero at the free surface position and positive towards the top of the flume and Y is normal to the flume sides and positive in sense of forming a positive XYZ trihedron.

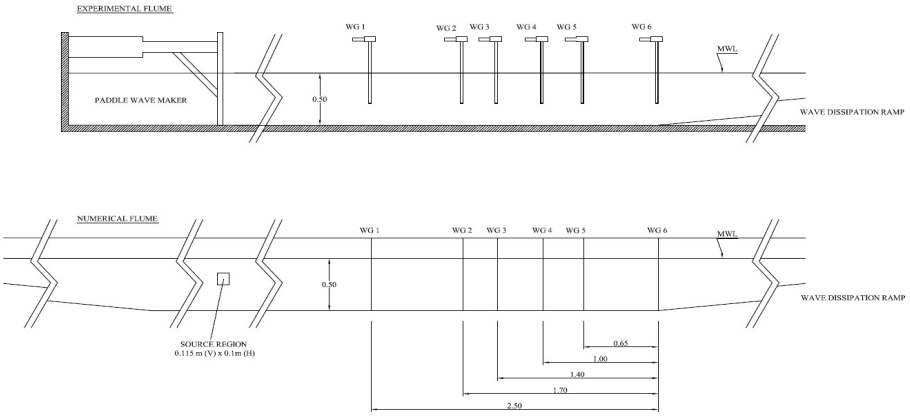


Figure 2: Numerical and experimental wave tank.

The wave generation in the numerical wave tank is conducted by means of an internal wave maker, a source function is set inside the computational domain, Figure 3. The internal wave maker is designed in order to avoid wave reflection following [10], in their work they propose a general method to generate different types of waves in numerical wave tank based on Navier-Stokes equations. The further theoretical background is given in [10]. Regular waves as well as irregular waves can be generated by means of an internal wave maker. A regular wave following linear theory [11] is defined as,

$$\eta(t) = \frac{H}{2}\sin(\omega t). \tag{6}$$

where ω is the wave frequency and H is the wave height. In terms of the source function, this expression is

$$s(t) = \frac{CH}{A}\sin(\omega t), \tag{7}$$

where C is the wave celerity, H is the wave height, A is the source region area and ω is the angular frequency.

An irregular wave is composed by a series of linear waves with different wave frequencies and wave heights. Therefore an irregular wave train can be generated by superimposing different regular waves,

$$s(t) = \sum_{i=1}^{n} \frac{C_i H_i}{A}\sin(\omega_i t + p_{si}), \tag{8}$$

Where p_{si} is the phase of each i wave. The irregular waves generated in the numerical model are defined by a JONSWAP spectrum, [12], with a peak factor of γ = 3.3. Once the spectrum is defined with the proper parameters, the wave components in the irregular wave train are calculated following [13] and the variables H_i, T_i and p_{si} are known and thus the function *s(t)* can be determined.

The geometry of the source function is a rectangle composed of *m* x *n* cells, a width *Ws* and *Hs* height. The vertical section crossing the centre of the source region can be considered the location of the numerical wave maker. Following the good practices given by [10] the dimensions of the source region are: *Ws* = 0.1 m, *Hs* = 0.115 m and *Lcs* = 0.200 m, Figure 3.

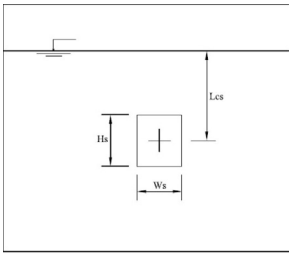


Figure 3: Source region geometry.

The discretization of the computational domain is conducted by hexahedral elements, these present variable size (in Z direction) for an optimal performance of the VoF scheme. Due to this is a 2D problem, just one cell in Y dimension is set, this cell has a thickness of 0.001 m. For the whole computational domain, the cell size in X dimension is the same, 0.05 m, being enough for resolving one wavelength (in our cases the wavelength is between L = 2.24 m and L = 5.09 m). In Z dimension the cell size is variable, this means that grid refinement is performed in the free surface area (between Z = -0.05 m and Z = 0.05m, where Z = 0 m is the mean water level) in order to allow a proper definition of the free surface, in this case the cell size is 0.01 m in Z dimension. In the rest of the computational domain the cell size in Z direction is 0.025 m.

Regarding the boundary conditions, all the wall sides as well as the dissipation ramps are set to wall no-slip boundary conditions, this means that there is no flow through these boundaries and the tangential flow velocity is zero. Also at the bottom a wall boundary condition was set, but in this case is a wall slip condition is used (the tangential flow velocity is nonzero) in order to avoid bottom friction and thus attenuation of the wave train. The top side of the domain is set to a pressure outlet boundary condition, where a constant pressure equal to the atmospheric pressure is applied. The lateral sides of the domain are set to symmetry conditions. The contours around the source region are established by an interface condition, which allows fluid crossing throughout itself.

Referring to the computational parameters, the time step is set satisfying the CFL condition, this means that the Courant number should be smaller than one in the whole computational domain,

$$\mu = \frac{\lambda \Delta t}{\Delta x} \leq 1. \tag{9}$$

Where μ is the Courant number, λ is the group celerity of incoming waves, Δt is the time step and Δx is the cell size in X direction. Satisfying this condition ensures that the method is stable and the solution converges. In this case the time step is set to Δt = 0.0025 s.

In the problem definition the following calculation constants are given. The acceleration of gravity is g = 9.81 m/s^2, the pressure of reference is P_{ref} = 101325 Pa (set equal to zero in the model), water density is ρ_w = 997.561 kg/m3 and air density is ρ_a = 1.184 kg/m3.

The recorded data from the numerical wave tank is compared with the experimental data. Five validation tests were performed in total, one validation test for regular waves and four for irregular waves were conducted simulating the conditions of the physical experiments. The wave conditions for the regular wave test (Test 001) are H = 0.04 m, T = 1.56 s and the testing time is 60 s, whereas for the irregular wave tests are reported in Table 1.

Table 1: Parameters for the validation of the irregular wave tests, H_s, significant wave height, T_p, peak period and t_t the testing time.

Test	H_s (m)	T_p (s)	t_t(s)
002	0.050	1.27	180
003	0.055	1.56	180
004	0.060	1.84	180
005	0.065	2.12	180

The validation in time domainis briefly presented in Figure 4, this figure represents the comparison between the experimental and numerical wave measurements at different locations in the flume for the irregular wave test 003, just 60 seconds of the record are presented for purpose of better visualization. The solid line represents the experimental data whereas the squared line represents the numerical measurements. Even if there are some little issues in some of the wave troughs and in consecutive wave heights representing high frequencies (around 65 seconds in the first subplot), in general one can notice rather good agreement between the experimental and the numerical wave profiles.

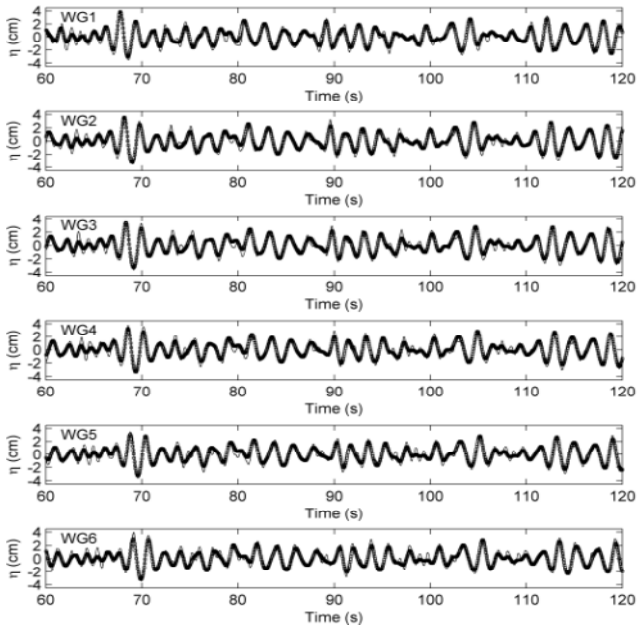


Figure 4: Validation test 003, (-) experimental data, (□) numerical data.

The comparison between the numerical and the experimental data is performed by means of the mean square error (MSE) and the correlation coefficient, *R*, these are defined as follows,

$$MSE = \frac{1}{N}\sum_{i=1}^{N}(\eta_i^M - \eta_i^E)^2, \tag{10}$$

$$R = \frac{\sum_{i=1}^{N}(\eta_i^M - \overline{\eta}_M)(\eta_i^E - \overline{\eta}_E)}{\sqrt{\sum_{i=1}^{N}(\eta_i^M - \overline{\eta}_M)^2 (\eta_i^E - \overline{\eta}_E)^2}}. \tag{11}$$

Where η_i^M is the free surface displacement recorded in the numerical wave tank, η_i^E is the registered free surface time series in the experimental wave tank, and $\overline{\eta_M}$ and $\overline{\eta_E}$ are the mean values of the registration, respectively.

The results at each wave probe are presented in table 2, as could be expected at the beginning of this work, the model works better for the regular waves, at all the locations the correlation coefficient is around 1, while for the irregular wave tests the correlation factor is around 0.9, even for the gauges located further downstream from the wave generation (WG5 and WG6), this means that the numerical wave tank is correctly modeling wave generation and wave propagation.

Table 2: Mean square error (*MSE*) and correlation coefficient (*R*) for the validation tests at different locations.

Test		WG1	WG2	WG3	WG4	WG5	WG6
001	MSE (cm^2)	0.0684	0.0746	0.0493	0.0487	0.0749	0.0420
	R	0.98	0.99	0.99	0.99	0.99	0.99
002	MSE(cm^2)	0.3457	0.3416	0.3512	0.3843	0.3762	0.4303
	R	0.9	0.9	0.9	0.89	0.88	0.88
003	MSE(cm^2)	0.2484	0.2449	0.2602	0.2918	0.3239	0.4059
	R	0.93	0.93	0.92	0.91	0.91	0.88
004	MSE(cm^2)	0.2635	0.2472	0.2839	0.3130	0.3693	0.4438
	R	0.94	0.94	0.93	0.92	0.9	0.88
005	MSE(cm^2)	0.3116	0.3639	0.4265	0.4922	0.5685	0.8177
	R	0.93	0.92	0.91	0.89	0.87	0.83

3.3 2D fixed model

All conditions (layout, wave generation, wave dissipation, etc.) are exactly the same as in the validated numerical wave tank above, but now a 2D model of the WaveCat is set at X = 11.85 m from the wave generation, Figure 5.

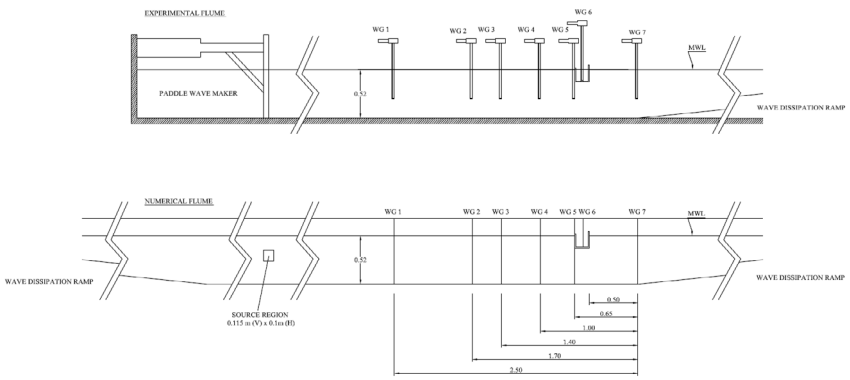


Figure 5: Experimental vs. Numerical layout for the 2D tests with the fixed model.

In addition, the cell size is smaller in the model area (between X = 19.20 m, X = 19.55 m and Z = -0.15 m and Z = 0.10 m) to optimize the overtopping capturing, the cell size is 0.005 m in X dimension and 0.0025 m in Z dimension. Concerning the boundary conditions, the model contours are set like wall-no slip condition.

As reported previously, the wave generation in the numerical wave flume is performed by means of an internal wave maker, following [13] the wave phases for the source function are calculated randomly between $-\pi$ and $+\pi$; this means that although the effort to faithfully reproduce the laboratory conditions and therefore the spectrum characteristics, direct comparison between series in time domain is not possible, thus the validation is performed in

frequency domain. Figure 6 presents the graphical verification for an irregular wave case, the conditions are: water depth, d = 0.517 m, freeboard, F = 0.033 m, significant wave height, H_s = 0.065 m and peak period, T_p = 1.84s.The figure represents the power spectral density for the wave profile recorded at wave gauges number 1 and 4, respectively. The solid line corresponds to the experimental data and the dotted line represents the numerical measurement. For wave probe 1 the correlation coefficient between the signals is R = 0.93 whereas the mean square error is MSE = 1.024 cm^4/Hz^2 over the whole frequency bandwidth; in the case of wave probe 4 the correlation coefficient is R = 0.91 and MSE = 1.381 cm^4/Hz^2. It can be observed that in general the numerical model overestimates the power spectral density around the central frequency for both gauges, this may be caused by the presence of the model (vertical smooth wall), in the numerical wave tank the wave reflection is bigger compared to the physical test because the wave dissipation at the wave generation is performed in a different way for the numerical case.

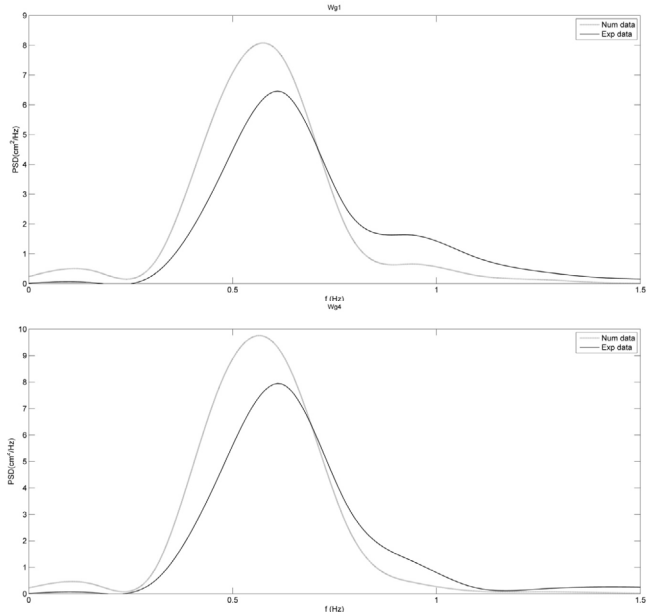


Figure 6: Graphical validation in frequency domain, (-) experimental data and (--) numerical data.

3.4 3D fixed model and 3D floating model

A WaveCat 3D fixed model was also implemented in the numerical model in order to exactly reproduce the physical experiments conducted with this model. The experimental layout is given in Figure 7. The conditions for the test are: convergence angle between the hull and the side wall of the flume, α = 60 °, freeboard, F = 0.02 m and water depth, d = 0.5 m. Symmetry is used to conduct the tests, this means that just one hull of the device is set in the numerical model and the axis of symmetry is the side wall of the flume.

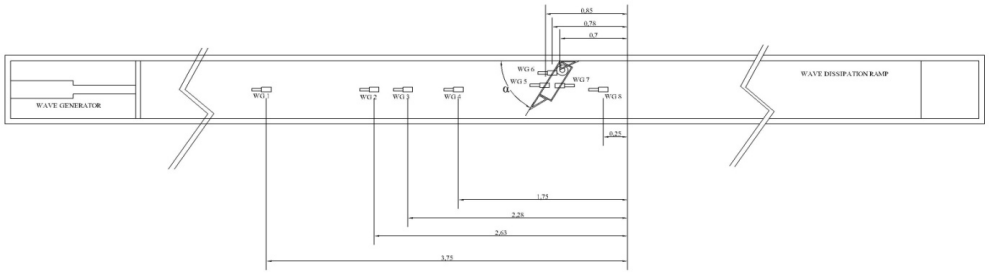


Figure 7: Experimental set-up for the tests with the 3D fixed model.

The wave generation is also conducted by means of the internal wave maker, this was also constructed following [10] good practices. The computational mesh is like in the 2D case formed by hexahedral volumes of variable size, in this case also grid refinement is conducted in the free surface area as well as in the model area; the cell size in X and Z direction is the same as in the 2D tests but as this is a 3D case, the cell size in Y direction is Δy = 0.05 m in the model area (to properly capture the overtopping bore) and Δy = 0.1 m in the rest of the computational domain. Figure 8 presents a frame during the simulation of this 3D numerical model, this figure shows an overtopping event occurring during the test.

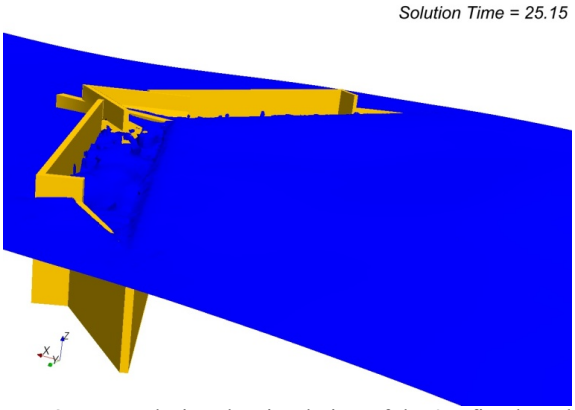


Figure 8: Frame during the simulation of the 3D fixed model.

Furthermore, a 3D floating model was implemented; the model is used to simulate the motion of the rigid body in response to pressure and shear forces caused by the incoming waves. The model calculates the resultant force and moment acting on the body due to all the influences and solves the governing equations of the rigid body motion to find the new position of the rigid body at each time step. In this case heave and pitch motions were enabled in the model, Figure 9 presents one snapshot of the simulation corresponding to this 3D floating model, here one can observe the wave overtopping occurring inside the reservoir placed on deck. Currently this model is under development and it requires more experience, but the first steps with this are very promising.

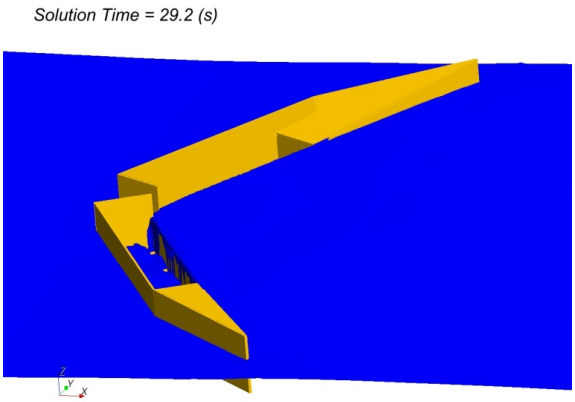


Figure 9: The numerical model of the 3D floating model.

4 CONCLUSIONS

Developing and optimizing reliable and efficient WECs is a key aspect to fully develop wave energy to a commercial stage. For this purpose, the WaveCat technology is developed by means of physical and numerical modelling, the numerical tool to carry out the WaveCat optimization is presented and described in this work.

A RANS-VoF model is used to simulate three different models of this WEC technology, detailed description of its implementation is given in this paper. Firstly, a time domain validation of the numerical wave tank is performed with rather good results, showing that the model accurately reproduces the wave generation and wave propagation. The second step is to implement a 2D fixed model in the validated numerical wave tank, in this case the validation is conducted in frequency domain and the results are reported, it is observed that the model overestimates the spectral density compared to the experimental wave tank. Besides, a 3D fixed model and a 3D floating model are implemented in the numerical model, although this is not validated yet, the numerical model is able to simulate a very non-linear problem like the wave-structure interaction in presence of wave overtopping with a very good stability and convergence in terms of simulation performance.

REFERENCES

[1] Iglesias G, López M, Carballo R, Castro A, Fraguela JA, Frigaard P. Wave energy potential in Galicia (NW Spain). Renewable Energy. 2009 11;34(11):2323-33.

[2] Smith HCM, Pearce C, Millar DL. Further analysis of change in nearshore wave climate due to an offshore wave farm: An enhanced case study for the wave hub site. Renewable Energy. 2012;40(1):51-64.

[3] Carballo R, Iglesias G. Wave farm impact based on realistic wave-WEC interaction. Energy. 2013(0).

[4] Babarit A, Hals J, Muliawan MJ, Kurniawan A, Moan T, Krokstad J. Numerical benchmarking study of a selection of wave energy converters. Renewable Energy. 2012 5;41(0):44-63.

[5] Margheritini L, Vicinanza D, Frigaard P. SSG wave energy converter: Design, reliability and hydraulic performance of an innovative overtopping device. Renewable Energy. 2009 5;34(5):1371-80.

[6] Tedd J, Peter Kofoed J. Measurements of overtopping flow time series on the wave dragon, wave energy converter. Renewable Energy. 2009 3;34(3):711-7.

[7] Fernandez H, Iglesias G, Carballo R, Castro A, Fraguela JA, Taveira-Pinto F, et al. The new wave energy converter WaveCat: Concept and laboratory tests. Mar Struct. 2012 12;29(1):58-70.

[8] Fernandez H, Iglesias G, Carballo R, Castro A, Bartolome P. Physical and numerical modeling of the WaveCat wave energy converter. Proc. of 32th international conference on coastal engineering. shanghai, china; ; 2010.

[9] Hirt CW, Nichols BD. Volume of fluid (VOF) method for the dynamics of free boundaries. Journal of Computational Physics. 1981 1;39(1):201-25.

[10] Lin P, Liu PL. Internal wave maker for navier-stokes equations models. Journal of Waterway, Port, Coastal and Ocean Engineering. 1999;125(4):207.

[11] Demirbilek, Z. and Linwood, V. Water wave mechanics, chapter II-1. In: Coastal Engineering Manual. US Army Corps of Engineers; 2008.

[12] Goda Y. Random seas and design of maritime structures. advanced series on ocean engineering, vo. 15. World Scientific Publishing; 2000.

[13] Lara JL, Garcia N, Losada IJ. RANS modelling applied to random wave interaction with submerged permeable structures. Coast Eng. 2006 4;53(5–6):395-417.

V International Conference on Computational Methods in Marine Engineering
MARINE 2013
B. Brinkmann and P. Wriggers (Eds)

REVIEW OF INDIVIDUAL BASED MODELLING TECHNIQUES IN A MARINE ENVIRONMENT

THOMAS LAKE, IAN MASTERS AND T. NICK CROFT

Marine Energy Research Group,
Room 136a, Talbot Building, Swansea University,
Swansea, SA2 8PP, United Kingdom
E-mail: marineenergy@swansea.ac.uk Web page: http://swan.ac.uk/engineering/marineenergy/

Key words: Computational Methods, Marine Engineering

Summary: Individual based modelling techniques offer an opportunity to explore the effects of animal behaviour on the environment, and the effects of changes in the environment on animal behaviour. This holds particular relevance in the growing fields of wave and tidal power, where developers are often required to investigate the potential effect of their devices. A number of approaches to IBMs are discussed, including some of the additional challenges faced applying these methods to the marine environment.

1 Introduction

Marine energy is a growing field, with up to 300MW of wave and tidal stream generation expected to be deployed around the UK by 2020. One of the concerns raised by developers is the burden placed on them to protect the marine environment from harm – both in terms of the ecology and the other users of an area. This burden is greater in areas containing protected species and areas designated as Marine Conservation Areas.[1,2]

The impact of marine energy devices can be investigated by monitoring resident populations of marine wildlife. New installations may be backed by several years of observational data, providing a baseline set of data for comparison after a device has been deployed. If the potential impact of a device on a wildlife population could be simulated during the development phase of a project, these results could then be used during the consent phase. The surveys conducted while investigating potential marine energy device deployment sites can also provide a variety of source data to be incorporated into a model.[3]

Individual Based Models (IBMs) are a form of computer model that simulates interactions between a population of entities and/or their surrounding environment. These entities are sometimes referred to as 'agents' or 'boids',[4] and the latter term will be used here. These boids are designed to react to their surroundings in a way that mimics that of the creatures that they represent, and allow us to investigate the outcomes of disturbances and environmental changes on a population.[5,6] These populations could be cetaceans, such as harbour porpoise, diving birds

such as cormorants or fish such as salmon. This contribution examines some of the different ways of planning and implementing an individual based model, and some of the challenges that must be dealt with.

2 Individual Based Modelling Methods

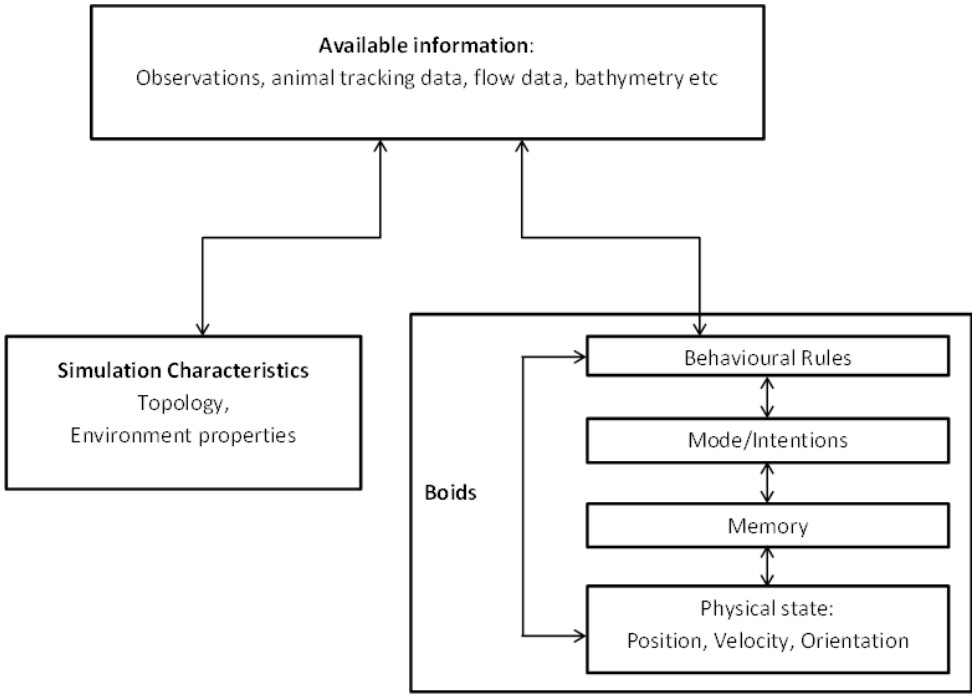


Figure 1: An example IBM in outline

Boids are given a set of rules that are used to determine how that boid will behave within the simulation. An outline of an example IBM is shown in figure 1. The number and detail of the rules used will vary depending on the simulation, but even a very simple set of rules can lead to behaviour that "corresponds to the observer's intuitive notion" of a behaviour.[4] In that example, 3 simple rules gave rise to plausible looking flocks of birds for a computer animation. For the purposes of simulating a specific species in a particular environment, a more detailed set of rules and environmental information is likely to be required.

Rule outputs that define the movement of a boid can do so in two main ways. If the boids are being treated as particles then the rules can calculate forces that act directly on the boid. This allows for drag and other hydrodynamic effects to easily be incorporated to calculate the resultant velocity of the boid at each timestep. In a more complex model, the movement rules can activate 'motors' that control movement in a more complicated model such as the three dimensional spring and node based model used in Tu and Terzopoulos.[7] In this case, the forces acting on the boid (a fish in this case) were generated by changing the shape of the fish by

changing the length of the springs making up it's skeleton.

In addition to influencing the movement of the boid the set of rules incorporated into a simulation may also be used to change how a boid will react to information in the future. Examples of this include switching the boid between different 'intents' or moods, with the movement of the boid governed by it's current intent and the information available to it.[7] An example of this would be that a boid may 'panic' if it identifies a nearby predator, and would then be more likely to move away from other nearby boids than if it were calm or feeding. A boid may also have a memory,[8] in which case the rules might add, remove or update information stored in memory. This information can then be used when the boid is deciding how to behave and how to move. These types of rules add additional complexity, but both reflect aspects of biological life that it is reasonable to assume influences the behaviour of an animal.

Before a boid can make any decisions about it's behaviour or movement, it needs to be aware of it's surroundings. How this happens is model dependent, and varies depending on the level of biological plausibility incorporated. A biologically plausible set of senses will limit the range over which information is available, and present the boid a more restricted set of information. As an example, rather than the boid having access to the bearing and distance to all of it's nearest neighbours, it might only have access to the number of boids that it can 'see' based on a limited field of view. Whether the boid then has access to further information about those boids or not is a design decision that needs to be made for each simulation. Similar considerations can be applied to other senses that animals may be using to determine information about their environment.

A further consideration is that of the effect of the boids on their environment. An example of this would be the depletion of resources in an area based on boid activity, for example depletion of quantities of food in an area due to feeding by the boids.[8] Food in this instance could represent a type of plant, or a species of prey that remains relatively localised. These area based properties require splitting the domain into patches, each patch then being associated with values for each of these properties.[9]

3 Parallelism and Implementation of Individual Based Models

Managing the computational cost of large populations is an important consideration in IBMs, particularly if the rules used are particularly complex or refer to many sources of information. As with many other processes, it is possible to decrease the time required to run a simulation by distributing the computations across multiple processors or nodes.[10] This does present some additional problems that must be considered when the model is being implemented.

The main computational cost of this sort of simulation arises from the time that each boid needs to run through it's decision making procedure. Every boid must process information from it's senses, with the time required dependent on the number of sources of information to be consulted. If the boids interact with each other, even if only in terms of movement decisions, then each boid must also search the list of all boids in the simulation to determine which boids are nearby and decide on their influences on it's movement. This cost can be reduced by partitioning the data spatially such that boids only need to query the list of boids in the local partition. Without this partitioning process, the computation time for the simulation increases according the the

square of the number of boids, $O\left(N^2\right)$, with the increase being reduced to $\sim O\left(N\right)$ by imposing suitable partitions on the data.[11,12] The experience of the Smoothed Particle Hydrodynamics community[13] can also be of use to determine ways of reducing the computational cost of these simulations.

In a partitioned simulation, the calculations that take longest are those that require other processes or nodes to be queried for information about their environment or the position of other boids. If the number of boids near the edges of each partition is minimised, the overall time taken to compute each step of the simulation can be reduced.[14] This allows each partition to be handled locally by a node, with queries to other nodes only being required where a boid is close enough to a border for the location of boids on the other side of the partition to be an influence. This can be done with a number of algorithms, including tree based algorithms, convex hull algorithms such as QHull, and genetic algorithms.[14] Rebalancing the partitions where necessary,[15] is important to minimise the number of inter-node queries, as these will take longer than local lookups.

Related to this is the difficulty of incorporating the different data sets efficiently, which requires taking into account the types of grid and resolution of the data, as well as how this data fits with the partitioning used. If the simulated environment has been split into patches or areas with properties associated with them to represent boid driven changes to the environment then these areas may add an additional constraint to the partitioning process.

4 Field and Background Data for Marine Life

Any attempt to predict the behaviour of marine life in the vicinity of turbines would be meaningless without sufficient understanding of their existing behaviour. It is also necessary to gain an understanding of how these behaviours relate to the environmental conditions around them.

Obtaining data to reach this understanding is one of the challenges for any sort of animal behaviour research, but is a particular issue when trying to examine the behaviour of animals in the marine environment. Observational data may be limited by sea states and prevailing weather conditions, and may not be able to capture the underwater behaviour of diving and swimming animals. The environment itself also adds additional variables to be considered - varying speeds and heights of water due to the tide, variation in that tidal cycle across spring and neap tides and so on - in addition to most of the variables that apply to land based models, such as time of day, season, weather and climate conditions and local topology. Electronic tagging of animals allows individuals to be tracked and their movements analysed, and can be applied to a number of species. These tags can transmit data via satellites, radio or GSM, or log data to be read when the tag is collected.[16,17] These tags are typically combined with GPS receivers and other sensors, allowing for further analysis of the animals' behaviour. The ability to track animals over longer periods of time and over long distances allows for a greater insight into the behaviour of these animals than would be possible with visual observations alone.

When it comes to the behaviour of marine life in water, the currents and characteristics of the water become important when determining their movement. This is particularly applicable to sites under consideration for wave and tidal energy extraction, as these sites by definition

have significant wave activity or strong currents. Depending on the size of the animal being simulated, these flows may be a dominant effect on the boid's overall velocity,[18,19] or may be something that the boid senses and uses as part of it's decision making process. The flow data used by the simulation may be obtained analytically for very simple simulated environments, but in more complex environments these results can be obtained using Computational Fluid Dynamics (CFD) calculations. These results can be compared to measured velocities, obtained using acoustic Doppler current profiler (ADCP) techniques or similar.[3,20,21] The impact of a marine energy device such as a tidal stream turbine can also be included in the CFD calculations, either by explicitly simulating the turbine or by using an approximation such as Blade Element Momentum theory.[19,22] This allows both the turbulence and change in flow speed to be incorporated into the model, including the effects of the turbine wake. These wakes can extend behind the turbine for up to 40 times the rotor diameter.[23]

Closely related to the availability of flow data is bathymetry. Where flow data is being obtained from a CFD model, this model can incorporate the bathymetry data in order to calculate the flow for the environment.[20] The bathymetry may also be used directly by the IBM in order to allow the boids to use that information to guide behaviour and movement. This may be coupled with other information regarding composition of the bed and sediment transport.[24] The depth and gradient of the sea bed have previously been found to correlate with the presence of Harbour Porpoise,[25] as well as with routes used for transit.[16]

Underwater noise is another potential contribution to animal behaviour which may be altered by the installation and operation of marine energy devices. There are many contributions to underwater noise including anthropogenic sources such as boats, shifting sand and sediments, turbulence, wind and rain and noises emitted by marine animals.[3,26] Noise due to turbulence and water flow is exacerbated in fast flowing currents, such as those where marine energy devices may be installed.

While it may not be directly useful for the purposes of creating behavioural rules, it is worth noting that physiological data regarding the species represented by the boids can be useful for determining the effect of interactions with the environment upon them. An notable example here is the study of turbine blade impacts on adult killer whales,[27] which made some conservative estimates of how an adult killer whale might be injured if it were to be struck by the moving blade of a tidal stream turbine. Physiological data regarding fish and smaller marine animals may be useful to determine the risk to these creatures due to pressure differences encountered while transiting through a turbine.[3,28] This may be useful to incorporate into an individual based model where fish are being modelled - either as the main focus of the model or as prey for larger marine life.

One approach to this is to create several models incorporating different possible influences on the behaviour of the animals and comparing these models to collected observational behaviour[25,29] . In Isojunno et. al.[25] this resulted in the creation of 3003 different mathematical models using combinations of 13 recorded environmental variables, varying from time of day to bed gradient. These models were then ranked according to their Akaike Weights[25,29] - a measure of how well a model fits a given set of data relative to the other models being compared.

With this approach, it is worth highlighting that the weights assigned to each model only provide information about the strength of each model relative to the other models being tested. This technique could be used as described to determine the influences worth including in the rules used by the IBM simulation, or could be used to rank the results of different IBM simulations.

In other scenarios, the influences chosen may be selected based on information from literature and the data available. If field data is available that the results can be measured against, then the rules and influences can be adjusted to obtain a suitable correlation between simulation results and the measured data. This may be another aspect of IBMs to which genetic algorithms can be applied. If the rules in use can be encoded as a genome, a suitable fitness function can be chosen to compare the simulated output to the desired result. Improved rule selections can then be generated based on successful genomes. This may be investigated in future work.

5 Conclusions

The term "Individual Based Model" covers a wide range of different models, centred on creating a virtual collection of creatures capable of taking independent actions based on a set of rules. Given sufficient information to choose sensible rules for the behaviour of the simulated animals, results can be obtained that can offer an insight into changes in how an area is used by a species or which illustrate why a species is distributed over an area in a particular fashion.

These models also offer the opportunity to explore how changes to an environment may affect the behaviour of a species resident in that area, something which is potentially useful for developers in the marine energy sector when considering the impact of their devices.

REFERENCES

[1] HM Government, "UK Renewable Energy Roadmap," tech. rep., Department of Energy and Climate Change, July 2011.

[2] D. Lusseau, F. Christiansen, J. Harwood, S. Mendes, P. Thompson, K. Smith, and G. Hastie, "Assessing the risks to marine mammal populations from renewable energy devices – an interim approach," tech. rep., The CCW, JNCC, NERC Knowledge Exchange Workshop, 2012.

[3] M. R. Willis, I. Masters, S. Thomas, R. Gallie, J. Loman, A. Cook, R. Ahmadian, R. Falconer, B. Lin, G. Gao, M. Cross, N. Croft, A. J. Williams, M. Muhasilovic, I. Horsfall, R. Fidler, C. Wooldridge, I. Fryett, P. Evans, T. O'Doherty, D. O'Doherty, and A. Mason-Jones, "Tidal turbine deployment in the bristol channel: a case study," in *Proceedings of the Institution of Civil Engineers - Energy*, vol. 163, pp. 93–105, August 2010.

[4] C. W. Reynolds, "Flocks, herds and schools: A distributed behavioral model," *ACM SIGGRAPH Computer Graphics*, vol. 21, no. 4, pp. 25–34, 1987.

[5] J. Willis, "Modelling swimming aquatic animals in hydrodynamic models," *Ecological Modelling*, vol. 222, no. 23–24, pp. 3869 – 3887, 2011.

[6] R. A. Stillman, A. D. West, R. W. G. Caldow, and S. E. A. L. D. dit Durell, "Predicting the effect of disturbance on coastal birds," *Ibis*, vol. 149, pp. 73–81, 2007.

[7] X. Tu and D. Terzopoulos, "Artificial fishes: Physics, locomotion, perception, behavior," in *Proceedings of the 21st annual conference on Computer graphics and interactive techniques*, pp. 43–50, ACM, 1994.

[8] H. Saarenmaa, N. D. Stone, L. Folse, J. Packard, W. Grant, M. Makela, and R. Coulsen, "An artificial-intelligence modeling approach to simulating animal habitat interactions," *Ecological Modelling*, vol. 44, pp. 125–141, 1988.

[9] R. Stillman, "MORPH - an individual based model to predict the effect of environmental change on foraging animal populations," *Ecological Modelling*, vol. 216(3–4), pp. 265–276, 2008. STP SEA Topic Paper Annexe, Fish Behaviour and Physiology (2009), DEFRA, UK.

[10] H. Lorek and M. White, "Parallel bird flocking simulation," 1993.

[11] B. Zhou and S. Zhou, "Parallel simulation of group behaviors," in *Proceedings of the 2004 Winter Simulation Conference R. G. Ingalls, M. D. Rossetti, J. S. Smith, and B. A. Peters, eds.*, 2004.

[12] G. Vigueras, M. Lozano, C. Pérez, and J. Orduña, "A scalable architecture for crowd simulation: Implementing a parallel action server," in *37th International Conference on Parallel Processing*, pp. 430–437, September 2008.

[13] J. Bonet and S. Kulasegaram, "Correction and stabilization of smooth particle hydrodynamics methods with applications in metal forming simulations," *International Journal for Numerical Methods in Engineering*, vol. 47, no. 6, pp. 1189–1214, 2000.

[14] G. Vigueras, M. Lozano, J. Orduña, and F. Grimaldo, "A comparative study of partitioning methods for crowd simulations," *Applied Soft Computing*, vol. 10, pp. 225–235, January 2010.

[15] R. Solar, R. Suppi, and E. Luque, "High performance distributed cluster-based individual-oriented fish school simulation," in *Proceedings of the International Conference on Computational Science*, vol. 4 of *Procedia Computer Science*, pp. 76–85, 2011.

[16] A. Read and A. Westgate, "Monitoring the movements of harbour porpoises (*Phocoena Phocoena*) with satellite telemetry," *Marine Biology*, vol. 130, pp. 315–322, 1997.

[17] D. Thompson, "Assessment of Risk to Marine Mammals from Underwater Marine Renewable Devices in Welsh waters (on behalf of the Welsh Government), Phase 2: Studies of Marine Mammals in Welsh High Tidal Waters, Annex 1 Movements and Diving Behaviour of Juvenile Grey Seals in Areas of High Tidal Energy." http://www.marineenergypembrokeshire.co.uk/publications-resources, July 2012. JER3688.

[18] R. J. H. Herbert, J. Willis, E. Jones, K. Ross, R. Hübner, J. Humphreys, A. Jensen, and J. Baugh, "Invasion in tidal zones on complex coastlines: modelling larvae of the non-native Manila clam, *Ruditapes philippinarum*, in the UK," *Journal of Biogeography*, vol. 39, pp. 585–599, 2012.

[19] A. J. Williams, T. Croft, I. Masters, and M. R. Willis, "Investigating environmental issues related to operation of tidal stream turbines using a bem-cfd model," in *World Renewable Energy Congress XI*, September 2010.

[20] T. O'Doherty, A. Mason-Jones, D. O'Doherty, P. Evans, C. Wooldridge, and I. Fryett, "Considerations of a horizontal axis tidal turbine," in *Proceedings of the Institution of Civil Engineers - Energy*, vol. 163, pp. 119–130, 2010.

[21] I. Fairley, P. Evans, C. Wooldridge, M. Willis, and I. Masters, "Evaluation of tidal stream resource in a potential array area via direct measurements," *Renewable Energy*, vol. 57, no. 0, pp. 70 – 78, 2013.

[22] R. Malki, A. Williams, T. Croft, M. Togneri, and I. Masters, "A coupled blade element momentum – computational fluid dynamics model for evaluating tidal stream turbine performance," *Applied Mathematical Modelling*, vol. 37, no. 5, pp. 3006 – 3020, 2013.

[23] R. Malki, I. Masters, A. J. Williams, and T. Croft, "The variation in wake structure of a tidal stream turbine with flow velocity," in *International Conference on Computational Methods in Marine Engineering MARINE* (L.Eça, E. Oñate, J. García, P. Bergan, and T. Kvamsdal, eds.), 2011.

[24] S. P. Neill, J. R. Jordan, and S. J. Couch, "Impact of tidal energy converter (tec) arrays on the dynamics of headland sand banks," *Renewable Energy*, vol. 37, no. 1, pp. 387 – 397, 2012.

[25] S. Isojunno, J. Matthiopoulos, and P. G. H. Evans, "Harbour porpoise habitat preferences: robust spatio-temporal inferences from opportunistic data," *MARINE ECOLOGY PROGRESS SERIES*, vol. 448, pp. 155–170, 2012.

[26] M. Broudic, T. Croft, M. R. Willis, I. Masters, and S.-H. Cheong, "Comparison of underwater background noise during spring and neap tide in a high tidal current site: Ramsey sound," in *Proceedings of the 11th European Conference on Underwater Acoustics*, July 2012.

[27] T. Carlson, B. Watson, J. Elster, A. Copping, M. Jones, M. Watkins, R. Jepsen, and K. Metzinger, "Assessment of strike of adult killer whales by an openhydro tidal turbine blade," Tech. Rep. PNNL-22041, Pacific Northwest National Laboratory, November 2012.

[28] M. R. Willis, M. Broudic, C. Haywood, I. Masters, and S. Thomas, "Measuring underwater background noise in high tidal flow environments," *Renewable Energy*, vol. 49, pp. 255–258, January 2013.

[29] S. Katsanevakis, "Modelling fish growth: Model selection, multi-model inference and model selection uncertainty," *Fisheries Research*, vol. 81, pp. 229 – 235, 2006.

V International Conference on Computational Methods in Marine Engineering
MARINE 2013
B. Brinkmann and P. Wriggers (Eds)

A MULTI-OBJECTIVE OPTIMIZATION ENVIRONMENT FOR SHIP-HULL DESIGN BASED ON A BEM-ISOGEOMETRIC SOLVER

A.-A.I GINNIS*, R. DUVIGNEAU†, C. POLITIS‡, K. KOSTAS‡, K. BELIBASSAKIS*, T. GEROSTATHIS‡ AND P.D. KAKLIS*

*School of Naval Architecture & Marine Engineering
National Technical University of Athens (NTUA)
9 Heroon Polytechneiou, Zografou 15773, Athens, GREECE
e-mail: ginnis@deslab.ntua.gr, web page: http://www.naval.ntua.gr/

†INRIA Sophia-Antipolis Méditerranée
Projet team OPALE
2004 route des Lucioles, 06902 Sophia-Antipolis, FRANCE
e-mail: Regis.Duvigneau@inria.fr web-page: http://team.inria.fr/opale/

‡Department of Naval Architecture Faculty of Technological Applications
Technological Educational Institute of Athens (TEI-Athens)
Agiou Spyridonos, 12210 Aigaleo, Athens, GREECE
e-mail: politis@teiath.gr web-page: http://www.na.teiath.gr/

Key words: Computer Aided Ship Design, Ship Parametric Model, Isogeometric Analysis (IGA), Optimization, Wave Resistance

Abstract. We present a ship-hull optimization environment integrating modern optimization techniques, a parametric ship-hull model and a novel BEM solver for the calculation of ship wave resistance. The environment is tested for a pair of optimization scenarios (local/global) for a container ship.

1 INTRODUCTION

Due to an increasing demand for efficiency and robustness in *Computer Aided Ship Design (CASD)*, the available modelling, analysis and evaluation techniques are being continuously pushed forward so that they can provide measurable improvements for both the design process and the resulting product. Fortunately, the current availability of computing power has allowed the employment of sophisticated *Computation Fluid Dynamic (CFD)* solvers and their coupling with advanced *Geometric Modeling* techniques and *Optimization* strategies, a combination that offers significant aid to meet the demanding requirements of contemporary CASD.

The optimization of a hull-form with respect to its resistance and resulting fuel consumption has been always posed as a major task in ship design. This work is focused on integrating three in-house developed components for ship-hull optimization. These components comprise a parametric CATIA®-based ship-hull design process, a Boundary Element Method (BEM) hydrodynamic solver and an optimization environment based on modern optimization techniques. Note that the hydrodynamic solver adopts the concept of *Isogeometric Analysis (IGA)*, which aims to intrinsically integrate CAD with Analysis by communicating the CAD model of the computation field to the solver without any approximation, e.g., panelization.
The rest of the paper is structured in four sections. In §2 we outline the construction, given a set of typical parent ship hulls, of the parametric ship model. Section 3 is devoted to present the basic features of the CFD solver for wave resistance, developed by combining the Neumann-Kelvin formulation with an IGA-based BEM approach. The optimization algorithms and the architecture of the associated software environment is described in § 4. Finally, we present two (local/global) optimization tests for a container ship. The first test deals with bow optimization against the criterion of minimum wave resistance under given displacement, while the second test involves ship-hull optimization against minimum resistance and minimum deviation from a reference deadweight.

2 The SHIP Parametric Model (SPM)

In this section we describe a methodology for constructing a parametric model for typical ship forms with the aid of CATIA [1], which is a featured parametric hybrid modeler, i.e., surface and solid modeler, providing a wide range of workbenches and multidisciplinary functionalities. The parametric capabilities in CATIA fully cover the requirements posed for generating the ship-hull parametric model (SPM). Finally, the automation offered in CATIA through various scripting languages can easily constitute the developing framework for the creation of the wrapper required in the optimization process; see §4,5.
To start with, the basic shape characteristics of a typical ship-hull comprise:

- a partition of the ship-hull into three main parts, namely the bow, the midsection and the stern,
- global dimensions (e.g., length between perpendiculars, beam, depth, draft) as well as dimensions characterizing each one of the aforementioned ship parts (e.g., extent of parallel deck and middle body),
- a set of control curves that are of boundary (e.g., stern profile, bow profile) or shape-transition character (e.g., FoS (flat-of-side) and FoB (flat-of-bottom) curves) and, finally,
- local geometrical characteristics (e.g., locations, angles, radii) that serve functional, structural and/or hydrodynamic purposes, e.g., bow-angle of entrance at waterline, bulb-top position, bilge radius, shaft height, etc.

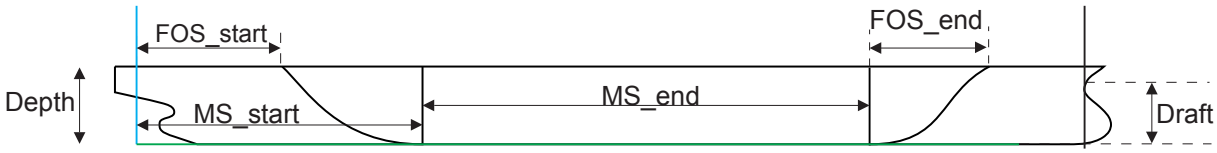


Figure 1: Lengths for defining mid-ship exposed parameters.

On the basis of the above coarse shape description and a set of parent ship-hulls, a list of *exposed* and *internal* parameters is devised. Exposed parameters will be accessible from the outside of the parametric modeling tool and initiate the modeling process, leading eventually to the production of a corresponding hull instance. On the contrary, internal parameters are not visible from the outside of the parametric tool and are used to control the surface construction process and eventually retain the basic shape characteristics of the parent hulls. Default values for both exposed and internal parameters are extracted from the parent ships. Furthermore, a domain of variation is assigned to each parameter assuring the modeling robustness while at the same time avoiding invalid geometrical models (e.g., self-intersections). These ranges can be thought as confidence intervals and have to be defined through extensive experimentation with the parametric model. Finally, SPM favors the use of non-dimensional parameters where possible, in order to avoid the interdependency between them.
Exposed parameters are categorized in four groups, according to whether they are global or associated to the midship, bow or stern areas of the ship. Parameters belonging to the global group correspond to ship's principal dimensions and their effect is of global nature, e.g., `G_Lpp`, `G_Beam`, `G_RiseOfFloor`. The second category includes parameters that are involved in the generation of the mid-ship part of the ship, e.g., `M_MS_start`, `M_FOS_end`; see Fig. 1) and, although not being global in nature, they also have a global effect as the mid-ship part is both the initial and supporting entity in the construction of the hull parametric model. The remaining two categories correspond to the bow and stern parts of the ship and are of more local character as they define shape forms in the areas of the bow and stern, respectively, see Fig. 2. The total number of exposed parameters is 30 and are split as follows: 5 global, 7 for the midship and 8,10 for the bow and stern parts respectively.

2.1 SPM construction process

We are targeting for a G^1-continuous hull, which will be based on a curve network and associated cross-tangent ribbons. Both exposed and internal parameters are used to parametrically describe the initial *Control Curve Network (CCN_0)*, which serves as the base for the ship-hull definition. CCN_0 comprises ship profile, FoS & FoB boundary curves, midship section and sections capturing shape transition in the bow and stern areas; see Fig. 3.
Apart from CCN_0, a number of auxiliary geometric entities is defined and employed in the

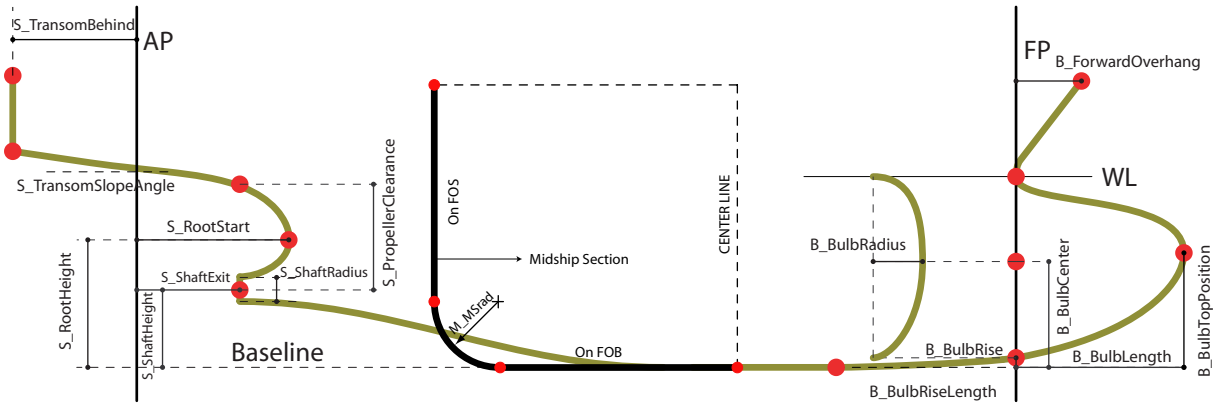


Figure 2: Exposed parameters for aft and bow parts of the ship and midship section

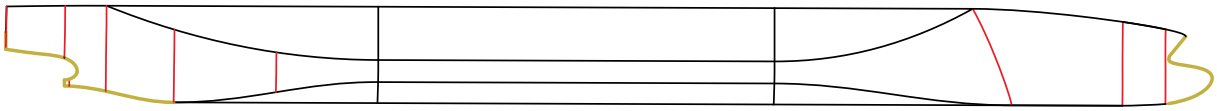


Figure 3: Initial Control Curve Network: CCN_0

modeling process. These entities include, among others, the fore- and aft-perpendicular, baseline and FoB & FoS planes. CCN_0 is used in conjunction with constraints apparently induced from ship's geometry, as e.g., symmetry with respect to the center plane, planarity of FoB/FoS areas, for producing cross-tangent ribbons over its elements. Attaching these ribbons to CCN_0 we get the so-called *augmented* CCN_0 *(*$aCCN_0$*)*.

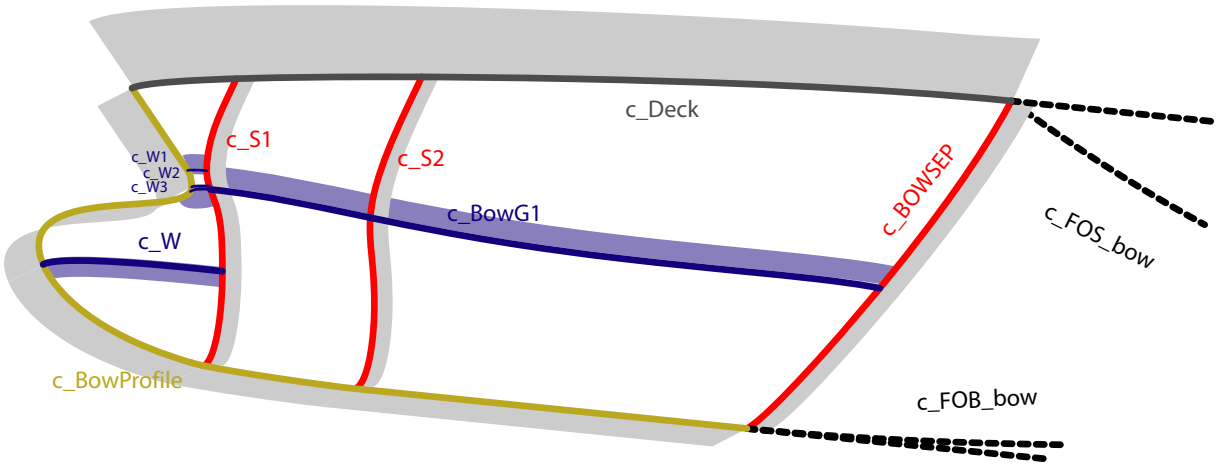


Figure 4: Bow part of $aCCN_1$

Using $aCCN_0$ various 3D control curves, capturing shape transitions in difficult areas (i.e., bow and stern), are created and attached to $aCCN_0$, producing a new curve network



Figure 5: The G^1-continuous composite surface interpolating $aCCN_1$

referred to as CCN_1; see blue curves in Fig. 4 for the bow part. Then, in analogy with the step: $CCN_0 \rightarrow aCCN_0$, additional cross-tangent ribbon information is added to CCN_1, leading to the final *augmented Control Curve Network (*$aCCN_1$; see Fig. 4. Based on $aCCN_1$ and using the appropriate CATIA functionalities, we employ a local construction scheme, that utilizes Hermite-type quadrilateral surface patch generation, thus ensuring tangent plane geometric continuity (G^1) for all surface patches constituting the ship-hull model; see Fig. 5.

3 The IGA-BEM wave resistance solver

The CFD solver adopted in the optimization process for calculating the wave resistance is based on the so-called Neumann-Kelvin wave source distribution over the wetted part of the hull. Following the formulation in Baar & Price [2], the wave-resistance problem is equivalently formulated as a *Boundary Integral Equation* (BIE) defined on the wetted surface S and the corresponding waterline ℓ,

$$\frac{\mu\left(\mathbf{P}\right)}{2}-\int_{S}\mu\left(\mathbf{Q}\right)\frac{\partial G\left(\mathbf{P},\mathbf{Q}\right)}{\partial n\left(\mathbf{P}\right)}dS\left(\mathbf{Q}\right)-\frac{1}{k}\int_{\ell}\mu\left(\mathbf{Q}\right)\frac{\partial G\left(\mathbf{P},\mathbf{Q}\right)}{\partial n\left(\mathbf{P}\right)}n_{x}\left(\mathbf{Q}\right)\tau_{y}\left(\mathbf{Q}\right)dl\left(\mathbf{Q}\right)=g\left(\mathbf{P}\right), \tag{1}$$

where μ is the density of the Neumann-Kelvin Green function $G\left(\mathbf{P},\mathbf{Q}\right)$, $g\left(\mathbf{P}\right)=-\mathbf{U}\cdot\mathbf{n}\left(\mathbf{P}\right)$ with $\mathbf{U}$ denoting the steady forward speed of the ship and $k=g/\left\|\mathbf{U}\right\|^{2}$ being the characteristic wave number.From the solution of the above integral equation, various quantities, such as velocity, pressure distribution, ship wave pattern and ship wave resistance can be obtained.

In the present work, a high-order Boundary Element Method (BEM) based on IsoGeometric Analysis (IGA) is applied for the numerical solution of the BIE (1), as described in detail in [3]. The IGA approach has been initially proposed by Hughes et al [4], in the context of Finite Element Method; see also [5] and [6]. In the context of IGA, field quantities are represented by the very same basis that is being used for representing the geometry of the body-boundary. For the latter, we shall presume that it can be accurately represented as a regular parametric NURBS surface as below:

$$\mathbf{x}\left(t_{1},t_{2}\right)=\sum_{i_{1}=0}^{n_{1}^{p}}\sum_{i_{2}=0}^{n_{2}^{p}}\mathbf{d}_{i_{1}i_{2}}^{p}R_{i_{1}i_{2},k_{1}^{p}k_{2}^{p}}^{p}\left(t_{1},t_{2}\right):=\sum_{\mathbf{i}=0}^{\mathbf{n^{p}}}\mathbf{d}_{\mathbf{i}}^{p}R_{\mathbf{i},\mathbf{k}^{p}}^{p}(t_{1},t_{2}), \tag{2}$$

$$\text{and } R^p_{\mathbf{i},\mathbf{k}^p}(t_1,t_2) := R^p_{i_1 i_2, k_1^p k_2^p}(t_1,t_2) = \frac{w^p_{i_1 i_2} N^p_{i_1,k_1^p}(t_1)\, N^p_{i_2,k_2^p}(t_2)}{\sum_{l_1=0}^{n_1^p}\sum_{l_2=0}^{n_2^p} w^p_{l_1 l_2} N^p_{l_1,k_1^p}(t_1)\, N^p_{l_2,k_2^p}(t_2)},\ p=1,\ldots,N, \tag{3}$$

where $\mathbf{i}=(i_1,i_2)$ and $\mathbf{k}^p=(k_1^p,k_2^p)$ are multiple indices, p is the patch identifier, $\mathbf{d}^p_{\mathbf{i}} := \mathbf{d}^p_{i_1 i_2}$ denote the control points of patch p and $N^p_{i_1}(t_1) := N^p_{i_1,k_1^p}(t_1)$, $N^p_{i_2}(t_2) := N^p_{i_2,k_2^p}(t_2)$ are the B-spline functions of degree k_1^p and k_2^p, respectively, which, in conjunction with the weights $w^p_{i_1 i_2}$ are used in (3) for building up the rational B-spline functions $R^p_{\mathbf{i},\mathbf{k}^p}(t_1,t_2)$ for patch p. Furthermore, ($t_k \in I_k^p$, $k=1,2$, which are partitioned appropriately by knot vectors J_k^p. As already mentioned above, in IGA context we employ the same representation for the unknown source-sink surface distribution

$$\mu(t_1,t_2) = \sum_{\mathbf{i}=0}^{\mathbf{n}^p+\mathbf{l}^p} \mu^p_{\mathbf{i}} R^p_{\mathbf{i},\mathbf{l}^p}(t_1,t_2)\ , \quad (t_1,t_2) \in\ \Omega_p,\ \Omega_p = I_1^p \times I_2^p,\ p=1,2,\ldots,N, \tag{4}$$

where, for the above representation, sequences of nested finite-dimensional spaces $S^{(\mathbf{l}^p)}_{\mathbf{k}} = S^p_{\mathbf{k}^p}(J^p_{1,l_1^p}, J^p_{2,l_2^p})$ are introduced on which the BIE (1) will be projected, with $\mathbf{l}^p := (l_1^p, l_2^p)$ denoting the additional knots inserted into I_1^p and I_2^p respectively. Substituting (4) into (1) and satisfying this equation over a set of collocation points, which are chosen to be the Greville abscissae of the associated knot vectors , we arrive at a discrete form of the BIE (1) which constitutes the linear system to be solved for the calculation of the unknown coefficients $\mu^p_{\mathbf{i}}$.

4 The multi-objective optimization environment

Simulation-based optimization is of growing importance in naval engineering, since it allows to improve ship performance for a moderate cost, in comparison with towing tank experiments. Moreover, the optimization is conducted in a rigorous algorithmic framework that can outclass the experience and intuitions of naval architects.

A major difficulty to apply an automated shape optimization procedure, in naval engineering as well as in other disciplines, is the development of a fully automated design loop. Indeed, for each set of parameters, a geometric hull model has to be constructed, allowing the generation of the computational domain used by the solver to provide the physical response and the performance analysis. All these steps should be fully automated, without hand-made repairing nor arranging process, in order to feed the optimization algorithm and finalize the design loop. In this context, the IGA paradigm offers a significant improvement over the classical grid-based methods, since it relies on a direct relationship between the design parameters and the solver, without any geometrical intermediate structures.

A second obstacle arises from the simulation process: for complex test-cases, CFD simulations are expensive, in terms of computational time. Moreover, the numerical solutions obtained can be polluted by errors arising from the discretization and iterative methods,

yielding noisy performance evaluations. Sometimes, this may lead the optimizer to spurious local optima or even yield the failure of the optimization procedure. Here again, the isogeometric context may be helpful because it allows to avoid geometrical approximations, which reduces the error level, and permits to construct high-order solutions yielding a better computational efficiency.
In summary, isogeometric analysis methods facilitate the development of a design optimization loop for practical engineering problems and make the resulting tool more efficient. The next sections present briefly the optimization algorithms considered in the present study and the software environment that gathers the geometric modeler, the solver and the optimizer.

4.1 Algorithms

Two single-objective and one multi-objective optimization algorithms have been included in the design optimization environment. As explained above, the robustness of the algorithms is critical to solve realistic problems. Therefore, derivative-free methods have been preferred to more efficient but fragile gradient-based approaches.
The numerical experiments carried out in the present study are based on the following algorithms:

- The multi-direction search algorithm from Dennis & Torczon [7].

  This is a deterministic direct-search algorithm, which leads to an optimum point by exploring iteratively a set of linearly independent directions from a starting point. It can be considered as an improvement of the well-known Nelder-Mead pattern-search method [8], since it relies on a strong convergence proof. This algorithm is well adapted to simulation-based optimization because it exhibits a low dependency on noisy performance evaluations.

- The standard (μ, λ) evolution strategy [9].

  Evolution strategies mimic the natural evolution laws to simulate a population of individuals that progressively converges to the optimum. In this paradigm, each individual is characterized by a set of parameters and its ability to survive is proportional to its performance. These methods, although far more expensive, are noticeable since they are able to avoid local minima thanks to random operators. The (μ, λ) evolution strategy is based on the evolution of a population of λ individuals, whose μ best individuals are used to generate the next generation.

- The Pareto archived evolution strategy from Knowles & Corne [10]

  This algorithm is a particular evolution strategy, which has been adapted to the context of multi-criterion optimization. In that case, the ability of an individual to survive is not related directly to the criteria values, but to the concept of dominance, introduced by the economist Pareto. In short, an individual is dominating an other

one if it has a better performance according to all criteria. This algorithm generates an archive of non-dominated individuals, which is used to determine the ability of a new individual to survive and have offsprings.

These three algorithms allow to solve a range of problems that are often encountered in naval engineering, by performing respectively a robust local search, an exploratory global search and a multi-objective Pareto front capturing.

4.2 Software environment

A design optimization software environment, depicted schematically in Figure 6, has been set up including the three main components: the optimizer, the solver and the modeler. Each of these components is wrapped in a corresponding wrapper, that manages the communication and data exchange among the components of the optimization environment. The wrappers are implemented using the python programming language and utilize the TCP/IP network protocol for the required communications. More Specifically:

1. Optimizer wrapper (Ow) communicates with the optimizer and broadcasts the generated parameter values to the parametric modeler wrapper (Mw).

2. Mw listens for data connections from Ow. When data, i.e., parameter values, are received, it triggers a CATIA construction script that produces the corresponding instance of the SPM and ultimately stores it as an IGES file at a specified ftp site. If the creation of this IGES file is successful, Ow establishes a connection with the Solver wrapper (Sw) and reports the IGES file creation. If the construction script fails a message is returned to Ow reporting the failure and requesting a new parameter set.

3. When a new IGES file is received, Sw initiates a connection to the site where the IGES file has been saved and retrieves it. IGA BEM solver is then started and performs the resistance calculations resulting, if successful, in the broadcasting of the objective function value to Ow. If computation fails, a network message is returned to Ow reporting the failure and requesting a new parameter set.

As it is obvious from the above discussion Ow, Mw and Sw work at the same time as client and server applications. This constitutes a flexible and efficient software environment for practical tests, presented in the next section.

5 Container-ship Optimization

5.1 Bow-optimization for minimizing wave resistance

The optimization environment has been firstly tested for optimizing the bow area of a container ship against the criterion of minimum wave resistance, under the constraint of

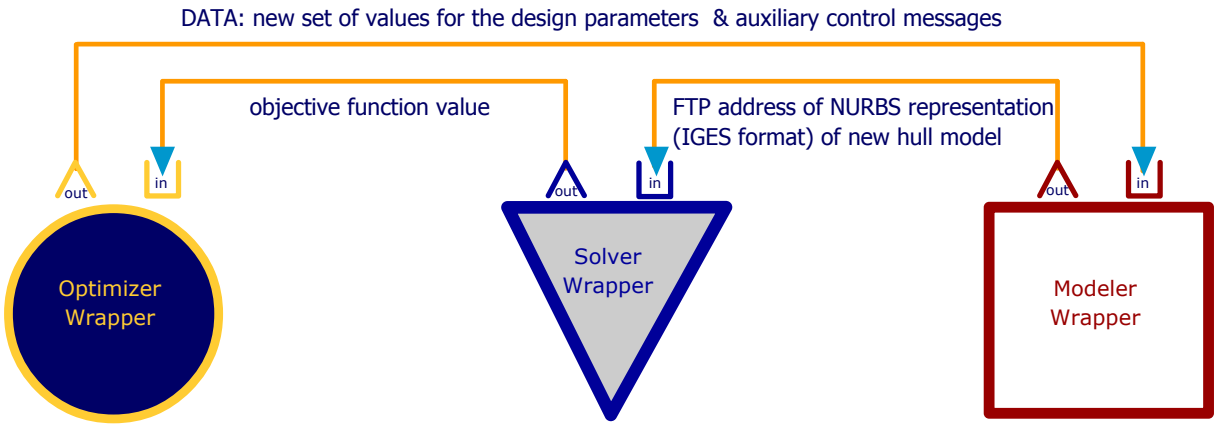


Figure 6: Schematic diagram of the optimization environment

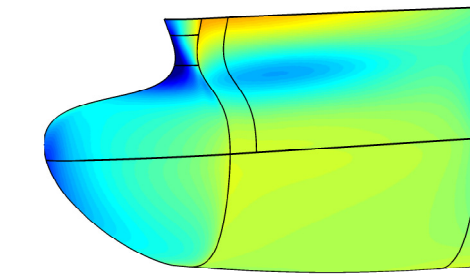
Table 1: 1st test of the optimization environment: range of variation of design parameters

B_BulbLength∈[6,11](m)	B_BulbTopPosition∈[4,10.5] (m)
B_BulbRadius∈[1.5,4.5] (m)	B_BulbRise∈[0,2] (m)

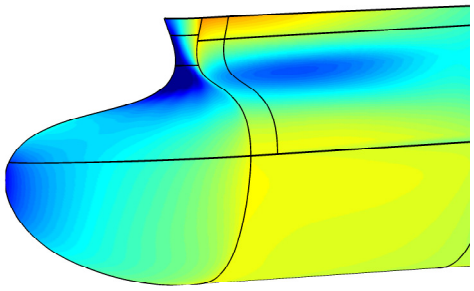
given displacement $\mathtt{V} = 80440$ m^3. The main particulars of the ship have as follows: $\mathtt{L}_{pp}$ = 277 m, $\mathtt{B} = 32.2$ m $\mathtt{T} = 13.0$ m, $\mathtt{C}_b = 0.6938$ and $\mathtt{V}_s$=26 knots. Since we are interested in optimizing the bow ship area, the design parameters are chosen to be: B_BulbLength, B_BulbTopPosition, B_BulbRadius and B_BulbRise; see Fig. 2. The range of variation of these parameters is given in Table 1. The direct-search optimization strategy described in § 4.1 is carried out to find optimal values for the design parameters of the bow. The bound constraints of Table 1 are implemented using a penalization approach while the displacement constraint is fulfilled within the SPM construction process.
Figure 7(b) illustrates the evolution of the wave resistance during the optimization procedure. More than half of the reduction is obtained during the first 15 simulations, whereas the convergence is then slower. This is due to the fact that the constraints become active after a first phase of straight descent. Especially, the displacement constraint is highly non-linear and is the cause of the observed irregular function decrease. Moreover, Figures 7(a) and (c) depict the bow-area shape along with the corresponding distribution of μ for two representative instances of the parametric model.

5.2 Shape optimization for minimizing resistance and deviation from a target deadweight

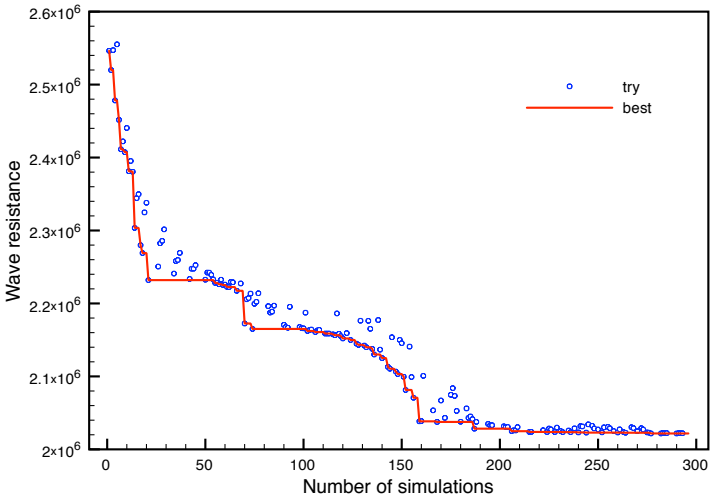
As a second test of the optimization environment we optimize a ship hull with respect to the following two criteria: a) minimum total resistance $\mathtt{R}_\mathtt{T}$ and b) minimum deviation from a reference deadweight of DWT=47000tons. Total resistance is evaluated using the solver described in §3 as regards its wave component and the standard ITTC relation for the



(a)



(c)



(b) Evolution of the wave resistance during the optimization process.



(d)

Figure 7: Evolution of wave-resistance & bow-area shape along with source distribution

frictional component. The deadweight of the ship is calculated as the difference between its displacement and its lightship, the latter being estimated via empirical formulae for containerships; see, e.g., [11].

Seven design parameters are chosen for the optimization process, namely, the length between perpendiculars, $\mathtt{L}_{pp}$, the breadth, `B`, the bilge radius, `M_MSrad`, the bulb length, `B_BulbLength`, the bulb radius, `B_BulbRadius` and the ratios `MS_startR` and `MS_endR`, defined as:

$$\mathtt{MS_startR} = \frac{\mathtt{MS_start}}{\mathtt{L_{pp}}}, \quad \mathtt{MS_endR} = \frac{\mathtt{MS_end}}{\mathtt{L_{pp}} - \mathtt{MS_start}},$$

where `MS_end` is the length of the parallel midbody of the ship while `MS_start` denotes the distance of its starting section from the after perpendicular; see Fig. 2. The above parameters range as in Table 2. The Pareto archived evolution strategy, presented in §4.1, is employed to calculate the Pareto front of the above optimization problem, which is depicted in Fig. 8. Figure 9 provides the optimization history of four of the design parameters along with their values on the Pareto front (green skeletal lines). Both figure correspond to a second stage of the optimization process. In the initial stage, the algorithm explores the feasible space with a large step length in order to catch a coarse approximation of the Pareto front, while the second stage refines the step length starting from a point near the Pareto front.

Table 2: 2nd test of the optimization environment: range of variation of design parameters

L_{pp}(m)	B(m)	MS_endR	MS_startR
[235,318]	[27,35]	[0.04,0.06]	[0.35,0.45]
M_MSrad(m)	B_BulbLength(m)	B_BulbRadius(m)	
[3,5]	[7.5,11.5]	[2.5,4]	

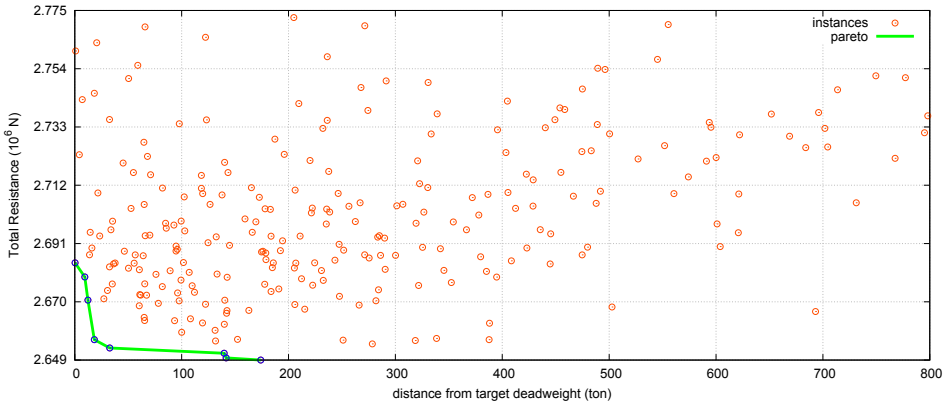


Figure 8: Pareto front for the resistance and the deadweight-deviation criteria

Acknowledgments

This research has been co-financed by the European Union (European Social Fund - ESF) and Greek national funds through the Operational Program *"Education and Lifelong Learning"* of the National Strategic Reference Framework (NSRF) - Research Funding Program: THALIS-UOA (MIS 375891).

REFERENCES

[1] CATIA V5 web site url: *www.3ds.com/products/catia/welcome*.

[2] Baar J.J.M. and Price W.G. Developments in the Calculation of the Wavemaking Resistance of Ships, *Proc. Royal Society of London. Series A, Mathematical and Physical Sciences* (1988) **416, 1850**:115-147.

[3] Belibassakis K.A., Gerostathis Th.P., Kostas K.V., Politis C.G., Kaklis P.D., Ginnis A.I. and Feurer C. A BEM-isogeometric method for the ship wave-resistance problem, *Ocean Engineering* **60**:5367 (2013).

[4] Hughes T.J.R., Cottrell J.A. and Bazilevs Y. Isogeometric analysis: CAD, finite elements, NURBS, exact geometry and mesh refinement, *Computer Methods in Applied Mechanics and Engineering* (2005) **194**:4135-4195.

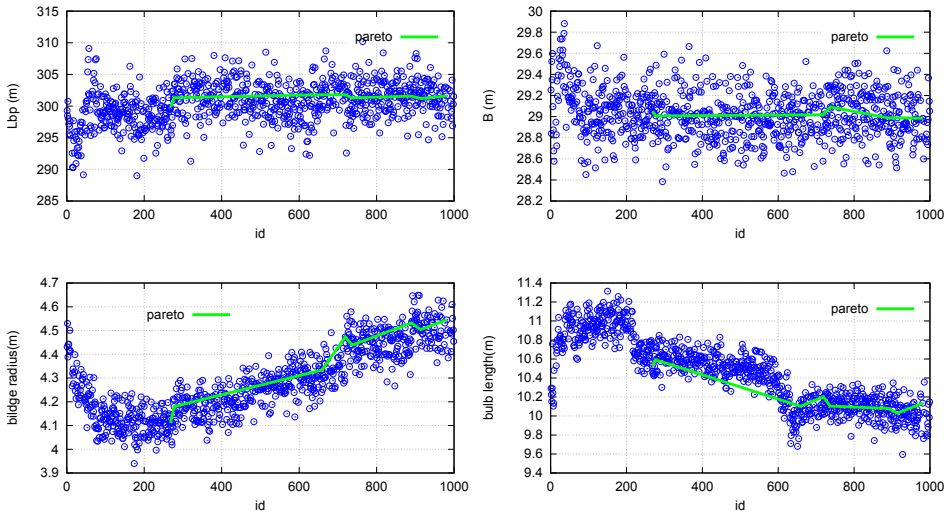


Figure 9: Variation of parameter values in the course of the optimization process

[5] Cottrell J.A., Hughes T.J.R. and Reali A.Studies of refinement and continuity in isogeometric structural analysis, *Computer Methods in Applied Mechanics and Engineering* (2007) **196, 41-44**:4160-4183.

[6] Cottrell J.A., Hughes T.J.R. and Bazilevs Y. *Isogeometric Analysis: Toward Integration of CAD and FEA* J. Wiley & Sons, New Jersey (2009).

[7] Dennis J.B. and Torczon V.B. Direct search methods on parallel machines. *SIAM Journal of Optimization*, **1, 4**:448-474 (1991).

[8] Nelder J. A. and Mead R. A simplex method for function minimization. *Computer Journal*, **7**:308-313 (1965).

[9] Michalewics Z.. *Genetic algorithms + data structures = evolutionary programs*. AI series. Springer-Verlag, New York (1992).

[10] Knowles J.D. and Corne D.W. Approximating the nondominated front using the pareto archived evolution strategy, *Evolutionary Computation*, **8, 2**:149-172 (2000).

[11] Chen Y. Formulation of a Multi-Disciplinary Design Optimization of Containerships, *MSc Thesis, Virginia Polytechnic Institute and State University* (1999).

V International Conference on Computational Methods in Marine Engineering
MARINE 2013
B. Brinkmann and P. Wriggers (Eds)

MODELING AND SIMULATION OF MAIN ENGINE EXCITATION ON BOARD VESSELS

CHRISTOPH TAMM* AND MATTHIAS KURCH†

*Fraunhofer Institute for Structural Durability and System Reliability LBF
Department of Structure Dynamics and Vibration Technology
Bartningstrae 47, 64289 Darmstadt, Germany
e-mail: christoph.tamm@lbf.fraunhofer.de, web page: www.lbf.fraunhofer.de

†Fraunhofer Institute for Structural Durability and System Reliability LBF
Department of Structure Dynamics and Vibration Technology
Bartningstrae 47, 64289 Darmstadt, Germany
e-mail: matthias.kurch@lbf.fraunhofer.de, web page: www.lbf.fraunhofer.de

Key words: Numerical Simulation, Engine Excitation

Abstract. The prediction of the vibro-acoustic behavior of vessels at every stage of the design process helps to identify acoustic problems and to optimize ship designs. In order to simulate the sound, noise and vibration transfer into ship structures, the sources of excitation need to be modeled. On board a vessel combustion engines are relevant sources of structure-borne noise, which introduce vibrations into the foundation as a result of the combustion process. A numerical model of the engine excitation is developed and system-level simulations are performed. A scaled torsional vibration test stand is used to verify the proposed simulation approach.

1 INTRODUCTION

In recent years, the passenger comfort on board vessels became of central importance. Owners and shipyards define low limit values for noise and vibration that must be observed during operation of the ship. On the other hand, light weight construction in combination with high propulsion power supplied by slow-running main engines lead to vibrations with negative effects on safety and comfort on board. Efficient prediction of the vibro-acoustic behavior of vessels can help to identify critical points in the ship design and to avoid costly rework subsequent to sea trials. Therefore, an approach, based on numerical system-level simulation, to estimate noise, vibration and harshness performance during each step of the design process is proposed.

This paper is focused on the development of a numerical model of a propulsion main engine. The main engine introduces excitation forces into the foundation and torsional

moments into the power train. The resulting torsional vibrations again induce structure-borne noise into the gear box, clutch and other parts of the power train.

A torsional vibration test stand is used to verify the proposed simulation approach. A numerical model is set up for a two-cylinder V engine and system-level simulations using Matlab/Simulink are performed. Both stationary operational conditions and transient excitations, e.g. engine run-ups and misfiring, are simulated. The numerical results are presented and the accuracy of the model is evaluated by comparing numerical and experimental data.

The numerical model presented in this paper is a part of a currently developed software toolbox to predict the vibro-acoustic behavior of a vessel efficiently. One of the aims of this toolbox is the identification of acoustic excitation mechanisms in an early phase of design and also in parallel to the development process. Therefore a modular and hierarchic modeling scheme is proposed, a numerical model is implemented and the results are presented.

2 NUMERICAL MODEL

The overall simulation model is built up modular and contains structural submodels of the engine block, foundation and power train as well as an excitation submodel. Both the mechanical structures and the excitation submodels are modeled separately with regards to their compatibility within the overall model. Therefore the connection ports between the submodels must be defined accurately. The advantage of modular modeling is the possibility to easily substitute each submodel describing the same component. With this proposed modeling approach not only the description depth of a submodel can be enhanced but also the numerical formulation can be varied [1]. In a pre-contractual phase an analytically determined model can be built up, which is easy to initialize and to parameterize. In the following design process each submodel can be replaced with a more accurate one, using more detailed modeling strategies or updating assumed parameters with experimentally determined.

In this paper the numerical submodels are all based on analytical equations. On the one hand the overall simulation model describes the foundation excitation through the engine mounts by means of dynamic forces $F(t)$ and accelerations $\ddot{z}(t)$. On the other hand the dynamic excitation torques $M(t)$ that lead to power train torsional vibrations are calculated. The main engine dynamic reaction forces and moments are schematically depicted in figure 1. Most of the initial parameters (see table 1) are taken from technical data sheets, installation drawing or supplier reports and some of them were experimentally determined. In sections 2.1 and 2.2 the excitation and structural models are described in detail.

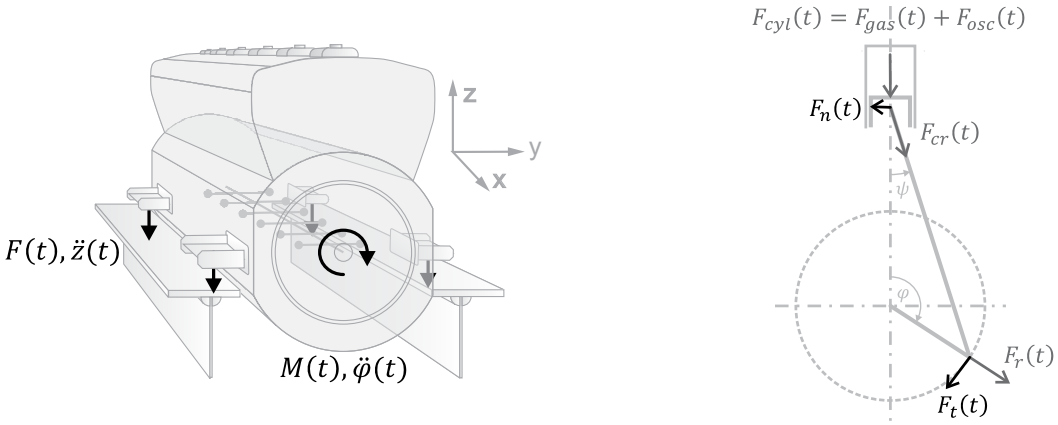


Figure 1: Scheme of a main engine and dynamic reaction forces and moment (left); dynamic forces acting at a crank drive (right)

2.1 Excitation submodel

As a result of the combustion process, both gas and inertia forces occur and excite vibrations in the mechanical structures. The calculation of the dynamic gas forces and moments are based on one cylinder's combustion pressure characteristics, determined at different mean effective pressures p_{mi}. The coefficients $a_k(p_{mi})$ and $b_k(p_{mi})$ of a *Fourier series* are calculated with the help of harmonic analyses. For each set of coefficients (e.g. $a_k(p_{mi,1})$ to $a_k(p_{mi,n})$) a continuous function is estimated using a polynomial interpolation. Thus, the cylinder pressure can be calculated for a user-defined number of revolutions $n(t)$ and an angle of revolution $\varphi(t) = \int 2\pi n(t)$ respectively. Setting a starting angle of revolution φ_0 for every cylinder, the ignition sequence of the engine is regarded. Considering only the impact of the gas forces, the cylinder pressure is calculated with the Fourier series

$$p_{cyl,gas}(t) = \sum_k \left(\rho a_k n(t) \cos\left(\frac{\pi}{T} k\varphi(t) - \varphi_0\right) + \rho b_k n(t) \sin\left(\frac{\pi}{T} k\varphi(t) - \varphi_0\right)\right) \qquad (1)$$

where k denotes the engine order and T the period of oscillation. With the coefficient ρ misfiring can be defined. In order to simulate the normal operation state, $\rho = 1$ must be set and the regular cylinder pressure is calculated. For values of $\rho < 1$ the cylinder pressure is decreased. Thus, it is possible to specify misfiring for each individual cylinder and simply vary the length and magnitude of the failure.

As a consequence of the alternating gas forces in the cylinder, the piston performs a oscillating linear motion. The connecting rod converts the linear into a rotary motion of the crank shaft. According to their type of motion, the accelerated masses cause oscillating and rotating inertia forces. The actual mass distribution of each crank drive is substituted with two concentrated masses [2]. The mass of the connecting rod is divided into a part moving with the piston and another part moving with the crank pin. In the excitation model presented in this paper the rotating inertia forces are neglected,

because the balancing of the rotating masses is general state of technology and common practice [3]. The oscillating mass is calculated with equation (2).

$$m_{osc} = \frac{1}{3} m_{conrod} + m_{piston} \tag{2}$$

The oscillating inertia force acting at one piston in z-direction is

$$F_{z,osc} = -r\omega^2(t) m_{osc} \ddot{z} \tag{3}$$

where r is the radius of the crank shaft, ω the rotational speed and $\ddot{z}$ the piston acceleration. Using a series expansion of the piston acceleration, equation (3) is approximated by

$$F_{z,osc} = -r\omega^2(t) m_{osc} \left[A_1 \cos 1\varphi + A_2 \cos 2\varphi + A_4 \cos 4\varphi + A_6 \cos 6\varphi + \ldots\right] \tag{4}$$

with the connecting rod ratio λ and following coefficients A_1 to A_6 [3]:

$$\begin{aligned} A_1 &= 1 \\ A_2 &= \lambda + \frac{1}{4}\lambda^3 + \frac{15}{128}\lambda^5 \\ A_4 &= -\frac{1}{4}\lambda^3 - \frac{3}{16}\lambda^5 \\ A_6 &= \frac{9}{128}\lambda^5 \end{aligned}$$

For the integration of the oscillating inertia forces in equation (1) the coefficients μ and

$$a_{m,i} = \frac{r\omega^2(t) m_{osc}}{A_K} A_i(\lambda) \tag{5}$$

are introduced. With $\mu = 1$ and $\mu = 0$ the calculation of the inertia forces can be set on and off respectively. Finally, the resulting cylinder pressure acting at one piston area can be derived from equations (1) to (5):

$$\begin{aligned} p_{cyl}(t) = \sum_k \Big(&(\rho a_k n(t) + \mu a_m n(t)) \cos\left(\frac{\pi}{T} k\varphi(t) - \varphi_0\right) \ldots \\ &\ldots + \rho b_k n(t) \sin\left(\frac{\pi}{T} k\varphi(t) - \varphi_0\right)\Big). \end{aligned} \tag{6}$$

The suggested analytical equation (6) was implemented using the Matlab/Simulink environment. With the resulting parametric excitation submodel the dynamic gas and inertia forces of a combustion engine can be simulated. The numerical results are dependent on several initial parameters (see table 1). The excitation model can be controlled with an user-defined rotation speed $n(t)$ and the above introduced coefficients $\rho(t)$ as well

as $\mu(t)$. Thus it is possible to define transient operational excitations like engine run-ups or misfiring.

All acting forces at the individual crank drives are depicted in figure 1. The dynamic connecting rod, normal, radial and tangential forces (F_{cr}, F_n, F_r and F_t) can be calculated depending on the cylinder force $F_{cyl} = F_{gas} + F_{z,osc}$, the crank shaft angle φ and the swivel angle ψ [4].

$$F_{cr} = \frac{F_{cyl}}{\cos\psi} \tag{7}$$

$$F_n = F_{cyl} \cdot \tan\psi \tag{8}$$

$$F_r = \frac{F_{cyl} \cdot \cos(\phi + \psi)}{\cos\psi} \tag{9}$$

$$F_t = \frac{F_{cyl} \cdot \sin(\phi + \psi)}{\cos\psi} \tag{10}$$

Summed over the length of the crank shaft, considering the phase relationship and ignition sequence these forces are used as the excitement in the overall simulation model.

2.2 Structural submodels

The structural submodel of the power train is modeled as a torsional harmonic oscillator. It consists of a finite number of mass moments of inertia Θ_i. These mass moments are coupled by discrete torsional springs and torsional dampers. Figure 2 shows a scheme of a torsional oscillator with n degrees of freedom.

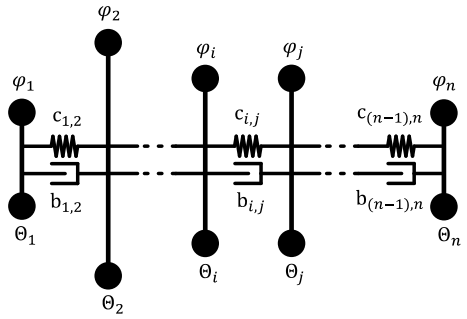


Figure 2: Scheme of a torsional harmonic oscillator with n degrees of freedom

The equation of motion for the i-th degree of freedom is given by [5]

$$\Theta_i\varphi_i = c_{i-1,i}(\varphi_{i-1} - \varphi_i) - c_{i,i+1}(\varphi_i - \varphi_{i+1}) + b_{i-1,i}(\dot{\varphi}_{i-1} - \dot{\varphi}_i) - b_{i,i+1}(\dot{\varphi}_i - \dot{\varphi}_{i+1}) \tag{11}$$

where Θ_i denotes the moment of inertia, $c_{i,j}$ is the torsional spring constant, $b_{i,j}$ is the torsional damping constant and φ_i represents the rotational degree of freedom. For

the complete torsional oscillator with n degrees of freedom results a system of ordinary differential equations

$$\mathbf{\Theta}\underline{\ddot{\varphi}} + \mathbf{B}\underline{\dot{\varphi}} + \mathbf{C}\underline{\varphi} = \sum \mathbf{M_T} \tag{12}$$

with the mass matrix $\mathbf{\Theta}$, the damping matrix $\mathbf{B}$, the stiffness matrix $\mathbf{C}$ of the system. $\mathbf{M_T}$ denotes the external excitation moments and $\underline{\varphi}$ denotes the vector of degrees of freedom. The systems of equation of motion for every installed component (e.g. combustion engine, gear box, clutch or propeller) are set up modularly. Finally, the complete power train is assembled by coupling the individual components. Thus it is easy to replace components or assembly groups to investigate their influence on the vibro-acoustic behavior.

The engine block is modeled as a rigid body with six degrees of freedom. The body can perform linear translations in the three direction x, y and z and small rotations about the axes. Figure 3 shows a scheme of a rigid body with the global coordinate system located in the body's center of gravity.

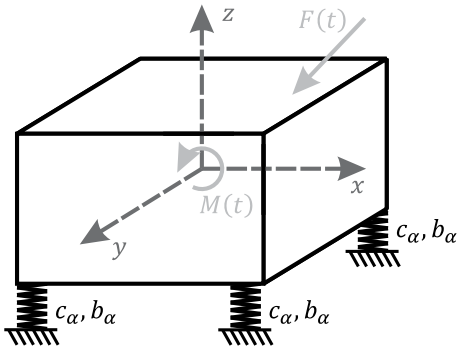


Figure 3: Scheme of a rigid body

The rigid body is mounted to a rigid foundation with a user-defined number of ideal three dimensional spring-damper systems. The mounts can be defined at a location α on the surface of the rigid body and the spring and damping coefficients c_α and b_α are time and frequency independent. External forces can be applied at any position in and on the rigid body and also external moments can be defined at the center of gravity. This leads to the following system of equations [3]

$$m\ddot{x} + \sum F_{\alpha x} = \sum F_x \tag{13}$$

$$m\ddot{y} + \sum F_{\alpha y} = \sum F_y \tag{14}$$

$$m\ddot{z} + \sum F_{\alpha z} = \sum F_z \tag{15}$$

$$\Theta_x\ddot{\varphi}_x + \sum F_{\alpha z} l_{\alpha y} + \sum F_{\alpha y} l_{\alpha z} = \sum M_x \tag{16}$$

$$\Theta_y\ddot{\varphi}_y + \sum F_{\alpha z} l_{\alpha x} + \sum F_{\alpha x} l_{\alpha z} = \sum M_y \tag{17}$$

$$\Theta_z\ddot{\varphi}_z + \sum F_{\alpha y} l_{\alpha x} + \sum F_{\alpha x} l_{\alpha y} = \sum M_z \tag{18}$$

where m and Θ_i are the mass and the moments of inertia of the rigid body, F_i and M_i are the external forces and moments, $F_{\alpha i}$ are the reaction forces at the mounts and $l_{\alpha i}$ are the distances from the center of gravity to the mounting positions. x, y, z, φ_x, φ_y and φ_z are the displacements and the rotation angles of the center of gravity.

The reaction forces $F_{\alpha i}$ and displacements $s_{\alpha i}$ at the mounts are calculated with following equations:

$$F_{\alpha z} = c_{\alpha z} s_{\alpha z} + b_{\alpha z}\dot{s}_{\alpha z} \tag{19}$$

$$F_{\alpha y} = c_{\alpha y} s_{\alpha y} + b_{\alpha y}\dot{s}_{\alpha y} \tag{20}$$

$$F_{\alpha x} = c_{\alpha x} s_{\alpha x} + b_{\alpha x}\dot{s}_{\alpha x} \tag{21}$$

$$s_{\alpha z} = z + l_{\alpha x}\varphi_y + l_{\alpha y}\varphi_x \tag{22}$$

$$s_{\alpha y} = y + l_{\alpha x}\varphi_z + l_{\alpha z}\varphi_x \tag{23}$$

$$s_{\alpha x} = x + l_{\alpha z}\varphi_y + l_{\alpha y}\varphi_z. \tag{24}$$

The overall simulation model can be used to estimate noise, vibration and harshness performance in an early phase of the ship design process. The proposed structural submodels (section 2.2) and the excitation submodel (section 2.1) are implemented using the Matlab/Simulink environment. First numerical system-level simulation are performed and torsional vibrations and foundation excitations (forces and accelerations) can be determined. Thus it might be possible to identify critical points in the ship design and to benchmark possible active and passive concepts for the reduction of vibrations in preliminary studies.

3 APPLICATION

The torsional vibration test stand depicted in figure 4 is used to verify the proposed simulation approach. The test stand was built up in order to reproduce operational conditions in power trains of vehicles. The operational loads and vibrations can be experimentally simulated with reduced amplitudes. This is necessary for an evaluation of active and passive concepts for the reduction of vibrations. The modular design allows variable configurations of the test stand and thus provides a tool for the developing of new components. In the standard configuration the test stand consists of a two-cylinder V engine, a rotor and an eddy current brake. The initial parameters of the submodels are shown in table 1. Nearly all parameter are available in the conceptual design phase.

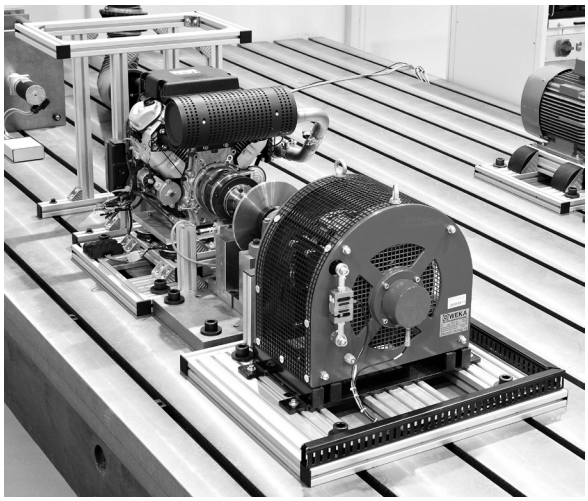




Figure 4: Torsional vibration test stand (left), Combustion engine (right)

Table 1: Initial parameters of the submodels

submodel	assembly	parameter
structure submodel	crank shaft	moments of inertia
		damping
		stiffness
	engine block	inertia properties
		mount positions
		mass
excitation submodel	piston	number
		stroke
		piston area
		mass
	connecting rod	length
		mass
		strokes
		V angle
	propeller power curve	rated speed (rpm)
		permitted rpm
		power
		firing order
		cylinder pressure

However, the moments of inertia, the center of gravity and principal coordinate system of the engine block were estimated, using the *Inertia Restraint Method* that is based on

measured frequency response functions [6, 7]. Furthermore, the cylinder pressure was determined experimentally. It was measured under on-load operation and coupled power train . The estimated combustion pressure characteristic used in the simulation model is based on the cylinder pressure measured at constant rotation speed of 1500, 2000, 2500, 3000 and 3600 rpm.

4 RESULTS

For the torsional vibration test stand described in section 3, an overall numerical model was set up and system-level simulations using Matlab/Simulink were performed. The results of the simulation are presented in this section. In the following figures 5 to 9 measured and simulated accelerations in the longitudinal (y), transverse (x) and vertical (z) direction of the engine are compared. All of them refer to a defined position P on the surface of the base plate of the engine (see figure 4). In order to validate the simulation model, an experimental operational modal analysis was accomplished. The accelerations were recorded during a constant run and a run up, using a *LMS SCADAS mobile* system and *PCB* $100\frac{mV}{g}$ triaxial accelerometers. The measured signals were interpreted with *LMS Test.Lab* software.

First, the measured and simulated results of a constant run at 3000 rpm are presented. In figures 5 and 6 the longitudinal, transverse and vertical accelerations are represented in the frequency domain. The dotted black curve is the amplitude spectrum of the simulated acceleration, while the gray curve shows the amplitude spectrum of measured ones. The axis of ordinates is scaled logarithmically to a reference value of $1\frac{m}{s^2}$.

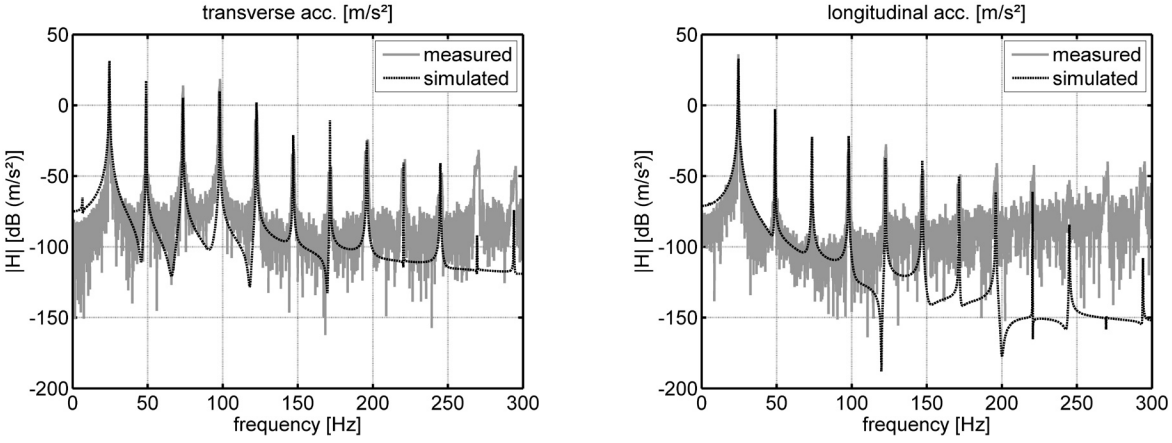


Figure 5: Measured and simulated transverse (left) and longitudinal accelerations (right)

The comparison illustrates that the excited frequencies match very well. Furthermore, in the range from 0 to 200 Hz the amplitudes can be predicted accurately. In addition, an engine run up from 1800 to 3800 rpm was performed. The experimental setup was retained the same. Figures 7 to 9 show Campbell diagram plots of the accelerations at

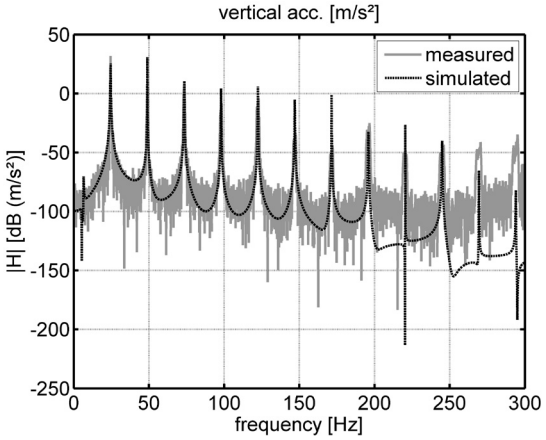


Figure 6: Measured and simulated vertical accelerations

position P determined in measured and simulated engine run ups. The plots represent the amplitude spectra as functions of the engine rotation speed.

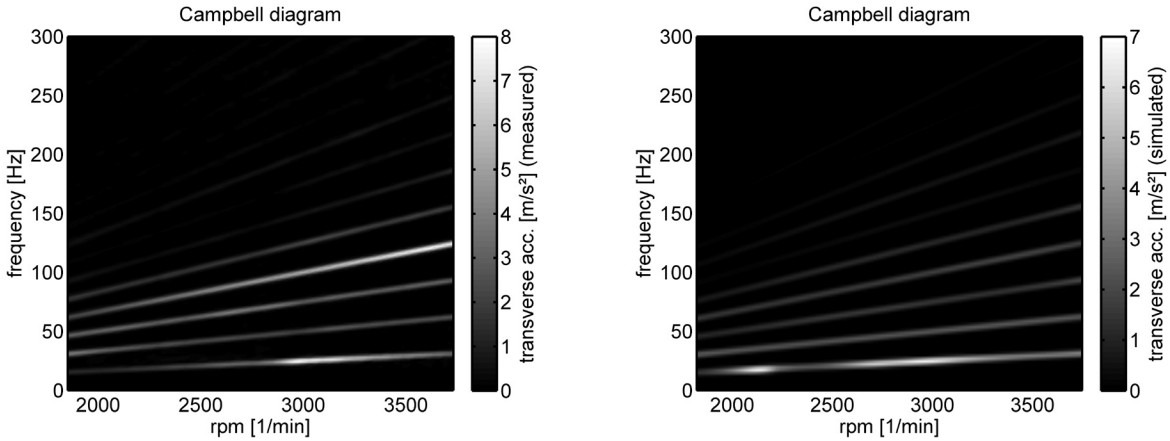


Figure 7: Campbell diagram of transverse acceleration [measured (left), simulated (right)]

The measured and simulated accelerations are pictured on the left and on the right side respectively. The amplitudes are plotted in absolute values. Both the natural frequencies of the system and the amplitudes can be predicted well.

5 CONCLUSION

In this paper a numerical modeling approach for the prediction of engine excitations on board vessels is presented. A modular and hierarchic overall model that is parametric and easy to initiate has been set up, using the Matlab/Simulink environment. The proposed methods have been applied to a torsional vibration test stand. The excitation forces of the combustion engines as well as the mechanical structure of the engine and the power

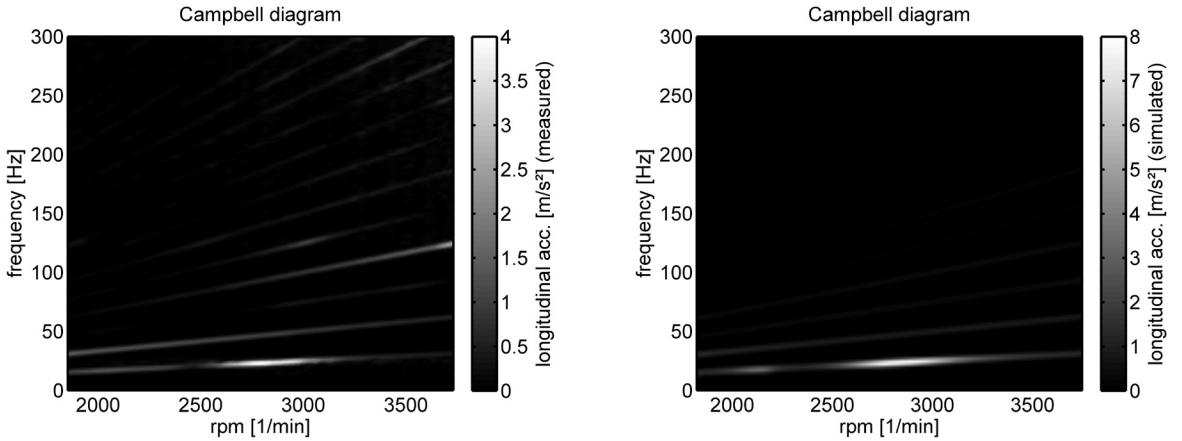


Figure 8: Campbell diagram of longitudinal acceleration [measured (left), simulated (right)]

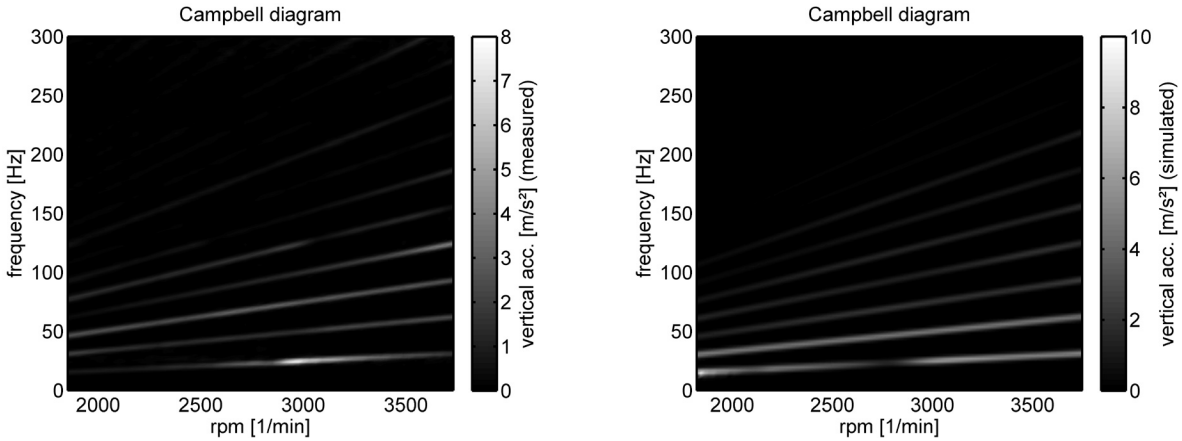


Figure 9: Campbell diagram of vertical acceleration [measured (left), simulated (right)]

train have been modeled. Numerical simulations and measurements of stationary and transient operational conditions have been performed. The numerical results have been presented and the accuracy of the model has been evaluated by comparing numerical and experimental data. It is found that the proposed methods can be used to predict the excitation forces and accelerations introduced into the engine foundation. Thus, in the future the developed model can be suitable for acoustic optimizations.

6 ACKNOWLEDGEMENTS

The results presented in this contribution were developed within the collaborative EPES project. It was funded by the German Federal Ministry of Economics and Technology (project ref. no. 03SX305). This financial support is gratefully acknowledged.

REFERENCES

[1] Herold, S., Jungblut, T. and Kurch, M., *A systematic approach to simulate active mechanical structures*, NAFEMS Seminar: 'Multi-Disciplinary Simulations - The Future of Virtual Product Development', Wiesbaden, Germany, (2009).

[2] Den Hartog, J. P., *Mechanical vibrations*, Dover books on engineering, Dover Publications, New York, (1985).

[3] Maass, H. and Klier, H., *Kräfte, Momente und deren Ausgleich in der Verbrennungskraftmaschine*, Die Verbrennungskraftmaschine Band 2. Springer, Wien, (1981).

[4] Tamm C., Atzrodt H. and Kurch M., *Modellierung der Motoranregung zur vibroakustischen Prognose im Schiffbau*, 38. Jahrestagung für Akustik, (2012).

[5] Hafner, K. E. and Maass, H., *Torsionsschwingungen in der Verbrennungskraftmaschine*, Die Verbrennungskraftmaschine Band 3. Springer, Wien, (1985).

[6] Toivola J., Nuutila O., *Comparison of three methods for determining rigid body inertia properties from Frequency Response Function*, Proceedings of IMAC XI, (1993).

[7] Tamm C. and Kurch M., *Determination of Rigid Body Inertia Properties of Combustion Engines based on measured Frequency Response Functions*, 39. Jahrestagung für Akustik, (2013).

V International Conference on Computational Methods in Marine Engineering
MARINE 2013
B. Brinkmann and P. Wriggers (Eds)

EFFECT OF THE BENDING STIFFNESS ON THE VOLUMETRIC STABILITY OF FISH CAGES WITH COPPER ALLOY NETTING

JUDSON C. DECEW[*], MICHAEL OSIENSKI[*], ANDREW DRACH[†], BARBAROS CELIKKOL[†], IGOR TSUKROV[†]

[*] Center for Ocean Engineering
University of New Hampshire
Durham, NH 03824, USA
e-mail: jud.decew@unh.edu

[†] Department of Mechanical Engineering
University of New Hampshire
Durham, NH 03824, USA
e-mail: igor.tsukrov@unh.edu

Key words: Aquaculture, Volumetric Stability, Numerical Modeling

Abstract. It has been well established that aquaculture will supply an increasing share of the world's seafood demand in the future. Most finfish are raised in marine fish cages consisting of a floating superstructure, polymer net chamber and a sinker weight(s). These systems are susceptible to large deformations, which can lead to reduction of the cage's volume and severely impact the health of the fish stock.

Net chamber deformation could be mitigated with the use of stiffer netting, such as copper alloy mesh. However, little is known regarding the bending characteristics of copper alloy nets and their relationship to the volumetric deformation of a fish cage. In this study, numerical modeling tools and techniques are developed and used to predict the dynamic structural behavior of gravity fish cages with copper alloy. An analytical model is validated by experimental testing to obtain an equivalent flexural rigidity. The model is used for finite element studies of the effect of bending resistance on the volume loss of fish cages with copper alloy netting. The contribution of the copper alloy's bending resistance to the volumetric stability is found to be minimal for the tested configurations. Thus, the traditional numerical modeling techniques (i.e. using truss elements) are sufficient for analyzing copper alloy cage configurations.

1. INTRODUCTION

The growth of global population, presently at 7 billion and projected to reach 9.3 billion in 2050, will continue to pressure the worldwide food supply [1]. Presently, 16% of the globally consumed animal protein comes from capture fisheries and aquaculture. With the wild fish stock population plateauing due to overfishing, aquaculture is expected to increase its seafood contributions by 8% a year for the foreseeable future [2].

The most commonly utilized containment system used by the marine aquaculture industry is called a gravity type cage. This type of cage system traditionally consists of a buoyant collar

made of high density polyethylene (HDPE), a polymer (nylon) net chamber suspended below the buoyant collar, and a weighted lower collar. The lower collar is typically filled with steel chain or other similar dense materials to keep the net vertical and resist deformation. This type of cage system relies on the difference in forces between the weighted net chamber and the main floatation collar to act as the restorative force which sustains the volume of a net chamber. In this configuration, fish cages are susceptible to net chamber deformation caused by substantial lateral forces or by inertial movements of components, which can decrease the net chamber volume. Significant reduction of the net chamber volume has been documented to occur when the system is subjected to high energy conditions (see for example [3, 4, 5]) and/or marine biological growth on the net chamber [6, 7]. An excessive chamber volume loss can lead to short-term crowding of the fish population, resulting in a hormonal stress response and reduced growth rates [8].

Copper alloy nets have been presented as a solution to fish cage volume loss due their inherent fouling resistance [9], high strength [10], and prevention of predation common in polymer nets [11]. However, most of the copper alloy research has focused on its fouling resistance, material loss rates [12], or the hydrodynamic characteristics of the netting [9, 13] and not on the effect of mesh bending stiffness on fish cage volumetric stability. In this study, the effective area moment of inertia of three copper alloys were found and used to investigate the effectiveness of this material to resist net chamber deformation using a combination of analytical models, finite element simulations, and laboratory experiments.

2. DESCRIPTION OF THE INVESTIGATED COPPER ALLOY MESHES

The most widely used copper alloy net in aquaculture cages is of the “chain-link” type. This net type (Figure 1) is typically hung with pickets in the vertical (warp) direction. In this orientation, wires (called pickets) are structurally independent of its interconnected/linked neighbors. Thus, if any single picket fails, the structural integrity of the net chamber is maintained. If the pickets were oriented in the horizontal direction, the failure of a single picket would lead to an expanding hole opened by the gravity forces. In the vertical orientation, the pickets provide certain bending resistance which could reduce the net chamber deformations. Note that the resistance to bending is only present when the mesh is loaded in the warp direction; in the weft direction, the pickets are effectively unrestricted.

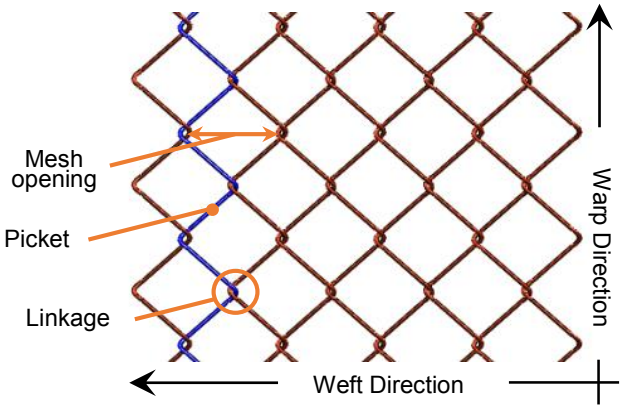


Figure 1: Chain-link mesh diagram.

Table 1: Material properties of the copper-alloy meshes.

Mesh parameters	Mesh type		
Mesh denomination	M2.5-25	M3.5-50	M2.5-30
Alloy name	Admiralty Brass, UR30	Silicon Bronze, SeaWire	Admiralty Brass, BlueSteel
Mesh opening, *mm*	25	50	30
Wire diameter, *mm*	2.5	3.5	2.5
Young's modulus, GPa	102	113	109
Shear modulus, GPa	38	42	41
Poisson's ratio	0.35	0.36	0.32
Density, kg/m^3	8300	8400	8400

Three of the most commonly utilized copper alloy mesh types were chosen for analysis. All three are of "chain-link" configuration: *M2.5-25* manufactured by Mitsubishi Shindoh; *M2.5-30* manufactured by Wieland-Werke; and *M3.5-50* manufactured by Luvata Appleton. Their material and geometric properties are shown in Table 1. Note that the denominations *M2.5-25*, *M2.5-30*, and *M3.5-50* are based on the wire diameter and the mesh opening size of the meshes.

3. ANALYTICAL METHOD FOR DETERMINING AREA MOMENT OF INERTIA

The first step is to construct an analytical model to describe the bending resistance, or more importantly, the equivalent area moment of inertia of pickets for each mesh. Due to the complex three dimensional geometry of the mesh, an average value for the area moment of inertia over the picket length is obtained. For this, each picket is assumed to act independently from the mesh as a whole. Only one repetitious segment of a picket can be considered due to the periodicity of its geometry, see Figure 2a.

Analytical modeling is based on the analysis of the picket's internal strain energy due to deformation. This energy can be represented as a sum of bending, shear, torsion, and axial components. To obtain the total strain energy of the system, an imaginary force F is applied to one end of the half segment, with the other end assumed to be rigidly fixed. For this type of loading, the contribution of axial and shear terms is much smaller than that of bending and torque. Thus, the strain energy is

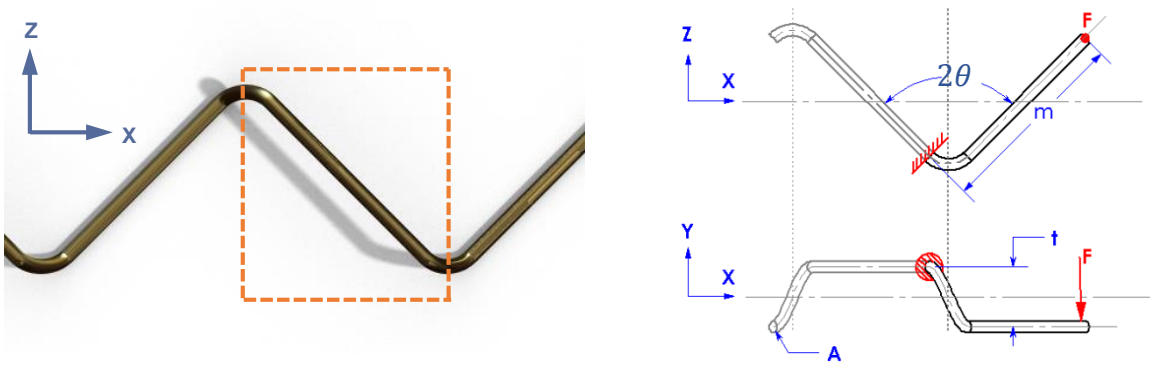


Figure 2: Chain-link picket geometry: (a) repetitious segment; (b) force diagram.

$$U_{Total} = \int_0^L \frac{M^2(x)}{2EI_{zz}} dx + \int_0^L \frac{T^2(x)}{2GJ_0} dx \tag{1}$$

where x is the distance along the warp direction; L is the total length of the picket segment along the warp direction; M is the bending moment; T is the torque; E is the Young's modulus; G is the shear modulus; I_{zz} is the moment of inertia; J_0 is the polar moment of inertia. Assuming a linearly elastic behavior, the total strain energy can be described as

$$U_{Total} = \frac{F^2(m\cos\theta)^3}{6E}\left[\frac{2(1+\nu)}{J_0} + \frac{\cos^2\theta}{I_{zz}}\right] \tag{2}$$

where ν is the Poisson's ratio; m and θ are defined in Figure 2b.

Thus, the equivalent moment of inertia (of an equivalent simply supported beam subjected to a point force) can be introduced as

$$\mathbb{I}_{eq} = \left[\frac{2(1+\nu)}{J_0} + \frac{\cos^2\theta}{I_{zz}}\right]^{-1} \tag{3}$$

It can be seen that the bending stiffness of chain-link mesh depends on the wire diameter, material's Poisson's ratio and the mesh weaving angle.

4. EXPERIMENTAL METHOD FOR DETERMINING AREA MOMENT OF INERTIA

A set of four-point bending experiments was conducted to compare the analytical predictions of bending resistance with the experimentally observed behavior. A servohydraulic uniaxial tension/compression testing machine (Instron 1350) with load capacity of 100 *kN* was used to apply the loads and measure the deflections with an integrated LVDT sensor. The loads were measured with a 1 *kN* S-beam load cell, manufactured by Futek, rigidly fixed to the testing machine. To obtain the four-point loading boundary conditions, a custom apparatus was constructed. It consisted of two frames (upper load and lower support frames) that provided a maximum support or load span of 0.75 *m*, see Figure 3.

The test procedure followed ASTM E855-90 [14]. The load applicators were centered at 2/3 of the support span distance, and the testing was conducted at two support spans: 0.75 *m* and 0.45 *m*. This was done to observe the effects due to different picket length to diamond size ratio. In addition, a series of tests were performed to study the sensitivity of the results to the setup parameters, such as picket orientation, tension in the mesh, specimen length).

Each test was repeated a minimum of six times to determine the variance in the resulting data. Prior to each set of experiments, the load cell was calibrated by zeroing it and checking it with a 100 *g* precision weight to ensure consistency. The data was recorded at the sampling frequency of 1.0 *kHz*. A crosshead velocity of 0.1 *mm*/*s* was used for all experiments.

From the sensitivity studies, the maximum displacement of all meshes in the elastic loading range was found to be 35 *mm*, resulting in a radius of curvature of 0.35 *m*. All experimental data showed significant trends of linearity. The bending resistance (*N*/*mm*) of each specimen was calculated by applying a linear regression to the measured data and calculating the slope of the curve, see Figure 4.

With the bending resistance of each specimen known, the Euler–Bernoulli linear beam theory was used to determine the picket's effective moment of inertia. The moment of inertia can be calculated using the following equation, based on a two point loaded simply supported beam [14]:

$$\delta_L = \frac{Pa}{48E\mathbb{I}_{eq}}(3L^2 - 4a^2) \tag{4}$$

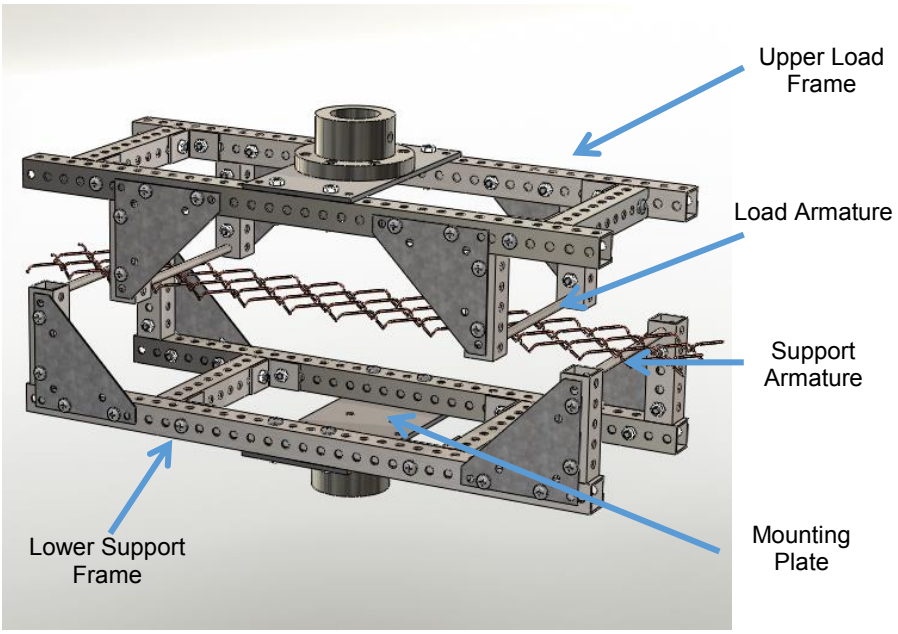


Figure 3: Schematics of the four-point bending fixture for testing of the chain-link meshes.

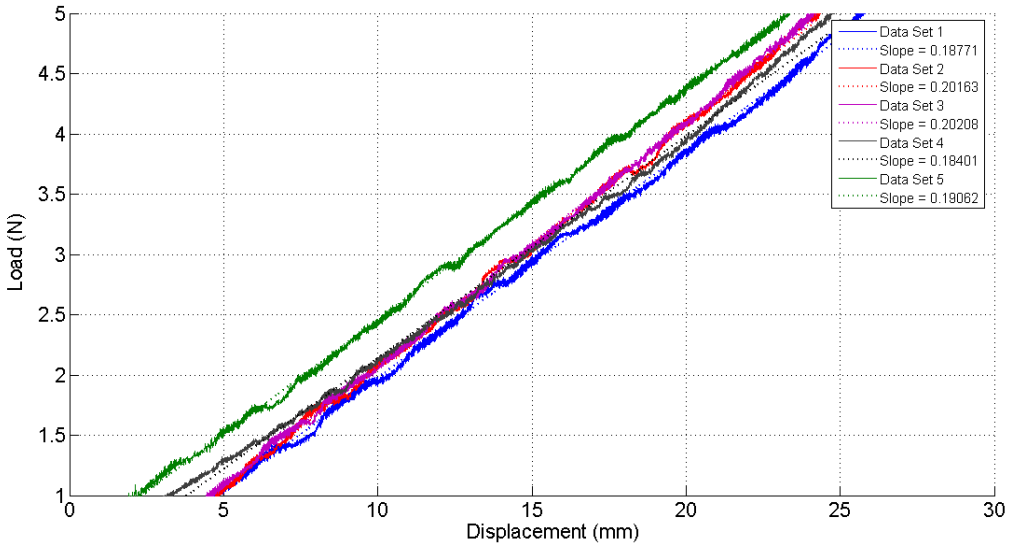


Figure 4: Example of the experimental data with linear regression slopes from a single picket bending test.

where δ_L is the deflection at the points of loading; P is the applied load; $\mathbb{I}_{eq}$ is the area moment of inertia at the origin of axes; E is the Young's modulus of the material; L is the span length between supports, and a is the distance from the support to the load point.

The results of experimental tests are presented in Table 2. It can be seen that the apparent stiffness significantly depends on the orientation of the bending plane (XY and XZ). Also, the analytical predictions and experimental values for the equivalent area moment of inertia of a single picket compare well, with a maximum relative difference lower than 17%.

It was observed that in the tests of a net panel consisting of four interconnected pickets, the observed stiffness was approximately four times higher than that of a single picket. This indicates that interaction between the pickets can be neglected in the predictions of chain-link mesh bending behavior.

Table 2: Comparison of the equivalent moments of inertia obtained from the experimental measurements and analytical predictions.

Specimen	Orientation	$\mathbb{I}_{eq}$ for 1 Picket, mm^4			$\mathbb{I}_{eq}$ for 4 Pickets, mm^4		
		Analytical	Experimental	δ^*,%	Analytical	Experimental	δ^*,%
M2.5-30	Y	1.23	1.27	3.5			
	Z	1.10	0.94	-16.8	4.39	3.82	-15.0
M2.5-25	Y	1.23	1.23	0.3			
	Z	1.10	1.04	-5.6	4.39	3.64	-20.6
Straight wire	Y	2.04	2.27	-10.4			
	Z	2.04	2.27	-10.4	8.12	9.08	-10.4
M3.5-50	Y	4.83	4.61	-4.8			
	Z	4.31	4.03	-7.0	17.3	16.8	-2.7

$$* \ \delta = \frac{\mathbb{I}_{exp} - \mathbb{I}_{ana}}{\mathbb{I}_{exp}} \cdot 100\%$$

5. NUMERICAL MODEL TO PREDICT VOLUMETRIC LOSS UNDER WAVES AND CURRENTS

A commercially sized, cylindrical gravity cage system was selected as the base framework flotation and support structure. The system has a diameter of 20 m and a net chamber depth of 10 m with a static net chamber volume of 3140 m^3. Such a system replicates a commercially sized cage presently utilized in down-east Maine fish farms. The buoyant rim is composed of two concentric floating collars constructed of 400 mm diameter HDPE pipes, and the lower rim made of a 90 mm pipe. To describe the drag forces on the net chamber, a recent study by Tsukrov et al. [13] was used. The copper alloy and nylon nets selected had a solidity of 17.1% (where solidity is the ratio of projected area to outline area). The detailed breakdown of cage framework design parameters is shown below in Table 3. The finite element mesh of the cage consisted of 1969 nodes and 2960 elements and is shown in Figure 5.

The net chamber was analyzed using both truss and beam elements to isolate the effect of the alloy's bending stiffness on the volumetric stability. For the beam elements, the effective moment of inertia was utilized as determined from the mechanical experiment.

Table 3: Cage framework model parameters.

Component parameters	Values
-FLOATATION COLLAR-	
Material	HDPE
Pipe Wall Thickness, *mm*	36
Pipe Diameter, *mm*	2x400
Collar Diameter, *m*	20
Total Mass, *kg*	5250
Young's Modulus, *GPa*	8.9
-LOWER SUPPORT COLLAR-	
Material	HDPE
Pipe Wall Thickness, *mm*	1.9
Pipe Diameter, *mm*	90
Collar Diameter, *m*	20
Young's Modulus, *GPa*	8.9
-NET CHAMBER (SIDE)-	
Twine Diameter, mm	2.54
Number of Twines per Element	35.52
-NET CHAMBER (BOTTOM)-	
Twine Diameter, mm	2.54
Number of Twines per Element	33.73

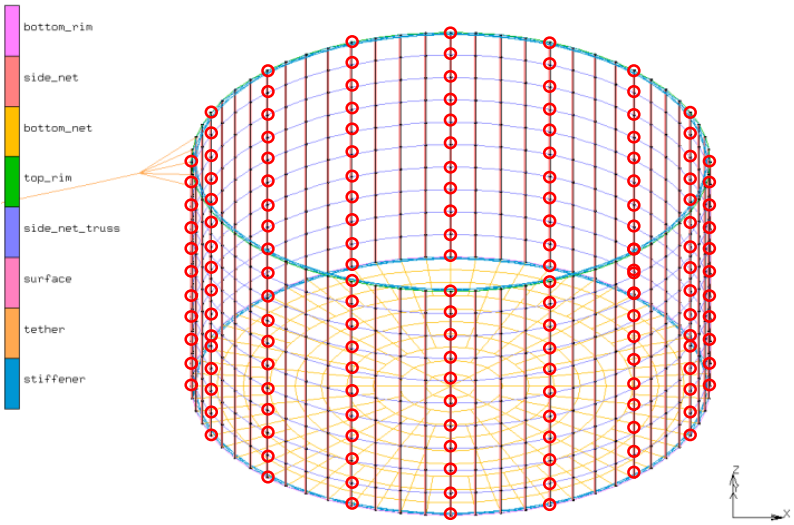


Figure 5: MSC Marc/Mentat copper-alloy cage model. Red circles indicate the tracked nodes.

Two major types of environmental loading were considered in simulations: ocean currents and waves. The wave periods and heights, and current velocities were based on the suggested off-shore aquaculture site conditions [15]. These exposed sites would experience significant wave heights between 1-3 meters (greater for storm events) with the majority of wave energy

density in the wave period range of 3 – 13 seconds [15]. To limit the number of simulations but still obtain a full range of conclusive results, a total of 11 different load cases were chosen (see Table 4). Load cases 1 through 3 (LC1-3) applied a current velocity that were constant with water depth. Load cases 4 through 7 (LC4-7) applied regular progressive waves with wave periods ranging from 5 to 11 seconds and wave heights ranging between 2 to 5 meters. Load case 8-11 (LC8-11) applied a co-linear combination of a 1 *m*/*s* current velocity with the waves.

A basic mooring system was needed to provide the vertical and horizontal freedom necessary to accurately predict the net chamber volume change. Since the applied forces are unidirectional, a simplified horizontal single point tether with length of 50 *m* was utilized.

Table 4: Simulated load cases.

Load case	Current velocity, *m*/*s*	Wave period, *s*	Wave height, m	Wave length, *m*
1	0.25	-	-	-
2	0.5	-	-	-
3	1.0	-	-	-
4	-	5	2	39
5	-	7	3	76
6	-	9	4	126
7	-	11	5	189
8	1.0	5	2	39
9	1.0	7	3	76
10	1.0	9	4	126
11	1.0	11	5	189

6. VOLUMETRIC DEFORMATION PREDICTED BY FEA

Finite element simulations were conducted to predict the volume reduction of a cage due to its deformation under waves and currents. The simulation time was set to 400 seconds with a time step of 0.0005 seconds.

Several methods are available to calculate the volume of a deformed cage based on the displacements of discrete points (nodes), for example Scalar Triple Product [3], the divergence method, and the Delaunay triangulation methods. For a detailed discussion of the volume calculation methods, see [16]. We used the divergence method and based our calculations on the data for 176 nodes evenly distributed over the net chamber, as shown in Figure 5. The volume deformation values calculated as the percentages of the remaining cage volume are shown in Table 5.

It can be seen that incorporation of the bending stiffness of netting (by using beam elements instead of truss elements) does not significantly change the predictions for the system's volume loss under the considered environmental loadings. The observed differences in volume do not exceed 3%. It appears that the ratio of beam length to resistance of bending for the analyzed system is so large that the bending stiffness of copper alloy pickets is negligible, and the netting behaves as though it was a catenary system.

Table 5: Remaining cage volume as predicted by MSC Marc simulations.

Model	Volume statistic	Load case 1	2	3	4	5	6	7	8	9	10	11
Beam elements	Mean, %	97	93	58	99	97	95	93	52	46	47	46
	Max, %				101	102	101	101	60	70	74	74
	Min, %				97	89	85	77	44	24	19	17
Truss elements	Mean, %	97	93	58	99	97	95	94	52	47	48	47
	Max, %				101	102	102	101	63	72	77	74
	Min, %				96	90	83	80	44	25	20	20

CONCLUSIONS

An experimental study was performed to characterize the bending stiffness of copper alloy chain-links meshes. The collected data was used to validate the developed analytical and numerical models. It was found that for commercial scale fish cages the bending stiffness of the copper alloy mesh does not significantly affect the predictions of volumetric loss due to environmental loading. It can be concluded that the implementation of the bending resistance of copper alloy mesh is not significant in determining the dynamic behavior of gravity type commercial fish cages. Thus, the traditional numerical modeling techniques (i.e. using truss elements) are sufficient for analyzing dynamics of copper alloy fish cage systems.

ACKNOWLEDGMENTS

The authors thank the manufacturers for supplying the test specimens. Langley Gace (International Copper Association) is acknowledged for sharing information on various copper alloy nets. The authors are grateful to Murat Yigit (Canakkale University) for providing mesh *M2.5-30* and Yannis Korkolis (University of New Hampshire) for invaluable discussions. Great thanks are extended to Paul Lavoie for help with the experiments.

REFERENCES

[1] UNFPA, "State of World Population 2011," United Nations Populations Fund, New York, NY, 2011.

[2] FAO, "Statistics and information Service of the Fisheries and Aquaculture Department," Food and Agriculture Organization of the United Nations, Rome, Italy, 2011.

[3] C.-C. Huang, H.-J. Tang and J.-Y. Liu, "Dynamical analysis of net cage structures for marine aquaculture: Numerical simulation and model testing," *Aquacultural Engineering,* vol. 35, no. 3, 2006.

[4] P. Lader, T. Dempster, A. Fredheim and O. Jensen, "Current induced net deformation in full-scale sea-cages for Atlantic salmon," *Aquacultural Engineering,* vol. 38, no. 1, pp. 52-65, 2008.

[5] Y.-P. Zhao, Y.-C. Li, G.-H. Dong, F.-K. Gui and B. Teng, "Numerical simulation of the effects of structure size ratio and mesh type on three-dimensional deformation of the fishing-net gravity cage in current," *Aquacultural Engineering,* vol. 36, no. 3, pp. 285-301, May 2007.

[6] S. Cheah and T. Chua, "A Preliminary Study of the Tropical Marine Fouling Organisms on Floating Net Cages," *Malayan Nature Journal,* pp. 39-48, 1979.

[7] R. Swift, D. W. Fredriksson, A. Unrein, B. Fullerton, O. Patursson and K. Baldwin, "Drag force acting on biofouled net panels," *Aquacultural Engineering,* vol. 35, no. 3, pp. 292-299, October 2006.

[8] J. Ortuno, M. A. Esteban and J. Meseguer, "Effects of short-term crowding stress on the gilthead seabream(Sparus aurata L.) innate immune response," *Fish Shell Immunology,* vol. 11, no. 2, pp. 187-197, 2001.

[9] R. Braithwaite, M. C. C. Carrascosa and L. McEvoy, "Biofouling of salmon cage netting and the efficacy of a typical copper-based antifoulant," *Aquaculture,* vol. 262, no. 2-4, pp. 219-226, 28 February 2007.

[10] A. Drach, I. Tsukrov, T. Gross, U. Hofmann, J. Aufrecht and A. Grohbauer, "Corrosion rates and changes in mechanical properties of copper alloys due to seawater exposure, IMECE2012-88156," in *Proceedings of the ASME 2012 International Mechanical Engineering Congress & Exposition*, Houston, TX, USA, 2012.

[11] H. Moe, R. H. Gaarder, A. Olsen and O. S. Hopperstad, "Resistance of aquaculture net cage materials to biting by Atlantic Cod (Gadus morhua)," *Aquacultural Engineering,* vol. 40, no. 3, pp. 126-134, May 2009.

[12] A. Drach, I. Tsukrov, J. DeCew, U. Hofmann, J. Aufrecht and A. Grohbauer, "Corrosion and biofouling performance of copper alloys investigated in the North Atlantic Ocean," in *CORROSION/2013*, Houston, TX, USA, 2013.

[13] I. Tsukrov, A. Drach, J. Decew, M. R. Swift and B. Celikkol, "Characterization of geometry and normal drag coefficients of copper nets," *Ocean Engineering,* vol. 38, no. 17-18, pp. 1979-1988, September 2011.

[14] ASTM E855-08, "Standard test methods for bend testing of metallic flat materials for spring applications involving static loading," ASTM International, West Conshohocken, PA, 2009.

[15] J. Ryan, "Farming the Deep Blue," Westport, Ireland, 2004.

[16] M. Osienski, "Dynamic and structural analyses of a gravity fish cage employing copper alloy netting," University of New Hampshire, Durham, NH, 2013.

V International Conference on Computational Methods in Marine Engineering
MARINE 2013
B. Brinkmann and P. Wriggers (Eds)

DESIGN AND MODELING OF SUBMERSIBLE FISH CAGES WITH COPPER NETTING FOR OPEN OCEAN AQUACULTURE

MARINE 2013

ANDREW DRACH[*], IGOR TSUKROV[*], JUDSON DECEW[†], M. ROBINSON SWIFT[*], BARBAROS CELIKKOL[†], CARLOS F. HURTADO[‡]

[*] Department of Mechanical Engineering
University of New Hampshire
Durham, NH 03824, USA
e-mail: igor.tsukrov@unh.edu

[†] Center for Ocean Engineering
University of New Hampshire
Durham, NH 03824, USA
e-mail: jud.decew@unh.edu

[‡] School of Marine Sciences
Pontificia Universidad Catolica de Valparaiso
Valparaiso, Chile
e-mail: felipe.hurtado@ucv.cl

Key words: copper alloy net, offshore aquaculture, submersible fish cage, design, finite element analysis

Abstract. Open ocean aquaculture is a rapidly growing industry with the potential to satisfy the global seafood demand in the environment of declining wild fish harvesting. However, technologies developed for inshore aquaculture are not easily transferrable to the exposed fish farm locations. In particular, the structural integrity of fish cage/mooring systems, and the high cost of the maintenance (cleaning of the biofouled netting) are two major concerns in the engineering for open ocean aquaculture.

This paper deals with introduction of copper alloy nets in open ocean aquaculture as a new technology to reduce biofouling, improve cage volume stability, its structural strength, and to provide additional protection from predators. Copper alloys have natural resistance to corrosion and biofouling combined with high strength and stiffness. However, these materials have higher density, different hydrodynamic properties and structural characteristics when compared to traditionally used nylon nets. The paper presents novel design and fabrication procedures needed for engineering of the offshore fish farms utilizing copper alloy netting. These procedures are illustrated on a commercial size gravity-type offshore fish cage, which was designed and successfully deployed in the Pacific Ocean near Isla Italia (Patagonia, Chile).

1 INTRODUCTION

In a typical marine aquaculture operation fish are raised in cages consisting of a framework and a net chamber [1,2]. The fish cages can be either surface-type (floating on the surface) or submersible to mitigate the effects of high energy surface conditions and improve the fish growing environment. Traditionally, net chambers are made of nylon netting in both inshore and offshore fish farms. However, potential improvements in fish farming operations and maintenance can be achieved by substituting polymer nets with copper alloy netting. Usage of the latter in offshore aquaculture requires new design techniques and revised analysis procedures due to a different set of physical properties (density, stiffness, strength) as compared to nylon and polyester which are traditionally used for fish cage netting.

This paper deals with introduction of copper alloy nets in open ocean aquaculture as a new technology to reduce biofouling, improve cage volumetric stability and its structural strength, and provide additional protection from predators. Development of anti-fouling, predator-resistant copper alloy netting technology started in 1970s with enclosures for salmon farming in the Northeast USA. Initial trials documented that after six years of deployment, enclosures had very little biofouling and minimal losses due to predator attacks [3–5]. To the best of the authors' knowledge, more than 300 cages utilizing copper alloy nets are currently installed in Australia, Chile and Japan. The use of copper alloy net materials has shown promising results in gravity-type and rigid-frame cages located in protected areas, such as bays or fjords [6–8]. Biological growth on copper alloy net chambers is minimal compared to the nylon net pens, allowing improved fish growth rates and oxygen flow, decreased maintenance and cleaning costs. Note that in the text to follow we refer to various copper alloy nets simply as "copper nets".

Fish cages with copper netting should be designed in such a way that existing aquacultural technologies and practices are used with few changes to accommodate the new netting type. This approach allows for easy integration of these systems to the existing industry (i.e. through retrofitting of the existing fish cage systems) and provides a lower economical barrier to the introduction of this technology. Advantages of copper netting can be summarized as follows:

- enhanced water flow through the cage, reduced parasites and infections due to significantly lower biofouling (see discussion of biofouling of copper alloys in [9])
- reduced mortality by avoiding stressful net changes and cleaning, better protection from predators
- lower maintenance and operational costs: no net changes; no net cleaning, no need for predator nets and lower use of antibiotics
- reduced environmental impact: copper alloys may be made of recycled materials and recycled after fish cage recovery, no bio-fouling to dispose of

It should be noted that as with any new technology, some obstacles and drawbacks are inherent. For copper nets, these include:

- higher initial costs due to high material costs of copper alloys and necessity to improve structural strength of the cage framework
- new design and installation techniques are required to integrate copper nets into the existing industry

- difficulties in handling components during cage fabrication and deployment due to the substantially increased weight of the system both onshore and in water.

Offshore aquacultural system consisting of a fishcage in a single-bay mooring grid and a manual feeder for submersible cages was designed in collaboration with EcoSea Farming S.A. (Chile) and deployed in the South Pacific. Two identical cages were successfully deployed in inshore and offshore sites, proving the flexibility of the design. In the sections to follow, the engineering approach to design and manufacturing of an offshore submersible gravity fish cage is demonstrated on the example of this system. More detailed information can be found in the project report [10].

2 DESIGN APPROACH AND CONSTRAINTS

High initial costs of offshore aquacultural systems (especially, the ones with copper alloy components) demand sound and systematic approach during all stages of design and analysis to ensure that the deployed system can withstand service loads as well as to survive without substantial damage through the storms inadvertent in the high-energy deployment locations. At the design stages, it is important to ensure that the structural strength is adequate and that the fish cage dynamic behavior is steady enough for successful farming. This can be achieved through the structural strength analysis and dynamic simulations under both service and storm loads. Recent developments of the computational techniques [11–14] allow for a robust analysis of the investigated design prior to the physical testing and field deployment. Proper engineering procedure for the development of an offshore fish cage system with copper alloy components should include the following steps:

- Establish the design constraints, operational limits and service life requirements
- Select the mooring system and deployment site, and collect historical environmental conditions data (if available)
- Generate several prototype sketches with the description of major components
- Analyze hydrostatics, design feasibility, and potential handling issues during assembly/construction/deployment
- Design suitable copper net attachments which ensure net pen integrity and limit wear of the netting
- Choose the best prototype and analyze corrosive compatibility of materials (i.e. make sure steel components are securely isolated from any copper parts)
- Develop the first design iteration including detailed drawings of all system components
- Analyze structural integrity and dynamic response of the individual components and system as a whole
- Iterate through a few cycles of design reviews with structural/dynamic analysts and construction/operations personnel
- Produce assembly/construction/deployment plans
- If possible, perform scaled physical testing
- Finalize the design and produce detailed documentation

The proposed design consists of a 20-meter diameter gravity-type cage (Figure 1) with the netting suspended from the top rim and attached to the bottom rim which is required to maintain volumetric stability. Framework consists of two surface pipes supported by brackets on top and a single pipe of the same diameter on the bottom. The entire net chamber is fabricated from the copper alloy wire woven into a chain-link configuration. An airlift–ballast assembly is added to the system to allow the cage to quickly surface and submerge. A single-bay grid mooring (with redundant anchor legs for safety) is utilized to secure the fish cage system. A hydraulic venturi-style feed device is used to feed the fish when submerged for extended periods of time.

The design is selected to satisfy the following requirements:

- Provide 3,000 m^3 net pen for fish farming
- Sustain net chamber integrity and volumetric stability in a variety of environmental conditions
- Provide sufficient reserve buoyancy for on-cage surface operations and maintenance
- Allow for quick submergence to avoid red tides / toxic algae outbreaks
- Withstand loads in a high-energy environment
- Be based on the existing technology and compatible with the existing infrastructure of the deployment region to allow easy integration into the local industry

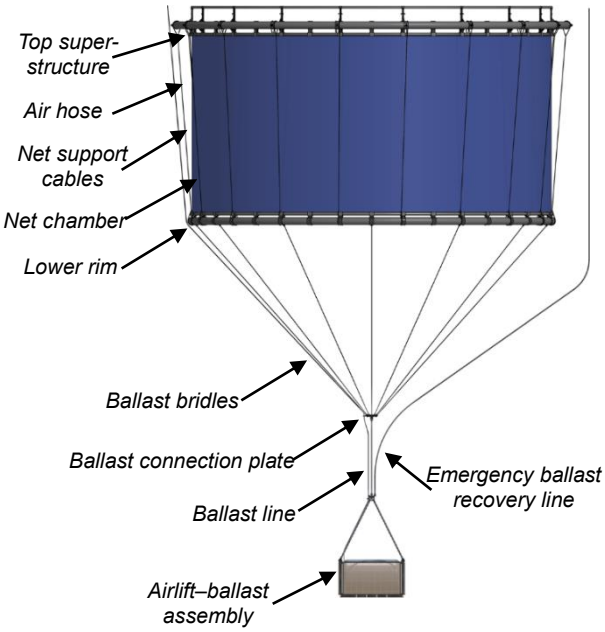


Figure 1. The submersible offshore fish cage design.

Although not a requirement, effort was also made to design a system that could be integrated into the existing cage frames. In effect, the proposed design was selected to allow retrofitting of existing aquaculture fish cages with nylon nets into those with copper netting. To accomplish these goals, analytical, numerical and physical modeling techniques were employed.

3 DESIGN STEPS

The design process started with a review of information on the environmental conditions and selection of an offshore site. Based on the available data, it was concluded that a load case representing storm events consisted of a 9-meter, 12-second wave with a collinear 1.5 *m/s* current. This loadcase was utilized for design and analysis purposes, along with a set of additional loadcases representing daily service conditions. It was also determined to limit surface operations and recommended to submerge the system for fish grow-out. Thus, life expectancy of the cage (specifically the net chamber) could be prolonged.

Next, preliminary cage and mooring configurations were developed for the selected environmental conditions. Overall cage design and mooring parameters such as diameter,

volume, and construction materials were established. Dynamic analysis (numerical simulations) of a surface cage was performed to get a first-order estimate of net and mooring loads. Using the obtained information, possible net chamber connections were proposed, analyzed and incorporated into the overall net pen. Preliminary finite element analysis was performed on all critical components to eliminate suspect cage configurations and component designs.

Several candidate designs were chosen for a more detailed study. Then hydrostatic characteristics were determined for each of the prototype designs [15]. The vertical centers of mass and buoyancy of the fish cage were calculated and compared to verify stability. The reserve buoyancy of each system was calculated to insure proper working conditions.

With a preliminary cage and mooring design established, a series of design reviews were performed with participation of structural analysts, EcoSea engineers and Chilean aquaculture industry personnel. Suggestions to the cage configuration, net attachments, mooring design, surface and submerging operations were reviewed and implemented. The system was re-examined and adjusted as necessary to insure that structural integrity, manufacturing techniques and planned operational logistics were adequate and compliant with the industry in the region.

Several copper net configurations with different chain-link weaving orientations and net attachment methods were considered. Galvanic corrosion concerns, optimal net usage and proper fish containment during submerged operations were analyzed as well. System operating procedures and methods to assemble the cage and netting were developed. The mooring line lengths, diameters and connections were specified, taking into account standard practices in use by the Chilean aquaculture industry. Geometric, physical and material properties of each component were examined for compatibility. All modifications were incorporated and the design configuration was finalized.

Next, the cage and mooring system dynamic and structural responses were analyzed. The dynamic performance of the cage was numerically modeled using the finite element analysis program AQUA-FE. This software package allows to perform the dynamic analysis of 3-D flexible structures in the marine environment. It was developed and maintained by the University of New Hampshire [12,16–18] and has been successfully used with multiple ocean engineering projects [19–21]. Note that this kind of analysis can also be performed using other software packages [22–25]. The system was first analyzed with no wave or current forcing. This static simulation insured the model was constructed properly, and allowed to study the net chamber shape. The model was then subjected to the selected environmental conditions to investigate the cage dynamic response (stresses and deformations) and mooring line tensions.

The results of the dynamic analysis were used as input to a structural model of the system and its components. Structural modeling was performed with a commercially available CAE software package SolidWorks. Finite element simulations of all load bearing components were conducted to investigate the structural integrity and establish the service load limits. Stresses at critical connections (e.g. mooring line and ballast bridles attachment points) were analyzed to optimize the material usage.

With the fish cage and mooring system analyses complete, the design was presented for review with the industry personnel. The design was finalized, full engineering documentation was generated, and later used for fabrication, assembly and deployment of two identical systems at different locations in the South Pacific.

4 FISH CAGE DESIGN ELEMENTS

A schematic of the cage system is presented in Figure 1. The top superstructure (Figure 2) consists of two pipes made of high density polyethylene (HDPE), a handrail, net support pipe (referred to as the "net pipe" in the text to follow) and 36 brackets. Both buoyancy pipes are 400 *mm* diameter DR9 pipes, providing the majority of the buoyancy and structural integrity of the system. These pipes are aligned with 18 brackets, as shown in Figure 3a, which support the handrail (110 *mm*) and net pipe (140 *mm*). Mooring attachments are located on the outside of each bracket. The other 18 brackets (Figure 3b), placed only over the inner buoyancy pipe, provide additional support to the net pipe. This allows for a more even distribution of the net chamber weight (ca. 5,400 *kg*) and dynamic loads on the structural pipe when subjected to waves.

The 10-meter deep net chamber was fabricated from admiralty brass (commercial modification of UNS C44400 alloy known as UR30) wire, woven into chain link mesh configuration, with a 4.0 *mm* wire diameter and a 40 *mm* bar length. The netting is suspended from the net pipe via individual "double loops" of brass wire (Figure 2, details A, B), located every 150 *mm* along the pipe. The bottom rim is attached via a similar method. The fish cage is designed to support a net chamber of this material on the sides and bottom of the circular chamber. For the top panel, nylon netting is chosen as a cheaper solution which also avoids accelerated corrosion concerns (splash zone corrosion when the system is floating on the surface).

A lower rim was incorporated into the design to help stabilize the volume of the net chamber, as well as provide some additional buoyancy to offset the net chamber weight. The rim was fabricated of HDPE pipes similar to the top superstructure, but without one buoyancy pipe and a handrail. Whereas the top rim has two sets of brackets, the lower rim assembly uses only one bracket modification (Figure 3c) with a pad-eye for attachment of the ballast bridles.

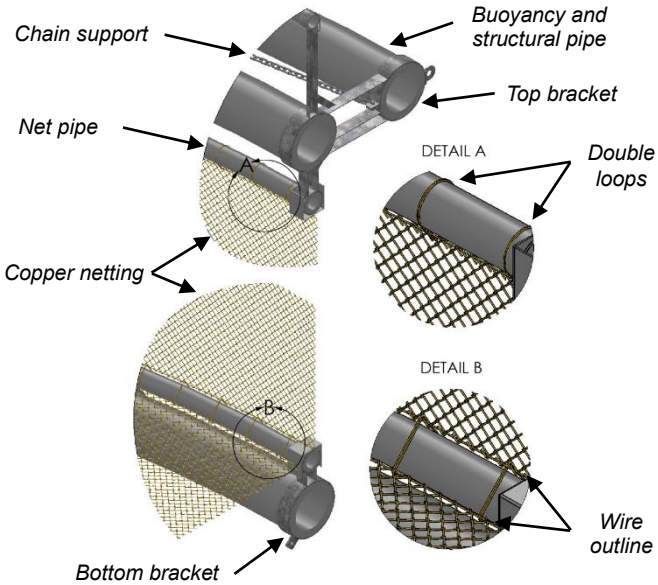


Figure 2. Top superstructure consists of a handrail, two main structural pipes and a net support pipe. The net chamber is attached to the net pipe on the top and bottom rims. The lower rim has only one structural pipe.

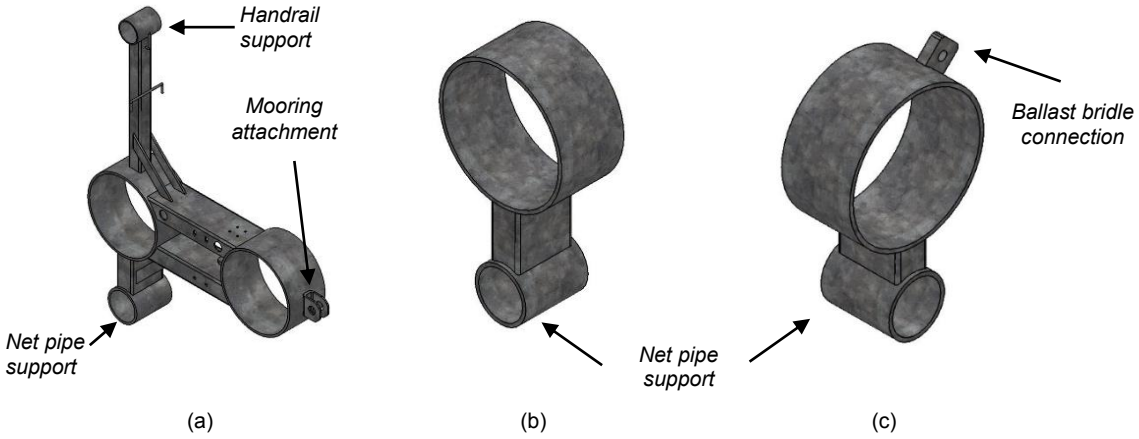


Figure 3. Brackets designed for the system: (a) main top rim bracket that secures all top rims. (b) top rim support bracket with additional support for the net pipe; (c) bottom rim bracket with a net support component and a pad-eye for the ballast bridle system.

5 NET CHAMBER AND ATTACHMENTS

The choice of net chamber attachment methodology was one of the most important steps in the design of this system. Several factors influenced the choice of a particular design of the net chamber attachments. First, it was important to design the attachments that provide sufficient strength to withstand the static and dynamic loads from the heavy netting. In addition to that, redundancy of the attachments was critical to ensure that in case of an attachment point failure, the whole system would not collapse. Another factor was the choice of net chamber attachment type (rigid, complaint or hybrid). The net assembly and attachment procedure was required to be straightforward to simplify cage system construction and *in-situ* maintenance. Finally, it was important to have the net constantly in tension to avoid excessive net wear (based on the previous experience with the chain-link mesh in offshore cages [8]).

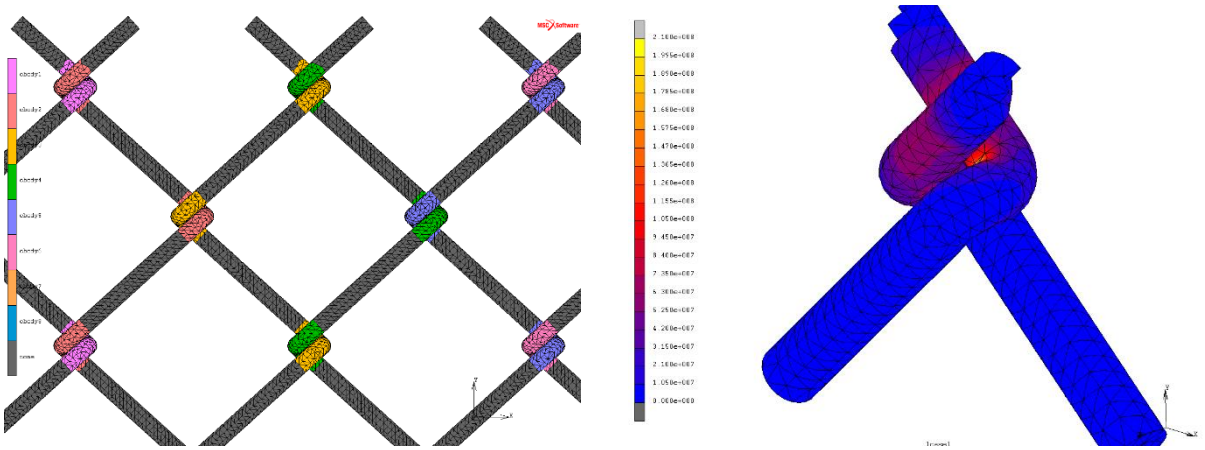
In the selected configuration the net is attached directly to a small diameter HDPE pipe located beneath the buoyancy pipes. Thus, copper netting is constantly submerged at least 0.5 *m* below the water surface and protected from accelerated corrosion in the splash zone. Net panels are outlined in 5 *mm* wire to reinforce the edges. The net is attached to the pipes with individual "double loops" as shown in Figure 2. This attachment method provides an extremely tight connection to the top and bottom net pipes, even distribution of the loads around the cage circumferences, and redundancy in the event of a single loop failure.

Dynamic analysis described in Section 3 indicates that the net chamber can experience significant snap loads under the applied environmental conditions. At the time of this research, only limited information was available on the strength of the chain-link brass mesh. Therefore, a finite element analysis study was performed (Figure 4) to determine the critical loads that this specific mesh can withstand. The analysis demonstrated that the stress concentrations at the joints can exceed the allowable limits. This observation was also supported by the results of a mechanical tension test on the chain-link mesh panel (Figure 5). To address this concern, additional load bearing members had to be incorporated for absorption of snap loads. Two solutions were considered:

- additional straight copper alloy wire woven through the netting and secured to the net pipes. However, a large number of additional wires (~200) was required to provide sufficient increase in strength;
- utilization of resin impregnated or coated steel cables adjacent to the net. As few as 18 cables were needed to protect the net chamber during the storm.

First method had an advantage of material compatibility, while the second one allowed for a more straightforward fabrication. Due to the limited supply of the copper alloy wire, the second option was employed. To insure that the cables absorbed the net loading, their length was specified slightly shorter than the height of the net chamber deformed due to its self-weight.

Finally, it was important to isolate the net from coming in contact with the galvanized steel brackets. To achieve this, a protective boot was designed to fit over the steel net supports, and held in place by the net pipes.



(a) (b)

Figure 4. Strength analysis of the chain-link mesh. (a) Joints are modeled as solid elements with contact regions shown in color. (b) Distribution of the equivalent stress at one of the joints.

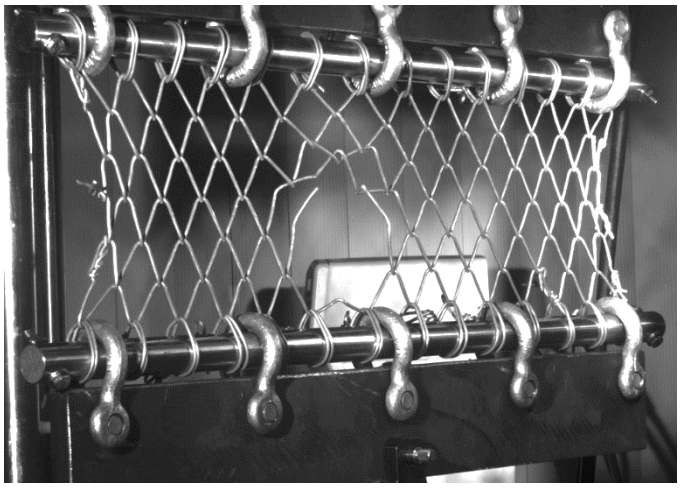


Figure 5. Tension testing of the strength of chain-link net panel.

6 AIRLIFT–BALLAST ASSEMBLY

To control position of the fish cage in the water column, an airlift–ballast assembly is used. This airlift device controls submergence through buoyancy adjustments. It consists of a steel and concrete framework with an inflatable airbag. The lift bag is placed inside the ballast structure with an air hose leading up to the surface. The airlift system is designed to be always negatively buoyant to prevent damage to the fish cage by the ascent of the airlift. The airlift-ballast assembly is supported below the cage by twelve ballast bridle lines. These lines are shackled into a ballast connection plate, designed to ease the installation and removal of each shackle. They are isolated from each other to limit the wear. In the event one of the lines fails, the remaining lines can operate as expected and allow the failed member to be replaced *in-situ*. A single ballast line runs from the connection plate to the airlift-ballast assembly. The ballast weight and bridle arrangement provide a dynamic restoring force that helps maintain volumetric stability when the two rims above (top superstructure and bottom rim) move relative to each other in waves, currents or during surfacing/submerging operations.

When the cage is operated at the surface, the bag is inflated, offsetting the weight of the ballast (Figure 6). To submerge the cage, the bag is deflated (via hose at the surface) reducing the system's reserve buoyancy. The cage stops its descent when the ballast weight reaches the seafloor. In the event the ballast becomes stuck in the seafloor sediment, a back-up pendant line can be used to free the system.

A lift bag can be operated via an HDPE hose that runs along the cage's exterior. Back up valves and break points in the line at several points along the length of the cage are incorporated to allow replacement of the hose sections if necessary. The hose at the surface is outfitted with two valves (one redundant) to insure that air does not escape during normal operations.

Several submersion technologies and techniques were investigated for providing submergence control, including utilization of various rim configurations as variable buoyancy chambers, integration of a variable buoyancy central spar inside the cage, and utilization of a separate airlift and a ballast weight below the cage. The described configuration with airlift-ballast assembly was chosen for the following reasons:

- Eliminates the possibility of losing buoyancy of the main cage frame in the event of a valve failure (if cage frame was used as a variable buoyancy chamber).
- The airlift-ballast assembly is located on the central axis of the system helping insure stable surfacing and submerging operations.
- The system is easy to use and can be submerged with small infrastructure and few personnel.
- The net pen can be utilized without the airlift-ballast assembly for surface operations.
- The cage system requires limited diving operations because filling and emptying the variable buoyancy member are performed at surface
- During the fish grow-out, the assembly can be removed, repaired, replaced, etc.
- The variable buoyancy member does not intake or exhaust water. The outside water pressure collapses the bag when air is released (at the surface). Pressurized surface air expands the bag, restoring buoyancy.

However, the choice of an external ballast system limits the net pen reserve buoyancy as compared to traditional surface cage systems or systems with an internal ballast system (such as the one in which main rims operate as variable buoyancy members). The reserve buoyancy of the system is linked to the variability in buoyancy associated with the airlift-ballast assembly. The more reserve buoyancy is required, the larger variable buoyancy member is needed, thus driving up the weight of the ballast. It is important to note that mooring systems should be compatible with the design of fish cage and choice of the submergence control device (e.g. airlift).

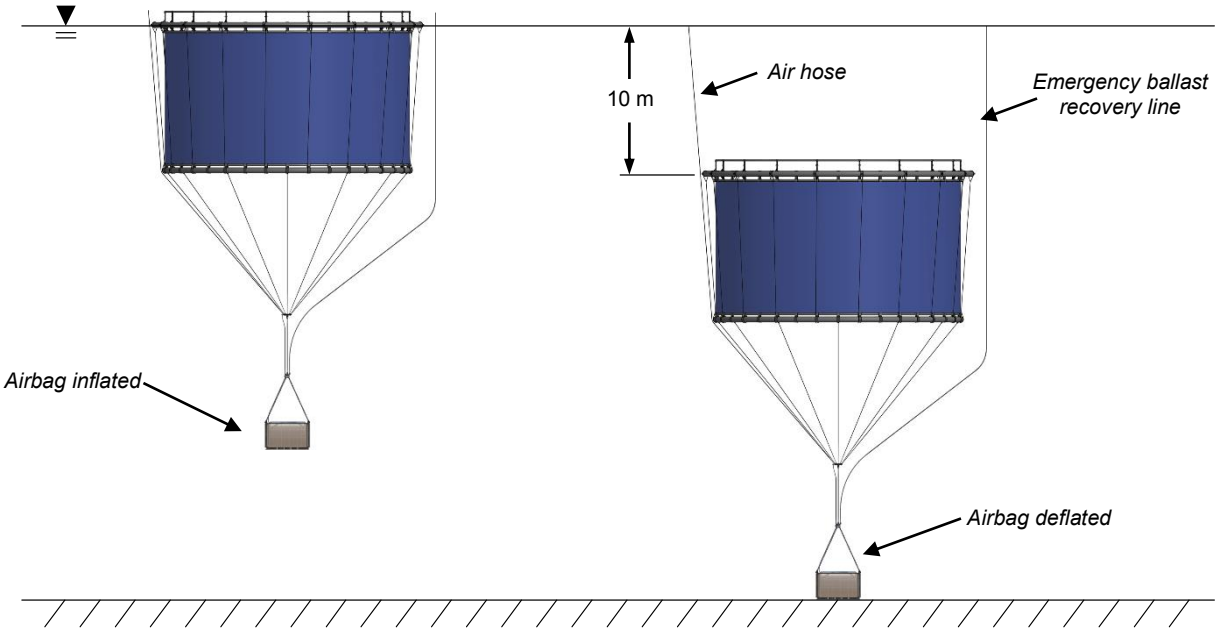


Figure 6. The fish cage in the surface (left) and submerged (right) positions.

7 CONCLUSIONS

Engineering procedures for design of a submersible fish cage with copper netting should include the following major steps: establishment of the design constraints, development and analysis of the conceptual design, review with construction and operational personnel, verification of the final design, and development of the construction and deployment procedures.

To illustrate this approach, design steps for the development of a submersible fish cage utilizing copper alloy net chamber are presented. To address the concerns associated with the introduction of a new netting material, robust net attachment methodologies were developed. In addition, the employed brackets were modified from the standard aquaculture bracket designs, providing not only adequate structural support to the system but also the opportunity to convert a standard gravity fish cage with nylon netting to the one with copper mesh. The airlift-ballast assembly was integrated into the design to protect the cage system from toxic algae blooms and heavy storms by submerging the cage below the surface.

To facilitate easy integration into the local aquaculture farming community, the cage system was designed for construction and deployment with small infrastructure. Two offshore aquaculture systems were fabricated and deployed in the South Pacific. One system is presently secured in a near-shore fish farm and stocked with Atlantic salmon for a trial grow-out. The second system is deployed in an exposed site having current velocities approaching 1 *m*/*s* and wave heights of 5 *m*. Both cage systems are being monitored for structural and operational issues that may develop, and have not shown significant degradation over the two-year period.

ACKNOWLEDGMENTS

This work was supported by the International Copper Association (ICA). Hal Stillman (ICA) is acknowledged for sharing information on various copper alloy nets and useful discussions. Great thanks are extended to Ryan Despins, Miles Amaral, Gonzalo Suazo and EcoSea Farming S.A. personnel for their help with design of the fish cage system.

REFERENCES

[1] Loverich G. F., and Gace L., 1997, "The effects of currents and waves on several classes of offshore sea cages," *Open Ocean Aquaculture '97*, Maui, Hawaii, pp. 131–144.

[2] Fredriksson D. W., DeCew J. C., Swift M. R., Tsukrov I., Chambers M., and Celikkol B., 2004, "The design and analysis of a four-cage grid mooring for open ocean aquaculture," *Aquacultural Engineering*, 32, pp. 77–94.

[3] Efird K. D., 1975, "The Inter-Relation of Corrosion and Fouling for Metals in Sea Water," *CORROSION/75*, National Association of Corrosion Engineers, Toronto, ON, pp. 124/1–124/14.

[4] Efird K. D., and Anderson D. B., 1975, "Sea Water Corrosion of 90-10 and 70-30 Cu-Ni: 14 Year Exposures," *Materials Performance*, November, pp. 37–40.

[5] Huguenin J. E., and Ansuini F. J., 1975, "The advantages and limitations of using copper materials in marine aquaculture," *Proceedings of the OCEAN 75 Conference*, Marine Technology Society, San Diego, CA, pp. 444–453.

[6] Ansuini F. J., and Huguenin J. E., 1978, "The Design and Development of a Fouling Resistant Marine Fish Cage System," *Proceedings of the Ninth Annual Meeting*, World Mariculture Society, Atlanta, GA, pp. 737–745.

[7] Huguenin J. E., Fuller S. C., Ansuini F. J., and Dodge W. T., 1981, "Experiences with a Fouling-Resistant Modular Marine Fish Cage System," *Proceedings of the Bio-Engineering Symposium for Fish Culture*, American Fisheries Society, pp. 201–209.

[8] DeCew J. C., Celikkol B., Drach A., and Chambers M., 2010, "Field Trials of a Small Scale Fish Cage with Copper Alloy Netting in the Gulf of Maine," *Proceedings of the World Aquaculture Society Conference*, San Diego, CA.

[9] Drach A., Tsukrov I., DeCew J. C., Hofmann U., Aufrecht J., and Grohbauer A., 2013, "Corrosion and Biofouling Performance of Copper Alloys Investigated in the North Atlantic Ocean," *CORROSION/2013*, National Association of Corrosion Engineers, Houston, TX, USA.

[10] Celikkol B., DeCew J. C., Drach A., Tsukrov I., and Swift M. R., 2010, "Submersible Offshore Salmon Cage Utilizing Copper Alloy Net Materials. Final Report submitted to EcoSea Farming S.A., Chile," University of New Hampshire, Durham, NH.

[11] Bessonneau J. S., and Marichal D., 1998, "Study of the dynamics of submerged supple nets (applications to trawls)," *Ocean Engineering*, 25(27), pp. 563–583.

[12] Tsukrov I., Eroshkin O., Fredriksson D. W., Swift M. R., and Celikkol B., 2003, "Finite element modeling of net panels using a consistent net element," *Ocean Engineering*, 30, pp. 251–270.

[13] Jensen Ø., Wroldsen A. S., Lader P. F., Fredheim A., and Heide M., 2007, "Finite element analysis of tensegrity structures in offshore aquaculture installations," *Aquacultural Engineering*, 36(3), pp. 272–284.

[14] Lee C.-W., Kim Y.-B., Lee G.-H., Choe M.-Y., Lee M.-K., and Koo K.-Y., 2008, "Dynamic simulation of a fish cage system subjected to currents and waves," *Ocean Engineering*, 35, pp. 1521–1532.

[15] Drach A., and DeCew J. C., 2009, "Fish Cage geometry, weight, configurations and static linear FEA. Project progress report submitted to EcoSea Farming S.A., Chile," University of New Hampshire, Durham, NH.

[16] Gosz M., Kestler K. J., Swift M. R., and Celikkol B., 1996, "Finite Element Modeling of Submerged Aquaculture Net-Pen Systems," *Open Ocean Aquaculture '96*, Portland, ME, pp. 523–554.

[17] Tsukrov I., Ozbay M., Swift M. R., Celikkol B., Fredriksson D. W., and Baldwin K., 2000, "Open Ocean Aquaculture Engineering: Numerical Modeling," *Marine Technology Society Journal*, 34(1), pp. 29–40.

[18] Kestler K. J., 2004, "Development of special finite elements for dynamic analysis of flexible structures in the moving fluid environment," Master's Degree Thesis, Mechanical Engineering Department, University of New Hampshire, Durham NH, USA.

[19] Fredriksson D. W., Swift M. R., Irish J. D., Tsukrov I., and Celikkol B., 2003, "Fish cage and mooring system dynamics using physical and numerical models with field measurements," *Aquacultural Engineering*, 27, pp. 117–146.

[20] DeCew J. C., Fredriksson D. W., Bugrov L., Swift M. R., Eroshkin O., and Celikkol B., 2005, "A Case Study of a Modified Gravity Type Cage and Mooring System Using Numerical and Physical Models," *IEEE Journal of Oceanic Engineering*, 30(1), pp. 47–58.

[21] DeCew J. C., Tsukrov I., Risso A., Swift M. R., and Celikkol B., 2010, "Modeling of dynamic behavior of a single-point moored submersible fish cage under currents," *Aquacultural Engineering*, 43(2), pp. 38–45.

[22] Bris F. Le, and Marichal D., 1998, "Numerical and experimental study of submerged supple nets: Applications to fish farms," *Journal of Marine Science and Technology*, 3, pp. 161–170.

[23] Lader P. F., Enerhaug B., Fredheim A., and Krokstad J., 2003, "Modelling of 3D Net Structures Exposed to Waves and Current," *3rd International Conference on Hydroelasticity in Marine Technology*, Oxford, UK.

[24] Takagi T., Shimizu T., Suzuki K., Hiraishi T., and Yamamoto K., 2004, "Validity and layout of 'NaLA': a net configuration and loading analysis system," *Fisheries Research*, 66, pp. 235–243.

[25] Zhao Y.-P., Li Y.-C., Dong G.-H., Gui F.-K., and Teng B., 2007, "A numerical study on dynamic properties of the gravity cage in combined wave-current flow," *Ocean Engineering*, 34, pp. 2350–2363.

V International Conference on Computational Methods in Marine Engineering
MARINE 2013
B. Brinkmann and P. Wriggers (Eds)

NUMERICAL STUDY OF THE FLOW FIELD AROUND FISHING NET

YUN-PENG ZHAO[*], CHUN-WEI BI[*], GUO-HAI DONG[*], YU-CHENG LI[*] AND FU-KUN GUI[†]

[*] State Key Laboratory of Coastal and Offshore Engineering
Dalian University of Technology
Dalian 116024, China
e-mail: Zhaoyp18@hotmail.com

[†] Marine Science and Technology School
Zhejiang Ocean University
Zhoushan, 316000, China

Key words: Flexible Fishing Net, Flow Field, Porous Media Model, Lumped-mass Model

Abstract. A numerical approach is proposed to simulate the interaction between flow and fishing net in steady current. The numerical approach is based on the joint use of the porous media model and the lumped-mass model. The configuration of flexible net can be simulated using the lumped-mass model and the flow field around plane nets can be simulated using the porous media model. Using an appropriate iterative scheme, the fluid-structure coupling problem can be solved and the steady flow field around flexible net is available. In order to validate the numerical approach, the numerical results are compared with the data obtained from the physical model tests. The comparisons show that both the configuration of the flexible nets and flow velocity results are in accordance with that of the corresponding physical model tests.

1 INTRODUCTION

In a deep-water net cage, water motion is beneficial to maintaining the water quality and sufficient water exchange is important for the fish health and growth. However, too intense water motion can cause serious deformation of the fishing net and the effective volume of the net cage reduced sharply which is disadvantageous to fish comfort. Numerous studies have shown that, the force on cage net is proportional to the square of the flow velocity. Even if small velocity differences exist, this may lead to great force differences. So in the investigation on the forces acting on the net cage, the flow velocity distribution around the cage net usually cannot be ignored. Furthermore, the flow field characteristics determine the distribution of nutrients, refuse and dissolved oxygen in the net cage.

To our knowledge, the first investigation of the flow filed of net cages was performed by Aarsnes *et al*. [1]. A series of experiments were carried out to study the velocity distribution within net cage systems, and flow velocity reduction formulae for the net cages were developed. Over the decades since, much progress has been made in the understanding the flow filed inside and around net cages by experimental approach. Fredriksson [2] studied the flow velocity in an open ocean cage with field measurements, and an approximate 10% velocity reduction was found. Lader *et al*. [3] conducted a series of experiments to investigate

the forces and geometry of a net cage in uniform flow, and an average of 20% velocity reduction was measured inside the cage. Li *et al*. [4] analyzed the shadowing effect of six practical gravity cage models by physical model tests, and the flow reduction coefficients within and downstream of the net cages were obtained. Johansson *et al*. [5] performed field measurements at four farms in Norway, and major current reduction was measured in the current passing through the cages. The measured current reduction was between 33% and 64%. Harendza *et al*. [6] conducted experiments in a towing tank with particle image velocimetry (PIV) configurations to investigate the flow field around cylinder fish cages with varying inclination angles and porosity, and the effects of inclination and porosity were described.

However, the efforts mentioned above are mainly concentrated on physical model tests. The numerical study of the flow field around net structure is complex due to the innumerable meshes and other properties like flexibility and discontinuity. Patursson *et al*. [7] developed a numercial model to simulate the flow field around a plane net without considering the net deformation by treating the net structure as a porous medium. Zhao *et al*. [8] proposed a three-dimensional numerical model using the porous media model and presented the flow field inside and around multiple net cages. Through the review of literature on numerical works, the existing efforts are mainly concentrated on the flow field around net structure with no deformation, and there are few numerical models considering the flexibility and movement of the fishing net. This paper introduces a three-dimensional numerical approach to simulate the interaction between flow and flexible nets in a steady current.

2 MODEL DESCRIPTIONS

The numerical approach to simulate the interaction between flow and the flexible net includes two numerical models: the porous media model and the lumped-mass model. The porous media model can simulate the flow field around the plane net with no deformation, and the lumped-mass model can simulate the configuration of flexible nets in certain current. The joint use of the above two models is presented to solve the fluid-structure coupling problem. The steady flow field around flexible nets can be obtained by using an appropriate iterative scheme as explained later in Section 2.3.

2.1 The porous media model

In this part, the porous media model is introduced to model the flow field around the plane net with no deformation, and the finite volume method is used to solve the governing equations of the numerical model. In this way, the numerical simulation of the flow field around the plane net is available.

2.1.1 Porous media resistance coefficients

The porous media model employs empirically determined flow resistance in the region of the domain that is occupied by the porous media. For flow through the porous media, the hydrodynamic forces acting on the porous media can be expressed as follows:

$$F = S_i \lambda A \tag{1}$$

where S_i is the source term for the momentum equation in the i direction, λ is the thickness of the porous media, A is the area of the porous media, and F is the hydrodynamic force in the i direction.

In Eq.(1), S_i is the source term for the momentum equation. When the region is outside the porous media model, $S_i = 0$. While, inside the porous media, S_i is calculated by the following equation:

$$S_i = -\left(D_{ij}\mu u + C_{ij}\frac{1}{2}\rho|u|u \right);$$
$$D_{ij} = \begin{pmatrix} D_n & 0 & 0 \\ 0 & D_t & 0 \\ 0 & 0 & D_t \end{pmatrix}, C_{ij} = \begin{pmatrix} C_n & 0 & 0 \\ 0 & C_t & 0 \\ 0 & 0 & C_t \end{pmatrix}. \quad (2)$$

where D_{ij} and C_{ij} are prescribed material matrices consisting of the porous media resistance coefficients, D_n is the normal viscous resistance coefficient, D_t is the tangential viscous resistance coefficient, C_n is the normal inertial resistance coefficient, C_t is the tangential inertial resistance coefficient.

Substituting Eq. (2) into Eq. (1) provides formulas for calculating the drag force (F_d) and the lift force (F_l) of the plane net. The drag force is parallel to the flow direction, and the lift force is perpendicular to the flow direction:

$$F_d = \left(D_n\mu u + C_n\frac{1}{2}\rho|u|u \right)\lambda A \quad (3)$$

$$F_l = \left(D_t\mu u + C_t\frac{1}{2}\rho|u|u \right)\lambda A \quad (4)$$

The porous coefficients in Eqs. (3) and (4) can be calculated from the drag and lift forces, while the drag and lift forces acting on the fish net have strong relationship with the features of fish net. So the connection between net features and flow field is considered by the porous coefficients in our numerical model. In a general way, the drag and lift forces of the plane net are obtained from the laboratory experiments. In addition, the forces can be calculated from the Morison equation:

$$F_d = \frac{1}{2}\rho C_d A u^2 \quad (5)$$

$$F_l = \frac{1}{2}\rho C_l A u^2 \quad (6)$$

where C_d and C_l are coefficients that can be calculated using empirical formulas proposed by Zhan *et al*. [9], Løland [10], Aarsnes *et al*. [1], etc.

When the plane net is oriented normal to the flow, the porous coefficients (D_n and C_n) are chosen from a curve fit between drag force data of the plane net and corresponding current velocities using the least squares method. The other two coefficients (D_t and C_t) can be ignored because the lift force is equal to 0 when α=90°. When the plane net is oriented with different attack angles (see Figure 1), the porous coefficients should be transformed into formulas (7) and (8) [11]. Then, the four porous coefficients can be obtained by minimizing the error between the theoretical values and existing data for the drag and lift forces using the least squares method, which is a common analytical method in error minimization.

$$D_n^{'} = \frac{D_n + D_t}{2} + \frac{D_n - D_t}{2}\cos(2\alpha^{'})$$
$$C_n^{'} = \frac{C_n + C_t}{2} + \frac{C_n - C_t}{2}\cos(2\alpha^{'}) \quad (7)$$

$$D_t^{'} = \frac{D_n - D_t}{2}\sin(2\alpha^{'})$$
$$C_t^{'} = \frac{C_n - C_t}{2}\sin(2\alpha^{'}) \quad (8)$$

where $\alpha^{'} = 90^{o} - \alpha$, and α is the attack angle.

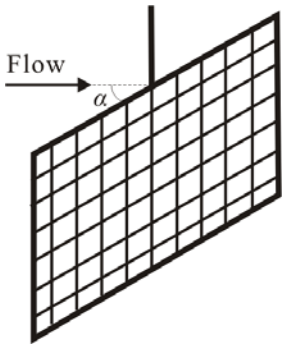


Figure 1: Definition of attack angle (α). Note that the attack angle describes the angle between the flow direction and the plane net in the horizontal plane.

2.1.2 Mesh grids and boundary conditions

An example of computational grids of a plane net at an attack angle α=90° is shown in Figure 2. The optimal mesh type and grid size can be achieved by using the tetrahedron mesh and a size fuction. The coordinate system for the numerical model is a right-handed, three-dimensional Cartesian coordinate system. The origin of the coordinate system is set to the center of the plane net on the free surface. In the coordinate system, x is positive along the flow direction, y is perpendicular to the flow direction on the horizontal plane and z is negative along the direction of the acceleration of gravity. The left boundary of the numerical flume is described by the velocity-inlet boundary condition, while the right boundary is described by the outflow boundary condition. The free surface is modeled using the wall boundary condition with zero shear force. The solid surfaces are modeled using no slip wall boundary. In the areas close to the solid surfaces, the technique of wall function and boundary layer mesh are adopted to solve the effect of the wall surfaces.

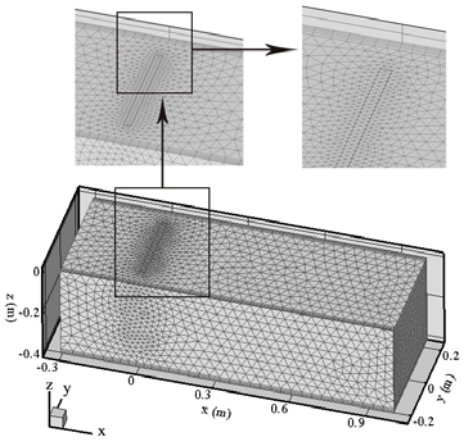


Figure 2: Example of the computational grids.

2.2 The lumped-mass model

The lumped-mass model is introduced to simplify the flexible net (see Figure 3), and the motion equation can be established mainly based on Newton's second law. Given an initial net configuration, the motion equations can be solved numerically for each lumped-mass point. Finally, the configuration of the flexible net in current can be simulated. The calculation method for the model has been explained fully in our previous articles [12,13]. Here only a brief outline is described.

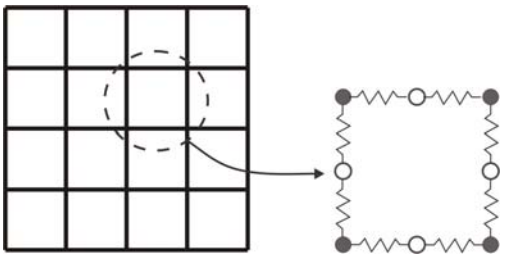


Figure 3: Sketch of the lumped-mass model.

2.2.1 Hydrodynamic forces and motion equations

In a uniform current, the motion equation of lumped-mass i can be expressed as follows:

$$(M_i + \Delta M_i)\vec{a} = \sum_{j=1}^{n} \vec{T}_{ij} + \vec{F}_d + \vec{B} + \vec{W}$$
$$\Delta M = \rho \forall C_m^{'}, C_m = 1 + C_m^{'} \tag{9}$$

where M_i and ΔM_i are the mass and added-mass of lumped-mass point i, $\forall$ is the volume of the point, C_m is the inertial force coefficient, $C_m^{'}$ is the added-mass coefficient, $\vec{a}$ is the acceleration of mass point, $\vec{T}_{ij}$ is the tension force in twine ij (j is the code for knots at another

end of the bar *ij*), *n* is the number of adjacent knots of point *i*, $\vec{F}_d$,$\vec{W}$ and $\vec{B}$ are the drag force, gravity force and buoyancy force, respectively.

Since the points at mesh bars are assumed to be cylindrical elements, the direction of the fluid forces acting on the point masses at each mesh bar should be considered. Therefore, the motion of the point mass *i* is set at the center of a mesh bar, and a local coordinates (τ, η, ξ) are defined to simplify the procedure (see Figure 4). The origin of the local coordinate is set at the center of a mesh bar and the η-axis lies on the plane including τ-axis and flow velocity $\vec{V}$.

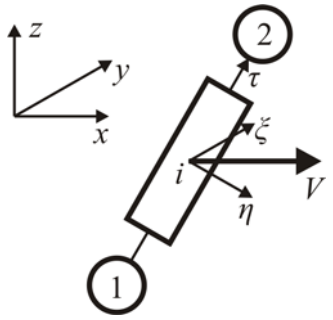


Figure 4: Sketch of the local coordinate for a mesh twine.

Besides the gravity and buoyancy, the drag force on lumped-mass point can be obtained by Morison Equation as follows:

$$\begin{aligned} F_{D\tau} &= -\frac{1}{2}\rho C_{D\tau} A_\tau \left|\vec{V}_\tau - \vec{\dot{R}}_\tau\right| (\vec{V}_\tau - \vec{\dot{R}}_\tau) \\ F_{D\eta} &= -\frac{1}{2}\rho C_{D\eta} A_\eta \left|\vec{V}_\eta - \vec{\dot{R}}_\eta\right| (\vec{V}_\eta - \vec{\dot{R}}_\eta) \\ F_{D\xi} &= -\frac{1}{2}\rho C_{D\xi} A_\xi \left|\vec{V}_\xi - \vec{\dot{R}}_\xi\right| (\vec{V}_\xi - \vec{\dot{R}}_\xi) \end{aligned} \tag{11}$$

where ρ is the density of water, $C_{D\tau}$, $C_{D\eta}$ and $C_{D\xi}$ are the drag coefficient in their respective directions, A_τ, A_η and A_ξ are the projected area of twine normal to their respective directions, $\vec{\dot{R}}_\tau$, $\vec{\dot{R}}_\eta$, $\vec{\dot{R}}_\xi$, $\vec{V}_\tau$, $\vec{V}_\eta$ and $\vec{V}_\xi$ are the velocity components of the lumped-mass point and water particle in their respective directions. The drag coefficients related to Reynolds number are described in the section 2.2.2.

The configuration of the fishing net in current at each time step can be calculated numerically by solving the motion equation with a given initial condition. The equations are simultaneously solved by using the Runge-Kutta-Verner sixth-order method in this paper. The tolerance for the global error is set to 0.001 to guarantee calculation accuracy. In all simulations, the time step is set to 0.001 and the simulation time is set to 40 s considering the calculation precision and efficiency.

2.2.2 Hydrodynamic coefficients of the net

For each mesh bar, the numerical procedure calculates the drag coefficient C_η and C_τ using a method described by Choo and Casarella [14] that updates the drag coefficients based on the Reynolds number (Re_n) as follows:

$$C_\eta = \begin{cases} \dfrac{8\pi}{\mathrm{Re}_n s}\left(1-0.87s^{-2}\right) & \left(0<\mathrm{Re}_n\le 1\right) \\ 1.45+8.55\,\mathrm{Re}_n^{-0.90} & \left(1<\mathrm{Re}_n\le 30\right) \\ 1.1+4\,\mathrm{Re}_n^{-0.50} & \left(30<\mathrm{Re}_n\le 10^5\right) \end{cases} \tag{12}$$

$$C_\tau = \pi\mu(0.55\,\mathrm{Re}_n^{1/2}+0.084\,\mathrm{Re}_n^{2/3}) \tag{13}$$

where $\mathrm{Re}_n = \rho V_{Rn} D/\mu$, $s = -0.077215665 + \ln(8/\mathrm{Re}_n)$, μ is the viscosity of water, C_η and C_τ are the normal and tangential drag coefficients for mesh bar, V_{Rn} is the normal component of the fluid velocity relative to the bar, and ρ is the density of water.

For the knot part, the Fredheim and Faltinsen [15] suggested it could be reasonable to use a drag coefficient in the range of 1.0–2.0 when modeling the knot part as a sphere. Here C_D is set as 2.0 for the knot part.

2.3 Joint use of the porous media model and the lumped-mass model

The lumped-mass model is introduced to simplify the flexible net, and the motion equation can be established The main concept of the numerical approach is to combine the porous media model and the lumped-mass model to simulate the interaction between flow and flexible nets. Taking single flexible net as example, a calculating flow chart for the numerical approach is shown in Figure 5. More detailed calculation procedure is given as follows. Step 1 is to simulate the flow field around a plane net without considering the net deformation using the porous media model. Step 2 is to calculate the drag force and the configuration of a flexible net in current using the lumped-mass model. The given initial flow velocity is exported from the upstream surface of the plane net in Step 1. In Step 3, according to the net configuration, the flow field around the flexible net can be simulated by dividing the net into several plane nets with different inclination angles. In Step 4, the drag force and the configuration of the flexible net is calculated again. Along the net height, different flow velocities are given which are exported from the upstream surface of the plane nets with different inclination angles. The terminal criterion of the calculation procedure is defined as $\Delta F = \left(F_{i+1} - F_i\right)/F_{i+1}$, where F_i and F_{i+1} are the drag forces of two adjacent calculations. If $\Delta F < 0.001$, it was determined that the force acting on the net structure is stable and the configuration of the flexible net is the equilibrium position considering the fluid-structure interaction. Otherwise, repeat Steps 3 and 4 until the criterion meets the precision requirement. Finally, the fluid-structure coupling problem can be solved and the steady flow field around flexible nets is available.

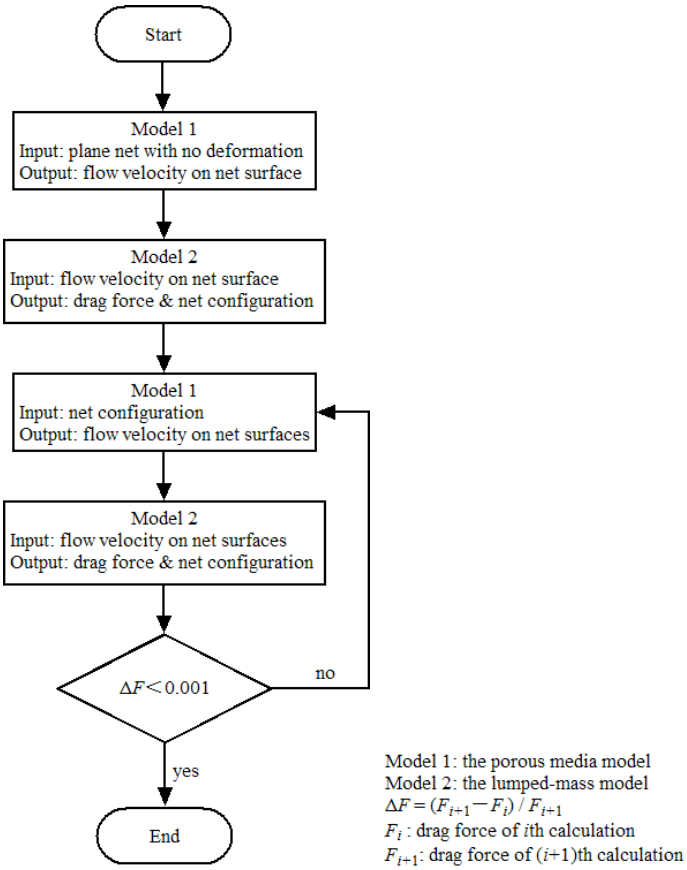


Figure 5: Flow chart for joint use of the porous media model and the lumped-mass model.

3 NUMERICAL SIMULATIONS OF THE INTERACTION BETWEEN FLOW AND FLEXIBLE NET

3.1 Laboratory setup

The tested net was a 0.3 m×0.3 m knotless polyethylene (PE) net with 15 meshes in width and 15 meshes in height. The twine diameter was 2.6 mm, and the mesh bar length was 20 mm. Mounted as square meshes, the net solidity ratio was 0.26. The flexible net, positioned from the water surface down, was centered on the width of the flume. A steel lower bar was mounted on the bottom of the net as sinker system. The diameter of the lower bar is 6 mm, and the mass is 73 g. Configuration of the flexible net was recorded using a CCD (Charge Coupled Device) camera at four different flow velocities, u_0=0.058, 0.113, 0.170 and 0.226 m/s. A load cell was attached to the top of the steel frame to measure the drag force on the flexible net. Meanwhile, flow velocities at three measurement points (see Figure 6) downstream from the flexible net were measured using an acoustic Doppler velocimeter (ADV).

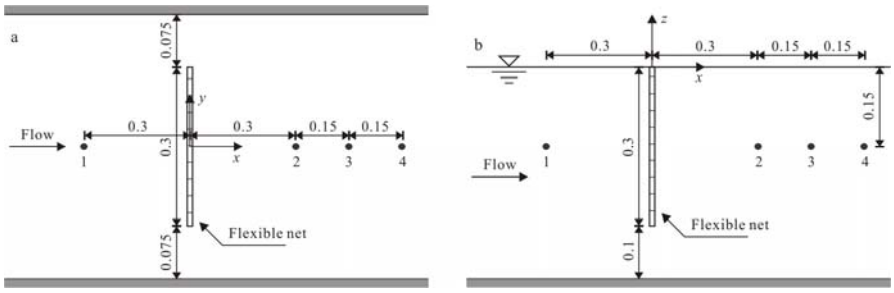


Figure 6: Physical model of a plane net and general setting of the measurement points (unit: m): (a) horizontal view and (b) vertical view.

3.2 Numerical model description

The three-dimensional numerical model was established according to the physical model. The characteristics of the fishing net are the same as in the physical model tests. The thickness of the porous media is 20 mm, and the porous coefficients, D_n=870,000 m^{-2}, D_t=153,500 m^{-2}, C_n=20.5 m^{-1}, and C_t=10.0 m^{-1}, can be obtained from the experimental data. The flexible net model is located 0.3 m downstream from the velocity-inlet boundary. The numerical simulations are performed with the incoming velocity u_0=0.226 m/s and u_0=0.170 m/s.

3.3 Results and discussion

The calculation precision and the equilibrium configuration of the flexible net can be obtained after the first iteration of Steps 3 and 4 in the numerical approach. In addition, the comparison of the equilibrium configuration of single flexible net between numerical simulation and physical model test presents a satisfactory result (see Figure 7).

The steady flow field around the flexible net is available according to the net configuration by dividing the net into several plane nets with different inclination angles. In the numerical results (see Figure 8), the streamlines present the flow direction around the flexible net. It was determined that the flow direction has no obvious diversion around the flexible net. That may be because the porosity of the net is quite large. As shown in the contour plots, there is a small region of flow velocity reduction upstream of the net, while there is a rather large velocity reduction region downstream from the net. As flow direction has no obvious diversion around the flexible net, the current reduction downstream from the net is mainly due to the shielding effect of the net. The width of the wake behind the net becomes narrower toward the centerline with increasing distance from the flexible net. The flow velocity increases at the flanks of the wake.

Comparisons of the flow velocity component u show that the flow velocity magnitude of the numerical simulation agrees well with the experimental data, and the maximum relative error is 1.9% (see Figure 9). Obvious flow velocity reduction of component u exists along the line through the net in the x direction. The maximum velocity reductions downstream from the single flexible net are 12.8% when u_0=0.226 m/s and 12.4% when u_0=0.170 m/s respectively according to our numerical results.

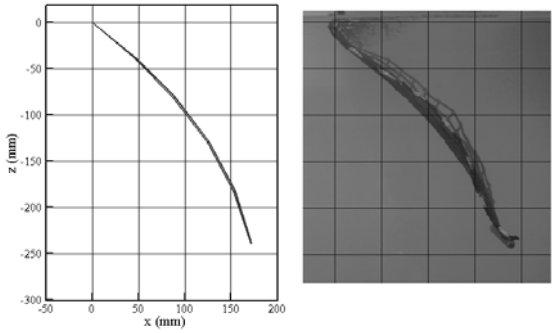


Figure 7: Comparison of the deformation of single flexible net between numerical simulation and physical model test when incoming velocity is 0.226 m/s.

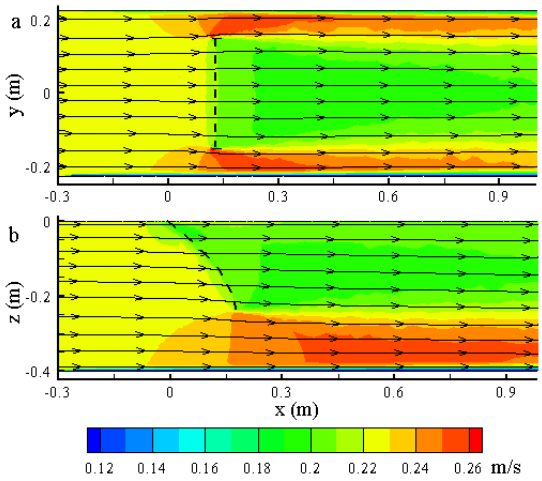


Figure 8: Flow velocity distribution around single flexible net calculated by numerical simulation when incoming velocity is 0.226 m/s: (a) contours on the horizontal plane z =−0.15 m and (b) contours on the vertical plane y =0.

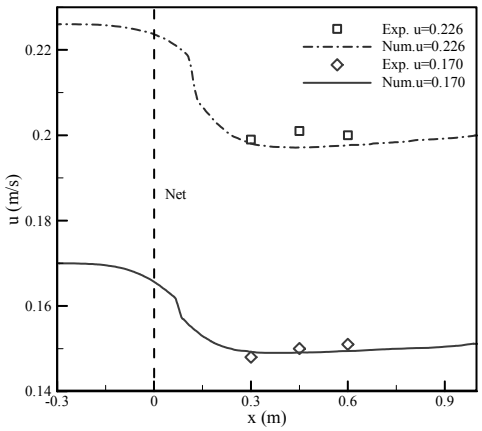


Figure 9: Comparisons of the flow velocity component u between numerical simulations and experimental data downstream from single flexible net.

4 CONCLUSIONS

- A numerical approach is proposed to simulate the interaction between flow and flexible nets based on the joint use of the porous media model and the lumped-mass model. Using an appropriate iterative scheme, the fluid-structure coupling problem can be solved and the steady flow field around flexible nets is available. The numerical results of the flexible net agree well with the experimental data. This study indicates that present numerical approach can simulate the interaction between flow and flexible net accurately.
- According to our numerical results, the diversion of flow direction around the flexible nets is relatively small. The maximum flow velocity reductions downstream from the single net are 12.8% and 12.4% respectively in two different currents.
- Present numerical approach is applicable to multiple flexible nets, and the number of iterations will not increase obviously. The incoming velocity is considered as the dominant factor for increasing the number of iterations.

ACKNOWLEDGEMENTS

This work was financially supported by the National Natural Science Foundation (NSFC) Project Nos.51239002, 51221961 and 51109187, the National 863 High Technology Project No.2006AA100301.

REFERENCES

[1] Aarsnes, J.V., Rudi, H. and Løland, G. Current forces on cage, net deflection. *In: Engineering for Offshore Fish Farming*. Thomas Telford, London, (1990) pp. 137–152.

[2] Fredriksson, D.W. *Open ocean fish cage and mooring system dynamics*. Ph.D. Dissertation, University of New Hampshire, Durham, NH, USA (2001).

[3] Lader, P.F., Enerhaug, B., Fredheim, A. and Krokstad, J. Modelling of 3D net structures exposed to wave and current. *In: 3rd International Conference on Hydroelasticity in Marine Technology* (2003) pp. 19-26.

[4] Li, Y.C., Chen, C.P., Li, C.L. and Mao, Y.C. A study on effectiveness of flow reducing by the net of gravity cage group. *Shipbuilding of China* (2005) **46**: 105-109. (in Chinese)

[5] Johansson, D., Juell, J.E., Oppedal, F., Stiansen, J.E. and Ruohonen, K. The influence of the pycnocline and cage resistance on current flow, oxygen flux and swimming behaviour of Atlantic salmon (Salmo salar L) in production cages. *Aquaculture*. (2007) **265**: 271-287.

[6] Harendza, A., Visscher, J., Gansel, L., Pettersen, B. PIV on inclined cylinder shaped fish cages in a current and the resulting flow field. *In: 27th International Conference on Offshore Mechanics and Arctic Engineering*, Estoril, Portugal, (2008) OMAE2008-57748.

[7] Patursson, Ø., Swift, M.R., Tsukrov, I., Simonsen, K., Baldwin, K., Fredriksson, D.W., Celikkol, B. Development of a porous media model with application to flow through and around a plane net. *Ocean Engineering* (2010) **37**: 314-324.

[8] Zhao, Y.P., Bi, C.W., Dong, G.H., Gui, F.K., Cui, Y., Xu, T.J. Numerical simulation of the flow field inside and around gravity cages. *Aquacultural Engineering* (2013) **52**: 1-13.

[9] Zhan, J.M., Jia, X.P., Li, Y.S., Sun, M.G., Guo, G.X. and Hu, Y.Z. Analytical and experimental investigation of drag on nets of fish cages. *Aquacultural Engineering* (2006) **35**: 91-101.

[10] Løland, G. *Current force on flow through fish farms*. Ph.D. Dissertation, Norwegian Institute of Technology, Trondheim, Norway (1991).

[11] Bear, J. *Dynamics of Fluids in Porous Media*. America Elsevier Publishing Company, Inc., New York (1972).

[12] Li, Y.C., Zhao, Y.P., Gui, F.K. and Teng, B. Numerical simulation of the hydrodynamic behaviour of submerged plane nets in current. *Ocean Engineering* (2006) **33**: 2352-2368.

[13] Zhao, Y.P., Li, Y.C., Gui, F.K. and Dong, G.H. Numerical simulation of the effects of weight system on the hydrodynamic behavior of 3-D net of gravity cage in current. *Journal of Hydrodynamics, Ser. B* (2007) **19**: 442-452.

[14] Choo, Y.I. and Casarella, M.J. Hydrodynamic resistance of towed cables. *Journal of Hydronautics* (1971) pp. 126–131.

[15] Fredheim, A. and Faltinsen, O.M. Hydroelastic anslysis of a Fishing net in steady inflow conditions. *In: Proceeding of 3rd International Conference on Hydroelasticity in Marine Technology*. University of Oxford, Oxford, Great Britain (2003).

V International Conference on Computational Methods in Marine Engineering
MARINE 2013
B. Brinkmann and P. Wriggers (Eds)

FAST SOLVERS FOR THERMAL FLUID STRUCTURE INTERACTION

PHILIPP BIRKEN*, TOBIAS GLEIM†, DETLEF KUHL† AND ANDREAS MEISTER*

*Institute of Mathematics
University of Kassel
Heinrich-Plett-Str. 40, 34132 Kassel, Germany
e-mail: {birken,meister}@mathematik.uni-kassel.de, web page:
http://www.mathematik.uni-kassel.de/

† Institute of Mechanics and Dynamics,
University of Kassel
Mönchebergstr. 7, 34109 Kassel, Germany
e-mail: {tgleim,kuhl}@uni-kassel.de - Web page: http://www.uni-kassel.de

Key words: Thermal Fluid Structure Interaction, Partitioned Coupling, Fixed Point methods, Vector Extrapolation

Abstract. We consider thermal fluid structure interaction to model industrial gas quenching in steel forging, where hot steel is cooled using cold high pressured gas. This allows to define properties of the finished steel part, as for example yield strength, locally at low cost and without environmental problems.

For the numerical simulation, a partitioned approach via a Dirichlet-Neumann coupling and a fixed point iteration is employed. In time, previously developed efficient time adaptive higher order time integration schemes are used. The respective models are the compressible Navier-Stokes equations and the nonlinear heat equation, where the parameter functions are obtained from measurements on a specific steel.

Here, the use of different vector extrapolation methods for convergence acceleration techniques of the fixed point iteration is analyzed. In particular, Aitken relaxation, minimal polynomial extrapolation (MPE) and reduced rank extrapolation (RRE) are considered.

1 INTRODUCTION

Thermal interaction between fluids and structures plays an important role in many applications. Examples for this are cooling of gas-turbine blades, thermal anti-icing systems of airplanes [3] or supersonic reentry of vehicles from space [12, 8]. Another is quenching,

an industrial heat treatment of metal workpieces. There, the desired material properties are achieved by rapid cooling, which causes solid phase changes, allowing to create graded materials with precisely defined properties.

Gas quenching recently received a lot of industrial and scientific interest [19, 7]. In contrast to liquid quenching, this process has the advantage of minimal environmental impact because of non-toxic quenching media and clean products like air [17]. Furthermore it is possible to control the cooling locally and temporally for best product properties and to minimize distortion by means of adapted jet fields, see [15].

To exploit the multiple advantages of gas quenching the application of computational fluid dynamics has proved essential [1, 17, 11]. Thus, we consider the coupling of the compressible Navier-Stokes equations as a model for air, along a non-moving boundary with the heat equation as a model for the temperature distribution in steel.

For the solution of a coupled problem, we use a partitioned approach [4], where different codes for the sub-problems are used and the coupling is done by a master program which calls interface functions of the other codes. This allows to use existing software for each sub-problem, in contrast to a monolithic approach, where a new code is tailored for the coupled equations. To satisfy the boundary conditions at the interface, the subsolvers are iterated in a fixed point procedure.

A fast solver is obtained by making use of a time adaptive higher order time integration method suggested in [2]. Namely, the singly diagonally implicit Runge-Kutta (SDIRK) method SDIRK2 is employed. Furthermore, it is imperative to reduce the number of fixed point iterations. Various methods have been proposed to increase the convergence speed of the fixed point iteration by decreasing the interface error between subsequent steps, for example Relaxation [10, 9], Interface-GMRES [13] or ROM-coupling [18]. Here, we consider Aitken Relaxation and two variants of polynomial vector extrapolation, namely MPE and RRE [16]. These are compared on the basis of the flow past a flat plate, basic test case for thermal fluid structure interaction.

2 GOVERNING EQUATIONS

The basic setting we are in is that on a domain $\Omega_1 \subset \mathbb{R}^d$ the physics is described by a fluid model, whereas on a domain $\Omega_2 \subset \mathbb{R}^d$, a different model describing a structure is used. The two domains are almost disjoint in that they are connected via an interface. The part of the interface where the fluid and the structure are supposed to interact is called the coupling interface $\Gamma \subset \partial\Omega_1 \cup \partial\Omega_2$. Note that Γ might be a true subset of the intersection, because the structure could be insulated. At the coupling interface Γ, coupling conditions are prescribed that model the interaction between fluid and structure. For the thermal coupling problem, these conditions are that temperature and the normal component of the heat flux are continuous across the interface.

We model the fluid using the Navier-Stokes equations, which are a second order system of conservation laws (mass, momentum, energy) modeling viscous compressible flow. We consider the two dimensional case, written in conservative variables density ρ, momentum

$\mathbf{m} = \rho\mathbf{v}$ and energy per unit volume ρE:

$$\begin{aligned} \partial_t \rho + \nabla \cdot \mathbf{m} &= 0, \\ \partial_t m_i + \sum_{j=1}^{2} \partial_{x_j}(m_i v_j + p\delta_{ij}) &= \frac{1}{Re}\sum_{j=1}^{2} \partial_{x_j} S_{ij}, \qquad i = 1, 2, \\ \partial_t(\rho E) + \nabla \cdot (H\mathbf{m}) &= \frac{1}{Re}\sum_{j=1}^{2} \partial_{x_j}\left(\sum_{i=1}^{2} S_{ij} v_i - \frac{1}{Pr} q_j\right). \end{aligned}$$

Here, $\mathbf{S}$ represents the viscous shear stress tensor and $\mathbf{q}$ the heat flux. As the equation are dimensionless, the Reynolds number Re and the Prandtl number Pr appear. The equations are closed by the equation of state for the pressure $p = (\gamma - 1)\rho e$. Additionally, we prescribe appropriate boundary conditions at the boundary of Ω_1 except for Γ.

Regarding the structure model, we will consider heat conduction only. For steel, we have temperature-dependent and highly nonlinear specific heat capacity c_p and heat conductivity λ. Thus, we have the nonlinear heat equation for the structure temperature $\Theta(\mathbf{x}, t)$

$$\rho(\mathbf{x}) c_p(\Theta) \frac{d}{dt}\Theta(\mathbf{x}, t) = -\nabla \cdot \mathbf{q}(\mathbf{x}, t), \tag{1}$$

where

$$\mathbf{q}(\mathbf{x}, t) = -\lambda(\Theta)\nabla\Theta(\mathbf{x}, t)$$

denotes the heat flux vector. Here, we use coefficient functions that have been suggested in [14] to model the steel 51CrV4 and are given by

$$\lambda(\Theta) = 40.1 + 0.05\Theta - 0.0001\Theta^2 + 4.9 \cdot 10^{-8}\Theta^3 \tag{2}$$

and

$$c_p(\Theta) = -10 \ln\left(\frac{e^{-c_{p1}(\Theta)/10} + e^{-c_{p2}(\Theta)/10}}{2}\right) \tag{3}$$

with

$$c_{p1}(\Theta) = 34.2 e^{0.0026\Theta} + 421.15 \tag{4}$$

and

$$c_{p2}(\Theta) = 956.5 e^{-0.012(\Theta - 900)} + 0.45\Theta. \tag{5}$$

For the mass density $\rho = 7836\ \mathrm{kg/m^3}$. Finally, on the boundary, we have Neumann conditions $\mathbf{q}(\mathbf{x}, t) \cdot \mathbf{n}(\mathbf{x}) = q_b(\mathbf{x}, t)$.

3 DISCRETIZATION

3.1 Discretization in space

Following the partitioned coupling approach, we discretize the two models separately in space. For the fluid, we use a finite volume method, leading to

$$\frac{d}{dt}\mathbf{u} + \underline{\mathbf{h}}(\mathbf{u}, \mathbf{\Theta}) = \mathbf{0}, \tag{6}$$

where $\underline{\mathbf{h}}(\mathbf{u}, \mathbf{\Theta})$ represents the spatial discretization and its dependence on the temperatures in the fluid. In particular, the DLR TAU-Code is employed [5], which is a cell-vertex-type finite volume method with AUSMDV as flux function and a linear reconstruction.

Regarding structural mechanics, the use of finite element methods is ubiquitious. Therefore, we will also follow that approach here and use quadratic finite elements, leading to the nonlinear equation for all unknowns on Ω_2

$$\mathbf{M}(\mathbf{\Theta})\frac{\mathbf{d}}{\mathbf{dt}}\mathbf{\Theta}(\mathbf{x}, \mathbf{t}) + \mathbf{K}(\mathbf{\Theta})\mathbf{\Theta}(\mathbf{x}, \mathbf{t}) = \mathbf{q_b}(\mathbf{x}, \mathbf{t}). \tag{7}$$

Here, $\mathbf{M}$ is the heat capacity and $\mathbf{K}$ the heat conductivity matrix. The vector $\mathbf{\Theta}$ consists of all discrete temperature unknowns and $\mathbf{q}_b(\mathbf{x}, t)$ is the heat flux vector on the surface. In this case it is the prescribed Neumann heat flux vector of the fluid.

3.2 Coupled time integration

If the fluid and the solid solver are able to carry out time steps of implicit Euler type, the master program of the FSI procedure can be extended to SDIRK methods very easily, since the master program just has to call the backward Euler routines with specific time step sizes and starting vectors.

Time adaptivity is obtained by using embedded methods as suggested in [2]. To this end, all stage derivatives are stored by the subsolvers. Then, the local error is estimated by the solvers separately, which then report the estimates back to the master program. Furthermore, if the possibility of rejected time steps is taken into account, the current solution pair $(\mathbf{u}, \mathbf{\Theta})$ has to be stored as well.

To comply with the condition that temperature and heat flux are continuous at the interface Γ, a so called Dirichlet-Neumann coupling is used. Namely, the boundary conditions for the two solvers are chosen such that we prescribe Neumann data for one solver and Dirichlet data for the other. Following the analysis of Giles [6], temperature is prescribed for the equation with smaller heat conductivity, here the fluid, and heat flux is given on Γ for the structure. Choosing the conditions the other way around leads to an unstable scheme.

In the following it is assumed that at time t_n, the step size Δt_n is prescribed. Applying a DIRK method to equation (6)-(7) results in the coupled system of equations to be solved at Runge-Kutta stage i:

$$\mathbf{F}(\mathbf{u}_i, \mathbf{\Theta}_i) := \mathbf{u}_i - \mathbf{s}_i^{\mathbf{u}} - \Delta t_n \, a_{ii} \underline{\mathbf{h}}(\mathbf{u}_i, \mathbf{\Theta}_i) = \mathbf{0}, \tag{8}$$

$$\mathbf{T}(\mathbf{u}_i, \mathbf{\Theta}_i) := [\mathbf{M} - \Delta t_n \, a_{ii} \mathbf{K}]\mathbf{\Theta}_i - \mathbf{M}\mathbf{s}_i^{\Theta} - \Delta t_n \, a_{ii} \bar{\mathbf{q}}(\mathbf{u}_i) = \mathbf{0}. \tag{9}$$

Here, $a_{ii} = 1 - \sqrt{2}/2$ is a coefficient of the time integration method and $\mathbf{s}_i^{\mathbf{u}}$ and $\mathbf{s}_i^{\Theta}$ are given vectors, called starting vectors, computed inside the DIRK scheme. The dependence of the fluid equations $\underline{\mathbf{h}}(\mathbf{u}_i, \mathbf{\Theta}_i)$ on the temperature $\mathbf{\Theta}_i$ results from the nodal temperatures of the structure at the interface. This subset is written as $\mathbf{\Theta}_i^{\Gamma}$. Accordingly, the structure equations depend only on the heat flux of the fluid at the coupling interface.

4 VECTOR EXTRAPOLATION

4.1 Basic fixed point iteration

To solve the coupled system of nonlinear equations (8)-(9), a strong coupling approach is employed. Thus, a nonlinear fixed point iteration is iterated until a convergence criterion is satisfied. In particular, we use a a nonlinear Gauß-Seidel process:

$$\mathbf{F}(\mathbf{u}_i^{(\nu+1)}, \mathbf{\Theta}_i^{(\nu)}) = \mathbf{0} \quad \rightsquigarrow \quad \mathbf{u}_i^{(\nu+1)} \tag{10}$$

$$\mathbf{T}(\mathbf{u}_i^{(\nu+1)}, \mathbf{\Theta}_i^{(\nu+1)}) = \mathbf{0} \quad \rightsquigarrow \quad \mathbf{\Theta}_i^{(\nu+1)}, \quad \nu = 0, 1, ... \tag{11}$$

Each solve is thereby done locally by the structure or the fluid solver. More specific, a Newton method is used in the structure and a FAS multigrid method is employed in the fluid.

The starting values of the iteration are given by $\mathbf{u}_i^{(0)} = \mathbf{s}_i^{\mathbf{u}}$ and $\mathbf{\Theta}_i^{(0)} = \mathbf{s}_i^{\Theta}$. The termination criterion is formulated by the nodal temperatures at the interface of the solid structure and we stop once we are below the tolerance in the time integration scheme divided by five.

$$\|\mathbf{\Theta}_i^{\Gamma\,(\nu+1)} - \mathbf{\Theta}_i^{\Gamma\,(\nu)}\| \leq TOL/5. \tag{12}$$

The vector

$$\mathbf{r}^{(\nu+1)} := \mathbf{\Theta}_i^{\Gamma\,(\nu+1)} - \mathbf{\Theta}_i^{\Gamma\,(\nu)} \tag{13}$$

is often referred to as the interface residual.

To improve the convergence speed of the fixed point iteration, different vector extrapolation techniques have been suggested. These are typically classic techniques, where a set of k vectors of a convergent vector sequence is extrapolated to obtain a faster converging sequence. We are now going to describe three techniques that we will test in this framework.

4.2 Aitken Relaxation

Relaxation means that after the fixed point iterate is computed, a relaxation step is added:

$$\tilde{\mathbf{\Theta}}_i^{\Gamma\,(\nu+1)} = \omega_{\nu+1}\mathbf{\Theta}_i^{\Gamma\,(\nu+1)} + (1-\omega_{\nu+1})\mathbf{\Theta}_i^{\Gamma\,(\nu)}. \tag{14}$$

Several strategies exist to compute the relaxation parameter ω.

The idea of Aitken's method is to enhance the current solution $\mathbf{\Theta}_i^{\Gamma\,(\nu+1)}$ using two previous iteration pairs $(\mathbf{\Theta}_i^{\Gamma\,(\nu+2)}, \mathbf{\Theta}_i^{\Gamma\,(\nu+1)})$ and $(\mathbf{\Theta}_i^{\Gamma\,(\nu+1)}, \mathbf{\Theta}_i^{\Gamma\,(\nu)})$ obtained from the Gauß-Seidel-Step (10)-(11). An improvement in the scalar case is given by the secant method

$$\tilde{\Theta}_i^{\Gamma\,(\nu+1)} = \frac{\Theta_i^{\Gamma\,(\nu-1)}\Theta_i^{\Gamma\,(\nu+1)} - \Theta_i^{\Gamma\,(\nu)}\Theta_i^{\Gamma\,(\nu)}}{\Theta_i^{\Gamma\,(\nu-1)} - \Theta_i^{\Gamma\,(\nu)} - \Theta_i^{\Gamma\,(\nu)} + \Theta_i^{\Gamma\,(\nu+1)}}. \tag{15}$$

The relaxation factor in equation (14) for the secant method (15) is then

$$\omega_{\nu+1} = \frac{\Theta_i^{\Gamma\,(\nu-1)} - \Theta_i^{\Gamma\,(\nu)}}{\Theta_i^{\Gamma\,(\nu-1)} - \Theta_i^{\Gamma\,(\nu)} - \Theta_i^{\Gamma\,(\nu)} + \Theta_i^{\Gamma\,(\nu+1)}}. \tag{16}$$

As customary, we use an added recursion on ω_i in which we use the old relaxation factor ω_ν:

$$\omega_{\nu+1} = -\omega_\nu \frac{r^{\Gamma\,(\nu)}}{r^{\Gamma\,(\nu+1)} - r^{\Gamma\,(\nu)}}. \tag{17}$$

In the vector case the division by residual $\mathbf{r}^{\Gamma\,(\nu+1)} - \mathbf{r}^{\Gamma\,(\nu)}$ is not possible. Therefore, we multiply nominator and numerator formally by $(\mathbf{r}^{\Gamma\,(\nu+1)} - \mathbf{r}^{\Gamma\,(\nu)})^T$ to obtain

$$\omega_{\nu+1} = -\omega_\nu \frac{(\mathbf{r}^{\Gamma\,(\nu)})^T(\mathbf{r}^{\Gamma\,(\nu+1)} - \mathbf{r}^{\Gamma\,(\nu)})}{\|\mathbf{r}^{\Gamma\,(\nu+1)} - \mathbf{r}^{\Gamma\,(\nu)}\|^2}. \tag{18}$$

Two previous steps are required to calculate the relaxation parameter. For the first fixpoint iteration, a relaxation parameter ν_1 is needed and therefore it must be prescribed.

4.3 Polynomial Vector Extrapolation

Another idea we will follow here are Minimal Polynomial Extrapolation (MPE) and Reduced Rank Extrapolation (RRE) [16]. Here, the new approximation is given as a linear combination of existing iterates with coefficients γ_ν to be determined:

$$\tilde{\mathbf{\Theta}}_i^{\Gamma\,(\nu+1)} = \sum_{j=0}^{\nu+1} \gamma_j \mathbf{\Theta}_i^{\Gamma\,j}. \tag{19}$$

For MPE, the coefficients are defined via

$$\gamma_j = \frac{c_j}{\sum_{i=0}^{\nu+1} c_i}, \quad j = 0, ..., \nu+1 \tag{20}$$

where the coefficients c_j are the solution of the problem

$$\min_{c_j} \left\| \sum_{j=0}^{\nu+1} c_j \mathbf{r}_j + \mathbf{r}_{\nu+1} \right\|_2. \tag{21}$$

For RRE, the coefficients are defined as the solution of the constrained least squares problem

$$\min_{\gamma_j} \left\| \sum_{j=0}^{\nu+1} \gamma_j \mathbf{r}_j \right\|_2, \quad \text{subject to} \sum_{j=0}^{\nu+1} \gamma_j = 1. \tag{22}$$

These problems are then solved using a QR decomposition.

5 NUMERICAL RESULTS

As a test case, the cooling of a flat plate resembling a simple work piece is considered. The work piece is initially at a much higher temperature than the fluid and then cooled by a constant air stream, see figure 1.

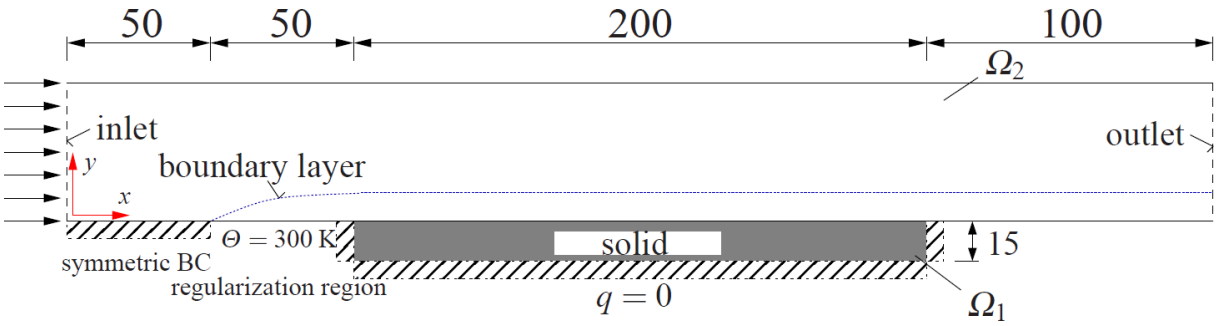
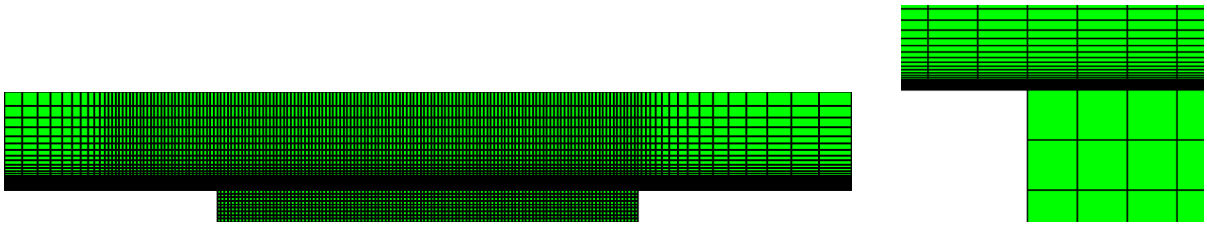


Figure 1: Test case for the coupling method

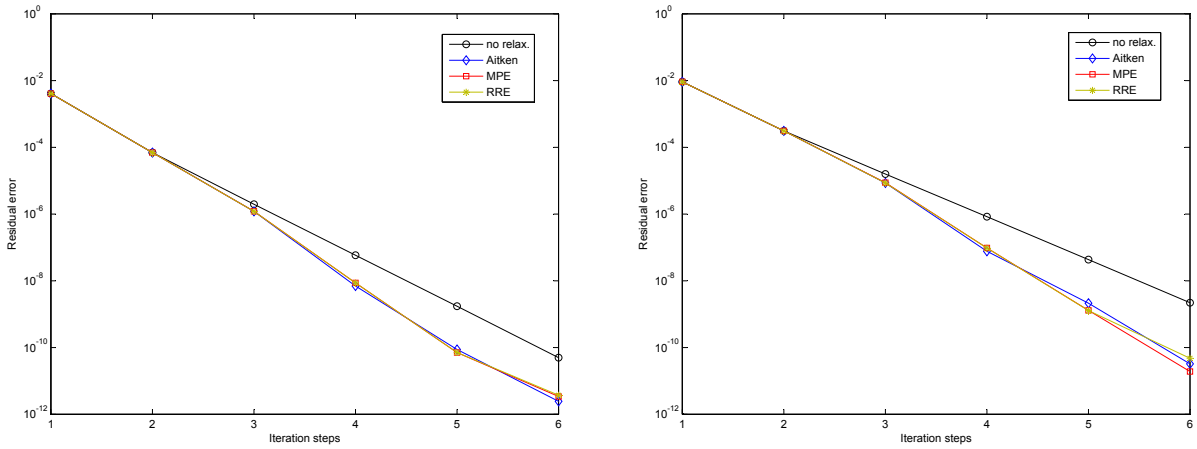
The inlet is given on the left, where air enters the domain with an initial velocity of $\mathrm{Ma}_\infty = 0.8$ in horizontal direction and a temperature of 273 K. Then, there are two succeeding regularization regions of 50 mm to obtain an unperturbed boundary layer. In the first region, $0 \leq x \leq 50$, symmetry boundary conditions, $v_y = 0$, $q = 0$, are applied. In the second region, $50 \leq x \leq 100$, a constant wall temperature of 300 K is specified. Within this region the velocity boundary layer fully develops. The third part is the solid (work piece) of length 200 mm, which exchanges heat with the fluid, but is assumed insulated otherwise, thus $q_b = 0$. Therefore, Neumann boundary conditions are applied throughout. Finally, the fluid domain is closed by a second regularization region of 100 mm with symmetry boundary conditions and the outlet.

Regarding the initial conditions in the structure, a constant temperature of 900 K at $t = 0$ s is chosen throughout. To specify reasonable initial conditions within the fluid, a steady state solution of the fluid with constant wall temperature $\Theta = 900$ K is computed.



(a) Entire mesh (b) Mesh zoom

Figure 2: Full grid (left) and zoom into coupling region (right)



(a) 1 time step with a time step size of 1 s (b) 1 time step with a time step size of 5 s

Figure 3: Comparison of the relaxation methods for 1 time step with different timestep sizes

The grid is chosen cartesian and equidistant in the structural part, where in the fluid region the thinnest cells are on the boundary and then become coarser in y-direction (see figure 2). To avoid additional difficulties from interpolation, the points of the primary fluid grid, where the heat flux is located in the fluid solver, and the nodes of the structural grid are chosen to match on the interface Γ.

To compare the effect of the different relaxation strategies on one fixed point iteration, we consider the first stage of the first time step in the test problem with a time step size of $\Delta t = 1$s and $\Delta t = 5$s. In figure 3, we can see how the interface residual decreases with the fixed point iterations. During the first two steps all methods have the same residual norm. This is because all methods need at least two iterations to start. For this example, the extrapolation methods outperform the standard scheme for target residual norms below 10^{-5}.

We now compare the different schemes for a whole simulation of 100 seconds real time when we choose different tolerances TOL. When we use a time adaptive algorithm, a total number of eight time steps is needed to solve the test case problem in 100 seconds.

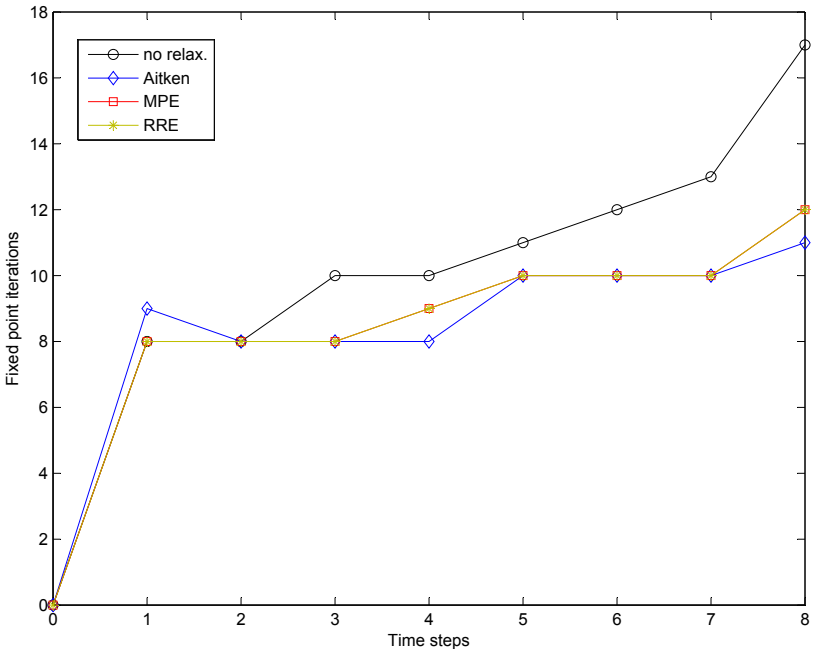


Figure 4: Number of fixed point iterations per time step

In figure 4, we see the number of fixed point iterations needed for each time step. The tolerance was chosen to be $TOL = 10^{-7}$. The dynamic relaxation methods needed a few less iterations. At the beginning of the time adaptive process, all of the methods started with the same time step size $\Delta t = 0.5$ s. With an increasing time and therefore an increasing time step size, caused by the adaptive algorithm, the normal (no relaxation) method needs more fixed point iterations in the end of that time interval, while the other methods have remained roughly constant. The total number of fixed point iterations is shown in tabular 1. As we can see, the extrapolation methods have an advantage over the normal (no relaxation) method for a tolerance of 10^{-7}. For $TOL = 10^{-4}$, all the methods need roughly the same number of iterations, which is also confirmed in Figure 3, where all methods overlap at 10^{-4}.

Table 1: Total number of iterations for 100 secs of real time

TOL		No relax.	Aitken	MPE	RRE
10^{-4}	#Iterations	53	48	50	50
10^{-7}	#Iterations	89	74	75	75

6 CONCLUSIONS

We considered a thermal fluid structure interaction problem where a nonlinear heat equation to model steel is coupled with the laminar compressible Navier-Stokes equations. The coupling is based on a Dirichlet-Neumann coupling. To obtain a fast solver, a higher order time adaptive method is used for time integration and different vector extrapolation techniques, namely Aitken Relaxation, MPE and RRE were compared for a test problem.

It turns out that for this simple problem, there is not much difference between the schemes for large tolerances, since the fixed point iteration terminates too quickly for the extrapolation schemes to make a difference. For tighter tolerances, the extrapolation schemes save 20% of iterations. Future work is on testing these schemes on more realistic examples.

REFERENCES

[1] A. L. Banka. Practical Applications of CFD in heat processing. *Heat Treating Progress*, (August), 2005.

[2] P. Birken, K. J. Quint, S. Hartmann, and A. Meister. A Time-Adaptive Fluid-Structure Interaction Method for Thermal Coupling. *Comp. Vis. in Science*, 13(7):331–340, 2011.

[3] J. M. Buchlin. Convective Heat Transfer and Infrared Thermography. *J. Appl. Fluid Mech.*, 3(1):55–62, 2010.

[4] C. Farhat. CFD-based Nonlinear Computational Aeroelasticity. In E. Stein, R. de Borst, and T. J. R. Hughes, editors, *Encyclopedia of Computational Mechanics*, volume 3: Fluids, chapter 13, pages 459–480. John Wiley & Sons, 2004.

[5] T. Gerhold, O. Friedrich, J. Evans, and M. Galle. Calculation of Complex Three-Dimensional Configurations Employing the DLR-TAU-Code. *AIAA Paper*, 97-0167, 1997.

[6] M. B. Giles. Stability Analysis of Numerical Interface Conditions in Fluid-Structure Thermal Analysis. *Int. J. Num. Meth. in Fluids*, 25:421–436, 1997.

[7] U. Heck, U. Fritsching, and K. Bauckhage. Fluid flow and heat transfer in gas jet quenching of a cylinder. *International Journal of Numerical Methods for Heat & Fluid Flow*, 11:36–49, 2001.

[8] M. Hinderks and R. Radespiel. Investigation of Hypersonic Gap Flow of a Reentry Nosecap with Consideration of Fluid Structure Interaction. *AIAA Paper*, 06-1111, 2006.

[9] U. Küttler and W. A. Wall. Fixed-point fluidstructure interaction solvers with dynamic relaxation. *Comput. Mech.*, 43:61–72, 2008.

[10] P. Le Tallec and J. Mouro. Fluid structure interaction with large structural displacements. *Comp. Meth. Appl. Mech. Engrg.*, 190:3039–3067, 2001.

[11] N. Lior. The cooling process in gas quenching. *J. Materials Processing Technology*, 155-156:1881–1888, 2004.

[12] R. C. Mehta. Numerical Computation of Heat Transfer on Reentry Capsules at Mach 5. *AIAA-Paper 2005-178*, 2005.

[13] C. Michler, E. H. van Brummelen, and R. de Borst. Error-amplification Analysis of Subiteration-Preconditioned GMRES for Fluid-Structure Interaction. *Comp. Meth. Appl. Mech. Eng.*, 195:2124–2148, 2006.

[14] K. J. Quint, S. Hartmann, S. Rothe, N. Saba, and K. Steinhoff. Experimental validation of high-order time integration for non-linear heat transfer problems. *Comput. Mech.*, 48(1):81–96, 2011.

[15] S. Schüttenberg, M. Hunkel, U. Fritsching, and H.-W. Zoch. Controlling of Distortion by means of Quenching in adapted Jet Fields. *Materialwissenschaft und Werkstofftechnik*, 37(1):92–96, 2006.

[16] A. Sidi. Review of two vector extrapolation methods of polynomial type with applications to large-scale problems. *J. Comp. Phys.*, 3(3):92–101, 2012.

[17] P. Stratton, I. Shedletsky, and M. Lee. Gas Quenching with Helium. *Solid State Phenomena*, 118:221–226, 2006.

[18] J. Vierendeels, L. Lanoye, J. Degroote, and P. Verdonck. Implicit Coupling of Partitioned Fluid-Structure Interaction Problems with Reduced Order Models. *Comp. & Struct.*, 85:970–976, 2007.

[19] U. Weidig, N. Saba, and K. Steinhoff. Massivumformprodukte mit funktional gradierten Eigenschaften durch eine differenzielle thermo-mechanische Prozessführung. *WT-Online*, pages 745–752, 2007.

V International Conference on Computational Methods in Marine Engineering
MARINE 2013
B. Brinkmann and P. Wriggers (Eds)

NUMERICAL SIMULATION OF HYDROACOUSTIC FLUID-SHIP INTERACTION BY FAST BEM & FEM COUPLING

Lothar Gaul, Dominik Brunner

Institute of Applied and Experimental Mechanics
University of Stuttgart
Pfaffenwaldring 9, 70550 Stuttgart, Germany
e-mail: gaul@iam.uni-stuttgart.de, web page: http://www.iam.uni-stuttgart.de

Key words: Fluid-Structure Interaction, Boundary Element Method, Fast Multipole Method, Halfspace Formulation

Abstract. The vibration behavior of ships is noticeably influenced by the surrounding water, which represents a fluid of high density. In this case, the feedback of the fluid pressure onto the structure cannot be neglected and a strong coupling scheme between the fluid domain and the structural domain is necessary. In this work, fast boundary element methods are used to model the semi-infinite fluid domain with the free water surface. Two approaches are compared: A symmetric mixed formulation is applied where a part of the water surface is discretized. The second approach is a formulation with a special half-space fundamental solution, which allows the exact representation of the Dirichlet boundary condition on the free water surface without its discretization. Furthermore, the influence of the compressibility of the water is investigated by comparing the solutions of the Helmholtz and the Laplace equation. The ship itself is modeled with the finite element method. A binary interface to the commercial finite element package ANSYS is used to import the mass matrix and the stiffness matrix. The coupled problems are formulated using Schur complements. To solve the resulting system of equations, a combination of a direct solver for the finite element matrix and a preconditioned GMRES for the overall Schur complement is chosen. The applicability of the approach is demonstrated using a realistic model problem.

Nomenclature

Ω_s, Ω_a	structural domain, acoustic domain	V, D	single layer potential, hypersingular operator
Γ_s, Γ_I	structural boundary, coupling interface	K, K'	double layer potential and its adjoint
Γ_H	half-space boundary	$\boldsymbol{K}^\mathrm{m}_\mathrm{BE}$, $\boldsymbol{C}^\mathrm{m}_\mathrm{BE}$	Galerkin matrices of mixed formulation
t_s, t_f	tractions on Γ_s and Γ_I	$\boldsymbol{K}^\mathrm{h}_\mathrm{BE}$, $\boldsymbol{C}^\mathrm{h}_\mathrm{BE}$	Galerkin matrices of half-space formulation
ϱ_s, λ, μ	structural density, Lamé constants	$\boldsymbol{K}_\mathrm{FE}$	dynamic stiffness matrix
n	unit normal direction of the fluid domain	$\boldsymbol{C}_\mathrm{FE}$	coupling matrix
u	structural displacements	$\boldsymbol{T}_\mathrm{q}$	transformation matrix
c_f, ϱ_f	speed of sound and density of the fluid	$\boldsymbol{S}$	Schur complement
p, q	acoustic pressure and flux	c_d	near-field parameter
$\bar{p}$, $\bar{q}$	prescribed pressure and flux	c_e	expansion length parameter
$\tilde{p}$, $\tilde{q}$	unknown pressure and flux	L	expansion length
f	excitation frequency	$h_l^{(1)}$	Hankel functions
ω, κ	wave number, circular wave number	P_l	Legendre polynomials
$P(x,y)$	fundamental solution	s	far-field direction
$P^*(x,y)$	half-space fundamental solution	D	distance vector between clusters

1 INTRODUCTION

Fluid–structure interaction deals with the mutual influence of an acoustic and a structural domain. If air is assumed as acoustic fluid, the influence of the surrounding fluid on the vibration behavior of the structure can usually be neglected. In contrast, this is typically not the case if the fluid is water. Due to its high density, the feedback of the acoustic pressure onto the structure has to be taken into account [5]. As a consequence fully coupled simulation schemes have to be applied which are computationally more expensive, since a structural problem and an acoustic problem have to be solved simultaneously.

For geometrically simple structures, analytical solutions exist [11]. Typically, the structure of engineering problems are more complex so that numerical schemes have to be used. The finite element method (FEM) is usually applied for the structural part [17]. For exterior acoustic fluid domains, the application of the boundary element method (BEM) is advantageous, since the Sommerfeld radiation condition is automatically fulfilled [16]. There are fast methods to overcome the drawback of the fully populated matrices like the fast multipole method (FMM) [13, 9] and $\mathcal{H}$-matrices [12]. With these fast methods it is possible to solve large scale problems in acoustics with some thousand degrees of freedom [6, 8]. If ship-like structures are considered, the water surface has to be incorporated. One possibility is to apply a mixed formulation [15] where only a finite part of the water surface in the vicinity of the ship is discretized. Alternatively, a half-space fundamental solution can be applied, which exactly fulfills the boundary condition on the water surface [14]. In this case, only the ship-hull needs to be discretized. There are various formulations for the coupling of the FEM and BEM [6, 10, 1]. Recently, fast BEM approaches were coupled with the FEM [6, 2], allowing the simulation of large–scale

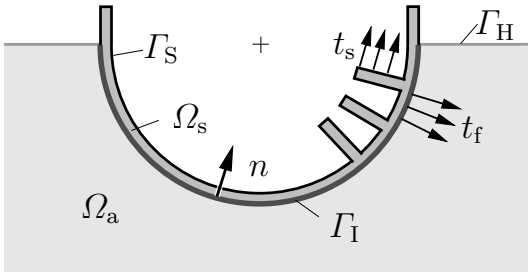


Figure 1: The coupled problem consists of a structural domain Ω_{s} and an acoustic domain Ω_{a}. The two domains are in contact to each other on the fluid-structure interface Γ_{I}. The water surface Γ_{H} is modeled with zero pressure boundary conditions.

coupled problems.

This paper starts with the governing equations of the coupled problem and presents two different formulations for the BEM. After this, the fast multipole method is introduced to accelerate the computations. A FEM representation for the structural part is discussed and a strong coupling scheme is presented. The different approaches are used to examine a realistic model problem. At the end the influence of the compressibility is investigated by comparing the results of the Helmholtz equation with the ones of the Laplace equation.

2 GOVERNING EQUATIONS OF THE COUPLED PROBLEM

In the following, the governing equations for the fluid-structure interaction problem are presented for the time harmonic case with the behavior $\mathrm{e}^{-\mathrm{i}\omega t}$. The wavenumber is denoted by $\omega = 2\,\pi\,f$, where f is the excitation frequency. The structural domain Ω_{s} (cf. Fig. 1) is assumed be linear elastic with the Lamé constants λ and μ. The material is homogeneous with the structural density ϱ_{s}. The corresponding elastodynamic problem for the displacements u is given by

$$\omega^2 \varrho_{\mathrm{s}}\, u(x) + \mu \Delta u(x) + (\lambda + \mu)\,\mathrm{grad}\,\mathrm{div}\, u(x) = 0 \qquad \text{for } x \in \Omega_{\mathrm{s}} \subset \mathbb{R}^3\,, \tag{1}$$

$$T\, u(x) = t_{\mathrm{s}} \qquad \text{for } x \in \Gamma_{\mathrm{s}}\,, \tag{2}$$

and by an additional transmission condition which is introduced later by (6). The Laplacian is denoted by Δ and T represents the traction operator. The structure is excited by the prescribed tractions t_{s}. The acoustic pressure p in the fluid domain Ω_{a} is either described by the time harmonic Helmholtz equation in case of a compressible fluid or by the Laplace equation in case of an incompressible fluid. Since the latter case is obtained by setting the speed of sound $c_{\mathrm{f}} \to \infty$, the derivations are only done for the more general case of the Helmholtz equation. In this paper, a partly immersed structure is investigated where the free fluid surface Γ_{H} is modeled by a Dirichlet boundary condition. The acoustic

boundary value problem has the form

$$\begin{aligned} \Delta p(x) + \kappa^2\, p(x) &= 0 \qquad \text{for } x \in \Omega_{\mathrm{a}}, && (3)\\ p(x) &= 0 \qquad \text{for } x \in \Gamma_{\mathrm{H}}\,, && (4)\\ \left| \frac{\partial p}{\partial R} - \mathrm{i}\,\kappa\, p \right| &< \frac{c_{\mathrm{f}}}{R^2} \qquad \text{for } R = |x| \to \infty\,, && (5) \end{aligned}$$

and an additional transmission condition which is presented later by (7). The circular wavenumber is denoted by $\kappa = \omega/c$. Equation (5) is called Sommerfeld radiation condition, which ensures an outgoing wave within the exterior acoustic domain [7]. Since a fluid with a high density is used, the feedback of the pressure onto the structure is not negligible. Therefore, a strong coupling scheme has to be applied, which is represented by the two transmission conditions

$$\begin{aligned} T\,u(x) &= t_{\mathrm{f}}(x) = -p(x)\,n_x \qquad \text{for } x \in \Gamma_{\mathrm{I}}, && (6)\\ q(x) &:= \frac{\partial p(x)}{\partial n_x} = \omega^2 \varrho_{\mathrm{f}} u(x)\,n_x \qquad \text{for } x \in \Gamma_{\mathrm{I}}\,, && (7) \end{aligned}$$

where the acoustic flux q is introduced. In the next two sections, the mixed BEM formulation and the half-space BEM approach are outlined.

3 MIXED BEM FORMULATION FOR THE ACOUSTIC DOMAIN

One possibility to model the acoustic problem of partly immersed structures is to discretize the water surface in the vicinity close to the structure. On the boundary Γ_{H}, the Dirichlet data vanish, i.e. $p = 0$ holds. Starting point are the boundary integral and the hypersingular boundary integral equation [12]

$$\begin{aligned} \frac{1}{2}\,p(x) &= \underbrace{\int_\Gamma P(x,y)\,q(y)\,\mathrm{d}s_y}_{(Vq)(x)} - \underbrace{\int_\Gamma \frac{\partial P(x,y)}{\partial n_y}\,p(y)\,\mathrm{d}s_y}_{(Kp)(x)}\,, \quad x \in \Gamma && (8)\\ \frac{1}{2}\,q(x) &= \underbrace{\int_\Gamma \frac{\partial P(x,y)}{\partial n_x}\,q(y)\,\mathrm{d}s_y}_{(K'q)(x)} - \underbrace{\int_\Gamma \frac{\partial^2 P(x,y)}{\partial n_x\,\partial n_y}\,p(y)\,\mathrm{d}s_y}_{-(Dp)(x)}\,, \quad x \in \Gamma && (9) \end{aligned}$$

which are valid for a general smooth boundary Γ. The single layer potential is denoted by V, K and K' are the double layer potential and its adjoint and D is the hypersingular operator. The free-space fundamental solution is denoted by

$$P(x,y) = \frac{\mathrm{e}^{\mathrm{i}\kappa|x-y|}}{4\pi|x-y|}\,. \qquad (10)$$

The pressure and flux are decomposed in a prescribed part ($\bar{\cdot}$) and an unknown part ($\tilde{\cdot}$)

$$p(x) = \tilde{p}(x) + \bar{p}(x) \quad , \quad q(x) = \tilde{q}(x) + \bar{q}(x)$$
$$\text{with} \begin{cases} \tilde{p}(x) = \bar{q}(x) = 0 & x \in \Gamma_{\mathrm{H}} \,, \\ \bar{p}(x) = \tilde{q}(x) = 0 & x \in \Gamma_{\mathrm{I}} \,. \end{cases} \tag{11}$$

Plugging (11) into (8) and weighting with constant functions ν^q on Γ_{H} yields

$$\begin{aligned} -\int_{\Gamma_{\mathrm{H}}} \nu^q(x) \left(V_{\mathrm{H}} \tilde{q}\right)(x) \,\mathrm{d}s_x \;+\; \int_{\Gamma_{\mathrm{H}}} \nu^q(x) \left(K_{\mathrm{I}} \tilde{p}\right)(x) \,\mathrm{d}s_x = \\ \int_{\Gamma_{\mathrm{H}}} \nu^q(x) \left(V_{\mathrm{I}} \bar{q}\right)(x) \,\mathrm{d}s_x \;-\; \int_{\Gamma_{\mathrm{H}}} \frac{1}{2} \nu^q(x)\, \bar{p}(x) \mathrm{d}s_x - \int_{\Gamma_{\mathrm{H}}} \nu^q(x) \left(K_{\mathrm{H}} \bar{p}\right)(x) \,\mathrm{d}s_x \,, \end{aligned} \tag{12}$$

where the subscript of the inner operator – H or I – represents the corresponding domain Γ_{H} and Γ_{I}. The same procedure is done on Γ_{I} for the hypersingular boundary integral equation (9) using linear functions ν^p for weighting

$$\begin{aligned} -\int_{\Gamma_{\mathrm{I}}} \nu^p(x) \left(K'_{\mathrm{H}} \tilde{q}\right)(x) \,\mathrm{d}s_x \;-\; \int_{\Gamma_{\mathrm{I}}} \nu^p(x) \left(D_{\mathrm{I}} \tilde{p}\right)(x) \,\mathrm{d}s_x = \\ \int_{\Gamma_{\mathrm{I}}} \nu^p(x) \left(K'_{\mathrm{I}} \bar{q}\right)(x) \,\mathrm{d}s_x \;-\; \int_{\Gamma_{\mathrm{I}}} \frac{1}{2} \nu^p(x)\, \bar{q}(x) \mathrm{d}s_x + \int_{\Gamma_{\mathrm{I}}} \nu^p(x) \left(D_{\mathrm{H}} \bar{p}\right)(x) \,\mathrm{d}s_x \,. \end{aligned} \tag{13}$$

Introducing a triangulation with piecewise linear shape functions for p and constant ones for q yields the system of equations

$$\underbrace{\begin{pmatrix} \boldsymbol{V}_{\mathrm{HH}} & -\boldsymbol{K}_{\mathrm{HI}} \\ \boldsymbol{K}'_{\mathrm{IH}} & \boldsymbol{D}_{\mathrm{II}} \end{pmatrix}}_{\boldsymbol{K}^{\mathrm{m}}_{\mathrm{BE}}} \begin{pmatrix} \tilde{\boldsymbol{q}} \\ \tilde{\boldsymbol{p}} \end{pmatrix} = \underbrace{\begin{pmatrix} -\boldsymbol{V}_{\mathrm{HI}} \\ \frac{1}{2}\boldsymbol{M}_{\mathrm{I}} - \boldsymbol{K}'_{\mathrm{II}} \end{pmatrix}}_{-\boldsymbol{C}^{\mathrm{m}}_{\mathrm{BE}}} \bar{\boldsymbol{q}} \,, \tag{14}$$

where the boundary condition $\bar{p} = 0$ has already been taken into account. Since not the whole infinity water surface can be discretized, it is desirable to have an formulation where the boundary condition on the water surface is included automatically. This can be achieved using a half-space fundamental solution as outlined in the next section.

4 HALF-SPACE BEM FORMULATION FOR THE ACOUSTIC DOMAIN

As pointed out in [3], the fluid domain which is bounded by the flat water surface can be seen as semi-infinite half-space. For such a problem, the use of the special half-space fundamental solution

$$P^*(x,y) = \frac{1}{4\,\pi} \frac{\mathrm{e}^{\mathrm{i}\,\kappa\,|x-y|}}{|x-y|} - \frac{1}{4\,\pi} \frac{\mathrm{e}^{\mathrm{i}\,\kappa\,|\tilde{x}-y|}}{|\tilde{x}-y|} \tag{15}$$

is advantageous, where x is mirrored on the half-space plane to obtain $\tilde{x}$. If $P^*(x,y)$ is plugged into (8) and (9) it can be shown, that the integrals over the water surface vanish

exactly. Thus, the boundary integral equations (8) and (9) are applicable in the same way but this time $P^*(x,y)$ is used instead of $P(x,y)$ and only Γ_I has to be considered [3]. To obtain a Galerkin formulation, both boundary integral equations are weighted with linear functions ν. Again a triangulation with piecewise linear shape functions for p and constant ones for q are applied, leading to

$$\left(\frac{1}{2}\boldsymbol{M}+\boldsymbol{K}\right)\boldsymbol{p}=\boldsymbol{V}\,\bar{\boldsymbol{q}} \qquad \text{and} \qquad -\boldsymbol{D}\,\boldsymbol{p}=\left(-\frac{1}{2}\boldsymbol{M}'+\boldsymbol{K}'\right)\bar{\boldsymbol{q}}\,, \tag{16}$$

where the matrices correspond to the operators introduced in (8) and (9), but this time with the fundamental solution $P^*(x,y)$. For exterior acoustic problems, spurious modes may occur. There are several possibilities to overcome this phenomenon. A widely applied strategy is to use a linear combination of the boundary integral equations (16) with a coupling constant α

$$\underbrace{\left(\frac{1}{2}\boldsymbol{M}+\boldsymbol{K}-\alpha\boldsymbol{D}\right)}_{\boldsymbol{K}^h_\mathrm{BE}}\boldsymbol{p}=\underbrace{\left(\boldsymbol{V}-\frac{1}{2}\alpha\boldsymbol{M}'+\alpha\boldsymbol{K}'\right)}_{-\boldsymbol{C}^h_\mathrm{BE}}\bar{\boldsymbol{q}}\,, \tag{17}$$

which is known as the Burton-Miller approach. A parameter $\alpha = {}^{-i}\!/_{\kappa}$ turns out to be stable and advantageous concerning the condition number. On possibility to implement the half-space fundamental solution is to mirror the elements and nodes at the water plane and call the standard integration routines for a combination of y with the non-mirrored point x and a second time for y with the mirrored point $\tilde{x}$. The result of the second integration simply has to be subtracted from the first one and inserted into the global matrices. Besides the additional memory consumption for storing the mirrored elements and nodes, no further increase of the storage requirements occur, since the size of $\boldsymbol{K}^h_\mathrm{BE}$ and $\boldsymbol{C}^h_\mathrm{BE}$ is not altered. However, for classical BE methods, these matrices are still fully populated. In order to overcome this drawback, the fast multipole method (FMM) is applied. The mirror-technique turns out to be advantageous for the FMM implementation, since the standard expansion can be applied.

5 FAST MULTIPOLE IMPLEMENTATION

For the introduced operators, one typically has to evaluate potentials of the type

$$\Phi(x_b)=\sum_{a=1}^{A}\frac{\mathrm{e}^{\mathrm{i}\kappa|x_b-y_a|}}{|x_b-y_a|}q_a, \tag{18}$$

where q_a denotes the source strengths of A sources. Standard BE methods typically consider the interaction of every combination of a load point with a field point. In contrast to this, the multipole algorithm sets up a clustering and sums up the contribution of all sources q_a in the center z_a of a cluster (see Fig. 2 left). At the next step, this so–called

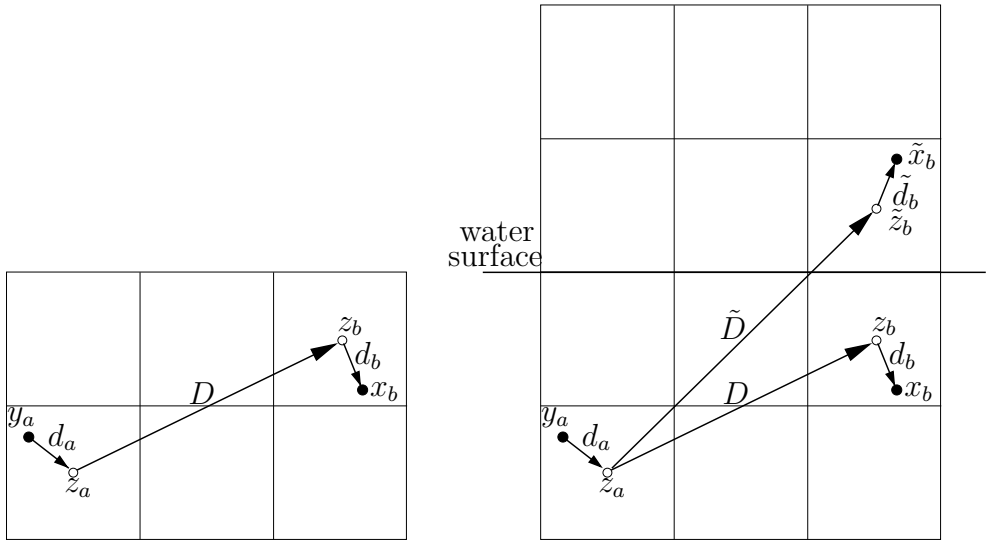


Figure 2: Clustering and splitting up of the vector between load point and field point into three parts for the symmetric formulation left (left) and the half-space formulation with geometrical mirroring (right).

far–field signature is translated to the center z_b of the other clusters and from there finally distributed to x_b.

From a mathematical point of view, the separation of the distance $|x_b - y_a|$ in the fundamental solution succeeds by using the diagonal form of the multipole expansion [13]

$$\frac{\mathrm{e}^{\mathrm{i}\kappa|x_b-y_a|}}{|x_b-y_a|} = \frac{\mathrm{i}\kappa}{4\,\pi}\sum_{l=0}^{\infty}(2l+1)\,\mathrm{i}^l h_l^{(1)}\left(\kappa|D|\right)\int_{\mathbb{S}^2}\mathrm{e}^{\mathrm{i}\kappa(d_a+d_b)\cdot s}P_l\left(s\cdot\hat{D}\right)\,\mathrm{d}s\,, \tag{19}$$

with the Hankel functions h_l and the Legendre polynomials P_l. The vectors which are local to the clusters are denoted by d_a and d_b (see Fig. 2), whereas D is defined by the centers of two interacting clusters. The unit distance vector is defined by $\hat{D} = {}^{D}\!/_{|D|}$. The integral over the unit sphere $\mathbb{S}^2$ is approximated by Gauss point quadrature using discrete values of the the far–field directions s [13]. Since one can not compute an infinite sum, the series has to be truncated. In this case the integration over the unit sphere $\mathbb{S}^2$ and the summation can be interchanged. Introducing the translation operator

$$M_L(s,D) = \sum_{\ell=0}^{L}(2\ell+1)\mathrm{i}^\ell h_\ell^{(1)}(\kappa|D|)P_\ell(s\cdot\hat{D})\,, \tag{20}$$

the original potential (18) can now be expressed in the form

$$\Phi(x_b) \approx \frac{\mathrm{i}\kappa}{4\pi}\int_{\mathbb{S}^2}\mathrm{e}^{\mathrm{i}\kappa\,d_b\cdot s}M_L(s,D)\underbrace{\sum_{a=1}^{A}\mathrm{e}^{\mathrm{i}\kappa\,d_a\cdot s}q_a}_{F(s)}\,\mathrm{d}s. \tag{21}$$

The choice of L in (20), which is called the *expansion length*, has a significant influence on the accuracy and the performance of the multipole algorithm. Proper choice helps to circumvent divergence of the series and will be discussed later in this section. The sum on the right hand of (21) is called the *far–field signature* $F(s)$. It is local to the cluster with the sources q_a, since only the vector d_a appears. In contrast to this, the translation operator M_L only depends on the vector D between two clusters' centers. Thus, if a regular cluster grid is used, the translation operators can be reused. Translating the far–field signature to another cluster using a translation operator forms the so called *near-field signature*. The solution is finally recovered by an exponential function of d_b and an integration over the unit sphere.

Since the multipole expansion is only valid for well separated load and field points, one has to split up the clusters into a near–field and far–field. All clusters which fulfill the condition

$$|D| < c_d \frac{d}{2} \tag{22}$$

form the near–field. Here, d denotes the cluster diameter and c_d is a constant. The arising near–field is represented by a sparse matrix. It has to be evaluated by classical BEM. All other clusters are in the far–field and form the so called *interaction list*.

To obtain an optimal efficiency, a hierarchical multilevel cluster tree is used. It is set up by consecutive bisectioning such that a mother cluster is divided into two son clusters on the next level. The procedure starts with the *root cluster*, which is the smallest parallelepiped containing all elements of the model. The division is stopped if a specified number of elements per cluster is reached. These final clusters, which do not have any sons, are called *leaf clusters*. The interaction list of every cluster is formed by those clusters, which are in the near-field of the *mother cluster* but not in its own near–field.

Obviously, the far–field signature has to be translated to the interaction lists on different levels. Since the cluster diameters are different on every level, the expansion length L has to be adapted to every level, too. Typically the well–established semi–empirical rule

$$L\left(\kappa\, d_\ell\right) = \kappa d_\ell + c_\mathrm{e} \log\left(\kappa\, d_\ell + \pi\right) \tag{23}$$

is used to estimate the number of series terms on level ℓ of the cluster tree [4]. The parameter c_e has to be chosen by the user and determines the desired accuracy. In order to maintain the accuracy of the multipole expansion when the cluster diameter increases on the next level, an interpolation and filtering strategy has to be applied. It is advantageous to use a fast Fourier transform for this purpose. This is because new far–field directions have to be added, which is only possible for the original form of the multipole expansion [9, 6]. The resulting *fast multipole method* (FMM) has a quasi linear complexity of order $\mathcal{O}(N \log^2 N)$ as outlined in [6].

The evaluation of the matrix-vector product for the symmetric formulation with the FMM algorithm is similar for all operators which are needed for the coupling formulations. Only slight modifications are necessary in order to take into account the different test and shape functions. The general procedure can be summarized with the following steps:

1. Compute the near-field part by a sparse matrix–vector multiplication.
2. Evaluate the far-field signature $F(s)$ for every leaf cluster.
3. Translate the far-field signature to all interaction cluster by means of the translation operators (Eq. 20) and sum it up as the near–field signature $N(s)$ there.
4. Shift the far-field signature to the mother cluster and repeat step 3 until the interaction list is empty.
5. Go the opposite direction and shift the near-field signature $N(s)$ to the son clusters until the leaf clusters are reached.
6. Recover the solution by integration over the unit sphere.

In case of the half-space problem, modifications are necessary for the near-field and the far-field [3]. The near-field also has to include the interaction to mirrored-clusters, which fulfill the near-field condition with a non-mirrored cluster. The multipole cycle is similar to the one of the symmetric formulation, however in step 3, the far-field signatures $F(s)$ also have to be translated to the mirrored clusters as depicted in Fig. 2 (right). In step 5, the shifting procedure also has to be done for the mirrored clusters. In step 6, the solution additionally needs to be recovered for the mirrored clusters and subtracted from the solution of the corresponding non-mirrored clusters. For a discussion of the computation time, the interesting reader is referred to [3].

6 COUPLED APPROACH

The structural problem given by (1) and (2) is discretized using the finite element method resulting in a system of linear equations

$$\underbrace{\left(-\omega^2 \boldsymbol{M}_{\mathrm{s}} - \mathrm{i}\omega \boldsymbol{D}_{\mathrm{s}} + \boldsymbol{K}_{\mathrm{s}}\right)}_{\boldsymbol{K}_{\mathrm{FE}}} \boldsymbol{u} = \boldsymbol{f}_{\mathrm{s}} + \boldsymbol{f}_{\mathrm{f}} \,, \tag{24}$$

where $\boldsymbol{M}_{\mathrm{s}}$ and $\boldsymbol{K}_{\mathrm{s}}$ denote the mass matrix and the stiffness matrix, respectively. In this paper, stiffness proportional damping is considered with the damping matrix

$$\boldsymbol{D}_{\mathrm{s}} = k_d \, \boldsymbol{K}_{\mathrm{s}} \,, \tag{25}$$

where k_d denotes a damping parameter. Vector $\boldsymbol{f}_{\mathrm{s}}$ incorporates the tractions t_{s} due to the driving forces. The finite element package ANSYS is utilized to set up the matrices $\boldsymbol{M}_{\mathrm{s}}$, $\boldsymbol{K}_{\mathrm{s}}$ and the right hand side vector $\boldsymbol{f}_{\mathrm{s}}$. They are imported into the research code by a binary interface. The data exchange only needs to be done once for a given model, since $\boldsymbol{M}_{\mathrm{s}}$ and $\boldsymbol{K}_{\mathrm{s}}$ are frequency independent. Typically, shell elements with six degrees of freedom are applied for thin structures.

The vector $\boldsymbol{f}_\mathrm{f}$ is defined by the first transmission condition (6). The nodal forces are computed from the fluid pressure by

$$\boldsymbol{f}_\mathrm{f} = -\boldsymbol{C}_\mathrm{FE}\,\boldsymbol{p} \qquad \text{where } \boldsymbol{C}_\mathrm{FE} \text{ is assembled from} \qquad \boldsymbol{C}_\mathrm{FE}^k = -\int_{\tau_k} \boldsymbol{N}_u^\mathrm{T}\,\boldsymbol{n}^k\,\boldsymbol{N}_p\,\mathrm{d}s_x\,. \quad (26)$$

The matrix with the structural shape functions is denoted by $\boldsymbol{N}_u$ and the one with the fluid shape functions by $\boldsymbol{N}_p$. According to the second transmission condition (7), the acoustic flux q on each boundary element τ_m is computed from the structural displacements of the adjacent nodes k by

$$\bar{\boldsymbol{q}} = \boldsymbol{T}_q\boldsymbol{u} \qquad \text{where each row is given by} \qquad q_m = \frac{1}{3}\varrho_\mathrm{f}\omega^2 \sum_{k\in m} \boldsymbol{u}_k \cdot \boldsymbol{n}^m\,, \qquad (27)$$

and ϱ_f denotes the density of the fluid. To obtain the coupled system of equations, (26) is plugged into (24) and (27) into (14) or (17) yielding

$$\begin{pmatrix} \boldsymbol{K}_\mathrm{FE} & \boldsymbol{C}_\mathrm{FE} \\ \boldsymbol{C}_\mathrm{BE}\boldsymbol{T}_q & \boldsymbol{K}_\mathrm{BE} \end{pmatrix} \begin{pmatrix} \boldsymbol{u} \\ \boldsymbol{x} \end{pmatrix} = \begin{pmatrix} \boldsymbol{f}_\mathrm{s} \\ 0 \end{pmatrix}\,, \qquad (28)$$

In case of the mixed formulation, $\boldsymbol{K}_\mathrm{BE}^\mathrm{m}$ and $\boldsymbol{C}_\mathrm{BE}^\mathrm{m}$ are used and $\boldsymbol{x} = (\tilde{\boldsymbol{q}}, \tilde{\boldsymbol{p}})^\mathrm{T}$, where $\tilde{\boldsymbol{p}}$ is the unknown pressure on the ship-hull and $\tilde{\boldsymbol{q}}$ is the unknown flux of the elements on Γ_H. For the half-space formulation, $\boldsymbol{K}_\mathrm{BE}^\mathrm{h}$ and $\boldsymbol{C}_\mathrm{BE}^\mathrm{h}$ are used and $\boldsymbol{x} = \boldsymbol{p}$ denotes the pressure on the ship hull. The coupled system (28) is rearranged using the Schur complement $\boldsymbol{S}$

$$\underbrace{\left(\boldsymbol{K}_\mathrm{BE} - \boldsymbol{C}_\mathrm{BE}\boldsymbol{T}_q\,\boldsymbol{K}_\mathrm{FE}^{-1}\boldsymbol{C}_\mathrm{FE}\right)}_{\boldsymbol{S}}\boldsymbol{x} = -\boldsymbol{C}_\mathrm{BE}\boldsymbol{T}_q\,\boldsymbol{K}_\mathrm{FE}^{-1}\boldsymbol{f} \qquad (29)$$

and a GMRES is applied to solve for $\boldsymbol{x}$. In each iteration step, $\boldsymbol{K}_\mathrm{FE}^{-1}$ must be applied to a vector. This is efficiently done using a LDL^T factorization, which only has to be computed once and can be reused in each iteration step. For the mixed formulation, a scaling of the different blocks of $\boldsymbol{K}_\mathrm{BE}$ is performed. As preconditioner, an ILU factorization of the near-field matrix of $\boldsymbol{K}_\mathrm{BE}$ is applied.

7 NUMERICAL RESULTS

In this section, the proposed fast BE-FE coupling schemes are compared for the container vessel depicted in Fig. 3 (left top). The model consists of 16547 nodes and 35836 structural degrees of freedom. The number of boundary elements on the ship hull is 2858 and 1343 nodes are in contact with the water. Water with the density $\varrho_\mathrm{f} = 1000^{\mathrm{kg}}/_{\mathrm{m}^3}$ and the speed of sound $c_\mathrm{f} = 1483.2^{\mathrm{m}}/_{\mathrm{s}}$ is assumed as acoustic fluid. The structure is excited by 691 forces caused by the pressure fluctuations of the ship propeller. For the mixed approach, a rectangular area of the water surface is meshed as shown for the rear half (cf.

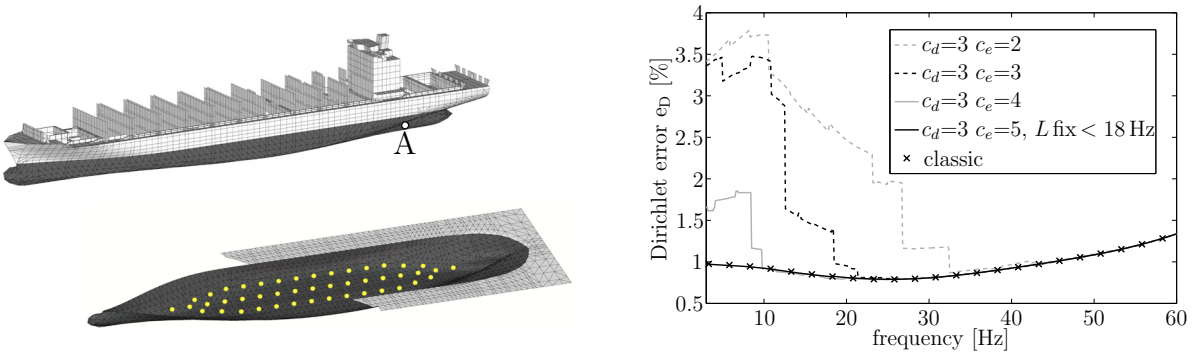


Figure 3: Discretized model of the investigated container-vessel (left top). The wet boundary elements are highlighted in dark gray. For the mixed formulation a part of the water surface is discretized as shown for the rear half. Light spots indicate the position of the used monopole sources (left bottom). Dirichlet error $\mathrm{e_D}$ for the half-space formulation and different multipole parameters (right).

Fig. 3 left bottom). The minimal distance d_w between the ship hull and the edge of the discretized water surface is chosen from the set $\{2.5\,\mathrm{m}, 5\,\mathrm{m}, 10\,\mathrm{m}, 20\,\mathrm{m}, 40\,\mathrm{m}$ and $80\,\mathrm{m}\}$. For the smallest water area with $d_\mathrm{w} = 2.5\,\mathrm{m}$, 639 nodes are located on the water surface which increases to 11799 nodes in case of the largest model. Before the simulations of the coupled approaches are presented, the BE part of the mixed formulation is compared with the half-space formulation concerning the accuracy and efficiency.

7.1 Accuracy of the fluid part

To examine the accuracy of the fluid part, an analytical field is created using 90 monopole sources. Half of them are located within the ship hull as decpicted in Fig. 3 (left bottom). To fulfill the Dirichlet boundary condition on the water surface, the monopole sources are mirrored and the strength multiplied by minus one. For this field, both the pressure and flux are known for a given point and normal direction. Hence, the analytical flux is used as boundary condition $\bar{\boldsymbol{q}}$ and the corresponding pressures $\boldsymbol{p}$ or $\tilde{\boldsymbol{p}}$ at the nodes on Γ_I are computed using (17) or (14). Since the analytical pressure $\boldsymbol{p}_\mathrm{mono}$ is known, the Dirichlet error

$$\mathrm{e_D} = \frac{||\boldsymbol{p} - \boldsymbol{p}_\mathrm{mono}||_{L_2}}{||\boldsymbol{p}_\mathrm{mono}||_{L_2}} \tag{30}$$

can be defined. In case of the mixed approach $\tilde{\boldsymbol{p}}$ is used instead of $\boldsymbol{p}$. First, the influence of the multipole parameters c_d and c_e as defined by (22) and (23) is investigated for the half-space formulation. As reference solution, the classical implementation without FMM is utilized. The corresponding Dirichlet errors are depicted in Fig. 3. For small frequencies and small expansion lengths, one observes a larger Dirichlet error. The error can be reduced by increasing the expansion length. A parameter $c_e = 5$ turned out to give a small error, if the expansion length is computed by (23) using a fixed frequency of 18 Hz for all frequencies $f \leq 18\,\mathrm{Hz}$. For this choice, hardly any difference between the

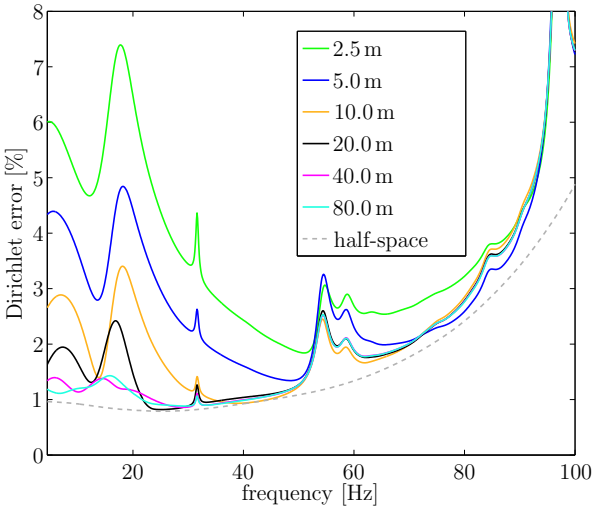


Figure 4: Container-Vessel: The Dirichlet error is visualized for different frequencies. The discretized water area of the mixed formulation is varied between 2.5 m and 80 m. The half-space result is plotted as comparison.

error of the classical implementation and the fast multipole implementation is observable any more. For this reason, this parameter set is chosen for all following simulations.

The Dirichlet errors are also computed for the mixed approach. The discretized water area is varied as mentioned above. The half-space solution is exact in the sense, that the Dirichlet boundary condition on the water surface is incorporated in an exact way and can therefore be seen as the achievable solution. Figure 4 shows the Dirichlet errors within a frequency range from 3 Hz to 100 Hz. All errors of the mixed formulation are larger than the half-space solution. For $d_w = 2.5\,\text{m}$, the errors reach almost 8% in the region around 20 Hz. The error curves of the mixed approach are wavy in contrast to the half-space formulation. This may lead to misinterpretation especially at 95 Hz where one observes an artificial resonance. If the discretized water area is enlarged, the errors tend to decrease. But this is not generally the case. For instance at a frequency $f = 55\,\text{Hz}$, the error is almost independent of the discretized water area and approximately twice as large as for the half-space formulation. The same holds for the resonance effect at 95 Hz, which occurs even for the largest water area. Hence, one concludes, that the half-space formulation is superior to the mixed formulation concerning the accuracy.

When using simulation tools for real life applications, also the efficiency is of major interest. Therefore, the computational times and the memory consumptions are discussed in the following. For all simulations a Intel Xeon 5160 CPU with 16GB RAM is used. The computational times for the models with the different water areas are depicted in Fig. 5 (left). The half-space approach does not need to discretize the water surface. Hence, the corresponding computational times are indicated by dashed horizontal lines in the same

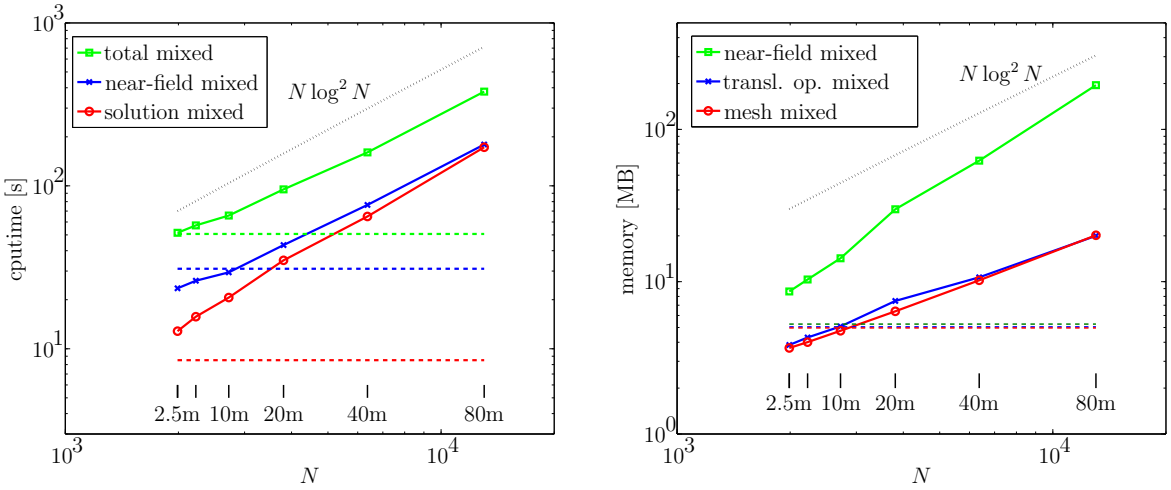


Figure 5: Computation time (left) and memory consumption (right) for the mixed formulation and different water areas with varying number of unknowns N. The corresponding values of the half-space formulation are indicated by dashed horizontal lines of the same color.

color. For small water areas with $d_\mathrm{w} \leq 10\,\mathrm{m}$, the mixed formulation is slightly faster concerning the set-up time of the near-field. However, the solution time for the half-space formulation is always smaller compared to the mixed approach. For this reason, the total simulation time including the reading of the model file and writing of the results files is always smaller for the half-space formulation. Thus one concludes, that the half-space formulation is also superior to the mixed formulation in terms of the computational time.

Besides the computational time also the memory consumption is compared. The results are visualized in Fig. 5 (right). Obviously, the near-field of the mixed formulation always requires more memory than the one of the half-space approach. Due to the mirrored mesh, the memory consumption for storing the model information is slightly larger for the half-space formulation compared to the mixed approach with small water areas. Due to the increasing number of elements for the larger water areas, the situation changes for water areas with $d_\mathrm{w} \geq 10\,\mathrm{m}$. The same holds for the memory consumption of the translation operators and near-field signatures. One concludes, that the overall memory consumption is smaller for the half-space formulation if not the smallest water area is chosen which yields inaccurate results.

So far, only the fluid part was investigated. In the next subsection, the coupled results are presented.

7.2 Coupled simulations

To compare the coupled simulation results, the velocity at node A (cf. Fig. 3) is investigated. Figure 6 (left) depicts the results for the mixed formulation and the half-space approach. In case of the mixed formulation, the water area is discretized using $d_\mathrm{w} = 10\,\mathrm{m}$. Both implementations use the fast multipole method with the parameters

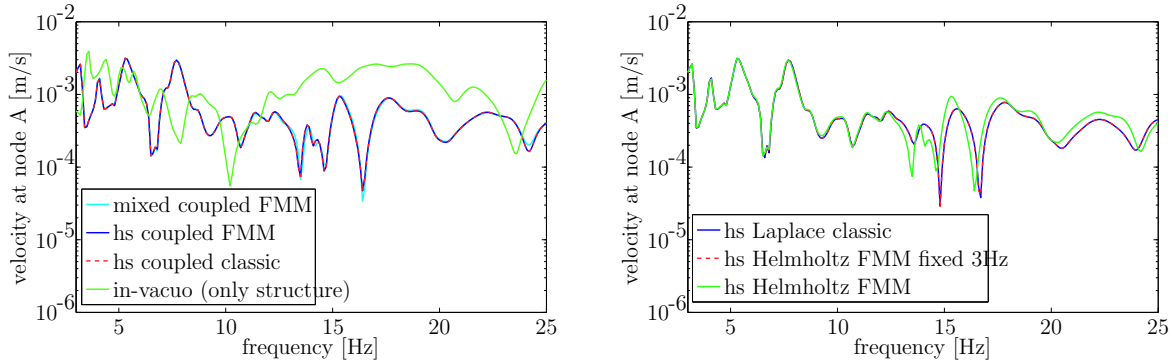


Figure 6: Velocity for the mixed and half-space (hs) formulation for the Helmholtz equation (left). Comparison of the velocity results for the Laplace and Helmholtz equation in case of the coupled half-space formulation (right).

mentioned above. The two graphs show hardly any differences. Only a slight deviation is observed at about 24 Hz. To show the correctness of the results, also the half-space formulation with classical implementation is plotted and shows a good agreement compared to the FMM version. To demonstrate the necessity of a fully coupled scheme, also the pure structural solution is plotted, which neglects the feedback of the acoustic pressure. Obviously, there is a significant difference and one concludes that the forces due to the acoustic pressure have to be taken into account.

So far, only the Helmholtz equation has been considered. It includes the so-called hydromass effect and also the sound radiation into the water. The frequency dependent Helmholtz equation can be replaced by the frequency independent Laplace equation, if only the hydromass effect is of significance and the water is assumed to be incompressible. To examine the influence of the compressibility, the velocity results at node A are shown in Fig. 6 (right). In the low frequency regime, the results of the Laplace equation and the Helmholtz equation are identical. For this reason, it is also possible to apply the Helmholtz equation and only perform one integration at a fixed frequency of 3 Hz. For higher frequencies, the results of this fixed Helmholtz approach are equivalent to the Laplace equation. However, above 12 Hz one observes slight differences between the Laplace and the Helmholtz equation. For higher frequencies, one expects an increasing influence. However, the structural discretization of the used model is not sufficient for this frequency regime. Hence, such test could not be performed with this model.

8 CONCLUSION

When dealing with ship vibrations, the influence of the surrounding water on the structure has to be considered. In this work, two boundary element methods in combination with a strong coupling scheme are compared. To overcome the restrictions caused by the fully populated matrices of classical boundary element methods, the fast multipole method is applied. A mixed approach, where a part of the water surface is discretized is

compared with a half-space approach, where a discretization of only the ship hull is sufficient. The latter one turns out to be superior in accuracy, computation time and memory consumption. Additionally, the influence of the compressibility of the water is investigated by comparing the results for the Laplace equation and the Helmholtz equation. One observes almost identical results in the low frequency regime. For higher frequencies, slight differences are visible.

REFERENCES

[1] Amini, S., Harris, P., and Wilton, D. *Coupled Boundary and Finite Element Methods for the Solution of the Dynamic Fluid-Structure Interaction Problem*. Springer Berlin, 1992.

[2] Brunner, D., Junge, M., and Gaul, L. A comparison of FE-BE coupling schemes for large scale problems with fluid-structure interaction. *Int. J. Numer. Meth. Eng. in press, DOI: 10.1002/nme.2412* (2008).

[3] Brunner, D., Of, G., Junge, M., Steinbach, O., and Gaul, L. A fast BE-FE coupling for partly immersed bodies. *Int. J. Numer. Meth. Eng. 81* (2010), 28–47.

[4] Coifman, R., Rokhlin, V., and Wandzura, S. The fast multipole method for the wave equation: A pedestrian description. *IEEE Antenn. Progag. M. 35* (1993), 7–12.

[5] Fahy, F. *Sound and Structural Vibration: Radiation, Transmission and Response*. Elsevier Press, Amsterdam, Heidelberg, 2007.

[6] Fischer, M. *The Fast Multipole Boundary Element Method and its Application to Structure-Acoustic Field Interaction*. PhD thesis, University of Stuttgart, 2004.

[7] Gaul, L., Kögl, M., and Wagner, M. *Boundary Element Methods for Engineers and Scientists. An Introductory Course with Advanced Topics.* Springer Berlin, 2003.

[8] Gumerov, N., and Duraiswami, R. *Fast Multipole Methods for the Helmholtz Equation in Three Dimensions*. Elsevier, Oxford, 2004.

[9] Gyure, M., and Stalzer, M. A prescription for the multilevel Helmholtz FMM. *IEEE Comput. Sci. Eng. 5* (1998), 39–47.

[10] Hughes, M., and Chen, K. An efficient preconditioned iterative solver for solving a coupled fluid structure interaction problem. *International Journal for Computer Mathematics 81* (2004), 583–594.

[11] Junger, M., and Feit, D. *Sound, Structures, and Their Interaction: Basic Concepts*, 2nd ed. The MIT Press, 1986.

[12] Rjasanow, S., and Steinbach, O. *The Fast Solution of Boundary Integral Equations*. Springer New York, 2007.

[13] Rokhlin, V. Diagonal forms of translation operators for the Helmholtz equation. *Appl. Comput. Harmon. A. 1* (1993), 82–93.

[14] Seybert, A., and Wu, T. Modified Helmholtz integral equation for bodies sitting on an infinite plane. *J. Acoust. Soc. Am. 85* (1989), 19–23.

[15] Stephan, E. Boundary integral equations for mixed boundary value problems in $\mathbb{R}^3$. *Math. Nachr. 184* (1987), 21–53.

[16] Wu, T. *Boundary Element Acoustics. Fundamentals and Computer Codes.* WIT Press Southampton, 2000.

[17] Zienkiewicz, O., and Taylor, R. *The Finite Element Method, Volume 1: The Basis.* Butterworth Heinemann Oxford, 2000.

V International Conference on Computational Methods in Marine Engineering
MARINE 2013
B. Brinkmann and P. Wriggers (Eds)

GPGPU-ACCELERATED SIMULATION OF WAVE-SHIP INTERACTIONS USING LBM AND A QUATERNION-BASED MOTION MODELER

C. F. JANSSEN, H. NAGRELLI AND T. RUNG

Institute for Fluid Dynamics and Ship Theory
Hamburg University of Technology (TUHH)
Hamburg, Germany
e-mail: {christian.janssen,heinrich.nagrelli,thomas.rung}@tuhh.de
web page: http://www.tuhh.de/fds

Key words: LBM, Free Surface Flow, Fluid-Structure Interaction, GPGPU

Abstract. The paper reports on the applicability of the Lattice Boltzmann based free surface flow solver elbe to the simulation of complex, fluid-structure interaction (FSI) problems in marine engineering. General purpose graphics processing units (GPGPUs) are used to accelerate the numerical calculations. The basic methodology and the initial validation of the solver for three FSI test cases are given in this paper. A more detailed validation and the application of the solver to the numerical simulation of the ditching of a free fall boat will be presented at the *Marine 2013 Conference*.

1 INTRODUCTION

Research on strongly nonlinear fluid-ship interactions has received an ever-increasing interest over the past few years, especially in naval architecture. As experimental studies are afflicted with scale effects which are generally difficult to quantify, efficient, robust and accurate computational approaches towards fluid-structure interaction are highly appreciated, particularly when emphasis is given to violant flow phenomena. In this work, we present a numerical wave tank on the basis of the Lattice Boltzmann Method (LBM) and a quaternion-based floating-body motion modeler. The LBM has recently matured as a viable alternative to classical CFD approaches, i.e. Eulerian Finite-Volume methods or particle-based Lagrangian approaches (e.g. SPH). LBM solves a discretized Boltzmann equation that describes the evolution of particle distribution functions, on Cartesian grids. Whilst modeling essentially similar physics as Navier-Stokes procedures, LBM features a number of performance-related advantages, particularly concerning data locality and parallel computing. The paper addresses the application of a GPGPU-accelerated, VOF-based LBM method [13] for the simulation of fluid-ship interactions. Attention is confined

to efficient models for rigid floating bodies. Such floating-body motions are traditionally performed by using deforming meshes or body-algned rigid grids or a combination of the two. A different option is conceivable in conjunction with LBM, which operates on fixed, equidistant Cartesian grids. Analogue to an immersed boundary approach, a grid update (i.e. remeshing) reduces to the calculation of subgrid distances of the Eulerian lattice nodes to the surface of the structure. The floating body motions themselves are described by a unit-quaternion motion modeler [16] that is coupled to the LBM in a bidirectional, explicit manner. After a brief description of the solver basics and the fluid-structure coupling approach in section 2, three illustrative validation cases are presented in section 3: drag on a sphere and the gravity-driven free fall of a rigid sphere, with and without water entry.

2 NUMERICAL METHOD

elbe is an efficient and accurate toolkit for the numerical simulation of complex two- and three-dimensional flow problems [14]. It considers nonlinear flow behavior with and without a free surface, effects of viscosity and turbulence and is based on a Lattice Boltzmann Method (LBM) on equidistant Cartesian grids. The LBM has become an efficient approach for solving a variety of difficult CFD problems, including those in the field of multiphysics. The numerical approximation is second-order accurate in space and time.

2.1 LBM basics

In contrast to classical CFD solvers which are dealing with the macroscopic Navier-Stokes equations, the LBM regards CFD problems on a microscopic scale. The primary variable of microscopic approaches is the particle distribution function $f(t, \boldsymbol{x}, \boldsymbol{\xi})$, which specifies the probability to encounter a particle at position $\boldsymbol{x}$ at time t with velocity $\boldsymbol{\xi}$. In order to obtain a model with reduced computational costs, the velocity space is discretized and discrete velocities $\boldsymbol{e}_i$ are introduced. In this work, the D3Q19 model [23] with 19 discrete microscopic particle velocities $\boldsymbol{e}_i$ and corresponding particle distribution functions $f_i(t, \boldsymbol{x})$ is used. The evolution of these discrete distribution functions is described by the discrete Boltzmann equation. A standard finite difference discretization on an equidistant grid finally leads to the *lattice* Boltzmann equation,

$$f_i(t + \Delta t, \boldsymbol{x} + \boldsymbol{e}_i \Delta t) - f_i(t, \boldsymbol{x}) = \Omega_i \tag{1}$$

The left-hand side of this equation is an advection-type expression,while the discrete *collision operator* Ω_i models the interactions of particles on the microscopic scale. Collision operators Ω_i of different complexity can be used. In a single relaxation time (SRT) model [1], the particle distribution functions are driven to an equilibrium state with a single relaxation rate (which relates to the kinematic viscosity of the fluid ν). In the more advanced MRT model [3] used in the present work, the particle distribution functions are transformed into moment space, where they are relaxed with several different relaxation

rates. This increases the stability and at the same time enables the development of more accurate boundary conditions [5]. The solutions of the lattice Boltzmann equation satisfy the incompressible Navier-Stokes equations up to errors of $\mathcal{O}(\Delta x^2)$ and $\mathcal{O}(\mathrm{Ma}^2)$ [15]. The macroscopic values for density fluctuation ρ and momentum $\rho_0 \boldsymbol{u}$ are the first two hydrodynamic moments of the particle distribution functions:

$$\rho = \sum_{i=0}^{18} f_i \quad \text{and} \quad \rho_0 \boldsymbol{u} = \sum_{i=0}^{18} \boldsymbol{e}_i f_i \tag{2}$$

As free surface flows usually occur at very high Reynolds numbers in the turbulent regime, a Smagorinsky large eddy model (LES) [18] is used to capture turbulent structures in the flow. The effect of the small sub-grid eddies on the large-scale flow structures is modeled through an additional turbulent viscosity ν_T, which - in a Smagorinsky model - depends on the local strain rate, $\nu_\mathrm{T} = (C_S \Delta x)^2 \|\mathbf{S}\|$, with Smagorinsky constant C_S and strain rate tensor $S_{\alpha\beta}$. For further details, see [18].

At the domain boundaries, the incoming particle distribution functions are missing after the advection step and are reconstructed with the help of boundary conditions. For no-slip and velocity boundaries, a simple bounce back scheme is used. The missing particle distribution function f_I is reconstructed as

$$f_I^{t+1}(\boldsymbol{x}) = f_i^t(\boldsymbol{x}) + 2\rho_0 w_i \frac{\boldsymbol{e}_i \bar{\boldsymbol{u}}}{c_s^2} \tag{3}$$

where i is the inverse direction to I, $\bar{\boldsymbol{u}}$ denotes the prescribed boundary velocity [2] and w_i are model-specific, constant weighting factors [11]. The subgrid wall distance is not taken into account in this model, so that the scheme is only second-order accurate for boundaries which are exactly located in the middle of two lattice nodes. At the free surface, the anti-bounce-back rule [17] balances the fluid pressure and the surrounding athmospheric pressure p_B:

$$f_I^{t+1} = -f_i^t + f_I^{eq}(\rho_B, \boldsymbol{u}_B) + f_i^{eq}(\rho_B, \boldsymbol{u}_B) \tag{4}$$

where $f_{i,I}^{eq}(\rho_B, \boldsymbol{u}(t_B, \boldsymbol{x}_B))$ are Maxwellian equilibrium distribution functions and ρ_B is related to the surrounding pressure by $\rho_B = p_B c_s^{-2}$. Gravity and other volume forces $\boldsymbol{F}$ are added directly to the distribution functions f_i in every time step [8]:

$$\Delta f_i = 3\omega_i \rho \boldsymbol{e}_i \cdot \boldsymbol{F}. \tag{5}$$

2.2 Free surface model

Free-surface flows are two-phase flows with high viscosity ratios and high density ratios between two immiscible phases. The flow is dominated by the denser phase and the interface is allowed to move freely. If capillary forces are neglected, the simulation of the denser and more viscous phase is sufficient and the influence of the second (less dense) phase on the flow dynamics can be represented by appropriate kinematic and dynamic boundary conditions at the interface. Numerically, the free surface represents a moving boundary, which is allowed to move freely, but at the same time has to be kept sharp. A couple of approaches have been developed to use the LBM for free surface flow simulations [6, 7, 12, 20]. Apart from the aforementioned methods, Koerner and Thuerey [17, 25] combine LBM with a VOF method and a flux-based advection scheme. Their algorithm initially was developed for the simulation of metal foams, but is capable of handling free-surface flow simulations as well, and was found to be robust and stable while keeping the interface sharp. Opposite to common VOF methods, the flux terms are expressed directly in terms of LBM distribution functions. In a VOF interface capturing approach, the interface is captured via the *fill level* of a cell, which qualifies the amount of a cell which is filled with fluid:

$$\varepsilon = \frac{V_{fluid}}{V_{cell}} \tag{6}$$

A fill level of 0.0 marks an empty cell in the inactive gas domain, a fill level of 1.0 corresponds to a filled cell inside the fluid domain. Fluid and gas cells are separated by a closed interface layer with a fill level between 0.0 and 1.0. The fill level changes in time, and the new fill level of a cell at time step $n+1$ is calculated via balancing the mass fluxes between the neighboring cells and updating the fill level via

$$\varepsilon^{n+1} = \frac{m^{n+1}}{\rho^{n+1}} = \frac{\rho^n \varepsilon^n + \sum_i \Delta m_i}{\rho^{n+1}}, \tag{7}$$

where $\rho^{n/n+1}$ is the fluid density at time step n resp. $n+1$ according to Eq. (2) and ε^n is the fill level at time step n [17, 25]. The mass flux terms m_i between neighboring cells are expressed in terms of particle distribution functions:

$$\Delta m_i = \left[f_I\left(\boldsymbol{x}, t\right) - f_i\left(\boldsymbol{x}, t\right) \right] \cdot A_i \cdot \Delta t \tag{8}$$

with the two antiparallel particle distribution functions $f_{i,I}$ entering or leaving the corresponding cell. A_i denotes the wet area between two cells and is calculated on the basis of a simplified surface reconstruction. It can be estimated e.g. as the arithmetic mean of the fill levels of two neighboring cells. Opposite to higher-order schemes (such as presented in [12]), the normal vector information is not considered here. To sum up, the Lattice Boltzmann VOF advection scheme can be considered as a specialized, geometry-based VOF method on the basis of a mesoscopic advection model.

2.3 Fluid-structure interaction

Floating-body motions follow from a motion modeler which converts the external and hydrodynamic forces exerted on the body into its motion. The latter involves appropriate descriptions of the spatial position and angular orientation. The most common way to describe the angular orientation of a rigid body is the use of Euler angles. They represent three composed elementary rotations of a body-fixed local coordinate system referring to a global system. In such an arrangement the effect of a Gimbal Lock can occur, when two axes are driven into a parallel configuration, which "locks" the system into a rotation in a degenerate two-dimensional space. To avoid this singularity and ensure that each motion is uniquely defined, unit-quaternions - also known as Euler parameters - are employed for the motion modeler [22].

For the coupling to the explicit LB method, a bidirectional, explicit coupling approach is used, which has been proposed and validated in [4]. First, the force acting on the rigid bodies is evaluated by means of the momentum exchange method [19]. The force $\boldsymbol{F}$ acting on an obstacle in the flow results from the momentum of the particles hitting the boundary. It can be computed by balancing the particle momentum before and after hitting the boundary:

$$\boldsymbol{F} = \sum_{i \in \Gamma} \boldsymbol{F}_i = -\frac{V}{\Delta t} \boldsymbol{e}_i \left(f_i(t + \Delta t, \boldsymbol{x}) + f_I(t, \boldsymbol{x}) \right) \tag{9}$$

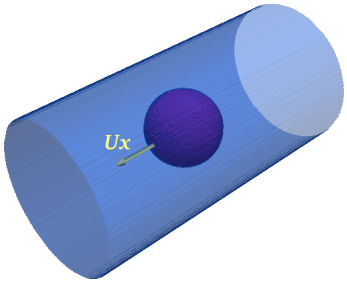
for all links i that are cut by the obstacle [21]. Since the rigid bodies do not allow elastic or plastic deformations, the evaluation of the integral force on the whole rigid body is sufficient. After the calculation of fluid loads, the force information is transferred to the structural solver and one time step of rigid body motion is computed. The resulting displacements and velocities are passed to the fluid solver, where the geometry is updated and the modified bounce back scheme (Eq. (3)) serves to incorporate the rigid body boundary velocity.

3 RESULTS

In the following, the numerical results for three validation cases are given. Since LBM usually operates on a finite difference grid, is explicit in time and requires only next neighbor interaction, it is very efficient in combination with GPGPUs and massively parallel hardware. In recent years, several authors accelerated their (LBM) computations on general-purpose graphics hardware, see e.g. the pioneering work of [28, 30, 29]. Later on, Toelke implemented two- and three-dimensional LB bulk flow models on nVIDIA GPGPUs [26, 27] and showed an efficiency gain of up to two orders of magnitude compared to a single-core CPU code. With the development of software development kits (SDKs), in combination with the recent hardware improvements, even complex flow simulations including free surfaces and fluid-structure interaction can be efficiently addressed. In this work, the GPGPU-accelerated elbe code is used [14]. The solver is based on the NVIDIA CUDA framework and basically follows the implementation strategies discussed in [12].

3.1 Drag on a sphere

The first test case is concerned with the drag force on a sphere moving with constant velocity in a cylindrical pipe. Fig. 1 shows the computational domain and the main simulation parameters. The simulation is carried out in the local sphere frame of reference: the sphere is fixed, and velocity boundary conditions are used at the inlet, outlet and the cylinder surface. Fig. 2 shows the converged velocity field in x direction.



Pipe length L_x $[m]$	16.0
Pipe diameter D $[m]$	4.0
Sphere diameter d $[m]$	2.0
Ratio $\lambda = \frac{d}{D}$ $[-]$	0.5
Initial sphere COG $[m]$	[16.0 4.0 4.0]
Re numbers $[-]$	10, 25, 50
Ma numbers $[-]$	0.02, 0.04, 0.08, 0.1

Figure 1: Sphere drag setup & calculation parameters

The force on the sphere is evaluated and validated in terms of the dimensionless drag coefficient C_d,

$$C_d = \frac{8\ F_x}{\rho u^2 \cdot d^2 \pi}, \tag{10}$$

for a sphere with diameter d moving with velocity u in a fluid with density ρ. To approximate C_d analytically, the extended Stokes solution by Schiller and Naumann [24] is used. The equation approximates the C_d coefficient for spheres in an infinite fluid with constant velocity. The influence of pipe walls surrounding the sphere is considered with an additional correction term [9], leading to the following final expression for the drag:

$$C_{d,\bigcirc} = \frac{24}{Re}\{1 + 0.15 \cdot Re^{0.687} + \frac{1 - 0.75857\lambda^5}{12.1050\lambda + 2.0865\lambda^3 1.7068\lambda^5 + 0.72603\lambda^6}\}, \tag{11}$$

depending on the ratio $\lambda = d/D$ of the diameters of the sphere and the pipe. This approximation leads to an accuracy of 95% for $\lambda < 0.6$ and $\mathrm{Re} < 50$. In Fig. 3, the results of a grid convergence study for the $\mathrm{Re} = 10$ case are shown for selected Mach numbers. It can be observed that the numerical results converge with increasing grid resolution, but do not converge to the analytical reference value for C_d based on Eq. (11). First studies suggest that this discrepancy depends on (i) the exact location of the sphere in the grid (due to the first-order simple bounce back rule), and (ii) the channel length (due to the disturbance of the flow pattern by the inlet and outlet boundary conditions). Both effects will be studied more carefully in future work. However, the numerical errors are in the same order of magnitude as the predicted accuracy of Eq. (11).

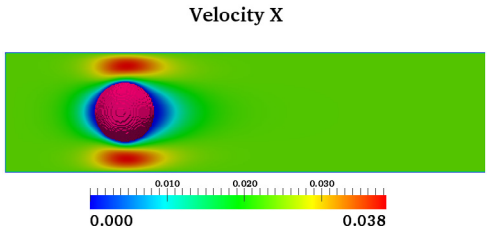


Figure 2: $v_{x,LB}$ for $Re = 10$

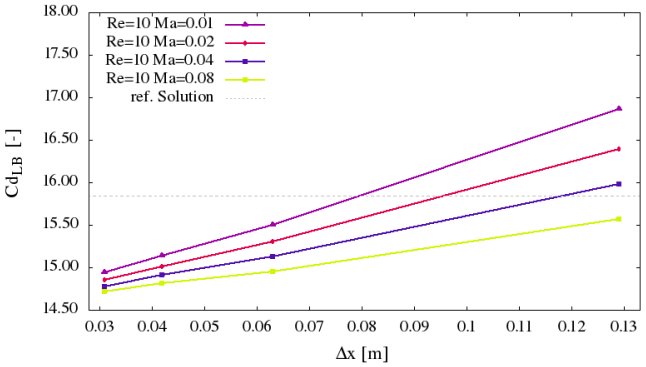
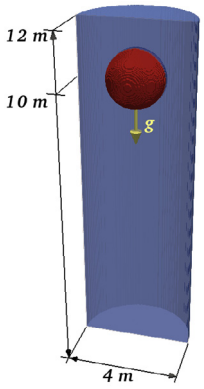


Figure 3: C_d grid convergence study for $Re = 10$

3.2 Falling sphere

For the validation of the explicit coupling of LBM and quaternion-based motion modeler, the gravity-driven sphere motion in a fluid at rest is examined, see Fig. 4. The simulation is started from a state of rest. During the initial stages of the simulation, the sphere is accelerated by the gravitational force. With increasing sphere velocity, the drag force increases, too, so that finally a terminal velocity v_z is reached.



Pipe height $[m]$	12.0
Initial sphere height $[m]$	10.0
Sphere diameter d $[m]$	2.0
Ratio $\lambda = \frac{d}{D}$ $[-]$	0.5
Re numbers $[-]$	10, 25, 50
Ma numbers $[-]$	0.02, 0.04, 0.08, 0.1

Figure 4: Rigid sphere in a fluid at rest - setup and simulation parameters

In our simulation, the ratio of fluid and sphere density is set to a constant value of $\rho_{Sph}/\rho_{Fluid} = 1.5$ and gravity is set to $g = 9.81[m/s^2]$. The fluid viscosity is artificially adjusted so that the final terminal velocity matches the given Reynolds number Re. For this purpose, the force balance on the sphere is considered. The force in z direction consists of two parts: the hydrostatic fluid pressure that causes buoyancy forces, and the viscous drag, which balances the effective sphere weight, $(\rho_{Sph} - \rho_{Fluid})$, so that

$$(\rho_{Sph} - \rho_{Fluid}) \cdot V_{Sph} \cdot g + \frac{1}{2}\rho_{Fluid} v_Z^2 \cdot C_{d,\bigcirc} \cdot A_{Sph} = 0 \tag{12}$$

holds, with sphere cross section A_{Sph} and sphere volume V_{Sph}. For given values of Re and λ, the drag coefficient $C_{d,\bigcirc}$ is obtained by evaluating Eq. (11)). The terminal velocity can be calculated by rearranging Eq. (12),

$$v_z = \sqrt{\frac{(\rho_{Sph} - \rho_{Fluid}) g \frac{4}{3} d}{\rho_{Fluid} \cdot C_{d,\bigcirc}}}, \tag{13}$$

and the corresponding (artificial) fluid viscosity ν yields $\nu = v_z d/\mathrm{Re}$. Fig. 5 shows the velocity field for selected time steps for the Re = 10 case.

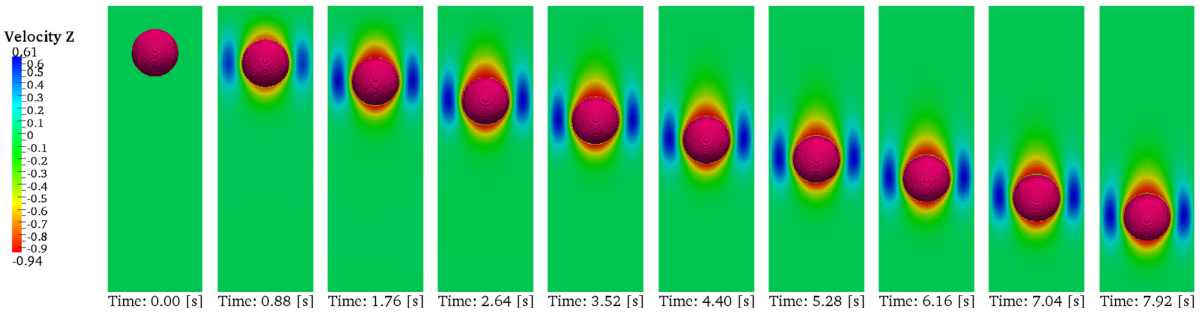
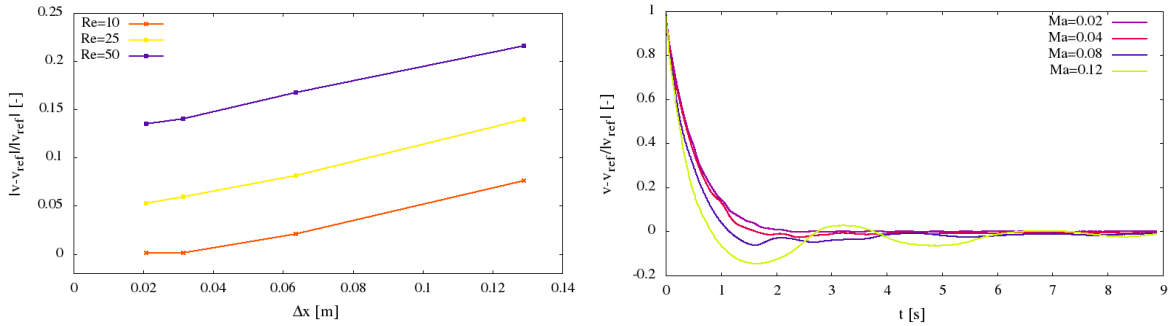


Figure 5: Falling sphere in a pipe, geometry and flow velocity in z direction$[\frac{m}{s}]$ for selected time steps (Ma = 0.04, Re = 10)

In Fig. 6a, the relative error of the terminal sphere velocity v_z is plotted against the grid resolution Δx for three selected Reynolds numbers. Convergence can clearly be observed. The numerical error increases with increasing Reynolds number, due to the limited accuracy of the C_d approximation (Eq. (11)). In Fig. 6b, the signed relative error in v_z is depicted for selected Mach numbers. For lower Mach numbers (corresponding to smaller time steps), less oscillations and a faster convergence is found. Note that the resulting terminal velocity is predicted very well, also for Re = 10. This supports the previous attempts to explain the error in C_d: here, the sphere moves (balancing the grid mapping errors), and no-slip boundary conditions are used at the top and bottom.



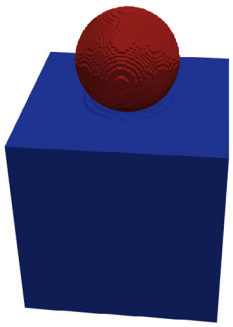
(a) Relative error of v_z as a function of lattice spacing Δx (Re = 10, 25, 50, Ma = 0.04)

(b) Relative error of v_z over time (Ma = 0.02, 0.04, 0.08, 0.12, Re = 10)

Figure 6: Results for the falling sphere test case

3.3 Sphere drop

The third and last test case deals with the water entry of a rigid sphere. As the sphere penetrates the water surface, its movement is damped due to buoyancy effects and additional contributions of the dynamic pressure gradient, i.e. drag. The sphere motion is damped, and the position of the sphere finally converges to the hydrostatic equilibrium.



Sphere diameter $[m]$	2.0
Initial water height $[m]$	4.0
Initial $COG[m]$	2.0, 2.0, 6.0
Domain size $[m]$	4.0, 4.0, 8.0
Density $\rho_{Sph}[\frac{kg}{m^3}]$	100, 200, 300, 400, 500, 600
Draft $T_{calc}[m]$	0.392, 0.574, 0.727, 0.866, 1.000, 1.134
Final $COG_{Zcalc}[m]$	4.634, 4.478, 4.352, 4.239, 4.131, 4.023

Figure 7: Water entry of the sphere at $0.5s$ & calculation parameters

The final sphere position depends on the ratio of sphere density and fluid density (ρ_{Sph}/ρ_{Fluid}) and is estimated with the principle of buoyancy, which requires the balance of buoyant force and sphere weight,

$$\rho_{Fluid} V_C = \rho_{Sph} V_{Sph} \tag{14}$$

where V_C denotes the volume of the submerged spherical calotte of height T,

$$V_C = \frac{T^2}{3}(3r - T). \tag{15}$$

Assuming $d = 1$, the draft T can be calculated by solving

$$0 = T^3 - 1.5T^2 + 0.5\frac{\rho_{Sph}}{\rho_{Fluid}} \quad with \quad T \leq 1.0 \quad \frac{\rho_{Sph}}{\rho_{Fluid}} \leq 1.0 \tag{16}$$

for T. For other sphere diameters d, the draft T can be scaled linearly. In our simulations, the fluid density is set to $\rho_{Fluid} = 1000\frac{kg}{m^3}$ and spheres of diameter $d = 2m$ and densities from 100 to 600 $[\frac{kg}{m^3}]$ are examined. The corresponding final positions of the sphere center of gravity (COG) are summarized in Fig. 7. In Fig. 8, the transient sphere trajectories are depicted and the convergence to the static swimming position can be seen. As expected, the higher the sphere density, the longer the oscillations last.

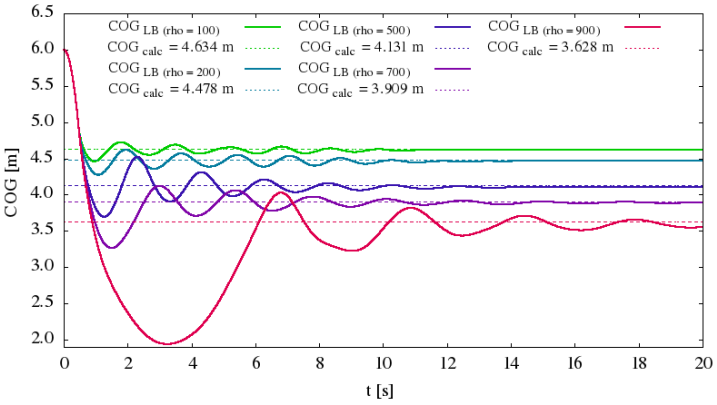


Figure 8: Sphere trajectories for different densities

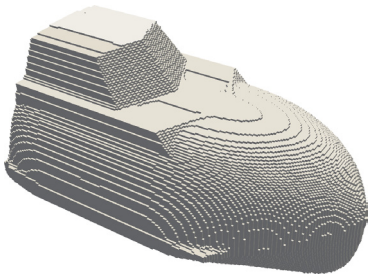


Figure 9: Voxel geometry of the Hatecke GFF(-T) 5.5 free fall boat

4 APPLICATION: FREEFALL LIFEBOAT

The validated code finally will be applied to the free fall and ditching of the freefall lifeboat Hatecke GFF(-T) 5.5M. A voxelized representation of geometry is depicted in Fig. 9. The numerical results and a comparison to reference data [10] will be presented at the conference.

5 CONCLUSIONS

In this paper, the validation of the Lattice Boltzmann based solver elbe for free surface flow problems involving nonlinear interactions of fluid and structure was presented. The model uses a VOF interface capturing approach and is coupled to a quaternion-based motion modeler in a bidirectional, explicit manner.

Three validation test cases with rather simple geometries were addressed. The results demonstrate that the proposed numerical methodology is generally able to produce accurate results for three-dimensional FSI applications, such as the water entry of a rigid sphere. Due to the straightforward grid generation, elbe is also applicable to more complex, three-dimensional geometries, as present in large-scale applications in marine engineering. The numerical results for the free fall and subsequent ditching of a free-fall rescue boat will be presented at the conference as an application example.

The authors gratefully acknowledge support for this research from the nVIDIA Academic Partnership Program (APP).

REFERENCES

[1] P. L. Bhatnagar, E. P. Gross, and M. Krook. A Model for Collision Processes in Gases. I. Small Amplitude Processes in Charged and Neutral One-Component Systems. Phys. Rev., 94(3):511–525, May 1954.

[2] M. Bouzidi, M. Firdaouss, and P. Lallemand. Momentum transfer of a lattice-Boltzmann fluid with boundaries. Physics of Fluids, 13:3452–3459, 2001.

[3] D. d'Humieres, I. Ginzburg, M. Krafczyk, P. Lallemand, and L.-S. Luo. Multiple-Relaxation-Time Lattice Boltzmann models in three dimensions. Royal Society of London Philosophical Transactions Series A, 360:437–451, 2002.

[4] S. Geller. Ein explizites Modell für die Fluid-Struktur-Interaktion basierend auf LBM und p-FEM. PhD thesis, Fakultät Architektur, Bauingenieurwesen und Umweltwissenschaften der Technischen Universität Carolo-Wilhelmina zu Braunschweig, 2010.

[5] I. Ginzburg and D. d'Humieres. Multireflection boundary conditions for lattice Boltzmann models. Physical Review E, 68(6):066614.1–066614.30, December 2003.

[6] I. Ginzburg and K. Steiner. Lattice Boltzmann model for free-surface flow and its application to filling process in casting. J. Comput. Phys., 185(1):61–99, 2003.

[7] A. K. Gunstensen, D. H. Rothman, S. Zaleski, and G. Zanetti. Lattice Boltzmann model of immiscible fluids. Phys. Rev. A, 43(8):4320–4327, Apr 1991.

[8] Z. Guo, C. Zheng, and B. Shi. Discrete lattice effects on the forcing term in the lattice Boltzmann method. Physical Review E, 65(4):046308.1 – 046308.6, April 2002.

[9] W. L. Haberman and R. M. Sayre. Motion of rigid and fluid spheres in stationary and moving liquids inside cylindrical tubes. Technical Report 1143, Dept. of the Navy, David Taylor Model Basin, Hydromechanics Laboratory, October 1958.

[10] J. Hatecke. Design Study Freefall Lifeboat GFF(-T) 5.5M. Technical Report Report No. 2006-20, Sachverständigenbüro Dipl.-Ing. Jan Hatecke, 2007.

[11] X. He and L.-S. Luo. Lattice Boltzmann model for the incompressible Navier-Stokes equation. Journal of Statistical Physics, 88:927–944, 1997.

[12] C. Janßen and M. Krafczyk. A lattice Boltzmann approach for free-surface-flow simulations on non-uniform block-structured grids. Computers and Mathematics with Applications, 59(7):2215 – 2235, 2010.

[13] C. Janßen and M. Krafczyk. Free surface flow simulations on GPGPUs using LBM. Computers and Mathematics with Applications, 61(12):3549–3563, June 2011.

[14] C. F. Janßen. elbe - efficient lattice boltzmann environment. http://www.tuhh.de/fds/research/current-projects/elbe.html.

[15] M. Junk and Z. Yang. Pressure boundary condition for the lattice Boltzmann method. Comput. Math. Appl., 58(5):922–929, 2009.

[16] N. Koliha. Development of a quaternion-based 6-DOF model for the simulation of floating bodies. Bachelor thesis, Schriftenreihe Schiffbau, TU Hamburg-Harburg, 2011.

[17] C. Körner, M. Thies, T. Hofmann, N. Thürey, and U. Rüde. Lattice Boltzmann Model for Free Surface Flow for Modeling Foaming. Journal of Statistical Physics, 121(18):179–196, October 2005.

[18] M. Krafczyk, J. Tölke, and L.-S. Luo. Large-eddy simulations with a multiple-relaxation-time LBE model. Int. J. Mod. Phys. B, 17:33–39, 2003.

[19] A.J.C. Ladd. Numerical simulations of particulate suspensions via a discretized Boltzmann equation. Part 1. Theoretical foundation. Journal of Fluid Mechanics, 271:285–309, 1994.

[20] P. Lallemand, L.-S. Luo, and Y. Peng. A lattice Boltzmann front-tracking method for interface dynamics with surface tension in two dimensions. Journal of Computational Physics, 226(2):1367–1384, 2007.

[21] N.Q. Nguyen and A.J.C. Ladd. Sedimentation of hard-sphere suspensions at low Reynolds number. J. Fluid Mech, 535:73 – 104, 2004.

[22] P.E. Nikravesh. Computer-Aided Analysis of Mechanical Systems. Prentice-Hall, 1988.

[23] Y. H. Quian, D. d'Humieres, and P. Lallemand. Lattice BGK models for Navier Stokes equations. Europhysics Letters, 17:479–484, 1992.

[24] L. Schiller and A.Z. Naumann. Ueber die grundlegenden Berechnungen bei der Schwerkraftaufbereitung. Zeitschrift des Vereines Deutscher Ingenieure, 77(12):318–320, 1933.

[25] N. Thürey and U. Rüde. Stable free surface flows with the lattice Boltzmann method on adaptively coarsened grids. Computing and Visualization in Science, page ., 2008.

[26] J. Tölke and M. Krafczyk. Implementation of a Lattice Boltzmann kernel using the Compute Unified Device Architecture developed by nVIDIA. Computing and Visualization in Science, 1:29–39, 2008.

[27] J. Tölke and M. Krafczyk. TeraFLOP computing on a desktop PC with GPUs for 3D CFD. International Journal of Computational Fluid Dynamics, 22:443–456, 2008.

[28] X. Wei, Y. Zhao, Z. Fan, W. Li, F. Qiu, S. Yoakum-Stover, and A. Kaufman. Lattice-based flow field modeling. IEEE Transactions on Visualization and Computer Graphics, 10(6):719–729, 2004.

[29] Y. Zhao. Melting and flowing in multiphase environments. Computers & Graphics, 30(4):519–528, 2006.

[30] H. Zhu, X. Liu, Lui Y., and E. Wu. Simulation of miscible binary mixtures based on lattice Boltzmann method. Computer Animation and Virtual Worlds, 17:403–410, 2006.

V International Conference on Computational Methods in Marine Engineering
MARINE 2013
B. Brinkmann and P. Wriggers (Eds)

A NEW TURBULENT THREE-DIMENSIONAL FSI BENCHMARK FSI-PFS-3A: DEFINITION AND MEASUREMENTS

Andreas Kalmbach, Guillaume De Nayer and Michael Breuer

Professur für Strömungsmechanik (PfS), Helmut–Schmidt–Universität Hamburg
Holstenhofweg 85, D–22043 Hamburg, Germany
e-mail: kalmbach / denayer / breuer@hsu-hh.de

Keywords: FSI, experimental investigation, PIV, turbulent flow, three-dimensional benchmark case

Abstract. *In the last decade, the demand for the prediction of complex multi-physics problems such as fluid-structure interaction (FSI) has strongly increased. For the development and improvement of appropriate numerical tools several test cases were designed in order to validate the numerical results based on experimental reference data [4, 12, 13, 8, 9, 10]. Since FSI problems often occur in turbulent flows also in the experiments similar conditions have to be provided. In the test-case FSI-PfS-1a [7] presented in the first contribution to this session, a cylinder is used with an attached flexible rubber plate. The resulting FSI problem is nearly two-dimensional regarding the phase-averaged flow and the structure deformations. The actual test case FSI-PfS-3a is the reasonable further development step of this two-dimensional benchmark to a forced fully three-dimensional flow, which now also leads to a significant three-dimensional structure deformation. The cylinder is replaced by a truncated cone. Similar to FSI-PfS-1a [7] a rubber plate is attached at the backside. This geometrical setup is exposed to a constant flow at Re = 32,000 which is in the subcritical regime. Due to the linearly increasing diameter of the cone the alternating eddies in the wake even become larger resulting in correspondingly increasing structural displacements. Owing to these challenging flow and structure effects, this benchmark will be the next step for validating FSI predictions for real applications. The experiments are performed in a water channel with clearly defined and controllable boundary and operating conditions. For measuring the flow a two-dimensional mono-particle-image velocimetry (PIV) system is applied. In order to characterize the three-dimensional behavior of the flow, phase-averaged PIV measurements are performed at three different planes. The structural deformations are measured along a line on the structure surface with a time-resolved laser distance sensor. The resulting FSI problem shows a quasi-periodic deformation behavior so that a phase averaging of the results is reasonable. By phase-averaging turbulent fluctuations are averaged out and thus a comparison with corresponding numerical simulations based on LES [3] and RANS [12, 13] approaches is possible.*

1 INTRODUCTION

Numerical predictions play more and more an important role in most engineering fields due to the high costs of experiments and the rise of computational resources. Furthermore, engineering problems tackled by numerical simulations always have become more challenging and nowadays often involve so-called multi-physics applications. Fluid and structure interaction (FSI) is an example of such a multi-physics engineering field: A rigid but elastically mounted body or a deformable structure, such as a rotor blade or a membranous awning, is exposed to a fluid flow. The fluid forces acting on the structure move or deform it. These displacements or deflections modify the flow resulting in a coupling process between the fluid and the structure.

The Department of Fluid Mechanics of HSU Hamburg is working on the long-term objective of coupled simulations of big lightweight structures such as thin membranes exposed to turbulent flows (outdoor tents, awnings...). In order to approach this goal, a FSI code was developed and the validation process is presented for example in [3]. The FSI program is based on two separate highly specialized solvers (one for the fluid, one for the structure) coupled by a third code. Both solvers were at first checked and validated separately. Then, the full multi-physics program was tested considering a laminar FSI benchmark [17, 18]. A 3D turbulent test case, denoted FSI-LES, was also taken into account to prove the applicability of the newly developed coupling scheme in the context of large-eddy simulations (LES). However, the validation was not complete, because of the lack of experimental data to compare with.
For this purpose several FSI test cases were recently developed. In the test-case FSI-PfS-1a [7] presented in the first contribution to this session, a cylinder is used with an attached flexible rubber plate. The resulting FSI problem is nearly two-dimensional regarding the phase-averaged flow and the structure deformations in the first swiveling mode. Detailed comparisons between experimental measurements and numerical LES predictions were carried out [7]. Another test case, denoted as FSI-PfS-2a [13], showed more complex swiveling behavior in the second mode which is achieved by applying a steel weight to the configuration of FSI-PfS-1a. This test case was also investigated by experimental measurements and numerical URANS predictions. The actual test case, FSI-PfS-3a, is the reasonable further development step of these two-dimensional benchmarks to a forced fully three-dimensional flow, which now also leads to a significant three-dimensional structure deformation. Therefore, the goal of this paper is to present a turbulent FSI test case relying on detailed experimental investigations for the deformation of the structure and the flow field carried out at PfS Hamburg.

The paper is organized as follows: The new test case is completely described in Section 2. The experimental investigations including the water tunnel and the measuring techniques are presented in Section 3. Due to cycle-to-cycle variations of the FSI phenomenon observed in the experiment and in the simulation, the results have to be phase-averaged prior to a detailed comparison. The process is given in Section 4. Finally, the experimental results are presented and discussed in Section 5.

2 DESCRIPTION OF THE TEST CASE FSI-PfS-3a

The fluid-structure interaction test case described in this paper is denoted FSI-PfS-3a. It is composed of a flexible thin structure with a distinct thickness h clamped behind a fixed rigid non-rotating truncated cone installed in a water channel (see Fig. 1). The mildly tapered cone (ratio $D_2/D_1 = 1.5$) has a central position in the experimental test section, which yields a blocking ratio of about 12.2 %. The geometrical dimensions are resumed in Table 1. In the experimental setup the sketched section of the water channel is turned 90 degrees. Therefore,

the gravitational acceleration g points in x-direction in Fig. 1. In the experiment the flexible structure has a width w slightly smaller than the width of the test section W. Hence a small gap of about 1.5 mm exists between the side of the deformable structure and both lateral channel walls.

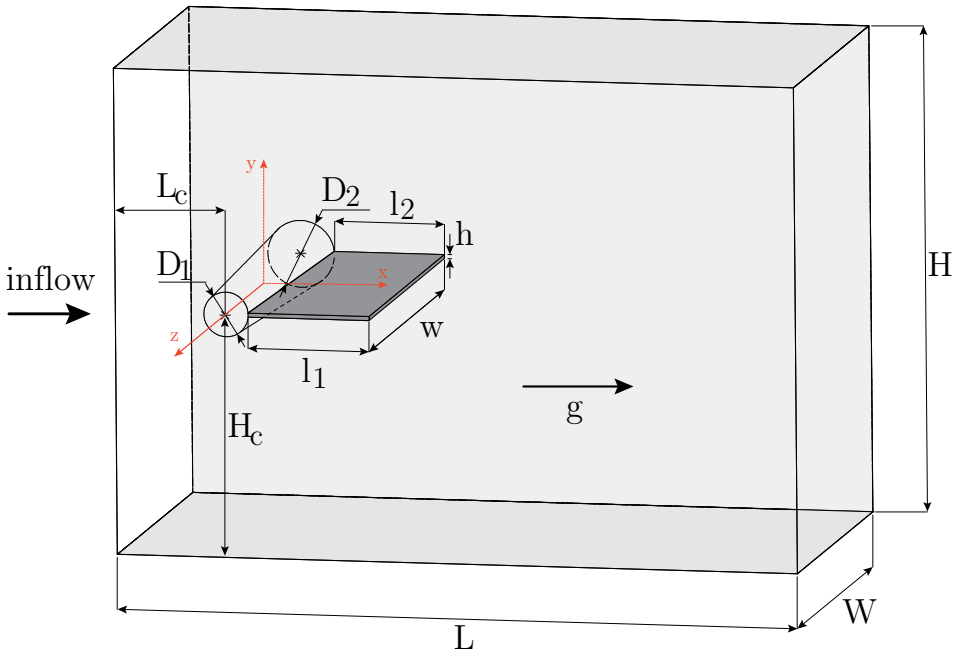


Figure 1: Sketch of the geometrical configuration of the benchmark case FSI-PfS-3a.

Small cone diameter	$D_1 = D$	$= 0.022$ m	
Large cone diameter	D_2	$= 0.033$ m	$D_2/D_1 = 1.5$
Cone center x-position	L_c	$= 0.077$ m	$L_c/D_1 = 3.5$
Cone center y-position	H_c	$= H/2 = 0.120$ m	$H_c/D_1 \approx 5.45$
Test section length	L	$= 0.338$ m	$L/D_1 \approx 15.36$
Test section height	H	$= 0.240$ m	$H/D_1 \approx 10.91$
Test section width	W	$= 0.180$ m	$W/D_1 \approx 8.18$
Long deformable structure length	l_1	$= 0.060$ m	$l/D_1 \approx 2.72$
Short deformable structure length	l_2	$= 0.0545$ m	$l/D_1 \approx 2.22$
Deformable structure thickness	h	$= 0.0021$ m	$h/D_1 \approx 0.09$
Deformable structure width	w	$= 0.177$ m	$w/D_1 \approx 8.05$

Table 1: Geometrical configuration of the FSI-PfS-3a benchmark.

The fluid used is water with an inflow velocity of $u_{\text{inflow}} = 0.969$ m/s. All experiments were performed under standard conditions at $T = 20°\text{C}$ ($\rho_f = 998.20\,\text{kg}\,\text{m}^{-3}$, $\mu = 1.0 \cdot 10^{-3}\,\text{Pa}\,\text{s}$). Based on the inflow velocity chosen and the cone diameter D_1 and D_2 the Reynolds number of the experiment is equal to $Re_{D1} = 2.13 \cdot 10^4$ and $Re_{D2} = 3.20 \cdot 10^4$, respectively. The material used for the flexible structure is rubber with a density $\rho_s = 1360\,\text{kg}\,\text{m}^{-3}$, a Young's modulus $E = 16$ MPa and a Poisson's ratio $\nu = 0.48$.

3 EXPERIMENTAL INVESTIGATIONS

The experimental investigations are carried out in the fluid mechanics lab of PfS with the help of a water channel, a particle-image velocimetry (PIV) system and a laser distance sensor. Several preliminary tests are performed to find the best working conditions in terms of good reproducibility of the results within the turbulent flow regime.

3.1 Description of the Water Channel and of the Flow

The water channel (Göttingen type, see Fig. 2) was designed and built at LSTM Erlangen [8, 9, 10] within the DFG research unit FOR 493 [5]. The channel ($2.8\,\mathrm{m} \times 1.3\,\mathrm{m} \times 0.5\,\mathrm{m}$, fluid volume of $0.9\,\mathrm{m}^3$) has a rectangular flow path and includes several rectifiers and straighteners to guarantee a uniform inflow into the test section. This test section has the geometry as described in Section 2 and possesses windows on three sides to allow optical measurement systems such as particle-image velocimetry. The structure (here the cone) is attached on the backplate of the test section and additionally fixed at the front glass plate. The water is put in motion by a 24 kW axial pump.

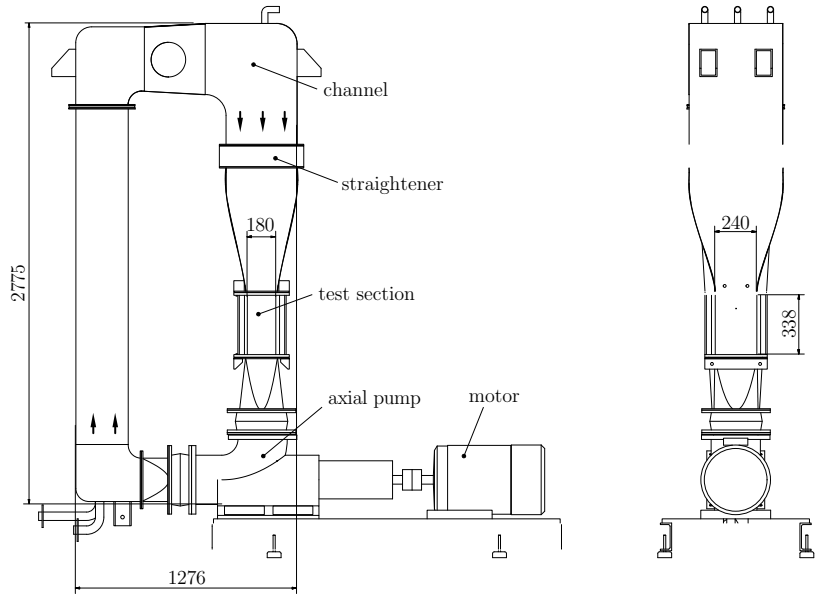


Figure 2: Sketch of the water channel (dimensions given in mm).

Based on the inflow velocity and the corresponding Reynolds number chosen, the flow around the cone is in the subcritical regime. Consequently, the boundary layers are still laminar, but transition to turbulence takes place in the free shear layers evolving from the separated boundary layers behind the apex of the cone. In the inflow section the velocity fields were measured by a laser-Doppler velocimetry system and was found to be nearly uniform except of course at the section walls. Furthermore, a low inflow turbulence level was measured ($\mathrm{Tu}_{\mathrm{inflow}} = 0.022$).

3.2 Measuring Techniques

The experimental investigations for a FSI problem have to describe both, the structure and the fluid coupled in time. In [8] the same camera was used to get the velocity fields and the

structural deflections. This method only works well for 2D FSI problems. In the present paper the turbulent flow regime causes cycle-to-cycle variations and significant three-dimensional deformations of the structure. Therefore, the displacement of the shell can not be extracted from the PIV images and a laser distance sensor is used instead. A 2D particle-image velocimetry (PIV) setup is applied to capture the velocity fields of the flow at three xy-planes at $(z/D)_{large} = -2.72$, $(z/D)_{middle} = 0$ and $(z/D)_{small} = 2.72$.

3.2.1 Particle-Image Velocimetry Setup

The particle-image velocimetry setup (cf. Adrian [1]) is classical: A single CCD camera measures the two components of the fluid velocity within the planar section illuminated by a laser light sheet (see Fig. 3). To assure a uniform illumination in front of and especially behind the structure, it was necessary to light up the flow field from both sides. The simultaneous illumination is realized by splitting the laser beam. Most of the flow field is illuminated by the first beam, which is directly coupled into a light sheet optic. The second beam is redirected by three specific laser mirrors to the other side of the test section forming a second light sheet on the backward region. The fluid is laden by small particles, which are following the flow and reflect the laser light. By taking two images of the reflection fields in a short time interval Δt, a cross-correlation technique can estimate the displacement of the particles using an equidistant grid. Using these displacements and the time interval Δt the velocity field in the illuminated plane can be calculated.

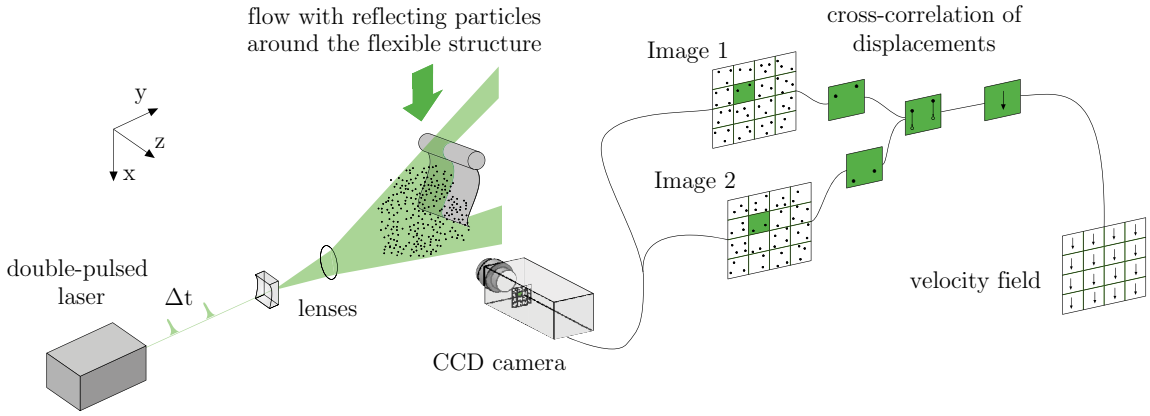


Figure 3: Measuring principle of a two-component PIV setup for the flow around the flexible structure.

Phase-resolved PIV-measurements (PR-PIV) are used to generate phase-averaged fluid velocity fields involving the structure deflections (see Section 4). The PR-PIV is carried out with a 4 Mega-pixel camera (TSI Powerview 4MP, charge-coupled device (CCD) chip) and a pulsed dual-head Neodym:YAG laser (Litron NanoPIV 200) with an energy of 200 mJ per laser pulse. The time between the frame-straddled laser was set to $\Delta t = 600\,\mu$s. Laser and camera are controlled by a TSI synchronizer (TSI 610035) with 1 ns resolution. The tracer particles are silver-coated hollow glass spheres (SHGS) with an average diameter of $d_{\text{avg,SHGS}} = 10\,\mu$m. The camera takes 12 bit pictures with a frequency of about $2.5\,\text{s}^{-1}$ and a resolution of 1910×1483 px with respect to the rectangular size of the test section. The grid used for the estimation of the displacements of the particles has a size of 169×169 cells and is calibrated with an average factor of 150 μm/px, covering three planar flow fields of $x/D \approx -3.0$ to 7.5 and $y/D \approx -4.0$ to 4.0

at $(z/D)_{large} \approx -2.72$, $(z/D)_{middle} \approx 0$ and $(z/D)_{small} \approx 2.72$. In order to generate one phase-resolved position (see Section 4), around 100 measurements are taken. Preliminary studies with more and fewer measurements showed that this number of 100 measurements represents a good compromise between accuracy and effort.

3.2.2 Laser Distance Sensor

In order to be able to capture the 3D structural deflections, a non-contact measurement method based on a laser distance sensor is applied. A laser triangulation technique is chosen because of the known geometric dependencies, the high data rates, the small measurement range and the resulting higher accuracy in comparison with other techniques such as laser phase-shifting or laser interferometry. The laser triangulation method is based on a laser beam which is focused onto the deformable object. A part of the light is reflected to a CCD-chip, located near the laser. When the object deforms itself, the distance between it and the sensor varies. This is detected on the CCD-chip. With this change on the CCD-chip and an internal length calibration adjusted to the applied measurement range, the deformation of the structure is calculated. To study simultaneously more than one point of the structure, a multiple-point triangulation sensor is applied (Micro-Epsilon scanControl 2750, see Fig. 4). This sensor uses a matrix of CCD chips to detect the displacements on up to 640 points along a laser line reflected on the surface of the structure with a data rate of 800 profiles per second. The laser line is positioned in a horizontal ($x/D \approx 3.1$, see Fig. 4(a)) and in a vertical alignment (see Fig. 4(b)) and has an accuracy of 40 μm. Due to the different refraction indices of air, glass and water a custom calibration is performed to take the modified optical behavior of the emitted laser beams into account.

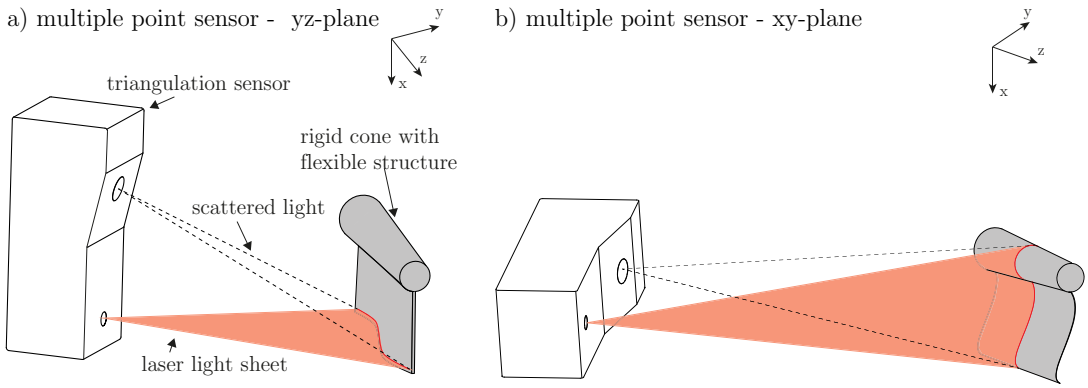


Figure 4: Setup and alignment of the multiple-point laser sensor on the flexible structure in a) yz-plane and b) xy-plane.

4 GENERATION OF PHASE-RESOLVED DATA

Each flow characteristic of a quasi-periodic FSI problem can be written as a function $f = \bar{f} + \tilde{f} + f'$, where $\bar{f}$ describes the global mean part, $\tilde{f}$ the quasi-periodic part and f' a random turbulence-related part (cf. [6, 16]). This splitting can also be written in the form $f = \langle f \rangle + f'$, where $\langle f \rangle$ is the phase-averaged part, i.e., the mean at constant phase. In order to be able to compare numerical results and experimental measurements, the irregular turbulent part f' has to be averaged out. Therefore, the present data are phase-averaged to obtain only the phase-resolved contribution $\langle f \rangle$ of the problem.

The present setup uses a reconstruction method for the phase averaging process. It consists of the multiple-point triangulation sensor (described in Section 3.2.2) and the synchronizer of the PIV system. Each measurement pulse of the PIV system is detected in the data acquisition of the laser distance sensor, which measures the structure deflection with a data rate of 800 profiles per second simultaneously with the PIV system.

The next steps for the post-processing of the experimental data are applied for each measurement plane separately and are processed as follows: Out of the structural data of the measurements in the three xy-planes ($z/D_{large} \approx -2.72$, $z/D_{middle} \approx 0$ and $z/D_{small} \approx 2.72$) the last reliable measurable point ($x/D \approx 3.1$) near the edge of the structure is monitored. With the resulting displacements as a function of time the reference period of the structure movement of this plane is calculated as follows. For this purpose the zero-crossings from negative to positive values of the y-displacements represent the beginning of a period. Applied to the whole time series of y-displacements, this method provides the beginning and the end of all periods independent of their period length as displayed in Fig. 5(a). The next step is the calculation of the average period duration by arithmetically averaging all period lengths found in the previous step leading to the reference period duration. A first averaging step calculates the average y-displacements covering all available measuring data from the laser distance sensor in time and space. For this purpose each period of the swiveling motion with varying interval length is divided into 137 equidistant parts. For each individual part an average of the y-displacements is predicted resulting in a reference period consisting of 137 data points. With this fine decomposition allowing a detailed representation of the structure deformation, each part only contains a small number of flow measurements. Therefore, the time or phase-angle interval per part has to be enlarged by a second averaging step for the structure data. The reference period and all recorded periods are now split into n parts covering larger equidistant phase-angle intervals (Fig. 5(b)) than before.

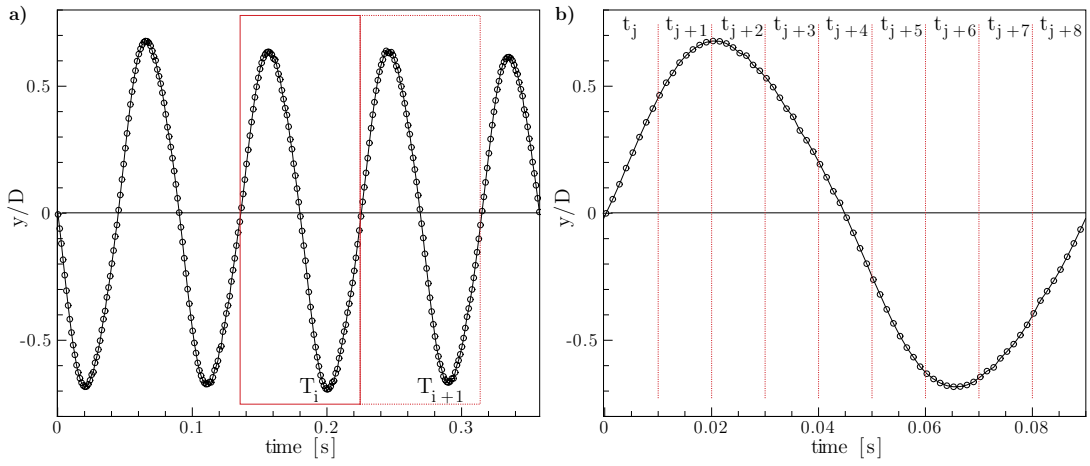


Figure 5: Phase-averaging procedure: (a) Period detection in y-displacements at a point near the trailing edge of the structure, (b) Period splitting into n parts (here for visibility only 9 parts) for the phase-averaging method.

In the present case n is set to 23 since it is a good compromise regarding a reasonable resolution of the phase-averaged motion and the number of measurements building each specific moment of the phase-averaged representation. A comparison of the corresponding 137 structure phase angles with the data of the newly defined reference period is performed for each part $n = 1$ to 23. The fluid and structure data of all matching profiles are assigned to the specific time-phase angle of the reference period, enabling the phase averaging of the PIV and structure

measurements. For the PIV experiments 2,000 single measurements per plane are taken. This is a compromise between the amount of data to be stored and the resulting post-processing costs and the limitations of the capture time of the laser distance sensor.
The phase-averaging procedure is also applied to the structure measurements in the yz-plane (see Fig. 4(a)) to receive simultaneous y-displacements in the monitored points z/D_{large}, z/D_{middle} and z/D_{small}. With these post-processing steps three separate phase-averaged reference structure and flow periods in the xy-plane and a single phase-averaged structure reference period in the yz-plane are obtained. A last post-processing step is necessary due to the phase-shift of the flow and structure movement between the three planes. Based on the phase-averaged results of the structural measurements in the yz-plane (see Fig. 4(a)) the precise phase shift between the planes is calculated. The displacements on the plane at the large cone diameter $(z/D)_{large} \approx -2.72$) are chosen to define the beginning and end of the reference period. Afterwards, the calculated phase shifts are separately applied to the phase angles of the flow fields in the three xy-planes.

5 RESULTS AND DISCUSSION

5.1 Deflection of the Structure

Similar to a flow around a cylinder, the flow behind a single truncated cone creates a von Kàrmàn vortex street. Several studies [15, 14, 11] describe different vortex shedding frequencies along the cone axis according to the three-dimensional geometry. This leads to a splitting of vortices (or vortex dislocation) in the wake behind the small cone diameter and therefore to a complex and fully three-dimensional flow. Furthermore, the size of the vortices are directly dependent on the local cone diameter. Nevertheless, in the present case the rubber plate acts like a splitter plate [2] and modifies the flow behavior in a significant way. The movement of the plate suppresses the different vortex shedding frequencies along the cone leading to only one shedding frequency like in the wake of a cylinder. Nevertheless, the influence of the linearly increasing cone diameter is still present in the flow field. The three-dimensional flow with wide vortices behind the large cone diameter and smaller vortices on the other side, induces inhomogeneous pressure forces on the rubber plate. Due to the periodic and alternating shedding of vortices this effect is also time-dependent and creates a wavelike deformation of the rubber plate (see Fig. 6).

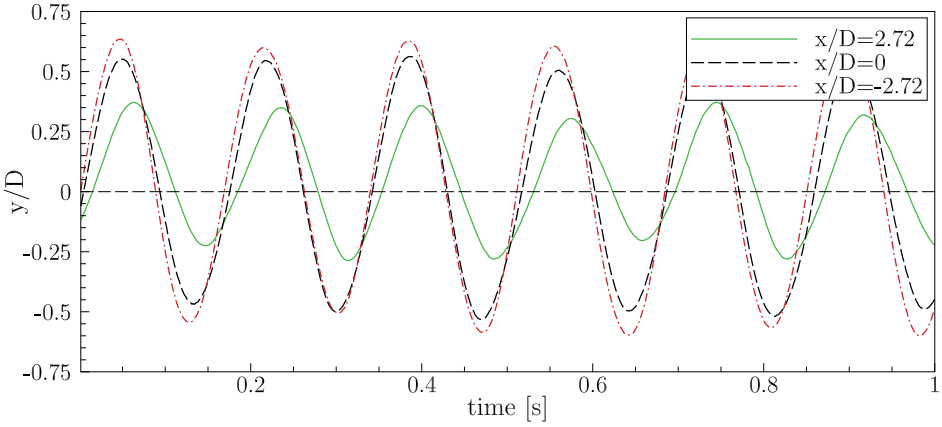


Figure 6: Structural results: raw signal of the deflection of the rubber plate at $(z/D)_{large} \approx -2.72$, $(z/D)_{middle} \approx 0$ and $(z/D)_{small} \approx 2.72$ measured in the yz-plane.

Summarizing these effects the FSI problem is quasi-periodic but fully three-dimensional with large structure deformations in negative z-direction (large cone diameter) and smaller deflections in positive z-direction (small cone diameter). In Fig. 6 the displacements of the structure within a time interval of one second (raw data) is presented. The plot is based on the displacement of three points located at the surface of the rubber plate and in a distance of 3 mm ($x/D = 3.1$) from the shell extremity. This point is chosen due to the measuring limitations of the structure sensor in resolution and illumination. The time series of these three displacement plots reveal cycle-to-cycle variations regarding the displacement amplitude and the swiveling frequency. Furthermore, the phase shift mentioned above is clearly visible. The structure at the large cone diameter is leading the structural motion. The structure in the middle of the domain follows with a phase shift of about 10 degrees. Finally, the structure at the small diameter reaches the same state with a phase delay of about 33 degrees with respect to the large diameter.

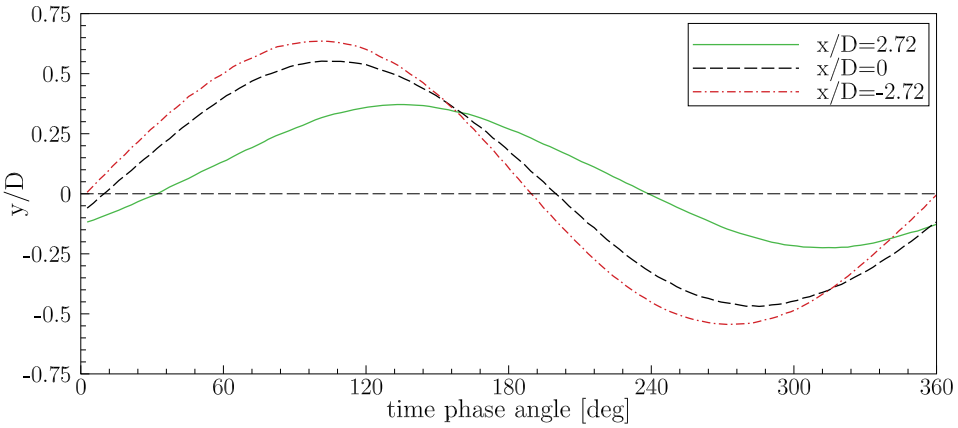


Figure 7: Structural results: phase-averaged period of the deflection of the rubber plate at $(z/D)_{large} \approx -2.72$, $(z/D)_{middle} \approx 0$ and $(z/D)_{small} \approx 2.72$.

In order to allow a quantitative comparison between the experimental results and numerical data all results are phase-averaged as explained in the previous section. With this process the mean period of the FSI phenomenon in flow and structure is generated. The results for the structure are presented in Fig. 7 for the three planes and in Fig. 8 for the entire line along the extremity. Based on the phase-averaged period of the deflections depicted in Fig. 7 the phase shift between the different planes is even more clearly visible. The phase difference between the small and middle diameter is significantly larger than between the middle and the large diameter. Thus the wave speed of the structural deflections in z-direction is not constant, which can be explained by minor pressure forces on this part ($z/D > 0$) of the structure and thus lower deformation rates there. Furthermore, the difference in the amplitudes also visibly differs between the small and the middle diameter compared to the middle and the large diameter.

The mentioned differences in the displacements along the truncated cone axis with mean extrema of the displacement are presented in Table 2. On first sight, the results in Figs. 7 and 8 seem to be not symmetric. But this asymmetry mainly occurs by the chosen measuring point on the surface of the structure. In Table 2 the measured mean y-displacements and those calculated for the chord are confronted. With respect to the calculated point at the chord of the structure the displacements are nearly symmetric. The remaining deviations from symmetry are perhaps caused by the slightly anisotropic material behavior of the rubber. The frequency of the FSI

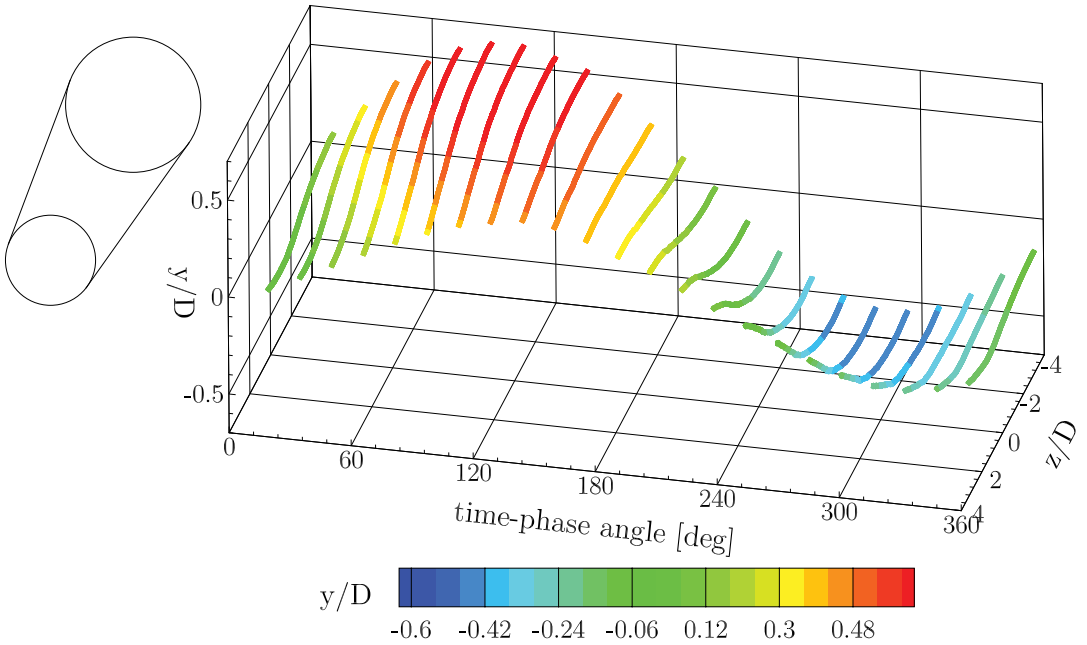


Figure 8: Structural results: phase-averaged period of the deflection of the rubber plate in the yz-plane near to the extremity of the structure (cone not in scale).

phenomenon, i.e., the frequency of the y-displacements, is about $f = 5.82$ Hz which correspond to Strouhal numbers of $St_{large} \approx 0.20$, $St_{middle} \approx 0.17$ and $St_{small} \approx 0.13$, respectively.

	$(y/D)_{max}$	$(y/D)_{min}$	$(y/D)_{max}$	$(y/D)_{max}$	$(y/D)_{max}$	$(y/D)_{max}$
plane	large	large	middle	middle	small	small
point at surface	0.635	−0.543	0.551	−0.469	0.372	−0.225
point at chord	0.59	−0.588	0.506	−0.514	0.327	−0.270

Table 2: Measured (surface) and calculated (chord) mean y-displacements.

In Fig. 9 the phase-averaged deflections in the three xy-planes and the displacements in the yz-plane are merged into a three-dimensional mesh, illustrating the three-dimensional deformation of the rubber plate. At a phase angle of 16 degree the deflections all over the rubber plate are small. In the further movement at 78 degree the displacements at the larger diameter nearly reach their maximum, where in positive z/D-direction (small cone diameter) only small deflections are noticeable. This part catches up at the next phase angle shown for 141 degree where the displacements on the extremity are almost constant in z-direction. The following phase angles at 203, 266 and 329 degrees depict similar states of the structure movement in the opposite direction.

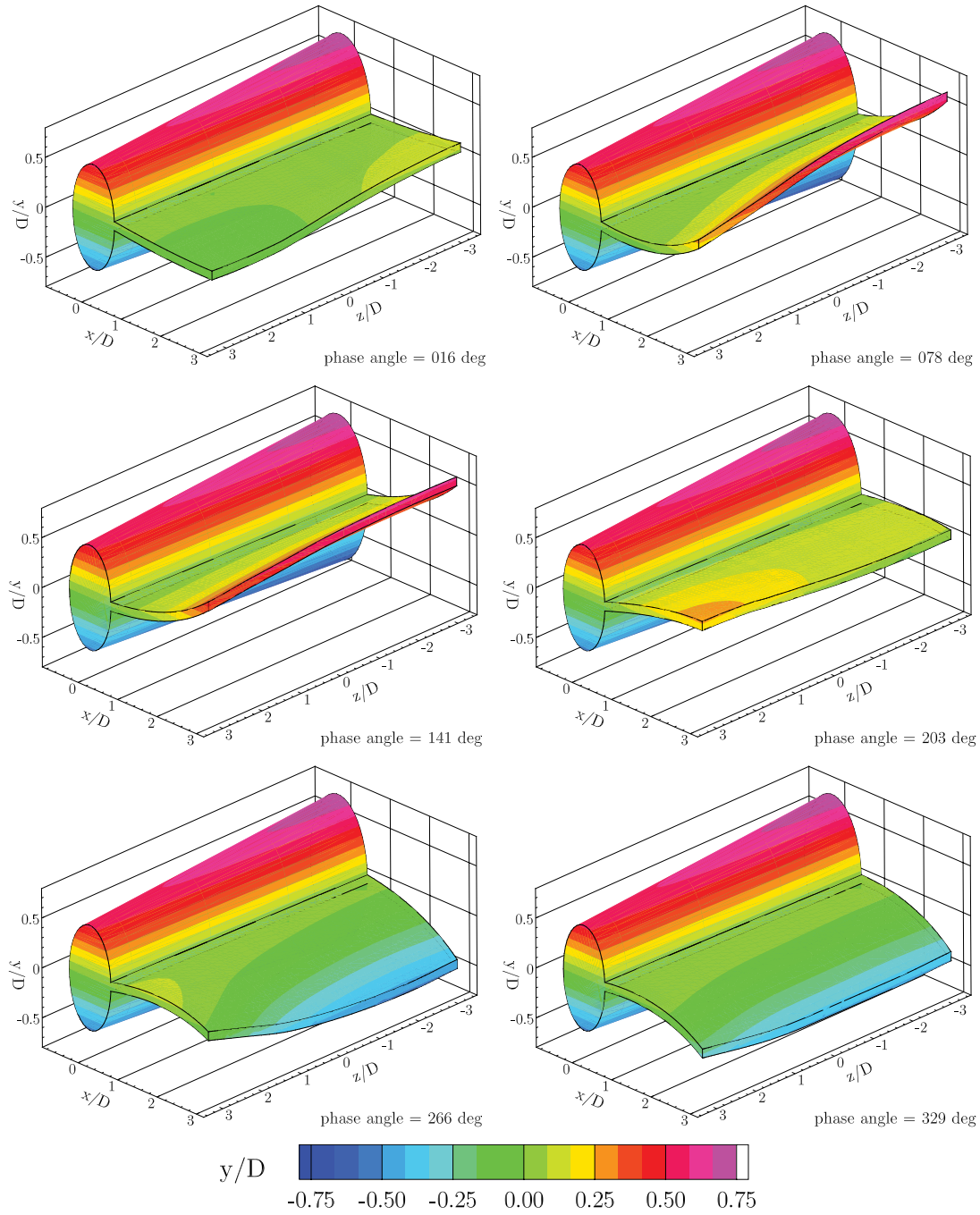


Figure 9: Structural results: interpolated and phase-averaged three-dimensional structure deformations for the reference period (note the axis ratio $(y/D)/(x/D) = 2$).

5.2 Flow Field

A selection of phase-averaged flow fields is depicted in Fig. 10. These six states of the mean period of the FSI problem illustrate the significant three-dimensional characteristic of the flow. The shed vortices are convected downstream leading to an alternating vortex pattern in the wake of the structure. In the wake of the structure the characteristic recirculation areas are observed. Finally, the shed vortices leave the region of interest. All planes ($(z/D)_{large} \approx -2.72$, $(z/D)_{middle} \approx 0$ and $(z/D)_{small} \approx 2.72$) at a single phase angle show the distinctive behavior

of this wake vortex. Nevertheless, compared to each other the three planes differ in the vortex size and the area of the wake influenced. The shed vortex on the plane $(z/D)_{large} \approx -2.72$ is much larger in size and velocity magnitude than on the plane $(z/D)_{small} \approx 2.72$. Also the mentioned phase shift between the large and the small cone diameter is visible through the staggered location of the vortex centers.

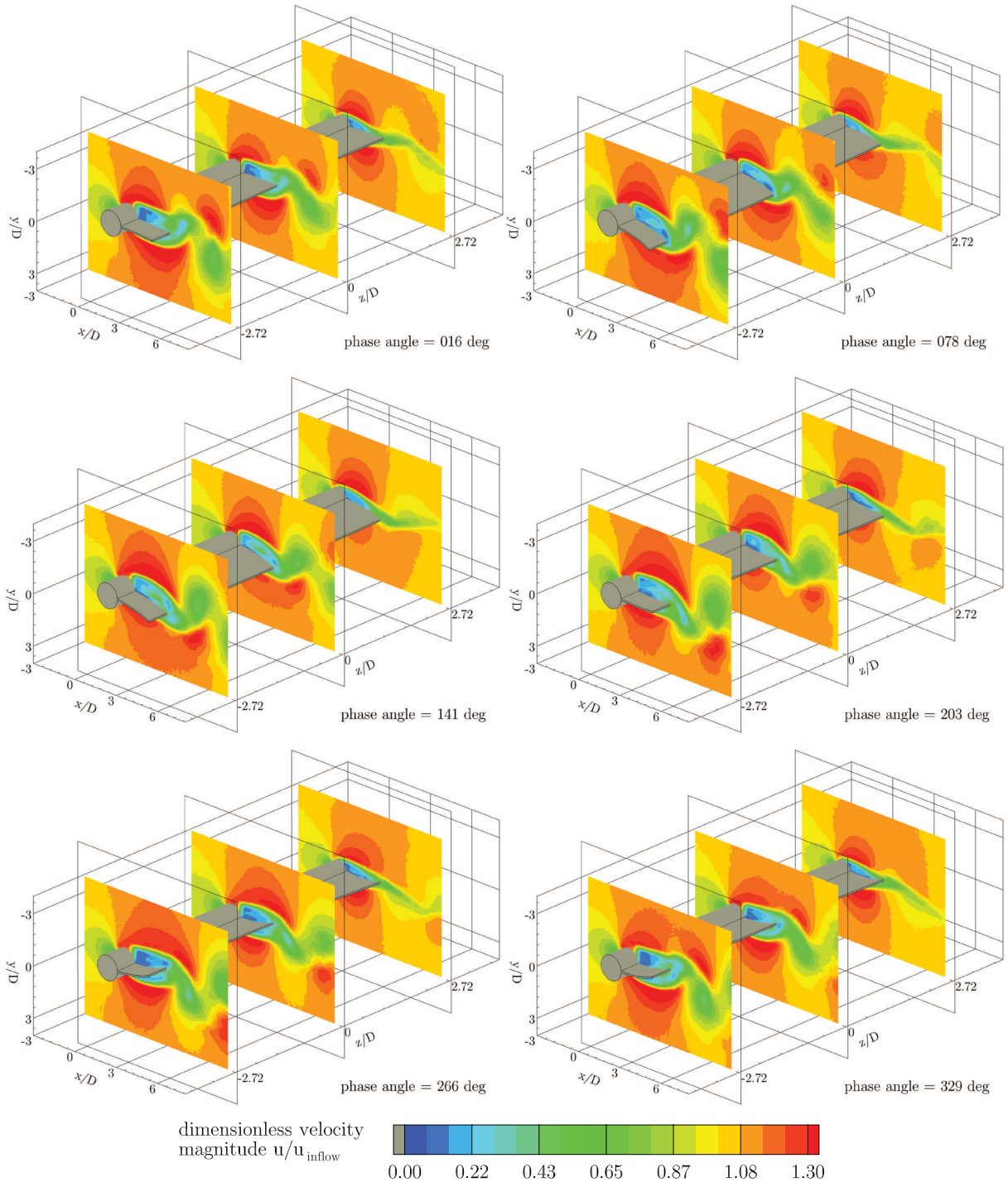


Figure 10: Phase-averaged PIV and structure results for the reference period.

6 CONCLUSIONS AND OUTLOOK

The paper presents a new three-dimensional FSI benchmark case denoted FSI-PfS-3a. The structure consists of a rigid truncated cone and a flexible membranous rubber tail fixed at the backside of the cylinder. According to the cone the flow is in the subcritical regime ($Re_{D1} = 2.1 \cdot 10^4$ or $Re_{D2} = 3.2 \cdot 10^4$). The FSI problem shows a quasi-periodic but fully three-dimensional behavior with larger structure deformations for increasing cone diameter. The detailed experimental investigations using optical measurements techniques for both, the fluid flow and the structure deformation, deliver comprehensive data for a reasonable validation process of FSI simulation tools.

7 AVAILABLE DATA FOR COMPARISON

This benchmark FSI-PfS-3a should help to evaluate and improve numerical FSI codes. Therefore, our department supports all interested groups with the experimental data presented in this paper and the first contribution to this session. Available for comparison are the 23 single phase-averaged two-dimensional reference velocity fields of the PIV measurement series at the three planes mentioned. For the flexible structure the raw and phase-averaged data of the displacements can be provided. Furthermore, static and dynamic material tests not mentioned in the paper are also available to prove the structural modeling. All data are stored in ASCII and Tecplot formats. Please contact the authors for more information or visit our website http://www.hsu-hh.de/pfs (see Section "Forschung/Fluid-Struktur-Wechselwirkung") for additional content (e.g., pictures, movies) concerning this and all other FSI benchmarks.

Acknowledgments: Partial financial support by DFG under contract number BR 1847/12-1.

REFERENCES

[1] R. J. Adrian. Particle-imaging techniques for experimental fluid mechanics. *Annual Review of Fluid Mechanics*, 23(1):261–304, 1991.

[2] E.A. Anderson and A.A. Szewczyk. Effects of a splitter plate on the near wake of a circular cylinder in 2 and 3-dimensional flow configurations. *Experiments in Fluids*, 23(2):161–174, 1997.

[3] M. Breuer, G. De Nayer, M. Münsch, T. Gallinger, and R. Wüchner. Fluid-structure interaction using a partitioned semi-implicit predictor-corrector coupling scheme for the application of large-eddy simulation. *Journal of Fluids and Structures*, 29:107–130, 2012.

[4] M. Breuer and A. Kalmbach. Experimental investigations on fluid-structure interactions based on particle-image velocimetry. In A. Thess, C. Resagk, B. Ruck, A. Leder, and D. Dopheide, editors, *Proc. der 19. Gala–Fachtagung 'Lasermethoden in der Strömungsmesstechnik', Sept. 6–8, 2011*, pages 35–1–35–8, Universität Ilmenau, 2011.

[5] H.-J. Bungartz, M. Mehl, and M. Schäfer, editors. *Fluid Structure Interaction II: Modelling, Simulation, Optimization*, volume 73 of *Lecture Notes in Computational Science and Engineering, LNCSE*. Springer, Heidelberg, 2010.

[6] B. Cantwell and D. Coles. An experimental study of entrainment and transport in the turbulent near wake of a circular cylinder. *Journal of Fluid Mechanics*, 136(1):321–374, 1983.

[7] G. De Nayer, A. Kalmbach, M. Breuer, S. Sicklinger, and R. Wüchner. A fluid-structure interaction benchmark in turbulent flow (FSI-PfS-1a) – A complementary numerical/experimental investigation. *Journal of Fluids and Structures*, 2013. submitted.

[8] J. P. Gomes and H. Lienhart. Experimental study on a fluid-structure interaction reference test case. In H.-J. Bungartz and M. Schäfer, editors, *Fluid-Structure Interaction – Modelling, Simulation, Optimization*, volume 53 of *Lecture Notes in Computational Science and Engineering, LNCSE*, pages 356–370. Springer, Heidelberg, 2006.

[9] J. P. Gomes and H. Lienhart. Experimental benchmark: Self-excited fluid-structure interaction test cases. In H.-J. Bungartz, M. Mehl, and M. Schäfer, editors, *Fluid-Structure Interaction II – Modelling, Simulation, Optimization*, volume 73 of *Lecture Notes in Computational Science and Engineering, LNCSE*, pages 383–411. Springer, Heidelberg, 2010.

[10] J. P. Gomes and H. Lienhart. Fluid-structure interaction-induced oscillation of flexible structures in laminar and turbulent flows. *Journal of Fluid Mechanics*, 715:537–572, 2013.

[11] C.S. Jagadeesh. Dynamics of vortex shedding from slender cones. *Ph.D. thesis*, 2009. Queen Mary University of London.

[12] A. Kalmbach and M. Breuer. Investigations on fluid-structure interactions using volumetric particle-image velocimetry. In *16th Int. Symp. on Applications of Laser Techniques to Fluid Mechanics, July 09-12, 2012, Lisbon, Portugal*, 2012.

[13] A. Kalmbach and M. Breuer. Experimental PIV/V3V measurements and numerical RANS predictions of vortex-induced fluid-structure interaction in turbulent flow – A new benchmark FSI-PfS-2a. *Journal of Fluids and Structures*, 2013. submitted.

[14] V.D. Narasimhamurthy, H.I. Andersson, and B. Pettersen. Cellular vortex shedding behind a tapered circular cylinder. *Physics of Fluids*, 21:044106.1 – 044106.12, 2009.

[15] P.S. Piccirillo and C.W. van Atta. An experimental study of vortex shedding behind linearly tapered cylinders at low Reynolds number. *Journal of Fluid Mechanics*, 246:163–195, 1993.

[16] W. C. Reynolds and A. Hussain. The mechanics of an organized wave in turbulent shear flow. Part 3. Theoretical models and comparisons with experiments. *Journal of Fluid Mechanics*, 54(2):263–288, 1972.

[17] S. Turek and J. Hron. Proposal for numerical benchmarking of fluid-structure interaction between an elastic object and laminar incompressible flow. In H.-J. Bungartz and M. Schäfer, editors, *Fluid-Structure Interaction*, volume 53 of *Lecture Notes in Computational Science and Engineering, LNCSE*, pages 371–385. Springer, Heidelberg, 2006.

[18] S. Turek, J. Hron, M. Razzaq, H. Wobker, and M. Schäfer. Numerical benchmarking of fluid-structure interaction: A comparison of different discretization and solution approaches. In H.-J. Bungartz, M. Mehl, and M. Schäfer, editors, *Fluid-Structure Interaction II – Modelling, Simulation, Optimization*, volume 73 of *Lecture Notes in Computational Science and Engineering, LNCSE*, pages 413–424. Springer, Heidelberg, 2010.

V International Conference on Computational Methods in Marine Engineering
MARINE 2013
B. Brinkmann and P. Wriggers (Eds)

DEVELOPMENT OF A HYBRID APPROACH USING COUPLED GRID-BASED AND GRID-FREE METHODS

N. KORNEV and G. JACOBI

Chair of Modeling and Simulation in Mechanical Engineering and Marine Technology (LeMoS)
University of Rostock
18059 Rostock, Germany
e-mail: nikolai.kornev@uni-rostock.de, web page: http://www.lemos.uni-rostock.de/

Key words: grid based method, vortex method, vortex dynamics

Abstract. The paper presents a novel hybrid approach developed to improve the resolution of concentrated vortices in computational fluid mechanics. The method is based on combination of a grid based and the grid free computational vortex (CVM) methods. The large scale flow structures are simulated on the grid whereas the concentrated structures are modeled using CVM. Due to this combination the advantages of both methods are strengthened whereas the disadvantages are diminished. The procedures of the separation of small concentrated vortices from the large scale vortices is based on LES filtering idea. The flow dynamics is governed by two coupled transport equations taking two way interaction between large and fine structures into account. The fine structures are mapped back to the grid represented large structures if their size grows due to diffusion. Algorithmic aspects of the hybrid method are discussed. Advantages of the new approach are illustrated on some simple canonic flows containing concentrated vortices.

1 INTRODUCTION

Insufficient resolution of vortex structures is one of the key problems in Computational Fluid Dynamics (CFD). First, the turbulent models used in Reynolds Averaged Navier Stokes Equations (RANSE) and Large Eddy Simulations (LES) approaches can be too diffusive. Second, the grid based methods possess rather high numerical diffusion which is proportional to the grid resolution. Both effects result in non- physical flow smoothing making difficult the reproduction of concentrated vortex structures with scales comparable with the cell size Δ. Some obvious movies illustrating this fact can be seen in http://www.lemos.uni-rostock.de/galerie-von-cfd-simulationen/. The numerical diffusion can be sufficiently diminished when the grid free Lagrangian methods like the Computational Vortex Method (CVM) [1] are applied. The vorticity domain is represented as a set of vortex particles tracked in the Lagrangian way. The CVM has the following advantages:

low numerical diffusion, no restrictions with respect to the CFL stability criteria, convenience in results interpretations in terms of vorticity, etc. Being developed many decades ago, the CVM is still not became a popular tool in the turbulence research because of the following difficulties: formulation of boundary conditions on solid boundaries, artificial noise typical for all particle methods, viscosity effects modeling, stability problems in three dimensional cases, etc. Taking the fact into account that many disadvantages of CVM can be easily solved within grid based methods and vice versa the authors came to idea to combine both methods to improve the resolution of vortex structures in CFD.

2 HYBRID GRID BASED AND GRID FREE METHOD

2.1 Choice of basic vortex elements

In [2] we proposed the procedure for derivation of axisymmetric vortices, referred to as the vortons, which being stochastic distributed reproduce the given spectra of turbulent kinetic energy. Particularly, the following formulae were derived for the vortex elements corresponding to the decaying turbulence spectra $E(k) \sim k^4 Exp[-\pi k^2/L^2]$, where L is the integral length:

• velocity induced by the n-th vorton at point $\mathbf{x}$:

$$\mathbf{u}(\mathbf{x}) = e^{-\pi|\mathbf{x}-\mathbf{x}_n|^2/2\sigma_n^2}\left(\boldsymbol{\gamma}_n \times (\mathbf{x}-\mathbf{x}_n)\right) \tag{1}$$

where $\boldsymbol{\gamma}_n$ and σ_n are the strength and the size of the vortex element.

• vorticity induced by the n-th vorton at point $\mathbf{x}$:

$$\boldsymbol{\omega}(\mathbf{x}) = e^{-\pi|\mathbf{x}-\mathbf{x}_n|^2/2\sigma_n^2}\left(\left(2-\frac{\pi}{\sigma_n^2}|\mathbf{x}-\mathbf{x}_n|^2\right)\boldsymbol{\gamma}_n + \frac{\pi}{\sigma_n^2}[(\mathbf{x}-\mathbf{x}_n)\boldsymbol{\gamma}_n](\mathbf{x}-\mathbf{x}_n)\right) \tag{2}$$

The derivatives $\partial u_i/\partial x_j$ and $\partial \omega_i/\partial x_j$ are calculated by direct differentiation of formulae (1) and (2). Note that new three dimensional vortex elements introduced in [2] induce the velocity and vorticity fields which are divergence free. Moreover, the distribution (2) obeys the diffusion equation $\partial_t \boldsymbol{\omega} = \nu\Delta\boldsymbol{\omega}$ if σ_n and $\boldsymbol{\gamma}_n$ are assumed to be function of time. Indeed, the fundamental solution of the diffusion equation for the vorton at the origin ($\mathbf{x}_n = 0$) is

$$\boldsymbol{\omega}(\mathbf{x},\mathbf{t}) = \frac{1}{(4\pi\nu t)^{3/2}}\iiint_{-\infty}^{\infty}\boldsymbol{\omega}(\boldsymbol{\xi},0)e^{-|\mathbf{x}-\boldsymbol{\xi}|^2/(4\nu t)}d\boldsymbol{\xi} = \tag{3}$$

$$= e^{-\pi|\mathbf{x}|^2/2\sigma_n^2(t)}\left(\left(2-\frac{\pi}{\sigma_n^2(t)}|\mathbf{x}-\mathbf{x}_n|^2\right)\boldsymbol{\gamma}_n(t) + \frac{\pi}{\sigma_n^2(t)}[\mathbf{x}\boldsymbol{\gamma}_n(t)]\mathbf{x}\right)$$

where

$$\sigma_n^2(t) = \sigma_n^2(0) + 2\pi\nu t \tag{4}$$

$$\boldsymbol{\gamma}_n(t) = \boldsymbol{\gamma}_n(0)(\sigma_n(0)/\sqrt{\sigma_n^2(0)+2\pi\nu t})^5 \tag{5}$$

2.2 Scale separation and approximation of concentrated vortices through the vortex elements.

The large scale flow field represented on the grid is separated from the small scale one represented by vortex elements using the filtration procedure taken from Large Eddy Simulation (LES). First, the original velocity field $\mathbf{u}(\mathbf{x},t)$ is filtered with some filter function $F(\mathbf{x}-\mathbf{s})$:

$$\overline{\mathbf{u}}(\mathbf{x},t)=\int\limits_{-\infty}^{\infty}\int\limits_{-\infty}^{\infty}\int\limits_{-\infty}^{\infty}\mathbf{u}(\mathbf{s},t)F(\mathbf{x}-\mathbf{s})d\mathbf{s} \tag{6}$$

The velocity field calculated as the difference between the original and filtered fields

$$\mathbf{u}'(\mathbf{x},t)=\mathbf{u}(\mathbf{x},t)-\overline{\mathbf{u}}(\mathbf{x},t) \tag{7}$$

should be approximated by vortex elements. Identification of vortices corresponding to the velocity field $\mathbf{u}'(\mathbf{x},t)$ is performed using one of the vortex identification criteria. The authors have gathered the best experience with the λ_{ci} criterion [3]. Vortex elements are placed into the flow regions with large λ_{ci} exceeding some threshold ε, i.e.

$$\lambda_{ci}>\varepsilon. \tag{8}$$

The condition (8) makes possible to separate strong vortices from weak ones which are then represented by vortex elements.

Representation of vorticity field $\boldsymbol{\omega}'=\nabla\times\mathbf{u}'$ is a problem which can have different numerical realizations. In the present paper we used a relative simple procedure assuming that the fine vortices have the form of local tubes with a certain cross section.

The method can be summarized as follows. For each time-step

i) : Sort out the regions of $\mathbf{u}'$ field with strong vortices:

$$\lambda_{ci}=\begin{cases}\lambda_{ci}, & \text{if } \lambda_{ci}>\varepsilon;\\ 0, & \text{otherwise.}\end{cases} \tag{9}$$

ii) : Find the point C_i with the maximum λ_{ci}. It is supposed that the point C_i is the local center of the vortex tube which is approximated by axisymmetric vortex element with the axis aligned with the local vorticity vector $\boldsymbol{\omega}(C_i)$.

iii) : Calculate the vorticity vector at point C_i:

$$\boldsymbol{\omega}(C_i)=\nabla\times\mathbf{u}'(\mathbf{x},t) \tag{10}$$

iv) : Determine the radius of the vortex structure at point C_i (see details in [4]).

v) : Calculate the vortex element strength and size.

The strength vector of the $i-th$ vortex element γ_i is found from the condition

$$\boldsymbol{\gamma}_i K(0)=\boldsymbol{\omega}(C_i) \tag{11}$$

where the coefficient $K(0)$ is the value of the vortex element kernel (inner distributions of vorticity at the center of the vortex element, $K(0) = -2$ for (2)). The vortex element size σ_i can be taken equal to the vortex tube radius

$$\sigma_i = R \tag{12}$$

vi) : Check the size and overlap with neighbors. If the radius is smaller than a certain threshold $R < \alpha\Delta$ the vortex element is generated. If a newly generated vortex element intersects with one of these appeared within the previous time steps both elements should be merged and replaced by a single element.

vii) : Eliminate the vortices close to C_i. The vortex element identified at the point C_i is ascribed to the vicinity $x - C_i \leq \beta\sigma_i$, where $\beta < 1$ is the overlapping parameter. At all adjacent points $x - C_i \leq \beta\sigma_i$ the values of λ_{ci} are set to zero.

viii) : If there are points with $\lambda_{ci} \neq 0$ return to the step ii).

Once the approximation is completed the velocities induced by vortex elements $\mathbf{u}^v$ are calculated. They are used to update the grid based velocities:

$$\mathbf{u}^g = \mathbf{u} - \mathbf{u}^v \tag{13}$$

Owing to this, the approximation procedure is conservative with the respect to the total velocity $\mathbf{u}$.

2.3 Equations of coupled evolution of grid- and particle represented flow fields

In this work we propose the splitting of Navier Stokes equation into a system of two coupled transport equations according to scales. The first equation describes the flow of the background u_i^g whereas the second one the flow induced by concentrated vortex structures u_i^v.

Substitution of the decomposition $\mathbf{u} = \mathbf{u}^g + \mathbf{u}^v$ and $\boldsymbol{\omega} = \boldsymbol{\omega}^g + \boldsymbol{\omega}^v$ into the vorticity transport equation gives:

$$\frac{\partial(\boldsymbol{\omega}^v + \boldsymbol{\omega}^g)}{\partial t} + ((\mathbf{u}^v + \mathbf{u}^g)\nabla)(\boldsymbol{\omega}^v + \boldsymbol{\omega}^g) = ((\boldsymbol{\omega}^v + \boldsymbol{\omega}^g)\nabla)(\mathbf{u}^v + \mathbf{u}^g) + \nu\Delta(\boldsymbol{\omega}^g + \boldsymbol{\omega}^v) \tag{14}$$

which we split into two following equations:

$$\begin{cases} \dfrac{\partial\boldsymbol{\omega}^g}{\partial t} + ((\mathbf{u}^v + \mathbf{u}^g)\nabla)\boldsymbol{\omega}^g = (\boldsymbol{\omega}^g\nabla)(\mathbf{u}^v + \mathbf{u}^g) + \nu\Delta\boldsymbol{\omega}^g \\ \dfrac{\partial\boldsymbol{\omega}^v}{\partial t} + ((\mathbf{u}^v + \mathbf{u}^g)\nabla)\boldsymbol{\omega}^v = (\boldsymbol{\omega}^v\nabla)(\mathbf{u}^v + \mathbf{u}^g) + \nu\Delta\boldsymbol{\omega}^v \end{cases} \tag{15}$$

The l.h.s of (15) is the full material time derivative $\frac{D}{Dt}$. The first equation describes the evolution of the grid based vorticity whereas the second one is responsible for concentrated vortices. The next task is to rewrite the first equation into $u - p$ variables.

$$\frac{\partial(\nabla \times \mathbf{u}^g)}{\partial t} + ((\mathbf{u}^g + \mathbf{u}^v)\nabla)(\nabla \times \mathbf{u}^g) = ((\nabla \times \mathbf{u}^g)\nabla)(\mathbf{u}^g + \mathbf{u}^v) + \nu\Delta(\nabla \times \mathbf{u}^g) \tag{16}$$

Taking the identities

$$(\boldsymbol{\omega}\nabla)\mathbf{u}-(\mathbf{u}\nabla)\boldsymbol{\omega}=\nabla\times(\mathbf{u}\times\boldsymbol{\omega}),(\boldsymbol{\omega}\nabla)\mathbf{u}-(v\nabla)\boldsymbol{\omega}=\nabla\times(\mathbf{u}\times\boldsymbol{\omega}),(\mathbf{u}\times\boldsymbol{\omega})=\frac{1}{2}\nabla u^2-(\mathbf{u}\nabla)\mathbf{u}$$

from the vector analysis into account one gets from (16) the $u-p$ formulation of the first equation (15). Finally we have the system:

$$\frac{\partial\mathbf{u}^g}{\partial t}+(\mathbf{u}^g\nabla)\mathbf{u}^g=\nabla\big(\pi+\frac{1}{2}\nabla(u^g)^2\big)+\nu\Delta\mathbf{u}^g+(\mathbf{u}^v\times\boldsymbol{\omega}^g) \tag{17}$$

$$\frac{d\boldsymbol{\omega}^v}{dt}=(\boldsymbol{\omega}^v\nabla)(\mathbf{u}^v+\mathbf{u}^g)+\nu\Delta\boldsymbol{\omega}^v \tag{18}$$

The first equation (17) is coupled with the second one (18) through the additional term $(\mathbf{u}^v\times\boldsymbol{\omega}^g)$. The physical meaning of this term can be revealed by applying the curl operator to the first equation. The term $(\mathbf{u}^v\times\boldsymbol{\omega}^g)$ describes the convective transport, amplification and rotation of the grid based vorticity vector $\boldsymbol{\omega}^g$ by the velocity field induced by concentrated vortex structures $\mathbf{u}^v$. The coupling of the second equation with the first one is due to the terms $(\mathbf{u}^g\nabla)\boldsymbol{\omega}^v$ and $(\boldsymbol{\omega}^v\nabla)\mathbf{u}^g$. The scalar function $\pi+\frac{1}{2}\nabla(u^g)^2$ is the grid based pressure Π.

The source term $\mathbf{u}^v\times\boldsymbol{\omega}^g$ is not necessary divergence-free, i.e. $\nabla(\mathbf{u}^v\times\boldsymbol{\omega}^g)\neq 0$. For the analysis of this term and its interpretation in terms on flow accelerations the pressure Π can be splitted within the each time step Δt into two terms $\Pi=\Pi^g+\Pi^v$ where Π^v is found from the Poisson equation $\Delta\Pi^v=-\nabla(\mathbf{u}^v\times\boldsymbol{\omega}^g)$. The contribution of vortices to the grid based flow acceleration is then $\nabla\Pi^v+\mathbf{u}^v\times\boldsymbol{\omega}^g$. The vector fields $\mathbf{u}^v\times\boldsymbol{\omega}^g$ and $\nabla\Pi^v+\mathbf{u}^v\times\boldsymbol{\omega}^g$ calculated for $\mathbf{u}^g=y^2/2\mathbf{i}$ and $\mathbf{u}^v=(1-e^{-25r^2})(-y\mathbf{i}+x\mathbf{j})/r^2$ are illustrated in Fig. 1. The uncompensated acceleration source $\mathbf{u}^v\times\boldsymbol{\omega}^g$ is clearly seen in Fig. 1 left whereas the term $\nabla\Pi^v+\mathbf{u}^v\times\boldsymbol{\omega}^g$ shows a dipole like distribution.

The equations (17) and (18) are solved sequentially. The first equation is solved on the grid whereas the second one using the grid free computational vortex method. The sum of these two equations written in the same variables retrieves the original Navier- Stokes equation.

The boundary conditions are explicitly formulated only for the grid solution. There is no boundary conditions for the vortex method. The generation of vorticity at boundaries due to induction u^v is taken by the grid solution into account.

2.4 Grid simulation

Numerical solution of the first equation (17) is obtained using the finite differential method (FDM) implemented on staggered grid. The convection step is treated explicitly whereas the diffusion step implicitly. The pressures Π^v and Π^g are found from the continuity equation (Poisson equation). The intermediate velocities obtained after the diffusion step are corrected by the gradient of a pressure $\Pi^v+\Pi^g$. The derivatives for the

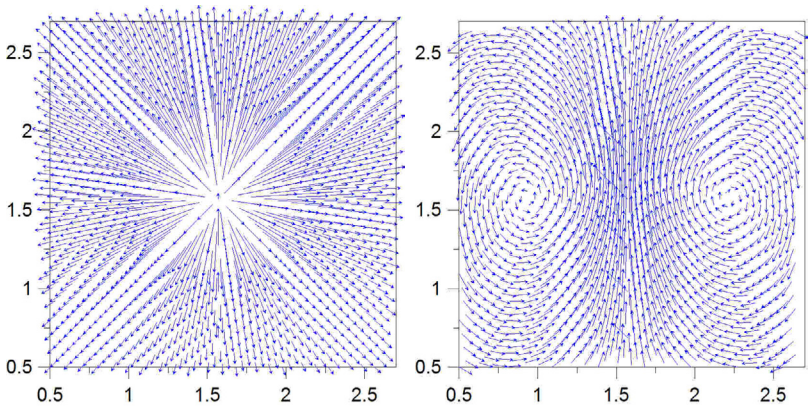


Figure 1: Vector fields $\mathbf{u}^v \times \boldsymbol{\omega}^g$ (left) and $\nabla\Pi^v + \mathbf{u}^v \times \boldsymbol{\omega}^g$ (right). Π^v is calculated within the domain $[0,\pi]\times[0,\pi]$ from the Poisson equation $\Delta\Pi^v = -\nabla(\mathbf{u}^v \times \boldsymbol{\omega}^g)$ with Neumann boundary conditions $\nabla\Pi^v = -\mathbf{u}^v \times \boldsymbol{\omega}^g$.

convection step are approximated using upwind, central differencing and a smooth transition between centered differencing and upwinding (mixed scheme). The poisson equation is solved using central differential scheme. A thorough description of the method is presented in [5]. Implementation of the grid simulation in OpenFOAM code is now being under progress. The velocity $\mathbf{u}^v$ is calculated directly from the formula (1).

2.5 Numerical implementation of the vortex method

The second equation (18) is solved using the explicit Euler method. Strictly speaking the vorticity at a point $\mathbf{x}$ is the sum of contributions of all vortons

$$\boldsymbol{\omega} = \sum_{n}^{N} \boldsymbol{\omega}_n, \tag{19}$$

where ω_n is found from (2). The right hand side of (18) is obtained by a formal differentiation of (19) on time:

$$\frac{d\boldsymbol{\omega}}{dt} = \sum_{n}^{N}\Big(\sum_{k=1}^{3} \frac{\partial\boldsymbol{\omega}_n}{\partial\gamma_{nk}}\frac{d\gamma_{nk}}{dt} + \frac{\partial\boldsymbol{\omega}_n}{\partial\sigma_n}\frac{d\sigma_n}{dt}\Big) \tag{20}$$

Formal substitution of (20) into (18) would result in a system of nonlinear[1] algebraic equations even if the explicit methods are used for the numerical solution of (18). Since it would make the numerical solution very complicated, this approach has never been used in vortex methods so far. Instead of this, one utilizes the fact that the function (2) decays rapidly and the mutual influence of vortons on r.h.s. of (18) is neglected. The derivatives

[1] nonlinear if $\sigma_n(t)$ depends on time. Otherwise, the system is linear with unknowns γ_{nk}

$\frac{\partial \boldsymbol{\omega}_n}{\partial \gamma_{nk}}$ and $\frac{\partial \boldsymbol{\omega}_n}{\partial \sigma_n}$ are calculated at the vorton centre $\mathbf{x} = \mathbf{x_n}$

$$\frac{\partial \omega_{nk}}{\partial \gamma_{nk}}(\mathbf{x} = \mathbf{x}_n) = 2, \frac{\partial \boldsymbol{\omega}_n}{\partial \sigma_n}(\mathbf{x} = \mathbf{x}_n) = 0 \tag{21}$$

Thus, the equation (18) is reduced to

$$2\frac{d\boldsymbol{\gamma}_n}{dt} = (\boldsymbol{\omega}^v \nabla)(\mathbf{u}^v + \mathbf{u}^g) + \nu \Delta \boldsymbol{\omega}^v \tag{22}$$

where the operator $(\boldsymbol{\omega}^v \nabla)\mathbf{u}^v$ is calculated analytically using (1) and (2). The grid velocity $\mathbf{u}^v$ at vortex place, which is necessary to calculate the operator $(\boldsymbol{\omega}^v \nabla)\mathbf{u}^g$ is determined using the M_2 interpolation procedure among adjacent grid points [1]. The diffusion $\nu \Delta \boldsymbol{\omega}^v$ is considered separately by the core spreading approach (see formulae (4) and (5)). If σ_n is getting due to diffusion larger than $\alpha\Delta$ it is mapped back to the grid. The velocities induced by this vortex are added to the background field $\mathbf{u}^g$ and the vortex is eliminated. Change of the element size σ_n due to amplification is found from the transport equation:

$$\frac{d\sigma_n}{dt} = -\frac{1}{2}\sigma_n \mathbf{e}\Big(\big(\mathbf{e}\nabla\big)\big(\mathbf{u}^v + \mathbf{u}^g\big) \Big) \tag{23}$$

3 RESULTS

In this section we present numerical solutions of some academic cases illustrating the advantages of the hybrid method.

The simulations have been performed in the rectangular domain $\pi \times \pi$ with the uniform grid of 100×100 cells and time step of 10^{-3}s. The kinematic viscosity is zero ($\nu = 0, Re = \infty$), i.e. only the artificial viscosity is present. The upwind scheme was applied for the grid based simulations using Finite Difference Method (FDM). Two Lamb- Oseen vortices with vorticity distribution $\omega = 2\gamma Exp[-r^2/\sigma^2]/\sigma^2$ are first placed onto the grid. The vortices with $\sigma = 0.1$m are well separated and have opposite signs $\gamma = \pm 0.5 m/s$. Within the hybrid method they are identified using the two dimensional version of the algorithm described in Sec.2.2 using the Lamb- Oseen vortex elements. As seen from Fig. 2 a) and b) the vortices are merged and diffuse in the pure grid based simulations whereas they rotate and keep their identity in hybrid simulations (Fig. 2 c) and d)). Moreover, the maximum vorticity is kept almost constant in hybrid simulations (Fig. 3). In upwind FDM simulations ω^2 losses almost 85 percent of its initial value in $1.3 sec$.

In the second test case the two dimensional turbulence was generated by placing five Lamb Oseen vortices with random sign of strength γ uniformly on the line ($x = 0.05, \pi/3 < y < 2\pi/3$) every 0.3 s. Then they move driven by the mean flow with the velocity $U_{mean} = 1 m/s$ and mutual induction. The strength of vortices was equal to $|\gamma| = 0.1 m^2/s$ and radius $\sigma = 0.02m$. Such a vortex occupies about three cells. Results presented in Fig. 4 show that the vortices disappear quickly in FDM simulation (Fig. 4 left) whereas they exist in the hybrid FDM+CVM simulations up to the outlet (Fig. 4

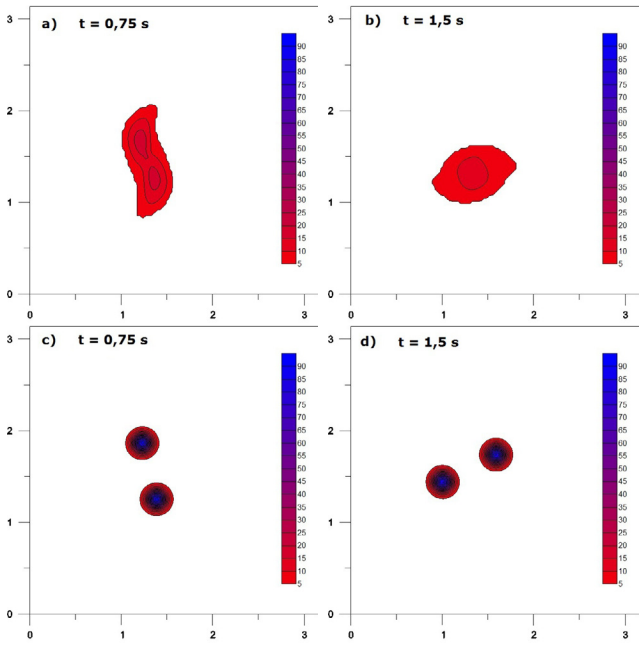


Figure 2: Simulation of dynamics of two vortices using Finite Difference Method (a,b) and Hybrid Method (c,d).

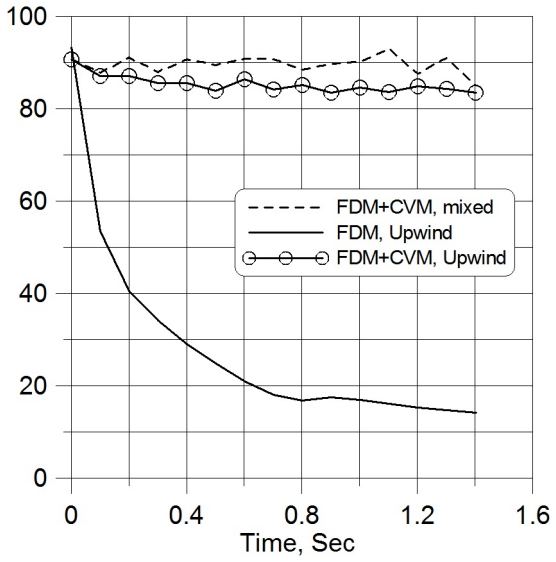


Figure 3: Maximum vorticity squared versus time. Simulation of two vortex rotation using FDM and hybrid.

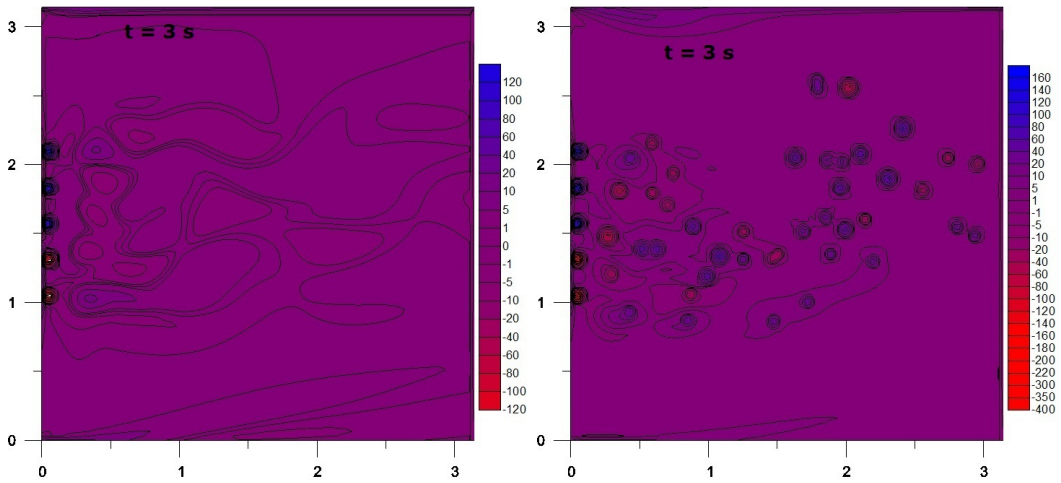


Figure 4: Simulation of two dimensional turbulence using Finite difference Method (left) and Hybrid Method (right).

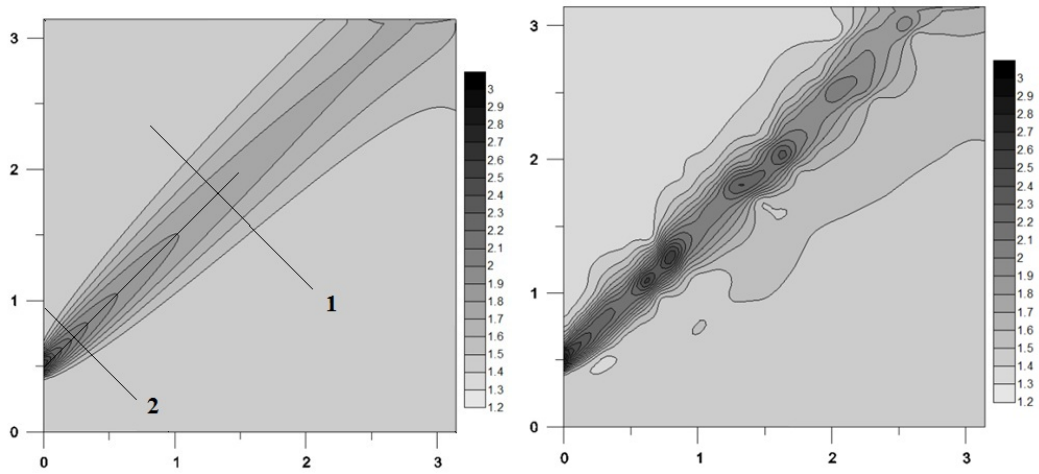


Figure 5: Simulation of planar jet development using Finite Difference Method (left) and Hybrid Method (right). Simulation time is 5 sec.

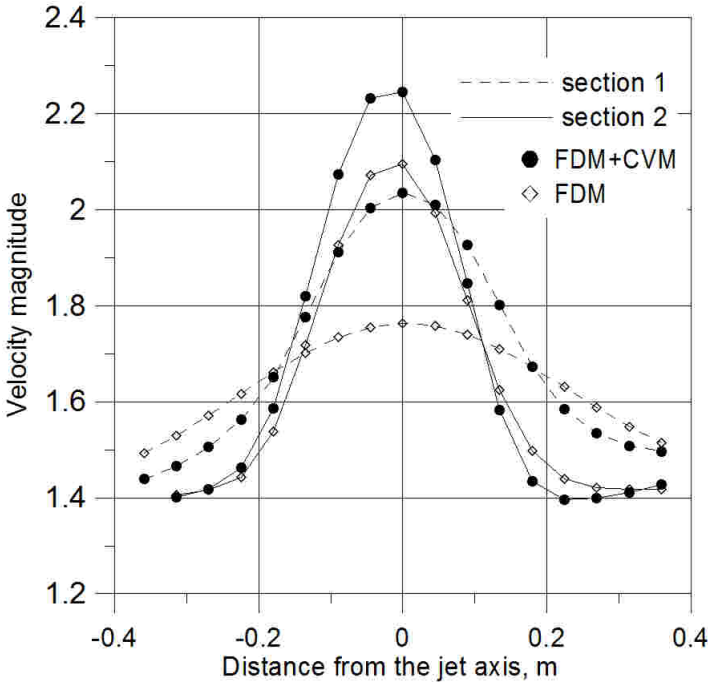


Figure 6: Velocity profile in two sections along the jet (shown in Fig. 5 left). Simulation of planar jet development using Finite Difference Method and Hybrid Method. Simulation time is 5 sec.

right).

The simulation of the planar jet development inclined under 45 degrees is presented in Fig. 5. The velocity distribution at the inlet is specified as:

$$u_x = \begin{cases} 100(y-(0.5-R_{jet}))((0.5+R_{jet})-y)+1.0 & 0.5-R_{jet} \le y \le 0.5+R_{jet} \\ 1.0 & 0.5-R_{jet} \ge y \ge 0.5+R_{jet} \end{cases} \quad (24)$$

$u_y = u_x$.

The calculations were performed for the jet radius $R_{jet} = 0.1$. The grid based pressure Π^g was set to zero at all boundaries excepting the outlet where the zero gradient boundary condition was enforced $\partial\Pi^g/\partial x = 0$. The unsteady convective boundary conditions for velocities were satisfied at the outlet. The vortex identification is carried out with the threshold of 0.1 for λ_{ci}. Since the viscosity is zero the jet spreading takes place only due to inviscid convective instability of the mixing layer arising at the jet boundary and artificial diffusion. The FDM solution obtained using upwind scheme demonstrates very fast spreading (Fig. 5 left)and velocity decay (Fig. 6). On the contrary, the jet maintains its energy longer in hybrid simulation than in FDM. Also the velocity decay is substantially slower in hybrid simulations.

4 CONCLUSIONS

The paper presents the first attempt to couple grid based and grid free simulations to improve the resolution of fine vortices in computational fluid dynamics. The separation of fine vortices is performed using the filtering procedure taken from Large Eddy Simulation. If the size of such vortices compared to cell size is small they get smoothed being modeled on grid because of artificial diffusion typical for grid based methods. To keep them we represent them explicitly by discrete vortex elements. The large scale motion being the difference between the original field and field induced by vortex elements is simulated on the grid, whereas the vortex elements evolution is treated with computational vortex method (CVM). The CVM like all grid free methods possess a small artificial diffusion and allows to keep identity of small vortices regardless of their size. Dynamics of large and small structures is governed by two coupled transport equations solved on grid and by CVM technique. The method principally differs from the existing hybrid approaches because the grid free simulation is embedded into the grid based one. With the other words, two coupled simulations are running simultaneously at each point within the whole computational domain. Numerical solution of some canonic problems shows the advantages of the hybrid method with respect to common grid based technique.

The general scheme of the presented method is open for all advanced techniques developed by different authors for vortex methods. Thus, the algorithms presented in the paper can be sufficiently improved using previous experience. First of all, the procedure of vortex identification and velocity field approximation through vortex elements can be optimized in future works. The computations of vorton induced velocities can be sufficiently accelerated with Fast Multipole Method (FMM) implemented on GPU cluster.

REFERENCES

[1] Koumotsakos P., and Cottet, J. (2000) Vortex methods: theory and practice. Cambridge university press, 2000.

[2] Kornev N., Hassel E., (2007), Synthesis of homogeneous anisotropic divergence free turbulent fields with prescribed second-order statistics by vortex dipoles, Physics of Fluids, Vol. 19, No. 5.

[3] Chakraborty, P. and Balachandar, S. and Adrian, R. J. (2005) On the relationships between local vortex identification schemes, J. Fluid Mech., Vol. 535, 189 - 214.

[4] http://www.lemos.uni-rostock.de/forschung/vortex-method/

[5] Seibold B. (2008) A compact and fast Matlab code solving the incompressible Navier-Stokes equations on rectangular domains,www-math.mit.edu/ seibold.

V International Conference on Computational Methods in Marine Engineering
MARINE 2013
B. Brinkmann and P. Wriggers (Eds)

UNSTEADY FSI SIMULATION OF DOWNWIND SAILS

NICOLA PAROLINI* AND MATTEO LOMBARDI†

*MOX - Dipartimento di Matematica
Politecnico di Milano
P.zza Leonardo da Vinci, 32, 20133 Milano, Italy
e-mail: nicola.parolini@polimi.it, web page: http://mox.polimi.it

†CMCS - Mathematics Institute of Computational Science and Engineering
Ecole Polytechnique Fédérale de Lausanne
Av. Piccard, Station 8, CH-1015 Lausanne, Switzerland
e-mail: matteo.lombardi@epfl.ch, web page: http://cmcs.epfl.ch

Key words: Sail dynamics, Fluid-Structure Interaction

Abstract. A numerical model for the simulation of the fluid-structure interaction (FSI) between the wind and the sails of a sailing boat is presented. This problem is characterized by an extremely light structure (in particular when downwind sails, spinnaker or gennaker, are considered) experiencing large displacements under the action of a complex (turbulent and separated) flow field. The model is based on a strongly coupled segregated FSI approach which guarantees adequate stability properties for the FSI problem at hand. A Dirichlet-Neumann coupling algorithm is adopted with a finite-volume Reynolds Averaged Navier-Stokes (RANS) flow solver interacting with a finite-element shell structural solver. Numerical results of unsteady FSI simulations are presented and discussed.

1 INTRODUCTION

Fluid-structure interaction (FSI) problems are still subject of intensive investigation in several application fields and many different formulations have been considered in the literature for their numerical solution.

In this work, we focus on a specific application where the interaction between a fluid flow (the wind) with a flexible (and light) structure (a sail) is considered. When upwind sailing configurations are considered, the flow around the sails is mainly attached and simplified flow models based on potential flow theory can usually be adopted, as in [1, 2]. Downwind configurations are much more demanding in terms of model complexity since, on one hand, the flow around gennaker (or spinnaker) is usually detached thus requiring the solution of the full Navier–Stokes equations [3, 4, 5, 6]; on the other hand, downwind

sails can often undergo large displacements, which should be accounted for by both the structural model and the mesh motion solver.

This paper is organized as follows: in Section 2 we briefly recall the structural and fluid models adopted and we introduce an unsteady strongly-coupled FSI scheme used for wind/sail interaction problems; in Section 3, we present a numerical (space and time) convergence analysis carried on for a benchmark FSI test case and then we present the results of the FSI simulation for an unsteady downwind two-sail configuration; finally, some conclusions are drawn in Section 4.

2 FLUID-STRUCTURE INTERACTION PROBLEM

Sails are flexible structures that deform under the action of the wind. The pressure field acting on the sail changes its geometry and this, in turn, alters the flow field.

The structural and fluid solvers are briefly introduced in the following sections before describing the coupling scheme that has been devised to simulate the FSI problem as well as the numerical techniques adopted for the interface data transfer and for the mesh motion. A detailed description of the different components of the FSI solver can be found in [7].

2.1 Structural solver

To model the structural behavior of the sails subjected to an external stress field we consider a shell finite element approach. Given a shell body of constant thickness h immersed in a fixed reference frame $\{\mathbf{e}_i\}$, $i = 1, 2, 3$ and based on the inextensible director shell theory, the geometry of the shell in the reference configuration is given by the mapping

$$\mathbf{X} = \mathbf{\Phi}(\bar{\boldsymbol{\xi}}) = \bar{\mathbf{\Phi}}(\xi^1, \xi^2) + \xi^3 \mathbf{L}(\xi^1, \xi^2), \qquad -\frac{h}{2} \leq \xi^3 \leq \frac{h}{2}, \tag{1}$$

where $\mathbf{X}$ is the position vector of a material point in the shell body identified by the convective system of coordinates $\bar{\boldsymbol{\xi}} = (\xi^1, \xi^2, \xi^3)$; $\bar{\boldsymbol{X}} = \bar{\mathbf{\Phi}}(\xi^1, \xi^2)$ are the points on the shell middle surface $\mathcal{M}(\xi^3 = 0)$, with boundary $\partial\mathcal{M}$, and the unit vector $\mathbf{L}(\xi^1, \xi^2)$ denotes the director field. We assume $\mathbf{L}$ to be normal to the middle surface in the original configuration but this property s, in general, lost during the deformation. Moreover, we assume that the material line originally normal to the shell midsurface in the reference configuration remains straight and unstretched during motion and that the stresses in the direction of the material line are zero.

A shell deformed configuration at time $t \in [0, T]$ is defined by the mapping $\mathbf{x} = \chi_t(\mathbf{X})$ where χ_t represents the motion. For this kinematics, the displacements $\mathbf{d}$ at a generic point $\mathbf{X}$ is given by

$$\mathbf{d}(\bar{\boldsymbol{\xi}}) = \mathbf{x}(\bar{\boldsymbol{\xi}}) - \mathbf{X}(\bar{\boldsymbol{\xi}}). \tag{2}$$

For a solid with density ρ_0 subjected to forces $\mathbf{B}$, the equation of motion (balance of momentum) in the reference configuration reads:

$$\rho_0 \frac{\partial^2 \mathbf{d}}{\partial t^2} = \nabla_R \cdot \mathbf{S} + \mathbf{B}, \tag{3}$$

where $\nabla_R \cdot$ is the divergence operator in the reference configuration and $\mathbf{S} = J\boldsymbol{\sigma}_S \mathbf{F}^{-T}$ is the first Piola-Kirchhoff stress tensor, $\boldsymbol{\sigma}_S$ is the Cauchy stress tensor, $\mathbf{F}$ is the deformation gradient defined as

$$\mathbf{F} = \frac{\partial \chi_t(\mathbf{X}, t)}{\partial \mathbf{X}} = \frac{\partial \mathbf{x}(\mathbf{X}, t)}{\partial \mathbf{X}},$$

and J is the determinant of $\mathbf{F}$.

The spatial discretization of problem (3) is based on the finite element method using the MITC4 elements [8]. This approach proved to be adequate [9] to simulate the dynamics of light structures, in particular with respect to the typical occurrence of post-buckled configurations triggered by local instabilities, known as *wrinkling*. A time adaptive explicit second-order scheme is considered for the time discretization (see [7]).

2.2 Fluid solver

In the context of sails simulations, potential flow models have been used extensively in case of upwind sailing configurations where the flow can be considered mainly attached. For downwind configurations, large flow separations usually occur and thus the solution of the full Navier-Stokes equations is required. Due to the typical Reynolds number characterizing the problem, a turbulence model approach is required and the Reynolds Averaged Navier-Stokes (RANS) equations are considered, which read

$$\begin{cases} \dfrac{\partial(\rho\mathbf{u})}{\partial t} + \boldsymbol{\nabla} \cdot (\rho\mathbf{u} \otimes \mathbf{u}) - \boldsymbol{\nabla} \cdot \boldsymbol{\sigma}_F = \mathbf{0}, & \text{in} \quad \Omega(t) \times (0,T), \\ \boldsymbol{\nabla} \cdot \mathbf{u} = 0 & \text{in} \quad \Omega(t) \times (0,T), \\ \mathbf{u} = \mathbf{u}_0 & \text{in} \quad \Omega(t=0), \\ \mathbf{u} = \mathbf{u}_D & \text{on} \quad \Gamma_D \times (0,T), \\ \boldsymbol{\sigma}_F \cdot \mathbf{n} = \mathbf{0} & \text{on} \quad \Gamma_N \times (0,T), \\ \mathbf{u} = \dot{\mathbf{d}} & \text{on} \quad \Gamma_{Sail}(t) \times (0,T) \end{cases} \tag{4}$$

where $\mathbf{u}$ and p are the averaged velocity and pressure, ρ is the air density, $\mathbf{w}$ is the mesh velocity and $\boldsymbol{\sigma}_w = \mu(\boldsymbol{\nabla}\mathbf{u} + \boldsymbol{\nabla}\mathbf{u}^T) - p\mathbf{I}$ is the stress tensor, with $\mu_{\text{eff}} = \mu + \mu_t$ denoting the total viscosity (sum of the dynamic and turbulent viscosity). On the portion Γ_D of the domain boundary (which usually includes the inlet), a Dirichlet velocity boundary condition $\mathbf{u}_D$ is imposed while on Γ_N (usually the outlet boundary) a Neumann-type condition imposes zero normal stress. The velocity on the moving sail is equal to $\dot{\mathbf{d}}$, the rate of deformation of the structure interpolated on the fluid interface. The turbulent

viscosity is evaluated using the Shear-Stress-Transport (SST) model [10] which requires the solution of two additional partial differential equations for the turbulent kinetic energy ε and for the specific dissipation ω, which are solved in a segregated fashion with respect to problem (4). Note that, in order to deal with the moving domain due to the sail deformation, a Arbitrary Lagrangian Eulerian (ALE) formulation of the RANS equations [11] has been adopted.

2.3 Mesh motion

The third computational ingredient of the FSI algorithm has to deal with the fluid mesh motion. Indeed, on one hand, the structural solver is based on a Lagrangian approach in which the problem is always recasted into a reference structural domain; on the other hand, the ALE approach adopted in the flow solution requires the extension of the sail displacement to the whole fluid domain. Different approaches can be adopted to face this problem. In this work, we have considered a technique based on the Inverse Distance Weighting (IDW) interpolation [12].

2.4 FSI coupling

Let us denote with $\mathcal{F}$ the fluid problem (4) defined on domain $\Omega_F(t)$ and with $\mathcal{S}$ the structural problem (3) defined on domain $\Omega_S(t)$. Moreover, we denote with $\mathcal{M}$ the mesh motion problem that is solved at each iteration to adapt the fluid computational grid to the updated sail geometry. In mathematical terms, the FSI problem can be defined as a coupled system that comprises the fluid problem $\mathcal{F}$, the structural problem $\mathcal{S}$ and the mesh motion problem $\mathcal{M}$. In abstract form, the problem can be formulated as follows

$$\begin{cases} \mathcal{F}(\mathbf{u}, p, \mathbf{w}) = 0 & \text{in} \quad \Omega_F(t) \\ \mathcal{S}(\mathbf{d}) = 0 & \text{in} \quad \Omega_S(t) \\ \mathcal{M}(\boldsymbol{\eta}) = 0 & \text{in} \quad \Omega_F^0 \\ & \\ \mathbf{u} = \dot{\mathbf{d}} & \text{on} \quad \Gamma(t) \\ \boldsymbol{\sigma}_F(\mathbf{u}, p)\mathbf{n}_F = \boldsymbol{\sigma}_S(\mathbf{d})\mathbf{n}_S & \text{on} \quad \Gamma(t) \\ \boldsymbol{\eta} = \mathbf{d} & \text{on} \quad \Gamma^0 \,, \end{cases} \tag{5}$$

where the three (fluid, structure and mesh motion) problems are coupled through three conditions over the interface $\Gamma(t)$ stating the continuity of velocity, the equilibrium of forces and the geometric continuity, respectively. In (5), $\boldsymbol{d}$ denoted the structural displacement, $\boldsymbol{\eta}$ the mesh displacement, Ω_F^0 and Γ^0 denote the reference fluid domain and interface, respectively. The fluid mesh motion velocity $\mathbf{w}$, needed in the ALE formulation of the RANS equations, is the time-derivative of the mesh displacement $\mathbf{w} = \dot{\boldsymbol{\eta}}$.

For the solution of problem (5), different FSI schemes can be devised. *Monolithic* schemes are based on the solution of a global system which is assembled and solved for

all the unknowns of the problem simultaneously; on the other hand, when existing (and independent) fluid and structural solvers have to be coupled, *partitioned* schemes, in which the fluid, structure and mesh motion problems are solved iteratively, are preferred. For the case at hand, a strongly-coupled partitioned scheme has been devised, which guarantees that at each time step the equilibrium is reached between the different sub-problems. To compute the solution at time t^{n+1}, a sub-iteration between the three sub-problems is required. The structural solution is first computed

$$\begin{array}{ll} \mathcal{S}(\mathbf{d}_{k+1}^{n+1}) = 0 & \text{in } \Omega_{S_k}^{n+1} \\ \boldsymbol{\sigma}_S(\mathbf{d})_{k+1}^{n+1}\mathbf{n}_{S_k}^{n+1} = \boldsymbol{\sigma}_F(\mathbf{u},p)_k^{n+1}\mathbf{n}_{F_k}^{n+1} & \text{on } \Gamma, \end{array}$$

followed by the mesh motion update

$$\begin{array}{ll} \mathcal{M}(\boldsymbol{\eta}_{k+1}^{n+1}) = 0 & \text{in } \Omega_F^0 \\ \boldsymbol{\eta}_{k+1}^{n+1} = \alpha\mathbf{d}_{k+1}^{n+1} + (1-\alpha)\mathbf{d}_k^{n+1} & \text{on } \Gamma^0, \end{array}$$

and finally the flow solution

$$\begin{array}{ll} \mathcal{F}(\mathbf{u}_{k+1}^{n+1}, p_{k+1}^{n+1}, \mathbf{w}_{k+1}^{n+1}) = 0 & \text{in } \Omega_{F_{k+1}}^{n+1} \\ \mathbf{u}_{k+1}^{n+1} = \alpha\dot{\mathbf{d}}_{k+1}^{n+1} + (1-\alpha)\dot{\mathbf{d}}_k^{n+1} & \text{on } \Gamma_{k+1}^{n+1}, \end{array}$$

where α is a coefficient computed using the Aitken relaxation. The iteration over the index k is stopped when a suitable convergence criterion is fulfilled, namely

$$\begin{cases} ||\mathbf{d}_{k+1}^{n+1} - \mathbf{d}_k^{n+1}||/||\mathbf{d}_0^{n+1}|| \leq \epsilon_d \\ ||\mathbf{u}_{k+1}^{n+1} - \mathbf{u}_k^{n+1}||/||\mathbf{u}_0^{n+1}|| \leq \epsilon_u \\ ||p_{k+1}^{n+1} - p_k^{n+1}||/||p_0^{n+1}|| \leq \epsilon_p \end{cases},$$

where both L^2 and L^∞ norms have been tested. In the numerical tests discussed in Section 3, a convergence criterion based on the L^2 norm has been used.

The FSI scheme described above can be adopted when non-conforming (at the interface) space discretizations are adopted for the fluid and structural problems. In this case, suitable interpolation operators for the data transfer at the interface are required. The approach adopted in this work is based on Radial Basis Functions and was introduced in [13]. Non-conforming interface grids are considered, for example, in the FSI sail simulation that will be presented in Section 3.2.

3 NUMERICAL RESULTS

The strongly-coupled FSI algorithm introduced in the previous sections has been applied for the simulation of different sail configurations. For an overview of the results, we refer to [7], where a large set of simulations on one- and two-sail configurations are discussed, together with an analysis of the effect of the sail trimming.

In order to assess the convergence properties of the model, we present here a simple benchmark test case comparing our results with those published in the literature. Moreover, to display the ability of the model in capturing complex sail dynamics, we report the result of an unsteady numerical simulation on a two-sail downwind configuration.

3.1 Cavity with flexible wall

As in the test case proposed in [14], a three-dimensional cavity with flexible bottom is considered with a pulsating flow field imposed on a small inlet section on the upper part of one side, while, on the opposite side a small outlet section is present.

On the inlet section, a pulsating linear velocity profile in $x-$direction, ranging from $\mathbf{0}$ to

$$\mathbf{u}_{\text{top}}(t) = (1 - \cos(2\pi t/5), 0, 0),$$

with a period of 5 s is considered. On the top surface, a uniform Dirichlet boundary condition $\mathbf{u} = \mathbf{u}_{\text{top}}$ is imposed, while on the outlet boundary the normal stress is set to zero. The flexible bottom surface is modeled using the shell finite element model described in Section 2.1 and the FSI interface conditions introduced in Section 2.4 apply. Finally, on the remaining boundaries homogeneous Dirichlet boundary conditions $\mathbf{u} = \mathbf{0}$ are imposed. The fluid and structural physical properties are reported in Table 1.

Fluid	Density [Kg/m^3]	Viscosity [m^2/s]	Cavity size [m]	Inlet size [m]
	1.0	0.01	1	0.125
Structure	Density [kg/m^3]	Poisson's ratio	Young's modulus [N/m^2]	Thickness [m]
	500	0.0	250.0	0.002

Table 1: Fluid and structural properties used in the cavity test case.

In Figure 1, the deformation undergone by the flexible bottom and the streamlines on the longitudinal vertical midplane are reported for different time instants. The pulsating flow field generates a suction pressure on the bottom and the creation of a large vortex inside the fluid domain.

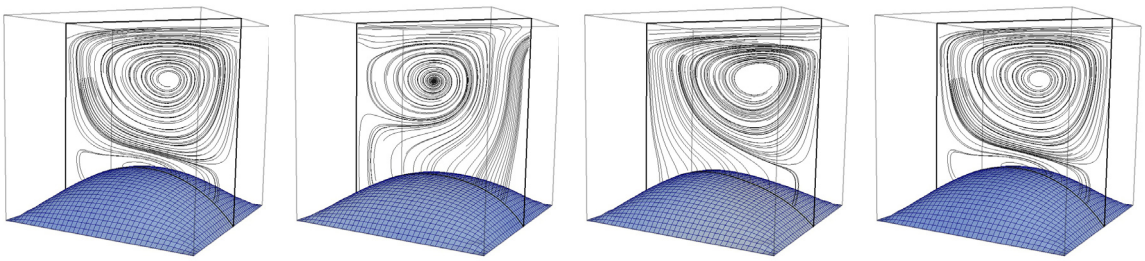


Figure 1: Structural surface deformation and fluid streamlines on a vertical cross section at different time instant over a period.

The time evolutions of the vertical displacement of the bottom surface midpoint are displayed in Figure 2 for different resolutions and show the space and time convergence of the method. The results are in agreement with those obtained in [14] where, however, no convergence analysis is reported.

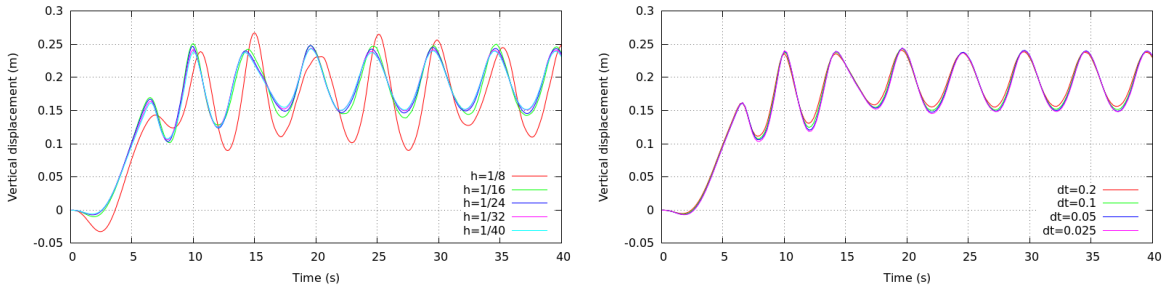


Figure 2: Time evolution of the bottom surface midpoint displacement: space (left) and time (right) convergence.

3.2 Unsteady FSI simulation for downwind sails

In this section, we present the results of the unsteady FSI simulation of a two-sail configuration. Only the sails are considered in this simulation and the computational domain is a parallelepiped surrounding them. The computational grid is based on a hybrid approach, where in the far field region a block structured grid is generated, while in a small region around the sails an unstructured grid is used (see Figure 3). The gennaker has two fixed vertices and the third one, attached to the trimming sheet, as the sheet is in tension, is constrained to stay at a fixed distance from the attachment point on the boat, thus moving on a spherical surface. The main sail motion is much more constrained, as the side attached to the mast is fixed (no mast deformation is considered), as well as the side attached to the boom.

The velocity boundary conditions imposed at the inlet of the domain is the composition of the opposite of the boat speed (here equal to 5.48 m/s in the $x-$direction) and the wind velocity (see Figure 4, left). The wind velocity magnitude is modeled with the following

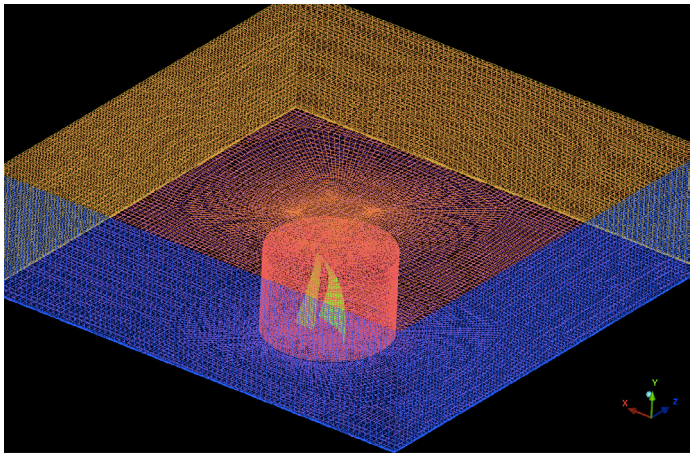


Figure 3: Hybrid structured-unstructured mesh for the gennaker-main sail simulations. The cylinder surface delimits the unstructured domain.

atmospheric boundary layer law (assuming y the vertical axis pointing upwards and the sea level being at y =0 m):

$$u(y) = u_{ref} \left(\frac{y}{y_{ref}} \right)^{C_r} \tag{6}$$

where u_{ref} is the reference wind velocity at the reference height y_{ref} and C_r is a constant reflecting the roughness of the surface over which the wind is blowing. In our simulations, we considered the reference wind velocity $u_{ref} = 6.632$ m/s, the reference height $z_{ref} = 10$ m and the roughness constant $C_r = 0.1$. In the downwind configurations considered here the boat is *reaching*: the wind is coming diagonally from behind, with an angle equal to 155 degrees to the bow direction.

These choices result in a twisted profile imposed on the inflow boundary: the resulting velocity profile is in fact the opposite of the boat speed at sea level but rapidly change direction and magnitude as the height increases (see Figure 4, right).

In order to be able to simulate such flow boundary layer accurately and preserve it inside the fluid domain, a refinement in the vertical direction of the computational grid in the area close to the sea level is required.

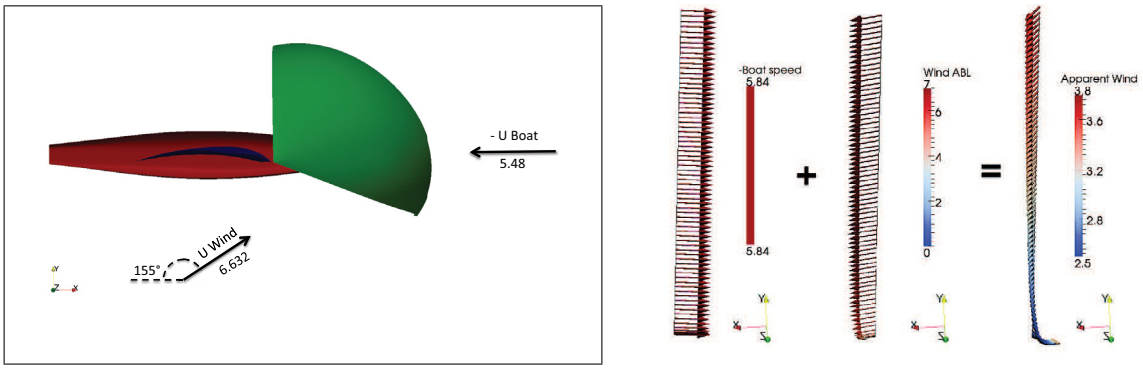
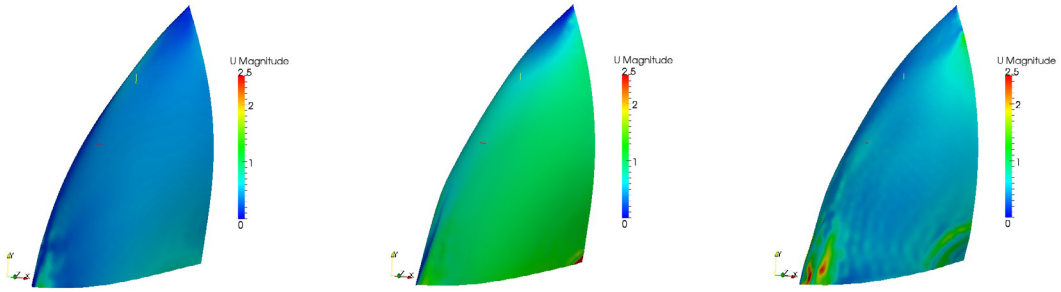


Figure 4: Boat velocity and wind speed directions (left) and resulting twisted inflow boundary condition (right).

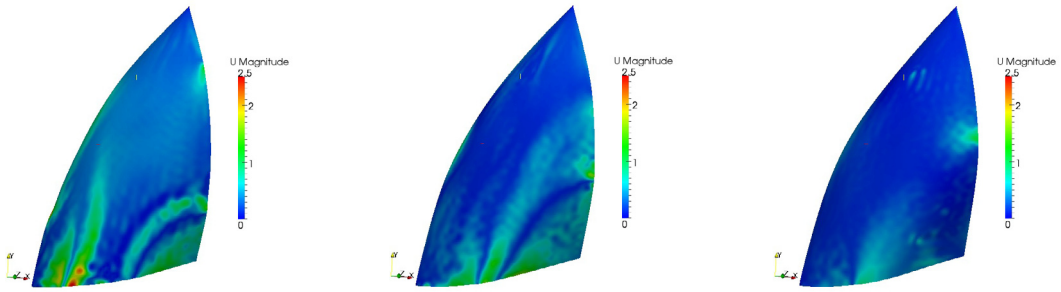
The sail fabric is modeled with a simple isotropic constitutive law, while the presence of battens (stiff elements inserted in the main sail to better control its shape) is accounted for considering local changes in the structure mechanical properties. The fluid and structural physical properties are reported in Table 2.

The deformation undergone by the sails can be observed in Figures 5 and 6. In the first instants, the vertex attached to the trimming sheet is free to move and travel forward under the pressure of the wind being the sheet not yet under tension (Figures 5, (a)). Being the bow vertex fixed, a wrinkle is generated in the lower forward part of the sail. When the maximum sheet length is reached, the motion of the sheet attached vertex is abruptly stopped and the sheet starts pulling down and backward: such impulse propagates very quickly from the vertex upward (Figure 5, (b)-(c)-(d)) and merges with the

one propagating from the bow wrinkle. After 2.8 seconds the deformation is already quite small and the simulation very close to a steady solution.



(a) Time = 0.5 $[s]$. (b) Time = 1.0 $[s]$. (c) Time = 1.2 $[s]$.



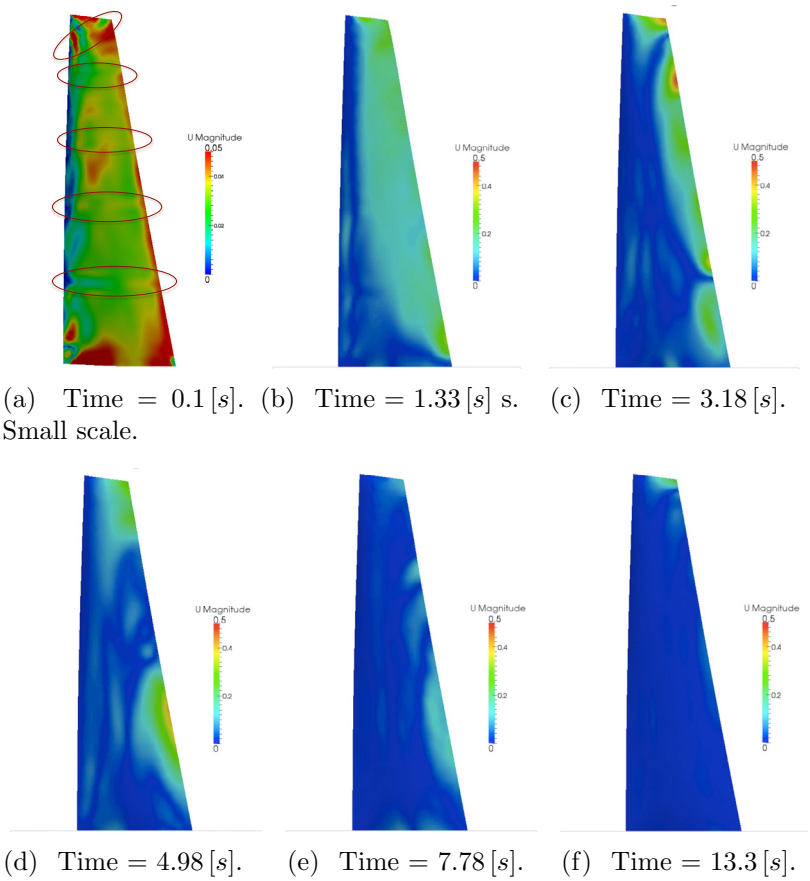
(d) Time = 1.5 $[s]$. (e) Time = 2.0 $[s]$. (f) Time = 2.8 $[s]$.

Figure 5: Two-sail transient FSI simulation: gennaker time evolution colored by displacement velocity contour.

The motion undergone by the main sail is much smaller if compared with the one of the gennaker due to the higher stiffness of the sail and, more importantly, to the very constraining boundary conditions. It is interesting to notice though that the presence of the battens, modeled with a local higher Young's modulus, has an influence on the motion, as can be observed in Figure 6, (a). The displacement of the main sail is characterized by deformation waves almost aligned with the vertical axis and propagating from the mast to the rear of the sail: once again this is physically compatible with the imposed constraints over the sail edges.

Fluid	Density $[Kg/m^3]$	Viscosity $[m^2/s]$		
Air	1.0	$1.5\ 10^{-5}$		
Structure	Density $[kg/m^3]$	Poisson's ratio	Young's modulus $[N/m^2]$	Thickness $[m]$
Gennaker	100	0.3	$3.76\ 10^{8}$	0.001
Main sail	340	0.3	$1.93\ 10^{9}$	0.003
Battens	500	0.3	$1.0\ 10^{10}$	0.012

Table 2: Fluid and structural properties used in the wind/sails FSI simulations.



(a) Time = 0.1 [s]. (b) Time = 1.33 [s] s. (c) Time = 3.18 [s]. Small scale.

(d) Time = 4.98 [s]. (e) Time = 7.78 [s]. (f) Time = 13.3 [s].

Figure 6: Two-sail transient FSI simulation: main sail time evolution colored by displacement velocity contour.

The time evolution of the forward force on the gennaker is displayed in Figure 7. In the first instants, the forward force on the gennaker drops to a very low value while the gennaker trimming sheet is not yet under tension and the sail is free to open up. When the trimming sheet starts pulling, the force abruptly rises to a large value and only slowly stabilize to an asymptotic regime when the sail is almost at rest. Nonetheless, a small fluctuation can still be observed even at convergence, showing that the asymptotic solution is unsteady and thus justifying the adoption of an unsteady FSI solver. In Figure 7, the present unsteady result is compared to the converged force value on the initial geometry configuration and to that obtained by a steady FSI simulation, where steady versions of both flow and structural solvers are considered.

Regarding the computational cost of such simulation, it is worth mentioning that, given a fixed FSI coupling tolerance, the residuals over the main sail converge much faster than those over the gennaker sail, due to much smaller motion magnitude. The structural solvers for the two sails are run independently, with the one simulating the main sail takes the longest time for each structural solution (being the sail stiffer, a smaller time step

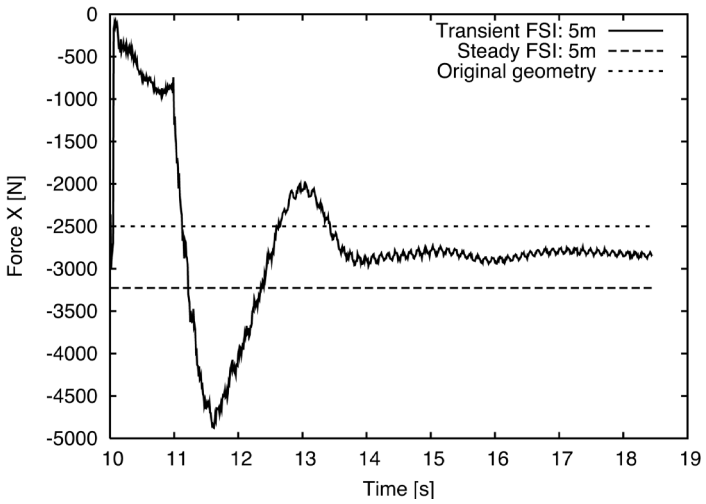


Figure 7: Two-sail transient FSI simulation: time evolution of the forward force on the gennaker.

constraint is imposed to the explicit solver to be able to catch the higher frequencies).

4 CONCLUSIONS

A model for the simulation of the unsteady dynamics of sails interacting with the wind has been presented. The model has been conceived in order to guarantee the strict stability requirements needed by fluid-structure interaction problems with light structure. In this respect, a strongly-coupled partitioned approach was considered with a FSI sub-iteration reaching a dynamic equilibrium at each time step. Moreover, an energy preserving interface data transfer between the fluid and the structure was used at the non-conforming interface. The convergence and robustness of the method have been assessed with numerical results on both an academic FSI test case and a real downwind sail dynamic problem.

REFERENCES

[1] T. Fukasawa and M. Katori. Numerical approach to aeroelastic responses of three-dimensional flexible sails. In *Proc. of 11th Chesapeake Sailing Yacht Symposium (Annapolis)*, 1993.

[2] J. Pilate. Development of a three-dimensional inverse sail design method. In *Proceedings 3rd High Performance Yacht Design Conference*, 2008.

[3] N. Parolini and A. Quarteroni. Mathematical models and numerical simulations for the America's cup. *Computer Methods in Applied Mechanics and Engineering*, 194:pp. 1001–1026, 2005.

[4] H. Renzsch, O. Müller, and K. Graf. Flexsail – a fluid structure interaction program for the investigation of spinnakers. In *Proceedings 2nd High Performance Yacht Design Conference*, 2006.

[5] D. Detomi, N. Parolini, and A. Quarteroni. Numerical models and simulations in sailing yacht design. In M. Peters, editor, *Computational Fluid Dynamics for Sport Simulation*, pages 1–31. Springer, 2009.

[6] Ignazio Maria Viola. Downwind sail aerodynamics: A cfd investigation with high grid resolution. *Ocean Engineering*, 36(1213):974 – 984, 2009.

[7] M. Lombardi. *Numerical simulation of a sailing boat: free surface, fluid structure interaction and shape optimization*. PhD thesis, EPFL, 2012.

[8] E. N. Dvorkin, D. Pantuso, and E. A. Repetto. A formulation of the MITC4 shell element for finite strain elasto-plastic analysis. *Computer Methods in Applied Mechanics and Engineering*, 125:pp. 17–40, 1995.

[9] D. Trimarchi, S. R. Turnock, D. J. Taunton, and D. Chapelle. The use of shell elements to capture sail wrinkles, and their influence on aerodynamic loads. In *The Second International Conference on Innovation in High Performance Sailing Yachts (Lorient, France)*, 2010.

[10] F. R. Menter, M. Kuntz, and R. Langtry. Ten years of industrial experience with the SST turbulence model. *Heat and mass transfer*, 4:pp. 625–632, 2003.

[11] J. Donea, S. Giuliani, and J.P. Halleux. An arbitrary Lagrangian-eulerian finite element method for transient dynamic fluid-structure interactions. *Computer Methods in Applied Mechanics and Engineering*, 33:pp. 689–723, 1982.

[12] J. Witteveen and H. Bijl. Explicit mesh deformation using inverse distance weighting interpolation. In *Proceedings of 47th AIAA Aerospace Sciences Meeting*, 2009.

[13] M. Lombardi, N. Parolini, and A. Quarteroni. Radial basis functions for inter-grid interpolation and mesh motion in fsi problems. *Computer Methods in Applied Mechanics and Engineering*, 256(0):117 – 131, 2013.

[14] J. G. V. Vázquez. *Nonlinear Analysis of Orthotropic Membrane and Shell Structures Including Fluid-Structure Interaction*. PhD thesis, Universitat Politècnica de Catalunya, 2007.

V International Conference on Computational Methods in Marine Engineering
MARINE 2013
B. Brinkmann and P. Wriggers (Eds)

STOCHASTIC NAVIER-STOKES EQUATIONS ARE A COUPLED PROBLEM

JOACHIM RANG* AND HERMANN G. MATTHIES*

*Institute of Scientific Computing
TU Braunschweig
Hans-Sommer Str. 65, 38106 Braunschweig, Germany
e-mail: {j.rang,wire}@tu-bs, web page: http://www.wire.tu-bs.de

Key words: stochastic Galerkin methods, uncertainty quantification, stochastic Finite Elements, Navier–Stokes equations

Abstract. In this paper we consider the stochastic incompressible Navier–Stokes equations. For the stochastic discretisation we use a stochastic Galerkin formulation and a polynomial chaos expansion. This approach leads to a huge nonlinear system of equations. We introduce partitioned methods like the Block–Jacobi and the Block–Gauß–Seidel method. These methods have the advantage that the huge nonlinear system is split into smaller systems. Numerical examples illustrate this idea.

1 INTRODUCTION

Nowadays many physical and engineering problems, e. g. the simulation of Newtonian fluids, are solved numerically with mathematical models and computer simulations. As input quantities of such models we have for example, boundary conditions, geometries, and coefficients, which are in general not exactly known since they may be the result of measurements.

There are two kinds of uncertainties. First there are the so-called aleatoric uncertainties. Here the uncertainties are described as inherent randomness inside the phenomenon. Then there are epistemic uncertainties which are related to our incomplete knowledge [NBH97, Eli99, Mat07, Jay03, RO10]. The uncertainties considered here are more or less epistemic uncertainties. Aleatoric uncertainties are nearly always described probabilistically [NBH97, Eli99, Mat07, Jay03, RO10, Gri02, Pap91]. For epistemic uncertainties different ansatzes are used: Fuzzy systems, convex sets, and intervals [NBH97, Eli99, RO10], as well as Bayesian probabilistic models [NBH97, Eli99, Mat07, Jay03, RO10, Chr92, KO01].

The identified uncertainties should not only be indicated and verbally described by modeling and simulation, they should also be quantified (see for example [Mat07]). The

quantification of uncertainties plays an important role in the determination of optimal processes and to find feedback controls, which are robust with respect to perturbations and uncertainties. There are different possibilities to describe and quantify uncertainties. In this article uncertainties are described with probabilistic or stochastic models since this approach offers a deep mathematical structure [Mat07].

A good probabilistic description can be achieved, for example, with Gaussian random variables if the random variables are continuous. As Wiener suggests [Wie38] every random variable $\mathsf{r}(\omega) \in L_2(\Omega)$ can be represented with polynomials, which depend on uncorrelated and independent Gauß variables [GS91, HØUZ96, Mal97, MBBS97, MB99, MK05]. This leads to functional approximations like the polynomial chaos expansion (PCE), which delivers a suitable representation of the stochastic process and of the random variable in independent identically distributed (**iid**) standard-Gauß variables.

In this paper we consider the incompressible Navier–Stokes equations. We assume that the right-hand side, the Reynolds number, and the solution are uncertain. For the spatial discretisation we use a Finite Element method (see [Joh04, Tur99]), and a stochastic Galerkin method is used for the discretisation in the stochastic part, i. e. we approximate the solution of the stochastic Navier–Stokes equations in a tensor-product space of both a spatial and a stochastic part. The unknown coefficients can be computed in two ways. First the so-called *non-intrusive method* should be mentioned, where the coefficients are computed in such a way that the deterministic code need not to changed. In this case the unknown coefficients can be approximated with the help of Monte Carlo simulations or stochastic collocation methods. In the case of *intrusive methods* the deterministic code needs some changes since a nonlinear system of coupled equations has to be solved.

This system is very large and a monolithic method may be not a good choice since the computations of the matrix-vector products need a lot of time and a lot of memory. A partitioned method may be a better choice. In this case we split the huge nonlinear system into smaller ones. This approach is known, for example, from the numerical solution of multi-field problems like fluid–structure interaction.

This paper is structured as follows: First we discretise the incompressible Navier–Stokes equations in the spatial and in the stochastic dimension. We receive a coupled and huge system of nonlinear equations. Then we introduce partitioned methods to solve this system, and finally we present a numerical result for the Burgers equations.

2 THE DISCRETISATION

2.1 The spatial discretisation

Let $\mathcal{G} \subset \mathbb{R}^d$, $d \in \{2, 3\}$, be a bounded domain. The motion of incompressible flows is modeled by the incompressible Navier–Stokes equations, which are given in dimensionless form by

$$\begin{aligned} -Re^{-1}\Delta\mathbf{u} + (\mathbf{u}\cdot\nabla)\mathbf{u} + \nabla p &= \mathbf{f} \quad \text{in } \mathcal{G} \\ \nabla\cdot\mathbf{u} &= 0 \quad \text{in } \mathcal{G}. \end{aligned} \tag{1}$$

Here, $\mathbf{u}$ is the velocity, p the pressure, $\mathbf{f}$ represents body forces and the parameter Re is the Reynolds number. The system of equations (1) has to be closed with appropriate initial and boundary conditions. If Dirichlet conditions are prescribed on the whole boundary $\partial\mathcal{G}$, a condition for the pressure, such as $\int_{\mathcal{G}} p(\mathbf{x})\ d\mathbf{x} = 0$, has to be added.

For the simplicity of presentation we consider the case that (1) is equipped with homogeneous Dirichlet boundary conditions in $[0, T]$. Then, the velocity ansatz and test spaces can be chosen in the same manner in the weak formulation of (1) as well as in the finite element method. Let $V = (H_0^1(\mathcal{G}))^d$, $Q = L_0^2(\mathcal{G})$, then the time–continuous weak or variational problem reads as: Find $(\mathbf{u}, p) \in V \times Q$ such that

$$\begin{aligned} (Re^{-1}\nabla\mathbf{u}, \nabla\mathbf{v}) + ((\mathbf{u}\cdot\nabla)\mathbf{u}, \mathbf{v}) - (p, \nabla\cdot\mathbf{v}) &= (\mathbf{f}, \mathbf{v}) \quad \forall\ \mathbf{v} \in V \\ (\nabla\cdot\mathbf{u}, q) &= 0 \quad \forall\ q \in Q. \end{aligned} \tag{2}$$

Here, $(\cdot,\cdot)$ denotes the inner product in $(L^2(\mathcal{G}))^d$, $d \in \{1, 2, 3\}$.

Finite element methods are a standard approach to perform the spatial discretization of (2), [GS00, Joh04]. The unique solvability of the arising discrete system requires that the velocity finite element space V_h is sufficiently large compared to the pressure finite element space Q_h. The precise description of this property is the so–called inf–sup condition [GR86]. To avoid technical difficulties in the presentation of the methods, we consider conforming finite element spaces, i.e. $V^h \subset V$ and $Q^h \subset Q$. The space–discretized Navier–Stokes equations read as follows: Find $(\mathbf{u}, p) \in V \times Q$ such that

$$(Re^{-1}\nabla\mathbf{u}_h, \nabla\mathbf{v}_h) + ((\mathbf{u}_h\cdot\nabla)\mathbf{u}_h, \mathbf{v}_h) - (p_h, \nabla\cdot\mathbf{v}_h) = (\mathbf{f}_h, \mathbf{v}_h) \tag{3}$$

$$(\nabla\cdot\mathbf{u}_h, q_h) = 0 \tag{4}$$

for all $\mathbf{v}_h \in V_h$ and all $q_h \in Q_h$. System (3)–(4) can be represented in algebraic form. Let

$$\{\boldsymbol{\phi}_{i,h}\}_{i=1}^{dN_u} = \left\{ \begin{pmatrix} \varphi_i \\ 0 \\ \vdots \end{pmatrix} \right\}_{i=1}^{N_u} \cup \left\{ \begin{pmatrix} 0 \\ \varphi_i \\ \vdots \end{pmatrix} \right\}_{i=1}^{N_u} \cup \quad \dots$$

be a basis of V_h and $\{\psi_{i,h}\}_{i=1}^{N_p}$ be a basis of Q_h. Here, N_u is the number of degrees of freedom for each component of the velocity, and N_p is the number of degrees of freedom for the pressure. Then, the solution of (3)–(4) can be written in the form

$$\mathbf{u}_h^{(k)}(\mathbf{x}) = \sum_{i=1}^{N_u} u_{i,h}^{(k)} \phi_i(\mathbf{x}), \quad k = 1, \dots, d,$$

$$p_h(\mathbf{x}) = \sum_{i=1}^{N_p} p_{i,h} \psi_{i,h}(\mathbf{x}).$$

Inserting these equations into (3)–(4) gives us

$$\sum_{j=1}^{N_u} u_{j,h}^{(1)}(Re^{-1}\nabla\phi_j,\nabla\phi_i)+\sum_{j=1}^{N_u} u_{j,h}^{(1)}(\mathbf{u}_h^{(1)}\partial_x\phi_j+\mathbf{u}_h^{(2)}\partial_y\phi_j,\phi_i)$$
$$-\sum_{j=1}^{N_p} p_{j,h}(\psi_j,\partial_x\phi_i)=(f_1,\phi_i),\quad i=1,\dots,N_u$$
$$\sum_{j=1}^{N_u} u_{j,h}^{(2)}(Re^{-1}\nabla\phi_j,\nabla\phi_i)+\sum_{j=1}^{N_u} u_{j,h}^{(2)}(\mathbf{u}_h^{(1)}\partial_x\phi_j+\mathbf{u}_h^{(2)}\partial_y\phi_j,\phi_i)$$
$$-\sum_{j=1}^{N_p} p_{j,h}(\psi_j,\partial_y\phi_i)=(f_2,\phi_i),\quad i=1,\dots,N_u$$
$$\sum_{j=1}^{N_u}(u_{j,h}^{(1)}(\partial_x\phi_j,\psi_i)+\sum_{j=1}^{N_u}(u_{j,h}^{(2)}(\partial_y\phi_j,\psi_i)=0,\quad i=1,\dots,N_p.$$

These equation can be written in matrix-vector formulation as follows

$$Re^{-1}L\mathbf{u}_h^{(1)}+A\left(\mathbf{u}_h^{(1)},\mathbf{u}_h^{(2)}\right)\mathbf{u}_h^{(1)}+B_1\mathbf{p}=\mathbf{f}_h^{(1)},$$
$$Re^{-1}L\mathbf{u}_h^{(2)}+A\left(\mathbf{u}_h^{(1)},\mathbf{u}_h^{(2)}\right)\mathbf{u}_h^{(2)}+B_2\mathbf{p}=\mathbf{f}_h^{(2)},$$
$$B_1^\top\mathbf{u}_h^{(1)}+B_2^\top\mathbf{u}_h^{(2)}=0,$$

where L is the discrete matrix for the Laplace operator, $A(\cdot)$ is the discrete matrix for the nonlinearity, and B_1, B_2 are the discrete matrices for the nabla operator.

2.2 The stochastic discretisation

In the next step we consider the stochastic incompressible Navier-Stokes equations, i. e. we consider equation (1), where the Reynolds number Re, the velocity u, the pressure p, and the right-hand side f are uncertain. Then our continuous problem reads as

$$\begin{aligned} -Re^{-1}(\omega)\Delta\mathbf{u}(x,\omega)+(\mathbf{u}(x,\omega)\cdot\nabla)\mathbf{u}(x,\omega)+\nabla p(x,\omega) &= \mathbf{f}(x,\omega) && \text{in } \mathcal{G}\\ \nabla\cdot\mathbf{u}(x,\omega) &= 0 && \text{in } \mathcal{G}, \end{aligned} \tag{5}$$

where ω is an elementary event (of a realisation) in a probability space $(\Omega,\mathcal{A},\mathbb{P})$ of random events. As in the previous subsection we first discretise (5) in the deterministic space. Then our discretised problem is given by

$$Re^{-1}(\omega)L\mathbf{u}_h^{(1)}(\omega)+A\left(\mathbf{u}_h^{(1)}(\omega),\mathbf{u}_h^{(2)}(\omega)\right)\mathbf{u}_h^{(1)}(\omega)+B_1\mathbf{p}(\omega)=\mathbf{f}_h^{(1)}(\omega), \tag{6}$$
$$Re^{-1}(\omega)L\mathbf{u}_h^{(2)}(\omega)+A\left(\mathbf{u}_h^{(1)}(\omega),\mathbf{u}_h^{(2)}(\omega)\right)\mathbf{u}_h^{(2)}(\omega)+B_2\mathbf{p}(\omega)=\mathbf{f}_h^{(2)}(\omega), \tag{7}$$
$$B_1^\top\mathbf{u}_h^{(1)}(\omega)+B_2^\top\mathbf{u}_h^{(2)}(\omega)=0. \tag{8}$$

For the stochastic discretisation we use a Galerkin approach, i. e. we look for a variational formulation. Therefore we multiply equations (6)–(8) with a testfunction H_γ and integrate over the stochastic domain Ω. We receive

$$\begin{aligned}
\int_\Omega \left[Re^{-1}(\omega)L\mathbf{u}_h^{(1)}(\omega) + A\left(\mathbf{u}_h(\omega)\right)\mathbf{u}_h^{(1)}(\omega) + B_1\mathbf{p}(\omega)\right] H_\gamma \mathbb{P}(d\omega) &= \int_\Omega \mathbf{f}_h^{(1)}(\omega) H_\gamma \mathbb{P}(d\omega),\\
\int_\Omega \left[Re^{-1}(\omega)L\mathbf{u}_h^{(2)}(\omega) + A\left(\mathbf{u}_h(\omega)\right)\mathbf{u}_h^{(2)}(\omega) + B_2\mathbf{p}(\omega)\right] H_\gamma \mathbb{P}(d\omega) &= \int_\Omega \mathbf{f}_h^{(2)}(\omega) H_\gamma \mathbb{P}(d\omega),\\
\int_\Omega \left[B_1^\top \mathbf{u}_h^{(1)}(\omega) + B_2^\top \mathbf{u}_h^{(2)}(\omega)\right] H_\gamma \mathbb{P}(d\omega) &= 0.
\end{aligned}$$

Any random variable $r(\omega) \in L_2(\Omega)$ can be represented as a series of polynomials in uncorrelated and independent Gaussian variables $\theta = (\theta_1, \dots)$ (see [Wie38]). This idea is called *polynomial chaos expansion* (PCE) and given by

$$\begin{aligned}
\mathbf{u}_h^{(k)}(\omega) &= \sum_\alpha \mathbf{u}_{h,\alpha}^{(k)} H_\alpha((\theta(\omega)), \quad k \in \{1,2\},\\
\mathbf{p}_h(\omega) &= \sum_\alpha \mathbf{p}_{h,\alpha} H_\alpha((\theta(\omega)),\\
\mathbf{f}_h^{(k)}(\omega) &= \sum_\alpha \mathbf{f}_{h,\alpha}^{(1)} H_\alpha((\theta(\omega)), \quad k \in \{1,2\},\\
Re(\omega)^{-1} &= \sum_\alpha Re_\alpha H_\alpha((\theta(\omega)).
\end{aligned}$$

For more details about we PCE we refer to [Mat07]. Inserting these formulas into our variational formulation leads to the following system

$$\begin{aligned}
L\sum_{\alpha,\beta} Re_\beta \mathbf{u}_{h,\alpha}^{(1)} \int_\Omega H_\alpha H_\beta \gamma \mathbb{P}(d\omega) + \int_\Omega A\left(\mathbf{u}_h^{(1)}(\omega), \mathbf{u}_h^{(2)}(\omega)\right)\mathbf{u}_{h,\alpha}^{(1)} H_\alpha H_\gamma \mathbb{P}(d\omega)&\\
+B_1 \sum_\alpha \mathbf{p}_{h,\alpha} \int_\Omega H_\alpha H_\gamma \mathbb{P}(d\omega) - \sum_\alpha \mathbf{f}_{h,\alpha}^{(1)} \int_\Omega H_\alpha H_\gamma \mathbb{P}(d\omega) = 0,& \quad (9)\\
L\sum_{\alpha,\beta} Re_\beta \mathbf{u}_{h,\alpha}^{(2)} \int_\Omega H_\alpha H_\beta H_\gamma \mathbb{P}(d\omega) + \int_\Omega A\left(\mathbf{u}_h^{(1)}(\omega), \mathbf{u}_h^{(2)}(\omega)\right)\mathbf{u}_{h,\alpha}^{(2)} H_\alpha H_\gamma \mathbb{P}(d\omega)&\\
+B_2 \sum_\alpha \mathbf{p}_{h,\alpha} \int_\Omega H_\alpha H_\gamma \mathbb{P}(d\omega) - \sum_\alpha \mathbf{f}_{h,\alpha}^{(2)} \int_\Omega H_\alpha H_\gamma \mathbb{P}(d\omega) = 0,& \quad (10)\\
B_1 \sum_\alpha \mathbf{u}_{h,\alpha}^{(1)} \int_\Omega H_\alpha H_\gamma \mathbb{P}(d\omega) + B_2 \sum_\alpha \mathbf{u}_{h,\alpha}^{(2)} \int_\Omega H_\alpha H_\gamma \mathbb{P}(d\omega) = 0.& \quad (11)
\end{aligned}$$

The polynomials H_α are chosen in such a way that the integrals can be solved analytically. One choice are multivariate Hermite polynomials which can be defined with a

recursion formula given by $h_{k+1}(t) = th_k(t) - kh_{k-1}$, $k \in \mathbb{N}$. The Hermite polynomials are orthogonal polynomials w.r.t. the standard Gaussian probability measure Γ, where $\Gamma(dt) = (2\pi)^{-1/2}e^{-t^2/2}$. The set

$$\{h_k(t)/\sqrt{k!} \mid k \in \mathbb{N}_0\}$$

forms a complete orthonormal system in $L_2(\mathbb{R}, \Gamma)$, since the Hermite polynomials satisfy

$$\int_{-\infty}^{\infty} h_m(t)h_n(t)\Gamma(dt) = n!\delta_{nm}.$$

A multivariate Hermite polynomial is defined by

$$H_\alpha(\mathbf{t}) := \prod_{j=1}^{d} h_{\alpha_j}(t_j), \qquad \forall \mathbf{t} \in \mathbb{R}^d,$$

where α is a multi-index. In Figures 1 and 2 we have visualised the Hermite polynomials H_{23}, H_{33}, H_{35}, and H_{55}.

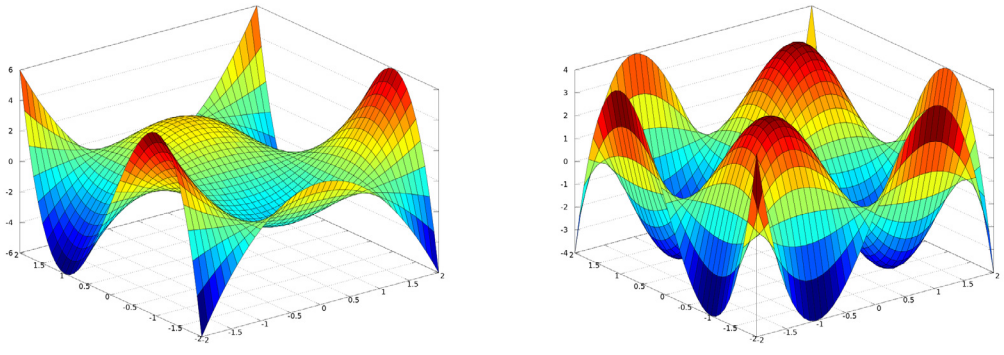


Figure 1: Hermite polynomials H_{23} and H_{33}

We can write each polynomial as a linear combination of Hermite polynomials. A product of two Hermite polynomials is again a polynomial which can be represented by Hermite polynomials, i. e.

$$h_k(t)h_l(t) = \sum_{n=|k-l|}^{k+l} c_{kl}^{(n)} h_n(t).$$

The coefficients $c_{kl}^{(n)}$ are only non-zero if $g := (k + l + n)/2 \in \mathbb{N}$ and if $g \geq k$, $g \geq l$ and $g \geq n$ (see [Mal97]).

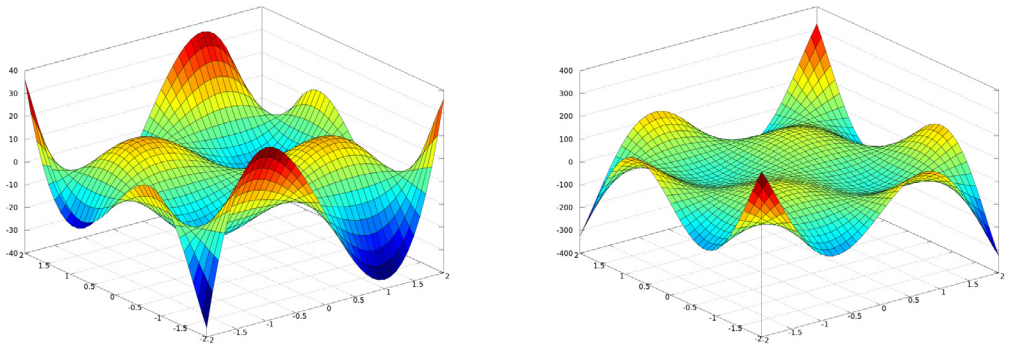


Figure 2: Hermite polynomials H_{35} and H_{55}

These properties of the Hermite algebra can be used to simplify equations (9)–(11). First of all we note that

$$\int_\Omega H_\alpha H_\gamma \mathbb{P}(d\omega) = \alpha! \delta_{\alpha\gamma}, \qquad \forall \alpha, \gamma$$

holds. The terms with three multivariate Hermite polynomials can be formulated as

$$\int_\Omega H_\alpha H_\beta H_\gamma \mathbb{P}(d\omega) = \sum_\eta c_{\alpha\beta}^{(\eta)} \eta! \delta_{\eta,\gamma}, \qquad \forall \alpha, \gamma.$$

A similar calculation can be done for the nonlinearities in (9) and (10), which can be written as follows

$$\begin{aligned}
&\int_\Omega \sum_{j=1}^{N_u} u_{j,h}^{(1)}(\omega)(\mathbf{u}_h^{(1)}(\omega)\partial_x\phi_j + \mathbf{u}_h^{(2)}(\omega)\partial_y\phi_j, \phi_i) H_\gamma \mathbb{P}(d\omega) \\
&= \sum_{j,k=1}^{N_u} \sum_{\alpha,\beta} u_{j,\alpha}^{(1)} u_{k,\beta}^{(1)} (\partial_x\phi_j, \phi_i) \int_\Omega H_\alpha H_\beta H_\gamma \mathbb{P}(d\omega) \\
&+ \sum_{j,k=1}^{N_u} \sum_{\alpha,\beta} u_{j,\alpha}^{(1)} u_{k,\beta}^{(2)} (\partial_y\phi_j, \phi_i) \int_\Omega H_\alpha H_\beta H_\gamma \mathbb{P}(d\omega).
\end{aligned}$$

In the next step we use all this information and put them into our discretised equations. Then we have a nonlinear system, which can be written as

$$L_\omega \mathbf{u}_{h,\omega}^{(1)} + A_{1,\omega}(\mathbf{u}_{h,\omega}^{(1)}, \mathbf{u}_{h,\omega}^{(2)}) + (B_1 \otimes I)\mathbf{p}_{h,\omega} = \mathbf{f}_{1,h,\omega} \tag{12}$$

$$L_\omega \mathbf{u}_{h,\omega}^{(2)} + A_{2,\omega}(\mathbf{u}_{h,\omega}^{(1)}, \mathbf{u}_{h,\omega}^{(2)}) + (B_2 \otimes I)\mathbf{p}_{h,\omega} = \mathbf{f}_{2,h,\omega} \tag{13}$$

$$(B_1^\top \otimes I)\mathbf{u}_{h,\omega}^{(1)} + (B_2^\top \otimes I)\mathbf{u}_{h,\omega}^{(2)} = 0. \tag{14}$$

3 SOLVING THE NONLINEAR SYSTEM

In this section we consider solution techniques for system (12)–(14). For further investigation we write our system in the form

$$\begin{aligned} f_1(u_1,\ldots,u_N) &= 0 \\ &\vdots \quad . \\ f_N(u_1,\ldots,u_N) &= 0 \end{aligned} \tag{15}$$

3.1 The monolithic approach

In the case of the monolithic approach the nonlinear system (15) is solved with a special method with a software, i. e. we apply a fixed point iteration or Newton's method on (15). The resulting linear system is solved with a direct or an iterative method. The disadvantage of this approach is that we have to deal with all degrees of freedom using one computer. Since we have a very high number of unknowns partitioned methods are considered as follows.

3.2 Partitioned methods

In the case of partitioned methods we split the system (15) into N nonlinear subsystems. Each subsystem is then solved by a method described in the subsection about the monolithic approach.

Often the so-called Block-Jacobi is applied. In this case we solve each subsystem independently from each other. At the end of each iteration we build the new iteration vector. This method can be easily parallelised and works as follows:

- Solve the nonlinear systems

  $$f_i(u_1^{(k)},\ldots,u_{i-1}^{(k)},u_i^{(k+1)},u_{i+1}^{(k)},u_N^{(k)}) = 0$$

  w.r.t. $u_i^{(k+1)}$ for $i = 1,\ldots,N$.

- Repeat this step until $\|\mathbf{u}^{(k+1)} - \mathbf{u}^{(k)}\|$ is sufficiently small.

Another approach is the Block–Gauß–Seidel method, which is given by the following algorithm:

- Solve the nonlinear systems

  $$f_i(u_1^{(k+1)},\ldots,u_{i-1}^{(k+1)},u_i^{(k+1)},u_{i+1}^{(k)},u_N^{(k)}) = 0$$

  w.r.t. $u_i^{(k+1)}$ for $i = 1,\ldots,N$.

- Repeat this step until $\|\mathbf{u}^{(k+1)} - \mathbf{u}^{(k)}\|$ is sufficiently small.

4 NUMERICAL RESULTS

As a numerical example we consider the two dimensional Burgers equation, which is given by

$$-\epsilon\Delta u + uu_x + uu_y = f \quad \text{in } (0,1)^2.$$

Moreover we need some boundary conditions to receive a unique solution. We discretise the problem with central differences and with a stochastic Galerkin method. For the spatial discretisation we use the stepsize $h = 1/20$ such that the deterministic problem has 400 degrees of freedom. In the case of the stochastic discretisation we choose $d = 2$ and $p = 5$, where p is the maximal degree of the Hermite polynomials. Then the stochastic problem has 21 unknowns. Together with the spatial problem our fully coupled problem has 10500 degrees of freedom. From the exact solution given by

$$u(x, y) = x^2 - 2x + 3$$

we compute the Dirichlet boundary conditions and the right-hand side.

We solve this nonlinear system of equations with a modified fixed point iteration which is already used in the area of solving the deterministic Navier–Stokes equations (see [JMR06, Joh04]). If Newton's method is applied for solving the nonlinear equations the solution process may fail if the stochastic dimension increases. In Figure 3 we have visualised the numerical error of the Galerkin coefficients w.r.t. the iteration number. We compare the monolithic approach with the Block–Jacobi and the Block–Gauß–Seidel methods. It can be observed that the monolithic approach needs less iteration steps. For a larger number of iteration steps the Block–Gauß–Seidel method produces more accurate results than the Block–Jacobi method.

5 SUMMARY AND OUTLOOK

In this article we considered the incompressible Navier–Stokes equations and their discretisation in the spatial and the stochastic domains. For the stochastic discretisation a stochastic Galerkin method is used which leads to a coupled system of nonlinear equations. This system is solved with partitioned methods like the Block–Jacobi and the Block–Gauß–Seidel method.

In future work this approach should be applied to the incompressible Navier–Stokes equations.

REFERENCES

[Chr92] G. Christakos. *Random field models in earth sciences.* Academic Press, San Diego, CA, 1992.

[Eli99] I. Elishakoff. *Whys and Hows in Uncertainty Modelling-Probability, Fuzziness, and Anti-Optimization.* Springer-Verlag, Berlin, 1999.

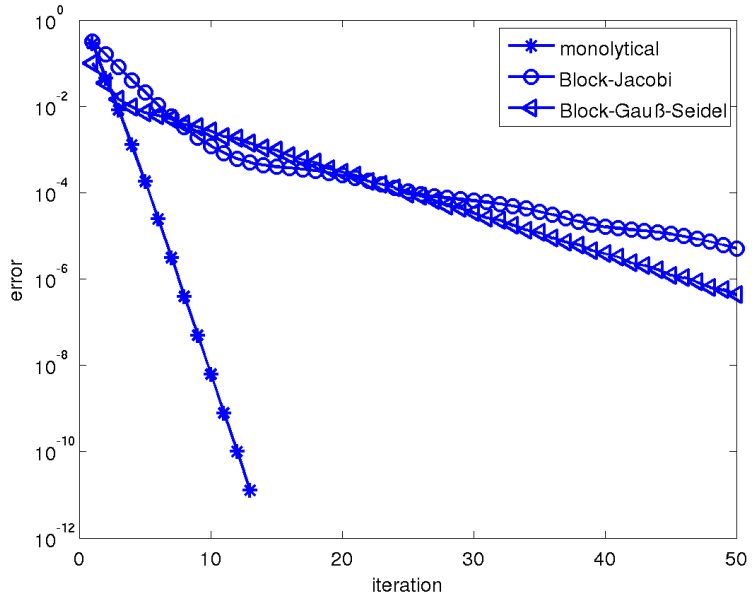


Figure 3: Numerical result for Burgers equation

[GR86] V. Girault and P.-A. Raviart. *Finite Element Methods for Navier-Stokes equations*. Springer-Verlag, Berlin-Heidelberg-New York, 1986.

[Gri02] M. Grigoriu. *Stochastic Calculus—Applications in Science and Engineering*. Birkhäuser Verlag, Basel, 2002.

[GS91] R. Ghanem and P. D. Spanos. *Stochastic finite elements—A spectral approach*. Springer-Verlag, Berlin, 1991.

[GS00] P.M. Gresho and R.L. Sani. *Incompressible Flow and the Finite Element Method*. Wiley, Chichester, 2000.

[HØUZ96] H. Holden, B. Øksendal, J. Ubøe, and T.-S. Zhang. *Stochastic Partial Differential Equations*. Birkhäuser Verlag, Basel, 1996.

[Jay03] E.T. Jaynes. *Probability Theory, the Logic of Science*. Cambridge University Press, Cambridge, 2003.

[JMR06] V. John, G. Matthies, and Joachim Rang. A comparison of time-discretization/linearization approaches for the incompressible Navier–Stokes equations. *Comput. Methods Appl. Mech. Eng.*, 195:5995–6010, 2006.

[Joh04] V. John. *Large Eddy Simulation of Turbulent Incompressible Flows. Analytical and Numerical Results for a Class of LES Models*, volume 34 of *Lecture Notes*

in Computational Science and Engineering. Springer-Verlag Berlin, Heidelberg, New York, 2004.

[KO01] M. Kennedy and A. O'Hagan. Bayesian calibration of computer models. *Journal of the Royal Statistical Society, Series B*, 63:425–464, 2001.

[Mal97] P. Malliavin. *Stochastic Analysis*. Springer-Verlag, Berlin, 1997.

[Mat07] H. G. Matthies. Uncertainty quantification with stochastic finite elements. In E. Stein, R. de Borst, and T. R. J. Hughes, editors, *Encyclopedia of Computational Mechanics*. John Wiley & Sons, Chichester, 2007.

[MB99] Hermann G. Matthies and Christian G. Bucher. Finite elements for stochastic media problems. *Comp. Meth. Appl. Mech. Engrg.*, 168:3–17, 1999.

[MBBS97] Hermann G. Matthies, Christoph E. Brenner, Christoph G. Bucher, and Carlos Guedes Soares. Uncertainties in probabilistic numerical analysis of structures and solids—stochastic finite elements. *Structural Safety*, 19(3):283–336, 1997.

[MK05] H. G. Matthies and A. Keese. Galerkin methods for linear and nonlinear elliptic stochastic partial differential equations. *Comp. Meth. Appl. Mech. Engrg.*, 194:1295–1331, 2005.

[NBH97] H.G. Natke and Y. Ben-Haim, editors. *Uncertainty: Models and Measures*. Akademie-Verlag, Berlin, 1997.

[Pap91] A. Papoulis. *Probability, random variables and stochastic processes*. McGraw-Hill, Singapore, 1991.

[RO10] C. J. Roy and W. L. Oberkampf. A complete framework for verification, validation and uncertainty quantification in scientific computing. *AIAA-Paper*, 2010-124, 2010.

[Tur99] S. Turek. *Efficient Solvers for Incompressible Flow Problems: An Algorithmic and Computational Approach*, volume 6 of *Lecture Notes in Computational Science and Engineering*. Springer, Berlin, 1999.

[Wie38] N. Wiener. The homogeneous chaos. *American Journal of Mathematics*, 60:897–936, 1938.

V International Conference on Computational Methods in Marine Engineering
MARINE 2013
B. Brinkmann and P. Wriggers (Eds)

CONCEPT AND REALIZATION OF THE COUPLING SOFTWARE EMPIRE IN MULTIPHYSICS CO-SIMULATION

T. WANG, S. SICKLINGER, R. WÜCHNER AND K.-U. BLETZINGER

Lehrstuhl für Statik
Technische Universität München
Arcisstr. 21, D-80333 München, Germany
e-mail: tianyang.wang@tum.de, stefan.sicklinger@tum.de, wuechner@tum.de, kub@tum.de,
web page: http://www.st.bv.tum.de

Key words: multiphysics, co-simulation, partitioned analysis, fluid-structure interaction

Abstract. The purpose of the software EMPIRE is to perform n-code co-simulation for solving multiphysics problems. EMPIRE provides a flexible way for constructing various co-simulation environments by introducing the concepts of *connection* and *filter*. It also provides data operations useful for general co-simulation including mapping between non-matching grids, extrapolation in time and relaxation in iterative coupling. The concepts and ingredients of EMPIRE are presented in this paper. Finally, the software is demonstrated by two FSI simulations.

1 INTRODUCTION

Multiphysics problems can be formulated by coupled systems of partial differential equations and ordinary differential equations. Two classical strategies for solving coupled systems are the monolithic strategy and the partitioned strategy. In the monolithic strategy, the global equation of the coupled systems is formulated and solved, whereas in the partitioned strategy, the single systems are solved separately and coupled together by exchanging information at the interfaces. With the partitioned strategy, different simulation codes can work together in a co-simulation to solve multiphysics problems, see Figure 1. From the software development point of view, partitioned strategy has a big advantage of reusing existing and well-tested simulation codes for single field problems.

One example of multiphysics is the simulation of wind turbines to study the fluid-structure-interaction (FSI) between the wind load and the turbine blades, see Figure 2. Usually, computational structural mechanics (CSM) and computational fluid dynamics (CFD) are coupled together to simulate the wind turbine with a fixed rotational speed. If the real time rotational speed of the wind turbine is needed, the model of the power

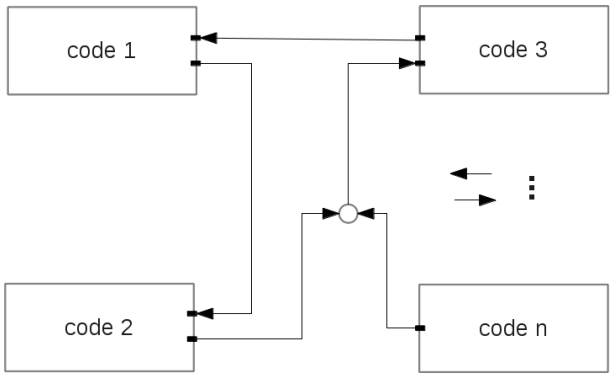


Figure 1: Co-simulation with n codes

generator should be added to the co-simulation. Additional simulation codes can be added to the co-simulation to simulate more complex scenarios.

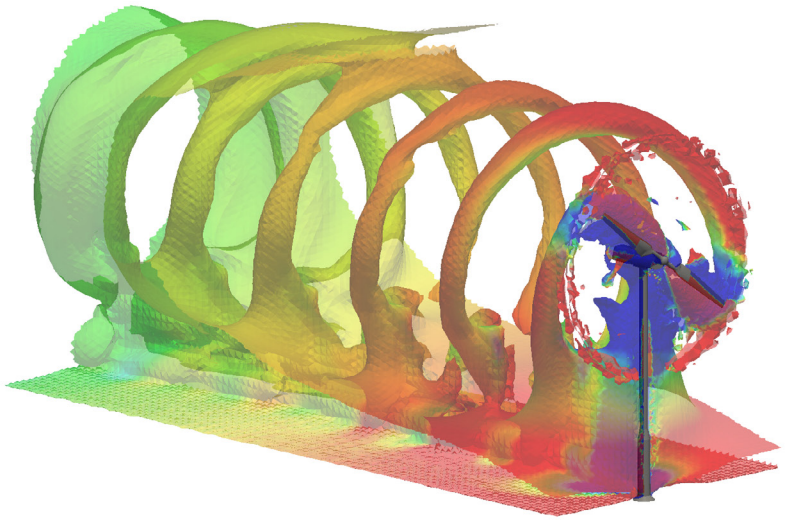


Figure 2: FSI simulation of a wind turbine

The newly designed software EMPIRE (Enhanced MultiPhysics Interface Research Engine) enables co-simulation with n-codes, to solve general multiphysics problems. The concepts of EMPIRE will be introduced in the next section.

2 CONCEPTS OF EMPIRE

Figure 3 shows co-simulation in the EMPIRE environment. The software EMPIRE has two components, the coupling code Emperor and the library EMPIRE_API for the simulation codes to communicate with Emperor. The data communication instance between codes is called *connection*. Inside a connection, the data can be manipulated by

operators called *filters*.

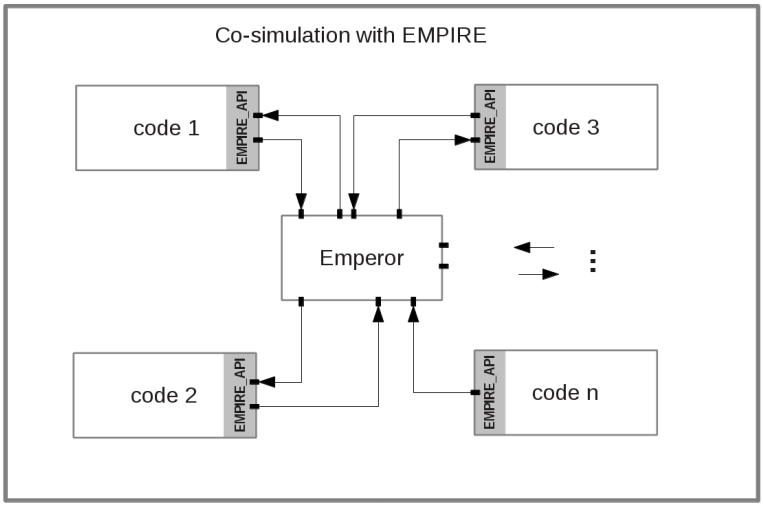


Figure 3: Co-simulation with EMPIRE

2.1 Coupling code Emperor

The coupling code Emperor couples all simulation codes together to perform co-simulation. Having a separate coupling code brings advantages including:

- the simulation codes only communicate with Emperor, without having the knowledge of the other codes in the co-simulation environment;
- unified format for data communication is defined by Emperor, which is followed by all simulation codes;
- the co-simulation environment can be defined in a single file that is read by Emperor;
- the data operations during communication are contained within Emperor which eliminates the need to modify existing simulation codes.

The server-client model is adopted with Emperor as the server and the simulation codes as the clients. The server opens a port at the beginning of the co-simulation to which an arbitrary number of clients can connect. The communication between the server and the client is performed using MPI-2.2.

2.2 Communication Library EMPIRE_API

The simulation codes communicate with Emperor using EMPIRE_API. It is a library containing functions such as connecting to and disconnecting from Emperor, communicating data of a certain type (e.g. mesh, degree of freedom, signal, etc) with Emperor.

EMPIRE_API is written in C++, but interfaced by C functions. As an example, the function of sending a finite element mesh to Emperor is quoted below:

```
void EMPIRE_API_sendMesh(int numNodes, int numElems, double *nodes, int
*nodeIDs, int *numNodesPerElem, int *elems);
```

where the input arguments consist of the number of nodes, the number of elements, the coordinates of all nodes, the IDs of all nodes, the number of nodes of all elements and the connectivity table of all elements.

EMPIRE_API can be compiled and linked together with simulation codes written in languages compatible with C, e.g. C, C++, Fortran, Python, Java, MATLAB, etc.

2.3 Definition of the Co-simulation Scenario by Connections

A connection is the data communication between different codes. It can have multiple inputs and outputs, which makes it more flexible for different scenarios. The inputs are the data sent from simulation codes and received by Emperor, and the outputs are the data sent from Emperor and received by simulation codes, see Figure 4. The co-simulation scenario can be defined by sequences and iterations of connections.



Figure 4: Connection in Emperor

To show how the co-simulation scenario is defined, the co-simulation of a wind turbine with three codes is taken as an example. The three codes are the CFD code, the CSM code and the generator code respectively. The CFD code can be expressed as

$$f_F = F(u_F), \tag{1}$$

where u_F is the displacements of the turbine, and f_F is the wind forces acting on the turbine. The code of the generator can be expressed as

$$T_R = G(T_A), \tag{2}$$

where T_A is the acting torque on the turbine shaft (computed from the wind forces on the turbine blades) and T_R is the reacting torque caused by the generator. The CSM code can be expressed as

$$u_S = S(f_S, T_{RS}), \tag{3}$$

where f_S is the fluid forces on the turbine, and T_{RS} is the reacting torque. The connections between the codes are defined in the left diagram in Figure 5 (where Emperor is omitted but the data must go through it). During the co-simulation, the CFD code computes the wind forces on the turbine and sends them to the generator code (connection 1). Then the generator computes the reacting torque according to the wind forces and sends it to the CSM code (connection 2). Then the CFD code also sends the wind forces to the CSM code (connection 3). Finally the CSM code can compute the displacements of the turbine according to both the wind forces and the reacting torque on the shaft and then send the displacements to the CFD code (connection 4). This completes one iteration. In the flowchart in Figure 5, the sequences and iterations of the connections are shown. The connections are put inside two nested iterations. The outer iteration is the time stepping, and the inner iteration is the iterative coupling which means the connections are run iteratively until the data are converged.

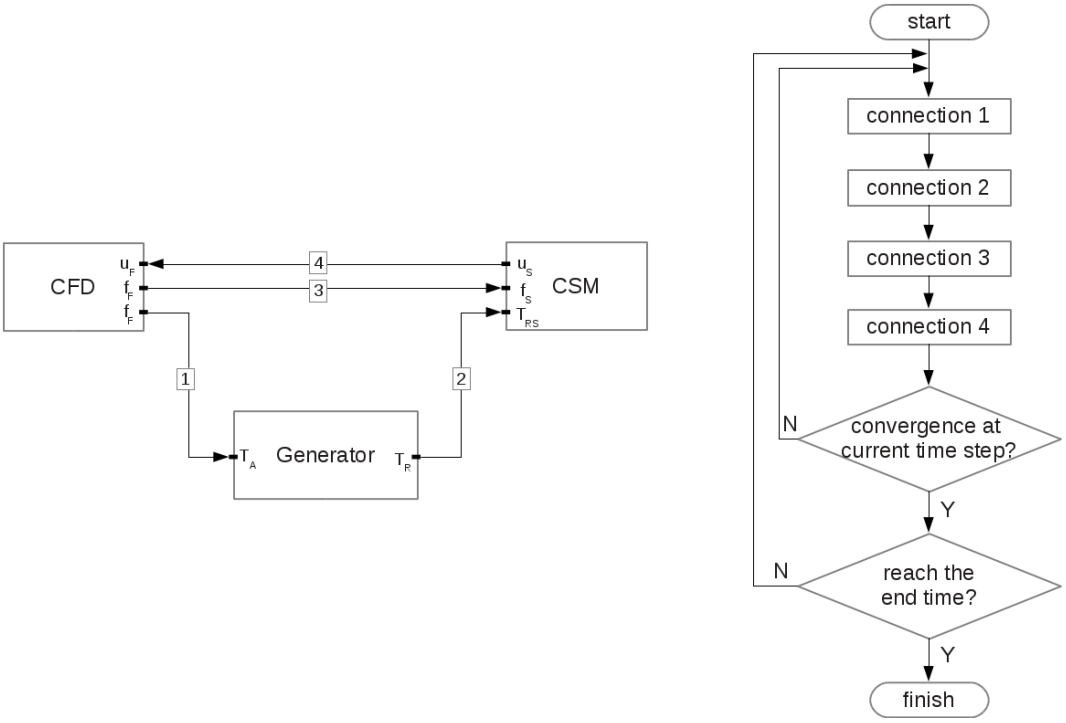


Figure 5: Co-simulation scenario of a wind turbine simulation

The connections are defined in the input XML file of Emperor, as well as the sequences and iterations of the connections. Emperor performs data communication accordingly, i.e. send or receive data at the expected time. However, because the simulation codes are running without being controlled by Emperor, the communication would fail if some simulation code does not send or receive data at the expected time. To assist a user in setting up a co-simulation, Emperor can output pseudo code for each simulation code

specifying how to do communication. The communication will work as expected if each simulation code follows the communication pattern in the pseudo code.

2.4 Filters in Connection

The inputs and outputs of a connection are generally different. Therefore, a sequence of operators may be applied which are named filters in EMPIRE. A filter can have multiple inputs and outputs. The filters inside a connection are shown in Figure 6.

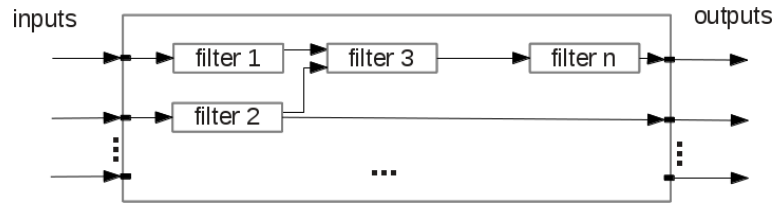


Figure 6: Filters inside a connection

Filters that are usually used in a co-simulation are introduced below.

2.4.1 Mapping Filter

At the interface between two surface coupled domains, the grids from both sides are usually non-matching, so the data cannot be assigned between the grids directly. In Emperor, the mortar method is implemented to map data between non-matching grids. The condition for mapping a data field from domain A to domain B is

$$u_B(x) = u_A(x), \tag{4}$$

where x is the coordinates, and $u_A(x)$ and $u_B(x)$ are the data field on A and B, respectively. By discretizing the fields with finite element method one has

$$\begin{aligned} u_A(x) &= N_A^T \cdot u_A, \\ u_B(x) &= N_B^T \cdot u_B, \end{aligned} \tag{5}$$

where u_A and u_B are values of $u_A(x)$ and $u_B(x)$ on grid points, and N_A and N_B are the shape function vectors of A and B, respectively. Mortar method applies weighted residual approach for (4) using N_B as the test function vector as

$$\int_B N_B(u_B(x) - u_A(x))\, dB = 0. \tag{6}$$

Apply (5) in (6) one has

$$\int_B N_B \cdot N_B^T\, dB \cdot u_B = \int_B N_B \cdot N_A^T\, dB \cdot u_A, \tag{7}$$

which can be reorganized in matrix-vector form as

$$C_{BB} \cdot u_B = C_{BA} \cdot u_A. \tag{8}$$

Since C_{BB} and C_{BA} are both sparse matrices, solving (8) takes much less computational effort than the case of full matrices. In (7), if the test functions are replaced by the dual shape functions, C_{BB} becomes a diagonal matrix [1, 2] so that (8) can be solved by computing the inverse matrix of C_{BB}. It is shown in [4] that using mortar method in FSI with a certain condition, both displacements and pressures can be mapped consistently while the energy being conserved. This is the advantage of mortar method compared with interpolation-like methods.

In Figure 7, it is shown that mortar method works well in mapping prototyped data field on a curved surface.

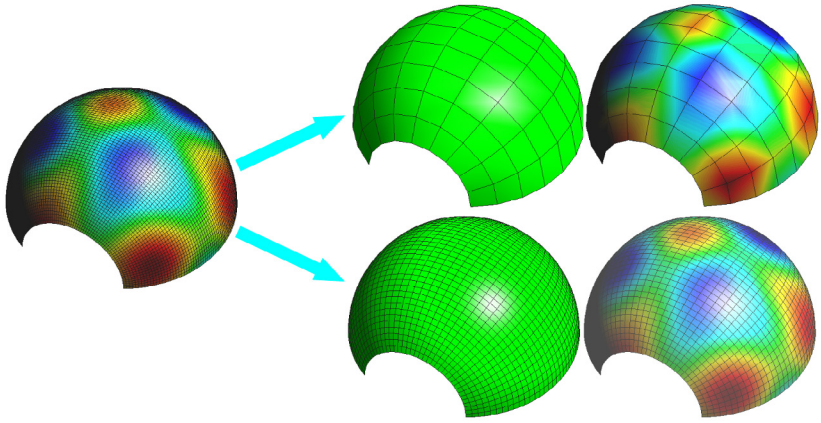


Figure 7: Mapping data field on a spherical surface with mortar method

2.4.2 Extrapolation Filter

At the beginning of a new time step, a prediction of the data at the coupled interface may have to be made. For example in Figure 5, at the beginning of time step $n+1$, the CFD code does not have the turbine displacements u_F^{n+1}. Therefore a prediction of it ($\hat{u}_F^{n+1}$) is computed and used in (1) as

$$f_F^{n+1} = F(\hat{u}_F^{n+1}). \tag{9}$$

The prediction is usually computed by extrapolation of values of previous time steps. The simplest extrapolation method is to use the value from the last time step as $\hat{u}_F^{n+1} = u_F^n$. More complicated extrapolation methods can be found in [5, 6].

2.4.3 Relaxation Filter

In iterative coupling, relaxation can be used to stabilize the simulation. Assume the input and output of the relaxation filter are x_{in} and x_{out} respectively, then at the $k+1$ iteration, the new output is computed by

$$\begin{aligned} x_{out}^{k+1} &= x_{out}^{k} + \omega(x_{in}^{k+1} - x_{out}^{k}) \\ &= (1-\omega)x_{out}^{k} + \omega x_{in}^{k+1}, \end{aligned} \tag{10}$$

where ω is the relaxation factor. It can be constant for all iterations, or can be computed dynamically in each iteration by Aitken's Δ^2 method to accelerate the convergence [7].

3 NUMERICAL EXAMPLES OF FSI

The example driven cavity with flexible bottom introduced in [9] is simulated, see Figure 8. The fluid domain is a 2D square with a periodic velocity imposed at the top. An inlet and an outlet are shown at the top of the left and right wall respectively. The bottom is modelled by a membrane structure. Figure 9 shows the result at the time $t = 4.25$(s).

Another example is the FSI benchmark by Turek [8], where the incompressible fluid flows around a cylinder and an elastic bar behind it, see Figure 10. The test case FSI3 in [8] is simulated, and the result at the time $t = 3.9$(s) is shown in Figure 11.

4 CONCLUSIONS

EMPIRE is designed and implemented for solving general multiphysics problems with n-code co-simulation. It has the following characteristics:

- Flexibility: co-simulation in a general scenario is available, since an arbitrary number of simulation codes and arbitrary connections among them is allowed.
- Modularity: partitioned strategy is used to apply existing simulation codes; the simulation codes are connected by Emperor; communication interface is provided in the library EMPIRE_API; object oriented programming with C++ is used to implement EMPIRE.
- Efficiency: communication is realized by using MPI; efficient mortar method is implemented for mapping data between non-matching grids; methods are implemented to accelerate co-simulation, e.g. extrapolation and relaxation.
- Usability: co-simulation is set up in a single file (input XML file of Emperor); simulation codes in all C-compatible languages can link to the library EMPIRE_API; various filters are provided for data operations including mapping, extrapolation and relaxation.

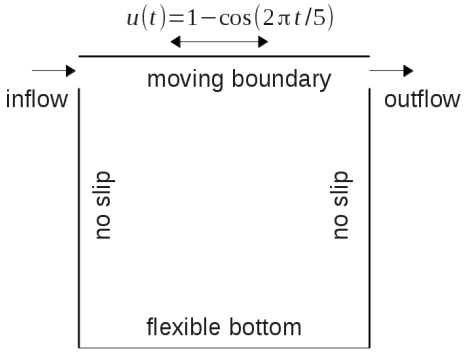


Figure 8: Driven cavity with flexible bottom

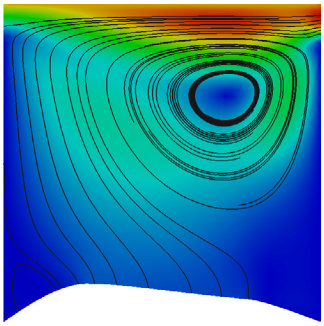


Figure 9: Result – velocity field and streamline at $t = 4.25$(s)

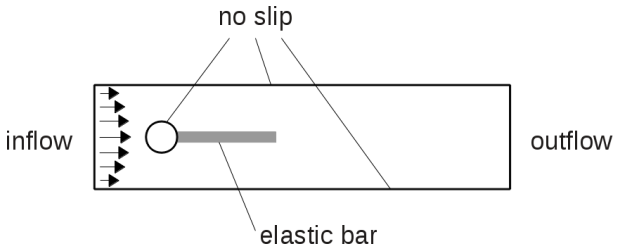


Figure 10: Flow around cylinder and an elastic bar behind it

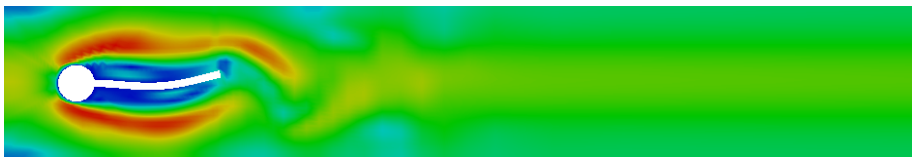


Figure 11: Result – velocity field at $t = 3.9$(s)

The next steps of EMPIRE include new coupling algorithms for n-code coupling where traditional coupling algorithms may have problems, and allowing adjustable time step length for simulation codes. The software will be further verified by examples of large scale n-code co-simulation.

REFERENCES

[1] Hartmann, S., Brunssen, S., Ramm, E. and Wohlmuth, B. Unilateral non-linear dynamic contact of thin-walled structures using a primal-dual active set strategy. *Int. J. Numer. Meth. Engng* (2007) **70**:883–912.

[2] Klöppel, T., Popp, A., Küttler, U. and Wall, W.A. Fluid-structure interaction for non-conforming interfaces based on a dual mortar formulation. *Comput. Methods Appl. Mech. Engrg* (2011) **200**:3111–3126.

[3] Unger, R., Haupt, M.C. and Horst, P. Application of Lagrange multipliers for coupled problems in fluid and structural interactions. *Computers & Structures.* (2007) **85**:796–809.

[4] Boer, de A., Zuijlen, van A.H. and Bijl, H. Comparison of conservative and consistent approaches for the coupling of non-matching meshes. *Comput. Methods Appl. Mech. Engrg* (2008) **197**:4284–4297.

[5] Felippa, C.A., Park, K.C. and Farhat, C. Partitioned analysis of coupled mechanical systems. *Comput. Methods Appl. Mech. Engrg* (2001) **190**:3247–3270.

[6] Farhat, C. and Piperno, S. Partitioned procedures for the transient solution of coupled aeroelastic problems – Part II: energy transfer analysis and three dimensional applications. *Comput. Methods Appl. Mech. Engrg* (2001) **190**:3147–3170.

[7] Küttler, U. and Wall, W.A. Fixed-point fluid-structure interaction solvers with dynamic relaxation. *Comput. Mech.* (2008) **43**:61–72.

[8] Turek, S. and Hron, J. Proposal for numerical benchmarking for fluid-structure interaction between an elastic object and laminar incompressible flow. In: Bungartz, H.J. and Schäfer, M. (Eds), *Fluid-structure interaction: modelling, simulation, optimization*, Springer, (2006) 371–385.

[9] Mok, D.P. and Wall, W.A. Partitioned analysis schemes for the transient interaction of incompressible flows and nonlinear flexible structures. In: Wall, W.A., Bletzinger, K.-U. and Schweitzerhof, K. (Eds), *Proceedings of trends in computational structural mechanics*, CIMNE, (2001) 689–698.

V International Conference on Computational Methods in Marine Engineering
MARINE 2013
B. Brinkmann and P. Wriggers (Eds)

MODELLING OF WATER FLOW WITH FREE SURFACE

MONIKA WARMOWSKA

Polski Rejestr Statków S.A.
Al. Gen. Józefa Hallera 126
80-416 Gdańsk, Poland
e-mail: m.warmowska@prs.pl, www.prs.pl

Key words: Free Surface, Harmonic wave, Sloshing, Shallow Water Problem, BEM

Abstract. Simulation of ship motion in irregular waves, modelling of sloshing inside ship tanks or flooded holds and flow of trapped water on fishing vessel deck requires special numerical methods to solve problems describing these phenomena. Accuracy of modelling of the deformed free surface in these phenomena significantly affects the solutions. The paper presents the assumptions, algorithms and results obtained in modelling the free surface and shows results of several years of research performed in Polski Rejestr Statków to enhance ship safety. The studies contribute to better awareness of ship behaviour, capsizing phenomenon, failure of ship structure and other undesired events.

1 INTRODUCTION

Modelling a vessel's motion in waves requires the following models of water flow:

- model of water flow around the ship,
- model of water flow inside ship's tank or damaged holds,
- model of trapped water flowing on vessel deck.

Generally the velocity field, the potential of the velocity (if the flow is potential), the pressure field, the free surface position or the changing water domain (e.g. the amount of water mass on fishing vessel) need to be determined in solving the ship hydrodynamics problems in order to simulate vessel motion in waves and motion of liquids in its tanks. Modelling of these phenomenon requires various assumptions to enable the use numerical method. For example, some hydrodynamics problems are solved neglecting the elevation of diffracted waves in determining the hydrodynamic forces acting on the vessel (linear models).

Boundary Element Methods [3], Volume of Fluid technique [1], Finite Elements Method [4], Shallow water method [2] and others [6] are used to solve the hydrodynamics problems.

It is important to choose a model as simple as possible but without loosing sight of the essence of water behaviour. The proper determination of hydrodynamic forces acting on the moving ship in waves is very important in terms of safety.

The paper focuses on the problem of free surface elevation and its importance in the modelling of some phenomenon in vessel motion in waves and motion of liquid in tanks.

2 PRESSURE FIELD IN REGULAR WAVE

The hydrodynamic forces induced by wave and ship motions result in the ship moving in waves. The linear model assumes a small wave amplitude. Thus the velocity field around the ship is potential and the irregular wave is assumed to be the superposition of regular waves. Assumption of the small wave amplitude in determination of the velocity flow is possible if the main dimensions of ship are significantly larger than wave height.

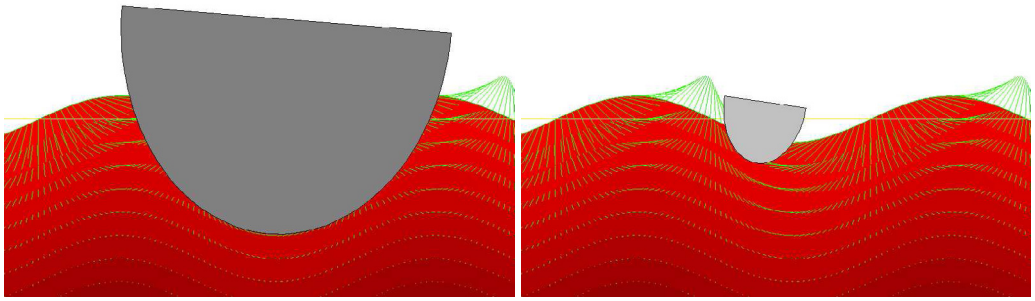


Figure 1 Big and small ship moving in a regular wave

In the linear model the velocity potential ϕ of harmonic wave is defined as follows:

$$\phi = \frac{r_0}{\omega} e^{kz} \sin(kx - \omega t), \tag{1}$$

where r_0 is the amplitude of harmonic wave, k is the wave number, ω is the frequency of harmonic wave oscillations ($\omega^2=kg$ for a deep water), (x, z) is the position of water particle, t is the time treated as a parameter. Axis OZ has an upward direction. The study refers to three methods. In the first method (linear) the pressure p_I is obtained from the linearized Bernoulli equation as follows:

$$p_I = p_0 - \rho g z + \rho g \zeta e^{kz}, \tag{2}$$

where p_0 is the pressure on the free surface, ζ is the elevation of the wave surface above a point on undisturbed surface $(x,0)$ defined as follows:

$$\zeta = r_0 \cos(kx - \omega t). \tag{3}$$

In the second method the pressure p_{II} depends on the position of a wave crest or a wave trough and is approximated by the formula:

$$p_{II} = p_0 - \rho g z + \rho g \zeta e^{k(z-\zeta)}. \tag{4}$$

In the third method (presented in report [12]) the wave is described as a cycling particles around their average position:

$$\begin{aligned} x(t) &= x_0 - r_0 e^{kz_0} \sin(kx_0 - \omega t), \\ z(t) &= z_0 + r_0 e^{kz_0} \cos(kx_0 - \omega t), \end{aligned} \tag{5}$$

where (x_0, z_0) is the average position of a water's particle. For harmonic wave in deep water it is the orbital motion. In this method the position of free surface is defined by equation (5) for z_0 equal to zero. If the average position (x_0, z_0) of liquid particle is given the value of pressure p_{III} is obtained from the following formulae:

$$p_{III} = p_0 - \rho g\left(z_0 + \zeta_0 - \zeta_0 e^{kz_0} + 0.5kr_0^2\left(1 - e^{2kz_0}\right)\right). \tag{6}$$

where the elevation of the wave surface ζ_0 is defined as:

$$\zeta_0 = r_0 \cos(kx_0 - \omega t). \tag{7}$$

If the wave amplitude r_0 is small the pressure may be approximated by the following formulae:

$$p_{IV} \approx p_0 - \rho g\left(z_0 + \zeta_0 - \zeta_0 e^{kz_0}\right). \tag{8}$$

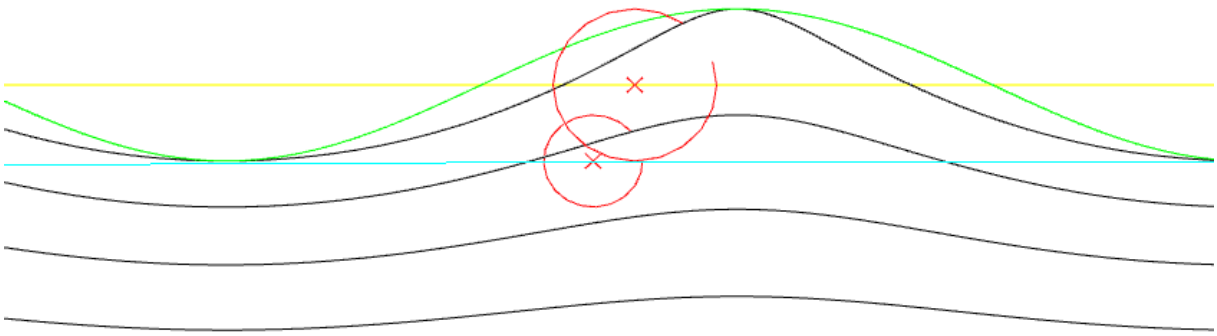


Figure 2 Orbital motion – position of surfaces for liquid particles with fixed z_0 and snapshot time t

In Figure 2, black lines show the surfaces created by cycling liquid particles for fixed z_0 (a yellow line is the still water level for particles with the vertical average position z_0 equals zero and a blue line for z_0 equal to $-r_0$), a green line is the free surface determined by equation (3), red cycles are tracks of liquid particles determined by equations (5).

Table 1 shows the pressures obtained using these four methods for the following wave parameters:

- the amplitude r_0 is equal to 2,25 meters,
- the period T of wave oscillation equals to 9,5 seconds,
- the average position (x_0, z_0) is situated at a point (0,–2).

The position of oscillating liquid particle (x, z) is calculated using equation (5). The wave elevation ζ in method I and II is determined by equation (3) and the wave elevation ζ_0 in method III and method IV – by equation (7).

The differences between method I and method III reaches 3.92Pa (for t equal to zero). The differences between method II and method III is not greater than 2,41Pa. The relative errors will increase if the cycling particle is reaching the wave surface and the errors will decrease if the cycling particle moves away from the wave surface.

The pressure calculations are simpler in the first and second method than in the third method. The method I and II are usually used to solve problems when the main dimensions of

the vessel exceed significantly the wave amplitude. In the case of fishing vessel motion, when the vessel draught is about 1to 3 meters, the third method, describing the orbital motion of the water particles, should be used [13].

Table 1: Pressure obtained by four methods

t [s]	x[m]	z[m]	ζ[m]	ζ_0[m]	p_I[Pa]	p_{II}[Pa]	p_{III}[Pa]	p_{IV}[Pa]
0.00	0.00	0.06	2.25	2.25	22.10	19.93	17.99	18.18
0.79	1.03	-0.22	2.00	1.95	22.09	20.39	18.25	18.44
1.58	1.78	-0.97	1.28	1.13	22.05	21.37	18.96	19.15
2.38	2.06	-2.00	0.21	0.00	22.01	21.99	19.93	20.11
3.17	1.78	-3.03	-0.97	-1.13	21.96	21.59	20.89	21.08
3.96	1.03	-3.78	-1.89	-1.95	21.94	20.52	21.60	21.78
4.75	0.00	-4.06	-2.25	-2.25	21.93	19.93	21.86	22.04
5.54	-1.03	-3.78	-1.89	-1.95	21.94	20.52	21.60	21.78
6.33	-1.78	-3.03	-0.97	-1.13	21.96	21.59	20.89	21.08
7.13	-2.06	-2.00	0.21	0.00	22.01	21.99	19.93	20.11
7.92	-1.78	-0.97	1.28	1.13	22.05	21.37	18.96	19.15
8.71	-1.03	-0.22	2.00	1.95	22.09	20.39	18.25	18.44
9.50	0.00	0.06	2.25	2.25	22.10	19.93	17.99	18.18

3 SLOSHING INSIDE SHIP TANK

Solving of the problem of water motion inside ship's tanks or holds focuses on determining of the free surface. A domain occupied by a fluid surrounded by the tank's walls changes during the simulation.

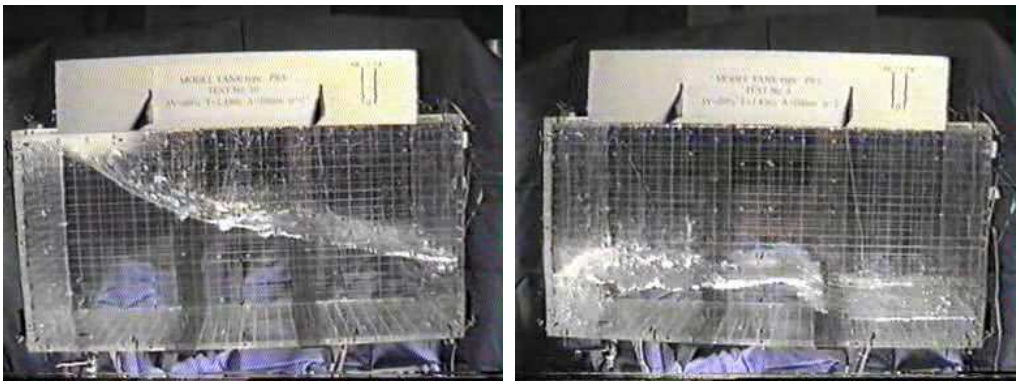


Figure 3 Sloshing phenomena in partially filled tank

Tank filled over 30%

If the tank is filled over 30% the free surface hitting a ceiling causes a dangerous consequences such as a construction failure. The forces induced by sloshing are taken into account in ship's motion equations [9].

If the oscillation of tank meets the natural period of fluid motion in the tank a standing wave is observed. The linear problem can be used only for wave of a small amplitude and when the volume of water does not reach the tank top. An observation of the standing wave velocity shows that the maximum value of velocity appears when moving free surface pierces the calm water plane (blue line in Figure 4). When a maximum elevation is achieved gravity forces generate accelerated wave motion.

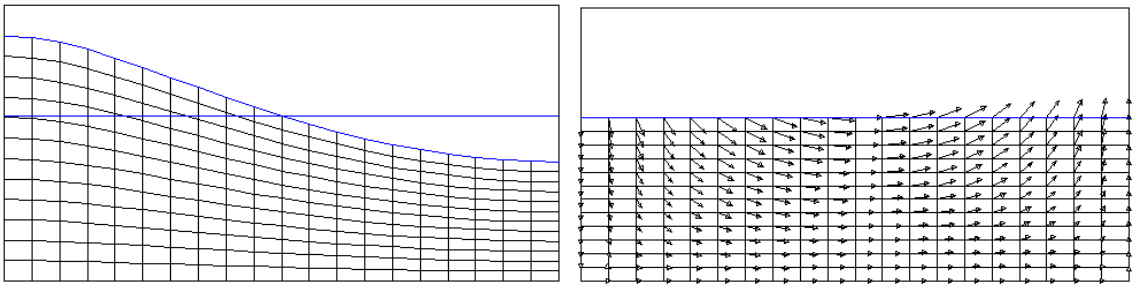


Figure 4 Free surface of standing and absolute velocity field

One of the best methods for determining the ship motion equations accounting for sloshing problems and forces generated by liquid motion in partially filled tank (over 30%) is the Boundary Element Method [10]. In this problem the domain occupied by liquid is bounded. The potential flow is assumed. The velocity potential satisfies Laplace problem with Neumann conditions on tank walls S_c and on the free surface S_F.

The boundary-value problem determining the velocity potential in the tank has the following form:

$$\begin{aligned} &\Delta\phi = 0, \qquad P \in \Omega, \\ &\frac{\partial\phi}{\partial\mathbf{n}} = \mathbf{n}\cdot\mathbf{v}, \quad P \in S_C, \\ &\phi = \phi_0, \qquad P \in S_F. \end{aligned} \tag{9}$$

The value of potential ϕ_0 on free surface S_F, occurring in boundary condition determining the shift of the free surface, is determined by (e.g. (12))

Figure 5 shows the method of surface shift in each time step of a simulation, [10].

There are different methods to determine a new surface of a liquid's domain [10]. In the first method points describing the free surface are shifted for fixed x. The value of the wave elevation is describe as follows:

$$\frac{\partial\xi}{\partial t} = -\frac{\partial\phi}{\partial n}\sqrt{1+\left(\frac{\partial\xi}{\partial x}\right)^2}. \tag{10}$$

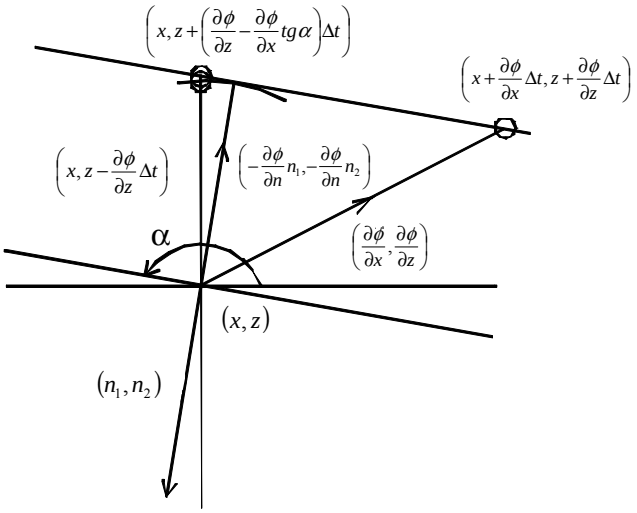


Figure 5 Methods of a free surface shift

When the inclination of the free surface is not too big the derivation of the elevation ζ with respect to horizontal direction *x* is negligible and the second method may be applied:

$$\frac{\partial\xi}{\partial t}=-\frac{\partial\phi}{\partial n}. \tag{11}$$

In the third method the free surface is moved according to formulae:

$$\frac{dx}{dt}=\frac{\partial\phi}{\partial x}, \frac{dz}{dt}=\frac{\partial\phi}{\partial z}. \tag{12}$$

Each of the methods mentioned above imply a different formula determining the derivatives of velocity potential ϕ with respect to time *t*. In the last method the velocity potential is obtained from the differential equation defined as follows:

$$\frac{\partial\phi}{\partial t}=\frac{1}{2}|\nabla\phi|^2-gz. \tag{13}$$

This method requires the setting of a new grid defining the domain boundaries in each time step of the simulation.

Low liquid level in a tank or in a damaged hold

When the level of liquid in a hold (e.g. in a damaged condition) is below 30% of the hold's height other methods are needed to solve the problem of sloshing. In this case a bore wave is observed (Figure 3). This problem is modelled with assumptions that vertical velocity is small thus vertical acceleration is negligible. It implies the assumption that horizontal velocities u_1 and u_2 do not depend on the vertical coordinate *z*. The dynamic water motion over the deck is directed along the hold.

One of the methods suitable for this kind of phenomenon is the method used for a shallow water problem. An algorithm of a solution is developed, which determines:

- the domain Ω occupied by water,
- the pressure field,
- the horizontal components u_1, u_2 of velocity u,
- the vertical component u_3 of velocity u,
- the forces and moments generated by moving water in the hold.

In this method the free surface shift is determined by the following equations:

$$\frac{dx}{dt} = u_1, \quad \frac{dy}{dt} = u_2, \quad \frac{dz}{dt} = u_3, \tag{14}$$

where velocity (u_1, u_2, u_3) describes the motion of water particles in relation to the bottom/deck of the hold. The pressure p in water over the bottom/deck is obtained as follows:

$$p(x,y,z) = p_a + \rho \int_{z_b + h(x,y,z_b)}^{z} f_3(x,y,s)\,ds, \tag{15}$$

where $h(t,x,y,z_b)$ is the distance between bottom/deck in the point (x,y,z_b) and the point $(x,y,z_b+h(t,x,y,z_b))$ belongs to the free surface and (f_x, f_y, f_z) is the external force (gravity and that generated by accelerating vessels).

The earlier assumptions, Euler equations of liquid motion and the principle of mass conservation result in the following formula determining the vertical velocity u_3:

$$u_3(x,y,z) = \left(-\frac{\partial u_1}{\partial x}(x,y) - \frac{\partial u_2}{\partial y}(x,y) + q \right)(z - z_b), \tag{16}$$

where q represents the change of water's mass on the hold bottom/deck due to the water flow in and out of the hole due to damage.

Shallow water method describes the problem of liquid motion in three-dimensional space but the solution is determined by the conditions on the liquid boundaries including the free surface (similarly to BEM). Figure 6 presents results of sloshing inside a tank (e.g. hold). Motion of the tank induces the motion of water.

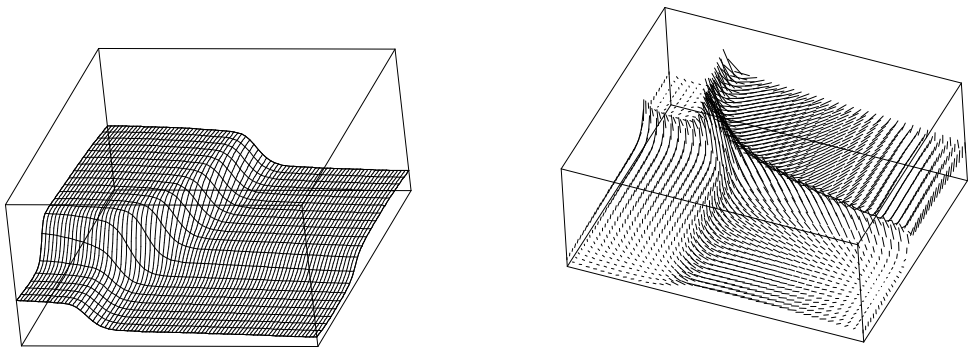


Figure 6 Free surface and velocity field obtained using shallow water method

4 WATER MOTION OVER THE FISHING VESSEL

The shallow water problem can be also used to model the flow of seawater on the vessel deck [11], [13]. The amount of the water mass trapped on deck keeps changing during the simulation as showed in Figure 7. This phenomenon significantly affects the flow of water on the vessel deck and therefore it is included to the shallow water problem approximating the flow on the deck (16). The mass of water entering the vessel deck in time is accounted for.

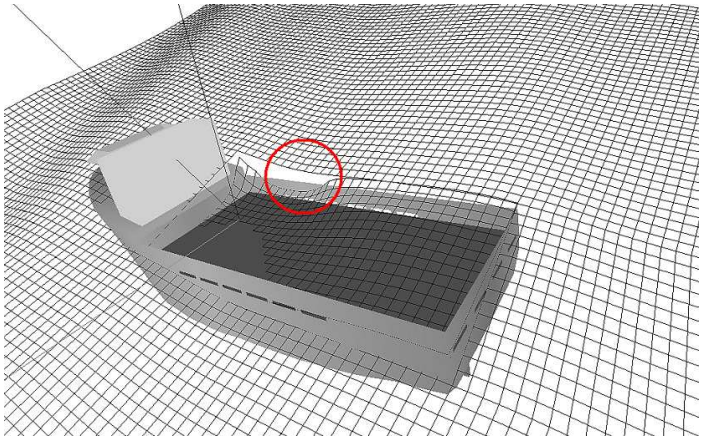


Figure 7 Flow over a bulwark

Other phenomena which significantly affect the flow of water on the vessel deck is showed in Figure 8. In this phenomenon water on the deck is connected with seawater and there is a boundary between these two domains. The velocity field of water around the ship affects the velocity field of water on the deck. It is taken into account as a boundary condition in differential equation (16).

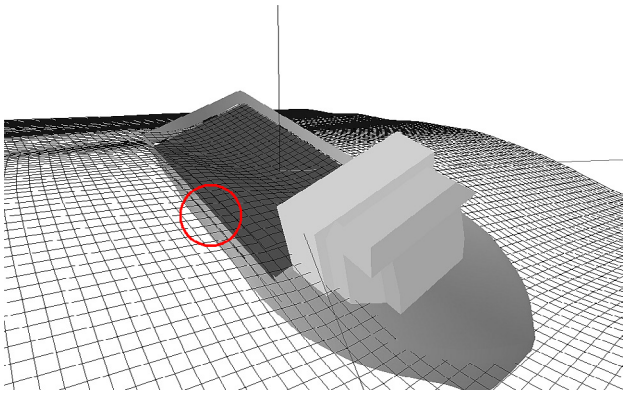


Figure 8 Deck submerged in water

The pressure obtained from formulae (15) determines the values of forces acting on the ship. The results obtained using shallow water method were compared to those using the simplified method [5], [8]. The simplified model is used in Ro-Ro ferries damage stability calculations where the volume of water on deck depends only on the distance between the

wave surface and deck water surface and does not depend on the velocity field on the deck. Figure 9 presents force F_{d3} (vertical component) generated by water on deck, increasing the draught, and Figure 10 the rolling moment F_{d4}, responsible for vessel capsizing.

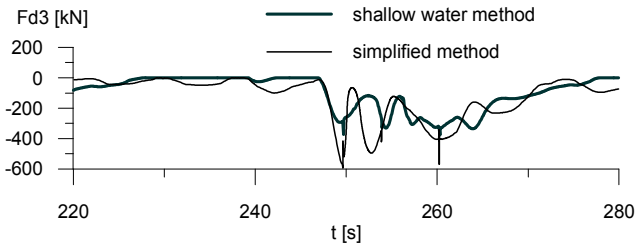


Figure 9 Time history of vertical force F_{d3} (increasing the draught)

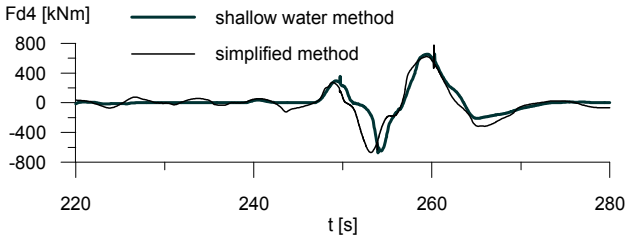


Figure 10 Time history of rolling moment F_{d4}

In the shallow water model the mass of water does not change as rapidly as in the simplified method used for calculating the mass of water in the Ro-Ro vessels in damage conditions. The rolling moment matches well for both methods.

5 CONCLUSIONS

Different numerical methods are used to solve problems describing ship motion in waves affected also by forces generated by sloshing of liquids in partially filled tanks, by trapped and moving water on the fishing deck etc. This paper focuses on the problem of free surface elevation as this phenomenon significantly impacts the determination the velocity field, and thus the pressure field and forces acting on the vessel.

For smaller vessels, for which the wave amplitudes are much bigger in relation to the vessel dimensions than in the case of big ships, more accurate methods determining the free surface should be used (equations (5) and (7)).

The potential flow can be used to approximate the flow in the ship tank (sloshing phenomenon) filled more than in 30%. This paper presents the Boundary Element Method used to solve the problem. The free surface is determined from equations (12) and the value of potential on the free surface from equation (13). When the level of liquid in a hold is below 30% the method of shallow water problem can be used to approximate the sloshing in the hold. The shallow water problem can be also used to model the flow of seawater on the vessel deck. This phenomenon is significantly affected by water flowing on and off of the deck, therefore, it is included in the method approximating the flow on the deck.

REFERENCES

[1] Hirt, C.W. and Nichols, B.D. „Volume of Fluid (VOF) Method for the Dynamics of Free Boundaries", *Journal of Computational Physics*, 1981.

[2] Zienkiewicz O.C. and Taylor, R.C. *The finite element method*, 4th Edition, Vol. 1, McGraw Hill, 1989.

[3] Faltisen, O.M. and Timokha A.N "Adaptive Multimodal Approach to Nonlinear Sloshing in a Rectangular Tank", *Journal of Fluid Mechanics*, Vol. 432, 2001.

[4] Wu, G.X. and Ma, Q.W. and Taylor, R.Eatock „Numerical simulation of sloshing waves in 3D tank based on finite element method", *Applied Ocean Research*, Vol. 20, No. 6, 1998.

[5] Belenky V., Luit D., Weems K., Shin Y.-S., „Nonlinear ship roll simulation with water-on-deck", *6th International Ship Stability Workshop*, *Webb Institute*, NewYork, 2002.

[6] Bertram, V. „*Practical Ship hydrodynamics*", Butterworth-Heinemann, 2002.

[7] Warmowska, M., „Numerical simulation of 2d sloshing in a rotating rectangular tank", *Marine Technology Transactions*, Vol. 15, Special issue – XXI SNO, 2004.

[8] Jankowski J., Laskowski A., „Capsizing of small vessel due to waves and water trapped on deck", *Proceedings of the 9th International Conference STAB 2006*, Brasil, 2006.

[9] Warmowska, M. and Jankowski, J. „Ship motion affected by moving liquid cargo in tanks", *Systems – Journal of Transdisciplinary Systems Science*, Vol. 11/1, Wrocław, 2006.

[10] Warmowska, M. „Numerical simulation of liquid motion in partly filled tank", *Opuscula Mathematica"*, Vol. 26/3, Kraków, 2006.

[11] Warmowska, M. „Problem of water flow on deck", *Archives of civil and mechanical engineering*, Vol. VII, No. 4, Wrocław, 2007.

[12] Warmowska, M. „Fala biegnąca", *Raport Techniczny Nr 50*, Polski Rejestr Statków, 2010.

[13] Warmowska, M. and Jankowski, J. „Safety of fishing vessels", *Symposium Safe Shipping on the Baltic Sea*, Gdańsk Polski Rejestr Statków, 2011.

V International Conference on Computational Methods in Marine Engineering
MARINE 2013
B. Brinkmann and P. Wriggers (Eds)

DYNAMIC MODELLING OF MOORING FOR FLOATING OFFSHORE STRUCTURES

MARINE 2013

GUTIERREZ J.E.[*], ZAMORA B. [‡], GARCÍA-ESPINOSA J.[†] AND ESTEVE J.[*]

[*] Depart. de Tecnología Naval, Universidad Politécnica de Cartagena
Paseo Alfonso XIII 48, 30203 Cartagena, Spain.
Email: jose.gutierrez@upct.es

[‡] Depart. de Ingeniería Térmica y de Fluidos, Universidad Politécnica de Cartagena
Doctor Fleming s/n, 30202 Cartagena, Spain.

† Centre Internacional de Mètodes Numèrics en Enginyeria (CIMNE)
Edifici C1, Campus Norte, UPC, C/ Gran Capitán s/n, 08034 Barcelona, Spain.

Key words: Mooring dynamics, Offshore structures, Lumped mass, Coupled analysis.

Abstract. There is a demand to develop and evaluate new concepts for offshore structures for harnessing ocean energy. Tools capable of calculating the behaviour of this kind of structures are also requested by the industry. An accurate analysis comprises fully coupled simulations and the use of complex models for non-linear dynamics analysis, including the modelling of mooring lines on floating offshore structures. In opposite of quasi-static modelling of mooring lines such as catenary lines [1], time - dependent models [2, 3] present some advantages.

This work presents a dynamic model of mooring lines for deep-water structures using LMM (Lumped Mass Method) [4, 5] formulation and its application on different kinds of floating devices. First, the mathematical model for mooring lines is presented. Then an application tool based on that mathematical model is showed. This tool is linked to the time-domain seakeeping solver SeaFEM [6]. The resulting model is able to obtain a fully coupled analysis of seakeeping and mooring dynamics of floating offshore structures. A preliminary study of mooring dynamics is presented over different solutions and configurations of mooring lines for several floating devices. Furthermore, an optimal design of mooring line configurations for different solutions of floating structures can be achieved.

This work also presents the study of different floating devices under several sea wave conditions. Finally some conclusions are remarked, and the future research lines are presented.

1 INTRODUCTION

The purpose of this work is to present a code for analysing the dynamics of mooring systems. Today, it is well known that the increase of developments of large offshore structures, (floating offshore wind turbines, for instance), requires a precise study of mooring arrangements. It is possible to find a wide variety of platform and mooring design concepts for offshore floating devices. Mooring systems are made by a set of cables, chains or wire

ropes, which are attached to offshore structures at different points with lower ends of these cables anchored at the seabed.

Several authors [7, 8] have proposed algorithms to analyse the dynamic behaviour of mooring arrangements in offshore structures.

Usually, floating offshore simulators can be found, which tend to use a quasi-static solution for mooring models. This approach has the advantage of computational efficiency. So, for cases where the waves are small and the movements of offshore devices and mooring arrangements are minimal, these solutions provide a good estimation of the line tension. However, for cases where the platform and mooring line motions are significant, quasi-static models neglect dynamic effect that may be important. The primary effect of mooring line dynamic is the increasing of platform damping. This effect improves the stability of the platform.

Thus, mooring lines should be investigated when the inertia of the line is important. The code employs a variation of Lumped Mass Method (LMM) for inelastic line [4, 5] and uses the Finite Difference method, as well as the implicit Newmark´s average acceleration method [9, 3] to solve the dynamic behaviour of mooring lines. Several authors have proved that LMM is an effective algorithm to calculate dynamic behaviour of different mooring configurations.

2 PROBLEM DESCRIPTION

2.1 Mathematical formulation

The mooring line is discretized by a finite number of nodes, which are called 'lumped masses' and all forces are applied in each node. So, the line is divided in a finite number of segments, which are considered as massless springs.

The equations of motion for the dynamic problem of the mooring line in two dimensions in local tangential, (t) and normal (n), directions are:

$$m\left\{\frac{\partial u}{\partial t}-\frac{\partial \theta}{\partial t}\right\}=\frac{\partial T}{\partial t}-w\sin\theta+F_t(1+e), \tag{1}$$

$$(m+\alpha)\frac{\partial v}{\partial t}+mu\frac{\partial \theta}{\partial t}=T\frac{\partial \theta}{\partial t}-w\cos\theta+F_n(1+e), \tag{2}$$

$$\frac{\partial e}{\partial t}=\frac{\partial u}{\partial s}-v\frac{\partial \theta}{\partial s}, \tag{3}$$

$$\frac{\partial \theta}{\partial t}(1+e)=\frac{\partial v}{\partial s}-u\frac{\partial \theta}{\partial s}, \tag{4}$$

where s is the unstretched length of the cable; u and v are the component of velocity vector; m is the mass per unit length; T is the tension vector; F is vector of external forces; e is the stretched length; w is the submerged weight per unit length of the cable; α is the two-dimensional added mass of the cable, and θ is the angle formed between the horizontal and the local tangential direction of the cable.

Material damping, bending and torsional moments are normally neglected. Discretization assumptions are shown in Figure 1.

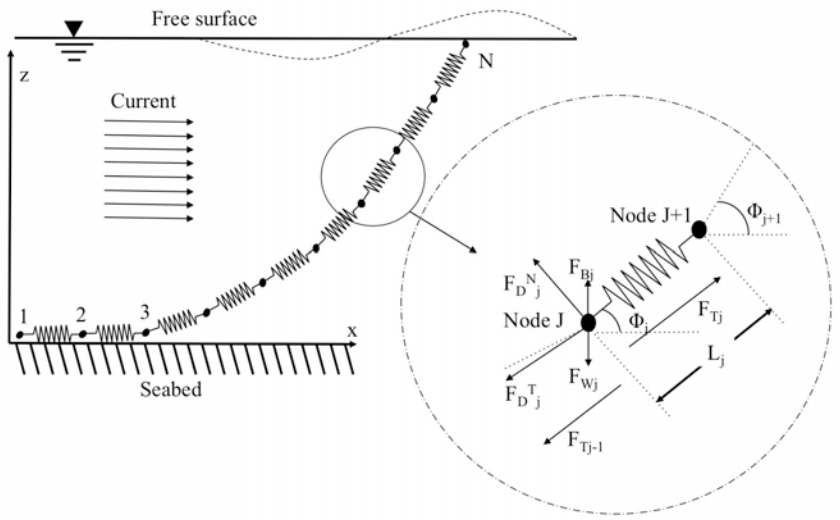


Figure 1: Scheme for the spatial discretization of the line. Balance of forces on line segment

Usually, mooring line is connected with floating offshore structures, and the motions of these structures on irregular waves are normally not affected by mooring line tension [5]. Applying the Newton's law to discretized line in global coordinates, it can be written,

$$\left([M_j] + [AM_j(t)]\right)\cdot\{\ddot{\vec{x}}_j(t)\} = \{\vec{F}_j(t)\}, \tag{5}$$

where M_j is the inertia matrix, AM_j is the hydrodynamic inertia matrix, t is the time, $\ddot{x}_j$ is the acceleration and F_j are the loads applied in the considered lumped mass. Note that drag forces and elastic stiffness are also included in the analysis.

The nodal force loads applied in each lumped mass are respectively given by:

$$\{\vec{F}_j(t)\} = \{\vec{F}_W\} + \{\vec{F}_B\} + \{\vec{F}_S\} + \{\vec{F}_T(t)\} + \{\vec{F}_D(t)\}, \tag{6}$$

where F_W is the weight of lumped mass, F_B is the buoyancy of lumped mass, F_S is the force caused by soil interaction, F_T is the tension of the line in each node and, and F_D is the drag forces in global coordinates.

The forces caused by seabed interaction can be modeled using Coulomb friction model to obtain the forces in horizontal direction, or using the Drucker-Prager friction model [10]. Some authors modeled the seabed as an elastic foundation with linear stiffness and damping properties [11]. In this case, the soil interaction is modeled through Coulomb friction,

$$\vec{F}_S(t) = \mu\cdot\vec{N}_j, \tag{7}$$

where μ is the coefficient of friction, and N_j the normal force.

On the other hand, drag forces are calculated in normal and tangential directions in each element of the line. Then, directional matrices are used to transform the local forces and velocities into global drag forces and velocities,

$$\begin{aligned} F_D^n(t) &= \frac{1}{2}\rho\cdot D_j\cdot l_j\cdot C_D^n\cdot u_j^n(t)\left|u_j^n(t)\right|, \\ F_D^t(t) &= \frac{1}{2}\rho\cdot D_j\cdot l_j\cdot C_D^t\cdot u_j^t(t)\left|u_j^t(t)\right|, \end{aligned} \tag{8}$$

where ρ is the water density, D_j the characteristic length of the element, l_j the segment length, and C_D the drag coefficient in normal and tangential directions (typical values are 2.0 for normal direction and 0.2 for tangential direction). Finally, u^n_j and u^t_j are the normal and tangential components of velocity of the fluid acting on the regarded j^{th} line segment.

2.2 Boundary conditions

To obtain an accurate analysis of mooring line, it is necessary to establish boundary conditions. These are related to position of the line, line extension and seabed contact.

As previous remarked, the seabed interaction is modeled by using Coulomb friction model. The value of the coefficient of friction μ will depends of soil type. In the treated cases a value of 0.4 it is considered for this parameter.

Regarding the line position, it is obvious that the line has not displacement in the lower end position. In each time step the movements of the line are checked to fix the position of the line in the lower end position and upper end position.

On the other hand, it is necessary to fix the line extension to avoid instabilities in numerical simulation; for this reason a predictor-corrector method based on Newmark method and Central Finite Difference method to predict the behaviour in each time step is employed. Then, line extension is calculated and checked to apply basic mechanical laws. So, new position is estimated in each time step.

3 DYNAMIC ANALYSIS OF THE BEHAVIOUR OF THE LINE

In order to solve the dynamic behaviour of mooring lines, some numerical methods are used. In this work, a predictor-corrector method based on the Central Finite Difference and the Newmark´s average acceleration methods is proposed. The procedure for solving the dynamic behaviour of mooring line is explained in a more detailed manner.

3.1 Proposed numerical scheme

The method is initialized using quasi-static solution of catenary equations. This solution supply an accurate initial position at t = 0 s for mooring line. Then, the Finite Difference Method is used to launch the calculation at t = Δt. The steps are the following:

I. Selection of the interval time $\Delta t < \Delta t_{critic}$.

II. Calculation of the position at t = $-\Delta$t.

$$\{\vec{x}_{t=-\Delta t}\} = \{\vec{x}_{t=0}\} - \Delta t\{\dot{\vec{x}}_{t=0}\} + \frac{\Delta t^2}{2}\{\ddot{\vec{x}}_{t=0}\}. \tag{9}$$

III. Estimation of the position at t = Δt, using Central Finite Difference scheme.

$$\{\tilde{\vec{x}}_{t=\Delta t}\} = \left[\frac{1}{\Delta t^2}M\right]^{-1}\left[\{\vec{F}_{t=0}\} + \frac{2}{\Delta t^2}M\{\vec{x}_{t=0}\} - \frac{1}{\Delta t^2}M\{\vec{x}_{t=-\Delta t}\}\right]. \tag{10}$$

IV. Evaluation of the velocities and acceleration of the line at t = 0 s.

$$\{\vec{\dot{x}}_{t=0}\} = \frac{1}{2\Delta t}[\{\vec{x}_{t=\Delta t}\} - \{\vec{x}_{t=-\Delta t}\}],$$
$$\{\vec{\ddot{x}}_{t=0}\} = \frac{1}{\Delta t^2}[\{\vec{x}_{t=\Delta t}\} - 2\{\vec{x}_{t=\Delta t}\} - \{\vec{x}_{t=-\Delta t}\}]. \quad (11)$$

V. Calculation of the stretched line e at t = Δt.

$$e = \{\vec{x}_{t=\Delta t}\} - \{\vec{x}_{t=0}\}, \quad (12)$$

VI. Calculation of the effective tension at t = Δt.

$$T_j = (EA_j/L_j)e. \quad (13)$$

VII. Recalculation of the tension in each lumped mass.

VIII. Correction of the initial position at t = Δt, applying boundary conditions.

IX. Selection of the correct values of γ and β for the Newmark method.

X. Estimation of the position at t = Δt, using Newmark method,

$$\{\vec{x}_{t=\Delta t}\} = \left[\frac{1}{\beta(\Delta t)^2}M\right]^{-1}\left\{\vec{F}_{t=\Delta t} + M\left(\frac{1}{\beta(\Delta t)^2}\{\vec{x}_{t=0}\}\right) + \frac{1}{\beta\Delta t}\{\vec{\dot{x}}_{t=0}\} + \left(\frac{1}{2\beta} - 1\right)\{\vec{\ddot{x}}_{t=0}\}\right\}. \quad (14)$$

XI. Determination of the velocity and acceleration vectors for the current time step.

$$\{\vec{\ddot{x}}_{t=\Delta t}\} = \frac{1}{\beta(\Delta t)^2}(\{\vec{x}_{t=\Delta t}\} - \{\vec{x}_{t=0}\}) - \frac{1}{\beta\Delta t}\{\vec{\dot{x}}_{t=0}\} - \left(\frac{1}{2\beta} - 1\right)\{\vec{\ddot{x}}_{t=0}\},$$
$$\{\vec{\dot{x}}_{t=\Delta t}\} = \{\vec{\dot{x}}_{t=0}\} + (1-\gamma)\Delta t\{\vec{\ddot{x}}_{t=0}\} + \gamma\Delta t\{\vec{\ddot{x}}_{t=\Delta t}\}. \quad (15)$$

XII. Repeating the procedure from III, to XII until the end of the simulation.

The employed procedure is shown in a simplified manner in Figure 2.

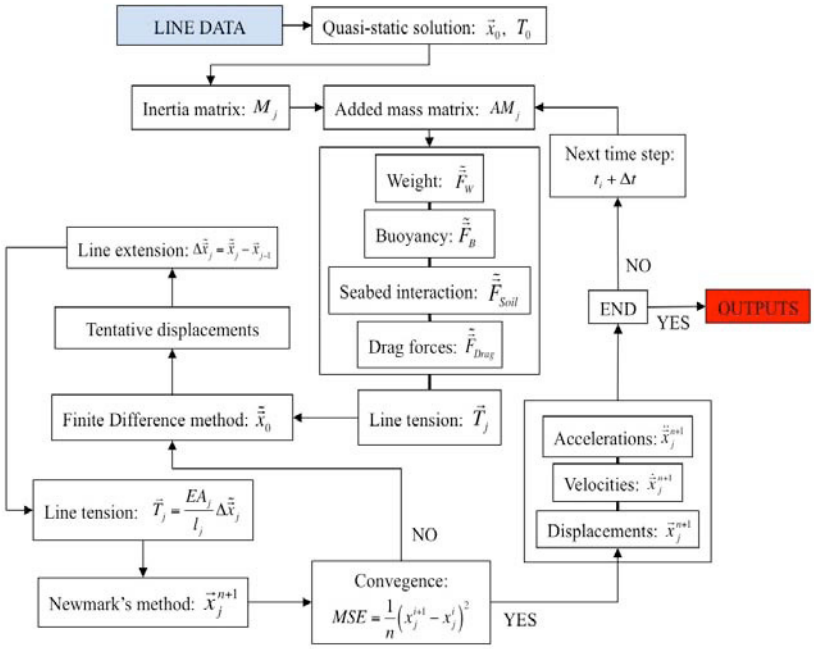


Figure 2: Proposed numerical scheme for solving mathematical model

3.2 Stability and discretization aspects

In order to obtain useful results, several aspects such as stability and accuracy of the employed methods must be considered. The number of lumped masses (nodes) should be sufficient to get an accurate estimation of the mooring line position. Furthermore, Van der Boom [5] observed that LMM might insert parasitical motions into the simulation. Increasing the numbers of elements of the line can prevent these parasitical movements; it is to say, by means of reducing the lumped mass for each node.

Usually, the reader can find in the bibliography other methods to solve the dynamic behaviour of mooring lines. For instance, Houbolt method [4, 5] is used to solve the specific problem. In this work is used the Newmark method, since dynamics of mooring line may be considered as typical vibration problem of structural dynamics.

As later remarks, the stability and error of this method depends basically on γ parameter. This method is unconditionally stable to values of $\gamma \geq 0.5$ and $\beta \geq 0.25(\gamma + 0.5)^2$. If the value of γ is equal to 0, a self-excited vibration gets into numerical procedure. However, if γ is equal to 0.5, a damping is added into the numerical scheme. So, for undamped cases the choice of these values leads to unconditionally stable time-integrator operator of maximum accuracy.

For damping cases, Newmark scheme remains stable as long as $\varepsilon < 1.0$, where ε is the modal damping coefficient. In general, damping has a stabilizing effect for moderate values of ε.

The knowledge of natural frequencies ω_n of continuous system results necessary to ensure the stability of numerical integration by Newmark method. In each case, the continuous system is discretized by LMM, so a simple one-dimensional bar can be considered for each segment line. The time step can be calculated as,

$$\Delta t = L_j / c, \tag{13}$$

where c is the longitudinal wave velocity [11], and L_j is the length of j-th element. The wave velocity is given by,

$$c = \sqrt{E/\rho}, \tag{14}$$

being E the Young Modulus and ρ the density per unit length.

It is important to avoid instabilities in numerical simulation due to discretization aspects. The touchdown point on seabed of mooring system should be locate in all time of the simulations, for this reason the authors have introduced an adaptive algorithm to divided the mooring line taking into account this point. The number of elements of the portion of the line, which rest on seabed may be different depending the upper end position of the line.

4 LINKING WITH SEAFEM

Fluid structure interaction is a topic of great interest in engineering, more specifically in offshore engineering. The interest in this field is growing due to renewable energy field in recent years. The coupled dynamic problems in offshore industry may be important in several applications like offshore wind energy or wave energy converters. These problems require a complex study, which involves several specialties; for instance, offshore wind energy implies aeroelastic calculations, wave-interaction problems, and mooring calculations.

Most of computer programs used in offshore engineering are based in frequency domain,

since the computational cost is cheapest than time domain simulations. Nowadays, the increasing on computer capabilities makes possible to carry out simulations in time domain. A great advantage of time domain simulations is to make easier the coupling with other phenomena, non-linear effects, etcetera.

So, it is possible to find some computer programs, which are capable of solving wave-structure interaction in time domain [6]. The reader can find bibliographic resources dedicated to solve fluid structure interaction in presence of waves surface using FEM formulation [13]. However, these works requires high computational costs. The use of potential flow theory with Stokes perturbation approximation allows to save computational costs in opposite of previous ones. SeaFEM is a useful program capable of solving wave-interaction problem using Finite Element method and unstructured meshes.

Borja et al. [6] have based SeaFEM on Stokes perturbation theory. This procedure is more efficient, and no re-meshing or moving mesh techniques are needed, which keeps computational costs and times low. These authors have adapted the algorithm to include non-linear external forces, like those used to define mooring systems, and variations on the pressure over the free surface. This motivates the development of an algorithm to calculate the forces and tensions due to mooring arrangements.

The governing equations for the first diffraction-radiation of a floating body are:

$$\nabla^2\phi = 0, \quad \text{in } \Omega \tag{15}$$

$$\partial_t\phi + g\eta = -\frac{P_a}{\rho} + C, \quad \text{in } z = 0 \tag{16}$$

$$\partial_t\eta - \partial_z\phi = 0, \quad \text{in } z = 0 \tag{17}$$

$$\partial_z\phi = 0, \quad \text{in } z = -H \tag{18}$$

$$\nabla\phi \cdot n_B = v_B \cdot n_B. \quad \text{in } \Gamma_B \tag{19}$$

where ϕ and η are the first order potential and free surface elevation, Ω is the fluid domain bounded by $z = 0$; P_a is the atmospheric pressure; ρ is the water density; C is a constant value; Γ_B represents the wetted surface of a floating body; and H is the water depth.

5 VALIDATION AND APLICATION EXAMPLES

5.1 Validation

The validation of the obtained results constitutes a primary objective to know the effectiveness of the code presented. Some bibliographic resources have been employed to get the validation of code. Mavrakos et al. [12] presented experiments, which were compared with numerical simulation using, both time and frequency domain computer codes. They showed the beneficial effects of buoys in reducing the mooring line dynamic tension. The Figure 3 shows a comparison between numerical results offered by Mavrakos et al. [12] and the results obtained by numerical procedure. These authors [12] established an experimental set-up, as well as the data acquisition procedures, and compared the experimental results with their numerical results.

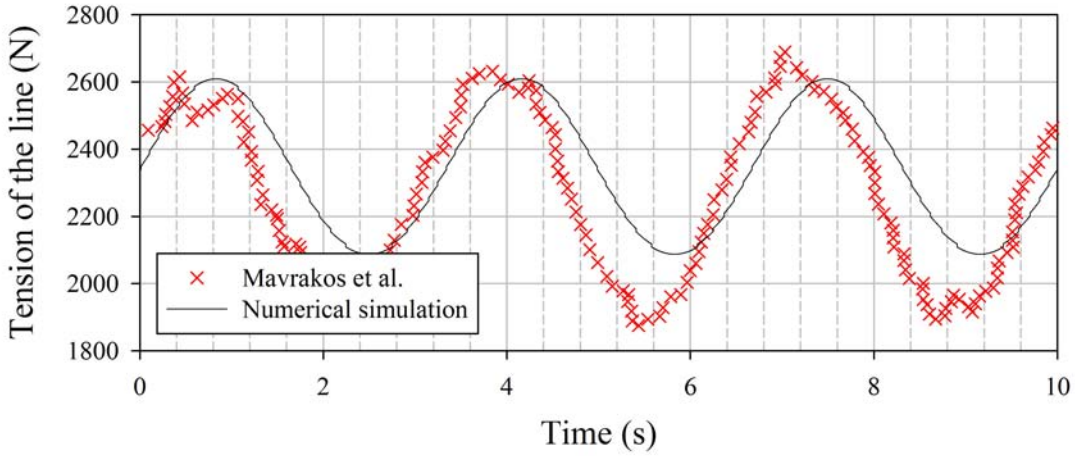


Figure 3: Comparison between numerical simulation and experimental results of Mavrakos et al. [12]

Figure 3 shows that the results obtained are in accordance with those experimentally obtained by Mavrakos et al. [12]. In this case, the line is divided in 100 nodes. The time step is established at $\Delta t = 1.0\times10^{-3}$ s to avoid stability problems (in fact, $\Delta t_{critic} = 2.3\times10^{-3}$ s). The simulation established a wave period of 3.33 s. It is remarkable that the maximum (peak) deviation between numerical and experimental results is less that 10%.

The second test case is based in the simulation of a cable subjected to the action of its self-weight and simply supported at its ends [14]. It is compared with analytical solution of the problem. The cable has the following characteristics: section area A = 0.0005 m^2; Young modulus of the material E = $5.01\cdot10^5$ N/m^2; length of the cable L = 7.07105 m; weight per unit length 0.49 N/m. The analytical reaction in the end of the cable is 34.681 N and the obtained vertical tension of the line is 34.684 N. The slightly difference may be caused by discretization errors.

The accuracy of the code is also verified applying classical test [15]. It consists of a horizontally suspended cable with one support free to slide laterally. For a cable of an unstretched length of L = 200 m, a weight per unit length of w = 1 kg/m, an extensional stiffness of EA = 10^5 N, and a horizontal load of F = 5.77 N applied at the free end, the theoretical static-equilibrium solution is for a horizontal span of X = 152.2 m and a vertical sag of Z = 58.0 m. It can be observed in Figure 4.

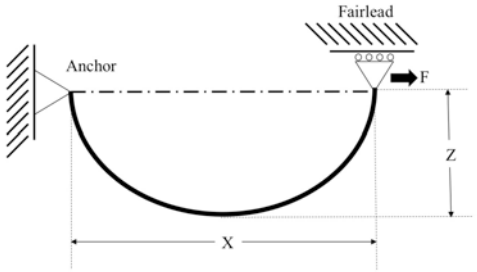


Figure 4: Benchmark problem for checking the accuracy of the program

This benchmark test showed that the displacement converged to analytical solution (see

Figure 5). The influence of several aspects may be important to obtain a stable and accuracy method to analyze the behaviour of mooring lines.

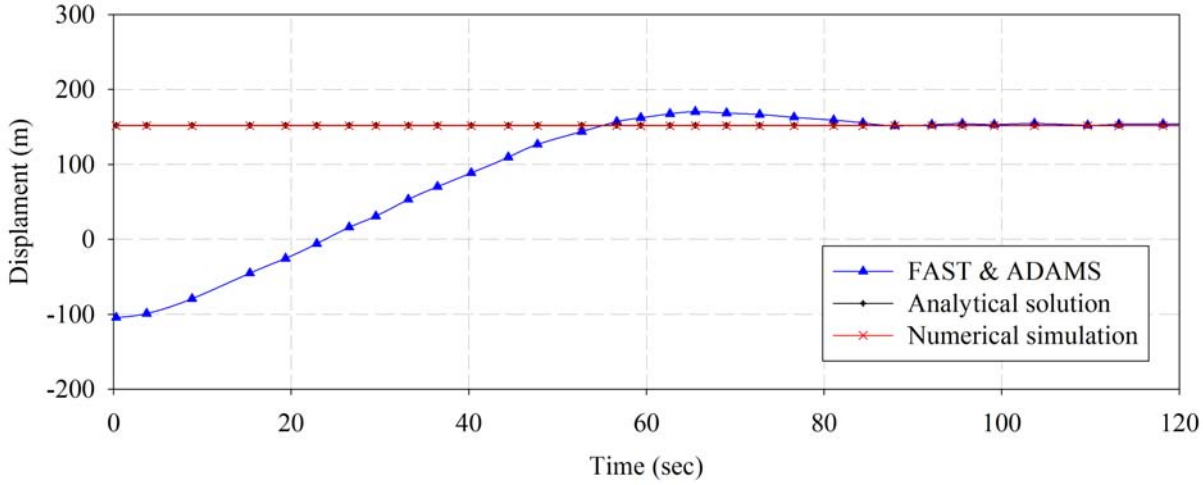


Figure 5: Solution for the benchmark problem

Figure 6 shows the time evolution of line tension at upper end position depending on the wave amplitude. This test is based on mooring system of monohull semisubmersible for North Sea oil production, which operates at 375 m water depth [12]. It can be noted an increase in the line tension with the wave amplitude, and the reader can observe that the average tension is the same in all cases.

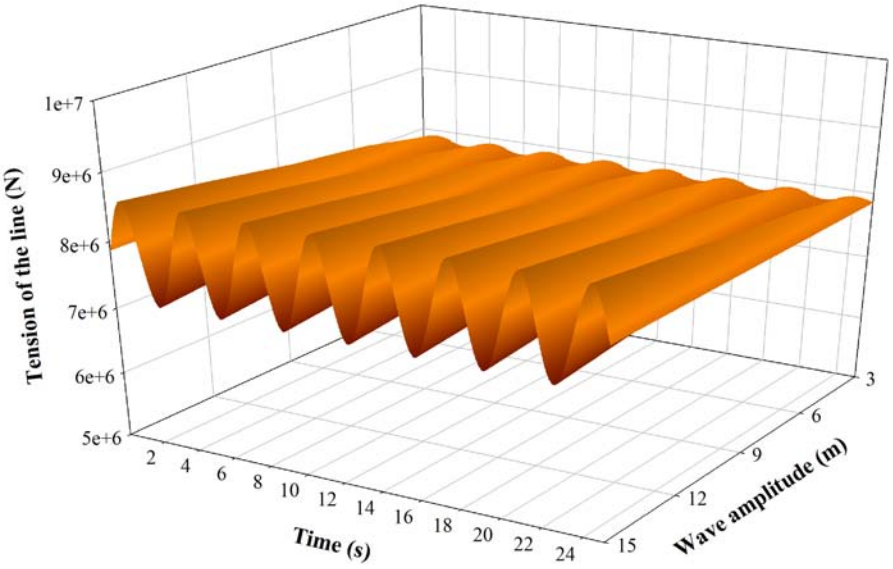


Figure 6: Response of the tension line at upper end position with incrementing in wave amplitude

We can analyse the displacement of upper end line position with the increment on current velocity. The characteristics of the line are the same as previous one. Table 1 shows the variation of the upper end position of the line with the current velocity before 30 s of

simulation.

Table 1: Horizontal displacement of the upper end line position with the increment in current velocity

Current velocity (m/s)	Position (m)	Increment (%)
0.0	1830.00	0.000
1.0	1830.04	0.002
5.0	1831.01	0.055
10.0	1834.05	0.221
15.0	1839.12	0.498

6 CONCLUSIONS AND FURTHER RESEARCHES

The easiness to implement non-linear external forces and moment acting on floating structures into SeaFEM program leads the authors to develop a code for mooring system. A solver for dynamic behaviour of mooring systems has been presented. The solver has been based on a Lumped Mass Method adding other features and capabilities. Central Difference Finite in combination with an implicit Newmark´s average acceleration methods are used to carry out the time domain integration.

The boundary conditions are related to seabed interaction, drag forces applied, mechanical characteristics of the line material and the wave-structure interaction. The solver has been compared with available results for a mooring line, and benchmark test. The agreement between the solutions shows that the implemented solver in this work performs well.

The algorithms are also linked with SeaFEM to obtain a full solver of dynamic behaviour of marine structures.

Finally, it can be noticed the importance of mooring analysis in offshore engineering. However, it is necessary to continue in the development of new model for mooring system, which include material damping, non-linear effects, and seabed interaction.

REFERENCES

[1] Faltinsen, O. M., *Sea loads on ships and offshore structures*, Cambridge University Press, ISBN: 0-521-45870-6, UK, 1990.

[2] Lindahl L., and Sjöberg, A., *Dynamic analysis of Mooring Cables*, The Second International Symposium on Ocean Engineering and Ship Handling, pp. 281-319, (1983).

[3] Zienkiewicz, O. C., and Taylor, R. L., *The finite element method*. McGraw Hill, Vol. I., (1989), Vol. II, (1991).

[4] Nakajima, T., Motora, S., and Fujino, M., *On Dynamic analysis of multicomponent mooring lines*, Offshore Technology Conference Paper, (1982).

[5] Van den Boom, H. J. J., *Dynamic behaviour of mooring lines*, Offshore Technology Conference Paper, (1977), Houston, Texas.

[6] Serván, B., and García, J., *Advances in the Development of a Time-domain Unstructured Finite Element Method for the Analysis of Waves and Floating Structures Interaction*, Marine 2011, Lisbon, Portugal.

[7] MARIN, DYNFLOAT. *Assesment of dynamic mooring system loads and tanker motions*, www.marin.nl, last accessed: 10-02-2013, Netherlands.

[8] Orcina Ltd, *OrcaFlex Manual*, ver. 9.6a, (2012), UK.
[9] Newmark, N. M., *A method or computation for structural dynamics*. ASCE Journal of the Engineering Mechanics Division (1959), 85: 67-94.
[10] Long, Y., Jia-hua, T., *Numerical investigation of seabed interaction in time domain analysis of mooring cables*, J. of Hydrodynamics (2006), 18(4): 424-430.
[11] Gobat, J.I. and Grosenbaugh M.A, *Time-domain numerical simulation of ocean cable structures*, Ocean Engineering (2006), 33(10): 1373-1400.
[12] Mavrakos, S. A., Papazoglou, V. J., Trianafyllou, M. S., and Hatjigeorgiou, J., *Deep Water Mooring Dynamics*, Marine Structures (1996), 9: 181-199.
[13] García, J., Valls A., and Oñate, E., ODDLS*: a new unstructured mesh finite element method for the analysis of free surface flow problems*, Int. J. Numer. Methd. Fluids 2008; 76(9): 1297-1327.
[14] Ortigosa, I., *Development of a decision support system for the design and adjustment of sailboat rigging*, PhD., Thesis (2011), UPC.
[15] Jonkman, J. M., *Dynamic modeling and load analysis of an offshore floating wind turbine*. Technical Report NREL/TP-500-41958 (2007).
[16] Bathe, K. J., *Finite Element Procedures*, Prentice Hall, ISBN: 0-13-301458-4, (1996). Ch.9.

V International Conference on Computational Methods in Marine Engineering
MARINE 2013
B. Brinkmann and P. Wriggers (Eds)

VIBRATION ANALYSIS OF PLATES WITH ARBITRARY STIFFENER ARRANGEMENTS USING A SEMI-ANALYTICAL APPROACH

LARS BRUBAK[*,a,b], JOSTEIN HELLESLAND[a] AND OLE J. HAREIDE[b]

[a]Mechanics Division, Department of Mathematics,
University of Oslo, 0316 Oslo, Norway

[b]Section for Ship Structures and Concepts, Technical Advisory
for Ship and Offshore Structures, Det Norske Veritas, 1322 Høvik, Norway

[*]e-mail: Lars.Brubak@dnv.com - Web pages: www.dnv.com and www.math.uio.no

Key words: Stiffened plates, Arbitrary stiffener orientations, Vibration analysis, Semi-analytical method, Rayleigh-Ritz method

Abstract. Vibration of plates with arbitrarily oriented stiffeners is studied. The plate may be subjected to in-plane loads and the plate boundaries may be simply supported or rotationally restained. The main objective is to present and validate an approximate, semi-analytical computational model for such plates subjected to in-plane loading. The formulations derived are implemented in a Fortran computer code, and numerical results are obtained for a variety of plate and stiffener geometries. The model may handle complex plate geometries, by using inclined stiffeners to enclose irregular plate shapes. The method allows for a very efficient analysis. Relatively high numerical accuracy is achieved with low computational efforts.

1 INTRODUCTION

Computationally efficient, semi-analytical methods are becoming more common as an alternative to finite element analyses (FEA) and explicit design formulas. The amount of published literature on semi-analytical methods for analysis of stiffened plates is growing. In a review paper by Liew, Xiang and Kitipornchai [1], most of the literature on vibration of stiffened plates till the year 1994 has been summarized. This literature study goes back to the well known study of vibration by Rayleigh [2] in 1877 and Ritz [3] in 1909. The latter approach is known as the Rayleigh-Ritz or Ritz method where a series of admissible trial functions are used. This approach is used in the present paper.

Semi-analytical methods such as the Rayleigh-Ritz approach and other mesh-less methods have been used to investigate many different aspect of vibration. For example, the

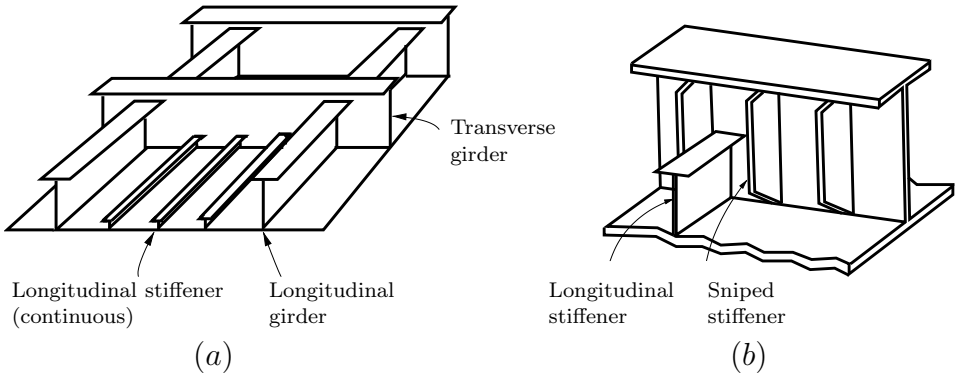


Figure 1: Examples of stiffened plates: (a) Stiffened plate enclosed by longitudinal and transverse girders, and (b) girder stiffened by sniped stiffeners.

Rayleigh-Ritz approach has been used to analyse free vibration of unstiffened plates with various boundary conditions [4, 5, 6], and vibration of plates subjected to in-plane loads [7, 8, 9]. Semi-analytical approaches have also been developed to investigate various aspects of vibration on stiffened plates [10, 11, 12, 13, 14]. In a research work by Xu, Du and Li [15], vibration of irregularly stiffened plates without in-plane loads is studied.

The semi-analytical methods mentioned above are restricted to irregularly stiffened plates without in-plane preloads, or to unstiffened or regularly stiffened plates. In the present work, the main objective has been to develop a computationally efficient semi-analytical model for eigenfrequency computations of stiffened plates subjected to in-plane prestress and with arbitrarily oriented stiffeners. Analyses by the present model can be performed for plates with simply supported, clamped of partially clamped boundary conditions, or combinations of these. The model may also handle interior supports, along lines with arbitrary orientations and lengths. By using inclined stiffeners or strong translational springs to enclose triangular, trapezoidal and other plate shapes, the present model may handle complex plate geometries.

2 PLATE DEFINITION AND BOUNDARY CONDITIONS

Typical engineering applications for stiffened plates are illustrated in Fig. 1(a) where a plate is enclosed by the strong longitudinal and transverse girders, and in Fig. 1(b) where the plate web is supported by a strong girder flange. Girder stiffeners may be be oriented horizontally or vertically. The stiffeners may be sniped at their ends (such as in Fig. 1(b)), and will then, unlike continuous stiffeners such as in Fig. 1(a), not be subjected to external axial loading (in the stiffener direction). Sniped stiffeners may also be used in conjunction with cases where a rather non-regular stiffener arrangement is required, such as for instance in the stern and in the bow of a ship hull.

In order to model such cases, the plate defined in Fig. 2 is considered. It may be subjected to in-plane shear stress and linear varying in-plane compression or tension stress. It may have none, one or more stiffeners, and the stiffener orientations may be

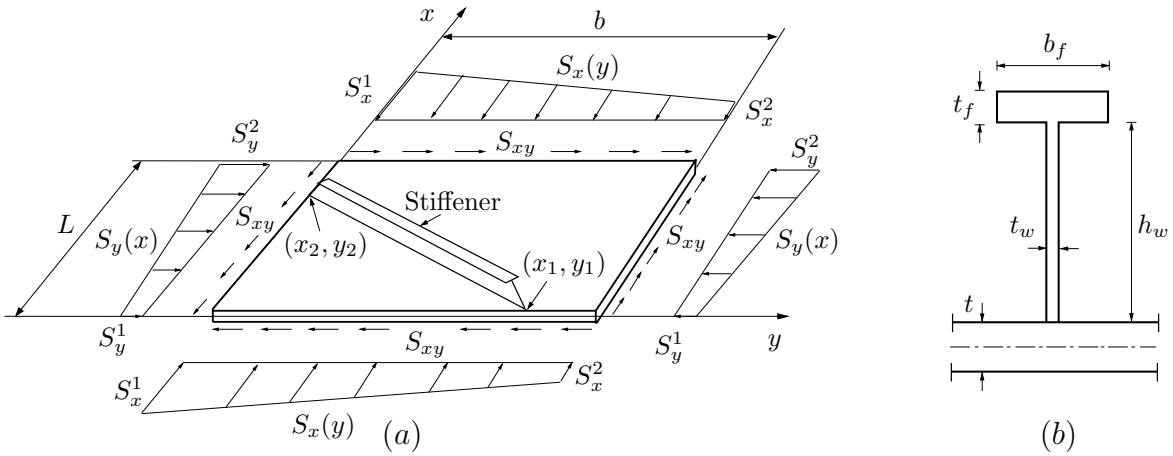


Figure 2: (a) Stiffened plate subjected to in-plane shear stress and in-plane, linear varying applied compression or tension stress, and (b) cross-section of an eccentric stiffener.

arbitrary. The stiffeners may have different cross-section profiles, and may be eccentric, as in Fig. 2(b), or symmetric about the middle plane of the plate. The stiffeners are modeled as simple beams. A boundary (plate edge) or a part of a boundary may be simply supported, clamped or something in between.

3 MATERIAL LAW AND KINEMATIC RELATIONSHIPS

The usual plane stress assumption for thin isotropic plates is adopted. The well known Hooke's law for this case is defined by

$$\sigma_x = \frac{E}{1-\nu^2}(\epsilon_x + \nu\epsilon_y) \tag{1}$$

$$\sigma_y = \frac{E}{1-\nu^2}(\epsilon_y + \nu\epsilon_x) \tag{2}$$

$$\tau_{xy} = \frac{E}{2(1+\nu)}\gamma_{xy} = G\gamma_{xy} \tag{3}$$

where σ_x, σ_y and τ_{xy} are the in-plane stresses, and ϵ_x, ϵ_y and γ_{xy} the in-plane strains, defined positive in tension, and the material coefficients E and ν are Young's modulus and Poisson's ratio, respectively. The total strain can be divided into a membrane strain (ϵ^m) and a bending strain (ϵ^b) and given by

$$\epsilon_x = \epsilon_x^m + \epsilon_x^b = \epsilon_x^m - zw_{,xx} \tag{4}$$

$$\epsilon_y = \epsilon_y^m + \epsilon_y^b = \epsilon_y^m - zw_{,yy} \tag{5}$$

$$\gamma_{xy} = \gamma_{xy}^m + \gamma_{xy}^b = \gamma_{xy}^m - 2zw_{,xy} \tag{6}$$

where w is the out-of-plane displacement in the z-direction (positive downwards in Fig. 2). The conventional notation $w_{,xy}$ for $\partial^2 w/\partial x\partial y$, etc., is adopted. The bending strain distribution complies with Kirchhoff's assumption [16].

4 VIBRATION ANALYSIS – EIGENVALUES

The eigenfrequencies of a perfect, stiffened plate are computed using the well known Rayleigh-Ritz method. The assumed displacement field, which satisfies the boundary conditions of a simply supported plate, is given by

$$w(x,y) = \sum_{i=1}^{M}\sum_{j=1}^{N} a_{ij}\sin(\frac{\pi i x}{L})\sin(\frac{\pi j y}{b}) \tag{7}$$

where a_{ij} are amplitudes, L the plate length and b the plate width.

By assuming harmonic vibrations, the usual eigenvalue problem [17] is

$$(K^M_{ijkl} + \Lambda^{pre} K^G_{ijkl} - \omega^2 M_{ijkl})a_{kl} = 0 \tag{8}$$

where

$$K^M_{ijkl} = \frac{\partial^2 U}{\partial a_{ij}\partial a_{kl}}\ ,\ \ \Lambda^{pre}K^G_{ijkl} = \frac{\partial^2 T}{\partial a_{ij}\partial a_{kl}}\ \text{ and }\ \omega^2 M_{ijkl} = \frac{\partial^2 H^{max}}{\partial a_{ij}\partial a_{kl}} \tag{9}$$

Here, ω denotes the natural circular eigenfrequencies and a_{kl} the corresponding eigenvectors. The desired prestress level is obtained by multiplying some initial (reference) applied in-plane stress by a load factor Λ^{pre}. In the eigenvalue problem, M is the mass matrix, K^M the material stiffness matrix and K^G is the geometrical stiffness matrix for the predefined in-plane stresses. These matrices are, as seen, expressed by U, T and H^{max}, which are the strain energy, potential energy due to external loads and the maximum kinetic energy, respectively. Each energy contribution is described in more detail below. In the common matrix notation, the eigenvalue problem above can be written

$$(\mathbf{K}^M + \Lambda^{pre}\mathbf{K}^G - \omega^2\mathbf{M})\mathbf{a} = \mathbf{0} \tag{10}$$

In an analysis of a clamped plate, it would be more appropriate to assume a displacement field defined with a series of cosine functions. However, although each component in a series of sine functions represents a simply supported condition, added together they are nearly able to describe a clamped, or partially restrained, condition at a negligible distance from the support. The sine curve assumption is therefore able to handle plates with various boundary conditions along the edges.

The elastic strain energy contribution from bending of the plate is given by

$$U^b_{\text{plate}} = \frac{D}{2}\int_0^b\int_0^L \Big((w_{,xx}+w_{,yy})^2 - 2(1-\nu)(w_{,xx}w_{,yy} - w^2_{,xy})\Big)\,dx\,dy \tag{11}$$

where $D = Et^3/12(1-\nu^2)$ is the plate bending stiffness and t is the plate thickness. By substituting the assumed displacement field, an analytical solution of this integral may be derived. More details can be found in Brubak [18] and Brubak, Hellesland and Steen [19]. The membrane strain energy of the plate and the stiffeners (below) is not included

as it does not affect computed eigenvalues, since small deflection theory is used. This will have some consequences that will be discussed in the results sections.

The curvature of the stiffeners is equal to the curvature in the plate along the stiffeners. Thus, the bending strain energy due to an arbitrarily oriented stiffener, with length L_s and cross-section area A_s, can be given by

$$U^b_{\text{stiff}}=\frac{EI_e}{2L_s^4}\int_{L_s}\left(L_x^2 w_{,xx}+2L_xL_y w_{,xy}+L_y^2 w_{,yy}\right)^2 dL_s \tag{12}$$

where (x_1, y_1) and (x_2, y_2) are the coordinates of the stiffener ends, $L_x = (x_2 - x_1)$, $L_y = (y_2 - y_1)$ and

$$I_e = \int_{A_s} (z - z_c)^2 \, dA_s + \, t \, b_e \, z_c^2 \tag{13}$$

is an effective moment of inertia about the axis of bending. Here, z_c is the distance from the middle plane of the plate to the centroidal axis (through the centre of area) of a cross-section consisting of the stiffener and an effective plate width b_e. The effective moment of inertia I_e reflects the fact that eccentric stiffeners tend to "lift" the axis of bending. For a symmetric stiffener, $z_c = 0$. This value also represents a reasonable simplification in many cases also for eccentric stiffeners. The strain energy integral in Eq. (12) may be solved analytically or by numerical integration. More details can be found in Brubak [18] and Brubak, Hellesland and Steen [19].

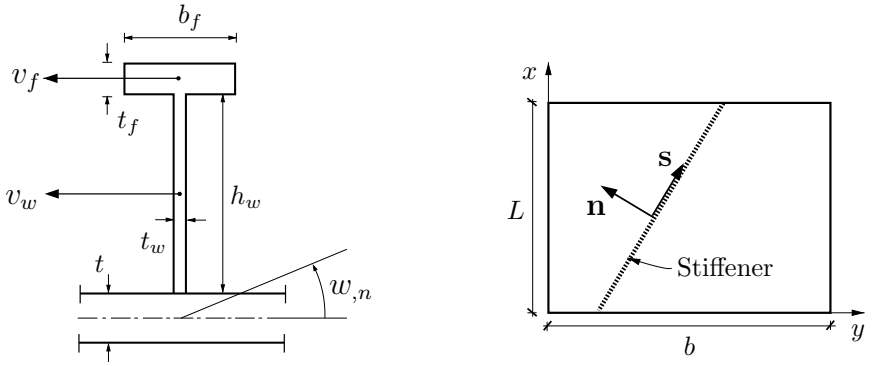
The potential energy of the external, in-plane prestress due to plate bending is given by

$$T = -\Lambda^{pre} \int_0^L \int_0^b \frac{t}{2}\left(S_{x0}(y)w_{,x}^2 + S_{y0}(x)w_{,y}^2 - 2S_{xy0}w_{,x}w_{,y}\right) dy \, dx \tag{14}$$

where $S_{x0}(y)$, $S_{y0}(x)$ and S_{xy0} are the initial (reference) stresses and Λ^{pre} the load factor for the prestress. More details can be found in Brubak [18] and Brubak, Hellesland and Steen [19].

The stiffeners in the example computations, presented below, are sniped. As a consequence, the in-plane stresses are applied at the midplane of the plate. Since the stiffeners will try to resist the corresponding strains, eccentricities (bending) will be introduced. However, such eccentricity effects are not accounted for in the model.

In line with the sniped stiffener assumption, Eq. (14) does not include any contribution from stiffeners. It would be reasonably straightforward to extend Eq. (14) to also include end loaded (continuous) stiffeners. However, in cases with local plate buckling, which are of most practical interest, the stiffeners will remain nearly straight and only contribute negligibly to T. Then it makes little difference whether the stiffeners are sniped or continuous. More details on how to include the energy contribution for end loaded stiffeners can be found in Brubak and Hellesland [20].



(a) (b)

Figure 3: (a) The velocity of the centroid of the web and flange due lateral displacement of the stiffener and (b) the stiffener orientation.

Both the displacements and the rotations along an arbitrary oriented line with length S may be restrained by applying translational and rotational springs, respectively. The strain energy due to these springs can be written

$$U_{\text{spring}} = \frac{1}{2}\int_S (k_r w_{,n}^2 + k_t w^2)\, dS \tag{15}$$

Here, $w_{,n}$ is the derivative of w normal to the line, and k_t and k_r are the stiffness of the translational springs and the rotational springs, respectively. More details can be found in Brubak [18] and Brubak, Hellesland and Steen [19]. Eq. 15 can also be applied for rotational springs at plate boundaries.

The maximum kinetic energy of the plate is given by

$$H_{\text{plate}}^{max} = \omega^2 \frac{\rho t}{2}\int_0^b \int_0^L w^2\, dx\, dy \tag{16}$$

where ρ is the density of the material, and the maximum kinetic energy of the vertical movement of the stiffener is given by

$$H_{\text{v,stiff}}^{max} = \omega^2 \frac{m_{st}}{2}\int_{L_s} w^2 dL_s \tag{17}$$

where $m_{st} = \rho(h_w t_w + b_f t_f)$ is the mass per unit length of the stiffener.

The kinetic energy of the rotational movement of the stiffener can be expressed by

$$H_{\text{r,stiff}} = \frac{1}{2}\int_{L_s} (m_w v_w^2 + m_f v_f^2) dL_s \tag{18}$$

where $m_w = \rho h_w t_w$ is the mass per unit length of the web and $m_f = \rho b_f t_f$ is the mass per unit length of the flange. As shown in Fig. 3(a), v_w and v_f is the lateral velocity of

the centroid of the web and the flange of the stiffener, respectively. By using geometrical considerations, these velocities can be written as

$$v_w = (0.5h_w + 0.5t)\frac{\partial w_{,n}}{\partial t} \quad \text{and} \quad v_f = (0.5t + h_w + 0.5t_f)\frac{\partial w_{,n}}{\partial t} \tag{19}$$

where $w_{,n}$ is the derivative of w normal to the stiffener orientation as illustrated in Fig. 3(b). By substituting Eq. (19) into Eq. (18), the expression for the maximum kinetic energy of the rotational movement of the stiffener can be written as

$$H_{\text{r,stiff}}^{max} = \omega^2 \frac{\bar{m}_{rot}}{2L_s^2} \int_{L_s} \left(L_y^2 w_{,x} + 2L_x L_y w_{,x} w_{,y} + L_x^2 w_{,y} \right) dL_s \tag{20}$$

where

$$\bar{m}_{rot} = m_w(0.5h_w + 0.5t) + m_f(0.5t + h_w + 0.5t_f) \tag{21}$$

The strain energy integral in Eq. (20) may be solved analytically or by numerical integration. The latter is used in the present work.

When all the expressions for the potential energy above are computed, the eigenvalue problem of Eq. (8) can be established and solved.

5 VALIDATION PREMISES

The present model was incorporated into a Fortran computer code and computed results have been compared with finite element analyses (FEA) using ABAQUS [21] for a variety of plate and stiffener dimensions, and in-plane prestress loads. Eigenfrequency results, presented as natural eigenfrequencies $f = \omega/2\pi$ [Hz], are verified by comparisons with FEA. Results, presented in subsequent sections, are limited to simply supported plates with sniped stiffeners.

The finite element model, based on shell elements (shell elements S4R both for plate and stiffeners), is supported in the out-of-plane direction along the edges of the plate, and the edges are forced to remain straight during deformation. The plate is also supported in the in-plane directions, just enough to prevent rigid body motions. Further, the ends of the stiffeners are completely free and not loaded (sniped).

The adopted elastic material properties in each computation are Young's modulus $E = 208000$ MPa and Poisson's ratio $\nu = 0.3$.

In the present model, 225 degrees of freedom (15x15) are used in all the cases. Comparable convergence studies carried out previously [19] have shown that this choice of degrees of freedom may overestimate the eigenfrequency predictions by, typically, about 1-2 %. In comparisons, the number of degrees of freedom used in the FEA analysis is typically about 20000, which is believed to be a sufficiently large number to ensure satisfactory results.

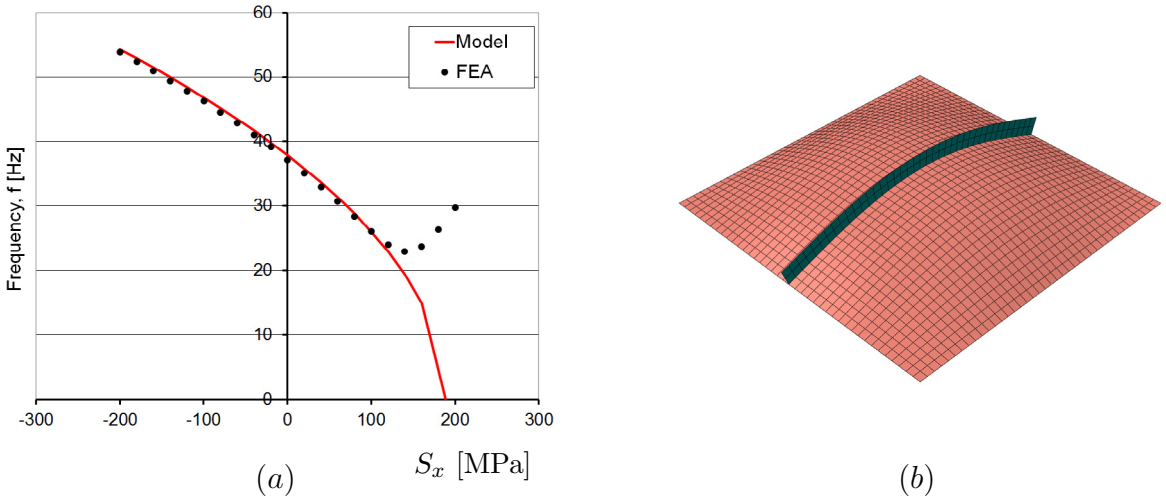


Figure 4: (a) Eigenfrequencies for a regularly stiffened plate subjected to uniaxial prestress S_x in the stiffener direction and (b) the eigenmode of the plate for free vibration.

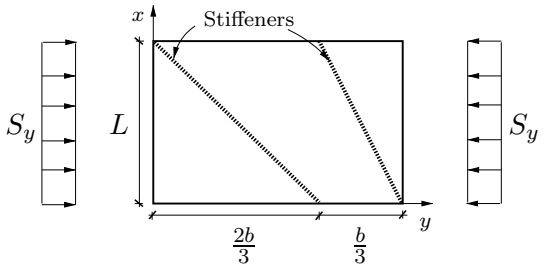
6 REGULARLY STIFFENED PLATE WITH IN-PLANE PRESTRESS

Stiffened plates subjected to in-plane prestress have been analysed. A typical case is shown in Fig. 4(a), where the eigenfrequencies for a plate is computed for various magnitudes of prestress in the stiffener direction for both compression and tension. The plate ($L/b/t = 2000/2000/20mm$) is simply supported and is provided with one regular, sniped stiffener with a flatbar section ($h_w/t_w = 100/12mm$).

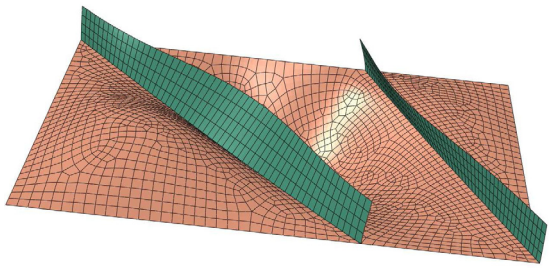
The agreement between the model and FE results is very good for external prestress smaller than about 120 MPa (Fig. 4(a)). This corresponds to about 63% of the elastic buckling stress, which has been found to be $S_{x,cr} = 189$ MPa in this case. Beyond this level, it can be seen that the model frequency results continues to decrease toward the elastic buckling stress (at the intersection with the S_x-axis) while the FEA results reaches a minimum value and then starts increasing for increasing prestress values. The reason for these differences is that the stiffness matrix in the FEA is computed using large deflection theory while the model is based on small deflection theory (in that the energy contribution from membrane strains does not affect the eigenvalues).

In large deflection theory, membrane stresses are redistributed from the interior of the plate fields to the stiffer parts, which are at the edges. This leads to a reduction in membrane compression stresses at the interior of the plate, which causes a larger eigenfrequency for the vibrations computed by FEA. It is worthwhile noting that this leads to solutions also for prestress values exceeding the classical elastic buckling stress. For plates without eccentricities (i.e., due to sniped stiffeners or imperfections), the membrane stress redistribution will start taking place at the classical buckling stress. With increasing eccentricities, the transition from the descending to the ascending portion of the frequency-prestress curve (FEA, Fig. 4(a)) becomes increasingly gradual. In the semi-analytical

	L	b	t	h_w	t_w
Plate 1	1200	2400	12	200	12
Plate 2	1600	2400	12	200	12



(a)



(b)

Figure 5: (a) Plate definitions and (b) eigenmode of Plate 1 subjected to prestress $S_y = 50$ MPa.

model, there is no redistribution of compression membrane stresses. Due to this, the frequency-prestress curve decreases continuously toward the elastic buckling stress. At and above this stress there is no solutions. In order to extend the model to include large deflection theory [22], it is expected that a similar formulation as in Brubak and Hellesland [23] for computing the post-buckling behaviour can be used.

The eigenmode for free vibration of the plate is shown in Fig. 4(b). This is a global mode where the stiffener deflection is one half wave. Similar modes with global deflections are also found when the plate is subjected to a prestress.

In its present form, application of the model should be limited to prestress values below about 60% of the classical elastic buckling stress for such cases, associated with global buckling modes and eccentric loads (sniped stiffeners). For local buckling modes such eccentricity effects are not that pronounced and the model will be able to handle prestress values closer to the elastic buckling stress (as shall be seen below).

7 IRREGULARLY STIFFENED PLATES

Typical results for two simply supported, irregularly stiffened plates defined in Fig. 5(a) are presented in Fig. 6 . The plates are provided with two inclined, eccentric stiffeners. The rather irregular stiffener locations are chosen such as to provide quite severe test cases for the present model. In this case, with a local eigenmode, the redistribution of compression stresses (discussed above) is less pronounced than above due to smaller eccentricity effects. This is reflected in the FEA results by a rather abrupt change in slope (sharp angle) for prestress values close to the elastic buckling stress. As already explained, the model does not reflect this phenomenon.

As seen (Fig. 6), the agreement between the model and the FE results is good for compression prestresses smaller than about 95% of the elastic buckling stress (as given by the intersection by the model results (full line) and the S_y-axis). For tensile prestress

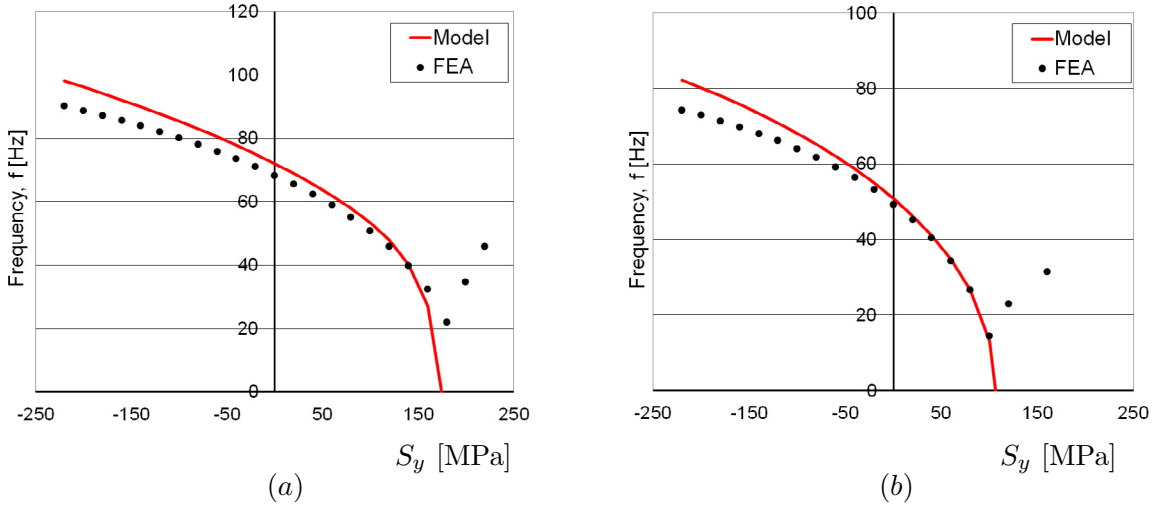


Figure 6: Eigenfrequency versus prestress S_y for (a) Plate 1 and (b) Plate 2.

values, the frequencies are somewhat overestimated, but still less than about 10% for prestress values as high as $S_y = -150$MPa. This is quite acceptable.

The shape of the first eigenmodes calculated by the present model and by FEA are quite similar in each case. Fig. 5(b) shows the first eigenmode of plate 2. This is a local mode with small out-of-plane deflections along the stiffeners.

8 CONCLUDING REMARKS

An efficient computational model for eigenfrequency computations of stiffened plates subjected to in-plane prestress with arbitrarily oriented stiffeners is presented, and results are obtained and compared with FEA results for cases with sniped stiffeners. The model is ideally suited in design optimisation studies and also in reliability studies that normally require a large number of case studies. A computer program based on this method is of a size that can easily be incorporated into a computerised design code. A minimal number of input parameters is required and the present model is therefore considerably more user friendly than commercial finite element programs, which requires experienced users to obtain reliable results.

Acknowledgments

The authors would like to thank dr. Eivind Steen at Det Norske Veritas (DNV), for his interest, suggestions and valuable discussions throughout the study.

REFERENCES

[1] K.M. Liew, Y. Xiang and S. Kitipornchai. Research on thick plate vibration: a literature survey, Journal of Sound and Vibration, 1995; 180(1): 163–176

[2] Lord Rayleigh. Theory of Sound. Volume 1, London: Macmillan; reprinted 1945 by Dover, New York, 1877

[3] W. Ritz. Über eine neue methode zur lösung gewisser variationsprobleme der mathematischen physik, Journal für Reine und Angewandte Mathematik, 1909; 135, 1–61

[4] J. Yuan and S.M. Dickinson. The flexural vibration of rectangular plate systems approached by using artificial springs in the Rayleigh-Ritz method, 1992, 159(1), 39–55

[5] R.B. Bhat. Natural frequencies of rectangular plates using characteristic orthogonal polynomials in Rayleigh-Ritz method, Journal of Sound and Vibration, 1985; 102(4), 493–499

[6] D.J. Dawe and O.L. Roufaeil. Rayleigh-Ritz vibration analysis of Mindlin plates, Journal of Sound and Vibration, 1980, 69(3): 345–359

[7] C.S. Kim, P.G. Young and S.M. Dickinson. On the flexural vibration of rectangular plates approached by using simple polynomials in the Rayleigh-Ritz method, Journal of Sound and Vibration, 1990; 143(3), 379–394

[8] O.L. Roufaeil and D.J. Dawe. Rayleigh-Ritz vibration analysis of rectangular Mindlin plates subjected to membrane stresses, Journal of Sound and Vibration, 1982; 85(2), 263–275

[9] M.M. Kaldas and S.M. Dickinson, Vibration and buckling calculations for rectangular plates subject to complicated in-plane stress distributions by using numerical integration in a Rayleigh-Ritz analysis, Journal of Sound and Vibration, 1981; 75(2), 151–162

[10] L.X. Peng, K.M. Liew, S. Kitipornchai. Buckling and free vibration analyses of stiffened plates using the FSDT mesh-free method, Journal of Sound and Vibration, 2006; 289(3), 421–449

[11] K.M. Liew, Y. Xiang, S. Kitipornchai, M.K. Lim Vibration of rectangular Mindlin plates with intermediate stiffeners Journal of Vibration and Acoustics, 1994; 116, 529–535

[12] R.B. Bhat. Vibrations of panels with non-uniformly spaced stiffeners, Journal of Sound and Vibration, 1982; 84(3), 449–452

[13] J.R. Wu and W.H. Liu. Vibration of rectangular plates with edge restraints and intermediate stiffeners Journal of Sound and Vibration, 1988; 123(1), 103–113

[14] M. Chiba and I. Yoshida. Free vibration of a rectangular platebeam coupled system, Journal of Sound and Vibration, 1996; 194(1), 49–65

[15] Hongan Xu, Jingtao Du and W.L. Li, Vibrations of rectangular plates reinforced by any number of beams of arbitrary lengths and placement angles, Journal of Sound and Vibration, 2010; 329(18), 3759–3779

[16] D.O. Brush and B.O. Almroth, Buckling of bars, plates and shells, McGraw-Hill Book Company, 1975

[17] A.K. Chopra, Dynamics of structures: theory and applications to earthquake engineering (third ed.), Prentice-Hall, 2007

[18] L. Brubak, Semi-analytical buckling strength analysis of plates with constant or varying thickness and arbitrarily oriented stiffeners. Research report in mechanics, No. 05-6, Norway: Mechanics Division. Dept. of Mathematics, University of Oslo; 2005. pp. 65

[19] L. Brubak, J. Hellesland and E. Steen. Semi-analytical buckling strength analysis of plates with arbitrary stiffener arrangements, Journal of Constructional Steel Research, 2007; 63 (4), 532–543

[20] Lars Brubak and Jostein Hellesland, Approximate buckling strength analysis of arbitrarily stiffened, stepped plates, Engineering Structures, 2007; 29(9), 2321–2333

[21] ABAQUS/Standard, User's Manual Version 6.7. volume Hibbitt, H. D. and Karlsson, B. I. and Sorensen, I. Hibbit, Karlsson and Sorenson Inc., Pawtucket; 2008.

[22] K. Marguerre, Zur theorie der gekrümmten platte grosser formänderung, Proceedings of The 5^{th} International Congress for Applied Mechanics, 1938; 93–101

[23] Lars Brubak, Jostein Hellesland. Semi-analytical postbuckling and strength analysis of arbitrarily stiffened plates in local and global bending, Thin-Walled Structures, 2007; 45(6), 620–633

V International Conference on Computational Methods in Marine Engineering
MARINE 2013
B. Brinkmann and P. Wriggers (Eds)

COMPARISON OF COMPUTATIONAL METHODS FOR EVALUATION OF WAVE-LOAD-INDUCED FATIGUE DAMAGE ACCUMULATION IN A CONTAINERSHIP STRUCTURE DETAIL

MARINE 2013

VIKTOR OGEMAN*, WENGANG MAO† AND JONAS W. RINGSBERG†

* Department of Shipping and Marine Technology
Chalmers University of Technology
SE-412 96 Gothenburg, Sweden
e-mail: ogeman@student.chalmers.se

† Department of Shipping and Marine Technology
Chalmers University of Technology
SE-412 96 Gothenburg, Sweden

Keywords: Direct calculation, Engineering beam theory, Fatigue damage, FEM, Panel method, Rainflow counting, Spectral fatigue methods, Strip theory, Structural stresses

Abstract. In this study different methods, from linear strip theory to more complex non-linear panel methods, are employed to estimate the hydrodynamic loads on a 4400TEU container ship. Subsequently, the structural stresses are computed using the finite element method and engineering beam theory. The calculated stresses are used to evaluate the fatigue damage in a detail of the ship structure using the rainflow counting method and different spectral methods. It is concluded that, for the studied part of the structure with governing uniaxial stresses due to wave loading, disregarding vibrational responses, it is sufficient to evaluate the fatigue damage using a spectral method, i.e. the so-called narrow band approximation, without any compensation.

1 INTRODUCTION

Ocean crossing vessels should be designed with sufficient fatigue strength. In the maritime industry, the stress-based fatigue assessment approach is used to predict the fatigue life of ship structures, using S-N curves combined with the Palmgren-Miner relationship [1]. In this approach, it is essential to have the stress range distribution for the structural details of interest. For conventional ships the stress range distributions are provided by classification society rules - these are mainly based on empirical experience. However, some discrepancy between the design and actual stress range distribution is reported due to differences in environmental loads encountered. For example, a ship may change its designated trade region or install a different routing system for route planning.

Furthermore, for novel ship designs, empirical data of fatigue loads is not available to guide the structural fatigue design [2]. Consequently, so-called direct calculation methods are introduced to compute the corresponding structural stresses for ship fatigue assessment [1]. This investigation aims to compare the result and reliability of using different computation methods for estimating the fatigue life of a ship structural detail, see Figure 1. Here linear strip theory is compared with linear and non-linear panel methods, engineering beam theory is

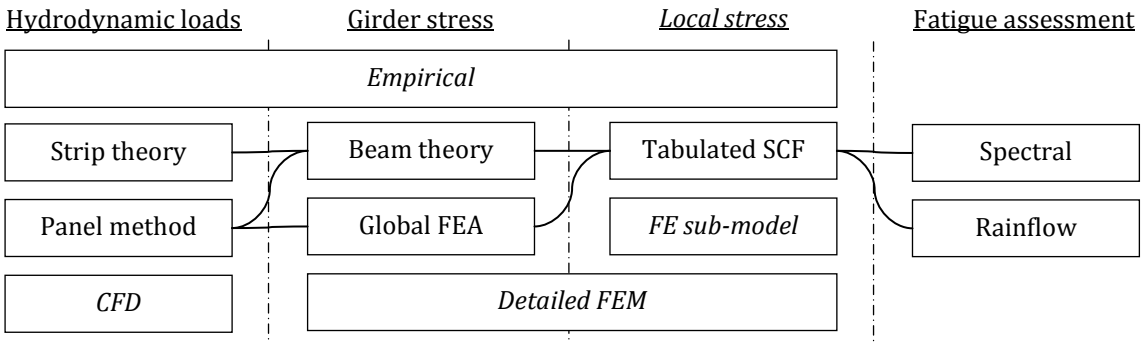


Figure 1: Overview of methods and different steps used to calculate fatigue damage. Methods marked in *italic style* are not considered in the current study. Note that some of the methods are used in the frequency domain.

compared with FEA, and direct rainflow counting is compared with various spectral fatigue estimations.

The fatigue assessment is split into four parts. The methods in each part can be interchanged to allow for many different calculation procedures. In the following, only the direct calculation methods are addressed. To investigate the difference between these methods, the current study first provides a quick overview of the methods considered in Section 2. Section 3 presents a container ship model used in a case study. In Sections 4 to 6, the results from the hydrodynamic load calculation, stress calculation and fatigue evaluation, respectively, are presented. The conclusions of the work are presented in Section 7.

2 FATIGUE METHODOLOGY

To evaluate the fatigue damage of a structural detail using the methodology outlined in Figure 1 the first step is to compute the hydrodynamic loads acting on the ship [1]. These can be computed using a linear frequency domain analysis, e.g. strip theory, or using more advanced time domain simulations such as panel methods or viscous CFD methods. The structural stresses caused by these wave loads are sought for. Engineering beam theory or a global FE model of the girder may be combined with either a tabulated stress concentration factor (SCF) or a detailed FE analysis to account for concentration of stresses due to the local geometry [1]. Finally, the fatigue damage is computed using either the rainflow counting method or a spectral method, based on an appropriate S-N curve [1].

2.1 Hydrodynamic loads

Linear strip theory is based on the assumption that 3D effects and ship motions are small. It also disregards forward speed effects. Strip theory is commonly used in the maritime industry for fatigue evaluation purposes because of its low computational requirements. Recently, the effects in the response due to the underlying assumptions, for example linearity, have been questioned [3].

Panel methods may mediate some of the issues with strip theory. Panel methods are based on 3D solutions to potential flow theory in the time domain. This combined with appropriate boundary conditions allow for solutions in arbitrary non-viscous wave descriptions and inclusion of some forward speed effects. Recently, computational fluid dynamics methods such as averaged Navier-Stokes have also been used - they are still under active development.

2.2 Girder stresses

Given the cross-sectional loads of a ship structure, engineering beam theory allows for calculation of stresses in any location. Based on the assumptions of small displacements, unchanged sectional geometry, an initial straight and prismatic beam and linear elasticity the stress in the section is given by:

$$\sigma_l = \frac{F_n}{A} + \frac{M_v}{I_v}\Delta z + \frac{M_h}{I_h}\Delta y + \sigma_w ,$$

where F_n, M_v, M_h are the longitudinal force, vertical and horizontal bending moment respectively. The properties A, I_v, I_h define the cross-sectional area and area moments of inertia while $\Delta z, \Delta y$ are the distances between the detail and the neutral axes, σ_w is the stress due to warping [4]. Despite its severe assumptions, engineering beam theory has proven to be applicable in many situations although these assumptions sometimes are violated, for example, usage in a ship where the cross-section may be considered only partly prismatic [1].

Alternatively, the girder stresses may be calculated using a global FE model of the ship. The ship is then typically discretized and described by a model consisting of beam and shell elements [5]. Instead of transferring sectional loads from the hydrodynamic calculation the calculated hydrodynamic water pressures may directly be transferred as pressures on the corresponding elements, also allowing for a locally more detailed analysis of the load effects.

2.3 Fatigue estimation

When the stress history of a structural detail is available, the rainflow counting method is often used to extract stress cycles. Based on the chosen S-N curve, fatigue damage accumulation can be estimated using the Palmgren-Miner relationship [6]. In the stress-based fatigue (high-cycle fatigue) assessment approach, a S-N curve describes the relationship between the number of harmonic stress cycles N until failure for a given stress range S. A one slope log-linear S-N curve, with parameters α, m, may for example be described as:

$$\log(N) = \alpha - m\log(S) .$$

Alternatively, the fatigue damage can be estimated using a spectral fatigue method given the spectrum of the structural stresses. The so-called narrow band approximation is often used for ship fatigue assessment. Given a stationary Gaussian load the narrow band approximation (NBA) is a proven upper bound to the rainflow damage and tends to the same value for narrow band processes [5]. The NBA may be calculated according to (same α, m as above):

$$D^{\mathrm{NB}} = \frac{T(2\sqrt{2})^m}{2\pi\alpha}\sqrt{\lambda_2}\lambda_0^{(m-1)/2}\Gamma(1+m/2)$$

where T is the considered period, λ_i is the i^{th} spectral moment and Γ is the gamma function.

There exist several corrections to the NBA for wider, two-peak load spectrums or even for non-Gaussian processes, see for example [2][7]. Such methods use spectral properties, often moments, or work by splitting the spectrum to approximate the damage.

3 COMPUTATIONS

To compare the results obtained using common combinations of the methods outlined in Figure 1 a 4400 TEU container ship [8], in fully laden condition and bow sea (heading angle $\theta = 135^\circ$) with a cruise speed of 10 m/s was used in all calculations. The results were expected to demonstrate the advantages and drawbacks of these methods, which may capture different effects. For example, plate buckling and the subsequent additional stress due to local water pressure is not described by strip theory but may be captured by panel methods followed by a FE analysis. The location for damage calculations was chosen to top of the outermost deck longitudinal for the upper deck in the middle of the central hold (133.5 m forward of AP), see Figure 2a. This location allows for the simplification of uniaxial load and is unaffected by the plate buckling due to local loads.

There exist many methods to approximate a stress concentration factor (SCF) and they may provide significantly different values [9]. However, since all methods considered in this study are subject equally to this factor the SCF was arbitrarily set to 2.0 in all the computations. Note that this does not affect any of the comparisons or the conclusions of the study. Further, the S-N curve in the investigation was chosen to be an empirical one slope curve for welded joints with $m = 3, \alpha = 12.164$ [1].

All simulations were performed in DNV Sesam [10] and the sea states used are described by a two parameter Pierson-Moskowitz (PM) spectrum with T_p chosen as the most probable for a given wave height on the North Atlantic [1], using a spreading factor of $\cos^2(\phi)$. Also note that as the "reference stress calculation" in this investigation engineering beam theory was used, but the effect of torsion was excluded due to the difficulty and longitudinal variation in estimation of torsional properties and boundary conditions.

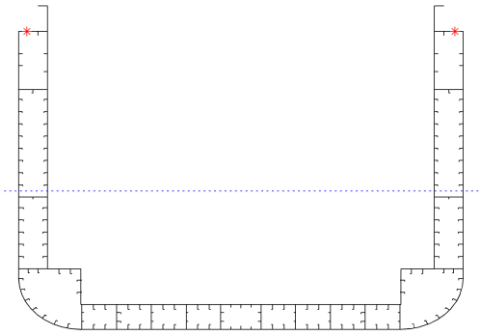


Figure 2a: Mid-ship cross-section with the considered points marked as red dots on starboard and port side. The vertical neutral axis marked with a dashed blue line. The cross-section is symmetric.

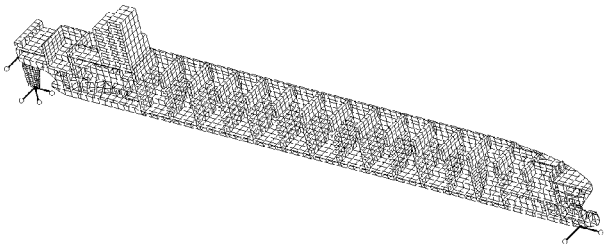


Figure 2b: View of half FE model of the considered container ship with constrained degrees of freedom illustrated. Note that a fully laden ship has been used for all calculations.

3.1 Hydrodynamic loads

All strip theory calculations were performed in Sesam Waveship using 58 strips and 10° heading increments, using an equal number of headings for the frequency domain calculations. The panel method solver used was Sesam Wasim. In both cases at least 30 wave lengths between 0.1 and 3.25 times the ship length have been used.

To eliminate instabilities in the predicted motion from the panel solver a relatively stiff spring system attached to bow and stern has been used, see Table 1a and the Wasim manual for a more detailed description [11]. Wasim allows for either a linear solver or a weakly non-linear solver including non-linearity in hydrostatic and Froude-Krylov forces, integrating pressures over the instantaneous wetted surface [11].

When extracting sectional loads from the panel method solver the resulting stress history shows unphysical occasional peaks, always of length just one sample. To eliminate the resulting significantly increased cycle amplitudes the sampling frequency was increased sufficiently to separate the noise from the highest frequency of interest and applying a linear phase filter to remove the noise. Note that no speed reduction, voluntary or involuntary, was applied in any of the considered sea states.

3.2 FE model and computation

The FE model used was developed by Li et al. [12]. To obtain a non-singular solution the FE model was constrained for translation in the after perpendicular (AP) and bow hull underside. Additionally, to prevent rotation about the lengthwise axis a node in the aft deck was constrained for translation in breadthwise direction, see Figure 2b [5].

The structural model was solved linearly and independently for each time step in Sesam Sestra [13]. This led to relatively large reaction forces in the three constricted nodes, approximately corresponding to the hydrostatic pressure on a 30 m^2 area. However, using inertial relief [13] for compensation of the inertial forces decreases the reaction forces to virtually zero whilst producing a difference in stresses in the considered points of considerably less than 5%. All solutions were therefore made without. The resulting stress history was calculated using a sampling frequency of 2 Hz.

3.3 Cross-sectional properties

When comparing different methods for finding the global stress at a certain position it is important to ensure that the same structural properties are used. In particular, when comparing the stresses obtained from engineering beam theory with that from a FE computation the properties of the FE model should be verified.

Table 1b shows the cross-sectional properties of the mid-hold section as estimated from the FE model. The values were obtained by repeating the middle hold including bulkheads to a long beam. By restricting all nodes in the two ends and in parallel displacing them in x, y and z direction the values for cross-sectional area and moments of inertia were obtained by comparing the resulting deformation to the Euler-Bernoulli beam equation.

Table 1a: Spring system properties in Wasim simulations [11].

	Surge	Sway	Yaw
Period	60s	30s	30s
Damp.c.	0.1	0.1	0.1

Table 1b: Cross-sectional properties of mid-hold section.

	A(m)	z_{na}(m)	I_v(m^4)	I_h(m^4)
Model	4.59	10.75	336.3	655.1

4 COMPUTATION OF HYDRODYNAMIC LOADS

To quantify the difference in fatigue damage using different wave descriptions an investigation of the ship in regular bow waves was made. Table 2 shows the difference in computed stress cycle range and fatigue damage when the ship was subject to harmonic waves and Stoke's fifth order waves [14] of the same height and using engineering beam theory for the stress calculation. The non-linear solver is used in both cases.

As expected the difference is larger for steeper waves, reaching a difference of up to 11% in 8 m waves. However, such high waves are exceedingly rare under ordinary circumstances and for smaller waves the difference is within a few percent and is therefore neglected. All further simulations were made using harmonic waves. The difference between the two sides might be explained by the π rad phase difference in σ_h leading to constructive respectively destructive interference with σ_v.

Table 2: Under-prediction of fatigue damage and stress amplitude using harmonic wave description as compared to fifth order Stoke's description with non-linear solver in 200 m long regular bow waves. The columns refer to under-prediction for the corresponding measure. Specifically, longitudinal stress in detail due to vertical, horizontal, horizontal and vertical bending as well as fatigue damage calculated using rainflow counting.

H_S (m)	Side	$\Delta\sigma_v^*$	$\Delta\sigma_h^*$	$\Delta\sigma_{h+v}^*$	d^*
8	Starboard	1.7%	-3.7%	3.8%	11%
8	Port	1.7%	-3.7%	0.56%	1.7%
4	Starboard	0.68%	0.0%	2.5%	5.1%
4	Port	0.68%	0.0%	0.44%	0.3%
2	Starboard	0.14%	0.37%	0.43%	1.4%
2	Port	0.14%	0.37%	0.0%	0.0%

4.1 Wave generation

In the hydrodynamic analysis, the waves as inputs were generated based on linear wave theory. Two different algorithms were used, randomly subdividing the spectrum into finite number of frequency components and uniformly spreading of the wave frequencies. Note that with the default option in DNV Wasim [11] of random subdivision, the generated wave surfaces are not Gaussian distributed, see Table 3. All generations in this investigation use the uniform option with 500 components and a spreading factor of $\cos^2(\phi)$.

Table 3: Excess kurtosis of wave surface γ_2 for various sea states described by a PM spectrum and generated by a random subdivision of 500 wave components. A normal distribution is expected to have γ_2=0. Increasing the number of components does not significantly change the values.

H_S (m)	Method	$E[\gamma_2]$	$\sqrt{Var[\gamma_2]}$
2.5	Random subdivision	-0.678	0.022
2.5	Uniform subdivision	-0.072	0.173
4.5	Random subdivision	-0.691	0.023
4.5	Uniform subdivision	0.079	0.162

4.2 Stationary period

To ensure that all sea state simulations were sufficiently long to obtain steady damage rate estimations the convergence for three different combinations of settings were studied. The results are presented in Figure 4a.

It was concluded that for reasonably small wave heights, 1800s is sufficient to obtain a steady damage rate and was used hereafter. For a significant wave height of 5.5 m, which is still relatively common in the North Atlantic [1], the coefficient of variation was found to be less than 7% which was considered acceptable.

4.3 Linear and non-linear panel method

When computing the hydrodynamic loads by a panel method in Wasim, both linear and non-linear solvers can be chosen. Let the structural stresses be calculated by engineering beam theory. For both harmonic waves and irregular seas, the difference in fatigue damage prediction using hydrodynamic loads computed between the linear and non-linear solvers is presented in Figure 4b. It is of interest to note how the large difference in predicted damage in the harmonic case does not imply a corresponding difference in the sea states. It was also found that for small wave heights the non-linear solver actually under-predicted the damage and that the zero crossing seemed to occur for a significant wave height of 3 m. Note that for the most common sea states on the North Atlantic the difference in damage prediction using the linear and non-linear solver is less than 10%.

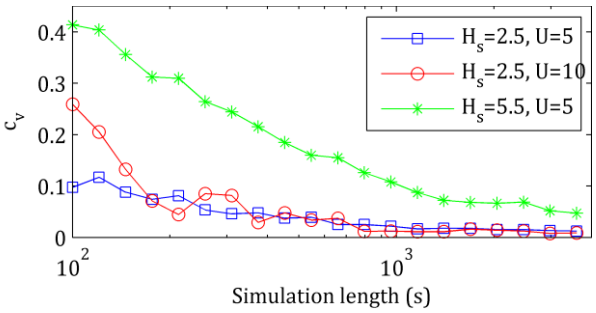


Figure 4a: Coefficient of variation in predicted damage rate from 200 realisations using the rainflow counting method and engineering beam theory to combine the vertical and horizontal bending moment. Linear panel method solver used for both cases with a speed of 5 m/s, non-linear for 10 m/s. Note the logarithmic abscissa scale.

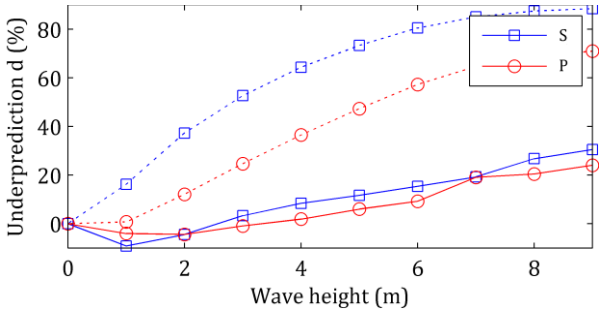


Figure 4b: Under-prediction of damage rate for linear solver as compared to the non-linear solver in harmonic bow sea $\lambda = 200$ m (top two dashed lines), and bow irregular seas (below two solid lines). The corresponding (significant) wave heights are given by the abscissa. In the legend, *S* and *P* refer to the point at starboard and port side respectively.

5 COMPUTATION OF GIRDER STRESSES

Table 4 shows the difference between calculated damage rate using the global FE model and engineering beam theory for a sea state with $H_s = 7.5$ m using the non-linear panel solver for the hydrodynamic loads. It is found that the FE calculations predict less damage than the engineering beam theory. Further, there is a large difference between starboard and port side, indicating that there is a difference in either the horizontal bending moment or warping. Note that warping was not accounted for in the engineering beam theory calculations.

Table 4: Over-predicted fatigue damage rate using engineering beam theory with vertical and horizontal bending moment as compared to global FE solution. *S*, *P* refer to the point at starboard and port side respectively.

	S	*P*
Over prediction	46%	271%

5.1 Structural stresses from full ship FE analysis

For the full ship FE analysis, the wave loads applied on the ship structure were directly transferred from the hydrodynamic analysis. In order to further understand the difference of the computed structural stress between FE analysis and engineering beam theory, we assume that there exists a linear relationship between the sectional forces and the longitudinal stress through a coefficient vector *C*:

$$\sigma_x = CF$$

where the sectional forces F come from the hydrodynamic analysis and the longitudinal stress σ_x is obtained from the FE calculation. In general, F is a vector of six components, three forces and three moments. However, using the engineering beam theory assumption that the longitudinal stress is independent of forces orthogonal to the cross-section, and the fact that the axial force is small the sectional force vector may be taken as:

$$F = \left[M_x, M_y, M_z\right]^T.$$

Regressing for *C* in least squares sense from $H_s = 7.5\,\text{m}$ for the two sides leads to:

$$C^S = \left[-0.216, 0.028, -0.0008\right]$$
$$C^P = \left[-0.360, 0.029, -0.0079\right].$$

The resulting stress calculated as CF corresponds well to the stress history obtained from the FE calculation, see Figure 5. This leads to a small prediction difference in fatigue damage compared to the FE calculation of 1% and 6%, respectively.

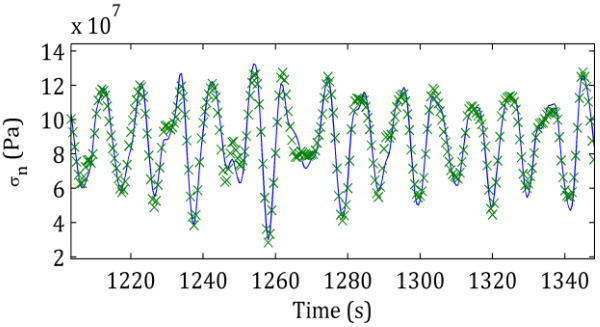


Figure 5: Stress history from sectional loads combined using regression represented as solid line. Sample points from FE-solution marked with crosses. History is for starboard side in a sea state described by $H_S = 7.5\,\text{m}$.

Only using six random time-samples for each regression rather than the entire series and using 500 trials, leads to similar coefficients with the following standard deviations:

$$\sqrt{Var\left[C^S\right]} = \left[0.111, 0.001, 0.012\right] .$$

Thus, the value of the vertical section modulus appears deterministic, whereas there is a large variation in the regressed values for warping and horizontal bending modulus. Using these different regressed values leads to coefficients of variation in damage over-prediction of 0.32 and 0.29 for starboard and port side, respectively. This indicates that the changing moduli for warping and horizontal bending largely affect the results.

Note that the reciprocal of the coefficients in the $C^{S,P}$ matrices corresponds well to the sectional modulus for vertical bending $35.7 \approx 29.9$, whilst the magnitude is clearly wrong for the horizontal bending, $-1250 \neq -50.3$. Further, both warping and horizontal bending stresses are expected to contribute symmetrically but with opposite signs to the starboard and port sides; this is clearly not the case in this relation.

6 FATIGUE DAMAGE COMPARISON

If the time series of structural stresses are available, the corresponding fatigue damage can be estimated by the rainflow counting (RFC) method. For ship fatigue assessment, structural stresses are often assumed to be Gaussian distributed and uniquely defined by a spectrum. Therefore, it is convenient to estimate the fatigue damage by a spectral method. Most of the current spectral methods are based on the so-called narrow band approximation (NBA) to approximate the RFC damage. Various correction procedures are introduce to decrease the overestimation from NBA, such as the method introduced by Benasciutti and Tovo [7] (denoted by BT), Zhao and Baker [15] (denoted by AB), the Wirsching-Light correction [16] (denoted by WL), the Dirlik method [17] (denoted by DL) and the method from Lutes and Larsen [18] (denoted by LL) respectively.

In order to investigate the discrepancy of different spectral methods from the RFC method for ship fatigue assessment, the structural stresses were computed using non-linear hydrodynamic analysis followed by the engineering beam theory for various sea states. It is found that for sea states with significant wave heights from 0.5 to 8.5 m, ship response appears very close to Gaussian with $E[\gamma_1] = 0.044$ and $E[\gamma_2] = 0.009$ for skewness and excess kurtosis and skewness respectively. Further, fatigue damages computed by some spectral methods, NBA, DL and LL, are compared with the RFC method in Figure 6.

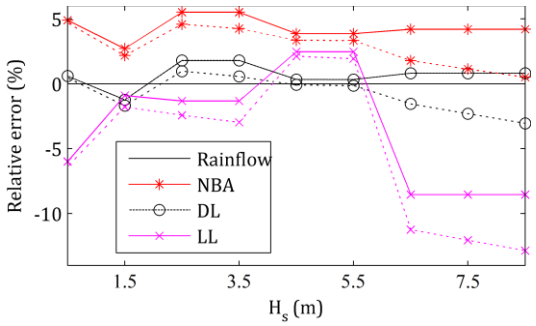


Figure 6: Relative error in damage prediction for some spectral methods as compared to direct rainflow counting. Dashed lines are using the non-linear solver, while solid lines are from the linear solver.

Note that the Lutes-Larsen method, the only to depend on only one moment, clearly perform the worst of the correction methods. The Wirsching-Light method provides an under-prediction. In fact, only the narrow band approximation itself provides a constantly conservative prediction. The damage predicted by the NBA is close to the value obtained by direct rainflow counting, in this case within 5%.

In order to find the most efficient way for a direct ship fatigue assessment, both the computation power and accuracy of different estimation procedures are compared in Table 5. The time is measured on an iCore5 workstation with 8 GB of RAM. The table presents results from four main types of calculations:

1) Panel method in sea state combined with global FE solution,
2) Panel method in sea state with stresses calculated using engineering beam theory,
3) Panel method to create RAOs combined with engineering beam theory
4) Strip theory with engineering beam theory.

In the table, the abbreviations "Non" and "Lin" refer to non-linear and linear hydrodynamic analysis, respectively; "P" denotes the panel method; "FEA" and "EBT" denote finite element analysis and engineering beam theory, respectively.

Table 5: Comparison of calculated damage rate D^* normalized against that for rainflow counting and approximate required computer time for simulation of an additional sea state on a low end desktop computer. All simulations using engineering beam theory calculated from 9 simulations with H_s ranging from 0.5 to 8.5 m in increments of 1m and evaluating damage from both port and starboard side. The simulations using the FE for structural stresses are only evaluated in one sea state as described in section 5.

Method	Type	$E[D^*]$	$Var[D^*]$	First calculation	Additional calculation
Non.P.+FEA+Rfc	1	<0.5	-	18 h	18 h
Lin.P.+FEA+Rfc	1	<0.5	-	15.5 h	15.5 h
Non.P.+EBT+Rfc	2	1.157	0.032	6 h	6 h
Lin.P.+EBT+Rfc	2	1.000	-	3 h	3 h
Lin.P.+EBT+NBA	2	1.036	0.014	3 h	3 h
Non.P.+EBT+NBA	2	1.187	0.029	6 h	6 h
Lin.P.+EBT+BT	2	0.980	0.013	3 h	3 h
Lin.P.+EBT+LL	2	0.984	0.014	3 h	3 h
Lin.P.+EBT+ZB	2	0.931	0.016	3 h	3 h
Lin.P.+EBT+WL	2	0.873	0.013	3 h	3 h
Lin.P.+EBT+DL	2	0.999	0.014	3 h	3 h
Lin.P.+EBT+LL	2	0.958	0.052	3 h	3 h
Freq.P.+EBT+NBA	3	1.057	0.134	49 h	60 s
Freq.P.+EBT+BT	3	0.998	0.127	49 h	60 s
Freq.P.+EBT+ZB	3	1.005	0.128	49 h	60 s
Freq.P.+EBT+DL	3	1.022	0.130	49 h	60 s
Strip+EBT+NBA	4	1.273	0.193	60 s	60 s
Strip+EBT+BT	4	1.168	0.178	60 s	60 s
Strip+EBT+ZB	4	1.170	0.180	60 s	60 s
Strip+EBT+DL	4	1.142	0.174	60 s	60 s

Comparing the damage prediction from time domain simulations using panel methods and frequency domain results constructed by combination of RAOs show that the average prediction over all sea states is very good. However, there is an over-prediction for lower wave heights and under-prediction for higher wave heights. Consequently, for damage from a long term sea state the frequency domain results would likely predict larger fatigue damages since the smaller wave heights are comparatively more common.

The damage predicted by the strip theory method is generally higher than the corresponding damage from the panel method, especially for the sea states with lower wave heights. No attempt has been made to decrease this difference. Table 5 also shows the approximated time required for using the method in question. The large difference between especially frequency domain computations and full hydrodynamic and FE solution provides a clear motivation to its common use.

7 CONCLUSIONS

The fatigue damage prediction using hydrodynamic loads from strip theory, frequency and time domain panel methods and structural stresses from FE and engineering beam theory analyses have been compared for a fully laden container ship in bow seas.

It is found that when considering a specific structural detail unaffected by local plate buckling due to water pressure in the mid-section and ignoring vibrational responses the narrow band approximation provides a good enough measure of the rainflow damage. This is shown by examples for both linear and non-linear panel method solvers combined with engineering beam theory. It is concluded that frequency domain analysis of fatigue damage for the same detail is a time saving alternative with an expected error of less than 6% compared to the damage from a linear time domain analysis. However, accounting for non-linear effects in the hydrodynamic load calculation creates noticeable differences in heavy seas.

The large difference between computed stress using engineering beam theory and the FE model is unexpected. It is of particular interest to notice that engineering beam theory predicts a considerably larger difference between starboard and port side than obtained in the FE analysis. It is however noticed that using only the stress due to vertical bending leads to a considerably better agreement. This issue clearly motivates further study and is currently under investigation.

8 ACKNOWLEDGEMENTS

The authors would like to thank Martin Kjellberg and Zhiyuan Li at Chalmers University of Technology, the Division of Marine Design, research group Marine Structures, for many valuable insights into panel methods and the Sesam software package.

REFERENCES

[1] DNV [Det Norske Veritas]. "Classification Note 30.7, Fatigue assessment of ship structures", Høvik, Norway, 2010.

[2] Mao, W. Fatigue assessment and extreme response prediction of ship structures. PhD thesis, Chalmers University of Technology, Gothenburg, Sweden, 2010.

[3] Zhiyuan, L. Ringsberg, J.W. Direct calculation of fatigue damage of ship structure details. In *Proceedings of the ASME 2011 30th International Conference on Ocean, Offshore and Arctic Engineering (OMAE2011)*, Rotterdam, the Netherlands, 2011.

[4] Thelandersson, S. Analysis of thin-walled elastic beams. Lund Institute of Technology, Lund, Sweden, 1987.

[5] DNV [Det Norske Veritas]. "Strength analysis of hull structures in container ships", July 2011, Høvik, Norway, 2011.

[6] Rychlik, I. On the 'narrow-band' approximation for expected fatigue damage. *Prob. Engng Mech.* (1993) **8**:1-4.

[7] Benasciutti, D. and Tovu, R. On fatigue damage assessment in bimodal random processes. *Int. J. Fatigue* (2007) **29**:232-244.

[8] Storhaug, G., Moe, E. and Holtsmark G. Measurement of wave-induced vibrations and fatigue loading onboard two container vessels operation in harsh wave environment. *J. Offshore Mech. Arct. Engng* (2007) **129**:279-289.

[9] Doerk, O., Fricke, W. and Weissenborn, C. Comparison of different calculation methods for structural stresses at welded joints. *Int. J. Fatigue* (2003) **25**:359-369.

[10] DNV [Det Norske Veritas]. "Sesam 2011 DVD Release, Release Notes", Høvik, Norway, 2011.

[11] DNV [Det Norske Veritas]. "SESAM User Manual Wasim", Høvik, Norway, 2011.

[12] Li, Z. and Ringsberg, J.W. Fatigue routing of container ships – assessment of contributions to fatigue damage from wave-induced torsion and horizontal and vertical bending. *Ships Offshore Struct*. (2011) **7**:119-131.

[13] DNV [Det Norske Veritas]. "SESAM User Manual Sestra", Høvik, Norway, 2011.

[14] Ditlevsen, O. "Stochastic wave loads on tubular offshore structures, models for dynamics and reliability analysis", Lecture notes for offshore structures course, 2nd edition. Technical University of Denmark, Copenhagen, Denmark, 2002.

[15] Zhao, W. and Baker, M.J. On the probability density function of rainflow stresses range for Stationary Gaussian processes. *Int. J. Fatigue* (1992) **14**:121-135.

[16] Wirsching, P.H. and Light, C.L. Fatigue under wide band random stresses. *J. Struct. Engng* (1980) **106**:1593-1607.

[17] Dirlik, T. Application of computers in fatigue analysis. PhD thesis, University of Warwick, Warwick, U.K., 1985.

[18] Lutes, L.D. and Larsen, C.E. Improved spectral method for variable fatigue prediction. *J. Struct. Engng* (1990) **116**:1149-1164.

V International Conference on Computational Methods in Marine Engineering
MARINE 2013
B. Brinkmann and P. Wriggers (Eds)

PROPAGATION OVER A SLOPING BOTTOM OF WAVES GENERATED BY SHIPS

SARA RODRIGUES[*], MARIA F. NASCIMENTO[1], NUNO FONSECA[2], JOÃO A. SANTOS[3] AND CLÁUDIO F. NEVES[4]

[*] Laboratório Nacional de Engenharia Civil, 1700-066 Lisboa, Portugal
e-mail: srodrigues@lnec.pt, www.lnec.pt

[1] Centro Estadual Universitário da Zona Oeste, 23070-200 Rio de Janeiro, Brasil
email: mfnascimento@yahoo.com, www.uezo.rj.gov.br

[2] Centro de Engenharia e Tecnologia Naval, Instituto superior Técnico, 1049-001 Lisboa, Portugal
email: nfonseca@ist.utl.pt, www.mar.ist.utl.pt

[3] Instituto Superior de Engenharia de Lisboa, 1959-007 Lisboa, Portugal
email: jasantos@dec.isel.pt, www.isel.pt

[4] Universidade Federal do Rio de Janeiro, 21949-900 Rio de Janeiro, Brasil
email: neves@peno.coppe.ufrj.br, www.oceanica.ufrj.br

Key words: Ship waves, FUNWAVE model, Pressure distribution

Abstract. This paper presents the results for the two additional pressure distribution functions included in the modified model FUNWAVE to simulate the propagation of waves generated by ships, where the ship is represented by a pressure distribution function. This modified model was adapted by Nascimento [1] in order to include a specified moving pressure at the free surface where the most of the phenomena involved in the transformation of the wave are reproduced. The value proposed by Nascimento [1] for the maximum value of the pressure distribution function of Li and Sclavounos [6] was used as reference in the two new pressure distribution functions.

1 INTRODUCTION

The propagation away from a ship of waves generated by it has been investigated because of their impact on erosion of the margins and on movements induced on moored ships.

The force associated with wave generation by a moving ship is an important part of ship's resistance, that is, the force along the longitudinal axis of the ship necessary for it to move with the desired speed setting. Several numerical models have been developed to determine this resistance to advance. In spite of their features, such models are not be used to simulate the propagation of these waves away from the ship, because the growth of computing time with the simulated area size leads to excessive time requirements.

The numerical models developed for the study of these waves propagation are based on the

shallow water equations, Stockstill and Berger [2], or on improved versions of the Boussinesq equations, Nwogu and Demirbilek [3], Dam et al. [4] and Nascimento [1]. In most of these models the ship is represented by a pressure distribution on the free surface at the position occupied by the ship.

The numerical model FUNWAVE is based on extended Boussinesq equations, Wei and Kirby [5] and it was adapted by Nascimento [1] to model the propagation of ship generated waves. For this the moving pressure distribution on the free surface proposed by Li and Sclavounos [6] was added to the momentum equations, to simulate the ship wave generation. This model reproduces most of the phenomena involved in the wave transformation over a variable depth, including the frequency dispersion, amplitude dispersion, diffraction, bottom and current refraction, energy transfer among harmonic components and energy dissipation by wave breaking and bottom friction.

The objective of this paper is to present the results obtained with the new pressure distribution functions implemented in the modified FUNWAVE model to present the pressure distributions of Pedersen [7] and Ertekin [8] that were implemented in the modified FUNWAVE model to generate ship waves. The results obtained with these new pressure distributions are compared to the ones from the Li and Sclavounos pressure distribution for a ship with a length of 1.5 m, a beam of 0.15 m and a draft of 0.06 m that sails along a channel with the geometry of Dam [4]: a slope of 1:50 that ends at a water depth of 0.22 m.

The structure of this paper is as follows. After this introductory section, section 2 describes the main features of the modified FUNWAVE model. In section 3 the maximum pressure value to be used in the pressure distributions functions is established. In section 4 some tests and their results with different pressures are presented. Finally, the paper closes with some conclusions of the presented work and directions for future work.

2 NUMERICAL MODEL FOR SHIP WAVES

The numerical model FUNWAVE is a hydrodynamic model based on the nonlinear Boussinesq equations derived by Wei and Kirby [5], which are able to simulate most phenomena associated to wave propagation into shallow water. In order to include ship generated waves, it was included in the momentum equation a pressure gradient which causes disturbances on the free surface, Figure 1. The continuity equation (1) and the momentum equation (2) for the modified model are:

$$\eta_t + \nabla.\left\{(h+\eta)\left[u_\alpha + \left(z_\alpha + \frac{1}{2}(h-\eta)\right)\nabla(\nabla.(hu_\alpha)) + \left(\frac{1}{2}z_\alpha^2 - \frac{1}{6}\left(h^2 - h\eta + \eta^2\right)\right)\nabla(\nabla.u_\alpha)\right]\right\} = 0 \tag{1}$$

$$\begin{aligned} &u_{\alpha t} + (u_\alpha.\nabla)u_\alpha + g\,\nabla\eta + z_\alpha\left\{\frac{1}{2}z_\alpha\nabla(\nabla.u_{\alpha t}) + \nabla(\nabla.(hu_{\alpha t}))\right\} + \\ &\nabla\left\{\frac{1}{2}\left(z_\alpha^2 - \eta^2\right)(u_\alpha.\nabla)(\nabla.u_\alpha) + \frac{1}{2}[\nabla.(hu_\alpha) + \eta\nabla.u_\alpha]^2\right\} + \\ &\nabla\left\{(z_\alpha - \eta)(u_\alpha.\nabla)(\nabla.(hu_\alpha)) - \eta\left[\frac{1}{2}\eta\nabla.u_{\alpha t} + \nabla.(hu_{\alpha t})\right]\right\} = -\frac{\nabla P}{\rho} \end{aligned} \tag{2}$$

where η is the surface elevation, h is the water depth, $u_\alpha = (u,v)$ is the horizontal velocity vector at level $z=z_\alpha=-0.531h$, g is the gravitational acceleration, t index represents the partial

time derivative, $\nabla = \left(\frac{\partial}{\partial x}, \frac{\partial}{\partial y} \right)$ is the horizontal gradient operator and P is the moving pressure source function.

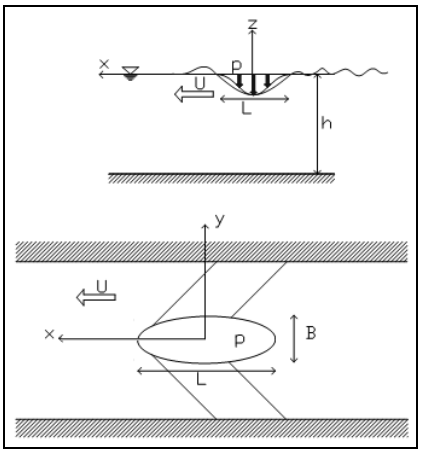


Figure 1: Representation of the moving pressure as the source function which generates the ship waves. (Adapted from Nascimento [1])

Although it is not difficult to include the pressure gradient in the Boussinesq equations to act as the diver for ship waves, one must ensure that the pressure distribution implemented in the model is compatible with the non linear and dispersive properties of the Boussinesq equations, i.e. to the same order of approximation.

The Boussinesq equations can be deduced from the dimensionless form of the Navier-Stokes equations assuming the shallow water hypothesis $h/l << 1$. Such a procedure induces two dimensionless independent parameters in equations, ε and μ^2. The parameter ε represents the ratio between the wave amplitude and the local water depth, $\varepsilon = \eta/h$, (that determines the magnitude of the nonlinear effects) whereas the magnitude of the dispersive effects are represented by the ratio between the local depth and the wave length, $\mu = h/l$.

Several assumptions can be made, resulting in different models of approximation which depend on the magnitude of these parameters. The relative importance of these effects is proportional to $\varepsilon/\mu^2 = \eta l^2/h^3$. For the Boussinesq equations there is a balance between dispersive and nonlinear effects, $\varepsilon = \mu^2$.

The first step in the analysis of the influence in the momentum equation is the expansion of the dependent variables in equations (1) and (2) into power series of the forcing dominant parameters. Such procedure allows the determination of the magnitude of the perturbation source that is compatible with the characteristics of the equations. For the dimensionless variables it is used a characteristic length, l_0, a typical wave amplitude, a_0, and a characteristic depth, h_0, that have the following relationships:

$$
\begin{aligned}
&x' = \frac{x}{l_0} \quad ; \quad y' = \frac{y}{l_0} \quad ; \quad z' = \frac{z}{h_0} \quad ; \quad t' = \frac{\sqrt{gh_0}}{l_0} t \\
&u' = \frac{h_0}{a_0 \sqrt{gh_0}} u \quad ; \quad v' = \frac{h_0}{a_0 \sqrt{gh_0}} v \\
&\eta' = \frac{n}{a_0} \quad ; \quad h' = \frac{h}{h_0} \quad ; \quad P' = \frac{P}{\rho g h_0}
\end{aligned}
\tag{3}
$$

Replacing (3) in (1) and (2), results the following continuity and momentum equations:

$$
\begin{aligned}
&\eta'_t + \nabla . \left\{ (h' + \varepsilon\eta') \left[u'_\alpha + \mu^2 \left\{ \left[\frac{1}{2} z'^2_\alpha - \frac{1}{6} \left(h'^2 - h'\varepsilon\eta' + (\varepsilon\eta')^2 \right) \right] \nabla (\nabla . u'_\alpha) + \right. \right. \right. \\
&\left. \left. \left. \left[z'_\alpha + \frac{1}{2} (h' - \varepsilon\eta') \right] \nabla (\nabla . (h' u'_\alpha)) \right\} \right] \right\} + O(\mu^4)
\end{aligned}
\tag{4}
$$

$$
\begin{aligned}
&u'_{\alpha t} + \varepsilon (u'_\alpha . \nabla) u'_\alpha + \nabla \eta' + \mu^2 V_1 + \varepsilon\mu^2 V_2 + \nabla P' = O(\mu^4) \\
&V_1 = \frac{1}{2} z'^2_\alpha \nabla (\nabla . u'_{\alpha t}) + z'_\alpha \nabla (\nabla . (h' u'_{\alpha t})) - \nabla \left[\frac{1}{2} (\varepsilon\eta')^2 \nabla . u'_{\alpha t} + \varepsilon\eta' \nabla . (h' u'_{\alpha t}) \right] \\
&V_2 = \nabla \left[(z'_\alpha - \varepsilon\eta') (u'_\alpha . \nabla) (\nabla (h' u'_\alpha)) + \frac{1}{2} \left(z'^2_\alpha - (\varepsilon\eta')^2 \right) (u'_\alpha . \nabla) (\nabla . u'_\alpha) \right] + \\
&\quad \frac{1}{2} \nabla \left[(\nabla . (h' u'_\alpha) + \varepsilon\eta' \nabla . u'_\alpha)^2 \right]
\end{aligned}
\tag{5}
$$

In equations (4) and (5) there is the need of a forcing term of order O(ε) for pulse generation, so η', u'_α and P' terms are expanded in power series of O(ε). As the real forcing in the momentum equation is $\nabla P'$ that moves along the *x* axis, this also implies the influence of dissipative terms and it is appropriate that the pressure distribution magnitude relates with ε and μ smaller that the magnitude of μ^4. Expanding the η', u'_α and P' terms in power series (the commas being omitted for convenience) one has:

$$
\begin{aligned}
&\eta = \eta_1 + \varepsilon\eta_2 + O(\varepsilon^2) \\
&u_\alpha = (u_\alpha)_1 + \varepsilon (u_\alpha)_2 + O(\varepsilon^2) \\
&P = P_1 + \varepsilon P_2 + O(\varepsilon^2) \\
&\nabla P = \nabla P_1 + \varepsilon\mu \nabla P_2 + O(\varepsilon^2)
\end{aligned}
\tag{6}
$$

Replacing (6) in (5), one gets a finite sequence of linear problems. For the first order approximation one has:

$$
u_{\alpha 1 t} + \nabla \eta_1 + \nabla P_1 + \left\{ \frac{1}{2} z_\alpha^2 \nabla (\nabla u_{\alpha 1 t}) + z_\alpha \nabla (\nabla (h u_{\alpha 1 t})) \right\} = 0 \tag{7}
$$

In a first approximation ∇P_1 in the equation (7) has to be equal to zero. For the second order approximation one has:

$$u_{\alpha 2t} + \nabla \eta_2 + \mu^2 \left\{ \frac{1}{2} z_\alpha^2 \nabla(\nabla u_{\alpha 2t}) + \nabla(h u_{\alpha 2t}) \right\} = -[(u_{\alpha 1} \nabla)(u_{\alpha 1})] - \mu^2 [\eta_1 \nabla(h u_{\alpha 1t})] - \mu \nabla P_2 \tag{8}$$

the terms on the right side represent the interaction of nonlinear terms the first order of η_1 and $u_{\alpha 1}$ and the second order of P_2 that serve as a forcing terms for the second order wave η_2 and $u_{\alpha 2}$.

In case of ship-wave generation it is assumed that at time t_0 the velocity and the free surface elevation are equal to zero and the pressure P is impulsive force that generates the waves, where

$$P = \varepsilon P_2 + O(\varepsilon^2) \tag{9}$$

the pressure P being dependent of P_2, due to the condition applied in (7), $\nabla P_1 = 0$. In equation (9) it becomes evident that P is of order ε, demonstrating the need for the source to be a nonlinear disturbance, ensuring that ∇P is of $\varepsilon\mu$ order.

As boundary conditions, the numerical model includes absorbing sponge layers to simulate energy dissipation in the momentum equation to control shore reflection effects.

3 PRESSURE DISTRIBUTION FUNCTION

Several pressure distributions are presented in the literature as nonlinear functions of O(ε) approximation, in a rectangle of width B and length L. Such pressure distributions on a rectangle can represent the effects of a moving ship along a water body whose bottom has topographical changes, where such movement can cause initial disturbances at the free surface inside the domain rectangle, that propagate along time with a pattern similar to the ones of ship generated waves. Such patterns are stationary, from the point of view of an observer moving with the ship.

A pressure distribution function was proposed by Li and Sclavounos [6] to study the solitary wave generated in front a ship that sails over a deep water region, equation (10). Pedersen [7] studied a similar wave pattern generated a pressure distribution that moves over a region with topographical changes and proposed equation (11). Ertekin et al [8] studied the generation of solitary waves in front of the ship as well as the stern transversal waves (equation 12). In the three equations *pa* designates the maximum value for the pressure distribution and it is assumed as constant value for the same order of ε, indicated in the nonlinear source in equation (9).

$$P(x,y) = pa \cos^2\left(\pi \frac{x}{L}\right) \cos^2\left(\pi \frac{y}{B}\right) \tag{10}$$

$$P(x,y) = pa \cos^2\left[\frac{\pi}{2}\left(\frac{x^2}{L^2} + \frac{y^2}{B^2}\right)\right] \tag{11}$$

$$P(x,y) = pa \cos^2\left(\frac{\pi(x - 0.5\alpha L)}{(1-\alpha)L}\right) \cos^2\left(\frac{\pi(y - 0.5\beta B)}{(1-\beta)B}\right) \tag{12}$$

with α=0.7 and β=0.4.

This equations are valid for $-L/2 \le x \le L/2$ and $-B/2 \le y \le B/2$, where L is the ship length, B is the ship beam, and (x,y) is the ship position given at any time as (x_0+V_xt ; y_0+V_yt), where (V_x,V_y) is the ship velocity.

The *pa* value corresponding to the maximum of the pressure distribution was established using the procedure of Nascimento [11], which made an analogy between ship generated waves and the waves generated by a solid body that slides into the fluid. Since the wave generated on the first case are also due to the motion of a solid body in the fluid, such analogy is possible once because the wave patterns are similar.

The classification of waves generated by the impact of a solid body is defined by theoretical solutions [9] and experimental results [10]. This classification was based in the relationship between the body height and the Froude number for sliding. The same concept was applied by Nascimento [11] which observes the same relationship between the height of the body and the Froude number in the characteristics of the generated wave pattern.

The dimensional analysis of the ship wave problem results in equation (13). The dimensionless parameters for this problem are similar to ones of the waves generated by the impact of a block. This confirms the analogy between the two phenomena and so studying this problem may be a viable way to analyze the problem of generated ship waves.

$$\frac{H}{h} = f\left(\frac{B}{h}, \frac{D}{h}, \frac{L}{h}, \frac{U}{\sqrt{gh}}, \frac{L_c}{h}, \frac{x}{h}, \frac{\rho_w}{\rho_{SE}}, T\sqrt{\frac{g}{h}}, \frac{l}{h}\right) \tag{13}$$

Where B is a ship beam, D is the ship draft, L is the ship length, U is the ship velocity, L_c is the channel width, x is the distance from the ship to shoreline, ρ_w is the density of the fluid, ρ_{SE} is the density of the ship, h is the wave height; T the wave period and l is the wavelength.

Making a transformation in (13) to include the block coefficient and the shoreline slope, quantities that are present in all relations that involve the ship characteristics and the local navigation, one has:

$$\frac{H}{h} = f\left(S, \frac{D}{h}, \frac{h}{L}, F_h, \frac{h}{L_c}, I_s, T\sqrt{\frac{g}{h}}\right) \tag{14}$$

with $S = BD/A$, $F_h = U/\sqrt{gh}$ and $I_s = h/x$, where A is the cross sectional area of the channel, F_h is the depth Froude number and I_s the shoreline slope.

From (14) it is expected that *D/h* has the same relation that the ratio between the block height and the depth of the channel, *e/h*. In this work, it will be assumed that the maximum pressure value equals the ratio between the draft and the channel depth:

$$pa = \frac{D}{h} \tag{15}$$

where $\frac{D}{h} = O(\varepsilon)$ and $\frac{h}{L} = O(\mu)$.

Following the methodology of Nascimento [1] which included the pressure distribution of Li & Sclavounos [6] in the FUNWAVE model equations, in this paper it was implemented two new functions of pressure distributions given by Pedersen [7] and Ertekin [8] in the modified model.

Figure 2 presents the behavior of these dimensionless pressure distributions as well as their x derivatives for y=0 (the ship representation in the numerical model), for *pa*=1 and for a ship whose length is 1.5 m and whose beam is 0.15 m. y derivatives were not presented because they are constant along y=0.

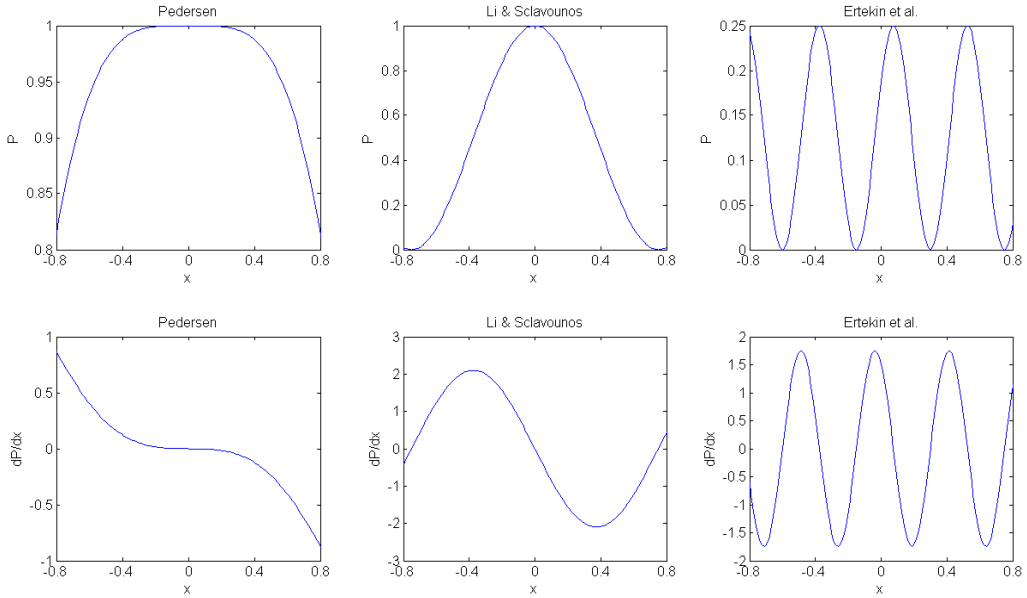


Figure 2: Pressure distributions and its derivatives for *pa*=1. The x axis represent the ship length with *L*=1.5m and *B*= 0.15m

Once the maximum pressure value is defined, those pressure distributions can be written in dimensional form. So for the pressure distribution function given by Li and Sclavounos [6]:

$$P(x,y) = \rho g h\, pa\ \cos^2\left(\pi\frac{x}{L}\right)\cos^2\left(\pi\frac{y}{B}\right) \tag{16}$$

Replacing *pa*, one has:

$$P(x,y) = \rho g D\ \cos^2\left(\pi\frac{x}{L}\right)\cos^2\left(\pi\frac{y}{B}\right) \tag{17}$$

The pressure distribution function of Pedersen [7] becomes:

$$P(x,y) = \rho g D\ \cos^2\left[\frac{\pi}{2}\left(\frac{x^2}{L^2}+\frac{y^2}{B^2}\right)\right] \tag{18}$$

And for the pressure distribution function given by Ertekin et al. [8], one has:

$$P(x,y) = \rho g D\ \cos^2\left(\frac{\pi(x-0.5\alpha L)}{(1-\alpha)L}\right)\cos^2\left(\frac{\pi(y-0.5\beta B)}{(1-\beta)B}\right) \tag{19}$$

4 TESTS AND RESULTS

To evaluate the new pressure distributions included to the modified FUNWAVE model, in this section, it will be presented some tests to analyze these pressure distribution functions and to compare their results with the ones from the pressure distribution used by Nascimento [1].

The ship has a length of 1.5 m, a beam of 0.15 m and a draft of 0.06 m and it is sailing along a coastal stretch that is 14 m long. This coastal stretch is made of a constant depth region (0.22 m deep) and of a 1:50 slope that ends on another constant depth region (0.006 m deep), as shown in Figure 3. The ship is sailing along the line defined by the two planes intersection with a constant velocity of 1.18 m/s, (F_h=*0.8*). Such geometry enables the study of wave propagation over the sloping bottom as well as over a constant depth region. Parallel to the sailing line, on both sides of the coastal stretch there are sponge layers, 3.0 m wide, to prevent the reflection into de domain of the waves propagated up to them.

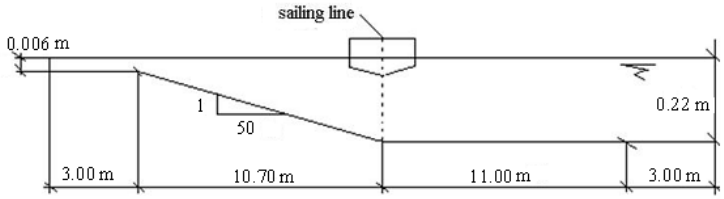


Figure 3: Channel geometry to use in the numerical model.

The Figure 4 shows the spatial representation of the free-surface elevation created by the pressure distribution function of Li and Sclavounos [6] for three instants 5 s, 22.5 s and 45 s.

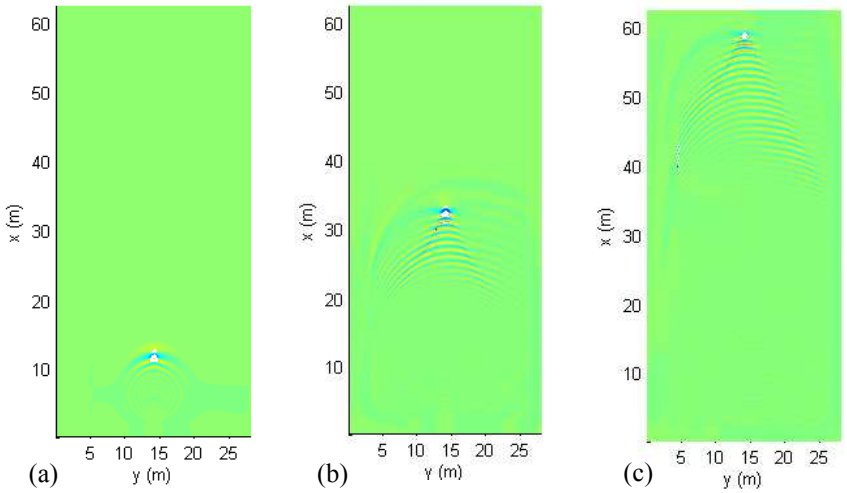


Figure 4: Surface elevation for the Sclavounos pressure distribution, *pa*: (a) t=5 s; (b) t=22.5 s; (c) t=45 s.

As it can be observed for instant 5 s the ship is still starting to generate waves, while for the instants 22.5 s and 45 s the figure shows the propagation of waves generated by ship along the channel. The waves travel at the same speed in water of a given depth but where the

bottom depth is changing their direction of travel changes and the waves become more parallel to the shore, as it can be seen on the left hand side of the channel (sloping bottom) where a bend in the wave crests is evident, Figure 5. In the right hand side of the channel (constant depth) the usual Kelvin wave pattern is found, a V shape with a 19.5 ° angle to the navigation line and two sets of waves (diverging and transversal).

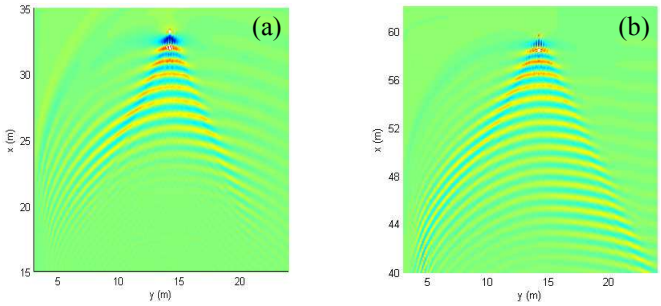


Figure 5: Zoom of the free-surface elevation given by Sclavounos distribution, *pa*: (a) t=22.5 s; (b) t=45 s.

The following figures show the evolution with the distance to the sailing line (y-coordinate) of the maximum free-surface elevation along the channel for the three pressure distribution functions presented in this paper, with the same maximum value *pa* for the pressure distribution.

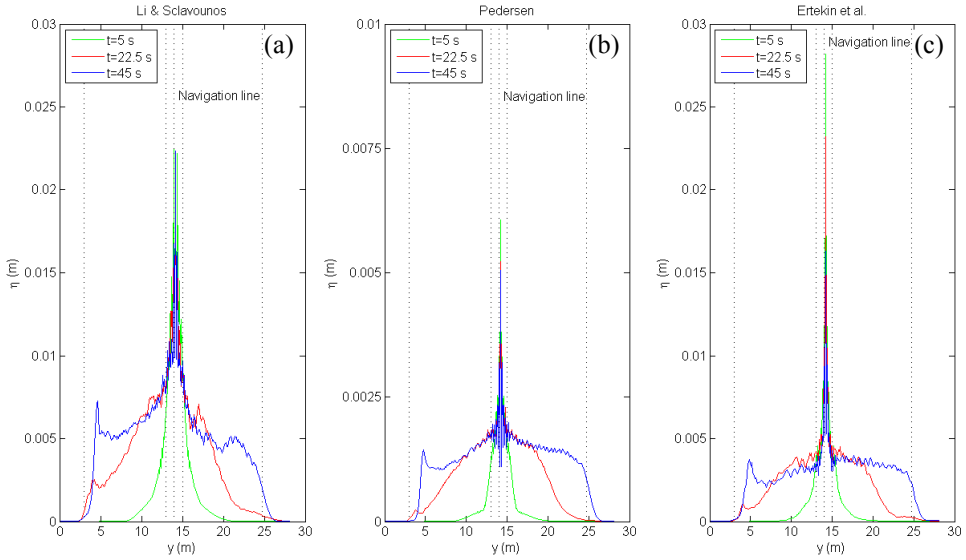


Figure 6: Maximum free-surface elevation for three instants of the value *pa* for: (a) Sclavounos; (b) Pedersen; (c) Ertekin.

The Figure 6 show that for instant 5 s the waves in the channel have not yet reached the maximum since the ship has just started to generate waves. As the ship travels along the channel, the waves grow and propagate along the channel width, as can been see in instant 45 s. Also it can be seen that the increase in the free-surface elevation is greater for the sloping side of the channel than for the constant depth side. The effect of the sponge layers can be

seen in the reduction of the maximum free-surface elevation in the last 3 m close to the domain boundaries.

Figure 7 illustrates the stationary character of the maximum free-surface elevation close to the ship for the three pressure distribution functions considered in this paper.

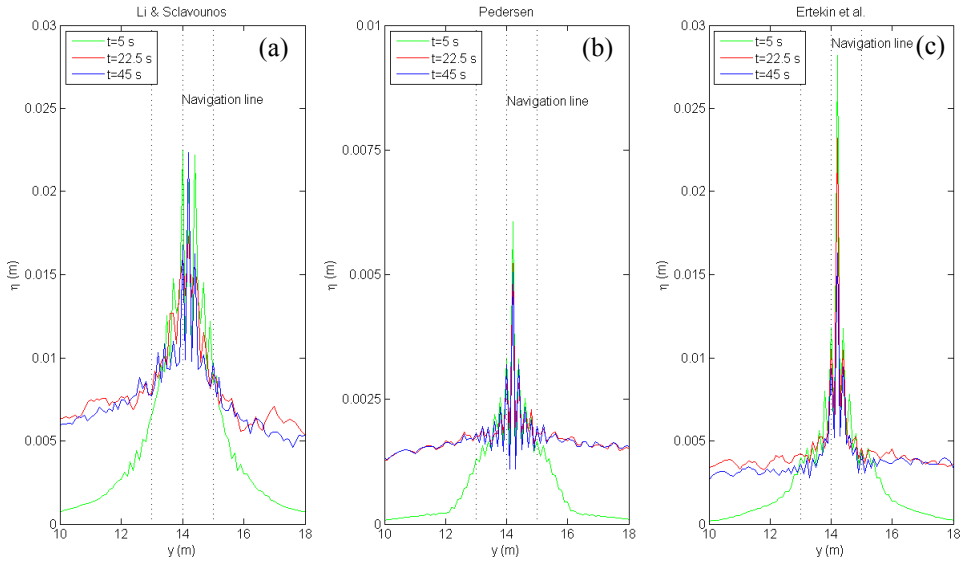


Figure 7: Behavior of the maximum free-surface elevation near the navigation line for: (a) Sclavounos; (b) Pedersen; (c) Ertekin.

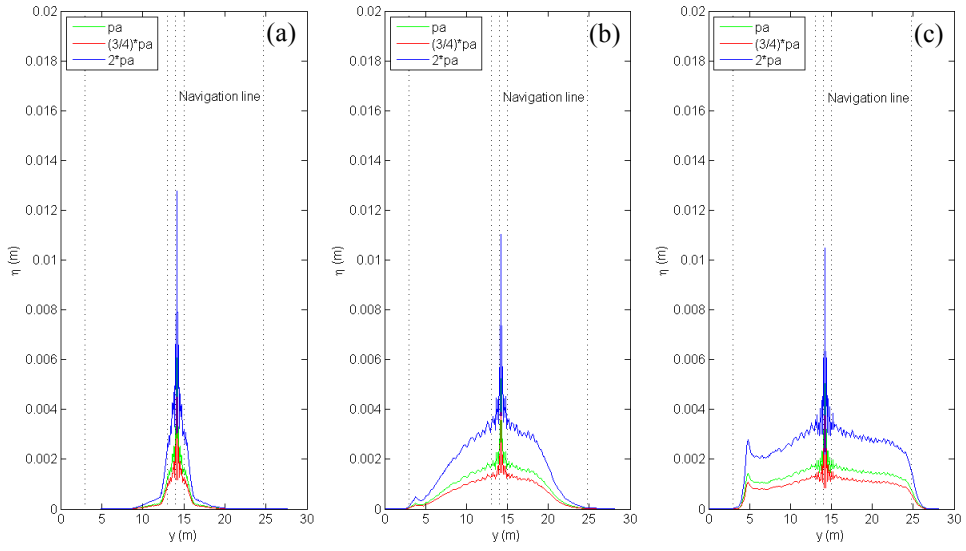


Figure 8: Maximum free-surface elevation for different values of the maximum (*pa, (3/4)*pa* and *2*pa*) in the Pedersen distribution: (a) t=5 s; (b) t=22.5 s; (c) t=45 s.

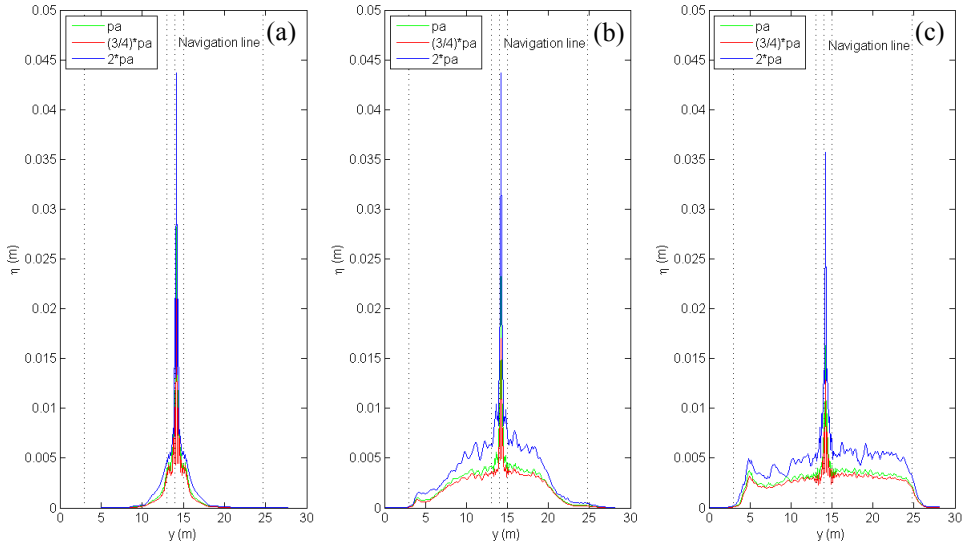


Figure 9: Maximum free-surface elevation for different values of the maximum (*pa, (3/4)*pa* and *2*pa*) in the Ertekin distribution: (a) t=5 s; (b) t=22.5 s; (c) t=45 s.

Figure 8 and Figure 9 show the evolution with the distance to the sailing line (y-coordinate) of the maximum free-surface elevation along the channel for each pressure distribution function presented in this paper, when three different values are considered (*pa*, *2*pa* and *(3/4)*pa*) for the maximum in the distribution.

The figures show a similar behavior for the three maximum values in the pressure distribution functions, an increase of the values of the free-surface elevation as pa value increases.

5 CONCLUSION

This paper presents the results for the two additional pressure distribution functions included in the modified model FUNWAVE to simulate the wave generating ability of a sailing ship.

Tests were made with a ship sailing along a coastal stretch made of a sloping bottom and a constant depth region. The ship sailed along the intersection of those two planes. In the sloping bottom the crests of waves are bent along the slope and in the constant depth the standards Kelvin waves can be found.

The three pressure distribution functions considered have a similar behavior: an increase in the free-surface elevation could be observed in the sloping side of the channel due the decreasing depth and a stationary character of the free-surface maximum elevation close to the ship.

Using the value proposed by Nascimento [1] for the maximum value of the pressure distribution function of Li and Sclavounos [6] in the two new pressure distribution functions produced results similar to the ones presented by Nascimento [1] although not exactly equal. Hence future work includes the definition of a procedure to establish the maximum pressure value. This study will include using the results from the FLUENT model to set the wave pattern close to the ship that is to be met by the results of the modified FUNWAVE version.

ACKNOWLEDGEMENTS

The first author acknowledges the support of Fundação para a Ciência e a Tecnologia, Portugal through the PhD grant SFRH/BD/75223/2010.

The cooperation between the authors is facilitated by the grant 4.4.1.00 CAPES awarded within the scope of the Portuguese – Brazilian technological and scientific cooperation 2013-2014 to the project "Amigos de Boussinesq – Modelação de ondas aplicada a navios e portos".

REFERENCES

[1] Nascimento, M.F. 2007. "Numerical study of ship-wave propagation in shallow water" (in Portuguese). Doctoral Dissertation. Ocean Engineering Department, Universidade Federal do Rio de Janeiro.

[2] Stockstill, R.L.; Berger, R.C. 2001. "Simulating barge drawdown and currents in channel and backwater areas", Journal of Waterway, Port, Coastal and Ocean Engineering, ASCE, pp.290-298.

[3] Nwogu, G.O.; Demirbilek, Z. 2004. "Numerical modeling of ship-induced currents in confined waterways". Proceedings of the 29th International Conference on Coastal Engineering, pp.256-268, Lisbon.

[4] Dam, K.T.; Tanimoto, K.; Nguyen, B.T.; Akagawa, Y. 2006. "Numerical study of propagation of ship waves on a sloping coast". Ocean Engineering, 33, pp.350-364.

[5] Wei, G.; Kirby, J.T. 1995. "Time-dependent numerical code for extended Boussinesq equations". Journal of Waterway, Port, Coastal and Ocean Engineering, ASCE, pp.251-261.

[6] Li, Y.; Sclavounos, P.D. 2002. "Three-dimensional nonlinear solitary waves in shallow water generated by advancing disturbance". Journal of Fluid Mechanics, v. 470, pp.383-410.

[7] Pedersen, G. 2004. "Waves generated by moving disturbances in shallow water".

[8] Ertekin, R.C.; Webster, W.C.; Wehausen, J.V. 1986. "Waves caused by a moving disturbance in a shallow channel of finite width". Journal of Fluid Mechanics, v. 169, pp.275-292.

[9] Noda, E. 1970. "Water waves generated by landslides". Journal of Waterway, Port, Coastal, Ocean Div., Am. Soc. Civ. Eng., v. 96(4), pp.835–855.

[10] Wiegel, R.L.; Noda, E.K.; Kuba, E.M.; Gee, D.M.; Tornberg, G.F. 1970. "Water waves generated by landslide in reservoirs", Journal of the Waterways and Harbors Division, 96(2), pp.307–333.

[11] Nascimento, M.F. 2001. "Approximation of the Boussinesq equations of in the process of wave generation in the solid-liquid interface. A numerical-experimental approach with commitment to engineering." Dissertation in Master civil engineering. Universidade Estadual Paulista.

V International Conference on Computational Methods in Marine Engineering
MARINE 2013
B. Brinkmann and P. Wriggers (Eds)

SIMULATION OF MOONPOOL WATER MOTION

HENRI J.L. VAN DER HEIDEN*, PETER VAN DER PLAS*, ARTHUR E.P. VELDMAN*, R. LUPPES* AND ROEL W.C.P. VERSTAPPEN*

*Computational Mechanics and Numerical Mathematics
Institute of Mathematics and Computing Science
University of Groningen
Groningen, 9747 AG
e-mail: h.j.l.van.der.heiden@rug.nl

Key words: Moonpool water motion, Viscous flow modeling, Turbulence

Abstract. The potentially violent free-surface motion of water in a moonpool is an important problem in the design and operation of various vessels. In this paper, improvements in the modeling of viscous flow effects of the free-surface simulation package ComFLOW are proposed. The improved modeling enables the simulation of events in which detailed viscous flow effects and free-surface motion are strongly coupled, such as the sloshing in a moonpool.

Attention will be given to the discretization of the convective term and the modeling of turbulence. The proposed stabilized central discretization of the convective term shows clear improvements over upwind schemes. State-of-the-art turbulence models, based on the physically relevant invariants of the rate-of-strain tensor, are proposed to model the interaction between resolved and subgrid scales.

The results of these improvements will be assessed for a moonpool sloshing test case.

1 INTRODUCTION

In offshore applications, details of viscous flow effects can become relevant in a variety of circumstances, e.g. when wave run-up on semi-submersible structures or the free-surface motion in a moonpool are concerned. The CFD simulation package ComFLOW has thus far concerned itself mostly with extreme wave impact, so the accurate modeling of viscous flow effects has not yet been a matter of concern. This motivates a novel approach for efficiently simulating viscous flow effects at high Reynolds numbers with the CFD simulation tool ComFLOW.

In ComFLOW, the Navier–Stokes equations can be solved for one-phase and for two-phase flow. The equations are discretized second-order in space, and second-order in time. An improved Volume-of-Fluid (IVOF) algorithm is used for free-surface displacement

[2, 6], which yields an accurate and robust algorithm. The latter property is important in violent flow cases.

Accurate modeling of viscous flow effects in high Reynolds number flows, requires two things. First, a turbulence model should be formulated and implemented that provides accurate results on coarse grids. Secondly, in regions of interest, a high local grid resolution should be achieved in a computationally efficient manner.

The focus of this paper is to assess the performance of improved viscous flow modeling for a practical offshore problem: simulation of the free-surface water motion in a moonpool. For more information on the subject, see [1] and the references therein. In [1], an older version of ComFLOW, which did not contain the detailed modeling of viscous flow effects, has been used to compute the water motion in a moonpool.

In the first section, the discretization of the Navier-Stokes equations is described, followed by an exposition of the turbulence models that have been implemented in ComFLOW. Finally, the performance of the improved viscous flow modeling in ComFLOW for simulating free-surface water motion in a moonpool is investigated.

2 DISCRETIZATION OF THE NAVIER–STOKES EQUATIONS

An excellent model for incompressible (turbulent) fluid flow is provided by the Navier-Stokes equations. The continuity equation

$$\mathcal{M}\mathbf{u} = 0, \tag{1}$$

where $\mathcal{M} = \nabla\cdot$ is the divergence operator, describes conservation of mass. Conservation of momentum is given by

$$\frac{\partial \mathbf{u}}{\partial t} + \mathcal{C}(\mathbf{u},\mathbf{u}) + \mathcal{G}p - \nu\,\mathcal{D}\mathbf{u} = \mathbf{f}, \tag{2}$$

based on the convection operator $\mathcal{C}(\mathbf{u},\mathbf{v}) = \mathbf{u}\cdot\nabla\mathbf{v}$, the pressure gradient operator $\mathcal{G} = \nabla$, the diffusion operator $\mathcal{D}(\mathbf{u}) = \nabla\cdot\nabla\mathbf{u}$ and forcing term $\mathbf{f}$. The kinematic viscosity is denoted by ν.

2.1 Finite-Volume Discretization

The second-order finite-volume discretization of the continuity equation (1) at the 'new' time level $n+1$ is given by

$$M\mathbf{u}_h^{n+1} = -M^{\Gamma}\mathbf{u}_h^{n+1}, \tag{3}$$

where M acts on the internal of the domain and M^{Γ} acts on the boundaries of the domain.

Regarding the discretized momentum equation, convection and diffusion term are discretized explicitly in time. The discrete diffusion operator is denoted by D, while $C(\mathbf{u}_h)$ denotes the discrete convection operator. The pressure gradient is discretized at the new time level. In this exposition the forward Euler time integration will be used. Taking the

diagonal matrix Ω to denote the matrix containing the volumes of the control volumes, gives the discretized momentum equation as

$$\Omega \frac{\mathbf{u}_h^{n+1} - \mathbf{u}_h^n}{\Delta t} = -C(\mathbf{u}_h^n)\mathbf{u}_h^n + D\mathbf{u}_h^n - G\mathbf{p}_h^{n+1} - \mathbf{f}. \tag{4}$$

The discrete convection operator is skew-symmetric, i.e.

$$C(\mathbf{u}_h^n) + C(\mathbf{u}_h^n)^* = 0. \tag{5}$$

To make the discretization symmetry-preserving, the discrete gradient operator and the divergence operator are each other's negative transpose, i.e. $G = -M^*$, thus mimicking analytic symmetry $(\nabla\cdot) = (-\nabla)^*$, as in [9].

The solution of this equation is split in two steps. The auxiliary variable $\mathbf{R}_h$ is defined through the equation

$$\Omega \frac{\mathbf{R}_h - \mathbf{u}_h^n}{\Delta t} = -C(\mathbf{u}_h^n)\mathbf{u}_h^n + D\mathbf{u}_h^n - \mathbf{f}. \tag{6}$$

Imposing discrete mass conservation (3) on the new time level $(n+1)$ results in a linear system for the pressure:

$$\Delta t \; M\,\Omega^{-1}\,G\mathbf{p}_h^{n+1} = M\mathbf{R}_h + M^{\Gamma}\mathbf{u}_h^{n+1}. \tag{7}$$

This equation is often referred to as the discrete pressure Poisson equation, as it can be regarded to be a discretization of the equation $\mathcal{M}\mathcal{G}\mathbf{p}_h = \mathcal{M}\mathbf{u}_h$. Note, that here the separate parts $\mathcal{M}$ and $\mathcal{G}$, rather than the the composed operator $\mathcal{M}\mathcal{G}$ are being discretized here.

2.2 Stability of the Spatial Discretization

The symmetry-preserving spatial discretization of the Navier–Stokes equations outlined above assumes a second-order central discretization of the convective term. However, if the (mesh-)Reynolds number of the flow is large, the central discretization can become unstable and show point-to-point oscillations when large gradients or (geometrical) singularities are present in the flow. Typically, the central discretization is stabilized by adding artificial diffusion to the central scheme, resulting in a first-order or second-order upwind discretization.

The damping that is introduced by the artificial diffusion in upwind methods dissipates the energy of scales of motion that can still be represented on the computational grid. Rather than resorting to an excessively dissipative upwind scheme, a slightly modified version of the stabilization procedure proposed by Shyy *et al.* [4] has been implemented. The stabilization procedure consists of a post-processing filter operation acting on the momentum velocities. In these steps, linear momentum is redistributed if point-to-point extrema are detected in the velocity field. The filter is constructed such that it conserves linear momentum.

3 LARGE EDDY SIMULATION MODELS

In order to simulate the high Reynolds number turbulent flows that are associated to offshore applications, large eddy simulation (LES) modeling is necessary. Simply put, the aim of LES is to simulate those scales of motion that can be represented on the computational grid as accurately as possible through modeling of the interaction between resolved and subgrid scales.

In a turbulent flow, the production of small scales takes place through the non-linear convective term. The only mechanism that counteracts the production of small scales of motion is diffusion. The equilibrium between production (by convection) and dissipation (by diffusion) of small scales cannot be reached on the computational grid. This consideration gives rise to two modeling options: either restrict the production of subgrid scales or increase the dissipation of subgrid scales.

3.1 Invariants of the rate-of-strain tensor

Important information of the physics of turbulent flows is contained in the invariants of the rate of strain tensor $S(\mathbf{u}) = \frac{1}{2}\left((\nabla\mathbf{u})^T + \nabla\mathbf{u}\right)$. As is shown in [8], the rate of dissipation of the scales contained in a domain Ω_Δ of size Δ, can be expressed in terms of the second invariant $q(\mathbf{u})$ of $S(\mathbf{u})$ as

$$Q(\mathbf{u}) \equiv \int_{\Omega_\Delta} q(\mathbf{u})\, \mathrm{d}\Omega \equiv \int_{\Omega_\Delta} \frac{1}{2}\mathrm{tr}\, S^2(\mathbf{u})\, \mathrm{d}\Omega. \tag{8}$$

The third invariant, denoted by $r(\mathbf{u})$ can be integrated over the same domain to give

$$R(\mathbf{u}) \equiv \int_{\Omega_\Delta} r(\mathbf{u})\, \mathrm{d}\Omega \equiv \int_{\Omega_\Delta} -\frac{1}{3}\mathrm{tr}\, S^3(\mathbf{u})\, \mathrm{d}\Omega = \int_{\Omega_\Delta} -\det S(\mathbf{u})\, \mathrm{d}\Omega. \tag{9}$$

When positive, the quantity (9) gives a measure for the convective production of scales $< \Delta$. If negative, energy is transferred from subgrid-scale structures to the resolved scales. In order to separate the scales properly, a turbulence model should close the transfer of energy in either direction.

3.2 QR eddy-viscosity model

The analysis in [8] shows that in order to arrive at an appropriate eddy-viscosity model, we evaluate the eddy-viscosity in terms of the invariants as

$$\nu_{\mathrm{eddy}} = \frac{3}{2}\frac{1}{\lambda_\Delta}\frac{|R(\mathbf{u})|}{Q(\mathbf{u})}, \tag{10}$$

where λ_Δ is the eigenvalue of the discrete diffusive operator corresponding to the scale Δ. Taking Δ identical to the grid size, this eigenvalue is a measure for the dissipation of the smallest *resolvable* scales. We will refer to this model as the QR model.

Note that the classical Smagorinsky turbulence model (see e.g. [3]) is formulated in terms of the invariant Q only, and dissipates energy also on well-resolved (even laminar) scales in the flow.

3.3 Regularization Modeling

In order not to interfere with the subtle energetic balance between the convection and diffusion in a turbulent flow on resolved scales, it is important to preserve the symmetries of the Navier-Stokes equations on a discrete level [9]. A symmetry-preserving regularization of the convective term smooths the original convective term while preserving its skew-symmetry. The smoothing takes place through a filter operation $\mathbf{u}_h \mapsto \overline{\mathbf{u}_h}$.

Verstappen [7] applies the filter to the convective term, which yields a family of symmetry-preserving regularization models. The discrete convective term is denoted by $C(\mathbf{u}_h) \cdot \mathbf{u}_h$. The second-order (in terms of the filter length) accurate regularization model from this family is given by

$$C_2(\mathbf{u}_h, \mathbf{u}_h) = \overline{C(\overline{\mathbf{u}_h}) \cdot \overline{\mathbf{u}_h}}. \tag{11}$$

Selfadjointness of the filter ensures the skew-symmetry of the original convective term.

The length scale over which the filter smooths the signal will depend on the local flow physics. The analysis in [5] shows that an expression for damping of the convective production of structures beyond length scale Δ can be derived. The damping factor, that we will denote by f_2, is a functional of the (local) filter length α, i.e. $f_2 = f_2(\alpha(\mathbf{u}))$. Balancing the convective production of subgrid scales and the natural diffusive dissipation gives

$$f_2(\alpha)\, \frac{|R(\mathbf{u})|}{Q(\mathbf{u})} = \nu |\lambda_\Delta|, \tag{12}$$

from which the filter length can be determined. The relation with (10) is evident.

3.4 A blended model

Another model that we discern is the blended model, in which both the QR eddy viscosity model and the regularization model play a role, depending on the physics of the flow. The transfer of energy from resolved to subgrid scales (i.e. (9) is positive) is modeled by the QR eddy-viscosity model. The backscatter of energy from subgrid scales to resolved scales (i.e. (9) is negative) is prevented by the regularization model.

The mixture of these models allows for a complete separation of resolved and subgrid scales. Only if the energy is transferred to smaller scales of motion, the kinetic energy is dissipated from the resolved flow structures. The model is closed for backscatter by the regularization of the nonlinear convective interaction between subgrid and resolved scales.

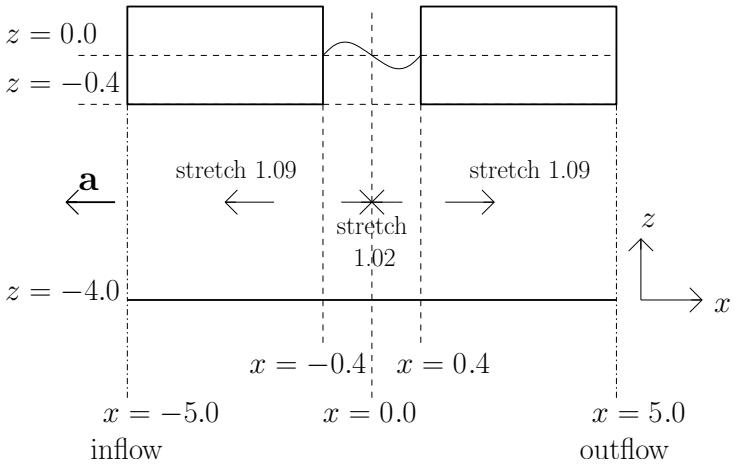


Figure 1: Simulation domain for the moonpool simulations. At the moonpool walls and at the (initial) free-surface position, the grid spacing in x and z direction is 0.01 m., indicated by the dashed line. The grid is stretched with a factor 1.09 towards the inflow and outflow boundaries and towards the bottom of the domain. The grid enclosed by the moonpool edges and the free-surface is slightly stretched (with a factor of 1.02) towards the center of the moonpool.

3.5 The turbulent boundary layer

From a computational point of view it is highly undesirable to refine the grid to the level at which the boundary layer can be resolved. In order to account for the influence of the turbulent boundary layer on the effective wall-shear stress that the outer flow experiences, the Werner-Wengle model is applied [10].

4 SIMULATION OF MOONPOOL WATER MOTION

The simulation of free-surface dynamics in moonpools is an example of an application where possibly violent free-surface motion is coupled to viscous flow details. A realistic simulation of free-surface motion is strongly dependent on the correct prediction of the vortex formation in the moonpool. The combination of coarse grids and upwind discretization techniques dissipate the perturbations that lead to the characteristic roll-up of the shear layer, thus preventing vortex formation at the edges of the moonpool.

In order to illustrate the performance of the stabilized central discretization, the first results of the simulation of water motion in a moonpool (in calm water) will be presented. In the simulations, the moonpool and the computational grid that is fixed to the moonpool geometry are accelerated to a constant speed.

4.1 Setup

In order to model moonpool dynamics in calm water (i.e. in the absence of waves) not the entire ship will be modeled. Instead, the moonpool is modeled as in figure 1. The domain has dimensions (in m.) $[-5.0, 6.0] \times [-0.5, 0.5] \times [-4.0, 0.5]$, and the stretched grid has dimensions $228 \times 10 \times 184$. As the setup of the problem is two-dimensional and most variation is expected to take place in the x-z plane, we hope that 10 uniformly spaced grid points in the are y direction are enough to capture the essential physics. The smallest grid spacing is 0.01 m. and the grid lines to which this spacing applies are indicated by the dashed lines in figure 1.

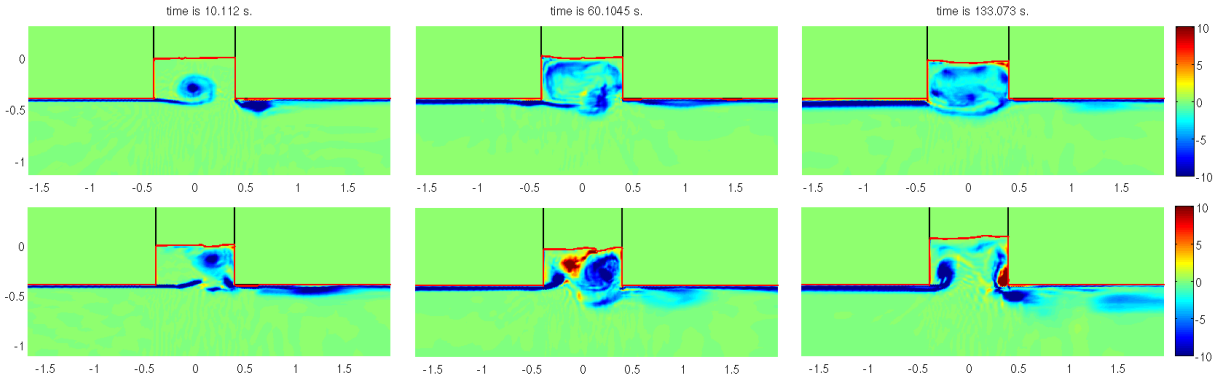


Figure 2: Development of vorticity in time (*from left to right:* 10 s, 60 s, and 133 s) for a final speed (after acceleration) of 0.7 m/s (*top*) and 1.0 m/s (*down*).

In rest, the flat free-surface ($z = 0$) is elevated 0.4 m. above the submerged bottom of the object, i.e. the *draft* is taken to be 0.4 m. The width of the moonpool is 0.8 m. in stream-wise (x) direction and 1.0 m. in cross-stream (y) direction.

Rather than moving the moonpool through the grid or to prescribe the inflow velocity, the moonpool and the grid fixed to the geometry are accelerated from rest. The acceleration is modeled through the forcing term in the Navier-Stokes equations. No-slip boundary conditions are applied at all the moonpool walls.

4.2 Results and discussion

The setup described above is able to capture the essential features of the water motion in the moonpool. Three stages of water motion in the moonpool are illustrated by the vorticity plots that are shown in figure 2. The moonpool is accelerated to two constant speeds: 0.7 m/s and 1.0 m/s.

In the first stage, during acceleration of the moonpool a big vortex is formed at the edge and shear layer roll-up is observed. The vortex travels upward in the moonpool and impinges on the free surface. For the lower speed (0.7 m/s) the vortices that are formed at the edge circulate through the moonpool, deforming the free-surface and inducing a small-amplitude oscillation of the water column (the piston mode).

For the higher speed (1.0 m/s), the elevation of the free-surface is more dramatic, which can clearly be seen from the oscillation of the water height in figure 3. The synchronization of vortex formation and the oscillation of the water column lead to resonant (piston mode) motion of water in moonpool. Moreover, a bore formed by the impinging vortex on the right-side wall of the moonpool is observed to travel back and forth between the right and left wall.

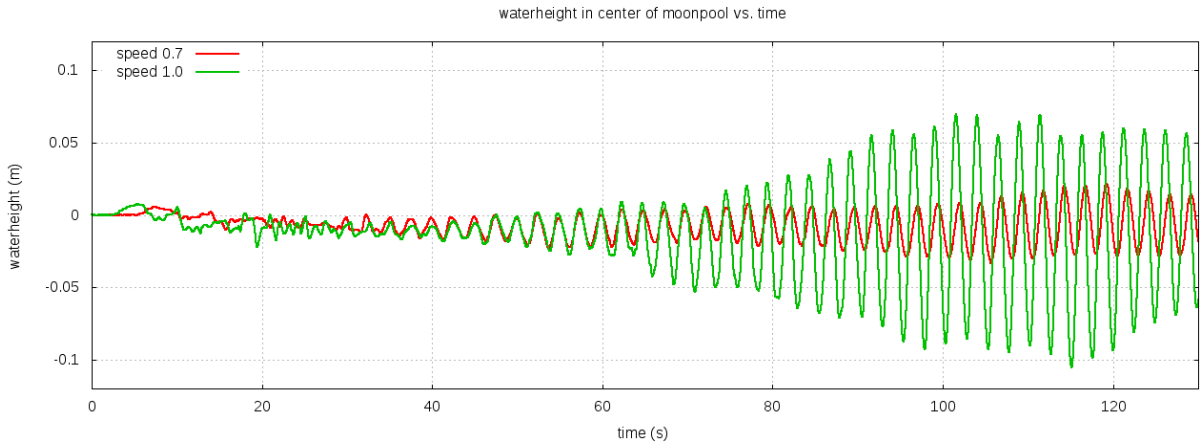


Figure 3: Water height as a function of time for the two final speeds (after acceleration). At a time of about 63 s, the water motion in the moonpool of speed 1.0 m/s resonance behavior is observed.

5 CONCLUSIONS

The free-surface water motion in a moonpool has been simulated with improved viscous flow modeling in ComFLOW. In order to simulate detailed viscous flow effects, it is necessary to employ a symmetry-preserving second-order central discretization of the convective term. As the central discretization is unstable in regions with high velocity gradients, the term is stabilized through the removal of the point-to-point oscillation that might appear around the large gradients. Simulations of the moonpool with the stabilized discrete convective term show that ComFLOW is able to simulate some essential features of water motion in the moonpool. The results are a clear improvement of the first-order (B2) and second-order (B3) upwind discretization which result in a steady state solution, with a stationary recirculation zone present in the moonpool (see the discussion in [1]).

These promising first results ask for a study of the behavior of the solution of the moonpool simulation upon grid refinement and upon the use of different turbulence models that have been described in this paper. A comparison with experimental data will also be possible in the near future.

Finally, the simulation of moonpool water dynamics in the presence of waves will be a subject of study in the near future.

REFERENCES

[1] Gaillarde G. and A. Cotteleer. Water motion in moonpools empirical and theoretical approach. Technical report, Maritime Research Institute Netherlands (MARIN), HMC Heerema, 2005.

[2] K.M.T. Kleefsman, G. Fekken, A.E.P. Veldman, B. Iwanowski, and B. Buchner. A volume-of-fluid based simulation method for wave impact problems. *Journal of Computational Physics*, 206(1):363–393, 2005.

[3] P. Sagaut. *Large Eddy Simulation for Incompressible Flows*. Springer–Verlag, 2001.

[4] W. Shyy, M.-H. Chen, R. Mittal, and H.S. Udaykumar. On the suppression of numerical oscillations using a non-linear filter. *Journal of Computational Physics*, 102(1):49 – 62, 1992.

[5] F.X. Trias and R.W.C.P. Verstappen. On the construction of discrete filters for symmetry-preserving regularization models. *Computers & Fluids*, 40(1):139 – 148, 2011.

[6] A.E.P. Veldman, R. Luppes, T. Bunnik, R.H.M. Huijsmans, B. Duz, B. Iwanowski, R. Wemmenhove, M.J.A. Borsboom, P.R. Wellens, H.J.L. van der Heiden, and P. van der Plas. Extreme wave impact on offshore platforms and coastal constructions. In *30th Conf. on Ocean, Offshore and Arctic Eng. OMAE2011*, Rotterdam, The Netherlands, June 19-24, 2011 (paper OMAE2011-49488).

[7] R.W.C.P. Verstappen. On restraining the production of small scales of motion in a turbulent channel flow. *Computers & Fluids*, 37(7):887–897, 2008.

[8] R.W.C.P. Verstappen. When does eddy viscosity damp subfilter scales sufficiently? *Journal of Scientific Computing*, 49(1):94–110, 2011.

[9] R.W.C.P. Verstappen and A.E.P Veldman. Symmetry-preserving discretization of turbulent flow. *Computers & Fluids*, 187:343–368, 2003.

[10] H. Werner and H. Wengle. Large-eddy simulation of turbulent flow over and around a cube in a plate channel. In *8th Symposium on Turbulent Shear Flows*, pages 155–168. Springer–Verlag, 1991.

V International Conference on Computational Methods in Marine Engineering
MARINE 2013
B. Brinkmann and P. Wriggers (Eds)

ADVANCES IN THE DEVELOPMENT OF A NEW CARTESIAN EXPLICIT SOLVER FOR HYDRODYNAMICS

P. BIGAY[†,*], C. LEROY[†], G. OGER[†], P.-M. GUILCHER[*] AND D. LE TOUZE [†]

[†] L'UNAM Université, Ecole Centrale Nantes, LHEEA lab., ECN / CNRS
1 Rue de la Noë , 44000 Nantes , France

[*] HydrOcean
1 Rue de la Noë CS 32122 44321 Nantes Cedex 3, France
www.hydrocean.fr

Key words: Explicit, Cartesian, Hydrodynamics, Weakly-compressible, Viscosity

Abstract. In order to efficiently address complex problems in hydrodynamics, the advances in the development of a new method are presented here. This new CFD solver aims at obtaining a good compromise in terms of accuracy, computational efficiency, and easy handling of complex geometries. The chosen method is an Explicit Cartesian Finite Volume method for Hydrodynamics (ECFVH) based on a compressible (hyperbolic) solver, with an embedded method for interfaces and geometry handling. The solver's explicit nature is obtained through a weakly-compressible approach chosen to simulate nearly-incompressible flows. The explicit cell-centered resolution allows for an efficient solving of very large simulations together with a straightforward handling of multi-physics. The use of an embedded Cartesian grid ensures accuracy and efficiency, but also implies the need for a specific treatment of complex solid geometries, such as the cut-cell method in the fixed or moving body frame. Robustness of the cut-cell method is ensured by specific procedures to circumvent small cell volume numerical errors. A characteristic flux method for solving the hyperbolic part of the Navier-Stokes equations is used and introduces numerical viscosity. This viscosity is evaluated prior to modeling viscous and turbulent effects. In a first approach presented here viscous effects are computed via a finite difference Laplacian operator introduced as a source term. This solver is validated on 2-D test cases.

1 INTRODUCTION

CFD has become an essential tool for engineers and tends to be more and more affordable in terms of computational costs or available resources. Most solvers in the field of hydrodynamics are implicit under incompressible flow assumption, for which large grid sizes can induce conditioning problems, parallelization difficulties, and nonlinear iterations increase on truly non-stationary problems. Thus, many physical problems such as flows around ships with air entrapment in the bow jet, presence of bubbles in the wake, sea-keeping of boats with complex moving appendages (thrusters...) cannot yet be easily solved. The explicit nature of the proposed method conversely allows for rather straightforward parallelization, robustness and multiphysic simulation handling (multiphase flows, fluid structure). The Cartesian nature of this method allows for a fast and accurate solver.

In this method upwinding is introduced. This, in turn, results in some numerical diffusion.

Prior to modeling physical diffusion and turbulence, a particular care is paid to the assessment of this numerical diffusion, especially according to slope limiters used in the MUSCL scheme of the hyperbolic solution. Then viscous effects are addressed. In the first part of this paper, the compressible core solver is presented. Validation of this solver is achieved through academic test cases and inviscid flow around a cylinder. The second part mainly deals with explicit viscosity modeling. A numerical viscosity study is presented using the Taylor-Green Vortex test case. Finally the explicit viscous solver is validated on classical 2-D test cases such as the Poiseuille flow and the lid-driven cavity flow.

2 ECFVH

2.1 The Navier-Stokes Equations

This method solves the compressible Navier-Stokes equations for viscous compressible flows:

$$\overrightarrow{W_t} + \overrightarrow{\varphi(W)_{x,y,z}} = \overrightarrow{Visc} \tag{1}$$

To close the system and relate pressure and density, we use the Tait isentropic equation of state, thus decoupling the energy equation. This equation is particularly adapted for modeling liquids::

$$P - P_0 = \frac{\rho_0 c_0^2}{\gamma}\left[\left(\frac{\rho}{\rho_0}\right)^{\gamma} - 1\right] \tag{2}$$

with the polytrophic constant γ, a reference pressure P0, the nominal density ρ_0 and the nominal speed of sound c_0.

This equation can be written in the following conservative form:

$$\begin{pmatrix}\rho\\ \rho u\\ \rho v\\ \rho w\end{pmatrix}_t + \begin{pmatrix}\rho u\\ \rho u^2+P\\ \rho uv\\ \rho uw\end{pmatrix}_x + \begin{pmatrix}\rho v\\ \rho vu\\ \rho v^2+P\\ \rho vw\end{pmatrix}_y + \begin{pmatrix}\rho w\\ \rho wu\\ \rho wv\\ \rho w^2+P\end{pmatrix}_z = \overrightarrow{Visc} \tag{3}$$

The viscosity terms in Navier-Stokes equations can be represented as viscous stress tensor components:

$$\overrightarrow{Visc} = \begin{pmatrix} 0 \\ \begin{pmatrix}\tau_{xx}\\ \tau_{xy}\\ \tau_{xz}\end{pmatrix}_x + \begin{pmatrix}\tau_{xy}\\ \tau_{yy}\\ \tau_{yz}\end{pmatrix}_y + \begin{pmatrix}\tau_{xz}\\ \tau_{yz}\\ \tau_{zz}\end{pmatrix}_z \end{pmatrix} \tag{4}$$

It can also be seen as a source term in a Laplacian operator manner as presented in this paper by assuming that compressibility effects in viscosity are negligible due to the weakly-compressible feature of the model.

$$F = \mu \begin{pmatrix} 0 \\ \Delta u \\ \Delta v \\ \Delta w \end{pmatrix} \tag{5}$$

For solving both hyperbolic and elliptic parts, two distinct procedures are setup and described in the next section

2.2 Finite volume characteristic flux scheme

Our solver is based on Finite Volume method, chosen to ensure conservativeness of the method. In this method, the unknowns are located at the center of cells.

To solve the Euler equations a new method originally developed by Ghidaglia et al. [1] in 1996 is used here. This method computes the fluxes needed at each edge by rewriting the equations with the flux Jacobian matrix and using its hyperbolic properties. The solution is then obtained via a projection on the solution in the characteristic base. These fluxes are not expressed in terms of conservative variables as in the Godunov scheme but directly in physical fluxes. For more details, the reader can refer to [2][4][5]. The solution flux is finally expressed as follows:

$$\phi_{Solution} = \left(\frac{F(\overrightarrow{w_L}) + F(\overrightarrow{w_R})}{2} + sign(\overline{\overline{J}}(\overrightarrow{w_{\text{int}}}, \vec{n})) \frac{F(\overrightarrow{w_L}) - F(\overrightarrow{w_R})}{2} \right) . \vec{n} \tag{6}$$

with w_R and w_L the conservative variables vector of left and right cells respectively, w_{int} $\overrightarrow{w_{\text{int}}}$ the value at the interface of the two cells and the Jacobian matrix defined as:

$\overline{\overline{J}} = \frac{\partial \Psi(W,\vec{n})}{\partial W}$. $sign(\overline{\overline{J}}(\overrightarrow{w_{\text{int}}}, \vec{n}))$ is a special matrix constructed with the reduction elements of the Jacobian. This method is an alternative to Roe schemes, HLLE and AUSM+ schemes. This method is general and applicable to any hyperbolic system, easy to implement and efficient in terms of computational costs. The explicit core of the method has been validated on classical test cases such as one and two dimensional shock tubes, backward facing step [2][4][5].

The hyperbolic solving method is based on an upwind method that uses both cell center and face conservative values. To enhance the method and evaluate the latter variables the classical MUSCL scheme [11] is used. Left and right interface values are computed using right and left cell gradients, together with a flux limiting procedure ensuring the Total Variation Diminishing property (TVD) and the non-inversion of the Riemann problem. Flux limiters used have a great deal of importance on the quality and diffusion property of the schemes. Limiters can have a diffusive and/or a dispersive behavior that needs to be evaluated regarding the targeted application. The reconstruction procedure and a few classical limiters are presented in the next page :

$$\begin{cases} u^{D}_{i+\frac{1}{2}} = u_{i+1} - \frac{1}{2}\Theta(\kappa_{i+1})\nabla^{D}u_{i+1} \\ u^{G}_{i+\frac{1}{2}} = u_{i} + \frac{1}{2}\Theta(\kappa_{i})\nabla^{D}u_{i} \\ u^{D}_{i-\frac{1}{2}} = u_{i} - \frac{1}{2}\Theta(\kappa_{i})\nabla^{D}u_{i} \\ u^{G}_{i-\frac{1}{2}} = u_{i-1} + \frac{1}{2}\Theta(\kappa_{i-1})\nabla^{D}u_{i-1} \end{cases} \qquad \kappa_i = \frac{\nabla^{G}u_i}{\nabla^{D}u_i} \tag{7}$$

Minmod (Roe, 1986)	$\Theta(\kappa_i) = Max[0, Min(1, \kappa_i)];$ $\lim_{\kappa_i \to \infty} \Theta(\kappa_i) = 1$
Superbee (Roe, 1986)	$\Theta(\kappa_i) = Max[0, Min(1, 2\kappa_i), Min(2, \kappa_i)];$ $\lim_{\kappa_i \to \infty} \Theta(\kappa_i) = 2$
Van Leer (Van Leer, 1974)	$\Theta(\kappa_i) = (\kappa_i + \lvert\kappa_i\rvert)/(1 + \lvert\kappa_i\rvert);$ $\lim_{\kappa_i \to \infty} \Theta(\kappa_i) = 2$

Table 1. Some of the classical limiters used in the MUSCL scheme.

2.3 Time stepping

Temporal integration stability of the scheme for solving the Euler equations is ensured by respecting the following Courant-Friedrichs-Lewy (CFL) condition based on the area Γ_{int} of the interface between two adjacent cells.

$$dt \leq \min_i \left(\frac{Vol_i}{\Gamma_{\text{int}} \max_k \left| (u_i + c)_k \right|} \right) \tag{8}$$

2.4 Weakly-compressible approach

The specificity of this method resides on the use of a weakly-compressible approach. We indeed use a full compressible model, time step is thus determined via the CFL stability criteria. This criterion leads to very small time steps for near boundary cells, increasing the overall computational costs of the simulations. In order to maximize the time steps and to conserve the physical behavior, the sound speed c_0 is chosen to be about 10 times the maximum value of velocity in the simulations. Simulations are therefore performed at Mach numbers $Ma \approx 0.1$. Under these assumption, it has been shown [6] that the compressible solution can be seen as the superimposition of the incompressible solution and an acoustic solution. Purely compressible effects are negligible ($O(Ma^2)$). Note that such approach is widely used in the SPH community for instance [3].

3 MESHING

Flow simulation around moving complex bodies is a challenging problem, especially when a fixed Cartesian grid is used to discretize the fluid. Local grid modification should be performed on the body surface, without significant increase of the computational cost. Our model is based on the use of cut-cells, together with cell merging procedures to avoid the well-known "small cell" problems, so that reasonable time steps can be preserved [2][4][5]. Cartesian meshing, cut-cell and cell merging techniques therefore allow for an automatic generation of computational meshes (given a surface mesh). An adaptive mesh refinement parallel model will be implemented in the following development steps of the model in order to speed up the computations and to allow massive simulations.

4 INVISCID VALIDATION OF FLOW AROUND A CYLINDER

To validate the hyperbolic solver and the geometry handling, we propose here to study an inviscid flow past a fixed cylinder, with an imposed incident velocity of 1 m/s .This cylinder is located in the center of a 20 meters long infinite tank. As a second step of this study, the pressure solution obtained on this fixed cylinder is then compared to the case of a cylinder moving with an imposed velocity of 1 m/s in a zero velocity flow field. Such conditions are equivalent, so that identical solutions can be expected. In both cases we use potential flow result as an analytical solution. The Van Leer limiter is used here and the results are shown for several grid sizes to show the convergence.

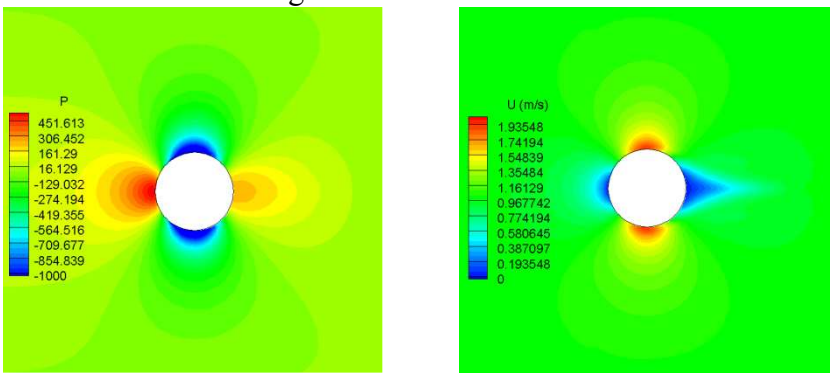


Figure 1. Pressure and velocity fields of the fluid flow around a cylinder.

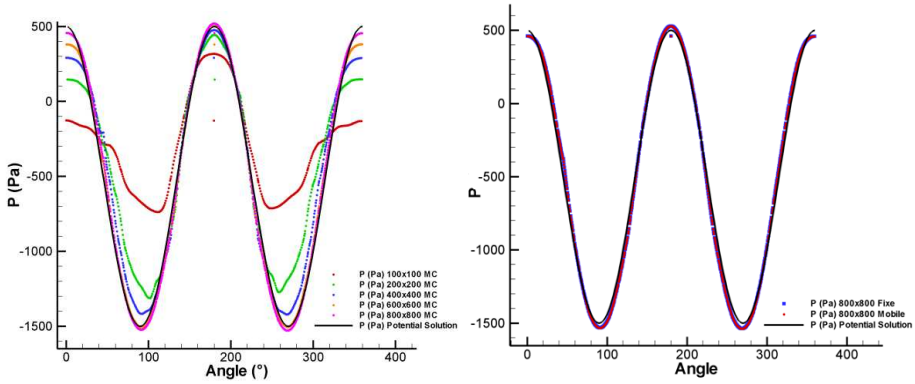


Figure 2. *Local steady pressure around the cylinder for different grid sizes with Van Leer limiter. (left) Local pressure comparison between fixed and moving cylinder(right).*

Previous figures validate the inviscid solver with fixed and moving geometries. Indeed given proper discretizations the pressure profile matches the theoretical potential solution. Fixed and moving solutions match very well thus validating the embedded boundary treatment.

5 VISCOSITY MODELING

5.1 Evaluation of the Numerical Viscosity

Solving the Euler equations requires the use of upwind methods. However these methods are known to be diffusive. In order to properly simulate viscous flows one needs to ensure that numerical viscosity stays negligible compared to physical viscosity. A study is then performed to evaluate this viscosity according to several important factors: discretization, use of MUSCL scheme and flux limiters, and the influence of sound speed.

The use of MUSCL scheme allows to reach second order accuracy for the hyperbolic part. Nevertheless it requires the use of limiters. TVD limiters are very numerous, they are more or less dispersive (overshoots, oscillations in shocks) and diffusive. One of the aims of this study is then to select the limiter with the best trade-off between diffusion and dispersion. The process of selection had a first step (not presented here) where its behavior was studied on 1-D shock tubes. Some limiters (e.g. Superbee) appear to be too dispersive and were not studied in the following test case. Among the tested limiters, only the Minmod and Van Leer limiters are shown in this paper.

To evaluate this numerical viscosity, the Taylor-Green Vortex test case is chosen [9]. This 2-D case consists in four eddies occurring in a square shaped domain of size L. Periodic boundary conditions are imposed at each side of the domain. The initialization is achieved as follows:

$$\begin{cases} u(x,y,t) = U_0 e^{\frac{-8\pi^2 \nu t}{L^2}} \sin\left(2\pi\frac{x}{L}\right)\cos\left(2\pi\frac{y}{L}\right) \\ v(x,y,t) = -U_0 e^{\frac{-8\pi^2 \nu t}{L^2}} \cos\left(2\pi\frac{x}{L}\right)\sin\left(2\pi\frac{y}{L}\right) \\ p(x,y,t) = \frac{\rho U_0^2}{4} e^{\frac{-16\pi^2 \nu t}{L^2}} \left[\cos\left(4\pi\frac{x}{L}\right)+\cos\left(4\pi\frac{y}{L}\right)\right] \\ U_0 = 1m/s, \quad L = 1m, \quad c_0 = 10m/s, \quad \rho_0 = 1000kg/m^3 \end{cases} \tag{9}$$

The initial pressure and velocity fields are presented in the following page.

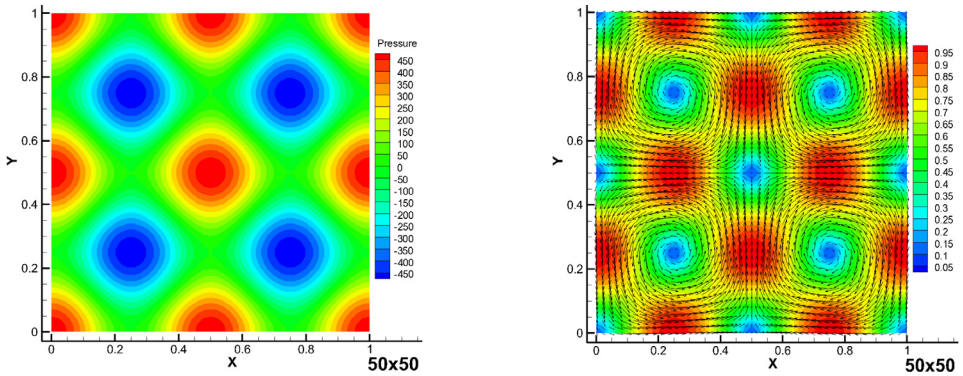


Figure 3. Pressure and Velocity fields of Taylor-Green Vortex test case.

In absence of physical viscosity, the solution is steady. In our case since the method exhibits numerical viscosity, the velocities of eddies decrease. Then by measuring the local velocity decay, it is possible to measure an equivalent numerical kinetic viscosity. Figure 4 shows the velocity decay in time of a point of the flow for different grid sizes.

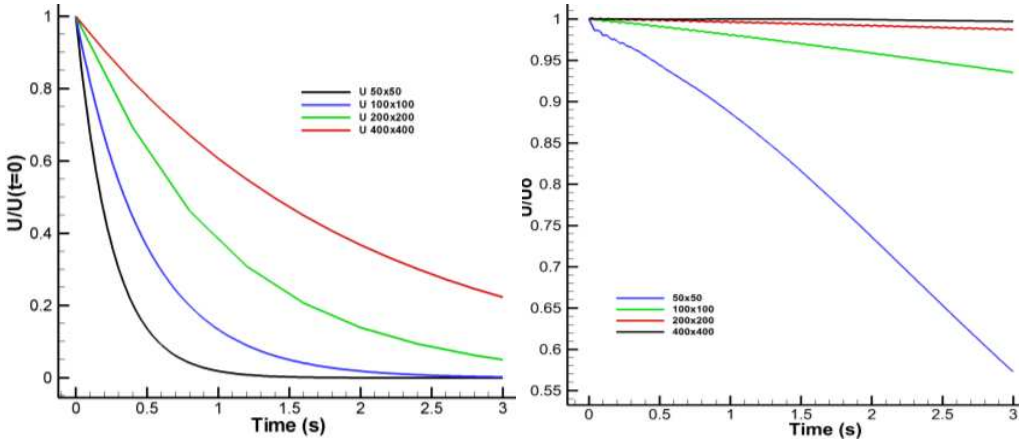


Figure 4. Local velocity of a point for different grid sizes without (left) and with (right) the MUSCL scheme.

As expected the method's upwindind leads to numerical dissipation. Without the MUSCL scheme numerical diffusion is much too important to enable simulating any physical viscosity except for the use of extremely fine grids (in about 3s the eddies are fully dissipated). With the MUSCL scheme, the velocity decay is much less important and will not mask physical viscous effects. To find the better compromise in the MUSCL scheme parametrization, limiters have to be tested in order to achieve the best diffusion/dispersion trade-off. Other than the use of the MUSCL scheme, grid discretization plays an important role: the finer the grids are the less dissipation there is.

The figure below shows the equivalent viscosity without MUSCL, and with MUSCL (Minmod and VanLeer Limiters). As expected, the level of numerical viscosity without MUSCL is too important and would hide all physical viscous effects.

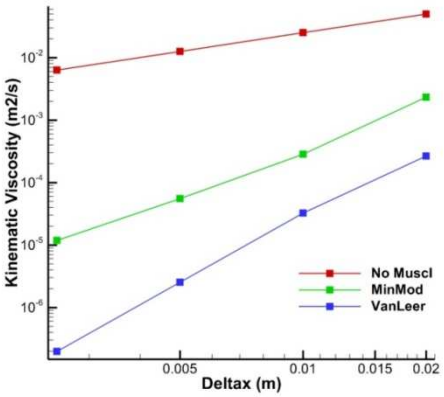


Figure 5. Equivalent kinematic viscosity computed for several discretizations and schemes

Different limiters have been tested, and among them the ones presented in Table 1. The results with the most interesting limiters are presented here. The Minmod limiter is a dissipative-only limiter and Van Leer's one is less diffusive but exhibits a dispersive behavior. According to all the tests performed the latter limiter appears to be the one presenting the best compromise in terms of diffusion and dispersion. A refined grid seems necessary with the Minmod limiter. Results with the Van Leer limiter are better and this limiter is finally adopted in our following simulations. As a conclusion, numerical viscosity will not be an issue for simulating viscous and turbulent flows, especially with turbulent viscosity of an order of magnitude of about 0.001 m^2/s.

5.2 Simulation of physical viscosity

As shown in equations (4) and (5), the elliptic part of Navier Stokes can be computed in two different manners: as a source term or as a viscous flux. In most hydrodynamic CFD codes, viscous terms are computed in an implicit manner. Our choice is to conserve a fully explicit scheme, so that an explicit viscous solver had to be developed.

In this first approach, the source term approach is adopted. To compute viscous effects, second spatial derivatives of velocities are computed at the cell centers. For this Finite Difference schemes, here second order or third order central differences are used (stencil on 3 or 5 points). Central differencing for elliptic schemes is always stable. This solution is robust and quite efficient.

Using this explicit viscous solver requires to respect another stability condition on the time step superimposed to the acoustic one, as:

$$dt \leq \min_i \left(\frac{Vol_i^{\,2}}{\Gamma_{\text{int}}^{\,2} \nu} \right) \tag{10}$$

5.3 Explicit viscous solver validation for low Reynolds number flows

Two different laminar test cases are used in this section to validate this explicit viscous solver: a periodic Poiseuille flow and a lid driven-cavity test cases.

5.3.1 Poiseuille flow

The fluid domain retained for this validation is a square shaped domain of size L = 1 m. The fluid is initialized in the whole domain with a uniform velocity of 1m/s. A longitudinal pressure gradient is imposed as a source term on the flow, while periodic boundary conditions are imposed on the left and right side of the domain to allow the fluid motion in the x direction. No-slip boundary conditions are imposed at top and bottom walls. The theoretical velocity profile expected is parabolic and should write:

$$v(y) = \frac{L^2}{8\eta}\frac{dP}{dx}\left(1 - \frac{4y^2}{L^2}\right) \tag{11}$$

Several simulations for different Reynolds numbers are performed and perfectly match the analytical solution. Here are the results for a 50x50 grid and Re = 1.

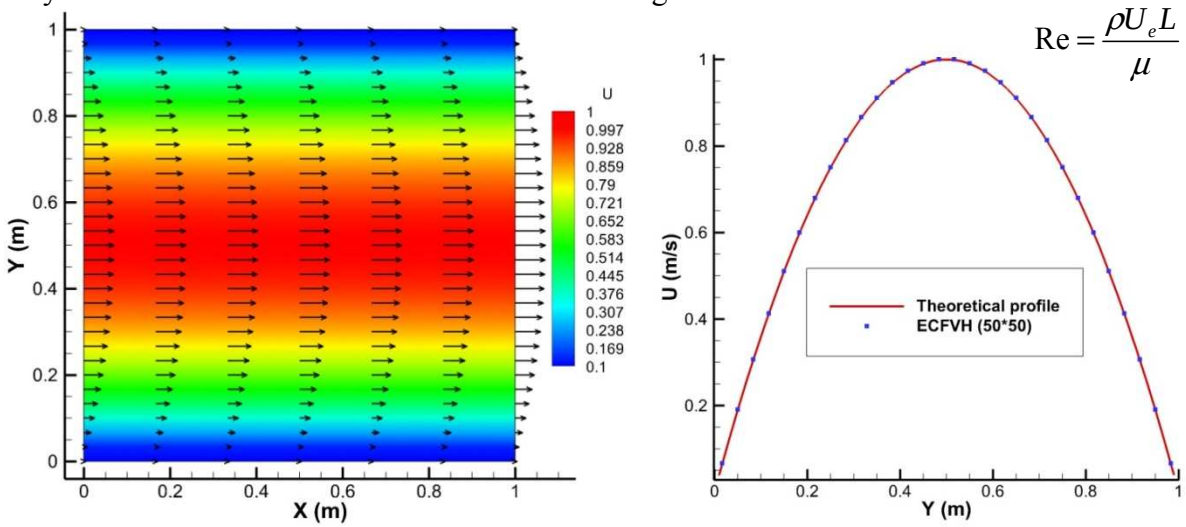


Figure 7. Poiseuille flow velocity field and velocity profile compared to theoretical profile.

5.3.2 Lid-Driven cavity flow

This test case is a classical incompressible test case and has been extensively studied, in particular by Ghia et al. [7]. In this test case, all boundaries are no-slip walls, and the fluid is set into motion by the moving upper wall. Results are available from Re=100 Re=10000. The validation consists in comparing streamlines, velocity profiles at location x=0.5 m and y=0.5 m, and the positions and dimensions of primary and secondary vortexes appearing in the corners.

Simulations have been carried out from Re=100 to Re=3200 for which the flow is still laminar. The velocity of the upper wall is imposed as 1 m/s, and the Reynolds number is varied via the value of the fluid viscosity. All these simulations show very good agreement to

the results available in [7]. In this paper, the results are compared to the reference for *Re*=100 for a grid size of 100x100.

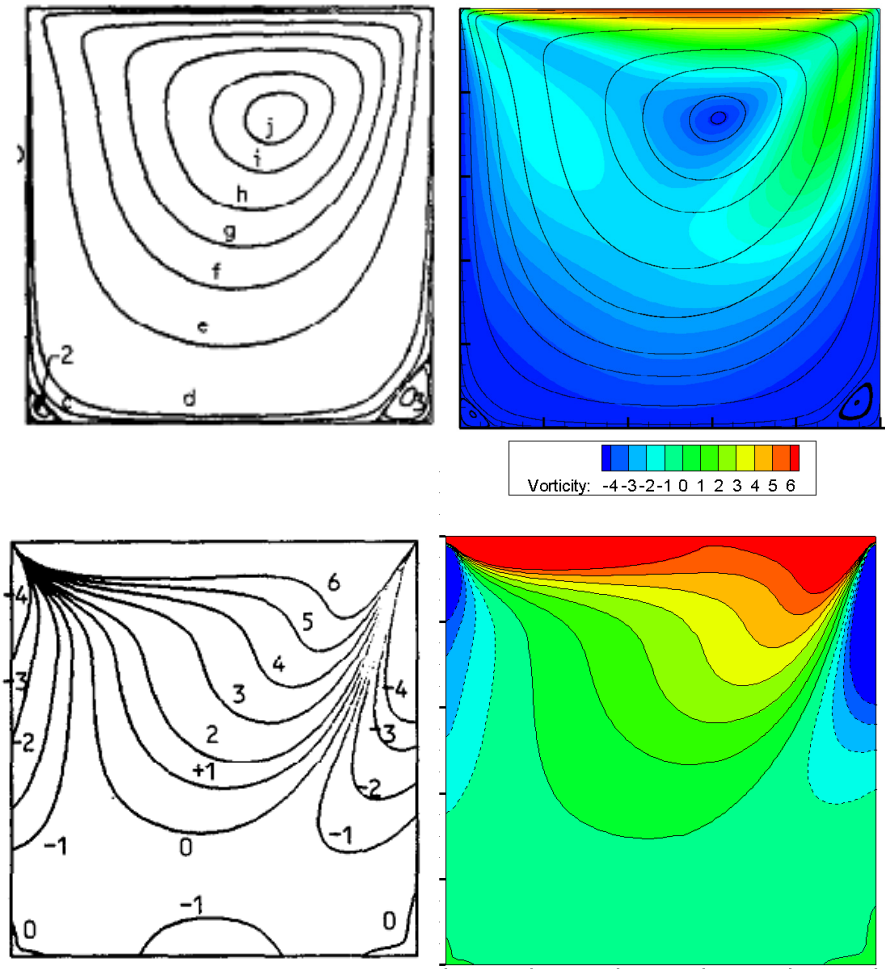


Figure 8. Lid-driven Cavity *Re*=100, Comparison of results with Ghia et al results , Velocity fields and streamlines , Vorticity fields .

The *Re*=100 lid-driven cavity results presented in figure 8 show an excellent agreement with the results from Ghia et al.. The relative errors in positions and dimensions of the vortexes are lower than 2%. Velocity profiles also compare very accurately with the reference.

6 CONCLUSION

A solver based on the Finite Volume method and using upwinded characteristic fluxes has been developed for hydrodynamic flows. This explicit solver relies on a fixed non-conform Cartesian grid into which bodies can freely move thanks to a dedicated cut-cell technique. Simulation of viscous effects has been addressed, namely by studying the influence of numerical viscosity. First validations have been presented on academic test cases, showing very encouraging results. Nevertheless, this method is not straightforward for complex

geometries. Another explicit viscous solver based on viscous fluxes is under development, and methods from [8] and [10] will be investigated. Then higher Reynolds numbers and turbulent simulations will be addressed by means of Large Eddy Simulation (LES). Further developments will also deal with Adaptive Mesh Refinement (AMR) in a parallel framework.

REFERENCES

[1] J.-M. Ghidaglia, A. Kumbaro, G. Le Coq, Une méthode volumes finis à flux caractéristiques pour la résolution numérique des systèmes hyperboliques de lois de conservation, C.R. Acad. Sc. Paris, Vol. 322, pp. 981–988, 1996.

[2] C. Leroy, D. Le Touzé, B. Alessandrini, Development of a cartesian-grid finite-volume characteristic flux model for marine applications, Materials Science and Engineering, Vol. 10, 2010.

[3] D. Le Touzé, G. Oger, B. Alessandrini, Smoothed Particle Hydrodynamics simulation of fast ship flows, Proceedings of the 27th Symposium on Naval Hydrodynamics, Seoul, Korea, 2008.

[4] C. Leroy, P. Bigay, G. Oger, Preliminary developments of a two-fluid Cartesian-Grid Finite-Volume Characteristic Flux model for marine applications. Proceedings of WCCM 2012.

[5] C. Leroy, Développement d'une méthode Volumes Finis à Flux Caractéristiques pour la simulation d'écoulements en hydrodynamique. Phd thesis , 2012.

[6] G. Capdeville, Modélisation numérique d'écoulements compressibles, partie I et II, Polycopié de cours de l'Ecole Centrale de Nantes, 142-149, 2006.

[7] U. Ghia, K.N. Ghia, C.T. Shin, « High-Re Solutions for Incompressible Flow Using the Navier-Stokes Equations and a Multigrid Method », Journal of Computational Physics, vol 48, p. 387-411, 1982..

[8] W.J Coirier, An Adaptively-Refined, Cartesian, Cell-Based Scheme for the Euler and Navier-Stokes Equations, Phd thesis, University of Michigan, 1994.

[9] M. de Leffe, Modélisation d'écoulements visqueux par méthode SPH en vue d'application à l'hydrodynamique navale, Phd thesis, 2011.

[10] M. Berger, M.J. Aftosmis, S. Allmaras, Progress towards a Cartesian cut-cell method for viscous compressible flow, AIAA 2012-1301, 2012.

[11] B.Van Leer, Towards the ultimate conservative difference scheme V. A second order sequel to Godunov's methods, Journal of Computational Physics, Vol. 39, pp. 101-136, 1979.

V International Conference on Computational Methods in Marine Engineering
MARINE 2013
B. Brinkmann and P. Wriggers (Eds)

A Hybrid Particle-Grid Scheme for Computing Hydroelastic Behaviors Caused by Slamming

H. MUTSUDA[*], S. BASO[**] AND Y.DOI[*]

[*] Division of Energy and Environmental Engineering,
Faculty of Engineering, Hiroshima University
1-4-1 Kagamiyama Higashi-Hiroshima, Hiroshima, 739-8527
e-mail: mutsuda@naoe.hiroshima-u.ac.jp, web page: http://home.hiroshima-u.ac.jp/mutsuda/
[**]Department of Naval Architecture,
Faculty of Engineering, Hasanuddin University
Km. 10 Tamalanrea, Makassar, 90245, Indonesia

Key words: Impact pressure; Ship slamming; Hydroelasticity; Grid based method; Particle based method

Abstract. Capable and accurate predictions of some effects of strongly nonlinear interaction wave-ship associated with hydroelastic behaviors are very required for simulation tool in naval architect and ocean engineering. It can guarantee ship safety at the sea state by producing proper design. Therefore, we have developed a hybrid scheme based on both grid and particle method. In order to clarify hydroelastic behaviors of a ship, a dropping test of a ship with elastic motion has been performed firstly. The developed scheme has been then validated on ship dropping case under the same conditions with experiment. The comparisons showed consistently in good agreement. Furthermore, evaluation on hydroelastic behaviors of ship motion under slamming, the impact pressure tends to increase in increasing Froude number (*Fn*). The bending moment and torque defined at the centre gravity due to hogging and sagging events can be predicted well, and their effects on the ship increase in increasing wave length even though the impact pressure decreases in increasing wave length after wave length is equal to 1.0. Moreover, hydroelastic behaviors affect the large heave and pitch amplitudes. Finally, the developed scheme can predict simultaneously hydrodynamic and hydroelastic effects on a ship caused by strongly nonlinear interaction between wave and ship.

1 INTRODUCTION

In sea state, a ship moving forward in severe wave condition can cause wave impact loads on its surface during short time such as slamming event and it is vulnerable to some effects caused by that slamming impact. In addition the wave load acting on a ship under strongly interaction wave-ship can generate a impact pressure and also accelerate a fatigue failure at the same time which influences on ship performance, ship structure and passenger comfort.

Moreover, a ship is not a really rigid construction and this means that a ship has elastic behaviors where it experiences strains and stresses because of its structural flexibility. This cannot be neglected that hydroelastic behaviors of a ship contributes some effects to ship

performances. Hence, hydroelastic behaviors of a ship have to be considered in predicting ship motions, pressure, bending moment and torque as resulted by the strongly interaction between wave-ship associated with hydroelastic effects toward proper ship design and ship safety.

Over the past 40 years, Faltinsen [1] gave a clear definition of the term ship hydroelasticity that the water pressure acts on the structure and the structure deforms. At the same time the speed of the structural deformation influences the pressure in the water. The hydroelastic formulation and model slamming was investigated by Bereznitski et al. [2] using numerical model, Tajima and Yabe [3] was simulated a vessel slamming by using CIP method. Then, wave loads on a ship in waves using an elastic model was studied and verified with full scale measurement. Moreover, Faltinsen [4] presented water entry of a wedge by hydroelastic orthotropic plate theory and an approximate three-dimensional theoretical investigation of hydroelastic wetdeck slamming, and also presented a theoretical study of representing the wetdeck as a beam model and accounting for dynamic hydroelastic effects. Senjanovic et al. [5] analyzed the hydroelastic effect on a flexible segmented barge motion in waves and distortion and slam events was characterized experimentally by using a hydroelastic segmented model [6].

Recently many ongoing research in marine engineering have been attempted to yield Computational Fluid Dynamics (CFD) tool toward accurate tool with considering CFD requirements. These can predict wave impact as hydrodynamic effects due to strongly nonlinear wave-body interactions, however, involvement of hydroelastic effects associated with capturing nonlinear free surface flows on a ship motion under severe wave condition is still rarely devoted and the results have been generally concerned on water entry problems with capturing technique of free surface phenomena or with a weakly interaction between wave and an elastic ship. The nonlinear free surface flows are difficult because it is a complex problem to keep the sharpness of the air-water interface tolerable and to handle moving free surface and elastic ship boundary. In addition, the solutions of CFD for ship motion simulation require more quantitative assessments in reproducibility and validation. Therefore, the developments of CFD techniques to predict accurately hydrodynamic and hydroelastic effects on ship motion in severe wave condition need tremendous efforts.

In our previous works, our developed method was applied to seakeeping performace in nonlinear waves with breaking (Baso et. Al.[7]). In present study our developed method, a hybrid particle-grid scheme, has been verified its usefulness in predicting hydroelastic effects on a ship motion in nonlinear wave with breaking. Here, the ship has been considered as an elastic body in both numerical simulation and experimental work. In addition, some phenomena of nonlinear free surface flow caused by strongly interaction between wave-elastic ship have been captured as well. The hybrid particle-grid scheme is a coupled Eulerian grid and Lagrangian particles which combines CIP method (Yabe and Wang [8]) and SPH method (Gingold and Monaghan [9]) to combine advantages and to compensate disadvantages of the both particle-grid methods. The advantages and disadvantages of the both methods are stated clearly in our previous publication [7]. The model has two kinds of Lagrangian particles, i.e. SPH and free surface particle, on Eulerian grids to correct interface tracking error. The two types of Lagrange particles are collocated and attracted with highly accurate captured nonlinear free surface under resolved region with Eulerian grid.

In this study, the experimental work of ship dropping test has been performed and it has been simulated numerically as well under the same conditions. Furthermore, the developed method, a hybrid particle-grid scheme, has been applied to elastic ship motion in nonlinear wave with breaking to predict and clarify impact pressure, bending moment, heave and pitch motions, and some phenomena caused by nonlinear interaction ship-wave with hydroelastic behaviors.

2 CONPUTATIONAL METHOD

In this section, the numerical method, which combines the Eulerian scheme and the Lagrangian particles by coupling the SPH method and CIP method with particle, are described concisely. More detail explanations were stated in the previous publications [7]. First, the CIP method with particles is introduced as a numerical scheme that combines the accuracy of Lagragian front tracking. Thereafter, the SPH method is employed to calculate deformation, strain, stress of elastic body, and 3D motion.

2.1 Arrangement of grids and particles

The developed Eulerian scheme with Lagrangian particles has been illustrated as shown in Fig.1. This scheme uses a staggered grid system and has two types of Lagrange particles, i.e. SPH particles to describe solid and free surface particles to capture free surface accurately. Density function defined on a grid node is corrected by using density function on free surface particles within referenced area with radius h. A smooth approximation of a density function can be constructed by using a Kernel function in the SPH method.

2.2 Governing equations for fluid phase

The governing equations for fluid phase consist of the mass conservation equation, incompressible Navier-Stokes equation and the equation of continuity, I-phase density function and its advection equation. The equations are expressed as follows:

$$\frac{\partial \overline{u}_i}{\partial x_i} = 0 \tag{1}$$

$$\frac{\partial \overline{u}_i}{\partial t} + \overline{u}_j \frac{\partial \overline{u}_i}{\partial x_j} = -\frac{1}{\rho}\frac{\partial \overline{P}}{\partial x_i} - \frac{\partial \tau_{ij}}{\partial x_j} + \frac{\mu}{\rho}\frac{\partial^2 \overline{u}_i}{\partial x_j \partial x_j} + g_i + \overline{F}_{fsi} \tag{2}$$

$$\frac{\partial \phi_I}{\partial t} + \overline{u}_j \frac{\partial \phi_I}{\partial x_j} = 0 \tag{3}$$

where, u_i is the velocity, μ the coefficient of fluid viscosity, ρ the fluid density, P the pressure, F_{fsi} the fluid-structure interaction, g_i the acceleration due to gravity, τ_{ij} the SGS stress term, and ϕ the density function. To reduce model parameters, the SGS stress term is solved by using the Dynamic SGS model proposed by Germano. More details are provided by Mutsuda

and Yasuda [10].

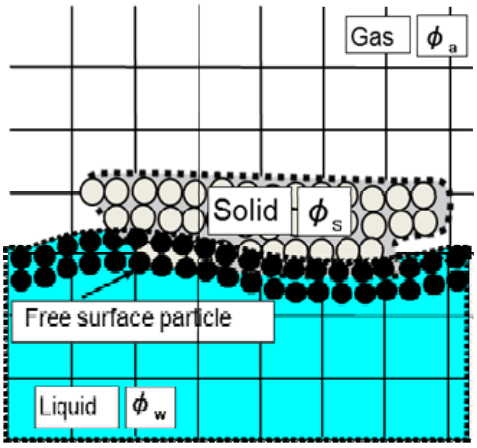


Fig. 1 Illustration of the proposed model (ϕ_I indicates density function; Lagrangian particles are located on Eulerian grid).

2.3 Advection step and non-advection step

The governing equations are solved by using the splitting method which is suitable for solving a multi-phase flow without smearing a density across interface between air and water. The advection step is calculated by the CIP method proposed by Takewaki and Yabe [11]. Then, the Type-M scheme of the CIP method is employed by using the third-order accuracy in time and space. On the other hand, the non-advection step is solved by using the second-order finite difference method.

2.4 Governing equations for Solid phase

The governing equations for solid phase are the continuity and momentum equations as follows:

$$\frac{D\rho}{Dt} + \rho \frac{\partial u^i}{\partial x^i} = 0 \tag{4}$$

$$\rho \frac{Du^i}{Dt} = \frac{\partial \sigma^{ij}}{\partial x^j} + g^i - F^i_{fsi} \tag{5}$$

where S^{ij} is the density, u_i the velocity, $P = -\sigma_{kk}/3$ the position vector of vector j components, the stress tensor of the solid phase, and F_{fsi} the fluid structure interaction term. The stress tensor σ_s^{ij} in Eq.(5) is given by

$$\sigma_s^{ij} = -P\delta^{ij} + S^{ij} \tag{6}$$

where S^{ij} is the deviatoric stress tensor, the pressure solved by the Poisson's equation (9) as mentioned below.

Our numerical model considers a large deformation of an elastoplastic body. The solid body changes at every calculation step by using the following equation:

$$\{dS^{ij}\} = [D^{ep}]\{d\varepsilon^{ij}\} \tag{7}$$

where D^{ep} is the elastoplastic matrix, $d\varepsilon^{ij}$ the time increment of the strain, and dS^{ij} the time increment of the deviatoric stress. To solve rotation of the solid phase during a deformation, the Jaumann derivative is used to ensure material frame indifference with respect to the rotation as follow:

$$\frac{dS^{ij}}{dt} = 2\mu\left(\dot{\varepsilon}^{ij} - \frac{1}{3}\delta_{ij}\dot{\varepsilon}^{ij}\right) + S^{ik}\Omega^{jk} + \Omega^{ik}S^{kj} \tag{8}$$

where $\dot{\varepsilon}$ is the strain rate tensor and Ω the spin tensor. Other details are given by Mutsuda *et al*. [31].

The pressure with specified jump conditions is solved by the Poisson's equation given by

$$\nabla\cdot\left(\frac{\nabla P^{n+1}}{\rho^{*}}\right) = \frac{\nabla\cdot u^{*}}{\Delta t} \tag{9}$$

where $*$ denotes a physical value after the advection step. The pressure for solid phase can be obtained by this equation and be applied in solving a solid deformation.

The fluid structure interaction F_{fsi} is solved by acceleration obtained from the pressure on the SPH particles interpolated using the pressure on grids solved by the Poisson's equation (9). In the model, the fluid structure interaction F_{fsi} in Eqs.(2) and (5) can be given by the following equation:

$$F_{fsi}(\mathbf{r}_a) = -\frac{1}{\rho(\mathbf{r}_a)}\sum_b m_b \frac{P(\mathbf{r}_b)}{\rho(\mathbf{r}_b)}\nabla_a W(\mathbf{r}_a - \mathbf{r}_b, h) \tag{10}$$

To keep computational efficiency and stability, the time increment in the solid phase is approximately 1/10 to 1/50 of that in fluid phase.

2.5 Ship Motions

A ship motion is solved by using information obtained from SPH particles because a ship hull consists of SPH particles capturing motion and deformation of a ship. Therefore, the 3D motion of a ship hull is represented by describing translation and rotation of the center of gravity of a ship hull by using the following equations:

$$\frac{\partial^2 x_{s,k}}{\partial t^2} = \frac{F_{s,k}}{m_i} - F_{fsi} \tag{11}$$

$$I\frac{\partial \omega_i}{\partial t} = T_i \tag{12}$$

$$\frac{\partial \theta_i}{\partial t} = \omega_i \tag{13}$$

where θ_I is the rotational angle, ω_i the angular velocity, T_i the torque, I the inertia moment, and F_{fsi} the fluid structure interaction. In addition, the center of gravity of a ship hull can be obtained by solving the inertia moment of SPH particles, and this is calculated by using Baraff theory [12]. Therefore, the coordinates of velocity of each SPH particle in every time step can be tracked by using the rotation matrix and the amount of the angle rotation of the center of gravity. The quaternion is also used instead of the rotation matrix $\boldsymbol{R}(t)$ in 3D to avoid the Gimbal lock phenomenon.

3 RESULTS AND DISCUSSIONS

3.1 Dropping Test of an Elastic Ship

We investigate firstly relationship between elastic motion and impact pressure caused by slamming by conducting a dropping test of an elastic ship. This is simply assumed that water impact load and strain caused by slamming would be obtained from a elastic ship dropping with deadrise angle to still water surface. Here, a model as an elastic ship is the monohull Ferry type. The experiment of the elastic ferry is performed for validating our developed method results in measuring strain which is acting within a deformable ferry model.

3.1.1 Experimental set up and computational conditions

The experimental set up was determined and designed based on the free fall theory with a constant falling speed. To consider an elastic motion, the ship model is divided into four parts as shown in Fig.2a. The separated part is connected using a backbone attachment made of metal. The flexural rigidity EI and the ship density are 351N/m^2 and 243kg/m^3, respectively. The main dimensions for the actual ship and the model in the experiment are presented in Table1.

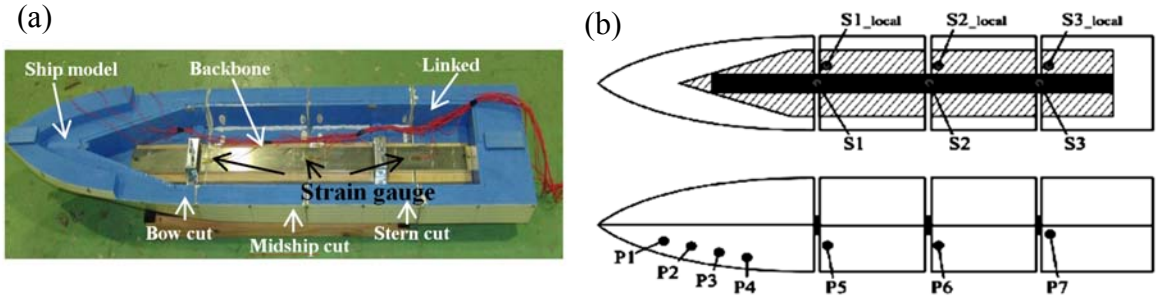


Fig. 2 a). Ship model; b) Location of pressure sensors and strain gauges.

Table 1. Main dimensions of actual ship and model

	Actual Ship	Model
Loa (m)	45	1.5
B (m)	9.6	0.3
H (m)	3.5	0.116
T (m)	1.2	0.04

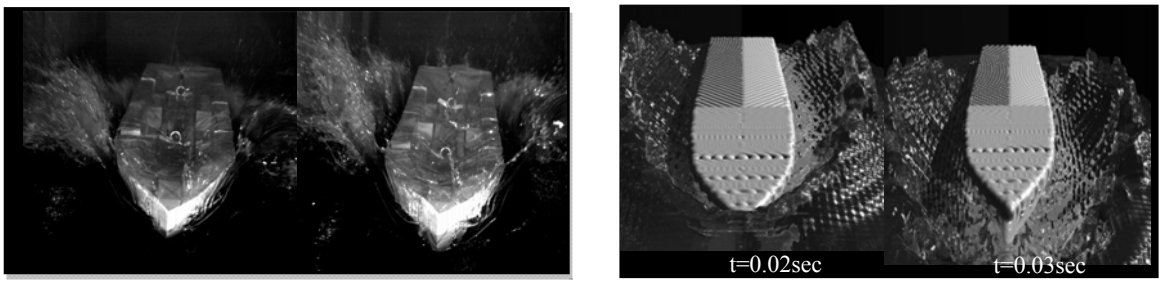
The pressure sensors are located in bow and bottom surface of the model at P1, P2, P3, P4, P5, P6 and P7 and the strains gauges with water proof are located on the backbone attachement at S1, S2 and S3 as shown in Fig.2b. The Pressure data measured from all points are grouped into three parts i.e. bow (P_{bow}), hull (P_{hull}) and stern (P_{stern}) to associate with strain data at S1, S2 and S3. Then, high speed video camera with 500*fps* is placed to capture the ship's motion during the dropping process.

In the experiment, a deadrise angle β of the ship model is defined as a colliding angle between still water surface and an inclined ship at initial condition. Then, the desired angle of the ship model is set and kept with wire before dropping. The deadrise angle β is strictly captured from video image.

For numerical simulation, the dropping test of the elastic ferry has been investigated numerically at the same initial conditions with the experiment as mentioned above. The Ferry model is represented by a large number of the SPH particles where the radius of the SPH particle is $0.0025L_{pp}$ and the total number is 29,434. The grid size is $0.01L_{pp}$ and the radius of free surface particle is $0.0025L_{pp}$ and the total number located near the free surface is 127,680. The density ratio between air and water is 800 and the viscosity ratio between them is 55 in the multiphase model. The flexural rigidity *EI* and the ship density are 351Nm^2 and 243kg/m^3, respectively. The initial dropping speed is used about 4.4m/sec recorded by high-speed video camera in the experiment.

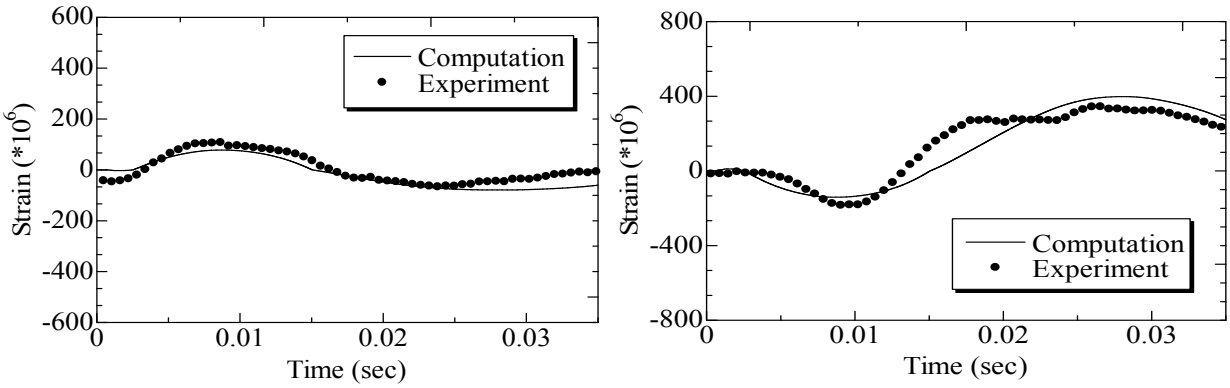
3.1.2 Comparison results

Figure 3 shows comparison of typical case of the elastic behavior and the free surface based on some snapshots between the experimental and the numerical results during the dropping and the entering process for deadrise angle β two degrees. Vertical location of the elastic ship, water splashing and free surface deformation change at each time step from 0.001sec to 0.03sec as shown in that figure. From the comparison, the numerical result is quite good agreement with the experimental one. However, there is small discrepancy between them during the entry process. When the ship bow contacted firstly on the water surface and then immersed, the water splashing near the bow and the generated short wave reflection along the ship are comparatively weak in the numerical results because small droplets and air bubbles less than the size of the free surface particles cannot be captured by our numerical model. We need to overcome this problem using another special technique in near future work.



(a) Experiment (b) Computation

Fig. 3 Comparison typical case of the elastic behavior and the free surface for $\beta = 2°$.



(a) Location : S1 (b) Location : S2

Fig. 4 comparison of the strain time histories between numerical and experimental results at S1 and S2 for β=2°.

Figure 4 shows an example comparison of the strain time histories between numerical and experimental results for deadrise angle $\beta = 2°$ at S1, S2 and S3, respectively. The numerical result is quite good agreement with the experimental result. However, the strain histories at S2 have some discrepancies because the strain at the stern part is caused by strongly interaction between the elastic ship model and the free surface with splashing during the elastic behavior response to the water.

3.2 Investigation of an Elastic Ship Motion in Nonlinear Wave

In this section, the investigation is emphasized to analyze hydroelastic behaviors under slamming by applying our numerical method to ship motion in heading regular wave with breaking. The main dimensions of a ship which are used in this section is the same with those of the dropping test as explained in previous section.

3.2.1 Computational conditions

In the computational conditions, the Froude numbers are set to 0.32 and 0.45. Then, Reynolds number is about 1.4 x 10^6. Young's modulus is 210GPa and Poisson ratio is 0.3 for the elastic ship. The incident wave height H_w/L_{pp} is 0.06, L_{pp} is a ship length and 12 cases are

performed based on the different wave length λ and the ship speed V. The grid size *dx,dy,dz* are $0.01L_{pp}$. The radius in both free surface particle and SPH particle are $0.0025L_{pp}$ and the number of particle is 542,000 for free surface and 29,306 for elastic ship (SPH particle).

3.2.2 Results and discussions

Figure 5 shows some snapshots of bow slamming and bottom slamming phenomena during the motion in nonlinear wave with breaking. The ship's bow hits the surface of wave crest and it is then categorized by bow slamming event and the bottom slamming event that bottom of the ship is lifted up and reenter into free surface due to the loading as shown in Fig. 5. In addition, the wave breaking can be captured well.

The ship experienced strain after the impact pressure acted to the ship. It was bended upward and downward. The reaction of strain on the deck that causes the bended ship is shown in Fig. 6. The localized strains S1, S2 and S3 grow up with increasing wave length. This means that the impact pressure is low where the impact pressure tends to decrease when $L_{pp}/\lambda \geq 1.0$. In addition, the localized impact pressure measured at S3 is highest in both cases based on Fn. The shape of the stern has a slightly flat of hull and a small draft, consequently these can contributes high strain. In future study, we will investigate local strain on along keel part. When wave load is applied, the shape of the ship could suffer hogging and sagging. This has been also explained previously.

Figure 7 shows the non-dimensional global impact pressure P* acting on the ship normalized by density ρ, gravity acceleration *g* and wave height H_w.

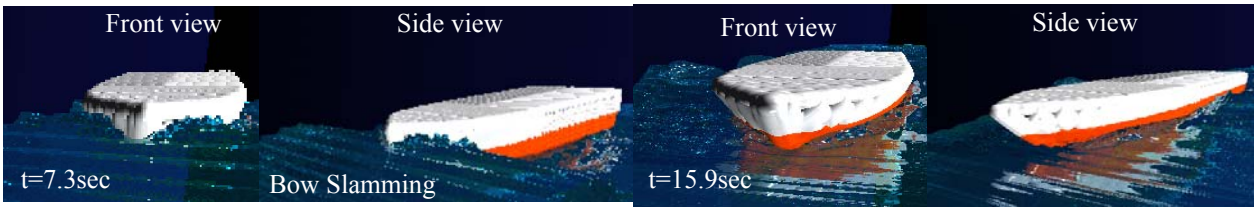
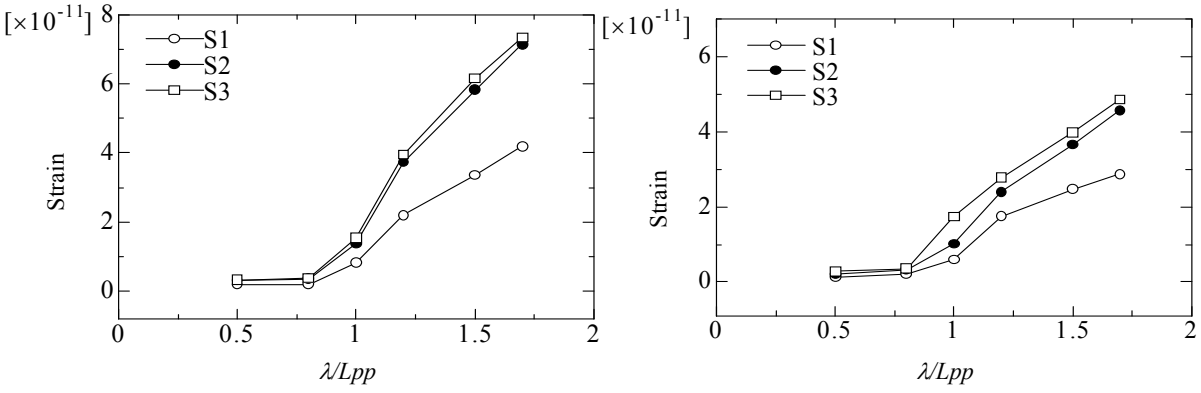


Fig. 5 Snapshots of bow slamming and bottom slamming with breaking.



(b) Fn=0.32 (a) Fn=0.45

Fig. 6 Typical localized strain response reacting on deck caused by hydroelastic behavior; a). *Fn*=0.32 and b). *Fn*=0.45.

High speed influence an magnitude of global impact pressure as shown in Fig. 7. The high global impact pressure occurs when L_{pp}/λ=1.0 and this is reasonable. Moreover, the shape of hogging and sagging are completely described when the wave is the same length with the ship L_{pp}/λ=1.0. Hogging that ship is where the crest of the wave is in a midship and sagging that ship is in the trough of two waves.

The global impact pressure is rarely investigated than the localized impact pressure. In fact, a mid of a ship is vulnerable to some disturbances due to loading because it can cause snap or crack. Therefore, in each case based on wave length, the high deflection of vertical bending load is defined at the centre gravity of the ship.

Figure 8 shows the non-dimensional vertical bending moment defined at the centre gravity of the ship. It can be seen also that high speed contributes strong bending moment because heave amplitudes of the ship becomes large. The vertical bending moment grows up in increasing the wave load level hereafter it tends to decrease about two times the ship length. This depends on a ship position related with that wave crest and trough even though a wave length is bigger or equal to two.

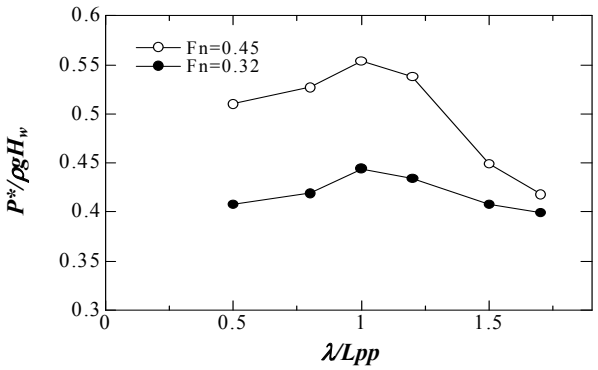


Fig. 7 Nondimensional global impact pressure acting along the ship for *Fn*=0.32 and *Fn*=0.45.

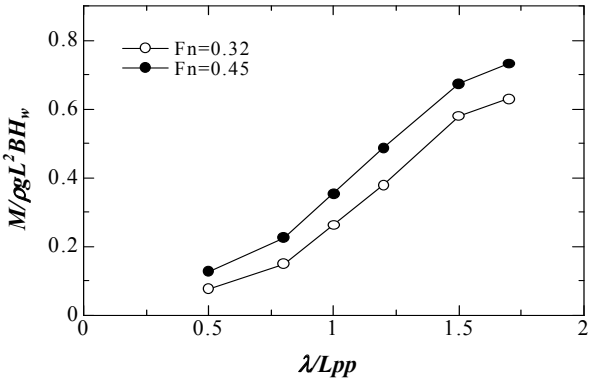
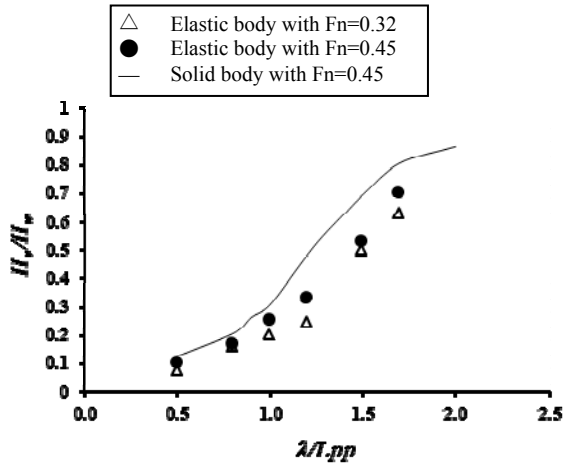
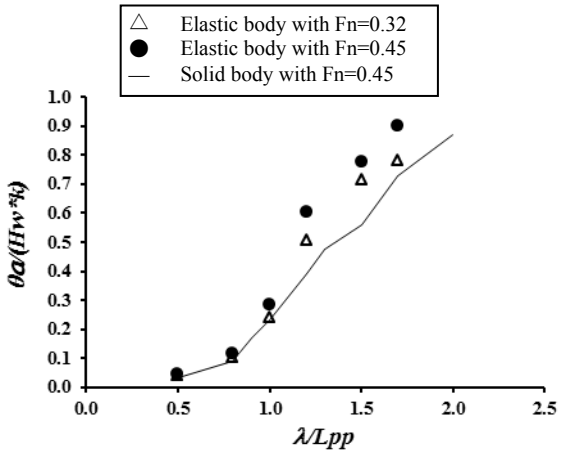


Fig. 8 Nondimensional vertical bending moment defined at centre gravity caused by global impact pressure.



(a) Heave



(b) Pitch

Fig. 9 Comparison of the nondimensional heave and pitch amplitudes between solid and elastic bodies.

Furthermore, comparison the non-dimensional heave and pitch amplitudes between elastic ship and solid ship is show in Fig. 9. The non-dimensional pitch and heave amplitudes are defined by H_v/H_w and $\theta_a/(H_w*k)$, where, H_v is heave motion amplitude, H_w the wave amplitude, θa the pitch motion amplitude and k the wave number.

Based on the comparison result of the non-dimensional heave amplitude, the heave amplitude of elastic ship is lower than solid ship in each wave length. In contrary, the no-ndimensional picth amplitude of the elastic ship is higher than the solid one. In addition, high Froude number *Fn* contributes large amplitude for the elastic case. Here, this can be seen significantly that ship motions are also influenced by hydroelasticity behaviors. Therefore, the performance of a ship in nonlinear wave with breaking depends on impact pressure, elastic structure and ship speed.

4 CONCLUSIONS

In the present study, the hybrid particle-grid scheme has been developed to investigate hydroelastic effects on both the dropping test of the ship and ship motion in nonlinear wave with breaking.

From the dropping test of the ship, the numerical result of vertical location of the elastic ship during the falling, water splashing and free surface deformation and strain history are overall in quite good agreement with the experimental results. However, there is small discrepancy between them during the entry process. These numerical errors were caused by small water droplets and air bubbles less than the size of the free surface particles.

The performance of a ship in nonlinear wave with breaking is influenced significantly by hydroelastic behaviors of the ship. These can be seen that hydroelastic effects address directly to impact pressure and vertical bending moment. The high Froude number *Fn* contributes large amplitude in both motion and bending moment for the elastic case. Here, this can be seen clearly that ship motions are also influenced by hydroelasticity behaviors. Therefore, the performance of a ship in nonlinear wave with breaking depends on impact pressure, elastic structure and ship speed.

The all result of the investigation of elastic ship motion in nonlinear wave with breaking by using hybrid particle-grid scheme needs to be validated with experimental work. Hence, in future work we will conduct experiment of an elastic ship motion in wave. Moreover, the size of the free surface particle will be considered also to capable handle a small water droplet and air bubble resulted by strongly interaction wave-ship.

ACKNOWLEDGEMENT

The authors would like to be grateful to Mr. Kawakami and Mr. Hashihira who kindly provided the experimental data of the dropping test of the elastic ship.

REFERENCES

[1] Faltinsen, O.M. (1997). "The effect of hydroelasticity on ship slamming", Phil. Trans. R. Soc., 355, pp.575-591.

[2] Bereznitski, A., Boon, B. and Postnov, V. (2001a). "Hydroelastic formulation in order to

achieve more accurate prediction of hydrodynamic loads", Proc. of 11th International Offshore and Polar Engineers Conference, Norway, Vol. 4, pp.337-342.
[3] Tajima, M. and Yabe, T. (1999). "Simulation on slamming of a vessel by CIP method", J. of the Phys. Soc. Of Japan, Vol. 68, No. 8, pp.2576-2584.
[4] Faltinsen, O. M. (1999), "Water entry of a wedge by hydroelastic orthotropic plate theory", Journal of Ship Research, 43, pp.180-193.
[5] Senjanovic, I., Malenica, S., and Tomasevic, S. (2008). "Investigation of ship hydroelasticity", Ocean Engineering, Vol.35, pp.523–535.
[6] Thomas, G. et al. (2010). "Slam events of high-speed catamarans in irregular waves", J Mar Sci Technol, 16, pp.8–21.
[7] Baso, S., Mutsuda, H., Kurihara, T., Kurokawa, T., Doi, Y., and Shi, J. (2010). "An Eulerian scheme with Lagrangian particles for evaluation of seakeeping performance of a ship in nonlinear wave", International Journal of Offshore and Polar Engineering, Vol.21, No.2: pp.103-110.
[8] Yabe, T., Mizoe, H., Takizawa, K., Moriki, H., Hyo-Nam Im, and Ogata, Y. (2004). "Higher-order scheme with CIP method and adaptive soroban grid towards mesh-free scheme", Journal of Computational Physics, Vol.194, pp.57-77.
[9] Gingold, R.A., and Monaghan, J.J., “Smoothed particle hydrodynamics, theory and application to non-spherical stars, *Mon. Not. Roy. Astr. Soc.*, Vol. 181, pp.375-389 (1977).
[10] Mutsuda, H. and Doi, Y. (2009). "Numerical simulation of dynamic response of structure caused by wave impact pressure using an Eulerian scheme with Lagrangian particles", Proceeding of the 28th International Conference on Ocean, Offshore and Arctic Engineering, OMAE2009-79736.
[11] Takewaki, H. and Yabe, T. (1987). "Cubic-interpolated pseudo particle (CIP) method application to nonlinear or multi-dimensional problems", Journal of Computational Physics, Vol.70 (1987), pp.355-372.
[12] Barraf, D. (1997). "An introduction to physically based modeling,: Rigid body simulationI ~Unconstrained rigid body dynamics~", SIGGRAPH’97 course note, D3.

V International Conference on Computational Methods in Marine Engineering
MARINE 2013
B. Brinkmann and P. Wriggers (Eds)

RESOLUTION REFINEMENT TECHNIQUE IN A SMOOTHED PARTICLE HYDRODYNAMICS NUMERICAL FLUME FOR COASTAL ENGINEERING APPLICATIONS

D.R.C.B. NEVES [*], E. DIDIER [*,†], P.R.F. TEIXEIRA [♦] AND M.G. NEVES [*]

[*] National Laboratory of Civil Engineering (LNEC)
Av. do Brasil, 101, 1700-066, Lisboa, Portugal
e-mail: dneves@lnec.pt, edidier@lnec.pt, gneves@lnec.pt, www.lnec.pt

[†] Faculty of Science and Technology – New University of Lisbon (FCT-UNL)
Monte de Caparica, 2829-516, Portugal
email: deric@fct.unl.pt, www.fct.unl.pt

[♦] Federal University of Rio Grande (FURG)
Campus Carreiros, 96201-900, Rio Grande, Rio Grande do Sul, Brazil
email: pauloteixeira@furg.br

Key words: SPH – Smoothed Particle Hydrodynamics, Wave-structure Interaction, Refinement Technique, Maritime Structures

Abstract. Numerical modeling of the wave interaction with coastal structures is a challenging issue due to the multi-nonlinear phenomena involved, such as, wave propagation, wave transformation, interaction among incident and reflected waves, run-up / run-down, wave breaking and wave overtopping. Numerical models based on a Lagrangian formulation, like SPH (Smoothed Particle Hydrodynamics), allow simulating complex free surface flows. This work presents the new developments on a SPH numerical model for studies on wave-structure interaction made at the National Civil Engineering Laboratory (LNEC). A new semi-automatic refinement technique of particles was applied to reduce the CPU time. Simulations with a specific geometry, a wave flume with a water chamber, were made regarding the application of this technique. An analysis was made on (i) convergence with resolution, i.e. particle dimension and (ii) semi-automatic refinement. Results were compared with the solution obtained with the finer resolution.

1 INTRODUCTION

Some of the maritime structures intend to use the wave action effects for the benefit of the communities as an advantage for the local economy. The study regarding the response of these structures is therefore important to ensure both their stability and functionality. Wave-structure interaction generates very complex phenomena involving nonlinear processes, like wave propagation and transformation, run-up / run-down, wave breaking and overtopping. Coastal structures may have different structural characteristics. The analysis of the hydraulic behavior of the structures is usually made by using semi-empirical formulae. However, direct application of these formulae is limited to simple structural configurations and to specific

wave conditions. In practical engineering studies, physical modeling tests are usually also undertaken, which permit a reliable evaluation of the structure's efficiency. The greatest disadvantages of the physical model tests are the required time for their construction and exploitation, the high cost and lack of flexibility to change the geometrical characteristics of the models. Moreover, scale effects could affect the results.

In recent years, due to the continuous increase in computational power, numerical models have been developed and their use has become increasingly attractive. Numerical modeling of the free-surface flow has attracted the interest of a large scientific community and wave interaction with coastal structures is a challenge due to the nonlinear phenomena involved.

The equations describing the flow are known for a long time, but with the improvement and the development of the computational techniques it has become easier to obtain approximate solutions to these equations and consequently to simulate realistic scenarios.

However, only a few numerical models allow simulating the very complex phenomena of wave breaking, overtopping and impact loads at vertical structures. Among the existing models, one can highlight the three different types of models that are currently in development and/or validated at LNEC: AMAZON [9], based on the nonlinear shallow water equations; IH-2VOF [2], based on the VARANS equations (Volume-Average-Reynolds-Navier-Stokes), and the SPHyCE [4] based on a Lagrangian method and the concept Smoothed Particle Hydrodynamics (SPH). The models AMAZON and IH-2VOF have already been successfully applied for wave-structure interaction studies, and the SPHyCE model is under development and validation.

Recently, models based on Lagrangian methods, such as the SPH approach, have emerged. This method is based on the Navier-Stokes equations and on a completely mesh-free technique. Monaghan [12] demonstrated that SPH is a very promising alternative for modelling free surface flows and wave breaking. Different models have been developed, based on the SPH formulation of the Navier-Stokes equations, and there are many different numerical implementations. The SPHyCE numerical model used and developed at LNEC is based on the original SPHysics model [8] and specially developed and improved for studies of wave interaction with impermeable and porous coastal structures and for applications of coastal engineering. Promising agreement with experimental data has been obtained for the free surface elevation, overtopping discharge and impact loads [2], [3], [4], [5] [6]. The present numerical model includes three specific developments, among others: i) a partial renormalization, i.e. partial filtering density, where renormalization is applied only for particles near the structure, which is an original method that allows simultaneously propagating waves, without diffusion, and modeling accurately the pressure field near the structure [5]; ii) an wavemaker with active absorption with paddle drift correction allowing the simulation of a semi-infinite numerical wave flume; and iii) a new semi-automatic refinement technique by the division of fluid particles. This work will be focused mainly on the semi-automatic refinement technique.

The analysis of the semi-refinement technique is fundamental to assure the limitations and potentialities of the new implemented technique in order to reduce the calculation time and to improve the model results.

To study the semi-automatic refinement technique, a simple water chamber was simulated. This geometry was chosen to avoid excessive nonlinear effects such as wave breaking, impact loads on a vertical wall and wave transformation over a sloping structure. The idea was to

simulate wave propagation regarding the semi-automatic refinement study, considering both an over simplified and a high complex wave propagation, focusing mainly on the wave effects that are directly connected with the new implemented technique of the semi-automatic refinement. An analysis of this technique was done, a convergence study with the resolution, i.e. the particle dimension, was performed to define the compromise between results accuracy and CPU time, and an analysis of semi-automatic refinement technique is carried out for several resolutions.

Therefore in section 2 the fundamental principle of the SPH method is explained and the new improvements of the SPH model are described. In section 3 the case study is described. In section 4, the free surface in the flume and the water chamber are analysed using the semi-automatic refinement technique. The conclusions are presented in the last section.

2 NUMERICAL MODEL

2.1 SPHyCE numerical model

The SPH method [12] is based on a Lagrangian formulation of Navier-Stokes equations. It is a mesh-free technique which allows modeling fluid particle trajectories. Numerically, the interaction between the particles is ensured by an interpolation function, the kernel [11].

Lagrangian Navier-Stokes equations are transformed into SPH forms, by integral equations using integral interpolants, which allows approximating any function *A(r)* by:

$$A(r) = \int_{\Omega} A(r')W(r - r', h)dr' \tag{1}$$

where r is the vector particle position, W is the kernel (weighting function), h is the smoothing length. The kernel allows determining the interaction among neighbouring particles included in the influence domain, a compact support within a circular region determined by a radius of $2h$, controlled by the smoothing length h, typically higher than the initial particle spacing, d_0.

The two-dimensional SPH equations are based on the Lagrangian formulation of the conservation of momentum and continuity:

$$\frac{dv}{dt} = -\frac{1}{\rho}\nabla P + \Pi + g \tag{2}$$

$$\frac{1}{\rho}\frac{d\rho}{dt} = -\text{div}\ (v) \tag{3}$$

where t is the time, Π represents the viscous terms, g = (0, -9.81) ms^{-2} is the acceleration of gravity, v, P and ρ are the velocity, pressure and density, respectively.

The standard SPH formulation [12], in which the fluid is considered weakly- compressible, is used and allows calculating the pressure by an equation of state [1]:

$$P = B\left[\left(\frac{\rho}{\rho_0}\right)^{\gamma} - 1\right] \quad \text{with} \quad B = \frac{c_0^2\rho_0}{\gamma} \tag{4}$$

with γ=7, ρ_0 the reference density (for water: 1000kg.m^{-3}) and c_0 the sound speed.

The trajectories of the particles are obtained from the following relationship:

$$\frac{dr}{dt} = v \tag{5}$$

SPHyCE numerical model, based on the SPHysics code [8], has been developed and improved for specifically solving coastal engineering problems and modeling complex free surface flows and wave interaction with coastal structures (impermeable and porous structures).

For numerical simulations of wave propagation and interaction with a vertical wall, the quadratic kernel is used to determine the interaction between the particles.

Integration in time is performed by the Predictor-Corrector model using a variable time step to ensure the CFL condition.

Particles are usually moved using the XSPH variant due to Monaghan [12]. The method is a correction for the particle velocity, which is recalculated taking into account the velocity of that particle and the average velocity of neighbouring particles. However, it was shown in [3] that instabilities appear during wave propagation due to the XSPH correction and fluid flow exhibits unphysical behaviours. Consequently, the XSPH correction is not used.

While the kinematics of SPH simulations is generally realistic, the pressure field of the particles can exhibit large pressure oscillations. One of the most straightforward and computationally least expensive methods to smooth out pressure oscillations is to perform a filter over the density of the particles, using the Shepard density filter, and to re-assign a density to each particle [5]. In the present study, SPHyCE model is applied using a partial renormalization technique developed in [5] and [6].

The boundary conditions are not displayed directly in the SPH formalism. In the present model the repulsive boundary condition, developed by [13], that imposes a repulsive force to the fluid particles from the boundary particles, is used and allows preventing the water particles to cross the solid boundary. Nevertheless, reinforcing this condition, some improvements were made in the SPHyCE model.

Initially, the water particles are placed in the flume using a regular Cartesian grid, i.e. particles are regularly distributed, with the spacing between particles defined by d_o. This is a condition of the SPH method when the smoothing length of the kernel is constant. The distribution of the solid particles at boundaries follows the one adopted for the fluid particles, namely the distance between the particles is equal to d_o independently of the boundaries direction. The velocity field is zero and the pressure is hydrostatic.

2.2 Semi-automatic refinement technique

A new semi-automatic refinement technique by division of fluid particles, in order to decrease the computational time without loss on results accuracy, was implemented in the SPHyCE code and analysis of this technique is the aim of the present work.

The model enables the division of one into 2, 3 or 4 smaller particles at any time during the calculations, allowing the refinement when it is most needed (Figure 1).

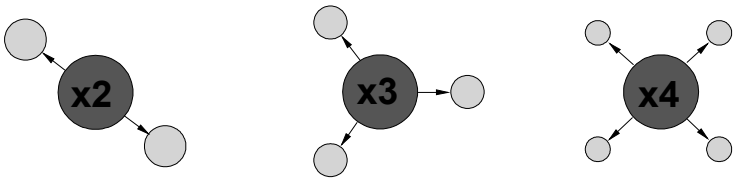


Figure 1: Division of the particles into 2, 3, or 4 smaller particles

This technique allows SPH simulations to start with a coarse resolution, producing relatively short CPU time in order to model the transient part of the flow, i.e. before stabilizing the interaction between the incident and reflected waves by the structure. After obtaining this flow stabilization the refinement technique is applied in order to split all the fluid particles in the computational domain (Figure 2), increasing the resolution in order to obtain more accurate results. This technique is to be applied for studies on a semi-infinite wave channel where the transient flow is not relevant to the results analysis.

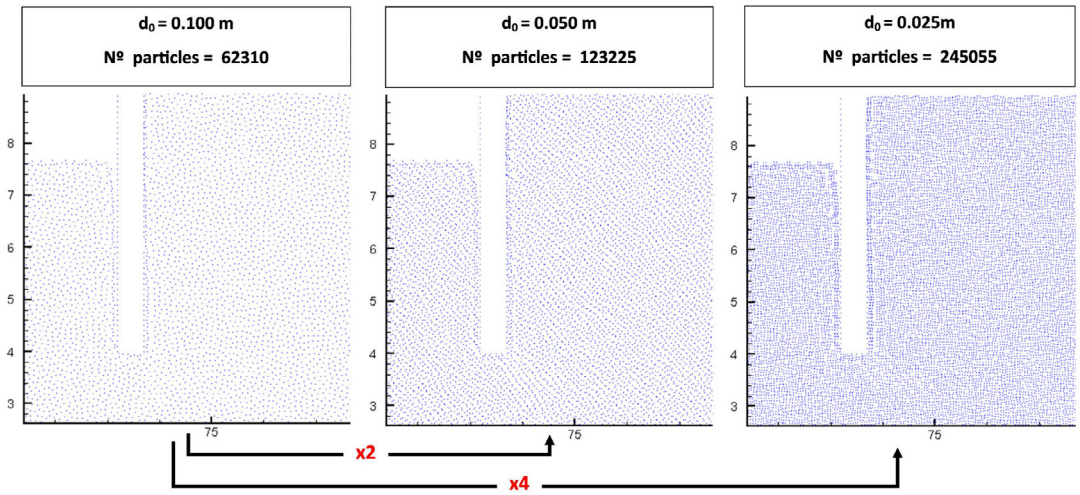


Figure 2: Division of the fluid particles into 2 and 4 smaller particles

3 CASE STUDY

A specific geometry for the computational domain was defined to study accurately the new implemented semi-automatic refinement technique.

The case study presents a wave flume with a water chamber to assess the influence of the new refinement technique for the wave propagation and for the nonlinear interaction with a simple structure.

The flume (Figure 3) is 80.0 m long and has a horizontal bottom. The water chamber begins at the distance of 72.3 m from the wavemaker and has a first vertical wall of 0.5 m thick and 5.0 m height and a second wall, coincident with the end of the flume. The first wall of the water chamber was defined to be submerged up to 4.0 m deep.

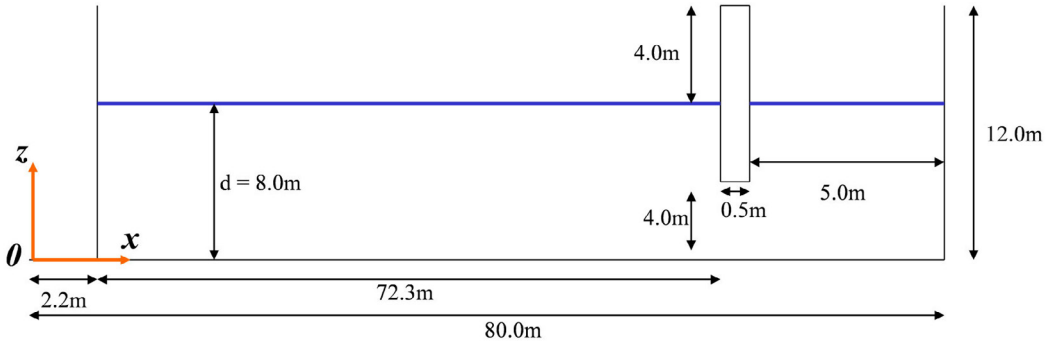


Figure 3: Schematic representation of the wave flume and water chamber

An incident regular wave was tested with 7.0 s wave period, T, and 2.0 m height wave, H. Water depth, d, is 8.0 m, which result in a wave length, L, equal to 55.2 m.

Active absorption of the reflected waves at the wavemaker was used in the numerical simulations and allows modeling a semi-infinite wave flume with a small computational domain, with approximately 1.3L length.

In order to study the free surface inside and outside the water chamber, 8 numerical wave gauges were placed along the wave flume (Figure 3). Two gauges, G1 closer to the wavemaker at x=8.2 m and G3 close to the front face of the wall at the water chamber entrance at x=72.9 m, and the mean level inside the water chamber are presented in this work.

The partial filtering density technique [6] [8] was applied to particles from x=70.0 m (before the wall that separates the water chamber) to x=80.0 m (inside the water chamber) each 30 time iterations.

4 RESULTS

As referred, in the present work the free surface at gauge G3 and the mean level inside the water chamber are presented and compared.

For the semi-automatic refinement study, two different analyses were made: (i) convergence study with particle dimensions, d_o, varying from 0.2 m to 0.05 m (i.e. 15918 to 246612 particles); and (ii) analysis of the semi-automatic refinement technique, comparing results with and without the semi-automatic refinement.

The mean free surface elevation inside the water chamber was calculated from the water volume inside the water chamber.

4.1 Convergence analysis

A convergence study is here performed varying the resolution, i.e. the particle dimension or/and particle volume. Table 1 shows the characteristics of the five computational domains used to check independence of the solution to the resolution. In this table, particle dimension, d_o, particle volume, total number of particles for each resolution and the number of particles per wave height are indicated ([5] specify that 40 particles are the minimum for a convergent solution in SPH simulations).

Figure 4 shows the time series of the free surface elevation outside the water chamber (G3) and the mean level inside the chamber.

Table 2 shows the average wave height at G3 and the mean level inside the water chamber for the five tested resolutions. CPU time, using a serial version of the SPHyCE code and a Personal Computer Intel(R) Core(TM) i7 CPU 920 @ 2.67GHz, and relative errors are also presented considering the solution obtained for the finer resolution (5A).

Table 1: Particle characteristics and number of particles used for the computational domain

Case	*do* (m)	Particle volume (m^3/m)	Number of particles	Number of particles per wave height
1A	0.200	$4.00x10^{-2}$	15918	10
2A	0.143	$2.04x10^{-2}$	30822	14
3A	0.100	$1.00x10^{-2}$	62310	20
4A	0.071	$5.00x10^{-3}$	123609	28
5A	0.050	$2.50x10^{-3}$	246612	40

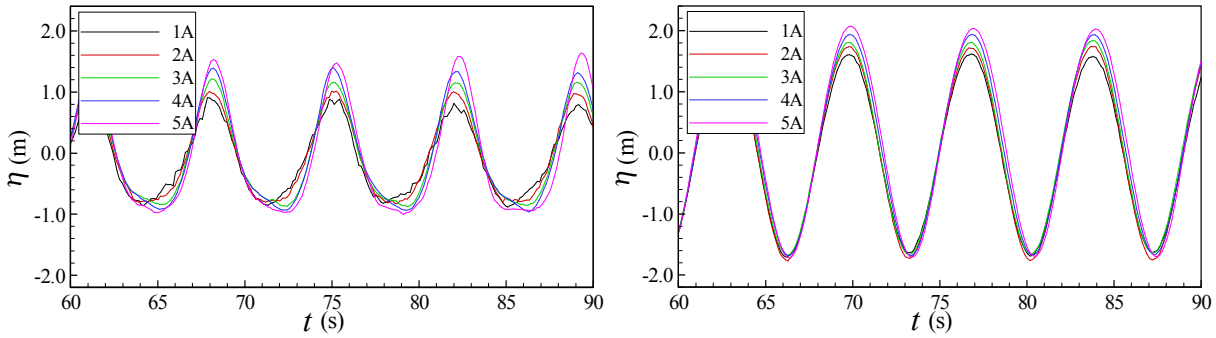


Figure 4: Convergence analysis with resolution - Free surface elevation at gauge G3 and mean level inside the water chamber

Table 2: Convergence analysis with resolution – CPU time, average wave height at G3 and mean wave heigth in the water chamber and relative errors

		Free surface at gauge G3		Mean free surface in water chamber	
Case	CPU time (hours)	Average wave height (m)	Relative error (%)	Average level (m)	Relative error (%)
1A	5.0	1.690	31.313	3.264	13.026
2A	15.0	1.783	27.539	3.469	7.558
3A	45.0	2.027	17.587	3.473	7.464
4A	131.3	2.294	6.746	3.588	4.382
5A	370.0	2.460	0.000	3.753	0.000

The convergence analysis demonstrates that, as expected, the quality of the results increases with the resolution. The results for the free surface elevation at gauge G3 reveal that the relative error can be reduced from 31% (1A) to 7% (4A) and for the mean level in the water chamber from 13% (1A) to 4% (4A), when comparing with the more refined case.

Differences are small between case 4A and 5A, particularly inside the water chamber. The CPU time increases sharply with the number of particles in the domain, as can be seen in Table 2. From case 1A to 5A the calculation time growths about 74 times, from 5 hours to 370 hours.

Figure 4 shows the CPU time versus the number of particles. Increasing the number of particles by a factor 2 induces that CPU time is multiplied by a factor 3. Based on the five resolutions, a trend line indicates that CPU time growths following the relationship $3x10^{-6}$ $N^{1.55}$, with N the number of particles.

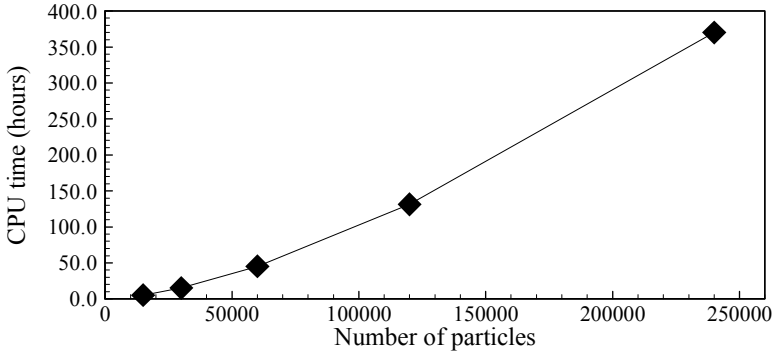


Figure 5: CPU time versus number of particles for the five resolutions

4.2 Semi-automatic Refinement

For the semi-automatic refinement technique, four refinements were obtained from two different particle resolutions, the 2A and 3A respectively, and both resolutions were refined by 2x and 4x. In Table 3 there are 4 cases to assess the semi-automatic refinement performance: (i) 2A-2x case is comparable with the 3A; 2A-4x case is analogous to the 4A; 3A-2x case is similar to the 4A; and finally the 3A-4x case is equivalent to the 5A case. Both resolutions will be compared with the respective simulations without refinement.

The refinement technique was applied after 55 s of simulation, when stabilized wave regime was obtained, considering a total simulation of 105 s.

Table 3: Refinement analysis - Cases with and without the semi-automatic refinement

Case	*do* (m)	Number of particles	Number of particles per wave height
2A	0.143	30822	14
2A-2x	0.101	60666	20
2A-4x	0.071	120354	28
3A	0.100	62310	20
3A-2x	0.071	123225	28
3A-4x	0.050	245055	40
4A	0.071	123609	28
5A	0.050	246612	40

In order to compare the non-refined with the refined test cases, Figure 6 to Figure 8 present the free surface elevation outside the water chamber (G3) and the mean level inside the water

chamber for the eight simulations.

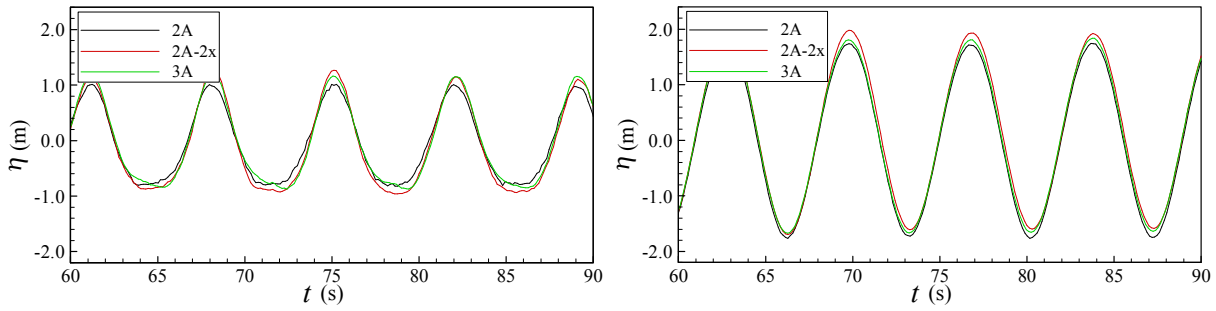


Figure 6: Refinement analysis - Free surface elevation at gauge G3 and mean level inside the water chamber for cases 2A, 2A-2x, and 3A

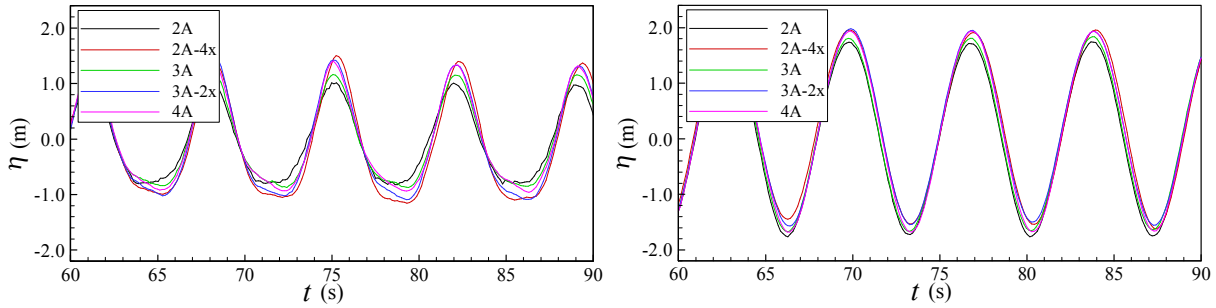


Figure 7: Refinement analysis - Free surface elevation at gauge G3 and mean level inside the water chamber for cases 2A, 2A-4x, 3A, 3A-2x and 4A

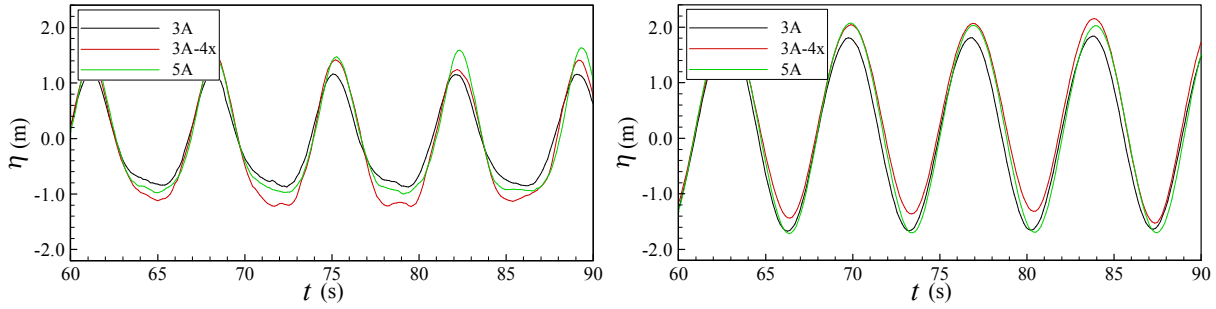


Figure 8: Refinement analysis - Free surface elevation at gauge G3 and mean level inside the water chamber for cases 3A, 3A-4x, and 5A

Table 4 shows the CPU time, the average wave height at G3 and the average height of the mean level in the water chamber for the 8 cases presented in Table 3. These 8 cases were grouped into 3 comparing tables to better analyze the effect of the semi-automatic refinement technique. Relative errors are also presented comparing the refined and non-refined cases with those with the highest initial resolutions.

The objective of the semi-automatic refinement technique is to firstly use a less refined calculation with the purpose of having a quickly stabilized wave regime and then, using the

semi-automatic refinement, simulate a well refined case in order to have approximately the same solution as the obtained with a more refined simulation (that would take a greater calculation time if using the same refinement for the whole simulation). Hereby, the new technique leads to a decreasing on the calculation time and maintains the same quality of the results.

The results presented in Table 4 show an agreement with the above hypothesis. In fact, observing the results, in most of the cases, the use of the semi-automatic refinement technique produces a solution that approximates to an even more refined simulation.

Table 4: Refinement analysis – CPU time, average wave height at G3 and mean wave height in the water chamber and relative errors

				Free surface at gauge G3		**Mean free surface in water chamber**	
	Case	Number of particles	CPU Time (hours)	Average wave height (m)	Relative error (%)	Average height for the mean level(m^3)	Relative error (%)
Evaluation 1	2A	30822	15.0	1.783	12.08	3.470	6.29
	2A-2x	60666	27.5	2.101	3.63	3.522	7.90
	3A	62310	45.0	2.027	0.00	3.264	0.00
Evaluation 2	2A	30822	15.0	1.783	22.30	3.470	3.32
	2A-4x	120354	68.8	2.423	5.63	3.538	1.41
	3A	62310	45.0	2.027	11.63	3.264	9.04
	3A-2x	123225	85.0	2.423	5.61	3.491	2.74
	4A	123609	131.3	2.294	0.00	3.589	0.00
Evaluation 3	3A	62310	45.0	2.027	17.59	3.264	13.03
	3A-4x	245055	215.6	2.571	4.51	3.616	3.65
	5A	246612	370.0	2.460	0.00	3.753	0.00

Considering Evaluation 1 at gauge G3, by doubling the number of particles (2A-ex) the solution reduces the relative error from the most refined solution (3A) from 12.08% to 3.63%. Inside the water chamber, the semi-automatic refinement produces the opposite effect, increasing the error from 6.29% to 7.90%. This might be due to the fact that these cases present a low resolution, with maximum of 20 particles per wave height that is considerably lower than the desirable for an acceptable solution [5].

For Evaluation 2, resolution is about 28 particles per wave height and results are more accurate. For the gauge G3, quadruplicating the number of particles of the case 2A (2A-4x), produces an increase of the results accuracy, reducing the relative error from 22.30% to 5.63%. The same tendency is showed by doubling the number of particles of the solution 3A (3A-2x) producing a decrease of relative error from 11.63% to 5.61%.

Finally Evaluation 3 presents simulations with 40 particles per wave height providing a suitable solution for the tested case [5]. Both gauge G3 and mean level inside the water chamber present better results when quadruplicating the number of particles of the 3A (3A-4x). At G3 and inside the water chamber, the relative error decreases from 17.59% to 4.51%

and from 13.03% to 3.65%, respectively.

Regarding the calculation time, main focus of the semi-automatic refinement technique, Table 4 proves a real improvement on the calculation time, with a CPU time reduction of about 35% to 47% when refining the particles by a factor of two or four. Comparing the case 3A-4x and 5A there is less than 5% differences between results and CPU time is 42% reduced, decreasing from 370 to 215.6 hours.

5 CONCLUSIONS

The paper presents the study and development of a new semi-automatic refinement technique based on the division of fluid particles. The case study presents a simplified structure of a wave flume with a water chamber. This structure allows analyzing of the wave propagation and its specific interaction with a vertical wall and a water chamber.

The analysis of free surface elevation near the entrance of the water chamber and mean level inside the water chamber are presented for: (i) the convergence with particles resolution; and (ii), the main purpose of this work, the semi-automatic refinement technique regarding two different resolutions and two types of refinement, doubling and quadrupling the number of particles.

The convergence analysis shows a clear convergence of the solution with the refinement of particles; the two most refined simulations (4A and 5A) only present a relative difference of 7% and 4% for the gauge G3 and the mean level inside the water chamber, respectively. However, for these two refined simulations, CPU time increases from 131.3 to 370 hours, i.e. doubling the number of particles of the CPU time reduces around 3 times.

Three different evaluations were made for the analysis of efficiency of the new semi-automatic refinement technique, considering a final resolution of about 60000, 120000 and 240000 particles, and multiplying by two and four the number of particles of the two coarser resolutions. The results prove that the CPU time using the refinement technique decreases considerably maintaining good agreement of the results when compared with those obtained without refinement. All simulations with the semi-automatic refinement present relative differences with the solution obtained with the finer resolution less than 6% for the free surface elevation outside and level inside the water chamber. Refining the particles by a factor of two or four the CPU time is considerably reduced, by 35% and 47%, respectively.

The semi-automatic refinement results show that the new implemented technique improves significantly both the final solution and the computational time.

For the future work, regarding the semi-automatic refinement technique further analyses are needed, other geometries and other physical phenomena (as wave overtopping) will be studied. Also the comparison and validation with physical tests will be performed.

6 ACKNOWLEGEMENT

The authors gratefully acknowledge the financial support of the Portuguese Foundation for Science and Technology, through project SPACE “A Smoothed Particle Hydrodynamic model development and validation for coastal engineering applications”, PTDC/ECM/114109/2009.

REFERENCES

[1] Batchelor, G.K. *Introduction to Fluid Dynamics*, Cambridge University Press, UK, (1974).

[2] Didier, E. Neves, M.G. Wave overtopping of a typical coastal structure of the Portuguese coast using a SPH model, *J.Coastal Research*, SI 56, (2009), pp. 496-500.

[3] Didier, E. Neves, M.G. Coastal flow simulation using SPH: Wave overtopping on an impermeable coastal structure, *Proc 4th ERCOFTAC SPHERIC workshop*, Nantes, France (2009), pp. 357-364.

[4] Didier, E. Neves, M.G. A Lagrangian Smoothed Particle Hydrodynamics – SPH – method for modelling waves-coastal structure interaction, *Proc CFD2010 ECCOMAS*, Lisbon, Portugal (2010).

[5] Didier, E. Martins, R. Neves, M.G. Vasco, J.R.G. Interaction between wave and coastal structure: validation of two Lagrangian numerical models with experimental results, *Proc. MARINE 2011*, Lisbon, Portugal (2011).

[6] Didier, E., Martins, R., Neves, M.G. Numerical and Experimental Modeling of Regular Wave Interacting with a Composite Breakwater. *International Journal of Offshore and Polar Engineering*, (2013). Accepted for publication.

[7] Didier, E. Neves, M.G. A Semi-Infinite Numerical Wave Flume using Smoothed Particle Hydrodynamics, *Int. J. of Offshore and Polar Eng.*, 22, Nº2, (2012), pp. 193-199.

[8] Gómez-Gesteira, M. Rogers, B.D. Dalrymple, R.A. Crespo, A.J.C. Narayanaswamy, M. User Guide for the SPHysics Code v1.4, Manchester, UK, (2008).

[9] Hu, K. High-Resolution Finite Volume Methods for Hydraulic Flow Modelling. PhD Thesis, *Manchester Metropolitan University*, UK, (2000).

[10] Lara, J.L. Ruju, A. Losada I.J. Reynolds averaged Navier-Stokes modelling of long waves induced by transient wave group on a beach, *Proc. R. Soc. A,* 467, (2011), pp. 1215-1242.

[11] Liu, G.R. Mesh free methods. Moving beyond the finite element method, *CRC press*, (2003).

[12] Monaghan, J.J. Simulating free surface flows with SPH, *J. Comp. Physics,* 110, (1994), pp. 399-406.

[13] Monaghan, J.J. Kos, A. Solitary waves on a Cretan beach, *Journal of Waterways, Ports, Coastal and Ocean Engineering,* 125, (1999), pp. 145-154.

V International Conference on Computational Methods in Marine Engineering
MARINE 2013
B. Brinkmann and P. Wriggers (Eds)

NUMERICAL ANALYSIS OF THE SHIP PROPULSION CONTROL SYSTEM EFFECT ON MANOEUVRING CHARACTERISTICS IN MODEL AND FULL SCALE

MARINE 2013

M. ALTOSOLE[*], M. FIGARI[*], M. MARTELLI[*], M. NATALETTI[*], S. VIGNOLO[†] AND M. VIVIANI[*]

[*] Department of Marine Technology, Electrical, Electronic and Telecommunication engineering (DITEN)

[†] Department of Mechanical, Energy, Management, Transportation and Mathematical engineering (DIME)

Università degli Studi di Genova
Via Opera Pia 11a, 16145 Genova, Italy
web page: http://www.ingegneria.unige.it

Corresponding author: michele.martelli@unige.it

Keywords: Numerical simulation, Marine propulsion plant, Control system, Ship manoeuvrability, Model and Full scale tests.

Abstract. A comprehensive approach to simulate the interaction between the ship propulsion system and manoeuvrability, during transients and off design conditions, is presented.

The increasing attention on the manoeuvring features of the vessel has forced designers to consider this aspect already in the preliminary stages of the project.

Data about manoeuvring characteristics may be obtained by means of several model tests (at planar motion mechanism or with free running models). However, differences between model tests and full scale trials exist. From the hydrodynamic point of view, some disagreements are due to the scale effects but also the effect of the propulsion control system, highly non-linear, may provide a considerable contribution to such differences.

These dynamical aspects cannot be taken into account with traditional methodologies and purely stationary approaches. For these reasons, the ship dynamic behaviour is evaluated by time domain simulators, developed by the authors, which include the ship dynamics, the propulsion plant dynamics and the propulsion control system logics.

At the end of the paper some simulation results are shown in order to better understand the effects and the differences of the propulsion control settings on the ship manoeuvrability in model and full scale.

1 INTRODUCTION

The dynamic behaviour of the propulsion system is mainly affected by the control system performance, in particular by the strategies adopted to perform the required task within the boundary conditions imposed by machinery or environment constraints. This is particularly evident when fast transients are present, as experienced in the case of tight manoeuvres.

To prevent possible failures, the control system must be properly set, through dedicated control functions, to maintain the shaft torque or the engine torque within the allowed limits, to reach and maintain the required rotational shaft lines speed, etc.

As it is well known, during manoeuvring of a twin-propeller vessel, like turning circle or zig-zag manoeuvres, significant unbalances on the shaft lines, in terms of torque and thrust loads, are experienced. As regards the propulsion and the control system design, this aspect has to be taken into account together with the general increase of the shaft torque with respect to the steady state value.

Usually the ship manoeuvring characteristics are evaluated by a series of model tests. In some cases, the model tests are performed with a free running model. The model hull geometry is perfectly reproduced by the scale factor, on the contrary, because of economic reasons, or technical problems, an exact scale propulsion plant (engines, propellers, etc.) cannot be installed on the free running model. Moreover, also the installed control system is simplified with respect to the full scale, often its interaction with the propulsion plant is not realistic (or even not existent at all) and consequently it does not affect the model manoeuvring characteristics.

As a consequence, possible unexpected behaviours may be experienced during sea trials, such as shaft lines revolutions drop, alarm activation in the control panel, propulsion system stopping due to the intervention of various protections. The best way to evaluate the different behaviours between the model and the full scale in preliminary design, is adopting simulation techniques. By means of these techniques, it is possible to evaluate the different behaviours of the propulsion plant (even in off design and/or potentially dangerous conditions) and to understand their causes.

On the basis of previous free running model experiments, general ideas about the simulation of the interaction of propulsion control and manoeuvring systems are outlined in this paper. The proposed simulation tools may be helpful to the designers for various tasks, such as the correct shaft line sizing or the propulsion control system tuning.

The considered ship for the present analysis is a fast twin screw / twin rudder ship, similar to those analysed in [1], whose range of main characteristics values is reported in Table 1, where L is the ship length, B is the ship beam, T is the draft and C_B is the block coefficient.

Table 1: Main characteristcs of ships analysed [1]

L/B	5.5 - 8.5
B/T	2.75 - 3.75
C_B	0.5 – 0.65

2 PROPULSION AND MANOEUVRING SIMULATOR

The simulation model has been developed starting from the methodology proposed by the authors in [2]. In particular, the numerical code, developed by Matlab® software, is a simulation platform that allows to study the vessel behaviour during transient conditions (acceleration, deceleration, etc.) as well as during steady state conditions (constant speed navigation). Such type of simulation models have proven their validity in a considerable number of previous works, including validation at sea [3][4].

Three different ship macro systems contribute to the global ship behaviour: the ship manoeuvrability, the propulsion plant and the control system. For each macro system, different elements have been modelled using differential and algebraic equations and tables. In detail, the following propulsion plant elements have been schematized: the main engines, the gearbox, the shaft lines. From the control system point of view, mathematical models, representing the propulsion plant supervisor controller as well as the local machineries controllers, are present. The ship motions have been evaluated by a numerical model characterized by three degrees of freedom; the model includes, as usual, forces due to the hull, the propulsors and the rudders, following the widely used modular approach. All the interactions among the different machineries/elements have been properly modelled, considering the ship like a whole system.

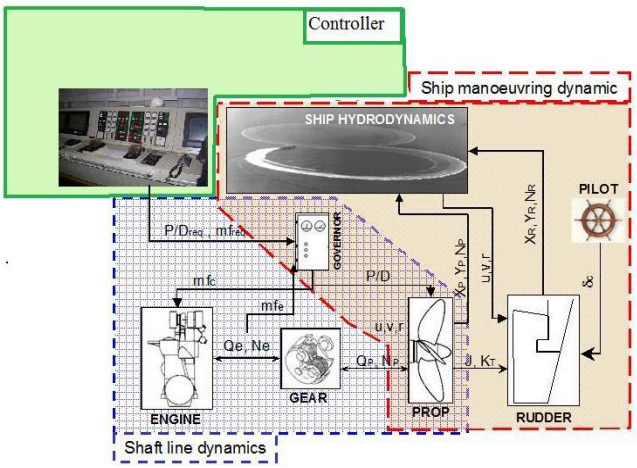


Figure 1: Simulator Architecture

As previously mentioned, a simulator was developed for both free running model and full scale ship. This step has been easily achieved by means of the simulator modular structure. The details of ships configurations are reported in the following sections.

2.1 Propulsion Plants

The main differences between the two developed simulators concern the propulsion plant. The free running model propulsion system is very simple, with two fixed pitch propellers driven by two Electric Propulsion Motors. The propulsion plant layout is shown in Figure 2.

The full scale (ship) propulsion plant is a CODLAG (COmbined Diesel eLectric And Gas turbine) system. As regards the prime movers, one gas turbine is used when a high power is required. One electric motor for each shaft is installed for low speed or silent operation. When the maximum power is needed, the main engines may be used all-together. A particular kind of gearbox is present, characterized by one input and two output shafts. Each shaft drives a controllable pitch propeller. The propulsion plant layout is shown in Figure 3.

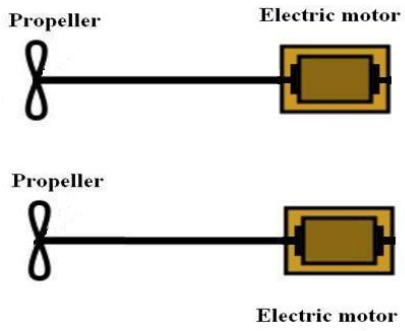


Figure 2: Model propulsion plant

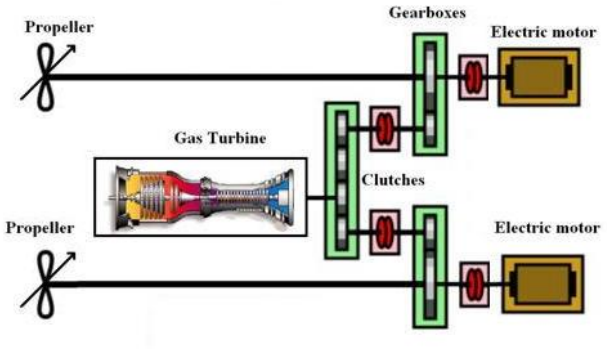


Figure 3: Full scale propulsion plant

The two shaft lines have been studied independently. By solving the differential equations of the shaft lines (1) it is possible to obtain the shaft lines dynamics.

$$2\pi J_p \frac{dn(t)}{dt} = Q_e(t) - Q_p(t) - Q_f(t) \tag{1}$$

Where:

J_p is the shaft line polar inertia
Q_e is the engine Torque
Q_p is the propeller Torque
Q_f is the torque due to the friction
n is the shaft line revolution

The aim of this paper is to focus attention on the propulsion controller, therefore a simplified model for the main engines has been used in order to reduce the computational time. Considering the electric motors, the torque has been modelled by a proper transfer function, applied to the shaft revolution error between setpoint and feedback. With regard to the gas turbine, the numerical dependence of power on shaft revolutions and fuel consumption flow rate has been used; the adopted data have been provided directly by the manufacturer. By an interpolation process, it is possible to obtain the gas turbine power (or torque). The fuel flow is evaluated by the gas turbine controller, on the basis of the gas generator rotational speed. Finally, the gearbox model includes the speed reduction ratio and the logics of the clutches activation.

2.2 Propulsion Control Systems

As remarked above, the propulsion control is usually very simple in model tests; in the present case, a series of free running model tests have been carried out preliminarily using various control system approaches, namely keeping constant (and equal to the value of the approach phase) revolution per minute (RPM), torque or power. The simulator in model scale has been calibrated on the basis of experimental results, showing a good correspondence in all the control system configurations, as reported in [5]. The constant RPM approach is more frequently adopted in free running model tests, because of its straightforwardness; this work mainly focuses on it.

In the full scale ship, and then in her simulation model, the use of a CODLAG propulsion system with two controllable pitch propellers led to the need of developing dedicated control functions [4]. First of all, the propulsion system is managed by a typical "combinator" law, where the equilibrium point for pitch and rpm have been implemented. For what concerns the engines, a limiting maximum torque, based on a PID algorithm was introduced.

Moreover, the over torque protection for shaft lines was also introduced, by means, at first, of a control function reducing propeller pitch; when this action is not sufficient, a fuel flow rate reduction acts in order to avoid shaft lines overload. Due to the particular gearbox, that forces the two shaft lines to operate at the same rpm, also a torque balance function has been designed. An overview on the considered control variables is shown in Figure 4.

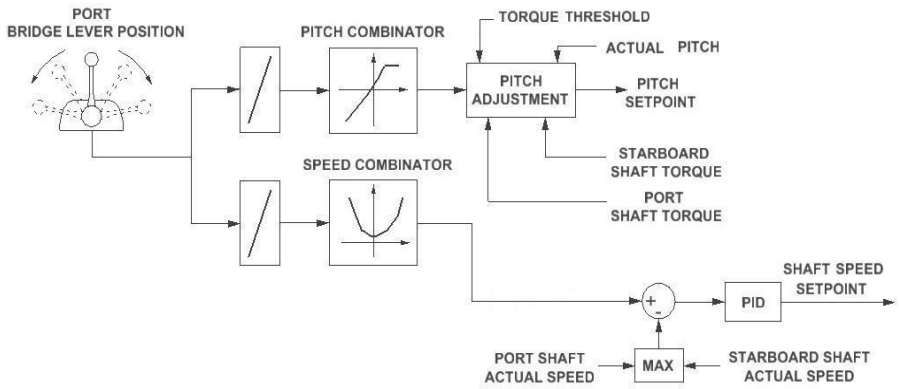


Figure 4: Control system layout

2.3 Manoeuvrability model

The model used in this work is fully described in [6] and [7], to which the reader is referred for a more detailed discussion. The model, characterized by a modular form, has been specifically developed in order to consider the peculiarities of a twin screw ship manoeuvrability, with particular attention to the appendages configuration, which may play a very important role. A further peculiarity of the adopted model is the possibility to consider shaft unbalances. In particular, the asymmetric behaviour of the two shafts is considered using an asymmetric variation of the wake fraction, as already proposed in [8].

In addition to this, the large amount of experimental data, recorded during the free running model tests, allowed to further validate the manoeuvrability model in order to take into

account a second asymmetry in propeller thrust, by means of an asymmetric correction factor applied to the propeller thrust during manoeuvres [5].

In particular, the values of the two correction coefficients were evaluated for the internal and external shafts on the basis of experimental data as a function of the ship drift angle (obtained at different rudder angles during manoeuvres) and of the ship speed.

The mathematical model is the same for the two simulators in model and full scale configuration and the hydrodynamic coefficients have been voluntarily considered constant; the total resistance of the hull has been opportunely scaled in accordance to usual practice.

3 SIMULATION RESULTS

In this section, some simulation results concerning both the free running model and the full scale ship are presented, allowing to outline some differences between the two cases. Three manoeuvres, corresponding to different rudder angles δ_R and Froude numbers Fn, have been proposed hereinafter (Table 2).

Table 2: Proposed manoeuvres

Test	δ_R [°]	[F_n]
Turning circle (A)	max	0.26
Turning circle (B)	max	0.39
ZIG-ZAG (C)	δ_0	0.39

For all the simulated manoeuvres, trajectory, heading, velocities and propulsion parameters have been considered. In the following figures, non-dimensional data are reported; propulsion parameters (propeller pitch, shaft revolutions, torque), have been made non dimensional with respect to the values corresponding to the rectilinear motion in the approach phase.

The first simulated manoeuvre (A) is a turning circle at medium speed. In this manoeuvre the influence of the control system is practically not visible, since all machineries operate below their operational limits and no protection actions are required. However, it is possible to see, in Figure 10, the asymmetrical behaviour of the two shafts with torque increasing more on the external shaft (about 60% with respect to 20% on internal shaft in correspondence to the stabilized phase of the manoeuvre) for both model and full scale ship. In Figure 6, 7 and 8 it is possible to appreciate some differences between velocities; these differences could be partly due to the different propeller working regimes in full and model scales (for example resistance scaling), and to the consequent different effect on the rudder. As a consequence, the predicted trajectory is slightly larger in full scale.

The second manoeuvre (B) is a turning circle corresponding to a higher speed, slightly lower than the maximum speed. In this case, it possible to appreciate larger differences between the model and the full scale ship. Figure 18 shows the shaft torque during the proposed manoeuvre, clearly showing the torque limitation for the external shaft in order to avoid over torque. This reduction is achieved acting on the propeller pitch (see Figure 15). In addition to this, in Figure 17 a decrease of shaft revolution for both shafts is visible; this reduction is due to the prime mover not being able to provide the required torque. As a consequence of this propulsion system running, it is possible to see (Figure 13, 14, 16) that the ship velocities drop is slightly larger in full scale than the previous manoeuvre.

Also the effect on the trajectory is slightly larger, even if still resulting in rather small variations.

The last proposed manoeuvre (C) is a Zig-Zag manoeuvre at a high speed. Also in this case, a propeller RPM reduction (Figure 23) is visible in full scale, due to the torque limits of the prime movers; moreover, a further (very limited) torque reduction on the external shaft during each counter-rudder, by means of the propeller pitch (Figure 25), is present. Notwithstanding these differences, it is clear that the effect on the manoeuvre is very limited, since the macroscopic parameters are almost invariant (Figure 26 and 19-22).

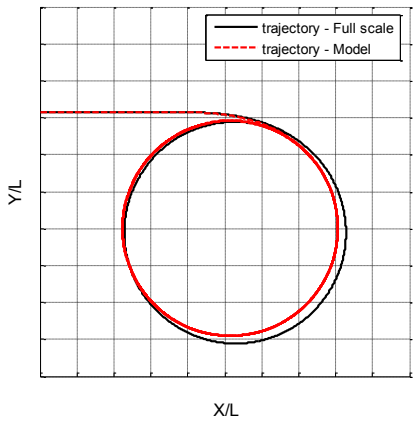


Figure 5: Ship trajectory (man A)

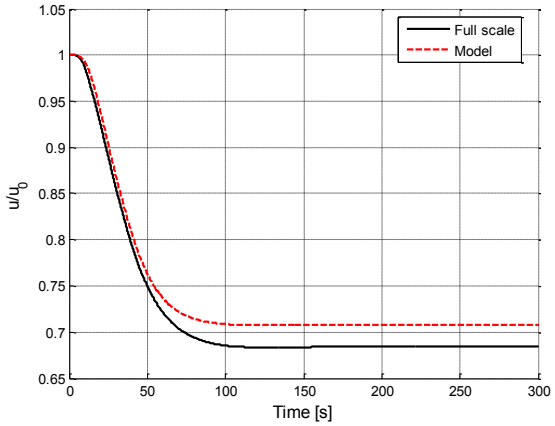


Figure 6: Surge velocity vs. Time (man A)

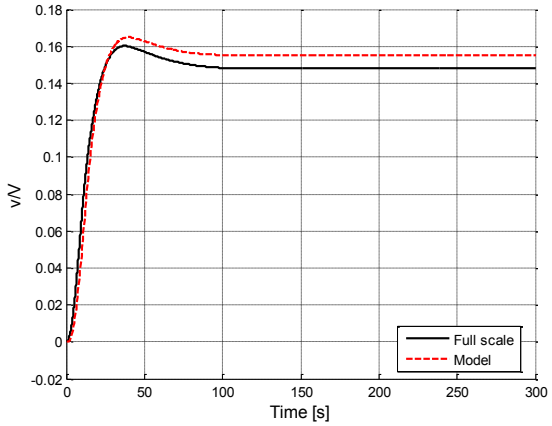


Figure 7: Sway velocity vs. Time (man A)

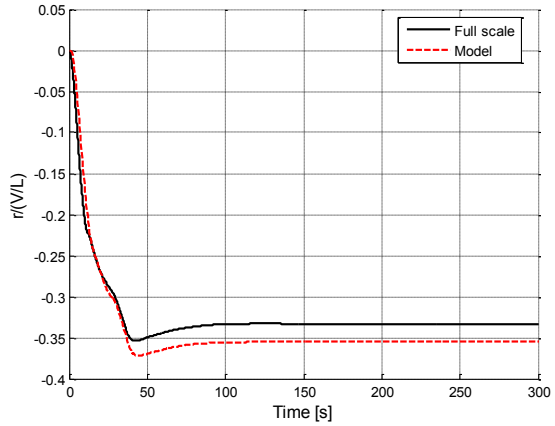


Figure 8: Yaw rate vs. Time (man A)

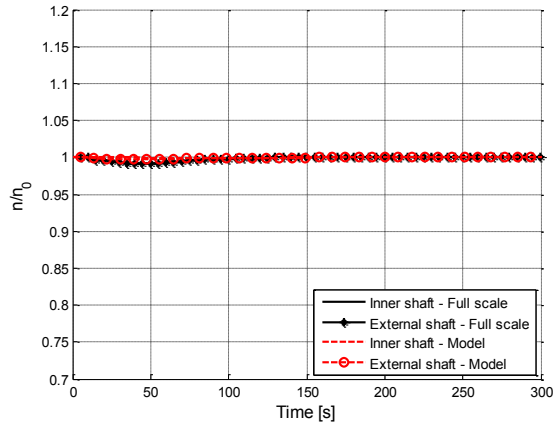


Figure 9: Shaft lines revolution vs. Time (man A)

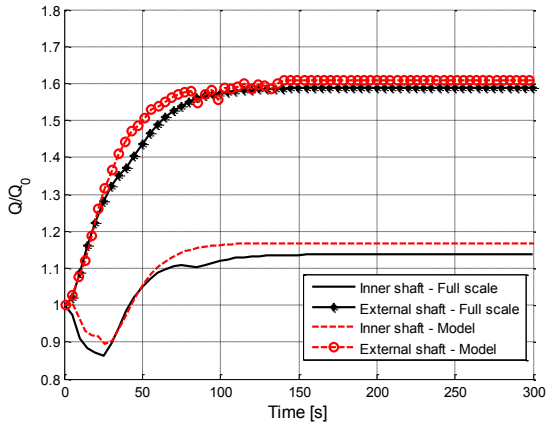


Figure 10: Torque vs. Time (man A)

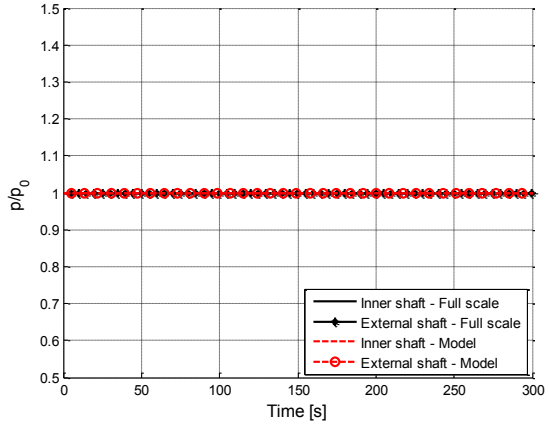


Figure 11: Pich angle vs. Time (man A)

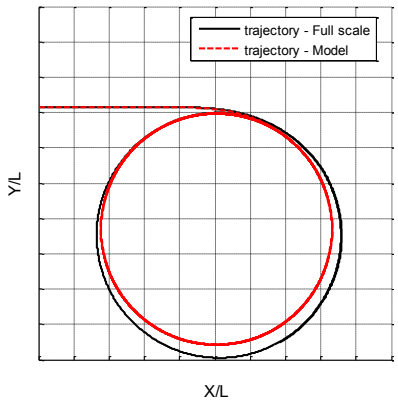


Figure 12: Ship trajectory (man B)

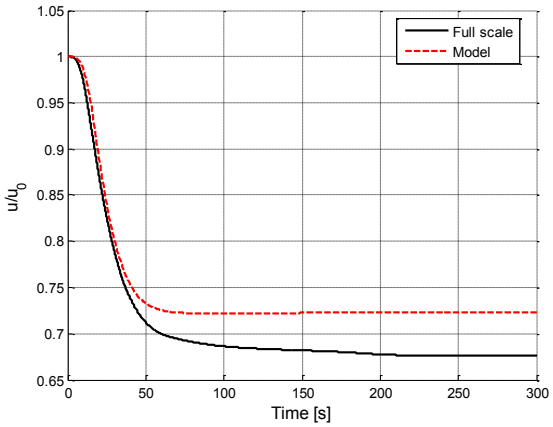


Figure 13: Surge velocity vs. Time (man B)

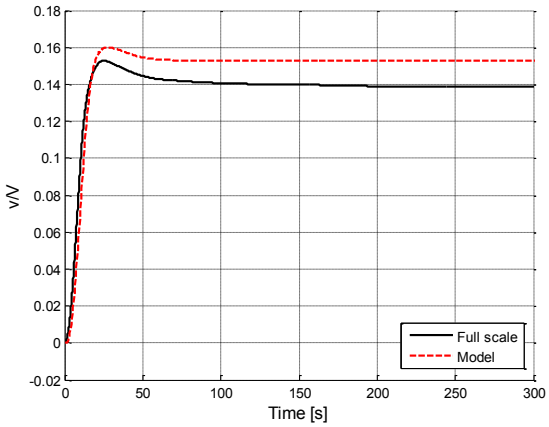


Figure 14: Sway velocity vs. Time (man B)

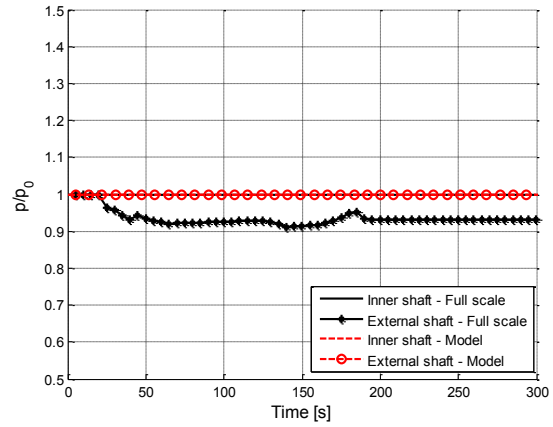


Figure 15: Pich angle vs. Time (man B)

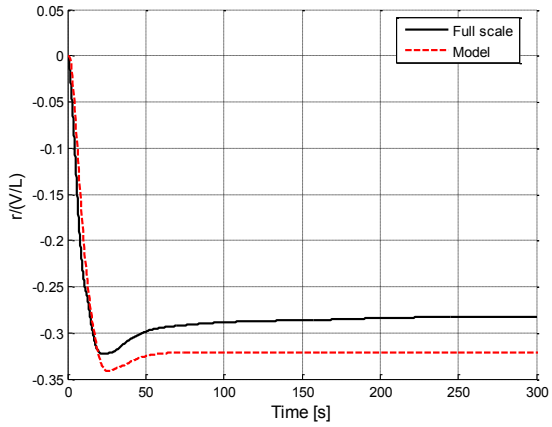


Figure 16: Yaw rate vs. Time (man B)

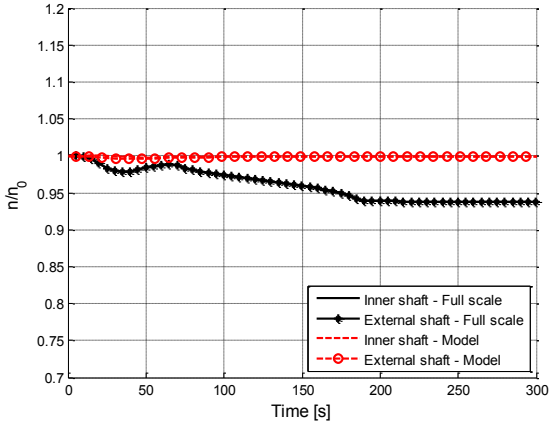


Figure 17: Shaft lines revolution vs. Time (man B)

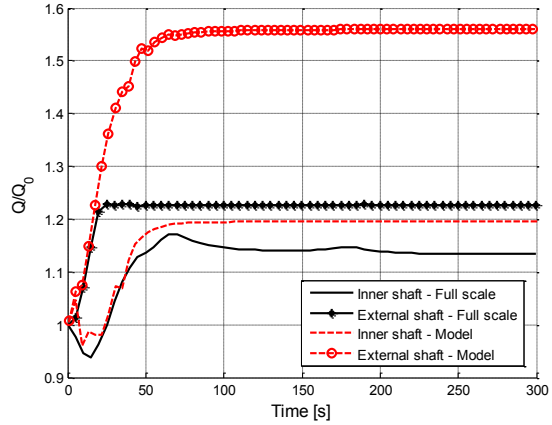


Figure 18: Torque vs. Time (man B)

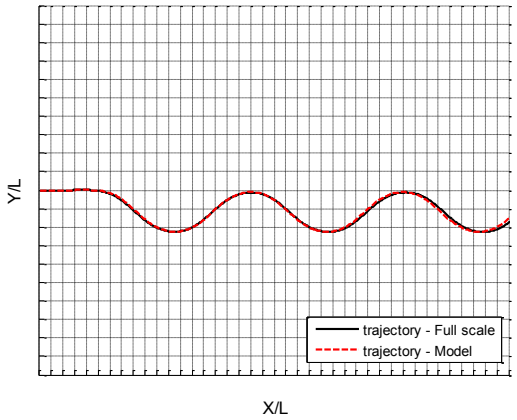


Figure 19: Ship trajectory (man C)

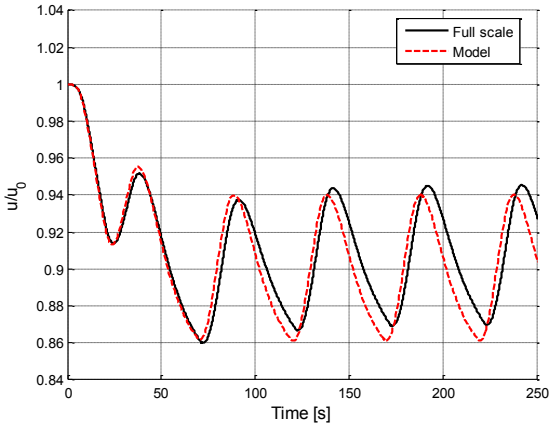


Figure 20: Surge velocity vs. Time (man C)

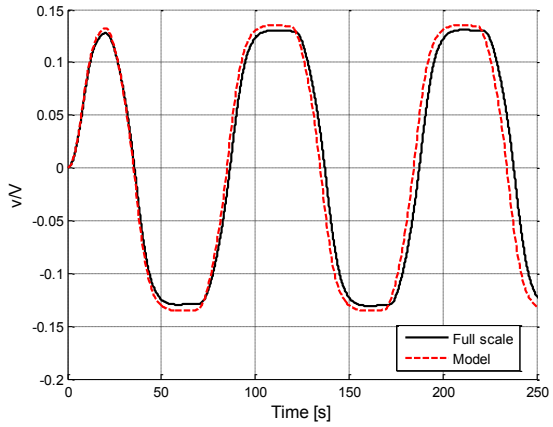


Figure 21: Sway velocity vs. Time (man C)

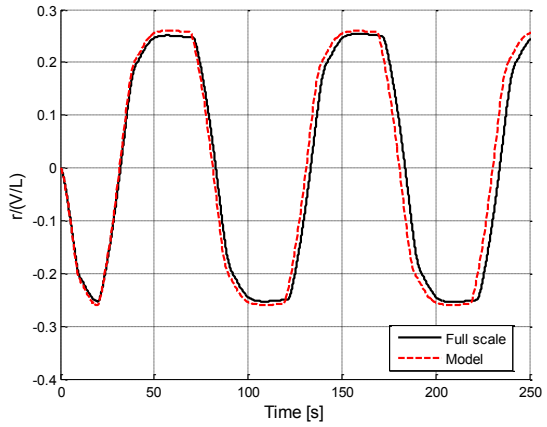


Figure 22: Yaw rate vs. Time (man C)

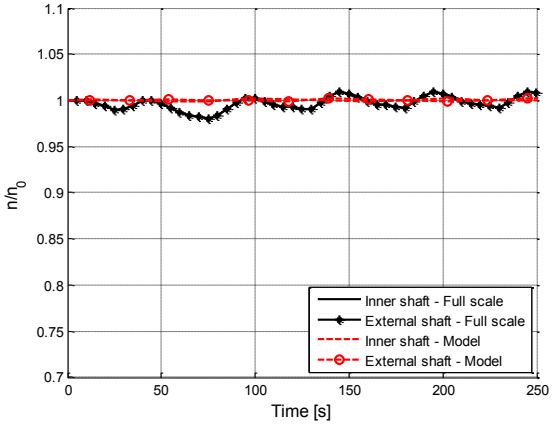


Figure 23: Shaft lines revolution vs. Time (man C)

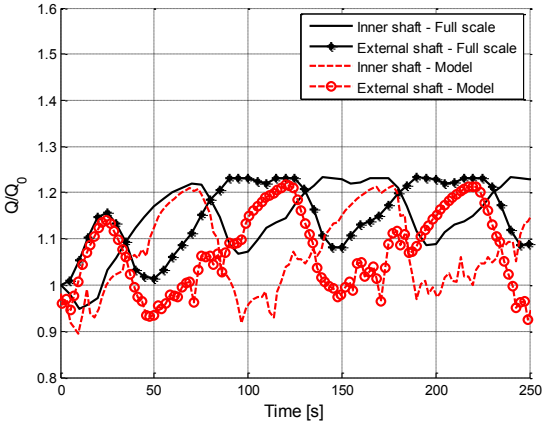


Figure 24: Torque vs. Time (man C)

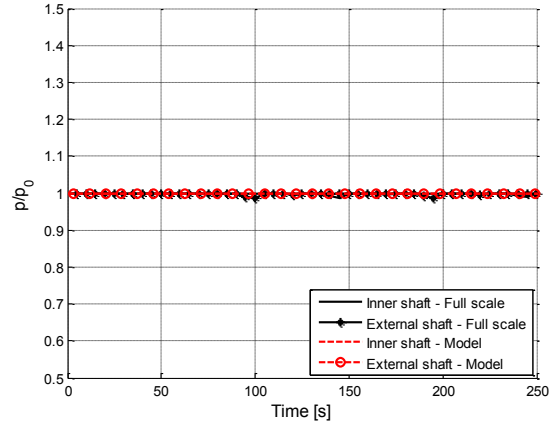


Figure 25: Pich angle vs. Time (man C)

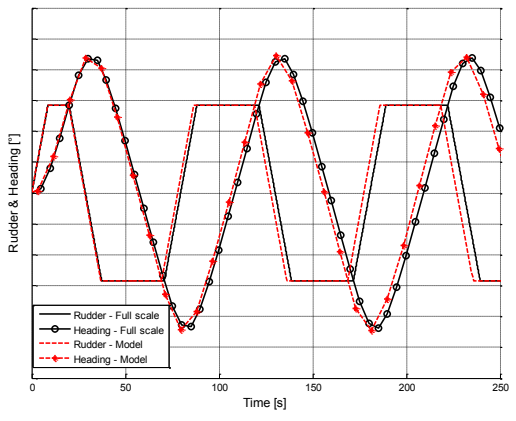


Figure 26: Rudder & Heading vs. Time (man C)

4 CONCLUSIONS

A comprehensive time domain manoeuvrability and propulsion plant simulator representing a twin screw ship both in model scale and in full scale, has been presented. The developed simulation models present the peculiarity of a modular structure that allows to represent the ship in different scales and with different propulsion configurations.

A series of simulations have been performed in order to analyse possible non-linear effects of automation on the propulsion plant behaviour during manoeuvres. For particular marine propulsion plants, these effects could not be analysed with model tests and would require the full scale ship availability.

The propulsion control effects resulted in a very limited influence on macroscopic manoeuvrability characteristics for low Froude numbers, as it could be expected, while differences are more significant when higher Froude numbers are considered.

It is believed that the simulation technique may be an essential tool in order to optimize the ship propulsion system control strategies or more generally the global ship performances. In order to increase the capability and reliability of the simulators, it is deemed of utmost importance to further validate the proposed methodology through full scale sea trials; the parallel analysis of model tests and full scale experimental data could be also useful in order to investigate other scale effects (e.g. variation of hydrodynamic coefficients) which have not been taken into account in the present work.

REFERENCES

[1] M. Viviani, C. Podenzana Bonvino, S. Mauro, M. Cerruti, D. Guadalupi, A. Menna, (2007). *"Analysis of Asymmetrical Shaft Power Increase During Tight Manoeuvres"*, Proceedings of the 9th International Conference on Fast Sea Transportation (FAST2007), Shanghai, China, September 2007.

[2] Altosole M., Figari M., Martelli M. (2012). *"Time domain simulation for marine propulsion applications"*, Proceedings of the 44th Summer Computer Simulation Conference, 2012 International Simulation Multi-Conference, Genoa, Italy, July 8-11, 2012. ISBN: 1-56555-348-9.

[3] Campora, U., Figari, M., (2003). *"Numerical Simulation of Ship Propulsion Transients and Full Scale Validation"*. Journal of Engineering for the Maritime Environment, Vol. 217.

[4] Altosole M., Benvenuto G., Campora U., Figari M., (2009). *"Real-Time Simulation of a COGAG naval Ship Propulsion System"*. Journal of Engineering for the Maritime Environment, Vol. 223, N. 1.

[5] Coraddu, A., Dubbioso, G., Guadalupi, D., Mauro, S., Viviani, M., (2012). *"Experimental investigation of asymmetrical propeller behavior of twin screw ships during manoeuvres"*, MARSIM2012, Singapore 23-27 April 2012.

[6] Di Mascio, A., Dubbioso, G., Notaro, C., Viviani, M. (2011) . *"Investigation of twin screw naval ships manoeuvrability behavior"*, Journal of Ship Research, Vol.55, N.4, December 2011, p. 221-248(28)- ISSN 0022-4502, Online ISSN: 1542-0604 - DOI: 10.5957/JOSR.55.4.090031

[7] Dubbioso, G., Viviani, M. (2012) *"Aspects of twin screw ships semi-empirical maneuvering models"*, Ocean Engineering 48 (2012) 69-80, ISSN 0029-8018, Elsevier, doi:10.1016/j.oceaneng.2012.03.007

[8] Viviani, M., Altosole, M., Cerruti, M., Menna, A., Dubbioso, G. (2008). *"Marine Propulsion System Dynamics During Ship Manoeuvres"*, 6th International Conference On High-Performance Marine Vehicles (Hiper 2008) , 18/19/09/2008 – Naples, ISBN: 8890117494, p.81-93.

V International Conference on Computational Methods in Marine Engineering
MARINE 2013
B. Brinkmann and P. Wriggers (Eds)

BULBOUS BOW SHAPE OPTIMIZATION

L. BLANCHARD*, E. BERRINI‡, R. DUVIGNEAU*
Y. ROUX†, B. MOURRAIN* & E. JEAN+

*INRIA Sophia-Antipolis Méditerranée
2004 route des lucioles, 06902 Sophia-Antipolis, France
e-mail: Regis.Duvigneau@inria.fr, web page: http://team.inria.fr/opale

‡ MyCFD
Le Busniess Pole, 25 Allée Pierre Ziller, 06650 Sophia-Antipolis, France
e-mail: elisa@mycfd.com - Web page:

† K-EPSILON
Espaces Antipolis, 300 routes des Cretes, 06902 Sophia-Antipolis, France
e-mail: yann@k-epsilon.com - Web page: http://www.k-epsilon.com

+ Jean & Frasca Design
9, Rue Plan Fourmiguier, 13 007 Marseille, France
e-mail: jfdesign@free.fr - Web page: http://www.jean-et-frasca.com

Key words: Bow, Shape optimization, Wave resistance

Abstract. The aim of this study is to prove the usefulness of a bulbous bow for a fishing vessel, in terms of drag reduction, using an automated shape optimization procedure including hydrodynamic simulations. A bulbous bow is an appendage that is known to reduce the drag, thanks to its influence on the bow wave system. However, the definition of the geometrical parameters of the bulb, such as its length and thickness, is not intuitive, as both parameters are coupled with regards to their influence on the final drag. Therefore, we propose to use an automated shape optimization procedure, based on a high-fidelity flow solver, a surrogate model-based optimizer and a CAD-based geometrical model, to derive the characteristics of the bow geometry allowing to maximize the achievable drag reduction. The numerical tools are first presented, and then applied to the optimization of a bow shape for a real fishing vessel, in order to determine the optimal length and thickness of the bow for drag reduction purpose.

1 INTRODUCTION

Simulation-based design optimization procedures are of growing interest in naval engineering, since CFD (Computation Fluid Dynamics) simulations are now reliable and this approach allows to obtain a significant performance improvement for a moderate cost, in comparison with experimental campaigns using towing tank facilities. Moreover, the optimization is based on a rigorous mathematical framework that can outclass the intuition and propose original design solutions.

To solve realistic problems, the design procedure should include several software components, such as a geometrical modeler, a grid generator, a flow solver and a design optimizer, each of them relying on complex numerical methods. Because of the computational costs related to high-fidelity simulations (unsteady turbulent flows with free-surface capturing), the efficiency of the overall procedure is a critical aspect for application to real-life problems.

In the present study, we present some recent numerical developments, originating from academic and industrial fields, to overcome the different issues that arise when solving realistic problems. In particular, we describe how the computational grid is generated automatically from a reduced set of parameters, via a CAD-based (Computer-Aided Design) model. We also make a focus on the use of surrogate models in this complex context. The optimization of a bulbous bow for a real fishing vessel is considered as test-case.

2 DESIGN PROCEDURE

The design optimization procedure gathers different software components: the *CAD modeler* in charge of constructing a geometrical hull model from a set of design parameters, the *grid generator* in charge of building the computational domain in accordance with the geometry, the *flow solver* in charge of computing the ship performance and finally the *optimizer* in charge of providing a new set of parameters according to the past simulations.

The optimization algorithm used for this study relies on the construction of a surrogate Gaussian model, that is used to derive new sets of design parameters at each iteration. Then, the evaluation of the performance values associated to these sets can be achieved independently, in a parallel way. The overall procedure is described schematically by Figure 1.

3 NUMERICAL METHODS

3.1 Hull geometric model

The construction of the geometrical model for design optimization purpose is a difficult task, since it has to fulfill several criteria, sometimes antagonistic. Firstly, the shape of interest should be precisely defined, but at the same time one would like to modify it with a few number of design parameters to facilitate the optimizer task. Secondly, a high regularity and accuracy is required to allow the fluid mesh generation, while some sharp edges should be maintained. Moreover, large deformations should be permitted, and the

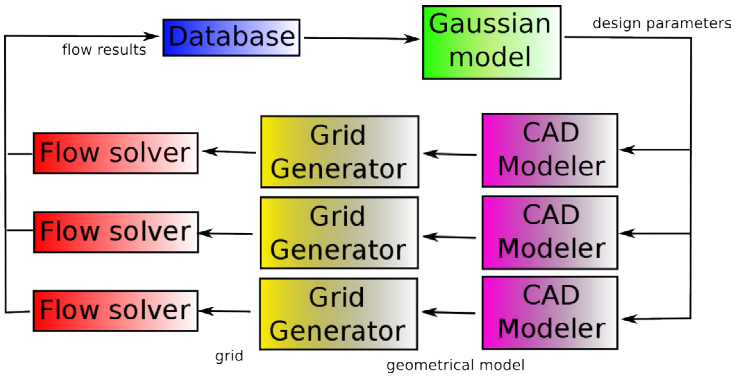


Figure 1: Overview of surrogate model-based optimization procedure.

final optimized shape should be compliant with respect a classical CAD systems, to allow a manufacturing process.

To try to fulfill most of these criteria, the construction of the geometric model is achieved with the help of the CAD platform Axel, developed at INRIA by Galaad Project-Team (`http://axel.inria.fr`). The baseline geometry of the fishing vessel without bow is imported in IGES format, yielding the definition of the geometry as a set of cubic NURBS patches, as illustrated by Figure 2. The white dots represent the NURBS control points.

To generate the bow shape, a restricted patch is defined by cutting the baseline patch along constant parameter curves, in blue on Figure 2. then, its control points can be moved to create the desired shape. Finally, the two patches are merged back into a single NURBS patch, which allows to ensure a C^2 surface regularity at the junction between the bow and the hull, as illustrated by Figure 2.

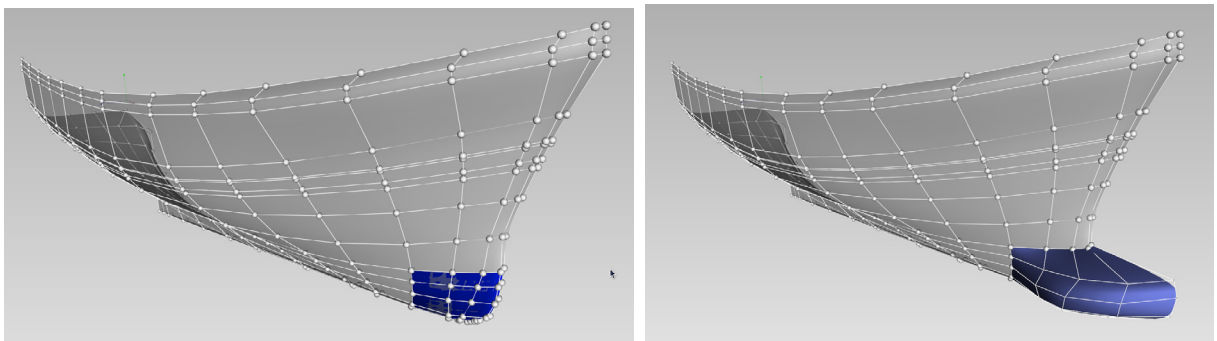


Figure 2: Baseline (left) and deformed (right) geometrical model.

This bow shape is obtained by moving approximately 20 control points, yielding a bow defined by 60 design variables. In the perspective of design optimization, the shape

definition has to be reduced to a smaller set of meaningful parameters, which avoid the generation of non-realistic bows. Therefore, a two-step approach is adopted: a baseline deformation is first defined by moving the control points, in order to generate a nearly cylindrical bow shape. In a second step, a family of bows is generated by applying some homothetic transformations, according to only two parameters: the bow length and thickness. Figure 3 shows some representatives of this family, that correspond to different length and thickness parameters. Finally, these two parameters are chosen as optimization variables for the forthcoming study.

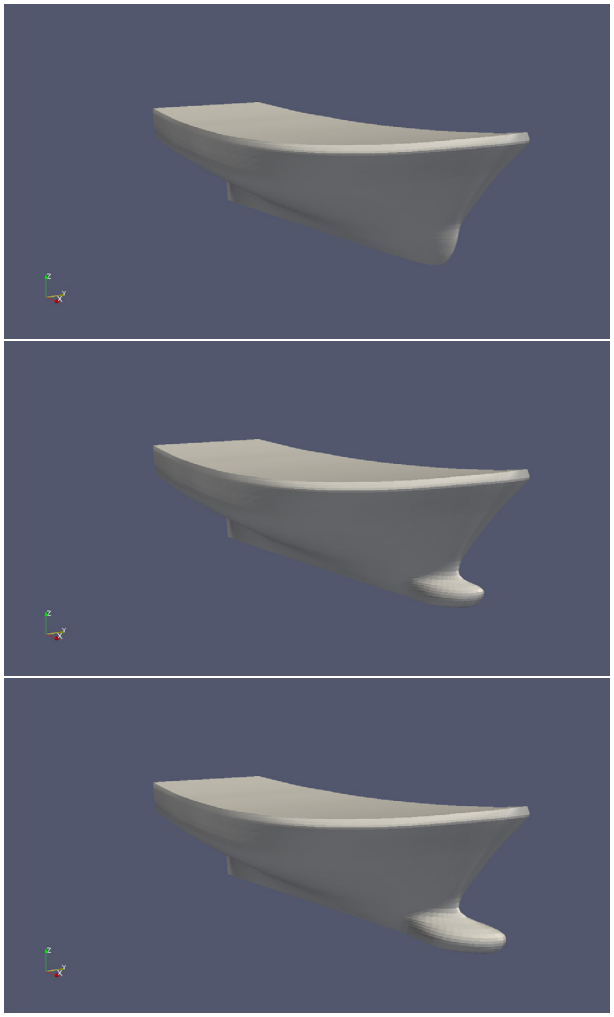


Figure 3: Some representatives of the generated hull shapes.

3.2 Mesh generation

To generate the computational grid, a closed water-tight triangularized volume, embedding the ship hull, should be generated. This task is carried out by defining additional NURBS patches on the plane surfaces limiting the computational domain and then discretizing all the patches along constant parameter values.

An body-fitted computational grid is then built using the software HEXPRESS^{TM}from Numeca International. HEXPRESS^{TM}generates non-conformal full hexahedral unstructured meshes on complex arbitrary geometries. In addition, the advanced smoothing capability provides high-quality boundary layers insertion [6, 7]. One of the meshes of our study case is illustrated by Figure 4. The grid generation process requires closed geometries to provide robust meshes. During the triangulation generation, a nonconforming mesh is produced, leading to the appearance of holes in the geometry. Therefore, the computational grid required human intervention in order to force HEXPRESS^{TM}to correct these discontinuities in the mesh. For some large bow deformations, involving large triangulation deformation, the computational grid could not be generated.

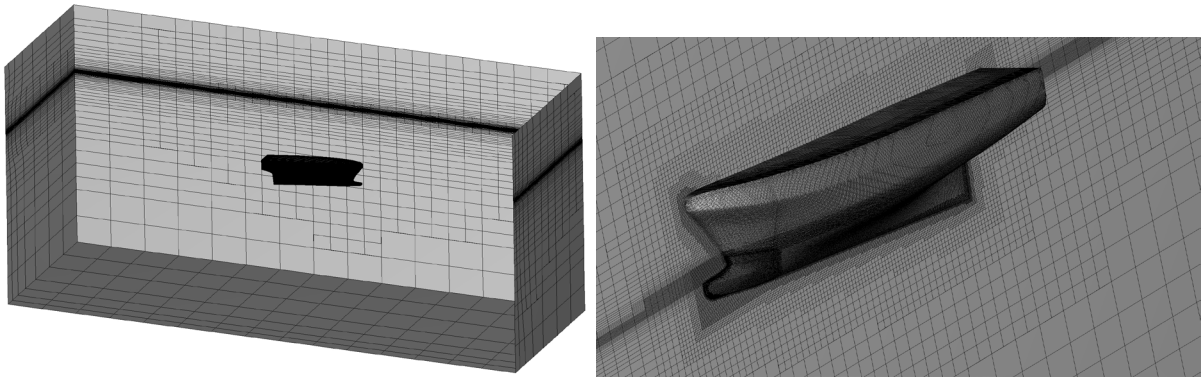


Figure 4: Some generated meshes of hull.

During the computation, the automatic mesh refinement feature has been used. Automatic, adaptive mesh refinement is a technique for optimising the grid in the simulation, by adapting the grid to the flow as it develops during the simulation. This is done by locally dividing cells into smaller cells, or if necessary, by merging small cells back into larger cells in order to undo earlier refinement. During the computation, the number of cells increases from 3 to 3.6 million cells.

3.3 Flow simulation

ISIS-CFD, available as a part of the FINE^{TM}/Marine computing suite, is an incompressible, unsteady Reynolds-averaged Navier-Stokes (RANS) solver [3, 4]. The solver is based on the finite volume method to build the spatial discretisation of the transport

equations. The unstructured discretisation is face-based, which means that cells with an arbitrary number of arbitrarily shaped faces are accepted. This makes the solver ideal for adaptive grid refinement, as it can perform computations on locally refined grids without any modification.

Free-surface flow is simulated with a multi-phase flow approach: the water surface is captured with a conservation equation for the volume fraction of water, discretised with specific compressive discretisation schemes [4]. Furthermore, the method features sophisticated turbulence models [3] and 6 DOF (Degree Of Freedom) motion simulation for free moving ships [5]. In our case, only 2 DOF are used. Post-processing for our test-case illustrates the simulation of the free surface motion on Figure 5.

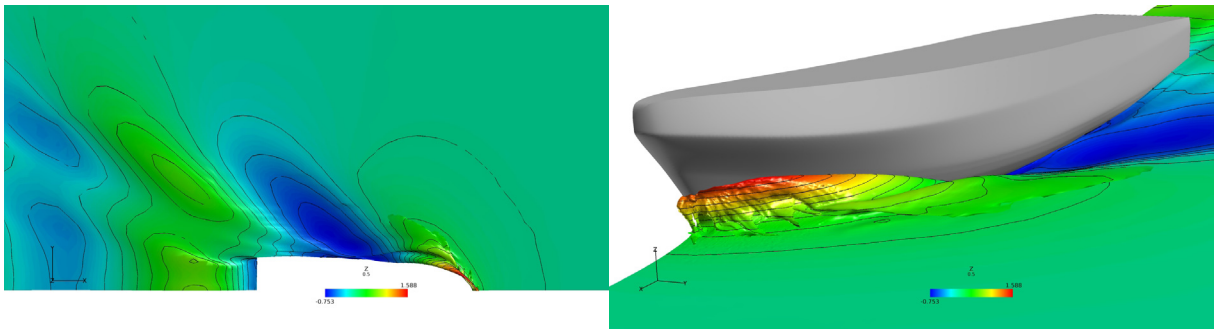


Figure 5: Post-processing of the ISIS-CFD^{TM}computation

3.4 Optimization

When dealing with three-dimensional turbulent flows, possibly unsteady flows, the main issue for the purpose of optimization is the computational burden. The evaluation of the objective function gradient using an adjoint approach is highly complex and the non-linearities underlying phenomena may generate multimodal objective functions exhibiting several local optima. Furthermore, simulation errors due to spatial and temporal discretization, partial convergence, etc, make the evaluations noisy. To address all these issues, the use of a surrogate model-based algorithm is adopted in the present study. In particular, this work is focused on the Efficient Global Optimization (EGO) algorithm.

The Efficient Global Optimization (EGO) is a global optimization algorithm that makes use of a stochastic surrogate model to drive the optimization [1]. One may be wondering about using a stochastic model, although the system is fully deterministic. This is justified by the fact that the model is constructed on the basis of a finite number of observations. The resulting uncertainty is modeled in a stochastic framework.

The algorithm starts from a Design of Experiments (DOE) phase: A database exploring the bounded search space is generated from simulation results. This database contains the objective function values, each of them being associated to a set of design parameters. In

a second phase, a Gaussian process model is constructed using this database, which allows the prediction of both the objective function value and an estimated model uncertainty at any point of the search domain. According to these predictions, the most interesting points are selected by means of a merit function. Usually, one selects the points that maximize the Probability of Improvement (PI) or the Expected Improvement (EI) merit function. Once evaluated, the corresponding objective function values are added to the database. This process is repeated until convergence, as illustrated on Fig. 1. A detailed description of the model construction and the merit function treatment can be found in [2]. The algorithm is part of the FAMOSA platform, developed at INRIA by Opale Project-Team.

4 APPLICATION TO A FISHING VESSEL

4.1 Initial fishing vessel without bow

The hull studied is an existing fishing vessel. Its main characterisics are :

- Boat speed : 6.687 m/s (12 nds)
- Length : 22m
- Center of gravity : (10.42, 0, -0.75)
- Displacement : 150 Tons

Simulation set up is the following :

Fluid characteristics

	$\rho(kg/m^3)$	$\mu(Pa.s)$
Water	1025	$1.07 * 10^{-3}$
Air	1.2	$1.85 * 10^{-5}$

Fluid domain

	min	max
X	-62	+61
Y	-41	0
Z	-41	+16

- Froude number 0.45
- Reynolds number $1.4 * 10^8$
- Turbulence model : SST $k - \omega$
- Motion : trim and sinkage solved
- Motion : imposed speed according to a half sinusoidal ramp law from 0 m/s to 6.687 m/s in 12 seconds

The reference drag computed for the initial half-hull without bow is $-7.4829 * 10^4$N

4.2 Design of experiments

As explained above, the first phase of the design procedure consists in exploring the design space using a DOE approach. Therefore, two admissible intervals are defined for the two selected design parameters (length l and thickness t), such as $1.4 < l < 2.8$ and $0.0 < t < 1.4$, and a distribution of design points is generated. A first set of points, corresponding to moderate bow dimensions, is created according to a Latin Hypercube Sampling (LHS). Additional points are then added to explore the possibility of larger deformations. Figure 6 shows the 22 design points in the parameter space.

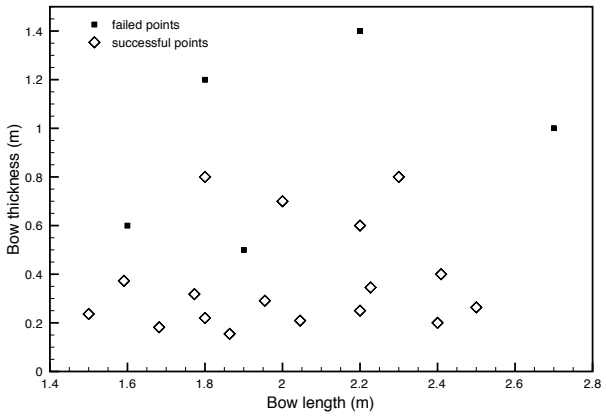


Figure 6: Design of experiments.

The evaluation of the performance corresponding to these points shows that about 20% of the evaluations fails, especially for large bow deformations (grid generation failures). . Therefore, the forthcoming study is restricted to mild shape deformation $l < 2.5$ and $t < 0.8$.

4.3 Optimization of length and thickness

A Gaussian surrogate model is constructed on the basis of the successful evaluations. A major difficulty arises here, due to the fact that the estimated resistance values are very close to each other. Actually, the variation of the total resistance observed over the computed set is about 5%, which is nearly the accuracy of the resistance prediction. Since the surrogate model construction permits to take into account some uncertainty on the evaluations (noisy observations), a range of models is built, from an interpolating model which supposes that the evaluations are exact, to models based on a prescribed error value, in terms of standard deviation. The three models are depicted in Figure 7.

The interpolating model exhibits some oscillations and several interesting areas. In particular, the most efficient bow shapes are found either for a long and thin bulb ($l \simeq 2.0$ and $t \simeq 0.2$), or for a longer and bulky bulb ($l \simeq 2.3$ and $t \simeq 0.8$), as shown in Figure 9.

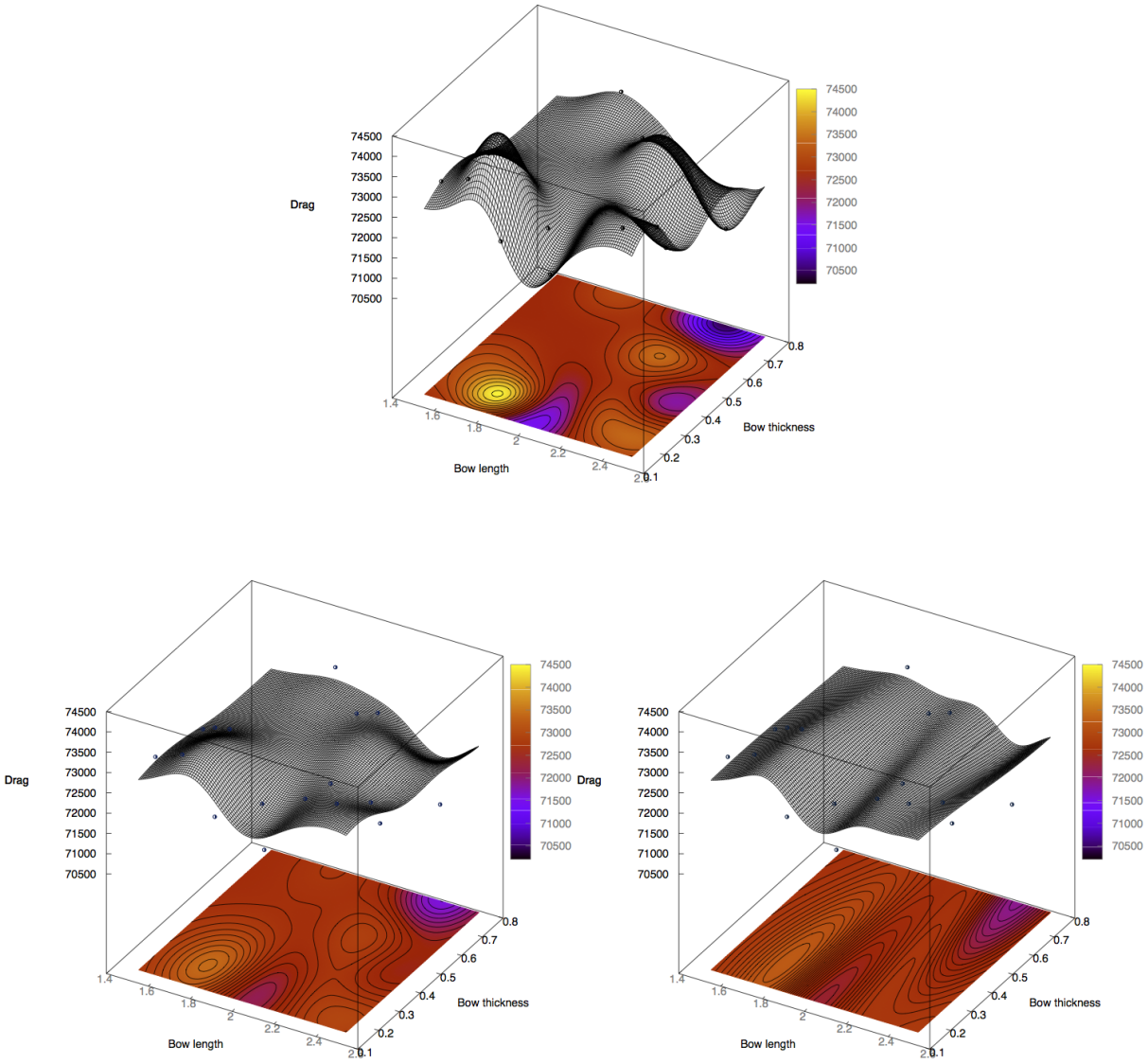


Figure 7: Surrogate model without error (top), with 1% error (left) and 2% error (right).

Unfortunately, the best design point found (6% drag reduction with respect to the original fishing vessel) is located on the boundary of the search domain. One should notice that all tested bows improve the estimated performance.

When a rather small evaluation error is taken into account, the model quickly becomes flat, which indicates that the numerical error plays a critical role here and it is difficult to identify a clear trend with the current set of evaluations. Nevertheless, the two interesting

regions already identified remain, even if their extent is not so obvious.

If one determines the design point that maximizes the Expected Improvement criterion, the first two models agree to select a point on the right boundary of the domain ($l \simeq 2.5$ and $t \simeq 0.5$), in black on Figure 9. For the last model, the flat behavior yields a point almost equal to the best point found so far, at the top right-hand corner of the domain.

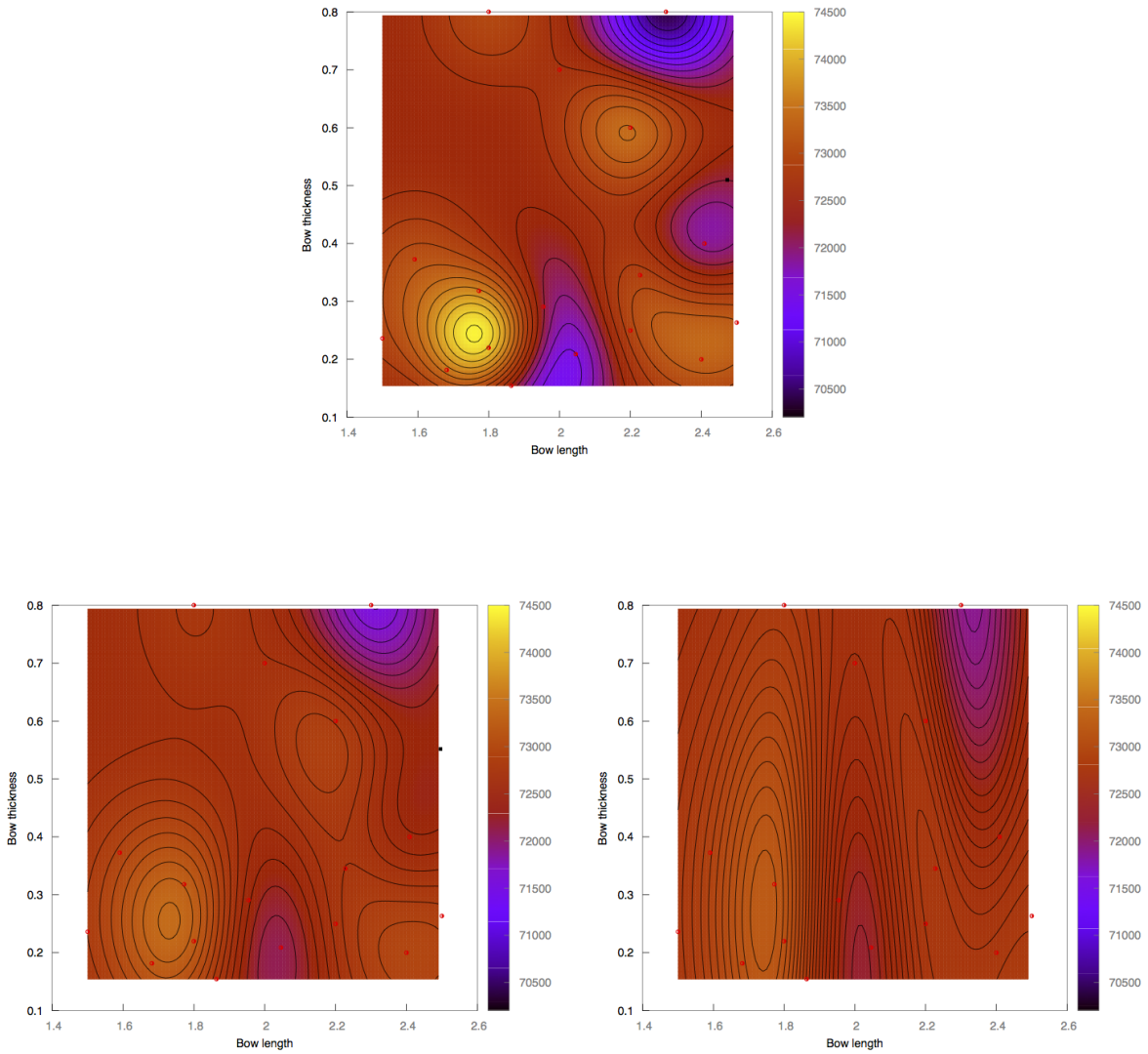


Figure 8: Performance map without error (top), with 1% error (left) and 2% error (right).

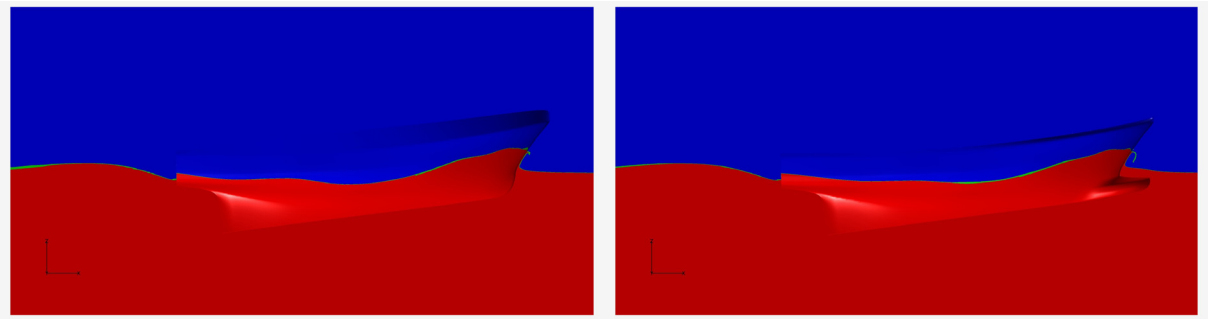


Figure 9: Reference Bulb and actual best bulb.

5 CONCLUSIONS

A design optimization procedure, based on a high-fidelity CFD analysis tool has been developed and applied to a realistic problem, dealing with the optimization of the bow shape of a fishing vessel. The difficulty to automatically generate a suitable computational grid from any set of design parameters has been reported, and has unfortunately restricted the admissible interval of design parameters. Another difficulty related to the construction of surrogate models in the presence of numerical errors arising from the simulation has also been pointed out.

Nevertheless, this study demonstrates that it is now possible to construct a design optimization loop based on sophisticated numerical tools in naval engineering context and apply it to real life problems. Forthcoming developments will extend the current methods and results.

6 ACKNOWLEDGEMENT

This study was achieved in the framework of the National project "Bulbe", funded by the "Fond Européen pour la Pêche" (FEP).

REFERENCES

[1] D. Jones. A taxonomy of global optimization methods based on response surfaces. *Journal of Global Optimization*, **21**:345–383 (2001).

[2] R. Duvigneau and P. Chandrashekar. Kriging-based optimization applied to flow control. *Int. J. for Numerical Methods in Fluids*, **69**, 11 (2012).

[3] R. Duvigneau, M. Visonneau, and G.B. Deng. On the role played by turbulence closures in hull shape optimization at model and full scale. J. Marine Science and Technology, 8(1), 125 (2003).

[4] P. Queutey and M. Visonneau. An interface capturing method for free-surface hydrodynamic flows. Computers & Fluids, 36(9), 14811510 (2007).

[5] A. Leroyer and M. Visonneau. Numerical methods for RANSE simulations of a self-propelled fish-like body. J. Fluid & Structures, 20(3), 975991 (2005).

[6] J. Wackers, G.B. Deng, A. Leroyer, P. Queutey, & M. Visonneau, Adaptive grid refinement algorithm for hydrodynamic flows, Computers & Fluids, Vol.55, pp. 85-100, 2012.

[7] J. Wackers, K. Ait Said, G.B. Deng, I. Mizine, P. Queutey & M. Visonneau Adaptive grid refinement applied to RANSE ship flow computation 28th ONR Symposium on Naval Hydrodynamics, Pasadena, October 2010, USA

V International Conference on Computational Methods in Marine Engineering
MARINE 2013
B. Brinkmann and P. Wriggers (Eds)

BEVEL GEAR CALCULATION OF A VESSEL DRIVE TRAIN WITH AZIMUTHING THRUSTERS

PROF. DR.-ING. BERTHOLD SCHLECHT*, DIPL.-ING. CHRISTIAN BAUER* AND DR.-ING. THOMAS ROSENLÖCHER*

*Institute of Machine Elements and Machine Design (IMM)
Technische Universität Dresden
01062 Dresden, Germany
e-mail: berthold.schlecht@tu-dresden.de, web page: http://www.me.tu-dresden.de

Key words: Computational Methods, Marine Engineering, Gear calculation

Abstract. Increasing requirements to modern vessels concerning performance and manoeuvrability led to very complex drive train designs. Therefore azimuthing thrusters became very common in the area of offshore supply vessels, tug boats and specialized research vessels. In order to extend the already huge field of operation and to better understand dynamic effects in such azimuthing thrusters the research project "EraNet HyDynPro" was started. The project focuses on the design of a robust drive train which contains a bevel gear stage. Therefore loads caused by propeller-water-interactions as well as loads while operating under ice conditions will be analysed. Based on this interdisciplinary project a contemporary way of gear calculation will be shown in this paper. For gear calculation it is necessary to acquire design loads. These can be measured at high costs or be simulated numerically. In the last few years the Multi-Body-System (MBS) Simulation got more and more popular to determine static and dynamic properties of large drive trains. This simulation can contain mathematical models of the propeller behaviour inside the water and under ice conditions as well as models of the electrical motor. Based on this a good prediction of gearing loads is possible. By the knowledge of the gearing load time series a complex tooth contact analysis can be made for every arbitrary point in time using specialized gearing software. Gear tiltings are considered in order to calculate the load distribution on the tooth flanks. By this knowledge a local comparison of the load and load capacity can be carried out. But how to handle the vast variety of load situations during different load cases and long time series? Therefore an appropriate classification of the different occurring states of gear deviations and gear loads will be presented. This way we are able to determine the risk of common gearing failures like pitting and tooth root breakages in detail for individual drive trains under different operating conditions. The paper will present the procedure of this contemporary way of designing gears. By using a simple spur gear set the general idea of simulating the operating conditions of a drive train and the subsequent complex tooth contact analysis

will be explained. On basis of this information a suitable approach to assess the risk of different gearing failures is carried out and the results will be illustrated.

1 INTRODUCTION

Modern ships are more and more subject to higher requirements. This specially applies to specialized ships like offshore supply vessels, tug boats and research vessels (see figure 1). In addition those vessels often operate under ice conditions, whereby specific requirements to the entire drive train arises. In the research project "EraNet HyDynPro" the total set of processes concerning the drive train are investigated more closely. At this the propeller-ice-interactions as well as the loads under ice conditions get analyzed. Influences caused by the driving engine as well as load alternations within the drive train caused by native mass and stiffness distributions are considered by a *multi-body-system simulation* (MBS-simulation). The focus of this paper is the calculation and design of the gearing system. One essential intermediate target of the research project is the generation of chronological load and position series of the gear wheels. These series get classified and every single class is applied to a *complex gearing load analysis*. Subsequently the local amount of damage is calculated and a local total damage sum gets generated using an appropriate damage accumulation approach for every kind of damage (pitting, tooth root breakage, flank breakage...). This damage sum represents the amount of locally utilized capacity of the gearing system with respect to the kind of damage.

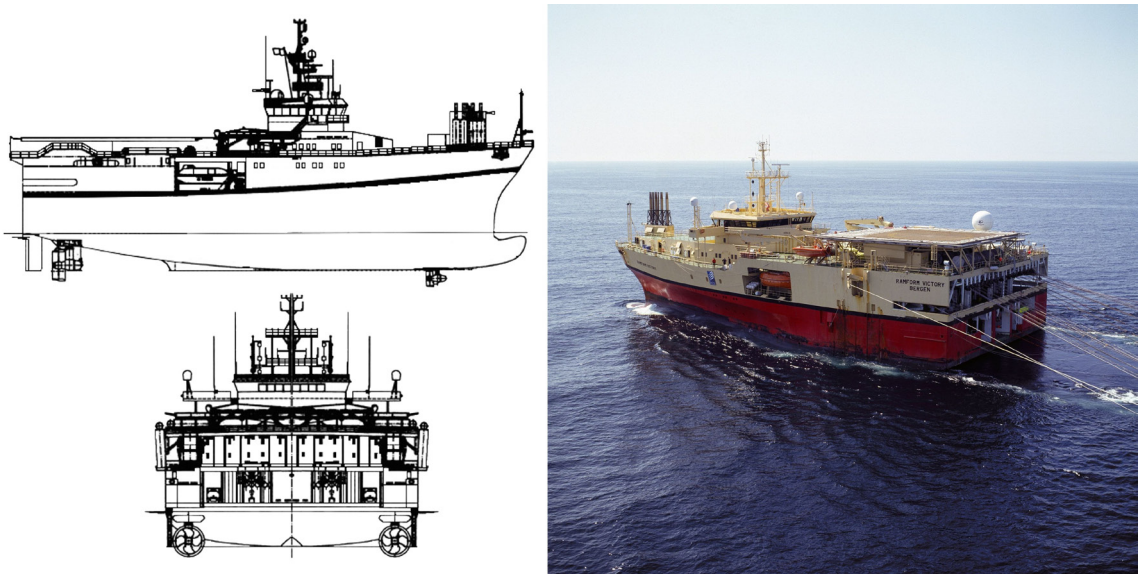


Figure 1: Research vessel with azimuthing thrusters

2 LOAD DETERMINATION

Usually the determination of design loads, or possibly their chronological trends, is the point of origin when calculating machine elements like the gearing system.

2.1 Determination of gearing loads and gearing displacements

In the case of stationarily operating and stiffly mounted drive trains the load alternation is very low. This way the nominal torque, which is necessary for the calculation of the toothing system, can be calculated using the input speed and power together with transmission ratios.

Conventional vessels operate in a quasi-stationary manner. Therefore the load alternations during operation are less important as long as resonance effects are avoided. However the mentioned specialized vessels are operating with severely alternating input power and speed during maneuvering. Beyond that the housing of an azimuthing thruster is a relatively flexible foundation for the drive train. For these circumstances it is necessary to perform detailed investigations of the dynamic behavior of the entire drive train system. Therefore a complex MBS-simulation model is built up (see figure 2). This model is a multi-dimensional oscillation system generated by masses, stiffness and damping. External loads caused by the motor and the propeller are applied to the model by co-simulations or characteristic curves. Based on this some chronological series of tooth forces and gear wheel positions can be calculated and recorded for a variety of operating conditions.

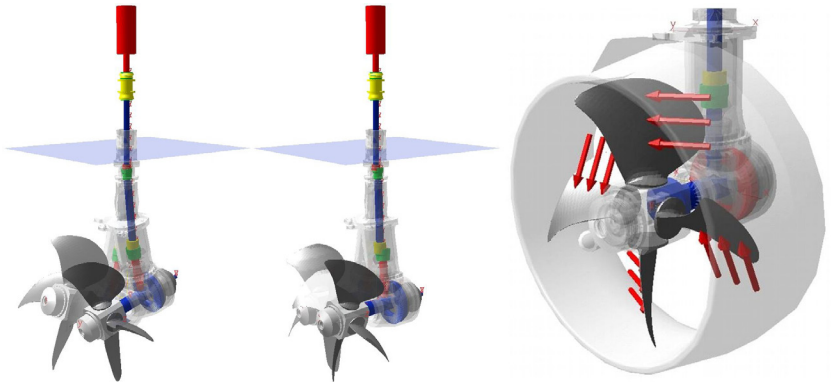


Figure 2: MBS-models of azimuthing thrusters: Two exemplary mode shapes (left, center), force application on the propeller (right)

2.2 Generation of combined load-displacement-spectra

A gearing calculation based on chronological series of the tooth forces and gearwheel displacements is hardly practicable. Hence a multi-dimensional classification of the tooth forces on the one hand and gear wheel displacements on the other hand is appropriate. In this way the tooth calculation for every point in time is not necessary. It is sufficient

to do this for every field of classification only, whereby the calculation effort decreases rapidly. [1]

In case of spur and helical gears an acting deviation of the flanks can be calculated using the displacements of the gear wheels. These, the tooth normal force and several geometrical parameters of the gearing are the required input data for the complex gearing load analysis (see figure 3).

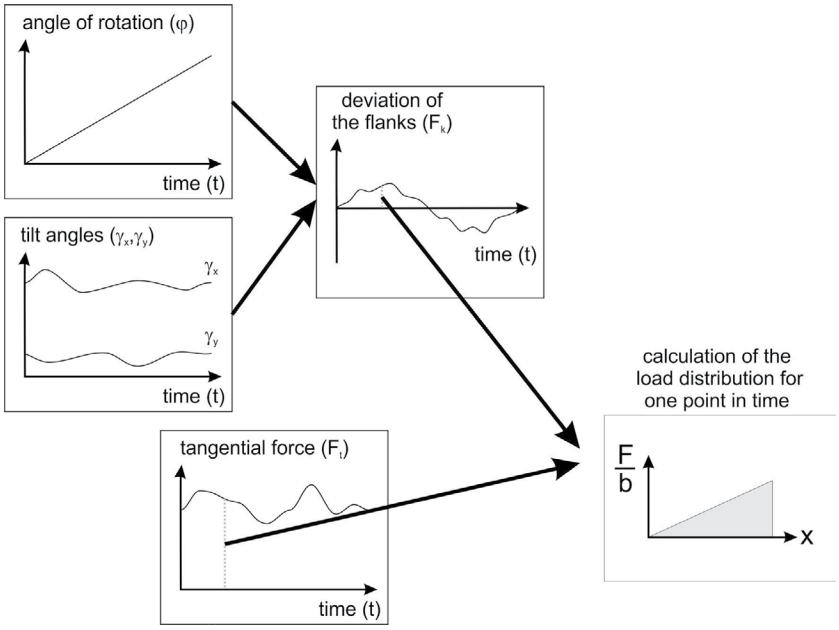


Figure 3: Scheme of data supply for the complex gearing load analysis

3 SPECIALISED GEARING CALCULATION

To avoid the common toothing failures like pitting and tooth root breakages at stationary operating and stiffly constructed drive trains a standardised gearing calculation according to DIN 3990, ISO 6996 or similar is applicable. If shaft, bearing, gearwheel or housing deformations influence the gearing system significantly, a verification by a complex gearing load analysis is advisable. Beyond that gearings of industrial applications more and more fail by a kind of damage called *flank breakage* or *tooth interior fatigue fracture* (TIFF). Up to now there is no standardized calculation available against this kind of failure. [2, 3]

3.1 Calculation of the tooth load distribution using the complex gearing load analysis

To perform a complex gearing load analysis the chair of machine elements of the technical university Dresden developed the computer software *LVR* for spur and helical gears

as well as *BECAL* for bevel gears. These programmes enable the determination of the local load distribution on the tooth flanks for all meshing positions at arbitrary torque (see figure 4). Thereby shaft deflections, gearwheel and bearing displacements as well as the tooth deformations are considered.

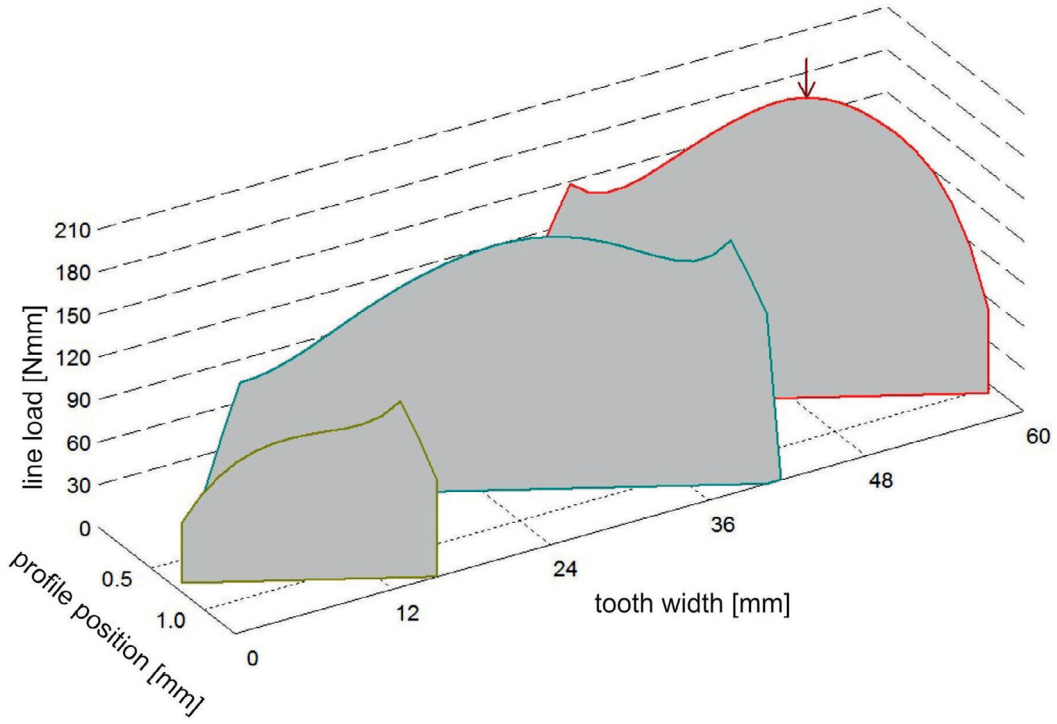


Figure 4: Complex gearing load analysis - load distribution at one meshing position

Based on the load distribution on the flanks at one meshing position it is also possible to figure out the load distribution for the entire field of meshing positions (see figure 5).

3.2 Calculation of relevant kinds of tooth stress

Based on the load distribution on the flanks within the entire meshing field also relevant local tooth stress conditions can be calculated. To calculate the gearing failures pitting and tooth root breakage the local calculation methods according to DIN 3990 are implemented in LVR and BECAL (see figure 6).

Up to now no standardized approach to calculate the risk of flank breakages is available. With respect to this, investigations are carried out within the research project. Hence local flank loads are used to calculate the stress conditions inside the tooth using analytical and numerical approaches (see figure 7). The global tooth stress condition (bending, shear stress, pressure) is calculated by the finite-element-method (FEM). The stress condition directly caused by the tooth contact (Hertzian pressure) is calculated in an analytical

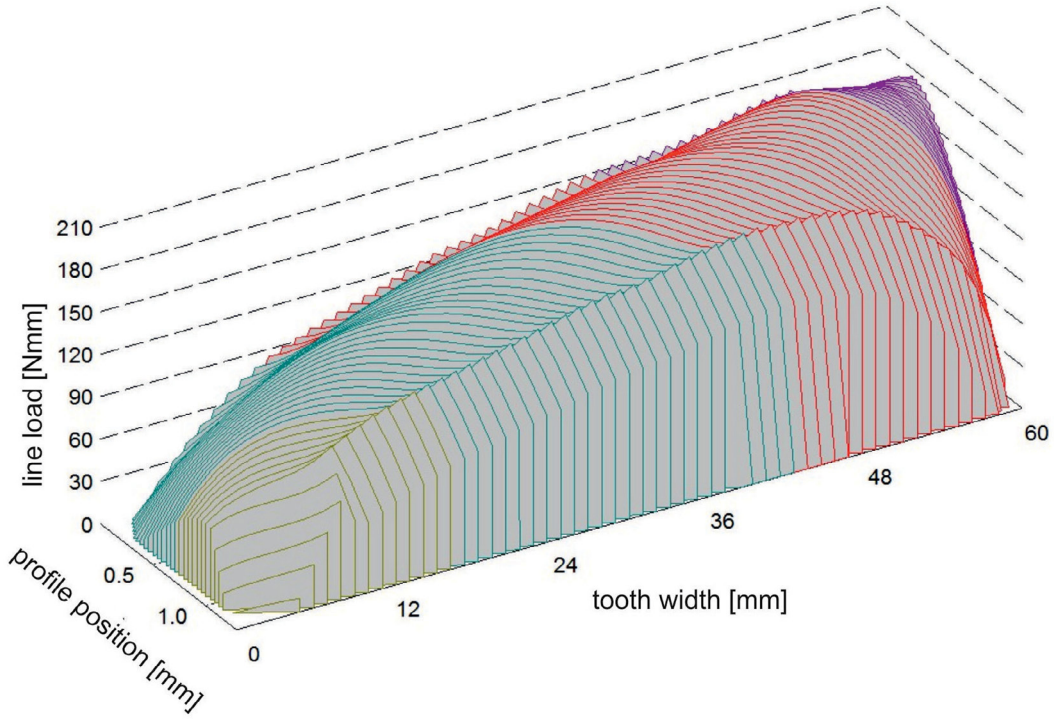


Figure 5: Complex gearing load analysis - load distribution for the entire field of meshing positions

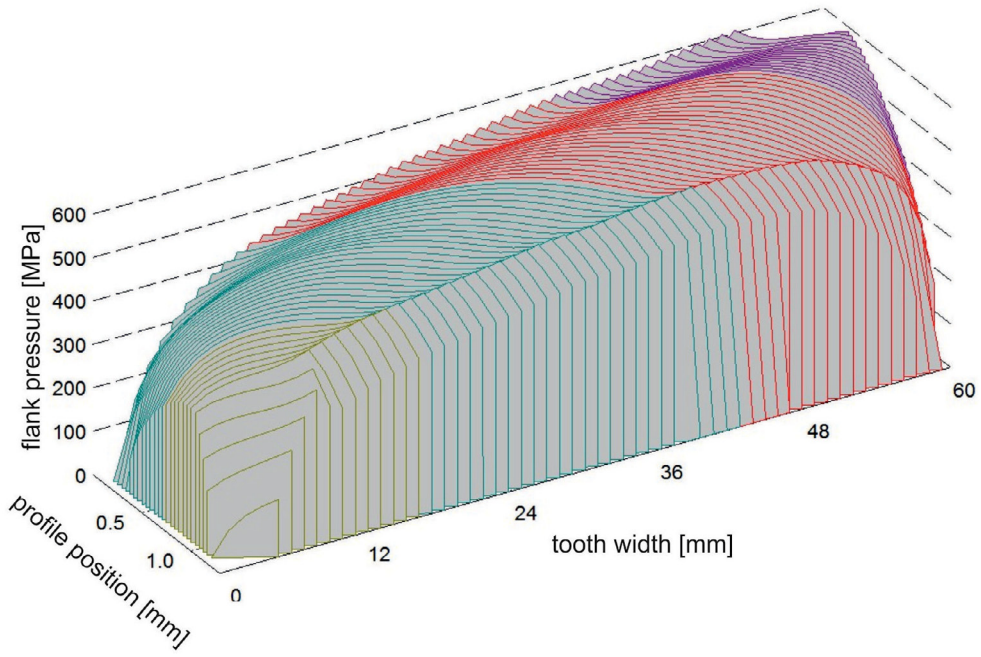


Figure 6: Complex gearing load analysis - distribution of contact pressures

manner, as well as residual stress conditions.

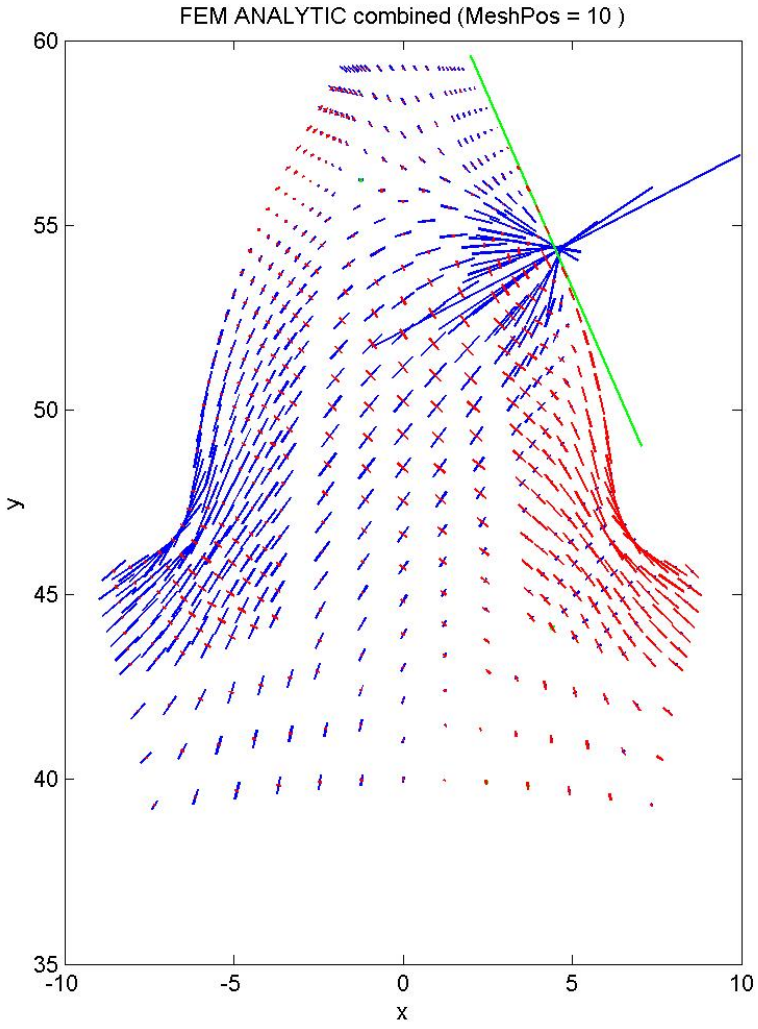


Figure 7: Principal stress inside the tooth by combination of numerical and analytical approaches

3.3 Calculation of the damage rates within the several load-displacement-spectra fields

The calculation of the damage rate of the gearing failures pitting and tooth root breakage is carried out by the mentioned standardized methods. For the calculation of the flank breakage many different approaches are published. Based on these approaches, complemented by own ones, the damage rate is supposed to get calculated for every spectra field. Test runs on a spur and a bevel gear test rig are planned for validation (see figure 8).

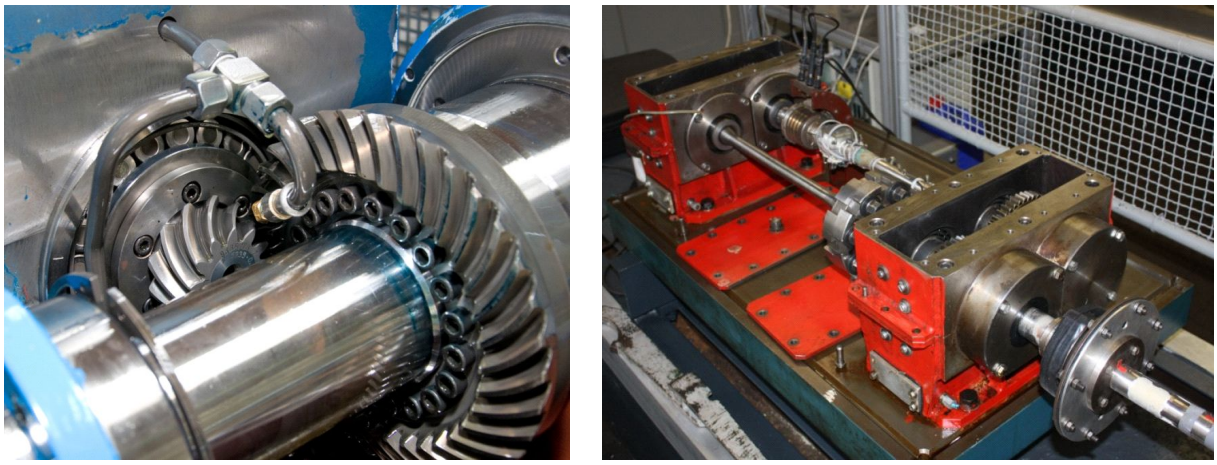


Figure 8: Test rigs - bevel gear (left), spur gear (right)

Listed below is the operating chart for the development of a method to calculate the risk of flank breakages (see figure 9). The best qualified approaches will be adapted on a variety of gearing geometries. If clear tendencies are appearing concerning the risk of flank breakage, some test runs will be performed on these gearings. With this the strength and weaknesses of the different approaches should be revealed as well as the implementation of own thoughts may be realised.

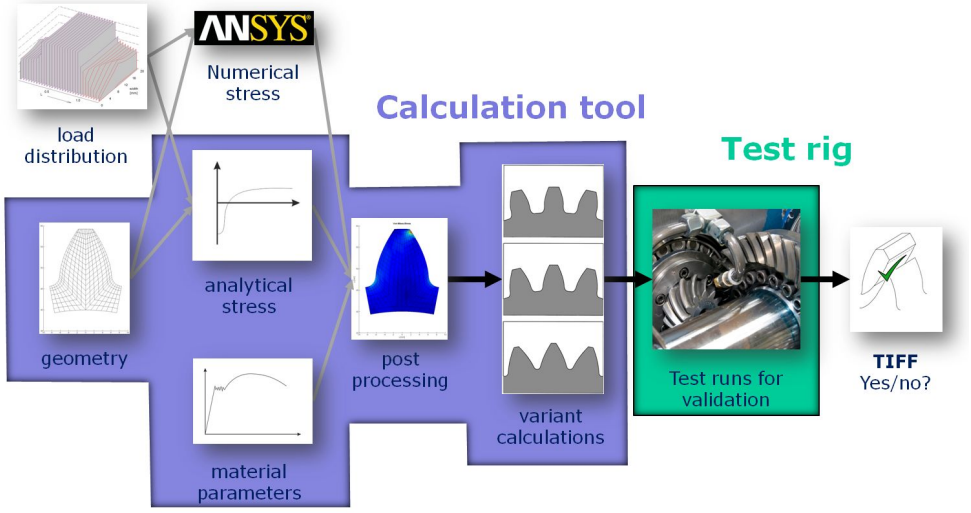


Figure 9: Operating chart for the development of a method to calculate the risk of flank breakage

3.4 Calculation of the total damage sum respectively service life

The several damage rates get collected to a local total damage sum using an appropriate damage accumulation approach. Further on several statements about the local service life in profile and width direction of the flank can be made. This is of importance especially on planetary gear stages with softly mounted or highly loaded planet carriers. Hence the deviation of the flanks is changing during the revolution of the planet carrier. In this case the consideration of the load displacement spectra in combination with the local tooth analysis as presented in this paper offers the possibility of determining appropriate flank modifications and service life statements. This would not be possible with standardised methods.

REFERENCES

[1] B. Schlecht, Chr. Bauer, *Stress Analysis of Gearings within their Elastic Environment under the Influence of its Dynamic Behaviour*, International Conference on Gears (VDI), Munich, 5. Oct. 2010

[2] B. Schlecht, *Maschinenelemente 2*, 1st Edition, Munich, Pearson, 2010

[3] H. Linke, *Stirnradverzahnungen*, 2nd Edition, Hanser, 2010

V International Conference on Computational Methods in Marine Engineering
MARINE 2013
B. Brinkmann and P. Wriggers (Eds)

COMPREHENSIVE ANALYSIS OF THRUSTER DRIVETRAINS TO DETERMINE RELIABLE LOAD ASSUMPTIONS

PROF. DR.-ING. B. SCHLECHT, DR.-ING. T. ROSENLÖCHER
DIPL.-ING. C. BAUER

Institute of Machine Elements and Machine Design, Chair of Machine Elements
Technische Universität Dresden
01062 Dresden, Germany
e-mail: thomas.rosenloecher@tu-dresden.de, web page: http://www.me.tu-dresden.de

Key words: Multibody System Simulation, Modelling Process, Thruster, Bevel Gear Stages

Abstract. The usage of modern thrusters allows to combine the functions of the drive and the ship rudder in one assembly, which are separated in conventional ship propulsions. The horizontally oriented propeller is supported in a vertically rotatable nacelle, which is mounted underneath the ship hull. The propeller can be directly or indirectly driven by an electric motor or combustion engine. The direct drive requires the installation of a low speed electric motor in the nacelle. The present paper concentrates on indirect drives where the driving torque is transferred by bevel gear stages and shafts from the ship to the propeller. Due to the closed and inaccessible construction high demands on the reliability have to be achieved. Especially for the design of the highly loaded bevel gear stage accurate information to the occurring loads are required. The experience of operating thrusters show that primarily rarely occurring special load cases have to be considered, which can only be determined by long-term measurements at very high cost. By means of a detailed multibody system simulation model of the thruster it is already possible to develop a basic knowledge to the dynamic properties of the drive train and to determine design loads for drivetrain components.

1 INTRODUCTION

The different drive train and ship concepts, the complicated operational conditions and the high demand on the reliability lead to many different tasks and conditions which have to be considered in the design process of thrusters. Therefor the occurring operational conditions are analysed using simple torsional oscillation models of the drive train up to now. In addition to the typical concept where the fixed propeller is driven by a long shaft, water jet engines, thrusters and also special solutions like the Voith-Schneider drive are used. The thrusters are mounted underneath the ship hull and the thruster housing can rotate around the vertical axes, so that they can be used as pushing or pulling drive and also as ship rudder. The driving power can directly be supplied by an electrical motor, installed in the nacelle (ABB, Rolls-Royce). Alternatively the driving torque is transferred by gearboxes and long shafts from the driving unit in the ship hull to the propeller of the thruster (Schottel, Rolls-Royce, Wärtsilä). Thruster which are driven by an electrical motor or combustion engine using a gearbox are able to operate with a constant driving speed if the provided thrust is adjustable by pitchable propeller

blades. Due to the good manoeuvrability thrusters are used in ferries and tug boats. Also if high demands on the positioning accuracy required by ships for gas- and oil production as well as for scientific marine research, thrusters are often used.

In comparison to the typical driving concepts using a long shaft, changed design loads have to be considered due to the combined function of driving and steering as well as the paired arrangement on both sides of the ship (figure 1, left). Further the discontinuously operation and the area of application can have influence on the design process. Next to the occurring torques also bending moments around the vertical axes resulting from the steering movements of the thruster have to been taking into account for the different operational conditions. A relevant design load case results from the positioning of the thrusters on both sides of the rear. In high waves an emersion of propeller can occur so that during the immersion the blade tips are slamming on the water surface. This leads to short time overloads which have to be transferred and supported by the drive train without damages.

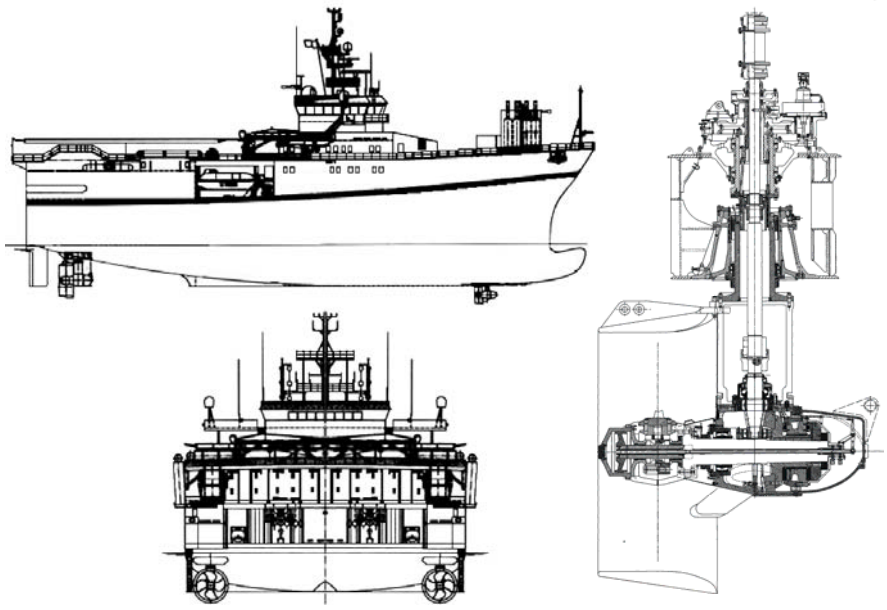


Figure 1: Positioning and design of the thruster

2 BASICS OF THE DRIVE TRAIN SIMULATION

The analysis of drivetrains operating under high dynamic loads presupposes the assembly of a detailed simulation model which is able to represent the dynamic behaviour of the drivetrain in the frequency and time domain. Even if high performance computers are available the level of detail of the simulation model has to correspond to the formulated question to ensure a feasible calculation effort. Despite the currently given possibilities of the simulation software the modelling process is very time-consuming. Based on the present data and the experiences of the engineer a discrete simulation model has to be assembled. A successive and modular assembly of fully parameterized simulation models allows a clear and reproducible modelling process compared to the combination of all drive train components in one unstructured model.

The modular concept requires in a first step the decomposition of the drivetrain into its substructures. According to this approach a simulation model of a thruster consists of the following substructures: propeller, propeller shaft, coupling, motor and an additional

subdivided gear box. Further the gearbox can be subdivided in different spur and helical gear stages, bevel gear stages and planetary gear stages whereby in the analysed thruster only bevel gear stages are used (figure 2). Each substructure consists of model components which can be subdivided into shafts, gear stages, bearings and supporting structures. The combination of single substructures finally leads to the complete simulation model of the thruster. Dependent from the present requirements an adjustment of the level of detail and the needed degrees of freedom for each submodel can be performed. Compared to the work with one single simulation mode for the complete drive train, the usage of different submodels enables an easy verification of the function and accuracy.

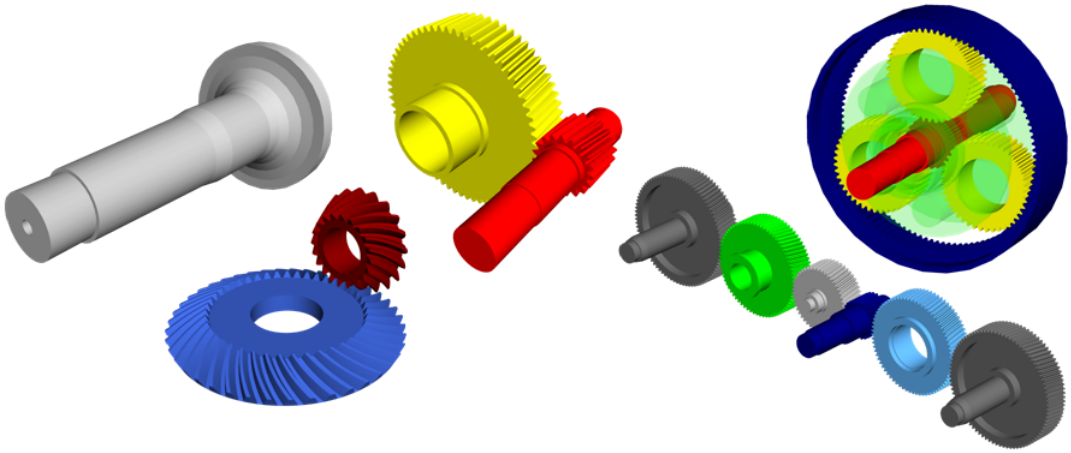


Figure 2: Different kinds of substructures which can be assembled to different drive trains

3 ASSEMBLY OF THE SIMULATION MODEL

The determination of the occurring drive train components loads and analysis of the dynamic behaviour can be achieved either by a complex measurement setup in the thruster nacelle or with the aid of detailed simulation models. The challenges of a measurement campaign are difficult environmental conditions and missing accessibility to install sensors after the assembly of the thruster. So, a measurement setup is time consuming and expensive. An availability of detailed measurement results for different drive train components will be an individual case and not be applicable to design thrusters. The determination of the component loads using the simulation results of complex drive train models can already performed during the product development process.

The assembly and functions of a thruster should be shown exemplary using the sectional drawing in figure 1, right. The nacelle with the function of the gearbox and cover of the drive train is mounted rotatable around the vertical axes in the ship hull und can be turned by an additional drive. The main driving machine in the ship hull transfers the required torque for a horizontal positioned driving aggregate by an elastically coupling and a bevel gear stage. For a vertical mounted driving machine the torque is transferred directly by a coupling to the vertical driveline in the nacelle. The segmented drive line is supported by several bearings in the housing. The shaft segments as well as the pinion of the bevel gear stage are connected by geared couplings. The wheel of the bevel gear stage is mounted on a carrier. The carrier is directly connected to the propeller shaft, which is supported by a roller and a sliding bearing. The axial mounted hub is used to support the four pitchable propeller blades, which can be

positioned by a hydraulically acting linkage.

The dynamic behaviour of the drive train is mainly characterised by the large motor- and propeller sided mass moment of inertias as well as the high flexibility. Dependent from the required thrust propeller diameter up to 5 meters are installed. The occurring torque and bending moment during operation presuppose a stiff design of the propeller shaft. By contrast thin shafts are used in the vertical drive line because the gear stage ratio lowers the torque and the resulting stress. The lower torsional and bending stiffness of these shafts has to be taken into account. Further the motor is connected by an elastic coupling with the drive train. Simplified the complete system can be described by two large mass of inertia, connected by a soft torsional stiffness. Additionally all drive train components are supported in the nacelle, which is also an elastic system and only connected at the top to the ship hull. Under consideration of the acting forces, the torque and the bending moments a simulation model representing the torsional degrees of freedom can only be used for a simplified and rough analysis of the dynamic behaviour. A comprehensive investigation of the entire system requires a detailed modelling of all relevant degrees of freedom in a simulation model.

All shafts of the drive train have to be modelled with the information to the torsional and bending stiffness, the mass and mass moment of inertia as well as with the rotatory and translatory degrees of freedom. The determination of the mass parameters can be performed using common three-dimensional CAD-software or by means of simple analytical approaches. A higher effort is demanded to calculate the stiffness of the components. The torsional stiffness of the drive train is mainly characterised by the flexibility of the shafts. Especially thin shaft have to be considered with their elastic properties. Additionally the bending stiffness of such shafts can have non negligible influences on the dynamic behaviour and the occurring displacements. A simulation model which is required to represent shafts can be assembled by means of the method of discretisation, by the implementation of beam models or by using modally reduced elastic structures (figure 3), [2], [4], [16], [18].

The consideration of axial and radial degrees of freedom supposes the modelling of the bearings. Essentially the modelling of the bearings is realized by a force element which introduces the reaction forces in the axial and radial directions as well as the reaction moments if necessary. The bearing properties can be described by average bearing stiffness, characteristic curves or complex models imported as DLL's [17].

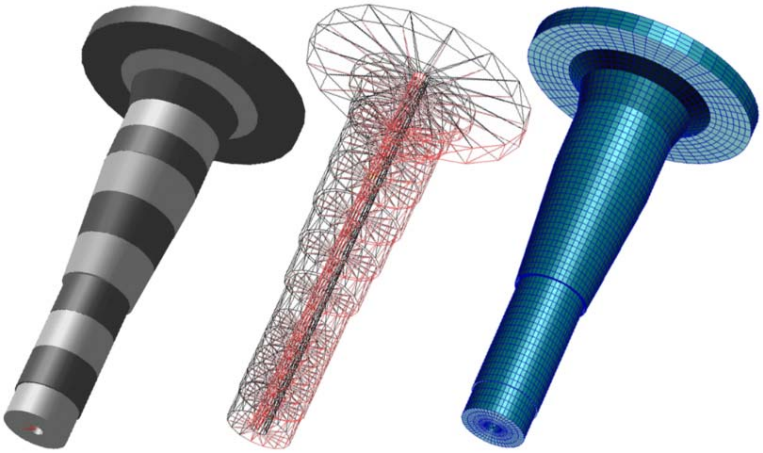


Figure 3: Possibilities to model the elasticity of a shaft

To support the shafts in the thruster housing the bearings are modelled as translatory spring-damper-elements, whereby the load dependent bearing stiffness is implemented, so that for all occurring load cases the approach can be used. Also the properties of the elastically and geared couplings are described by spring-damper-elements. For the motor sided coupling information of the stiffness characteristics are required which must be provided by the manufacturer. According the current knowledge the stiffness of geared couplings can only be determined using analytical approaches [1], [5], [8]. Information to the radial stiffness and stiffness against inclination due to the comprehensive influence factors and uncertain calculation methods are not available. As first approach all possible degrees of freedom are locked by constraints or high stiffness and the occurring influences on the dynamic behaviour have to be determined by sensitivity analysis.

The model of the bevel gear stage between the vertical drive line and the propeller shaft must describe the transfer behaviour for the torque as well as for all force components so that the dynamic properties of the complete drive train can be correctly represent. Next to the description of the nonlinear characteristic of the stiffness resulting from the changing contact conditions, the backlash have to be considered during the calculation of the acting forces. For each step of the integration the determination of the equilibrium between the acting forces, displacements, the inclination of the shafts and the inner gearing forces must be ensured. The simulation software SIMPACK offers the tool boxes GEARWHEEL and GEARPAIR to model gearings and to describe the transfer behaviour in detail.

An alternative modelling approach offers the mathematical description of the resulting forces in the gearing by means of user routines. Based on the calculation of the tooth normal force in the ideal pitch point, the complete tooth contact is simplified and described in one point. The tooth normal force consists of stiffness and damping dependent parts. Information about the displacements and velocities in tangential, radial and axial directions resulting from the relative position of the gears can be determined by the joint states and the corresponding trigonometric relationships. The gearing stiffness can be considered as average contact stiffness according to DIN 3990 and variable gearing stiffness over the path of contact using Fourier coefficients (figure 4).

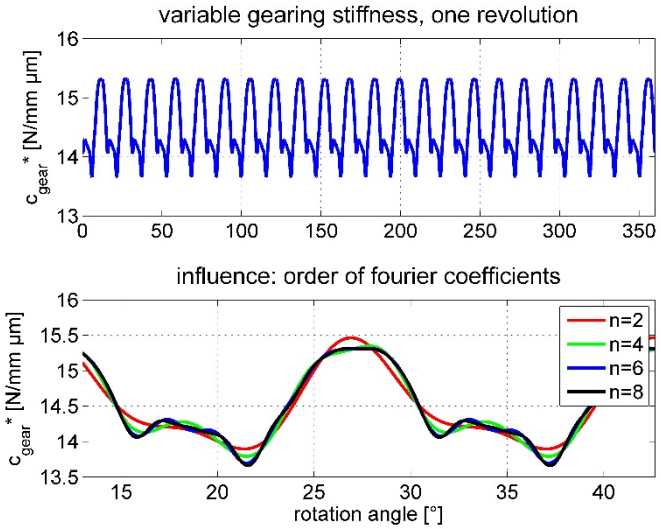


Figure 4: Variable gearing stiffness over the contact path using Fourier coefficients

The rigid modelled hub is mounted axially on the propeller shaft and supports the four pitchable propeller blades. To consider the flexibility and resulting deformations of the blades under the high loads, the material and shape dependent elasticity has to be considered. Due to the complex geometry the method of discretisation or beam approaches cannot be used so that on basis of a detailed finite-element model and the dynamic reduction the propeller blades are represented by modal reduced elastic structures (figure 5, left). The implementation of a flexible structure in SIMPACK is based on a meshed finite-element model of the component geometry and the definition of the material properties. Additionally the modelling of the connection points between the elastic structure and the rigid bodies of the multibody system model is required. The connection points to the supporting spring-damper elements can be modelled by means of multipoint constraints (MPC). However, the resulting FE-model is assembled by many shell or solid elements and has therefore much more degrees of freedom as necessary to describe the rigid body motions in the MBS model. Because such complex models cannot be handled by a classic MBS solver, the level of detail of the finite element model has to be reduced to the transfer behaviour between the connection points. All additional information to the displacement of nodes, which are not used as connection points in the MBS model, are not available in the reduced model of the structure. The application of the reduction approach according to Craig-Bampton requires the definition of the connection points between the flexible structure and the rigid bodies. The mode shapes of the reduced model are used to determine the deformation under load [3], [6]. The number of natural frequencies chosen for the modal reduction defines the valid frequency range and the accuracy of the model, which is also influenced by the choice of frequency response modes in the SIMPACK Add-On Module FEMBS [7].

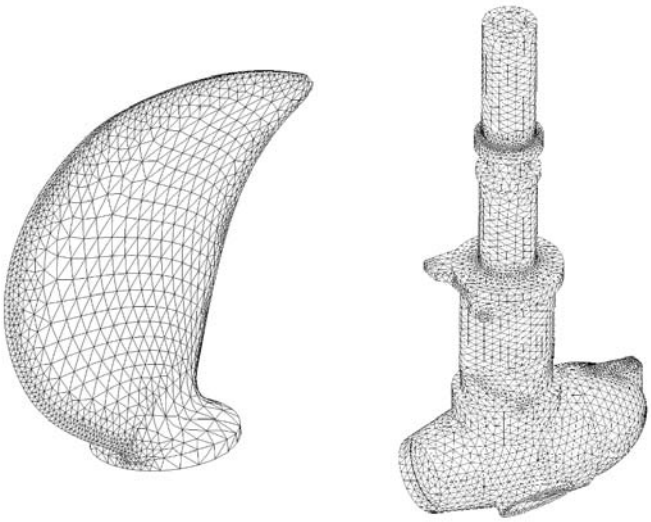


Figure 5: Finite-element-model of the propeller blade and the thruster housing

A comparable proceeding has to be performed to represent the elastic properties of the thruster housing. The large mass of the propeller and the propeller shaft with the bevel gear wheel as well the propeller sided loads have to be supported by the structure of the thruster housing and have to be transferred to the large bearing in the ship hull. The expected deformations under the load will have an influence on the dynamic behaviour of the drive train. Based on the geometry of the thruster housing a finite-element model can be assembled (figure

5, right). The connection points for the support in the ship hull and the positions of the bearings for the drive train components are linked by constraints to a number of surface nodes in the area of the bearing seats. After the implementation of the reduced finite-element model the spring-damper elements which are representing the bearings will be defined between these connection nodes and the body marker of the MBS model. So all introduced loads are directly transferred as torque or supported by the bearings in the thruster housing and the ship hull.

4 INVESTIGATIONS IN THE FREQUENCY DOMAIN

To realise the described modularisation consequently, the simulation model of the thruster consist of the submodels motor, coupling, the vertical drive line, the bevel gear stage, the propeller shaft and the propeller. All components are assembled in a complete model of the thruster and supported in the modally reduced finite-element model of the thruster housing. The release of all degrees of freedom und consideration of all supporting and connecting spring-damper-elements allows by comparison of natural frequencies and excitation frequencies the determination of critical operational speeds and the analysis of the dynamic behaviour of drive train components and the supporting structure (figure 6). Possible excitations are the rotation frequency of all drive train components in the first and second order, the gear meshing frequency of the bevel gear stage with the first order and higher harmonics, the rotation frequency of the propeller with the first order und higher harmonics corresponding to the number of installed blades and disturbance of the flow due to the nacelle design. The named sources can excite torsional, bending, radial and axial mode shapes which has to be analysed for each determined critical operational speed. Especially the propeller sided excitations has an important influence on the dynamic behaviour of the complete system because the torque as well as the acting forces can lead to resonances with different harmonics of the rotation frequency of the propeller shaft.

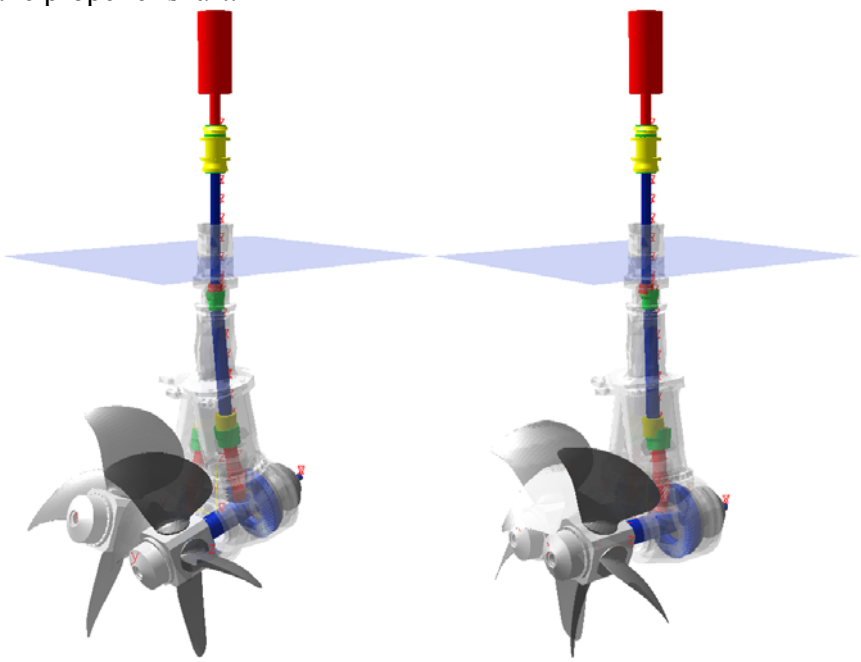


Figure 6: Mode shapes of the thruster (10 Hz, 11 Hz)

In figure 7 the Campbell diagram for the thruster with all natural frequencies and excitations up to 140 Hz shown exemplarily. The first natural frequency of the complete system at 10 Hz is characterised by a bending mode shape of the thruster housing against the support in the ship hull. The fourth order of the propeller rotation frequency could cause a resonance with this mode shape at an operational speed of 635 rpm (figure 6, left). In addition to the stiffness of the housing also the stiffness of the bearing which supports the thruster in the ship hull has an influence on the mode shape. The first torsional mode shape of the drive train at 11 Hz is superposed by a second bending mode shape of the housing. This natural frequency can also be excited by the fourth order of the propeller rotation frequency at an operational speed of 720 rpm (figure 6, right). The mentioned excitation frequency is caused by flow disturbance, which occurs if a blade pass the thruster housing. The changing torque, bending moments and forces can lead to an excitation of both mode shapes.

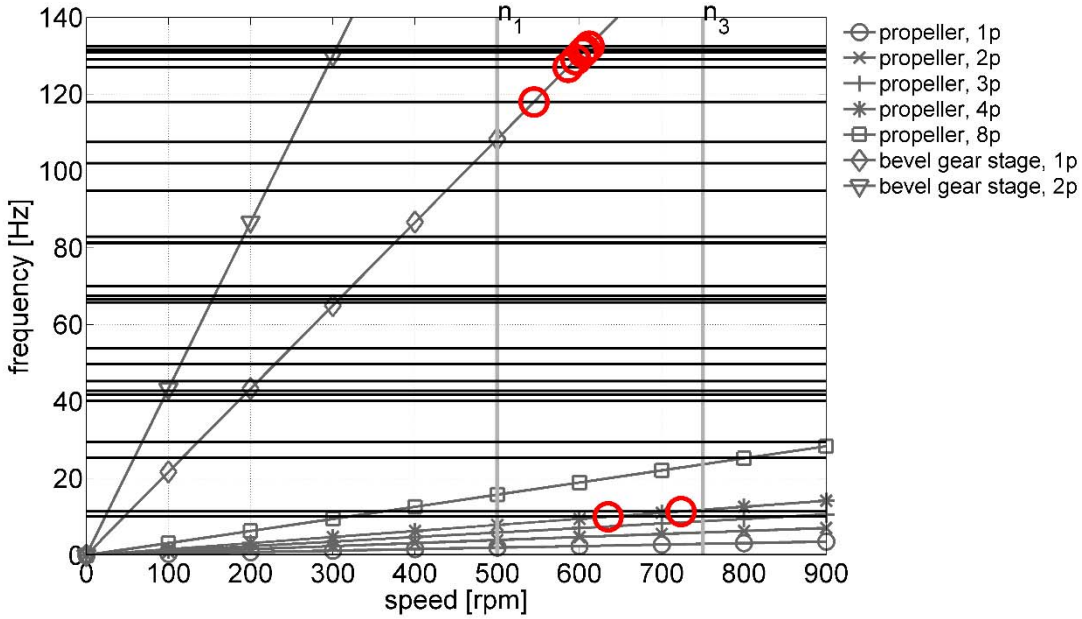


Figure 7: Campbell diagram

Also the higher natural frequencies of the drive train are characterised by the superpositioning of housing and drive train mode shapes and can be excited by higher harmonics of the propeller rotation frequency. For the analysed drive train only the fourth and eighth order of the propeller rotation frequency are relevant. For the further investigations the interesting frequency/speed range is limited by the lower border of the operational speed and the gear meshing frequency of the bevel gear stage at approximately 110 Hz.

In the analysis of the higher frequency range all possible intersections between the gear meshing frequencies and the determined mode shapes have to be taken into account. Due to the exciting gearing force components in tangential, radial and axial direction an excitation of torsional, axial and bending mode shapes as well as mode shapes against the shaft support are possible. In addition to the theoretically investigations using the Campbell diagram, a comprehensive evaluation of the excitability can only be performed by the simulation of a slow run up and a detailed analysis of the simulated velocities, accelerations and torques.

5 ANALYSIS IN THE TIME DOMAIN

Besides the analysis of possible excitations of natural frequencies in the range of the operational speed by means of the detailed simulation model the occurring loads for all drive train components and different operational conditions can be analysed. This requires an enlargement of the mechanical model to characterise the acting motor and propeller sided loads in detail.

The description of the electric motor can be realised by modelling the different control loops in MATLAB/SIMULINK. Important for a realistic motor model is the knowledge of all motor parameters. These parameters must be provided by the manufacturer of the electric motor. In the case of the presented thruster only some rough information to the motor are available, so that by means of speed-torque characteristics a simplified model are used to describe to motor behaviour. The modelling of the propeller sided loads requires a comprehensive discussion to the proper modelling approach. To analyse a simple torsional vibration model the information to the occurring torque is sufficient and allows already a first evaluation of the dynamic behaviour and testing of the model. The simplified consideration of the torque neglects the important influences of the thrust forces and bending moments which are also applied at the propeller. These load components cause the bending of the thruster housing, the displacements of the propeller shaft and have also an impact on the contact conditions in the bevel gear stage. Next to the analysis of operational states under full load for different flow angles, especially extreme load cases like the immersion of the propeller at maximum input power can be seen as critical for the reliable operation of the thruster and should be investigate with the model [12]. Until today no comprehensive measurement results for such thrusters are available so that the occurring loads during the immersion and emersion of the propeller were analysed only with scaled models in water tanks. When the propeller approaches the water surface, the surrounding water is already mixed with air, so that the thrust and the acting torque decreases. The speed of the motor increases due to the lower resisting torque. A further emersion of the propeller causes at first a water free movement of the upper blade. At the moment of the blade immersion the resisting force increases suddenly which leads to a short-time increase of the torque in the drive train [9], [10], [11].

To determine the occurring component loads during such load cases, a very detailed propeller force model is necessary. The introduction of the water resisting forces is carried out by modelling a discrete load distribution over the blade length for the tangential and axial force component, separable for each blade. The calculation of the acting forces for each load introduction point occurs dependent from the rotation angle, the distance from the water surface and measurement based assumptions for the force progression by means of a MATLAB/SIMULINK model. The introduction of the resulting forces on the propeller blades in the MBS model allows a first analysis of the occurring loads for shafts, bearings and gearings. Figure 8 shows the torque of the propeller shaft and the motor speed over the simulation time as comparison between measurement and simulation results.

Further possibilities for the description of the propeller sided loads are given by the computational fluid dynamics. The method is used to analyse the ship hull and the interactions between ship hull and thruster already during the design process. Because of the detailed, computational intensive models a CFD simulation can only be done for single revolutions of the propeller and defined environmental conditions. A combination of CFD- and MBS-

simulation is due to long simulation time by using the currently available computer performance for the dynamic simulation not applicable. But the propeller forces and torques can be precalculated for defined quasi static load cases and introduced in the MBS model using force elements [14]. To improve the propeller force models and to validate the mechanical simulation model the measurement of the different real occurring operational loads by means of an extensive measurement setup over a long period is mandatory.

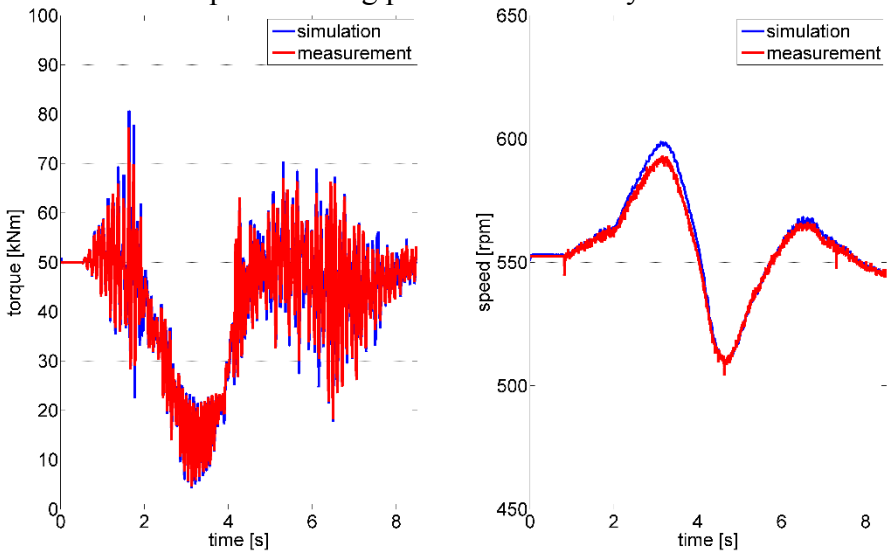


Figure 8: Time series for the immersion and emersion of the thruster

6 CONCLUSION

The described methods can be used to model the mechanical components as well as the acting propeller loads, so that basic statements to the dynamic behaviour of the thruster drive train can be given. The comparatively simply constructive design of the drive train is characterised by the high flexibility of the drive line and the thruster housing. This leads in combination with the large propeller and motor inertias as well as the acting forces to high dynamic states in the drive train. If a sudden increase or decrease of the propeller sided torque occurs, first the twist of the drive train must be resolved, before the backlash in the gearings or couplings can affect the dynamic drive train behaviour. The occurrence of back flank contact in the bevel gear stage gets possible, if the propeller load changes with an amplitude and for the duration, so that a twist free drive train exists. The motor sided coupling can reduce overloads at the motor. Damages in the drive train can only be avoided by an overload protection at the propeller shaft. The challenge is the design of an overload protection which can limit the torque reliable and is small enough for an installation in the available space in the thruster housing [13], [15].

REFERENCES

[1] Benkler, Helmut: Berechnung von Bogenzahnkupplungen. Fortschritt-Berichte VDI, Reihe 1, Nr. 27. Düsseldorf: VDI Verlag, 1970

[2] Claeyssen, Julio R.; Soder, Rosa A.: A dynamical basis for computing the modes of Euler-

Bernoulli and Timoshenko beams. In: Journal of Sound and Vibration (2003), 259(4), S. 986-990

[3] Craig, Roy R.; Bampton, Mervyn C.: Coupling of Substructures for Dynamic Analyses. In: AIAA Journal (1968), Vol. 6, No. 7, S. 1313

[4] Dresig, Hans: Schwingungen mechanischer Antriebssysteme. Berlin: Springer, 2006

[5] Fleiss, Rainer: Das Radial- und Axialverhalten von Zahnkupplungen. Darmstadt, Technische Hochschule Darmstadt, Dissertation, 1977

[6] Guyan, Robert J.: Reduction of Stiffness and Mass Matrices. In: AIAA Journal (1965), Vol. 3, No. 2, S. 380

[7] Heckmann, Andreas; Otter, Martin; Dietz, Stefan; Lopez, Jose Diaz: The DLR FlexibleBodies library to model large motions of beams and of flexible bodies exported from finite element programs. Modelica 2006, 4. – 5. September 2006

[8] Heinz, Rudolf: Untersuchung der Kraft- und Reibungsverhältnisse in Zahnkupplungen für große Leistungen. Darmstadt, Technische Hochschule Darmstadt, Dissertation, 1976

[9] Koushan, Kourosh: Dynamics of Propeller Blade and Duct Loadings on Ventilated Ducted Thrusters Due to Forced Periodic Heave Motion. In: Proceedings of International Conference on Violent Flows, Kyushu University, Fukuoka, Japan, 2007

[10] Koushan, Kourosh; Spence, Silas J. B.; Hamstad, Toralf: Experimental Investigation of the Effect of Waves and Ventilation on Thruster Loadings. In: First International Symposium on Marine Propulsors, SMP´09, Trondheim, Norway, 2009

[11] Kozlowska, Anne M.; Steen, Sverre; Koushan, Kourosh: Classification of Different Type of Propeller Ventilation and Ventilation Inception Mechanism. In: First International Symposium on Marine Propulsors smp´09, Trondheim, Norway, 2009

[12] Mork, Lynn R.: Slamming on propeller blade. Trondheim, Norwegian University of Science and Technology, Department of Marine Technology, Pre project thesis, 2006

[13] Neikes, Kai: Untersuchungen zur Funktionstrennung bei der Antriebswelle eines Ruderpropellers. Dresden, Technische Universität Dresden, Lehrstuhl Maschinenelemente und Maschinenkonstruktion, Kleiner Beleg, 2011

[14] Polter, Marko: Dynamische Analyse eines Strahlruderantriebes unter Berücksichtigung detaillierter Lastannahmen auf Grundlage von CFD-Berechnungen. Dresden, Technische Universität Dresden, Lehrstuhl Maschinenelemente und Maschinenkonstruktion, Diplomarbeit, 2010

[15] Polter, Marko: Entwicklung und Konstruktion einer Überlastkupplung. Dresden, Technische Universität Dresden, Lehrstuhl Maschinenelemente und Maschinenkonstruktion, Kleiner Beleg, 2008

[16] Ruge, Peter; Birk, Carolin: A comparison of infinite Timoshenko and Euler-Bernoulli beam models on Winkler foundation in the frequency- and time-domain. In: Journal of Sound and Vibration (2007), 304, S. 932-947

[17] Wiche, E: Radiale Federung von Wälzlagern bei beliebiger Lagerluft. In: Konstruktion 19, Heft 5, S. 184 - 192, 1967

[18] Wünsch, Dieter; Carcia del Castillo, Luis: Experimentelle Modellfindung und modellhafte Ermittlung dynamischer Belastungen torsionsschwingungsfähiger Systeme. Frankfurt am Main: Forschungsvorhaben FVA Nr. 95, Forschungshefte 213 und 214 der Forschungsvereinigung Antriebstechnik e.V., 1986

V International Conference on Computational Methods in Marine Engineering
MARINE 2013
B. Brinkmann and P. Wriggers (Eds)

NUMERICAL ANALYSIS OF IMPACT OF ENERGY BUOY ANCHORING CONFIGURATIONS ON ITS MOTION AND EFFICIENCY

MARINE 2013

PAWEL DYMARSKI*, CZESLAW DYMARSKI†

* Gdansk University of Technology (GUT)
Politechnika Gdańska
ul. Narutowicza 11/12, PL 80233 Gdansk, Poland
e-mail: padymar@pg.gda.pl, web page: http://www.pg.gda.pl

† Gdansk University of Technology (GUT)
Politechnika Gdańska
ul. Narutowicza 11/12, PL 80233 Gdansk, Poland
e-mail: cpdymars@pg.gda.pl, web page: http://www.pg.gda.pl

Key words: Devices for Capturing Sea Wave Energy, offshore hydrodynamics, numerical computations.

Abstract. This document provides results of the numerical analysis of impact of energy buoy anchoring configuration on its motion and efficiency. Results of these analysis presented in the paper are a continuation of the works [1], [2].

1 INTRODUCTION

This paper presents a numerical analysis of the impact of energy buoy mooring configurations on its movement on the wave and effectiveness. The method used to analyse the buoy movement modelling in six degrees of freedom was described in a paper presented at the Conference MARINE 2011.

The buoy is shown in fig. 1 and fig 2. It consists of the hull (1), column (2) with shaft, turbine (3), torque meter (4), unidirectional clutch (5) , flywheel (6), two stage chain gear (7), electric generator (8) and anchor wires (9).

A more detailed description of construction and equipment of the buoy and of the method of its operation can be found in the article [2]

Presented below simulations of the buoy movement in regular wave and power calculations were conducted for several configurations of anchoring systems, but only for wave height equal 0,4 m, in the frequency ranges of (0,30 ÷ 0,44) Hz, it means for one of such conditions as were created during model tests at the scale of 1:5 in the towing tank.

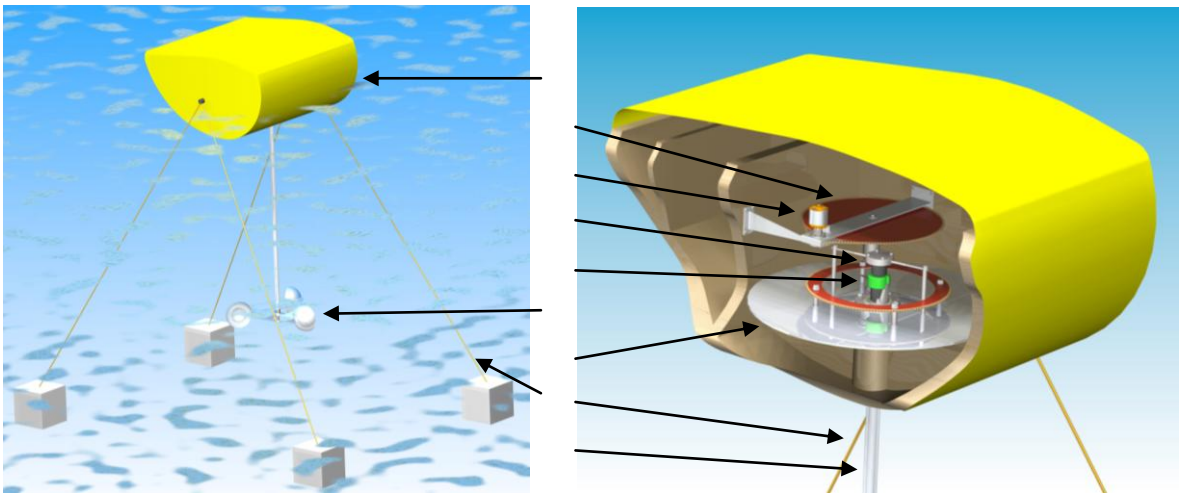


Figure 1: Drawing of view and cross-section of the buoy for capturing of sea wave energy



Figure 2: Photos of the buoy model during its launching in the towing tank and during the test on regular wave

2 VARIANTS OF THE ANCHOR SYSTEMS USED IN SIMULATIONS

All variants of the anchoring systems were calculated for wire ropes located symmetrically relative to the plane of symmetry of the buoy. They differed only in the number and location of the anchors at the bottom of sea and also in the anchor ropes tension value.

The first numerical simulation was performed for the variant 1of the anchoring system, the same as the one which has been used during of the model tests in the towing tank. This system, marked **As 2-0** (Anchor system, 2 – number of the main ropes, 0 – angle of the rope from the vertical), is shown in a simplified way in fig. 3, consisted of two main wire ropes and two auxiliary lines. In side

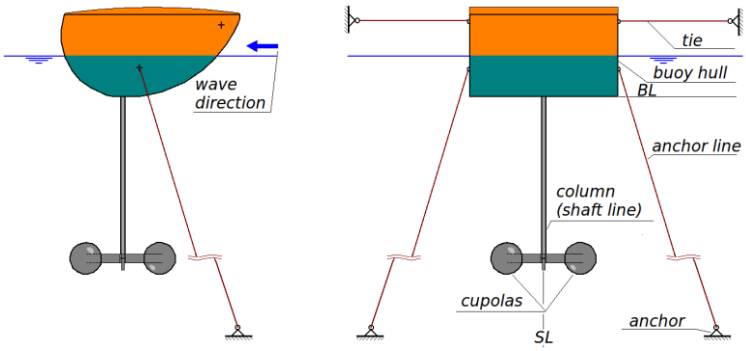


Figure 3. Sketch of the modelled anchoring system As 2-0

view the main ropes look vertical at calm water. They are attached to both sides of the buoy before and slightly above the center of its buoyancy and strained to increase draught of the buoy. The lower ends of these ropes were attached to a larger hard box laid on the bottom of the towing tank. The auxiliary lines are horizontal, their role is to prevent yawing. The stiffness of the main ropes is high to prevent heave motions. However the horizontal lines are flabby, in order to minimize yawing without reducing pitching.

The buoy turbine is moving progressively (due to pitch motion) and rotating. The hydrodynamic reaction on rotor is calculated as the sum of forces induced on the canopies and additional elements to which the canopies are attached. Hydrodynamic reaction induced on singular (isolated) canopy was calculated after defining and evaluation of the characteristics of the drag and lift coefficients using RANSE-CFD method. The total torque of the turbine is the difference between hydrodynamic interactions and torque response to the generator. The torque on the generator is a function of turbine rotational speed. In this model, we have assumed that this is a linear function.

Further simulations were carried out for three variants of anchoring systems consisting of four lines differing only in the position of the bottom. Simplified drawing of these kind anchoring systems of the buoy with shown basic geometrical parameters is presented in fig. 5. Calculations were performed for the following combinations of the system, symmetric relative to the plane of the buoy symmetry:

- varint 2 – **As 4-15x15 – (**Anchor system, 4 – number of the main ropes, 15x15 – α_1 x α_2);
- varint 3 – **As 4-30x30 – (**Anchor system, 4 – number of the main ropes, 30x30 – α_1 x α_2);
- varint 4 – **As 4-15x45 – (**Anchor system, 4 – number of the main ropes, 15x15 – α_1 x α_2);

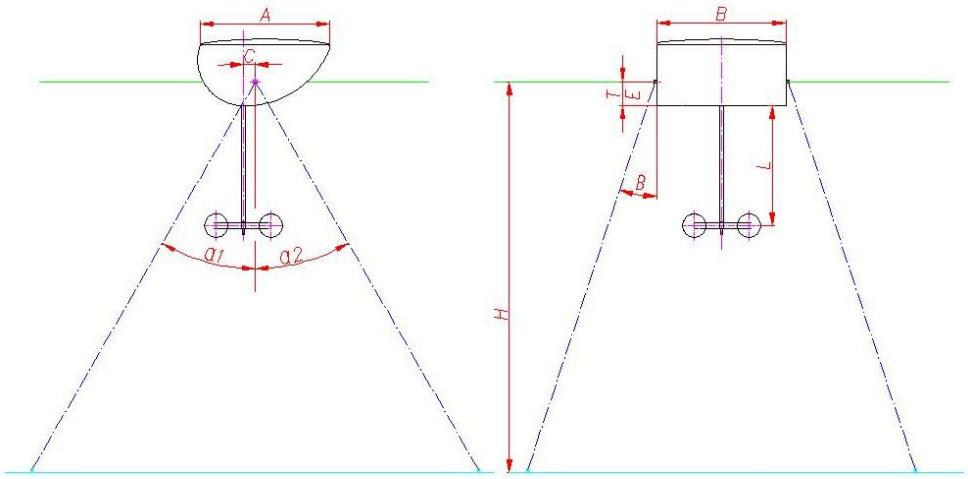


Figure 4. View of the anchored system of the buoy with shown basic geometrical parameters

The calculation of the following parameters were buoy geometric model tested in towing tank and set in fig. 5.: A = 2,0 m; B = 2,0 m; C = 0,162 m; L = 2,64 m; E = 0,370 m; H = 6,0 m; β = 18˚; α_1 , α_2; - are different for each variant;

- T_0 = 0,32 m – draught of the buoy's hull before tensioning of the anchor wire;
- T_k = 0,37m – draught of the buoy's hull after tensioning of the anchor wire;
- d = 0,005 m – diameter of the anchor wire;

- H_w = 0,4 m – height wave height

The last, variant 5, of the presented anchoring system consists of six main ropes arranged symmetrically around the vertical axis located slightly before the center of the buoy buoyancy, as it is shown in fig. 5. It is marked **As 6x40 – (**Anchor system, 6 x40 – number of the main ropes x α). In order to better compare the characteristics of the analyzed mooring systems, it was assumed that the relevant geometric parameters as well as weight, and moment of inertia of the buoy are the same as for previous variants of the anchoring system.

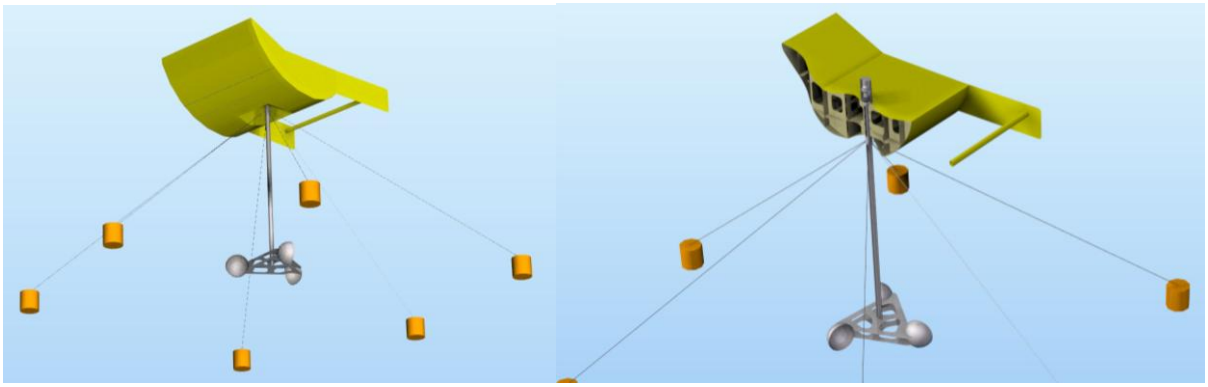


Figure 5: Drawing of view and cross-section of the buoy with symmetrical anchor system marked **As 6x40**

3 RESULTS OF NUMERICAL SIMULATIONS

3.1. Results for variant 1

The values of the basic parameters of the buoy motion on regular wave such as: pitch, heaving and horizontal displacement as well as energetic parameter on the turbine shaft such as: torque, rotary speed and power calculated for real scale for the same range of the wave angular speed are presented in fig. 6.

The values of these calculation results show very low efficiency of wave energy capturing by the device for the anchoring system. It was confirmed by the results of model tests. This can be explained by the low rigidity of the system on the horizontal displacement of the buoy in the direction of the surge. These displacements for the wave frequency ω = ~ 1.1, corresponding to the maximum efficiency in its operations, reaching a value of about 1.6 m and further grow to 2.4 m for ω = ~ 0.8. This means that much of the extracted wave energy is consumed for the horizontal displacement of the buoy at the expense of reducing the amplitude of the pitch and because of this also the energy of rotation of the turbine.

It was concluded that increasing the efficiency of the device required magnification of the rigidity of the mooring buoy system, and thus reducing its linear motion. Therefore, further buoy simulations were carried out for mooring systems with increased rigidity, which is obtained by increasing the number of anchor ropes, and by appropriate selection of their location configuration.

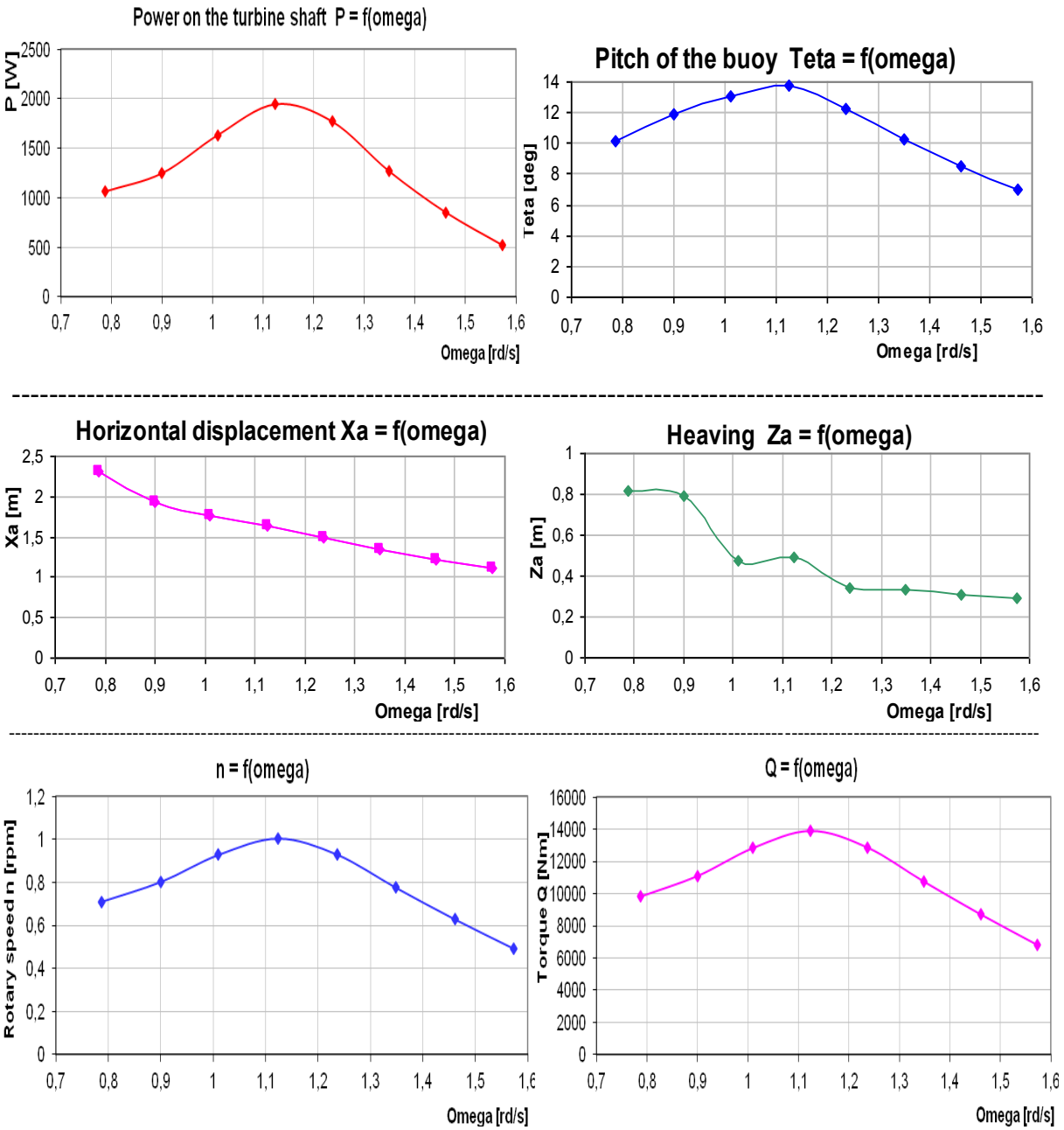


Figure 6: The captured power of the waves and pitch, horizontal and vertical displacement of the buoy as well as torque and rotary speed of the turbine shaft, calculated for variant 1 **As 2-0** of the anchoring system

3.1. Results for variant 2

The results of the similar simulations conducted for variant 2 anchoring system **As 4-15x15** are presented in fig. 7.

As expected the use of four anchor ropes symmetrically spaced and deviated from the vertical caused a reduction of the horizontal displacements of the buoy and thus increased the amplitude of the pitch motion and captured energy.

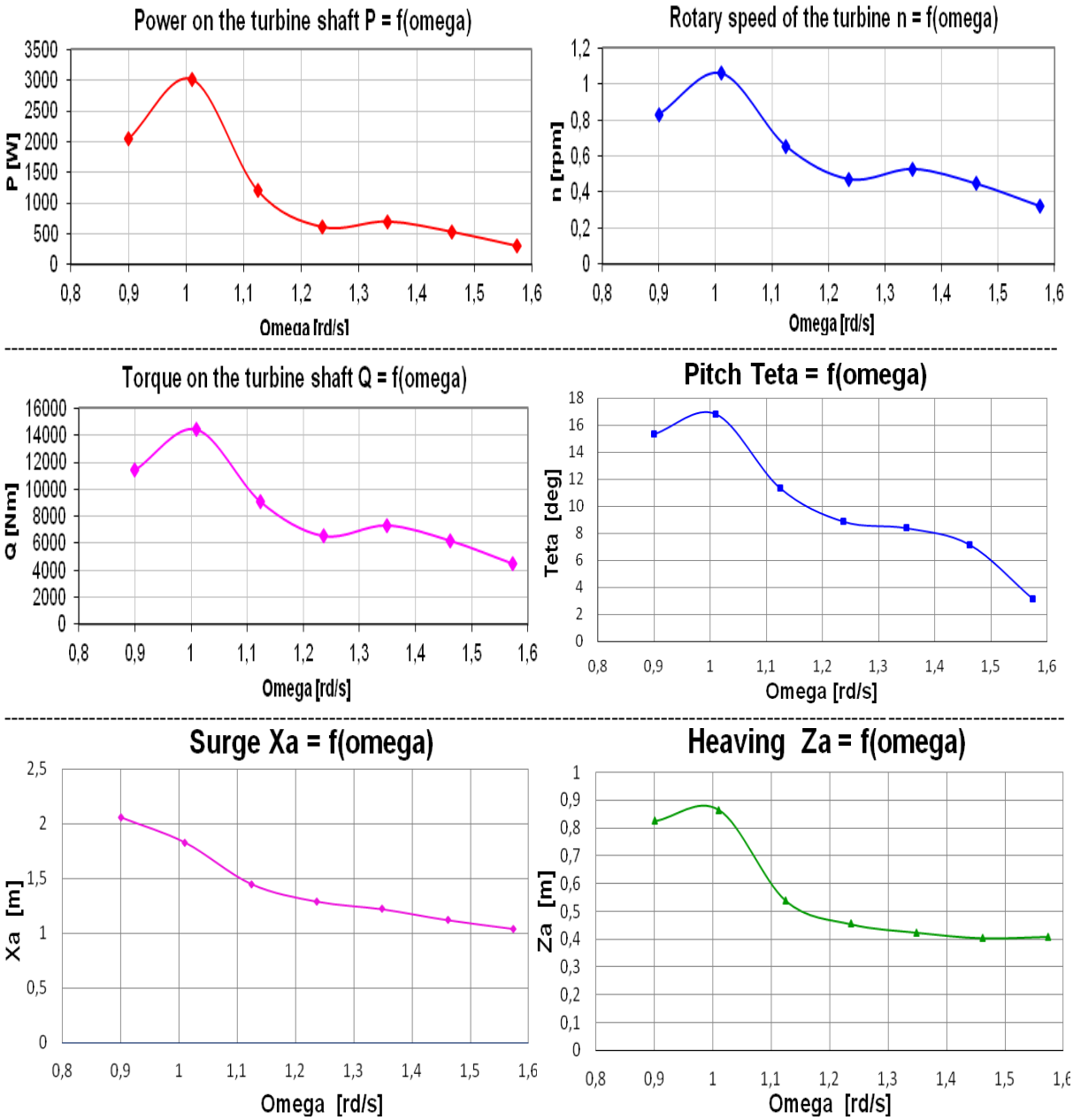


Figure 7: Captured power of the waves as wel as torque and rotary speed of the turbine calculated for variant 2 **As 4-15x15** of the anchoring system

3.1. Results for variant 3

Variant 3 of anchoring system is symmetrical, similar to variant 2, but the angle of anchor lines in this case is twice as high. Because of this the rigidity of the system increased in the horizontal direction and at the same time decreased in the vertical direction. Calculated values of the individual parameters of captured energy and motion of the buoy are shown in fig. 8.

The results presented below relate to somewhat reduced range of frequency ω for this variant of the anchoring system because it was difficult to achieve convergence solutions for

small values of ω. As expected, however, these results clearly demonstrated that the efficiency of sea wave capturing energy has increased significantly.

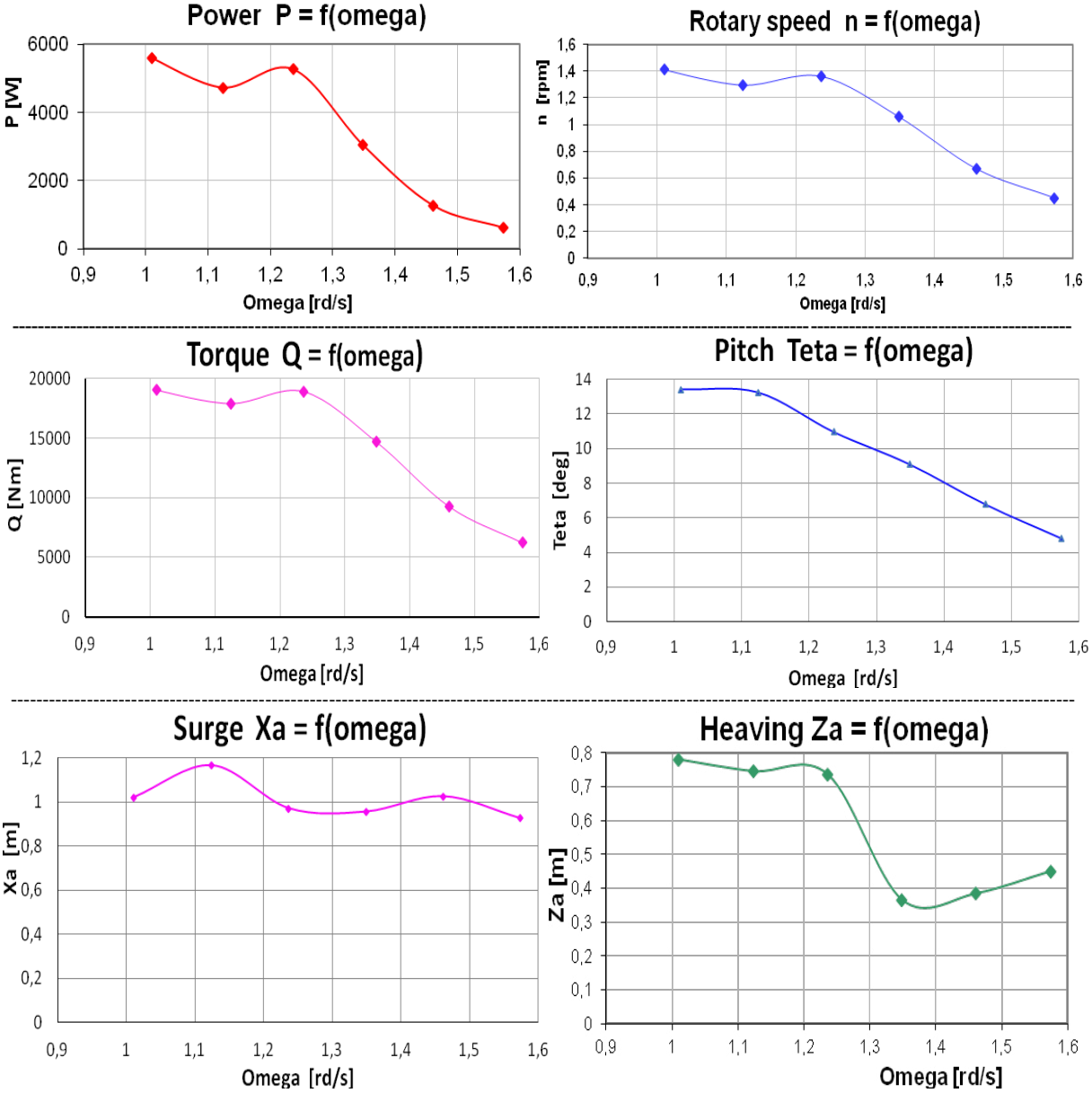


Figure 8: The curves of such parameters as: power, rotary speed, torque, picht, surge and heaving of the buoy as afunction of frequency of the waves calculated for anchoring system **As 4-30x30**

3.1. Results for variant 4

In variant 4 (As 4-15x45) there were still used four anchor lines, but not in a symmetrical arrangement. Due to the fact that the main load acting on the buoy and generated by the wave is directed to the front part, it was considered that it would be preferable to increase angles of the both front ropes what in effect give higher stiffness of the system in the direction of the load. While, the rope should be tilted back from the vertical direction by a smaller angle to

better limit heaving of the buoy. The results of the simulation performed for this configuration of the anchoring system is shown in Fig. 9.

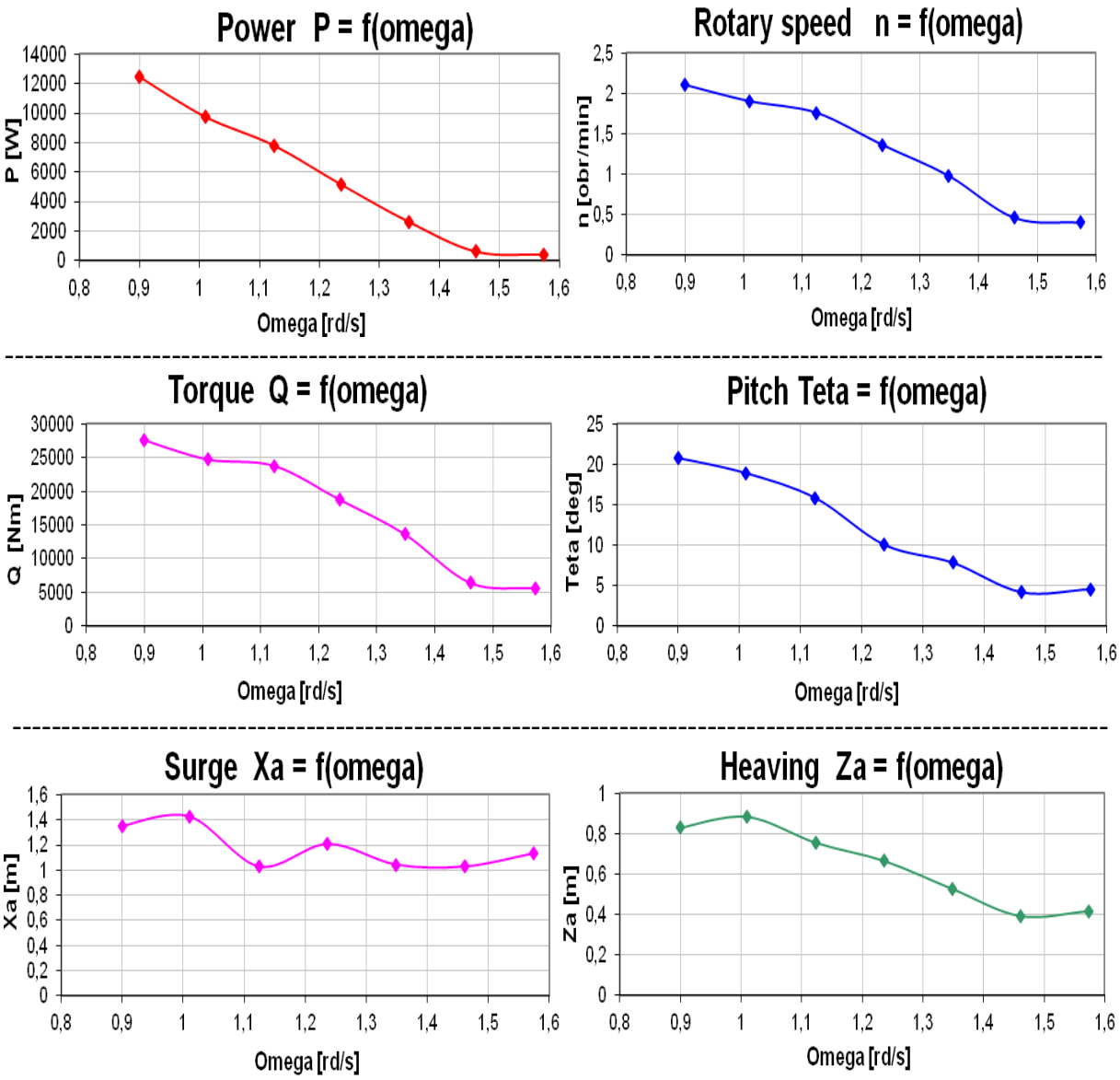


Figure 9. The curves of such parameters as: power, rotary speed, torque, picht, surge and heaving of the buoy as afunction of frequency of the waves calculated for anchoring system As 4-30x30

For this variant of the anchoring system value of the captured sea wave energy surpassed 12 kWand pitch was over 20 deg. It is much beter than in previous cases, but all these presented above configurations of the anchoring system are adjusted to one direction of the wave. It is significant disadvantage because waves seldom keep steady direction.

3.1. Results for variant 5

Bearing in mind above-mentioned disadvantage of the previous systems it was decided to change a little shape of the buoy and replace current anchor configurations symmetric with

respect to the plane of symmetry by axially symmetric as it is shown in fig. 5. The upper ends of the anchor ropes are connected to the bearing housing mounted on the vertical axis fixed to the buoy hull. Because the axis of the bearing is slightly forward of the center of buoyancy, the buoy will always set in the most favorable position facing the wind and waves. It was concluded that this changed shape of the buoy and new variant of the anchoring system will allow at list significantly increase the period of effective work of the device regardless of wave direction. The results of the simulation performed for this configuration of the anchoring system is shown in Fig. 10.

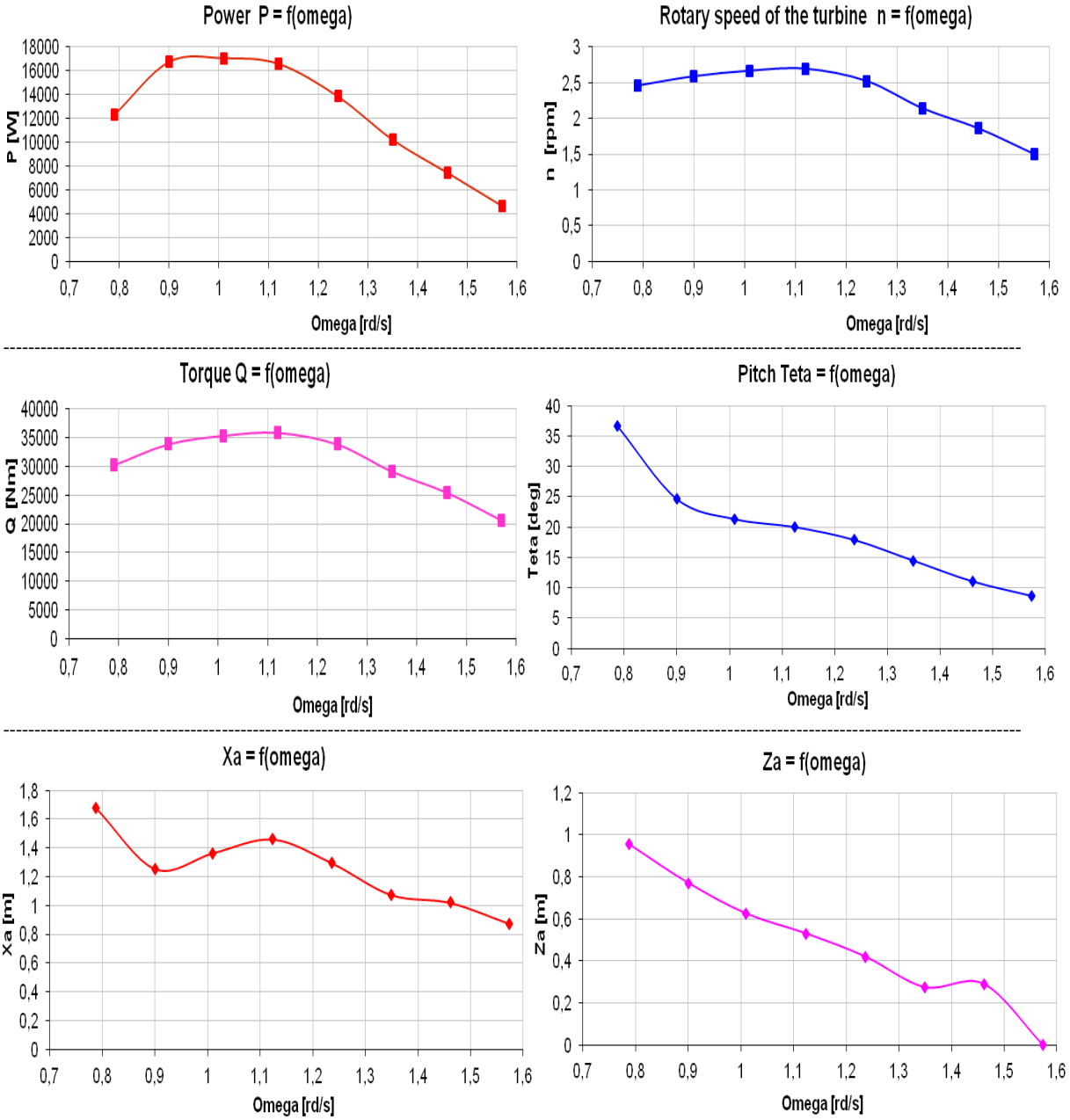


Figure 10: The curves of such parameters as: power, rotary speed, torque, picht, surge and heaving of the buoy as afunction of frequency of the waves calculated for variant 5 of the anchoring system **As 4-30x30**

As can be seen from these graphs the results of the simulations for this variant of the anchoring system are the best. Not only value of the sea wave captured energy is the highest, but also the range of wave frequency with such high power is the widest.

In order to show the impact of the anchor rope tensioning on the efficiency of the buoy in fig. 11 presented the results of the main parameters of the captured wave energy calculated for the same configuration of the anchoring system, but with not tight ropes.

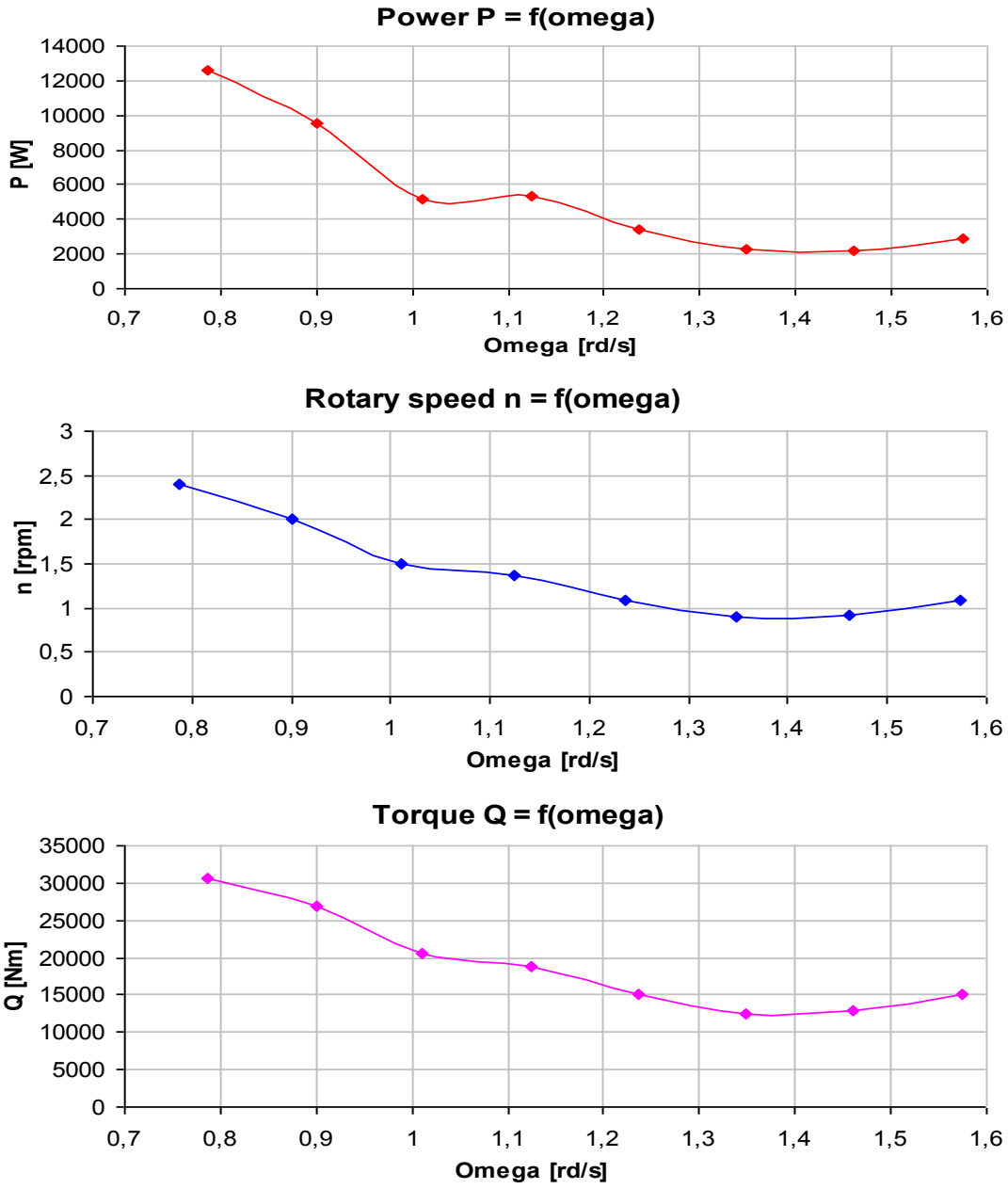


Figure 11. The curves of such parameters as: power, rotary speed and torque as afunction of frequency of the waves calculated for variant 5 of the anchoring system **As 4-30x30**, but with not tight anchor ropes

As might be expected the results show a significant deterioration in both the quality and efficiency of work of the buoy. The highest value of the captured sea wave energy was less than 74% in comparison with value calculated for the buoy with pre-tensioning anchor ropes, and in a narrow range of low frequencies only.

4 CONCLUSIONS

The paper presents the results of numerical simulations of the motion and efficiency of the energy buoy on regular wave. These results show a significant impact of the configuration of the anchoring system and the pre-tensioning of the anchor rope on the efficiency of capturing the sea wave energy. It turns out that an appropriate choice of these two parameters can radically increase the efficiency of acquiring the energy –13.6% of the wave energy for the analyzed conditions. This may not be a satisfactory value, but it should be considered that up to now the effect of a number of other parameters has not been analyzed. The appropriate selection of these additional parameters could lead to a further increase of the efficiency. These additional parameters include geometric parameters of the hull, column length, number and diameter of the spheres and the diameter of their deployment. The research on determining these dependencies will be continued and we hope to present the results next year on the MARINE 2014 conference.

REFERENCES

[1] Dymarski P., Dymarski Cz.: *Numerical simulation of energy buoy motion in wave.* IV International Conference on Computational Methods In Marine Engineering IMARINE 2011 Lisbon, Portugal, 28 – 30 September 2011.

[2] Dymarski C. Dymarski P. Litwin W.: *Novel Design of an Ocean Wave Power Device*; KEY ENGINEERING MATERIALS 2012 s. 206-215.

V International Conference on Computational Methods in Marine Engineering
MARINE 2013
B. Brinkmann and P. Wriggers (Eds)

SIMULATION OF MOORING CABLE DYNAMICS USING A DISCONTINUOUS GALERKIN METHOD

JOHANNES PALM[⋆], GUILHERME MOURA PAREDES[†], CLAES ESKILSSON[⋆], FRANCISCO TAVEIRA PINTO[†] AND LARS BERGDAHL[⋆]

[⋆] Department of Shipping and Marine Technology
Chalmers University of Technology
SE–412 96 Gothenburg, Sweden
Email: johannes.palm@chalmers.se - Web page: www.chalmers.se

[†] Departamento de Engenharia Civil
Faculdade de Engenharia, Universidade do Porto
Rua Dr. Roberto Frias, s/n, 4200–465 Porto, Portugal
Email: moura.paredes@fe.up.pt - Web page: www.fe.up.pt

Key words: Mooring cable, Discontinuous Galerkin method, High-order finite elements

Abstract. A new numerical model for simulating the dynamics of mooring cables is presented. The model uses the *hp* formulation of the discontinuous Galerkin method. Verification against analytical solutions for a static and a dynamic case is carried out and the model is shown to exhibit exponential convergence with increasing polynomial order of the expansion basis. A simulation of the cyclic movement of a cable endpoint is compared to experimental results, and there is a good agreement between the computed and measured tension force.

1 INTRODUCTION

Snap loads have always been an important aspect of mooring cable dynamics. Within the field of floating wave energy converters (WECs), the importance of snap loads will most likely be even greater. Unlike the typical moored offshore structures, these devices will be installed in relatively shallow water in energetic wave climates. Their working principle of operation in many cases requires them to oscillate at the water surface with large amplitudes and close to their resonant frequency. These characteristics will make the mooring cables of floating WECs more prone to snap load effects, requiring tools that can accurately model this.

Many numerical models for cable dynamics have been proposed since the early 1960's and the work of Walton and Polachek [1]. Some of the more frequently used methods include the finite difference method, e.g.[1, 4], and the popular lumped mass method, e.g.

[2, 3]. Linear finite element methods have been used by e.g. [5] and, more recently, studies employing higher-order finite elements including cubic splines [6] and mixed *hp* elements [7] have been presented.

The formulation presented in this paper uses the discontinuous Galerkin (DG) method of arbitrary spatial order to model a perfectly flexible cable with no bending or torsional stiffness. The hallmark of the DG method is that the solutions are allowed to be discontinuous over elemental boundaries and that the elements are coupled by numerical fluxes, as in the finite volume method. Thus the discrete space of the DG method can be argued to be better suited for handling shock waves such as snap loads. Although the final aim of the new mooring cable solver is directed towards snap loads, in this paper only the first step towards accomplishing this is presented: verification and validation of the fundamental DG model using *hp* elements.

The paper is organised as follows. In Section 2 the equations governing the cable dynamics are presented and in Section 3 the numerical discretization, focusing on the DG method, is described. The results of the numerical model are presented in Section 4. First, to verify the model and to establish the accuracy of the formulation, the model is compared against well known analytical solutions for the static elastic catenary and a linear transverse wave on a string. Then, model simulations of a submerged cable with forced cyclic end point motion are presented and compared to measurements of a physical model test. Finally, concluding remarks are found in Section 5.

2 GOVERNING EQUATIONS

The dynamics of a perfectly flexible cable are described by a one-dimensional second-order non-linear wave equation, see e.g. [5, 7]. Let $\mathbf{r}$ and s denote the cable position vector and the curvilinear abscissa along the unstretched cable, respectively, and let t denote the time. Following [12], the equations are made non-dimensional by scaling $\mathbf{r}$ and s with a characteristic length L_c and by scaling the time with a characteristic time t_c. The cable dynamics in non-dimensional form are then given as

$$\frac{\partial^2 \mathbf{r}}{\partial t^2} - \frac{\partial}{\partial s}\left(c^2 \frac{\partial \mathbf{r}}{\partial s}\right) = \mathbf{f}\,, \tag{1}$$

$$c^2 = \frac{t_c^2}{L_c^2}\frac{EA_0}{\gamma_0}\frac{\epsilon}{1+\epsilon}\,, \tag{2}$$

$$\epsilon = \left|\frac{\partial \mathbf{r}}{\partial s}\right| - 1\,, \tag{3}$$

where c is the non-linear and non-dimensional celerity of the wave propagation and the source term $\mathbf{f}$ represents all external forces acting on the cable segment. In the expression for the celerity, EA_0 and γ_0 are the axial stiffness and mass per unit length of the cable, and ϵ represents the strain. For the typical problems treated in this study the characteristic length of the problem is chosen to be the unstretched length of the cable, and the characteristic time is given by the period of oscillation.

The external forces in $\mathbf{f}$ can be divided into four separate forces: $\mathbf{f} = \mathbf{f}_1 + \mathbf{f}_2 + \mathbf{f}_3 + \mathbf{f_4}$. Here $\mathbf{f}_1$ is the sum of gravity and buoyancy, $\mathbf{f_2}$ is the added mass force, and the tangential and normal drag forces are given as $\mathbf{f}_3$ and $\mathbf{f}_4$. Introducing the unit tangential vector $\mathbf{t}$, defined as

$$\mathbf{t} = \frac{\partial \mathbf{r}}{\partial s} \Big/ \left| \frac{\partial \mathbf{r}}{\partial s} \right| = \frac{\partial \mathbf{r}}{\partial s} \Big/ (1+\epsilon) \ , \tag{4}$$

the expressions for the external forces on the cable segment read

$$\mathbf{f}_1 = -\frac{\gamma_\mathrm{e}}{\gamma_0} \frac{t_c^2}{L_c} \mathbf{g} \, , \tag{5}$$

$$\mathbf{f}_2 = C_\mathrm{M} \frac{A \rho_\mathrm{w}}{\gamma_0} \left(\mathbf{a}_\mathrm{rel} - (\mathbf{a}_\mathrm{rel} \cdot \mathbf{t}) \, \mathbf{t} \right) (1+\epsilon) \ , \tag{6}$$

$$\mathbf{f}_3 = \frac{1}{2} C_\mathrm{Dt} \frac{\rho_\mathrm{w} d L_c}{\gamma_0} \left(\mathbf{v}_\mathrm{rel} \cdot \mathbf{t} \right)^2 \mathbf{t} \, (1+\epsilon) \ , \tag{7}$$

$$\mathbf{f}_4 = \frac{1}{2} C_\mathrm{Dn} \frac{\rho_\mathrm{w} d L_c}{\gamma_0} \left| (\mathbf{v}_\mathrm{rel} - (\mathbf{v}_\mathrm{rel} \cdot \mathbf{t}) \, \mathbf{t}) \right| \left(\mathbf{v}_\mathrm{rel} - (\mathbf{v}_\mathrm{rel} \cdot \mathbf{t}) \, \mathbf{t} \right) (1+\epsilon) \ . \tag{8}$$

Here $\gamma_e = \left((\rho_c - \rho_w) / \rho_c \right) \gamma_0$ is the effective mass per unit length of the submerged cable, ρ_c and ρ_w are the cable and fluid densities. The terms C_M, C_{Dt} and C_{Dn} denote the hydrodynamic coefficients of added mass, tangential drag and normal drag forces, respectively. The last three forces are functions of the relative velocity and relative acceleration of the water with respect to the mooring cable, $\mathbf{v}_\mathrm{rel}$ and $\mathbf{a}_\mathrm{rel}$, given by

$$\mathbf{v}_\mathrm{rel} = \mathbf{v}_\mathrm{w} - \frac{\partial \mathbf{r}}{\partial t} \, , \tag{9}$$

$$\mathbf{a}_\mathrm{rel} = \mathbf{a}_\mathrm{w} - \frac{\partial^2 \mathbf{r}}{\partial t^2} \, . \tag{10}$$

3 NUMERICAL MODEL

3.1 Discontinuous Galerkin method

Let Ω_h denote the partition of the domain Ω into N_{el} elemental domains $\Omega^e = \{ s \,|\, s_l^e \leq s \leq s_u^e \}$ with size boundaries $\partial\Omega^e$ at s_u^e and s_l^e (see Figure 1). The size of the e^{th} element is $h_e = s_u^e - s_l^e$. The first step in the discretization of (1) is to rewrite it as a system of first order differential equations in space, with the use of an auxiliary variable $\mathbf{q}$:

$$\frac{\partial^2 \mathbf{r}}{\partial t^2} = \frac{\partial}{\partial s} \left(c^2 \mathbf{q} \right) + \mathbf{f} \, , \tag{11}$$

$$\mathbf{q} = \frac{\partial \mathbf{r}}{\partial s} \, . \tag{12}$$

Within the e^{th} elemental region the solution, for an arbitrary function f, is approximated by setting $f(s,t) \approx f^e(s,t) = \sum_{i=0}^{i=p} \phi_i(s) \tilde{f}_i^e(t)$. Here $\tilde{f}_i^e(t)$ denotes the local degrees of

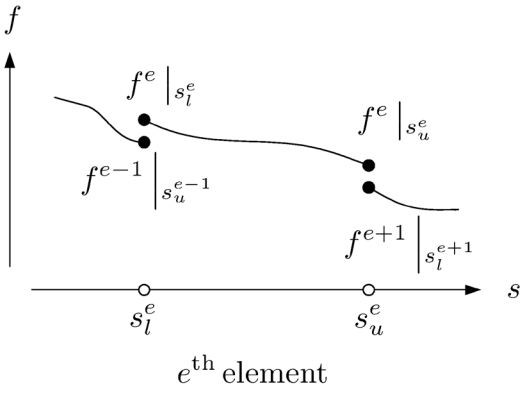


Figure 1: Notation for elemental discretization.

freedom of expansion coefficients and ϕ_i are the expansion basis of order p. In the tests in Section 4 the so-called modal p-type basis [8] is used. This is a hierarchical basis made up of two linear boundary modes and the interior modes given by of Jacobi polynomials.

Taking the inner product $(\cdot\,,\cdot)$ of eqs. (11)–(12) with respect to the basis functions $\phi_k(s)$ we obtain the elemental Galerkin approximation:

$$\left(\phi_k, \frac{\partial^2 \mathbf{r}_h}{\partial t^2}\right)_{\Omega^e} = \left(\phi_k, \frac{\partial}{\partial s}\left(c_h^2 \mathbf{q}_h\right)\right)_{\Omega^e} + \left(\phi_k, \mathbf{f}_h\right)_{\Omega^e}\,, \qquad \forall\ k\,, \tag{13}$$

$$\left(\phi_k, \mathbf{q}_h\right)_{\Omega^e} = \left(\phi_k, \frac{\partial \mathbf{r}_h}{\partial s}\right)_{\Omega^e}\,. \tag{14}$$

Integrating the terms involving derivatives of s by parts, exchanging the boundary flux terms with numerical fluxes, denoted by $\widehat{\cdot}$, and integrating by parts once more yields the following formulation

$$\left(\phi_k, \frac{\partial^2 \mathbf{r}_h}{\partial t^2}\right)_{\Omega^e} = \left(\phi_k, \frac{\partial}{\partial s}\left(c_h^2 \mathbf{q}_h\right)\right)_{\Omega^e} + \left[\phi_k(\widehat{c_h^2 \mathbf{q}_h}^{\,e} - c_h^2 \mathbf{q}_h^e)\right]_{s_l^e}^{s_u^e} + \left(\phi_k, \mathbf{f}_h\right)_{\Omega^e}\,, \tag{15}$$

$$\left(\phi_k, \mathbf{q}_h\right)_{\Omega^e} = \left(\phi_k, \frac{\partial \mathbf{r}_h}{\partial s}\right)_{\Omega^e} + \left[\phi_k(\widehat{\mathbf{r}_h}^{\,e} - \mathbf{r}_h^e)\right]_{s_l^e}^{s_u^e}\,. \tag{16}$$

For the numerical fluxes, a modified version of the local discontinuous Galerkin (LDG) method developed by Cockburn and Shu [9] is used,

$$\widehat{\mathbf{r}_h} = \{\mathbf{r}_h\} + \beta\,[\mathbf{r}_h]\,, \tag{17}$$

$$\widehat{c_h^2 \mathbf{q}_h} = \{c_h^2 \mathbf{q}_h\} - \beta\left[c_h^2 \mathbf{q}_h\right] + \frac{\eta_1}{h}\,[\mathbf{r}_h] + \eta_2 h\,[\mathbf{v_h}]\,, \tag{18}$$

where η_1 and η_2 are constant mesh-independent parameters, h is the non-dimensional element size, $\beta \in [-1/2, 1/2]$ controls the level of up- and downwinding of the fluxes, and the trace, $\{x\}$, and jump ,$[x]$, operators are introduced as

$$\{x_h^e\}|_s = \frac{1}{2}\left(x_h^e|_{s_u^e} + x_h^{e+1}|_{s_l^{e+1}}\right) \quad \text{if} \quad s = s_u^e\,, \tag{19}$$

$$\{x_h^e\}|_s = \frac{1}{2}\left(x_h^e|_{s_l^e} + x_h^{e-1}|_{s_u^{e-1}}\right) \quad \text{if} \quad s = s_l^e\,, \tag{20}$$

$$[x_h^e]\,|_s = \left(x_h^e|_{s_u^e} - x_h^{e+1}|_{s_l^{e+1}}\right) \quad \text{if} \quad s = s_u^e\,, \tag{21}$$

$$[x_h^e]\,|_s = \left(x_h^{e-1}|_{s_u^{e-1}} - x_h^e|_{s_l^e}\right) \quad \text{if} \quad s = s_l^e\,. \tag{22}$$

The choice of β and η_1 will give rise to different computational stencils affecting the convergence rates [9, 8]. In the test cases presented in Sections 4, $\beta = 0$ is used which gives a centred flux with a wide stencil, but typically allows for larger time steps to be used. The η_1 penalty term is employed to obtain optimal convergence. The use of the additional penalty term η_2, which is non-standard, was found to increase the robustness of the scheme for the validation tests. A more in-depth investigation into the behaviour of the penalty terms is ongoing work.

Dirichlet and Neumann boundary conditions are implemented weakly through the definition of the numerical fluxes [9]

$$\widehat{\mathbf{r}_h} = \mathbf{g}_\mathrm{D} \quad \text{on } \Gamma_\mathrm{D}\,, \qquad \widehat{\mathbf{r}_h} = \mathbf{r}_h^e \quad \text{on } \Gamma_\mathrm{N}\,, \tag{23}$$

$$\widehat{c_h^2\mathbf{q}_h} = (c_h^e)^2\mathbf{q}_h^e + \frac{\eta_1}{h}\left(\mathbf{r}_h^e - \mathbf{g}_\mathrm{D}\right) \quad \text{on } \Gamma_\mathrm{D}\,, \qquad \widehat{c_h^2\mathbf{q}_h} = \mathbf{g}_\mathrm{N} \quad \text{on } \Gamma_\mathrm{N}\,, \tag{24}$$

where $\mathbf{g}_\mathrm{D}$ and $\mathbf{g}_\mathrm{N}$ are the non-dimensionalised values at the cable end points.

3.2 Time-stepping scheme

Presently the numerical model uses explicit time-stepping schemes, either the third-order Runge-Kutta scheme [9] typically associated with DG schemes or a simple second-order central differencing scheme. The computations presented in this paper have used the central differencing scheme. Writing the semi-discrete equations as

$$\frac{\partial^2 \mathbf{r}_h}{\partial t^2} = \mathbf{L}_h\left(\mathbf{r}_h\right)\,, \tag{25}$$

advancing from time level n to $n+1$ for the central differencing scheme is simply

$$\mathbf{r}_h^{n+1} = 2\mathbf{r}_h^n - \mathbf{r}_h^{n-1} + \Delta t^2 \mathbf{L}_h\left(\mathbf{r}_h\right)\,. \tag{26}$$

It should be noted that the time step restriction for explicit schemes for second-order spatial derivatives is very restrictive as $\Delta t \propto p^{-4}$ [8]. Thus implicit schemes will be considered in later studies.

4 TEST CASES

The convergence of the model and the quality of the simulation results are verified by comparison with analytical solutions for known cases. The error in the L_2-norm of the results is computed for different choices of polynomial order p and element size h. The L_2 error is defined as

$$\|f\|_{L_2} = \sqrt{\int_\Omega (f_{exact} - f)^2 \, \mathrm{d}\Omega}\,, \tag{27}$$

and is evaluated using the quadrature points inside every element e.

4.1 Static verification - elastic catenary equation

The analytical solution to the static equilibrium of an elastic catenary can be found in e.g. [10] and is well known:

$$x = a_\mathrm{T} \mathrm{sinh}^{-1}\left(\frac{s}{a_\mathrm{T}}\right) + a_\mathrm{T}\frac{\gamma_\mathrm{e} g}{EA_0} s\,, \tag{28}$$

$$z = \sqrt{a_\mathrm{T}^2 + s^2} + \frac{\gamma_\mathrm{e} g}{2EA_0} s^2 - a_\mathrm{T}\,, \tag{29}$$

$$a_\mathrm{T} = \frac{T_\mathrm{H}}{\gamma_\mathrm{e} g}\,. \tag{30}$$

The horizontal component of the tension force, T_H, is constant along the cable and the origin of the x, z and s coordinates is the lowest point of the catenary. The equations are implicit when T_H is unknown, and are solved numerically for each set of cable conditions.

The computed cable has a stiffness of $EA_0 = 200$ kN/m, a mass of $\gamma_e = 1.738$ kg/m and an unstretched length L of 100.5 m. The attachment points of the cable are horizontally aligned and distanced by 100 m. Three cases are examined:

- p-type refinement ($N_{el} = 2$ with $p = 1\,, \ldots\,, 9$),
- h-type refinement using linear elements ($N_{el} = 1\,, 2\,, 4\,, \ldots\,, 20$ with $p = 1$),
- h-type refinement using quadratic elements ($N_{el} = 1\,, 2\,, 4\,, \ldots\,, 20$ with $p = 2$).

The computational results in terms of L_2 error of the cable position versus total degrees of freedom are presented in Figure 2. Both the expected exponential convergence of the p-type refinement (as illustrated by the straight line for $h = 2$ in the semi-log plot to the left in Figure 2) and the algebraic convergence of the h-type refinement (as demonstrated by the straight lines in the logarithmic plot to the right of Figure 2) are shown in the result. The benefit in using high-order methods for smooth problems in terms of accuracy per degree of freedom is obvious.

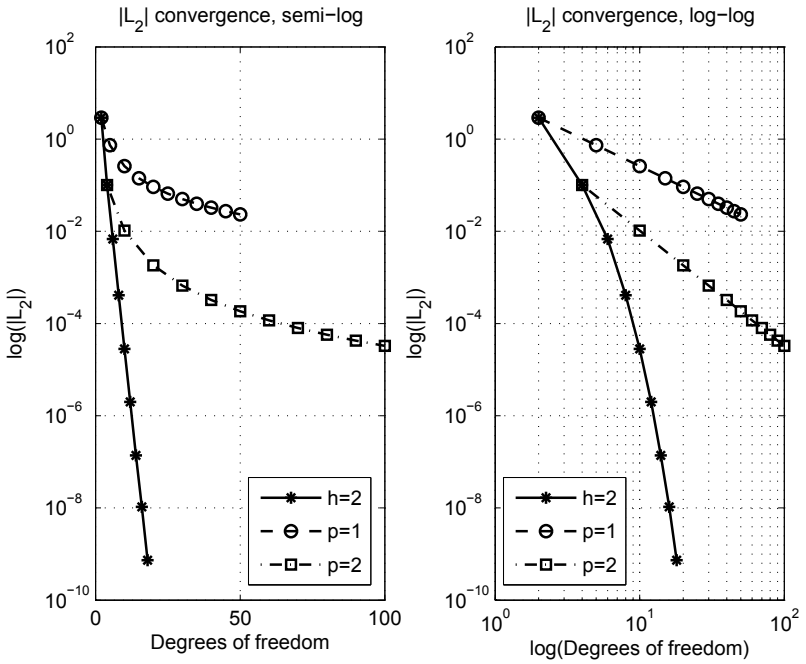


Figure 2: L_2 error of the cable position as a function of the total number of degrees of freedom for the elastic catenary case.

4.2 Dynamic verification - standing wave on a taut cable

Consider a cable with constant tension and strain, no external forces applied and only transverse displacements allowed. Then eq. (1) simplifies to the standard linear wave equation

$$\frac{\mathrm{d}^2 r}{\mathrm{d}t^2} = \frac{T}{\gamma_0(1+\epsilon)} \frac{\partial^2 r}{\partial s^2} \,. \tag{31}$$

The term $T/\left(\gamma_0(1+\epsilon)\right)$ in eq. (31) is the square of the celerity of the wave in the unstretched computational domain s. The celerity of the wave in the physical domain is

$$c_p = \sqrt{\frac{T}{\gamma_\mathrm{p}}} = \sqrt{\frac{T(1+\epsilon)}{\gamma_0}} \,, \tag{32}$$

where γ_p is the mass per unit length of the stretched cable. Let the end points of the cable be horizontally aligned and stretch it to form a half sine arch that is centred at the midpoint of the cable. The analytical solution to this problem then reads [11]:

$$y(x,t) = A\cos\left(c_p \frac{\pi}{L(1+\epsilon)} t\right) \sin\left(\frac{\pi}{L(1+\epsilon)} x\right) \,, \tag{33}$$

where A is the maximum amplitude of the displacement.

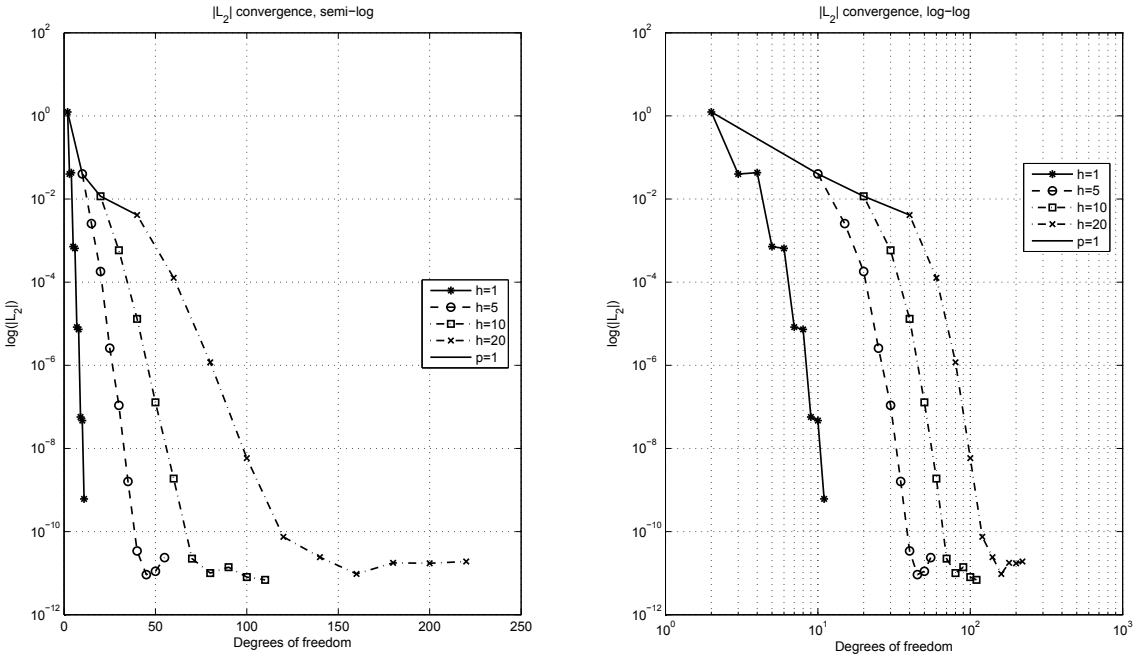


Figure 3: L_2 error of the cable position as a function of the total number of degrees of freedom for the elastic standing wave case.

The computed cable has a constant tension $T = 1\,\mathrm{N}$, a mass of $\gamma_0 = 1\,\mathrm{kg/m}$ and an unstretched length L of $0.5\,\mathrm{m}$. The attachment points are distanced by $1\,\mathrm{m}$ and the wave amplitude is set to $1\,\mathrm{m}$. The domain is divided into $N_{el} = 1\,, 5\,, 10\,, 20$ elements with $p = 1\,, \ldots\,, 10$. For this case no penalty term is used in the model. The solution is integrated for $2\,\mathrm{s}$ (one complete oscillation cycle) using a sufficiently small time step to ensure spatial errors dominate.

The computational results in terms of L_2 error of the cable position versus total degrees of freedom are presented in Figure 3. It is shown that – as for the static catenary case – p-type refinement yields exponential convergence until the error get saturated around machine precision ($\approx 1 \times 10^{-12}$ for the present case). It should be mentioned that the convergence rates are generally sub-optimal and of order p. This is as expected since centred numerical fluxes without penalty terms is known to loose an order of convergence [9].

4.3 Validation test - comparison against the experiments of Lindahl

The model test of Lindahl [12] is used for validating the dynamic behaviour of the cable solver against experimental measurements. In this section, the measured cable top end force results will be compared to those computed by the numerical model.

The experimental set-up is shown in Figure 4. The experimental measurements were

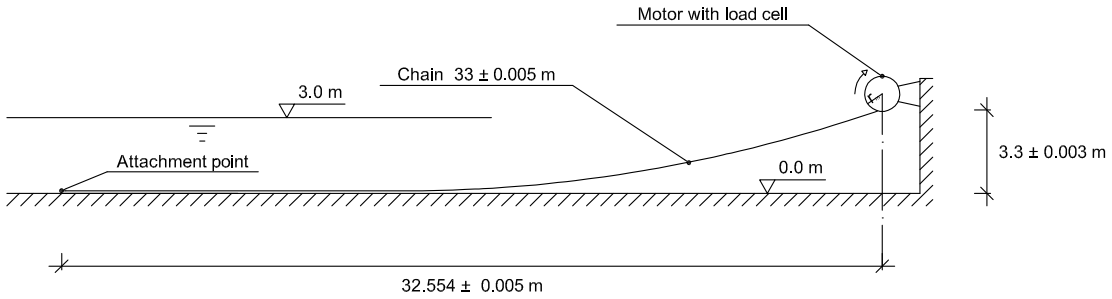


Figure 4: The geometrical setup of the experimental tests by [12].

made on a 33m steel chain ($\rho_c = 7800$ kg/m^3) submerged in 3m of water ($\rho_w = 1000$ kg/m^3). One end was attached to the concrete floor and the other end was attached to a circular plate with a fixed rotation speed. The radius of motion in the cases compared in this study was 0.2 m. The cable characteristics suggested in [12] are presented in Table 1.

In the experiments the top part of the chain was suspended in air and the rest was submerged in water. This is taken into account in the numerical model by the use of the dry weight for the gravity force and by excluding any added mass- or drag forces acting on the cable segment above the height of 3 m.

The interaction between cable segments and the concrete floor is handled by a ground interaction model made up of a bilinear spring and damper system in the normal (vertical) direction and a dynamic friction in the tangential direction [13, 3]. The characteristics of the ground model are presented in Table 1. Please note that $G_{\mathrm{v_c}} = 0.01$ m/s is the velocity at which the dynamic, tangential friction force reaches its maximum value. Up to that value, the friction force is ramped up from 0. The forces acting on the cable when it is interacting with the ground are given by:

$$\mathbf{F}_{\mathrm{Gz}} = -G_{\mathrm{K}}\, d\, \Delta z - 2\, G_{\mathrm{C}} \sqrt{\frac{G_K d}{\gamma_0}} \min\left(0\,, v_z\right) + \gamma_e\, g\,, \tag{34}$$

$$\mathbf{F}_{\mathrm{Gxy}} = -\gamma_{\mathrm{e}}\, g\, G_\mu \min\left(\frac{v_{\mathrm{xy}}}{G_{\mathrm{v_c}}}, 1\right)\,, \tag{35}$$

where $\Delta z \geq 0$ is the ground penetration depth, v_z is the vertical velocity of the cable and $v_{\mathrm{xy}} = \sqrt{v_{\mathrm{x}}^2 + v_{\mathrm{y}}^2}$ is the velocity of the cable tangential to the ground.

In the computations the cable is divided into 10 elements with polynomial order $p = 7$. Two cases with rotational periods of $T_r = 3.5$ s and $T_r = 1.25$ s, respectively, are investigated. The simulations are integrated in time for 15 rotational periods. The resulting forces in the top end are shown in Figures 5 and 6.

As seen in Figures 5 and 6 the values match very well. The maximum value of the tension force is correct within a few percent, and the high frequency oscillations that

Table 1: Characteristics of the cable and the ground interaction model used in the Lindahl cases.

Name	Value	Unit	Description
L	33	m	Cable length
γ_0	0.018	kg/m	Mass per length
EA_0	10000	N	Cable stiffness
d	0.002	m	Nominal cable diameter
C_{Dt}	0.5	-	Tangential drag coefficient
C_{Dn}	2.5	-	Normal drag coefficient
C_{M}	3.8	-	Added mass coefficient
G_{K}	3	GPa/m	Ground normal stiffness per unit area
G_{C}	1	-	Fraction of critical damping of ground
G_{μ}	0.3	-	Friction coefficient
$G_{\mathrm{v_c}}$	0.01	m/s	Cut-off velocity of friction

appear for very low tension force magnitude are small in amplitude. The end force is never completely slack for the $T_r = 3.5$ s case, however other parts of the cable has tension force that vanishes completely. In the more high frequency case of $T_r = 1.25$ s the end point force does however vanish completely. As the entire cable looses stiffness at some instances in time, the numerical oscillations after the slack are larger in the case of higher frequency of excitation. These numerical oscillations are quickly damped out as the cable tension increases, and the inaccuracy is only evident for very low tension force magnitudes. The computed maximum force however is still in excellent agreement with the experimental data. It is worth to point out that the results presented here are unfiltered and have not been smoothed in any way. It should also be mentioned that the ground interaction model has a large influence on the solutions and that further studies into the effect of the ground model for high-order solutions are required.

5 CONCLUDING REMARKS

The presented high-order DG formulation for the solution of cable dynamics shows good agreement with both experimental and analytical data, confirming the accuracy of the model formulation. The model is shown to exhibit the expected exponential convergence associated with p-type refinement. The DG approach allows for discontinuities in the solution – often appearing due to the cable becoming slack, as seen in the Lindahl cases. However, Gibbs-type oscillations, typically associated with the use of high-order schemes in the presence of discontinuities, are occurring in the absence of any artificial viscosity, limiters or filters. In the Lindahl cases stability of the solutions is obtained through the use of the penalty terms. Optimising the penalty terms as well as adding additional shock-capturing capabilities in order to better handle snap loads is ongoing work.

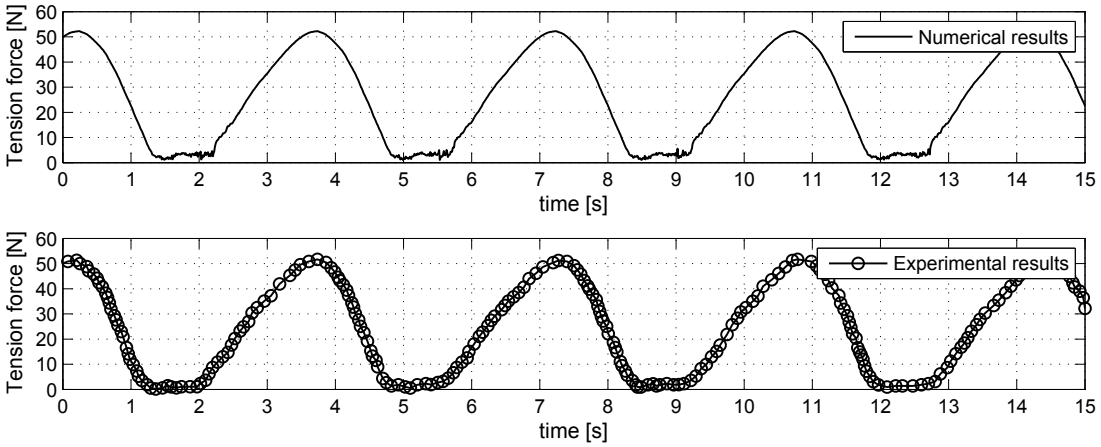


Figure 5: Comparison between the experimental and numerical cable top end forces. $r = 0.2\,\mathrm{m}$ and $T_r = 3.5\,\mathrm{s}$.

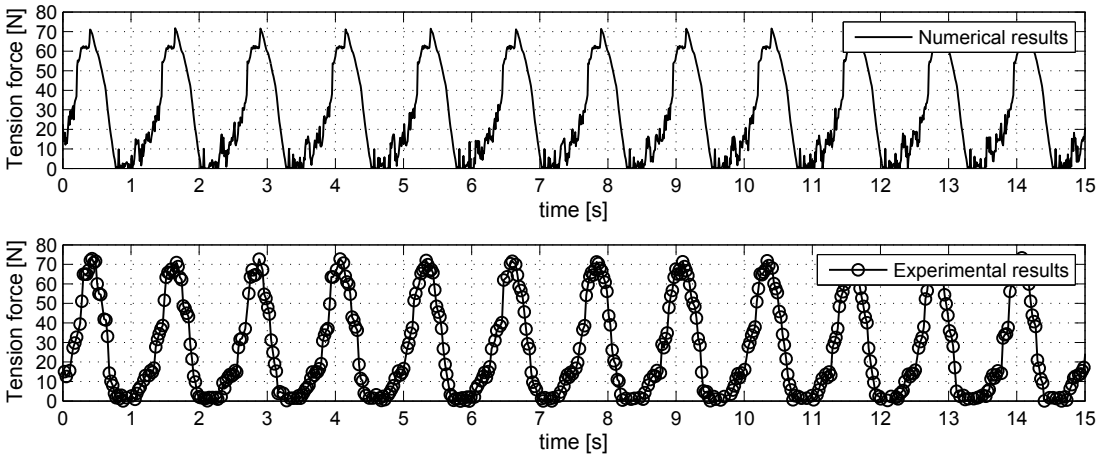


Figure 6: Comparison between the experimental and numerical cable top end forces. $r = 0.2\,\mathrm{m}$ and $T_r = 1.25\,\mathrm{s}$.

ACKNOWLEDGEMENTS

This work was funded by the Swedish collaboration platform Ocean Energy Centre (hosted by Chalmers University of Technology and supported by a grant from Region Västra Götaland, the regional development agency of Västra Götaland in Western Sweden) and by the Portuguese Foundation for Science and Technology (FCT – Fundação para a Ciência e Tecnologia) through research grant SFRH/BD/62040/2009.

REFERENCES

[1] Walton, T.S. and Polachek, H. Calculation of transient motion of submerged cables. *Math. Comp.* (1969) **14**:27–46 .

[2] Khan, N.U. and Ansari, K.A. On the dynamics of a multicomponent mooring line. *Comp. Struc.* (1986) **22**:311–334.

[3] Orcina Ltd. *OrcaFlex manual – version 9.5a.* (2012).

[4] Roussel, P. Numerical solution of static and dynamic equations of cables. *Comp. Meth. Appl. Mech. Engng.* (1976) **9**:65–74.

[5] Aamo, O.M. and Fossen, T.I. Finite element modelling of mooring lines. *Math. Comp. Sim.* (2000) **53**:415–422.

[6] Escalante, M.R., Sampaio, R., Rosales, M.B. and Ritto, T. A reduced order model of a 3D cable using proper orthogonal decomposition. *Mec. Comp.* (2011) **XXX**:1143–1158.

[7] Montano, A. and Restelli, M. and Sacco, R. Numerical simulation of tethered buoy dynamics using mixed finite elements. *Comp. Meth. Appl. Mech. Engng.* (2007) **196**:4117–4129.

[8] Karniadakis, G.Em. and Sherwin, S.J. *Spectral/hp element methods for CFD.* Oxford University Press, 2nd edition, (2003).

[9] Cockburn, B. and Shu, C.-W. Runge-Kutta discontinuous Galerkin methods for convection-dominated problems. *J. Sci. Comp.* (2001) **16**:173–261.

[10] Sjöberg, A. and Bergdahl, L. *Förankringar och förankringskrafter.* Report Series B:30, Department of Hydraulics, Chalmers University of Technology, (1981).

[11] Greiner, W. *Classical mechanics: systems of particles and Hamiltonian dynamics.* Springer, (2003).

[12] Lindahl, J. *Modellförsök med en förankringskabel.* Report Series A:12, Department of Hydraulics, Chalmers University of Technology, (1985).

[13] Lindahl, J. *Implicit numerisk lösning av rörelseekvationerna för en förankringskabel.* Report Series A:11, Department of Hydraulics, Chalmers University of Technology (1984).

V International Conference on Computational Methods in Marine Engineering
MARINE 2013
B. Brinkmann and P. Wriggers (Eds)

NUMERICAL SIMULATION OF THE BEHAVIOUR OF A MOORED SHIP INSIDE AN OPEN COAST HARBOUR

LILIANA V. PINHEIRO*, CONCEIÇÃO J.E.M. FORTES*, JOÃO A. SANTOS†, JOSÉ L.M. FERNANDES ‡

* Laboratório Nacional de Engenharia Civil - Ports and Maritime Structures Division
Av. do Brasil 101, Lisbon. Portugal.
e-mail: {lpinheiro, jfortes}@lnec.pt, www.lnec.pt

†Department of Civil Engineering - Instituto Superior de Engenharia de Lisboa
Rua Conselheiro Emídio Navarro 1, 1959-007, Lisbon. Portugal.
e-mail: jasantos@dec.isel.pt, www.isec.pt

‡Department of Mechanical Engineering - Instituto Superior Técnico
Av. Rovisco Pais, 1, 1049-001 Lisbon. Portugal.
e-mail: leonel@dem.ist.utl.pt, www.ist.utl.pt

Key words: wave propagation, ship – wave interaction, finite elements method, panel method.

Abstract. Sea waves inside harbors can affect scheduled port operations. Hence it is important to correctly predict and characterize the wave field inside ports and to describe the movements of the ship and forces acting upon it. A classical approach is to assume that ship-wave interaction is linear, [1]. Then it is possible to decompose it in the so-called radiation and diffraction problems. Numerical models that solve such problems have been developed and used by the offshore industry for quite a while, [2], to study the interaction of sea-waves with floating objects. However, these models cannot be used to solve the diffraction problem of ships inside harbor basins where nearby reflecting boundaries and shallow depths create very complex nonlinear wave fields.
A new set of procedures using coupled models is proposed in this work. First, a Boussinesq-type finite element wave propagation model is used to determine the wave field in the numerical domain containing the harbor. Then the velocity potentials are evaluated at the ship's hull and finally, the Haskind relations [3] are used to determine the wave forces on the ship along the six modes of motion (heave, sway, surge, roll, pitch and yaw). This new methodology for the evaluation of diffraction forces on a ship inside a harbor basin is presented and tested in this paper. Movements of the moored ship and tensions on the mooring system are obtained using a numerical solver for the motion equations of a moored ship. An application to an open coast harbor is presented.

1. INTRODUCTION

Sea waves inside a sheltered basin can cause excessive motions on moored ships which can lead not only to interruption of loading and unloading operations but also to collisions with other ships or port infrastructures with significant economic losses.

Coupling a numerical model for wave propagation with a numerical model for moored ship behavior subjected to the wave action can identify potentially adverse sea states and help planning safe harbor activities.

A numerical tool called SWAMS has been developed to tackle this problem. The great advantage of such a tool is the ability to provide time series of ship's movements, as well as of forces and extensions in the mooring elements once the offshore sea-wave characteristics are known. This information can be derived from buoy measurements or prediction models, making this a very useful tool, both for design of port infrastructures and for planning of port activities.

For sea-wave propagation SWAMS may use a linear model based upon the mild slope equation, DREAMS [4], that is able to simulate the propagation of monochromatic waves into sheltered areas taking into account refraction, diffraction and reflection or a more complex model, BOUSS-WMH, [5], that is capable of a more accurate description of sea states evolution along varying-depth sheltered regions by taking into account also nonlinear interactions and energy dissipation due to bottom friction and wave breaking.

To simulate moored ship behaviour, SWAMS uses the numerical package MOORNAV [6] which resorts to the frequency domain results of the WAMIT model [2] for the radiation and diffraction problems of a free floating body to get the hydrodynamic forces necessary to BAS model [7]. This model assembles and solves, in the time domain, the moored ship motion equations taking into account incident sea waves and the geometry and constitutive relations of mooring system elements.

WAMIT was initially developed to evaluate the wave-induced stresses on floating structures deployed offshore. Within a harbor basin, waves are diffracted by the harbor structures which invalidates the use of WAMIT model to solve the diffraction problem unless one considers several floating bodies, some of them immobile and occupying the whole of the liquid column. However, this implies the solution of a huge system of linear equations. A possible alternative is to use the so-called Haskind relations [3] involving the potential flow associated with the waves radiated by the ship and the potential of incident waves at the position where the ship is placed.

In this paper we describe: the basic equations of moored ship behaviour, the SWAMS package, the application of this package to evaluate moored ship motions in a very special condition in which the model can be used directly with WAMIT; the new implemented procedures based on Haskind relations and the first test results obtained with these procedures. The paper ends with the presentation of final remarks on the work.

2. MOORED SHIP EQUATIONS

Assuming small amplitude of the ship movements along each of its six degrees of freedom, it is easy to define the part corresponding to the quasi-static variation of submerged hull form. This leads to the hydrostatic restoring matrix C_{kj} whose coefficients are the force along mode k due to a unit change, in still water, of the ship position along mode j.

The same assumption on ship movement amplitude leads to the linearity of the interaction between the hull and the incident waves. Such linearity allows the decomposition of that problem into two simpler problems, [1]: The radiation problem in which one determines the forces along each degree of freedom that are needed for an arbitrary hull movement in

otherwise calm water, and the diffraction problem in which one determines the force along each degree of freedom k that is exerted by incident sea waves on the motionless ship hull.

The motion equation for the moored ship can then be written as

$$\sum_{j=1}^{6}\left[(M_{kj}+m_{kj})\ddot{x}_j(t)+\int_{-\infty}^{t}K_{kj}(t-\tau)\,\dot{x}_j(\tau)\,d\tau+C_{kj}x_j(t)\right]=F_k^d(t)+F_k^m(t)+F_k^f(t) \tag{1}$$

where M_{kj} is the mass matrix of the ship and $F_k^m(t)$ and $F_k^f(t)$ are the instantaneous values of the forces due to mooring lines and fenders. Strictly speaking, this is a set of six equations whose solutions are the time series of the ship movements along each of her six degrees of freedom as well as of the efforts in mooring lines and fenders.

In the above equation the mass matrix and the hydrostatic restoring matrix depend only on the ship geometry and on the mass distribution therein. The forces due to mooring lines and fenders can be determined from the constitutive relations of these elements of the mooring system and from the changes in the distance between their ends (for fenders one has account for the no-length variation associated to absence of contact between the ship and the fender).

The impulse response function, $K_{kj}(t)$ (the time-evolution of the force along k coordinate after a ship movement with impulsive velocity at $t=0$ along j coordinate), the infinite-frequency added mass matrix, m_{kj} and the excitation forces due to waves, F_k^d, that arise in the equation above depend on hull shape and on the disturbance caused in wave propagation flow by the motionless hull or on flow generated by hull movement in otherwise calm water.

Assuming that any sea state that acts on the ship can be decomposed into sine waves of known period and direction, the diffraction force associated with this sea state can be obtained from the superposition of the stationary diffraction forces due to each of these sinusoidal components. That is, results from the diffraction problem in the frequency domain may be used to produce a time domain result.

Also the impulse response functions and the infinite-frequency added masses can be determined from results obtained for the radiation problem in frequency domain:

$$K_{kj}(t)=\frac{2}{\pi}\int_0^{\infty}b_{kj}(\omega)\cos(\omega t)d\omega \tag{2}$$

$$m_{kj}=a_{kj}(\omega)+\frac{1}{\omega}\int_0^{\infty}K_{kj}(t)\sin(\omega t)d\omega \tag{3}$$

where $b_{kj}(\omega)$ is the damping coefficient for frequency ω and $a_{kj}(\omega)$ the added mass coefficient for the same frequency. The added mass and damping coefficients result from decomposing the stationary force associated to the radiation problem for a sinusoidal movement of frequency ω into a part that is in phase with the body velocity (the damping coefficient) and a part in phase with the body acceleration (the added mass coefficient).

3. FREQUENCY DOMAIN APPROACH

The use of frequency-domain results to generate data for a problem in the time domain is due to the greater availability of numerical models to solve, in the frequency domain, the

interaction problem of a floating body with the waves.

WAMIT [2] is one of these models. It was developed at the former Department of Oceanic Engineering of the Massachusetts Institute of Technology and it uses a panel method to solve in the frequency domain the diffraction and radiation problems of a free floating body. This model uses Green's second identity to determine the intensity of source and dipole distributions over the panels used in discretization of the hull wetted surface. With such distributions it is possible to generate the harmonic flow potentials of the radiation and diffraction problems of a free ship placed in a constant-depth zone not limited horizontally.

3.1. Velocity potentials

Let X_j designate the j coordinate of a point P in the floating body. Due to the linearity of the floating body / waves system, if ω is the angular frequency of the incident wave then the motion described by X_j has the same angular frequency:

$$X_j = \mathrm{Re}\left[\varepsilon_j e^{-i\omega t}\right] \tag{4}$$

where ε_j designates the complex amplitude of the body motion along j coordinate.

Using the factorization proposed by [8], which assumes that the potential associated to the motion along j coordinate is proportional to the velocity complex amplitude of that motion, the flow potential when the ship moves under sea-wave action can be written as

$$\phi = \left[\varphi_0 + \varphi_7 + \sum_{j=1}^{6} -i\omega\varphi_j\varepsilon_j\right] e^{-i\omega t} \tag{5}$$

where φ_j is a complex stationary potential. This approach enabled the separation of the flow problem from the ship motion problem thus requiring the evaluation of flow potentials for unit velocity along each of the generalized coordinates, only. Each φ_j potential has to satisfy the usual Laplace equation in the whole fluid domain, the linearized free-surface boundary condition at $z = 0$ and the zero flow across the sea bottom boundary condition.

In addition to these equations, φ_j potential must satisfy also a boundary condition at the wetted surface of the floating body. For the φ_0 and φ_7 potentials, associated to the diffraction problem, the sum of the velocity components orthogonal to the ship hull produced by these two potentials must be zero because the body is motionless

$$\frac{\partial\varphi_0}{\partial n} + \frac{\partial\varphi_7}{\partial n} = 0\ . \tag{6}$$

For the φ_1 to φ_6 potentials, at any point on the ship hull, the component of the flow velocity orthogonal to the ship hull must equal the same component of the ship local velocity.

$$\frac{\partial\varphi_j}{\partial n} = n_j \tag{7}$$

n_j being the generalized outer normal to the wetted surface of the ship (component of the ship local velocity normal to the wetted surface when the ship oscillates along j coordinate).

Once the flow potential is known, pressure on the floating body can be evaluated from the

linearized Bernoulli equation and from this the force along the k coordinate is given by

$$F_k = i\rho\omega\int_S (\varphi_0 + \varphi_7) n_k e^{-i\omega t} dS + \sum_{j=1}^{6} -\rho\omega^2 \varepsilon_j \int_S \varphi_j n_k e^{-i\omega t} dS \tag{8}$$

The first term in the sum is the force associated to the diffraction problem whereas the second term is associated to the radiation problem. In the previous equations S is the wetted surface of the ship hull and n_k is the normal to that surface along generalized coordinate k. The decomposition of the force associated to the radiation problem into a part that is in phase with the body motion velocity and a part in phase with the body acceleration gives respectively the damping coefficient, b_{kj}, and the added mass coefficient, a_{kj}.

3.2. Haskind relations

The solution of the previous equations produce the quantities needed to model the interaction the floating body with monochromatic waves. As is, they are valid for the interaction of one floating body only with incident waves. By extending the concept of the generalized outer normal, n_j it is possible to study the interaction of monochromatic waves with several bodies some of which may be stationary, i.e. that are obstacles around which waves are diffracted.

Although it is possible to use the WAMIT model to solve the diffraction problem of a ship within a harbor basin, the number of equations that would be attained is too much for most of the currently available computers. An alternative to solve such a diffraction problem is to use the relations established in [3].

Using Green's second identity it is possible to show that there is no need to compute the potential of the wave diffracted by the body, ϕ_7, to evaluate the components of the force associated to the diffraction problem, equation (8). In fact, according to such identity, given a volume Ω where functions φ_j and φ_k are twice differentiable and whose boundary is $\partial\Omega$

$$\int_\Omega \left(\varphi_j \nabla^2 \varphi_k - \varphi_k \nabla^2 \varphi_j\right) dV = \int_{\partial\Omega} \left(\varphi_j \frac{\partial \varphi_k}{\partial n} - \varphi_k \frac{\partial \varphi_j}{\partial n} \right) dS \tag{9}$$

n being the boundary outer normal. $\partial\Omega$ is made of the solid boundaries of the domain, the free-surface, the body wetted surface, S, and of a vertical cylindrical surface away from the body. Since both φ_j and φ_k satisfy the Laplace equation in the whole domain, the volume integral at (9) is zero. The linearized boundary condition at the free-surface leads to the conclusion that at this part of the $\partial\Omega$ boundary the integral on the right hand side is zero. At the vertical cylindrical surface away from the body, φ_1 to φ_7 potentials comply with a radiation boundary condition. For such potentials the surface integral on that part of the $\partial\Omega$ boundary is also zero. Then it may be concluded that for φ_1 to φ_7 the following is valid

$$\int_S \varphi_j \frac{\partial \varphi_k}{\partial n} dS = \int_S \varphi_k \frac{\partial \varphi_j}{\partial n} dS \tag{10}$$

Given this and the boundary conditions for the radiation and diffraction problems at the solid boundaries of the domain, the diffracted force can be written in the form presented in [3]

usually known as Haskind relations:

$$F_k^D = -i\rho\omega \int_S \left(\varphi_0 \frac{\partial \varphi_k}{\partial n} - \varphi_k \frac{\partial \varphi_0}{\partial n} \right) dS e^{-i\omega t} \tag{11}$$

So, instead of evaluating the diffraction potential φ_D to compute the force along k coordinate exerted by the incident waves on the stationary ship, using the previous equations it suffices to know the incident wave potential at the wetted body surface, φ_0, as well as the radiation potential at the same surface, φ_k.

3.3. Numerical Implementation

The Green theorem is used to transform the differential equations for radiation and diffraction potentials into integral equations that are assembled and solved by the numerical model WAMIT. Instead of having a set of equations valid in the whole domain one ends up with a set of equations to be satisfied at the domain boundaries, which happens to be the relevant region when flow induced forces are to be evaluated. By approximating the average position of the floating body wetted surface by a set or triangular or quadrangular panels where a constant value of the flow potential can be assumed, the integral equations become a set of linear equations for velocity potential values at each of those panels.

The surface integral in equation (11) is computed using the same panel discretization for the ship hull and a four-point Gauss quadrature formula. The normal derivative of the radiation potential φ_k at the Gauss quadrature points on each panel can be evaluated from the kinematics of the moving ship, equation (7). The value of the radiation potential is constant at each panel and is computed by the WAMIT model.

So, what needs to be evaluated are the incident wave potential, φ_0 and its normal derivative, $\partial\varphi_0/\partial n$, at the Gauss quadrature points. These quantities can be evaluated from the complex amplitude of the free surface elevation, $\eta(x_i, y_i)$, and of the horizontal components $U_0(x_i, y_i)$ and $V_0(x_i, y_i)$ of the wave-induced flow velocity.

Assuming that the mild slope hypothesis is valid, the vertical variation of the velocity potential can be written as $\varphi_0(x_i, y_i, z_i) = \varphi_0(x_i, y_i, z = 0)\cosh[k(d + z_i)]/\cosh kd$. Then, once the free-surface elevation is known, the potential $\varphi_0(x_i, y_i, z_i)$ can be evaluated by

$$\varphi_0(x_i, y_i, z_i) = \frac{g}{\omega}\eta(x_i, y_i)\frac{\cosh[k(d + z_i)]}{\cosh kd} \tag{12}$$

The same mild slope hypothesis enables the relation between the complex amplitudes of the velocity horizontal components at any level and their complex amplitudes at $z = 0$:

$$\frac{\partial \varphi_0}{\partial x} = u(x_i, y_i, z_i) = U_0(x_i, y_i)\frac{\cosh[k(d + z_i)]}{\cosh kd} \tag{13}$$

$$\frac{\partial \varphi_0}{\partial y} = v(x_i, y_i, z_i) = V_0(x_i, y_i)\frac{\cosh[k(d + z_i)]}{\cosh kd} \tag{14}$$

To get the complex amplitude of the vertical component of the wave induced flow velocity one just has to derive equation (12) in order to z to get

$$\frac{\partial \varphi_0}{\partial z} = \frac{gk}{\omega} \eta(x_i, y_i) \frac{\sinh[k(d + z_i)]}{\cosh kd} \tag{15}$$

From the scalar product of the velocity vector by the panel normal one gets the velocity vector component normal to the panel or the normal derivative of the flow potential associated to the incident wave.

4. SWAMS NUMERICAL TOOL

SWAMS - Simulation of Wave Action on Moored Ships - is an integrated tool for numerical modeling of wave propagation and of moored ship behavior inside ports to help in the decision making process for planning port operations.

It consists of a graphical user interface and a set of modules for running numerical models. The user interface enables data storage and manipulation, numerical model execution and enables graphical visualization of results. Each model corresponds to a module to which are attached the databases that bring together all the project information. With this application one may conduct studies in a more efficient way since the work related with the construction of the data files for each model, the model calculations and results visualization are easier.

SWAMS was developed in Microsoft Access™, which has the advantage of including the event-driven object programming language Visual Basic for Applications (VBA). An advantage of this language is the possibility to use and handle different Microsoft Windows applications.

The SWAMS ensemble includes:

- DREAMS module, corresponding to the numerical model DREAMS, [2], which is based on the mild-slope equation for monochromatic wave propagation;
- BOUSS-WMH module, based on the nonlinear finite element model BOUSS-WMH, [5], which solves the nonlinear Boussinesq equations presented in [9];
- MOORNAV module, [6], that assembles and solves the moored ship motion equations assuming the linearity of the floating body / waves system, proposed in [1]. This module is made of two numerical models: WAMIT, [2], that solves, in the frequency domain, the radiation and diffraction problems associated to the interaction between incident waves and a free-floating body; BAS, [7], that assembles and solves, in the time domain, the motion equations of a moored ship at berth taking into account the time series of the wave forces on the ship, the impulse response functions of the ship and the constitutive relations of the mooring system elements (mooring lines and fenders).

SWAMS databases are MS Access ™ databases, corresponding to the numerical models modules, which contain all the project information together with several folders where all the created files are stored.

The graphical representation of data and results in SWAMS is made with Tecplot™ (for DREAMS and BOUSS-WMH modules) and with MS Excel ™ (for WAMIT and BAS modules) and with Autocad (for WAMIT module). All these graphical visualization programs are run by event-driven macros that automate the entire process of creating maps and graphs.

5. MOORED SHIP IN A SCHEMATIC HARBOUR

This section presents one application of the numerical package for the evaluation of the behavior of a ship moored inside a schematic harbor basin under a sea state whose characteristics outside that basin are known. This numerical application illustrates SWAMS functioning, ie, of the set of models BOUSS-WMH, WAMIT, and BAS and draws attention to the modifications needed for a widespread application. It must be pointed out that Haskind relations produced diffraction forces in the frequency domain. For this the monochromatic incident wave field at the ship location was evaluated with numerical model DREAMS.

The wave propagation calculations were performed on a LINUX CORVUS workstation with four AMD Opteron ™ 265, 2GHz and 8GB of RAM, while the calculations of the behavior of the ship are made on a personal computer Intel Quad Core ™ Q6600 2.4Ghz and with 1.97GB of RAM.

5.1. Incident waves

The computational domain is 2000 m wide and 4000 m long. The schematic port located on the right hand side of the domain consists of two breakwaters: the North breakwater with two stretches, one horizontal and the other vertical of 750 meters and 1000 meters in length, respectively and the South Breakwater with one horizontal stretch, 400 m long, defining a quadrangular basin whose side length is approximately 700m, Figure 1.

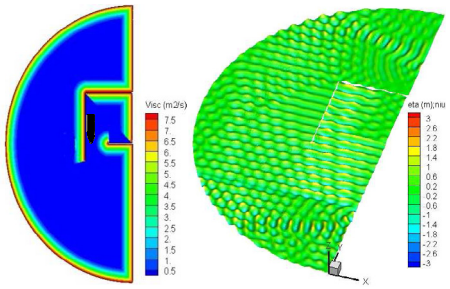


Figure 1: Calculation domain. Regular waves with a period of 10 s and amplitude 0.6 m from South (North coincides with the direction of the y axis).

The finite element mesh of the harbor domain was generated having a minimum of 8 points per wavelength, the depth in the whole area is 17 m and the incident regular waves had a period of 10 s and an amplitude of 0.6 m, resulting in a mesh with 185 599 elements, 93 616 points, 1 631 boundary points and a bandwidth of 322.

Figure 2 shows the time series of free surface elevation at a point within the port, where the ship is to be moored 600 s after the start of the calculation with the BOUSS-WMH module with regular waves from South (propagating in the positive direction of the y-axis) with 10 s period and 0.6 m amplitude.

5.2. Moored ship response

The ship has a volume of 108 416 m3, a waterline length of 243 m, a maximum beam of 42 m and a draft of 14 m. Since it is intended to illustrate the operation of the numerical model for moored ship behaviour only, the adopted mooring scheme was very simple, with

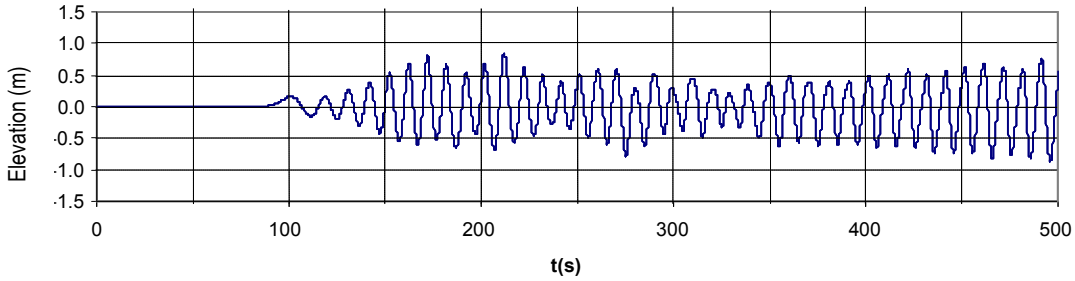


Figure 2: Free surface elevation in the area where the ship is moored.

only two breast lines (l1 and l4), two spring lines (l2 and l3) and two fenders (f1 and f2) as shown in Figure 3. The ship's longitudinal axis is parallel to the jetty, her bow being 98 away from the south end of that jetty. All mooring lines were made of polyethylene with the same maximum traction force of 1274 kN and had the same length (hence the same constitutive relations). The constitutive relation of one of these mooring lines is shown in Figure 3a). The pneumatic fenders had a maximum compression force of 3034 kN, the constitutive relations shown in Figure 3b) and the hull´s friction coefficient is 0.35. In this study, it is assumed that the wave hitting the ship propagates with straight crests perpendicular to the jetty where the ship is moored. This assumption makes the analysis simpler and allows one to use directly the results of the numerical model WAMIT for the free ship diffraction problem.

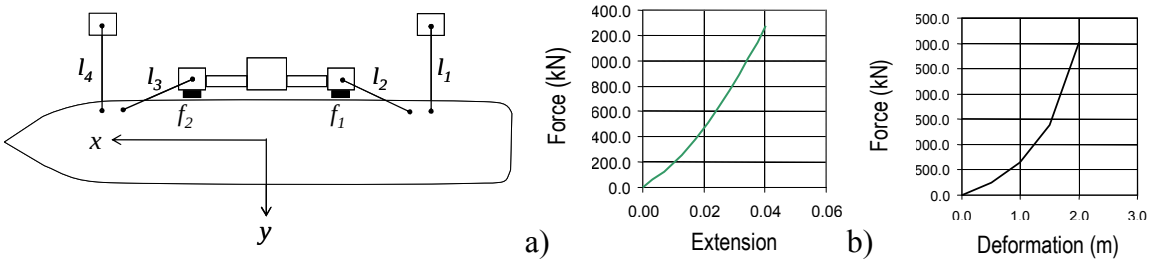


Figure 3: Mooring scheme. Constitutive relations: a) lines; b) fenders.)

For the interaction between the free ship and the incident waves (in the frequency domain), it was considered that only the pier wall close to the ship has some influence in this interaction. Thus it was modeled the ship near a vertical wall 750 m long, 50 m wide that occupied the whole of the water column, that is, with a height of 17 m. The ship's side close to the wall was 30 m apart from the wall and the ship's bow was 98 m away from the end wall.

The wet surface for the ship hull was divided into 3732 panels whereas the wall surface was divided into 1284 panels. Figure 4 shows a perspective of those panel distributions. The numerical model WAMIT was used to solve the radiation problem of the ship for 76 frequencies evenly spaced between 0.0125 rad / s and 0.95 rad / s.

Forces due to incident monochromatic waves were calculated using the Haskind relations with the incident wave field given by the DREAMS numerical model. As expected, the proximity of the vertical wall destroys the symmetry of the flow around the ship that existed when there was no wall. An example of this is the transverse force and the yaw torque on the ship that appear for head waves when there is a wall near the ship, Figure 5.

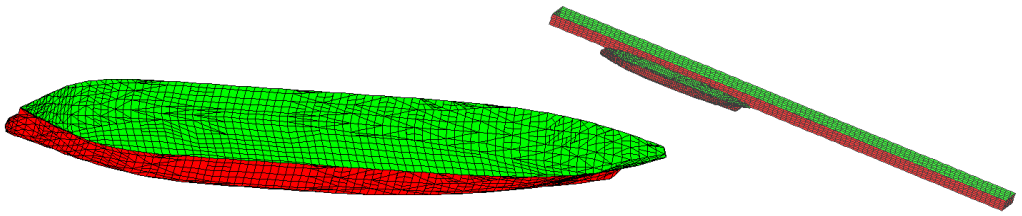


Figure 4: Panel discretization of the ship and the wall.

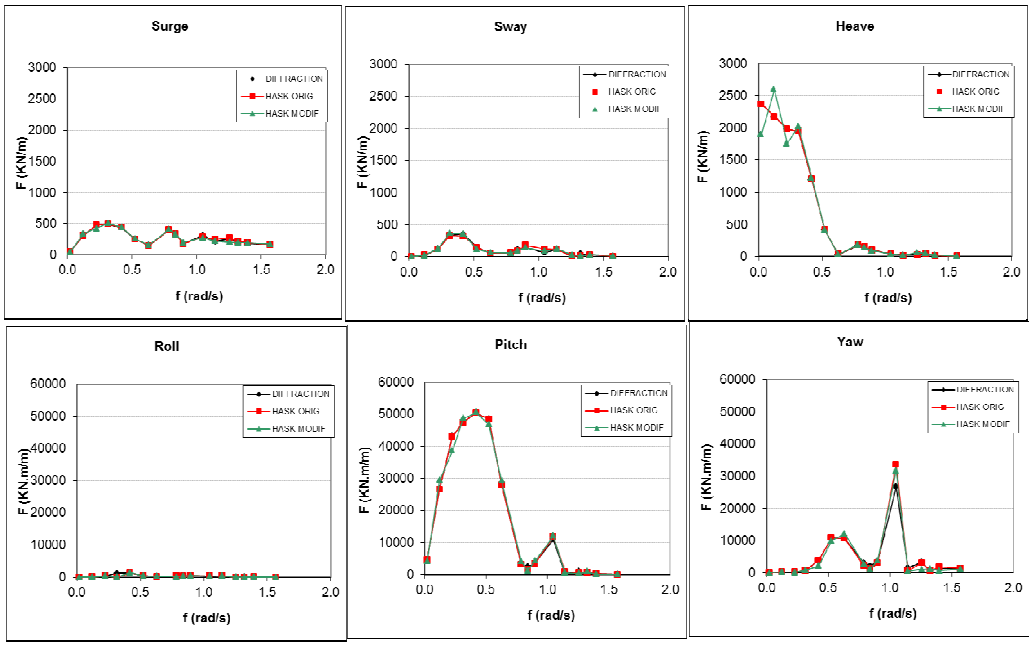


Figure 5: Forces due to incident head waves along the six degrees of freedom of the ship.

With the results from the frequency domain radiation and diffraction forces, it was possible to determine impulse response functions and the infinite-frequency added mass coefficients that are needed to mount the moored ship motion equations. All impulse response functions were calculated with a time interval of 0.1 s and a maximum duration of 200 s.

Starting from the impulse response functions for the 36 possible pairs (force along k coordinate due to motion with impulsive velocity along j coordinate) and the corresponding added mass coefficients for the various frequencies for which the radiation problem was solved in the frequency domain and using equation (3) several estimates for the infinite-frequency added mass added were obtained.

The time series of the forces due to incident waves on the ship were determined by using the time series of the free wave elevation estimated for a point in the area where the ship is to be moored together with the results from the frequency-domain diffraction problem for bow waves. Given the limitations of the procedure for obtaining the force time series, which is based on the Fast Fourier Transform, one might only consider the first 500 s of the free-surface elevation time series. Figure 6a) shows the time series of longitudinal force exerted by the incident waves on the ship. In the figure it can be seen another limitation of the procedure

implemented to calculate time series: oscillations in the force time series do occur before the incident wave arrival to the location where the ship is moored (around t = 90 s) something which is not physically possible.

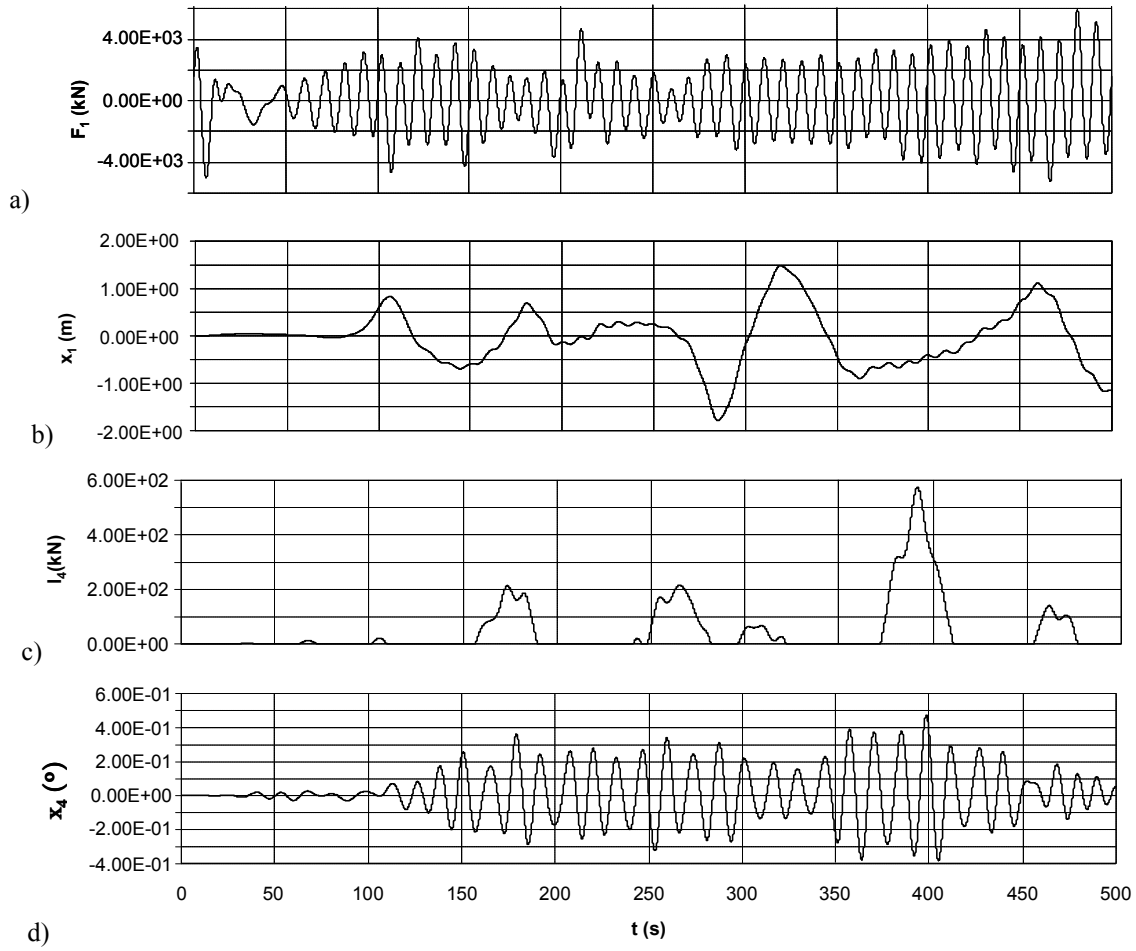


Figure 6: Moored ship time series: a) Longitudinal forces; b) Longitudinal motion; c) Tension on mooring line l1; d) Roll motion.

The time series of the movements along the longitudinal axis of the moored ship shown in Figure 6b), illustrates the non-linear response of the ensemble ship + mooring system. In fact, for oscillations in the free-surface elevation whose period is about 10 s, there are moored ship oscillations with a much higher period. The period of these oscillations is controlled by the existence of mooring lines and fenders, as can be confirmed in Figure 6c) with the time series of the forces in the bow breast line. Since the mooring system elements produce forces acting on the ship in the horizontal plane only, it is for the movements in this plane that the non-linear behavior is most evident. This can be confirmed with the time series shown in Figure 6d) with the roll motion where it is observed that the oscillation period is similar to the period of the incident wave on the ship.

6. FINAL REMARKS

This paper presents the results obtained with the numerical package SWAMS in modeling the behavior of a moored ship inside a schematic harbor. The time series of the ship's movements and tensions in the mooring system clearly illustrate the nonlinear behavior of the system ship-moorings-fenders.

A Boussinesq-type model was used to determine the time series of the incident waves. Results were obtained for a wave whose propagation direction coincided with the breakwater's length, which facilitated the determination of the diffraction forces. To solve more complex problems, where the incident waves are significantly diffracted by the harbor's infrastructures or other obstacles, a new procedure was tested based on so-called Haskind relations. So far, the velocity potentials of incident waves needed for this were obtained with a linear wave propagation model. The initial results presented here are very promising and the wave propagation model will soon be replaced by a more complex Boussinesq-type model.

ACKNOWLEDGMENTS

The authors acknowledge funding from FCT through grant SFRH/BD/82637/2011 PhD and project HIDRALERTA - PTDC/AAC-AMB/120702/2010 and EROS - PTDC/CTE-GIX/111230/2010.

REFERENCES

[1] Cummins, W. E., 1962. Impulse response function and ship motions. Schiffstechnik, 9, 101-109.

[2] Korsemeyer F.T., Lee C.-H., Newman J.N. e Sclavounos P.D., 1988. The analysis of wave effects on tension-leg platforms, 7th International Conference on Offshore Mechanics and Arctic Engineering, Houston, Texas, pp. 1-14.

[3] Haskind, M.D. 1957. The exciting forces and wetting of ships in waves, Izvestia Akademii Nauk S.S.S.R, Otdelenie Tekhnicheskikh Nauk, 7, 65-79. (David Taylor Model Basin Translation Nº.307, March 1962).

[4] Fortes, C.J.E.M., 1993. Mathematical modelling of combined sea-wave refraction and diffraction (analysis by the finite element method). Master's degree dissertation in Mechanical Engineering, IST. (in Portuguese)

[5] Pinheiro, L. V., 2007. A finite element method for the discretization of the extended Boussinesq equations. Master's degree dissertation in Mechanical Engineering, IST. (in portuguese).

[6] Santos, J.A., 1994. MOORNAV – Numerical model for the behaviour of moored ships. Final report. Lisbon: Report 3/94-B, Projecto NATO PO-Waves.

[7] Mynett, A.E., Keunig, P.J. e Vis, F.C., 1985. The dynamic behaviour of moored ships inside a harbour configuration. Int. Conf. on Numerical Modelling of Ports and Harbours, Birmingham, England: 23-25 April 1985. Cranfield: BHRA, The Fluid Engineering Centre.

[8] Tuck, E. O., 1970. Ship motions in shallow water. Journal of Ship Research, 14, 4, 317-328.

[9] Nwogu, O., 1993. Alternative form of Boussinesq equations for near-shore wave propagation. J. Waterway, Port, Coastal, and Ocean Engineering, 119(6):618-638.

V International Conference on Computational Methods in Marine Engineering
MARINE 2013
B. Brinkmann and P. Wriggers (Eds)

SIMULATION OF A PENDULUM WITH FLUID INTERACTION AND EXPERIMENTAL VALIDATION

Florian Beck, Florian Fleissner and Peter Eberhard

Institute of Engineering and Computational Mechanics
University of Stuttgart
Pfaffenwaldring 9, 70569 Stuttgart, Germany
[florian.beck, florian.fleissner, peter.eberhard]@itm.uni-stuttgart.de
www.itm.uni-stuttgart.de

Key words: Smoothed Particle Hydrodynamics; Multibody System; Coupled Simulation; Experimental Comparison; Pendulum in Water

Abstract. The coupling of different simulation approaches allows the simulation of complex systems. One interesting combination in this context is to simulate rigid bodies moving in a fluid. In this work, the coupled simulation of a rigid pendulum in a water tank is presented. The simulation results for different immersion depths of the pendulum in the fluid are compared with experimental data.

When using a coupled simulation it is possible to merge several advantages of different simulation techniques in one common simulation. This way, several effects that influence the dynamic behavior of complex systems can be investigated. The deceleration of a solid body while moving in a fluid and the free surface of a fluid can be analyzed in one joint simulation. The setup used in this work allows the pendulum to plunge fully or partly into the fluid. The pendulum in a water tank is a simple example for a complex system for which several effects have to be taken into account in order to reproduce the dynamic behavior of the whole system precisely.

In a first step, the mechanical model is set up and simulated and, afterwards, experiments were performed. For the experiments the simulation model is transferred with a scale 1:1. Besides the simulation and its results, the experimental setup for this pendulum and a comparison are presented. The simulation of the pendulum in the water tank shows nice agreement with the experimental data.

1 INTRODUCTION

Many systems in engineering applications are getting more and more complex. The modeling and simulation of such complex systems can be a very challenging task. One typical example for such a complex system is a floating wind turbine. This kind of system consists

of several components, which require different simulation techniques when the dynamic behavior of the entire system is investigated. A floating wind turbine is subjected to different load types, e.g. wind and wave loads [1]. Therefore, both aerodynamic and hydrodynamic forces have to be taken into account.

One possible approach when analyzing the structural response of complex systems subjected to different load types are coupled simulations. In a coupled simulation, two different simulation techniques can be combined in order to be able to simulate such complex systems. In this work, one example of such a complex system is presented. It consists of a pendulum with a rigid body, which immerses into a fluid. The setup allows the pendulum to plunge fully or partly into the fluid. There are different phases during one swing of the pendulum. In the initial phase the pendulum is totally outside of the water. In the beginning the pendulum is moving in the air with little resistance. Then, the impact of the pendulum into the water follows and it is decelerated by the damping from the fluid. In this example, there are several points that have to be considered when studying the dynamic behavior. The motion of the rigid body due to water resistance, the description of the free surface and the fluid body interface are investigated. To handle the challenging points when simulating the pendulum, the coupled simulation is divided into two submodels. The Multibody System (MBS) approach is chosen for the submodel for the rigid body pendulum, whereas the Smoothed Particle Hydrodynamics (SPH) method is employed for the submodel of the fluid. The SPH method is a mesh-less method. Some advantages of this method are the description of the free surface and the interface between the two submodels. When using classical grid-based methods the computational effort to simulate the free surface and the interface is much higher, thus, we have chosen a mesh-less method.

The aim of this work is, on the one hand, to introduce a simulation tool for simulating these complex systems and to show the advantages when applying the mesh-less SPH method. On the other hand, it is to present the experimental framework for a pendulum in a water tank. The experimental setup of the pendulum in the tank allows comparing the performed simulations with experimental data. The work is therefore divided into three parts. The theoretical background and simulation part, the description of the experimental setup and, finally, the comparison of the simulation with the experiment. In the theoretical background and simulation part some theory of the applied simulation methods is presented. Then, the coupling technique is introduced before discussing some details of the results of the simulation. Then the description of the experimental setup and the results of the experiments follow. In the last part the comparison of the simulation and the experiment is made.

2 Theoretical Background and Simulation Model

2.1 Smoothed Particle Hydrodynamics

For each submodel of the coupled simulation a different simulation method is used. In Figure 1, a sketch of the pendulum with the water tank is shown. The SPH method is used for the simulation of the fluid. Due to its mesh-less character, the SPH method can handle the free surface naturally. Another advantage is that no special treatment for the fluid solid interfaces is needed. Because of these two advantages, the dynamic behavior of the pendulum due to water resistance can be analyzed in the simulation.

Originally, the SPH method was designed to investigate astrophysical phenomena. But nowadays, there are other applications of the SPH method like fluid dynamics, e.g. for free surfaces [2], [3] or fluid-structure interaction [4], [5] or multiphase flows [6], [7]. An overview about other field of applications can be found in [8].

The SPH method has been implemented in our particle simulation software Pasimodo [9], which is designed for mesh-less particle methods. Due to its modular structure, it is possible to couple Pasimodo with different other simulation software packages [10].

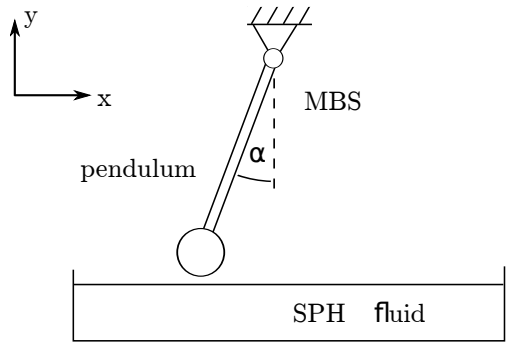


Figure 1: Sketch of the pendulum.

Using the SPH method, the Navier-Stokes (N-S) equations for describing a fluid can be discretized. For a fluid with density ρ, pressure p, viscosity ν, and velocity $\mathbf{v}$ the equation used to describe the conservation of momentum and the equation for the conservation of mass are

$$\rho\left(\frac{\partial \mathbf{v}}{\partial t}+\mathbf{v}\cdot\nabla\mathbf{v}\right)=-\nabla p+\mu\nabla^2\mathbf{v}+\mathbf{f} \text{ and} \tag{1}$$

$$\frac{\partial \rho}{\partial t}+\nabla\cdot(\rho\mathbf{v})=0\ . \tag{2}$$

In (1), $\mathbf{f}$ is the vector of the body forces acting on the fluid. To obtain the SPH formulation of the N-S equations basically two steps are required. The first step is a kernel

approximation and the second one is referred to as particle approximation [8]. The continuum, which is described using the N-S equations, is discretized into so called particles. At these particles any quantity is described with the function

$$A(\mathbf{r}) = \sum_j m_j \frac{A_j}{\rho_j} W(|\mathbf{r} - \mathbf{r}_j h_j|) \ . \tag{3}$$

Here, the subscript j refers to the particle number, m_j to the mass, $\mathbf{r}$ to the position, ρ_j to the density of a particle, and W is the kernel function. In this work, the classical Gaussian kernel is used for all simulations. For a more detailed description of the method see [8]. The solid body of the pendulum is modeled using the MBS method which is briefly outlined in the next section.

2.2 Multibody System Method

The MBS method can be applied for the analysis of many engineering systems which consists of rigid bodies. It is also possible to take elastic deformations into account. To achieve this, classical Multibody Systems are extended by elastic bodies [11], [12]. Several rigid bodies connected with coupling elements, e.g. springs or dampers, form a classical Multibody System. A detailed description can be found in [13]. The equation of motion can be derived with classical principles of mechanics and yield for the complete MBS

$$\mathbf{M}(\mathbf{q}) \cdot \ddot{\mathbf{q}} + \mathbf{k}(\dot{\mathbf{q}}, \mathbf{q}, t) = \mathbf{g}(\dot{\mathbf{q}}, \mathbf{q}, t) \tag{4}$$

with the mass matrix $\mathbf{M}$, the vector $\mathbf{k}$ for the generalized gyroscopic forces, the vector $\mathbf{g}$ with generalized applied forces, and the vector $\mathbf{q}$ of generalized coordinates.

The MBS simulation is performed with Neweul-M^2 [14]. For the coupling of the two simulation software packages Pasimodo and Neweul-M^2, the possibility of C-export is used. In this way, it is possible to write the complete symbolic description of an MBS model to a shared library. In the next section, the coupling of the MBS and the SPH method is discussed.

2.3 Coupled Simulation

The simulation of complex systems with different dynamic behavior can be realized by dividing the system in several subsystems. This separation into subsystems leads to several advantages, e.g. it is possible to apply for each subsystem another integration scheme. There are various approaches to couple these subsystems [15].

The approach which is applied in this work, is separate modeling and separate simulation. The simulations of the subsystems are coupled, therefore, this is called coupled simulation or modular simulation. The time step size of each subsystem can be different, so, the simulation of the entire system is similar to a multi rate method [16]. In each time step of the simulation the necessary system information, like forces and motions, is transferred between the subsystems. The flow of information can be seen in Figure 2.

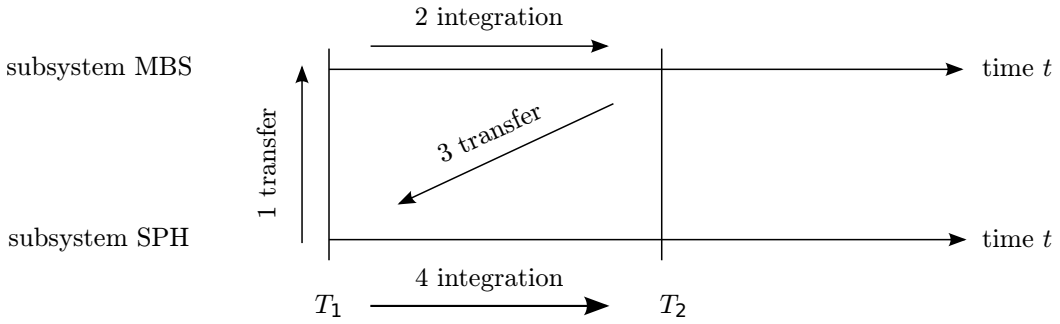


Figure 2: Scheme of the data exchange between the two submodels.

An important point is the stability of the simulation. The information is exchanged at discrete time steps. In [17] is shown for coupled MBS that instability of the modular simulation can occur, if a non-iterative simulator coupling is applied. Therefore, to maintain the stability of the simulation, the exchange scheme is applied in an iterative process.

Another point is the computational effort of the simulation. For the coupling in this work an adaptive exchange time interval is applied. The exchange time interval is then increased or decreased depending on the interaction of the two subsystems. In each simulation step a neighborhood search of the particle simulation is performed. During the neighborhood search the contact detection of the fluid and the solid body takes place. The positions and the velocities are evaluated and the exchange time interval is adapted. The adaptive exchange time interval can be seen in Figure 3, showing also the x-position of the pendulum. When the pendulum immerses into the fluid the exchange time interval is decreased. During the phases when the pendulum is outside the fluid it is increased.

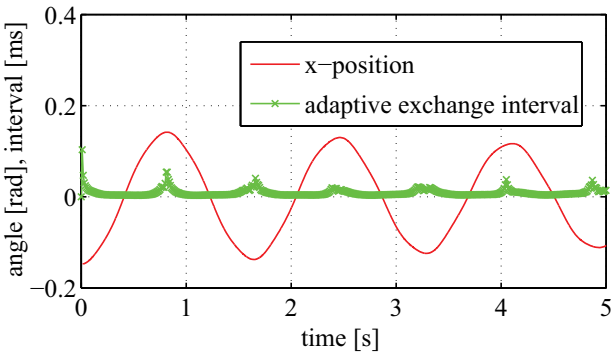


Figure 3: Adaptive exchange time interval.

The calculation of the forces acting between the two subsystems is based on the repulsive force model from [2]. The distance and the difference in the velocities of the solid body and the fluid are determined and the force is calculated. The solid body structure

is represented by triangular meshes in Pasimodo. In case that an interaction between the mesh and the particles occurs, the calculated force $\mathbf{f}_c$ is applied to the two subsystems. The equations of motion for the MBS (4) and the momentum equation (1) for the fluid yield

$$\mathbf{M}(\mathbf{q}) \cdot \ddot{\mathbf{q}} + \mathbf{k}(\dot{\mathbf{q}}, \mathbf{q}, t) = \mathbf{g}(\dot{\mathbf{q}}, \mathbf{q}, t) + \mathbf{f}_c \text{ and} \tag{5}$$

$$\rho \left(\frac{\partial \mathbf{v}}{\partial t} + \mathbf{v} \cdot \nabla \mathbf{v} \right) = -\nabla p + \mu \nabla^2 \mathbf{v} + \mathbf{f} + \mathbf{f}_c \quad . \tag{6}$$

For a fixed immersion depth of the pendulum the parameters are analyzed that take the distance and the difference in velocity into account. Exemplary the x-position for different simulations is shown in Figure 4. On the left side, the influence of the distance parameter is shown and, on the right side, the parameter for the velocity difference. As it can be seen the influence is not significant.

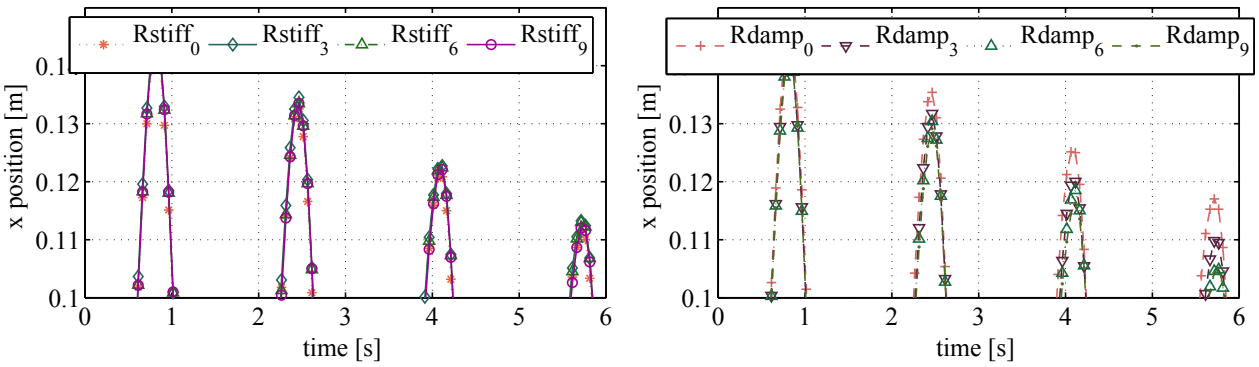


Figure 4: Simulation results when varying the stiffness (left) and the damping (right) parameters.

In the next section, the description of the employed experimental setup as well as the evaluation of the measurement data in order to recreate the trajectory of the pendulum is presented. Later on, the trajectory of the experiment and the simulation are compared.

3 Experiment

3.1 Experimental setup

For the comparison of the simulation and the experiment, measurements are performed in our laboratory. Therefore, the simulation model is transferred in scale 1:1 to the reality. The experimental setup of this work can be seen in Figure 5. It consists of a frame to which the pendulum is attached to using low-friction bearings. The size of the frame is width 0.78 m × height 1.08 m × length 1.18 m. This framework allows the pendulum to plunge fully or partly into the fluid in the tank. The dimensions of the tank are width 0.3 m × height 0.13 m × length 0.4 m. The pendulum itself consists of a rigid metal rod, and a sphere at its tip. The dimension of the rod made of Carbon steel 1.1274

are width 50.0 mm × height 5.0 mm × length 500.0 mm. The diameter of the sphere made of V2A steel is 30 mm. The rigid body, the sphere and the tank are exchangeable, e.g. an elastic pendulum or a larger tank is possible.

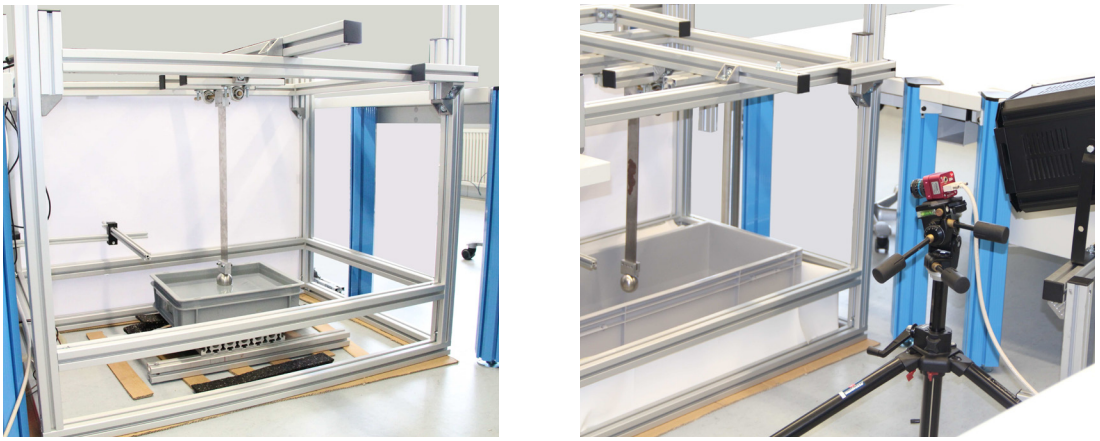


Figure 5: Experimental setup showing a small tank on the left and a larger one on the right side.

3.2 Measurements

In the case of a rigid pendulum, the rotation angle of the pendulum can be determined using an incremental encoder. The encoder is connected to the pendulum with a clutch to compensate a possible shift of the axis. The trajectory can be calculated from this angle. Another possibility for obtaining the trajectory would be to measure the velocity. The used incremental encoder has a maximum resolution of 10000 pulses/round. The maximum sample frequency is 750 kHz. In addition to this highspeed video recordings are made. With these recordings it is possible to track the free surface of the water and compare the experiment with the simulation.

Here, a monochrome camera is used for the highspeed video recordings. Up to 2000 frames per second are possible with this kind of camera, depending on the resolution of the highspeed video recordings. For the lighting of the scene three extremely bright metal-halide spots are used. The highspeed video recordings of the experiments are used for the comparison of the free surface. An example of the highspeed video recording is shown in Figure 6.

4 Results

The results of the coupled simulation of the MBS model and the SPH model are discussed in this section. The simulation is divided into different phases. In one phase, the pendulum is not immersed into the water and there is very little resistance to its motion. After the impact of the pendulum into the fluid, the pendulum is decelerated by the fluid.

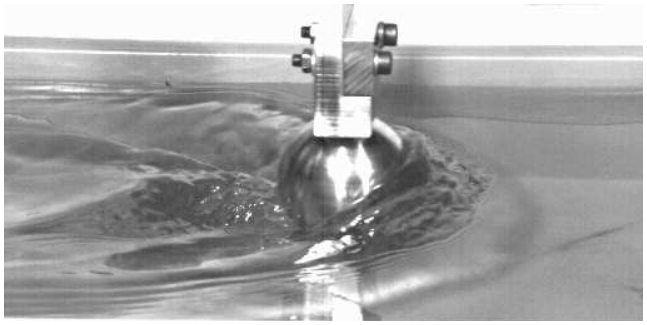


Figure 6: Highspeed video made during the immersion phase.

The whole simulation model is shown for two different times in Figure 7. In Figure 8, the trajectory of three different simulations can be seen. In these simulations the immersion depth of the pendulum is varied, from 1 cm in the lowest point up to 3 cm. The surface of the simulation is shown in Figure 9.

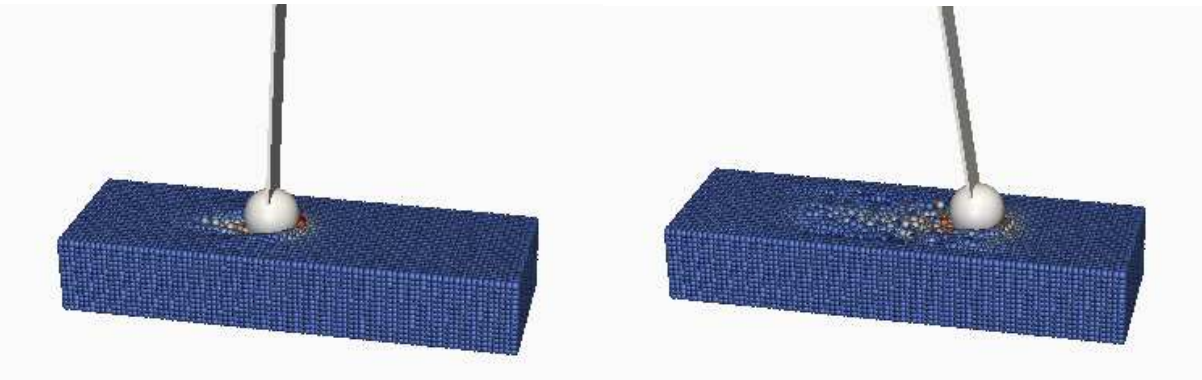
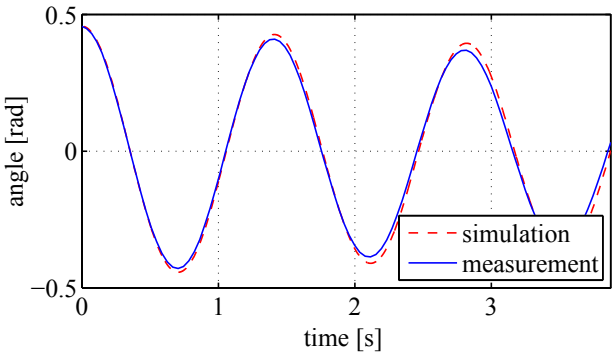


Figure 7: Two different states of the simulation.

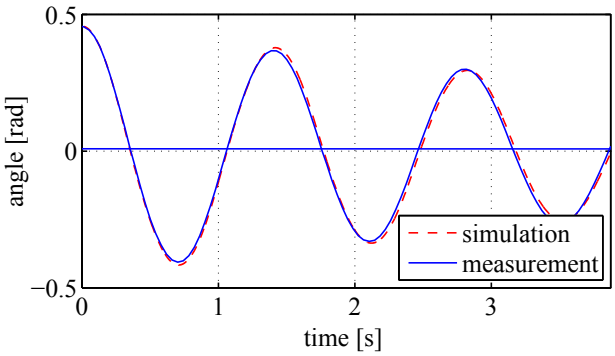
The shape of the free surface is varying during the phase when the pendulum is immersed into the fluid. Using only the pure MBS model it is not possible to get precise results due to the influence of the different shapes of the free surface. But, as it can be seen in the figure, using a coupled simulation gives good results.

5 Conclusion

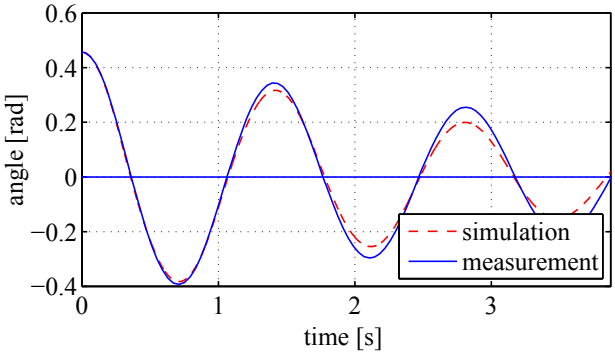
In this work, a simulation framework that allows the coupled simulation of solid bodies and a fluid is presented. The fluid is modeled with the SPH method. The motion of the solid body is modeled using the MBS method. The two subsystems are coupled to an explicit



(a) Immersion depth 1cm

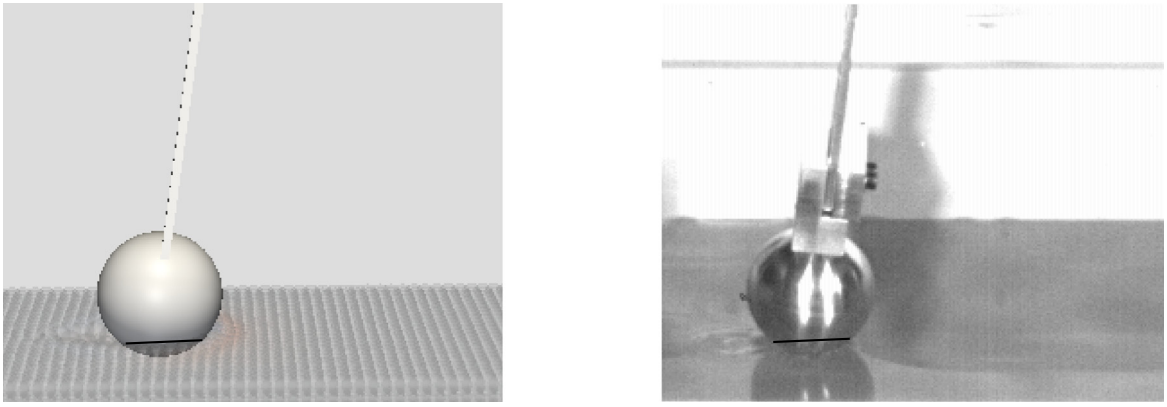


(b) Immersion depth 2 cm

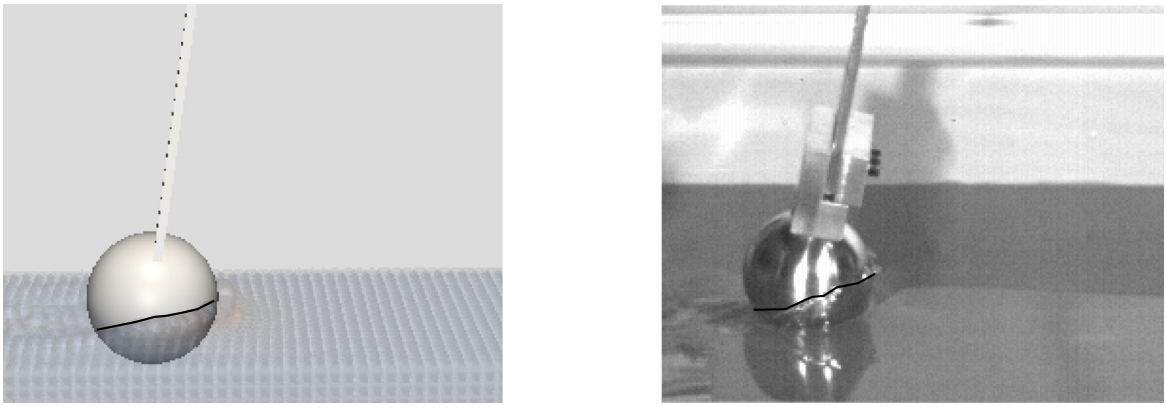


(c) Immersion depth 3 cm

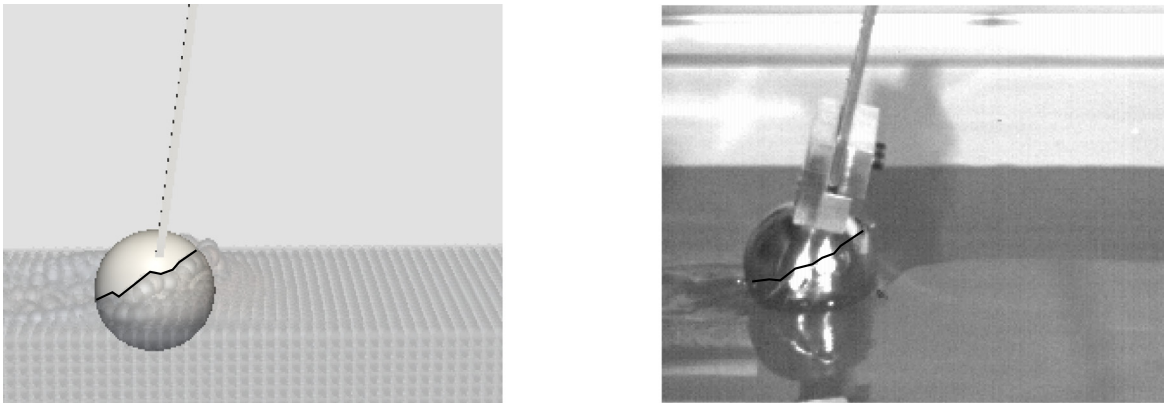
Figure 8: Trajectories of the simulation and the experiment of three different immersion depths.



(a) Immersion depth 1 cm



(b) Immersion depth 2 cm



(c) Immersion depth 3 cm

Figure 9: Simulation and experiment for three different immersion depths. The fluid surface is highlighted with a black line.

modular co-simulation. Furthermore, the simulation model was built in hardware in scale 1:1 and experiments were performed. The motion of the pendulum was recorded with a highspeed video camera. The trajectories and the free surface of the coupled simulation were compared with the experiment and are in good agreement. A most interesting point in the context of the coupled simulation is the possibility to reproduce the free surface of the fluid in a correct way. In this work a rigid body was used for the coupled simulation. It will be a very interesting task to study the dynamic behavior when taking its elastic deformations into account. A further issue will be the use of the so called incompressible SPH method.

REFERENCES

[1] Karimirad M, Meissonnier Q, Gao Z, Moan T. Hydroelastic Code-to-Code Comparison for a Tension Leg Spar-Type Floating Wind Turbine. Marine Structures. 2011;24(4):412–435.

[2] Monaghan JJ. Simulating Free Surface Flows with SPH. Journal of Computational Physics. 1994;110:399–406.

[3] Takeda H, Miyama SM, Sekiya M. Numerical Simulation of Viscous Flow by Smoothed Particle Hydrodynamics. Progress of Theoretical Physics. 1994;92(5):939–960.

[4] Campbell J, Vignejevic R, Libersky L. A Contact Algorithm for Smoothed Particle Hydrodynamics. Computer Methods in Applied Mechanics and Engineering. 2000;184:49–65.

[5] Kulasegaram S, Bonet J, Lewis RW, Profit M. A Variational Formulation Based Contact Algorithm for Rigid Boundaries in Two-Dimensional SPH Applications. Computational Mechanics. 2004;33:316–325.

[6] Colagrossi A, Landrini M. Numerical Simulation of Interfacial Flows by Smoothed Particle Hydrodynamics. Journal of Computational Physics. 2003;191:448–475.

[7] Hu XY, Adams NA. A Multi-Phase SPH Method for Macroscopic and Mesoscopic Flows. Journal of Computational Physics. 2005;213:844–861.

[8] Liu MB, Liu GR. Smoothed Particle Hydrodynamics (SPH): an Overview and Recent Developments. Archives of Computational Methods in Engineering. 2010;17:25–76.

[9] Pasimodo. www.itm.uni-stuttgart.de/research/pasimodo/pasimodo_en.php.

[10] Fleissner F, D'Alessandro V, Schiehlen W, Eberhard P. Sloshing Cargo in Silo Vehicles. Journal of Mechanical Science and Technology. 2009;23(4):968–973.

[11] Schwertassek R, Wallrapp O. Dynamik flexibler Mehrkörpersysteme (in German). Braunschweig: Vieweg; 1999.

[12] Shabana AA. Flexible Multibody Dynamics: Review of Past and Recent Developments. Multibody System Dynamics. 1997;1(2):159–223.

[13] Schiehlen W, Eberhard P. Technische Dynamik (in German). 3rd ed. Wiesbaden: Vieweg+Teubner; 2012.

[14] Kurz T, Eberhard P, Henninger C, Schiehlen W. From Neweul to Neweul-M^2: Symbolical Equations of Motion for Multibody System Analysis and Synthesis. Multibody System Dynamics. 2010;24(1):25–41.

[15] Geimer M, Krüger T, Linsel P. Co-Simulation, gekoppelte Simulation oder Simulatorkopplung? Ein Versuch der Begriffsvereinheitlichung (in German). O + P Zeitschrift für Fluidtechnik. 2006;50(11-12):572–576.

[16] Gear CW, Wells DR. Multirate Linear Multistep Methods. BIT Numerical Mathematics. 1984;24:484–502.

[17] Kübler L, Schiehlen W. Modular Simulation in Multibody System Dynamics. Multibody System Dynamics. 2000;4:107–127.

V International Conference on Computational Methods in Marine Engineering
MARINE 2013
B. Brinkmann and P. Wriggers (Eds)

FLUID STRUCTURE INTERACTION ANALYSIS OF AN HYDROFOIL

C. LOTHODE*, M. DURAND*, A. LEROYER†, M. VISONNEAU†, M. DELAITRE*, Y. ROUX*, L. DOREZ+

*K-Epsilon
Espaces Antipolis, 300 route des Crêtes - CS 70116
06902 Sophia-Antipolis, France
e-mail: mathieu@k-epsilon.com, web page: http://www.k-epsilon.com/

† Laboratoire de recherche en Hydrodynamique, Énergétique et Environnement Atmosphérique
École Centrale de Nantes
1 rue de la Noë BP 92101, 44321 Nantes Cedex 3, France
e-mail: alban.leroyer@ec-nantes.fr - web page: http://www.ec-nantes.fr/

+ Groupama Sailing Team
56100 Lorient
e-mail: loic@groupamasailingteam.com - web page: http://www.cammas-groupama.com/

Key words: Fluid Structure Interaction, VIV, RANSE, Racing Yacht

Abstract. In this paper, a dynamic computation of the Groupama 3 foil is performed. Foils are thin profiles, placed under the hull of a ship, allowing it to provide a lifting force. This study is placed in the context of the 2013 America's Cup, which will see the appearance of a new kind of high performance multihull.

At high speeds, the foils are subject to intense hydrodynamic forces and to movement due to the sea. The deformations are then sizable and there is a risk of ventilation, cavitation or vibration that could lead to important modification of the hydrodynamic forces or to the destruction of the foil. It is therefore necessary to quantify correctly its deformation and its response to dynamical efforts.

The foil/water interaction is a strongly coupled problem, due to the thickness of the object. In this paper, the problem is solved using a segregated approach. The main problems resulting of such a method are the numerical stability and remeshing. These problems are detailed and some results presented.

As a first test case, the simulation of a vortex excited elastic plate proposed by Hübner is presented. This case is very demanding in terms of coupling stability and mesh deformation.

Then, the foil of Groupama 3 is modelled in a simplified form without hull and free surface, and then in a more realistic conditions with free surface and waves.

1 Numerical method

The strategy used to solve the fluid structure interaction problem is a partitioned coupling between a fluid solver and a structural solver. The two solvers are described in the following as well as the coupling algorithm.

1.1 Fluid : ISIS-CFD

The solver ISIS-CFD included in FINE/Marine^{TM}is developed by the DSPM team of LHEEA laboratory. This solver can solve the Reynolds-Averaged Navier-Stokes Equations in a strongly conservative way. It is based on the finite volume method and can work on structured or unstructured meshes with arbitrary polyhedrons [WKR$^+$11].

The velocity field is obtained from the momentum conservation equations and the pressure field is obtained according to the incompressibility constraint. The pressure-velocity coupling is obtained using the SIMPLE algorithm. All the variables are stored in a cell-centered manner. Volume and surface integrals are evaluated according to second order schemes. The time integration is an explicit scheme of order two. At each time step, an internal loop is performed (called a non-linear iteration) associated with a Picard linearization in order to solve the non-linearities of the Navier-Stokes equations.

The equations are formulated according to the Arbitrary Lagrangian Eulerian paradigm and therefore can easily take into account mesh deformations. Several turbulence models are implemented in ISIS-CFD. In this study, we used the SST-$k-\omega$ model[MKL03].

1.2 Structure: ARA

The solver ARA was developed by the company K-Epsilon during the project VOILE-nav [ABHD12]. The code was initially aimed at simulating the dynamic behaviour of sailboat rigs : sails, mast and cables.

The finite element method is used. At each time step, we seek an equilibrium between all the elements and forces. The elements receive as an input the position, the speed and the acceleration of each of its nodes. It can contain internal variables in the case of elastic deformation, and the element computes the derivatives of forces according to those variables. These derivatives are assembled into a mass matrix $[M] = \frac{\partial F}{\partial \ddot{x}}$, damping matrix $[D] = \frac{\partial F}{\partial \dot{x}}$ and stiffness matrix $[K] = \frac{\partial F}{\partial tx}$. The elements can be composed of different kinds of finite elements (cable, beam, shell, membrane). It is also possible to use elements with a penalization method such as contact or sliding elements. In the coupling algorithm, the fluid-structure interface itself is considered as an element.

The time scheme used is Newmark-Bossak. This scheme has been chosen for its compromise between the necessary filtering of the high frequencies, the accuracy of the low frequencies and the lack of numerical energy creation in case of high nonlinearities.

Elements used

While numerous element types have been implemented in the structural code, in the present study, only beam elements are used. Those elements are Timoshenko elements, with the hypothesis of small deformations. We therefore have a constant matrix in the local frame. Each beam element is defined thanks to two points (for position) and two quaternions (for the tangent directions). More details on the nonlinear algorithm used can be found in [Dur12].

1.3 Coupling

The fluid-structure coupling leads to four problems: the continuity of constraints at the interface, the deformation of the interface, the deformation of the fluid mesh and the coupling algorithm.

1.3.1 Continuity of constraints

The perfect continuity of constraints cannot be assured because of the difference between the fluid discretisation and the structural discretisation. Thus, a consistent method is used (see [Dur12]). It corresponds to an integration of the forces on the fluid faces :

$$\boldsymbol{F}_M = \int_\Gamma (p\,\boldsymbol{n} + \tau \cdot \boldsymbol{n})\, d\Gamma$$

and then a projection of those efforts on the degree of freedom of the closest beam element.

1.3.2 Interface deformation

The fluid structure interface is entirely defined by the fluid faces. Each fluid node is projected on the beam elements in order to get a parameterized position of the projected point but also a vector linked to the local frame of the beam. When the beam is deformed, the 3D deformation of the neutral axis is computed with the variation of the local frame from one end to the other end of the beam. The local frame evolves smoothly according to a cubic spline law. Therefore, the new fluid node position is computed from the new position of neutral axis and its local frame (see FIGURE 1).

1.3.3 Mesh deformation

Following the interface deformation, the whole mesh of the fluid domain needs to be deformed. This deformation occurs at each coupling iteration. The number of call to this procedure being non-negligible, the mesh deformation needs to be fast. To do that, a new method was developed that propagate the deformation state to the fluid mesh. The algorithm is described more thoroughly in [Dur12]. The rigid displacement (translation and rotation) of each face of the interface is computed. This displacement is propagated to its neighbours and so on iteratively until the boundaries of the mesh are reached.



(a) Fluid node projection (red) on the beam (blue segment)

(b) Fluid node position is computed according to the neutral axis (cubic spline) and the local frame

Figure 1: Fluid structure interface deformation.

1.3.4 Quasi-monolithic algorithm

The global solution algorithm is based on a quasi-monolithic approach. This approach is an implicit coupling adapted to a partitioned solver while conserving the property of convergence and stability of the monolithic approach. To obtain such a result, the structural computation is performed at each nonlinear iteration of the fluid (inner loop). The fluid algorithm is not modified. The nonlinear iterations include a fluid subiteration and a structural convergence. The nonlinear iterations are performed until convergence, therefore fluid-structure convergence is reached at each time step. Furthermore, an "interface" element is added to the structural solver. This element is computed from the Jacobian matrix of the interface. In the case of an exact Jacobian matrix, the algorithm is the same as a monolithic algorithm. With the same idea as the quasi-Newton method where a simplified Hessian matrix is used, here a simplified Jacobian is computed.

The Jacobian matrix is not necessary, even for strongly coupled problems. Nonetheless, its use permits the elimination of under-relaxation, implying a significant reduction in the number of coupling iterations required.

With the present method, the ratio between the time of fluid structure interaction and fluid only computation is in between 1 and 2.

2 Test cases

2.1 Hubner test

To start, an academic test was studied [HWD04]. This case is itself a modification of [RW98] by changing certain boundary condition and characteristics of the structure. With the case of Hubner, the structure is more bendable and the deformations are larger. The case is therefore harder to study.

The parameters of Hubner were studied by Valdès et Vázquez [VMO09] and also by Guillaume De Nayer in 2008 [DN08]. The later modified the dimensions of the domain which he found to be too small. Those dimensions are used here (cf. FIGURE 3 and

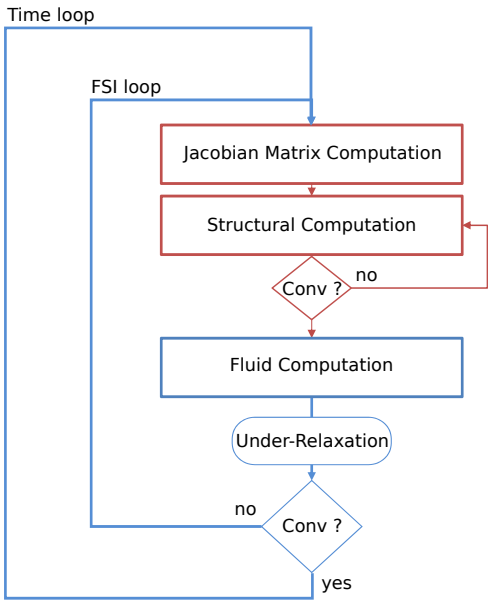


Figure 2: Dynamic coupling algorithm. In blue, the fluid solving scheme. In red, the added structural iteration with the Jacobian computation.

TABLE 1).

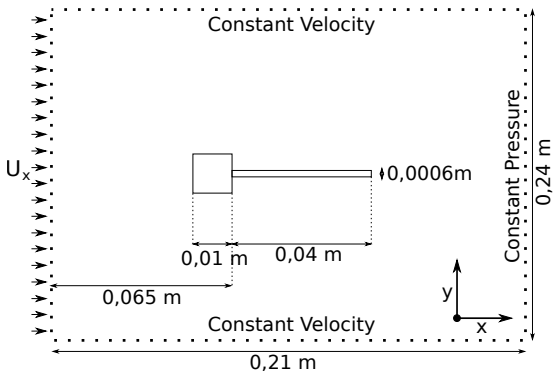
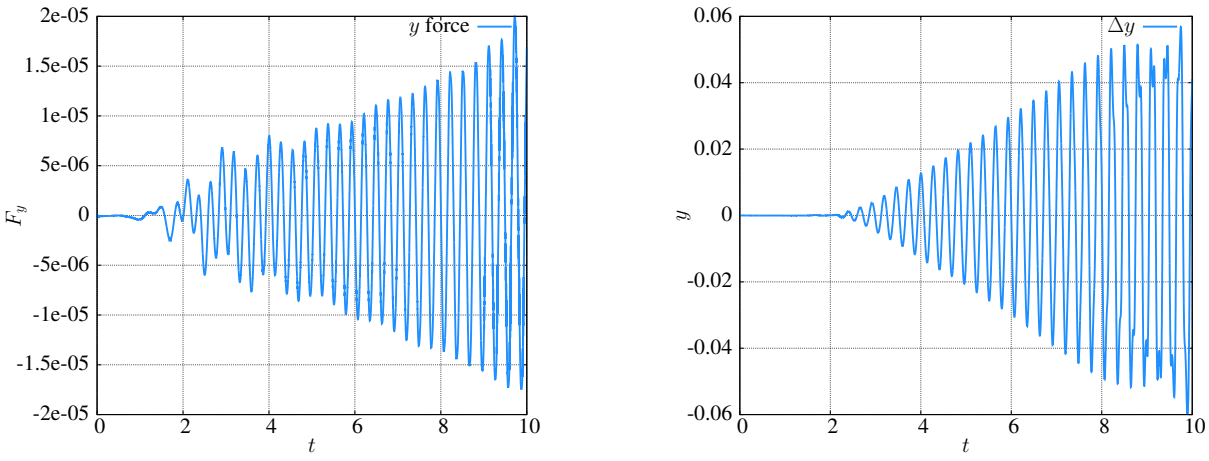


Figure 3: Diagram of the simulation

Fluid data			
Fluid density	ρ_f	$1,18$	$kg.m^{-3}$
Dynamic viscosity	μ_f	$1,82 \times 10^{-5}$	$Pa.s$
Inlet velocity	U_x	$0,315$	$m.s^{-1}$
Structural data			
Square size	a	$0,01$	m
Length of the tip	L	$0,04$	m
Tip thickness	d	$0,0006$	m
Young modulus	E	$0,2$	MPa
Tip density	ρ_s	2000	$kg.m^{-3}$
Poisson coefficient	ν	$0,35$	

Table 1: Properties of the fluid and the structure

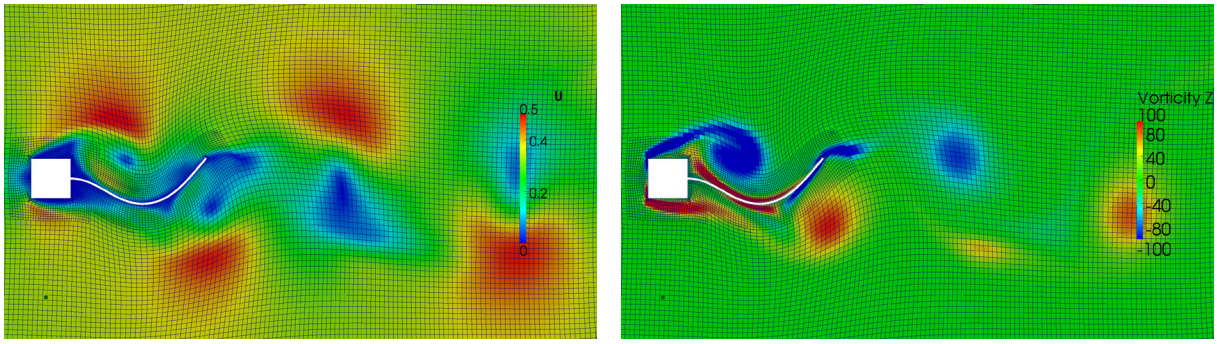
According to the data, the Reynolds number is 200. The assumption of a laminar flow was used. The physical time of the computation is approximately 25 s and the time step is $\Delta t = 0.001s$. The fluid mesh was generated by HEXPRESS^{TM}, the mesher of the software FINE/Marine^{TM}. It has 111452 cells and 132782 vertices. The structural beam is made out of 100 beam elements.



(a) y force ($N.m^{-1}$) (b) y deflection (m)

Figure 4: Evolution of forces and deformation

The results obtained by Hübner show an amplitude of $6cm$ and correspond to the results obtained by the method presented here. Furthermore, the frequency ($3.15 \pm 0.05Hz$) is also in the ranged obtained by Hübner and De Nayer ($3.22Hz$ for De Nayer, $3.10Hz$ for Hübner).



(a) $\| \boldsymbol{u} \|$ (b) ω_z

Figure 5: Visualization of the mesh deformation and creation of vortices in established flow

The FIGURE 5 shows the results of the mesh deformation. The cell quality and orientation is preserved even with relatively large deformation.

The tip oscillates in phazse with the creation of vortices by the square block. We can see those vortices advected in the flow FIGURE 5b.

2.2 Hydrofoil

An hydrofoil is the equivalent of an airfoil, but for a boat. Its use can vary from an lift assist purpose[1] to a full flight purpose[2]. Hydrofoils on sailing multihulls are positionned at the two opposite hulls. Most of the time, their influence can be modified by modifiying their orientation and position.

The study is done on the foil of Groupama 3, trimaran of 105 feet (32 m) and 18 tons. The boat broke the Jules Vernes record (fastest circumnavigation around the world) in 2010. This boat represents a break through in the concept of oceanic racing yachts by being lighter and by including hydrofoils.



Figure 6: Groupama 3

The foil used by Groupama 3 is a C foil, which is the shape you can see by looking at it by the front side. It also has a winglet to reduce the induced drag.

2.2.1 Foil alone

In this case, a simplified version of the foil is used. The foil is simply an extrusion of a NACA 4512 profile, with a curvature radius of $3m$, without the winglet. Furthermore, we do not take into account the free surface. The structural properties are listed below:

Length	4 m	Bending inertia (I_x)	7×10^6 mm^4
Width	0.7 m	Bending inertia (I_y)	1×10^9 mm^4
Mass	75 kg	Shear modulus (G)	3×10^4 MPa
Young modulus	2×10^5 MPa	Torsion inertia (I_0)	3×10^6 mm^4
Mean section area	8×10^3 mm^2		

Table 2: Simplified structural data

[1] to reduce the drag by reducing the immersed volume of the hull, which is the case of most sailing multihulls

[2] hull out of the water, like the Hydroptère

The structural mesh is given by 14 beam elements, with the node at the highest elevation blockfixed in position and rotation.

The first step is a quasi-static computation to predict the equilibrium position of the foil. Fluid iterations are performed alone until convergence, then a structural convergence is performed. The mesh is updated and a new fluid convergence with the new deformed mesh is performed. The quasi-static loop is done until convergence of the geometry. This convergence is assured only if the problem is stable.

The results obtained are in the TABLE 3. Those results were obtained with an inlet velocity of $15m \cdot s^{-1}$.

	Position z	z force
Undeformed foil	-1.351 m	7.434×10^4 N
Deformed foil	-0.756 m	9.316×10^4 N
Difference	0.595 m	1.882×10^4 N

Table 3: Differences between a computation with or without fluid structure interaction

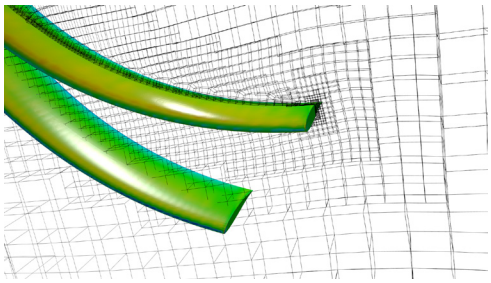
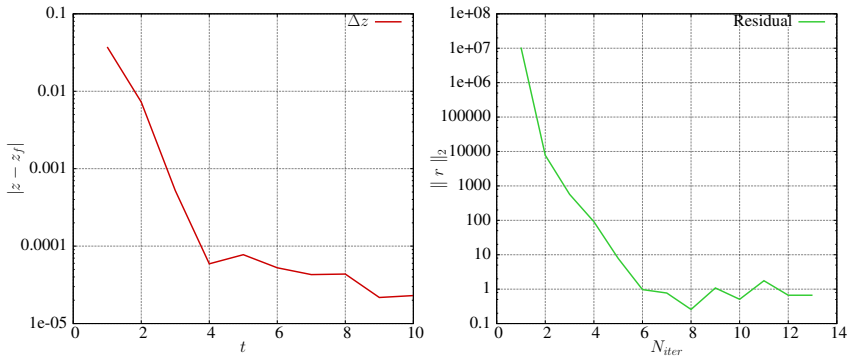


Figure 7: Undeformed and deformed foil and visualization of the deformed mesh

The gain in lift is big (+25%) whereas the drag is only augmented by a small factor (+3%) (see TABLE 3). By adjusting correctly the neutral axis and the center of effort, this behaviour can be optimized. At this speed, for a deformed foil, the lift represent 50% of the weight of the boat.



(a) Convergence to the solution

(b) Initial residual forces (before the structural computation is performed)

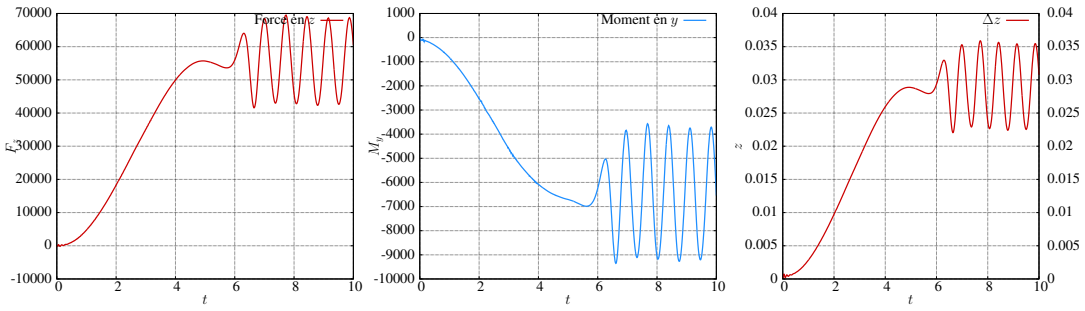
Figure 8: Convergence

The FIGURE 8 shows the quasi-static convergence. We notice that the deflection obtained is converged. The initial residual of the coupling (before computation of the structure) is decreasing by an order of magnitude at each coupling iteration. With only 6 quasi-static iterations, the solution is converged.

2.2.2 Foil with hull and waves

In this section, the real geometry of the foil (including the winglet) is used and the hull is added. Unsteady fluid structure interaction computations were performed with the foil fixed at the interface of the hull. A free surface is imposed at $z = 0$ as an initial condition. The hull is fixed and all of the nodes of the beam inside the hull are fixed in both translation and rotation.

At $t = 0$, the speed of the boat is 0. The imposed motion is done according to a $\frac{1}{4}$ sinusoidal law until $15m \cdot s^{-1}$. The waves are starting at $t = 0s$, $45m$ in front of the foil and reach the foil at $t = 6s$. The waves are Stokes first order potential waves 1 with $\pm 0.5m$ amplitude in z and a period of $3s$.

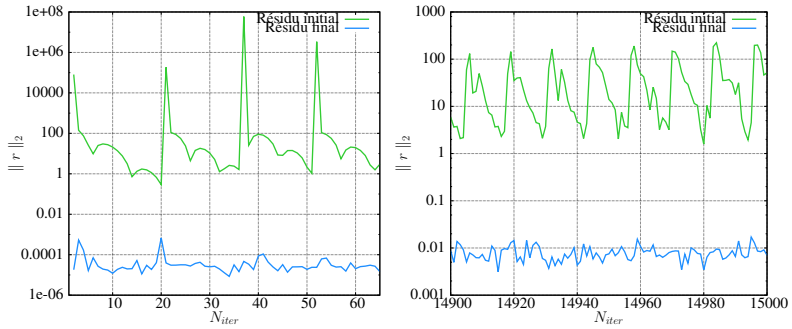


(a) z forces (b) y momentum (c) z deflection

Figure 9: Forces and momentum acting on the foil with respect to time

FIGURES 9a and 9b show the variation of the lift forces and torsion moment in the foil local frame. The variation of lift is $56 \pm 12 \times 10^3 N$.

The foil is very stiff and therefore does not bend very much. Nonetheless, the amplitude observed in waves is not negligible because it induce a vertical velocity that changes the incident flow, and thus the lift and drag.



(a) Start of the simulation (b) End of the simulation

Figure 10: Initial residual on the structure

The FIGURE 10 permits us to conclude on the convergence of the coupling. It can be seen that the initial residual decreases quickly during the nonlinear iterations until convergence. Furthermore, using the Jacobian matrix of the interface allows a convergence in 20 subiterations where a classic implicit coupling with under-relaxation would require about a hundred subiterations. A computation without fluid structure interaction needs about 10 iterations to reach convergence.

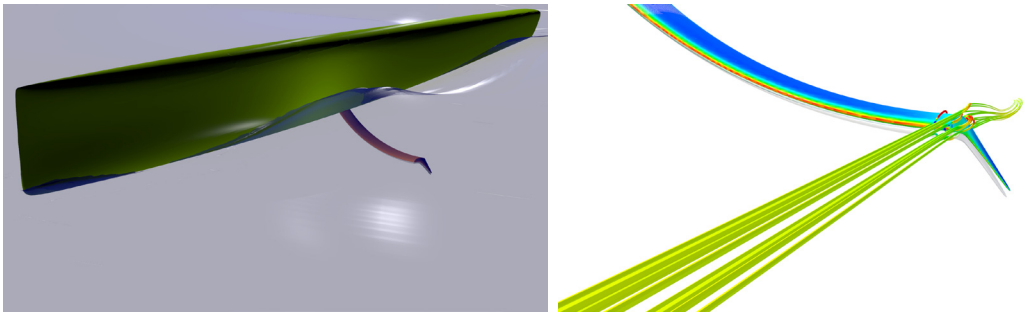


Figure 11: Computation results

Conclusion

The results of a partioned coupling between a viscous, incompressible fluid solver and a structural finite element analysis software are presented for strongly coupled problems. The Hubner case permitted the validation of the fluid-beam interaction. The quasi-static and dynamic results for the foil of a high performance multihull were then presented.

Furthermore, the scope of work of this boat was to do oceanic races and therefore it was designed to be both very reliable and safe. Thus, the foils used are smaller compared to what can be used for smaller, 60 feet (18 m) IMOCA multihulls of the same generation. To use bigger foils on that kind of boat, it will be necessary to predict the dynamic stability of the boat and also to dimension their structure.

Vibratory phenomena such as flutter, which can lead to structrual failure of the foil has not been investigated in the present study, but would of interest to determine the suceptiability to detrimental vibratory modes for the foil.

The boundary conditions for the structure play an important role in the determination of the structural deflections, hence it would be of interest to investigate a freely moving foil inside the hull with pinned connections at the lower and upper hull surfaces which corresponds more to what is happenning in reality.

Acknowledgment

We would like to thank PACAGrid and INRIA for providing the computational power required to undertake this study.

REFERENCES

[ABHD12] B. Augier, P. Bot, F. Hauville, and M. Durand, *Experimental validation of unsteady models for fluid structure interaction: Application to yacht sails and rigs*, Journal of Wind Engineering and Industrial Aerodynamics **101** (2012), 53–66.

[DN08] G. De Nayer, *Interaction fluide-structure pour les corps élancés.*, Ph.D. thesis, École Centrale de Nantes, 2008.

[Dur12] M Durand, *Interaction fluide-structure souple et legere, applications aux voiliers*, Ph.D. thesis, Ecole Centrale Nantes, 2012.

[HWD04] B. Hübner, E. Walhorn, and D. Dinkler, *A monolithic approach to fluid–structure interaction using space–time finite elements*, Computer methods in applied mechanics and engineering **193** (2004), no. 23, 2087–2104.

[MKL03] FR Menter, M. Kuntz, and R. Langtry, *Ten years of industrial experience with the sst turbulence model*, Turbulence, heat and mass transfer **4** (2003), 625–632.

[RW98] E. Ramm and WA Wall, *Fluid-structure interaction based upon a stabilized (ale) finite element method.*

[VMO09] J.G. Valdés, J. Miquel, and E. Oñate, *Nonlinear finite element analysis of orthotropic and prestressed membrane structures*, Finite Elements in Analysis and Design **45** (2009), no. 6–7, 395 – 405.

[WKR+11] J. Wackers, B. Koren, HC Raven, A. van der Ploeg, AR Starke, GB Deng, P. Queutey, M. Visonneau, T. Hino, and K. Ohashi, *Free-surface viscous flow solution methods for ship hydrodynamics*, Archives of Computational Methods in Engineering **18** (2011), no. 1, 1–41.

V International Conference on Computational Methods in Marine Engineering
MARINE 2013
B. Brinkmann and P. Wriggers (Eds)

LOCAL GRID REFINEMENT FOR FREE-SURFACE FLOW SIMULATIONS IN OFFSHORE APPLICATIONS

PETER VAN DER PLAS*, HENRI J. L. VAN DER HEIDEN*, ROEL LUPPES* AND ARTHUR E. P. VELDMAN*

*Institute for Mathematics and Computer Science
University of Groningen (RuG)
P.O. Box 407, 9700 AK Groningen, The Netherlands
Corresponding author: P.van.der.Plas@rug.nl

Key words: Computational Methods, Marine Engineering, Local Grid Refinement, Free-Surface Flow

Abstract. A local grid refinement approach is presented for free-surface flow simulations. A semi-structured approach is used based on rectangular refinement regions, inside which the grid is locally structured, allowing for the application of efficient solution methods. At refinement interfaces a simple data structure facilitates the look-up of neighbouring cells. Near refinement interfaces, a modified discretization stencil is introduced for the Navier-Stokes equations. To allow for efficient grid configurations, the interface scheme also needs to perform well near objects and free-surface boundaries. Therefore, special attention is paid to designing a compact interface scheme that can perform well in a wide variety of industrial applications. Numerical results are presented for flow around a square cylinder as well as the simulation of a breaking dam.

1 INTRODUCTION

In offshore applications, extreme events of wave impact on rigid and floating structures are of high interest. In the past the CFD simulation tool ComFLOW [1, 2] has been successfully used for these purposes. For accurate prediction of wave run-up and wave loading on offshore structures high resolution is only required in the areas of interest, whereas in the far field coarse grids are sufficient. Up to now, further reduction of grid points was only possible by means of grid stretching which typically results in large deformation of grid cells and due to its poor locality is not very efficient. In the ComFLOW-3 project one of the aims is to increase numerical efficiency by introducing local grid refinement.

2 DISCRETIZATION OF THE NAVIER–STOKES EQUATIONS

An excellent model for incompressible fluid flow is provided by the Navier-Stokes equations. The set of equations consists of the continuity equation

$$\mathcal{M}\mathbf{u} = 0, \tag{1}$$

where $\mathcal{M} = \nabla\cdot$ is the divergence operator, and the momentum equation

$$\frac{\partial \mathbf{u}}{\partial t} + \mathcal{C}(\mathbf{u},\mathbf{u}) + \mathcal{G}p - \mathcal{D}\mathbf{u} = \mathbf{f}, \tag{2}$$

based on the convection operator $\mathcal{C}(\mathbf{u},\mathbf{v}) = \mathbf{u}\cdot\nabla\mathbf{v}$, the pressure gradient operator $\mathcal{G} = \nabla$, the diffusion operator $\mathcal{D}(\mathbf{u}_h) = \nabla\cdot\nabla\mathbf{u}_h$ and forcing term $\mathbf{f}$.

The continuity equation (1) is discretized at the 'new' time level $n+1$ to give

$$M\mathbf{u}_h^{n+1} = -M^\Gamma\mathbf{u}_h^{n+1} \tag{3}$$

where M acts on the internal of the domain and M^Γ acts on the boundaries of the domain.

Convection and diffusion are discretized explicitly in time. The divergence and the pressure gradient are discretized at the new time level. If we denote the diagonal matrix containing the fluid volumes of the momentum cells by Ω, the discretized momentum equation is given by

$$\Omega\frac{\mathbf{u}_h^{n+1}-\mathbf{u}_h^n}{\Delta t} = -C(\mathbf{u}_h^n)\mathbf{u}_h^n + D\mathbf{u}_h^n - G\mathbf{p}_h^{n+1}. \tag{4}$$

Finding the solution to the system of equations (3) & (4) is split in two steps. First an auxiliary variable $\mathbf{u}_h^*$ is defined by the equation

$$\Omega\frac{\mathbf{u}_h^{*}-\mathbf{u}_h^n}{\Delta t} = -C(\mathbf{u}_h^n)\mathbf{u}_h^n + D\mathbf{u}_h^n. \tag{5}$$

Using this variable in (4) gives

$$\Omega\frac{\mathbf{u}_h^{n+1}-\mathbf{u}_h^{*}}{\Delta t} = -G\mathbf{p}_h^{n+1}. \tag{6}$$

Substitution of equation (6) in the continuity equation (3), gives rise to the following system of equations

$$\Delta t M\Omega^{-1}G\mathbf{p}_h^{n+1} = M\mathbf{u}_h^{*} + M^\Gamma\mathbf{u}_h^{n+1}, \tag{7}$$

which is often referred to as the discrete pressure Poisson equation, as it can be viewed as a discretization of the equation $\mathcal{M}\circ\mathcal{G}\mathbf{p} = \mathcal{M}\mathbf{u}$. Note, however, that we are not directly discretizing the composed operator $\mathcal{M}\circ\mathcal{G}$ here, but its separate parts $\mathcal{M}$ and $\mathcal{G}$. Hence, of sole importance is the accuracy of the discretization of the divergence and gradient operators $\mathcal{M}$ and $\mathcal{G}$, respectively. This should be kept in mind when assessing the accuracy of the method.

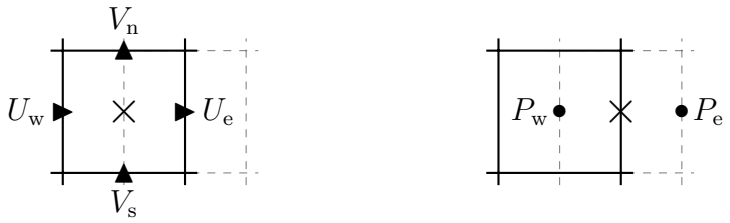


Figure 1: Regular discretization stencil for $M\mathbf{u}_h$ (left) and $G\mathbf{p}_h$ (right, horizontal component only) applied at the location indicated with $\times$.

3 LOCAL GRID REFINEMENT

The Navier–Stokes equations are discretized on an Arakawa C-grid as illustrated in fig. 1. For brevity the third dimension, which is treated similarly, is omitted. The subscript ℓ is used to indicate the local refinement level, where $\ell = 0$ refers to the unrefined base grid (indexing is discussed in section 3.1.)

In the regular parts of the grid the divergence operator is discretized as follows (for the subscript convention consult fig. 1)

$$M\mathbf{u}_h|_\ell = \Delta y_\ell (U_{\mathrm{e};\ell} - U_{\mathrm{w};\ell}) + \Delta x (V_{\mathrm{n};\ell} - V_{\mathrm{s};\ell}) \tag{8}$$

In order to let the discrete operators satisfy the adjoint condition,

$$G = -M^* \tag{9}$$

the pressure gradient is discretized as $G\mathbf{p}_h = -M^*\mathbf{p}_h$. This gives the following second-order central discretization:

$$\frac{P_{\mathrm{e};\ell} - P_{\mathrm{w};\ell}}{\Delta x_\ell} \qquad \frac{P_{\mathrm{n};\ell} - P_{\mathrm{s};\ell}}{\Delta y_\ell} \tag{10}$$

3.1 Refinement approach

A semi-structured approach is followed in which a cell (i, j) at refinement level ℓ is *replaced* by a set of $r_i \times r_j$ smaller cells at refinement level $\ell+1$ having indices $(2i+m, 2j+n)$ at offsets $0 \leq m < r_i, 0 \leq n < r_j$. The semi-structured indexing system is illustrated in fig. 2. On block-shaped refinement regions the method is locally structured, hence the computational efficiency of the original array-based solution methods can be exploited as much as possible. Only at the boundaries of the refinement regions where the actual refinement takes place a new treatment is required.

For describing the grid layout an auxiliary array is introduced storing only one integer for each potentially occuring cell $(i, j; \ell)$ pointing at the memory location of the subgrid in which it is contained (or null if the cell does not exist). Along the lines of [3] a data structure results that allows for fast and efficient look-up when compared with typical tree-based storage methods.

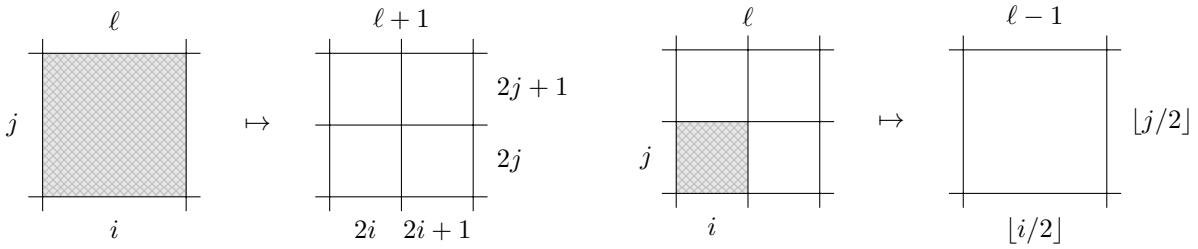


Figure 2: Illustration of semi-structured indexing for refinement ratios $r_i = 2, r_j = 2$. *Left*: From coarse to fine indices. *Right:* From fine to coarse indices.



Figure 3: *Left*: refinement approach based on interpolation of missing refined pressure variable, *Right*: refinement approach (as followed here) with shifted pressure gradient which is equal for both refined cell faces. Missing variables are denoted by "○".

3.2 Poisson equation near interfaces

Near refinement interfaces the discretization stencil is incomplete due to missing coarse or fine grid variables. Typically, a large stencil is used for the approximation of missing pressure or velocity variables along the refinement interface. Interpolation of missing variables increases the number of non-zero coefficients in the pressure Poisson matrix, which might result in a non-symmetric matrix, putting higher demands on the solver. Most authors use a non-overlapping interface and apply linear (or even higher-order) interpolation for missing variables on the other side of the interface [4]. Another approach is to apply linear interpolation inside an overlapping interface [5]. In all cases the discretization results in a non-symmetric system of equations.

In the present approach, a compact discretization scheme is designed (in particular for the implicit part), which results in a small and symmetric scheme for the discrete composition of M and G. This makes it possible to employ an efficient linear solver. Furthermore, it facilitates the use of adjacent refinement regions as well as the interface discretization near objects and free-surface boundaries.

3.2.1 Spatial discretization

Remark (i) *As an example we consider refinement interfaces in the "x=constant"-plane where the refined cells are located to the left of the interface. Five other interface orientations are possible, which are treated similarly. To further simplify discussion we assume a base grid with uniform grid spacings* Δx_0 *and* Δy_0.

Remark (ii) *In the current discussion we take refinement ratios* $r_i = 1$ *and* $r_j = 2$. *In words, no refinement is applied perpendicular to the refinement interface and local refinement is only applied along the refinement interface. For the grid spacings this implies* $\Delta y_{\ell+1} = \Delta y_\ell/2$ *and* $\Delta x_{\ell+1} = \Delta x_\ell$. *Since* $r_i = 1$, *for the latter, the level subscript will be omitted.*

Extending the discretization to the three-dimensional case, non-uniform grids and other refinement directions or refinement ratios is straightforward.

There are two ways of obtaining a first-order accurate discretization of the pressure gradient. Either by using a linear interpolation for the missing pressure variable outside the refinement region (see left of fig. 3) or by slightly shifting the location of the pressure gradient (see right of fig. 3). Both approaches result in a first-order accurate discretization scheme introducing an error term that is proportional to respectively $\Delta\frac{\partial^2 p}{\partial y^2}$ and $\Delta\frac{\partial^2 p}{\partial y \partial x}$, where for brevity we use Δ which has the same order of magnitude as Δx and Δy. However, the first approach results in a relatively large stencil whereas the second approach uses a smaller interpolation stencil consisting of pressure variables that already form part of the regular stencil.

For this reason, the second approach is followed, which can be described as "using a constant pressure gradient along a refined cell face" (see e.g. [6, 7]). Correspondingly, we use a uniform velocity across the entire refined cell face and only place coarse computational velocity variables at the interface.

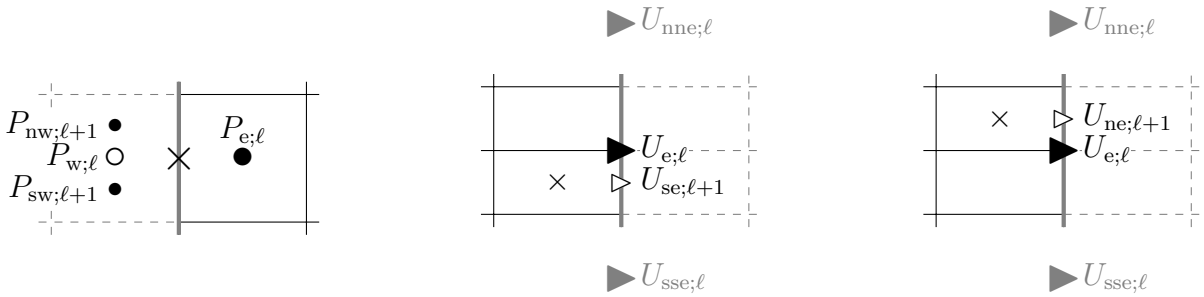


Figure 4: *Left:* Missing *coarse* pressure variable (○) for the gradient operator applied at the location indicated with ×. *Right:* Missing *refined* velocity variable (▷) for the divergence operator applied at the location indicated with ×, together with the variable used for constant extrapolation (▶) and linear correction (▶).

For the missing coarse pressure variable $P_{\mathrm{w};\ell}$ (see fig. 4) a simple average of the neighbouring fine pressure values is used. This results in the following discretization of the pressure derivative at the refined cell face

$$\frac{2P_{\mathrm{e};\ell} - P_{\mathrm{sw};\ell+1} - P_{\mathrm{nw};\ell+1}}{2\Delta x} = \frac{\partial p}{\partial x}(\mathbf{x}^u_\ell) + O(\Delta).$$

Note that the approximation for the missing pressure variable is second-order accurate, but one order of accuracy is lost due to the loss of symmetry in the central scheme. Hence the approximation of the pressure gradient across the refinement interface is first-order accurate.

For the discretization of the divergence at the fine side of refinement interfaces, an approximation is needed for the missing fine velocities. As a first approach, a discretization is obtained by means of the adjointness condition (9), so the divergence operator is defined as the negative transpose of the gradient operator. This implies that missing velocities are simply approximated using constant extrapolation (see fig. 4)

$$U_{\mathrm{se};\ell+1} \quad := U_{\mathrm{e};\ell} = u(\mathbf{x}^U_{\mathrm{se};\ell+1}) + O(\Delta), \qquad U_{\mathrm{ne};\ell+1} := U_{\mathrm{e};\ell} = u(\mathbf{x}^U_{\mathrm{ne};\ell+1}) + O(\Delta).$$

The corresponding divergence operator for interface cells is then given by

$$\begin{aligned}\left(\overline{M}\mathbf{u}_h\right)_{\mathrm{s};\ell+1} &= \Delta y_{\ell+1}\left(U_{\mathrm{e};\ell} - U_{\mathrm{sw};\ell+1}\right) + \Delta x\left(V_{\mathrm{c};\ell+1} - V_{\mathrm{s};\ell+1}\right)\\ \left(\overline{M}\mathbf{u}_h\right)_{\mathrm{n};\ell+1} &= \Delta y_{\ell+1}\left(U_{\mathrm{e};\ell} - U_{\mathrm{nw};\ell+1}\right) + \Delta x\left(V_{\mathrm{n};\ell+1} - V_{\mathrm{c};\ell+1}\right)\end{aligned}$$

Taking a uniform velocity along the refined cell face is conform the earlier remark of using a uniform pressure gradient along the refined cell face. However, it can be seen that the scheme for the divergence operator is not consistent yet because the velocities in the central difference are not well aligned in the y-coordinate.

$$\begin{aligned}\frac{1}{\Delta x\Delta y_{\ell+1}}\left(\overline{M}\mathbf{u}_h\right)_{\mathrm{s};\ell+1} &= \frac{\partial u}{\partial x}(\mathbf{x}^P_{\mathrm{s};\ell+1}) + \frac{\partial v}{\partial y}(\mathbf{x}^p_{\mathrm{s};\ell+1}) + \frac{1}{2}\frac{\Delta y_{\ell+1}}{\Delta x}\frac{\partial u}{\partial y}(\mathbf{x}^u_{\mathrm{e};\ell}) + O(\Delta)\\ \frac{1}{\Delta x\Delta y_{\ell+1}}\left(\overline{M}\mathbf{u}_h\right)_{\mathrm{n};\ell+1} &= \frac{\partial u}{\partial x}(\mathbf{x}^P_{\mathrm{n};\ell+1}) + \frac{\partial v}{\partial y}(\mathbf{x}^p_{\mathrm{n};\ell+1}) - \frac{1}{2}\frac{\Delta y_{\ell+1}}{\Delta x}\frac{\partial u}{\partial y}(\mathbf{x}^u_{\mathrm{e};\ell}) + O(\Delta)\end{aligned}$$

The inconsistency can be resolved by adding corrections for the observed error terms. In order to satisfy mass conservation it is important that these corrections sum up to zero for each refined cell face. For this we can make use of the symmetry observed in the above error terms and correct the operator $\overline{M}$ with the following linear correction terms:

$$\frac{1}{\Delta x\Delta y_{\ell+1}}\left(M^+\mathbf{u}_h\right)_{\mathrm{s};\ell+1} = -\frac{1}{2}\frac{\Delta y_{\ell+1}}{\Delta x}\left[\delta_y\mathbf{u}_h\right]_{\mathrm{e};\ell} \tag{12}$$

$$\frac{1}{\Delta x\Delta y_{\ell+1}}\left(M^+\mathbf{u}_h\right)_{\mathrm{n};\ell+1} = \frac{1}{2}\frac{\Delta y_{\ell+1}}{\Delta x}\left[\delta_y\mathbf{u}_h\right]_{\mathrm{e};\ell} \tag{13}$$

where δ_y is a central differencing operator which is applied along the refinement interface (see fig. 4)

$$[\delta_y \mathbf{u}_h]_{\mathrm{e};\ell} = \frac{U_{\mathrm{nne};\ell} - U_{\mathrm{sse};\ell}}{2\Delta y_\ell} \tag{14}$$

The divergence operator with correction, i.e. $\overline{M} + M^+$ is now first-order accurate.

We remark that the correction operator M^+ is similar for other interface orientations. Note that in the three-dimensional case the operator would also include a difference term in the secondary direction tangential to the interface.

4 NUMERICAL RESULTS

In order to investigate the performance of the local grid refinement scheme, two-dimensional simulations of flow around a square cylinder have been performed. All simulations at Reynolds numbers 10 and 100 have been performed using a second-order central discretization without the use of a turbulence model.

cyl.	grid	L	# pts	C_d
2×4	80×80	0	6k	3.1374
	40×40	1	3k	3.1598
3×6	120×120	0	14k	3.2590
	60×60	1	6k	3.2589
4×8	160×160	0	26k	3.2918
	80×80	1	19k	3.2917
	40×40	2	4k	3.2908
6×12	240×240	0	58k	3.3138
	60×60	2	9k	3.3133
	30×30	3	3k	3.3099
12×24	480×480	0	230k	3.3297
	60×60	3	12k	3.3290
	30×30	4	5k	3.3243
24×48	960×960	0	922k	3.3383
	60×60	4	19k	3.3373
	30×30	5	9k	3.3323

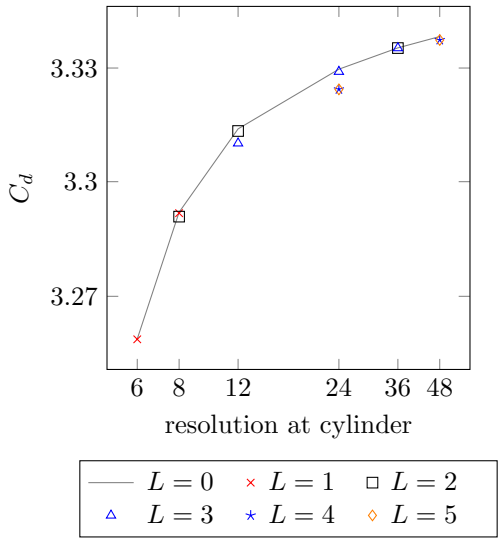


Table 1: Drag-coefficient predictions (C_d) for flow around a square cylinder (Re=10) on uniform, and locally refined grids. The column 'cyl.' displays the grid resolution at the boundary of the cylinder. The column 'grid' shows the resolution of the base grid to which the local grid refinement is applied. In all cases a refinement ratio of 2×2 is used and L indicates the number of local refinement regions. In the column '# pts' the total number of grid points is displayed.

In order to get a good view of the efficiency gain that is obtained with the local grid refinement approach, the analysis is best performed from a "coarsening" point of view. Near the object the grid resolution is kept constant while the grid is coarsened towards the boundaries of the domain.

4.1 Flow around a square cylinder

In this 2-D test case a square cylinder is placed of dimensions $[-0.5, 0.5] \times [-0.5, 0.5]$ in a computational domain covering the region $[-10, -10] \times [30, 10]$.

At a Reynolds number of 10 the flow readily converges to a steady-state solution. The resulting solution is smooth and is not expected to pose any difficulties for refinement interfaces. The numerical results presented in table 1 show that the drag-force predictions are accurate even on grids that are very coarse close to the boundaries of the domain. By accepting a 0.5% difference in the prediction of the drag force it is possible to reduce the computational time by up to factor of 100. The resolution of the grid close to the object is of main importance, and it is seen that good convergence behaviour is obtained when increasing the number of cells around the cylinder.

At a Reynolds number of 100 the flow is unsteady, as the flapping shear layer results in an oscillating drag and lift force on the cylinder. This test case clearly provides a more challenging test for the local grid refinement method. A local grid refinement ratio of 3×3 is used and the results of the locally refined grids are compared to their uniform counterparts. The results shown in table 2 illustrate again that the number of grid points can be reduced significantly while useful predictions for the drag and lift coefficients can still be obtained.

cyl.	grid	L	#pts	St	C_d	$C_\mathrm{l,rms}$
6×12	240×240	0	58k	0.152	1.6275	0.2567
	80×80	1	19k	0.153	1.6273	0.2554
9×18	360×360	0	129k	0.150	1.5687	0.2231
	40×40	2	12k	0.150	1.5687	0.2208
18×36	720×720	0	0.5M	0.150	1.5234	0.2009
	80×80	2	48k	0.150	1.5232	0.1998

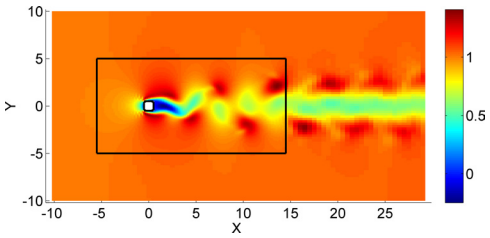


Table 2: Numerical predictions of the Strouhal number (St), mean drag force C_d, and the root-mean-square of the lift coefficient $C_\mathrm{l,rms}$ for flow around a square cylinder (Re=100) on uniform and locally refined grids. In all cases a refinement ratio of 3×3 is used. Again, the 'cyl.' denotes the grid resolution around the cylinder, 'grid' the resolution of the base grid, L the number of refinements, and '# pts.' the total number of grid points.

4.2 Dambreak experiment

To demonstrate the validity of the local refinement method for more practical cases, it is tested for the simulation of a breaking dam. ComFLOW has been used before for this classical test [1], therefore it provides good material for assessing the performance of the local refinement method.

As starting point a grid is used of $200 \times 36 \times 50$ points. In order to save computational time, the original resolution is only maintained around the block; to the right as well as towards the sides of the domain it is coarsened (as illustrated in fig. 5).

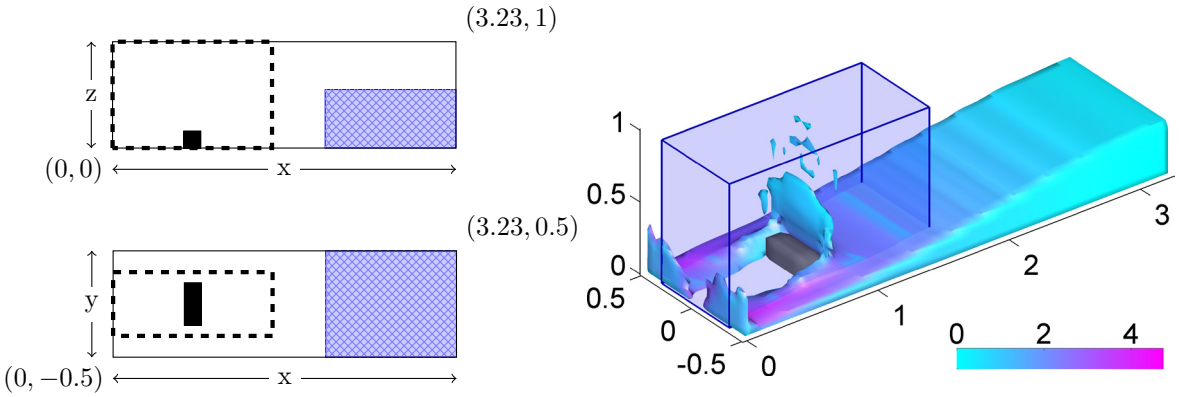


Figure 5: *Left:* Cross sections of the domain illustrating the grid configuration. The original resolution is only kept inside the dashed box. *Right:* Isosurface of the volume fractions colored by the absolute velocity of the free surface.

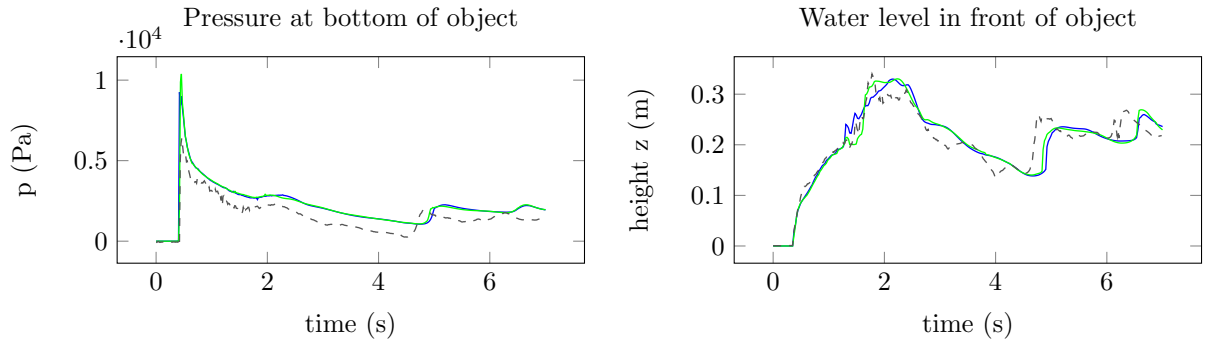


Figure 6: Numerical results and measurements for the 3-D dambreak experiment. *Legend:* —— coarsened grid; —— uniform grid; - - - experiment.

The simulation results show good correspondence to the measurements and it can be seen that coarsening in the region of the reservoir does not affect the prediction of the impact pressure. The differences between the locally coarsened and uniform grid are much smaller than the actual modelling error while the computational time has been reduced from 8h05 to 0h38. This illustrates that for typical "impact" problems a significant computational saving can be made by coarsening in the far away regions.

5 CONCLUSIONS

In this paper a local grid refinement approach has been presented for the simulation of free-surface flow. Special attention was paid to designing a compact stencil because the method needs to be accurate and robust in a wide variety of settings. In particular this facilitates the interface discretization near cut-cells and the modification of the Volume-of-Fluid scheme. Furthermore, the compact interface scheme is easily adapted to support refinement corners that occur when concatenating rectangular refinement regions, hence allowing for even more efficient grid configurations.

The local refinement approach has been succesfully applied to the simulation of turbulent flow, wave simulations and (wave) impact problems. Several simulation results were presented to verify and validate the method. In particular for calculating drag forces or (wave) impact forces the reduction of computational costs can be significant. Currently the refinement method is being extended to support two-phase flow and moving objects.

REFERENCES

[1] K.M.T. Kleefsman, G Fekken, A.E.P. Veldman, B Iwanowski, and B. Buchner. A volume-of-fluid based simulation method for wave impact problems. *Journal of Computational Physics*, 206(1):363–393, 2005.

[2] A.E.P. Veldman, R. Luppes, T. Bunnik, R.H.M. Huijsmans, B. Duz, B. Iwanowski, R. Wemmenhove, M.J.A. Borsboom, P.R. Wellens, H.J.L. van der Heiden, and P. van der Plas. Extreme wave impact on offshore platforms and coastal constructions. *30th Conf. on Ocean, Offshore and Arctic Eng. OMAE2011, Rotterdam, Netherlands, June 19-24*, 2011.

[3] M.D. de Tullio, P. De Palma, G. Iaccarino, G. Pascazio, and M. Napolitano. An immersed boundary method for compressible flows using local grid refinement. *Journal of Computational Physics*, 225(2):2098–2117, 2007.

[4] M.L. Minion. A projection method for locally refined grids. *Journal of Computational Physics*, 127(1):158–178, 1996.

[5] Q. Liu. A stable and accurate projection method on a locally refined staggered mesh. *International Journal for Numerical Methods in Fluids*, 67(1):74–92, 2011.

[6] E. Uzgoren, R. Singh, J. Sim, and W. Shyy. Computational modeling for multiphase flows with spacecraft application. *Progress in Aerospace Sciences*, 43(4):138–192, 2007.

[7] F. Losasso, F. Gibou, and R. Fedkiw. Simulating water and smoke with an octree data structure. In *ACM Transactions on Graphics (TOG)*, volume 23, pages 457–462. ACM, 2004.

V International Conference on Computational Methods in Marine Engineering
MARINE 2013
B. Brinkmann and P. Wriggers (Eds)

TESTING A SEMI-AUTOMATED TOOL FOR THE OPTIMISATION OF FULL-SCALE MARINE PROPELLERS WORKING BEHIND A SHIP

STEPHAN BERGER, MARKUS DRUCKENBROD, MARKUS PERGANDE AND MOUSTAFA ABDEL-MAKSOUD

Institute M-8 for Fluid Dynamics and Ship Theory
Hamburg University of Technology
Schwarzenbergstraße 95c, 21073 Hamburg, Germany
e-mail: stephan.berger@tuhh.de, web page: http://www.tuhh.de/fds and
http://www.panmare.de

Key words: Propeller optimisation, evolutionary algorithm, sheet cavitation, pressure pulses, propulsion efficiency

Abstract. A procedure for the optimisation of full-scale marine propellers working behind a ship is presented. This procedure consists of two stages: the actual optimisation and a detailed investigation of a few selected propeller geometry variants. In the first step, an evolutionary algorithm in combination with the in-house panel code *pan*MARE is used to solve the multi-objective propeller optimisation problem. An efficient method for the evaluation of the individuals and a parameterisation strategy for propeller shapes are presented. Proceeding from the results of the optimisation, a set of selected propeller variants is investigated in detail in the second stage of the procedure. The applied algorithm is based on coupling *pan*MARE with a viscous flow solver. An enhancement of this method allows investigating several propeller variants sequentially without stopping the solvers.

1 INTRODUCTION

Usually, the final propeller design of a ship is developed when the hull form design and the machinery selection are nearly completed. Assuming that the ship designer creates a hull form that leads to the lowest resistance and the most homogenous wake field possible, the only way to improve propulsion efficiency, propeller-induced hull structure vibrations and propeller noise is to optimise the propeller shape. Unfortunately, at this stage of the design many measures for improving the propulsion efficiency come into conflict with measures for the reduction of hull structure vibrations and propeller noise, which are significant factors for the comfort on board. Propeller designers need to find a compromise between these demands. Their importance can vary for different ship types:

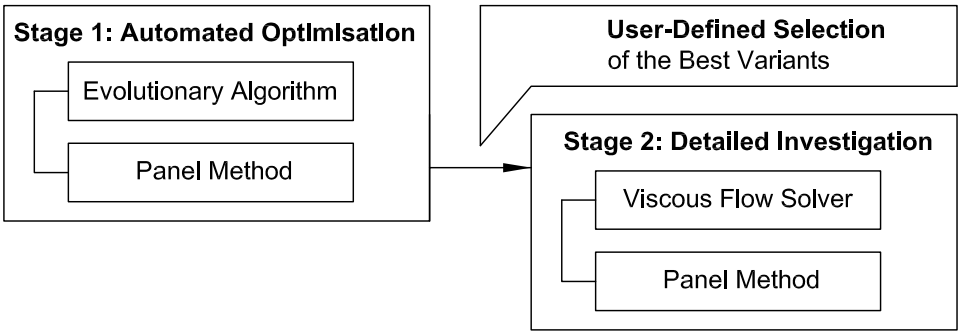


Figure 1: The two process stages of the optimisation tool.

for a container ship, propulsion efficiency is more important than comfort, whereas for a passenger ship comfort is the dominating factor. The tool introduced and tested in this paper assists the propeller designer with finding a propeller design for a given hull form which meets the demands named above in a better way than a given initial solution. In the following, an outline of the optimisation tool, which operates in two stages, is given (see Figure 1).

(1) *Stage 1: Automated Optimisation.* The first stage is the actual optimisation. Different optimisation algorithms are investigated for the optimisation of propeller shapes in [1], evolutionary algorithms are tested in [2] and [3]. In the present paper an evolutionary algorithm is also employed. In this context, the formulation and evaluation of the objective function is a crucial aspect. During the optimisation process a few hundreds of individuals (i.e. propeller variants) need to be simulated. Only potential theory-based methods can handle this in a reasonable amount of time. These methods allow for incorporating the ship's wake field, but all aspects of the interaction between the flow around the hull and the propeller cannot be captured. In order to account for this, a subsequent second stage is necessary.

(2) *Stage 2: Detailed Investigation of the Best Propeller Variants.* As a result of the optimisation in the first stage, a large set of propeller variants is offered to the designer. The designer can select a small number of promising variants from this set by means of appropriate criteria depending on the design requirements. This selection is then investigated by a numerical method that is based on coupling a viscous flow solver with a potential theory-based boundary element method. The employed coupling approach is able to capture all relevant interaction effects between the flow around the hull and the propeller. Based on the results of this investigation, the designer can make a final decision.

The next section is devoted to the underlying numerical methods for the hydrodynamic analysis of the propeller variants. After that, the optimisation tool is presented in detail on the basis of a case study. Finally, the paper ends with a discussion of the results and some notes on future work.

2 UNDERLYING METHODS FOR THE HYDRODYNAMIC ANALYSIS

In this section, the underlying numerical methods for the evaluation of the propeller variants in Stage 1 and the detailed investigation of the best variants in Stage 2 are briefly described.

2.1 Potential Theory-Based Boundary Element Method

The method used here for the evaluation of the propeller variants in Stage 1 is the in-house boundary element solver *pan*MARE, which is aimed to simulate arbitrary potential flows in marine applications including sheet cavitation effects [4]. This boundary element code is based on a three-dimensional panel method with flat quadrilateral panel elements and a constant source and dipole distribution over each panel.
The governing equations for the numerical scheme are derived from the potential flow assumptions, where the flow is considered to be irrotational, incompressible and inviscid. The equations for the conservation of mass and momentum are then simplified to Laplace's equation for the total potential Φ^* and the Bernoulli equation for the pressure p [5]:

$$\nabla^2\Phi^* = \nabla^2(\Phi + \Phi_\infty) = 0 \tag{1}$$

and

$$p + \frac{1}{2}\rho|\mathbf{V}|^2 + \rho\frac{\partial\Phi}{\partial t} + \rho g z = const, \tag{2}$$

$\forall \mathbf{x} \in \Omega$, where Ω is the domain of the potential flow, Φ is the induced potential, Φ_∞ is the undisturbed free stream potential, and $\mathbf{V} = \nabla\Phi^*$ and $\mathbf{V}_\infty = \nabla\Phi_\infty$ are the total velocity and the reference velocity, respectively. Arbitrary velocity distributions can be described as reference velocity, e.g. the wake field of a ship. The induced velocity is the difference between the total and the undisturbed reference velocity $\mathbf{V}_{ind} = \mathbf{V} - \mathbf{V}_\infty$. The constants ρ and g are the constant water density and gravity constant, respectively.
The continuous solution of the Laplace equation is obtained by Green's third identity as a distribution of sources and dipoles on the body's surface [5]:

$$\int_{\partial\Omega} \Big[\mu(\mathbf{x})\nabla\Big(\frac{1}{\|\mathbf{x}_0 - \mathbf{x}\|}\Big)\cdot\mathbf{n} - \frac{\sigma(\mathbf{x})}{\|\mathbf{x}_0 - \mathbf{x}\|}\Big] dS(\mathbf{x}) = 0, \tag{3}$$

where

$$\sigma(\mathbf{x}) := -\nabla\Phi(\mathbf{x})\cdot\mathbf{n} \text{ and } \mu(\mathbf{x}) := -\Phi(\mathbf{x}). \tag{4}$$

$\mathbf{x}_0$ are collocation points inside a solid body. To obtain a unique solution for the above equation, boundary conditions are required on the boundaries of the flow domain Ω. There are three types of boundaries where different boundary conditions are applied: the cavitating parts of the body surface S_{B_C}, the non-cavitating parts of the body surface S_B/S_{B_C}, where S_B is the body surface, and the wake surface S_W. The boundary conditions are formulated as follows:

- On the non-cavitating body surface S_B/S_{B_C}, the Neumann boundary condition is applied: $\nabla\Phi^* \cdot \mathbf{n} = 0, \forall \mathbf{x} \in S_B/S_{B_C}$, where the vector $\mathbf{n}$ represents the normal vector on the point $\mathbf{x}$. From this condition an equation for the source strengths can be derived: $\sigma = \mathbf{V}_\infty \cdot \mathbf{n}, \forall \mathbf{x} \in S_B/S_{B_C}$.
- On the non-cavitating wake surface S_W, the physical Kutta condition is applied to model the vorticity: $\Delta p = 0, \forall \mathbf{x} \in S_W$, where $\Delta p = p^+ - p^-$ is the pressure jump between the pressure value on the upper and lower side of the trailing wake.
- On the cavitating parts of the body surface S_{B_C}, additional kinematic and dynamic boundary conditions are postulated to describe the physics of sheet cavitation: no flow is allowed to penetrate the cavity sheet, and the pressure on S_{B_C} must be equal to vapour pressure of water p_v: $p = p_v, \forall \mathbf{x} \in S_{B_C}$. The extent of the surface S_{B_C} and the cavity thickness η need to be determined iteratively [6].

Equation (3), combined with the above boundary conditions on the body and sheet cavity surface, results in a continuous boundary value problem that is discretised by the panel method. Hereby, the body and trailing wake surfaces are discretised in flat quadrilateral elements and the boundary conditions are applied on a collocation point $\mathbf{x}_0$ of each panel element. The collocation points are defined in *pan*MARE as the midpoints of the surface panels, which are slightly displaced inside the body. On each body panel element a source and a dipole is distributed with a constant strength over one panel. On the trailing wake panels only dipoles are distributed since no displacement is induced by the wake. The wake surface S_W is aligned along the streamlines of the velocity field $\mathbf{V}$ iteratively in order to account for the trailing vortex roll-up. The described procedure results in a set of linear equations that can be easily solved numerically by the Gauss method. Friction effects are not captured inherently by this method; they have to be corrected with empirical models.

2.2 Viscous Method

For the detailed investigation of the best propeller variants in Stage 2 with respect to propulsion efficiency, fluctuations of hull pressure and propeller thrust as well as the occurrence and behaviour of cavitation, it is essential to capture the interaction between the propeller and the flow around the hull. The latter is strongly influenced by viscous effects and is therefore calculated by a viscous method solving the RANS equations and the continuity equation:

$$\rho \left(\frac{\partial}{\partial t} + \mathrm{J}\overline{\mathbf{u}} \right) \cdot \overline{\mathbf{u}} = -\nabla \overline{p} + \nabla \cdot \left(\overline{\boldsymbol{\tau}} + \boldsymbol{\tau}_T \right) + \mathbf{f} \tag{5}$$

and

$$\nabla \cdot \overline{\mathbf{u}} = 0, \tag{6}$$

$\forall \mathbf{x} \in \Lambda$, where Λ is the domain of the viscous flow. In Equations (5) and (6), the variable $\overline{\mathbf{u}}$ denotes the Reynolds-averaged velocity, $\overline{p}$ the Reynolds-averaged pressure, $\overline{\boldsymbol{\tau}}$

the Reynolds-averaged molecular stress tensor and $\boldsymbol{\tau}_T$ the Reynolds stress tensor due to the Reynolds-averaging, whose components are approximated by appropriate turbulence models. $\mathrm{J}\overline{\mathbf{u}}$ is the Jacobian matrix of the velocity field and $\mathbf{f}$ is a volume specific force source term. For the numerical solution of the RANS equations under consideration of appropriate boundary conditions on the boundaries of the domain of the viscous flow Λ, the ANSYS CFX code based on a finite volume element method, which can be applied for both structured and unstructured numerical grids, is used [7].
Nowadays, viscous methods are a sophisticated tool for the simulation of the ship flow with operating propeller, but full-scale simulations taking account of cavitation effects are prohibitively expensive and therefore not applicable in the day-to-day design process. To reduce the computational effort, the real propeller can be replaced by a distribution of body forces emulating the impact of the propeller on the hull flow. The flow around the propeller including sheet cavitation effects is calculated by means of the panel method described in the previous section. To account for the interaction between hull flow and propeller, a coupling method is applied (see Section 3.2.1).

3 DETAILED DESCRIPTION OF THE OPTIMISATION TOOL

After having introduced the principles of the design process and the most relevant components in the previous sections, the design process is described in detail. As an illustrative example, a given initial propeller design[1] for the KRISO Container Ship (KCS) shall be improved. The basic propeller dimensions as the number of blades z_P, the number of revolutions n and the propeller diameter $D = 2R$ are kept constant during the optimisation.

3.1 Stage 1: Automated Optimisation

As mentioned in the introductory section, the task is to improve the propeller shape with respect to propulsion efficiency and comfort level in terms of propeller-induced hull structure vibrations. It is possible to formulate this as a constrained multi-objective optimisation problem:

$$\min \left\{ \epsilon_{eff}\left(A\right), \epsilon_{com}\left(A\right) \right\} \text{ subject to } \frac{|T - T_0|}{T_0} \leq \delta, \tag{7}$$

where ϵ_{eff}, $\epsilon_{com} : \Psi \rightarrow \mathbb{R}^+$ are appropriate objective functions quantifying the propulsion efficiency of a propeller variant $A \in \Psi$ and the tendency of the propeller to induce hull vibrations, respectively. Ψ denotes the set of all possible propeller variants. The problem is considered to be a minimisation problem, i.e. smaller values of the objective functions signify a better propeller. In this case, the only constraint is that the difference between propeller thrust T and reference thrust T_0 is smaller than a certain limit $\delta \cdot T_0$. Regardless

[1]The propeller data and relevant experimental results are provided by a propeller manufacturer. We therefore are only allowed to publish dimensionless quantities.

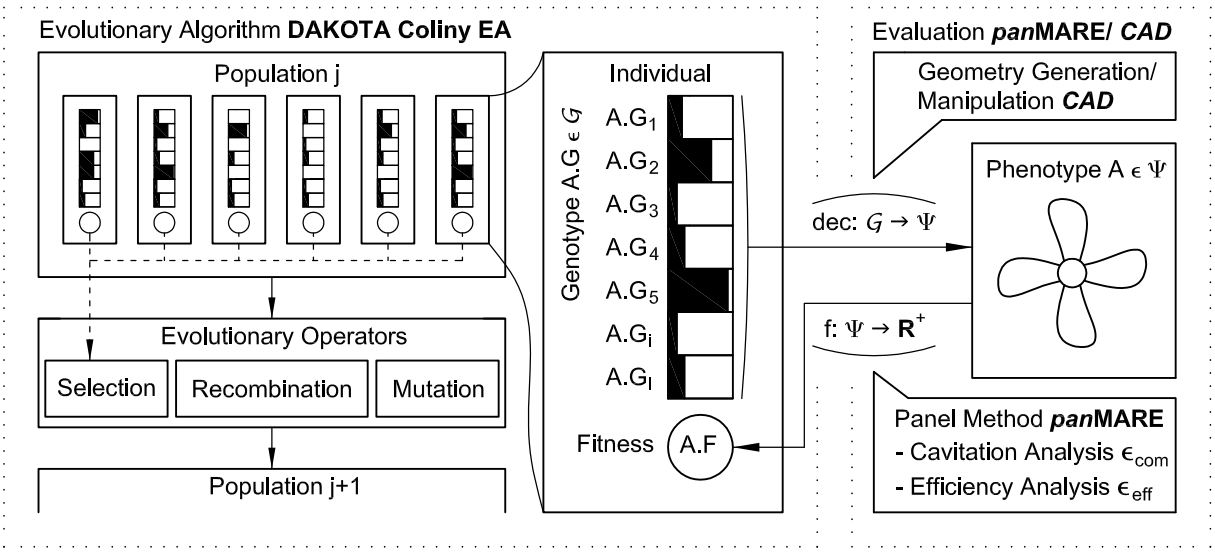


Figure 2: Principle of the evolutionary algorithm.

of the exact definition of the objective functions and the search space, which is to be done later in Sections 3.1.1 and 3.1.3, the present optimisation problem is obviously complex. Without knowing more about the problem, it has to be assumed to be non-linear and discontinuous. Evolutionary algorithms are suitable for these kinds of problems because they are not problem-specific in general. The disadvantage is that these all-purpose algorithms require a longer period of time to find a solution for the optimisation problem and it cannot be guaranteed that the found solution is a good solution or even the best [10]. If more detailed information about the optimisation problem is available, the use of deterministic or local optimisation methods is the better choice.

Figure 2 shows the principle of the optimisation method.[2] The jth population consists of a number of individuals, i.e. propeller variants. An arbitrary individual A is characterised by its genome $A.G \in \mathcal{G}$, where $\mathcal{G} \subset \mathbb{R}^l$ is defined as the genotypic search space (see Figure 3). Generally, the genome of an individual consists of $l \in \mathbb{N}$ components $A.G_i \in \mathbb{R}$ $(1 \leq i \leq l)$. In other words, each propeller variant is determined by l geometry parameters. The probability of survival for each individual is quantified by its fitness $A.F \in \mathbb{R}^+$, which depends on the objective functions introduced in Equation (7). Usually, evolutionary algorithms operate on the genotypic search space $\mathcal{G}$, but for the evaluation of the fitness it is necessary to transform the individuals into a phenotypic representation $A \in \Psi$ by means of a decryption function $dec : \mathcal{G} \to \Psi$, which means that a concrete propeller is generated using a set of l geometry parameters. After investigating this propeller variant numerically by the method introduced in Section 2.1, the fitness $A.F \in \mathbb{R}^+$ can be expressed by $A.F = f(A)$, where $f : \Psi \to \mathbb{R}^+$ is defined as fitness function.

[2]Evolutionary algorithms try to apply the process of biological evolution to optimisation problems. Thus, the terminology is borrowed from evolutionary biology [10].

Genome component/ Parameter		*Range*
$A.G_1$	$\frac{P}{D}$ at $\frac{r}{R} = 0.175$	[0.80, 1.02]
$A.G_2$	$\left(\frac{r}{R}\right)_{mid,P}$	[0.40, 0.90]
$A.G_3$	$\frac{P}{D}$ at $\frac{r}{R} = \left(\frac{r}{R}\right)_{mid,P}$	[0.80, 1.40]
$A.G_4$	$\frac{P}{D}$ at $\frac{r}{R} = 1.0$	[0.80, 1.20]
$A.G_5$	$\frac{Ca}{c}$ at $\frac{r}{R} = 0.175$	[0.00, 0.22]
$A.G_6$	$\left(\frac{r}{R}\right)_{mid,Ca}$	[0.20, 0.80]
$A.G_7$	$\frac{Ca}{c}$ at $\frac{r}{R} = \left(\frac{r}{R}\right)_{mid,Ca}$	[0.00, 0.13]
$A.G_8$	$\frac{Ca}{c}$ at $\frac{r}{R} = 1.0$	[0.00, 0.04]

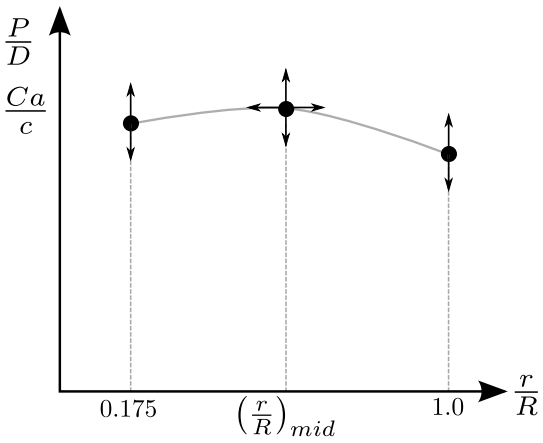


Figure 3: Genotypic search space $\mathcal{G}$ and meaning of the genome components/ parameters.

The $(j+1)$th population is created by applying the evolutionary operators *selection*, *recombination* and *mutation* to the jth population (see Figure 2). The procedure is repeated until an appropriate user-defined convergence criterion is fulfilled.
After this rather general description, the most important components of the algorithm and their implementation are explained in a more detailed way.

3.1.1 Search Spaces and Implementation of the Decrypting Function

Care must be exercised when the search space and the decrypting function are laid out. On the one hand, an adequate scope is needed for a noticeable propeller improvement, but on the other, it should be avoided that individuals are created whose design is obviously inappropriate. In the present study, the radial distribution of pitch $P(r)$ and the radial distribution of camber $Ca(r)$, which is defined as the maximal distance between the chord line and the mean line of the radial profile section, are varied during the optimisation.[3] All the remaining propeller characteristics are kept constant. The table in Figure 3 shows the definition of the genotypic search space. The genome of an individual consists of 8 components, which means that $\mathcal{G}$ is a search space with $l = 8$ dimensions. $A.G_1 ... A.G_4$ determine the radial distribution of pitch, $A.G_5 ... A.G_8$ the radial distribution of camber. For the genotype-phenotype conversion, the in-house geometry manipulation tool CAD is used. The genome components are interpreted as supporting points of a cubic interpolation spline (see Figure 3). CAD modifies the initial propeller shape using these splines as new radial distributions of pitch and chamber. Hereafter, the numerical grid is generated by means of this tool as well. Since the propeller skew or the sectional chord length are not modified, degenerated or ill-conditioned numerical grids are avoided.

[3]The dimensionless notation used in the following reads $\frac{P}{D}\left(\frac{r}{R}\right)$ for the pitch distribution and $\frac{Ca}{c}\left(\frac{r}{R}\right)$ for the radial distribution of camber, where c is the chord length of the radial profile section.

3.1.2 Notes on the Applied Evolutionary Algorithm

In this work, the Coliny evolutionary algorithm, which is a part of the open-source DAKOTA framework, is used [11]. Originally, the Coliny EA is intended for single-objective optimisations. A simple approach to carry out constrained multi-objective optimisations with this type of evolutionary algorithms is the application of aggregating fitness functions with penalty term [10], which is the pursued strategy in this work.
As shown in Figure 2, the evolutionary operators are a fundamental component of evolutionary algorithms. The way of applying these operators and their adjustment have a great impact on the convergence behaviour of the algorithm, and the setup of the evolutionary operators should be adapted to the particular problem [10], but this is hardly possible. Hence, a slightly modified standard setup is used.
The jth population consists of 25 individuals. The selection operator is applied to this population in order to choose a number of best individuals. This *parental selection* is based on a deterministic approach where only the fitness $A.F$ of an individual is considered. Next, 15 child individuals are generated from this set of parental individuals. 80% of the child individuals result from mating, where the recombination operator merges the genomes of two parental individuals to a new genome of a child individual. The remaining 20% are randomly chosen and then mutated parental individuals. In order to perform this mutation, the mutation operator affects a stochastical small change of the genome. This measure prevents the evolutionary algorithm from running into local optima. The fitness of each of the 15 new child individuals is evaluated by means of the panel method *pan*MARE and they are added to the 25 individuals of the jth population. Finally, the selection operator is applied again to reduce the current number of 40 individuals to 25, which results in the $(j+1)$ population. This *environmental selection* is based on both deterministic and stochastic criteria. One optimisation run has a total number of 400 individuals.

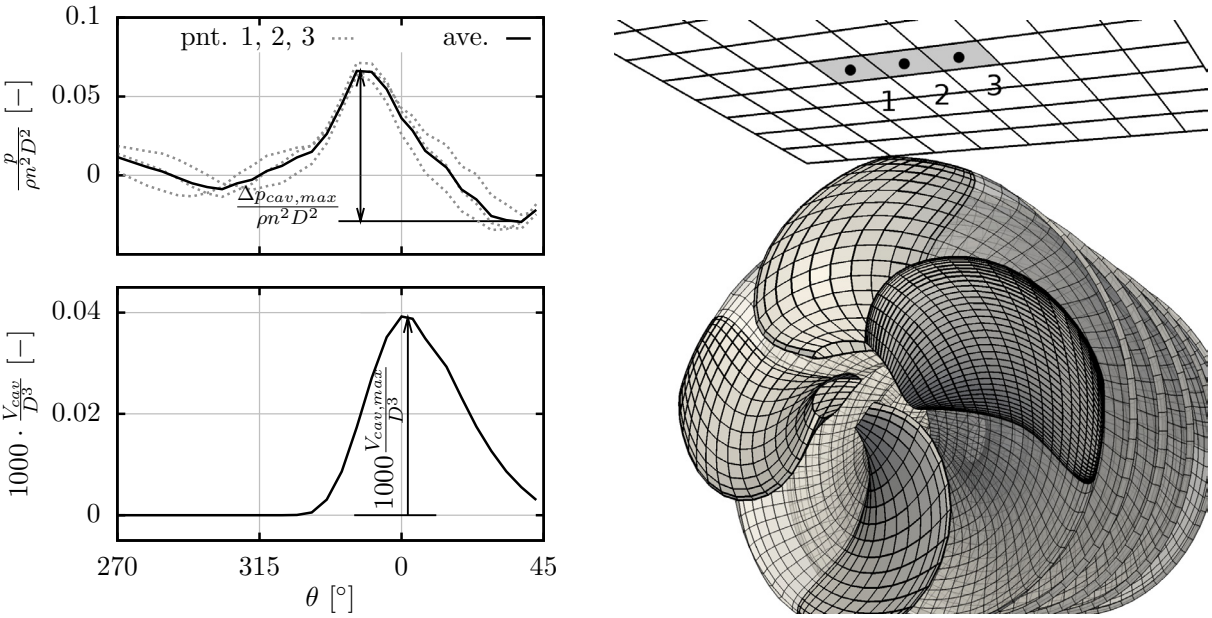
3.1.3 Evaluation of the Fitness of an Individual

The baseline formulation of the aggregating fitness function reads as follows:

$$f(A) = w_{eff}\epsilon_{eff}(A) + w_{com}\epsilon_{com}(A) + pen(A), \tag{8}$$

where w_{eff}, w_{com} with $w_{eff} + w_{com} = 1.0$ are weighting factors and $pen(A) : \Psi \to \mathbb{R}^+$ is a penalty function depending on the severity of the constraint injury (see Equation (7)). Apart from the setup of the evolutionary operators, the convergence behaviour of the evolutionary algorithm depends strongly on the exact formulation of the fitness function. Since no specific rules exist for the formulation, starting with an intuitive guess is the only possibility.

- The first term of Equation (8) quantifies the propulsion efficiency of the evaluated



(a) Definition of $V_{cav,max}$ and $\Delta p_{cav,max}$.

(b) Numerical grid used for the calculation of ϵ_{com}.

Figure 4: Calculation of ϵ_{com} using the example of the initial propeller design.

propeller variant:

$$\epsilon_{eff}\left(A\right) = \gamma_1 \frac{Q^{[0]}}{D \cdot T^{[0]}} + \gamma_2 \left(\frac{T^{[1]}}{T^{[0]}} + \frac{Q^{[1]}}{Q^{[0]}} \right), \tag{9}$$

where $T^{[0]}$ and $Q^{[0]}$ are the mean propeller thrust and mean propeller torque. $T^{[1]}$ and $Q^{[1]}$ denote the amplitudes of the thrust and torque fluctuations occurring with blade frequency nz_P. For the calculation of these values, 2.0 revolutions of the investigated propeller variant A are simulated by means of the panel method *pan*MARE (see Section 2.1) using the nominal wake field of the ship as reference velocity $\mathbf{V}_\infty$. The values can then be retrieved by a Fourier analysis of the time-dependent results. γ_1 and γ_2 are calibration factors making ϵ_{eff} equal to 1.0 for the initial propeller shape and pronouncing the first term of Equation (9). The employed numerical grid is similar to that shown in Figure 4b, the only difference is that each of the four blades are discretised by a coarse mesh and the absence of the flat plate above the propeller.

- Cavitation and pressure pulses due to cavitation are considered to be the most important drivers for propeller-induced vibrations and consequently for the level of comfort. However, even when panel methods are employed, a comprehensive analysis of cavitation effects is not possible for the evaluation of a few hundreds of individuals in a reasonable amount of time. To overcome this dilemma, a formulation

is chosen which considers cavitation effects and requires only a short simulation time for the evaluation.

$$\epsilon_{com}(A) = \gamma_3 \frac{\Delta p_{cav,max}}{\rho n^2 D^2} + \gamma_4 \frac{V_{cav,max}}{D^3}. \tag{10}$$

$V_{cav,max}$ is the maximum cavitation volume occurring during the blade passage through the wake field peak, $\Delta p_{cav,max}$ the corresponding pressure jump (see Figure 4a). The signal is recorded at three monitoring points, slightly smoothed and averaged. The cavitation model is activated for only one blade (recognisable by the fine discretisation). Note that only sheet cavitation is concerned, other relevant types of cavitation, such as tip and hub vortex cavitation are not captured by the present method. Again, the nominal wake field is used as reference velocity and the passage of this blade through the wake field peak is simulated. Thus, only 0.5 revolutions are necessary. The calibration factors γ_3 and γ_4 are chosen again in a way that ϵ_{com} is 1.0 for the initial propeller shape. Figure 4b shows the numerical grid employed.

- The penalty function *pen* assigns a bad fitness to those individuals violating the constraint that the thrust must be within a certain range. An intuitively chosen formulation reads as follows:

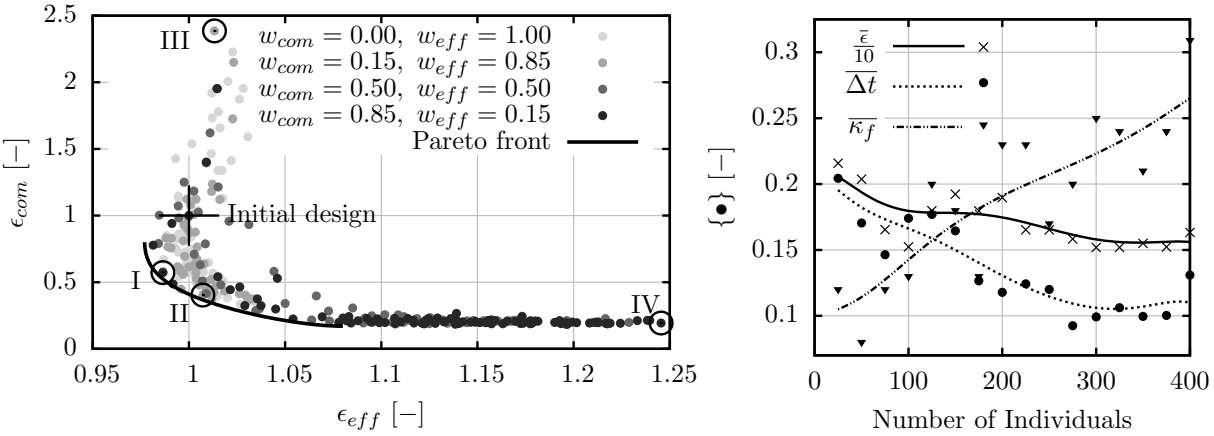
$$pen(A) = \begin{cases} 0, & \text{if } \frac{|T^{[0]} - T_0|}{T_0} \leq \delta \\ \xi \left(\frac{|T^{[0]} - T_0|}{T_0} - \delta \right)^2, & \text{if } \frac{|T^{[0]} - T_0|}{T_0} > \delta \end{cases}, \tag{11}$$

where ξ is a calibration factor and T_0 the mean thrust of the initial propeller design. δ is set to 0.04. A stricter restriction could compromise the convergence behaviour of the optimisation algorithm.

3.1.4 Results of the Optimisation

Figure 5a shows the objective function values of all generated feasible individuals $A \in \Psi_f \subset \Psi$, i.e. all generated propeller variants not violating the thrust constraint, which leads to $pen(A) = 0$. As mentioned in the introductory Section 1, efficiency and comfort are two conflicting objectives and at a certain point it is no longer possible to simultaneously improve them both. Hence, multi-objective optimisations result not in a single optimal solution, but in a set of optimal solutions, which are located on the *Pareto front* $\mathcal{P} \subset \Psi_f$: for all individuals in $\mathcal{P}$ it can be said that it is not possible to improve one objective without worsening the other (see Figure 5a).
In order to capture the Pareto front as good as possible, four optimisation runs with different weighting factors w_{eff} and w_{com} were carried out. It can be seen in Figure 5a that the individuals of each run form agglomerations which concentrate in different locations. For instance, the run with $w_{eff} = 0.15$ and $w_{com} = 0.85$ pronounces the comfort objective. As a result, most of the individuals are located on the horizontal flank, whereas the individuals originating from the run with $w_{eff} = 1.00$ are mostly located on

the vertical flank and the rest is somewhere in between. Figure 5b shows the averaged convergence behaviour of all four optimisation runs. It can be seen that the percentage of feasible individuals $\overline{\kappa_f}$ steadily grows from 0.1 to 0.25 during the simulation and at the



(a) ϵ_{com} and ϵ_{eff} for all feasible individuals.

(b) Convergence behaviour.

Figure 5: Objective function values of all feasible individuals and convergence behaviour.

same time, the average thrust deviation $\overline{\Delta t}$ of the unfeasible individuals is reduced. The average aggregated objective functions of the feasible individuals $\overline{\epsilon_{com} + \epsilon_{eff}} = \bar{\epsilon}$ can be improved, but after 300 evaluated individuals, the improvement stagnates.
For the further detailed investigation, four propeller variants are selected. Figure 6 shows the distributions of pitch and camber and the radial thrust distribution in terms of the sectional thrust coefficient $k_{T_r} = {}^{dT}/_{\rho n^2 D^2 c dr}$, where dT is the thrust of a blade section with the small radial extent dr and the chord length c.

- *Variant I* is a Pareto-optimal variant and shows a good improvement of the objectives (see Figure 5a). Nevertheless, it is dropped because the distribution of pitch and the corresponding thrust distribution are obviously inappropriate. The high loaded tip would generate an immense cavitating tip vortex. As mentioned in Section 3.1.3, this crucial aspect has not been taken into account for the calculation of ϵ_{com} and should be addressed in later work.

- *Variant II* is also a Pareto-optimal variant with a better comfort level but with a slightly lower efficiency compared to the initial design. This variant has a reduced pitch which is compensated by an increased camber. The main thrust load is shifted to inner blade sections.

- *Variant III* and *Variant IV* are extreme cases with a relatively good efficiency but a low comfort level and vice versa. They are located at the end points of the flanks in Figure 5a and are not part of the Pareto front. *Variant III* has a high overall pitch

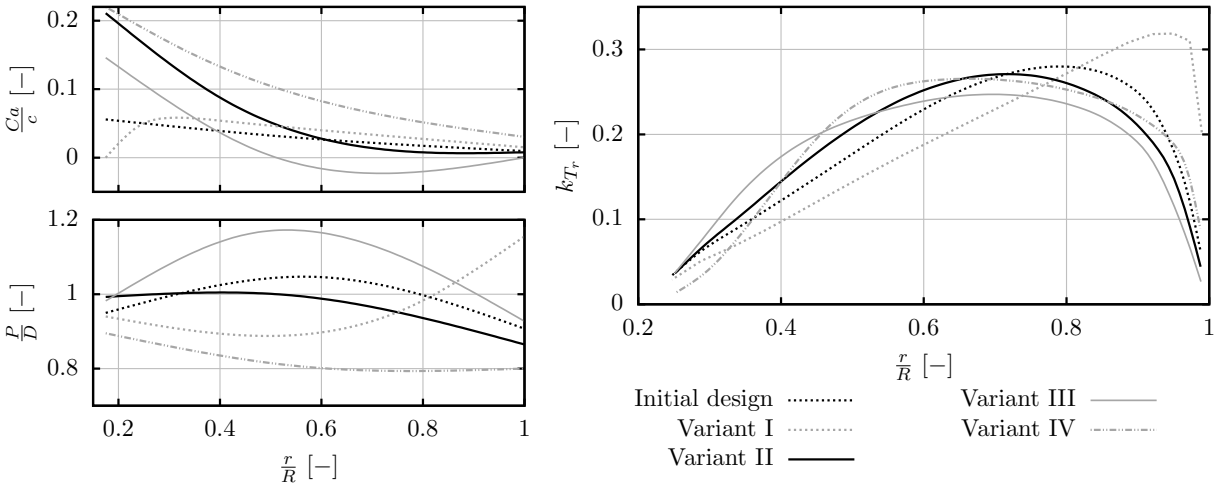


Figure 6: Radial distributions of camber $\frac{Ca}{c}$, pitch $\frac{P}{D}$ and thrust k_{T_r} of the selected variants.

(which is even compensated by a partially negative chamber), whereas the overall pitch of *Variant IV* is the lowest of all selected variants. However, to generate the prescribed thrust, this variant is highly cambered and more of a bucket wheel than a propeller. The high overall pitch of *Variant III* makes the blade sections susceptible to stall and provokes cavitation. Both variants are not considered to be good alternatives, but they are investigated in the next section for academic reasons.

3.2 Stage 2: Detailed Investigation of the Selected Propeller Variants

As a result of the optimisation in Stage 1, the designer is offered a set of propeller design alternatives whose efficiency and comfort level have been evaluated in a simplified manner without taking into account propeller-hull interactions. The second stage aims for answering two questions: (1) Is a certain selected propeller variant really better then the initial design? (2) If yes, how big is the improvement in terms of propeller-induced hull vibrations and fuel consumption?

3.2.1 Description of the Employed Method

In this section, the method used for the detailed investigation is described. The principal component is the viscous/inviscid coupling algorithm mentioned before. This algorithm consists of two steps[4] (see [8] and [9]):

(1) In the first step, the viscous flow solver is used to calculate the effective wake field of the ship. For this purpose, the velocity distribution $\overline{\mathbf{u}}$ is extracted for an adequate number of reference points $\mathbf{x}_{ref,j} \in \Lambda$ on a circular plane located $0.1D$ upstream of

[4]Whereas in Section 2 the theory has been described in a continuous form, it is proceeded now in a discretised form, as indicated by the additional indices.

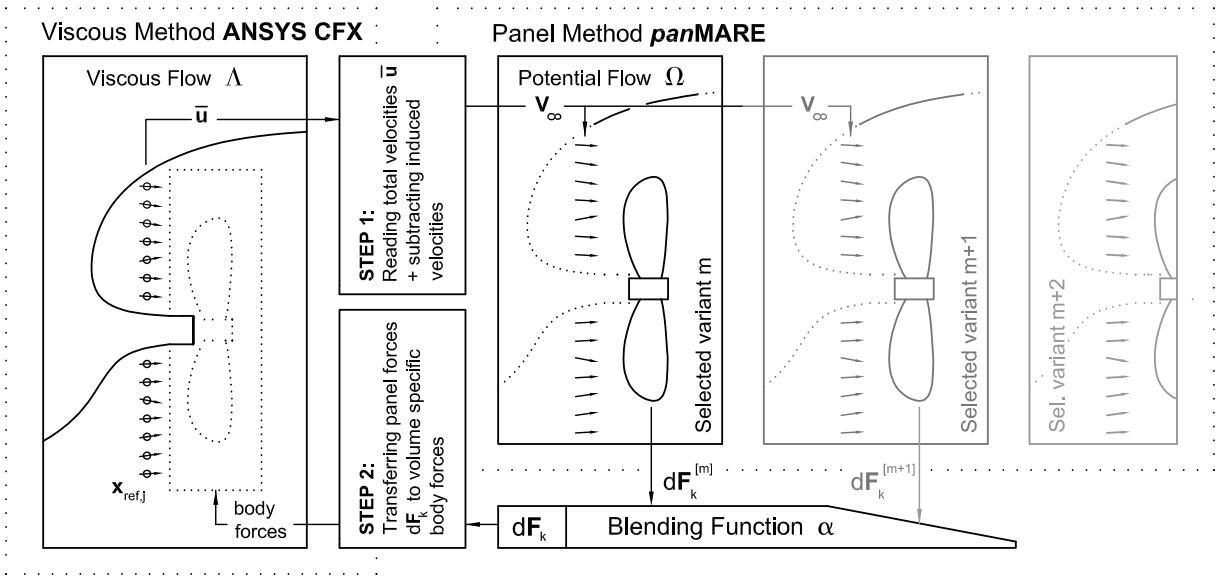


Figure 7: Layout of the coupling algorithm with blending function.

the propeller position. Because of the body forces applied, this velocity distribution is affected by the induced velocities of the propeller $\mathbf{V}_{ind} = \mathbf{V} - \mathbf{V}_\infty$ (see Section 2.1). In order to obtain the effective wake field of the current time step $t_{[i]}$, the induced velocities have to be subtracted. The effective wake field is then used as reference velocity $\mathbf{V}_\infty$ for the panel method *pan*MARE:

$$\mathbf{V}_\infty\left(t_{[i]}\right) \approx \overline{\mathbf{u}}\left(t_{[i]}\right) - \mathbf{V}_{ind}\left(t_{[i-1]}\right), \forall \mathbf{x}_{ref,j}. \tag{12}$$

Since the induced velocities for the current time step are unknown, the values from the previous step $t_{[i-1]}$ are used for approximation.

(2) In the second step, the integrated pressure distribution on the propeller blades calculated by *pan*MARE is passed to the viscous flow solver in terms of a body force distribution. For each blade panel element k with the area A_k, the normal $\mathbf{n}_k$, the panel midpoint $\mathbf{x}_k$ and the derived pressure p_k, one resulting force $\mathrm{d}\mathbf{F}_k = p_k A_k \mathbf{n}_k + \mathrm{d}\mathbf{F}_{k,fric}$ containing both a part due to pressure and empirically estimated part due to friction is provided. These forces are converted into a corresponding distribution of volume specific body forces, which is added to the source term $\mathbf{f}$ of the RANS Equations (5). The algorithm takes into account the blade form and makes a distinction between suction and pressure side of the blades.

After applying the body force distribution, the first step is repeated and the updated effective wake field is passed to the panel method again. As indicated in Figure 7, not only the propeller is considered by the panel method, but also the part of the hull directly above the propeller. In doing so, the propeller-induced hull pressure fluctuations can be

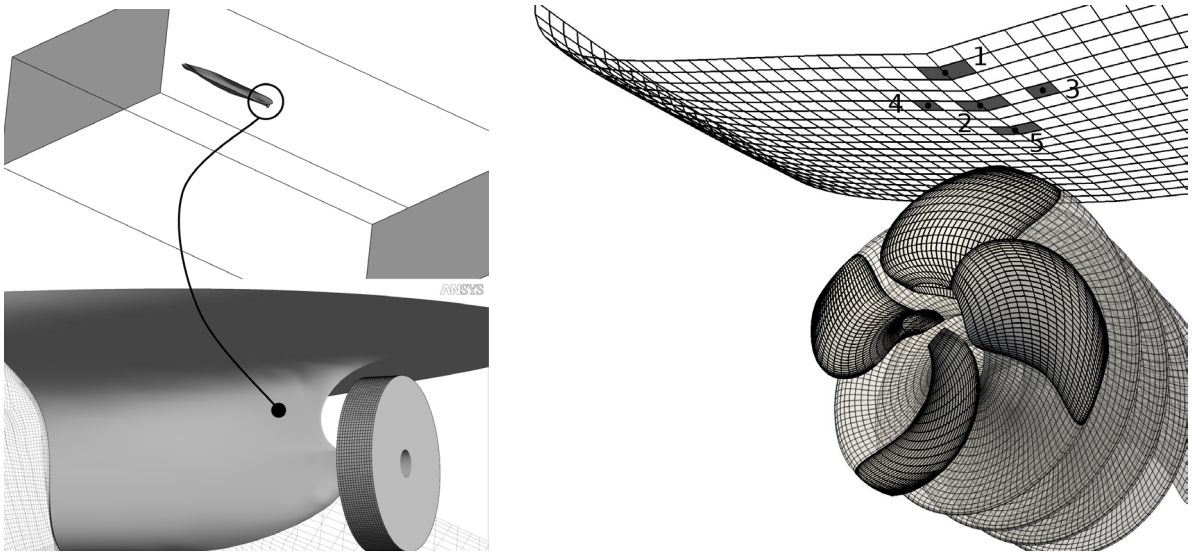
calculated directly by means of the panel method [9]. It would be possible as well to observe propeller-induced pressure fluctuations in the domain of the viscous flow, but there are two reasons why it is better to observe them in the domain of the potential flow. Firstly, the displacement effect of the propeller blades, which is a rather small but not negligible contributor to pressure fluctuations, cannot be captured properly when the propeller is only represented by a distribution of body forces. However, in the domain of the potential flow, the blades are really existent and the displacement effect is captured. The second reason is that pressure fluctuations calculated by a RANS solver can be subject to numerical damping and they therefore are likely underestimated.
The algorithm described so far needs up to 2.0 simulated propeller revolutions to reach a converged mean thrust and converged pressure fluctuations. This start-up period is inevitable, since the impact of the propeller on the velocity field $\overline{\mathbf{u}}$ needs a certain span of time to develop [9]. For the sequential investigation of more than one selected propeller variants, a remarkable amount of time can be saved by smoothly switching from one instance of *pan*MARE to another while the viscous method ANSYS CFX keeps running. Assuming that the number of panel elements is constant for all propeller variants and the investigated propeller variants differ only slightly from each other, this is possible without any problems. The forces $\mathrm{d}\mathbf{F}_k$ and the force application points $\mathbf{x}_k$ become:

$$\mathrm{d}\mathbf{F}_k = \alpha \cdot \mathrm{d}\mathbf{F}_k^{\langle m \rangle} + (1.0 - \alpha) \cdot \mathrm{d}\mathbf{F}_k^{\langle m+1 \rangle} \text{ and } \mathbf{x}_k = \alpha \cdot \mathbf{x}_k^{\langle m \rangle} (1.0 - \alpha)\, \mathbf{x}_k^{\langle m+1 \rangle}, \qquad (13)$$

where the blending function $\alpha = \alpha\left(t_{[i]}\right)$ is 1.0 during the simulation of the mth propeller variant with one instance of *pan*MARE and decreases stepwise to 0.0 during the blending process to the subsequent instance simulating variant $m + 1$.

3.2.2 Notes on the Methodology of Investigation

Two runs of investigation are carried out: one without accounting for cavitation and the other with a cavitation number of $\sigma_{n0.8} = 1.52$. The exact operation point of the initial propeller variant is set in accordance with model test results that are provided by a model basin [12]. Since a maximum relative thrust deviation of $\delta = 0.04$ was allowed during the optimisation in the first stage (see Section 3.1.3), the propeller diameters of the investigated propeller variants *II*, *III* and *IV* are corrected in order to harmonise the mean thrust. Because of $T^{[0]} \propto D^4$, the necessary changes are only of the very small magnitude $\mathcal{O}\left(\sqrt[4]{1 \pm \delta}\right)$. The number of revolutions is still kept constant.
Figure 8a shows the numerical model of the viscous flow domain Λ. It contains the full-scale bare hull without any appendages. Free water surface effects are not taken into account. The entire mesh counts 6.0M cells, thereof 0.1M cells belong to the part of the mesh where the body forces gained by the calculations in the potential flow domain Ω are applied. For the simulation of turbulence, the SST turbulence model is used. In the potential flow domain Ω, the part of the hull located directly above the propeller is discretised by 990 equilateral panels. The propeller blades are discretised by 20 panels in the radial and 70 panels in the tangential direction (see Figure 8b).



(a) Numerical grid of the viscous flow domain Λ.

(b) Numerical grid of the potential flow domain Ω and position of pressure monitoring points.

Figure 8: Numerical grids used for the detailed investigation.

3.2.3 Results of the Detailed Investigation

In Figure 10, the dimensionless pressure amplitudes $k_{p^{[i]}} = {}^{p^{[i]}}/_{\rho n^2 D^2}$ and the dimensionless predicted propulsive power $k_{P_D} = {}^{P_D}/_{\rho n^3 D^5}$ with $P_D = 2\pi n Q^{[0]}$ of all investigated propellers are compared. The predicted pressure amplitudes for the initial propeller show a good agreement with the experimental data. Greater deviations occur for the second harmonic $p^{[2]}$. This may be related to the fact that tip vortex cavitation is not considered yet. The simulated propulsive power of the initial propeller differs from the experimentally found power. A part of this difference can be explained by the fact that the experimental model is equipped with a rudder, the numerical model not.
The results of the detailed investigation confirm that the formulation of the objective functions ϵ_{com} and ϵ_{eff} in Section 3.1.3 is suitable for the evaluation of different propeller shapes. In particular, the formulation of ϵ_{com} estimates the tendency of a certain propeller shape to induce hull pressure fluctuations in a very efficient way. The values of the objective function ϵ_{com} reflect the level of pressure amplitudes $p^{[i]}$ and the extent of the cavity sheet quite well (see Figure 9). The preferred *Variant II* displays reduced pressure fluctuations and a smaller extent of the sheet cavity shape without losing too much efficiency.

4 CONCLUSIONS AND FUTURE WORK

It could be demonstrated that the two-stage optimisation method introduced in this paper is able to optimise a given initial propeller design and to quantify the improvement. However, there is still some room for improvement.

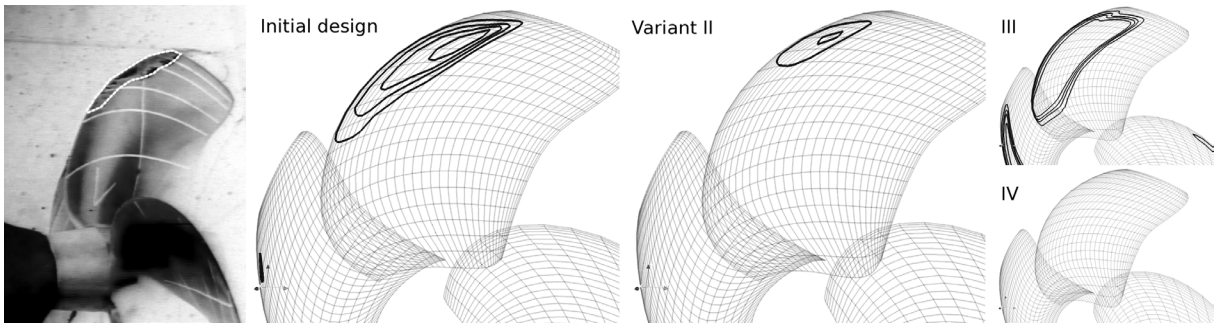


Figure 9: Computed sheet cavitation shapes for the investigated propeller variants in the 0°-position.

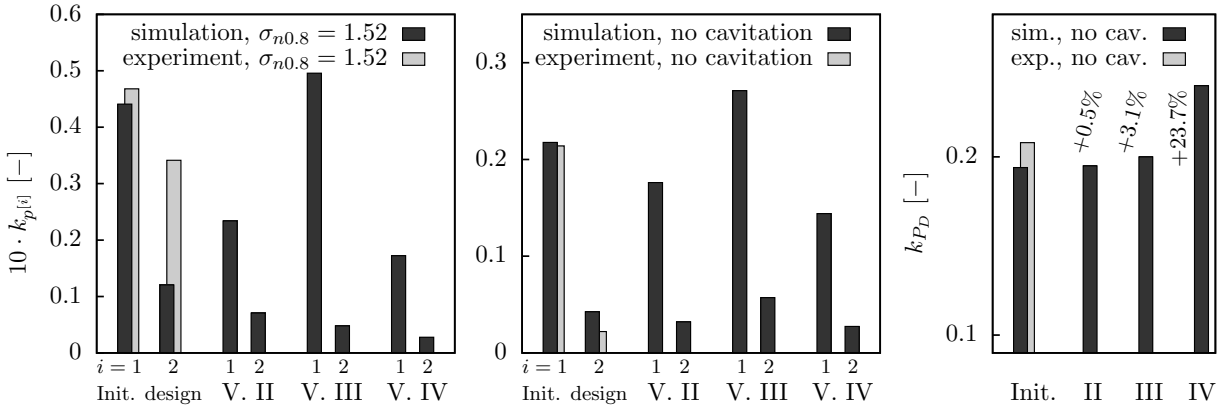


Figure 10: Computed pressure amplitudes for monitoring point 2 and predicted propulsive power.

- Although many propeller variants display better values for both of the objective functions than the initial variant, many of these variants are nevertheless unusable (e.g. *Variant I*) because the inherited distribution of pitch will lead to a highly loaded tip or hub region. This incites the formation of cavitating tip and hub vortices. The problem can be addressed by implementing a semi-empirical vortex cavitation model. Alternatively, a prescribed maximal thrust load at the blade ends could serve as additional constraint for the optimisation. As an intermediate measure, an appropriate restriction of the genotypic search space $\mathcal{G}$ could ease this problem.

- For the detailed investigation of the selected propeller variants in Stage 2, the same operation point is set for all propeller variants. This simplification involves the assumption that the effect of thrust deduction is nearly independent of the particular propeller shape. The method can be improved by a correction of the operation point with respect to a propeller-specific thrust deduction.

ACKNOWLEDGEMENTS

All model test results were kindly provided by the Potsdam Model Basin SVA. The initial propeller was designed by Mecklenburger Metallguss GmbH MMG. The first and second authors are funded by the BMWi-projects "Correlation of Cavitation Effects Under Consideration of the Wake Field (KonKav II)" and "Boss Cap Efficiency (BossCEff)".

NOMENCLATURE

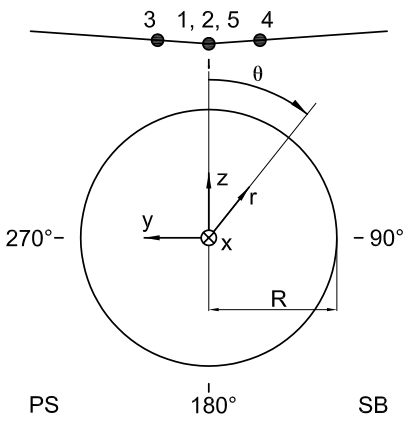


Figure 11: Coordinate system, view f. behind

General variables and constants	
$\mathbf{x} = (x, y, z)$	Space variable in Cartesian coordinates
r, θ	Polar coordinates in the propeller plane (see. Figure 11)
t	Time variable
g	Gravity constant
ρ	Density of water
p_v	Vapour pressure of water

Variables: potential flow domain Ω	
$\mathbf{x}_0$	Collocation point
$\mathbf{n}$	Normal vector
$\mathbf{\Phi}_\infty$, $\mathbf{\Phi}$, $\mathbf{\Phi}^*$	Undisturbed, induced, total potential
$\mathbf{V}_\infty$, $\mathbf{V}_{ind}$, $\mathbf{V}$	Reference, induced, total velocity
p	Pressure
μ, σ	Dipole strength, source strength
η	Cavity thickness
V_{cav}	Cavity volume

Variables: viscous flow domain Λ	
$\overline{\mathbf{u}}$	Reynolds-averaged velocity
$\overline{p}$	$\sim$ pressure
$\overline{\tau}$	$\sim$ molecular stress tensor
τ_T	Reynolds stress tensor
$\mathbf{f}$	Source term

Variables and notations in the context of EAs	
Ψ	Set of all indiviuals, i.e. phenotypic search space
Ψ_f	Set of all feasible indiviuals
$\mathcal{G}$	Set of all genomes, i.e. genotypic search space
$\mathcal{P}$	Pareto front
ϵ_{com}, ϵ_{eff}	Objective functions
f, pen	Fitness function, penalty $\sim$
w_{com}, w_{eff}	Weighting factors
γ_1, γ_2, γ_3, γ_4, ξ	Calibration factors
δ	Relative constraint injury
A, $A.G$, $A.F$	Individual, genome of A, fitness of A
$\overline{\kappa_f}$, $\overline{\Delta_t}$, $\bar{\epsilon}$	Auxiliary quantities for the estimation of the convergence behaviour of the EA

Variables and notations: viscous/inviscid coupling	
$\mathrm{d}\mathbf{F}_k$	Resulting force acting on a blade panel element k
$\mathbf{x}_{ref,j}$	Reference point
α	Blending function

Relevant propeller parameters	
R, D	Propeller radius, diameter
z_P	Blade number
n	Number of revolutions
$\sigma_{n0.8}$	$= \frac{p_{stat0.8} - p_v}{\rho/2 n^2 D^2}$ Cavitation number
$p_{stat0.8}$	Static pressure at $z = 0.8R$
P, Ca, c	Sectional pitch, camber, chord length

Variables and notations: hydrodynamic analysis	
T	Propeller thrust in general
$T^{[i]}$	Thrust fluctuation of the order i, $i = 0$ for mean value
$Q^{[i]}$	Propeller torque fluctuation
$p^{[i]}$, $k_{p^{[i]}}$	Pressure amplitude of the order i, dimensionless $\sim$
k_{T_r}	Sectional thrust coefficient
P_D, k_{P_D}	Propulsive power, dimensionless $\sim$

Indices	
i, j, k, l, m, n	Context-dependend meaning

REFERENCES

[1] Han, K.-J., Bark, G., Larsson, L. and Regnström, B.: A Procedure for Optimizing Cavitating Propeller Blades in a Given Wake. *Ship Technology Research*, Vol. 53, (2006)

[2] Hundemer, J., Naujoks, B., Hachmann, T. and Abdel-Maksoud, M.: Evolutionary Algorithms in Propeller Design. *Annual Report of the The German Society for Maritime Technology*, Vol. 100, (2006)

[3] Vesting, F. and Bensow, R.: Propeller Optimisation Considering Sheet Cavitation and Hull Interaction. *Proceedings of 2nd International Symposium on Marine Propulsors (SMP 2011)*, Hamburg, Germany, (2011)

[4] Bauer, M. and Abdel-Maksoud, M.: A Boundary Element Method for the Computation of Unsteady Sheet Cavitation Effects in Marine Propeller Flows. *Proceedings of 8th International Conference on Engineering Computational Technology*, Dubrovnik, Croatia, (2012)

[5] Katz, J. and Plotkin, A.: *Low-Speed Aerodynamics*. Cambridge University Press, (2001)

[6] Vaz, G. N. V. B.: *Modelling of Sheet Cavitation on Hydrofoils and Marine Propellers Using Boundary Element Methods*. PhD Thesis, Instituto Superior Técnico, Lisbon, Portugal, (2006)

[7] NN: *ANSYS CFX 14.0 Documentation*. ANSYS, Canonsburg, USA, (2012).

[8] Greve, M., Wöckner-Kluwe, K., Abdel-Maksoud, M. and Rung, T.: Viscous-Inviscid Coupling Methods for Advanced Marine Propeller Applications. *International Journal of Rotating Machinery*, (2012)

[9] Berger, S., Bauer, M., Druckenbrod, M. and Abdel-Maksoud, M.: Investigation of Scale Effects on Propeller-Induced Pressure Fluctuations by a Viscous/Inviscid Coupling Approach. *Proceedings of 3rd International Symposium on Marine Propulsors (SMP 2013)*, Launceston, Australia, (2013)

[10] Weicker, K.: *Evolutionäre Algorithmen*. Teubner, Stuttgart, Germany, (2007)

[11] NN: *DAKOTA Version 5.2 Reference Manual*. Sandia National Labroratories, Albuquerque, USA, (2011)

[12] Heinke, H.-J. and Jaksic, D.: *Kavitationsuntersuchungen und Druckschwankungsmessungen mit fünf Propellern am Dummymodell des KRISO Containerschiffs KS 621*. Report 3036, SVA Potsdam, Germany, (2004)

V International Conference on Computational Methods in Marine Engineering
MARINE 2013
B. Brinkmann and P. Wriggers (Eds)

SHIP ENERGY ASSESSMENT BY NUMERICAL SIMULATION

MARINE 2013

A. CORADDU, M. FIGARI AND S. SAVIO

Department of Electrical, Electronic, Telecommunications Engineering, and Naval Architecture
University of Genova
Via Opera Pia 11a, 16145 Genoa, Italy

e-mail:
andrea.coraddu@unige.it
massimo.figari@unige.it
stefano.savio@unige.it

Key words: Energy management, Marine Engineering, Energy modelling, Simulation

Abstract. Traditionally, the environmental performance of marine systems in terms of exhaust emissions has never been among the primary concerns of the maritime industry. However, this situation is going to quickly change, as in the shipping sector Energy Efficiency Design and Operation IMO Indexes testify. In such a context it is worth mentioning that the greening of shipping operations can be effectively achieved by a suitable system design and energy management. Ship Energy Efficiency Management Plan (SEEMP) should be a tool to monitor and to optimize ship and fleet efficiency performance; as a consequence it will have a deep impact on the reduction not only of the exhaust gas emissions but also of the operational costs. To reach this goal energy modelling represents the keyword. In particular, the estimate by simulation, of onboard power generation, consumption and losses plays a fundamental role for driving, for instance, a decision support tool toward the optimal choices as far as energy management is concerned. To this purpose, in the paper the authors present the outcomes of the activities carried out to develop a simulation tool able to represent an overall ship system from the energetic point of view. Modelling approach and the results of numerical simulations performed by the authors to estimate vessel fuel consumption in a real case study are shown and discussed.

1 INTRODUCTION

Sea shipping is a relatively environmentally friendly mean of transport when compared to others modes, however it is still an important source of air pollutants, mainly due to exhaust emissions of sulphur dioxide (SO_2), carbon dioxide (CO_2) and nitrogen oxides (NO_x). The impacts on the environment represent an increasing concern in coastal areas and harbors with heavy traffic. As a matter of fact, the reduction of ship emissions into the air is both a constant challenge for all interested parties and an increasingly dominant policy driver. IMO has introduced greenhouse gas (GHG) emission reduction in its agenda since 1995. In recent years the effort to reduce emissions from the shipping sector has strengthened.

Many studies about CO_2 shipping emission demonstrated that, for many goods, shipping is the most efficient way of transport. Despite this, high potential of improvement certainly does

exist and IMO is thrusting the maritime sector toward a more rational approach to ship energy and GHG emissions management. IMO is developing some technical and economical instruments in order to introduce an emission regulation for the global fleet [1, 2, 3]. As far as technical instruments are concerned, two different emission indexes for vessels are proposed and already in use for some vessels: the Energy Efficiency Design Index (EEDI) and the Energy Efficiency Operational Indicator (EEOI). The former is used to assess the design of the vessel, the latter is adopted to evaluate the vessel in operation. Both indexes are measured by the ratio between emissions, in mass of CO_2, and the transported cargo quantity per sailed distance.

At moment MARPOL Annex VI contains the 'baseline' values for three ship types (general cargo, bulk and tankers) while an important debate is focusing on the definition of the 'baseline' values for other ship categories, like ferry and cruise. The ship efficiency has always been a commitment for ship designers but in the past its formal evaluation and eventual optimization were usually addressed qualitatively. Only very recently, due to the concurrent situation of high bunker costs and IMO CO_2 cap approach, ship efficiency has been raised to be the "primary" driver of ship design and operation and, as a consequence, more detailed calculation procedures need to be adopted.

The Department of Electrical, Electronic, Telecommunications Engineering, and Naval Architecture (DITEN) of the University of Genova has a long time experience in ship propulsion simulation, optimization techniques and emission reduction procedures.

In this paper the authors present a procedure to model onboard main actors involved in the different energy processes, such as auxiliary engines, Diesel Generators, mechanical and electrical loads, in order to estimate vessel fuel consumption. The proposed approach has been applied by the authors on a real case study during their participation to the EU research project REFRESH – Green retrofitting of existing ships. Starting from data collected on board of a tanker equipped with a conventional propulsion system, the authors have modelled the electrical network, from the diesel-generators to the main auxiliary loads, in order to estimate compliance degree between the outcomes of the models implemented in the tool and the real behavior of the system.

The starting point of the proposed approach was a code, developed by the authors, able to evaluate the fuel consumption and the exhaust emissions of a ship in a seaway both in steady state and in transient conditions. The first real application of the studies was for the Italian aircraft carrier "Cavour" where the propulsion control system was optimized also with respect to minimum fuel consumption [4, 5, 6]. More recently, the same technique was adopted to optimize the Italian frigate FREMM propulsion system [7]. The analysis of the various aspects affecting the carbon footprint of ships, in lieu of the recent MARPOL requirements, was carried out for two Italian shipping companies and improvements of fleet energy management techniques were investigated [8, 9, 10].

2 ENERGY MODELLING

The electrical power network of a generic ship could be represented by a set of Diesel Generators (DGs) feeding electrical loads (rotating machines or other electrical subsystems) through power transformer units and distribution cables. Once known the behavior of the mechanical load at each motor shaft (resistant torque) and the (active and reactive) power required by the other electrical subsystems, an integrated analysis should be carried out to

estimate the power demand at the bus-bars of each Diesel Generator in steady state conditions. Assuming load request known (mechanical or electrical) and regulated voltage at DG bus-bars, a typical non-linear problem should be solved. In fact, line current for each electrical item is a function of its feeding voltage, which is in turn a function of the absorbed current. Such a problem becomes not trivial if the behavior of the network has to be studied taking into account model and mutual interactions of the electrical items.

On the contrary, a simplified analysis based on the assumption each electrical item is fed at the rated voltage (at the connection point) would avoid the management of non-linear constraints. A preliminary study carried out by the authors has demonstrated that such simplifications brings an acceptable error (a few percent) on the estimate of fuel consumption whenever distribution lines are correctly sized and taking into account daily operating conditions. The proposed approach can be effectively utilized to solve any kind of electrical network lay-out by suitably interfacing different machine models.

In such a context, the Marine Technology team of DITEN has developed a simulator consisting of a set of routines that represent the various elements of the ship electrical power network, namely Diesel engine, Synchronous Generator, Induction Motor, Transformer and Distribution line.

As far as modeling is concerned, Diesel engine routine allows to estimate, by means of a suitable set of iso-consumption curves [11], fuel consumption starting from the knowledge of mechanical brake power and revolution. Electrical items are modelled through conventional single phase equivalent circuits in steady state conditions. For instance, the Induction Motor equivalent model allows to compute the active and reactive power absorbed by stator windings once known mechanical load torque.

The implementation of the numerical code has been made in Matlab-Simulink® software environment, a wide used platform for system simulation.

3 CASE STUDY

The Case Study identified by the authors refers to a VLCC tanker whose main data are described in Table 1. The behavior of the electrical plant of the vessel has been studied over a 24-hour time window, mainly devoted to discharging operations.

In Figure 1, a schematic lay-out of the electrical plant is presented. Due to the aim of this analysis, in the mentioned figure just the two Diesel Generators and the two Induction Motors of the ballast pumps are clearly identified as single items, being the remaining electrical loads included all together as “Base Load” blocks.

Table 1: VLCC tanker main data

Variable	Symbol	Value
Length (O.A.)	L_{OA}	332.0 m
Length (B.P.)	L_{BP}	320.0 m
Breadth (mld)	B	58.0 m
Depth (mld)	D	31.0 m
Draft (mld)	T	22.5 m

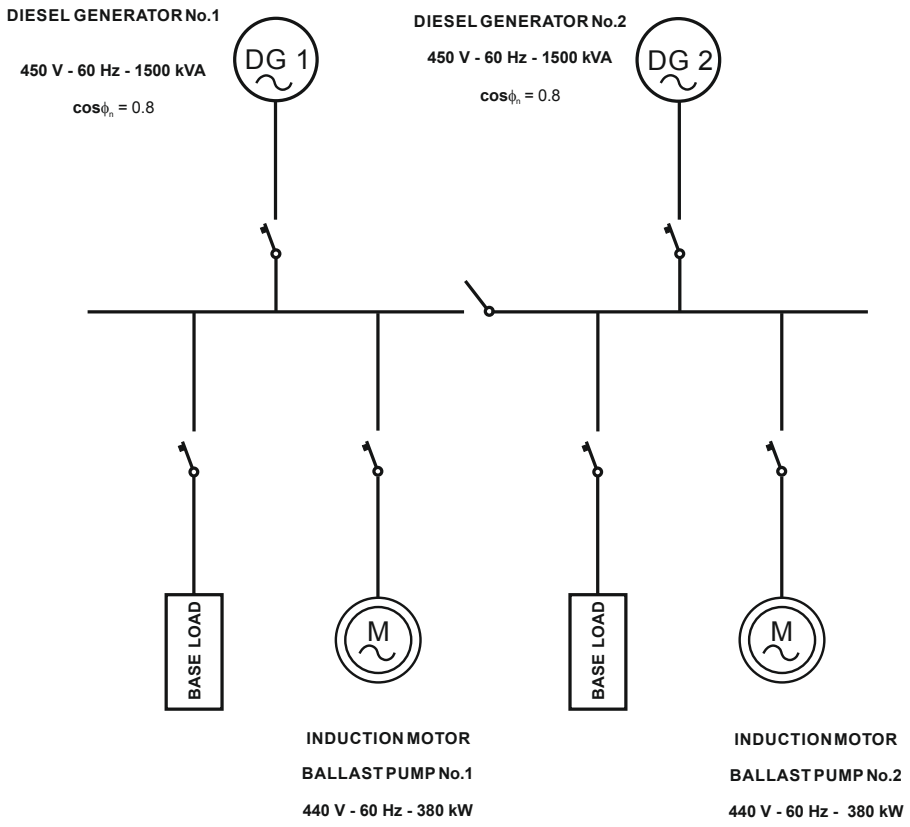


Figure 1: Schematic lay-out of the electrical plant

As far as electrical generation is concerned, each group is composed of a 1280 kW Wärtsilä Diesel Engine coupled with a 1500 kVA TAIYO 3 – phase brushless Synchronous Generator. Main data of TAIYO brushless Synchronous Generator are reported in Table 2, while in Table 3 plate data of TAIYO Induction Motors utilized to drive ballast pumps are presented.

Table 2: Plate data of 3–phase brushless AC Synchronous Generator

Variable	Symbol	Value
Rated Power	A_N	1500 kVA
Rated Voltage	V_N	450 V
Rated Current	I_N	1925 A
Number of poles	P	8
Rated Frequency	f_N	60 Hz
Rated Speed	n_N	900 rpm
Rated power factor	pf_N	0.8

Table 3: Plate data of ballast pump 3–phase Induction Motor

Variable	Symbol	Value
Rated Power	A_N	380 kW
Rated Voltage	V_N	440 V
Rated Current	I_N	610 A
Number of poles	P	6
Rated Frequency	f_N	60 Hz
Rated Speed	n_N	1170 rpm
Rated Torque	T_N	3100 Nm

During the analyzed time window, value of main electrical quantities at Diesel Generators bus-bars have been recorded. In the following Figure 2 the time behavior of the recorded quantities is presented for both Diesel Generators. In the mentioned figure and in the others presented in this paper reactive power always refers to the request of items whose impedance is characterized by a phase lag. Starting from the total active and reactive power request, the authors have then estimated the power request of the Induction Motors driving the ballast pumps (when operating). Assuming the induction motors are running at a constant speed during operation, it has been assumed each of them is absorbing an active power of 190 kW and a reactive power of 85 kVAR (phase lag), providing a shaft torque of 1420 Nm at 1186 rpm. As a consequence, total active and reactive power request at the bus-bars of the two Diesel Generators can be assumed equal to the request of two electrical base loads, whose time total behavior is depicted in Figure 3, plus a continuous request of 380 kW and 170 kVAR in the following times windows (when Induction Motors are running):

from t = 0 s to t = 7870 s
from t = 64880 s to t = 70000 s
from t = 82100 s to t = 86220 s

assuming t = 0 s represents the start of the recording.

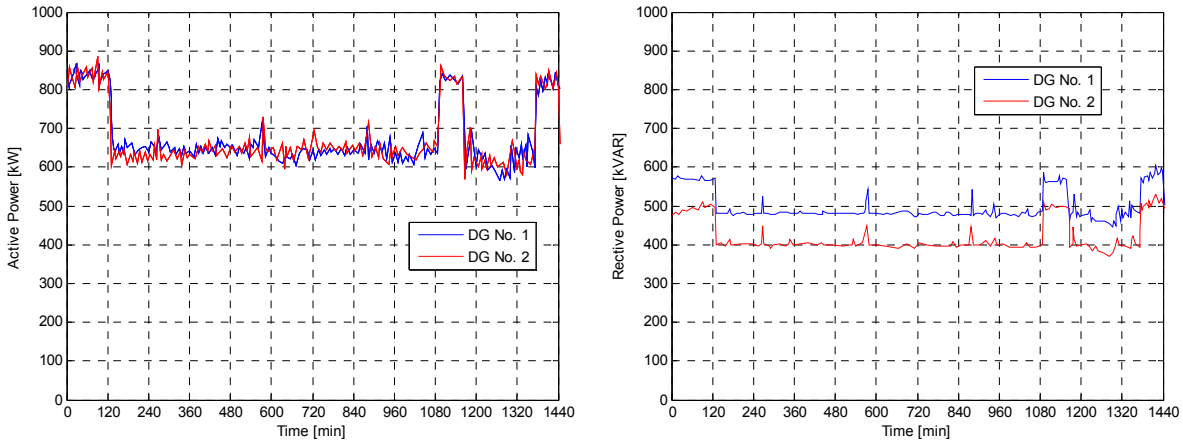


Figure 2: Time behaviour of active and reactive power at Diesel Generator bus-bars

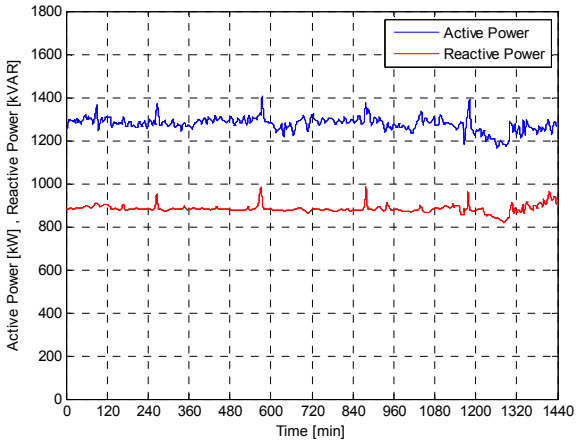


Figure 3: Time behaviour of base loads active and reactive power at Diesel Generator bus-bars

Once identified the architecture of the electrical plant and the operating characteristics, a Matlab-Simulink® model has been created in order to perform the simulation. The overall Simulink® model of the electrical plant (for one line) is presented in Figure 4 and mainly consists of one Diesel Generator and one Induction Motor. Electrical base load has been simply modeled by an active and reactive power request, whose behavior has been derived taking into account the curves shown in Figure 3.

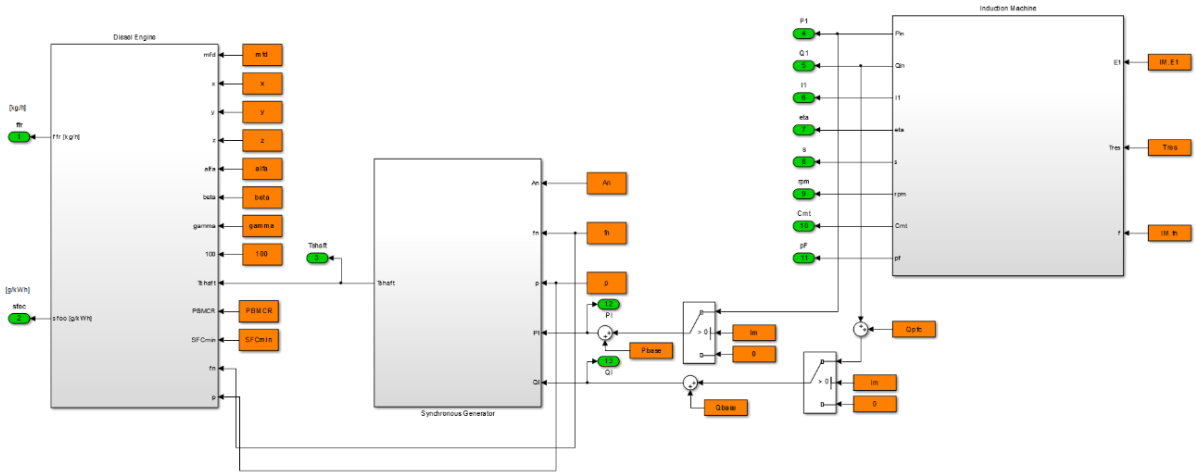


Figure 4: Simulink® model of the overall electrical system (one line)

As far as the Induction Motor is concerned, the model has been parameterized thanks to a procedure defined by the authors starting from the plate data reported in Table 2. Induction Motor has been loaded with a resistive torque of 1420 Nm in order to model the operating point previously described. So doing, the machine absorbs from the network 190 kW, running at 1186 rpm.

It is worth mentioning that in this operating point the reactive power absorbed by the motor would equal 139 kVAR (phase lag).This is the reason why in the Simulink® model a node is present, where the reactive power of the Induction Motor is summed to the reactive power of a three-phase capacitor bank absorbing 54 kVAR (phase lead). This allows to model a total reactive power request of 85 kVAR (phase lag).

As far as the Synchronous Generator is concerned, a simplified model based on efficiency curves, as a function of the power factor at DG bus-bars, has been adopted. To this aim the efficiency curves of a machine of analogous power rating have been utilized, being unavailable the information from the data sheets of the manufacturer.

As far as the Diesel engine is concerned, model has been parameterized considering a rated power of 1280 kW and the minimum SFOC equal to 191 g/kWh, this latter quantity derived from the SFOC behavior provided by the manufacturer.

The diesel engine modeling is based on an algebraic equation that describes the fuel consumption map in terms of engine power and speed. The general form of the equation [11] contains engine power and shaft revolution at maximum rating, minimum specific fuel consumption at optimizing point. The equation is integrated within the Diesel Generator model by the differential equation of the shaft dynamics, from the knowledge of the required torque the shaft speed is kept constant by a suitable engine torque and corresponding fuel flow rate.

Such a modeling approach implies identical behavior of the two electrical lines, it is to say the same power request for each DG. In the analyzed case study this simplification turns out acceptable (having in mind the final purpose of the analysis) if the recorded behavior of active power of each DG is considered.

4 RESULTS COMPARISON

The results of the simulation are reported in the following Figure 5 and Figure 6. In particular, Figure 5 presents the time behavior of the fuel flow rate for DG No. 1 and No. 2 in both simulated and real conditions, while the behavior of their sum is shown in Figure 6.

In such a context, the behavior in real conditions has been computed by merging the active power request for each generator (Figure 2) and the SFOC behavior evaluated from Wärtsilä Diesel engine plate data.

Graphical results are very satisfactory and to quantify the compliance degree between simulated and real overall consumption over the considered 24-hour operations, the behaviors depicted in Figure 6 have been integrated in the time domain. The outcome of this further analysis has been 7114 kg for the simulated consumption, against a value of 6707 kg for the measured one, with a difference of about 6 %.

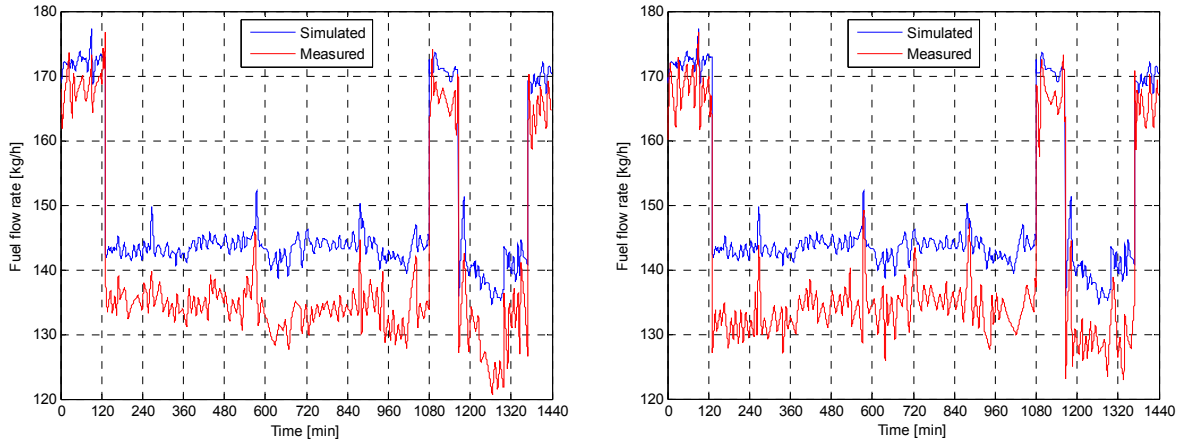


Figure 5: Time behavior of fuel flow rate for DG No. 1 (left) and DG No. 2 (right)

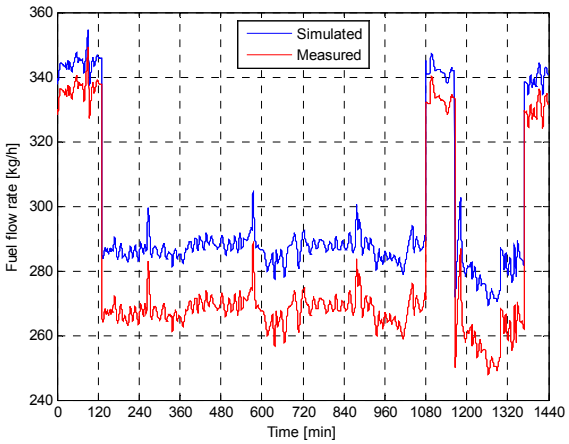


Figure 6: Time behavior of total fuel flow rate for the two Diesel Generators

The main reason of such difference is due, in this case, to the very simple model utilized for the Diesel engine. This clearly turns out by analyzing the following Figure 7, where SFOC behavior vs. bus-bars active power is shown, in both simulated and real conditions. In the simulated conditions SFOC behavior has been prepared by utilizing the simplified model of the Synchronous Generator and assuming a power factor equal to 1.

It is worth reminding that the Diesel engine model utilized in the simulation is parameterized just providing the value of the minimum SFOC, and so consumption estimate is really good near this point (in this case for an electrical power at DG bus-bars of 850 ÷ 1050 kW), while model effectiveness decreases when the operating point departs from such an interval.

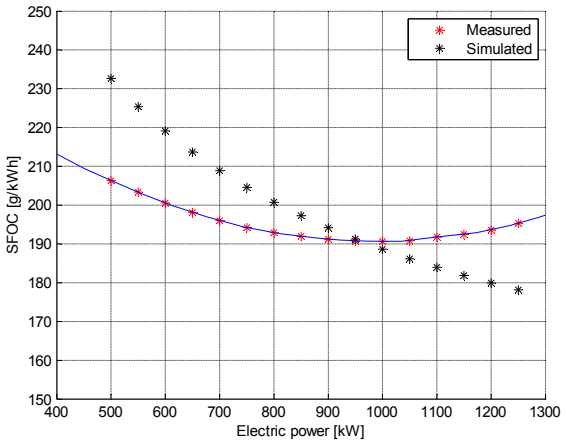


Figure 7: SFOC vs. electric power behavior for one Diesel-Generator

In such a context, the analyzed Case Study is really penalizing for the model because each Diesel Generator always works at a power well below the minimum SFOC point (providing on average about 650 kW when the Induction Motors are off and about 850 kW when they are on).

Although it would be nice to have always operating points very close to the one characterized by the minimum SFOC, because maximum would be the benefit, being maximum the efficiency, such a situation is not obviously easy to obtain due to (more or less heavy) power request oscillations in daily operating conditions.

If this happens, whatever is the amplitude of the oscillations, the consumption estimate would be characterized by an approximation better than the computed 6%, due to a sort of compensation clearly detectable from the behavior of Figure 7.

Although an approximation of 6% (or less) could be considered satisfactory, taking into account the negligible amount of data required to customize the Diesel engine model, the authors have decided to carry out another analysis by modelling the Diesel engine in a bit more detailed way. The idea is to collect three values of the SFOC as a function of the mechanical power P_{mech} provided at the engine shaft, modelling the Diesel engine with the SFOC vs. mechanical power curve identified by a polynomial of degree 2 that fits the data in a least squares sense.

Utilizing this model for the Diesel (identified in the following as “three-point model”), an estimate of fuel consumption has been carried out and the results compared with the ones related to real operating conditions. Figure 8 presents the time behavior of the fuel flow rate for DG No. 1 and DG No. 2 in both simulated and real conditions, while the behaviors of their sum is shown in Figure 9. In such a context, the behavior in real conditions has been once again computed by merging the active power request for each generator (Figure 2) and the SFOC behavior presented in Figure 7. Graphical results testify a quasi-overlap between the curves and to quantify the approximations the behaviors of Figure 9 have been integrated in the time domain to compute the overall consumption over the considered 24-hour operations, with the following results. The outcome of this last analysis has been 6664 kg for the simulated consumption, against the same value as before (6707 kg) for the measured one, with a difference of less than 1 %.

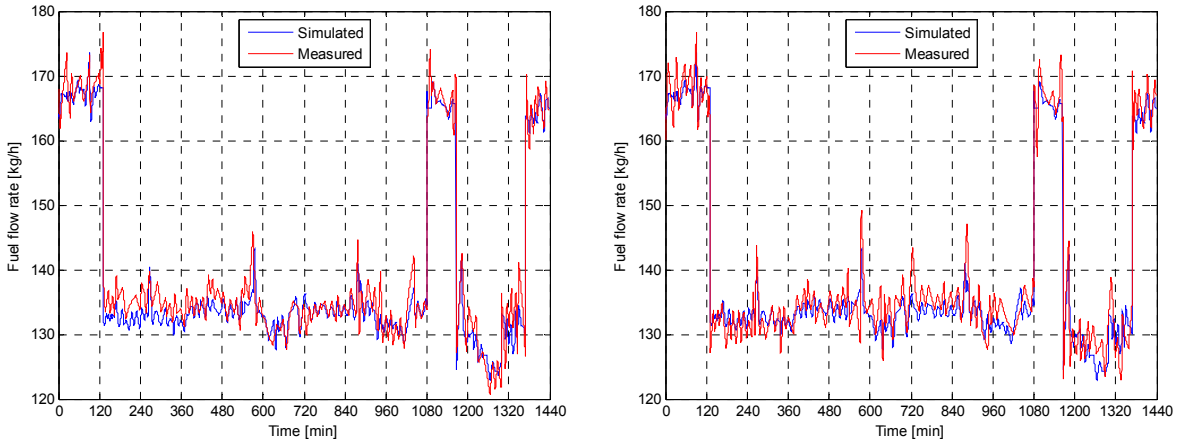


Figure 8: Time behaviour of fuel flow rate for DG No. 1 (left) and DG No. 2 (right) – three-point model

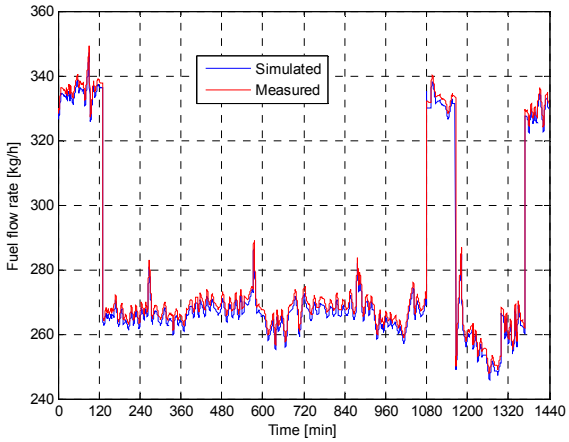


Figure 9: Time behaviour of total fuel flow rate for the two Diesel Generators – three-point model

7 CONCLUSIONS

New requirements introduced by IMO will force maritime community to adopt design and management approaches aimed at reducing worldwide greenhouse gas emission. This will have a direct positive impact on the reduction of fuel consumption and consequently on the operating costs. In this paper, a simulation based approach to evaluate fuel consumption of a vessel has been proposed and its effectiveness verified starting from data collected on board of a VLCC tanker equipped with a conventional propulsion system. To this aim the authors have modelled the electrical network, from the Diesel Generators to the Induction Motors driving ballast pumps and main auxiliary loads. A simulation of 24-hour time window, mainly devoted to discharging operation, has been performed and compared with energy audit carried out onboard.The results of this study have shown a good agreement between the simulated results and the measured ones, testifying the software code developed by the authors represents a valid tool in performing the energetic analysis of a vessel. In order to allow the whole energy

optimization of the vessel such a code could be profitably integrated with other codes representing the ship propulsion and eventually other major onboard consumers.

ACKNOWLEDGMENTS

The work presented in the paper was partially funded by EU FP7-SST-2011-RTD-1 Collaborative project REFRESH – Green Retrofitting of Existing Ships.

REFERENCES

[1] IMO, Interim guidelines for voluntary verification of the energy efficiency design index, MEPC.1/Circ.682, (2009).
[2] IMO, Guidelines for voluntary use of the ship energy efficiency operational indicator, MEPC.1/Circ. 684, (2009).
[3] IMO, Interim guidelines on the method of calculation of the energy efficiency design index for new ships, MEPC.1/Circ.681, (2009).
[4] M. Figari and M. Altosole, Dynamic behaviour and stability of marine propulsion systems, Proceedings of the Institution of Mechanical Engineers, Part M: Journal of Engineering for the Maritime Environment (2007) **221(4)**: 187-205.
[5] M. Altosole, G. Benvenuto, M. Figari and U. Campora, Real-time simulation of a COGAG naval ship propulsion system, Proceedings of the Institution of Mechanical Engineers, Part M: Journal of Engineering for the Maritime Environment (2009) **223(1)**: 47-62.
[6] C. G. Soares and M. Figari, Fuel consumption and exhaust emissions reduction by dynamic propeller pitch control, Analysis and Design of Marine Structures, CRC Press (2009): 543-550.
[7] M. Altosole, G. Dubbioso, M. Figari, M. Viviani, S. Michetti and A. Millerani Trapani, Simulation of the dynamic behaviour of a CODLAG propulsion plant, Warship 2010: advanced technologies in naval design and construction, London (2010).
[8] M. Figari, M. D'Amico and P. Gaggero, Evaluation of ship efficiency indexes, Sustainable Maritime Transportation and Exploitation of Sea Resources, CRC Press (2011): 621-627.
[9] A. Coraddu, M. Figari and S. Savio, Energy efficiency index statistical analysis through vessel operating data, Proceedings of the 2012 International Research Conference on Short Sea Shipping (2012).
[10] A. Coraddu, M. Figari and S. Savio, Probability of achieving the energy efficiency index by Monte Carlo simulation, Proceeding of International Conference on Managing Reliability, Maintainability and Safety in the Maritime Industry (2012).
[11] M. Altosole and M. Figari, Effective simple methods for numerical modelling of marine engines in ship propulsion control systems design, Journal of Naval Architecture and Marine Engineering (2011) **8(2)**: 129-147.
[12] A. Coraddu, S. Gaggero, D. Villa and M. Figari, A new approach in engine-propeller matching, Sustainable Maritime Transportation and Exploitation of Sea Resources, CRC Press (2011): 631-637.

V International Conference on Computational Methods in Marine Engineering
MARINE 2013
B. Brinkmann and P. Wriggers (Eds)

SHIP PROPULSION PREDICTION WITH A COUPLED RANSE-BEM APPROACH

G. Deng*, P. Queutey*, M. Visonneau*, and F. Salvatore†

*Dynamics of Marine Propulsion Systems, LHEEA Lab. (ex. LMF) CNRS UMR 6598
Hydrodynamics, Energetics, Atmospheric Environment, Ecole Centrale de Nantes
1, Rue de la Noe, 44321 Nantes, France
e-mail: Ganbo.Deng@ec-nantes.fr, web page: http://www.ec-nantes.fr/

† Marine Propulsion and Cavitation Lab, Ocean Renewable Energy Team
CNR-INSEAN - Italian Ship Model Basin
Via di Vallerano, 139 - 00128 Roma, Italy
e-mail: francesco.salvatore@cnr.it - Web page: http://www.insean.it

Key words: RANSE-BEM Coupling, Propeller-Hull Interaction, Self-Propulsion

Abstract. This paper is devoted to the validation of a RANSE-BEM coupling procedure for propeller-hull interaction simulation with the ISIS-CFD RANSE solver developed by the DSPM team of the LHEEA laboratory in Nantes coupled with the PRO-INS BEM code developed by INSEAN. The hybrid simulation approach is first validated with an open water test case. Then, propeller-hull interaction issue is investigated with several test cases to assess the accuracy of the RANSE-BEM coupling approach. A special way to evaluate the effective wake at the propeller plane is proposed. With this approach, good predictions are obtained with the RANSE-BEM coupling computations.

1 INTRODUCTION

Propeller-hull interaction is an important topic for ship design. Accurate prediction of ship self-propulsion is a challenging task for CFD computations as it requires not only an accurate prediction of resistance and wake flow, but also a good prediction of propeller perturbation. Although such kind of computation can be performed with a RANSE solver using sliding grid or overlapping grid, the CPU cost of such kind of full RANSE simulation is about one order higher than a conventional resistance computation [1]. While full RANSE simulation is preferred for very complex situation such as propeller ventilation, an interesting alternative for routine design such as ship propulsion prediction is the hybrid RANSE-BEM coupled approach where propeller induced perturbation is modelled through an inviscid-flow model based on a boundary element method (BEM) while the RANSE solver is used to describe the flow field around the ship. The

present paper focuses on the validation of such a coupled procedure. The RANSE approach is based on the unstructured finite-volume flow solver ISIS-CFD developed by the DSPM team of the LHEEA laboratory in Nantes. BEM is based on a boundary integral formulation for marine propellers in arbitrary onset non-cavitating and cavitating flow conditions. The computational model is implemented into the PRO-INS solver [2, 3, 4]. Recently, a RANSE/BEM coupling approach for propeller-hull interaction has been developed in a joint research work between ECN/CNRS and CNR-INSEAN during the EU-FP7 STREAMLINE project. The RANSE code provides the velocity field in front of the propeller to the BEM code as inflow condition. Propeller loading by BEM is recast as volume force distribution at the propeller plane. This body force representing the propeller action is added as source term in the momentum equation of RANSE simulation. Time-averaged or unsteady propeller effects can be described.

2 NUMERICS

A brief description of the RANSE code and the BEM code is given in this section. Then, the coupling strategy is presented.

2.1 RANSE Flow Solver: ISIS-CFD

ISIS-CFD, available as a part of the $FINE^{TM}$/Marine computing suite, is an incompressible unsteady Reynolds-averaged Navier-Stokes (URANS) method. The solver is based on the finite volume method to build the spatial discretisation of the transport equations. The unstructured discretisation is face-based. While all unknown state variables are cell-centred, the systems of equations used in the implicit time stepping procedure are constructed face by face. Fluxes are computed in a loop over the faces and the contribution of each face is then added to the two cells next to the face. This technique poses no specific requirements on the topology of the cells. Therefore, the grids can be completely unstructured; cells with an arbitrary number of arbitrarily-shaped faces are accepted.

Pressure-velocity coupling is obtained through a Rhie & Chow SIMPLE type method: at each time step, the velocity updates come from the momentum equations and the pressure is given by the mass conservation law, transformed into a pressure equation. In the case of turbulent flows, transport equations for the variables in the turbulence model are added to the discretisation. Free-surface flow is simulated with a multi-phase flow approach: the water surface is captured with a conservation equation for the volume fraction of water, discretised with specific compressive discretisation schemes, see [5].

The method features sophisticated turbulence models: apart from the classical two-equation k–ϵ and k-ω models, the anisotropic two-equation Explicit Algebraic Stress Model (EASM), as well as Reynolds Stress Transport Models, are available, see [6, 7]. The technique included for the 6 degrees of freedom simulation of ship motion is described by Leroyer & Visonneau [8]. Time-integration of Newton's law for the ship motion is combined with analytical weighted or elastic analogy grid deformation to adapt the fluid

mesh to the moving ship.

Parallelization is based on domain decomposition. The grid is divided into different partitions; these partitions contain the cells. The interface faces on the boundaries between the partitions are shared between the partitions; information on these faces is exchanged with the MPI (Message Passing Interface) protocol. This method works with the sliding grid approach and the different subdomains can be distributed arbitrarily over the processors.

2.2 BEM Solver: PRO-INS

In the proposed hybrid viscous/inviscid model, propeller effects are determined through a hydrodynamic model based on a Boundary Element Method (BEM). The methodology is valid under inviscid flow assumptions and allows to describe the flowfield around a marine propeller operating in a prescribed onset flow. Considering as input the non-homogeneous velocity distribution representing the hull-induced wake, propeller operation in behind hull conditions can be analysed.

The computational model involves the numerical solution of the Laplace equation for the velocity potential via a boundary integral formulation implemented into the PRO-INS code developed by CNR-INSEAN. In its more general formulation, the PRO-INS solver includes a wake alignment model to correctly describe trailing vorticity shedding process, as described in [2].

A simple two-phase flow model is integrated with the BEM solver to describe the effects of transient sheet cavitation on propeller loads and on induced velocity and pressure fields radiated to the surrounding flow, see [3] and [4]. In the present work, hydrodynamic loading distribution on propeller blade surface predicted by BEM is recast as a volume force distribution to define body force terms for the RANSE solver.

2.3 RANSE/BEM Coupling

A RANSE/BEM coupling approach contains following steps:

- The RANSE code computes the flow around the hull. The velocity field is interpolated to a interface plane located in front of the propeller. This is the total velocity required for the potential code.

- Using the total velocity provided by the RANSE code, the potential code performs a simulation for a rotating propeller. Effect of the propeller is represented by body forces.

- Those body forces are added into the right hand side of the Navier-Stokes equation in the RANSE code. They are also taken into account when solving the motion equation for the boat.

The ISIS-CFD code can handle any number of boats (limited to 99) with any prescribed and/or solved motion. An arbitrary number of propellers can be attached to each boat. Parallelized computation with adaptive mesh refinement and automatic load balancing is fully supported. Each block interpolates the velocity at the interface plane located at a prescribed position in front of the propeller for all points at the interface plane found inside the block. The interpolated results are collected and distributed to all blocks so that each block contains required total velocity for all propellers. Those total velocity as well as all other information such as the kinematics for all boats are transferred to the potential code using a user defined dynamic subroutine. The potential code can be either integrated directly into this dynamic subroutine, or launched from it using a system call as it is the case in the present study. Data exchange is accomplished with disk files in the latter case.

Body force transfer from the BEM code to the RANSE code, the distance of the interface plane to the propeller, and the way the propeller induced velocity is computed are the key points in a RANSE/BEM coupling implementation. The most accurate way to achieve the body force transfer is to communicate all cells in the RANSE mesh within the swept volume by propeller blades to the BEM code, and then map the forces acting at the blades to those grid cells directly. However, such implementation is not only too complex, but also too expensive, especially when an unstructured grid, possibly updated dynamically by adaptive grid refinement, is employed by the RANSE code. In the present study, a very simple procedure is adopted. The forces acting on the propeller blades are mapped to a two dimensional cylindrical grid. Based on this two-dimensional distribution, body forces are distributed into a cylindrical volume swept by the propeller blades in the RANSE code. A uniform body force distribution in the axial direction is assumed. Such simple implementation has an impact on the choice of interface plane distance to the propeller.

The BEM code needs the effective velocity which is the difference between the total velocity provided by the RANSE code and the propeller induced velocity. In our implementation, the propeller induced velocity is computed by the BEM code using the real geometry of the propeller, while the total velocity is computed by the RANSE code using body forces. Due to the simplification made for the body force transfer from the BEM code to the RANSE code, it is expected that numerical error increases as the interface plane moves toward the propeller. On the other hand, even without the propeller, the velocity field always changes in space in the wake. To obtain a better prediction, it is desirable to locate the interface plane as close as possible to the propeller. As the objective of the present computation is self-propulsion simulation, a steady BEM computation is performed. The inflow velocity is averaged in the circumferential direction for such computation. The output body force from the BEM code is also averaged in the circumferential direction. To save computational time, only half domain computation is performed by the RANSE code. Tangential body force is not taken into account in the computation.

3 NUMERICAL VALIDATION

3.1 Open water computation with total velocity obtained from a full RANSE computation

Propeller open water is a special test case for RANSE/BEM coupling computation. As the effective velocity (a uniform flow) is known, the BEM code can give the expected solution without using a coupling procedure. This provides a reference solution for the validation of RANSE/BEM procedure. We have performed a very simple validation exercise in which the total velocity at the interface plane is computed with a RANSE computation in which the rotating propeller is taken into account with its real geometry. Such a computation is referred as a full RANSE hereafter in the paper. If the total velocity is computed correctly by the RANSE code, and the propeller induced velocity is computed correctly by the BEM code, then, a uniform effective wake should be recovered, and the RANSE/BEM coupling procedure should give the same result as that obtained by the BEM code using the exact effective velocity. The configuration chosen for this exercise is the KP505 propeller of the KCS benchmark [9] with the advance coefficient J=0.7. Instantaneous velocity at the interface plane is provided to the BEM code as total velocity. The measurement data obtained by NMRI and MOERI as well as the predicted numerical results obtained by the BEM code and the full RANSE computation are provided in table 1 as reference solution. Relative error compared with measurement result by NMRI is also given. The RANSE/BEM coupling computation is performed with different interface plane positions (noted as D_{In} in the table, D=0.25 being the diameter of the propeller). D_{In} is an important parameter used by the RANSE code to interpolate the total velocity at the interface plane, and by the BEM code to compute the propeller induced velocity at the same location. As expected, the predicted result by the hybrid RANSE/BEM coupling procedure is insensitive to the location of the interface plane as long as the interface plane does not intercept the propeller blade, D_{In}/D=0.12 being the minimum distance that fulfills this requirement. ¿From D_{In}/D=0.5 to D_{In}/D=0.12, Kt decreases by about 1.2%, while Kq decreases by 0.7%. The predicted Kt with the hybrid approach is almost the same as that predicted by the BEM code. While numerical predictions for Kt are about 4% smaller than the measurement data obtained by NMRI, they agree well with the measurement result obtained by MOERI using exactly the same propeller model.

The success of this validation exercise demonstrates that:

- The velocity field is computed correctly by the RANSE code.
- The velocity field is correctly interpolated at the interface plane.
- The propeller induced velocity at the interface plane is correctly computed by the BEM code.
- An instantaneous total velocity obtained with a URANSE computation can be used as a total velocity by the BEM code in a steady run to obtain a correct steady

result.

Table 1: Open water result with a full RANSE total velocity

Type	D_{In}/D	Kt	Kt error	10Kq	Kq error
Exp(NMRI)	-	0.185	-	0.311	-
Exp(MOERI)	-	0.1770	-4.3%	0.2992	-3.8%
BEM	-	0.1791	-3.2%	0.3153	+1.0%
RANSE	-	0.1740	-5.9%	0.3240	+4.2%
RANSE/BEM	0.12	0.1773	-4.2%	0.3248	+4.4%
RANSE/BEM	0.15	0.1777	-3.9%	0.3251	+4.5%
RANSE/BEM	0.18	0.1782	-3.7%	0.3256	+4.7%
RANSE/BEM	0.25	0.1787	-3.4%	0.3261	+4.9%
RANSE/BEM	0.50	0.1794	-3.0%	0.3269	+5.1%

3.2 Open water computation with total velocity obtained from a RANSE/BEM coupling computation

This validation exercise is similar to the previous one except that the total velocity is obtained with a RANSE/BEM coupling computation in which the effect of the propeller is represented by body forces provided by the BEM code. Consequently, there is an approximation made in the RANSE computation. Effect of tangential forces is investigated. Predicted results obtained with and without tangential forces are shown in table 2 and table 3, respectively. It is expected that the error due to this approximation increases as the location of the interface plane moves toward the propeller. Numerical results shown in table 2 and 3 indicate that it is indeed the case. In RANSE computation, body forces are added in a cylindrical region from -0.12D to 0.12D, corresponding to the swept area by propeller blade. When tangential forces are taken into account, almost the same prediction is obtained between D_{In}/D=0.5 to D_{In}/D=0.13. Error begins to increase at D_{In}/D=0.12. At D_{In}/D=0.1 for which the interface plane is located inside the region where body forces are added into the source term of the RANSE equation, a 9% overprediction on Kt is obtained compared with measurement value. When tangential forces are not taken into account, error in Kt keeps increasing as the interface plane approaching the propeller plane. It jumps quickly after D_{In}/D=0.12. Without taking into accout the tangential forces, propeller thrust is about 3% smaller. Based on this validation exercise, we can conclude that the body forces approximation implemented in the present study can give satisfactory result as long as the interface plane is located outside the region where body forces are added. Error is acceptable when the tangential force is neglected.

Table 2: Open water result with a RANSE/BEM total velocity (with tangential force)

Type	D_{In}/D	Kt	Kt error	10Kq	Kq error
RANSE/BEM	0.10	0.2014	+8.9%	0.3528	+13.4%
RANSE/BEM	0.12	0.1785	-3.5%	0.3262	+4.9%
RANSE/BEM	0.15	0.1797	-2.9%	0.3275	+5.3%
RANSE/BEM	0.18	0.1803	-2.5%	0.3281	+5.5%
RANSE/BEM	0.25	0.1799	-2.8%	0.3275	+5.3%
RANSE/BEM	0.50	0.1793	-3.1%	0.3268	+5.1%

Table 3: Open water result with a RANSE/BEM total velocity (without tangential force)

Type	D_{In}/D	Kt	Kt error	10Kq	Kq error
RANSE/BEM	0.10	0.1933	+4.5%	0.3433	+10.4%
RANSE/BEM	0.12	0.1712	-7.5%	0.3173	+2.0%
RANSE/BEM	0.15	0.1738	-6.1%	0.3203	+3.0%
RANSE/BEM	0.18	0.1753	-5.2%	0.3220	+3.5%
RANSE/BEM	0.25	0.1761	-4.8%	0.3230	+3.8%
RANSE/BEM	0.50	0.1777	-3.9%	0.3247	+4.4%

3.3 Propeller-hull interaction with total velocity obtained from a full RANSE computation

This validation exercise concerns a propeller-hull interaction simulation. The total velocity is obtained with a full RANSE computation using sliding grid to simulate a rotating propeller. The test case is the KCS self-propulsion test case proposed for Tokyo 2005 CFD Workshop and Gothenburg 2010 CFD Workshop [9]. It is a self-propulsion test case with the boat at fixed trim and sink position with a ship speed U=2.196m/s, leading to a Froude number of 0.260. The propeller revolution rate n=9.50 rps is fixed in our computation both in the full RANSE computation and in the BEM computation. The mesh employed in the RANSE computation contains about 2M cells around the hull, and 1.5M cells around the propeller. The RANSE code under estimates the propeller thrust by about 4.1%. This error is about of the same order for the open water computation as shown previously for similar advance coefficient. Unlike the open water test case, with the total velocity provided by a full RANSE computation, the BEM code over predicts the propeller thrust by more than 7%. However, the error decreases when the interface plane approaches the propeller plane as shown in table 4. When D_{In}/D is larger than 0.25, the computational result becomes uncertain. We believe that such over-estimation is not due to the accuracy of total velocity prediction, since the full RANSE

computation under estimates the propeller thrust. Unlike the open water configuration, effective velocity depends on the position of interface plane. As the error decreases when the interface plane approaches the propeller plane, it is reasonable to conclude that in a RANSE/BEM coupling computation, it is the effective wake at the propeller plane that should be used by the BEM code for the propeller computation. However, effective wake at the propeller plane can not be computed directly due to the propeller geometry and the body forces added in the RANSE computation. An approach to estimate the effective wake is proposed in the next sub-section. Based on this validation exercise, we can conclude that in a propeller-hull interaction computation with RANSE/BEM coupling procedure, it is desirable to locate the interface plane as much as possible close to the propeller plane. But it should be located outside the region swept by the propeller blade. D_{In}/D=0.15 appears to be a good choice. It will be used later on in all computations.

Table 4: Propeller interaction result with a full RANSE total velocity

Type	D_{In}/D	Kt	Kt error	10Kq	Kq error
Exp	-	0.170	-	0.288	-
RANSE	-	0.163	-4.1%	0.303	+5.2%
RANSE/BEM	0.12	0.1823	+7.2%	0.3205	+11.3%
RANSE/BEM	0.13	0.1829	+7.6%	0.3210	+11.4%
RANSE/BEM	0.15	0.1831	+7.7%	0.3212	+11.5%
RANSE/BEM	0.18	0.1859	+9.4%	0.3246	+12.7%
RANSE/BEM	0.25	0.1790	+5.3%	0.3165	+9.9%
RANSE/BEM	0.30	0.1860	+9.4%	0.3252	+12.9%

3.4 Propeller-hull interaction with RANSE/BEM coupling approach

Propeller-hull interaction computation is performed with the RANSE/BEM coupling procedure for 4 different test cases, namely the KCS test case [9], the STREAMLINE tanker test case (noted as STL in the following table), the HTC test case, and the DTC test case [10]. For all computations, half domain is simulated and the tangential force is not taken into account. Propeller revolution rate n is fixed. k-ω SST model is employed. Interface plane is located at 0.15D. The mesh contains about 1M cells. Except for the KCS test case, trim and sinkage are free, and rudder is included. The predicted Kt and Kq are compared with the experimental results as well as the full RANSE computation in table 5. Except for the DTC test case, propeller thrust is over predicted. Based on grid independent study not shown in this paper, numerical error on Kt is about 1-2%. As a full RANSE computation always under estimates Kt, it is unlikely possible that the over estimation of Kt in the RANSE/BEM coupling computation is due to the accuracy of total velocity computation. As mentioned in the previous sub-section, we believe that

the main reason for this over estimation is due to the fact that the effective wake at the interface plane is employed by the BEM code for the propeller computation, while it is the effective wake at the propeller plane that should be used. Although it is impossible to evaluate the effective wake at the propeller plane directly, nominal wake at the propeller plane can be computed without difficulty. Then a rational way to estimate the effective wake at the propeller plane U_{eff_Prop} can be proceeded as follow:

$$U_{eff_Prop} = U_{tot_In} - U_{ind_In} + U_{nom_Prop} - U_{nom_In}$$

Here U_{tot_In} is the total velocity at the interface plane given by the RANSE code. U_{ind_In} is the propeller induced velocity at the interface plane provided by the BEM code. U_{nom_Prop} and U_{nom_In} are nominal wake at the propeller plane and at the interface plane, respectively, given by another RANSE resistance computation. When the effective wake is computed in this way, good predictions are obtained for all test cases as shown in the table 6. Slightly high error observed for the HTC test case might be due to the accuracy of the propeller geometry used in the computation. Under-estimation of Kt for the DTC test case is due to the effect of grid resolution. Result obtained with a 2M grid for the DTC test case predicts Kt with about +1% error.

Table 5: Propeller interaction result with RANSE/BEM coupling computation

Type	n (rps)	Kt	Kt error	10Kq	Kq error
KCS-Exp	9.5	0.170	-	0.288	-
KCS-RANSE	9.5	0.163	-4.1%	0.303	+5.2%
KCS-RANSE/BEM	9.5	0.1786	+5.1%	0.3154	+9.5%
STL-Exp	8.92	0.2491	-	0.4101	-
STL-RANSE	8.92	0.2346	-5.8%	0.4030	-1.8%
STL-RANSE/BEM	8.92	0.2575	+3.4%	0.4242	+3.4%
HTC-Exp	8.28	0.1920	-	0.2812	-
HTC-RANSE	8.28	0.1725	-10.1%	0.2664	-5.3%
HTC-RANSE/BEM	8.28	0.2130	+10.9%	0.3040	+8.1%
DTC-Exp	13.27	0.2203	-	0.3626	-
DTC-RANSE	13.27	0.2057	-6.6%	0.3652	+0.7%
DTC-RANSE/BEM	13.27	0.2185	-0.8%	0.3653	+0.2%

4 CONCLUSIONS

A RANSE/BEM coupling procedure is applied for propeller-hull interaction computation in the present study. It has been found that the interface plane needs be located as near as possible to the propeller plane without intercepting the region where body

Table 6: RANSE/BEM coupling computation with corrected effective wake

Type	n (rps)	Kt	Kt error	10Kq	Kq error
KCS-RANSE/BEM	9.5	0.1690	-0.6%	0.3038	+5.5%
STL-RANSE/BEM	8.92	0.2470	-0.8%	0.4157	+1.4%
HTC-RANSE/BEM	8.28	0.1935	+2.8%	0.2902	+3.2%
DTC-RANSE/BEM	13.27	0.2156	-2.1%	0.3597	-0.8%

forces are added. When the effective wake evaluated at the interface plane is employed for propeller computation by the BEM code, propeller thrust is over-predicted. A way to compute the effective wake at the propeller plane is proposed in this paper. When the effective wake at the propeller plane thus computed is employed for propeller computation, the RANSE/BEM coupling procedure provides reliable prediction for all test cases investigated in the present study. With this hybrid approach, ship propulsion prediction can be obtained with the same accuracy and the same CPU cost as a resistance prediction. It is a reliable alternative to a full RANSE computation for this kind of application.

5 Acknowledgments

This work was granted access to the HPC resources of IDRIS under the allocation 2011-21308 made by GENCI (Grand Equipement National de Calcul Intensif). Part of the work was supported by the STREAMLINE project, a collaborative R&D project, partly funded by the 7th Framework Programme of the European Commission.

REFERENCES

[1] Visonneau, M., Queutey, P., Deng, G. B., Wackers, J., Guilmineau, E., Leroyer, A., and Mallol, B., 2012. "Sliding grids and adaptive grid refinement for rans simulation of ship-propeller interaction.". In 11th International Conference on Computer Applications and Information Technology in the Maritime Industries, COMPIT'12.

[2] Greco, L., Salvatore, F., and Felice, F. D., 2004. "Validation of a quasi–potential flow model for the analysis of marine propellers wake". In Twenty-fifth ONR Symposium on Naval Hydrodynamics.

[3] Pereira, F., Salvatore, F., and Felice, F. D., 2004. "Measurement and modelling of propeller cavitation in uniform inflow". *Journal of Fluids Engineering,* ***126***, pp. 671–679. DOI: 10.1115/1.1778716.

[4] Salvatore, F., Testa, C., and Greco, L., 2009. "Coupled hydrodynamics-hydroacoustics BEM modelling of marine propellers operating in a wakefield". In First Int. Symposium on Marine Propulsion, SMP 2009. ISBN: 978-82-7174-263-8.

[5] Queutey, P., and Visonneau, M., 2007. "An interface capturing method for free-surface hydrodynamic flows". *Computers and Fluids,* ***36***, pp. 1481–1510.

[6] Deng, G. D., and Visonneau, M., 1999. "Comparison of explicit algebraic stress models and second-order turbulence closures for steady flow around ships". In 7th Symposium on Numerical Ship Hydrodynamics, pp. 4.4–1–4.4–15.

[7] Duvigneau, R., Visonneau, M., and Deng, G. B., 2003. "On the role played by turbulence closures in hull ship optimization at model and full scale". *Journal of Marine Science and Technology,* ***8***, pp. 11–25.

[8] Leroyer, A., and Visonneau, M., 2005. "Numerical methods for RANSE simulations of a self-propelled fish-like body". *Journal of Fluids and Structures,* ***20***, pp. 975–991.

[9] Hino, T. "Test case 2". In Proceedings of CFD Workshop Tokyo 2005, see also http://www.gothenburg2010.org/instructions_KCS/Case2.3a/Case_2-3a.htm.

[10] el Moctar O., Shigunov, V., and Zorn, T., 2012. "Duisburg test case: Post-panamax container ship for benchmarking". *Ship Technology Research Journal,* ***59***, pp. 50–64.

V International Conference on Computational Methods in Marine Engineering
MARINE 2013
B. Brinkmann and P. Wriggers (Eds)

A THROUGHFLOW METHOD FOR THE ANALYSIS OF MIXED FLOW WATERJET PUMP

G. RICCI, C. COSTA AND A. SATTA

Dipartimento di Ingegneria Meccanica, Energetica, Gestionale e dei Trasporti (DIME)
Sezione Macchine, Sistemi Energetici e Trasporti (MASET)
Università degli Studi di Genova
Via Montallegro 1, 16145 Genova, ITALY
e-mail: gianluca.ricci@unige.it, carlo.costa@unige.it, ansat@unige.it

Key words: Computational Techniques, Throughflow, Propulsion, CFD, Mixed-flow pumps

Abstract. Due to the large availability of cheap and powerful computational resources, and due to the high level of reliability of modern CFD tools, fully three dimensional Navier Stokes computations have become the state of the art for the final design stage even in complex turbomachinery geometries. Nonetheless, there is still need for fast, yet accurate simplified modelling for quicker parametrical analysis during the preliminary design of turbomachinery. In this work a throughflow mass flow rate based meridional approach has been developed. The code is based upon the fundamental assumptions of permanent, axisymmetric and incompressible flow. In order to evaluate the spanwise gradient of fundamental unknowns along the control stations, the method is based on the employ of radial equilibrium equation in its full formulation, without neglecting any terms. The method is able to calculate the flow unknowns inside the bladed zones of meridional channel through the evaluation of blade force source term inside the radial equilibrium equation. In order to simplify the management of geometric parameters inside the process, a parametric representation of blade geometry has been developed. The evaluation of streamline curvature has been carried out by means of the parametric formulation using a natural cubic spline representation. Moreover a geometric curvature has been introduced and opportunely combined with the analytical calculated curvature in order to improve the stability. An automatic semi-empirical procedure, based on the proposed method, has been developed. It employs qualified correlative models for the evaluation of both energy losses and deviation angles. The code has been used for the analysis of a mixed flow waterjet pump. The results obtained have been compared with those circumferentially averaged of a viscous full 3D commercial calculation and show a good agreement. This achievement confirms the coherence of the procedure with 3D viscous methods, thus making the simplified approach consistent with more complex approaches.

NOMENCLATURE

f	General function	G	Function of blade angles [dimensionless]
f_ε	Flow deviation correlative function	gH	Specific head [J/kg]
f_σ	Energy loss correlative function	k_m	Streamline curvature [m^{-1}]

L	Specific work [J/kg]
$\dot{m}$	Mass flow rate [kg/s]
n	Rotational speed [rpm] or streamline normal direction
P	Absolute (p_t) or relative total pressure (p_{tr}) [Pa]
p	Static pressure [Pa]
$s.l.$	Streamline
t	$\tan\varepsilon$ [dimensionless]
t_f, t_f'	Fluid-dynamics parameter for correlative equation
$\bar{t}_g, \bar{t}_g'$	Geometrical parameter for correlative equation
th	Blade thickness [m]
u	Blade speed [m/s]
v	Absolute (c) or relative (w) speed [m/s]
X	Quasi-orthogonal direction: X' circumferential projection on meridional plane
X'	Motion equation projection line lying on S_2 flow surface or camber surface
z_p	Number of blades [dimensionless]

Greeks

γ, φ	Characteristic angles of quasi-orthogonal X [deg]
ε	Absolute (α) or relative (β) flow angle [deg]
η	Angle between X and X': "lean angle" [deg]
η_{idr}	Hydraulic efficiency [dimensionless]
ϑ, m, n	Orthogonal Coordinates with Axial Symmetry
ϑ, R, z	Axisymmetric cylindrical coordinate system
Λ	Flow angular momentum [m^2s^{-1}]
λ	Streamline slope angle [deg]
ρ	Density [kg/m^3]
$\sigma = \frac{P_2}{P_1}$	Energy loss coefficient based on total pressure ratio [dimensionless]
ω	Angular speed [s^{-1}]

Subscripts

1	Upstream control station
2	Downstream control station
c	Blade
i, j	Calculation grid indexes
m	Meridional
n	Normal
t	Total
tr	Total relative
ϑ	Tangential

1 INTRODUCTION

In both academic and industrial context various calculation procedures are still employed. They can be divided in two overall categories: the CFD methods and the so-called semi-empirical procedures based upon the employment of experimental correlations both for energy losses and blade flow exit angle evaluation. A good prediction of turbomachine fluid-dynamical performance can be obtained only after an accurate choice of correlative equations since these two classes of correlative models are usually fitted to a specific family of machine. The use of such different procedures often leads to results that in most cases are not consistent. These different results, often accepted by industries because of the uneven potential of such codes, is a hard issue to be cleared if the target consist in integrating the different procedures widely employed in industries. The management simplicity, the quick usability of results and the short time required for collecting input data are aspects that should not be ignored, above all for the possibility of creating tools easily available for

turbomachines designers. These peculiarities have led semi-empirical codes to be the most employed tools for preliminary design and analysis of turbomachines in particular within company design activities.

The final target of this work is to develop a simplified procedure able to provide a quick but complete solution, where the results are consistent with the ones provided by CFD codes. With this background the proposed code is a semi-empirical procedure with high stability and robustness in order to properly evaluate reliable radial distributions for the fundamental unknowns of axisymmetric flow. Moreover the flexibility of the code is a feature which permits to accurately predict the overall performance of turbomachineries in several operating conditions and at different blade configurations.

A throughflow method for the analysis of pumps is presented and applied to the analysis of a mixed flow waterjet pump for marine propulsion.

2 CALCULATION METHOD

The proposed method is based upon the development of a fixed mass-flow rate procedure which employs the radial equilibrium equation formulated in terms of velocity [1], [2], [3], [4]. The assigned mass flow rate approach is the most adopted formulation when incompressible and subsonic flows are analysed. It does not present relevant differences from fixed outlet pressure approach when low compressibility physical condition is verified because, in such case, both formulations are well-posed [5].

In the most general condition a fluid-dynamical problem has to be studied in four dimensions namely the time and the three spatial coordinates. Basic simplifying hypothesis of considering the flow as steady and axisymmetric reduce dimensions to two. The choice of adopting the OCAS, Orthogonal Coordinates with Axial Symmetry (ϑ,m,n), identifies the two spatial coordinates with the meridional and normal direction, respectively m and n. For convenience the quasi-orthogonal direction, indicated with X, is taken as the second spatial dimension instead of the n direction [6]. The quantities needed to characterize the flow properties in each point of the fluid domain, called the fundamental unknowns, are five if no additional simplifying assumptions are made: two thermodynamic variables and the three components of the velocity vector. Due to the axisymmetry of the flow, axisymmetric stream surfaces exist, consequently w_n is null everywhere and the unknown components of the velocity vector are decreased to two provided that λ is known. The flow of water inside the turbomachine is considered incompressible [7]. For this reason the momentum and the energy equation are decoupled. Therefore, assuming that the process is adiabatic, the thermodynamic state of the flow is univocally described by one single variable being temperature an arbitrary constant value. So it's necessary to choose only three fundamental unknowns instead of five. It's convenient to select as fundamental unknowns the velocity v, the flow angle ε and the total pressure P of the reference frame considered, in order to minimize the number of auxiliary unknowns introduced in the calculation process [8]. In fact it's necessary to introduce as many additional equations, called auxiliary equations, as the number of auxiliary unknowns present in the fundamental equations.

The working conditions of the machine are determined specifying the control parameters, in detail the rotational speed n and the inlet mass flow rate $\dot{m}$, together with inlet boundary

conditions. Concerning the latter, on the quasi-orthogonal representing the inlet of the fluid domain absolute total pressure P and flow angular momentum $\Lambda=c_\vartheta R$ are set.

2.1 Fundamental equations

Because the number of fundamental equations has to be equal to the number of fundamental unknowns three expressions are required. The continuity equation and the two correlative equations, providing the flow angle and the total pressure loss, are employed. Writing the latter with respect to each streamline the following equations set comes out:

$$P_2(X_2) = P_1(X_1)\sigma_{1-2} = P_1(X_1) f_\sigma(\bar{t}_g, t_f) \tag{1}$$

$$\varepsilon_2(X_2) = f_\varepsilon(\bar{t}_g', t_f') \tag{2}$$

$$d\dot{m}_2 = d\dot{m}_1 =$$

$$= \rho v_2(X_2)\cos\varepsilon_2(X_2)\cos[\lambda_2(X_2)+\varphi_2(X_2)]\left[2\pi R_2 - \frac{z_p\, th_2(X_2)}{\cos\varepsilon_{c2}(X_2)\cos\eta_{c2}(X_2)}\right]dX_2 \tag{3}$$

it's worth noting that in Eqn. (1), Eqn. (2) and Eqn. (3) subscripts 1 and 2 indicate respectively inlet and outlet control station of each row (rotor or stator). How to apply Eqn. (1) and Eqn. (2) when throughflow, instead of ductflow, calculation is carried out can be found in [9]. Application of Eqn. (3) is, on the contrary, straightforward even in throughflow analysis if subscripts *i-1* and *i,* specifying two consecutive quasi-orthogonal lines, take the place of 1 and 2.

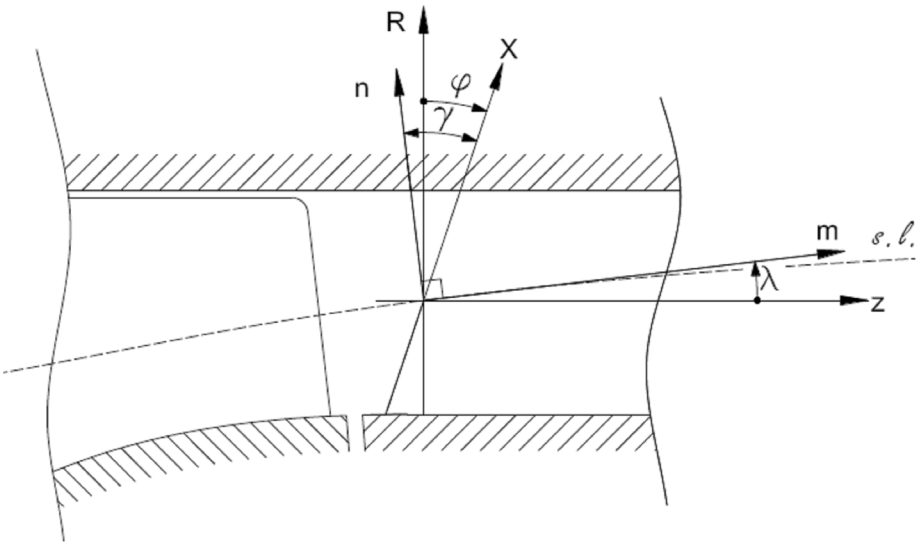


Figure 1: Angles φ, λ and γ

The whole geometrical quantities of the machine, hence $\bar{t}_g'$ and $\bar{t}_g$ too, are known since the present case is an analysis application. On the other hand every fluid-dynamical variable

t_f' and t_f, on which correlative relations depend, is to be expressed, through the employment of so-called closure auxiliary equations, as function of fundamental unknowns only. The continuity equation introduces streamtube thickness dX_2 and streamline meridional slope λ_2 as new unknowns.

In trivial one-dimensional problem (one single streamtube), dX_2 becomes the geometrical height of meridional channel, λ_2 the mean value of hub and shroud slope. Both of them are known geometrical parameter. In such case the set of Eqn. (1), Eqn. (2) and Eqn. (3) solve the problem. If we make use of several streamline we need two more auxiliary equations. Let's suppose λ_2 is known. Then it's necessary to use another relation identifiable in the velocity gradient equation. It's a first order nonlinear ordinary differential equation and derives from the projection of motion equation on the X direction. In its full formulation it can be written as follows:

$$\frac{d\left(v^2/2\right)}{dX} = \frac{dP}{dX}\frac{1}{\rho} - \left(G\frac{dP}{dm}\frac{1}{\rho}\right) - \left[\frac{\left(v_m t\right)^2}{R} + 2\omega v_m t\right]\frac{dR}{dX} + \\ + \frac{v_m}{R}\frac{d\left(v_m Rt + \omega R^2\right)}{dm}\tan\eta + \frac{d\left({v^2}_m/2\right)}{dm}\sin\gamma + k_m {v_m}^2\cos\gamma \tag{4}$$

with $t = \tan\varepsilon$, $\gamma = \lambda + \varphi$, Fig. 1, and $G = -\dfrac{t\tan\eta + \sin\gamma}{1+t^2}$.

Unlike velocity gradient equation present in [10], Eqn. (4) has been derived modelling friction force per unit mass through the employment of energy equation written in mechanical form instead of Horlock's formulation [11]. The integration constant for Eqn. (4) is obtained by imposing that the mass flow conservation is satisfied:

$$\int_X \rho v(X)\cos\varepsilon(X)\cos[\lambda(X)+\varphi(X)]\left[2\pi R - \frac{z_p\, th(X)}{\cos\varepsilon_c(X)\cos\eta_c(X)}\right]dX = \dot{m} \tag{5}$$

The resolution approach is based upon a classical procedure [9]. Tentatively both the fundamental unknowns values and the streamline distribution are assigned as initial condition. The system of Eqn. (1), (2) and (4) is solved searching for the velocity value at hub of the control station, for which the condition expressed in Eqn. (5) is satisfied. Such algorithm is applied to each control station in the computational domain. At the end of this internal iterative process the streamline position distribution has to be reallocated through Eqn. (3). The computation has to be repeated up to convergence. It's useful to remember that the stator rows are investigated in the absolute reference frame while the rotor ones are analysed in the relative reference frame [6]. This choice leads to use the same equations set for both type of rows, but it also requires the introduction of "changing equations" that allow to transfer the fundamental equations from a reference frame to another. Moreover flow angles are measured with respect to the meridional direction and the tangential component of velocity vector is assumed positive if directed like the blade speed u.

A computer code, written in FORTRAN, based on the just described method is developed. The code is organized in subroutines, thus allowing quick maintenance and updates.

3 APPLICATION

The proposed method is applied to a mixed flow waterjet pump and the obtained results are compared with 3D Navier-Stokes CFD calculation [12] both at design and off-design conditions. The studied pump has been derived by scaling a previous design developed at DIMSET [13] in order to obtain higher values of power. This waterjet pump is made up of two rows of blades, one rotating and another stationary, and it is characterized by a low weight to power ratio, that is to say its performance is high in relation to its small dimensions. The rotor has been designed to give a constant outlet absolute flow angle. Its blades are twisted and their solidity is high. Its geometry is similar to that of an inducer and so it is hard to represent. The stator has been designed so that the flow approaches it with an optimum angle of incidence and outlet tangential velocity is almost zero. In relation to its blades the stagger angle is constant along the span and the lean angle is high.

As regards CFD calculation a structured grid with about one million nodes is used and Spalart Allmaras turbulence model is introduced. The obtained results are circumferentially mass averaged in order to have radial distributions of the quantities of interest on the quasi-orthogonals. used by developed computer code.

The main code calls subroutines that implement semi-empirical correlations proposed in open literature. As concerns flow angle, determined by Eqn. (2), Howell correlative relations [14], for rotor row, Lieblein ones [15], revised by Thomas [16], for stator row, are employed for evaluating profile flow deviation angle. As concerns total pressure, determined by Eqn. (1), both rotor and stator row, makes use of Lieblein correlations [17], for computing profile energy losses, and of Howell ones [18], for calculating globally estimated secondary losses. The main program provides as outputs the radial distributions of both fundamental unknowns and auxiliary ones on each quasi-orthogonal chosen as control station. Furthermore it computes global parameters necessary to identify waterjet performance namely hydraulic efficiency η_{idr}, specific head gH based on absolute total pressure rise and specific work L.

The results obtained in design condition are widely presented. The calculation process has shown a stable convergence, Fig. 2, thanks to streamlines initial distribution which divides the meridional channel into equal parts.

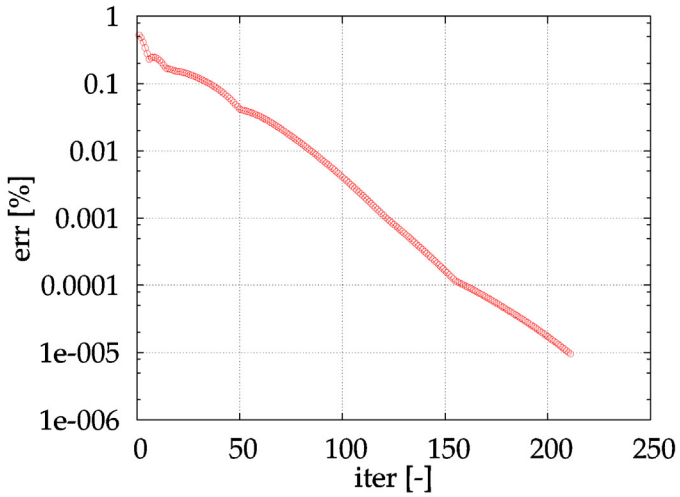


Figure 2: Convergence diagram in logarithmic scale

An excellent coherence between streamtubes thicknesss provided by the proposed method and CFD ones can be observed from meridional streamlines trend, Fig. 3.

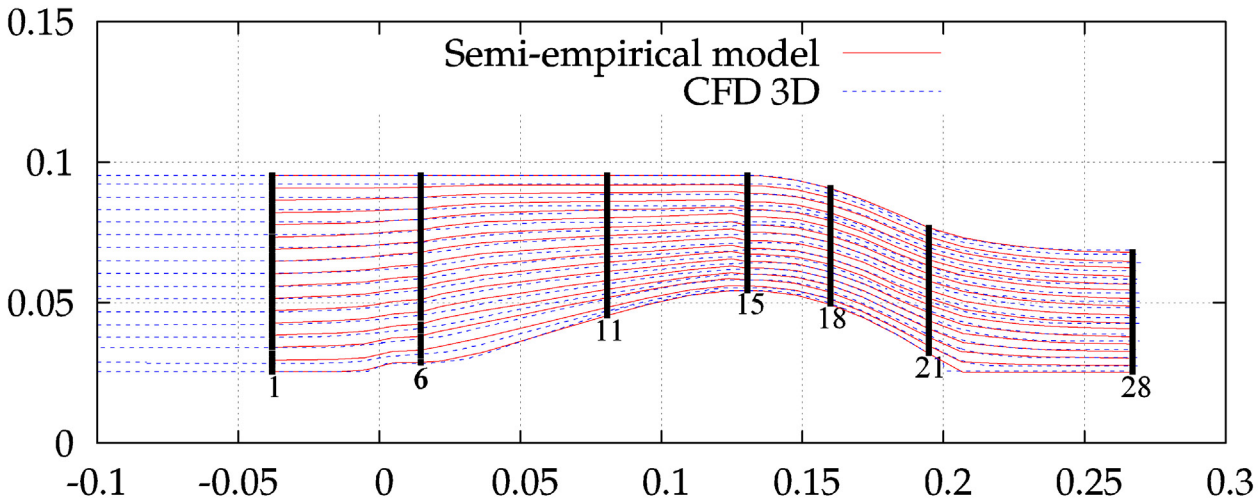


Figure 3: Streamlines trend in meridional plane

Moreover in Fig. 3 the most significant quasi-orthogonals, among the ones employed in calculation, are marked. In particular the 1st and the 28th ones are respectively the inlet and the outlet control stations of the calculation domain, the 6th, the 15th and the 21st ones are the quasi-orthogonals placed at inlet and outlet of each row while the 11th and the 18th are positioned respectively within rotor and stator row. These latter two are specific of a throughflow code and do not exist in a ductflow code. In Fig. 4, Fig. 5, Fig. 6 and Fig. 7 unknowns P, ε and v_m, calculated on significant control stations located outside of rows, are shown in comparison with averaged CFD results. Radial distributions on first quasi-orthogonal are not shown since boundary conditions are set on it. Agreement is good, mismatches are mainly due to gap and secondary flows effects which global correlations are not able to capture.

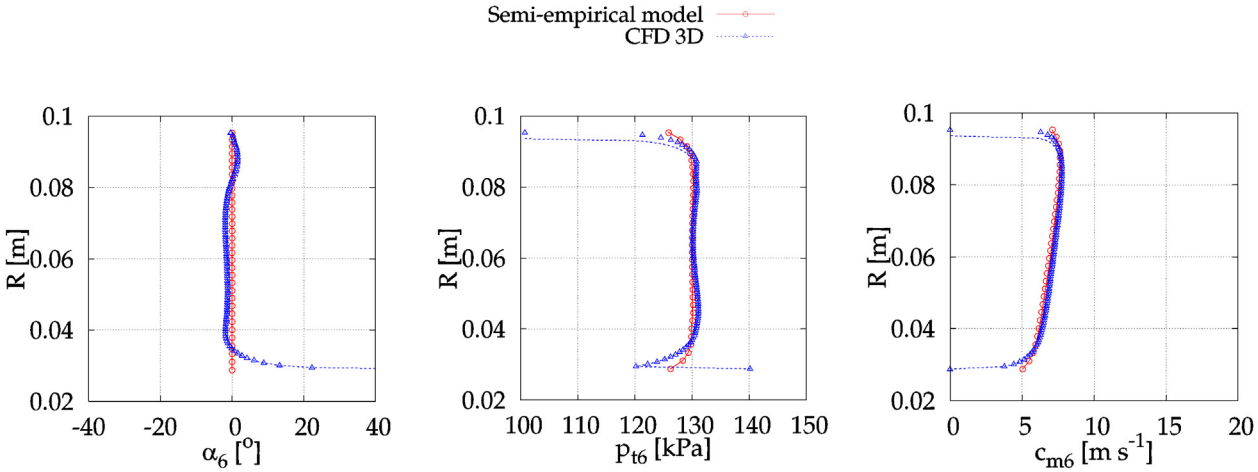


Figure 4: Unknowns at inlet of rotor row

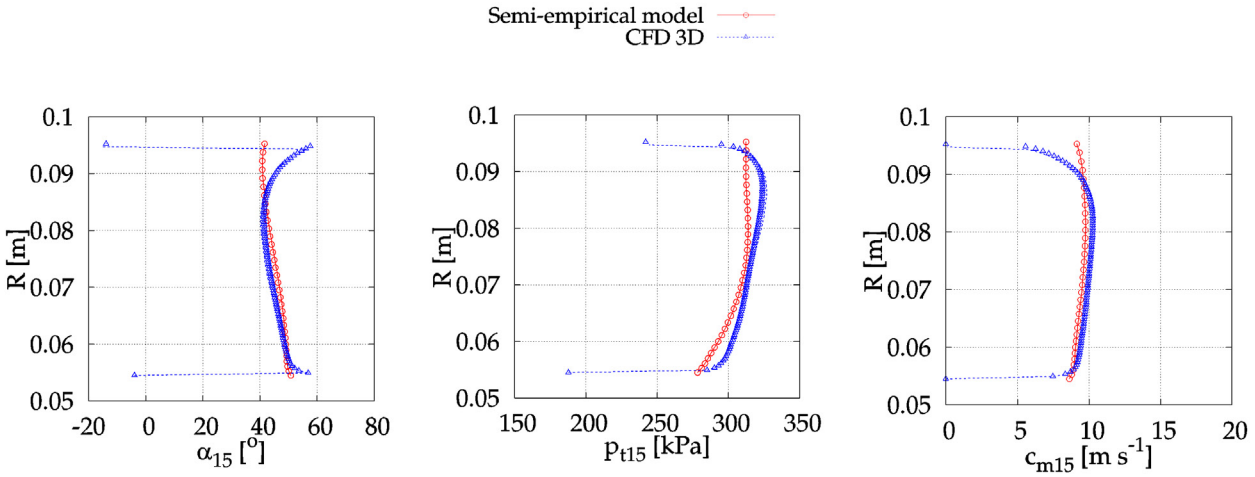


Figure 5 Unknowns at outlet of rotor row

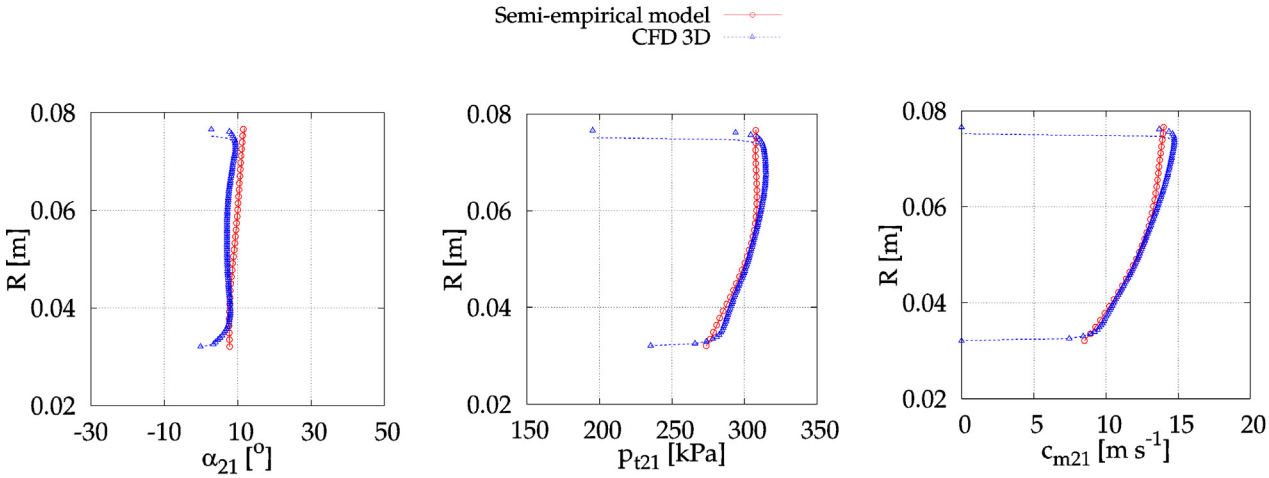


Figure 6: Unknowns at outlet of stator row

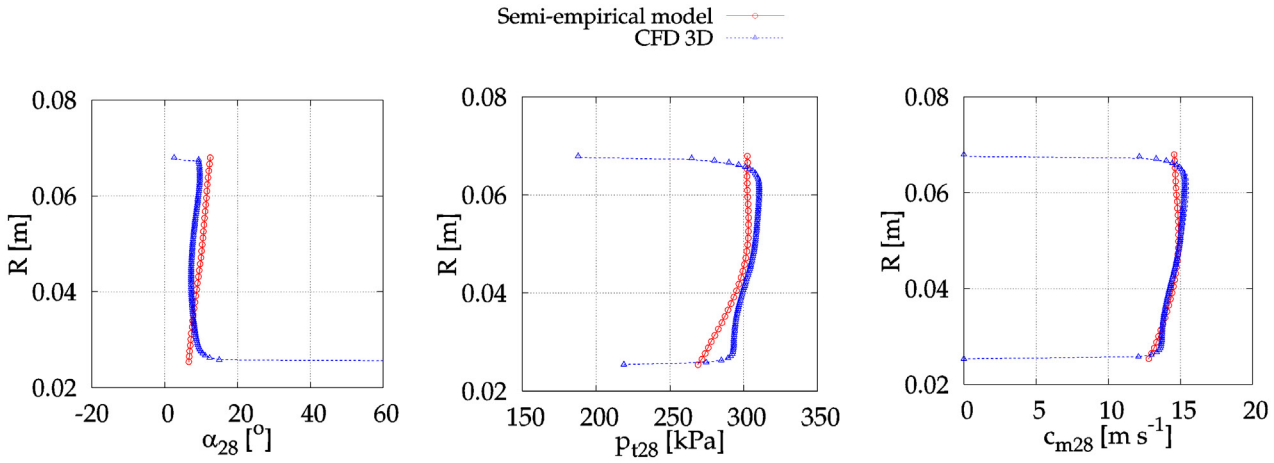


Figure 7: Unknowns at outlet of waterjet

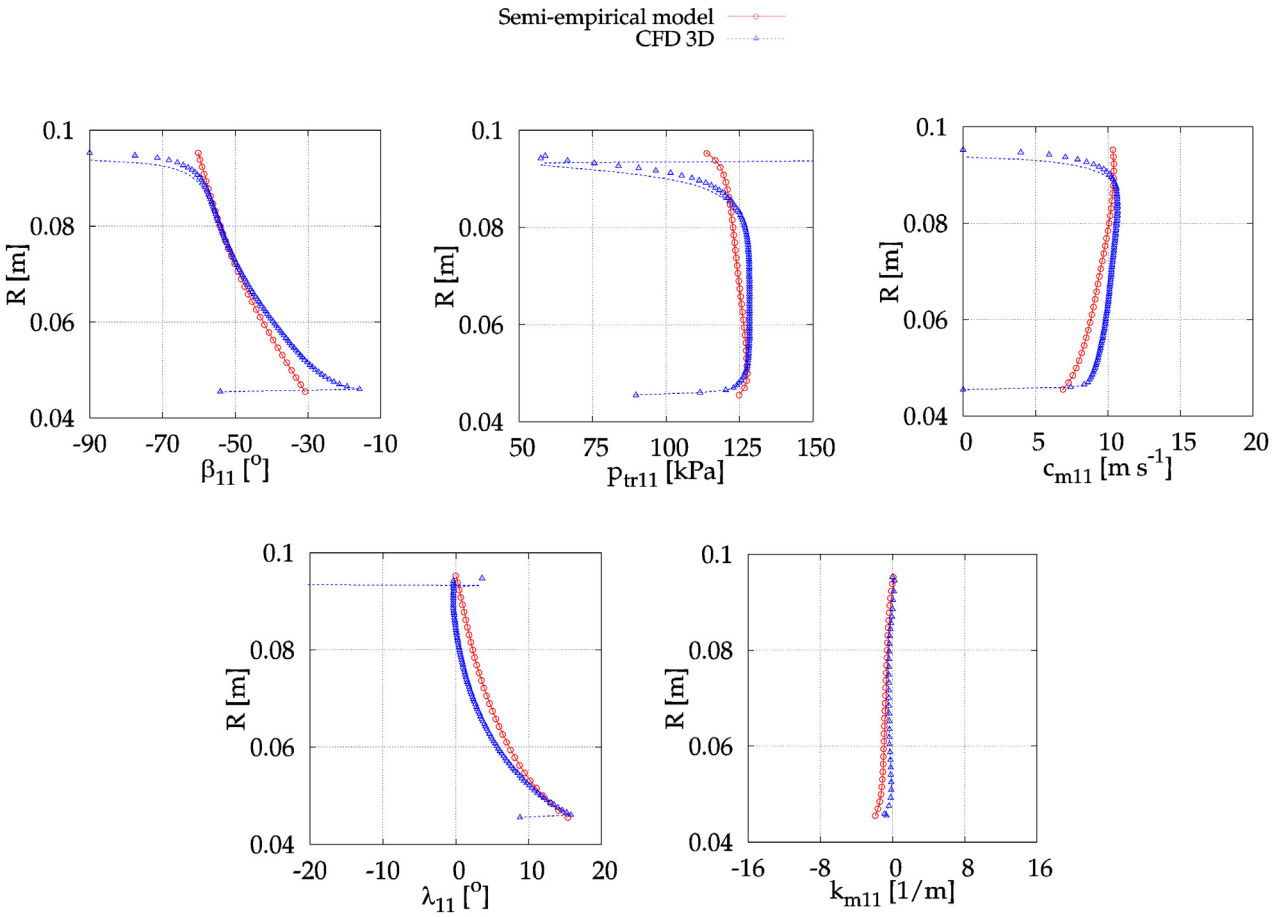


Figure 8: Unknowns on the quasi-orthogonal placed in the middle of rotor row

As concerns quasi-orthogonals within rows, where calculation is more critical, the two auxiliary unknowns λ and k_m as well as P, ε and v_m are shown in Fig. 8 and Fig. 9.

Also in these control stations mismatches with respect to CFD reference are small and due to correlations employed. The evidence that auxiliary unknowns, involved in throughflow calculation process, show minimal differences with respect to CFD ones confirms this statement.

Finally, in order to test flexibility of method, code is applied to diagram gH and η_{idr} characteristic curves of machine at nominal rotational speed, Fig. 10. Mass flow rate is changed between the range 166 and 247 [kg/s]. Errors relative to CFD reference are lower than 5%.

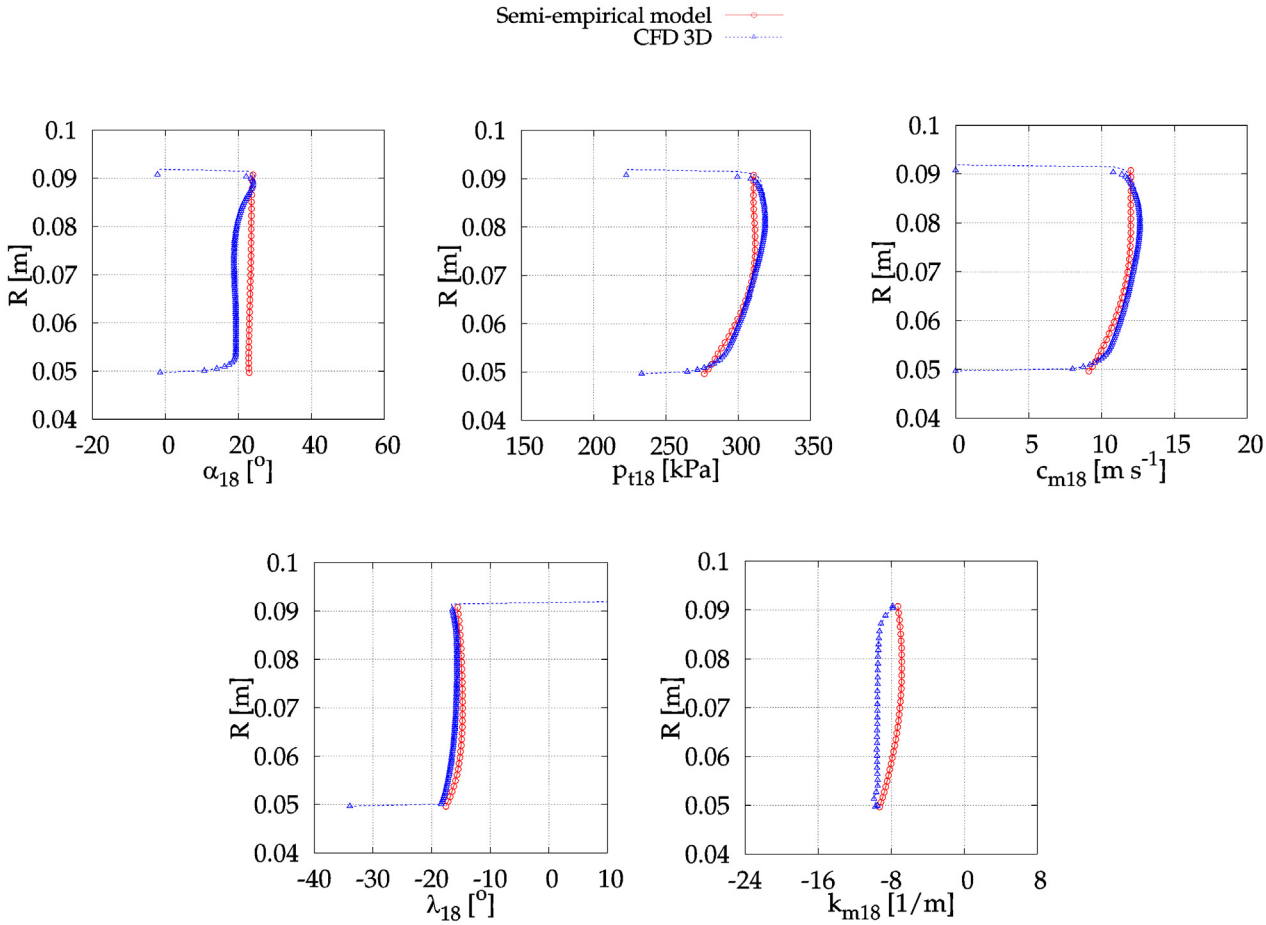


Figure 9: Unknowns on the quasi-orthogonal placed in the middle of stator row

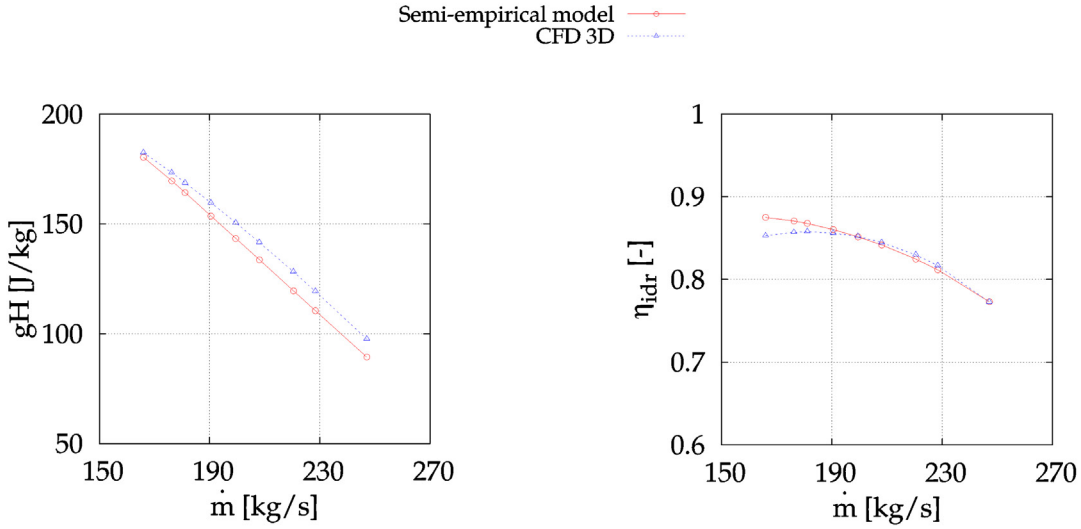


Figure 10: gH and η_{idr} characteristic curves of waterjet

4 CONCLUSIONS

In this work a calculation code based on a semi-empirical throughflow methodology has been developed and applied to pumps analysis. Thanks to flexibility of method the procedure has been employed to study mixed flow pumps. The mass flow rate based meridional approach is semi-empirical because it makes use of relations, both theoretical and experimental, for evaluating energy loss and flow angle. The proposed method solve velocity gradient equation, Eqn. (4), without neglecting any term. In particular specific formulations for computing streamline meridional curvature k_m , streamline meridional slope λ and lean angle η have been implemented.

The procedure has been used to analyze a waterjet system for marine propulsion. As concerns design working condition, radial distributions of quantities of interest have been widely presented referring to control stations positioned both in duct flow regions and within rows of machine. Such values, compared with circumferentially mass averaged CFD results, show good agreement. Moreover several working conditions have been tested. Specific head gH and hydraulic efficiency η_{idr} characteristic curves have been plotted in order to visualize global performance of waterjet. Also these global results are in accordance with the ones provided by CFD procedure.

REFERENCES

[1] Casey M. and Robinson C., 2008. "A new streamline curvature throughflow method for radial turbomachinery". In Proceedings of ASME Turbo Expo, GT2008-50187.

[2] Bosio A., Croce G., Marini M. and Satta A., 1996. "L'equazione del gradiente della velocità per il calcolo through-flow nelle turbomacchine". In Proc. Turbomachine '96, U. of Genoa, ed.

[3] Jennions I. K., Stow P., Hirsch C. and Railly J. W., 1985. "A quasi-three-dimensional turbomachinery blade design system. I: Throughflow analysis. – II: Computerized system. Discussion". Journal of engineering for gas turbines and power, 107(2), pp. 301-316.

[4] Wennerstrom A., 1975. "On the treatment of body forces in the radial equilibrium equation of turbomachinery". Progress report 75-0052, Aerospace Research Laboratories.

[5] Croce G., Dedicato E., Gazzano R., Ratto L. and Satta A., 2008. "Procedure for the axial multi stage turbomachineries performance analysis". ISROMAC-12.

[6] Vavra M. H., 1974. "Aerothermodynamics and flow in turbomachines". Robert Krieger Publ. Comp.

[7] Osif T., 1988. "The effects of salt, gas, temperature, and pressure on the compressibility of water". SPE Reservoir Engineering, 3(1), pp. 175-181.

[8] Ratto L. and Satta A., 2010. "A simplified method with local correlations for the analysis of multistage axial turbines". In Proceedings of ASME Turbo Expo, GT2010-23491.

[9] Katsanis T., 1966. "Use of arbitrary quasi-orthogonals for calculating flow distribution in the meridional plane of a turbomachine". Tech. Rep. TN D-2546, NASA.

[10] Noera F. and Satta A., 1998. "Through flow calculation in axial flow turbines using a quasi-orthogonal solver". In Proceedings of ASME Turbo Expo, 98-GT-503.

[11] Horlock J. H., 1971. "On entropy production in adiabatic flow in turbomachines".

Journal of basic engineering, pp. 587-593.
[12] Various Authors, 2012. NUMECA FINE/Turbo User Manual.
[13] Gazzano R., Ratto L. and Satta A., 2009. “Optimised design and analysis of a small waterjet propulsion system”. In Proceedings of III International conference on computational methods in marine engineering MARINE 2009.
[14] Howell A. R., 1945. “Design of axial compressors”. Proc. Instn. Mech. Engrs., 153.
[15] Lieblein S., 1960. ”Incidence and deviation angle correlations for compressor cascades”. ASME J. Basic Eng., 82, pp. 575-584.
[16] Thomas K. D., 2005. “Blade row and blockage modelling in an axial compressor throughflow code”. Master Thesis, U. of Stellenbosch, South Africa.
[17] Lieblein S., 1959. ”Loss and stall analysis of compressor cascades”. ASME J. Basic Eng., 81, pp. 387-400.
[18] Howell A. R., 1945. “Fluid dynamics of axial compressors”. Proc. Instn. Mech. Engrs., 153.

V International Conference on Computational Methods in Marine Engineering
MARINE 2013
B. Brinkmann and P. Wriggers (Eds)

TECHNICAL-ECONOMICAL ANALYSIS OF COLD-IRONING: CASE STUDY OF VENICE CRUISE TERMINAL

CRISTIANO MARINACCI†, ROBERTO MASALA†, STEFANO RICCI*, ANTONIO TIERI†

Sapienza University of Rome – DICEA – Transport Area
Via Eudossiana 18, 00154 Rome, Italy
e-mail: cristiano.marinacci@uniroma1.it
e-mail: roberto_masala@libero.it
e-mail: stefano.ricci@uniroma1.it
e-mail: antonio.tieri@uniroma1.it
web page: http://www.uniroma1.it

Key words: Cold-Ironing, Port, Feasibility, Venice

Abstract. Cold-ironing is the practice that enables to power commercial ships by a link to fixed electricity network, in order to reduce pollutant emissions in the port areas caused by marine fuels in auxiliaries engines feeding on board installations during ships stops at quays. The present paper aims to provide an overview of the most important technical and functional features of the concerned ships power systems and to analyze the technical, economic and financial feasibility of this system. In the first part the main technical-constructive elements for the application of Cold-ironing to different types of ship (such as voltage, frequency, power supply and power demand on the quay) are analyzed. The variety of functional situations does not allow to establish general constructive solutions since the cold-ironing system is depending both on the operational mode and the layout of each terminal. In the second part of the paper it has been analyzed the case study of the cruise terminal in Venice (VTP Spa Venice Passenger Terminal) with the aim of verifying the feasibility of a cold-ironing system for power supply of cruise ships on quays. The analysis was based on ships timetable for the year 2012, which includes the arrivals and the departures of 86 different ships with a global volume of 570 movements. Starting from data on dwell times, following the guidelines of the MEET methodology for estimating emission factors [3] it has been estimated pollutant emissions (nitrogen oxide NOx, sulfur oxides SOx, volatile organic compounds VOC, particulates PM, carbon monoxide CO) as a basis to calculate externalities to be considered for the Cost-Benefit Analysis (CBA). Based on a probabilistic analysis of the terminal occupation by ships (disposal of ship stalls on each quays) five operational scenarios were defined. Each scenario has been defined on the basis of an economic evaluation by means of a cost-benefit parametric analysis with the aim of providing the maximum financial results for assigned budgets. From a comparison of the results of the cost-benefit analysis and an estimate of possible investment costs obtained from USA case studies, it is noticed that the scenario providing coverage of both financial and economic investment includes the minimum number of electrified stalls and a ships journeys reorganization. It was also proposed a sensitivity analysis of CBA for the evaluation of indicators variations according to reference conditions variation.

1 INTRODUCTION

In order to reduce the emissions of a ship during its stop at the dock, a process, called cold-ironing, has been designed and adopted in some regions. It provides the electricity supply for onboard electric generator through a connection to fixed electricity network instead of to use the ship's engines. The power supply is provided through high tension line and a main substation to reduce the voltage. Afterwards, the current is carried out in the different docks, via underground cables, where it is converted into the frequency required for the specific ship. The frequency conversion is an important aspect because the most part of ships' generators use 60 Hz frequency, while the fixed electricity network normally provides 50 Hz standard frequency. The last step of the process is the connection, through the cables, of the dock's station with sockets placed on-board. Furthermore, depending on the voltage of on-board generators, it may be required an additional transformer inside the ship for the end use of electricity. Normally, during navigation the main engines, supported by auxiliary ones, generates the power for the motion and all other services of the ship, but in ports the main engine is switched off and, therefore, all the energy need is normally satisfied by auxiliary engines. Nevertheless some big and modern cruise ships use diesel-electric propulsion systems and are not equipped with auxiliary engines.

2 GENERAL SPECIFICATIONS

The use of cold-ironing on the dock requires the consideration of some basic parameters of the ship, such as the feeding voltage of the generators, the frequency and the power need to ensure the primary functions of the ship during the stop. Depending on the typology of ship these parameters may change relevantly [7]. These parameters are briefly analyzed, as an example, for 4 different typologies of commercial ships: container (deep sea and feeder), Ro-Ro and bulk ships (Table 1).

Table 1: Example of the construction of one table

	Power	Voltage	Frequency
Container ship deep sea	2 MW÷8 M	380-440 V÷6,6 kV	60÷50 Hz
Container ship feeder	200÷400 kW	Low	50÷60Hz
Ro-Ro ship	700 kW÷2 MW	400-460 kV	60÷50Hz
Bulk ship	1 MW e 2,5 MW	380-440 kV	60÷50 Hz

3 OPERATIONAL CRITICALITY

The variety of ships' technical situations leads to standardization problem for cold-ironing. In addition to different power needs, differences of voltage and frequency supply are problematic. The voltage of current reaching quays is normally variable between 6 and 20 kV. For vessels supplied with lower voltage a further processing is requires. The diagram in Figure 1 shows the situation with the transformer located on-board, but it is also possible a location on the dock. Deciding on the best location of the transformer is a key variable for the optimal process management. The major problems in locating the transformer on-board are the need for additional space and the cost of equipping each ship. It seems more economically

viable to install the transformer on the dock to be used by each moored vessel but the presence of handling equipment would limit the availability of space also for this location.

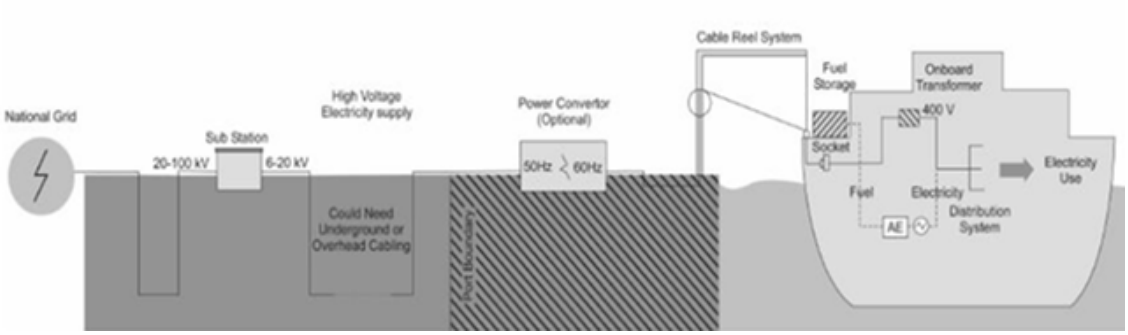


Figure 1: Cold-ironing system components basic scheme

The differences of power supply frequencies require converter on docks and affects the distribution mode from the main substation to the quay substations. The number of connection cables can vary from a few units up to ten, depending upon the type of ship, as well as different types of sockets may be required. All these varieties further complicate the operational aspects of the cold-ironing [7], which would be strongly simplified by unified procedures. For the final connection cables are matched to the ship by a dock crane, which holds them in suspension (Figure 2).



Figure 2: Ship connection

4. CONNECTIONS' SPECIFICATION

It is possible to consider different patterns of connection depending upon the mode of electricity distribution from the main port substation to the ship; normally three different connection systems exist, where the key variable is the allocation of frequency converters:

1. decentralized system: each dock is equipped with a converter;
2. centralized system: a single centralized converter is installed;
3. power distribution system: the current is remotely rectified and converted.

Strengths and weaknesses of the three connections are summarised in Table 2.

Table 2: Strengths and weaknesses of cold-ironing configurations

Configuration	Strengths	Weaknesses
1	Possible failures affect a single dock	High space need. Redundancy in converter use. Converter dimensioning according to maximum power average. Need of many transformers.
2	Limited space need. Converter used under request only.	Vulnerability. High cost of switches.
3	Limited space need. Reduction of losses in cables.	Lack of applications. Vulnerability

5 CASE STUDY: VENICE CRUISE TERMINAL

The cruise terminal in Venice is one of the most important terminal in the Mediterranean, the third in Europe and the eleventh in the world for passengers traffic. A large part of the traffic consist of cruise ships. In 2011 the total number of passengers in Venice reached the record level of 2,248,453, of which 1,777,073 from/to cruise ships. In 1997, operations management and traffic control are assigned to the new corporate Venice Passenger Terminal SpA (VTP), with the aim to improve all aspects of the provided services by reaching an increase of about 218% in 14 years. The facilities are spread over 260,000 square meters of land area in addition to 123,700 square meters of water surface and 3,300 meters of quays. The position is strategic as it allows easy access to the city (just 3 minutes by People Mover connecting the passengers terminal to the train station area). It is also well connected with the Marco Polo International Airport (about 13 km and 200 daily flights). The terminal can accommodate vessels having a maximum length of 340 m and a maximum draft of 8.70 m divided into 7 quays (17 stalls) of different sizes:

- Piave: 549,57 m, 2 stalls;
- Testata Marmi: 203,00 m, unique stall;
- Tagliamento: 726,70 m, 4 stalls;
- Isonzo: 630,00 m, 2 stalls;
- Santa Marta: 465,24 m, 4 stalls;
- San Basilio: 342,57 m, 4 stalls;
- Riva Sette Martiri: 360,40 m, inland cruises only.

5.1 The case-study methodology setting

The envisaged complexity of applications into real contexts has directed the work towards the implementation of a tool for evaluating the feasibility of the cold-ironing system using a technical and economic analysis applied to the case study of the port of Venice. The problem focuses on the sustainability aspects, in particular on the reduction of the emissions, providing inputs to a wide spectrum cost-benefit analysis. The study includes:

- data collection regarding the stay of ships in dock and the use of the terminal;
- estimation of emissions by all ships docked in 2012;
- probabilistic analysis of the terminal to identify the different operating scenarios according to the implementation degree of the cold-ironing;
- parametric cost-benefit and sensitivity analysis of the single scenarios;
- assessments of the economic and financial feasibility of the proposed measures.

5.2 Data collection and analysis

The database used for this work is the timetable (arrivals and departures) of the year 2012: 86 different ships have been handled for a total of 570 calls. The data collected for each ship are:

- name;
- shipping company;
- moorage (Marittima, San Basilio, Santa Marta);
- dock and stall of mooring;
- arrival and departure time.

5.3 Analysis of the staying time

The staying time of the ships have been estimated on the basis of departure and arrival times by stall. The average and maximum values are summarized in Table 3.

Table 3: Average and maximum values of staying time per stall

	Dock										
	Tagliamento		Piave		Isonzo		Santa Marta			San Basilio	
Stall	VE 107	VE 110	VE 117	VE 123	VE 18	VE 20	VE 24	VE 25	VE 27	VE 29	VE 30
Average staying time [hours]	11,3	10,8	12,8	9,2	12,5	9,8	14,9	14,1	10	12,1	12,2
Maximum staying time [hours]	144,5	24,5	72,5	24,5	49	96,5	48,5	49	10	96,5	25

The staying time of the ships in the dock is a key factor, together with the power required to feed all the devices of the ships themselves, to estimate the contribution to energy consumptions and emissions of various pollutants.

5.4 Terminal utilization

It has been estimated the utilization of the terminal by considering the number of daily arrivals and presences of ships in the dock, where the difference is due to multiple days staying of several ships resulting by staying times data. Table 4 contains a summary of docks occupation times.

Table 4: Docks utilization (frequency)

	Docks				
Ships at dock	Tagliamento	Piave	Isonzo	S. Marta	S. Basilio
2	59	10	60	5	4
1	109	115	124	77	114
0	197	240	181	283	247
Total	365	365	365	365	36

This operational analysis is crucial for the identification of the docks to be equipped with cold-ironing devices. Due to different situations considered, it has been developed a more detailed probabilistic study, including the realization of different scenarios depending on the degree of use of the terminal.

5.5 Emissions assessment

To estimate the emissions it has been followed the guidelines proposed in the MEET ("Methodologies for estimating air emissions from transports pollutant") project [3]. This European project is the first presenting a worldwide methodology for estimating the emissions of air pollutants generated by navigation. The methodology was developed by physicist Carlo Trozzi in 1996, was updated in 2008-2009 [4] and is still considered in studies that regard emissions by naval activity [5]. Starting from the staying times data, it has been possible to calculate the quantity of emissions produced as follows:

$$\textit{Emissions (g) = Power required (kW) x Stopping time (h) x Emission factors (g/kWh)} \quad (1)$$

The calculation was performed for all planned ships. The global annual emissions due to the whole traffic of cruise ships in the port of Venice, calculated for a total of 8478 hours, potentially avoidable by cold-ironing implementation, are summarized in Table 5.

Table 5: Total emissions for the year 2012 generated by all operated ships

Engine emissions [t]				
NOx	SOx	VOC	PM	CO
705,62	30,85	103,76	62,26	114,15

6 PROBABILISTIC ANALYSIS OF SCENARIOS

By a probabilistic analysis carried out on the timetable of cruise ships, it has been identified a minimum number of stalls occupied equal to 4, corresponding to a coverage of 80% of the traffic. The following scenarios (number of stalls to be electrified, served ships and supply energy summarized in Table 6) to be assessed by CBA, have been defined on the basis of the following assumptions:

- number of stalls actually used;
- maximum number of moored ships per day;
- presence of stalls in the same docks, for possible technical installations;
- forecast of more polluting ships in 4 more used quays.

Table 6: Scenarios key parameters

	Scenario 1	Scenario 2	Scenario 3	Scenario 4	Scenario 4 bis
Number of stalls	11	8	6	4	4
Requested energy [kWh]	69.177.749	68.983.441	62.358.146	46.956.516	58.245.860
Number of ships	86	84	58	54	26

7 COST-BENEFIT ANALYSIS OF PROPOSED SCENARIOS

For a comparison between the various proposed techno-economic scenarios it has been implemented a careful CBA, in order to estimate the most effective scenarios in specific economic contexts [1] [6]. Due to the difficulties to obtain data about the costs to install cold-ironing systems it was decided to perform a parametric study based on preliminary assessments of investment and operational costs. The analysis is based on an initial Net Present Value (NPV) threshold set to 30% of those costs. The investment will be considered convenient insofar as the NPV will be at least 30% of the investment costs (evaluated as a limit value that a possible investor may accept to undertake the investment). It is assumed that the investment will be concentrated in the first year, but amortized over 5 years (5.5% per year for 5 years = 30% approximately) and the project life cycle was assumed at 15 years.

7.1 Financial analysis

The benefits considered in the financial analysis are related to the saving in operational costs due to fuel and electric energy consumptions.

$$B = [C_o\text{-}C_{sc}]_{internal} \tag{2}$$

- C_o is the cost of fuel in the present situation (reference scenario);
- C_{sc} represents the cost of electricity consumption in the reference scenario.

7.2 Economic analysis

In the economic analysis additional benefits are due to the difference in external costs related to pollutant emissions.

$$B = [C_o\text{-}C_{sc}]_{internal}+[C_o\text{-}C_{sc}]_{external} \tag{3}$$

where:

- C_o is the cost of fuel in the present situation (reference scenario);
- C_{sc} represents the cost of electricity consumption in the reference scenario;
- C_o is the external cost of emissions in the reference scenario due to fuel consumption;
- C_{sc} is the external cost of emissions in the reference scenario due to electric energy consumption.

In figure 3 are reported the results obtained in the 5 scenarios.

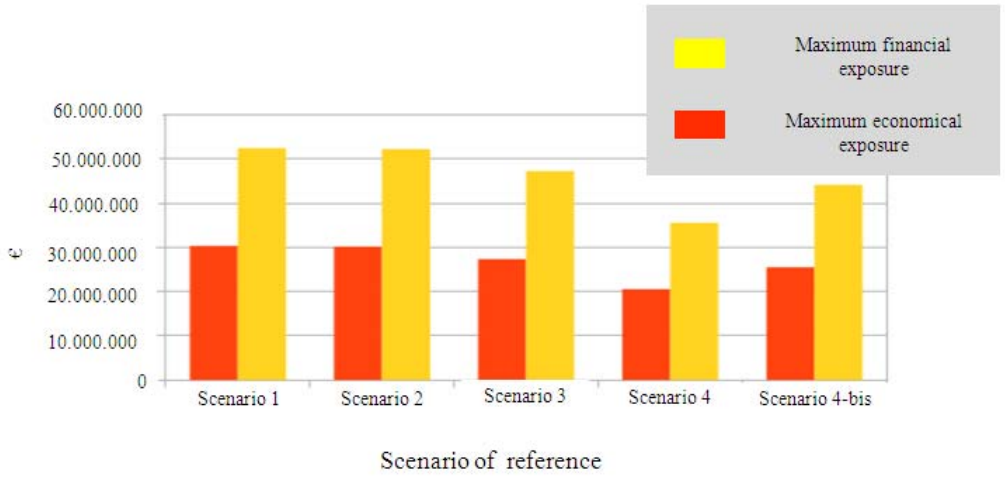


Figure 3: Results of CBA (red: maximum financial exposure – yellow: maximum economic exposure)

The CBA results highlight that the benefits are proportional to the quantity of energy that is provided by means of the cold-ironing system, as well as the financial exposure of the project. On the other hand, the bigger is the number of electrified quays and vessels to be converted to the new supply system the higher is the investment costs to be incurred. Therefore the feasibility of the project is not absolutely granted. In scenario 4-bis, despite the same number of electrified docks and a smaller number of vessels to be converted, there is a relevant increase of the financial and economic exposures. Indeed this scenario achieves larger benefits with lower costs, due to the use of the docks by the most polluting vessels.

7.3 Sensitivity analysis

For the most effective scenario (4-bis) it has been performed a sensitivity analysis based on the variation of fuel and electricity prices used for financial analysis and calculating once more the threshold of maximum financial exposure (Table 7).

Table 7: Threshold of maximum financial exposure related to scenario 4-bis [M€]

Fuel price [€/t]	Electric Energy price [€/Mwh]									
	90	**100**	**110**	**127**	**135**	**145**	**160**	**180**	**195**	**215**
500	10,96	5,86	0,76	-	-	-	-	-	-	-
550	16,65	11,55	6,45	-	-	-	-	-	-	-
605	22,90	17,80	12,70	4,04	-	-	-	-	-	-
670	30,29	25,19	20,09	11,43	7,35	2,25	-	-	-	-
794	44,39	39,29	34,19	25,52	21,45	16,35	8,70	-	-	-
810	46,21	41,11	36,01	27,34	23,26	18,17	10,52	0,32	-	-
890	55,30	50,21	45,11	36,44	32,36	27,26	19,61	9,42	1,77	-
975	64,97	59,87	54,77	46,10	42,03	36,93	29,28	19,08	11,43	1,24
1075	76,34	71,24	66,14	57,47	53,4	48,3	40,65	30,45	22,8	12,61
1180	88,28	83,18	78,08	69,41	65,33	60,23	52,59	42,39	34,74	24,54

The two factors are incremented by 10% steps, starting from the initial value proposed. The empty cells in the table are negative values (high electricity price and low fuel price) with ships powered by fuel. In Figure 4 each value of energy price is associated with a coloured curve versus the maximum financial exposure thresholds.

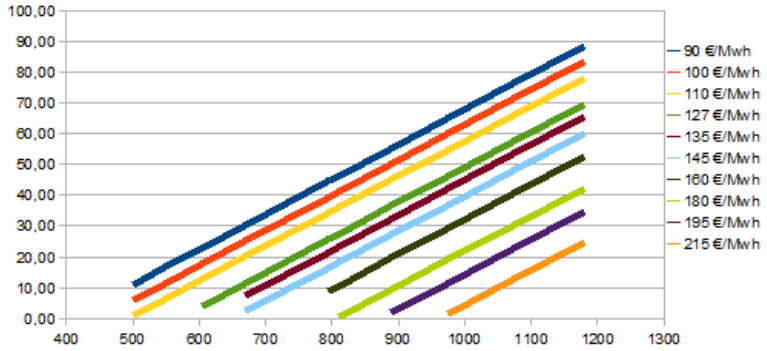


Figure 4: Variation of the threshold maximum financial exposure for the scenario 4-bis according to the prices of fuel and electricity

The relationship between the analysed parameters is linear. On this basis it is possible to estimate the threshold of maximum financial exposure corresponding to the prices of the two parameters (by entering the chart with a certain value of fuel price, intersecting the curve of electricity price curve and then reading the result on the horizontal axis).

7.4 Cost-benefit analysis summary

The analysis (summarised in Table 8) showed that the cold-ironing can offer benefits both financially (electricity cost lower than fuel cost) and economically, thanks to relevant emissions reductions. The sensitivity analysis showed that Scenarios 1 to 4 are almost invariant with respect to the combination of parameters, as well as Scenario 4-bis lets achieve significantly better results.

8 ECONOMIC-FINANCIAL FEASIBILITY OF PROPOSED SCENARIOS

Starting from the proposed scenarios, some assumptions about electrification docks equipment based on USA studies on cold-ironing have been taken and the corresponding costs items have been estimated to define an order of magnitude of the global costs [2]. In Table 9 a comparison among scenarios in terms of economic indicators is showed. Scenario 4-bis turns out to be the most efficient because it is the only one that ensures financial coverage of the investments. The remaining scenarios only provide economical coverage. The efficiency of scenario 4-bis is conditioned by the docking of the 26 most polluting ships on Isonzo and Tagliamento docks, which should be ensured by the reorganization of ship moorage aside the stalls organization for year 2012.

Table 8: Summary of CBA parameters and results

		Scenario 1	Scenario 2	Scenario 3	Scenario 4	Scenario 4-bis
Number of stalls to be electrified		11	8	6	4	4
Required energy [kwh]		69,177,749	68,923,441	62,358,146	46,956,516	58,245,860
Number of ships to be converted		86	84	58	54	26
Reduction of emissions [t/year]	NOx	674.23	671.76	607.77	457.66	567.69
	SOx	-12.98	-12.93	-11.70	-8.81	-10.93
	VOC	103.52	103.14	93.31	70.27	87.16
	PM	60.52	60.29	54.55	41.08	50.95
	CO	100.71	100.34	90.78	68.36	84.79
Maximum financial exposure [€]		30,315,203	30,203,760	27,326,704	20,577,373	25,524,610
Maximum economic exposure [€]		52,424,178	52,231,459	47,256,157	35,584,517	44,139,791

Table 9: Comparison among scenarios

	Possible investment cost	Maximum financial exposure	Investment coverage	Maximum economic exposure	Investment coverage
Scenario 1	57,000,000	30,315,203	NO	52,424,178	YES
Scenario 2	55,200,000	30,203,760	NO	52,231,459	YES
Scenario 3	38,900,000	27,326,704	NO	47,256,157	YES
Scenario 4	35,800,000	20,577,373	NO	35,584,517	YES
Scenario 4-bis	19,000,000	25,524,610	YES	44,139,791	YES

9 CONCLUSIONS

The use of the cold-ironing system is characterised by a very high level of complexity for the wide range of aspects and for the great number of stakeholders, whose primary goals are sometime different. Therefore the adoption of joint decisions meeting the needs of all operators is rather complicated. In the analysed case study are mainly faced the technical and economic aspects of the project, with a focus on the reduction of the emissions, without considering all technical details concerning the equipment required for the implementation of the cold-ironing. The cold-ironing system provides an important contribution for the reduction of emissions, mainly because the energy consumption of the cruise ships is high in comparison with other typologies of commercial ships. This high consumption is due to the energy need of a wide range of on-board equipment, in order to satisfy the passengers' needs. Different implementation scenarios have been proposed. The most efficient scenario (4-bis) requires additionally a change into the assignment of ships to docks in comparison with the present situation. The other scenarios lead to a further reductions of the emissions, since they consider a higher amount of equipped ships and docks, but the economic and financial

indicators proposed are lower due to higher investment costs. Only the 4-bis scenario ensures both financial and economic coverage. The other scenarios reach the economic coverage only, therefore their feasibility depends on the adoption of incentive schemes to cover the total investment.

REFERENCES

[1] Environ International Corporation. *Cold ironing cost effectiveness port of Long Beach*. Volume I – Report - Long Beach, California (2004).

[2] Ericsson P. and Fazlagic I.. *Shore side power supply. A feasibility study and a technical solution for an on-shore electrical infrastructure to supply vessels with electric power while in port*. Master of Science Thesis. Chalmers university of technology – Goteborg, Sweden (2008).

[3] Trozzi C., Vaccaro R..*Methodologies for estimating future air pollutant emissions from ships*, Techne report MEET RF98b (August 1998)

[4] Trozzi C., De Lauretis R. EMEP/EEA *Emission inventory guide book* (2009)

[5] Trozzi C.. *Update of Emission Estimate Methodology for Maritime Navigation*, Techne Consulting report ETC.EF.10 DD (2010).

[6] Environ International Corporation. *Final Report Shoreside Power Feasibility Study for Cruise Ships Berthed at Port of San Francisco*, San Francisco California (2005)

[7] ARB. (2006). Cold ironing report. Available on: http://www.arb.ca.gov/ports/marinevess/documents/coldironing0306/report.pdf [access on 20th December 2012]

MATHEMATICAL SIMULATION AND COMPUTER SYSTEM FOR PRE-PROCESSING OF PROPELLER GEOMETRY FOR CFD ANALYSIS AND PRODUCTION APPLICATIONS

MARINE 2013

ALEKSEY Yu. YAKOVLEV, NIKOLAY V. MARINICH, ANNA A. SENYUSHKINA

FSUE Krylov State Research Centre
Moskovskoe shosse 44, St. Petersburg, Russia
e-mail: krylov@krylov.ru, web page: http://www.krylov.spb.ru

Key words: propeller, approximation, 3D model, software

Abstract. The paper presents a method for mathematical description of the propeller geometry. The method is implemented using a set of software modules and makes it possible to describe the propeller geometry for analysis and production purposes. The propeller geometry representation contains an approximation of blade surfaces including the sharpened trailing edges as well as the hub and fillet between the blade and the hub. The paper gives analytical expressions of the above-said surfaces, the algorithm for data pre-processing and transmission with subsequent generation of the 3D model. An example of 3D propeller model obtained by this method is given.

1 INTRODUCTION

The digital geometry representations of various products are nowadays used in practically all phases of product development from the preliminary design to final production. This is also done in the development of ship propellers noted for their complex shapes. In view of the specific requirements in propeller design and production a range of specific software tools are used to meet the needs of each specific phase in propeller development, and therefore, different methods of data presentation are applied. Based on the preliminary comparison of various software tools it has been found that not only the data processing software and preferable data presentation formats are different, but also the requirements regarding the accuracy of surface description as well as the methods of surface approximation are widely ranging at different stages of development. In practice the most accurate source of propeller geometry data remains to be the propeller drawing, which requires generation of a new 3D model at each stage. This is a costly and time-consuming situation. Therefore, it is advisable to have one common mathematical model for propeller geometry representation to be used as a basis for easy generation of the 3D model applicable throughout the propeller development from design to production.

2 PROBLEM STATEMENT

As it was mentioned above, the most traditional and commonly accepted approach is to specify all the main propeller geometry details on the propeller drawing. In this case the actual propeller geometry details are given in the tabulated format with manual graphical interpolation of the tabulated values. In the 1970s – 1980s the methods of propeller geometry description drastically changed with the advent of numerically controlled machines, automatic drawing equipment and computational analysis tools introduced in the production workshops and design offices. At that time some theoretical studies on the propeller geometry description were undertaken in the Soviet Union to develop new methods and software for propeller geometry representation and production of propeller drawings. The milestones of these studies are described in ref. [1, 2] and in the monograph [3] summarizing the results of studies by N. Yu. Zavadovsky recognized as a leading authority in this field.

The method developed in these studies was based on the approximation of the main geometrical details of propeller blades. However, even at that time it was noted [3] that for CNC-machines it would be preferable to have the blade geometry description based on the surface approximation using a set of specified points. This approach was developed using standard software packages [4]. The requirement for such specification of the propeller geometry was growing with the implementation and development of CAD/CAM systems, CFD techniques and graphical software packages. The modern specialist systems for propeller development are able to generate the 3D model in a range of widely used formats [8], [9]. However, such model would inevitably be different from the initial theoretical geometry and this discrepancy would grow with the number of transformations. In this context it is advisable to develop a method for distortion-free transmission of the propeller geometry to allow the end user obtain the accurate geometry in the most convenient format for his specific applications. The method proposed in ref. [3] is believed to be the most suitable tool for this purpose. However, it needs to be significantly improved and extended to present the whole propeller rather than its individual blades. Also, the method of ref. [3] was earlier used for generation of drawings, while in our case it should be modified to solve various problems for a wide range of users as well as to generate 3D models. In the following sections it will be shown how these issues are dealt with.

3 MATHEMATICAL MODEL OF PROPELLER

3.1 Coordinate systems

Traditionally, the propellers are analyzed using a number of different coordinate systems. Each of these systems is used to solve certain specific issues.

The most common system is the propeller-fixed Cartesian coordinate system 0xyz (Fig. 1). In this system the 0x-axis coincides with the axis of propeller rotation and it is positive in the ship advance direction (whence comes the inflow). 0y-axis is positive vertically upward and it usually coincides with the propeller axis line which is used as reference for arranging all blade elements. The axes origin is at the intersection of propeller axis of rotation and propeller axis line. 0z-axis is positioned with respect to the above-defined axes to form the right-hand coordinate system.

Apart from the rectangular coordinate system, it is also common to apply for propellers the cylindrical coordinate system 0xrθ. This system is introduced traditionally as follows

$$\begin{cases} x = x \\ y = r \cdot \cos\theta \\ z = r \cdot \sin\theta \end{cases} \quad \text{and} \quad \begin{cases} x = x \\ r = \sqrt{y^2 + z^2} \\ \theta = arctg\, {}^{z}\!/_{y} \end{cases} \tag{1}$$

where r – radial coordinate and θ – angular coordinate (Fig. 1).

The cylindrical coordinate system is orthogonal like the Cartesian coordinate system, which facilitates manipulations.

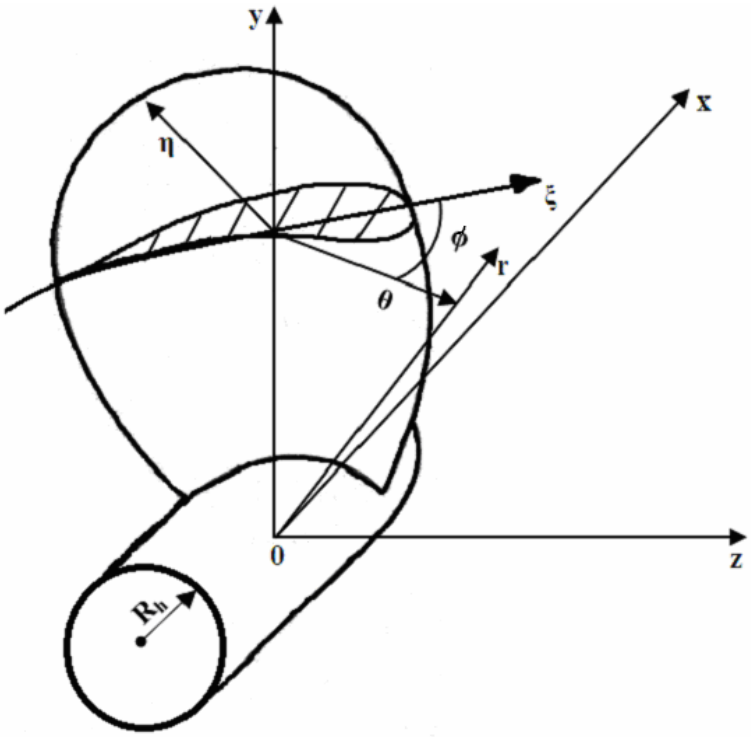


Figure 1: Coordinate systems used for propeller geometry description

For the analysis of propeller geometry the helical coordinate system 0rξη is introduced (Fig. 1). In this system the radial coordinate is defined like in the cylindrical coordinate system. The 0ξ-axis is directed along the chord of the blade cylindrical section. Since the angle between the chord and propeller disk plane (pitch angle) □ depends on the radius, the coordinate system is no longer rectangular. The third axis 0η is normal to the 0ξ-axis and directed from the blade pressure side to the blade suction side.

$$\begin{cases} r = \sqrt{y^2 + z^2} \\ \xi = x \cdot \sin\phi + r \cdot \theta \cdot \cos\phi \\ \eta = x \cdot \cos\phi - r \cdot \theta \cdot \sin\phi \end{cases} \quad \text{and} \quad \begin{cases} x = \xi \cdot \sin\phi + \eta \cdot \cos\phi \\ y = r \cdot \cos\left(\dfrac{\xi \cdot \cos\phi - \eta \cdot \sin\phi}{r} \right) \\ z = r \cdot \sin\left(\dfrac{\xi \cdot \cos\phi - \eta \cdot \sin\phi}{r} \right) \end{cases} \tag{2}$$

Where □ – pitch angle.

Unfortunately, since the 0rξη system is not orthogonal, the tensor analysis tools have to be used.

3.2 Parametric representation of blade geometry

The propeller geometry is generally specified by a number of characteristic parameters in function of r and ξ [7]. Usually the radius functions of width C, pitch P, maximum cylinder section thickness t and cylinder section camber f_M are used. The blade pitch can be expressed in terms of the earlier introduced pitch angle $\phi = arctg\left(\dfrac{P}{2\pi r} \right)$. Since the blade may have an asymmetric shape, i.e. have an angular or axial displacement of blade sections, the radius functions of skew Cs and rake i_G are introduced. The skew defines the displacement of blade sections along 0ξ-axis, while the rake defines the blade section displacement along the 0x-axis. Skew can be represented in terms of skew angle θ_S: $C_S = \dfrac{r \cdot \theta_S}{\cos\phi}$. The above–mentioned directions of displacements are not independent, which complicates the task of geometry representation. In addition, the functions $F_t\left(r, \tilde{\xi}\right)$ and $F_c\left(r, \tilde{\xi}\right)$ are used for representation of the cylinder blade section outline. These functions give the chord-wise distribution of the thickness ratio and camber line at each radius. These values are ratios because they are related to the maximum thickness and camber of blade section at respective radii. The variable $\tilde{\xi}$ used here is more convenient than ξ for the geometry description and it has a linear relation with ξ.

$$\xi = C_S\left(\bar{r}\right) + \frac{C\left(\bar{r}\right)}{2}\tilde{\xi} \tag{3}$$

Moreover, this relation shows that the variable $\tilde{\xi}$ is non-dimensionalized with respect to the blade width at each radius, so that $\tilde{\xi} = 1$ at the leading edge and $\tilde{\xi} = -1$ at the trailing edge of the blade.

Thus, the mathematical description of the blade geometry using the above-defined parameters is represented as coordinates of the point on blade surface $\vec{r}_b$ in function of curvilinear coordinates r and $\tilde{\xi}$

$$\vec{r}_b = \vec{r}_b\left(r,\tilde{\xi}\right) = x_b\left(r,\tilde{\xi}\right)\cdot\vec{i} + y_b\left(r,\tilde{\xi}\right)\cdot\vec{j} + z_b\left(r,\tilde{\xi}\right)\cdot\vec{k} \tag{4}$$

Where $\vec{i}$, $\vec{j}$, $\vec{k}$ are Cartesian vectors.

The components of vector $\vec{r}_b$ are expressed as follows

$$\begin{aligned} x_b &= i_G(\bar{r}) + \left(C_S(\bar{r}) + \frac{C(\bar{r})}{2}\tilde{\xi}\right)\cdot\sin\phi + \eta\left(\bar{r},\tilde{\xi}\right)\cdot\cos\phi \\ y_b &= r\cdot\cos\left(\frac{C_S(\bar{r}) + \frac{C(\bar{r})}{2}\tilde{\xi}}{2}\cdot\cos\phi - \eta\left(\bar{r},\tilde{\xi}\right)\cdot\frac{\sin\phi}{r}\right) \\ z_b &= r\cdot\sin\left(\frac{C_S(\bar{r}) + \frac{C(\bar{r})}{2}\tilde{\xi}}{2}\cdot\cos\phi - \eta\left(\bar{r},\tilde{\xi}\right)\cdot\frac{\sin\phi}{r}\right) \end{aligned} \tag{5}$$

This expression is traditionally used for representing the propeller blade geometry [8]. In these relations the following representation of the pressure and suction sides of the blade is used

$$\eta\left(\bar{r},\tilde{\xi}\right) = F_c\left(\bar{r},\tilde{\xi}\right)\cdot f_M \pm F_t\left(\bar{r},\tilde{\xi}\right)\cdot\frac{t}{2} \tag{6}$$

Where the plus sign corresponds to the suction side, while the minus sign corresponds to the pressure side of the blade.

3.3 Blade surface approximation

The above-given mathematical representation of the blade (5) (6) requires that the above-mentioned blade parameters be specified in function of the variables r and $\tilde{\xi}$. For approximating these relations a special spline-approximation technique was developed [8]. The splines in this case are used to smooth the initial data at the propeller design stage, and in this case it is required to visually check the generated functions.

The smoothing splines for the parameters C, Cs, i_G, t, f_M and P are generated by minimization of functional J for the class of functions with continuous second derivative

$$J = \alpha\int_{r_0}^{r_N}\left|f''(r)\right|^2 dx + \sum_{i=0}^{N}\frac{\left[f(r_i) - f_i^*\right]^2}{\rho_i} \tag{7}$$

Where $\alpha \geq 0$, $\rho_i \geq 0$, $f(r)$ - approximating function, f_i^* - values of respective parameters specified at radii r_i.

The lower are α and ρ_i values, the closer is the function bringing the min J to the interpolation spline plotted on the basis of f_i^* values.

For approximating the geometric particulars of blade surface it is convenient to impose the

following additional requirements on the smoothing spline:
- the spline is to pass the extreme radius values r_0 and r_N exactly, i.e. $f(r_0) = f_0^*$ and $f(r_N) = f_N^*$
- the spline is to satisfy the boundary conditions defining the parameter behavior at blade edges to obtain a smooth shape for the whole blade;
- weight factors ρ_i take two values: 1 or 0 depending on whether it is allowed for the curve to pass beside this point or not;
- the spline is to meet the following condition $\max_i \left| f(r_i) - f_i^* \right| \le \varepsilon$, where ε – given allowed deviation of the spline from the ordinates f_i^*.

The surfaces have to be smoothed only by approximation of the functions $F_t(r, \tilde{\xi})$ and $F_c(r, \tilde{\xi})$. The problem of generating a bi-cubic spline approximating these functions based on given f_{ij}^* and boundary conditions is solved in three steps. First, one-dimensional smoothing splines over the radius are generated for all values of $\tilde{\xi}_j$; secondly, the cubic splines are constructed based on the values of the first splines for different r_i for all i, thirdly, the interpolation bi-cubic spline is obtained.

3.4 Mathematical description of propeller blade surface

Equations (5) allow us to describe the point coordinates on blade surface as a function of curvilinear coordinates r and ξ. If in this case the relation $\eta = \eta(r, \xi)$ of form (6) is used for surface description, a smooth blade shape is generated. However in practice it is common to specially profile, e.g. sharpen blade edges. Also, relations (5) (6) do not take into account the blade fillet.

Therefore, a special representation of the function η is applied to include modifications in the smooth blade geometry introduced while developing the real propeller. In this case the smooth blade shape corresponding to (6) is taken as the basis. This shape is obtained using the necessary modifications introduced in certain local areas.

As an example the relationship is given below, which is used for the case of sharpened trailing edge

$$\eta(\bar{r}, \tilde{\xi}) = \begin{cases} F_c(\bar{r}, \tilde{\xi}) \cdot f_M \pm F_t(\bar{r}, \tilde{\xi}) \cdot \dfrac{t}{2}, & \tilde{\xi} > \tilde{\xi}_L \\ \pm \left[\dfrac{e_T}{2} \cdot \dfrac{\tilde{\xi}_L - \tilde{\xi}}{L} + F_t(\bar{r}, \tilde{\xi}_L) \cdot \dfrac{t}{2} \cdot \dfrac{\tilde{\xi}_L + 1}{L} \right], & \tilde{\xi} < \tilde{\xi}_L \end{cases} \quad (8)$$

Where $\tilde{\xi}_L$ - defines the starting point of trailing edge sharpened section, e_T – thickness at the sharpened edge tip.

Other types of modifications can also be introduced in the initial smooth propeller blade geometry for practical applications such as rounding of trailing edges, smoothing of blade tip, etc.

Since it becomes rather difficult to specify the blade geometry by expression (5) including

the relations similar to (8), the surface elements are usually determined numerically by calculations rather than described analytically. For example, it should be noted that the normal to surface can be found from the formula

$$\vec{n}_b = \frac{\frac{\partial \vec{r}_b}{\partial r} \times \frac{\partial \vec{r}_b}{\partial \tilde{\xi}}}{\left| \frac{\partial \vec{r}_b}{\partial r} \times \frac{\partial \vec{r}_b}{\partial \tilde{\xi}} \right|} \tag{9}$$

3.5 Mathematical description of propeller hub

The propeller hub surface is an axisymmetric body whose axis of symmetry coincides with the axis of propeller rotation (0x-axis) (Fig. 1). Therefore, the hub surface can be represented well in the cylindrical coordinates $\vec{r}_h = \vec{r}_h(x, \theta)$. This relation can be expressed as

$$\begin{aligned} x_h &= x \\ y_h &= R_h(x) \cdot \cos\theta \\ z_h &= R_h(x) \cdot \sin\theta \end{aligned} \tag{10}$$

Where $R_h(x)$ – hub meridian section shape.
It is simple to calculate the normal vector at each point of the hub surface using the vector product of basis vectors in curvilinear coordinates.

$$\vec{n} = \frac{R_h'(x)}{\sqrt{1+\left[R_h'(x)\right]^2}} \cdot \vec{i} + \frac{\cos\theta}{\sqrt{1+\left[R_h'(x)\right]^2}} \cdot \vec{j} + \frac{\sin\theta}{\sqrt{1+\left[R_h'(x)\right]^2}} \cdot \vec{k} \tag{11}$$

Where the prime sign means the derivative with respect to x.

The shape of meridian section $R_h(x)$ is approximated based on a given set of points using the interpolation quadratic spline, which makes it possible to model hubs of complex shapes.

3.6 Definition of fillet surface

The fillet transition between the blade surface and hub is an important detail of propeller geometry to be considered in the strength and hydrodynamic analyses. The issues related to the fillet surface definition were analyzed in [3], however the integrated description of propeller geometry was not available at that time because it was not required for practical applications. In this study it is attempted to develop the mathematical description of the propeller as a whole and this representation should include the fillet transition.

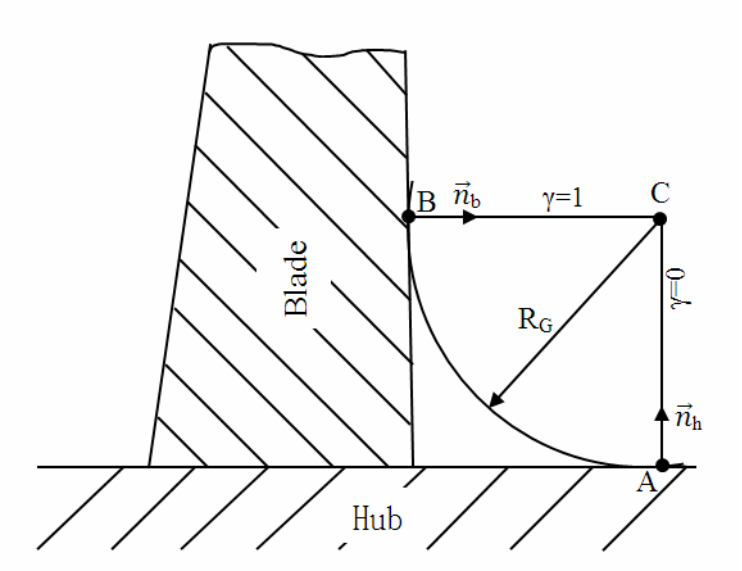


Figure 2: Construction of fillet transition

Usually, it is assumed that the blade and hub are joined by a circle of given radius. Based on this condition it is required to find the coordinates $\vec{r}_C$ of the center in the circle forming the fillet in the given section (at given $\tilde{\xi}$). The point $\vec{r}_C$ shall be located at the same specified distance from the blade and hub surface equal to the fillet radius R_G. Based on this requirement and using eq. (11) it is easy to derive a set of equations for finding the fillet radius and fillet/hub attachment point

$$\begin{cases} x_b\left(r,\tilde{\xi}\right)+R_G\cdot n_{bx}\left(r,\tilde{\xi}\right)=x_A+R_G\cdot\dfrac{R_h'(x_A)}{\sqrt{1+\left[R_h'(x_A)\right]^2}}=x_C \\ y_b\left(r,\tilde{\xi}\right)+R_G\cdot n_{by}\left(r,\tilde{\xi}\right)=\left[R_h(x_A)-\dfrac{R_G}{\sqrt{1+\left[R_h'(x_A)\right]^2}}\right]\cdot\cos\theta_A=y_C \\ z_b\left(r,\tilde{\xi}\right)+R_G\cdot n_{bz}\left(r,\tilde{\xi}\right)=\left[R_h(x_A)-\dfrac{R_G}{\sqrt{1+\left[R_h'(x_A)\right]^2}}\right]\cdot\sin\theta_A=z_C \end{cases} \quad (12)$$

Where, the unknown values are the radius r at which the fillet is joined with the blade and the cylindrical coordinates x_A and θ_A of the point where the fillet is attached to the hub.

By solving numerically this non-linear system of equations one can find the above unknowns for all coordinates $\tilde{\xi}$. It should be noted that the fillet radius may vary in function of this coordinate $R_G=R_G\left(\tilde{\xi}\right)$. After the unknown values are found, Equations (12) give coordinates $\vec{r}_C$ of the center in the circle forming the fillet

$$\vec{r}_G\left(\tilde{\xi},\gamma\right)=\vec{r}_C-R_G\cdot\left[\left(1-\gamma\right)\cdot\vec{n}_h+\gamma\cdot\vec{n}_b\right] \tag{13}$$

Where γ – coordinate along the fillet circle arc variable from 0 to 1, $\vec{n}_h$ and $\vec{n}_b$ are normal to the hub and blade surfaces defined in the fillet attachment points.

4 PROPELLER GEOMETRY DATA GENERATION AND FLOW CHART

The flow chart of propeller geometry data is given in Fig.3. At first the design specifications are worked out. Based on these specifications the main propeller parameters are determined and its blade system is designed. The obtained blade parameters are smoothed using spline approximations (see item 3.3). Then a special-purpose software module is used to create a file containing the propeller blade and hub descriptions as well as the fillet and blade edge sharpening details. The data generated by this module are to be transmitted by e-mail or local network.

The end users can be propeller or model manufacturers, CFD designers or strength analysts. All end users have a special-purpose data interpretation module. This module will check the propeller data received and represent the propeller geometry in the formats as required by this specific user.

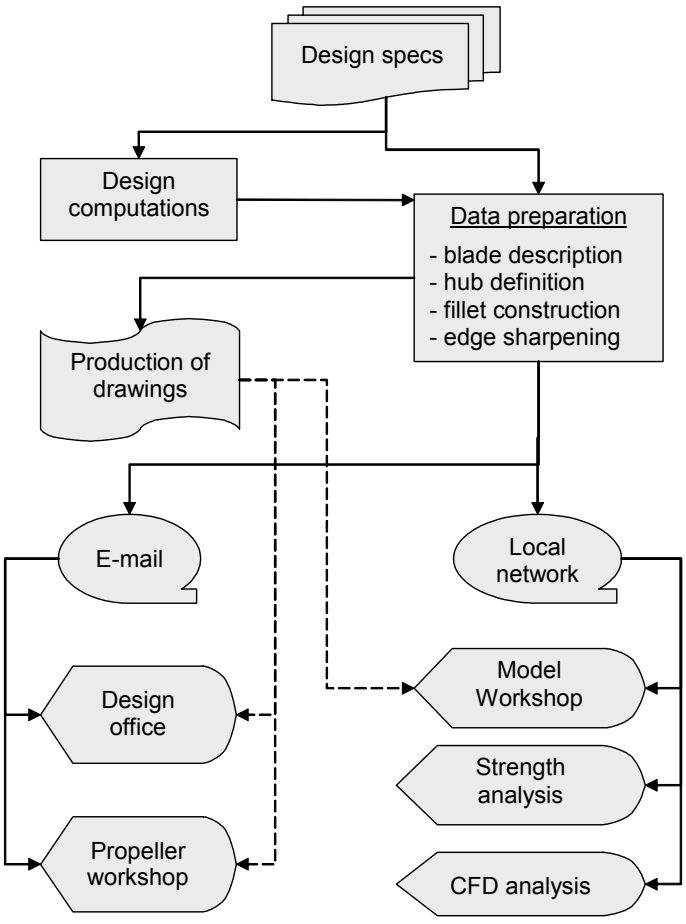


Figure 3: Flow chart of propeller geometry data

5 GENERATION OF 3D MODEL USING RECEIVED DATA

Based on the mathematical description of propeller it is required to generate and format the data as necessary to deal with specific task. The main principle in formatting these data is as follows. Sets of points are generated on the propeller surface based on the user-specified mesh size of the grid on this surface. Further, these coordinates are either directly converted in the geometry description format or in a set of micro-commands, which can be interpreted by the appropriate software package or code.

5.1 Preparation of data for generating the geometry

The following calculations are done to construct the 3D propeller model. The propeller blades outside the fillet attachment area are broken down into sets of points located at the same cylindrical sections.

$$\vec{r}_{ij} = \vec{r}_b\left(r_i, \tilde{\xi}_j\right), \quad i = \overline{1, N}, \quad j = \overline{1, M} \tag{14}$$

Where N – number of cylindrical sections used for generating the model, M – number of points in each section.

Usually the number of points at all sections is the same, and their coordinates $\tilde{\xi}$ are repeated for each section. This makes it easy to find the guiding lines for surface generation.

The fillet area is described by other sets of points. In this case the curvilinear coordinates are $\tilde{\xi}$ and parameter γ. Thus, we have an additional set of points

$$\vec{r}_{ij} = \vec{r}_\gamma\left(r_i, \tilde{\xi}_j\right), \quad i = \overline{N+1, N+N_G}, \quad j = \overline{1, M_G} \tag{15}$$

Where N_G – number of the parameter γ values used for generation of the model , M_G – number of grid points along the hub.

Finally, the hub surface can be defined in different ways for modeling. In some packages it is sufficient to specify points on one meridian section, and the package itself can use these points to construct the body of revolution. In this case

$$\vec{r}_{i0} = \vec{r}_h\left(x_i, 0\right), \quad i = \overline{N+N_G+1, N+N_G+N_H} \tag{16}$$

Where N_H – number of points at the meridian section.

However in a general case one has to specify points on the hub surface. It can be done by specifying a number of meridian sections or by break-down of hub surface in the coordinate system $0r\xi\eta$.

5.2 Examples of data preparation in different software packages

One of the examples of open formats is STL format. Under this format the propeller surface is broken down into triangular elements. This format is convenient for viewing the general view of propeller, but for practical tasks other data formats are used.

Let us consider the case when the data are transmitted to a model workshop. The propeller models are manufactured on CNC machines using CAD/CAM software of DELCAM (PowerShape, PowerMill) [9]. The package PowerShape is used for generating the propeller surface. The obtained surface is then translated into the propeller model machining software

PowerMill.

The data interpretation module creates a file readable in PowerShape. This file specifies the coordinates of points in cylindrical blade sections, coordinates of guiding lines connecting these sections and a set of circles defining the fillet transition. The fillet is constructed by mating the hub surface and propeller blades using a circle of given radius. Fig.4 shows an example of propeller model geometry ready to be passed to model workshop.

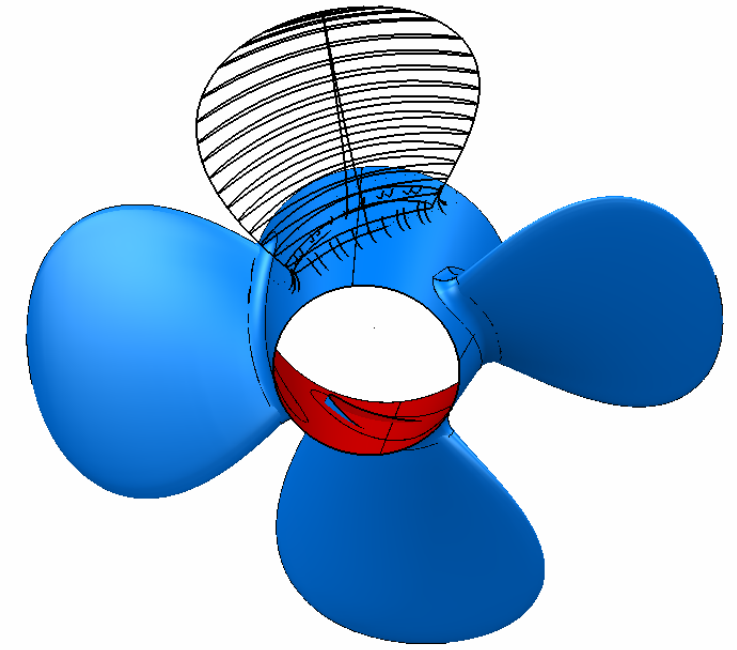


Figure 4: 3D model of propeller and framework for its generation obtained by the method described in the paper

6 CONCLUSIONS

- A modified mathematical representation of propeller geometry has been developed based on the conducted investigations. This representation gives full description of the propeller surface including blades, hub and fillet. It allows introduction of blade modifications, the simplest example being sharpening of blade trailing edges. The fillet can be constructed with a variable rounding radius.
- Algorithms for construction of 3D propeller models and surface grids based on mathematical geometry representation have been developed and implemented.
- The developed method is implemented by a number of software modules able to transmit propeller geometry without distortions to propeller designers and manufacturers.

REFERENCES

[1] Zavadovksy N. Yu. Computer-aided design and manufacturing system for propellers. *Voprosy sudostroeniya. Seria proektirovania sudov.* (1974) vyp. 5, 41-46. (In Russian)

[2] Zavadovksy N. Yu., Maslennikov S. S., Rusetsky A. A. Mathematical representation of propeller surfaces and its application. *Voprosy sudostroeniya. Seria proektirovania sudov.*

(1983) vyp. 36, 98-101. (In Russian)
[3] Zavadovksy N. Yu., *Theory and methods for design of complex geometry propellers.* Krylov Shipbuilding Research Institute, St. Petersburg (2004). (In Russian)
[4] Kerr, C. J. Use of CAD/CAAAM in Propulsor Design / Production at David Taylor *Propellers'88 Symposium.* Virginia Beach. (1988) Pp. 18.1-18.9.
[5] B. P. Epps, M. J. Stanway, and R.W. Kimball OpenProp: An Open-source Design Tool for Propellers and Turbines / *SNAME Propellers and Shafting Conference* (2009).
[6] *Practical propeller modeling: from concept to 3D CAD model.* A HydroComp technical report, Report 131.
[7] *ITTC – Recommended Procedures and Guidelines*. (1999) 7.5 – 01 02 – 01
[8] Bavin V.F., Zavadovksy N. Yu, Levkovsky Yu.L., Mishkevch V.G. *Propellers. Modern design methods*. Leningrad. Sudostroenie (1983). (In Russian)
[9] B. L. Baskov, A. V. Bitsulya, V. V. Saitov, A. A. Stroganov Practical application of DELCAM software packages for production of ship and propeller models / *Ratsionalnoe Upravlenie Predpriyatiem* (2007), #3 (In Russian).

V International Conference on Computational Methods in Marine Engineering
MARINE 2013
B. Brinkmann and P. Wriggers (Eds)

AXISYMMETRIC TRANSIENT MODELLING OF A WIND TURBINE FOUNDATION IN COHESIONLESS SOIL USING THE PREVOST'S MODEL

B. CERFONTAINE*,†, S. LEVASSEUR† AND R. CHARLIER†

*FRIA, FRS-FNRS, National Fund for Scientific Research
Brussels, Belgium
e-mail: b.cerfontaine@ulg.ac.be

† Geomechanics and Geological Engineering
Department ArGEnCo, University of Liege
Sart-Tilman, Liege, Belgium

Key words: Prevost's Model, Suction Caisson, Constitutive Law

Abstract. Suction caissons are more and more used for offshore foundations. This paper deals with the cyclic modelling of suction caissons using the Prevost's model. The case study is a 8m large diameter caisson embedded in dense No. 0 Lundsand. Parameters for the model are calibrated using drained triaxial tests. A parametric study concerning the influence of the constitutive law, the skirt length and permeability is carried out.

1 INTRODUCTION

Nowadays, offshore power plants are gathering momentum [1]. Developers are planning new wind farms in deeper waters and further away from the coasts for economical and environmental purpose as well. Wind turbines are growing in size and power, increasing the foundation requirements. Developing an accurate design approach is a crucial issue for private companies that aim to decrease building costs. Foundation costs may represent up to 30 % of the total [2]!

Suction caissons are a serious alternative to piling for offshore structures. These are lighter, easier to install and cheaper than classical foundations [3]. The caisson is set up by reducing the water pressure inside the bucket by pumping. The differential pressure on the top of the caisson induces a downward force that digs the foundation into the soil.

Numerical modelling of this kind of offshore foundations is not trivial. Simple numerical models exist, based on in-situ test measurements, semi-empirical methods or macro-elements [3, 4, 5, 6]. Classical isotropic-hardening models are not able to truly represent the cyclic loading paths which involve elastic and plastic deformations in both loading and unloading cases. One should consider more sophisticated models such as the Prevost's

model [7] which is dedicated to represent cyclic behaviour of cohesive or frictionless soils. An improved version of this model is available in [8] in the scope of earthquake modelling. An application to offshore gravity structures is available in [9] for cohesive soil.

The Prevost's model is applied in this paper to a suction caisson case study to highlight the main features of the cyclic loading of offshore foundations. The main objective is to test the possibilities and limitations of the model for this purpose. A parametric study is carried out on both skirt length and permeability.

2 THE PREVOST'MODEL

2.1 Definitions

The sign convention of soil mechanics is adopted : compressive stresses and strains are positive. The Macauley brackets $\langle\rangle$ are defined according to

$$\langle f \rangle = \begin{cases} 0, & f < 0 \\ f, & f \geq 0 \end{cases} \tag{1}$$

The symbol":" indicates a dot product between two tensors (in bold characters). For example, if $\boldsymbol{\sigma'}$ is the effective (Cauchy) stress tensor, the product $\boldsymbol{\sigma'} : \boldsymbol{\sigma'} = \sigma_{ij} \cdot \sigma_{ij}$ in index notation. The identity tensor is written $\boldsymbol{\delta}$, then the mean effective stress is defined as $p' = 1/3 \cdot \boldsymbol{\sigma'} : \boldsymbol{\delta}$. The deviatoric stress tensor and the invariant of deviatoric stresses are defined through

$$\mathbf{s} = \boldsymbol{\sigma'} - p' \cdot \boldsymbol{\delta} \qquad \text{and} \qquad \mathrm{q} = \sqrt{\frac{3}{2} \cdot \mathbf{s} : \mathbf{s}} \tag{2}$$

2.2 Constitutive equations

The Prevost's model lies within the framework of elasto-plasticity. Constitutive equations are written in incremental form. The equation below links the effective stress rate $\dot{\boldsymbol{\sigma}}'$ to the elastic deformation rate $\dot{\boldsymbol{\epsilon}} - \dot{\boldsymbol{\epsilon}}^p$

$$\dot{\boldsymbol{\sigma}}' = \mathbf{E} : \dot{\boldsymbol{\epsilon}} - \dot{\boldsymbol{\epsilon}}^p \tag{3}$$

where $\mathbf{E}$ is the fourth-order tensor of elastic coefficients, $\dot{\boldsymbol{\epsilon}}$ is the total deformation rate and $\dot{\boldsymbol{\epsilon}}^p$ is the plastic deformation rate defined through

$$\dot{\boldsymbol{\epsilon}}^p = \mathbf{P} \cdot \langle \mathrm{L} \rangle \tag{4}$$

$\mathbf{P}$ is a symmetric second-order tensor defining a non-associated plastic potential. The plastic loading function, L, is a scalar that depicts the amount of plasticity deformation and is defined in the following

$$\mathtt{L} = \frac{1}{\mathrm{H'}} \cdot \mathbf{Q} : \dot{\boldsymbol{\sigma}}' \tag{5}$$

where $\mathbf{Q}$ is a second-order tensor defining the unit outer normal to the yield surface and H' the plastic modulus associated to this surface. This normal tensor can be decomposed into its deviatoric and volumetric part as

$$\mathbf{Q} = \mathbf{Q}' + \mathrm{Q"} \cdot \boldsymbol{\delta} \tag{6}$$

2.3 Yield functions

The model is made of conical nested yield surfaces in principal stress space [7]. Their apex is fixed at the origin of axes but could be translated on the hydrostatic axis to take cohesion into account if necessary. The i-th surface is the locus of the stress states that verify

$$\mathrm{f}^i \equiv \frac{3}{2} \cdot \left(\mathbf{s} - \mathrm{p}' \cdot \boldsymbol{\alpha}^i\right) : \left(\mathbf{s} - \mathrm{p}' \cdot \boldsymbol{\alpha}^i\right) - \left(\mathrm{p}' \cdot \mathrm{M}^i\right)^2 = 0 \tag{7}$$

where $\boldsymbol{\alpha}^i$ is a kinematic deviatoric stress tensor defining the coordinates of the yield surface centre in deviatoric space and M^i is a material parameter denoting the aperture of the cone.

2.4 Plastic flow rule

The plastic potential $\mathbf{P} = \mathbf{P}' + \mathrm{P}" \cdot \boldsymbol{\delta}$ is decomposed into its deviatoric part which is associative

$$\mathbf{P}' = \mathbf{Q}' \tag{8}$$

and its volumetric part which is non-associative

$$\mathrm{P}" = \frac{1}{3} \cdot \frac{\eta^2 - \bar{\eta}^2}{\eta^2 + \bar{\eta}^2} \qquad \text{where} \qquad \eta = \frac{\sqrt{3/2 \cdot \mathbf{s} : \mathbf{s}}}{\mathrm{p}'} = \frac{\mathrm{q}}{\mathrm{p}'} \tag{9}$$

The material parameter $\bar{\eta}$ takes into account the phase transformation line defined by Ishihara [10]. This parameter rules the dilationnal behaviour and separates the p'-q plane into two zones. Stress ratios (η) lower than $\bar{\eta}$ indicate a plastic contractive behaviour whilst the other zone depicts a dilative plastic behaviour.

2.5 Hardening rule

The hardening rule of the surfaces is purely kinematic. During loading, the active surface moves up to come into contact with the next one. All surfaces inside the active one stay tangential at the current stress state. The relationship between plastic function and kinematic hardening is determined through the consistency condition [7] and leads to

$$\mathrm{p}' \cdot \boldsymbol{\alpha}^i = \frac{\mathrm{H}'}{\mathbf{Q}' : \boldsymbol{\mu}} \cdot \langle \mathrm{L} \rangle \cdot \boldsymbol{\mu} \tag{10}$$

where $\boldsymbol{\mu}$ is a tensor defining the direction of translation of the active surface in the deviatoric space. At this step, any direction of translation could be used depending on the strategy used to integrate the constitutive law (explicit or implicit). The only requirement is that the outermost activated surface has to be at most tangential to the next one, at the end of a given step. Overlapping of the surfaces is then avoided. In this paper, an implicit integration is adopted.

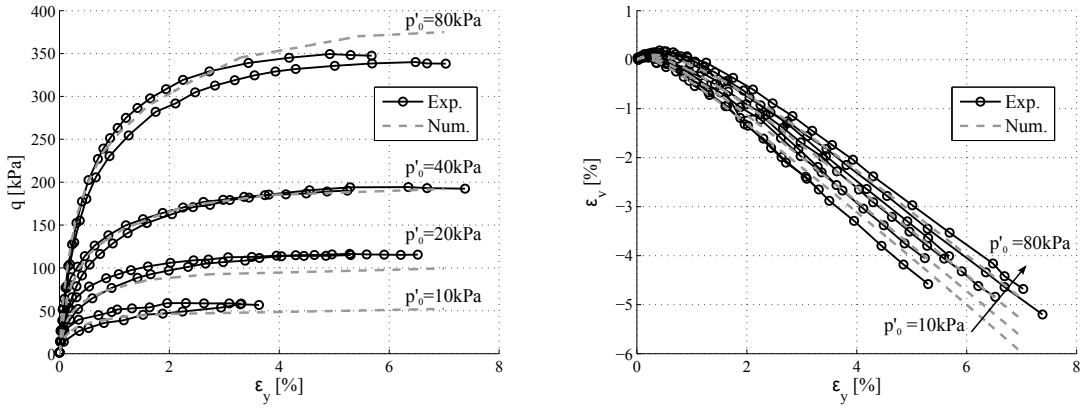
3 CALIBRATION

According to [7], calibrating the model only requires drained triaxial tests (both compressive and extensive curves are needed). Then the tensorial equation (7) describing each yield surface is simplified into

$$\mathrm{f}^i \equiv \left(\mathrm{q} - \mathrm{p}' \cdot \beta^i\right)^2 - \left(\mathrm{m}^i \cdot \mathrm{p}'\right)^2 = 0 \tag{11}$$

and the procedure of calibration is thus straightforward. Firstly, the compression q-ϵ_y curve is delineated into segments along which a plastic modulus is constant. Each transition from a segment to another gives the inital upper bound ($u^i > 0$) of each yield surface. Secondly, the same procedure is carried out for extension curves. Plastic moduli associated with each surface are still known and but initial lower bounds ($l^i < 0$) of surfaces aren't. Then, initial positions (β^i) and sizes (m^i) of the surfaces can be computed

$$m^i = \frac{u^i - l^i}{2} \qquad \beta^i = l^i + m^i \tag{12}$$



(a) q-ϵ curve (b) $\epsilon_v - \epsilon_y$ curve

Figure 1: Experimental (from [11]) and numerical drained triaxial compressive tests on Lund sand No. 0 at different initial mean effective stress (p'_0).

In the scope of this study, test on Lund sand No 0 at high relative density (around 90%, mass density of grains = $\rho_s = 2650$ kg/m^3) are assumed to represent seabed. Data are obtained from triaxial tests given in [11]. The $\mathrm{p}'_0 = 40$kPa curve is adopted as reference curve for calibration (see in Figure 1(a) and 1(b)). Unfortunately, these tests only involve compression curves. Then to characterize the soil behaviour in extension, we formulate a hypothesis We consider that behaviour in extension is similar to behaviour in compression but with a weaker resistance (as shown in [12]). The extension curve of the soil is thus assumed to be the compressive one scaled to a factor 2/3. Plastic parameters identified for the model are given in the Table 1. A dependency of stiffness on the mean effective stress is taken into account through the following relations

$$\mathrm{X}(\mathrm{p}') = \mathrm{X}_0 \cdot \left(\frac{\mathrm{p}'}{\mathrm{p}_{ref}}\right)^{\mathrm{n}} \qquad \text{where} \qquad \mathrm{X} = [\mathrm{G}, \mathrm{K}, \mathrm{H}'] \qquad \text{and} \qquad \mathrm{p}_{ref} = 100\mathrm{kPa} \tag{13}$$

The reference shear and bulk moduli are taken equal to 47MPa and 65MPa respectively. The permeability of the soil is assessed equal to 10^{-5} m/s, [3].

Table 1: Parameters describing the soil for the Prevost's model : initial position of the surfaces (α), aperture of the surfaces (M), reference plastic modulus associated (H'_0), parameter defining the volumetric plastic potential ($\bar{\eta}$), n for the dependency of stiffness on the mean effective stress.

Surf. Nb.	1	2	3	4	5	6
$\alpha[-]$	0.0917	0.1333	0.1583	0.1750	0.200	0.2250
M [−]	0.4583	0.6667	0.7917	0.8750	1.0000	1.1250
H'_0 [MPa]	50	30	20	12	5	2.5
Surf. Nb.	7	8	9	10	11	12
$\alpha[-]$	0.2467	0.2583	0.2733	0.2850	0.2950	0.3033
M [−]	1.2333	1.2917	1.3667	1.4250	1.4750	1.5167
H'_0 [MPa]	1.2	0.8	0.4	0.3	0.1	0.025
$\bar{\eta}$	1.15					
n	0.5					

4 CASE STUDY

4.1 Geometry

The case study adopted here is the modelling of a suction's caisson part of a tripod foundation in shallow water. This paper focuses on the soil behaviour and the superstructure is not modelled, nor the part of the foundations into the sea. The suction caisson is a half cylinder of 8m diameter. To a first approximation, the horizontal load is neglected and the foundation can be idealized as an axisymmetric case (see in Figure 2). The soil modelled is a 24m long times 22m high rectangular domain. The horizontal boundary at the top as well as the outermost vertical one are considered drained. In this case study, the soil and the caisson are considered perfectly stuck. The initial coefficient of lateral earth pressures is assumed to be equal to 0.7. The first metre of soil of the sea bed is not modelled and is replaced by a 10kPa confinement. A small cohesion of 2.5kPa is added to parameters calibrated above for numerical purpose.

4.2 Loading

The design of the suction caisson is based on the bearing capacity procedure developed in [15]. Then the acting vertical forces are estimated. The first step consists in applying

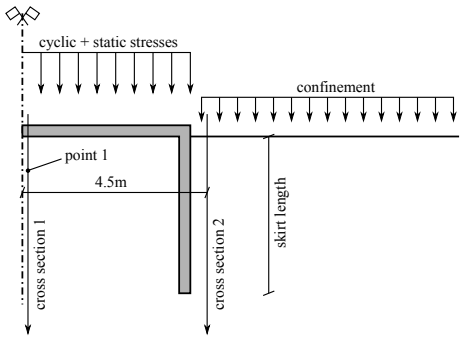
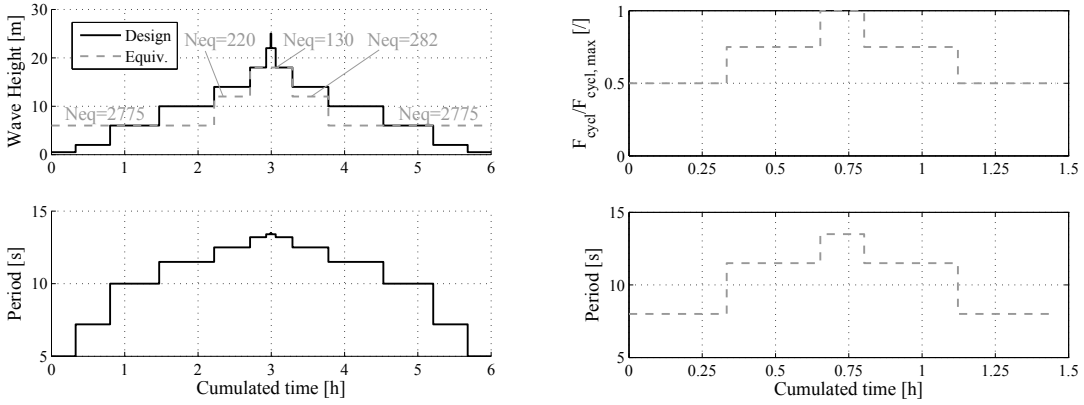


Figure 2: Geometry of the foundation. The first cross section is under the centre of the caisson, the second one is 0.5m outside the caisson. The point no 1 is located 0.5m under the centre of the caisson.

the dead weight of the wind turbine and foundation following a drained stress path. The second step concerns the cyclic loading.



(a) Histogram for the 100-year design and equivalent storm for the Ekofisk site [13].

(b) Equivalent vertical cyclic loading adopted for the modelling of suction caisson.

Figure 3: Equivalent cyclic loading of the foundation

During a storm, waves and wind are random processes that involve a loading on the wind turbine. They don't necessary have the same principal direction nor frequency content. Then their action on the wind turbine eventually entails a loading of the suction caisson which depends on the structural response of the wind turbine.

Describing the characteristics of waves requires two components : their heights and periods [13]. The typical content of a storm can be limited to different classes of waves of given height and period. In the normal course of a storm, waves of small height and period are followed by waves of higher and higher height and period. Following this tendency, [13] obtained an equivalent cyclic loading on the soil for the 100-year design storm for the Ekofisk site (see in Figure 3(a)), based on work of [14]. Firstly, the storm is decomposed

in successive wave packets of a given height (see in Figure 3(a)). Afterwards, this loading is transformed into an equivalent number of cycles of a given shear amplitude in the soil.

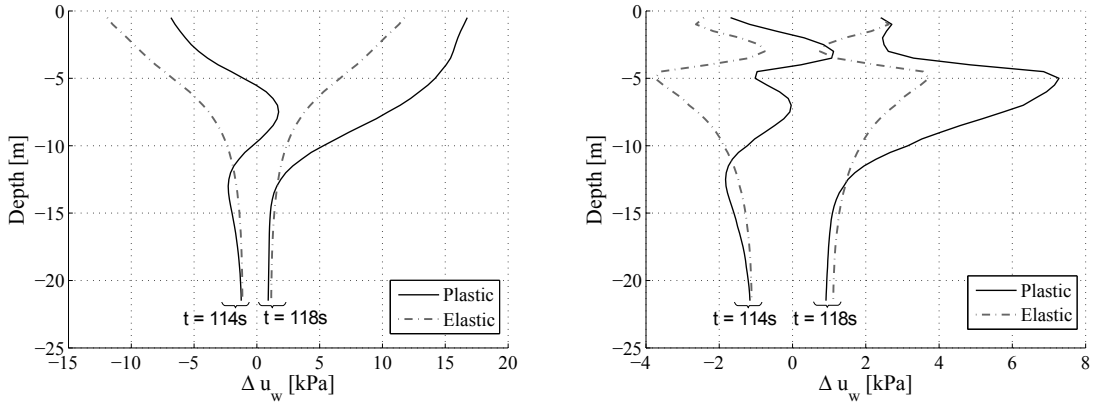
In order to simplify the loading, a similar procedure is followed. The synthetic cyclic loading adopted is made of different stages of increasing amplitude and period of vertical stresses then followed by a symmetric effect of decreasing amplitude and period, see in Figure 3(b). The static vertical stress is estimated to 80 kPa while the cyclic maximal vertical stress is chosen equal to 40 kPa.

5 RESULTS

Results consist in a parametric study on factors affecting the response of the suction caisson to a cyclic loading. The influence of the constitutive law, the skirt length and the permeability, are investigated. They are provided either in a cross section for a fixed time step or at a fixed point for every time step (see in Figure 2).

5.1 Constitutive law

The first parameter investigated is the constitutive law (see in Figure 6). This first comparison shows clearly that at the beginning of a new wave packet, the effect of the elasto-plastic constitutive law is to shift the curve of pore pressure variation to greater values, probably due to contractancy of the soil. However, the influence of the contractancy seems limited to the first 10-15 metres of the soil where deviatoric stresses are of greater importance. Downwards the elasto-plastic curves tend to elastic ones and nearly become symmetric.



(a) Elastic/Elasto-Plastic constitutive law : variations in water pore pressure (cross section 1)

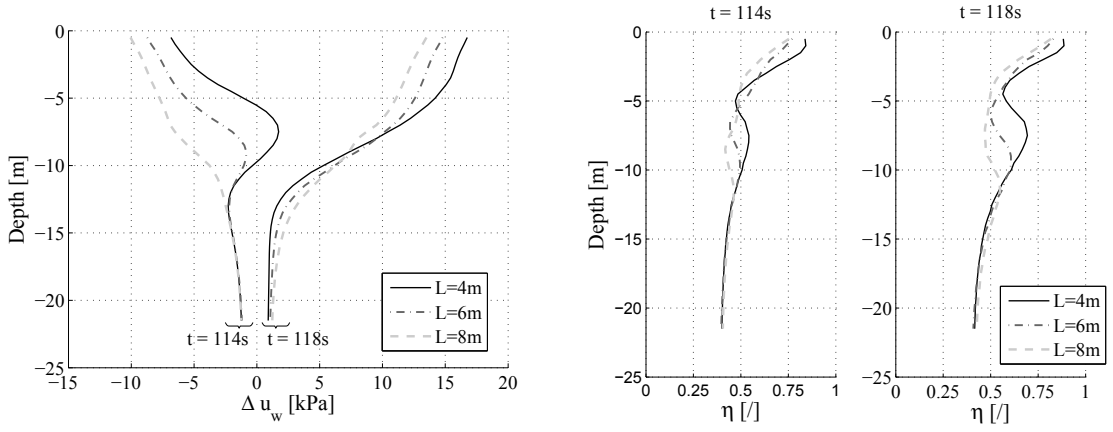
(b) Elastic/Elasto-Plastic constitutive law : variations in water pore pressure (cross section 2)

Figure 4: Cross section of the variations in pore water pressure for minimum (t= 114s) and maximum (t= 118s) vertical stresses, during the first wave packet.

5.2 Skirt length

Figure 5 depicts cross sections of pore pressure variations and mean effective stress at the beginning of the storm (first wave packet). The time steps $t = 114$s and $t = 118$s correspond to a half period where the cyclic amplitude is respectively minimum and maximum.

These figures summarize the two main effects of the skirt length. Firstly, the length of the skirt modifies the flow regime around the caisson. A higher skirt length implies a greater time to dissipate pore pressure generated at its top. On the other hand, the soil inside the caisson is confined, hence the stress ratio ($\eta = q/p'$) decreases with depth up to a reversal point (see in Figure 5(b)). This point lies at a depth slightly deeper than the skirt length. Downwards a local peak in stress ratio is clearly visible where the deviatoric stresses develop. The skirt length affects both the position and the sharpness of the local peak in η. Therefore, depending on its value, a contractive or dilative volumetric behaviour appears hence a pore pressure generation or dissipation.



(a) Variations in water pore pressure

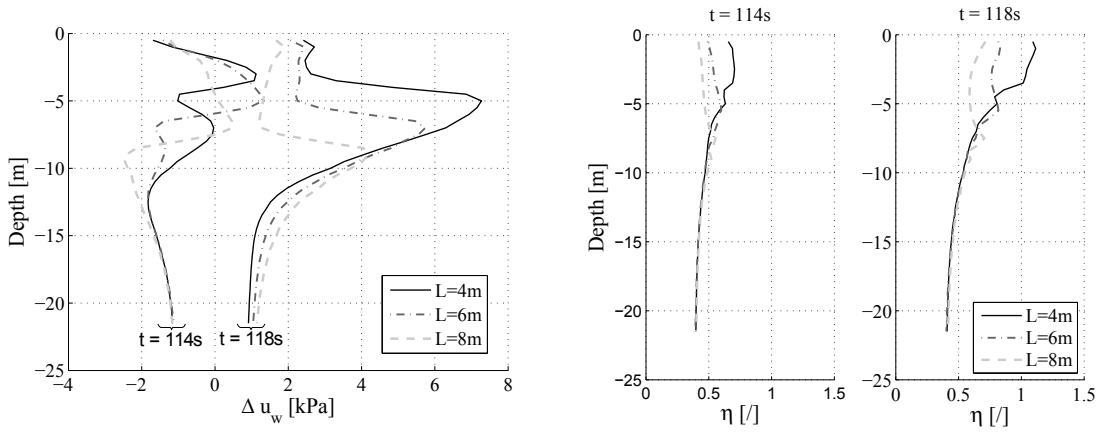
(b) Variations in stress ratios $\eta = q/p'$

Figure 5: Influence of the skirt length : cross section 1 for minimum (t= 114s) and maximum (t= 118s) vertical stresses, during the first wave packet.

The higher the skirt length the lower the plasticity around the soil (see in Figure 5(b)). As a consequence the shift of the curve of pore pressure variation (5(a)) is lower and the local peak is smoothed. The curve for a 8m skirt length tends to the symmetric elastic distribution.

It's worth noting that outside the caisson (cross section 2), the soil is highly plastified (see in Figure 6(b)). Indeed, due to the hypothesis of sitcky contact between the soil and the caisson, high deviatoric stresses develop whilst the mean effective stress is weak. This implies a greater shift of the pore pressure curve compared with an elastic curve (see in Figures 4(b) and 6(a)). This effect is smoothed again by the skirt depth.

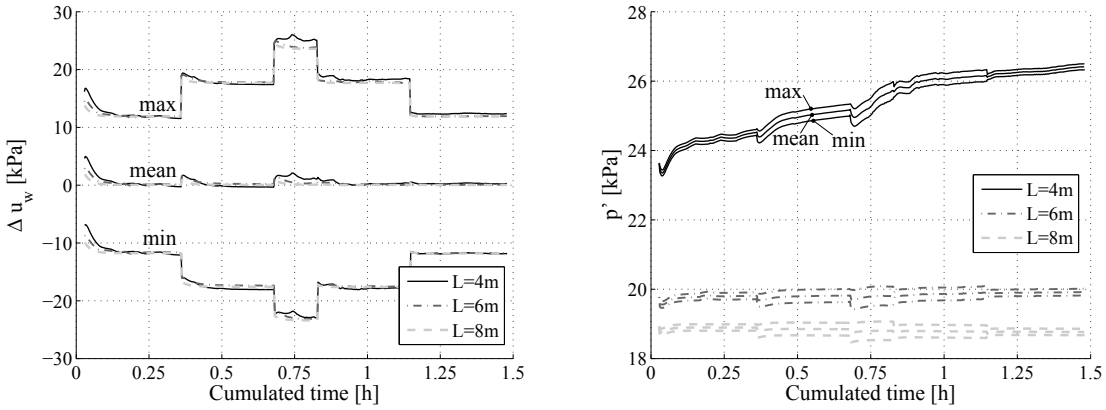
The evolution of pore pressure variations in time at point 1 is given in Figure 7(a).



(a) Variations in water pore pressure

(b) Variations in stress ratios $\eta = q/p'$

Figure 6: Influence of the skirt length : cross section 2 for minimum (t= 114s) and maximum (t= 118s) vertical stresses, during the first wave packet.



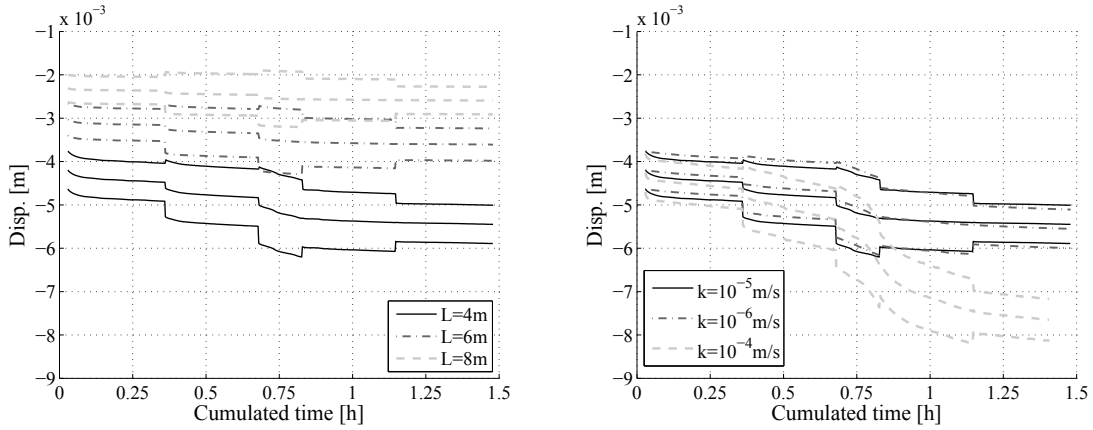
(a) Variations in water pore pressure : mean tendency and envelop curve.

(b) Mean effective stress : mean tendency and envelop curve.

Figure 7: Influence of the skirt length : evolution of pore pressure variation and mean effective stress with time at point 1.

All the curves depict the same behaviour. During the two first wave packets of the storm ($\sigma_{v,cycl} = 0.5/0.75 \cdot \sigma_{v,cycl,max}$), the pore pressure variation firstly rises up to a peak, then decreases and stabilizes. The symmetric effect is clearly visible in Figure7(b) that depicts the variations of mean effective stresss.

During the stabilized phase, the pore pressure created during cycle is dissipated within the same cycle [16]. The mirror effect of the mean effective stress is a tendency to increase as the volumetric deformation rises up and the soil densifies. Accumulation of vertical permanent displacement is greater during the transient than during the stationary phase (see in Figure8(a)). It's worth noting that the transient behaviour coupled with greater



(a) Dependency on the skirt length : mean tendency and envelop curve.

(b) Dependency on the permeability : mean tendency and envelop curve.

Figure 8: Evolution of the displacement with time at point 1.

displacement accumulation disappears for the steps where the storm calms down (wave packets 4 and 5).

The evolution of the mean effective stress (see in Figure 7(b)) highlights the partially drained behaviour of the soil. Both variables don't have the same amplitude of variation (see in Figures 7(b) and 7(a)). During a cycle, the major part of the loading is transferred to pore water pressure. Overpressure cannot dissipate totally before unloading. Hence, only a small part of the loading passes from pore water pressure to soil skeleton. A smaller skirt length involves that a greater part of the loading stresses the soil at the top of the caisson. The initial mean effective stress is greater but the deviatoric stress as well leading to greater plasticity and displacement of the caisson.

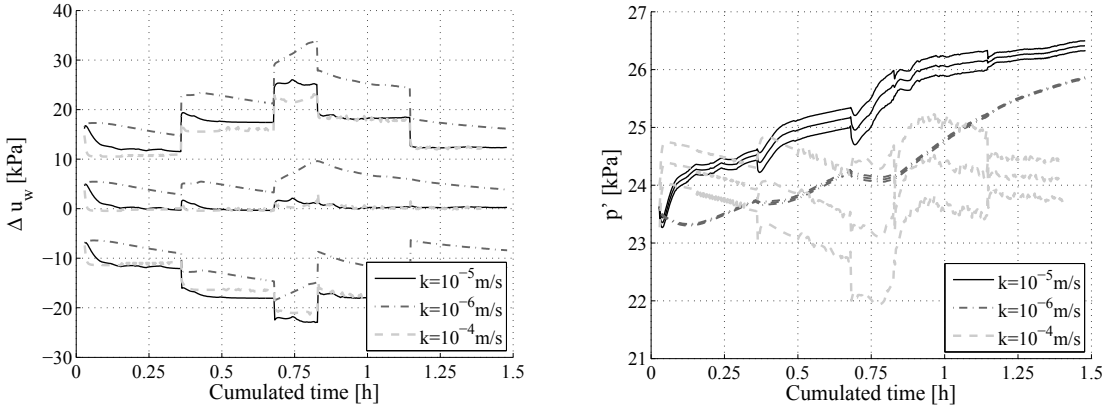
5.3 Permeability

Reducing permeability leads to a weaker dissipation of the pore water pressure and a build up of this pressure for the greatest loading amplitude ($\sigma_{v,cycl} = \sigma_{v,cycl,max}$, see in Figure 9(a)). The loading is essentially supported by the pore water pressure. As a consequence, the tendency of the mean effective stress is to evolve more slightly and the variation around this tendency is weaker. Then, the soil is not prone to rearrange and deform. As a consequence, the displacement is quite the same (see in Figure 8(b)).

On the other hand, a greater permeability involves a greater variation of both mean effective and deviatoric stresses. Then the soil is submitted to a greater loading and its deformation is larger (see in Figure 8(b)).

6 CONCLUSIONS

The main purpose of this paper was to capture the main features of the cyclic loading of suction caissons modelled using the Prevost's model. A parametric study was carried



(a) Variations in water pore pressure : mean tendency and envelop curve.

(b) Mean effective stress : mean tendency and envelop curve.

Figure 9: Influence of the permeability : evolution of pore pressure variation and mean effective stress with time at point 1.

out to better understand the influence of the key factors such as permeability and skirt length. Experimental results are not really scattered in literature because of commercial purpose. Then only numerical simulations are presented in this paper.

Couplings between soil plasticity and flow around the caisson are not easy to predict, *a priori*. In the case presented here, the pore water pressure, unable to dissipate, sustains the main part of the cyclic loading. Then the soil skeleton is only submitted to a fraction of the total cyclic loading and its deformation is weaker than for a drained loading. Two parameters are shown to affect the total displacement : the skirt length (the greater the length the smaller the displacement) and the permeability. The role of the latter depends on several factors. It was shown in this case than a 10^1 times greater permeability entails a greater displacement whilst a 10^{-1} times smaller permeability nearly doesn't influence the displacement.

This paper was a first step to an accurate modelling of suction caissons. The future work will focuses on the improvement of simulations. Contact elements should be added to take into account the sliding between the soil and the caisson. Improvements of the model are also necessary to represent the cyclic path of the soil more accurately and to overcome "local failures". Finally a switch to 3D is unavoidable to take into account the horizontal load transmitted to the soil.

REFERENCES

[1] Stuyts, B. and Irvine, J. and Cathie, D., Assessing the stability of tripod foundations for offshore win turbines under cyclic loading. *Proc. of he the 8th Int. Conf. on Structural Dynamics, EURODYN 2011*, (2011) 3482-3489

[2] Senders, M., Suction caissons in sand as tripod foundations for offshore wind turbines.

Thesis, University of Western Australia, (2008)

[3] Byrne, B.W and Houlsby, G.T., Experimental investigations of response of suction caissons to transient vertical loading. *J. of the Geotech. and Geoenv. Eng.*, (2002) **128**:926-939

[4] Houlsby, G.T., Suction caissons for wind turbines. *Proceedings of the international symposium on frontiers in offshore geotechnics*, (2005) 75-94

[5] Houlsby, G.T. and Kelly, R.B. and Huxtable, J. and Byrne B.W, Field trials of suction caissons in sand for offshore wind turbine foundations *Géotechnique*, (2006) **56**:3-10

[6] Taiebat, H.A., Three dimensional liquefaction analysis of offshore foundations. *Thesis*, University of Sydney, (1999)

[7] Prevost, J.H., A simple plasticity theory for frictional cohesionless soils. *Soil Dynamics and Earthquake Engineering*, (1985) **4**:9-17

[8] Yang,Z. and Elgamal, A., Multi-surface cyclic plasticity sand model with lode angle effect. *Geotechnical and Geological Engineering*, (2008) **26**:335-348

[9] Prevost, J.H. and Hughes, T.J.R. and Cohen, M.F., Analysis of gravity offshore structure foundations *Journal of Petroleum Technology*, (1980) **32**:199-209

[10] Ishihara, K. and Tatsuoka, F. and Yasuda, S. , Undrained deformation and liquefaction of sand under cyclic stress. *Soils and Foundations*, (1975) **15**:29-44

[11] Ibsen, L.B. and Jakobsen, F.R. , *Lund sand No 0, Data Report 8401, 8402, 8801 & 8901*, (1996) Soil Mechanichs Laboratory, Aalborg University, Denmark

[12] Hyodo, M. and Hyde, A.F.L. and Aramaki, N. and Nakata, Y., Undrained monotonic and cyclic shear behaviour of sand under low and high confining stresses. *Soils and Foundations*, (2002) **42**:63-76

[13] Rahman, M.S. and Seed, H.B. and Booker, J.R., Pore pressure development under offshore gravity structures. *J. of the Geotech. Eng. Div.* ASCE, (1977) **103**:1419-1436

[14] Lee, K.L. and Focth, J.A., Liquefaction potential at Ekofisk tank in North Sea *J. of the Geotech. Eng. Div.* ASCE, (1975) **101**:1-18

[15] DNV, Foundations, classification notes No 30.4, - Foundations, Det Norske Veritas, Høvik, Norway, (1992)

[16] Ibsen, L.B., The mechanism controlling static liquefaction and cyclic strength of sand *Proc. of Int. Workshop on Physics and Mechanics of Soil Liquefaction*, Baltimore, (1998) Soil Mechanichs Laboratory, Aalborg University, Denmark

V International Conference on Computational Methods in Marine Engineering
MARINE 2013
B. Brinkmann and P. Wriggers (Eds)

THE EFFECT OF DIFFERENT VOLUME-OF-FLUID (VOF) METHODS ON ENERGY DISSIPATION IN SIMULATIONS OF PROPAGATING WAVES

BULENT DUZ*, MART J.A. BORSBOOM‡, PETER R. WELLENS‡, ARTHUR E.P. VELDMAN† AND RENE H.M. HUIJSMANS*

*Department of Ship Hydrodynamics
Technical University of Delft
Mekelweg 2, 2628 CD Delft, The Netherlands
e-mail: b.duz@tudelft.nl, r.h.m.huijsmans@tudelft.nl, www.tudelft.nl

‡Deltares
P.O. Box 177, 2600 MH Delft, The Netherlands
e-mail: mart.borsboom@deltares.nl, peter.wellens@deltares.nl, www.deltares.nl

†Institute for Mathematics and Computer Science
University of Groningen
P.O. Box 407, 9700 AK Groningen, The Netherlands
e-mail: a.e.p.veldman@rug.nl, www.rug.nl

Key words: Volume-of-fluid, Propagating waves, MACHO, COSMIC, Energy dissipation, Free surface advection

Abstract. Spurious energy dissipation in numerical wave simulations due to numerical diffusion is a widely-known problem that can have several causes. The numerical diffusion can be due to the discretisation method used for the governing equations applied inside the flow domain, but can also be due to the numerical implementation of the moving free surface and the boundary conditions applied at the free surface. A technique to model an arbitrary 3D free surface efficiently is the volume-of-fluid (VOF) method. In this paper, the attention is focused on the effect of various VOF methods on spurious wave energy dissipation. For this purpose, we will compare several VOF methods in simulations of propagating waves where strong nonlinear behavior is dominant in the flow. The VOF methods in question are based on two methodologies: Simple Line Interface Calculation (SLIC) and Piecewise Linear Interface Calculation (PLIC). Additionally, a grid convergency study will be performed to better understand the numerical behavior of the methods. In the end, comparisons and discussions will be provided to address how numerical wave energy dissipation can be reduced by implementing more accurate VOF methods.

1 INTRODUCTION

Volume-of-fluid (VOF) methods have been successfully used in computational fluid dynamics (CFD) simulation of interfacial and free surface flows for several decades. Typically, the VOF approach presents a model based on a scalar indicator function to transport the fluid according to the underlying velocity field on a fixed computational mesh. This function is characterized by the volume fraction f occupying one of the fluids within each cell. If a cell is completely filled with one fluid, the volume fraction takes the value of 1, and 0 if only the second fluid is present. The values between these two limits indicate the presence of the interface or free surface.

To advect the volume fraction field in time, the following transport equation is solved,

$$\frac{\partial f}{\partial t} + \mathbf{u} \cdot \nabla f = 0, \tag{1}$$

where $\mathbf{u}$ denotes the fluid velocity. Assuming a solenoidal velocity field (incompressible flow) modeled by $\nabla \cdot \mathbf{u} = 0$, Eq. (1) can alternatively take the form:

$$\frac{\partial f}{\partial t} + \nabla \cdot (\mathbf{u} f) = 0. \tag{2}$$

In the VOF context, the discrete volume fraction field is not smoothly distributed at the interface. On the contrary, it displays sharp discontinuous changes between 0 and 1. To preserve the steep profile of the interface, the explicit location of the interface is locally reconstructed and corresponding volume fluxes are computed to update the the volume fraction field to the next discrete time level using Eq. (2). Thus, the interface reconstruction is the first stage of a VOF method. Using the values of the volume fraction in a compact cell stencil, the orientation and location of the interface in a grid cell can be calculated in a piecewise constant, piecewise linear or piecewise parabolic fashion. Among the three classes, the piecewise linear reconstruction is nowadays the most popular approach, and the methods which fall into this category are usually referred to as Piecewise Linear Interface Calculation (PLIC) methods. For a review of interface reconstruction methods, see, e.g., [1, 2].

Once the interface is reconstructed, the volume fraction field is conservatively advected in time via Eq. (2). This equation can be solved using either an unsplit advection or a direction split advection scheme. Although both strategies have been successfully applied in simulation of interfacial flows, direction split advection schemes are more common in standard VOF methods due to ease of implementation: treating individual velocity components to compute 1D fluxes for a sequence of updates in each spatial direction, as opposed to treating velocity components acting in all directions to compute multidimensional fluxes using inherently difficult geometric tasks. For an analysis on these two advection strategies, see, e.g., [2–4]. Regardless of the strategy for advection, conservation of mass must be satisfied and the resulting volume fraction values must be bounded, $0 \leq f \leq 1$, during the transport process of the volume fraction field.

In this paper, the main objective is to compare the performance of several interface reconstruction/advection combinations in simulations of propagating waves. In these tests, we will use two direction split advection schemes of Leonard et.al. [5] which, to the best knowledge of the authors, have not been used in the context of interfacial or free surface flows. The schemes are Multidimensional Advective-Conservative Hybrid Operator (MACHO) and Conservative Operator Splitting for Multidimensions with Inherent Constancy (COSMIC). Besides these two advection schemes, the Eulerian Implicit-Langrangian Explicit (EI-LE) scheme explained in [6] has been considered for comparison. We will also compare these methods with the current VOF implementation in the CFD simulation tool ComFLOW, see [7, 8] for an overview of the features of this flow solver. It employs the VOF technique introduced by Hirt and Nichols [9] and a local height function (LHF) to overcome the bottlenecks which originate from this VOF technique such as violation of mass conservation and spurious flotsam and jetsam. For a detailed description of the LHF, see [10].

2 INTERFACE RECONSTRUCTION

In a PLIC-VOF method, the interface in each cell is approximated by a line (or a plane in three dimensions). Within each cell, the approximated interface can be defined by the equation:

$$\mathbf{m} \cdot \mathbf{x} = \alpha, \tag{3}$$

where $\mathbf{m}$ is the local surface normal, $\mathbf{x}$ is the position vector of a point on the interface and α is a constant. Essentially, the interface reconstruction involves two procedures: the determination of $\mathbf{m}$ and α. For a given discrete volume fraction field, $\mathbf{m}$ in each cell is usually calculated using the data from the surrounding cells. However, since the discrete volume fraction field is not smoothly distributed at the interface, computation of $\mathbf{m}$ with high accuracy can be complicated and expensive. Since the CFD tool ComFLOW is specifically designed to simulate extreme wave loading on structures in three dimensions, the required reconstruction method must be considerably cheap and easily applicable in 3D while retaining a reasonable accuracy for estimation of the linear interface, although the present study is mainly focused on 2D problems. Among many techniques that are available in the literature, we will show results for three methods: Youngs' algorithm [11], the least-square gradient (LSG) technique by Rider and Kothe [3] and the Mixed-Youngs-Centered (MYC) implementation of Aulisa et al. [12].

Once the normal vector is known, the planar interface within the cell is located so that local volume conservation is satisfied. In other words, the resulting plane should pass through the cell in such a way that the truncated volume lying below the plane is equal to the exact material volume in that cell. As Eq. (3) suggests, the location of the planar interface results from the computation of α. With the available knowledge of the normal vector $\mathbf{m}$ and the volume fraction f within the cell, we can calculate α either iteratively or analytically. Here, we use the analytical relations derived by Scardovelli and Zaleski [13].

3 INTERFACE ADVECTION

After we determine the orientation and location of the planar interface, the volume fraction field is advected in time via Eq. (2). Among many direction split methods, we will consider the MACHO and COSMIC schemes which can be given in 2D as,

the MACHO scheme:

$$\begin{aligned} f^* &= f^n - \Delta t \frac{\partial u f^n}{\partial x} + \Delta t f^n \frac{\partial u}{\partial x} \,, \\ f^{n+1} &= f^n - \Delta t \left(\frac{\partial u f^n}{\partial x} + \frac{\partial w f^*}{\partial z} \right), \end{aligned} \tag{4}$$

and the COSMIC scheme:

$$\begin{aligned} f^X &= f^n - \Delta t \frac{\partial u f^n}{\partial x} + \Delta t f^n \frac{\partial u}{\partial x} \,, \\ f^Z &= f^n - \Delta t \frac{\partial w f^n}{\partial z} + \Delta t f^n \frac{\partial w}{\partial z} \,, \\ f^{n+1} &= f^n - \Delta t \left[\frac{\partial}{\partial x} \left(u \frac{f^n + f^Z}{2} \right) + \frac{\partial}{\partial z} \left(w \frac{f^n + f^X}{2} \right) \right]. \end{aligned} \tag{5}$$

An advantage of the MACHO and COSMIC schemes is that both methods can be readily extended to 3D while the EI-LE scheme does not naturally extend to 3D. A clear advantage of the COSMIC scheme is its inherent symmetric feature [5]. However, the COSMIC scheme requires one additional interface reconstruction in 2D at each time step. In 3D, this scheme becomes even more expensive which makes it necessary to implement a computationally cheap interface reconstruction algorithm.

4 NUMERICAL RESULTS

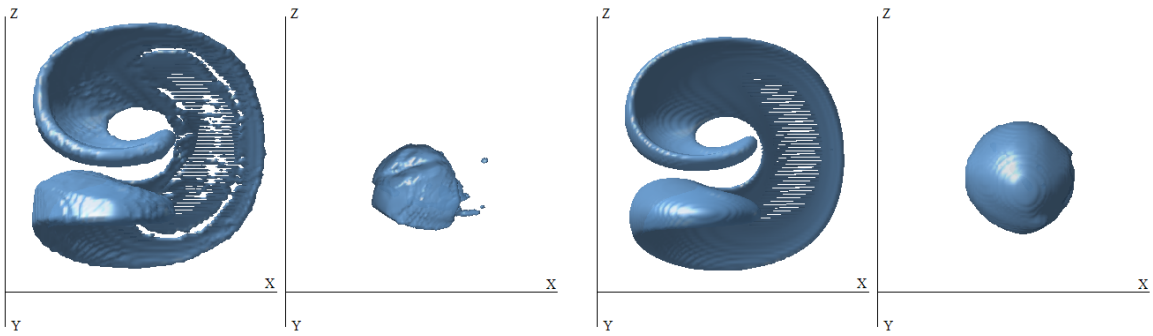
The order of accuracy of the reconstruction methods used in this work has been extensively studied by various researchers, see, e.g., [2–4, 6, 12, 14]. Therefore, we focus our attention on the following advection tests.

4.1 3D deformation field

In this test problem, a sphere of radius 0.15 and center $(0.35, 0.35, 0.35)$ is immersed in a 3D reversible deformation field inside a unit sized cube. The flow is formed by the velocity field:

$$\begin{aligned} u &= 2\sin^2(\pi x)\sin(2\pi y)\sin(2\pi z)\cos(\pi t/T)\,, \\ v &= -\sin(2\pi x)\sin^2(\pi y)\sin(2\pi z)\cos(\pi t/T)\,, \\ w &= -\sin(2\pi x)\sin(2\pi y)\sin^2(\pi z)\cos(\pi t/T)\,, \end{aligned} \tag{6}$$

where $T = 3$ is used. Due to this velocity field, the sphere undergoes severe deformation until it reaches maximum stretching at $t = 1.5$, then returns to its initial shape and



(a) H&N + LHF (b) LSG + COSMIC

Figure 1: 3D reversible deformation field test on a 128^3 grid at CFL = 0.5. Snapshots are taken at maximum deformation ($t = 1.5$), and after the flow returns back ($t = 3$).

position at $t = 3$ by means of the Leveque cosine term [15]. As we employ staggered grid arrangement where the velocity components are defined at cell faces, the velocity field (6) is applied in a discretely divergence-free manner.

Fig. 1 shows the results on a $128 \times 128 \times 128$ grid using the H&N + LHF method versus the LSG + COSMIC combination at time $t = 1.5$ and $t = 3$. The LSG + COSMIC scheme clearly outperforms the H&N + LHF method. However, as the sphere reaches the maximum thinning, holes appear in the deformed fluid body in both results. The recovered shape in the end is roughly a sphere with some minor coalescence when the LSG + COSMIC method is used.

Mesh	Error (Youngs + COSMIC)	Error (LSG + COSMIC)	Error (Youngs + direction-split)	Error (H&N + LHF)
32^3	7.66×10^{-3}	7.51×10^{-3}	7.71×10^{-3}	1.06×10^{-2}
	1.56	1.68	1.47	1.05
64^3	2.59×10^{-3}	2.34×10^{-3}	2.78×10^{-3}	5.1×10^{-3}
	1.78	1.81	1.87	1.08
128^3	7.50×10^{-4}	6.64×10^{-4}	7.58×10^{-4}	2.4×10^{-3}

Table 1: Errors defined by (7) for the 3D deformation field at CFL = 0.5. The order of accuracy of a method is given between the errors. The result on the third column is taken from [4] for comparison.

Tab. 1 shows the the geometrical error E in L_1 which is defined as

$$E = \sum_{i,j,k} \left| f_{i,j,k} - \tilde{f}_{i,j,k} \right| \Delta x_i \Delta y_j \Delta z_k \tag{7}$$

where $\tilde{f}_{i,j,k}$ and $f_{i,j,k}$ are the volume fraction fields at time $t = 0$ and $t = 3$, respectively. In terms of the magnitude of the errors, COSMIC shows a superior performance over the direction-split scheme used in [4] for the same Youngs reconstruction method. Using the LSG method with COSMIC improves the results further.

4.2 Application example: Propagating Rienecker-Fenton waves

The final example is propagating Rienecker-Fenton waves [16] in shallow water. Here, we particularly focus our attention on investigating the effect of various interface-reconstruction /advection combinations on energy dissipation in wave simulations.

4.2.1 Mathematical modeling of the flow solver

If we consider water as a homogeneous, incompressible, viscous fluid, we can describe fluid motion in a three-dimensional domain Ω by the continuity equation and the Navier-Stokes equations in a conservative form as,

$$\oint_{\Gamma} \mathbf{u} \cdot \mathbf{n} \; d\Gamma = 0, \tag{8}$$

$$\oint_{\Omega} \frac{\partial \mathbf{u}}{\partial t} d\Omega + \oint_{\Gamma} \mathbf{u}\mathbf{u}^T \cdot \mathbf{n} d\Gamma = -\frac{1}{\rho} \oint_{\Gamma} (p\mathbf{n} - \mu \nabla \mathbf{u} \cdot \mathbf{n}) d\Gamma + \oint_{\Omega} \mathbf{F} d\Omega \; . \tag{9}$$

In Eqns. (8) and (9), Ω denotes a volume with boundary Γ and normal vector $\mathbf{n}$, $\mathbf{u} = (u, v, w)^T$ is the flow velocity, ρ is the fluid density, p is the pressure, μ is the dynamic viscosity, ∇ is the gradient operator and $\mathbf{F} = (F_x, F_y, F_z)^T$ represents external body forces acting on the fluid such as gravity. Detailed explanation of how the individual terms in these equations are treated is beyond the scope of this paper. For this purpose, see, e.g., [17, 18].

4.2.2 Propagating Rienecker-Fenton waves

Four Rienecker-Fenton waves with the same period but different heights are generated, see Tab. 2. Steepness of the waves ranges from 3% to 10.3% which indicates strong nonlinear behavior in the flow. All the three waves are started from rest, and within the first three periods, wave heights are gradually increased until full heights are reached. The length of the domain in the direction of propagation is defined in such a way that the waves do not reach the end of the domain during the simulations. This procedure guarantees that there is no reflection in the computational domain, and hence the solution

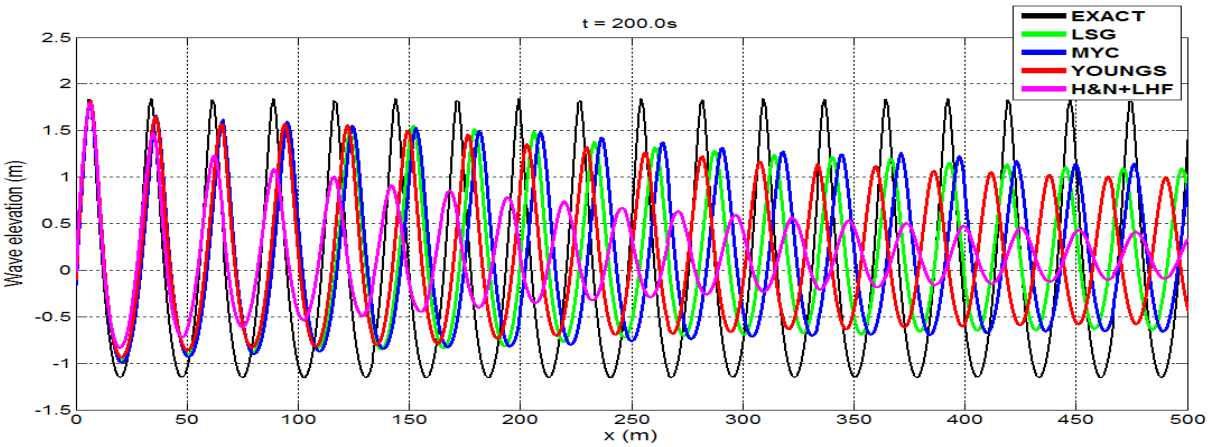
	Rienecker-Fenton waves			
	period	height	length	steepness
	T (s)	H (m)	L (m)	H/L (%)
WAVE3	4	0,75	24,88	3,0
WAVE7	4	2	26,1	7,6
WAVE10	4	3	28,9	10,3

Table 2: Characteristics of the Rienecker-Fenton waves.

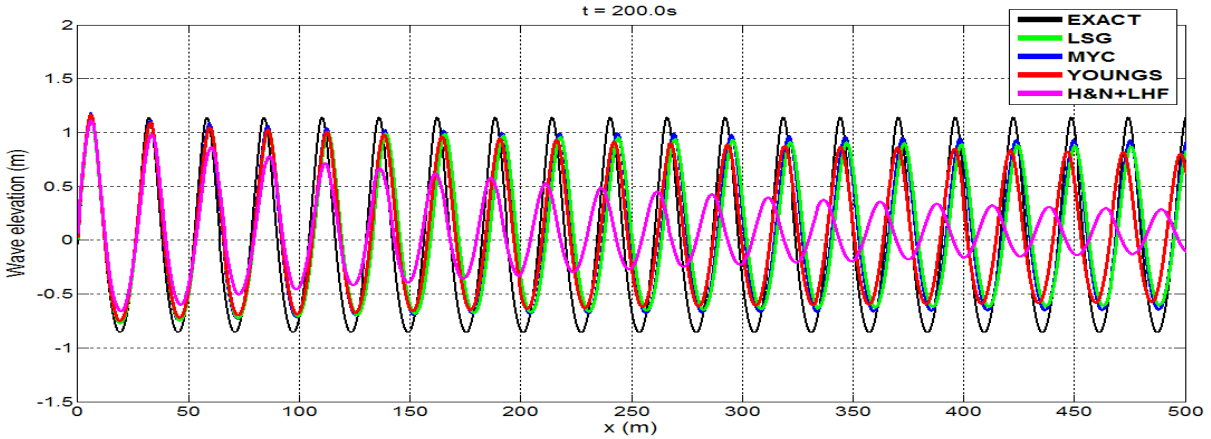
is not perturbed. The duration of the simulations should allow us to have a comprehensive picture regarding wave damping. Therefore, a stable wave system for a large number of wave periods is required. In this analysis, we performed simulations for 200 seconds to have a stable wave system for at least 17 consecutive wave lengths, and correspondingly the domain length is computed as 2000 meters considering the fastest propagating wave component. The water depth in all simulations is 9.5 meters. Two uniform grid resolutions are considered for the grid convergence study: 1.0m and 0.5m in both directions.

Fig. 2 shows the surface elevations as a function of the horizontal position at time $t = 200s$ for the three Rienecker-Fenton waves on the coarse grid, and Fig. 3 on the fine grid. These results are obtained from several PLIC algorithms with the COSMIC advection scheme. Also, the analytical results from the Rienecker-Fenton theory and the Hirt-Nichols' VOF with local height function (H&N + LHF) are plotted in the figures.

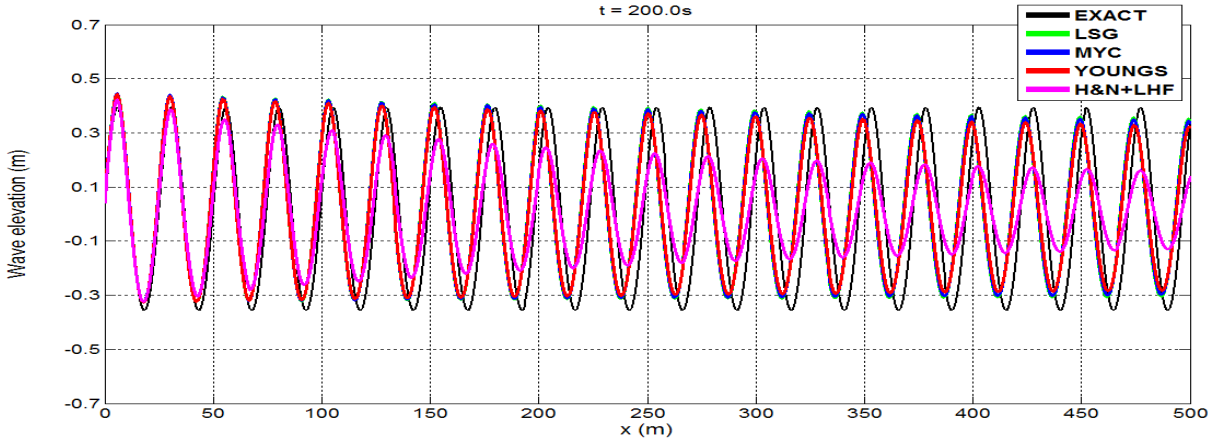
The results on the coarse grid ($\Delta x = \Delta z = 1m$) in Fig. 2 demonstrate that the behavior of the Hirt-Nichols' VOF + LHF is considerably dissipative: WAVE3 lost nearly 59% of the initial wave height after 17 consecutive wave lengths. For WAVE7, this amount is 78%, and for WAVE10 it is 83%. Additionally, this method causes a clear phase shift with respect to the analytical solution. The results indicate that larger phase shifts occur as the steepness of the waves increases. When the PLIC algorithms + COSMIC advection combinations are used, results improve substantially as less dissipation and phase shift are observed. For WAVE3, all the three reconstruction algorithms perform almost the same, somewhat in favor of LSG and MYC. For WAVE7, we observe differences especially as the waves propagate in the computational domain. The Youngs reconstruction algorithm yields the largest wave damping while the LSG and MYC methods perform similarly: 70% of the initial wave height remains with the Youngs method after 17 wave lengths whereas 75% remains with the LSG and MYC methods. In terms of phase shift, there is only a slight difference between the reconstruction methods. In the results for WAVE10, we see that nearly 57% of the initial wave height dissipated when the Youngs method is used. From the LSG and MYC methods, this amount is 51%. After 4 wave lengths from the inflow boundary, we observe three distinct wave signals from the three reconstruction methods.



(a) Results for WAVE10 (steepness: 10.3%)

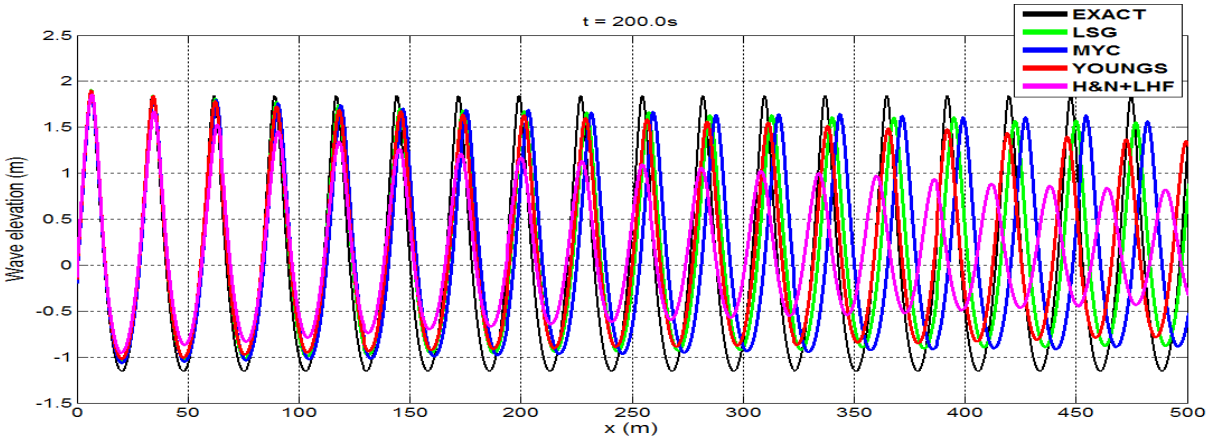


(b) Results for WAVE7 (steepness: 7.6%)

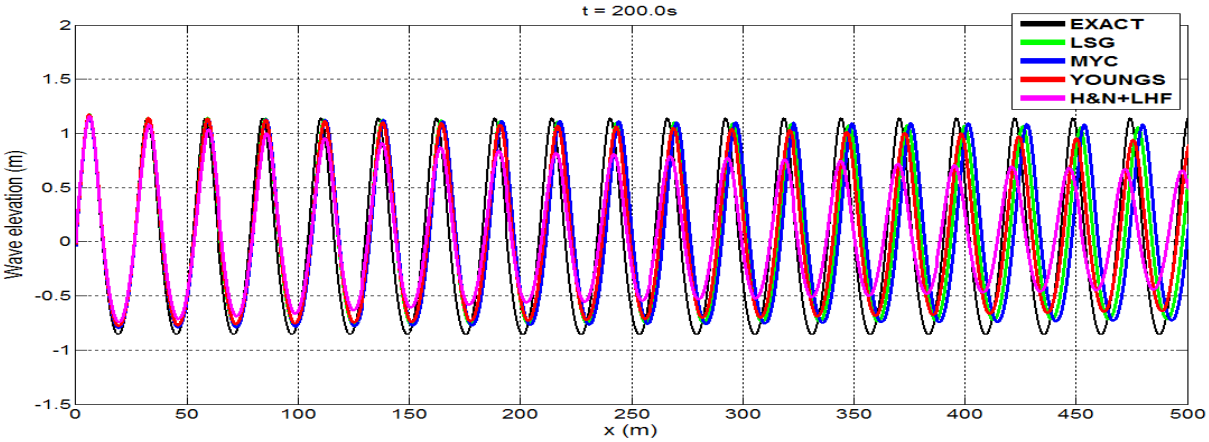


(c) Results for WAVE3 (steepness: 3.0%)

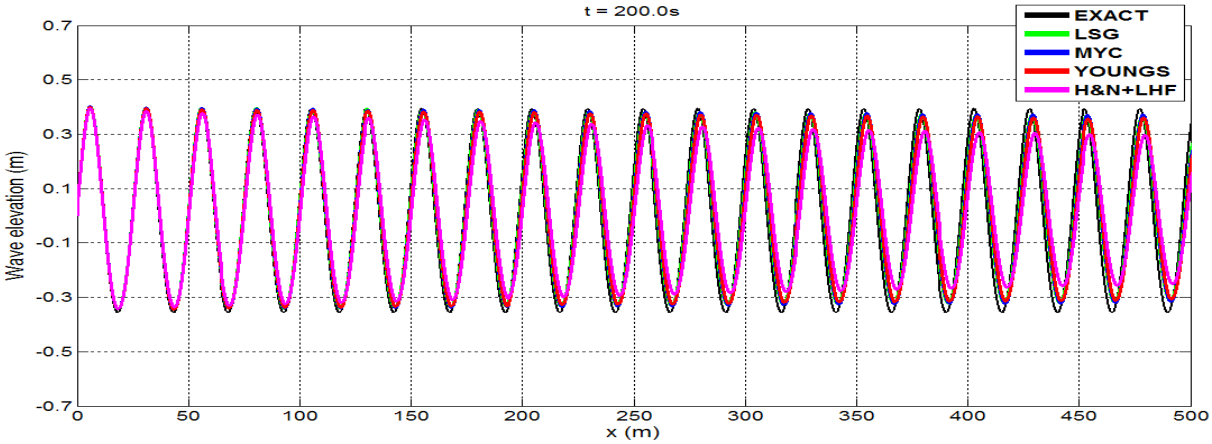
Figure 2: Wave elevations as a function of horizontal location for the waves in Tab. 2. The LSG, MYC and Youngs methods are combined with the COSMIC advection scheme. Grid resolution is $\Delta x = \Delta z = 1m$.



(a) Results for WAVE10 (steepness: 10.3%)

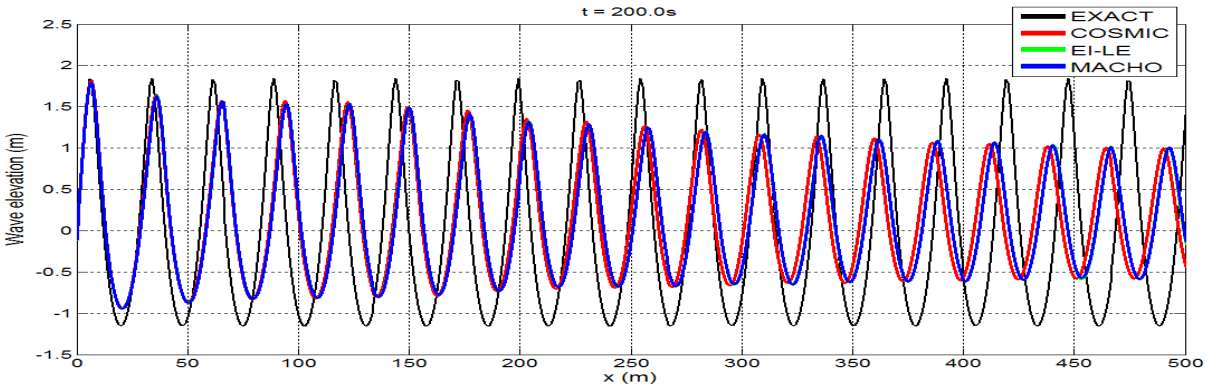


(b) Results for WAVE7 (steepness: 7.6%)

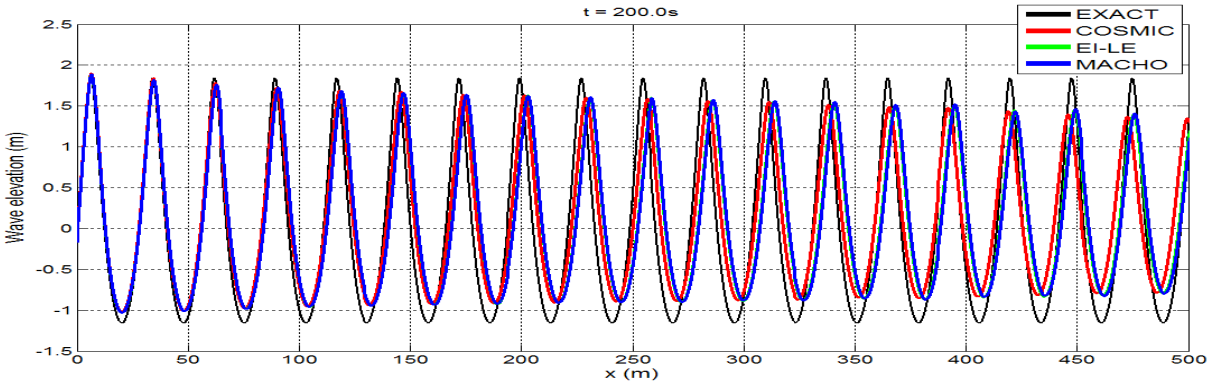


(c) Results for WAVE3 (steepness: 3.0%)

Figure 3: Wave elevations as a function of horizontal location for the waves in Tab. 2. The LSG, MYC and Youngs methods are combined with the COSMIC advection scheme. Grid resolution is $\Delta x = \Delta z = 0.5m$.



(a) Grid resolution is $\Delta x = \Delta z = 1m$



(b) Grid resolution is $\Delta x = \Delta z = 0.5m$

Figure 4: Wave elevations as a function of horizontal location for WAVE10. The COSMIC, EI-LE and MACHO advection schemes are combined with the Youngs reconstruction method.

When the grid resolution is increased ($\Delta x = \Delta z = 0.5m$), significant improvements in the results are noticed, see Fig. 3. When Hirt-Nichols' VOF + LHF is used, WAVE3 lost nearly 26% of its initial wave height after 17 wave lengths, WAVE7 lost 44%, and WAVE10 lost 58%. Similar to the behavior on the coarse grid, H&N + LHF produces substantial errors in terms of phase shift as the steepness increases. With PLIC methods + COSMIC combinations, we observe significant improvements in the results concerning both wave damping and phase shift. For WAVE3, the wave signals obtained with three reconstruction methods are almost the same: 90% of the initial wave height remains with very small phase shift. For WAVE7, 80% of the initial wave height remains with the Youngs method whereas 88% remains with the LSG and MYC methods. Regarding phase shift, the LSG and Youngs method have slight advantage over the MYC method. For WAVE10 we observe clear differences between the three reconstruction methods. When Youngs method is used, only 71% of the initial wave height remains. This amount is 81% with the LSG and MYC methods. The result for WAVE10 also indicate that three wave

signals from the three PLIC methods show different behaviors in terms of phase shift: the MYC method produces the largest phase shift while the Youngs and LSG method produce small phase shifts.

Fig. 4 illustrates the results to compare the performance of the advection schemes. The combinations of the LSG and MYC methods with the MACHO, EI-LE and COSMIC advection schemes resulted in almost the same profiles for the three waves at two grid resolutions. In fact, we observed different wave profiles only when we use the Youngs method with the three advection schemes for the simulation of WAVE10. In case of the WAVE3 and WAVE7, once again we did not notice any differences between the advection methods. Fig. 4 shows that the behavior of the advection methods is almost the same in terms of wave damping, and is only slightly different in terms of phase shift. The difference between the MACHO and EI-LE schemes can be hardly seen at both resolutions while COSMIC produces slightly different wave signals.

5 CONCLUSIONS

We studied the effect of VOF algorithms on spurious energy dissipation in propagating wave simulations. By implementing more accurate interface reconstruction/advection combinations, spurious energy dissipation as well as phase shift are reduced substantially.

Acknowledgment
This research is supported by the Dutch Technology Foundation STW, applied science division of NWO and the technology programma of the Ministry of Economic Affairs in The Netherlands (contracts GWI.6433 and 10475).

REFERENCES

[1] Benson, D.J. Volume of fluid interface reconstruction methods for multi-material problems. *Appl. Mech. Rev.* (2002) **55**:151–165.

[2] Pilliod, J.E. and Puckett, E.G. Second-order accurate volume-of-fluid algorithms for tracking material interfaces. *J. Comput. Phys.* (2004) **199**:465–502.

[3] Rider, W.J. and Kothe, D.B. Reconstructing volume tracking. *J. Comput. Phys.* (1998) **141**:112–152.

[4] Liovic, P., Rudman, M., Liow, J-L., Lakehal, D. and Kothe, D. A 3D unsplit-advection volume tracking algorithm with planarity-preserving interface reconstruction. *Comput. Fluids* (2006) **35**:1011–1032.

[5] Leonard, B.P., Lock, A.P. and MacVean, M.K. Conservative explicit unrestricted-time-step multidimensional constancy-preserving advection schemes. *Mon. Weather Rev.* (1996) **124**:2588–2606.

[6] Scardovelli, R. and Zaleski, S. Interface reconstruction with least-square fit and split Eulerian-Langrangian advection. *Int. J. Numer. Meth. Fluids* (2003) **41**:251–274.

[7] Veldman, A.E.P., Luppes, R., Bunnik, T., Huijsmans, R.H.M., Duz, B., Iwanowski, B., Wemmenhove, R., Borsboom, M.J.A., Wellens, P.R., van der Heiden, H.J.L. and van der Plas, P. Extreme wave impact on offshore platforms and coastal constructions. *In Proc. 30th Conf. on Ocean, Offshore and Arctic Engineering OMAE 2011* OMAE2011-49488.

[8] Luppes, R., Duz, B., van der Heiden, H.J.L., van der Plas, P. and Veldman, A.E.P. Numerical simulation of extreme wave impact on offshore platforms and coastal constructions. *In Proc. 5th Conf. on Computational Methods in Marine Engineering MARINE 2011.*

[9] Hirt, C.W. and Nichols, B.D. Volume of fluid (VOF) method for the dynamics of free boundaries. *J. Comput. Phys.* (1981) **39**:201–225.

[10] Gerrits, J. *Dynamics of liquid-filled spacecraft.* Ph.D. Thesis, University of Groningen, The Netherlands, (2001).

[11] Youngs, D.L. An interface tracking method for a 3D Eularian hydrodynamics code. AWRE Design Math. Div. (1987) AWRE/44/92/35.

[12] Aulisa, E., Manservisi, S., Scardovelli, R. and Zaleski, S. Interface reconstruction with least-squares fit and split advection in three-dimensional Cartesian geometry. *J. Comput. Phys.* (2007) **225**:2301–2319.

[13] Scardovelli, R. and Zaleski, S. Analytical relations connecting linear interfaces and volume fractions in rectangular grids. *J. Comput. Phys.* (2000) **164**:228–237.

[14] Wang, Z., Yang, J. and Stern, F. A new volume-of-fluid method with a constructed distance function on general structured grids. *J. Comput. Phys.* (2012) **231**:3703–3722.

[15] Leveque, R. High-resolution conservative algorithms for advection in incompressible flow. *SIAM J. Numer. Anal.* (1996) **33**:627–665.

[16] Rienecker, M.M. and Fenton, J.D. A Fourier approximation method for steady water-waves. *J. Fluid Mech.* (1981) **104**:119–137.

[17] Verstappen, R. W. C. P. and Veldman, A. E. P. Symmetry-preserving discretization of turbulent flow. *J. Comput. Phys.* (2003) **187**:343–368.

[18] Kleefsman, K. M. T., Fekken, G., Veldman, A. E. P., Iwanowski, B. and Buchner, B. A Volume-of-Fluid based simulation method for wave impact problems *J. Comput. Phys.* (2005) **206**:363–393.

ANALYSIS OF THE INFLUENCE OF COMPLEX MATERIAL BEHAVIOUR ON FUSION WELDING SIMULATIONS

MARINE 2013

JP. LEFEBVRE[*], N. POLETZ[†], L. D'ALVISE[♠], M. CAZUGUEL[♦], A. FRANCOIS[†] AND E. WYART[†]

[*] Cenaero France SASu
462 Rue Benjamin Délessert – BP 83
ZI de Moissy-Cramayel – 77554 Moissy-Cramayel - France
e-mail: jean-pierre.lefebvre@cenaero.fr, www.cenaero.fr

[†] Cenaero
Rue des Frères Wright 29
6041 Gosselies - Belgium
e-mail: nicolas.poletz@cenaero.be, arnaud.francois@cenaero.be, eric.wyart@cenaero.be,
www.cenaero.be

[♠] GeonX
c/o SONACA, Route Nationale Cinq
6041 Gosselies - Belgium
e-mail: laurent.dalvise@geonx.com, www.geonx.com

[♦]DCNS Ingénierie Sous-Marins
CSE/CSB/Groupe Calcul – Rue Choiseul –
56311 Lorient Cedex - France
e-mail: mikael.cazuguel@dcnsgroup.com, www.dcnsgroup.com

Key words: Fusion welding, Metallurgy, Phase transformation

Abstract. Numerical simulation of welding processes allows the assessment of the residual stresses and deformations. Accurate results require the precise knowledge of the operating conditions and the materials. Because of the large temperature range the material overcomes during the process, complex phenomena may occur. The material can therefore be modeled using different levels of complexity. This paper presents a discussion of the influence of the material modeling, applied to a welding process, on the final results.

1 INTRODUCTION

Welding processes are among the most common techniques to assemble metallic parts together in the industry. However, the sequence of heating up and cooling down phases generates residual stresses and deformations that can have non negligible effects for further assembly or usage. In order to avoid manufacturing expensive prototypes, numerical

simulations of manufacturing processes are helpful during the design phase.

Because of the temperature range the material is subjected to, its modeling must take into account all phenomena such as material flow and phase transformation effects. In this paper, the welding process assembling a stiffener onto a panel is numerically simulated. Different material models (with or without phase transformation) are analyzed, and their influence on the accuracy of the results is discussed. Numerical welding simulations are performed using the software Morfeo/Welding, which is dedicated to simulate manufacturing processes, such as machining and welding [3].

2 DESCRIPTION OF THE CASE

2.1 Geometry and Mesh

In order to improve the mechanical characteristics of the structures, assemblies made up of panels and stiffeners are commonly used. Shipbuilding industry encountering the same issues, the validation case is defined as a stiffener welded onto a panel through two T-welding joints. The panel dimensions are 500x500x4 mm, while the stiffener dimensions are 500x100x4 mm. Figure 1 presents an overview of the analyzed geometry, as well as the associated mesh. In order to capture in an accurate way the gradients occurring during the welding process, specific mesh refinements are required in the Heat Affected Zone (HAZ). Mesh size is therefore fixed to 1.0 mm in the volumes close to both welding beads. Outside of these areas, element size is increasing with the distance to the melting pool. However, in order to avoid over-estimation of the panel stiffness and to capture accurately potential bending, a minimum of two elements is kept across the plate thickness.

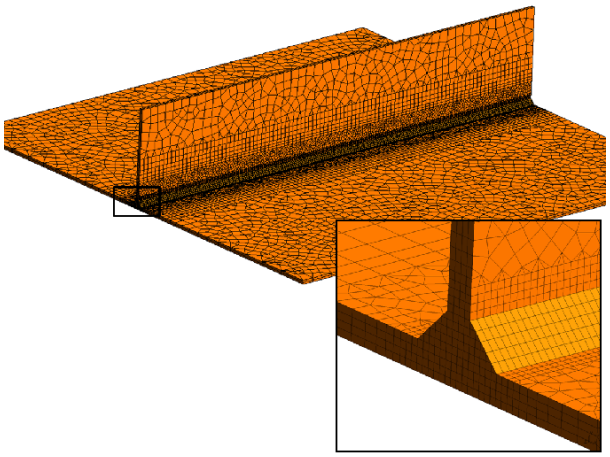


Figure 1: Mesh of the assembly Stiffener-Panel

The mesh is composed by degree 1 hexaedra and prisms elements. The presented mesh is constituted by 119 000 nodes and 152 000 elements.

2.2 Material behavior

Both parts of the assembly – stiffener and panel – are manufactured using the same steel alloy. The objective of the analysis is to examine the influence of the mechanical modeling of

the material. In order to simplify the model, and to save computation time, the quantities characterizing the thermal behavior are kept constant independently of the thermal evolution. Common values for steel alloys are therefore considered for the density, the thermal conductivity and the specific heat.

The constitutive law governing the mechanical response of the material is more complex, since it includes viscous effects and metallurgy and phase transformation. The elasto-plastic behavior is defined through a pure isotropic hardening (Eq. 1). The J2 yield function defining the elasticity domain follows the same formulation whatever the current phase is.

$$f(\sigma,R) = J_2(\sigma) - \sigma_y - R \tag{1}$$

with J_2 the second invariant of the stress tensor, σ_y the initial yield stress, and R the hardening stress defined as

$$R = Q[1 - \exp(-b\,p)]^{\beta} \tag{2}$$

where p refers to the accumulated plastic strain.

The viscous effects are also taken into account in the mechanical law. The retained formulation is the Cowper-Symonds overstress power law [4], defined as follows

$$\dot{p} = D\left[\frac{|\sigma| - R}{R}\right]^n \tag{3}$$

where $\dot{p}$ refers to the plastic rate, D and n are respectively the modulus and exponent of viscosity.

In order to complete the description of the mechanical behavior, metallurgy and phase transformation can be integrated into the model. The considered steel alloy is defined by two different phases: the ferrite-pearlite and the austenite. Phase transformation is modeled thanks to the Leblond-Devaux modeling approach, which defines the phase transformation velocity as a function of the temperature T and the proportion of the phase z (eq. 4), z_{eq} being the phase proportion reached at the equilibrium for the given temperature T and τ a characteristic time constant:

$$\dot{z} = \frac{z_{eq}(T) - z(T)}{\tau(T)} \tag{4}$$

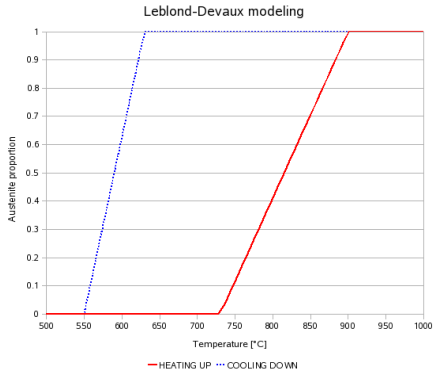


Figure 2 : Phase transformation : Leblond-Devaux modeling

These last two parameters can be deduced from dilatometric curves: using quasi-static heating-up velocity for z_{eq}, so that each state can be considered as equilibrate. τ is identified using faster heating-up velocities in order to get the right temperatures at the beginning and the end of the transformation.

Phase transformation integration induces changes in the expansion coefficient curve: during the heating-up phase, the transformation from ferrite-pearlite phase to austenite introduces the volumetric contraction (or expansion during the cooling down phase), effects being not considered for a single phase material description. The integration of the metallurgy allows taking into account the transformation plasticity induced. The formulation is given below (Eq. 5), where K is a material constant, z describes the progress of the new phase generation and σ_{dev} is the deviatoric stress tensor.

$$\dot{\varepsilon}^{pt} = K\,\phi'(z)\,\dot{z}\,\sigma_{dev} \qquad (5)$$
$$\phi(z) = z(2-z)$$

2.3 Operating conditions

The Metal Active Gas welding process is fully modeled. A phenomenological approach is used to model the heat input: the welding energy is integrated as an equivalent heat source with a volumetric power distribution through the workpiece thickness [1]. The sequence is also included in the model (torch trajectories, welding velocities, and cooling-down periods). Metal deposition is not taken into account in this case: elements modeling the weld joints are active from the beginning of the simulation.

The equivalent heat source is correlated to the experiment thanks to a metallographic analysis, which allows to determine easily the dimensions of the melted pool. Figure 3 compares the melted pools of the numerical simulation (defined by the isotherm 1500°C) and the experiment.

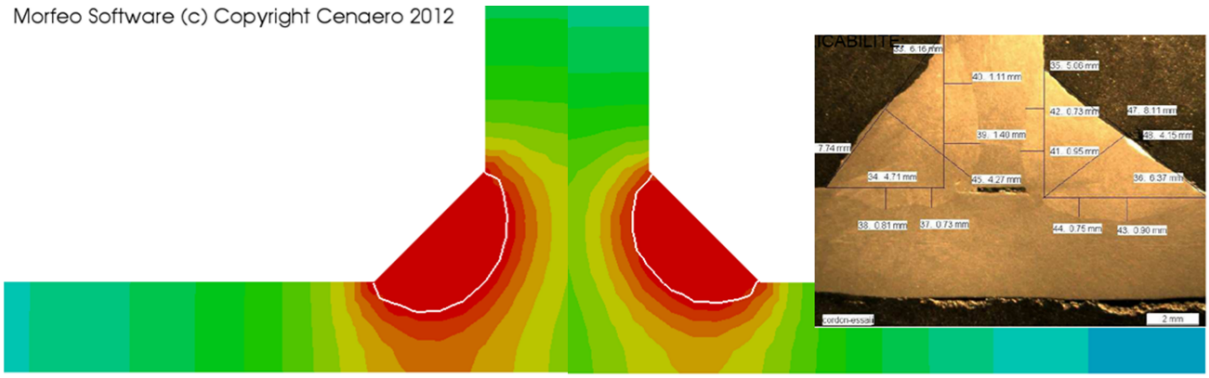


Figure 3 : Comparison between experimental and numerical melted pools

The welding power of 2440 W is applied into the model, and the weld torch is moving at the constant velocity of 5.30 mm/s.

2.4 Thermal and mechanical boundary conditions

Thermal exchange with the environment must be taken into account. It includes radiation and convection. Both contributions are gathered in one unique condition, applied on every free surface of the assembly, with an equivalent exchange coefficient evolving with the temperature.

Mechanical clamping is applied on surfaces on the thickness of the panel, as plotted in Figure 4. Each of these two surfaces is located at 24 mm from the plate side, and is 24 mm long.

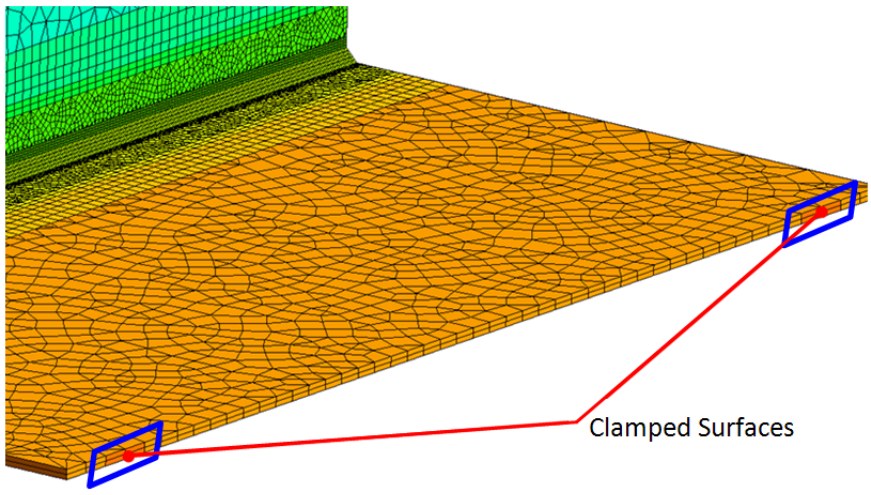


Figure 4 : Mechanical clamping system

3 NUMERICAL SIMULATION OF THE WELDING PROCESS

The numerical simulation of the fusion welding simulation is performed as a transient thermo-mechanical computation, using the dedicated software Morfeo/Welding. Resolution of

the problem is performed using a weak coupling method between both thermal and mechanical computations. The thermal analysis is based on a transient non-linear conduction formulation as expressed in Eq. 6

$$\rho C \frac{\partial T}{\partial t} = D \Delta T + P \tag{6}$$

where ρ is the material density, C the specific heat, D the conductivity tensor (reduced to the thermal conductivity as isotropy is considered) and P the heat source density.

The variation of the temperature field induces the generation of thermal strain. The generalized Hooke's law (Eq. 7) is solved to compute the thermo-elasto-plastic response of the structure for each time step.

$$\sigma = C \varepsilon^{el} = C\left(\varepsilon^{total} - \varepsilon^{plastic} - \varepsilon^{thermal}\right) \tag{7}$$

where C is the elasticity tensor.

The time increment has to be chosen carefully, specifically during the welding phase: it depends mainly on the mesh size and on the operating conditions (equivalent heat source dimensions and welding velocity). A compromise must be found in order to get accurate results without spending too much computation time. In this particular case, the increment has been chosen as the duration requested for the torch to move for 2 mm (which is twice as the element length in the welding joints). During the cooling down phases, the time step increases as the temperature gradients become lower and lower.

Within Morfeo, two main solver categories are available: iterative or direct solver. The iterative solver has been applied to solve the thermal analysis, while the parallel direct one was chosen for the mechanical resolution. Main criteria in the solver choice are the results restitution time and the influence of the solver settings (which are more delicate to adjust in the case of the iterative solver).

Thanks to the parallelism of Morfeo, results can be exploited within a reasonable time. 16 processors, using each less than 2 Gbytes, were used to perform the simulations, and complete results were available after less than 24 hours of computation.

4 PRESENTATION OF THE RESULTS

Two different simulations are performed with an increasing level of complexity in the material modeling: in the first simulation, only the elasto-visco-plastic response is considered, without any metallurgy, while it is taken into account in the second simulation.

Results are presented for three different time steps, respectively corresponding to the end of both weld joints, and after cooling down. All quantities are normalized with respect to the maximal value, common for both computations.

4.1 Simulation without metallurgical effects

In this model, one single phase is considered all over the complete temperature range.

The evolution of the normalized Von Mises stress field is presented in Figure 5.

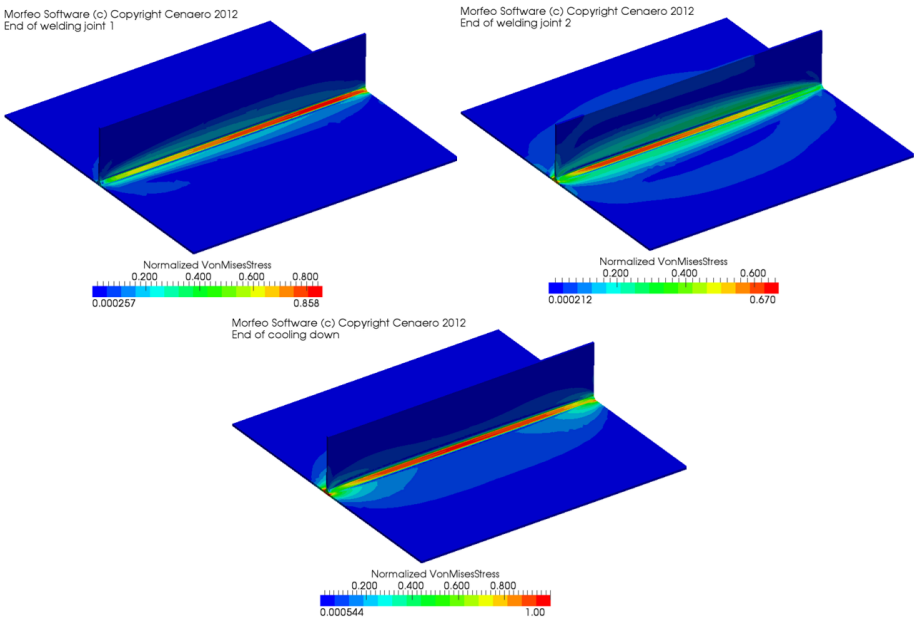


Figure 5 : Simulation without metallurgy - Von Mises stress map

The maximal stress values are located in the welding joints, areas where the thermal strain is the largest. It can be observed that maximal stress values at the end of the second weld are lower than those computed at the end of the first pass. This is can be explained by the temperature field that is higher in the welds because of the two heating-up phases, and tends to relax the stresses.

The analysis of the deflection of the assembly, and mainly of the panel is of great interest for further assembly in a larger structure. The evolution of the normalized vertical displacement is displayed in the following Figure 6.

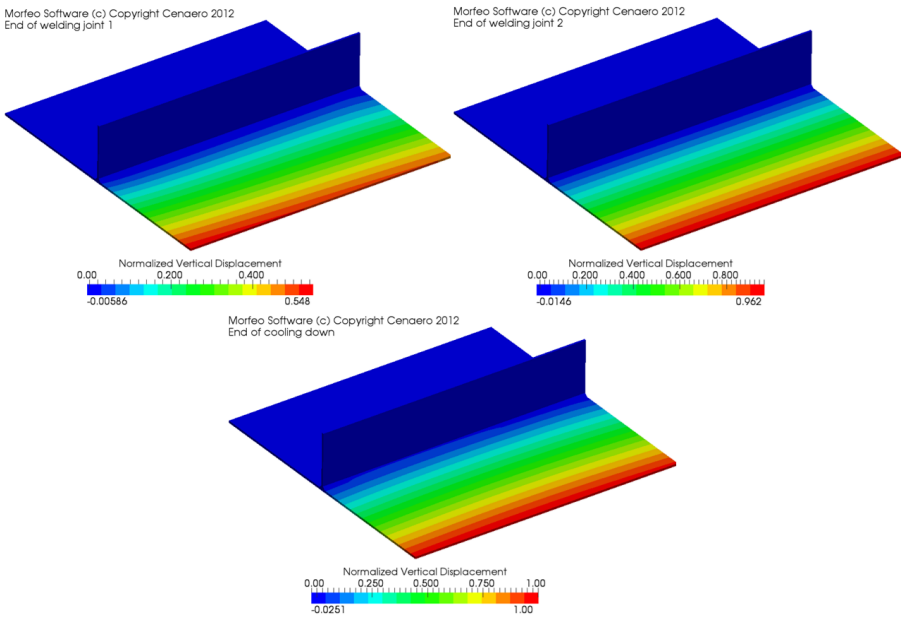


Figure 6 : Simulation without metallurgy - Vertical displacement

The cooling down phase induces volume contraction of the joint that generates bending of the panel. Figure 6 shows that the bending of the panel is uniform, and that no torsion occurs as the iso-lines are parallel to the welding trajectories.

Advanced phenomena such as the phase transformation, the transformation plasticity induced are not considered in this material model. They can however affect the final solution [2], and the influence has to be quantified. Metallurgy is therefore included in the material modeling, and the same process is analyzed

4.2 Simulation with metallurgical effects

Normalized Von Mises stresses and vertical displacement are post-processed for the same three time steps, as it was done previously. Results are presented below (Figure 7 and Figure 8).

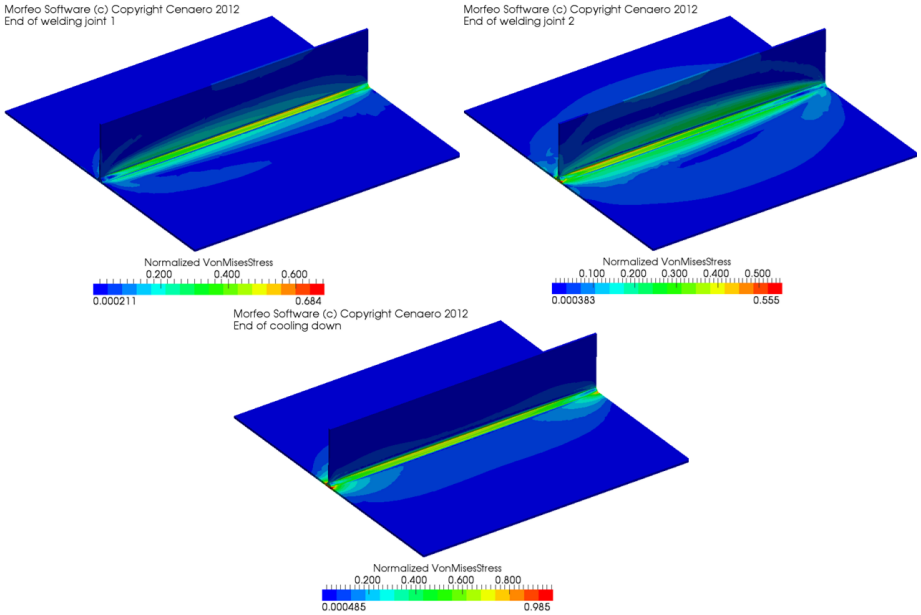


Figure 7 : Simulation including the metallurgy - Von Mises stress map

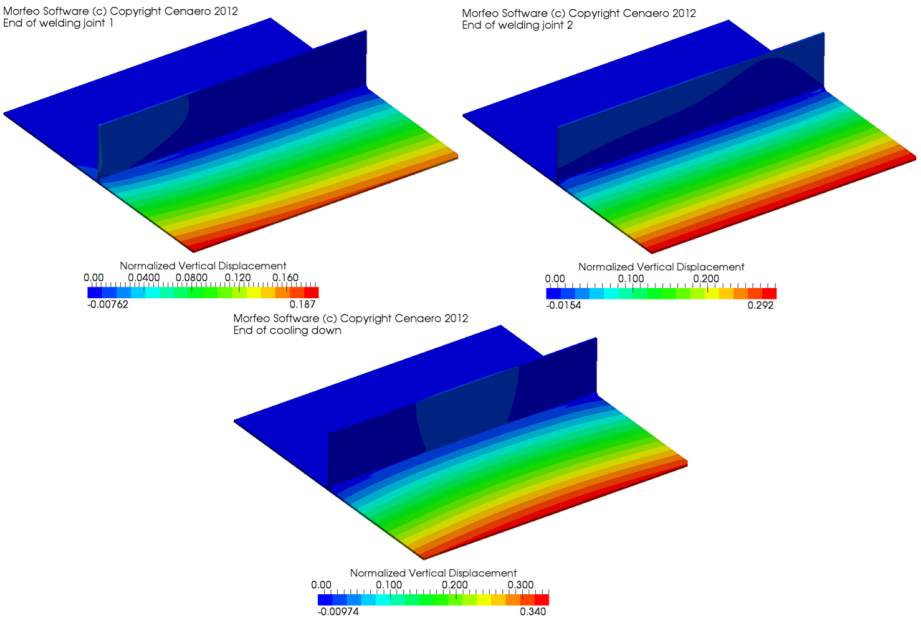


Figure 8 : Simulation including the metallurgy - Vertical displacement

The maximal stress values are about 15% lower than those computed without metallurgical effects. Maximal stress levels are located around the melting pool, where no phase transformation occured. The general shape of the deformed structure is similar to the one presented in Figure 6, although the final deflection is almost three times lower.

4.2 Influence of the metallurgy on the final results

Taking into account the metallurgy influences the results of the numerical simulation and

the resources (CPU time and memory) usage. It induces an increase of the CPU Time in the mechanical task of 12% (there is no change in the thermal model, so that the computation time are identical), and requires 25% more memory: computations are completed respectively in less than 21 and 23 hours, using respectively 8.7 Gbytes and 10.8 Gbytes.

The maximal stress levels are not located exactly at the same place: without metallurgy, maximal values are located in the welding beads, where the thermal strain was the higher. This is not the case in the second model: during the cooling down phase, the phase transformation austenite->ferrite+pearlite induces some volume expansion, which relieves the stresses in and around the melting pool. Maximal stress values are therefore lower than those computed in the first model, and located in the surrounded areas, where no phase transformation occurred, as illustrated in Figure 9.

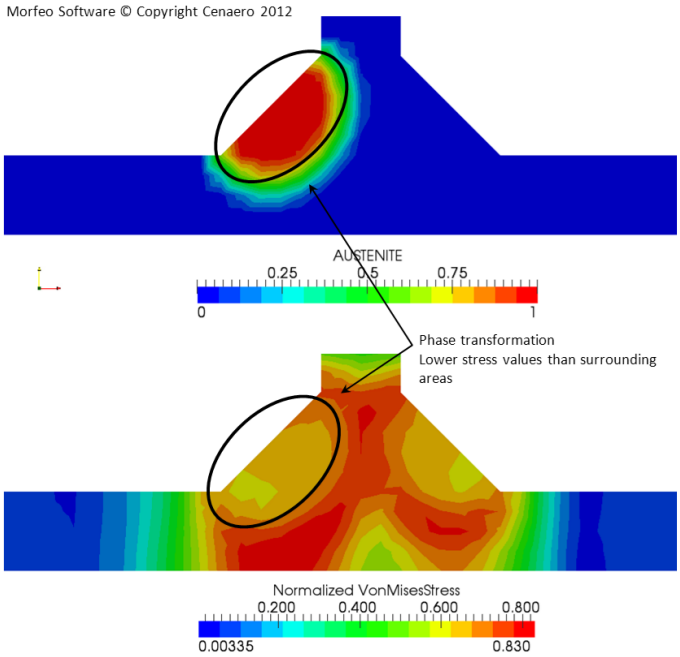


Figure 9 : Domain subjected to phase transformation - Location of the highest stress values

The structures overcome similar deformed shape: the panel's bending (Figure 6 and Figure 8). Nevertheless, the final deflection is three times larger when metallurgy is not considered. In this case, the bending is indeed due to the volume contraction during the cooling down phase. When the metallurgy is applied into the model, the transverse stress map is slightly different. Because of the volume expansion happening during the austenite to ferrite+pearlite transformation, the compressive stress becomes lower, and therefore the induced deflection of the panel.

Unfortunately, experimental measurements are not reliable for this application case. For a finer investigation of the benefit of taking into account of metallurgy within fusion welding simulations, a smaller and simpler instrumented case, made of two plates butt welded, could be analyzed numerically and experimentally.

The previous comparison clearly shows that material modeling plays a key role in the accuracy of the simulations. However, increasing the complexity of the material model requires an even more complex and precise characterization to return accurate results.

5 CONCLUSIONS

In order to analyze the influence of complex material modeling, the MAG fusion welding process is applied on a shipbuilding typical structure, made up of a stiffener and a panel. The constitutive law is defined as elasto-visco-plastic. Two different material models are analyzed in this paper : the first model considers the material as a single phase material, while the second one takes into account the metallurgical effects, such as phase transformation, transformation induced plasticity and thermal contraction/expansion during the phase changes.

The material model plays a key role in the assessment of the residual stresses: with metallurgical effects, residual stresses predicted are lower than those computed with a simpler material model. The higher stress values are located outside of the HAZ (where no phase transformation occurred), whereas the initial model predicts them in the welding beads. It also has a great influence on the deflection computation. On this application case, it has been proved that a factor 3 was applied to the final deflection.

The main conclusions of this analysis are relative to the crucial importance of the material characterization, and the reliability of the welding tests that could be performed to correlate and validate the model. The integration of advanced phenomena in the material behavior requires a precise characterization, and a strong validation on instrumented samples.

6 AKNOWLEDGMENT

The authors would like to show their gratitude to DCNS who provided the studied case and the financial support to perform these analyses.

REFERENCES

[1] Modelling and Simulation of Welding and Metal Deposition, A. Lundbäck, Department of Applied Physics, Mechanical and Materials Engineering, Luleà University of Technology, Luleå, Sweden, 2010

[2] Three-Dimensional Finite Element Simulation of Laser Welded Stainless Steel Plate, D. Berglund, L.E. Lindgren & A. Lundbäck, Computer Aided Design, Luleà University of Technology, Luleå, Sweden, 2001

[3] Morfeo 1.7 User's Manual, Cenaero, Belgium, 2012

[4] Abaqus 6.10 User's Manual, Dassault Systèmes Simulia Corp., Providence, RI, USA, 2010

V International Conference on Computational Methods in Marine Engineering
MARINE 2013
B. Brinkmann and P. Wriggers (Eds)

COMPUTATIONAL MODELLING OF TWO-PHASE FLOW AROUND A SAVONIUS TYPE WAVE ENERGY CONVERTER IN A TWO-DIMENSIONAL NUMERICAL WAVE TANK

M. TUTAR[*†] AND C. ERDEM[††]

[*] Department of Mechanical and Manufacture
Mondragon Goi Eskola Politknikoa
Loramendi 4, Apartado 23, 20500 Mondragon, Spain

[†]IKERBASQUE, Basque Foundation for Science, 48011, Bilbao, Spain
E-mail: mtutar@mondragon.edu www.mondragon.edu

[††] Department of Aerospace Engineering, Middle East Technical University, 06531, Ankara, Turkey
E-mail: ceyhanerdem@gmail.com

Key words: Computational Methods, Wave Energy, Volume of Fluid (VOF) Method, Savonius Turbines

Abstract. In the present study, the main objective is to develop a finite volume method (FVM) based numerical modelling approach incorporated with a Volume of fluid (VOF) method to investigate the effect of wave on the performance of Savonius rotor in a two-dimensional numerical wave tank (NWT). A Savonius rotor, whose rotational axis is normal to the direction of wave generation, is introduced to computationally investigate flow around the rotor structure at selected wave height conditions. The geometry of the blades is such that wave motion produces a positive force on the rotor and is constructed using CAD software. Followed by importing the orthogonal mesh domain constructed in FLOW-3D software environment, defined in Cartesian coordinates, into the finite volume environment of FLOW-3D for fluid flow analysis. A body-fixed reference system ("body system"), introduced for the rotor, and the space reference system ("space system") is employed to scrutinize a two-dimensional unsteady turbulent flow around the rotor structure. At each time step equations of motion are solved for the rotor under coupled motion with consideration of hydraulic, gravitational and control forces. The flow simulations are then performed using Reynolds-averaged Navier-Stokes (RANS) based two-equation RNG k-ε turbulence model with dynamically computed turbulent length scale, under the assumption of incompressible, viscous, and transient two-phase turbulent flow conditions.

From the numerical results obtained and validated against the theoretical data obtained from the no-rotor flow condition, it can be concluded that the flow characteristics is strongly dependent upon differing wave propagation conditions and energy conversion rate can be increased with a proper combination of selected wave height and frequency for the investigated parametric value range. Flow visualization, which is represented by qualitative contours of velocity vector field also show different flow patterns at different wave height conditions.

1 INTRODUCTION

Worldwide interest in ocean wave energy options has given rise to emergence of new wave turbine designs. Some of the most recent models on the market are Savonius type hydraulic turbines, which are considered to be simple, efficient with good starting capabilities and to operate at relatively low rotational speeds There have been now considerable efforts in combined experimental and computational studies [1-5] of power performance analysis of Savonius turbines, which are used to transfer the wave's force directly to the rotor shaft, which is directly connected to a generator that converts the energy into electricity for their high efficient diversified applications.

Orbital motion of water particles in experimental wave tank (EWT) has been investigated through several experimental studies [4,5] to determine the performance of the Savonius rotor in shallow waters for different parameters. Ahmed et al. [4] and Faizal et al. [5] well documented the flow around the rotors placed parallel to the incoming waves in a 2-D EWT using particle image velocimetry (PIV) measurements. The frequency of the wave generator which produced the sinusoidal wave, the rotor speed and the rotor submerged level were varied for these experimental studies as well as the number of rotors used in a well-aligned array arrangement to determine the performance of the Savonius rotor for different governing parameters. These studies showed that rotational speeds increased with an increase in the wave frequency, as it amplified the wave height and hence the kinetic energy of the water particles in their orbital motion. However, increase in the wavelength reduced the rotational speed and the maximum rotational speed was achieved close to the surface. The experimental study of Hindasageri et al. [6] also demonstrated the influence of water depth on the rotor rotational speed. They noted that the number of blades on the rotor and the number of rotors in the array would be influential on the rotor performance and computational fluid dynamics (CFD) simulations would be required for further analysis of rotor performance.

There have been also very limited number of numerical studies [7,8] on wave flow analysis around Savonius rotor in the literature. Zullah and Lee [7] adopted a finite volume method (FVM) based numerical modelling approach devoted to investigate the effect of wave on performance and internal flow of the Savonius turbine in the components of an oscillating water column (OWC) system used for the wave energy harnessing. Their principal findings stated that the shape of the rotor would be influential on the efficiency and self-starting capability of the rotor and a higher curvature rotor would receive a higher value of net positive torque. Their obtained result also indicated that the developed numerical models would be well suitable to analyse the water flow through the Savonius rotor.

The purpose of the present study was numerically explore the non-linear, two-dimensional, viscous, unsteady and two-phase turbulent flow motion around a Savonius rotor placed in a 2-D NWT using FVM method based numerical modelling approach [9] in comparison with the experimental work [6]. Since a very limited literature available for the numerical analysis of Savonius rotor performance in shallow waters, and this was also motivation for the present study.

2 GOVERNING EQUATIONS

The fundamental flow equations governing the present 2-D turbulent flow behavior around the Savonius rotor structure are continuity, Reynolds averaged Navier-Stokes (RANS)

equations (momentum equations) and turbulence transport equations. These conservation equations written in non-linear differential form of vector notation for incompressible, viscous fluid flow conditions can be summarized below.

$$\frac{\partial \overline{u}_i}{\partial x_i} = 0 \tag{1}$$

$$\rho \frac{\partial \overline{u}_i}{\partial t} + \rho \overline{u}_j \frac{\partial \overline{u}_i}{\partial x_j} = -\frac{\partial \overline{P}}{\partial x_i} + \frac{\partial}{\partial x_j}\left(\mu \frac{\partial \overline{u}_i}{\partial x_j} - \rho \overline{u_i' u_j'} \right) + \rho g_i \tag{2}$$

The Full ρ is the fluid density, $\overline{u}_i$ is the time averaged velocity, x_i is the coordinate direction, u_i' is the deviation from the time averaged velocity, $\overline{P}$ is the time averaged pressure, g_i is gravity acceleration, μ is the dynamic viscosity of the fluid, - $\rho \overline{u_i' u_j'}$ is the Reynold's stress tensor which is required to be modeled using a turbulence model for closure of RANS equations. The temporal and spatial co-ordinates correspond to *t* and x_i, respectively. In 2-D Cartesian coordinates the continuity and RANS equations can be re-defined by simply dropping the over bar for brevity for the time averaged quantity as below:

$$\frac{\partial u}{\partial x} + \frac{\partial v}{\partial y} = 0 \tag{3}$$

$$\rho\left(\frac{\partial u}{\partial t} + u\frac{\partial u}{\partial x} + v\frac{\partial u}{\partial y} \right) = -\frac{\partial P}{\partial x} + \frac{\partial}{\partial x}\left(\mu \frac{\partial u}{\partial x} - \rho \overline{u'u'} \right) + \frac{\partial}{\partial y}\left(\frac{\partial u}{\partial y} - \rho \overline{u'v'} \right) + \rho g_x \tag{4}$$

$$\rho\left(\frac{\partial v}{\partial t} + u\frac{\partial v}{\partial x} + v\frac{\partial v}{\partial y} \right) = -\frac{\partial P}{\partial y} + \frac{\partial}{\partial x}\left(\mu \frac{\partial v}{\partial x} - \rho \overline{u'v'} \right) + \frac{\partial}{\partial y}\left(\frac{\partial v}{\partial y} - \rho \overline{v'v'} \right) + \rho g_y \tag{5}$$

In eddy viscosity based *k*-ε turbulence models, Reynolds stress tensor is related to the mean flow straining field for incompressible flow as below:

$$-\rho \overline{u_i' u_j'} = \frac{2}{3}\rho k \delta_{ij} + 2\mu_t \overline{S}_{ij} \tag{6}$$

Where *k* denotes the turbulence kinetic energy, μ_t is the eddy viscosity related to turbulence kinetic energy, *k* and its dissipation rate, ε, and $\overline{S}_{ij}$ is the time averaged strain rate tensor related to mean velocity gradient in the flow. The turbulent kinetic energy, *k* and its dissipation rate,ε for isothermal are then defined by the turbulence transport equations to determine the eddy viscosity term, which is used to calculate the Reynolds stress term to closure the RANS equations.

3 COMPUTATIONAL FRAME WORK

Below summarizes a computational frame work, which describes briefly the computational principles of the current flow modeling solution employed, and addresses some important aspect of the computational details of this solution.

3.1 Flow geometry

A 2-D schematic diagram of a numerical wave tank (NWT) is constructed as a representation of the experimental wave tank (EWT) study of Hindasageri et al. [6] as seen in Fig. 1. The overall size of the NWT flow domain in the *x* and *z* directions ranges from 0 to 41.5 m and -0.6 to 0.5 m, respectively. The Savonius rotor placed in the NWT is generated in accordance with the rotor structure used in the experiment. The location of the Savonius rotor is subject to change in accordance with the experimental study at different rotor submergence levels of to make a direct comparison with the experimental results [6]. The boundaries are also illustrated in Fig. 1.

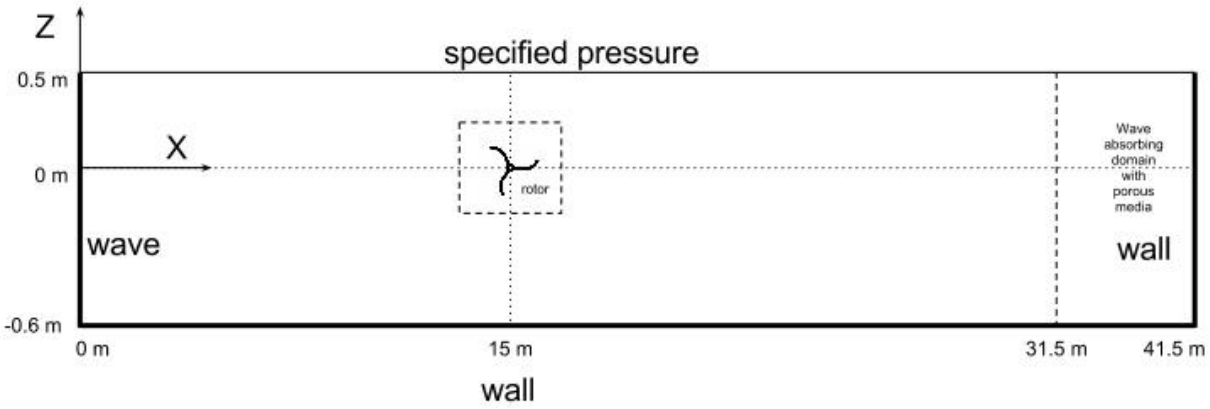
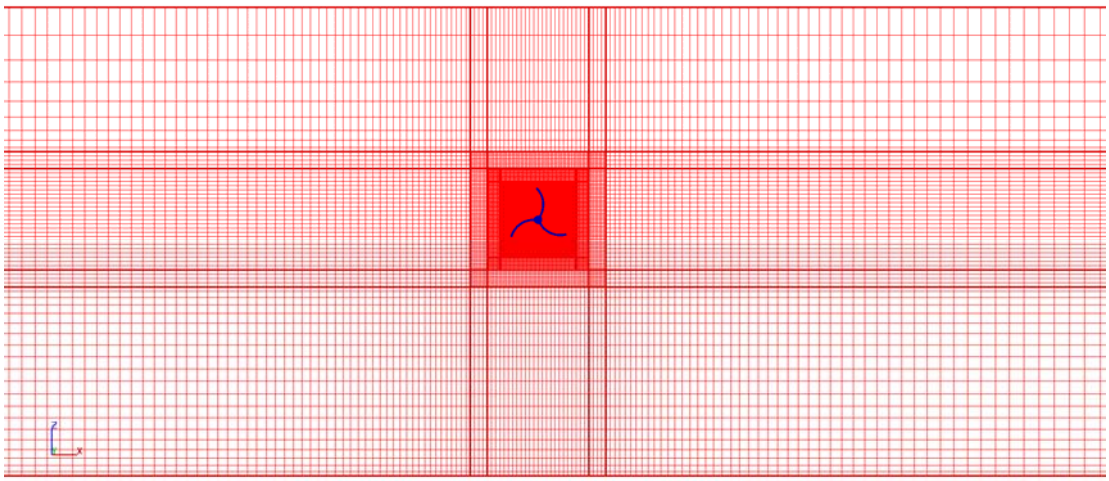


Figure 1: Numerical wave tank (NWT) representation of the present flow problem

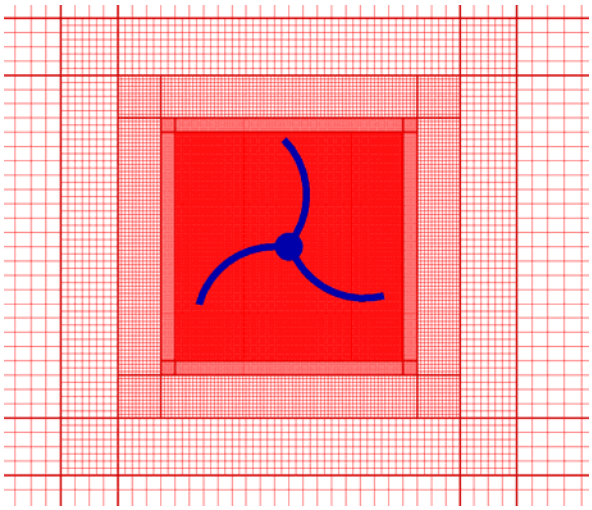
3.2 The computational grid and boundary conditions

The multi-block meshing modeling is utilized for more efficient use of computational resources and fast flow solution. The computational domain is constructed with non-uniformly spaced 2-D quadrilateral mesh elements (Fig. 2) with fine resolution near wall surfaces and interface between air and water to successfully resolve the air-water surface movement due to wave propagation and to improve the numerical accuracy for measuring velocity and pressure gradients.

Different mesh resolutions are adopted for flow simulations with and without Savonius rotor based flow solutions. The global 2-D mesh domain includes three different local mesh zones coupled with each other: 1) The wave generating boundary and the wave surface domain ($0 < x < 31.5$ m); 2) Wave absorbing domain- porous media defined in the flow exit zone (31.5 m $< x < 41.5$ m); 3) The fine inner mesh zone where the rotor movement takes place. Different mathematical models are adopted for resolution of the flow in each mesh zone and these models are briefly discussed as below:



(a)



(b)

Figure 2: The mesh configuration used in the present simulations; a) Global mesh; b) Local mesh surrounding the rotor surface

Wave generating boundary and wave surface domain:

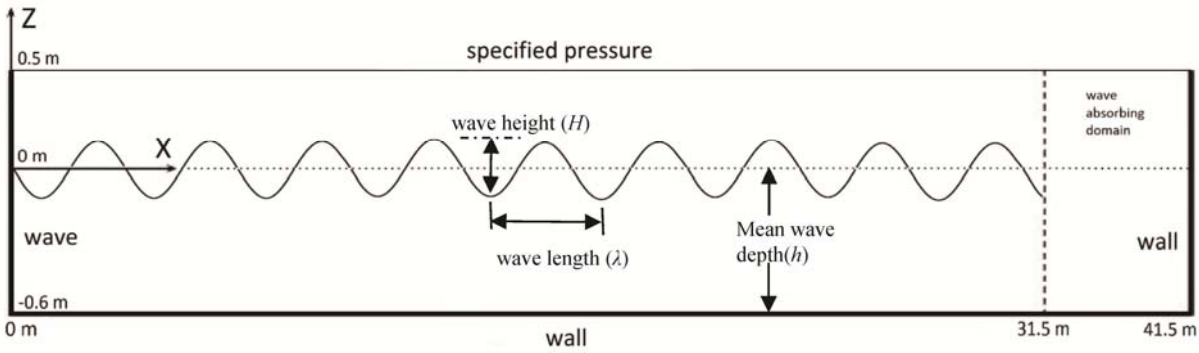


Figure 3: Stokes wave entering the computational domain at the left boundary (x = 0 m) in the NWT

As shown in the figure above, a wave train is simulated to come from x=0, wave boundary into the computational domain. The reference system (x, z) is established with its origin fixed at 0.6 m above the NWT bottom, +x going in the wave propagation direction and +z in the upward direction. The wave is characterized by the wave height H, wavelength λ and wave frequency ω. The mean wave depth h is constant. The wave frequency ω and the wave speed c in are related to other parameters as

$$\omega = \frac{2\pi}{T} \text{ and } c = \frac{\lambda}{T} \tag{7}$$

where k is the wave number ($k = 2\pi/\lambda$).

The Stokes wave theory assumes potential flow, i.e. the fluid flow is incompressible and irrotational. The stream function ψ thus exists and satisfies the Laplace equation;

$$\nabla \psi = 0 \tag{8}$$

Hence fluid velocity components in x and z directions are;

$$u = \frac{\partial \psi}{\partial x} \text{ and } w = -\frac{\partial \psi}{\partial z} \tag{9}$$

With the further assumption that a wave crest exists at x=0 at t=0, the Laplace equation for ψ, along with its boundary conditions at the free surface and the bottom, are solved using a perturbation method. The perturbation parameter is the dimensionless wave amplitude, $\varepsilon = kH/2$, which is also known as the wave steepness. The solution for the water elevation and velocity with second-order accuracy with respect to ε is given below in consideration of applicability ranges of the present generated waves as provided in Fig. 4.

Surface profile:

$$\eta = \frac{H}{2}\cos(kx - \omega t) + \frac{H^2 k}{16}\frac{\cosh(kg)}{\sinh^3(kh)}(2 + \cosh 2kh)\cos 2(kx - \omega t) \tag{10}$$

x-velocity:

$$u = \frac{H}{2}\frac{gk}{\omega}\frac{\cosh k(h+z)}{\cosh kh}\cos(kx - \omega t) + \frac{3H^2 \omega k}{16}\frac{\cosh 2k(h+z)}{\sinh^4(kh)}\cos 2(kx - \omega t) \tag{11}$$

z-velocity:

$$w = \frac{H}{2}\frac{gk}{\omega}\frac{\sinh k(h+z)}{\cosh kh}\sin(kx - \omega t) + \frac{3H^2 \omega k}{16}\frac{\sinh 2k(h+z)}{\sinh^4(kh)}\sin 2(kx - \omega t) \tag{12}$$

The free surface domain:

In the present numerical approach free surface is modelled with a new volume of fluid (VOF) advection method, namely TruVOF technique. This technique is a modified version the Volume of Fluid (VOF) technique originally proposed by Hirt and Nichols [12] and consists of three ingredients: a scheme to locate the surface, an algorithm to track the surface

as a sharp in the interface moving through a computational grid, and a means of applying boundary conditions at the surface [9].

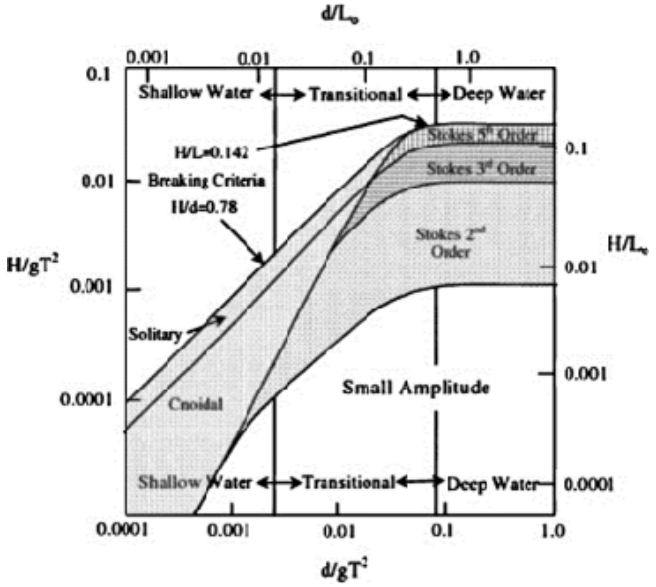


Figure 4: Applicability ranges of various wave theories (after Le Méhauté [10] and USACE [11]). d: mean water depth; H: wave height; T: wave period; g: gravitational acceleration

Wave absorbing domain:

For the modeling of the wave absorbing domain; D'Arcian model is used, in which flow resistance is linearly proportional to velocity by the *permeability*, κ:

$$u_{superficial} = -\frac{\kappa}{\mu}\nabla p$$

where $u_{superficial}$, κ, μ and ∇p are apparent velocity, intrinsic permeability, dynamic viscosity and pressure gradient in real space within the porous material, respectively. The purpose of using porous media at the end of the NWT domain is to damp the velocity components of the water in the NWT, so that any reflection which may affect the upstream flow conditions will be eliminated.

3.3 Numerical Solver

A FDM/FVM based numerical flow modeling approach of FLOW-3D [9] is used to solve the partial differential equations (continuity, momentum and energy equations) governing rotor movement and surface tracking. The momentum equation is closely coupled with the viscosity constitutive relation. To increase the convergence rate, momentum equations and the pressure based continuity equation are also coupled with a pressure-velocity coupling scheme of Generalized Minimal Residual Solver (GMRES) scheme [13] and the first order upwind scheme for discretization of the momentum equation. A variable time step size with an initial value of 1.5×10^{-5} s is used in all simulations. The size of the time step can be controlled and adapted using the stability and convergence criteria during the solution. The one fluid VOF model is

chosen for free surface, the Fractional Areas/Volumes Obstacle Representation (FAVOR) is chosen for efficient geometry definition. In the FAVOR method, a surface is allowed to cut through an element compared to the BFC (body fitted coordinate). The location of solid surface in FAVOR is recorded by the fractional face areas and fractional volume of the element covered by the solid.

4 RESULTS AND DISCUSSIONS

Numerical verification of the proposed computational modeling approach is initially established for a no-rotor flow case by generating wave propagation with a range of wave length or frequency in comparison with the theoretical solutions based on Stokes Second 2nd order wave theory for different mesh resolutions. The computations are later extended to the rotor-flow solution and a series of simulations are performed for different wave height conditions of 100 mm, 120 mm, 140 mm and 160 mm at a submerged level of the rotor at z = 0 m to directly compare the results with those obtained from Hindasageri et al. [6].

4.1 No-rotor flow condition: Wave propagation

The generation of linear waves based on Stokes 2nd order wave formulation is completed in a time period of around 2.1 s and wave length of 4.62785 m for different wave height conditions of H = 100 mm for three different mesh resolutions of 12,456 cells (coarse mesh), 29,064 cells (medium mesh) and 114,125 cells (fine mesh) and or H = 160 mm for a fine mesh resolution of 114,125 cells. As seen in Figs. 4 and 5, the numerical data is found to be in very good correspondence with the theory, and in the shape of the surface waves is represented almost sinusoidal function throughout the domain with different surface elevation height depending on the wave height imposed at the inflow boundary.

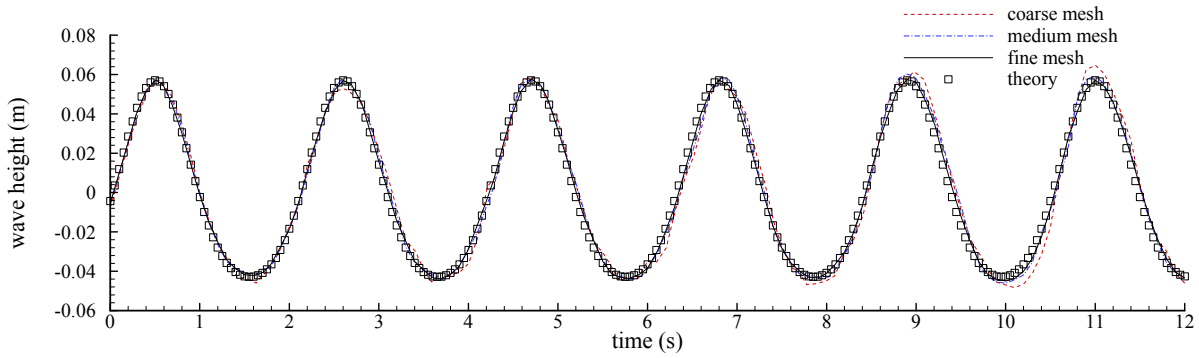


Figure 5: Wave elevation history for three-different mesh systems in comparison with the theory at a probe position of x = 15 m for a selected wave height of H = 100 mm

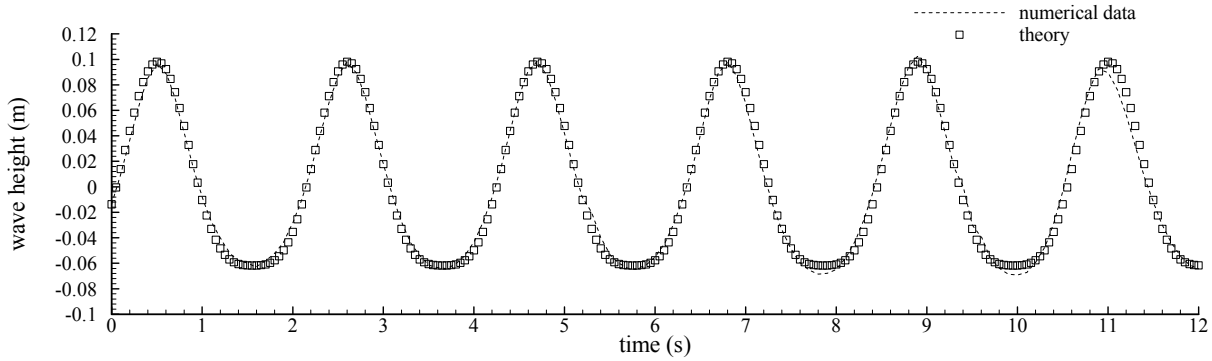


Figure 6: Wave elevation history for the fine mesh solution in comparison with the theory at a probe position of x = 15 mm for a selected wave height of H = 160 mm

The probe position at which the surface elevation history is plotted is illustrated in Fig. 7.

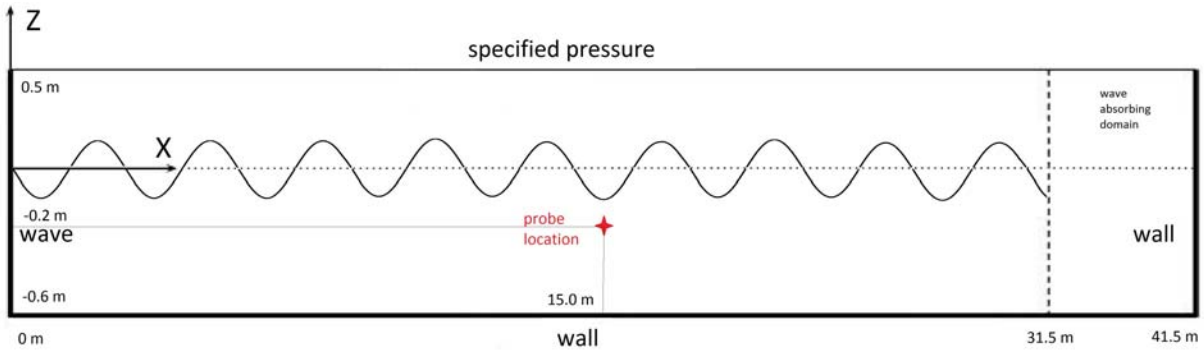
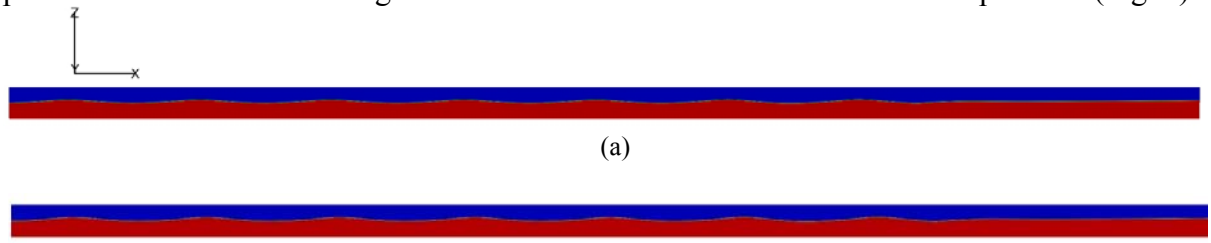


Figure 7: The probe position used for evolution of surface elevation for different wave height values.

After nearly 5 wave generation periods, the wave approaches to its quasi-steady profile while it is dissipated in the wave absorbing domain, which is generated as a resistance of the porous medium for smoothing the surface waves to overcome the reflection problem (Fig. 8).



(a)

(b)

Figure 8: Instantaneous phase contours illustrating wave surfaces at t = 5 s; a) Wave height of H =100 mm; b) Wave height of H = 140 mm

4.2 Simulations with rotor flow condition

Figures 9 (a) to (d) illustrate the instantaneous phase contours together with velocity vector fields at the same simulation time of 11.5 s. for the case of flow interaction with three-bladed Savonius rotor for different wave heights. Distinguished phase contours and corresponding velocity vectors obtained for each case suggests that flow characteristics is strongly dependent upon differing wave propagation conditions and energy conversion rate may be increased with a proper combination of selected wave height.

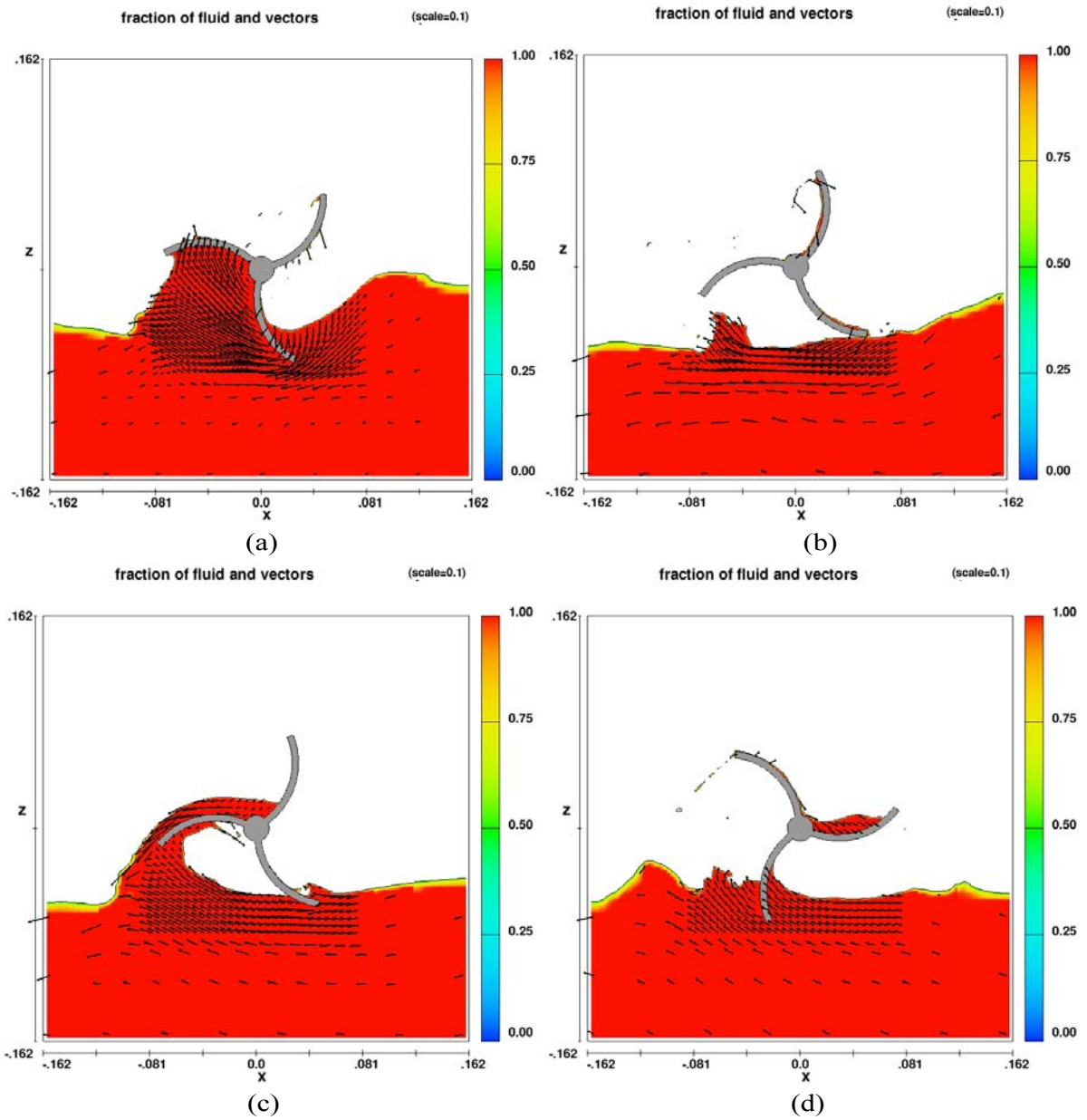


Figure 9: Instantaneous phase contours and local velocity vectors in the inner mesh domain at a simulation time of 11.5 s; a) H = 100 mm; b) H = 120 mm; H = 140 mm; d) H = 160 mm

The time history of rotor speed at different wave height represents highly fluctuating evolution pattern as an indication of non-steady rotational motion in the clock and anti-clock wise direction for each wave height as seen in Figs. 10 (a) to (d). This behavior is possibly due to non-continuous flow through the rotor blade which is located at a sub-merged level of z = 0 m and through investigations may be required for the analysis of this rotational behavior. Nevertheless, the maximum rotational speed obtained in the clock wise directions are found to be in good correspondence with those obtained from the experimental study of Hindasageri et al. [6] and slightly higher rotational speed is obtained as the wave height increases as an indication of positive effect of wave height increase on the rotational torque.

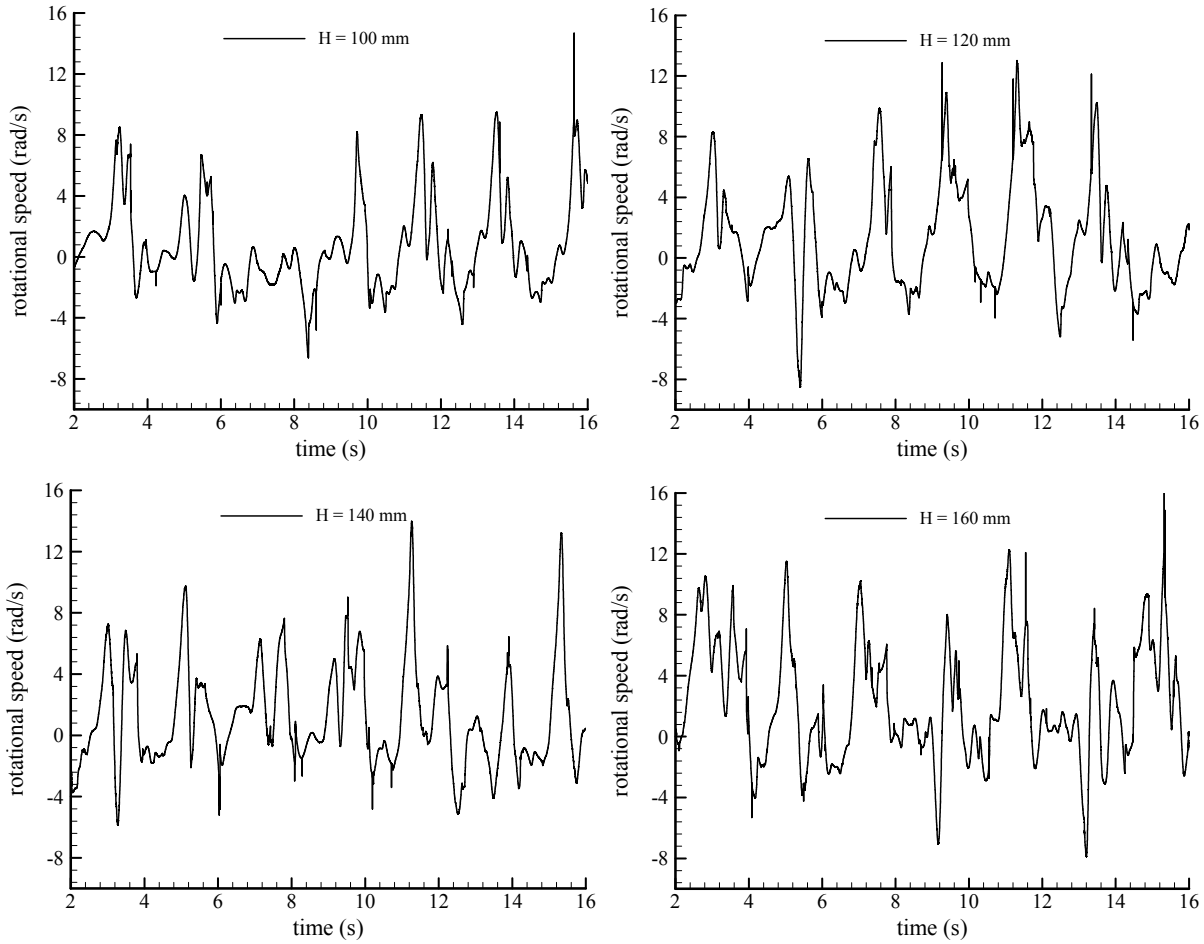


Figure 10: Time evolution of rotational speed at different wave height, *H*.

5 CONCLUSIONS

In the present study, generation and propagation of regular surface waves and their interaction with a three-bladed Savonius rotor are numerically investigated with use of FVM based numerical flow solver, FLOW-3D. A summary of findings of the present study are presented below:

- The present numerical code, FLOW -3D successfully reproduces linear waves with ease and reasonable accuracy and models the interaction of these waves with a Savonius rotor for

different wave height conditions.

- The propagation of generated waves at the inflow boundary in the NWT.is found to be stable.
- The higher wave heights the higher rotational speed of the Savonius rotor.
- Non-continuous flow through the rotor, which is located at zero submerged surface level, causes fluctuating rotational motion.

ACKNOWLEDGEMENTS

This work was funded under the project of the Gobierno Vasco- Basica y Aplicada- PI 2011-8. The partial financial support was also acknowledged under the project of the Spanish Ministry of Economy and Competitiveness MTM2010-16511.

REFERENCES

[1] Wang H-W., Huang, C-J. and Wu, J. Simulation of 3D numerical wave tank, *Journal of Engineering Mechanics* (2007) 761-772

[2] Dong, C-M., Huang, C-J., Generation and propagation of water waves in a two-dimensional numerical viscous wave flume. *Journal of Waterway, Port, Coastal and Ocean Engineering (ASCE)* (2004) 143-153

[3] Nakajima, M., Lio, S., and Ikeda, T. Performance of double-step savonius rotor for environmentally friendly hydraulic turbine. *J. of Fluid Science and Technology* (2008) **3(3):** 410-419

[4] Faizal, M., Ahmed, M.R., and Lee, Y-H. On utilizing the orbital motion in water waves to drive a Savonius rotor. *Renewable Energy* (2010) **35**:164-169

[5] Ahmed M.R., Faizal, M., Prasad, K., Cho Y-J., Kim, C-G., Lee Y-H., Exploiting the orbital motion of water particles for energy extraction from waves. *J. of Mechanical Science and Technology* (2010) **24(4):** 943-949

[6] Hindasageri, V., Ramesh, H., and Kattimani, S.C. Performance of Savonius rotors for utilizing the orbital motion of ocean waves in shallow waters. *J. of Sustainable Energy & Environment* (2011) **2**: 117-119

[7] Zullah, M.A., Lee, Y-H. Performance evaluation of a direct drive wave energy converter using CFD. *Renewable Energy* (2012) 1-5

[8] Zullah, M.A; Prasad D. Ahmed, M.R., and Lee, Y-H. Performance analysis of a wave energy converter using numerical simulation technique. *Science China-Technological Sciences* (2010) **53**(**1**):13-18

[9] FLOW 3D, User Manual Version 10.0.1, Flow Science. Inc., Santa Fe (2012)

[10] Le Méhauté, B., An introduction to hydrodynamics and water waves, Springer-Verlag. (1976)

[11] USACE (U.S. Army Corps of Engineers), Coastal Engineering Manual EM 1110-2-1100, Part II, Washington, DC. (2008)

[12] Hirt, C.W. and Nichols, B.D., Volume of Fluid (VOF) method for the dynamics of free boundaries. *Journal of Computational Physics* (1981) **39**:201.

[13] Saad Y. and Schultz, M.H. GMRES: A generalized minimal residual algorithm for solving nonsymmetric linear systems. *SIAM J. Sci. Stat. Comput.*(1986) **7**:856-869.

V International Conference on Computational Methods in Marine Engineering
MARINE 2013
B. Brinkmann and P. Wriggers (Eds)

COMPUTATIONAL PREDICTION OF NEAR AND FAR FIELD NOISE DUE TO PILE DRIVING FOR OFFSHORE WIND FARMS

K. HEITMANN, T. LIPPERT, S. LIPPERT AND O. VON ESTORFF

Institute of Modelling and Computation
Hamburg University of Technology
Denickestr. 17, D-21073 Hamburg, Germany
e-mail: k.heitmann@tuhh.de - web page : http://www.mub.tuhh.de/

Key words: Simulation, Underwater Noise, Offshore Windfarms, Pile Driving, Time Domain, Frequency Domain

Abstract. One major long-term goal of the German government is to decrease the greenhouse gas emissions by 40 %. This results in a key role of offshore wind farms regarding the turnaround in energy policy. In most cases, offshore wind turbines are erected by pile driving leading to a significant noise impact. In consequence, limiting values for emitted underwater noise have been prescribed to avoid a negative influence on marine mammals. To fulfill these requirements, different sound damping systems are currently developed or under investigation. Thereby, the numerical prediction of the resulting sound pressure level is an important tool to prevent cost-intensive offshore tests.

As a general approach different numerical modeling techniques are used to study the generated pressure wave, taking into account the near and far field propagation separately. To model the area near the pile of the wind turbine, a detailed finite element approach is used. For the far field propagation, numerically highly effective methods are needed to predict the sound pressure level at large distances of several kilometers from the pile. In a combined model, results of the area close to the pile are transferred to a separate model using wavenumber integration to compute the sound pressure in the far field of the pile. Detailed investigations of the far field model and the setup of the combined near field-far field model can be found in corresponding publications of the authors [1]-[4]. The focus of this contribution is on the transformation of the near field model from the time domain to a formulation in the frequency domain to be able to consider frequency-dependent effects, like, e.g., the damping characteristics of bubble curtains.

1 INTRODUCTION

One key technology towards the extension of renewable energy is electricity generation by offshore wind farms. In water depths of 10 to 50 m, pile driving is still the best available technology. Thereby, high energy levels are required to drive the piles into the soil. To protect the marine mammals, limiting values for emitted underwater noise have been introduced by the German Federal Ministry for the Environment, Nature Conservation and Nuclear Safety. In most cases, these limiting values can only be fulfilled by using sound mitigation systems like, e.g., the bubble curtain. The numerical prediction of the resulting sound pressure level with and without sound mitigation system is an important tool to avoid cost-intensive offshore tests and to get a better understanding for the emitted pressure field. To take into account the near and the far field propagation, the model is divided into two parts, for which different modeling techniques are used. While the near field model is based on the finite element method (FEM), the far field propagation to distances of several kilometers from the pile is computed by using a wavenumber integration approach (see [1]-[4]).

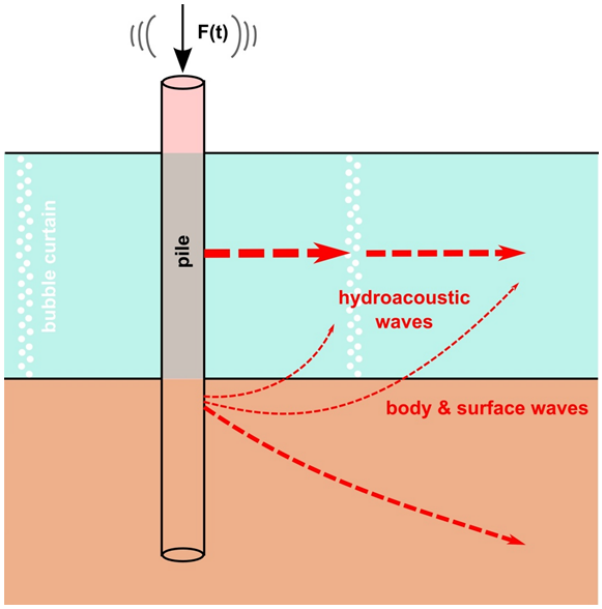


Figure 1: Visualisation of the different possible sound paths of the structure-borne noise and water-borne noise due to pile driving through a bubble curtain

A big challenge for the finite element near field model is to consider the pile driving process combined with a sound mitigation system like, e.g., the bubble curtain. On the one hand, the impact of the hammer on the pile is a highly time-dependent process, on the other hand, a simulation of the rising bubbles is not possible in such a finite element model and the characteristics of the bubble curtain like the speed of sound in a water air-bubble mixture are frequency dependent. In [5] and [6] an approach is shown to calculate

the sound speed und density of this mixture. The sound speed of fluids is given by:

$$c = \sqrt{\frac{1}{\rho\kappa}}. \tag{1}$$

The expression for the density ρ and the compressibility κ are:

$$\rho_{mix} = (1 - V)\rho_{water} + V\rho_{air} \tag{2}$$
$$\kappa_{mix} = (1 - V)\kappa_{water} + \Delta\kappa \tag{3}$$

The occurrence of the bubbles in the water causes the frequency-dependent additional compressibility $\Delta\kappa(f)$. Instead of computing the near field in the time domain, which was done so far [1]-[4], it would therefore be desirable to enable near field calculations also in the frequency domain. To compare both approaches, a time-domain simulation is set up and the accelerations of the pile and the soil are transferred to a frequency-domain simulation.

2 Time Domain Near Field Model

A sketch of the geometry and the boundary conditions of the 2D axis symmetric time domain finite element model for the near field is shown in figure 2. The steel pile has

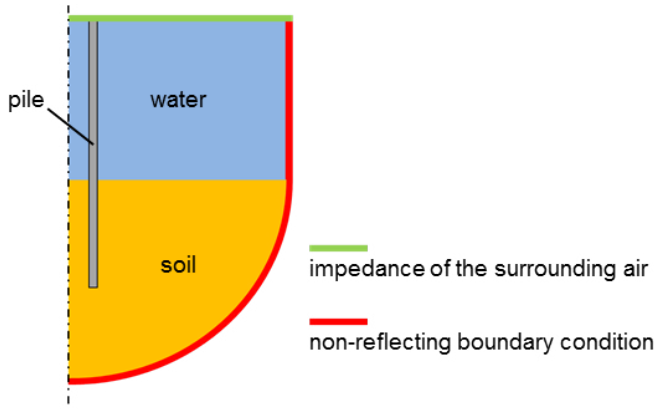


Figure 2: Geometry and boundary conditions of the 2D axis symmetric time domain model

a total length of 15 m and is penetrated 6.5 m into the soil. The resulting height of the water column is 8.5 m with a horizontal expansion of the model of 15 m. In this first approach, the pile and the soil are modeled as solid. The material properties are summarized in table 1.

Table 1: Material properties of soil and pile

	Young's Modulus	Density	Poisson's ratio
soil	$30 \cdot 10^8 MPa$	$1000 \frac{kg}{m^3}$	0.3
steel pile	$210 \cdot 10^9 Pa$	$7850 \frac{kg}{m^3}$	0.28

To describe the characteristics of the force applied by the impact hammer to the pile, the approach of Deeks [7] was chosen (see figure 3). Pile and soil are coupled with a spring-damper connection. Different non-reflecting boundary conditions are selected for soil and water to satisfy the radiation condition (see figure 2). For the water column, a mesh size of 15 cm was chosen to allow for calculations up to 1 kHz with 10 elements per wavelength.

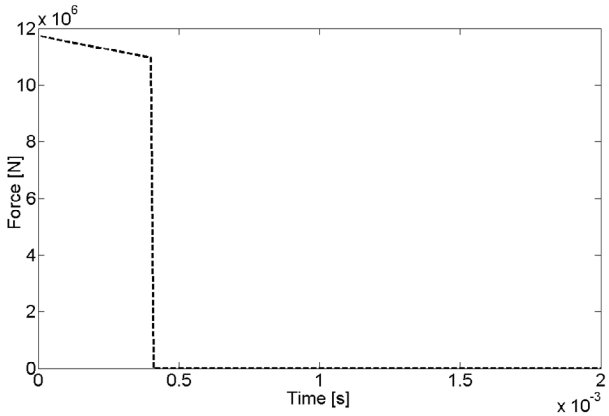


Figure 3: Characteristic behaviour of the time-dependent force applied to the pile

3 Frequency Domain Near Field Model

The frequency domain finite element model for the near field contains only fluid elements to model the water. As in the time domain model, the mesh size is 15 cm. Instead of using a coupled fluid-structure model, the excitation of the water by both pile and soil is applied by corresponding boundary conditions. In a first step, the normal accelerations of the bounding surface of the pile and the soil to the water are extracted from the time domain model, fourier transformed and transferred to the frequency domain finite element model. After the transfer of the data sets, these transformed accelerations are defined as boundary conditions to the model. The cut-off of the soil requires a selection of another boundary condition to replace the influence of the soil to an incident pressure wave. In this case, a solid ground impedance boundary condition was chosen.

In both models, the typical wave propagation observed for pile driving with a inclination of about 17° can be seen in the results. By reason of the principles of the linear acoustics, the entire pressure can be assembled from the pressure field according to the influence of the pile accelerations and the pressure field according to the soil accelerations.

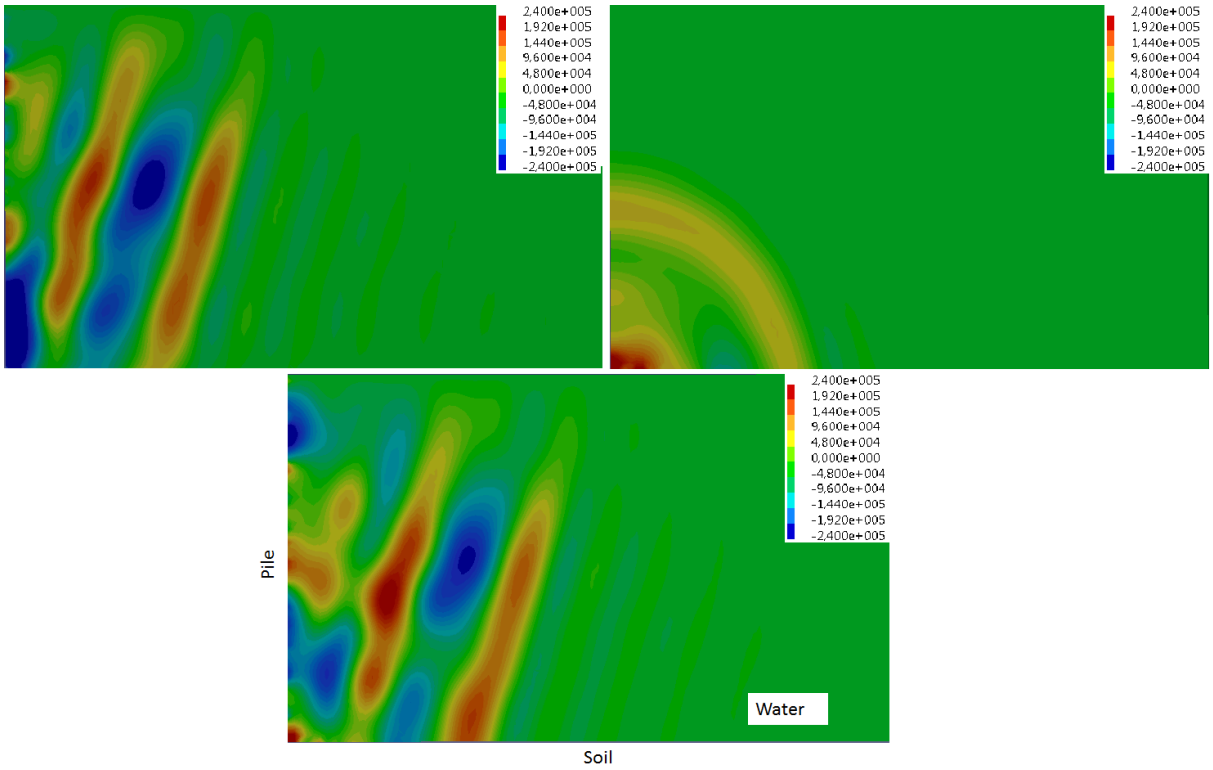


Figure 4: Pressure field in the water column of the frequency domain model, left: pressure field according to the pile accelerations, right: pressure field according to the soil accelerations, bottom: combined pressure field of the pile and soil accelarations due to pile driving

An evaluation of the pressure at different nodes of the water domain indicates the good accordance of both models (figure 5). The difference in the peak pressures can

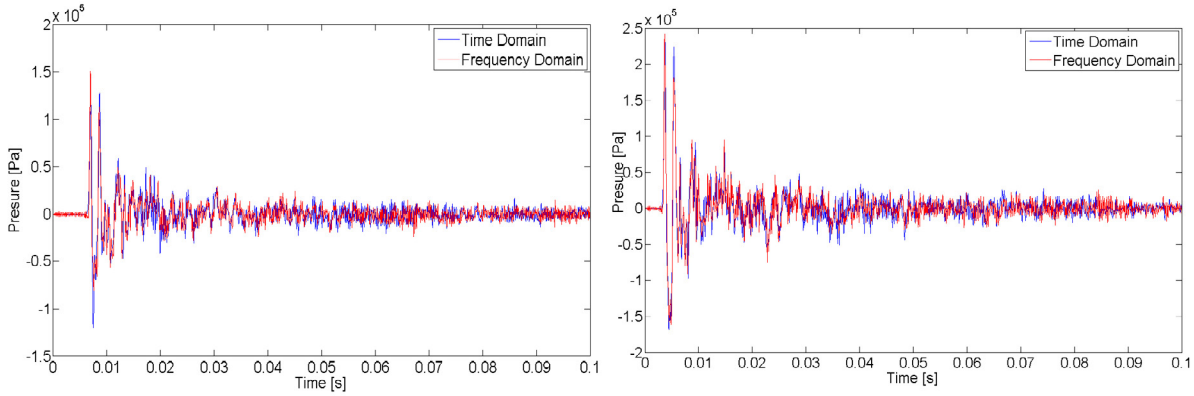


Figure 5: Comparison of the pressure in the water domain at two nodes in a water depth of 4.75 m, left: 10 meter distance to the pile, right: 5 meter distance to the pile

be explained in the frequency step, which results from the fourier transformation and differences of both models in the high frequency range depending on the mesh size. In a range from 0 to 2 kHz the amplitude and the phase of the pressure of both models match well (figure 6).

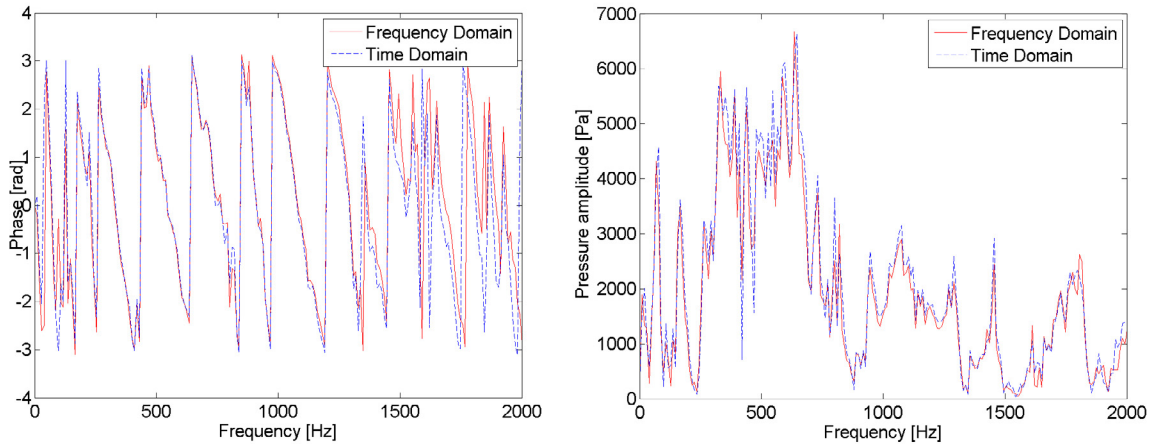


Figure 6: Comparison of the phase and the amplitude of the pressure in a distance of 10 meter to the pile and a water depth of 4.75 m of both models

4 Conclusions and Outlook

Up to now, the near field model for the prediction of pile driving noise has been formulated in the time domain. To be able to efficiently consider frequency-dependent

parameters, as for example when applying sound mitigation measures, an approach to formulate the near field model in the frequency domain has been shown. A comparison of the results calculated in the time domain and the frequency domain, respectively, showed a very good agreement. By reason of modeling only the fluid elements in the frequency domain model, the computation time further decreases significantly compared to the time domain model. Based on these results, it is planned to develop and investigate modeling techniques for the bubble curtain in the frequency domain. Furthermore, the coupling of the soil with the water will be studied more extensive. To get a more realistic model, a two phase soil model will be implemented in the time domain model and boundary conditions for the frequency domain model will be analyzed to get an identity between the results in both domains. Finally, the simulation results will be validated with measured data from extensive offshore tests that are performed with in the BORA project.

5 Acknowledgements

The research on the prediction model for the pile driving noise and its validation is carried out in the frame of the BORA project at Hamburg University of Technology together with project partners at the University of Kiel and the University of Hannover. The authors gratefully acknowledge the funding of the BORA project by the Federal Ministry for the Environment, Nature Conservation, and Nuclear Safety due to an act of the German Parliament (project ref. no. 0325421). For further information, please visit the project homepage at www.bora.mub.tuhh.de.

REFERENCES

[1] Lippert, T., Lippert S.,*Modelling of pile driving noise by means of wavenumber integration.* Acoustics Australia 40(3),178-182 (2012).

[2] Lippert, S., Lippert, T., Heitmann, K., von Estorff, O.*Prediction of underwater noise and far field propagation due to pile driving for offshore wind farms.* Proceedings of the 21st International Congress on Acoustics ICA 2013, Montreal, Canada (2013) (in publication)

[3] Lippert, T., Heitmann, K., Ruhnau, M., Lippert, S., von Estorff, O., *On the prediction of pile driving induced underwater sound pressure levels over long ranges.*, Procedings of the 20th international Congress on Sound an Vibration, ICSV20, Bangkok, Thailand, (2013) (in publication)

[4] Lippert, S., Lippert, T., von Estorff, O. *Prediction of underwater sound due to pile driving for offshore wind farms - A challenge for numerical simulation.* Procedings of the 41st International Congress on Noise Control Engineering, Inter-Noise (2012), New York City, Ny, USA

[5] Novarini, J.C., Keiffer, R. S. and Norton,G.V., *A Model for Variations in the Range and Depth Dependence of the Sound Speed and Attenuation Induced by Bubble Clouds Under Wind-Driven Sea Surfaces*. IEEE Journal of Oceanic Engineering, 23(4) (1998).

[6] Rustemeier, J., Grießmann, T.,Rolfes R., *Underwater sound mitigation of bubble curtains with different bubble size distributions.* Proceedings of the 11th European Conference on Underwater Acoustics ECUA 2012, Edinburgh, UK (2012).

[7] Deeks, A.J.*Numerical Analysis of Pile Driving Dynamics.* Doctoral Thesis, University of Western Australia, Perth, Australia (1992).

New development of cost-efficient Multi-pile Concrete Foundation (MCF) for offshore wind turbine

Ki-Du Kim,[*] Anaphat Manovachirasan[**], Hye-kwan Jeon**

Department of Civil and Environmental System Engineering, Konkuk University

120 Neungdongro, Gwangjin-gu, Seoul 143-701, Republic of Korea.

[*] E-mail: kimkd@konkuk.ac.kr, 822-2049-6074

[**] E-mail: m.anaphat@hotmail.com

*** ACEENC.Inc B-1203, Digital Empire Bld., 906-4, Gwanyang-dong, Dongan-gu, Kyunggi-do, Korea E-mail:hkj444@daum.net

ABSTRACT

A hybrid type of cost-efficient supported structure combined with concrete cone and steel shaft has been developed for wind turbine farms. A new type of structure which is supported by driven piles, termed Multi-pile Concrete Foundation (MCF), is suggested. Finite element analyses for support structures under hydrostatic load are carried out, using both a shell and frame element of the XSEA program. The Morrison equation with three dimensional wave load is applied in XSEA simulation software, which are particularly directed at concrete structures. The optimized structures based on the preliminary design concept resulted in an efficient structure, which reasonably reduces fabrication costs.

Keywords: Offshore wind turbine, fine element analysis, Multi-pile concrete foundation, hybrid

1. Introduction

From past to present, most offshore wind farms have used steel foundations; however, the main disadvantage of steel foundations are high corrosion and costs. On the other hand, government sectors in some countries have developed new materials to prevent these problems. In Denmark, using concrete material in the ocean has been developed, and used with success [1]. Not only is the construction cost of concrete foundation cheaper, at half the steel foundation cost, concrete structure can also be installed rapidly, and the period is shorter, than in the case of a steel jacket structure. Additional advantages of concrete material are its durability, low maintenance, resistance to abrasion, and higher damping properties [2]. Prestressed concrete provides specific advantages of durability, low cost maintenance, rigidity against buckling, fatigue properties under a large number of loadings, freedom from vibration, ease of repair of local damage, and resistance to fire and external explosion.

Gravity foundations using prestressed concrete are already used in wind farms at depths up to 27 meters. Each comprises a hollow conical stem, and a circular raft footing, with continuous reinforcement of passive and prestressed steel. The dimension of the stem is designed to provide the required anchoring for the tower. This prestressed concrete transfers the overturning bending moments to the raft. Thus, the dimension of the raft footing is determined by the overturning moment at the foot of the stem, and the allowable bearing pressures on the seabed [3]. It is therefore site-specific; for deeper water, greater wind loads, more severe sea states and weaker seabed, a greater diameter is needed. However, the basic design of a circular raft stiffened by prestressed concrete radial ribs, which transfers the overturning moment from the foot of the stem to the seabed, remains the same for all applications. The fatigue design study of a concrete framed tripod structure is suggested by J. Grünberg et al. [4].

In this paper, the optimum foundation selection is a function of the variables of water depth, turbine size, and wind farm location conditions. As the water depth and turbine size increase in weak soil foundation, the applicability of the gravity base foundation becomes limited by the heavy gravity loading. Therefore, the concrete gravity foundation and driven-pile has been developed, to abolish the disadvantage of each type of foundation. This limit is further constrained by the concept design of a new hybrid model, termed Multi-pile concrete foundation (MCF). This structure responds with an optimum solution for shallow and deep water level. The general arrangement of substructure was studied, and investigated through behavior and natural frequency analyses. The objectives of the study were to assess of new hybrid structures: (1) the acceptable natural frequencies of the structure; and (2) the behavior of the structure under environmental loads, with principle attack angles. In this paper, the characteristics of sea conditions of a demonstration offshore wind farm in the west sea of Korea are considered [5]. In addition, a wind energy conversion system with a concrete substructure is fully modeled, using the finite element method to simulate the various conditions.

2. Design environment and analytical model

The new innovative concept of an offshore wind turbine substructure, shown in Figure 1, is developed by using concrete material. The starting point of the design basis of the structural concept is to use static analysis under the extreme environmental parameters and loads of the west sea of Korea.

The geometry of the concrete structure with piles support is shown in Table 1, for the structural analysis in XSEA. The concept model from the conventional gravity based foundation is developed

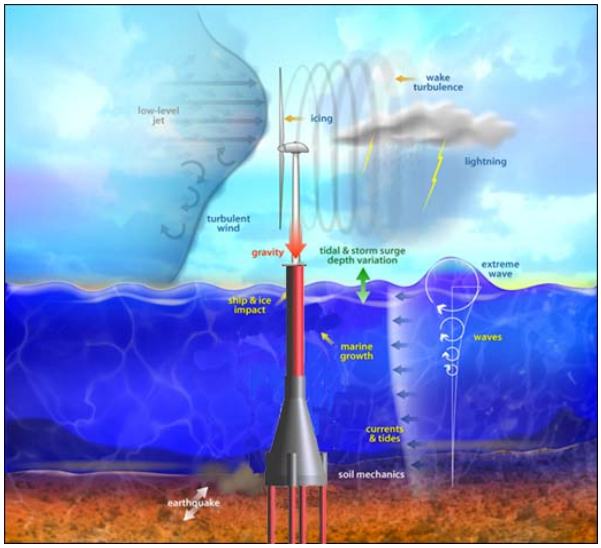
by modifying the concrete material and structural configuration. The concrete substructure is composed of central concrete-steel structure, steel shaft, concrete wing and concrete leg sleeves.

Table 1. Geometry of concrete substructures

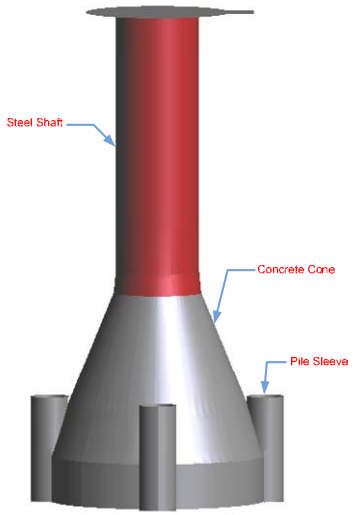
Structural Components	Elevation from (m)	Elevation to (m)	Length (m)	Outer Dia. (m)
Concrete Cone	0.00 (base)	15.00 (base)	15.00	15.00
Concrete Sleeve	0.00	7.00	7.00	3.00
Steel Shaft	15.00	33.00	18.00	6.60

3. The Environmental condition

The metocean condition is applied to the sub-structure for primary design, using the extreme condition. The objective is the feasibility study that the structure is able to withstand storm attack. The applicability of the load case refers to extreme turbulent wind as an abnormal turbine operation mode. The 1 hour mean wind speed, significant wave height, water level, storm surge heights, Tide height and current speed magnitude are assigned with 50 year-return period.



(1-1) Modified from NREL report figures



(1-2) MCF Substructures

Figure 1. Multi-pile Concrete Foundation (MCF) in offshore wind turbine

Table 1. Geometry of concrete substructures

Structural Components	Elevation from (m)	Elevation to (m)	Length (m)	Outer Dia. (m)
Concrete Cone	0.00 (base)	15.00 (base)	15.00	15.00
Concrete Sleeve	0.00	7.00	7.00	3.00
Steel Shaft	15.00	33.00	18.00	6.60

3.1 Wind modeling

The mean wind velocity is determined by a database in which values are recorded near the site, and evaluated and applied to the substructure and tower above the water surface. The wind model analysis is the variation of the mean velocity, with a height of 10 meter over a horizontal surface of homogeneous roughness, describe by the exponential power law. This is given by [6].

$$u(z) = U_{10}(H) \cdot \left[\frac{z}{H}\right]^{\alpha} \quad u(z) = U_{10}(H) \cdot \left[\frac{z}{H}\right]^{\alpha}$$

3.2 Hydrodynamic Modeling

Offshore turbines are those whose foundation may be subjected to hydrodynamic loading. The offshore wind turbine substructure is subjected to hydrodynamics that depend on the foundation system and water depth for the offshore turbine installation. In this case, they consist of current and wave loading.

3.2.1 Current model

The most common currents considered in offshore structural analysis are tidal currents. The magnitude and direction of the tidal currents at the tower surface are generally estimated from local field measurement, the direction of the current reversing with the rise and fall of the tide. The ocean current caused by tidal wave propagation in shallow water can be characterized by a practically horizontal velocity field, in which intensity is slowly increased and decreased by the water depth. The variation of current velocity with depth is given by [8]

$$v(z) = v_{tide}(z) + v_{wind}(z) \quad \text{Where} \quad v_{tide}(z) = v_{tide0} \cdot \left[\frac{h+z}{h}\right]^{1/7}, \qquad v_{wind}(z) = v_{wind\,0} \cdot \left[\frac{h_0+z}{h_0}\right]^{1/7}$$

3.2.2 Wave modeling

The force exerted on a sub-structure by surface waves was considered by Morison (1950). The excitation force is created by drag term and inertia term. These two terms are seen to be proportional to the square of the water velocity and acceleration, respectively. The values of velocity and acceleration are calculated from an appropriate wave theory. By applying a regular wave with period, wave height and water depth to the Regular wave theory selection diagram [7], a seven order stream function wave theory is selected to be used in this case. The general stream function wave form is illustrated below,

where, $$\psi = cz + \sum_{n=1}^{N} X(n) \cdot \sinh\left(nk(z+d)\right) \cdot \cos(nkx)$$

3.3 Turbine Loading

In this research, 5MW of wind turbine under wind excitation cause the loading conditions to the offshore substructure. Top tower loads are applied to the substructure, as shown in the table below. Yaw bearing fore-after shear force, yaw bearing side-to-side shear force, yaw bearing axial force, rotating yaw bearing roll moment, rotating yaw bearing pitch moment and yaw bearing yaw moment are applied quasi-statically at the top of the tower in the x, y and z directions, respectively [8].

Fx	Fy	Fz	Mx	My	Mz
(kN)	(kN)	(kN)	(kNm)	(kNm)	(kNm)
1.21E+02	-2.94E+01	3.40E+03	1.24E+02	-8.58E+01	-1.44E+03

3.4 Self Weight Modeling

The dead load or permanent load is the sum of the loads that are relatively constant over time, including the self-weight of the structure itself. The designer can also be relatively sure of the magnitude of dead loads, as they are closely linked to the density and quantity of the construction materials. The self-weight of the offshore wind turbine structure is analyzed by using the commercial software XSEA. The structural weight is automatically calculated by the self-weight module of XSEA to be equal to 1,173 Ton. Shell and frame element are used to apply to the concrete-steel sub-structure and beam part, respectively.

3.5 Environment site parameters

Extreme wave conditions are assumed for a recurrence period of 50 years per wave direction. A parameter of hydrodynamic load for finite element analysis, considering the characteristics of a candidate site, is introduced. To select the parameter for a wind farm, not only wind resources, but also diverse factors, including the water depth and the use of the sea, must be taken into account. Through an analysis of these factors, the Korea Electric Power Corporation Research Institute (KEPCO Research Institute) has determined that the area near the island Wi-do in the West Sea (Yellow Sea) is the optimal site for a demonstration offshore wind farm. The metocean parameter data are represented in the table below, which is given by Ref. [5]

Water depth	Surge + Tide Height	Effective water Depth	Significant Wave Height	Wave Period	Wind Speed (1hr @ 10m)	Current Speed

(m)	(m)	(m)	(m)	(sec)	(m/s)	(m/s)
15	2.9	17.9	7.22	11.90	25.00	1.55

4 The analysis result

4.1 Natural frequency analysis

In general, the nacelle generates electricity on offshore wind turbine structure by inducing the rotor's rotation, having the characteristic of rotational frequency effects. An operational wind turbine is subjected to harmonic excitation from the rotor. The rotor's rotational frequency is the first excitation frequency, and is commonly referred to as 1P. The second excitation frequency to consider is the blade passing frequency, often called 3P (for a three-bladed wind turbine), at three times the 1P frequency. The turbine manufacturer advises an additional safety margin of 10% for the lower boundary and upper boundary. Outside the additional safety margin, the dynamic response due to turbine loading is neglected. Therefore, the natural frequency of the design should not coincide with the rotational frequency of the turbine (1P), or the blade passing frequency (3P). If the natural frequency is in the same interval, resonance will occur, with significant fatigue damage (even failure) as a consequence. The first natural frequency of the MCF is 0.970, which is in the safety margin of the Stiff-Stiff zone, as shown in Figure 2. Generally, a concrete structure is designed in the Stiff-Stiff range design, which is cost-effective, and has good durability. Moreover, the concrete gravity base design has the natural frequency of 0.95 Hz, which is nearly same as this new concept structure. However, the MCF has less weight and cost than the gravity base foundation, which is good for an in situ construction site. For fatigue consideration, sea states with a high frequency (0.10 Hz.) of occurrence have the largest effect. These are generally relatively short waves. Because waves have various periods, they span a wide range in the frequency band. Thus, it shows that this structure will not be damaged by wave or blade.

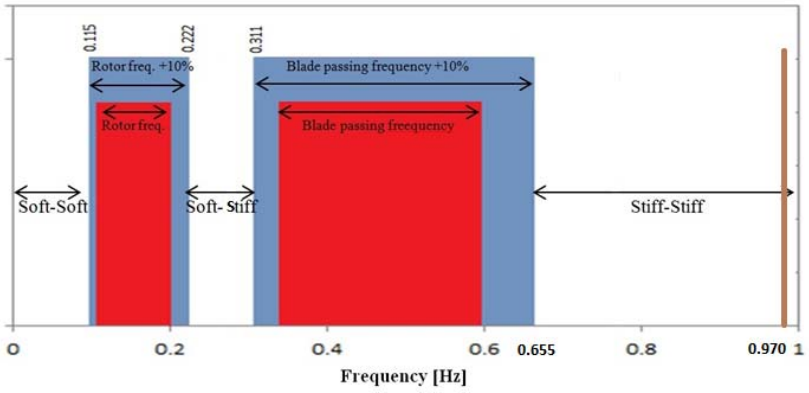


Figure 2. Design ranges for the fundamental frequency of the support structure

Furthermore, the XSAE program provides a mathematical model to calculate the Eigen-vector. In this paper (refer Table 2), five modes shape are illustrated, to see the realistic physical behavior of the MCF in Figure 3.

Table 2. Natural frequency and Natural period

Mode	Axis	Natural Frequency	
		Frequency	Period
		(Hz)	(sec)
1st-Mode	X-axis	0.970	10.300
	Y-axis	0.970	10.300
2nd-Mode	X-axis	3.256	0.307
	Y-axis	3.257	0.307
3rd-Mode	X-axis	7.223	0.138
	Y-axis	7.224	0.138
4th-Mode	Twist	11.590	0.086
	Twist	12.290	0.086
5th-Mode	X-axis	13.080	0.076
	Y-axis	13.140	0.076

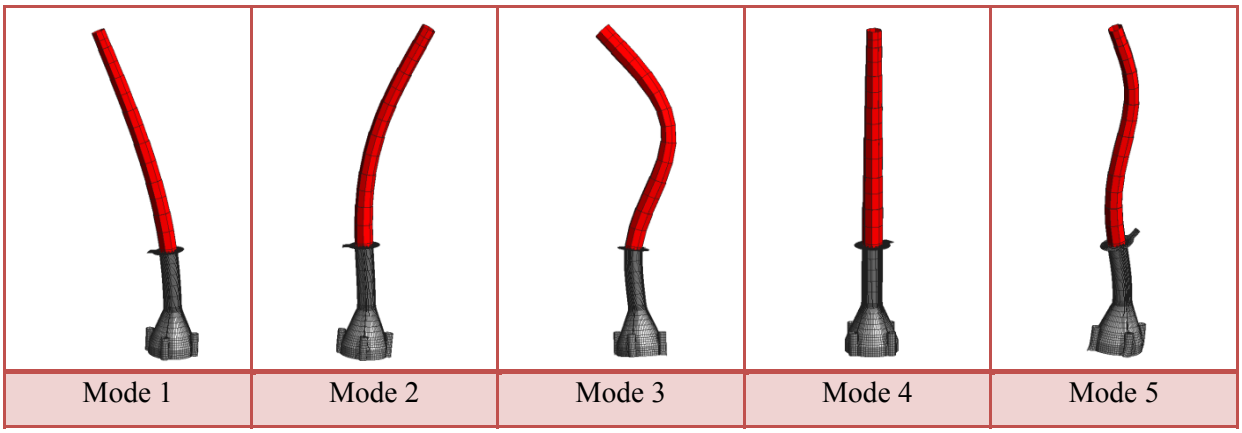


Figure 3. Mode shapes simulation of the MCF

4.2 Load combination analysis

The load combination of wind, wave, current, turbine and self-weight loads is completed by the superposition method. Load combination cases are selected by attack angle, as shown in Figure 3. Due to the symmetry of the Multi-piles concrete foundation along the x and z axis, load cases were

reduced from 8 to 2 load cases, as illustrated in Figures 4 and 5, respectively. In this paper, loads are automatically combined, by using the XSEA offshore simulation program, which provides the load combination analysis of the sea state to apply to the offshore wind turbine sub-structure.

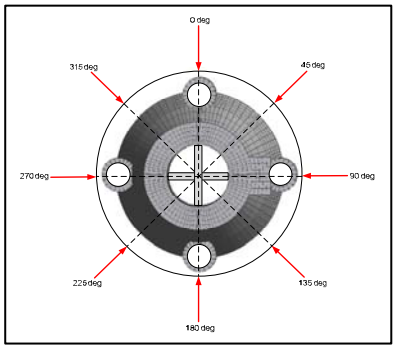


Figure 4. Load Direction Cases

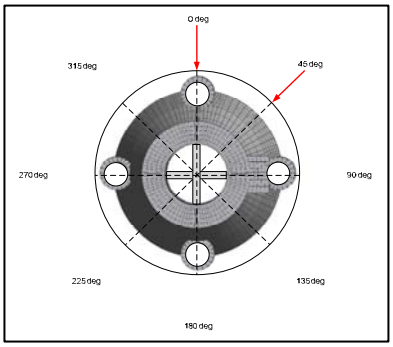


Figure 5. Principle Load Simulations in XSEA

Based on the properties of the MCF, this structural modeling strategy is characterized by the use of a four nodes shell element called XShell-4-ANS, to model the concrete structure and steel shaft. Moreover, a frame element called XFrame is used to model the concrete cross beam of the bottom structures. These two elements are selected, based on the characteristic and dimension of the structure. The finite element analysis is analyzed by applying the hydrostatic load based on the Morrison equation, and turbine load, at the top, and body of the structure, respectively.

According to the analysis, the response of the MCF system during the quasi static loading is illustrated by the deformation and stress distribution over the entire body of the structure. Applied load combinations are varied along the attack angle direction. Figs. 6 and 7 illustrate the characteristic of its response in the simulation. In the present analysis, the displacement of the structure at the top of tower has been considered as the main parameter. The top of the tower is displaced 0.1267 and 0.1251 meters in the direction of 0 and 45 degrees at the top of tower, respectively. Since, there is no verification for the top tower displacement; the vertical deflection that is given in the design code [6] is used to check the requirement. Due to the design code, the allowable vertical deflection is 2L/200, where L is the length of cantilever beam. Therefore, the allowable value is 2*101/200=1.01 meters, at the top of the tower.

Due to the earlier mentioned structural model, the stress and displacement contour are presented. The acting loads considered in this analysis were self-weight, wave and top tower load. In this case, the wave load was applied horizontally to the structural alignment. The wind load was calculated according to the procedure described on the Definition of a 5-MW reference wind turbine for offshore [9]. The computed Bending stress contour is shown with the MCF from the XSEA [9] program, where

the stress distribution can be seen in the outer zone, not just in its value, but even in its sign. The inner zone of the steel shaft receives compressive stress (B), due to the combination load. On the other hand, the outer zone of the shaft is in tensile stress state (A), since the outer zone is elongated.

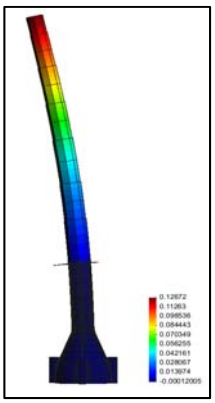


Figure 6. Displacement contour

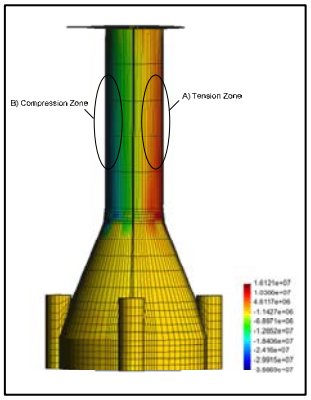


Figure 7. Bending stress contour.

5. Conclusion

Although offshore wind turbine structures are traditionally created from steel for almost the entire structure, concrete has also been used in wind farms. Recently, the wind offshore industry has recognized the great possibilities offered by concrete material. As compared to steel, there are many advantages: of lower maintenance and lower fabrication costs, longer life of the structure and better motion behavior. A new innovative technology of wind turbine substructure, termed the Multi-pile Concrete Foundation (MCF), is suggested in this paper, which is developed from the conventional gravity based foundation and driven pile. The structural analyses show that it can withstand the allowable displacement in the extreme condition. In addition, natural frequency analysis is also used. There are many reasons to compute the natural frequencies and mode shapes of a structure. All of these reasons are based on the fact that real eigenvalue analysis is the basis for many types of dynamic response analyses, which will be the further study of this structure. The result of eigenvalue analysis of Multi-piles concrete foundation can confirm that this structure is in the safety range to avoid resonance. In conclusion, it is possible to infer that the new concept of foundation design in this paper can withstand the extreme condition in the west sea of Korea.

Further study, involving optimum design by hydrodynamic and aerodynamic load, is required to develop a stable model. The basic design, transportation and installation method of the MCF to be installed in the West Korean Sea will also be studied. Moreover, the pile size can be studied from the reaction at the supports of structure, under the load conditions.

Acknowledgement

This research was a part of the project titled "Development of design basis and concrete technologies for offshore wind turbine support structures/20120093" funded by the Ministry of Land, Transport and Maritime Affairs, Korea

REFERENCES

[1] P. Volund, “Concrete is the future for offshore foundations”, Wind Engineering, Vol. 29 (2005).

[2] H. C. Cotton, “Materials Requirements for Offshore Structures”, Philosophical Transactions of the Royal Society of London. Series A, Mathematical and Physical Sciences, Vol. 282, No. 1307 (1976).

[3] W. Brook-Hart, P. A. Jackson, M. Meyts, P. Sayer, “Competitive Concrete Foundations For Offshore Wind Turbine”, Gifford (2008).

[4] J. Grünberg, J. Göhlmann, C. Ertel, “Concrete Foundations for Offshore Wind Energy Converters subjected to fatigue loading”, Institute of Concrete Constructions, University of Hannover, Copenhagen Offshore Wind (2005).

[5] K.-Y. Oh, J.-Y. Kim, J.-S. Lee, “Preliminary evaluation of monopole foundation dimensions for an offshore wind turbine by analyzing hydrodynamic load in the frequency domain”, KEPCO Research Institute, Korea (2012).

[6] DNV-OS-J101, “Design of Offshore Wind Turbine Structures”, Det Norske Veritas, offshore standard (2011).

[7] DNV-RP-C205, “Environmental Conditions and Environmental Loads”, Recommended Practice, Det Norske Veritas, offshore standard (2007).

[8] J. Jonkman, S. Butterfield, W. Musial, and G. Scott, NREL/TP-500-38060, “Definition of a 5-MW Reference Wind Turbine for Offshore System Development” , National Renewable Energy Laboratory (2009).

[9] XSEA: www.xfinas.com, Konkuk University (2013).

Quantity and Type Forecasting Tool for Offshore Wind Power Plant Spare Parts

Dipl.-Ing. Robert Rauer*,
Dipl.-Ing. oec. Torsten Münsterberg†,
Prof. Dr.-Ing. Carlos Jahn†

* Institute of Maritime Logistics MLS
Hamburg University of Technology
Schwarzenbergstrasse 95 D, 21073 Hamburg, Germany
Email: robert.rauer@tuhh.de, Web page: www.tuhh.de/mls

† Fraunhofer Center for Maritime Logistics and Services CML
Schwarzenbergstrasse 95 D, 21073 Hamburg, Germany
Email: info@cml.fraunhofer.de - Web page: www.cml.fraunhofer.de

Abstract: In this paper a forecasting model for offshore wind power plant spare parts is presented. The paper starts with an overview about the German offshore wind energy market and the expected future development. To reach a high availability of the turbines, the right amount of spare parts is needed and therefore the authors introduce a tool to forecast the quantity / type of spare parts by a given availability and maintenance strategy. In this context essential terms as reliability, availability, maintenance and service are described.

1. Introduction & Background

The German offshore wind branch is a very young industry. The target for the offshore wind energy output in 2020 is an installed capacity of 10 Gigawatt (GW) and in 2030 of up to 25 GW (today installed capacity is approximately 200 MW) (Bundesverband WindEnergie, 2013). This means that in 2030 there will be nearly 6000 offshore wind turbines, which have to be maintained. Offshore conditions present new challenges related to operation and maintenance (O&M). The main differences compared to onshore farms persist in accessibility, foundations, transport and installation equipment, which bring the need for different maintenance strategies, specific equipment and vessels, inventory and storage approach. For German offshore wind farms, the situation compared to the UK or Denmark, is very different because of the higher water depth and distance to shore (cf. Figure 1).

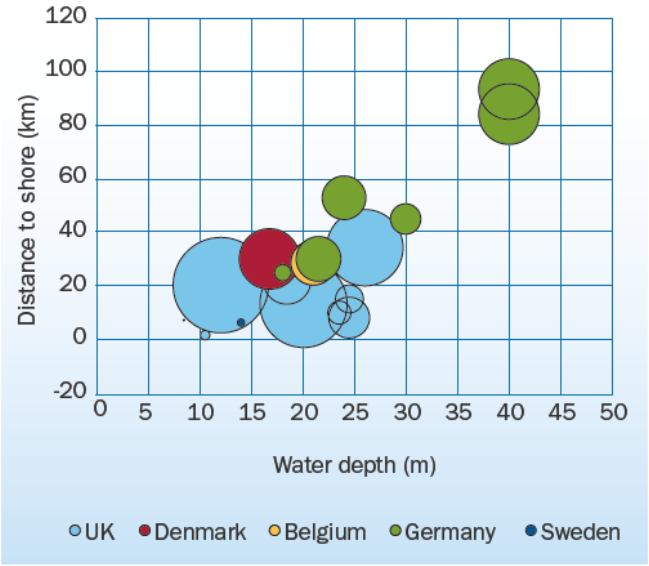


Figure 1: Water depth, distance to shore and size of offshore farms under construction 2012 (EWEA, 2013)

Today, the operational phase for offshore wind farms is laid out for 20-25 years (Vattenfall, 2010) and the main objective is to have offshore wind turbines available to produce electricity. Because if a 5MW offshore turbine is down, the loss of revenue for one day is up to 12.000 EUR; 500 EUR for one hour. (Schmidt, 2011) The wind turbines have to be reliable, and in cases of failure, maintenance procedures have to bring the turbine back to operation in short time. The offshore operational conditions for offshore wind farms are different to the conditions of onshore parks, because of the rough weather conditions. In certain periods of the year it's impossible to access the offshore wind park to repair or maintain the turbine. (Echavarría, 2009) Accessibility, availability of equipment, spare parts, transport logistics and personnel are essential for maintaining an offshore farm.

Availability of wind turbines under these conditions can be highly hindered by wind turbine's reliability. Especially in winter it is hardly impossible to maintain the turbines to provide availability levels (~98% cf. Figure 2) compared to onshore wind turbines. Important for accessibility is the wave height and wind force. The reliability of common offshore turbines therefore is not satisfying and the availability is lower than onshore. Strong wind makes it hard to access by boat or helicopter. (DENA, 2010, p.84) The German offshore wind pilot project "alpha ventus" achieved in 2011 an average technical availability of 95%. (IWES, 2013) The first offshore wind farm Horns Rev, built by Elsam 2002 (Denmark), in the North Sea achieved 95% (DENA, 2010), and the offshore wind farm Egmond aan Zee achieved 95,4% (Pijkeren et. al, 2012).

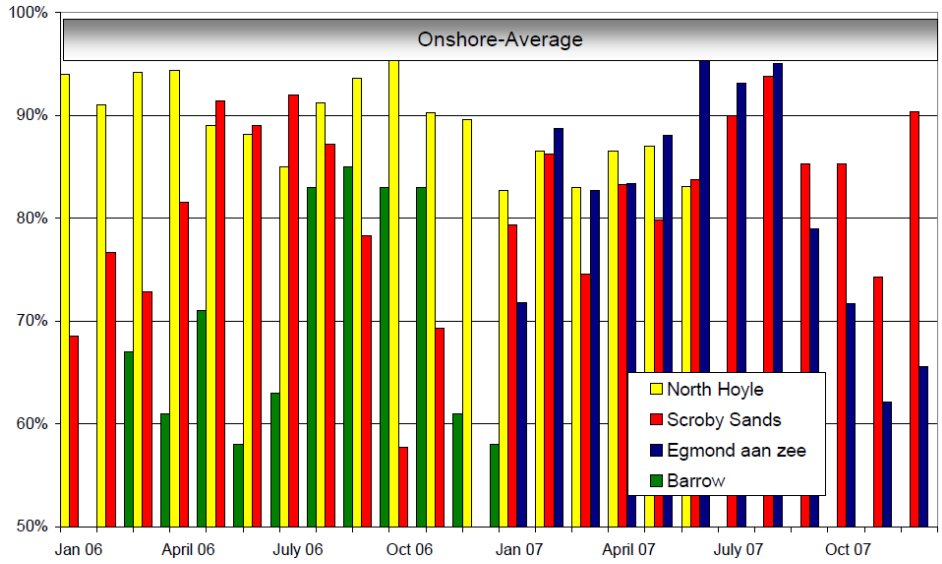


Figure 2: Availability of early offshore wind turbines (Faulstich et. al, 2010)

In offshore wind farms a simple failure implies the risk of stopping the turbine until it can be accessed by a maintenance crew. In the North Sea, these periods can last days or several weeks. The offshore conditions also increase the O&M costs – 25% to 30% of the kWh cost for offshore turbines, but only 10% to 15% for onshore turbines (EWEA, 2013, p.10). Considering that for some wind turbines, helicopter access is an option to reduce the downtime of the turbine, also the costs will be higher. The availability of offshore wind turbines is important for the success of renewable energies, but there is a lack of reliability records for the offshore wind farms.

To increase the availability of offshore wind turbines, it could be possible to use general findings from the onshore experience and evaluate the need of spare parts. The existence of the right spare part, if a turbine is down, is essential to bring it back on track in the shortest possible time . To achieve this goal, it is important to develop a model to forecast the amount of spare parts in a predefined time window. With such a model it could be possible to reduce the O&M costs for storage, decrease the downtime and reach higher availability.

2. Research goals

As a first step this paper will explain essential terms of maintenance for offshore wind farms (e.g. reliability, availability). Based on these terms common maintenance strategies are presented and their direct influence of the availability to offshore wind turbines. The following section describes the implementation of a tool to forecast the needed spare parts of a specific offshore wind farm, and consider the influence of a variety of factors like used logistics concepts (ship/helicopter) (Münsterberg et. al, 2012) and stock size.

3. Problems relating to offshore wind farms

The operational phase deals with four problems (RAMS – reliability, availability, maintenance and service), which will be described shortly (based on Echavarría, 2009) regarding the amount and type of spare parts and the need of an IT-Tool to forecast quantity and type.

Reliability in this paper is defined *"as the ability of a system or component to perform its required functions under stated conditions for a specified period of time"*. (IEEE, 1990) But the problem is that the data for the life time of an offshore wind turbine (20-25 years) is today not existent. The manufactures of wind turbines developing bigger turbines in shorter periods of time, turbines built 20 years ago, are much smaller and rather simple compared to the offshore wind turbines today. Also the operational conditions in the North Sea are not very well known. Early designs of offshore turbines were not very reliable and so the availability was lower than expected (e.g. gearboxes), because the design was similar to onshore turbines and not developed for the conditions in the North Sea. In offshore wind parks, today the reliability levels of offshore wind turbines are not public available. The wind industry started late to document and process the available data (Echavarría, 2009). Reliability figures of offshore turbine parts could be a good basis to forecast needed spare parts, but as described the data is missing yet. But reliability figures exist for onshore wind turbines, for each of the main component e.g. rotor, gearbox and generator – data about subcomponents is missing.

Operational availability is besides reliability one of the most important problems regarding offshore wind turbines. Only when a turbine is available for operation, it can produce and deliver electricity. So, "the capability of the wind turbine to maintain operation" is a good definition for availability. An offshore turbine which is technically not available, cannot produce "money". Reducing the downtime and get the turbine available is very important for the wind farm owner. Operational availability of a turbine depends on the accessibility and location of the needed spare part – if the spare part is available. The kind of spare part influences directly the logistics concept and involved costs, because of the needed storage, transport vehicle and personnel.

Maintainability and Serviceability To identify the number of spare parts it should be known if a broken or failing system / component is repairable. Serviceability describes the planned schedule to maintain a turbine. Important is here, which kind of spare parts have to be exchanged or to maintain and which type of e.g. vessel is needed to transport the part. A broken blade is hard to replace by helicopter because of the dimensions ranging over 60 meters.

Maintenance strategy

The availability of an offshore wind turbine is directly connected to the chosen O&M and spare part strategy. In general maintenance strategies can be divided into preventive and corrective maintenance (Matyas, 2010, p.29). The preventive maintenance is conducted before a component of the site fails or condition monitoring system identifies a fault in the system, parts are controlled and some are exchanged. On the opposite site the corrective maintenance is performed when a failure occurs and is reported to the maintenance office. The purchase of an offshore wind turbine is often connected with a warranty by the manufacturer for five years and a guaranteed availably of 95% (e.g. Areva M5000). This includes full-service of the site, spare parts management on site, service-personnel, heavy lift logistics and spare-parts e.g. nacelle or the blades. (Balz, 2012, p. 15) This means that the manufacturer handles the complete maintenance, provides the personnel and spare parts storage for the farm.

Like described before, the maintenance strategy is associated with the operational availability and so the availability of a system can be defined as:

$$A = \frac{MTBF}{MTBF + MDT}$$

(Jung et. al, 2002, 158pp.) where MTBF stands for *mean time between failures* and MDT is *mean downtime*. Downtime is the time, when the offshore wind turbine is unavailable and fails to produce energy. MTBF is the result of the technical design of the system (e.g. reliability). MDT depends on the chosen maintenance strategy described before and split up into three main parts (Lindqvist et. al, 2010, p.24)

$$MDT = MTTR + MLDT + MWT$$

where MTTR is the abbreviation for *mean time to repair*, which is the repair time on site. The time needed to "find" and repair / replace the damaged item with a spare part and bring the system back online. MLDT is *mean logistic delay time* and is the average time for the personnel to reach the broken site. This includes the transportation time and also the time when the site is not accessible because of the bad weather conditions. MWT is the *mean waiting time* for spare parts and is crucial for the availability. This time depends on stock levels and the lead time.

To improve the operation availability it is clear that a long MTBF and low MDT is needed. But an improvement on MTBF and MDT is expensive. (Lindqvist et. al, 2010, p. 24pp) The MTBF is not in focus of this work. More important is the MDT, because it can be improved by

- Faster transportation of staff and items,
- Stock optimization and
- Shortening of lead times.

With the end of the manufacturer warranty the offshore farm owner wants to keep the costs as low as possible. To ensure supply in case of a turbine downtime, the owner needs to know how many spare parts to keep in stock and of which type to bring the system back online in the shortest time. But today no public data of needed spare parts in the lifetime of an offshore wind turbine exists. These turbine manufacturers are strict on revealing data about their turbines especially the occurring failures and item costs. A possibility could be to transfer the knowledge of failures rates from onshore to offshore turbines. Improving the reliability of offshore wind turbines is important to the success of German offshore wind energy in the future. The experience has shown that the profitability of wind farms is directly affected by the reliability and high maintenance costs. (Richardson, 2010) One possibility is to improve reliability by changing used technology. For example remove the gearbox and use a direct drive turbine configuration and so reducing the moving parts. Another way to reduce the down time of a turbine is to use a well-defined spare part management concept. The maintenance strategy for offshore wind farms will have to be much more planned than it is the case for onshore turbines, because of the likelihood of a higher number of failures and the bad accessibility of an offshore turbine due to rough weather conditions. Also the journey time to an offshore turbine is often longer than onshore. The ability to access the wind farm quickly and cost-effectively will be crucial to achieve the required turbine availability. Especially for German offshore wind farms, because they are located further away from shore than farms in the UK or Denmark.

4. Forecasting of offshore turbine spare parts

The first step to forecast is to analyze given data of the operations of an offshore wind farm. Therefore historical data of spare parts is analyzed and evaluated. This kind of data is mostly available in form of time-series. A time-series is a set of data of quantities related to a process taken at regular intervals. Time-series analysis provides tools for selecting a model that can be used to forecast future events. The goal of this research work is to determine a model that

explains the observed data and allows extrapolation into the future to provide a forecast. With the tool it will be possible to predict the amount of spare parts for a period of time to accomplish a defined availability and to determine which kind of transport equipment is needed (cf. Figure 3).

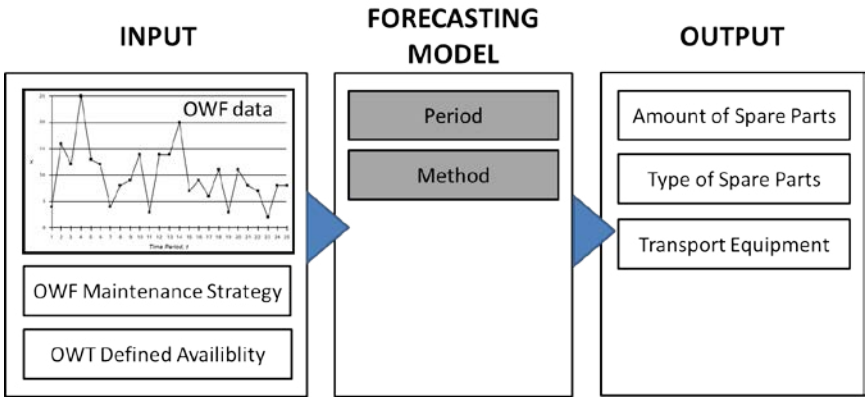


Figure 3: Forecasting model for offshore spare parts

For the forecasting model the bad offshore weather conditions and so the accessibility of the turbines have to be considered. For example, if a site like an onshore turbine is always accessible, the spare part stock size can be smaller, because components can directly being exchanged. For an offshore wind farm it is different. A site is only available on a certain number of days (van Bussel et. al, 2001) – in the operation phase up to 200 days. So it can be, that a turbine fails and powers down but cannot be repaired because of the bad weather. When in this time another turbine fails than we need a larger storage because of multiple replacements and that results in a higher stock size.

For the replacement of a large turbine component a crane ship is always needed. These ships are very expensive to charter and have often a long lead time (1-12 months) (Lindqvist et. al, 2010, p.80). The problem depends on the lead time of the crane ship, so it can be possible that an item is reordered before the crane ship is available. Another point could be a tactical decision, that a crane ship is early ordered if several maintenance tasks have to be fulfilled. These results again in a larger storage and stock size. As described before, it is also possible that an item is exchanged as a preventive action. To remove the boundary condition of an available ship, a company can buy his own ship. Then it's permanently available for operation and maintenance, but with the tradeoff higher costs.

To implement the tool it's planned to use the Software MATLAB, which is a numerical computing environment. It provides a toolbox for time series (TSA-toolbox) to identify patterns and forecast values. With the tool it will be possible to import data by a graphical user interface and to forecast spare parts by different computational methods.

5. Conclusion

The authors of this paper showed that for the availability the amount of spare parts is a crucial factor in the operations phase of offshore wind farms. Spare parts management and maintenance strategy influences directly the profit of a wind farm. The spare parts define the storage and stock size. To forecast these spare parts a framework for a forecasting tool was introduced. The tool based on time-series and fixed predefined availability of an offshore wind farm with the result to determine the number and type of needed spare parts. Because the turbine

manufacturers are strict on revealing data about their turbines, especially the occurring failures and item costs, the next step is to gather the needed data and then implement the tool to demonstrate the capability to forecast the right amount of spare parts for an given offshore wind farm.

References

Balz (2012) Willi Balz, Die Rolle der Offshore-Windenergie im Rahmen der Energiewende, HOCHTIEF Symposium auf der Husum Windenergy 2012, 19. September 2012.

Bundesverband WindEnergie (2013) Offshore, Bundesverband Windenergie, http://www.wind-energie.de/politik/offshore, access 25.02.2013.

DENA (2010) dena-Netzstudie II / Integration erneuerbarer Energien in die deutsche Stromversorgung im Zeitraum 2015 – 2020 mit Ausblick auf 2025, Deutsche Energie-Agentur GmbH, Berlin, 2010.

Echavarría (2009) Erika Echavarría, RAMS for Offshore Wind farms / Operation and Maintenance Concepts, We@Sea R&D Programme, TU Delft, We@Sea project 2004-012, 2009.

EWEA (2013) The European offshore wind industry - key trends and statistics, European Wind Energy Association, 2012.

Faulstich et. al (2010) S. Faulstich, B. Hahn, P. Lyding, P. Tavner, Reliability of offshore turbines – identifying risks by onshore experience, 2010.

IEEE (1990) IEEE standard glossary of software engineering terminology, IEEE Std 610.12-1990, 1990.

IWES (2013) Pressemitteilung - alpha ventus: Forschung und Industrie präsentieren gemeinsame Erfolge, Fraunhofer IWES, , http://www.iwes.fraunhofer.de/de/Presse-Medien/Pressemitteilungen/2012/alpha_ventus_forschungundindustriepraesentierengemeinsameerfolge.html, access 8.2.2013.

Jung et. al (2002) Volker Jung, H.-J. Warnecke (2002), Handbuch für die Telekommunikation, Berlin 2002.

Lindqvist et. al (2010) Mattias Lindqvist and Jonas Lundin, Spare Part Logstics and Optimization for Wind Turbines / Methods For Cost-Effective Supply and Storage, Universität Uppsala, 2010.

Matyas (2010) Kurt Matyas, Instandhaltungslogistik / Qualität und Produktivität, Hanser Verlag, München / Wien, 2010.

Münsterberg et. al (2012) Torsten Münsterberg and Robert Rauer, Design and evaluation tool for operations and maintenance logistics concepts for offshore wind farms, DEWEK 2012 Proceedings, 2012.

Pijkeren et. al (2012) Laurens van Pijkeren; Bart Hoeffaker, NoordzeeWind - Offshore Windfarm Egmond aan Zee / 5 years of Operation, MEP workshop, Ijmujiden, 2012.

Richardson (2010) Paul Richardson, Relating onshore wind turbine reliability to offshore application, Durham theses, Durham University, 2010.

Schmidt (2011) Martin Schmidt, Offshore-Windenergie in Schleswig-Holstein / Eine Chance für die regionale Wirtschaft?, windcomm schleswig-holstein, 2011.

van Bussel et al. (2001) G.J.W. van Bussel, A.R. Henderson, C.A. Morgan, B.Smith, R.Barthelmie, K. Argyriadis, A. Arena, G. Niklasson, E. Peltola, State of the Art and Technology Trends for Offshore Wind Energy: Operation and Maintenance Issues, CA-OWEE, 2001.

Vattenfall (2010) alpha ventus - Deutschlands erster Offshore-Windpark, presentation, Sächsisches Fachsymposium Energie, 22.11.2010.

V International Conference on Computational Methods in Marine Engineering
MARINE 2013
B. Brinkmann and P. Wriggers (Eds)

FATIGUE STRENGTH ASSESSMENT OF HP STIFFENER JOINTS WITH FILLET-WELDED ATTACHMENTS USING THE PEAK STRESS METHOD

C. FISCHER°, W. FRICKE°, G. MENEGHETTI* AND C.M. RIZZO#

°Institute for Ship Structural Design and Analysis
Hamburg University of Technology
Schwarzenbergstr. 95, 21071 Hamburg (Germany)
e-mail: claas.fischer@tuhh.de, w.fricke@tu-harburg.de

*Department of Industrial Engineering
University of Padova
via Venezia 1, 35131 Padova (Italy)
email: giovanni.meneghetti@unipd.it

#Department of Naval Architecture, Electrical, Electronic and Telecommunication Engineering
University of Genova
Via Montallegro 1, 16145 Genova (Italy)
email: cesare.rizzo@unige.it

Key words: Computational Methods, Peak Stress Method, Finite Element Analysis, Marine Engineering, Fatigue, Welded Joints

Abstract. The Peak Stress Method (PSM) is a simplified, finite element-based technique to readily estimate the Notch Stress Intensity Factors (NSIFs) at the tip of sharp-V-shaped notches. More precisely, it was shown that the maximum principal stress evaluated at the V-notch tip by means of a rather coarse finite element analysis is proportional to the mode I NSIF, as far as mode II and mode III stresses are negligible. When fatigue strength assessment of fillet welded joints is performed according to the NSIF approach, the weld toe profile is modeled as a sharp V-notch having the toe radius equal to zero (the worst case hypothesis) and the peak stress can be used as design stress combined with a properly calibrated design scatter band. Due to its computational simplicity, the PSM appears rather useful for the everyday design practice of the shipbuilding industry. In the present paper the PSM is briefly described and applied to assess the fatigue strength of joints between HP stiffeners with fillet-welded cover plates adopted by the shipbuilding industry, for which full scale fatigue test data are available. By applying the PSM, good agreement between theoretical and experimental fatigue lives is obtained despite the complex geometry and the different loading conditions of the tests.

1 INTRODUCTION

In the context of fatigue design of fillet welded joints the local approach based on the notch stress intensity factor (NSIF) assumes the weld toe profile as a sharp V-notch having a tip radius equal to zero and an opening angle equal to 135° (typical value) [1,2,3]. Recently, it

has been shown that the ratio between the mode-I NSIF and the elastic peak stress evaluated at the point of singularity (i.e. the notch tip) by the finite element method depends only on the type and size of the elements adopted in the discretization, according to the following expression [4]:

$$K_{FE}^{*} = \frac{K_1}{\sigma_{11,peak} \cdot d^{(1-\lambda_1)}} \cong 1.38 \tag{1}$$

where K_1 is the exact value of the mode I NSIF, $\sigma_{11,peak}$ is the maximum principal stress as calculated from a linear elastic finite element analysis where the mean size of the FE mesh surrounding the weld toe is *d* and $(1-\lambda_1)$ is the stress singularity exponent, which equals 0.326 for a V-notch having opening angle 2α equal to 135° [5] (typical value of the weld toe profile for a fillet-welded joint). The mode I NSIF is taken according to the definition given by Gross and Mendelson [6] (see Figure 1):

$$K_1 = \sqrt{2\pi} \cdot \lim_{r \to 0} \left[(\sigma_{\theta\theta})_{\theta=0} \cdot r^{1-\lambda_1} \right] \tag{2}$$

Concerning the FE mesh used to calibrate expression (1), the following conditions were fulfilled [4]:

- two-dimensional models discretized with four-node, plane elements as implemented in Ansys™ software (Plane 42 on the Ansys element library);
- FE mesh patterns like that shown in figure 2, where only two elements share the node located at the point of stress singularity of the weld toe.

It is worth noting that the FE mesh of figure 2 was readily obtained by running the free-mesh generation algorithm available in the software, after imposing the so-called 'global element size' parameter equal to *d*. No additional procedures were executed in FE mesh preparation.

To consider the maximum principal stress in expression (1), mode II as well as mode III stresses must be negligible, otherwise only the mode I (opening) stress must be computed in Eq. (1) [7]

Thanks to expression (1), the peak stress may substitute the NSIF in fatigue strength assessments and enables one to adopt the so-called Peak Stress Method (PSM). In order to calibrate a design scatter band to use with the peak stress, a number of fatigue test results relevant to simple T- or cruciform arc-welded joints in structural steel were analysed in terms of peak stress [8]. All joints were tested in the as-welded conditions under load ratio (ratio between the minimum and the maximum applied load) close to zero and failed from the weld toe. The main plate thickness ranged from 6 mm to 100 mm, while the attachment to main plate thickness ratio varied from 0.03 to 8.8. Figure 3 reports the resulting design scatter band, which will be used later on. The correction coefficient f_w, multiplying the range of the linear elastic peak stress, accounts for the material, the flank angle at the weld toe and the mean size *d* of the finite element mesh adopted to evaluate the peak stress [8]. For welded joints in structural steel, flank angle around 45° (i.e. V-notch opening angle $2\alpha \cong 135°$ in figure 1) and mean finite element size *d* equal to 1 mm, then f_w equals 1.064.

So far, the PSM was used in combination with two-dimensional FE models like that shown in figure 2. Recently, the PSM has been extended to three-dimensional FE models meshed

with eight-node brick elements (SOLID 45 of the Ansys™ Element Library) and it has been shown that the calibration coefficient 1.38 found using expression (1) using two dimensional numerical analyses is still valid [9].

For welded joints having plate thickness greater than about 5 mm, an element size of 1 mm was seen to be appropriate in order to estimate the stress field intensity at the weld toe. Such an element size is some order of magnitudes greater than that needed for a direct evaluation of the mode I NSIF according to definition (2). Moreover, by using the PSM, only the elastic peak stress at the notch tip can be considered as design stress rather than the whole local stress field. The above mentioned features appear rather useful for the everyday design practice of the shipbuilding industry. As a matter of fact, a ship contains a very large number of geometrically complex welded details, whose fatigue assessment is rather cumbersome. In the present paper the PSM [4] is briefly described and applied to assess the fatigue strength of joints between HP stiffeners with fillet-welded cover plates adopted by the shipbuilding industry for which full scale fatigue test data are available [10-12]. By applying the PSM, good agreement between theoretical and experimental fatigue lives is obtained despite the complex geometry and the different loading conditions of the tests.

2 THE TEST CASE: HP STIFFENER JOINTS

The fatigue strength of butt joints between the typical shipbuilding stiffener, the bulb plate or Holland Profile (HP), was recently assessed by comparing and re-analyzing some available tests data.

In [12] and [13] various point-wise approaches proposed in IIW Guidelines as well as in scientific literature were applied to different joint configurations, namely a few versions of the structural stress approaches and the notch stress approach considering the well known 1-mm weld toe rounding. Scattered results, only in partial agreement with experimental data, were found.

Indeed, the application of the above mentioned methods in the captioned cases is not always straightforward nor sometimes possible, neither effective. Difficulties in following the IIW suggestions for the FE modelling of relatively complex geometries were highlighted.

Basically, the bulb itself is a three-dimensional component interacting with two-dimensional shells surrounding it: the three-dimensional vs. two-dimensional mismatch is the main source of complexity. Since a reference thickness of the bulb cannot be identified, even identification of stress extrapolation points in post-processing of FE analyses is difficult, being often cause of scatter and/or disagreement among different approaches.

Tests on large-scale specimens of various attachments of bulb plate profiles were carried out in the Marine Structures Testing Lab of the University of Genova, see Fig. 4 top, [10], as well as by the Institute of Ship Structural Design and Analysis of the Hamburg University of Technology (TUHH), see Fig. 4 bottom, [11].

The two joint geometries with special reinforcing attachments at the profile bulb shown in Fig. 4 are considered in the following.

It is worth noting that experimental data used as targets of numerical calculations have been derived from component tests that are relatively different from each other: the Italian specimens (joints between HP 120x7) had larger dimensions and included four joints each; they were affected by typical defects and irregularities of shipbuilding both as far as

misalignments and weld defects are concerned. The German specimens (joints between HP 160x7) were simpler and built for laboratory testing and, although in full scale, they were affected by a lower level of imperfections.

Table 1 shows the outcomes of the statistical analysis of test data as well as the re-analysis of them, having reduced the scatter to obtain a standard deviation in agreement with conventional testing (standard deviation of log. life = 0.20). The aim is to eliminate the influence of test-related effects, existing in both cases, and to obtain more reliable target values for the considered details.

3 FE ANALYSIS ACCORDING TO THE PEAK STRESS METHOD

It was then decided to apply the PSM to the joints shown in Fig. 4. Especially, these cases among those tested and assessed according to other approaches are considered interesting for the assessment of the PSM because local notch geometries are relatively challenging and complex stress field is induced by both the bulb profile and the reinforcing attachments.

The loading conditions are in principle rather simple but the resulting stress field at weld toes could be complex because of the geometry: the HP120x7 joints with the patch onto the bulb head were fatigue tested at stress ratio $R<0.1$ in bending conditions as shown in Fig. 5 top, while the HP160x7 joints (named Variant 3 in [11]) were tested in pure tension with stress ratio R=-1.

The nominal stress range could be easily defined for both details applying the beam theory for the HP stiffener without reinforcement.

Taking advantage of the already built finite element (FE) models from previous calculations on the joints shown in Fig. 4, [12-13], it was decided to apply the sub-modeling technique to obtain three-dimensional finite element models for the PSM. Sub-modeling technique, available in most FE software environments as well as in the Ansys™ one adopted in this case, allows generating an independent, more finely meshed model of only the region of interest considering the displacements calculated on the cut boundaries of the more coarse model as boundary conditions of the sub-model.

Fig. 5 shows the whole FE models (left) and the sub-models (right) with results in terms of the first principal stresses for both details. Eight node solid elements were used to calculate the design stress as required by the PSM. The weld seam was rounded at reinforcing plate edges to avoid fictitious stress concentrations induced by sharp corners at edges.

Fig. 6 shows the detail of the meshing at the weld toe: only two solid 8 node elements (SOLID 45 of the Ansys™ software [9] or, equivalently, SOLID185 with element key option 2 set to 3) at the notch according to the requirements of the PSM were used for models of both details.

4 COMPARISON BETWEEN EXPERIMENTAL RESULTS AND THORETICAL ESTIMATIONS

Fig. 7 compares the experimental data expressed as peak stress values with the design scatter band shown in previous Fig. 3. The maximum value of the first principal stress along the weld toe was taken into account and the weighting factor $f_w=1.064$ was applied, since the notch opening angle is 135° for both details. Good agreement is found, also in case of the HP 160x7 (Variant 3) joints, which were tested at stress ratio R=-1 and therefore a bonus factor of

about f(R)≈1.3 could be considered in case of a limited level of residual stresses, according to the IIW recommendation [14]. However, since the joints were tested in the as-welded condition, Fig. 8 does not consider any bonus factor. As a second remark, it should be noted that the design scatter band reported in Figs. 3 and 7 was calibrated on experimental results generated from welded *specimens*, where most of the fatigue life is spent for initiation and short crack propagation inside the small zone governed by the NSIF. When full scale welded joints or real structures are considered, the fatigue life to propagate a macro-crack outside the structural volume governed by the NSIF could be significant. Then, strictly speaking, the PSM-based scatter band should be used to estimate the fatigue life to initiate a technical crack and not the total fatigue life of the joint. This might be another reason to explain the longer life than estimated for the HP 170x7 joints, where failure was defined after the whole bulb was fractured.

12 CONCLUSIONS

- The peak stress method was applied to perform the fatigue strength assessment of a HP stiffener joints with weld toe failures subject to full scale tests. Three-dimensional finite element analyses were performed to estimate the peak stress (i.e. the design stress) at the weld toe. A design fatigue scatter band previously calibrated on experimental results was used to assess the fatigue strength of the HP joints. Experimental results were found in fair agreement with the theoretical estimations.
- The peak stress method proved to combine the robustness of a local approach based on the Notch Stress Intensity Factor with the simplicity of a point related method.
- Due to its computational simplicity, the PSM appears rather useful for the everyday design practice of the shipbuilding industry.

REFERENCES

[1] Lazzarin, P. and Livieri, P. Notch stress intensity factors and fatigue strength of aluminium and steel welded joints. *Int. J. Fatigue* (2001) **23**: 225-232.

[2] Atzori, B. and Meneghetti, G. Fatigue strength of fillet welded structural steels: finite elements, strain gauges and reality. *Int. J. Fatigue* (2001) **23(8)**: 713-721.

[3] Radaj, D., Sonsino, C.M. and Fricke, W. *Fatigue assessment of welded joints by local approaches*. 2nd ed. Cambridge/Boca Raton Fla: Woodhead Publishing/CRC Press (2006).

[4] Meneghetti, G. and Lazzarin, P. Significance of the Elastic Peak Stress evaluated by FE analyses at the point of singularity of sharp V-notched components. *Fatigue Fract. Engng Mater. Struct.* (2007) **30**: 95-106.

[5] Williams, M.L. Stress singularities resulting from various boundary conditions in angular corners on plates in tension. *J Appl Mech* (1952) **19**: 526-528.

[6] Gross, R. and Mendelson, A. Plane Elastostatic Analysis of V-Notched Plates. *Int. J. Fract. Mech.* (1972) **8**: 267-272.

[7] Meneghetti, G. The use of peak stresses for fatigue strength assessments of welded lap joints and cover plates with toe and root failures. *Eng. Fract. Mech.* (2012) **89**: 40-51.

[8] Meneghetti, G. and Lazzarin, P. The peak stress method for fatigue strength

assessments of welded joints with weld toe or weld root failures. *Welding in the World* (2011) **55(7/8)**: 22-29.

[9] Meneghetti, G. and Guzzella, C. The peak stress method combined with three-dimensional finite element models to estimate the mode I notch stress intensity factor at the toe of fillet-welded joints. *Eng. Fract. Mech*. (2013), *submitted*.

[10] Carrera, G., Rizzo, C.M. and Tedeschi, R. Reports # 05CRI06 - 05CRI09: *Collapse and fatigue tests of welded joints in bulb stiffeners*. DINAV, University of Genova, 2005.

[11] Fricke, W. Untersuchungen zur Schwingfestigkeit von Längsspantstößen aus HP-Profilen *Schiff & Hafen.* (1986) **38(2)**: 50–54. [in German].

[12] Rizzo, C.M. and Fricke, W. Fatigue assessment of bulb stiffener joints according to local approaches. *Ships and Offshore Structures* (2012), in press.

[13] Rizzo, C.M. and Fricke, W. Verifica a fatica di giunti di profilati a bulbo mediante approcci locali (Fatigue strength assessment of bulb plate profiles joints according to local approaches). *Rivista Italiana della saldatura* (2012) **2**: 177-187. ISSN0035-6794. [in italian].

[14] Hobbacher, A. *Recommendations for fatigue design of welded joints and components*. IIW-Doc. 1823-07. New York: Welding Research Council Bulletin 520 (2009).

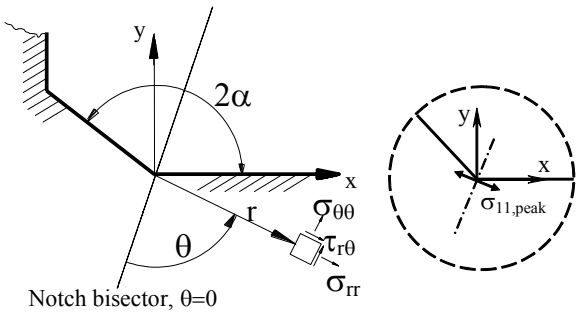


Figure 1: Local stresses and peak stress at the weld toe of a fillet-welded joint.

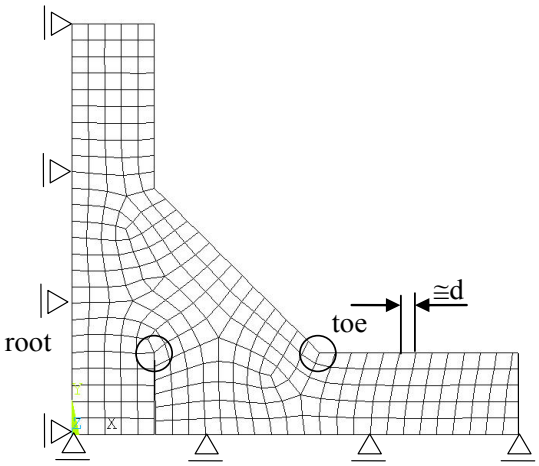


Figure 2: Typical two-dimensional free-mesh to apply the PSM at the toe or the root of a fillet-welded joint. *d* is the mean size of the four-node plane elements [4].

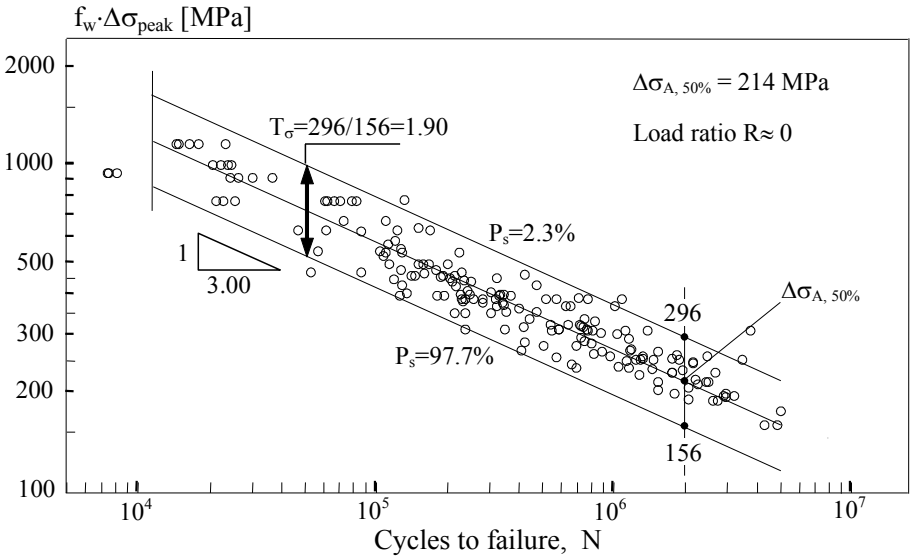
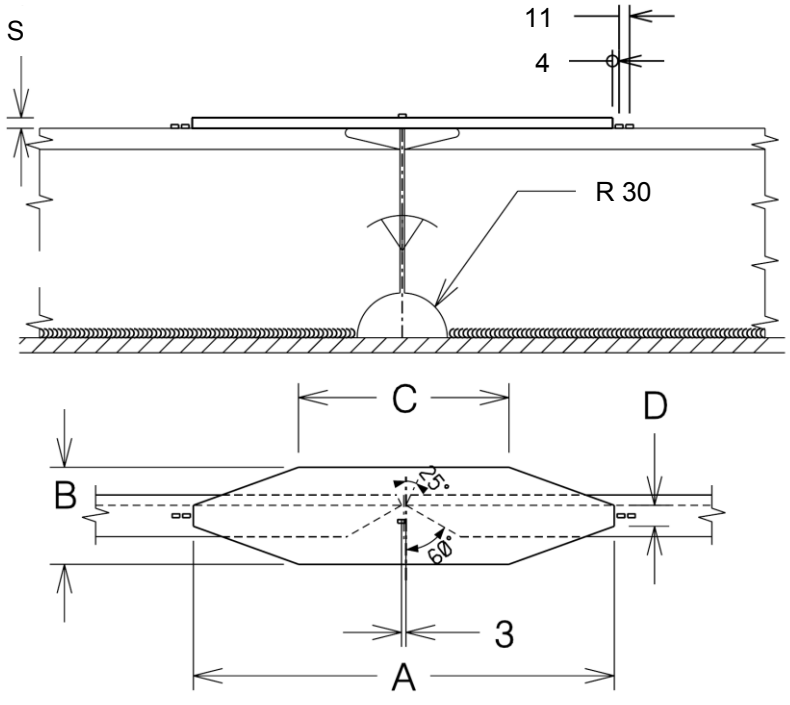


Figure 3: Fatigue strength of steel fillet-welded joints in terms of equivalent peak stress evaluated by using two-dimensional finite element models like that reported in Figure 2 ([8]).

HP 120x7 butt joint with patch on bulb head



H PROF.	A	B	C	D	S
⌜120X7	240	55	120	10	7

HP 160x7, Variant 3

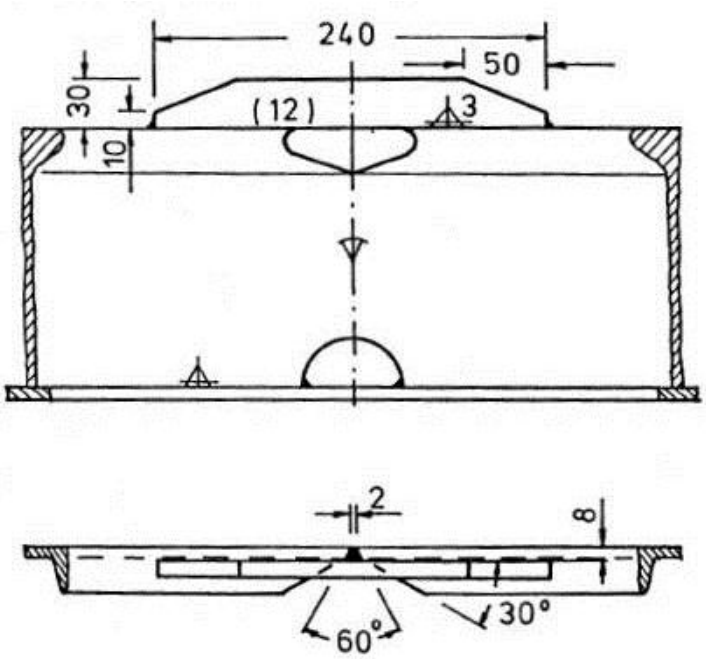


Figure 4: Geometries of the HP stiffener joints (HP120x7 top, HP160x7 bottom).

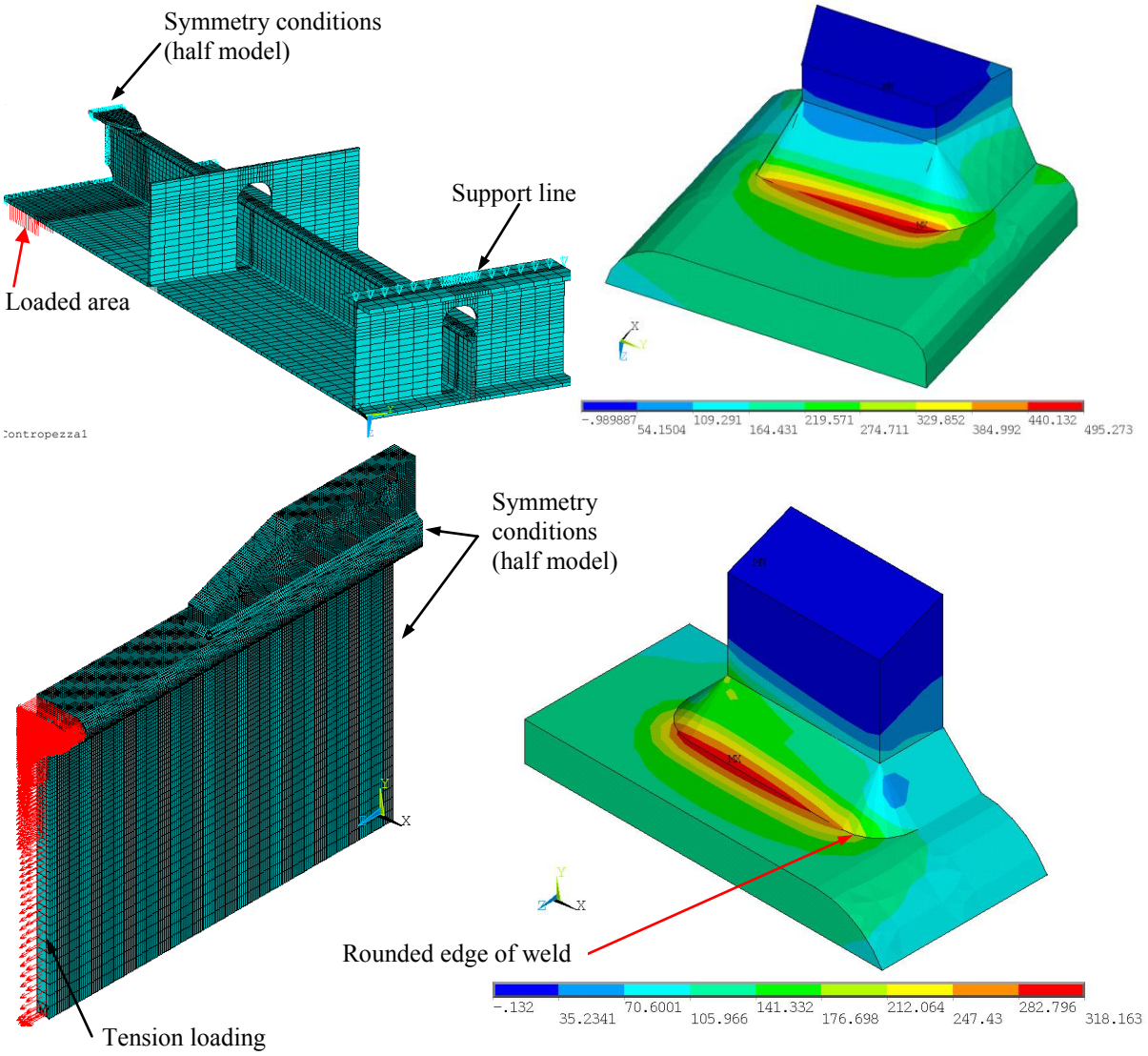


Figure 5: Available FE models and results of the 1st principal for the newly built sub-models (HP120x7 top and HP160x7 bottom).

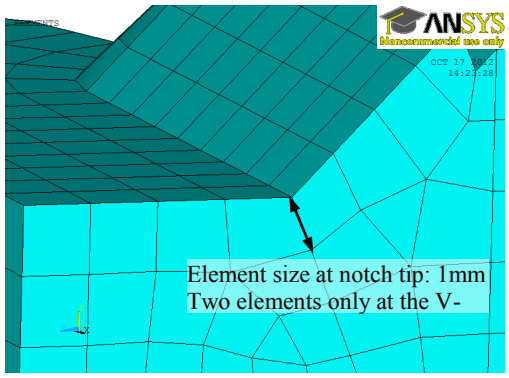


Figure 6: Detail of the mesh, cross section at weld toe.

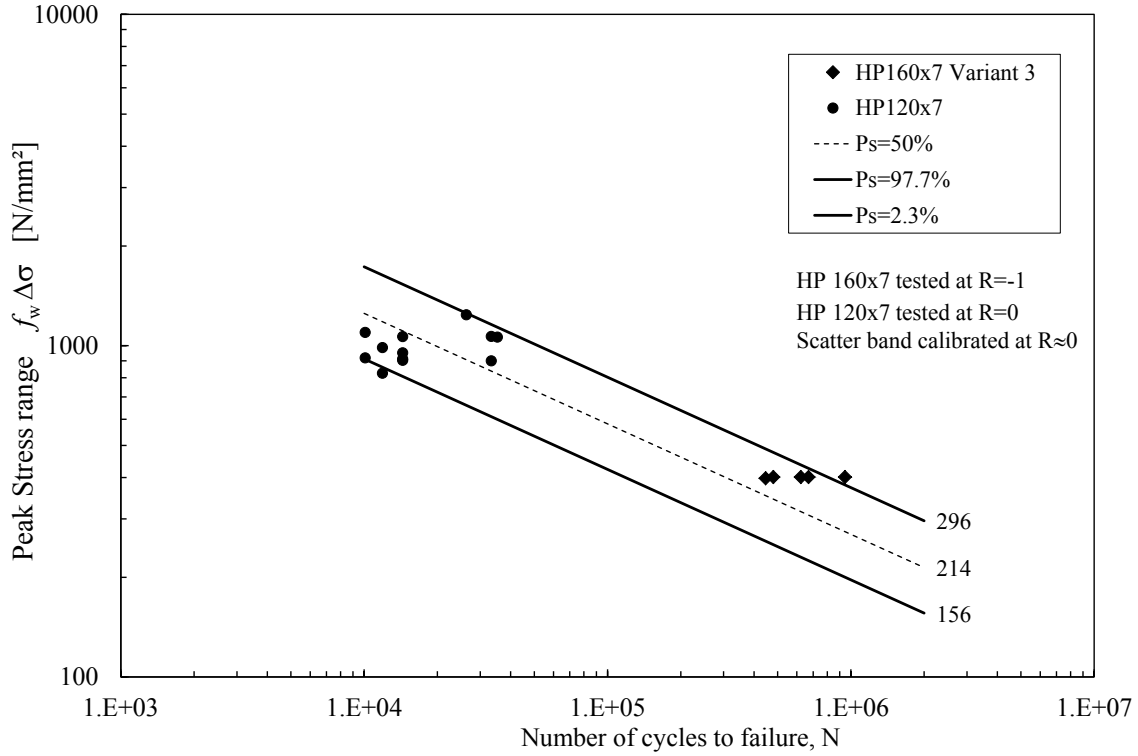


Figure 7: comparison between experimental results and PSM estimations for the analysed stiffener joints. The scatter band is that reported in figure 3.

Table 1: Cycles N to fracture, applied stress range $\Delta\sigma$ and scatter index T_N between survival probability Ps = 90% and 10% assuming slope exponent of S-N curve m = 3 [12]

Tests statistical re-analysis		HP 120x7, Top plate	HP 160x7, Variant 3
Parameters of mean S-N curve from experiments	$N(P_S=50\%)$	1.7×10^4	6.1×10^5
	$\Delta\sigma(P_S=50\%)$	345 MPa	126 MPa
	T_N (St. Dev.)	1:5.88 (0.30)	1:1.93 (0.11*)
Characteristic values of S-N curve Normalized standard deviation St. Dev. = 0.20	N ($P_S=97.7\%$)	2×10^6	2×10^6
	$\Delta\sigma(P_S=97.7\%)$	52 MPa	63 Mpa
	T_N	1:3.25	1:3.25

(*: includes all 7 available tests)

V International Conference on Computational Methods in Marine Engineering
MARINE 2013
B. Brinkmann and P. Wriggers (Eds)

A Preliminary Study on Ultrasonic Non-Destructive Testing of Concrete in Maritime Environment

Abid. A. Shah*, Yuri L. Ribakov† and Ch. Zhang*

*Chair of Structural Mechanics, Department of Civil Engineering,
University of Siegen,
Paul-Bonatz-Str. 9-11,
D-57076 Siegen, Germany
E-mail: abidalishah@bauwesen.uni-siegen.de - Web page: http://www.statics.uni-siegen.de

† Ariel University
40700 Ariel, Israel
Email: ribakov@ariel.ac.il - Web page: http://www.ariel.ac.il

Key words: Concrete, Non-destructive testing, Marine, Through-transmission, Attenuation, Wave reflection factor.

Abstract. This paper describes an experimental study in which non-destructive testing (NDT) of concrete in marine and a non-marine environment was performed. Nine (150mm x 150mm x 150mm) cubic specimens from three batches of concrete with w/c of 0.40, 0.50, and 0.60 and with appropriate variations in cement and sand were prepared.

The hardened concrete specimens were cured under controlled laboratory conditions for 28 days. In the first stage the cubic specimens were tested using through-transmission NDT technique lying simply on laboratory floor, representing a typical of non-marine environment. Afterwards, for simulating marine-like environment, the cubic specimens were retested lying in a water tank. The underwater through-transmission of the specimens was performed.

The results obtained from both ways of testing were recorded and plotted in time and frequency domains. P-wave velocities and attenuation of the wave signals were measured and compared. Additionally, the wave reflection factor (WRF) was calculated and compared for specimens tested under water.

The results show that the wave attenuation, the P-wave velocities in concrete, and the WRF are highly influenced by the w/c ratio. The outcomes of this study can be useful in conducting research on testing actual maritime concrete structures.

1 INTRODUCTION

The growing concern of the present day engineers is to effectively inspect the deteriorated concrete infrastructure [1,2]. Their priorities are increasingly shifting away from building new structures towards inspection, assessment and maintenance of the existing infrastructure [3]. Before appropriate rehabilitation can be prescribed, it is therefore necessary that the condition of a structure should be assessed. Non-destructive test (NDT) techniques that can detect, localize and characterize damage and flaws in the infrastructure are of great interest for this purpose [4].

The concrete infrastructure is comprised of a wide range of structure types including bridges, beams, columns, pavements, piers and pipes. Each of these structures, some of which

are also constructed in marine environment, may contain damage or embedded flaws. Elastic wave-based non-destructive test (NDT) methods are useful for detecting flaws or defects in all kinds of concrete structures [5]. However the application of elastic wave-based NDT methods for concrete structures is severely limited by the physical coupling between sensors and concrete surface, which reduces testing efficiency [1].

Most NDT techniques require good contact between the sensor and tested concrete surface to obtain reliable data. But the surface preparation is often very time- and labor consuming due to the rough surface or due to limited access particularly in case of underwater concrete structures. The easiest approach to speed up the data collection process is to eliminate the need for physical contact between the sensor and tested structure. Commonly used non-contact techniques include radiography with penetrating radiation, RADAR with electromagnetic pulsed waves and infrared thermography [6]. However, these techniques limited safety provision and are very expansive.

In this study a special through transmission test setup is developed as a solution that enable the elastic wave-based NDT method to test the concrete not only in non-marine environment but also perform the underwater NDT of concrete. This method describes the location, size and shape of embedded damage or flaws. It provides a direct way to help engineers evaluate the condition of both surface and under water concrete structures. Additionally, the through transmission test (Figure 1) can evaluate the velocity and attenuation of an ultrasonic wave traveling through the concrete. By knowing the pulse time of flight and the thickness of the concrete member the velocity can be calculated.

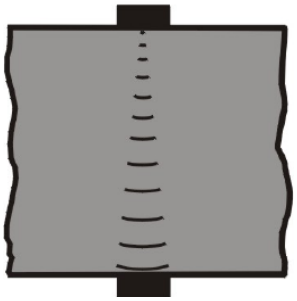


Figure 1. Ultrasonic through transmission method.

The proposed test setup was applied to evaluate the cubic specimens, prepared with different w/c, in two stages. In the first stage the specimens were tested lying simply on laboratory floor. Afterwards, for simulating marine-like environment, the cubic specimens were retested lying in a water tank. The underwater through-transmission testing of the specimens was performed. The results obtained from both ways of testing were recorded and plotted in time and frequency domains. P-wave velocities and attenuation of the wave signals were measured and compared. Additionally, the wave reflection factor (WRF) was calculated and compared for specimens tested under water. The results show that the wave attenuation, the P-wave velocities in concrete, and the WRF are highly influenced by the w/c ratio.

2 EXPERIMENTAL PROGRAM

Nine (150mm x 150mm x 150mm) cubic specimens from three batches of concrete with

w/c of 0.40, 0.50, and 0.60 and with appropriate variations in cement and sand were prepared. Two sizes of coarse aggregates were used, one with size varied from 2 to 8 mm and second with size varied from 8 to 15 mm. The aggregate quantities were kept constant in all the three batches. After 24-hour of casting the steel moulds were opened and the hardened concrete specimens were kept in water tub for 28-day of curing under the laboratory controlled temperature. Details of the mix proportions are given in Table 1.

Table 1: Mix proportions and compressive strength of concrete

W/C	Cement (kg/m^3)	Water (kg/m^3)	Sand (kg/m^3)	Crushed stone (kg/m^3)	Air entraining agent (kg/m^3)	Water reducing agent (kg/m^3)	Slump (cm)	Compressive strength (MPa)
0.40	425	170	799	910	0.034	0.026	8.0	56
0.50	340	170	871	910	0.034	0.017	10.0	45
0.60	283	170	919	910	0.034	0.010	10.50	38

Figures 2 and 3 show the test setups for testing cubic specimens outside and inside of water. The test setup used for testing of the concrete specimens outside of water consisted of a tone burst pulsar, a broadband receiver, two sensors, an agilent (function generator), and an oscilloscope (see Figure 1). One of the sensors was connected with the pulsar for wave transmission in the specimens and the other with receiver for wave reception. Each sensor had a central frequency of 500 kHz. In the current experimental program the ultrasonic waves were generated into the concrete specimens at a frequency range of greater than 100 kHz.

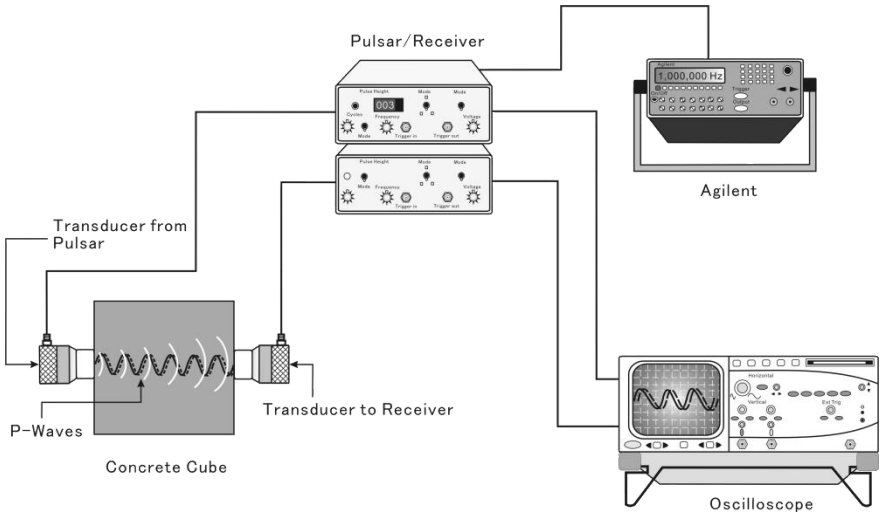


Figure 3. Ultrasonic through transmission testing of a cubic specimen outside of water

Similarly, for NDT of concrete specimens in water, the test setup consisted of a water tank, Master and Slave sensors, a loading pedestal for placement of the concrete cube, a control system, a computer and an oscilloscope (see Figure 2).

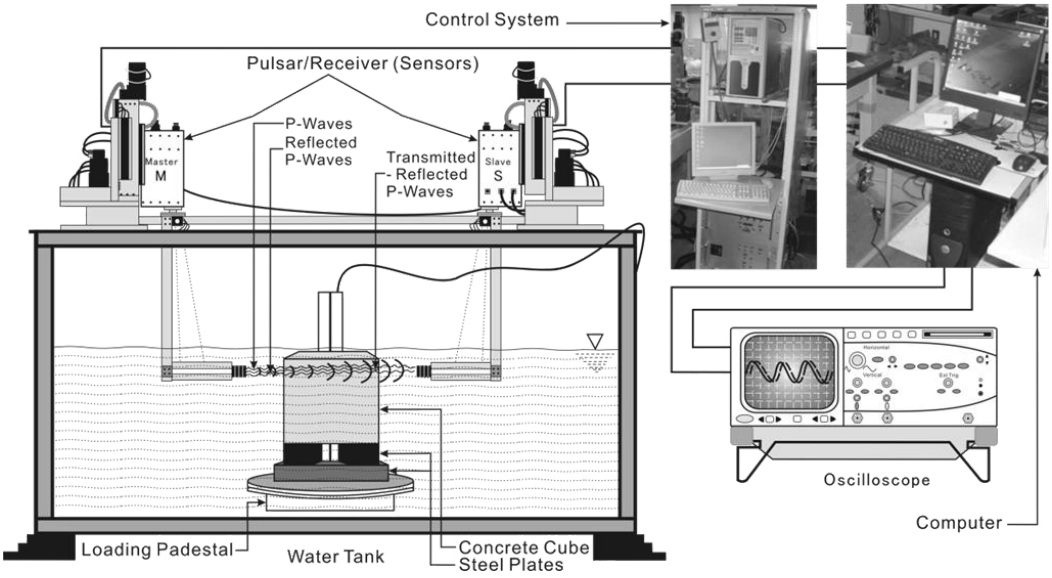
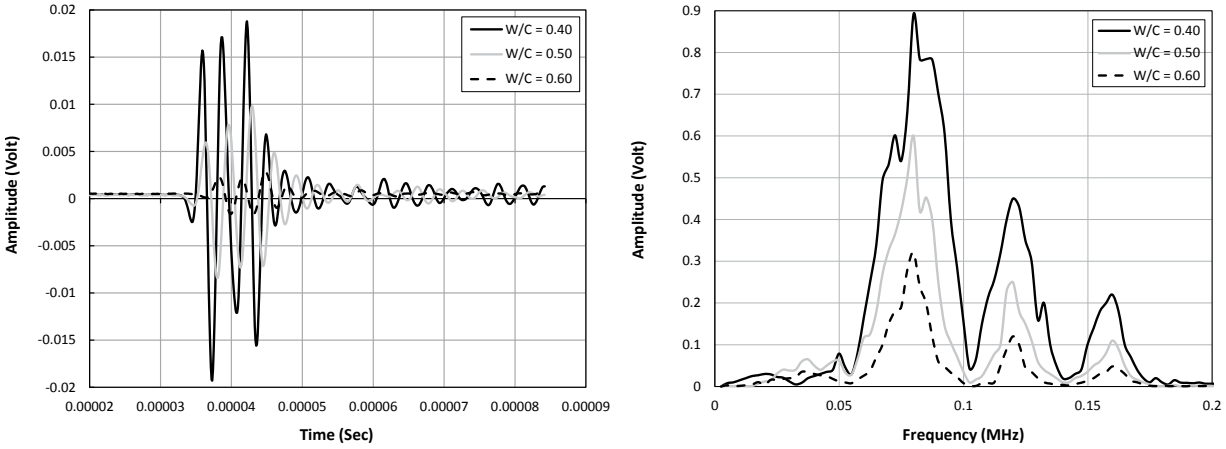


Figure 4. Ultrasonic through transmission testing of a cubic specimen inside of water

3 DISCUSSION OF TEST RESULTS

Figure 5 (a) shows the captured wave signals in time domain for the cubic specimens cast with w/c of 0.40, 0.50, and 0.50. The mean values of three specimens tested outside of water (Figure 3) at each w/c are plotted for comparison. As was expected, the effect of w/c is very pronounced in the plotted results. The experimental results illustrate that the amplitude of the waveforms decreases as w/c increases.



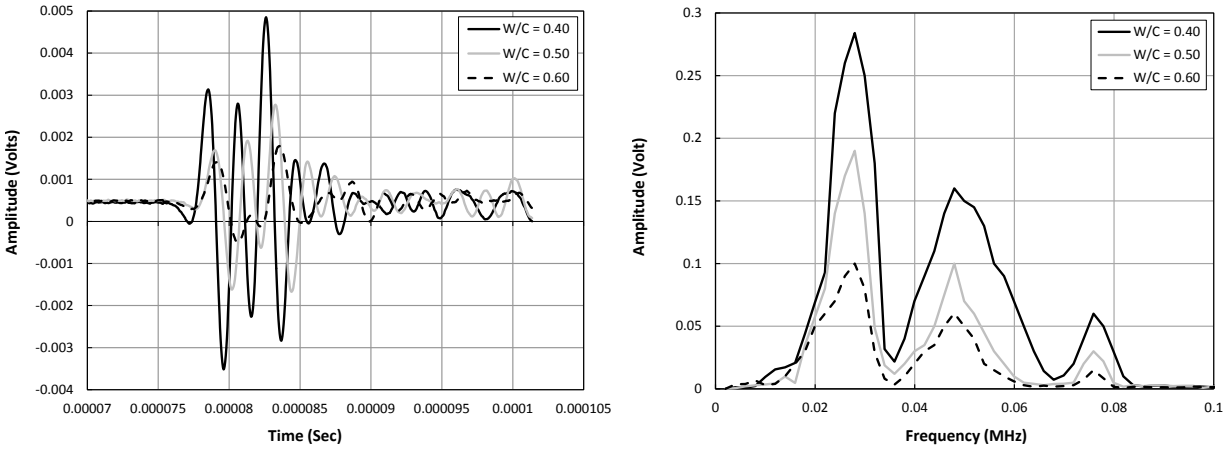
(a) (b)

Figure 5. Ultrasonic waveforms for outside of water tests (a) time domain (b) frequency spectrum

The Fourier transformed values of the time domain wave signals, as plotted in Figure 5 (a), are given in Figure 5 (b). At each w/c, the frequency spectrum appeared in three distinct

peaks. The test results show that the amplitude of the ultrasonic waveforms decreases as w/c increases. The comparison of the relative amplitudes of these two frequency peaks can be used to calculate attenuation. It was observed that the wave attenuation increases as frequency level increases. The highest attenuation of the ultrasonic waveforms was observed for frequency level greater than 150 kHz.

Similar trends for the change in the ultrasonic amplitude in time and frequency domain were obtained for the underwater experimentation (Figure 4). The average results of three specimens at different w/c were used for comparison. Figures 7 and 8 show these changes graphically. It can be seen that signal amplitude decreases as w/c increases (see Figure 7). Similarly, it was noticed that signal attenuation increases as frequency level increases.



(a) (b)

Figure 5. Ultrasonic waveforms for underwater tests (a) time domain (b) frequency spectrum

The comparison of test results revealed that the magnitudes of ultrasonic waveforms in both time and frequency domains were greater for the specimens evaluated outside of water than those for inside of water. The reduction in ultrasonic amplitude for under water evaluation was because of the fact that when an ultrasonic wave traveling through a medium hits an interface, defined as a boundary between two materials (water and concrete) with different acoustic properties, it is partially reflected back and partially transmitted into the medium on the other side of the interface. Therefore, the partially transmitted waves through the concrete were more prone to attenuate and resulted into signals reduction from the outside of water state to inside of water state by about 68% for all w/c concretes.

The wave reflection factor (WRF) for specimens tested underwater was additionally calculated, which describes the amount of wave energy reflected at the interface of water and concrete. The WRF for P-waves is determined by the acoustic impedances of the two materials that form the interface. When the wave travels from Material 1 (fluid/water) into Material 2 (concrete) the WRF is

$$WRF = \frac{\rho_c v_c - \rho_f v_f}{\rho_c v_c + \rho_f v_f} \tag{1}$$

with ρ_f and ρ_c as the densities while v_f and v_c as the P-wave velocities of fluid and concrete respectively.

From the test results analysis it was found that WRF increases as w/c decreases and vice versa. Table 2 shows the P-wave velocity and WRF values for cubic specimens tested under water. P-wave velocities of cubic concrete specimens tested outside of water are tabulated in Table 3. Both tables consist of the mean values of three tests with different w/c.

Table 2: Wave velocities and WRF for cubic specimens tested in water

W/C	Volume (m^3)	Mass (kg)	Concrete Density (kg/m^3)	Fluid density (kg/m^3)	v_c (m/s)	v_f (m/s)	WRF
0.40	0.0016	3.67	2370	1000	2851	1479	0.764
0.50	0.0015	3.64	2360	1000	2827	1479	0.763
0.60	0.0015	3.60	2350	1000	2817	1479	0.762

Table 3: P-wave velocities of cubic specimens tested outside of water

W/C	v_c m/s
40	4688
50	4615
60	4451

The tabulated results (tables 2 and 3) show that in each case concrete wave velocity decreases as w/c increases. However, the wave velocity values for specimens tested outside of water were found higher than those for inside of water, independent of w/c. This is perhaps because of the fact that underwater the non-contact NDT sensors generated weaker ultrasonic wave signals. It was, therefore, difficult to identify the onset, which resulted in a decreased pulse velocity. It might be an interesting finding towards evaluating concrete behavior applying through transmission testing technique to under water concrete structures. However, to validate this finding future research based on extensive experimentation in this direction is strongly recommended.

4 CONCLUSIONS

This research is focused on conducting an experimental study in which the through transmission NDT of concrete in marine and a non-marine environment was performed in order to examine the P-wave velocity and signal attenuation. Nine cubic specimens were cast. Three batches of concrete with w/c of 0.40, 0.50, and 0.60 and with appropriate variations in cement and sand were prepared.

The test results show that the testing technique appears to be reliable in both surface and underwater NDT evaluation of concrete. In both cases the results obtained for testing cubic specimens are reasonable and satisfactory. The P-wave velocities, however, for concrete specimens tested outside of water are greater than the specimens tested inside of water.

As the w/c decreases, the amplitude, the peak frequency levels, the P-wave velocity in concrete, and the wave reflection factor (which is a measurement of attenuation) increase. As

a result for the specimens tested underwater high attenuation of ultrasonic signals at frequency levels higher than 50 kHz was observed.

On the other hand, due to stronger signals for outside of water testing, the ultrasonic waves obtained at each w/c were found more prone to attenuate as soon the frequency levels exceeded 150 kHz. Additionally, attenuation can easily be calculated by comparing the relative amplitude levels of the different frequency peaks.

The research findings presented in this study can be very useful in conducting research on testing actual maritime concrete structures.

REFERENCES

[1] ACI Committee 228. Nondestructive test methods for evaluation of concrete in structures. Report ACI 228.2R-98, *American Concrete Institute*, Farmington Hills, MI., (1998).

[2] Asano, M., Kamada, T., Kunieda, M., Rokugo, K. and Kodama, I. Impact acoustics methods for defect evaluation in concrete. in *Non-Destructive Testing in Civil Engineering 2003*, Vol. Proceeding BB 85-CD, DGZIP, Berlin, Germany, Sept. (2003).

[3] Richart, F., Hall, J. and Woods, R. *Vibrations of soils and foundations*. Prentice-Hall Inc., Englewood Cliffs, New Jersey, (1970).

[4] Shah A. A. and Ribakov Y. Damage detection in concrete using nonlinear signal attenuation ultrasound. *Latin American Journal of Solids and Structures* (2012) 9(6):713-730.

[5] Shah, A. and Hirose S. Non-linear ultrasonic investigation of concrete damaged under uni-axial compression step loading. *ASCE Journal of Materials in Civil Engineering* (2010) 22 (5): 476-484.

[6] Malhotra, V.M. and Carino N.J. *Handbook on nondestructive testing of concrete*. Ann Arbor.: CRC Press, (2004).

V International Conference on Computational Methods in Marine Engineering
MARINE 2013
B. Brinkmann and P. Wriggers (Eds)

THE EFFECTIVE AXIAL FORCE CONCEPT FOR OFFSHORE LINED AND CLAD PIPES

KNUT VEDELD* HÅVAR SOLLUND* AND OLAV FYRILEIV†

* Mechanics Division,
Department of Mathematics, University of Oslo,
Moltke Moes vei 35, Pb. 1053 Blindern,
0316 Oslo, Norway

†Det Norske Veritas A/S
Veritasveien 1
1363 Høvik

E-mail: knutved@math.uio.no - Web page: http: // www.math.uio.no

Key words: : Lined pipes, clad pipes, effective axial force, pipeline

1 INTRODUCTION

Pipelines, risers and piping systems are subject to internal and external pressures as well as variations in temperature due to natural variations in the surrounding environment and variations in content temperature. Pressures and, depending on the boundary conditions, temperature will cause stresses in the pipe wall. Integrating the axial stresses over the cross section of a pipe gives the so-called true wall axial force [1]. The global bending behavior of pipes is affected by the axial force through 2nd order effects. However, due to the effect of the internal and external pressures it is the so-called effective axial force that governs the global response of the pipe. By using Archimedes' law, Sparks [2] demonstrated that the overall effects of pressure on a pipe may be expressed by an equivalent force system where equivalent axial forces replace complicated pressure integrals over doubly curved surfaces. Note that these equivalent axial forces do not cause axial stresses in a pipe, hence the distinction between true wall axial force and effective axial force, but they do, however, govern static and dynamic beam bending behavior and buckling [1-3].

The somewhat confusing definitions of the effective axial force and the distinction between the effective and true wall axial force concepts elude many, and historically have caused open disagreements between engineers and researchers in mechanics alike [4,5]. Even recently, the concept of effective axial force has been questioned [6], demonstrating that there is a need to solidify the theoretical background for the effective axial force concept.

Pipelines, risers and piping systems are often composed of layered cylinders. The dominating material is carbon manganese (CMn) steel for its cost and capacity to bear pressure and bending loads, but other materials are often applied for various other reasons. Thin stainless steel liners are sometimes applied to avoid corrosion in the CMn steel [7,8]. Variations in the Poisson's ratio and thermal expansion coefficients in the layers will alter the stress configurations through the thickness of the combined cross-section as compared to a monolithic cross-section, and ultimately result in axial reactions between the layers. The effective axial force concept for a layered cross-section will consequently be different from that of a monolithic cross-section. In this paper, a novel approach to the effective axial force concept is presented accounting for layered pipe cross-sections. The importance of variation in stiffness, Poisson's ratios and thermal expansion coefficients to the effective axial force and true wall axial force will be illustrated by applying the novel theory on typical lined and

clad pipeline cross-sections.

2 THEORETICAL BASIS FOR THE EFFECTIVE AXIAL FORCE

Archimedes' law states that "*the effect of the water pressure on a submerged body is an upward directed force equal in size to the weight of the water displaced by the body*". Formulated mathematically, Archimedes' law states that

$$\int_S -p_e \mathbf{n} dS = \rho_w V g \mathbf{k} = b\mathbf{k} \tag{1}$$

where S is the closed surface surrounding the submerged body, $\mathbf{n}$ is the normal vector to the surface S, p_e is the external pressure from the water, ρ_w is the density of the water, V is the volume of the body, b is the buoyancy, g is the gravitational constant and $\mathbf{k}$ is the unit normal vector in vertical direction. The mathematical formulation is further illustrated in Fig. 1a)-b).

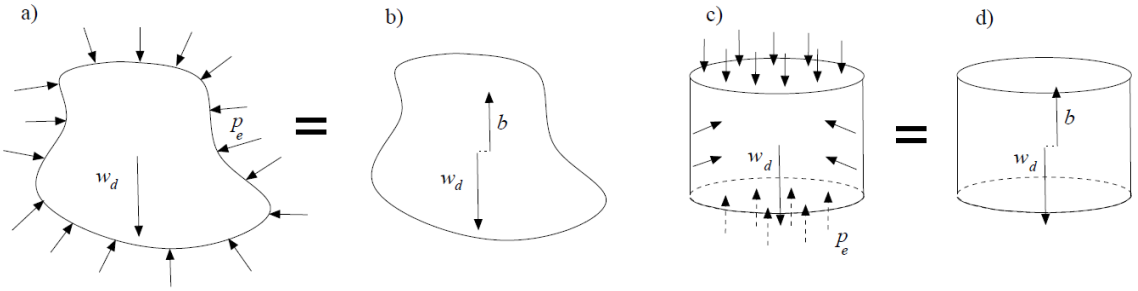


Figure 1: Archimedes' principle applied to a general body submerged in water and a cylinder.

In Fig. 1c)-d), Archimedes' law is restated for a vertical cylinder with end caps. If we adjust the dry weight w_d of the vertical cylinder to be exactly equal to the buoyancy b, the net force acting on the cylinder according to Figure 1d) is zero. Hence, if we apply Archimedes' law, we can express mathematically that, unless influenced by other forces, the cylinder will remain still in the water. If we only consider the load case illustrated in Fig. 1d), i.e. replacing the external pressure with a concentrated load acting on the center of gravity, the stresses in the cylinder wall are necessarily zero. From the load case in Fig. 1c) we can easily establish, however, the mean non-zero hoop stresses in the cylinder by equilibrium

$$\sigma_{\theta\theta} = -\frac{p_e D}{2t} \tag{2}$$

where $\sigma_{\theta\theta}$ is the mean hoop stress, D is the outer diameter of the cylinder and t is the cylinder wall thickness.

Furthermore, the approximate axial stresses in the cylinder wall must balance the pressure force acting on the end-caps, i.e.

$$\sigma_{zz} = -\frac{p_e A_e}{A_s} \tag{3}$$

where σ_{zz} is the axial stress, A_e is the area of the end caps and A_s is the cross-sectional area of the cylinder wall, and p_e is approximated as constant over the height of the cylinder.

We can observe that Archimedes' law will predict an equivalent vertical force equaling the buoyancy, which can replace a pressure integral. We can also, importantly, observe that this equivalent force cannot replace the actual pressures over the surfaces when establishing stresses and strains in the body. If we, on the other hand, allow the dry weight to be smaller than the buoyancy for the case described in Fig. 1d), the cylinder will move upwards towards the surface of the water if unconstrained. If we place a hand on the cylinder, the force we will feel in our hand is the difference between the dry weight and the buoyancy. Consequently, even if the force from the Archemedian upthrust cannot be applied to understand the stresses and strains in the cylinder, this is still the force we can measure when a body is submerged in water, and the force which will govern its displacements, albeit not its deformations. Hence we postulate the following observation or corollary to Archimedes' law:

The Archimedian upthrust is a measurable force equal to integrating the external pressure acting on a submerged body. It governs the displacements of the body, but not the stresses and strains on the interior of the body.

When we look at a pipe exposed to internal and external pressure, we find that we can add and subtract the end cap pressures to achieve an equivalent load system, as shown in Figure 2.

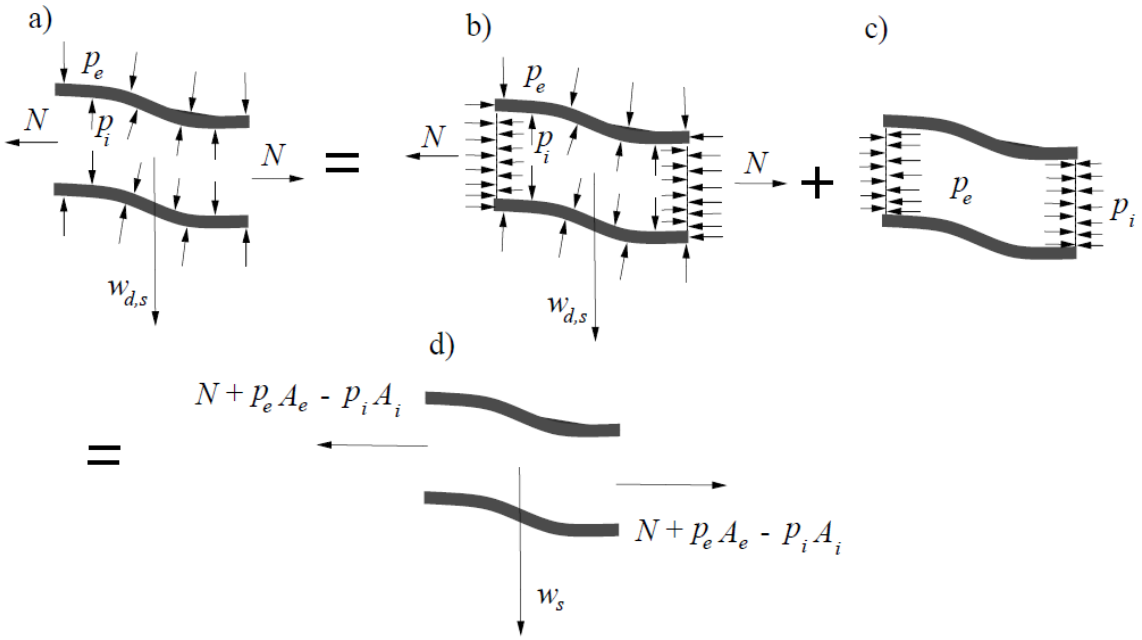


Figure 2: Archimedes' law applied twice to an internally and externally pressurized cylinder.

In Fig. 2a) an original cutout of a pipe is shown, and the forces acting on it are the pressures, the true wall axial force and the dry weight of the steel wall cross-section, drawn as w_d. In order to apply Archimedes' law we need pressures acting over closed surfaces. To make the pressure surfaces continuous and closed, we add (and subtract) the external and internal pressures to the external area A_e and the internal area A_i respectively, as shown in Fig. 2b) and 2c). By Archimedes' law, the pressures over the closed surfaces can be replaced by the buoyancy b in terms of the external pressure, and the weight of the content fluid w_{cont} in

terms of the internal pressure. Thus the weight of the pipe itself w_d, plus the weight of the content and subtracting the buoyancy gives the submerged weight w_s. Thereby the submerged weight can replace the initial pipe weight and the pressures over the closed surfaces, as shown in Fig. 3d). The only loading which remains is the submerged weight and the opposite axial loadings, including the contributions added to create pressures over closed surfaces. Thus the effective axial force in a cylindrical structure, free to expand axially, subject to internal and external pressure is defined by:

$$S_{eff} = N - p_i A_i + p_e A_e \tag{4}$$

It is, however, important to note that since we have utilized Archimedes' law to arrive at the expression for the effective axial force, the effective axial force cannot be used to express stresses and strains in the pipe, according to our previous observation. For an axially free pipe, the axial stresses must, consequently, be based on the true wall axial force N, and the pressures will contribute to radial and hoop stresses, but not axial stresses for the case described in Figure 2, and Eq. (4).

3 GENERAL ASSUMPTIONS

Exact displacement fields for multi-layer cylinders exposed to temperature, internal and external pressure, as well as axial forces, have been determined by Vedeld and Sollund [9].

$$u_r = \frac{C_{r1}}{r} + C_{r2} r, \quad u_\theta = 0, \quad u_z = \frac{C_z}{L} \tag{5}$$

In Eq. (5), u_r is the displacement in radial direction, u_θ is the displacement in hoop direction, u_z is the displacement in axial direction, and C_{r1}, C_{r2} and C_z are undetermined coefficients. Temperature expansion coefficients, Young's moduli and Poisson's ratios of the two layers in the cylinders are assumed to not be equal. Consequently, due to loading, finite cylinder length and differences in thermal expansion coefficients, the cylinders will be exposed to axial forces, and stresses and strains will be coupled by Poisson's ratio effects.

The boundary condition is shown in Figure 3, i.e., the pipe is exposed to an axial force N, as well as to internal pressure p_i, external pressure p_e and a uniform temperature change ΔT.

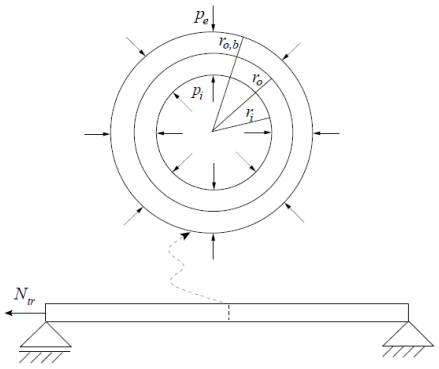


Figure 3: Boundary conditions for a segment of the heated, pressurized pipeline

The layers in Fig. 3 are assumed axially coupled, i.e. no axial sliding is accounted for.

4 DEDUCTION OF THE EFFECTIVE AXIAL FORCE

Based on full three dimensional elasticity, the stress fields in the two layers can be derived from Eq. (5).

$$\begin{bmatrix}\sigma_{rr}\\ \sigma_{\theta\theta}\\ \sigma_{zz}\end{bmatrix} = \hat{E}\begin{bmatrix} -(1-2v)\dfrac{C_{r1}}{r^2} + C_{r2} + v\dfrac{C_z}{L} - (1+v)\alpha\Delta T \\ (1-2v)\dfrac{C_{r1}}{r^2} + C_{r2} + v\dfrac{C_z}{L} - (1+v)\alpha\Delta T \\ 2vC_{r2} + (1-v)\dfrac{C_z}{L} - (1+v)\alpha\Delta T \end{bmatrix}$$
$$\begin{bmatrix}\sigma_{rr,b}\\ \sigma_{\theta\theta,b}\\ \sigma_{zz,b}\end{bmatrix} = \hat{E}_b\begin{bmatrix} -(1-2v)\dfrac{C_{r1,b}}{r^2} + C_{r2,b} + v\dfrac{C_{z,b}}{L} - (1+v)\alpha_b\Delta T \\ (1-2v)\dfrac{C_{r1,b}}{r^2} + C_{r2,b} + v\dfrac{C_{z,b}}{L} - (1+v)\alpha_b\Delta T \\ 2vC_{r2,b} + (1-v)\dfrac{C_{z,b}}{L} - (1+v)\alpha_b\Delta T \end{bmatrix} \tag{6}$$

In Eq. (6), σ_{rr} is the radial stress, $\sigma_{\theta\theta}$ is the hoop stress and σ_{zz} is the axial stress for the stainless liner or clad part of the pipe, and the subscript $_{,b}$ has been assigned to equivalent properties of the CMn backing steel. E is the Young's modulus where

$$\hat{E} = \frac{E}{(1+v)(1-2v)} \tag{7}$$

In order to derive the expression for restrained effective axial force in a lined or clad pipe, we will first illustrate the solution technique on the simpler case of a pipe with a monolithic (CMn) cross-section.

Eq. (6), now applying only to the single CMn layer, contains three unknown displacement coefficients. These quantities can be obtained by applying the known relations for pressure balance on the inner and outer pipe boundaries, together with force balance in the longitudinal direction, given by

$$\begin{aligned}\sigma_{rr}(r_i) &= -p_i \\ \sigma_{rr}(r_o) &= -p_e \\ \sigma_{zz}A_s &= N\end{aligned} \tag{8}$$

Applying Eq. (6) to solve for the three displacement coefficients gives

$$\begin{aligned} C_{r1} &= \frac{1+v}{E}\frac{r_i^2 r_o^2 (p_i - p_e)}{r_o^2 - r_i^2} \\ C_{r2} &= \frac{1-v}{E}\frac{p_i r_i^2 - p_e r_o^2}{r_o^2 - r_i^2} - \frac{v}{E}\frac{N}{A_s} + \alpha\Delta T \\ C_z &= \frac{NL}{EA_s} - 2\frac{vL}{E}\frac{p_i r_i^2 - p_e r_o^2}{r_o^2 - r_i^2} + L\alpha\Delta T \end{aligned} \tag{9}$$

The strain in the longitudinal direction can be found based on Eq. (9).

$$\varepsilon_{zz} = \frac{\partial u_z}{\partial z} = \frac{C_z}{L} = \frac{N}{EA_s} - 2\frac{\nu}{E}\frac{p_i r_i^2 - p_e r_o^2}{r_o^2 - r_i^2} + \alpha\Delta T \tag{10}$$

At lay down, the effective axial force H_{eff} is equal to the lay tension and the true wall axial force N_1 is given by:

$$N_1 = H_{eff} + p_{i,1}A_i - p_e A_e \tag{11}$$

The effective axial force will change when the pipe goes into operation when heat and a new internal pressure is applied. However the effective axial force expression, Eq. (4), still holds generally and consequently

$$N_2 = S_{eff} + p_{i,2}A_i - p_e A_e\,, \tag{12}$$

where N_2 is the true wall axial force in operational condition, $p_{i,2}$ is the internal pressure in operational condition and S_{eff} is the effective axial force in operational condition. Since the pipe is assumed fully fixed axially in operational condition, for instance due to pipe-soil axial friction between the pipe and the seabed, the longitudinal strain remains constant between the laying and the operational conditions.

$$\varepsilon_{zz,1} = \varepsilon_{zz,2} \quad \Rightarrow \quad \frac{C_{z,1}}{L} = \frac{C_{z,2}}{L}\,, \tag{13}$$

In Eq. (13), $\varepsilon_{zz,1}$ is the longitudinal strain after laying and $\varepsilon_{zz,2}$ is the longitudinal strain in operation. The longitudinal strain is assumed constant over the steel cross-section and can be found by inserting for N, p_i, p_e and ΔT in Eq. (10) for the laying and operational conditions respectively.

$$\begin{aligned}&\frac{H_{eff} + p_{i,1}A_i - p_e A_e}{EA_s} - 2\frac{\nu}{E}\frac{p_{i,1} r_i^2 - p_e r_o^2}{r_o^2 - r_i^2} + \alpha\left(T_1 - T_0\right)\\ &= \frac{S_{eff} + p_{i,2}A_i - p_e A_e}{EA_s} - 2\frac{\nu}{E}\frac{p_{i,2} r_i^2 - p_e r_o^2}{r_o^2 - r_i^2} + \alpha\left(T_2 - T_0\right)\end{aligned} \tag{14}$$

Solving Eq. (14) for the effective axial force S_{eff} yields

$$S_{eff} = H_{eff} - \Delta p_i A_i\left(1 - 2\nu\right) - EA_s\alpha\Delta T\,, \tag{15}$$

where $\Delta p_i = p_{i,2} - p_{i,1}$ and $\Delta T = T_2 - T_1$. Eq. (15) is identical to the equation for the effective axial force in a fully axially restrained pipe on the seabed, as found in DNV-OS-F101 [3].

The aim is, however, to solve for two-layer cylinders rather than the simple monolithic case. For two-layer cylinders, the same displacement field as was determined for the single layer case can be applied, i.e. the Lamé field, Eq. (5), can be applied successively for each layer [11]. The necessary solutions for the present problem are for axially unrestrained pipes of finite length, exposed to temperature and pressure. The solutions for temperature and pressure, derived in [11], are shown separately due to their significant length. The effects of

temperature and pressure may be superimposed, since we assume linear material behavior.

The solution for a lined pipe exposed to a uniform temperature change ΔT over the cross-section is:

$$C_{r1,b}^T = \frac{R_1^T K_{22}^T - R_2^T K_{12}^T}{K_{11}^T K_{22}^T - K_{12}^T K_{21}^T} \quad \wedge \quad C_{r2,b}^T = \frac{-R_1^T K_{21}^T + R_2^T K_{11}^T}{K_{11}^T K_{22}^T - K_{12}^T K_{21}^T}$$
$$C_z^T = \frac{L}{v_b}\alpha_b \Delta T(1+v_b) + \frac{L(1-2v_b)}{r_{o,b}^2 v_b} C_{r1,b}^T - \frac{L}{v_b} C_{r2,b}^T \tag{16}$$

where

$$K_{11}^T = \frac{\hat{E}_b(1-2v_b) - \hat{E}(1-2v)}{r_o^2} + (1-2v_b)\frac{\hat{E}v - \hat{E}_b v_b}{r_{o,b}^2 v_b} - \frac{c_A(1-v)}{vA_s}\left(\frac{1-2v_b}{r_{o,b}^2}\right)$$
$$K_{12}^T = -\hat{E}\left(1-2v+\frac{v}{v_b}\right) - \frac{\left(2v_b\hat{E}_b A_{s,b} - c_A\right)(1-v)}{vA_s}$$
$$K_{21}^T = \frac{v(1-2v_b)}{v_b r_{o,b}^2} - \frac{1-2v}{r_i^2} - \left(1+(1-2v)\frac{A_o}{A_i}\right)\frac{c_A(1-2v_b)}{2v\hat{E}A_s r_{o,b}^2}$$
$$K_{22}^T = -(1-2v)\frac{A_o}{A_i} - \frac{v}{v_b} - \left(1+(1-2v)\frac{A_o}{A_i}\right)\frac{2v_b\hat{E}_b A_{s,b} - c_A}{2\hat{E}vA_s} \tag{17}$$
$$R_1^T = \Delta T\left(\hat{E}\alpha(1+v) - \frac{\hat{E}v\alpha_b(1+v_b)}{v_b} - \frac{1-v}{vA_s}\left(\hat{E}A_s\alpha(1+v) - c_B\right)\right)$$
$$R_2^T = \Delta T\left(\alpha(1+v) - \frac{v}{v_b}\alpha_b(1+v_b) - \left(1+(1-2v)\frac{A_o}{A_i}\right)\frac{\left(\hat{E}A_s\alpha(1+v) - c_B\right)}{2v\hat{E}A_s}\right)$$
$$c_A = \frac{\hat{E}A_s(1-v) + \hat{E}_b A_{s,b}(1-v_b)}{v_b} \quad \wedge \quad c_B = \alpha_b(1+v_b)\frac{\hat{E}A_s(1-v) + \hat{E}_b A_{s,b}(1-2v_b)}{v_b}$$

For the pressure solution we get the following expression:

$$C_{r1}^p = \frac{K_{22}^p R_1^p - K_{12}^p R_2^p}{K_{11}^p K_{22}^p - K_{12}^p K_{21}^p} \quad \wedge \quad C_{r1,b}^p = \frac{-K_{21}^p R_1^p + K_{11}^p R_2^p}{K_{11}^p K_{22}^p - K_{12}^p K_{21}^p}$$
$$C_z^p = \frac{L}{v_b - v}\left(\frac{p_i}{\hat{E}} - \frac{p_e}{\hat{E}_b} - C_{r1}^p\frac{r_i^2 + r_o^2(1-2v)}{r_i^2 r_o^2} + C_{r1,b}^p\frac{r_{o,b}^2 + r_o^2(1-2v_b)}{r_{o,b}^2 r_o^2}\right) \tag{18}$$

where

$$
\begin{aligned}
&K_{11}^{p} = \hat{E}\left(1-2v\right)\left(\frac{1}{r_i^2}-\frac{1}{r_o^2}\right) \quad \wedge \quad K_{21}^{p} = 2vA_s\hat{E}\frac{1-2v}{r_i^2} - c_L\frac{r_i^2+r_o^2\left(1-2v\right)}{r_i^2 r_o^2} \\
&K_{12}^{p} = \hat{E}_b\left(1-2v_b\right)\left(\frac{1}{r_o^2}-\frac{1}{r_{o,b}^2}\right) \quad \wedge \quad K_{22}^{p} = 2v_bA_{s,b}\hat{E}_b\frac{1-2v_b}{r_{o,b}^2} + c_L\frac{r_{o,b}^2+r_o^2\left(1-2v_b\right)}{r_{o,b}^2 r_o^2} \\
&R_1^{p} = p_i - p_e \quad \wedge \quad R_2^{p} = N + 2vp_iA_s + 2v_bA_{s,b}p_e - c_L\left(\frac{p_i}{\hat{E}}-\frac{p_e}{\hat{E}_b}\right) \\
&c_L = \frac{EA_s + E_bA_{s,b}}{v_b - v}
\end{aligned}
\tag{19}
$$

Inserting for Eqs. (16) and (18) into (13) and solving for the effective axial force yields:

$$
\begin{aligned}
S_{eff} = \left(\frac{C}{A}\right)\Bigg(&\frac{p_{i,1}-p_{i,2}}{\hat{E}} - C_{r1}^{P1}S_1 + C_{r1,b}^{P1}S_2 + \frac{v_b - v}{v_b}\left(1+v_b\right)\alpha_b\left(\Delta T_1 - \Delta T_2\right) \\
&+ \frac{\left(1-2v_b\right)\left(v_b-v\right)}{r_{o,b}^2 v_b}\left(C_{r1,b}^{T1}-C_{r1,b}^{T2}\right) - \frac{v_b-v}{v_b}\left(C_{r2,b}^{T1}-C_{r2,b}^{T2}\right)\Bigg) - \frac{B}{A}
\end{aligned}
\tag{20}
$$

where

$$
\begin{aligned}
&S_1 = \frac{r_i^2 + r_o^2\left(1-2v\right)}{r_i^2 r_o^2} \quad \wedge \quad S_2 = \frac{r_{o,b}^2 + r_o^2\left(1-2v_b\right)}{r_{o,b}^2 r_o^2} \\
&A = K_{12}^{P}S_1 + K_{11}^{P}S_2 \;\wedge\; B = -\left(K_{22}^{P}S_1 + K_{21}^{P}S_2\right)R_1^{P2} + AR_{2,rem}^{P2} \;\wedge\; C = K_{11}^{P}K_{22}^{P} - K_{12}^{P}K_{21}^{P} \\
&R_{2,rem}^{P2} = p_{i,2}A_i - p_eA_e + 2vp_{i,2}A_s + 2v_bA_{s,b}p_e - \frac{EA_s + E_bA_{s,b}}{v_b - v}\left(\frac{p_{i,2}}{\hat{E}}-\frac{p_e}{\hat{E}_b}\right)
\end{aligned}
\tag{21}
$$

The rather complex formulae expressed in Eq. (20) will be proposed substituted with a much simpler expression:

$$
S_{eff,approx} = H_{eff} - \Delta p_iA_i\frac{\left(1-2v\right)A_s + \left(1-2v_b\right)A_{s,b}}{A_s + A_{s,b}} - \Delta T\left(E\alpha A_s + E_b\alpha_bA_{s,b}\right) \tag{22}
$$

A simple and common way to estimate the effective axial force for a lined or clad pipe, is to ignore the material properties of the liner or clad layer and apply the expression from DNV-OS-F101, Eq. (15), on the combined cross-section, which then is assumed to consist of CMn steel only, but with the liner thickness included in the CMn steel thickness. This manner of calculating the effective axial force will in the following be termed $S_{eff,OS\text{-}F101}$, but it should be noted that this procedure is not described in DNV-OS-F101 [3]. This methodology has been applied in the present context to create a comparative basis to the novel formulae in Eqs. (20) and (22) and making it possible to isolate the effects of variation in material properties between the layers.

$$S_{eff,OS-F101} = H_{eff} - \Delta p_i A_i (1-2\nu_b) - \Delta T E_b \alpha_b \left(A_s + A_{s,b}\right) \tag{23}$$

5 RESULTS AND COMPARISONS

Pipelines with outer diameters in the range of 6 inches to 40 inches, and D/t ratios from 8 to 40 have been systematically studied for three separate loading cases. In all cases, a constant liner thickness of 3 *mm* has been assumed. The loading cases are presented in Table 1.

Table 1: Load cases for comparisons of effective axial force formulae.

Load case	Δp_i	ΔT
1	260	120
2	220	0
3	0	50

Load case 1 represents a high pressure, high temperature pipeline (HTHP), load case 2 represents a standard pipeline operating at ambient temperature and load case 3 represents a depressurized pipe which has not had time to cool off yet. Load case 1 is included since it represents a pipe for which the effective axial force is a critical design parameter whereas loading cases 2 and 3 are included to investigate the effect of the liner or clad on the effective axial force as a function of pressure and temperature individually. In Table 2, the material properties for the corrosion-resistant alloy (CRA) and the CMn steel are given.

Table 2: Material properties for liner and backing steel.

Material	Young's modulus E [GPa]	Poisson's ratio ν [-]	Temperature expansion coeff. A [°C^{-1}]
Liner (CRA)	191	0.29	$1.70 \cdot 10^{-5}$
Backing steel (CMn)	207	0.30	$1.17 \cdot 10^{-5}$

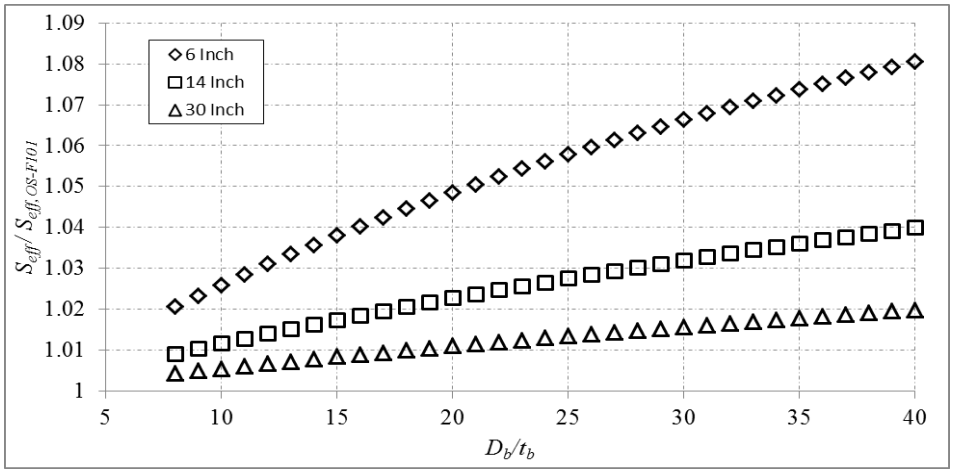


Figure 4: Effect of liner on effective axial force for different pipe diameters and steel diameter-to-thickness ratios. Both internal pressure and temperature have been applied (load case 1).

Fig. 4 shows how the accuracy of Eq. (23) varies with steel D/t ratio for HTHP pipes with three different outer diameters of 6 inches, 14 inches and 32 inches, respectively. The figure clearly shows that the effect of the liner on the compressive effective axial force is increasing with D/t for the steel, and also that the effect declines with increasing outer diameter. Since the effect of the liner on the effective axial force depends on both the D/t ratio and the outer diameter as individual parameters, a different, more general parameter is desirable in order to isolate the effect of the liner to a single representative variable. The $A_{s,b}/A_s$ ratio is proposed, since one would expect that the effect of ignoring the liner material properties decreases monotonically for increasing values of this ratio, as shown in Figure 5 for load cases 2 and 3.

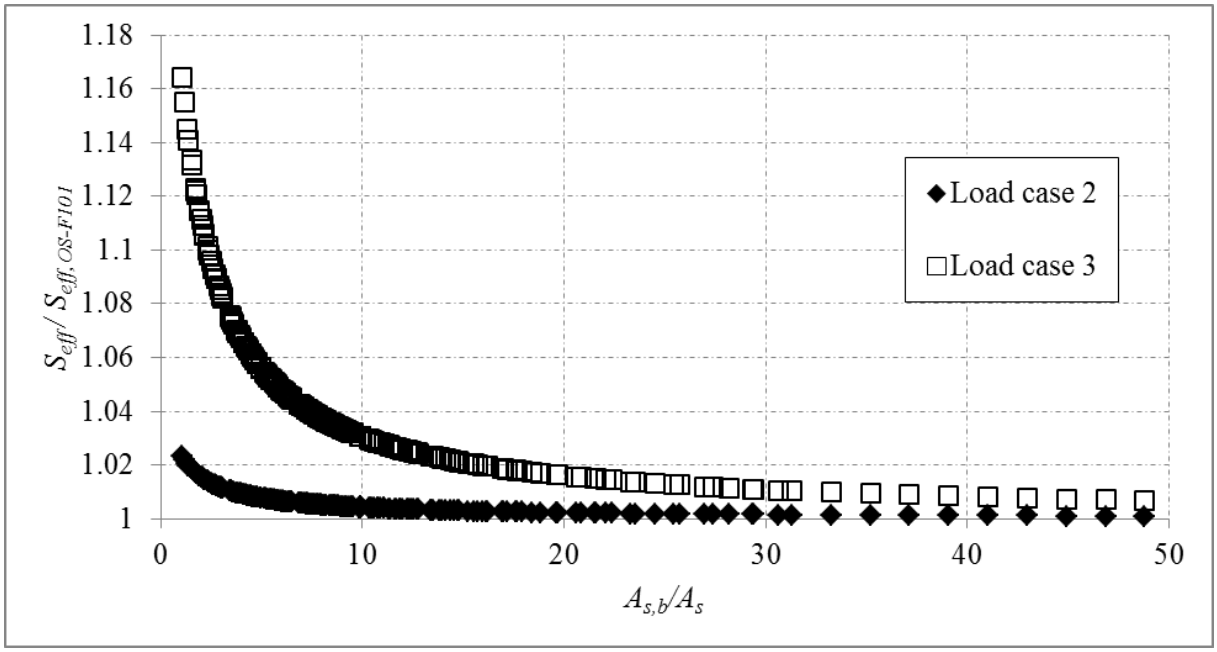


Figure 5: Effect of liner on effective axial force as a function of the cross-sectional ratio $A_{s,b}/A_s$. Load case 2 (pressure only) and load case 3 (temperature only) have been applied.

From Figure 5, it is observed that the effect of temperature is much more significant than the effect of pressure for the relative change in effective axial force from the liner. This is to be expected, since the difference in temperature expansion coefficients is much more pronounced than the differences in Poisson's ratios between CMn steel and stainless steels.

In Figure 6, below, the effect of the liner or clad on the effective axial force is demonstrated for the HTHP pipeline. It is observed that the functional relationship is no longer one-to-one, but it is also seen that the accuracy of applying Eq. (23) rather than the exact expression, Eq. (20), still may be determined with good precision based on the $A_{s,b}/A_s$ ratio.

Based on the observations of the relation between cross-sectional areas of the steels and the outcome to the effective axial force, Eq. (22) is tested to determine its accuracy. It is reasonable to expect a good relation due to the clear dependence on the $A_{s,b}/A_s$ parameter to the effect of the liner. The results for load case 1 are presented in Figure 7.

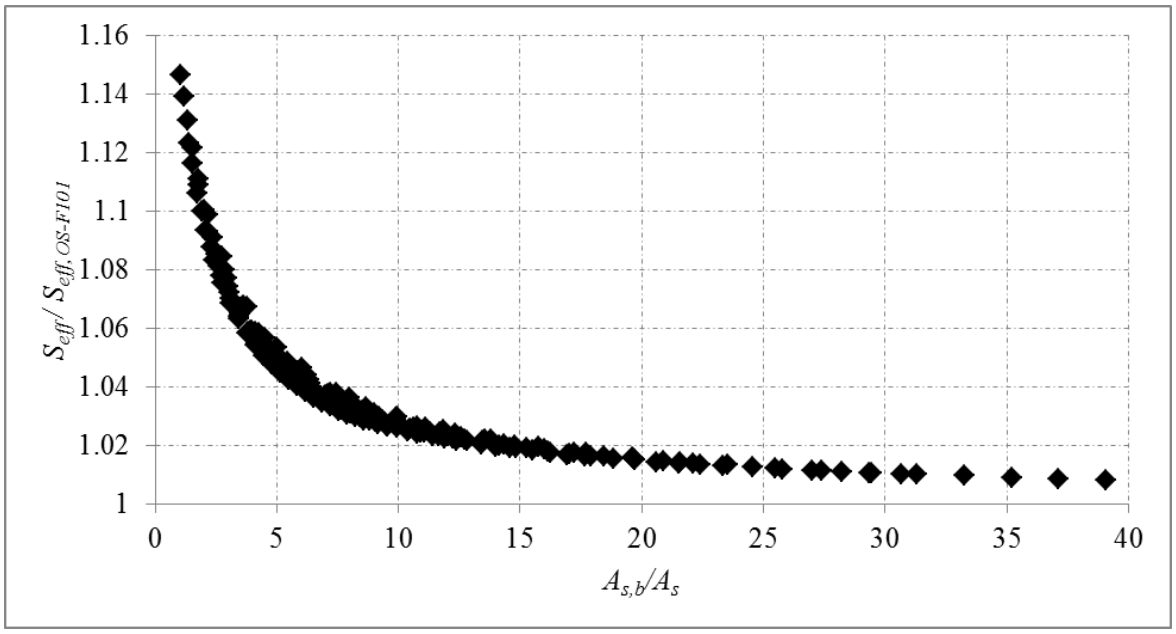


Figure 6: Effect of liner on effective axial force as a function of the cross-sectional ratio $A_{s,b}/A_s$. Load case 1 (pressure and temperature) has been applied.

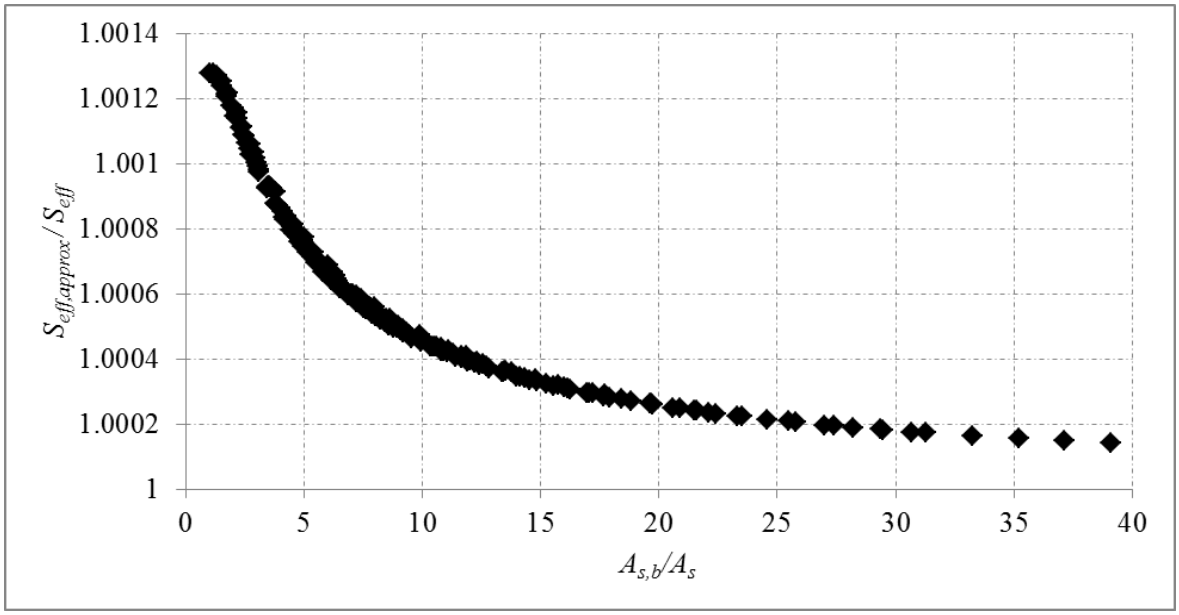


Figure 7: Accuracy of the proposed simplified expression, Eq. (22), compared to the exact expression, Eq. (23), as a function of the cross-sectional ratio $A_{s,b}/A_s$.

As shown in Figure 7, Eq. (22) gives an excellent prediction of the effect of the liner on the effective axial force. Load cases 2 and 3 (not shown) exhibit the same accuracy for the proposed Eq. (22). It is also positive that the slight (negligible) inaccuracy is consistently conservative in terms of the effective axial force. Moreover, it should be noted that the alternative approximate expression, Eq. (23), was not only found to be less accurate than Eq.

(22), but was also consistently non-conservative for the cases examined in the present study.

12 CONCLUSIONS

- The effect of liner and clad materials on the effective axial force has been determined by an exact analytical deduction.
- Liner and clad materials increase the compressive effective axial force since their thermal expansion coefficients are higher and their Poisson's ratios lower.
- Particularly for small diameter pipes with moderate to high D/t ratios it is important to include the effects of the liner or clad materials on the effective axial force.
- A (much) simplified formula to predict the effective axial force for lined and clad pipes has been proposed, and its accuracy is excellent.

REFERENCES

[1] Fyrileiv, O. and Collberg, L. Influence of pressure in pipeline design – effective axial force. *Proc. of 24th Int. Conf. on Offshore Mechanics and Arctic Engineering, OMAE 2005*, Halkidiki, Greece, June 12-17 (2005).

[2] Sparks, C.P. The influence of tension, pressure and weight on pipe and riser deformations and stresses. *ASME transactions* (1984) **106**: 46-54.

[3] DNV-OS-F101. *Submarine pipeline systems*. Det Norske Veritas, Norway (2012).

[4] Galgoul, N.S., Massa, A.L.L. and Claro, C.A. A discussion on how internal pressure is treated in offshore pipeline design. *Proceedings of IPC 2004*, Calgary, Canada (2004).

[5] Carr, M., Bruton, D. and Leslie, D. Lateral buckling and pipeline walking, a challenge for hot pipelines. *Offshore Pipeline Technology conference, OPT 2003,* Amsterdam, The Netherlands (2003).

[6] Lupinacci, M. Galgoul, N.S., Guevara, N.O., Fernandes, A.C., Coelho, F.M. and Neto, S.F.S. The influence of internal pressure on pipeline natural frequency. *Proc. of 28th Int. Conf. on Ocean, Offshore and Arctic Engineering, OMAE 2009*, Honolulu, Hawaii, USA, May 31 – June 5 (2009).

[7] Vedeld, K., Osnes, H. and Fyrileiv, O. Analytical expressions for stress distributions in lined pipes: Axial stress and contact pressure interaction. *Marine Structures* (2012) **26**(1): 1-26.

[8] Vedeld, K., Osnes, H. and Fyrileiv, O. New interpretations of gripping force tests for lined pipes. *Marine Structures* (2012) **29**(1): 152-168.

[9] Vedeld, K. and Sollund, H. Explicit analytical solutions for heated, pressurized multi-layer cylinders of finite length *Research Report in Mechanics, No. 13-1, Mechanics Division, Department of Mathematics, University of Oslo, Norway* (2013).

V International Conference on Computational Methods in Marine Engineering
MARINE 2013
B. Brinkmann and P. Wriggers (Eds)

CNOIDAL WAVE INDUCED FORCES ON A SUBMARINE PIPELINE

XIAO-HE XIA, YUN-FENG XU, JIAN-HUA WANG†, JIN-JIAN CHEN

Department of Civil engineering, Shanghai Jiao Tong University
800 Dongchuan Road, 200240 Shanghai，China
† email: wjh417@sjtu.edu.cn

Key words: Cnoidal water wave; Biot equation; Submarine pipeline; Pore pressure

Abstract. Forces acting on a submarine pipeline by cnoidal water waves is analyzed with Biot equation. Parametric studies are carried out to examine the influence of air content in pore water and the soil hydraulic conductivity on the forces. It has been shown that the air content and the soil hydraulic conductivity can significantly affect the pore pressure, horizontal and vertical forces acting on the pipeline. An increase in the air content and a reduction of the soil hydraulic conductivity as well as an increase of the soil hydraulic anisotropy will reduce the pore pressure on the surface of the pipeline. The maximum uplift force acting on the pipeline approaches 0.2 times of the pipeline buoyancy and, a high soil hydraulic anisotropy can make the magnitude of the horizontal force approaches 0.15 times of the pipeline buoyancy.

1 INTRODUCTION

Numerous researches had been focused on ocean waves induced transient response on a seabed and submarine pipelines. Mei and Foda [1] gave an analytical approximation on stresses in a semi-infinite seabed with a pipeline fixed on the seafloor. In the study on waves induced pore pressure around a pipelines, Spierenburg [2] gave the uplift force on the pipeline based on the potential theory. Furthermore, a physical experiment was set up to model the breakout of the half buried pipeline in sand by Foda, Law and Chang [3]. Cheng and Liu [4] investigated waves induced seepage force on a rigid pipeline buried in a seabed with the boundary integral equation method. Magda et al. [5-7] analyzed the pore pressure around the pipeline and the uplift force with a finite element method approach on the base of Biot equation. In addition, analogous laboratory and numerical studies have been published [8-10].

In view of that waves are usually nonlinear especially in shallow water, Mostafa and Mizutoni [11]; Gao and Wu [12] investigated the nonlinear wave force on marine pipeline with a coupled FEM-BEM model. Naturally, the seabed in coastal frequently become unstable before the ultimate design conditions of pipeline, Teh et al. [13, 14] and Sumer et al. [15, 16] studied the stability of submarine pipeline laid in a liquefied seabed.

The preceding researches present sufficient, multi-perspective and comprehensive knowledge about the response of the the seabed and pipelines to waves. The linear wave theory is frequently applied in the preceding analytical analysis. Whereas, waves are usually nonlinear in the coastal region, and the linear wave is not adequately suitable. Cnoidal wave theory is an explicit theory mainly applicable for shallow water. Much work has been devoted to facilitate the application of that wave theory [17-19]. This paper considers a poro-elastic seabed embedding a pipeline under cnoidal waves herein.

Consequently, the natural seabed is very complex in composition and texture. Properties about the air content in pore water and soil hydraulic conductivity are very difficult to measure. In this paper parametric studies are carried out to indicate the influence of the air content and soil hydraulic conductivity on the forces on the pipeline.

2 PROBLEM FORMULATION

Problem analyzed in this study is illustrated in Fig. 1. A pipeline is fully buried in a semi-infinite seabed. The seafloor is horizontal and the pipeline is weightless. Interaction between the pipeline and the seabed is not considered. Biot equation on poro-elastic media is employed to describe the response of the seabed, which has been generally accepted as the governing equation for the soil displacement and pore pressure. Adopting the sign of compression positive for stress which is frequently used in geotechnical engineering, the governing equations may be written as

$$G\nabla^2 u + (\lambda + G)\frac{\partial \varepsilon_v}{\partial x} = \frac{\partial p}{\partial x} \tag{1}$$

$$G\nabla^2 v + (\lambda + G)\frac{\partial \varepsilon_v}{\partial z} = \frac{\partial p}{\partial z} \tag{2}$$

$$k_x \frac{\partial^2 p}{\partial x^2} + k_z \frac{\partial^2 p}{\partial z^2} = n\beta\gamma_w \frac{\partial p}{\partial t} + \gamma_w \frac{\partial \varepsilon_V}{\partial t} \tag{3}$$

in which *u(x, z, t), v(x, z, t)* denote the soil displacement in horizontal and vertical direction, and *p(x, z, t)* represents the pore pressure. ε_v is the bulk strain (i. e. $\frac{\partial u}{\partial x} + \frac{\partial v}{\partial y}$), γ_w is the specific weight of water. *t* is the time, *n* is the soil porosity. k_x, k_z are the hydraulic conductivity in x and z directions. β denotes the compressibility of the pore water including a small amount of air, i. e.

$$\beta = \frac{1 - d_a}{K_w} + \frac{d_a}{P_{abs}}$$

where K_w is the bulk elasticity modulus of the pure water (taken as 2.3×10^9Pa), d_a is the percentage of air content in pore water, P_{abs} is the absolute pore pressure. The pore water in seabed is not always completely saturated and contains a small quantity of bubbles. Whereas, even a very few amounts of bubbles in the water can decrease the effective bulk modulus of

the pore water significantly [20-22].

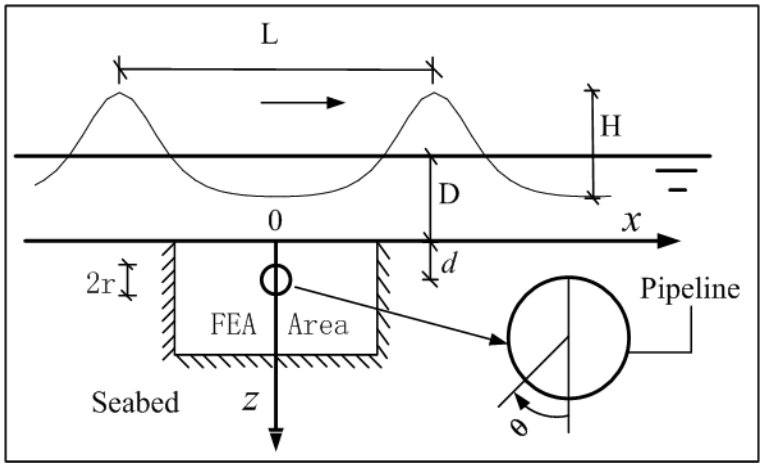


Fig. 1 Problem analyzed.

When cnoidal waves pass over the seabed, the oscillatory water pressure on the surface of seabed can be approximated as

$$p(x,t) = p_0 + \mathrm{g}(x,t) \tag{4}$$

where $p_0 = \gamma_w H\left(\frac{1}{m^2} - \frac{E}{m^2 K} - 1\right)$, $g(x,t) = \gamma_w Hcn^2\left[2K\left(\frac{x}{L} - \frac{t}{T}\right)\right]$, H is the wave height, L is the wave length, T is the wave period, m is the modulus. K and E are the first and second kinds of complete elliptic integral**.**

The boundary conditions on the seafloor are that the pore pressure is given by Eq. (4) and there is no normal and shear stress. Referring to Fig. 1, we consider a finite seabed which is bounded from below and sides by rigid and rough surfaces. The boundary conditions for the pore pressure flux is $\frac{\partial p}{\partial n} = 0$ in which n is the outward normal of the boundary. And for the soil skeleton, the boundary condition is $U_n = 0$ where U_n is the normal component of the displacement. In general, there is a soft impermeable layer on the surface of a pipeline which can prevent the pipeline from corrosion by the sea water. Then the boundary condition for the pore pressure is no water flux and the soil skeleton is free along the pipeline surface.

The initial conditions of Eqs. (1-3) are given with the assumption that the soil displacement and the pore pressure are negligible at the beginning, i. e. $u(x,z,0) = 0$, $v(x,z,0) = 0$ and $p(x,z,0) = 0$.

The horizontal and vertical forces acting on the pipeline can be found by integrating the pore pressure along the pipeline outer contour Γ, i. e.

$$F_h = \int_\Gamma p n_x dl \tag{5}$$

$$F_v = -\int_\Gamma p n_y dl \tag{6}$$

in which F_h is the horizontal seepage force (right positive) and F_v is the vertical force (upward positive).

3 NUMERICAL CALCULATION

3.1 Verification

Pore pressures on the surface of the pipeline was measured by Cheng and Liu [4] in an laboratory test. A numerical modeling of the problem is accomplished with COMSOL 4.3 package and compared with Cheng and Liu (Fig. 2). A linear water wave is employed with wave height H=0.143m, wave period T=1.75s and water depth D=0.533m, the corresponding wave length is L=3.54m. Parameters for the seabed are: shear modulus G=640kPa, Poisson constant $\upsilon = 0.33$, soil porosity n=0.42, soil hydraulic conductivity k_z=1.1×10^{-3}m/s, air content in the pore water d_a=5%. Radius of the pipeline is $r = 0.084\text{m}$ and the buried depth d=0.167m. Fig. 2 shows that the agreement of the current solution and the results of Cheng and Liu is excellent.

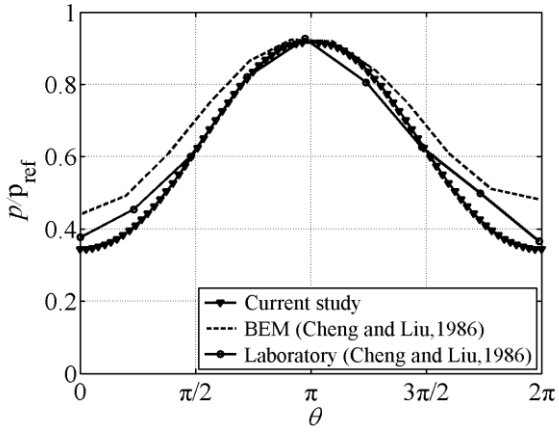


Fig. 2 Pore pressures on the surface of the pipeline. Notation: $p_{ref} = \frac{1}{2}\frac{\gamma_w H}{\cosh(2\pi D / L)}$

3.2 Solution

This section shows the seabed response under cnoidal waves. The input data for the wave are as followed: the wave height H=2.0m and wave period T=10s travelling in a water depth of D=6.5m. The calculated modulus of the cnoidal wave is m=0.979876 with a wave length of L=80.03m. The normalized wave pressure on the seabed with respect to time is shown in Fig. 3. It indicates that the normalized wave crest approaches 0.7 and the wave trough is near -0.3. Properties about the seabed are given as: the soil shear modulus G=20MPa, the Poisson constant $\upsilon = 0.3$, the porosity of the soil n=0.5, the soil hydraulic conductivity $k_x = k_z = 2.0\times10^{-4} m/s$ and the air content in pore water d_a=1%.

Fig. 4 gives the soil displacement along the pipeline under waves. Fig. 4(a) and Fig. 4(b) represent respectively the displacement under the wave crest and wave trough. It is clear that the soil horizontal displacement is negligible compared to the vertical. The maximum normalized value of the soil vertical displacement is approximate to 0.001, corresponding to

the maximum vertical displacement $v = 2$ mm. Fig. 5 shows the pore pressure on the pipeline. It states that the magnitude of the pore pressure on the top varies more sharply than that on the bottom. Fig. 6 gives the horizontal and vertical forces acting on the pipeline. It is clear that the horizontal force is much smaller that the vertical. The maximum vertical force is approximate to $0.2F_{\text{buo}}$, which is in accordance with the analysis of Cheng and Liu [4].

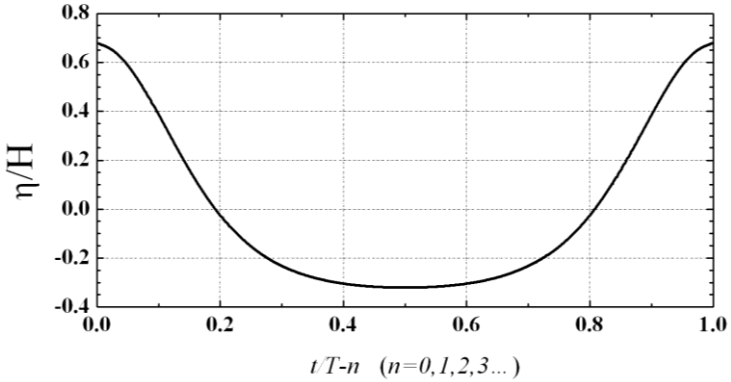
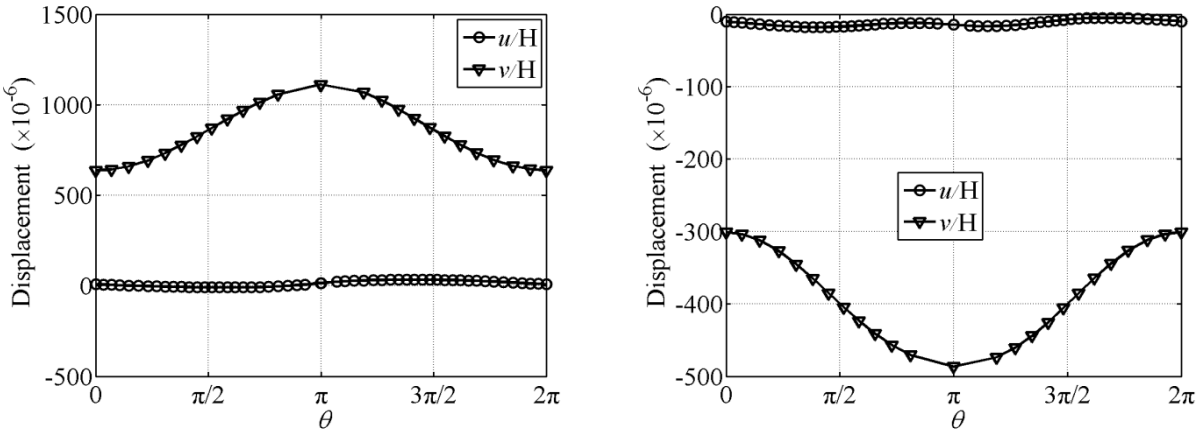


Fig. 3 Profile of the cnoidal water wave



(a) Under the wave crest

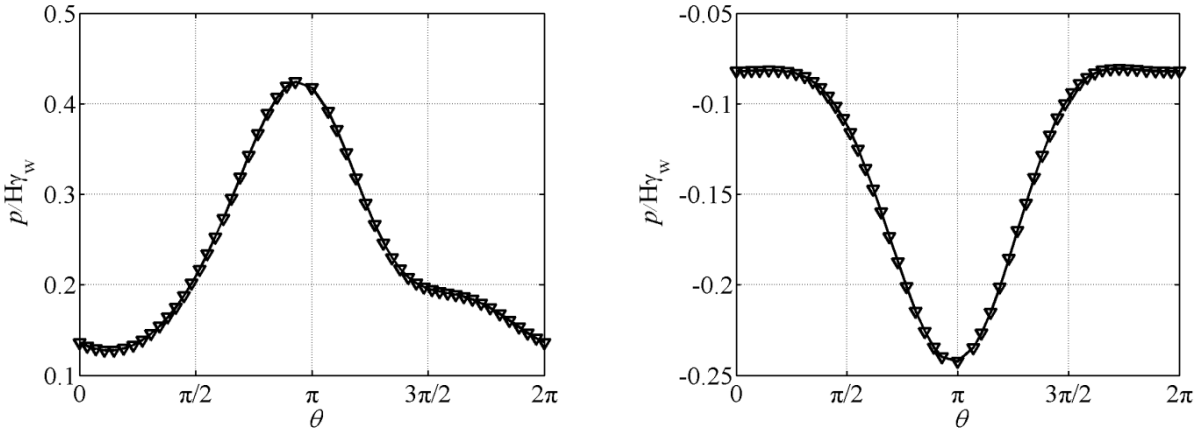
(b) Under the wave trough

Fig. 4 Soil displacement along the pipeline

4 PARAMETRIC STUDIES

Naturally, the seabed is layered with complex composition and distinct hydraulic anisotropy. However, it is difficult to determine the exact values of the air content in pore water and the soil hydraulic conductivity as well as the soil hydraulic anisotropy in engineering practice. Therefore, parametric studies are necessary to provide useful insight on the sensitivity of forces on a pipeline with these parameters. In this section, parametric studies are carried out to investigate the influence of the air content in the pore water, as well as the soil hydraulic conductivity and the soil hydraulic anisotropy. The air content d_a varies from 0

to 2% and the hydraulic conductivity k_x=k_z varies from 1.0×10^{-4} to 2.5×10^{-3} m/s, consequently k_x/k_z varies from 1 to 25. Parameters about the seabed and the wave are the same as given in section 3.2.



(a) Under the wave crest (b) Under the wave trough

Fig. 5 Pore pressure around the pipeline

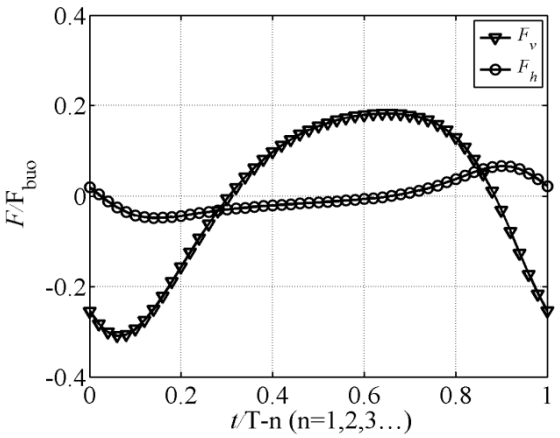


Fig. 6 Forces acting on the pipeline. Notation: $F_{\text{buo}} = \gamma_w \pi r^2$

4.1 Influence of the air content

Fig. 7 illustrates the influence of the air content on the pore pressure along the pipeline (Fig. 7a) and forces acting on the pipeline (Fig. 7b, c). For simplicity, this section only gives pore pressure under the wave crest. The soil hydraulic conductivity in the study is $k_x = k_z = 1.0 \times 10^{-4}$ m/s . It is clear that the pore water pressure is very sensitive to the air content. An increase of the air content can decrease the magnitude of pore pressure and forces acting on the pipeline. Nevertheless, the maximum of the vertical force on the pipeline is near $0.2F_{buo}$.

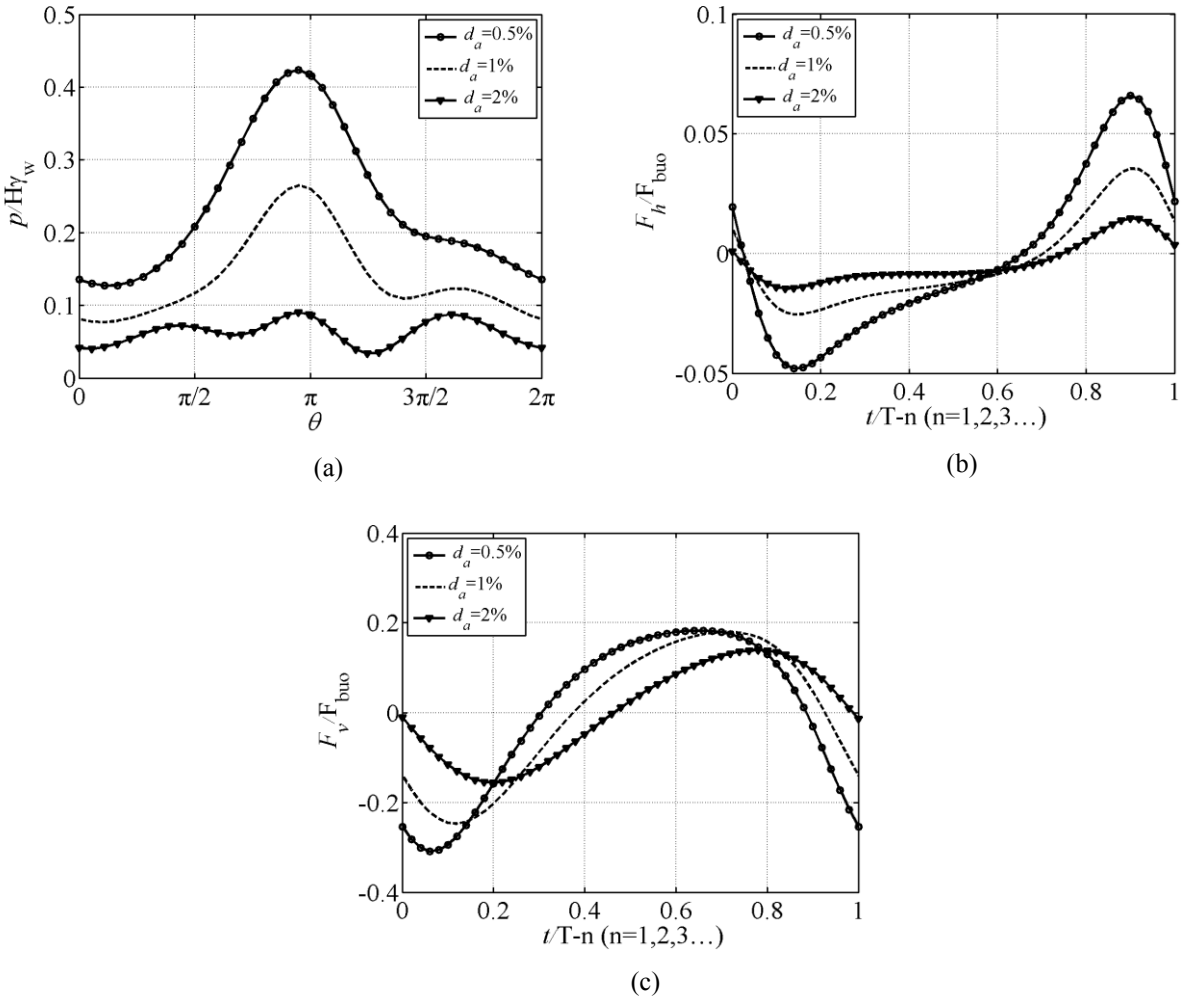


Fig. 7 Influence of the air content

4.2 Influence of the soil hydraulic conductivity

Fig. 8 illustrates the influence of the soil hydraulic conductivity on the pore pressure (Fig. 8a), forces on the pipeline (Fig. 8b, c). The air content in the calculation is $d_a = 1\%$. It is clear that the soil hydraulic conductivity can affect the pore pressure significantly. An decrease of k_z can decrease the magnitude of the pore pressure and forces on the pipeline. Similarly as above, the maximum of the vertical force on the pipeline approaches $0.2F_{buo}$.

4.3 Influence of the soil hydraulic anisotropy

Fig. 9 illustrates the variation of the pore pressure (Fig. 9a) and forces (Fig. 9b, c) acting on the pipeline when k_x/k_z varies from 1 to 25. It is clear that the magnitude of the pore pressure decrease as the value of k_x/k_z increases, whereas, an increase of k_x/k_z will increase the horizontal force acting on the pipeline with a maximum of $0.15F_{buo}$. Nevertheless, the vertical force on the pipeline varies slightly with k_x/k_z and the maximum is close to $0.2F_{buo}$.

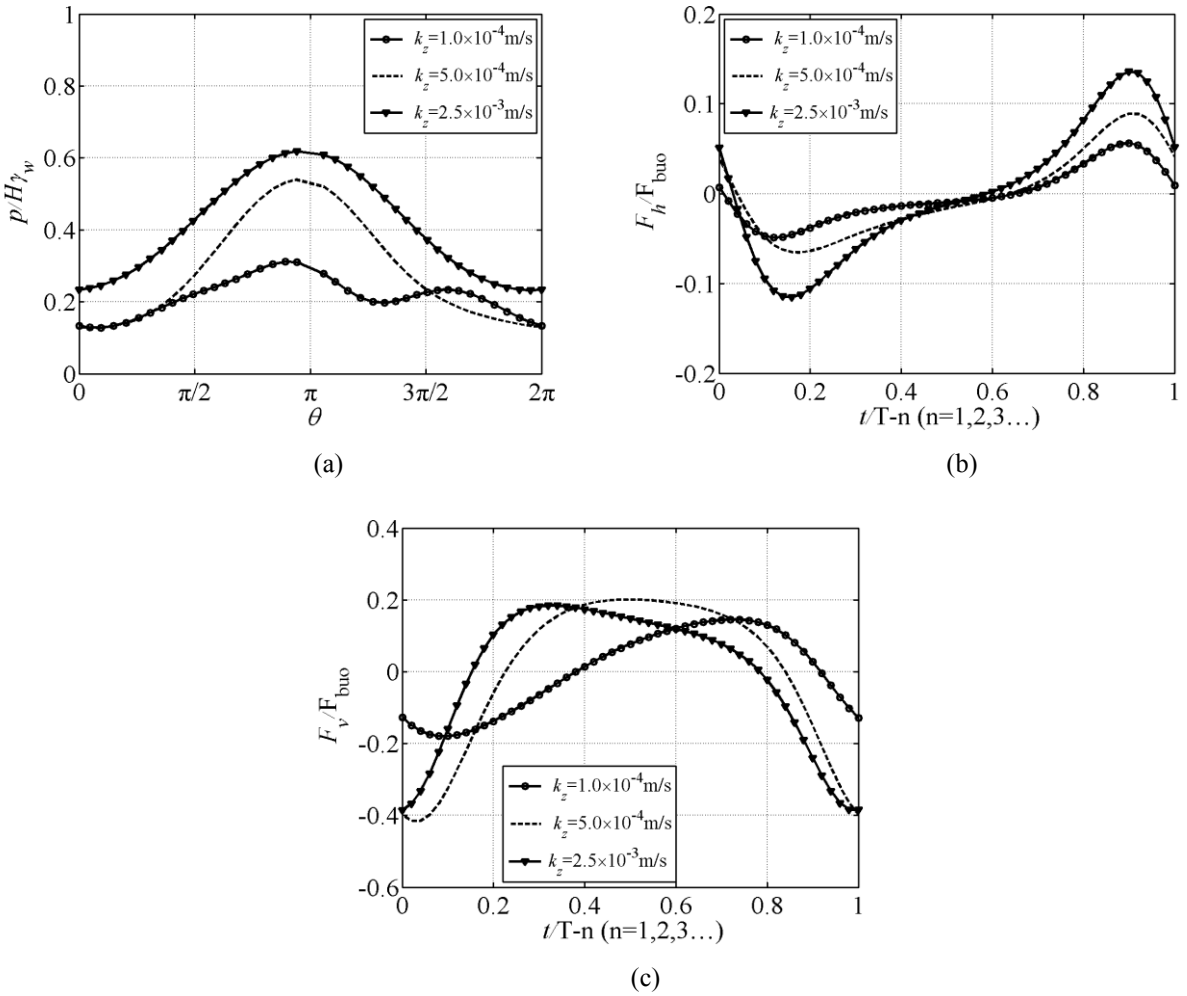


Fig. 8 Influence of the soil hydraulic conductivity on pore pressure

5 CONCLUSIONS

Biot equations can be used to evaluate forces acting on a submarine pipeline under cnoidal water waves without the consideration of the interaction between the seabed and the pipeline. The air content in pore water and soil hydraulic conductivity can significantly affect the forces. When the air content in the pore water varies from 0 to 2% and the soil hydraulic conductivity varies from 2.0×10^{-5} to 2.5×10^{-3} m/s, an increase of the air content in pore water and a decrease in the soil hydraulic conductivity as well as an increase of the soil hydraulic anisotropy can decrease the magnitude of the pore pressure on the pipeline. The maximum vertical force acting on the pipeline is near $0.2F_{buo}$, which is independent of the air content and the soil hydraulic conductivity. Nevertheless, a high anisotropy ratio k_x/k_z can make the magnitude of the horizontal force approaches $0.15\ F_{buo}$.

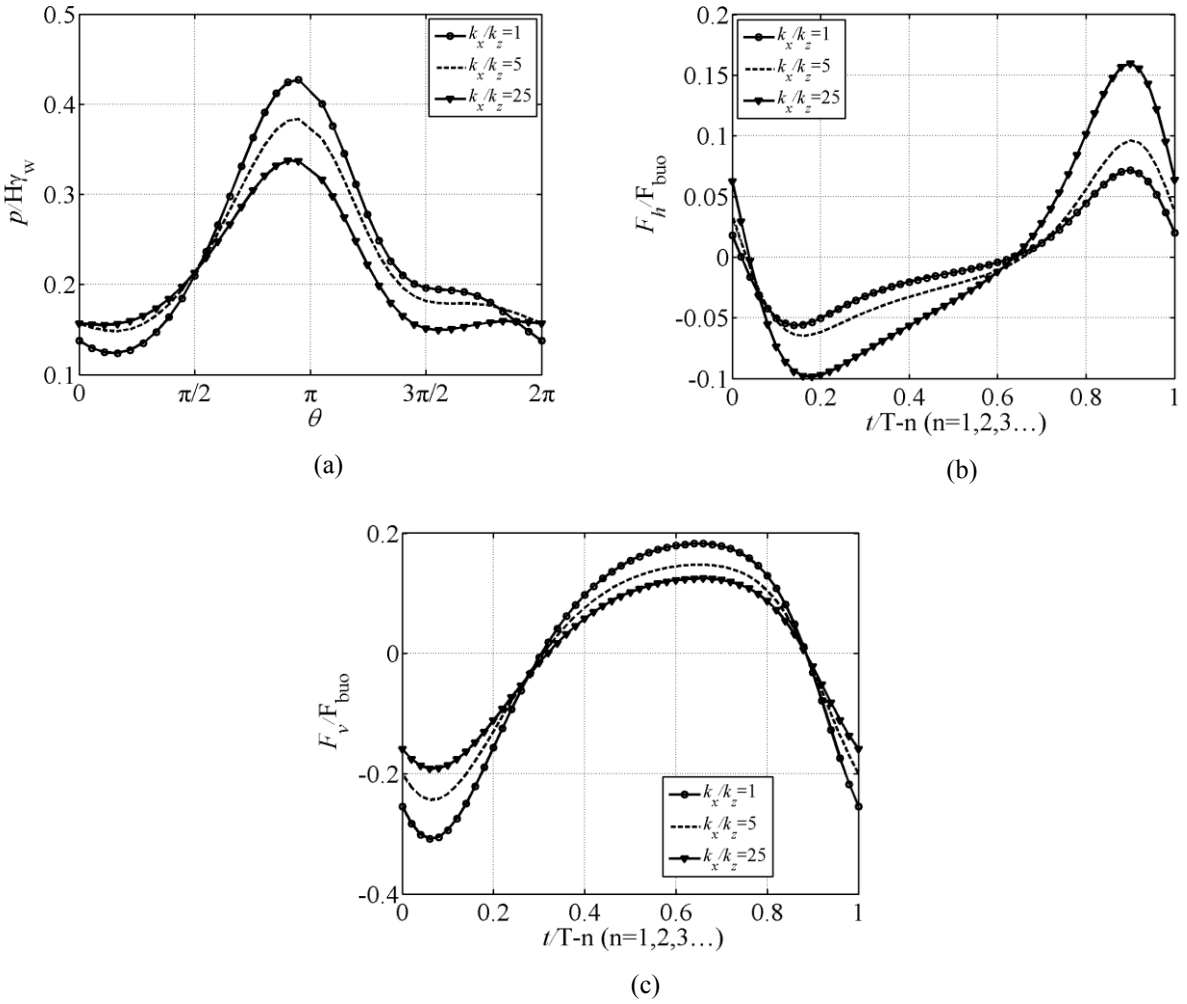


Fig. 9 Influence of the soil hydraulic anisotropy

REFERENCES

[1] Mei, C.C., and Foda, M.A. Wave-induced stresses around a pipe laid on a poro-elastic sea bed. *Geotechnique* (1981) 31(4): 509-517.

[2] Spierenburg, S.E.J. Wave-induced pore pressures around submarine pipelines. *Coastal Engineering* (1986) 10(1): 33-48.

[3] Foda, M.A., Chang, J.Y.H., and Law, A.W.K. Wave-induced breakout of half-buried marine pipes. *Coastal Engineering* (1988) 116(2): 1464-1481.

[4] Cheng, A.H.D., and Liu, P.L.F. Seepage force on a pipeline buried in a poroelastic seabed under wave loadings. *Applied Ocean Research* (1986) 8(1): 22-32.

[5] Magda, W. Wave-induced uplift force acting on a submarine buried pipeline: Finite element formulation and verification of computations. *Computers and Geotechnics* (1996) 19(1): 47-73.

[6] Magda, W. Wave-induced uplift force on a submarine pipeline buried in a compressible seabed. *Ocean Engineering* (1997) 24(6): 551-576.

[7] Magda, W., Maeno, S., and Nago, H. Wave-induced pore-pressure response on a submarine pipeline buried in seabed sediments-experiment and numerical verification. *The Journal of the Faculty of Environmental Science and Technology, Okayama Univer&ity* (1998) 3(1): 75-95.
[8] Madhu Sudhan, C., Sundar, V., and Narasimha Rao, S. Wave induced forces around buried pipelines. *Ocean Engineering* (2002) 29(5): 533-544.
[9] Gao, F., Gu, X., and Jeng, D.S. Physical modeling of untrenched submarine pipeline instability. *Ocean Engineering* (2003) 30(10): 1283-1304.
[10] Gao, F.P., Jeng, D.S., and Sekiguchi, H. Numerical study on the interaction between non-linear wave, buried pipeline and non-homogenous porous seabed. *Computers and Geotechnics* (2003) 30(6): 535-547.
[11] Mostafa, A.M., and Mizutani, N. "Nonlinear wave forces on a marine pipeline buried in a sand seabed." *Proc., Proceedings of the twelfth International Offshore and Polar Engineering Conference, Japan*, 68-75.
[12] Gao, F.P., and Wu, Y.X. Non-linear wave-induced transient response of soil around a trenched pipeline. *Ocean Engineering* (2006) 33(3): 311-330.
[13] Teh, T., Palmer, A., and Damgaard, J. Experimental study of marine pipelines on unstable and liquefied seabed. *Coastal Engineering* (2003) 50(1): 1-17.
[14] Teh, T., Palmer, A., Bolton, M., and Damgaard, J. Stability of submarine pipelines on liquefied seabeds. *Journal of Waterway, Port, Coastal, and Ocean Engineering* (2006) 132(4): 244-251.
[15] Sumer, B., Hatipoglu, F., Fredsøe, J., and Hansen, N. Critical flotation density of pipelines in soils liquefied by waves and density of liquefied soils. *Journal of Waterway, Port, Coastal, and Ocean Engineering* (2006) 132(4): 252-265.
[16] Sumer, B., Truelsen, C., and Fredsøe, J. Liquefaction around pipelines under waves. *Journal of Waterway, Port, Coastal, and Ocean Engineering* (2006) 132(4): 266-275.
[17] Xu, Y.F., Xia, X.H., and Wang, J.H. Calculation and approximation of the cnoidal function in cnoidal wave theory. *Comput. Fluids* (2012) 68244-247.
[18] Isobe, M. Calculation and application of first-order cnoidal wave theory. *Coastal engineering* (1985) 9(4): 309-325.
[19] Cho, Y.S. A note on estimation of the Jacobian elliptic parameter in cnoidal wave theory. *Ocean Engineering* (2003) 30(15): 1915-1922.
[20] Tørum, A. Wave-induced pore pressures—air/gas content. *Journal of Waterway, Port, Coastal, and Ocean Engineering* (2007) 133(1): 83-86.
[21] Sandven, R., Husby, E., Husby, J., Jønland, J., Roksvåg, K., Stæhli, F., and Tellugen, R. Development of a sampler for measurement of gas content in soils. *Journal of Waterway, Port, Coastal, and Ocean Engineering* (2007) 133(1): 3-13.
[22] Breul, P.B.P., Haddani, Y.H.Y., and Gourvès, R.G.R. On site characterization and air content evaluation of coastal soils by image analysis to estimate liquefaction risk. *Canadian Geotechnical Journal* (2008) 45(12): 1723-1732.

V International Conference on Computational Methods in Marine Engineering
MARINE 2013
B. Brinkmann and P. Wriggers (Eds)

PREDICTION OF THE SCALE EFFECT FOR THE HULL-PROPELLER INTERACTION FACTORS

DMITRY V. BAGAEV, MICHAIL P. LOBACHEV, NIKOLAI A. OVCHINNIKOV, ANDREY E. TARANOV

Krylov State Research Centre (KSRC)
44, Moskovskoe Shosse, St.Petersburg, 196158, Russia
e-mail: krylov@krylov.spb.ru

Key words: interaction factors, URANS, scale effect, roughness

Abstract The paper is focused on the possibility of scale effect calculations using unsteady solution of the Reynolds equations (URANS method) for arbitrary hull shapes. URANS method is used for simulation of a flow around the tanker 12990 with rotating propeller in both model and full scales. The computational results have been verified against the model and full scales experimental data for the drag, thrust and moment. The scaling of the wake factor is done using 4 different semi-empirical approaches.
Effects of the surface roughness of the hull and propeller on the propulsion characteristics are considered. Some advantages and disadvantages of the presented method are discussed in the paper.

1. INTRODUCTION

Nowadays prediction of the ship propulsion characteristics in design practice is usually based on the experiments (towing tank, wind tunnel and so on). During model tests we have to neglect some similarity relations, i.e. the model tests are performed with partial similarity modeling. Therefore the problem of appropriate scaling from the model to the full scale is very important. Huge amount of investigations in the towing tanks have been done world-wide, but still the modern methods of scaling are imperfect. Variety of different existing approaches confirms it very well. That situation was stated in the final report [1] of 23rd ITTC although the recommended scaling procedure exists (ITTC QM Procedure 4.9-03-03-01.2).

The ITTC-78 procedure was recommended for the using in the speed prediction of the single-screw transport vessels [2]. Considering the significance of this procedure which takes into account all components of the ship propulsion characteristics, it is necessary to point out that ITTC-78 procedure in its essence is a mix from outer (estimation of the characteristics depending on the non-modeled similarity criterions) and inner (examination of the methodological uncertainty) problems [3]. This is connected with the fact that not all regulations of the ITTC-78 are well-grounded physically. Some basic regulations of ITTC-78 were criticized in [4].

In consequence of insufficient foundation of the ITTC-78 procedure and limitation of its applicability (single-screw transport vessels) the development of the new methods of scaling from the model test to the full scale is in progress up to now. The present work is focused on the method of the scale effects calculations using unsteady solution of the Reynolds equations (URANS method) for the ship hull equipped with propeller. Due to the complexity of such

calculation and high performance computer requirements, this type of scaling methods starts to be propagated recently. Additionally to use computational fluid dynamic (CFD) for scaling methods effectively it is necessary to develop special procedure to speed up the pre-processor setup and mesh generation and therefore to reduce the overall computational time. Previously applied computer methods [5, 6] use a combination of URANS approaching and semi-empirical relations.

At present the existed URANS-based computational methods do not allow to predict ship propellers characteristics with the accuracy corresponding to the experiment. However one can suppose that discrepancies are caused by poor resolving of the tip vortices shedding from the ship propeller. This fact has effect on the estimation of the pressure distribution so the same errors should take place both for the model and the full scales. Therefore it is possible to use successfully the URANS-based methods for prediction of the scale effects.

2. NUMERICAL SETUP

The calculation of interaction factors using unsteady solution of the Reynolds equations was performed for the tanker hull 12990. Main dimensions of the hull 12990 and its model 11409 manufactured in scale 32.5 are listed in the Table 1. All calculations were performed for the design loaded condition.

Table 1: Main dimensions of the hull 12290 and model 11409

Main dimensions	model	full scale
Length on waterline, L_{WL} m	7.231	235.0
Breadth, B m	0.994	32.3
Draught, T m	0.3815	12.4
Displacement, V m^3	2.167	74400
Wetted surface area, Ω m^2	10.777	11383

Propeller model 7849 was chosen for the numerical study and has the following parameters: number of blades, n = 4, diameter, D = 200 mm, pitch ratio P/D = 0.658, blade area ratio $A_E/A_0 = 0.713$, skew angle 0°. The specific feature of the propeller 7849 is increasing of the pitch angle from the hub to the blade tip. Although it does not comply with the modern design practice, which recommends reducing pitch angle in the tip area to decrease vibration, two tankers ("Pobeda" and "Marshal Vasilevsky") were equipped with the propeller 7849 and comprehensive tensometric propeller data were recorded during the sea trials.

For simulation of the flow around the hull including the rotating propeller the CFD (computational fluid dynamics) software Star-CCM+ version 7.0 was used. Reynolds equation for the incompressible flow is solved using the nonlinear k-ε turbulence model in the high Reynolds number formulation.

Rotation of the propeller is simulated using the "sliding grid" interface. The computational grid is divided into two regions. The cylindrical region is formed around the propeller. The external surface of the region forms the sliding interface between the rotating region (propeller) and the fixed region (hull). The rotating region completely covers the propeller

and neither intersects nor touches the hull. There should be a sufficient gap between the hull and rotating region to generate the proper grid between the propeller and interface surface as well as between the interface surface and the hull surface. The flow inside the cylindrical region is solved in rotating coordinate system.

The main aims of the work are interaction factors between hull and propulsor, therefore the free surface effects were not considered. For the conventional displacement ships the influence of the free surface effects on the interaction factors is rather weak [7]. In numerical setup the symmetry boundary condition was used on the design waterline.

To estimate the interaction factors between the hull and propulsor the set of numerical simulations was done in accordance with experimental procedure [7]. To reduce the computational time the constant velocity mode was chosen as preferable.

The estimation of the interaction factors is performed in 4 steps:

Step 1. The flow around the hull without the propeller is simulated.

Step 2. The flow around the propeller in open water condition is simulated for different inflow velocities. As opposed to experiments the flow is considered to be turbulent a priory and there is no need to provide some kind of turbulization.

Step 3. The flow around the hull with rotating propeller is simulated for the different rotational speeds and fixed towing speed. The data for the hull resistance, propeller thrust and torque depending on the advance ratio are obtained.

Step 4. The interaction factors are estimated using the appropriate procedure [7] and previously obtained data.

The calculations were performed for the extend Reynolds number range, starting from the corresponding to the model experiment and ending with the corresponding to the sea trials. The operational points for the model and full scale are presented in the Table 2. The Reynolds numbers for the ship hull and propeller are defined as following:

$$\mathrm{Rn} = \frac{\mathrm{VL_{WL}}}{\nu}, \qquad \mathrm{Rn_p} = 5\frac{\mathrm{nD^2}}{\nu}\frac{\mathrm{A_E}}{\mathrm{A_0}}\frac{1}{\mathrm{z}}, \tag{1}$$

where V is the vessel speed, L is the hull length on waterline, D is the diameter of the propeller, n is the rotational speed, A_E is the expanded blade area, A_0 is the propeller disc area, z is the number of blades. The advanced ratio J corresponding to the operational point is equal to 0.6087.

Table 2: Operational points

Condition	Rn	Rn_p
Model scale	$8{,}872 \cdot 10^6$	$3{,}593 \cdot 10^5$
	$1{,}000 \cdot 10^8$	$4{,}050 \cdot 10^6$
Full scale	$1{,}632 \cdot 10^9$	$6{,}611 \cdot 10^7$

3. RESULTS

3.1 Viscous resistance.

The comparison between the numerical solution and approximation according to Prohaska [8] for the viscous resistance of the tanker 12990 is presented on the Fig.1. Estimation of the form-factor using Prohaska method was performed on the basis of multiple measurements for the small Froude numbers. This approach allows us to reduce inaccuracy of form-factor estimation significantly. Two different extrapolation curves were used in Prohaska method for the friction resistance of the flat plate: ITTC-57 curve and curve of Pustoshny-Kotlovich. Dependence of the friction resistance on the Reynolds number is described as follows:

$$C_{Fo} = \frac{0.075}{(\lg \mathrm{Rn} - 2)^2} \qquad \text{ITTC-57 curve;}$$

$$C_{Fo} = \frac{0.323}{(\lg \mathrm{Rn})^{2.45}} \qquad \text{curve of Pustoshny-Kotlovitch.}$$

For the Reynolds number $\mathrm{Rn}=1.521\cdot 10^9$ the difference between the results obtained in the numerical simulation and the results of the Prohaska method achieves 1.6% for the curve of Pustoshny-Kotlovitch and 9.5% for the ITTC-57 curve.

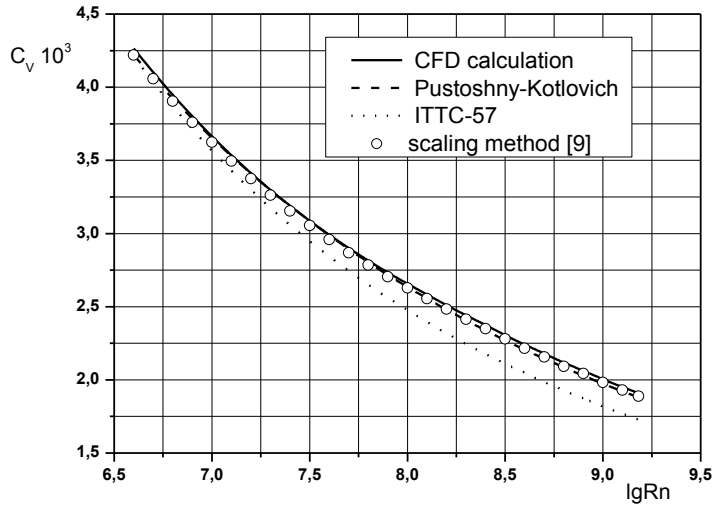


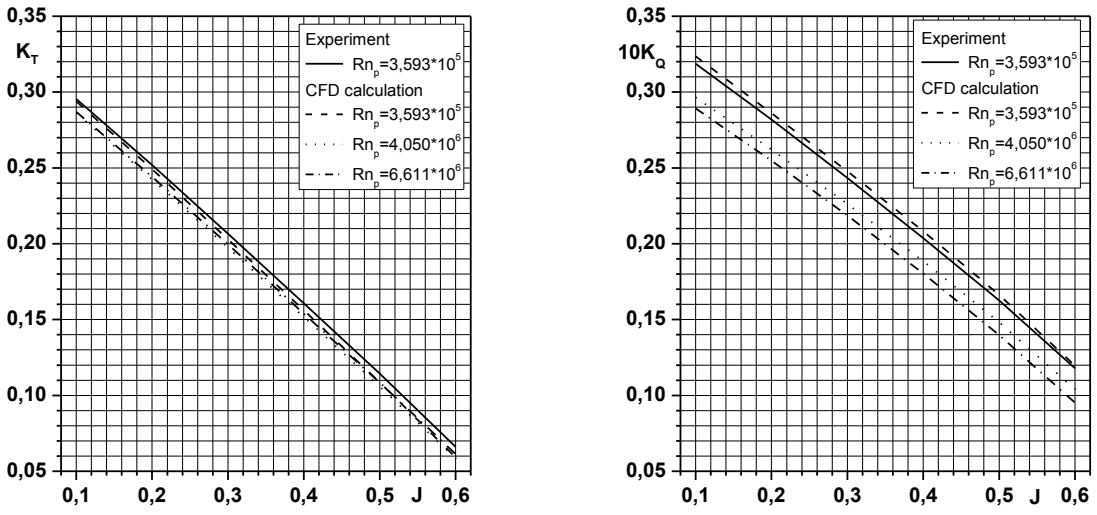
Figure 1: Tanker 12990. Viscous resistance for the different Reynolds number

The fact that curve of Pustoshny-Kotlovitch provides the results which are very similar to the URANS solution has a simple explanation. The curve of Pustoshny-Kotlovitch was derived with assumption that logarithmic velocity profile exists inside the boundary layer of the flat plate. This assumption complies with the logarithmic wall function in the URANS solution and based on the numerous measurements of the velocity profile inside the boundary layer. The ITTC-57 curve is a simple extrapolation curve, which was chosen on the basis of the best agreement between the scaled experimental data and the sea trials data. The ITTC-57

curve differs substantially from the relations based on the semi-empirical theory of the boundary layer. The curve of Pustoshny-Kotlovitch seems to be more physically grounded. Additionally the URANS based scaling method proposed by Pustoshny et al.[9] plotted on the Fig.8. The results of procedure [9] are very close to CFD calculation and Pustoshny-Kotlovich curve.

3.2 Performance curves of the marine propeller in open water

The comparison between the numerical solution and the experimental data for the thrust coefficient $K_T(J)$ of the marine propeller 7849 at different advance ratios J is plotted on the Figure 2a. Figure 2b represents the same dependency for the moment coefficient $K_Q(J)$ values. Both numerical and experimental investigations were completed in open water conditions for the model Reynolds numbers. There are some discrepancies between experiment and URANS solution. The value of the thrust coefficient is slightly lower than obtained experimentally; while the moment coefficient values are slightly higher. It should be noted that numerical solution for the modern ship propellers with unloading on the blade tip provides usually more accurate results. Apparently the disagreement between experimental tests and calculations for the marine propeller 7849 can be explained by insufficient resolution of the tip vortices which are quite strong due to increased pitch at the blade tip. Nevertheless the influence of the scale effect on the performance curves completely corresponds to the modern conception. In opposition to the ITTC-78 procedure one can state the scale effect of the thrust coefficient takes place as well as the scale effect of the moment coefficient. Moreover the scale effect of the thrust coefficient depends on the advance ratio. It is obviously connected with the repositioning of the critical point on the leading edge.



a b

Figure 2: Marine propeller 7849. Performance curves; open water condition

The comparison between the numerical solution and the experimental data for the propeller efficiency η_0 for the marine propeller 7849 at different advance ratios J is plotted on the Figure 3a. Although the propeller efficiency in calculations is lower than in experimental

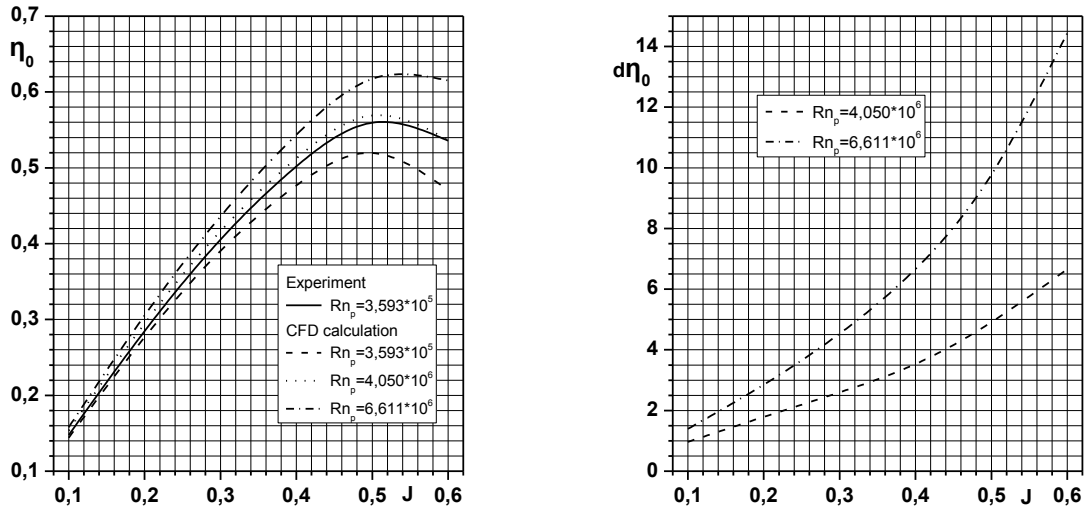
data, the shape of the curve seems to be very similar to the experimental one. That allows us to use the numerical results for the estimation of the scale effect. Dependencies of the propeller efficiency on advance ratio are showed on the Figure 3b. As a basis for the comparison the propeller efficiency corresponding to the model Reynolds number was taken:

$$d\eta_0 = (\eta_{0Rn} - \eta_{0Rnm}) \cdot 100\%, \quad (2)$$

where Rn denotes an arbitrary Reynolds number, Rnm denotes a model Reynolds number. One can estimate the advance ratio J, which takes the full scale wake factor into account:

$$J = 0.6087 * (1 - 0.361) = 0.389. \quad (3)$$

According the Figure 3b the variation of the propeller efficiency corresponding to this advance ratio is 6.37%, which is quite expectable.



a b

Figure 3: Marine propeller 7849. Propeller efficiency for different Reynolds numbers; open water condition

3.3 Performance curves of the marine propeller operated behind the hull

The comparison between dependency of the coefficient $K_T(J)$ on the advance ratio obtained experimentally and calculated for the marine propeller 7849 operated behind the model hull 11409 is shown on the Figure 4. Moment coefficient for the same problem is plotted on the Figure 5. The experiment was conducted using standard ITTC procedure. Additionally the multiple (14 times) measurements for 4 different advance ratios were implemented. It allowed to estimate the random errors as well as to increase the measurement accuracy using the statistical analysis.

The quality of the results remains close to the previous paragraph - the thrust coefficient is slightly lower than in experimental data. Insufficient resolution of the tip vortices results in similar errors in the process of the numerical simulation of the marine propeller in open water condition as well as behind the hull. This similarity allows us to expect the wake factor values to be correct.

During the sea trials of the tankers “Pobeda” and “Marshal Vasilevsky” the tensiometric measurements of the shaft moment were carried out. The moment coefficients obtained from those measurements are plotted on the Figure 5 as well. The numerically predicted moment coefficient is slightly lower than experimental one. The fact that propeller roughness was not considered in the URANS simulation can probably explain such discrepancies between the experiment and calculation. Since the used CFD software supports modeling of the roughness, this fact has been proved through additional calculations with rough propeller. As the average size of the propeller roughness the values of 7 and 10 μm were taken. This range of roughness corresponds to the cathode deposits. Figure 6 presents the comparison between the sea trial data and calculated moment coefficient for smooth and rough propeller. Taking into account the roughness on the propeller allows achieving better agreement between the CFD calculations and sea trials data.

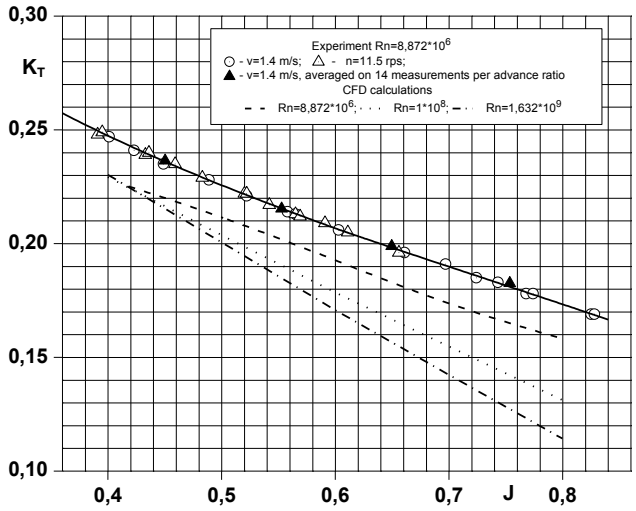


Figure 4: Thrust coefficients of the marine propeller 7849 operated behind the model 11409

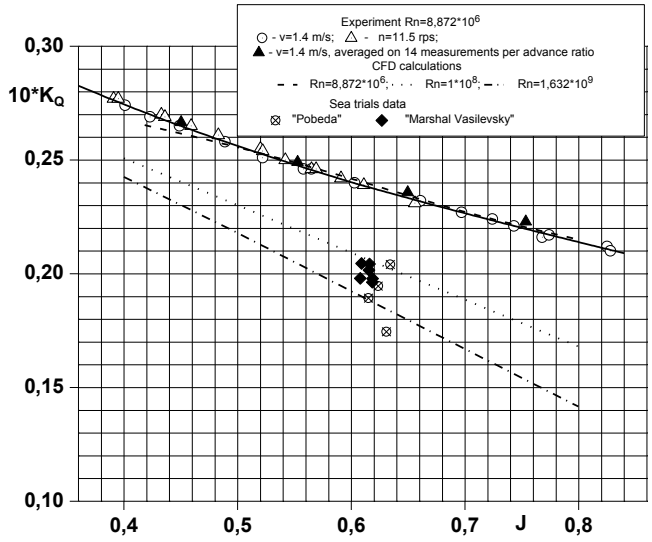


Figure 5: Moment coefficients of the marine propeller 7849 operated behind the model 11409

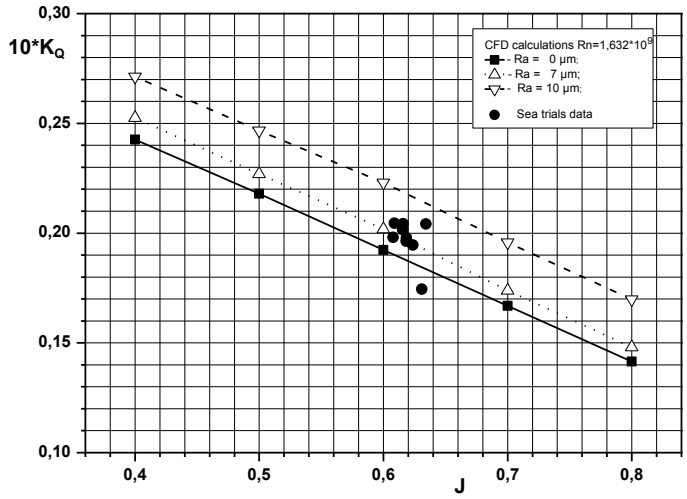


Figure 6: Moment coefficients of the marine propeller 7849 operated behind the model 11409. Influence of roughness

3.4 Interaction factors

Figure 7 helps us to understand the accuracy of the presented method. Numerically estimated interaction factors are plotted on the Figure 6 in comparison with experimental data. The calculations were conducted for the model scale. The agreement is not comprehensive, but seems to be rather good. Underestimation of the propeller thrust in open water conditions is close to the losses of thrust behind the hull, therefore the predicted wake fraction W is sufficiently accurate. That can be clearly recognized from the Figure 7.

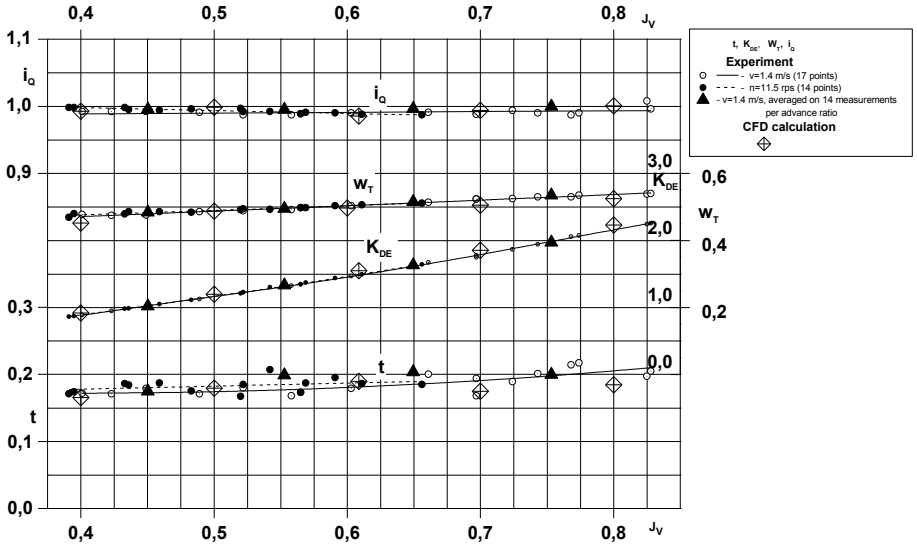


Figure 7: Interaction factors of the marine propeller 7849 and the model hull 11409

Analyzing the interaction factors computed for the wide range of Reynolds number, starting from corresponding to the model experiment and ending with corresponding to the sea trials, one can state that scale factor has very weak impact on the thrust deduction factor t and relative rotative efficiency i_Q. This fact fully corresponds to the ITTC assumptions. Of course, there are some deviations for different Reynolds numbers, but they are within the measurement uncertainty for the model scale. Therefore the results for the thrust deduction factor and relative rotative ratio are not in the scope of the present work.

Numerical and experimental data for the wake factor W_T are plotted on the Figure 8. The model measurements were conducted in pure water and in polymer solution. The wake factors defined on the basis of the sea trials using different statistical analysis and results of the scaling using 4 different methods are presented on the Figure 8 as well. The methods of the scaling are defined as following:

Method 1. This procedure is based on the combination of the URANS calculation of the ship hull without propeller and semi-empirical assumptions, which allow defining the wake factor W_T using the nominal wake factor W_N. This is a modification of the Pustoshny-Titov method performed in Krylov Shipbuilding Research Institute [4,12]. According to this method the following relation between wake factor W_T and nominal wake factor W_N is used:

$$W_T = \frac{W_N \cdot \sqrt{2}}{\sqrt{1+\sqrt{1+C_{TA}}}}. \tag{4}$$

Herein the main features of the flow around the hull will be taken into account through the nominal wake factor only.

Thrust loading coefficient C_{TA} can be calculated using the effective thrust loading coefficient K_{DE} as follows:

$$C_{TA} = \frac{8}{\pi} \cdot \frac{1}{1-t} \cdot \frac{1}{(1-W_T)^2} \cdot \frac{1}{(K_{DE})^2}, \; K_{DE} = DV \cdot \sqrt{\rho / T_E}. \tag{5}$$

Finally the nonlinear equation for wake factor W_T will be solved iteratively. Wake factor for the full scale ship can be obtained in following way:

$$W_{TS} = W_{TM} + (W_{TS}^{calc} - W_{TM}^{calc}), \tag{6}$$

where index *calc* denotes the calculated quantities, index S - full scale, index M – model scale.

Method 2. This method was proposed by Kanevsky [14]. It is based on the investigation of the hull roughness and its influence on the hull-propeller interaction [13]. Kanevsky offered an approximation for the wake factors depending on the viscous resistance ratio:

$$\frac{W_{TS}}{W_{TM}} = 0.4 + 0.6 \cdot \frac{C_{VS}}{C_{VM}}, \tag{7}$$

which has been successfully used in Krylov Shipbuilding Research Institute for the speed prediction. C_{VS} is the viscous resistance of the ship; C_{VM} is the viscous resistance of the model.

Method 3 - "Speed prediction method ITTC-78". After extensive investigation through

model-ship analysis, the following correlation formula for the wake fraction was adopted by ITTC-78 [2]:

$$W_{TS} = (t + 0.04) + (W_{TM} - t - 0.04) \cdot \frac{(1+k) \cdot C_{FoS} + \Delta C_F}{(1+k) \cdot C_{FoM}}. \quad (8)$$

Equation (8) is based on the assumption that viscous part of the wake fraction depends linearly on the viscous coefficient C_V. C_{F0} is the friction coefficient of the flat plate according to the ITTC-57; t is the thrust deduction factor; ΔC_F is the roughness correction.

Method 4. Denisov and Tumashek have proposed the following approximation based on the results obtained in [13]:

$$\frac{W_{TS}}{W_{TM}} = 1.5 \cdot \frac{C_{VS}}{C_{VM}} - 0.5 \cdot \left(\frac{C_{VS}}{C_{VM}} \right)^2 \quad (9)$$

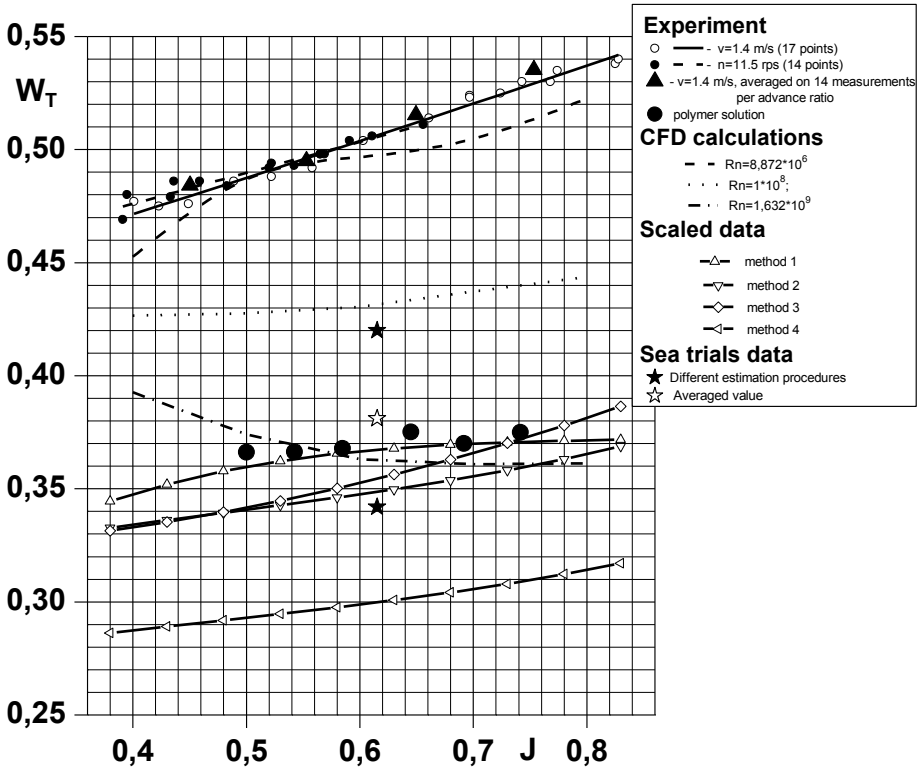


Figure 8: Wake factors W_T for model and full scales. Different approximation procedures

As it can be seen from Figure 8 all described methods except method 4 estimate the wake factor at the operational point J=0.6078 with acceptable quality. It must be admitted that lower values of the wake factor seem to be more plausible including the minimal value of W_{TS}=0.342. The results obtained by Orlov in polymer solution [15] confirm this suggestion. Wake factor obtained in polymer solution at operational point is about 0.37. Considering the

increased resistance coefficient obtained in polymer solution, one can suggest that wake factor of 0.37 is rather overestimated. Thus, it is more likely that the wake factor at operational point lies between 0.342 and 0.37. It can be proposed to repeat the statistical analysis of sea trials data using the scale effect estimation obtained in the present work for the performance curves. The wake factor of 0.342 was obtained from the sea trials data using ITTC-78 procedure for the estimation of the performance curves.

The results almost all of used scaling procedures for the tanker 12990 are very close to each other. It should be noted that measured and simulated flow around this hull is rather conventional, without any specific features. It was reported in the work [6] that speed prediction for this kind of hull shapes can be done with high accuracy using the most of numerical methods. The same paper demonstrated that for the hulls with separation of the flow only the URANS-based method [5] allowed obtaining results agreed with sea trials data. While the method [5] is applicable for single-screw ships only, the URANS-method used in the present work allows us to simulate the flow around an arbitrary hull shape.

4 CONCLUSIONS

URANS-based method for the simulation of the viscous flow around the ship hull is applied to the 12990 tanker equipped with rotating propeller 7849 in both model and full scales. The results of the present study demonstrate that prediction of the scaling effect of the resistance, performance curves of the marine propeller (operated in open water condition as well as in the ship wake) and interaction factors can be performed in the same way without any additional empirical assumptions, except the embedded in URANS method (e.g. turbulence or roughness models). That allows us to conduct the calculation of the scaling effect for the arbitrary hull shape provided that the applicability of URANS method has been validated for this hull shape in the model scale. It should be noted that comprehensive experience in CFD accumulated in Krylov State Research Centre indicates that URANS methods are quite universal.

The significant requirements in computational time on the high performance computer can be considered as drawback of the presented method. The study of the scaling effect including numerical calculations for the 5 advance ratios in the model and full scales can be done on the cluster with performance of 1 TFlop in 2-3 weeks. Such requirements can be compensated by the fact that URANS calculations provide a lot of additional information concerning the local and integral flow characteristics. For example the pressure distribution on the propeller blades at any point of time can be obtained and consequently the estimation of the cavitation margin for the full scale can be done. Other time-averaged and instantaneous flow characteristics can be obtained as well.

The further development of the presented method can be done for better prediction of the propeller thrust and detailed analysis of the roughness effects.

REFERENCES

[1] The Resistance Committee. Final Report and Recommendations to the 23rd ITTC // *Proceedings of the 23rd ITTC*, Venice, Italy, 8-14 September. 2002.

[2] Report of Performance Committee / *Proceedings of 15th ITTC*, Hague,1978.

[3] Pustoshny A.F. Analysis of some model series. NTO SP, Leningrad, 1963, (46):62-90 (in Russian).
[4] Turbal V.K., Shpakov V.S. and Shtumpf V.M. *Design of the hull forms and propulsors of the transport ships*. Leningrad: Sudostroenie, 1983 (in Russian).
[5] Lobachev M.P. Scaling effect in the shipbuilding – state of art. *XLIII Alexey Krylov readings – marine workshop*, St. Petersburg, 2009: 9–13. (in Russian).
[6] Egorova E.Yu., Lobachev M.P. and Chicherin I.A. Speed prediction and estimation of the hull-propeller interaction factors. *XXXVIII Alexey Krylov readings – marine workshop*. St.Petersburg, 1997:62–63. (in Russian).
[7] *Handbook of the ship theory*. Ed. Ja.I.Vojtkunsky. Leningrad: Sudostroenie, 1985. Vol 1. (in Russian).
[8] Prohaska C.W. A simple method for the evaluation of the form factor and the low speed wave resistance, Written contribution, Report of the Resistance Committee, 11th ITTC, Tokyo, 1966
[9] Chicerin I.A., Lobachev M.P. and Pustoshny A.V. Scaling of towing resistance using RANS code, *Proceedings of 10th International Conference on Hydrodynamics*, St.Petersburg, Russia, 2012
[10] Egorova E.Yu., Lobachev M.P. and Chicherin I.A. Numerical prediction of the hull-propeller interaction factors. *Proceedings of Krylov Shipbuilding Research Institute*, 1997, vol 6(290):86-93. (in Russian).
[11] Chicherin I.A., Egorova E.Yu. and Lobachev M.P. Development of RANS Code and its Application in Performance Prediction Procedure // *Second International Shipbuilding Conference (ISC'98)*: Proceedings: 24–26 November 1998: Section B. St.Petersburg, 1998:101–110.
[12] Pustoshny A.F. and Titov I.A. Some aspects of the hull-propeller interaction. // *Collected articles on the ship hydrodynamics*. Krylov Shipbuilding Research Institute 1980. (in Russian).
[13] Denisov W.I., Pashin W.M. and Tumashik A.P. Investigation into the influence of ship hull roughness and scale effect upon hull-propeller interaction // *Proceedings of Fourth international symposium on PRADS*. Varna, 1989.
[14] Kanevsky G.I. and Kruglova S.N. Improvement of the speed prediction procedures. *XXXVI Alexey Krylov readings – marine workshop.* St.Petersburg, 1993:21–23. (in Russian).
[15] Orlov O.P. and Pashin V.M. Real possibility to obtain the hydrodynamic characteristics of the hull in the towing tank, *150th anniversary of A.N. Krylov*, edited by Pashin V.M., (in Russian, accepted for publication 2013).

V International Conference on Computational Methods in Marine Engineering
MARINE 2013
B. Brinkmann and P. Wriggers (Eds)

ZIG-ZAG MANEUVER SIMULATION BY CFD FOR A TANKER LIKE VESSEL

G. DUBBIOSO*, D. DURANTE*, AND R. BROGLIA*

*CNR-INSEAN, the Italian Ship Model Basin, via di Vallerano 128, Rome, Italy
e-mail: giudubbioso@libero.it, danilo.durante@cnr.it, e-mail: riccardo.broglia@cnr.it

Key words: Zig-Zag maneuver, Tanker vessel, Yaw checking ability, Propeller modeling, Dynamic Overset Grids

Abstract. The zig-zag maneuver of a tanker like vessel has been simulated by means of the globally second order accurate finite volume solver χnavis. The aim is to stress the capability of the solver in predicting the yaw checking ability of a ship model characterized by a poor directional stability, an aspect that is usually exploited when performing zig-zag maneuvering. Numerical results have been compared to free running model tests. The effect of rudder rate and propeller modeling have been also investigated. The latter topic is crucial in order to draw the potentialities and further improvements of a simplified and computationally efficient propeller models.

1 INTRODUCTION

In this work the maneuvering behavior of the tanker like vessel recently considered in previous works [1, 2, 3] has been further exploited by means of the general purpose Computational Fluid Dynamic (CFD) solver χnavis. The interest on this non-standard test case is supported by the fact that the original version of this model, i.e. twin screw with a single rudder, experienced a marked unstable behavior that was impossible to predict by means of neither system based mathematical models nor the most popular hydrodynamic coefficients regressions [4]. Moreover, the comparison with the modified (and established) version, characterized by a twin rudder control system plus a central skeg, may provide a valuable insight in the effect of stern appendages and control system configuration on the dynamic response of the vessel. On these basis, this model is therefore attractive, and, at the same time, extremely challenging for the verification and validation of the capabilities of a CFD solver for predicting ship control and maneuvering qualities. Previous research was centred on the prediction of the turning circle maneuver at higher rudder angle ($\delta = 35°$). For both configurations, numerical results were in good agreement with respect to experiments, and their relative differences in terms of dynamic quality response during the transient and the stabilized phase of the maneuver were correctly

reproduced. Moreover, the use of a novel approach for modeling the presence of the propeller let it possible to emphasize the effect of propeller in-plane loads (side forces) on the dynamic response of the vessel and a closer description of rudder-propeller interaction (in case of the twin rudder configuration).

In the present work the $10° - 10°$ zig-zag maneuver of the twin rudder configuration has been numerically simulated, in order to further verify and validate the capabilities of the CFD solver in predicting a fully unsteady maneuver; this kind of maneuver is more challenging with respect to the turning circle one, because, in addition to the correct distribution of the hydrodynamic forces and moment on the hull, their time rate variation is also crucial for a correct estimation of the dynamic response. A further issue that should be further enlightened is concerned with the validity of the hybrid propeller model presented in [1] for simulating transient maneuvers; as will be described in the following, the propeller loads are computed in the framework of quasi-steady theory and, consequently, unsteady phenomena (lead-lag of self-induced velocity field or added mass) typical of a rotor functioning within a time-varying inflow have been neglected.

In this preliminary research the modeling aspects related to propeller side force and propeller loading have been addressed. Moreover, the effect of changing the rudder rotational rate has been further considered. Numerical results are compared to the experiments [12, 13] carried out at the CNR-INSEAN outdoor maneuvering basin in terms the typical yaw checking parameters (overshoot angles and overshoot times).

2 NUMERICAL METHOD

The numerical solution of the governing equations is computed by means of the solver $\chi navis$, which is a general purpose simulation code developed at CNR-INSEAN; the code yields the numerical solution of the unsteady Reynolds averaged Navier Stokes equations for Unsteady High Reynolds Number (turbulent) free surface flows around complex geometries. The main features of the numerical algorithm are briefly summarized for the sake of brevity; the interested reader is referred to [6, 7, 14] and [8] for details.

The solver is based on a finite volume formulation with conservative variables co-located at cell centred. The spatial discretization of the convective terms is done with second order ENO-type scheme. The diffusive terms are discretized with second order centred scheme. The time integration is done by second order implicit scheme (three points backward); the solution at each time step is done by pseudo-time integration by means of Euler implicit scheme with approximate factorization with local pseudo time step and multi-grid acceleration. The turbulent viscosity has been calculated by means of the one–equation model of Spalart and Allmaras [9]. Free surface effects are taken into account by a single phase level-set algorithm [6]. Complex geometries and multiple bodies in relative motion are handled by a dynamical overlapping grid approach [7]. High performance computing is achieved by an efficient shared and distributed memory parallelization [8].

3 PROPELLER MODEL

In CFD applications of marine hydrodynamics, the propeller is often modeled instead to be directly resolved: in fact, the characteristic time and spatial scales required to solve accurately propeller blade hydrodynamics differ up to two order of magnitude with respect to those characterizing the hull. Usually, the presence of the propeller is described by the "body force" approach: axial and tangential momentum sources are added to the Navier Stokes equations and distributed in a toroidal disk of finite thickness representing the propeller. Body forces are usually determined by actuator disk theories that assume axial-symmetric inflow conditions and optimal distribution of circulation, and therefore may provide an incomplete description of the propeller operating in maneuvering conditions, which is characterized by strong oblique flow effects. In this work, the same propeller model described in [1] has been further improved in order to account more accurately of the propeller loading (crucial for the correct estimation of rudder propeller interaction); in the following, the key points of the model are summarized:

- The axial and circumferential body forces follow the radial distribution suggested by Hough and Ordway [10]. In order to simulate the propeller dynamic behavior during a maneuver, the thrust and torque coefficients (i.e. K_T and K_Q) are not prescribed; instead, they are interactively evaluated from the real propeller open water curves. In particular, at each time step the propeller advance coefficient is evaluated by averaging the effective wake in correspondence of the first plane of the disk, and consequently:

$$J_{eff} = \frac{\iint \vec{V}(r,\theta) \cdot \vec{n} \; dr \; d\theta}{ND} \tag{1}$$

  where $\vec{V}(r,\theta)$ is the local velocity, $\vec{n}$ the normal to the propeller disk, N is propeller rate of revolution and D is the diameter. J_{eff} represent an effective advance coefficient, and, in order to be consistent with the propeller open water curves, should be properly corrected for the self-induction effect. To this aim, the longitudinal self-induction factor a (averaged) has been evaluated on the basis of the one–dimensional actuator disk theory, namely:

$$a = \sqrt{1 - 8\frac{K_T}{J^2\pi}} \tag{2}$$

  where K_T is the thrust coefficient and J is the advance coefficient. In order to match the strict relation between propeller load and self induction factor, a non linear equation should be solved at each time step; however, this is avoided for the sake of computational efficiency. In particular, at the end of each time step the actual advance coefficient is computed by means of the induction facto evaluated at the previous time step, i.e.:

$$J_{nom} = J_{eff}(1 - a_{n-1}) \tag{3}$$

It has to be noticed that the self–induction coefficient can be computed considering the propeller load distribution over infinitesimal circumferential sections, thus leading to a radially varying distribution of a or the complete actuator disk theory that accounts for the circumferential momentum imparted to the flow. However, as shown in 3, an average value is required in present application.

- In order to model the performance of the propeller functioning in oblique flow, the semi-empirical method of Ribner [11] has been followed for the evaluation of propeller in–plane force, defined as:

$$Y_P = k_s Z \frac{3}{4\pi} \frac{\partial C_L}{\partial \alpha} A_{side} \frac{F(a)}{1 + k_a \frac{3}{4\pi} \frac{\partial C_L}{\partial \alpha} A_{side}} \beta \tag{4}$$

with $F(a)$ the propeller load factor, defined as:

$$F(a) = \frac{(1+a)[(1+a) + (1+2a)^2]}{1 + (1+2a)^2} \tag{5}$$

being a the longitudinal induction factor, which should be evaluated at the actual time step. In the previous equations, β is the flow angle of attack in correspondence of the propeller disk, k_s and k_a are semi-empirical constant introduced for taking into account hub effects and non homogeneous distribution of the inflow over the propeller disk and A_{side} is the blade projected lateral area; Z is the number of propeller blades. In this case propeller force is the total in plane force, i.e. the resultant of the lateral and vertical components; the inflow angle is properly evaluated by averaging the velocity components of the fluid over the propeller disk.

In order to gain more insight into the effect of propulsion system to the response of the model, different simulations have been carried out: in particular, the effect of the lateral force and the self-induction velocity (i.e. underestimating the propeller loading) have been switched off (separately), and the resulting maneuvers compared to the one obtained with the complete propeller model.

4 GEOMETRY AND TEST CONDITIONS

A twin screw twin rudder tanker-like model is considered for the numerical simulations (figure 1); the model is fully appended with bilge keels, struts, A-brackets and shafts for two propellers) and a single rudder. The main non dimensional characteristics are reported in table 1. For this model an extensive free running test program has been carried out at the lake of Nemi[12, 13], and numerical results are compared with those experimental data in terms yaw-checking parameter (rudder-heading angle plot). The data are shown only in non-dimensional form because of restriction on diffusion. All the quantities in the following are non-dimensionalized by a reference length $L = L_{pp}$ and the

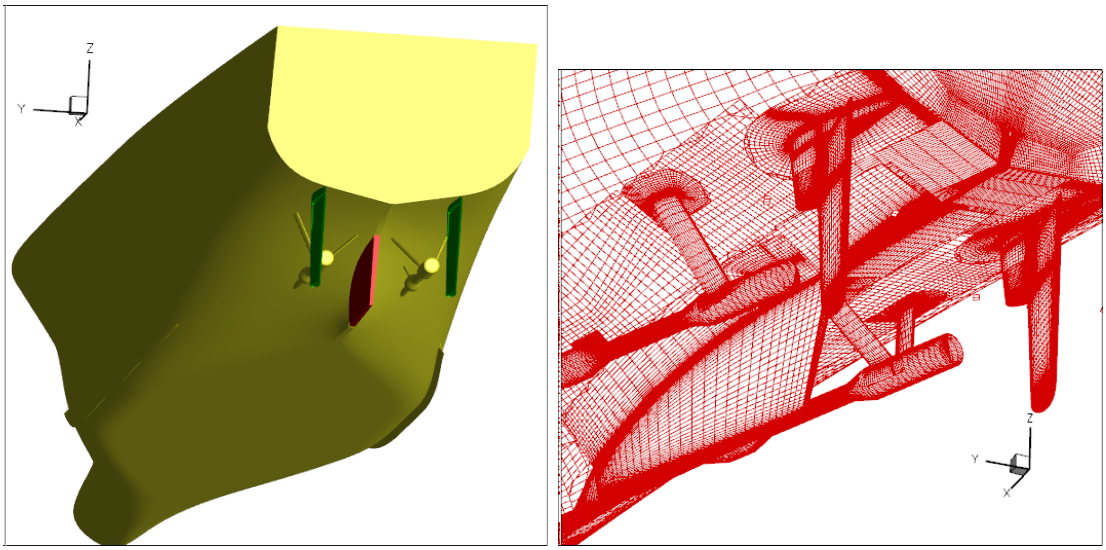


Figure 1: Left: model geometry overview. Right: mesh details around the stern region

approach velocity U_∞ (at model scale). This gives a Reynolds number $Re = 5.0 \times 10^6$ and a Froude number $F_N = 0.217$. Test cases considered are listed in 2; it has to be noticed that the effect of rudder angle rate of execution has been also investigated. The zig–zag tests are carried out at fixed turning rate of the propeller; the propulsion point is evaluated by means of a self–propulsion simulation.

Table 1: Ship model characteristics

L_{pp}	1
Speed	1
Displacement	$5.0987\,10^{-3}$
J	0.865
$Arud$	0.0023

5 COMPUTATIONAL MESH

The physical domain is discretized by means of structured blocks with partial overlap; overlapping grids capabilities are exploited to attain a high quality mesh and for refinement purposes. The whole mesh consists of a total of about 7.8 million of computational volumes. A detail of the discretization of the individual part of the vessel is summarized in table 3. Grid distribution is such that the thickness of the first cell on the wall is always below 1 in terms of wall units (y+=O(1) i.e. $\Delta/L_{pp} = O(20/Re)$, Δ being the thickness of the cell). In figure 1 detailed view of the mesh in the stern region is shown; the use of

Table 2: Test Matrix

TEST	$\dot{\delta}$ [deg/s]	Lateral Force	a
NUM.1	15	yes	yes
NUM.2	7.5	yes	yes
NUM.3	15	yes	no
NUM.4	15	no	yes

overlapping grid capability allowed to take into account for all the details, in particular for the mesh around the rudder where both the fixed and the mobile parts are carefully discretized.

Table 3: Test Matrix

Zone	N. of Blocks	N. of Cells
Background	2	184,320
Free surface	2	933,888
Hull	18	2,738,176
Bilge keels	8	655,360
Shafts and struts	24	733,184
Rudder	68	2,195,456
Skeg	34	299,008
Actuator disk	2	65,536

In the present work numerical computations have been carried out only on the medium mesh level, the activity on the finest mesh is still in progress.

6 RESULTS

In this paragraph numerical results for the cases listed in table 2 are discussed and compared with respect to the free running experiments. In table 4 the series of experimental data available are summarized in terms of the first and second overshoot angles and the equivalent overshoot times. The average value of the first and second overshoot angles are close to 8° and 9°, respectively; moreover, despite the relatively low number of experimental tests, the quantitative information of the measurement can be considered reliable, considering that the free running tests were carried out in an outdoor basin,

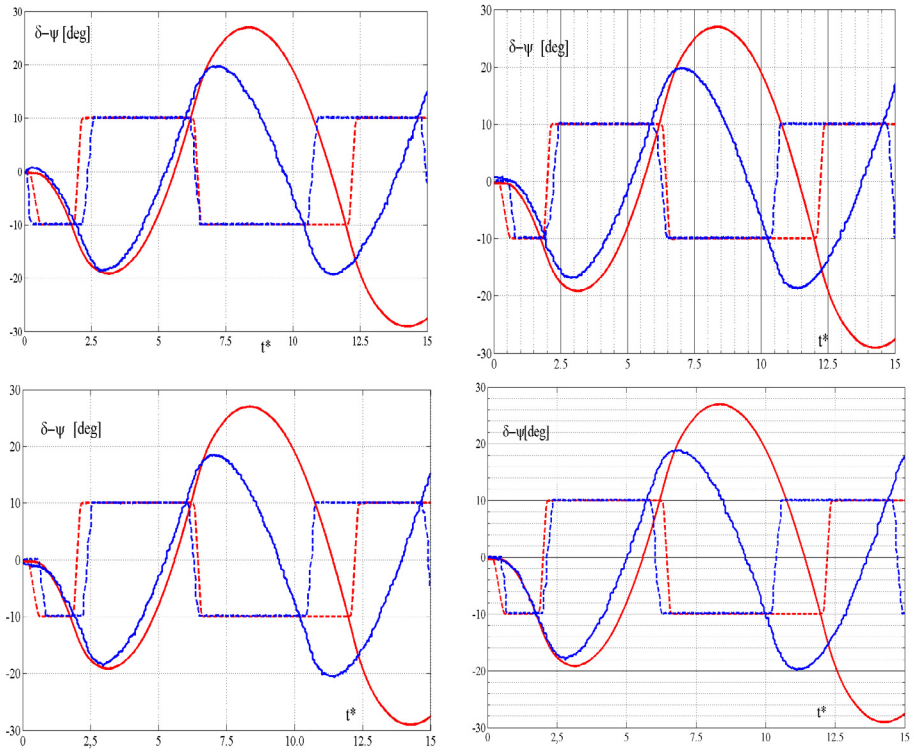


Figure 2: Comparison between simulated (–) and free running model tests (–)

and therefore some level of disturbance caused by wind can be expected. In table 4 yaw–checking parameters are reported.

Only the simulated maneuver with the complete propeller model (NUM.1) is compared with the experimental tests; the effect of propulsion and rudder rate is evaluated by comparing simulated maneuvers only. In the following discussion, the time is scaled by the characteristic time (i.e., $t^* = t\frac{U_\infty}{L_{pp}}$). In figure 2 the simulated maneuver is compared with all the free running tests available; the response of the vessel to the first rudder angle is in good agreement with measurements as well as the first overshoot angle. In the second part of the maneuver the discrepancy is noticeably higher: during the transient phase after the first counter-execution of the rudder (approximately at unit time $t = 2.5$), the yaw rate is higher and the vessel is less reactive to the rudder inversion at the second "yaw reach" (at time unit $t = 7$), leading to an excessive overshoot angle. It has to be noticed that the overestimation of the yaw rate could have been affected by discrepancies among the rotational mass of gyration, presently estimated by the equivalent ellypsoid method, i.e. $I_{zz} = \rho_\Delta \Delta$, where Δ is the model displacement and ρ_Δ represents the radius of gyration set equal to $0.25 L_{pp}$). Moreover, unsteady effects mainly related to propeller added mass, actually not included in the actuator disk model, may play a relevant role on the dynamic response of the vessel.

Table 4: Experimental results

TEST	$1^{st}ov$ [deg]	T_{1ov}	$2^{st}ov$ [deg]	T_{2ov}
EXP.1	8.51	1.12	9.65	1.29
EXP.2	6.79	1.06	9.73	1.17
EXP.3	8.68	1.12	8.41	1.05
EXP.4	8.17	1.06	8.74	1.17

Table 5: Numerical results

TEST	$1^{st}ov$ [deg]	T_{1ov}	$2^{st}ov$ [deg]	T_{2ov}
NUM.1	9.13	1.45	16.98	2.13
NUM.2	14.05	1.77	24.5	1.77
NUM.3	9.02	1.33	17.36	2.24
NUM.4	9.02	1.33	16.22	1.96

The propulsion system does not provide any remarkable effect on the model maneuvering response (see table 5 and figure 3); this is supported by comparison of simulation $NUM.1$ (red line) with $NUM.3$ (light blue line) and $NUM.4$, respectively. It can be evidenced that in the first transient phase (up to the 1^{st} overshoot angle) the vessel response very similar in all three cases. Discrepancies are more evidenced approaching the second overshoot phase: without the propeller lateral force the model experiences a slight improvement in yaw checking ability, with an overshoot angle lower than 2° with respect to $NUM.1$ and $NUM.4$, i.e., the propeller effect is destabilizing. As deeply discussed in [3], this effect has to be mainly addressed to a strong blockage of the rudders (which are located behind propellers) that causes a (lateral) up–wash in correspondence of the propeller plane. On the other hand, propeller loading slightly reduces the yaw checking ability of the vessel (the 2^{nd} overshoot angle is higher than in case of $NUM.1$): this effect is mainly related to propeller–rudder interaction, namely the decrease of propellers slipstream velocity affects rudder lift efficiency. Finally, it has to be emphasized that the rudder rate strongly affects the model response; this is evidenced since the 1^{st} overshoot angle and is dramatic in the second phase of the maneuver (2^{nd} overshoot angle close do 25°).

In order to gain further insight into the behavior of the rudder–propeller system during an unsteady maneuver, in figures 4-6 propeller forces in terms of thrust and lateral force ratio (i.e., $\frac{K_Y}{K_T}$, where K_Y represents the propeller lateral force coefficient) and rudder lateral force have been investigated for the reference maneuver $NUM.1$ and the most unstable one $NUM.2$. As evidenced in the plots, vertical lines are drawn for identifying the

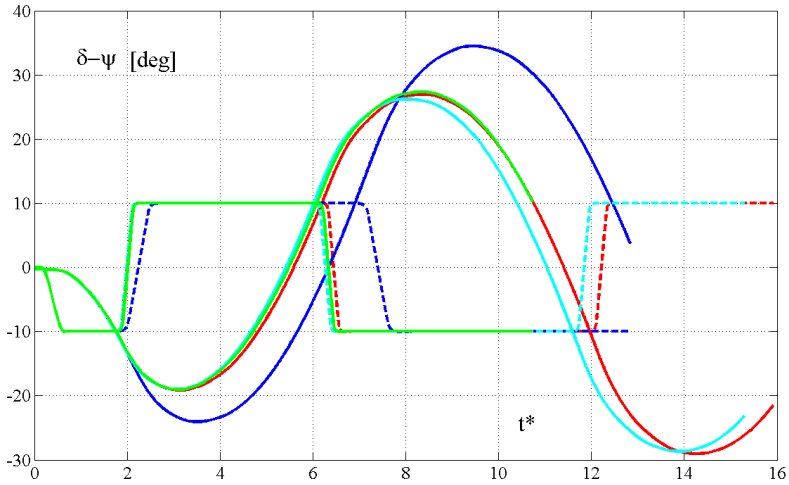


Figure 3: Simulation results; (–)$NUM.1$;(–)$NUM.2$;(–)$NUM.3$;(–)$NUM.4$

time instants relative to "yaw reach" (i.e. $\delta = \psi$, green lines) and to the heading overshoot (dark lines). The thrust coefficient (figure 4) for the $STBD$ and $PORT$ propellers shows a similar trend in both maneuvers; after the first rudder execution, the thrust exerted by the two propellers reduces.

Across the overshoot phase ($2 < t^* < 3$) the $STBD$ propeller is more loaded than the $PORT$ one; in fact, during this phase, this propeller changes the position with respect to the instantaneous center of rotation, i.e. it is in a leeward side as the maneuver starts and is on the windward side before reaching the 1^{st} overshoot; vice-versa, the $PORT$ propeller changes its relative position from the wind to the lee side, probably when it starts to decrease around $t^* = 2.5$. Moreover, immediately after the overshoot, the thrust on the windward propeller ($STBD$ side) decreases, whereas the thrust increases on the leeward propeller until $t^* = 4$. Thereafter, the loads on the two propellers experience a similar value and decrease up to the second "yaw reach". It has to be emphasized that the thrust variation around the overshoot is related to transient variations of the propeller inflow (mainly due to the change of the yaw rate and rudder blockage) that stabilize when a quite constant yaw rate is established ($4 < t^* < 6.5$). This phenomenon is different for the lee and windward propeller, because of the different flow straightening coefficient of the hull on the internal and external sides [2, 3]. This phenomenon is repeated during the second overshoot phase ($7.5 < t^* < 9$), with higher values of thrust because in this phase the model drift is relatively larger than before. Highest peaks are evidenced in case of $NUM.2$, because the model experiences a large drift and, consequently, a greater speed drop with respect to $NUM.1$. The propellers exert side–forces with opposite sign (see figure 5), and consequently, a negligible contribution to the dynamic response of the vessel is provided; it is worth of note the peaks in correspondence of the two "yaw checking" points ($t^* = 2$ and $t^* = 6.5$), probably caused by the rudder angle inversion which changes

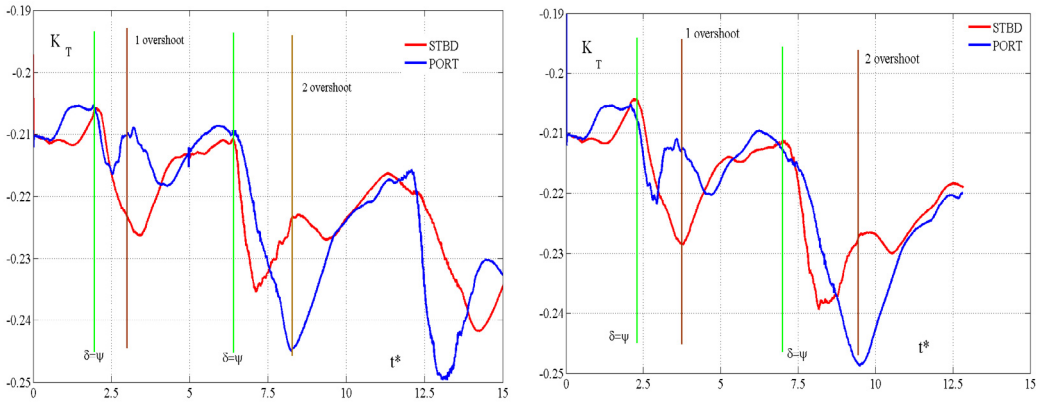


Figure 4: Thrust variation on the STBD and PORT propellers. Left: $NUM.1$ Right: $NUM.4$

the inflow drift angle in correspondence of the propellers (see also figure 6). Moreover, the trends of lateral forces across the yaw speed inversion show a similar behavior of the thrust coefficient K_T. Simulation $NUM.2$ shows a similar trend, with slightly larger peaks, consistently with the previous discussion. As discussed previously, effects of these transient on the propeller behavior is not entirely captured by the quasi-steady approach at the basis of the adopted propeller model. For the sake of completeness, time variation of the $STBD$ and $PORT$ rudders lateral force is depicted in figure 6; in the approach phase, the rudder forces are oppositely directed due to the flow "closure" direction at the stern. Consequently to the first rudder execution, the incidence angle of the $STBD$ rudder increases, whereas the one on the $PORT$ rudder decreases approximately with same rate and the model response is not immediate; after this short transient the model starts to yaw, and the rudder incidence angle progressively reduces. At the first rudder inversion, on both sides the lateral force increases noticeably until reaching a peak ($t^* = 2.3$) and then reduces due to the vehicle response (for the same reason as before). It has to be emphasized that during some intervals, the lateral force exerted by the rudder is opposite, i.e. one of the rudder is working like a stabilizing fin. Moreover, in correspondence of the overshoot transient, both rudders experiences stall phenomena (evidenced by the high frequency oscillations); the $STBD$ rudder is not affected by stall after the first rudder inversion, because the amplitude of hull motion is relatively lower.

7 CONCLUSIONS

In this work a preliminary investigation of the yaw checking ability of a twin screw twin rudder vessel experiencing poor course stability qualities has been carried out by means of an high accurate CFD solver. Different simulations have been carried out in order to validate a simplified propeller generalized for capturing oblique flow effects and, at the same time, to analyze the propeller contribution on unsteady maneuvering response of this challenging hull model. As a result, propeller effect as well as propeller loading

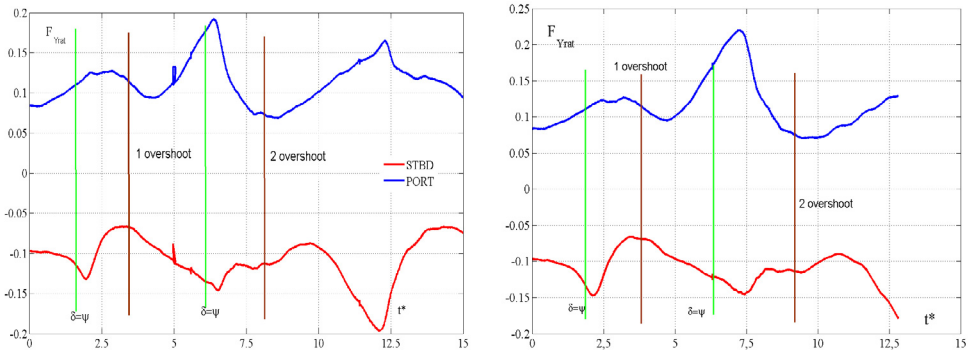


Figure 5: Lateral force coefficient on the STBD and PORT propellers. Left: $NUM.1$ Right: $NUM.2$

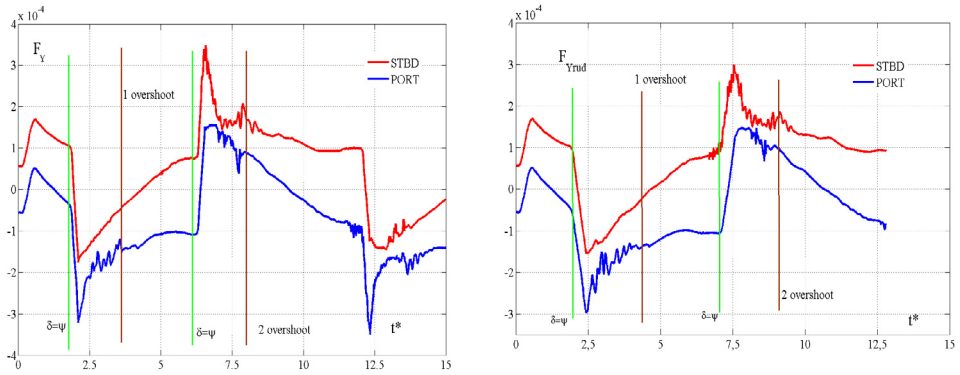


Figure 6: Lateral force on the STBD and PORT rudders. Left: $NUM.1$ Right: $NUM.2$

provide a negligible effect on this type of maneuver, because hull drift angle is low as well as the speed reduction. Comparison with free running experiments have been carried out in terms of yaw checking parameters; comparison is satisfactory in terms of first overshoot angle, whereas the second overshoot angle is over–predicted. Further work is required in order to investigate propeller effects that are still not included in the propeller model (i.e. added mass) and the vehicle behavior during tighter unsteady maneuver (i.e. zig-zag 20°-20°) and different stern appendage configuration (single rudder).

8 ACKNOWLEDGEMENTS

The authors are grateful to Dr. Salvatore Mauro for providing experimental data and for his useful suggestions and discussion on ship maneuvering related topics.

REFERENCES

[1] Broglia, R. and Dubbioso, G. and Durante, D. and Di Mascio, A. Simulation of Turning Circle by CFD: Analysis of different propeller models and their effect on

manoeuvring response *Applied Ocean research* (2013) **39**:1–10.

[2] Dubbioso, G., Durante, D., Broglia, R. and Di Mascio, A. CFD Manoeuvering Prediction of a Twin Screw Vessel with different stern appendages configuration 29^{th} *Symposium on Naval Hydrodynamics* (2012) Gothenburg, Sweden, 26–31 August.

[3] Broglia, R., Durante, D., Dubbioso, G. and Di Mascio, A. Turning ability characteristic study of a twin screw vessel by CFD *V Int. Conf. on Comp. Meth. in Marine Eng.* (2011), Lisbona

[4] Dubbioso, G. Maneuvering Behavior of Twin Screw Naval Vessels. *Phd Thesis* (2011) University of Genova, Italy.

[5] Amini, H. and Steen, S. Theoretical and experimental investigation of propeller shaft loads in transient conditions. *Int. Ship. Progress* (2012), **59**:55–82.

[6] Di Mascio, A. and Broglia, R. and Muscari, R. On the Applications of the One-Phase Level–Set Methods for Naval Hydrodynamic Flows *Computer and Fluids* (2007),**36(5)**:868–886.

[7] Di Mascio, A. and Muscari, R. and Broglia, R. An overlapping Grids Approach for the Moving Bodies Problems *Proc. of* 16^{th} *Offshore and Polar Engin. Conf.* (2006), San Francisco, California (USA).

[8] Broglia, R. and Di Mascio, A. and Amati, G. A Parallel Unsteady RANS Code for the Numerical Simulations of Free Surface Flows *Proc. of* 2^{nd} *International Conference on Marine Research and Trasportation* (2007), Ischia, Napoli (Italy).

[9] Spalart, P.R. and Allmaras, A. A One Equation Turbulence Model for Aerodynamic Flows *La Recherce Aerospatiale* (1994),**1**:5–21.

[10] Hough, G.R. and Ordway, D.E. The generalized actuator disk. *Development in Theorethic and Applied Mechanics* (1965), **2**:317–336.

[11] Ribner, H. Propellers in yaw. *NACA annual report* (1945),**31**:193–215.

[12] Mauro, S. (1999a). *Prove di Manovrabilità su Modello di Unità Logistica*. INSEAN Technical Report, N6/C 2280.

[13] Mauro, S. (1999b). *Prove di Manovrabilità su Modello di Unità Logistica*. INSEAN Technical Report, N8/C.2280.

[14] Di Mascio, A., Broglia, R., and Muscari, R. (2009). Prediction of hydrodynamic coefficients of ship hulls by high-order Godunov-type methods. *J. Marine Sci. Tech.*, 14:19–29.

V International Conference on Computational Methods in Marine Engineering
MARINE 2013
B. Brinkmann and P. Wriggers (Eds)

COMPARISON OF DIFFERENT APPROACHES FOR THE DESIGN AND ANALYSIS OF DUCTED PROPELLERS

STEFANO GAGGERO*, MICHELE VIVIANI*, GIORGIO TANI*, FRANCESCO CONTI†, PAOLO BECCHI‡ and FEDERICA VALDENAZZI‡

*Department of Naval Architecture, Electrical and Electronic Engineering
University of Genoa
Via Montallegro, 1, 16145 Genoa, Italy

† Fincantieri Naval Vessels Business Unit
Via Cipro, 11, 16129 Genoa, Italy

‡ CETENA
Via Ippolito d'Aste, 5, 16129 Genoa, Italy

Key words: Decelerating Ducted propellers design, Panel Method, RANS,

Abstract. In the present paper, different approaches for the design and analysis of ducted propellers are presented and discussed, starting from the conventional lifting line / lifting surface approach and considering more complex (and computationally demanding) panel methods and RANS solvers. Attention is posed on the more challenging case of decelerating duct configuration, and a design case is presented for a thorough analysis of the various approaches. Two different propellers geometries have been defined, and the results of the experimental campaign at towing tank and cavitation tunnel carried out on them are shown, demonstrating the capabilities and limits of the adopted approaches. Finally, general guidelines for the design of this kind of propulsor are briefly outlined.

1 INTRODUCTION

Ship design requirements are always increasing in time, with new and challenging tasks for the designers, in order to be able to grant a higher quality and to face a very competitive shipbuilding market. Considering propeller design, the increasing requirements, especially for what regards the higher segment in the shipbuilding activity, focused on high added value ships, have led to the necessity of providing not only a propeller with high efficiency and avoidance of erosive cavitation, but with also good characteristics in terms of low induced vibrations and radiated noise. In the present paper, the activities carried out by Fincantieri, in cooperation with CETENA and the University of Genoa (DITEN), in the framework of the European Project BESST, are presented. In particular,

attention has been focused on ducted propellers for medium/high speed applications and improved cavitation behaviour. As a consequence of this second requirement, decelerating duct configuration has been chosen, since they are thought to be an interesting alternative to free running propellers for ship propulsion, being potentially very performing in terms of reduced cavitation, vibration and noise. As it is well known, ducted propellers are currently mainly used in accelerating duct configuration for low speed applications where bollard pull is of great interest; in this case concepts and design methods related to these propulsors are well known since the early 70s [9], and many different works have been presented during years. On the contrary, the decelerating duct configuration has received lower attention, and design examples and/or experimental data are much more limited. This may be partly due to higher difficulties in the prediction of the propeller-duct interaction and, more in general, of the duct decelerating effect; as a consequence, in this case the propeller performance prediction is more challenging with the usual design and analysis tools. Recent developments in CFD provide new tools to support the design of ducted propellers and open new perspectives in exploiting their potential. In the activity carried out, aimed to the development of design guidelines for this kind of propulsor, different approaches for the design, optimisation and analysis of decelerating ducted propellers have been analysed. In particular, conventional lifting line/lifting surface approach [9], panel methods (coupled to genetic algorithms as optimizing tools [4, 1]) and RANS [2] calculations (in 2D and 3D) are considered. A brief description of methods considered is reported in section 2. In order to exploit the capabilities of these different approaches, a possible realistic design case has been considered, as described in section 3. At first, the design has been performed using the methodology usually adopted by Fincantieri for this kind of propellers [10]; this methodology, already applied with satisfactory outcomes, couples iteratively an in-house lifting line/lifting surface code (named "Elintub") and a commercial RANS solver (Ansys CFX). In order to further improve this procedure two more numerical methodologies have been investigated and described in this paper and concern the possibility of duct and blade geometry optimization. These different approaches rely on a quasi 2D actuator disk model for the duct design, analysis and optimization and a potential method coupled with a genetic algorithm for the blade geometry optimization. It is believed that these two approaches may be conveniently included in the design process, which of course includes, as represented in figure 1, towing tank and cavitation tunnel tests as final verification of mechanical characteristics and cavitating behaviour.

2 THEORETICAL BACKGROUND

2.1 Lifting Line / Lifting Surface Design Approach

The code, named "Elintub", used for the design activity described in this paper, is a lifting line/lifting surface based software, developed by Fincantieri and CETENA. As usual for a design tool, the definition of the propeller blade geometry is based upon the

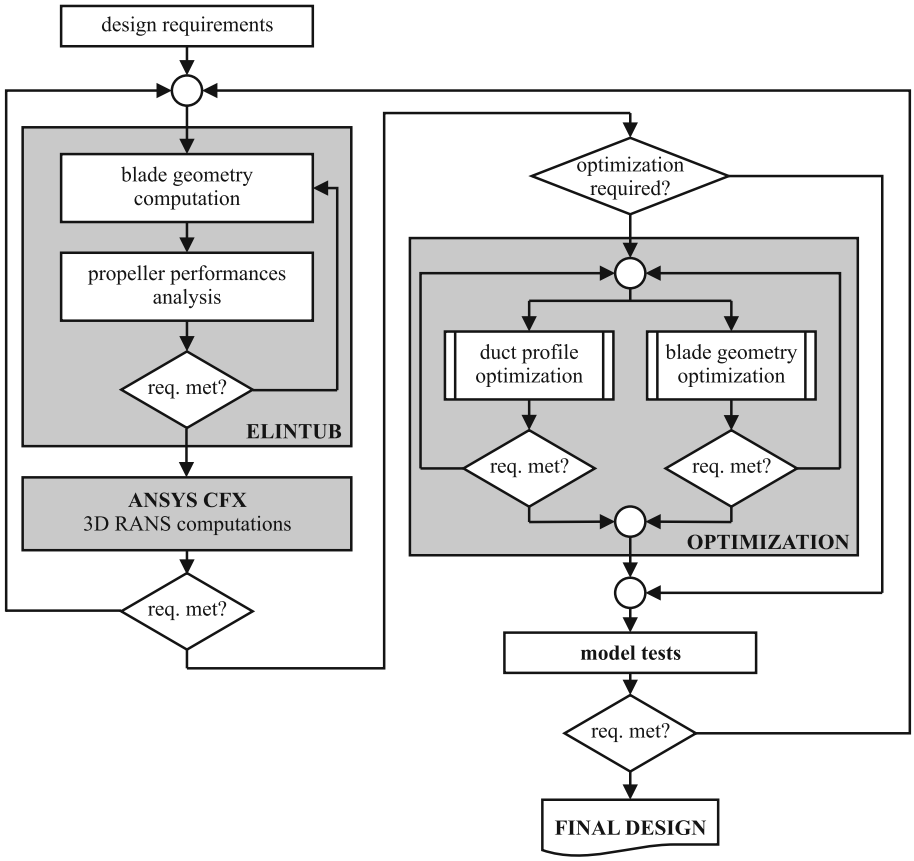


Figure 1: Ducted propeller design flow chart.

assumption of non-viscous, incompressible axi-symmetric and steady flow, with the blade represented by a lattice of vortexes, with unknown intensity and placed on an iteratively adjusted lifting surface. The influence of the duct is accounted through the linearized annular airfoil theory and is approximated by a distribution of ring vortices and sources. The design is carried out iteratively, until convergence is achieved in terms of the flow induced by the duct at the propeller and of the flow induced by the propeller at the duct.

2.2 Panel Method / Optimization by genetic algorithms

An alternative strategy to the classical lifting line/lifting surface approach is represented by optimization. The definition of a new geometry can be performed, in fact, testing thousands of different geometries, automatically generated by a parametric definition of the main geometrical characteristics of the propeller (as in [5, 4, 1]), and selecting only those able to improve performances (in terms of efficiency and cavity extension, for instance) together with the satisfaction of defined design constraints. The core of the design by optimization is represented by an accurate, reliable and fast flow solver and by a robust parametric representation of the propeller geometry. A potential panel method,

such as the one developed at the University of Genova [6] complies the first requisite. The code has been specifically customized for the solution of cavitating ducted propellers with the inclusion of the tip gap flow correction as in [8]; a thorough description of the code may be found in [7]. With respect to lifting line/lifting surface approaches, a panel method allows to directly compute the influence of the hub and, especially, of the duct, both in terms of the additional load on the blade tip region and in terms of the velocity disturbance on the whole propeller, avoiding the simplified representation of the duct only by vortex rings and sources. The results accuracy versus computing time ratio is, moreover, extremely good (if compared with RANS solver) making this kind of solver suitable for the automatic analysis of thousands of geometries. The classical design table is the natural, robust, parametric description of the propeller geometry, that can be easily fitted by means of a set of B-Spline curves whose control points turn into the free variables of the optimization procedure. A genetic algorithm drives the optimization procedure: from an initial population (whose members are randomly created from the original geometry altering the values of the free parameters within prescribed ranges), successive generations are created via cross-over and mutation: the members of the new generations arise from the best geometries of the previous computations that satisfy all the imposed constraints (thrust identity, for instance) and grant better values for the selected objectives.

2.3 RANS 2D computations

The design of a ducted propeller requires the flow field around the blade tip area to be analyzed in detail, because viscous effects are known to have a primary role in what occurs in the gap between the blade and the duct, especially in terms of cavitation and then noise. As modelling a complete 3D RANS computations could be very time expensive in the design phase, both for meshing and computing needs, in the adopted design approach the complete 3D RANS computations are performed just in the advanced phase of the design procedure, in order to check an already well established blade and duct geometry and, if needed, give some indication to make the design closer to the requirements. However, in this way the whole flow field around the blade and the duct (and their interaction) can be known only at the end of the design procedure. For this reason, the feasibility of a simplified RANS approach has been studied and added to the traditional design procedure. The aim of this approach is the definition of a quick meshing and computing RANS simulation able to evaluate the flow field around the duct, its cavitation behaviour, its induced flow field on the propeller, in order to carry out a customized duct design/optimization. For this purpose, a quasi-2D actuator disk model has been developed. This kind of approach can lead to:

- very detailed mesh size around the duct, keeping the whole fluid domain size at least ten times smaller than a complete 3D computation,
- very fast and easy geometrical modification and re-meshing of the duct, making it possible to optimize the flow field around the duct by RANS simulation,

- estimate the induced flow field on the propeller and, in case, perform some modifications on the design input data in order to make the lifting line/surface evaluation closer to target needs.

The fluid domain is modelled considering a narrow slice of domain, with an angular extension of 2-3 degrees. The effect of the propeller is simulated inside the CFX solver by the actuator disk model, where the thrust and the torque distributions are provided by external sources (panel code or lifting line/surface code, for instance). This kind of approach can represent a very powerful optimization tool, especially in the case it is coupled with the panel method optimization tool, because both the blade and the duct geometry can be made closer to the design needs.

2.4 RANS 3D computations

The final step of the ducted propeller design is a fully 3D RANS analysis, able to accurately simulate the viscous phenomena that typically occur in the blade tip area. Despite the good results that can be obtained by the panel methods, the flow field between the blade tip and the duct is strongly characterized by viscosity and then both the velocity field and the cavitation behaviour can be properly evaluated only by viscous numerical computations. In the present work, the Ansys CFX code has been applied, considering two different meshes for evaluating the propeller mechanical characteristics and the cavitation behaviour.

3 DESIGN CASES

3.1 Ducted Propeller Design point

The propellers have been designed for the propulsion of a medium/high speed twin screw vessel at an advance ratio close to 1 and a cavitation index (σ_N) of about 1.5.

For confidentiality reasons the performance of the propeller will be provided in terms of thrust and torque coefficients (K_T and $10K_Q$) expressed as a percentage of the design coefficients.

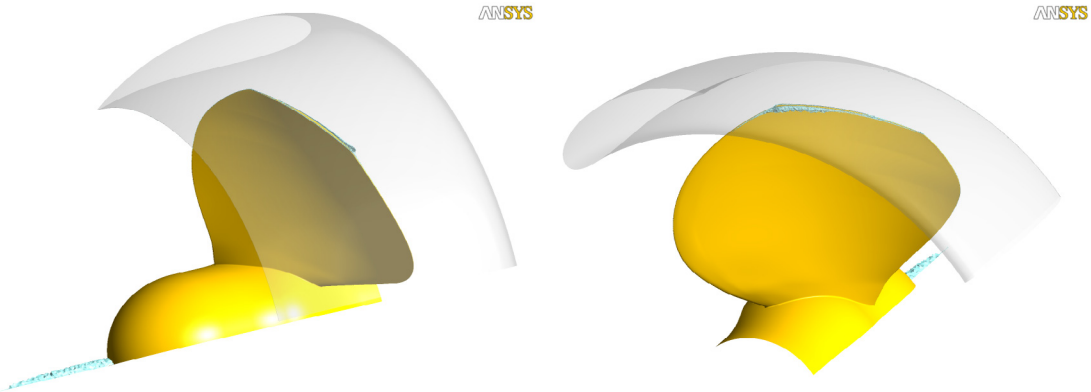
3.2 Ducted Propeller Designed via Lifting Line/Lifting Surface and 3D RANS Computations - Propeller 1

As already remarked, the methodology usually adopted, with satisfactory outcomes, by Fincantieri, involves the coupling of the "Elintub" code, which evaluates the blade geometry meeting the design performance requirements, and CFX, which is able to investigate the propeller and the duct hydrodynamic behaviour. The analysis of the RANS results makes it possible to identify the modifications that have to be implemented in the design input data (load distribution, geometrical restriction, for instance) in order to optimize propeller performances. Usually a couple of iterations are necessary because the viscous phenomena, occurring especially at the blade tip and between blade and duct,

strongly affect the propeller performances, especially in terms of cavitation inception and extension. During this work the RANS simulations used for the design have been set with a "coarse" unstructured mesh with 7.7 millions cells. Then, another "finer" mesh has been realized, using 15.6 millions cells. In particular, the flow domain geometry has been realized in order to focus the cells in the region close to the blade and the duct, consistently with the expected stream tube. The aim of this activity was the study of the effect of the mesh accuracy on the cavitation phenomena extension, on the pressure and forces results and the overall performances.

The two grids are adopted, respectively, to compute the overall propeller performance (K_T, K_Q, and η_o) and to check cavitation and appreciate the viscous phenomena in the gap between the blade tip and the duct. To this regard, it is necessary to remind that the computations have been carried out in "wetted" condition, i.e. without activating the cavitation (two phase flow) model; the cavitation pattern has been obtained at the design cavitation index by identifying the blade/hub areas where the pressure is lower than the vapour pressure. For what regards mechanical characteristics, the predicted propeller thrust in the final iteration is 99% of the design value. As it will be seen, this prediction has been verified by experimental results, thus confirming the validity of the adopted approach.

Figures 2(a) and 2(b) show the cavitation pattern from the computations, highlighting the presence of tip leakage vortex and hub vortex; also in this case, experimental results confirmed numerical predictions.



(a) Propeller 1 - Pressure side (b) Propeller 1 - Suction side

Figure 2: Cavitation on Propeller 1 by isosurfaces at $C_p = -\sigma$.

3.3 Ducted Propeller optimized by genetic algorithm - Propeller 2

Propeller optimization has been carried out in order to obtain a new geometry (Propeller 2), able to maximize efficiency and to reduce the back cavitation at the design

cavitation index delivering the same numerical thrust of the initial propeller (the Propeller 1): in order to speed up the convergence, a thrust variation of ±2% is admitted. Propeller 1 design table has been used to define the range of the free parameters. The numerical predictions of thrust and torque obtained with the panel method for the Propeller 1 showed some differences with respect to the available experimental measures carried at towing tank (and with respect to the viscous computations previously presented); namely, total propulsive thrust was overestimated by about 7% and torque by about 12%. For the optimization it has been assumed that these differences, ascribed to the numerical approach, remain the same also for the newly designed propellers and the numerical predictions for the Propeller 1 have been taken as the reference point of the optimization procedure. Also in terms of cavity extension some limitations of the panel approach have to be be highlighted. The previous experience with Propeller 1 at the cavitation tunnel showed, at the design point, only a cavitating tip leakage vortex (plus less significant hub vortex) whose prediction is beyond the capabilities of the cavitating panel method. The sheet cavitation, that has been numerically evidenced at the blade tip of Propeller 1 (figure 7) can be, however, correlated with the occurrence of the tip cavitating vortex and its extension (to be, as a consequence, minimized) can be considered a measure of the risk of cavitating tip leakage vortex. In order to numerically amplify the sheet cavity bubble at the blade tip, to include a certain margin for the occurrence of bubble cavitation and let the optimization work at a more convenient point (for which cavity extension is not constrained by the dimension of few panels at the blade leading edge), the design of the new propeller via optimization has been carried at a slightly lower cavitation index with respect to the design point.

The optimization activity for the design of the new geometry has been carried out investigating only global parameters, i.e. maintaining the blade and duct profiles shape adopted for Propeller 1. In particular (control points of) chord, maximum camber and pitch distributions along the radius have been taken as free variables. Structural considerations have been limited, in present activity, to constraining the maximum thickness to the chord distribution in order to maintain the same blade strength of Propeller 1. About 10 thousands different geometries have been generated and analysed by the panel method, and the results of the optimization are reported in the Pareto diagram of figure 3. The optimal selected propeller, as highlighted in the diagram, is a compromise between reduction of computed cavity area and increased efficiency. As shown in figure 3, with respect to the computed values of efficiency and cavity area of Propeller 1, the new geometry, at the same working point, presents, numerically, a reduction of the cavity extension of about 30% and an increase in efficiency of 2%. Delivered total thrust of the new Propeller 2 is 1% lower than that computed for the Propeller 1 but, as expected, within the prescribed numerical tolerance of ± 2%. Reductions in cavity extensions only affect the cavitating strip of panels at the blade tip, whose significance (and correlation) in terms of cavitating tip leakage vortex would merit a deep investigation. The chosen propeller represents an optimal choice for the verification purpose of the reliability of the

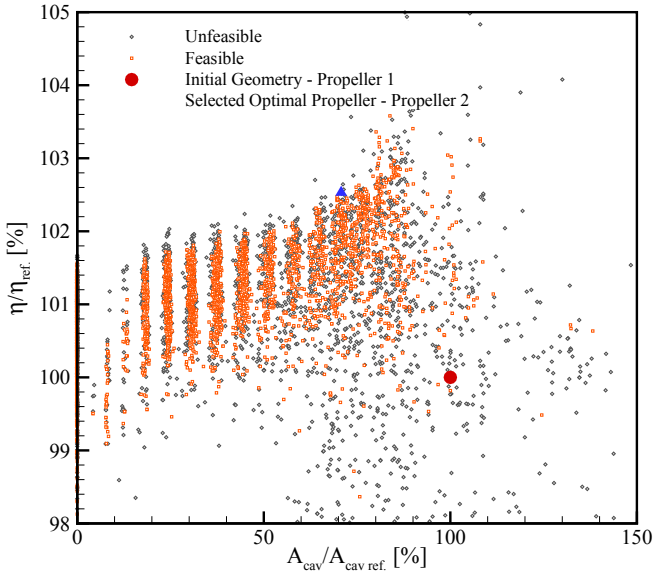


Figure 3: Pareto distributions of optimal geometries.

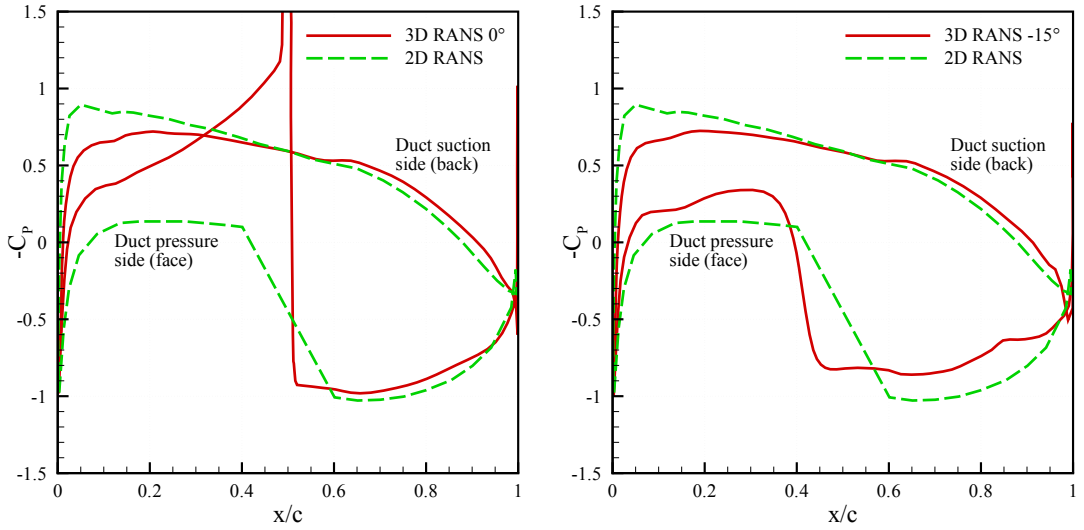
optimization approach, since efficiency can be better estimated and compared than the cavitating tip vortex strength; moreover, the design assumption about the risk of bubble cavitation may be also verified.

3.4 Application of 2D RANS computations in the optimization loop

In order to check the applicability of the quasi-2D approach described above, a test has been made considering Propeller 1. In particular, an actuator disk has been built based on the results from the 3D RANS computations of the propeller itself. Specifically, the actuator disk has been loaded with the thrust and the torque distributions computed for the propeller inside the duct, in a way to obtain the same total thrust and torque of the 3D computations. The computation results have been compared with those of the full 3D RANS model; this has provided the means to assess the reliability of using a quasi-2D approach instead of a full 3D approach.

Figure 4 shows the comparison of the pressure coefficients $(-C_P)$ on the pressure side (face) and on the suction side (back) of the duct. Because the 2D simulation is characterized by axial symmetry, the pressure coefficient distribution over the duct profile is compared with what obtained by the 3D analysis, considering two different positions, the first one in correspondence to the blade passage, the second one in correspondence to 15 degrees toward the propeller leading edge. As it can be seen, a fairly good agreement is found in the second case (figure 4(b)), both for the back and the face of the duct. Otherwise, when the blade passage position is considered, it may be observed that (C_P) curves have a good agreement on the back of the duct while on the face, the pressure

distribution from the 3D calculations features a sharp peak, which is associated to the flow field passing through the blade-duct clearance and then to the tip leakage vortex detected by the complete 3D computations. In the same longitudinal positions of the peak, the pressure distribution from 2D calculations features a linear pressure variation due to the presence of the actuator disk; the peak is absent, as the actuator disk cannot take such effect into account and also because the body forces characterizing the actuator disk are distributed over the whole disk volume. Since the total thrust (and torque) applied by the actuator disk on the flow is the sum of all the forces acting on all the cells of the disk volume, the effect of the propeller increases linearly moving along the shaft. In any case downstream of the propeller the pressure distributions are satisfactory close each other.



(a) $\theta = 0^o$ (b) $\theta = -15^o$

Figure 4: Comparison between 2D and 3D computed duct pressure distributions.

As a result of this analysis, it can be said that, as far as the global duct behaviour is concerned, the comparison between 3D and quasi-2D is good and makes quasi-2D computations a feasible alternative to 3D ones, especially in the propeller and duct design phase, allowing to capture the global functioning characteristics of the duct. Of course, effects such as tip leakage vortex and the local accelerating effect of the blade, are not captured by quasi-2D computations, as visible, and fully 3D computations need to be carried out at some point in the design process to account for these effects. As a conclusion, it can be said that quasi-2D RANS computations can be used to investigate the duct behaviour, provided that data are available to set-up the actuator disk. Considering both the meshing and computing time needs, the 2D model looks very attractive as a design tool (coupled with lifting line/lifting surface computations) because it makes it

possible to investigate in detail the hydrodynamic behaviour of the duct profile, consistently with the load distribution characterizing the propeller blade. Furthermore, this kind of approach can increase in efficiency in the case of it is coupled with a propeller analysis and optimization tool, such as that described in the previous section. However, full 3D computations need to be carried out if information on cavitation and local effects in the blade tip area are to be predicted with care.

4 EXPERIMENTAL CAMPAIGN

4.1 Experimental Setup

Model tests (open water tests and cavitation tunnel tests) have been performed in order to validate the numerical results and the adopted design procedures.

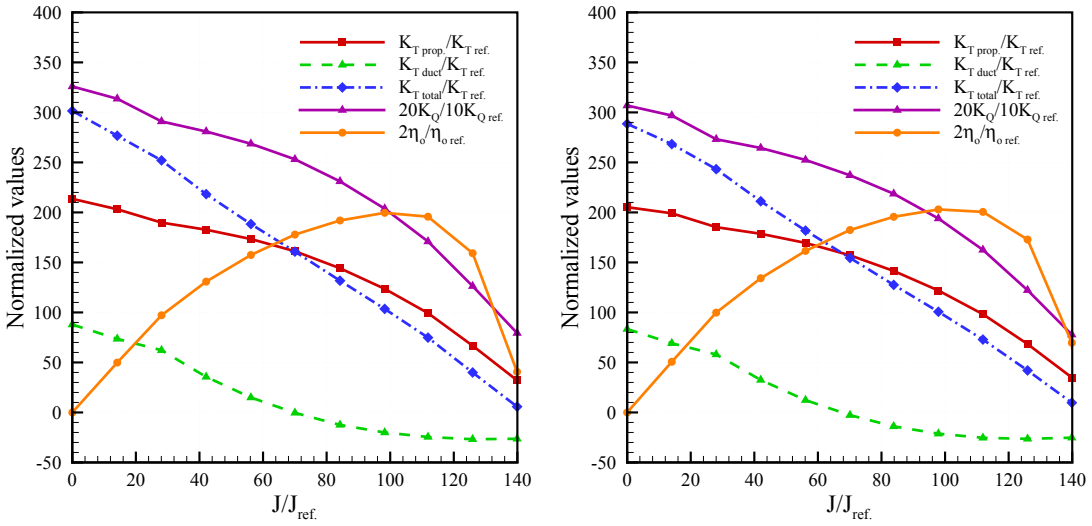
In particular, open water tests have been carried out at SVA towing tank, using a Kempf & Remmers propeller dynamometer H39 and a R35X balance for the measurement of duct thrust. A constant propeller rate of revolution (15 Hz) was adopted during tests. Cavitation tunnel tests have been carried out, instead, at the University of Genoa cavitation tunnel. The tunnel is equipped with a Kempf & Remmers H39 dynamometer, which measures the propeller thrust, the torque, and the rate of revolution. As regards the duct forces, an in-house developed measuring device has been adopted, allowing to perform not only usual cavitation observations, but also direct measurements of different forces components (and thrust breakdown, if present) in cavitating conditions. A detailed description of the measuring device may be found in [3]. All tests were carried out without propeller shaft inclination and in an uniform wake, consistently with the design assumptions previously described. A constant propeller rate of revolution (25 Hz) was adopted.

4.2 Open Water tests

Results from model scale open water tests carried out at SVA towing tank are shown in figure 5. The reported values are normalized with respect to the design point. Open water tests substantially confirm the reliability of the two different adopted design procedures, showing for both the propellers a good agreement with the required design performances; Propeller 1 has a thrust coefficient almost equal to the required one, confirming the numerical results presented in section 3.2 while Propeller 2 delivers, in line with the numerical results of the optimization, a little lower thrust (about 3%). On the other hand, as expected, Propeller 2 presents a slightly increased efficiency (about 2%), confirming from this point of view the reliability of the optimisation procedure.

4.3 Cavitation observations

The aim of the cavitation tunnel tests has been the determination of the cavitation bucket for the two propellers, as well as the collection of a set of cavitation observations at a number of functioning points in order to validate the numerical predictions. The

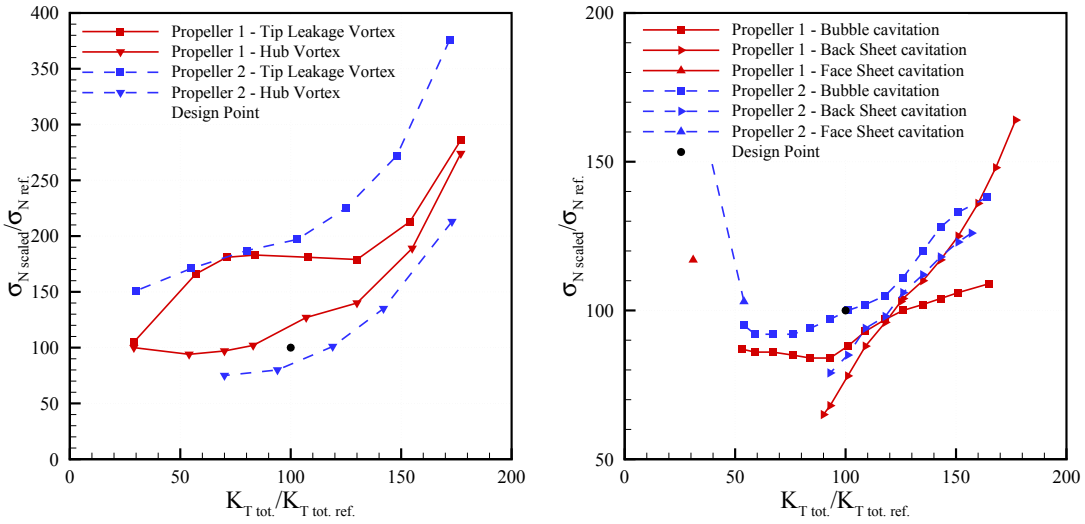


(a) Propeller 1 (b) Propeller 2

Figure 5: Normalized Open Water Performances.

inception points of the various cavitating phenomena are reported in figure 6(a) for what regards the vortex type occurrences (tip leakage and hub vortex), while in figure 6(b) Propeller 1 and Propeller 2 are compared in terms of the inception of the bubble and sheet cavitation related phenomena. The two propellers showed a satisfactory cavitating behaviour. At design point (figure 7(a) and 7(b)) tip leakage vortex and hub vortex are present for the Propeller 1 while only tip leakage affects the hydrodynamic behaviour of Propeller 2. However, this phenomenon is slightly anticipated, contrarily to what expected from the optimisation process, with respect to Propeller 1. This unwanted behaviour is probably due to the intrinsic limitation of the code, which does not allow to correctly rank the two propellers in terms of tip vortex inception merely by the predicted sheet cavity bubble at the last strip of panels at tip. From this point of view, it is believed that a final verification by means of RANS codes (including cavitation prediction) of a series of selected designs may overcome this problem, allowing to accurately characterize the propellers in terms of cavitating tip vortex inception and strength. The tip leakage vortex is present at any loading condition and its inception index seems less influenced by the propeller load if compared to the inception of the conventional propellers tip vortexes: in particular for Propeller 1 this phenomenon does not depend on the thrust coefficient for a wide range of values around the design point. This quite different behaviour of the tip leakage vortex inception (together with a different margin for what regard bubble cavitation at tip trailing edge) is probably the most clear difference between the propellers in cavitating conditions. For both the propellers, however, the buckets are quite wide, therefore confirming the capability of the decelerating ducts to postpone cavity inception also in off-design conditions and the general capability of both the design strategies to

provide satisfactory geometries.



(a) Vortex phenomena

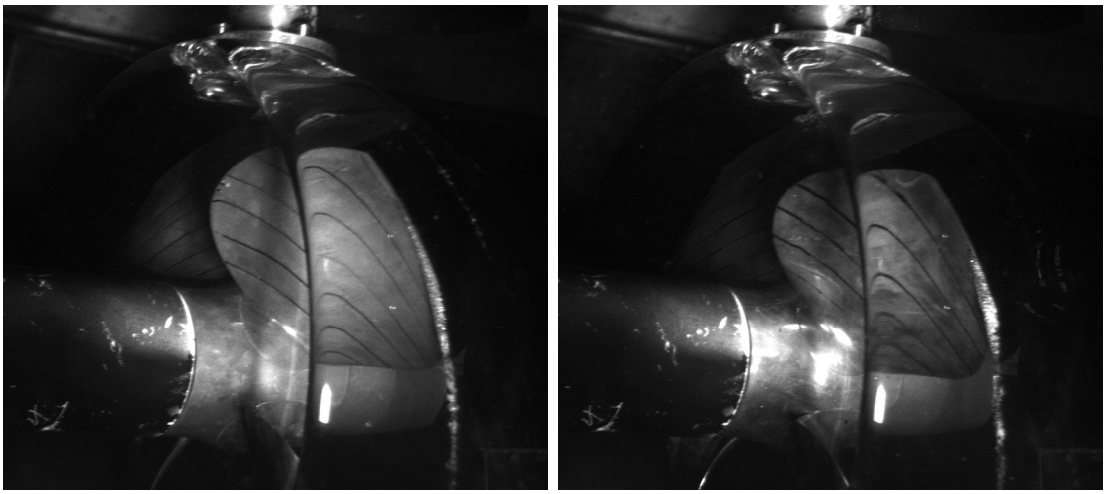
(b) Bubble phenomena

Figure 6: Normalized Cavitation Buckets.

The propellers look also free from bubble cavitation, which appears only at cavitating indexes lower than the design point. Margins, however, are very different. Propeller 1 is quite safe with respect to this phenomenon, while Propeller 2 experiences tip back bubble cavitation at the blade trailing edge just below the design point, as clearly visible from figure 6(b). These differences partially confirm the numerical calculations. Even if, as already mentioned, during the optimization activity a certain margin has been adopted (carrying out the new design at a cavitation index 10% lower than the design point), the analysis of the pressure distribution for a radial section near to the tip shows a pressure distribution at midchord closer, for Propeller 2, to the cavitation limit, confirming that the optimized propeller is more inclined to be subjected to bubble cavitation with respect to Propeller 1. Reasons for the discrepancy between predicted and observed bubble cavitation inception point have to be further investigated in future studies.

5 CONCLUSIONS

The present work shows the design of a decelerating ducted propeller, performed by a lifting surface code, checked and tuned by RANS calculations and optimized by a potential method coupled with a genetic algorithm. While the main design activity represents the traditional shipyard design methodology, that is the use of a own lifting surface design code coupled with some RANS simulations, the propeller geometry optimization was aimed to check the possibility of improve the design and make it closer to design requirement. Then, this study have led to two propeller geometries, the first obtained by the



(a) Propeller 1 (b) Propeller 2

Figure 7: Observed Cavitation for Propeller 1 and 2 at design point.

traditional shipyard design tool the second by the numerical optimization. The reliability of numerical codes adopted has been validated by means of the experimental campaign at towing tank and cavitation tunnel. Furthermore, the hydrodynamic behaviour of the duct has been studied by a quasi-2D RANS method, based on the actuator disk model. Considering both the meshing and computing time needs, this method looks very attractive because it leads to accurate information keeping the time restricted and consistent to the design time requirements. As expected, the application of the shipyard traditional design procedure has led to a good agreement between numerical prediction and experimental data; however the analysis performed by a panel method coupled with a optimization algorithms has shown to be very powerful and effective, making it possible to modify the propeller geometry in accordance with design restrictions and target. Nevertheless, panel methods presented an intrinsic limitation in completely correctly capturing phenomena which are characterized by a predominant viscous nature; in particular, despite cavitating tip leakage vortex occurrence is somehow predicted by the presence of cavitating panels at tip, the code is not capable of ranking different propellers correctly. From this point of view, therefore, it is believed that RANS calculations including cavitation may provide a better insight in the phenomenon, overcoming the problem and allowing to choose among a set of possible optimal designs the best solution including also design characteristics which may not be completely captured with less accurate approaches.

6 ACKNOWLEDGEMENTS

The research leading to these results has received funding from the European Community's Seventh Framework Programme (FP7/2007-2013) under grant agreement n 233980.

REFERENCES

[1] Becchi, P., Grasso, A., Bruzzone, D. and Valdenazzi, F. An integrated CFD-based tool for propeller blade design and evaluation. *International Conference on marine Research and Transportation, ICMRT 2005, Ischia, Italy* (2005).

[2] Becchi, P. and Pittaluga, C. Comparison between RANS Calculations and Panel Method Results for the Hydrodynamic Analysis of Marine Propellers. *MARINE CFD 2005 Conference, Southampton, England* (2005).

[3] Bertetta, D., Bertoglio, C., Conti, F., Rizzo, C.M. and Viviani M. Cavitation Tunnel Tests on Ducted Propellers. *17th International Conference on Ships and Shipping Research, Naples, Italy* (2012).

[4] Bertetta, D., Brizzolara, S., Gaggero, S., Savio, L. and Viviani M. CPP propeller cavitation and noise optimization at different pitches with panel code and validation by cavitation tunnel measurements. *Ocean Engineering* (2012). **53**:177–195.

[5] Gaggero, S. and Brizzolara, S. Parametric CFD Optimization of fast marine propellers. *10th International Conference on Fast Sea Transportation, Athens, Greece* (2009).

[6] Gaggero, S. and Brizzolara, S. A panel method for trans-cavitating marine propellers. *7th International Symposium on Cavitation, Ann Arbor, Michigan* (2009).

[7] Gaggero, S., Brizzolara, S. and Villa, D. Design and Analysis of Conventional and Ducted Propellers: a Numerical Approach. *17th International Conference on Ships and Shipping Research, Naples, Italy* (2012).

[8] Hughes, M.J. Analysis of multi-component ducted propellers in unsteady flow. *Ph.D. Thesis, Massachussets Institute of Technology* (1993).

[9] Oosterveld, M.W.C. Wake adapted ducted propellers. *MARIN Pubblication 345* (1970).

[10] Valdenazzi, F., Sebastiani, L. and Becchi, P. CFD based design oriented tools at CETENA. *International Conference on Computational Methods in Marine Engineering, Oslo, Norway* (2005).

V International Conference on Computational Methods in Marine Engineering
MARINE 2013
B. Brinkmann and P. Wriggers (Eds)

INFLUENCE OF PROPELLER TIP ROUGHNESS ON TIP VORTEX STRUCTURE - MARINE 2013

Christian Krueger*, Nikolai Kornev*, Christian Semlow† Matthias Paschen†

*Chair of Modelling and Simulation (LEMOS)
University of Rostock (URO)
Albert-Einstein-Str. 2, 18059 Rostock, Germany
e-mail: christian.krueger@uni-rostock.de, web page: http://www.lemos.uni-rostock.de/

† Chair of Ocean Engineering (LMT)
University of Rostock (URO)
Albert-Einstein-Str. 2, 18059 Rostock, Germany
e-mail: christian.semlow@uni-rostock.de - Web page: http://www.lmt.uni-rostock.de

Key words: Tip Vortex Cavitation, Marine Propellers

Abstract. This paper investigates the effects of propeller tip roughness on the tip vortex formation. It was shown, that sand grain roughness can lead to a significant drop in angular vortex momentum and therefore reduced vortex vacuum. Due to additional viscous stresses between propeller blade and detached tip vortex, the momentum is transformed into turbulent kinetic energy. As the turbulent scales are dissipated partly, the energy content of the system is reduced. This effect shows to be sensitive to application area and roughness height.

1 INTRODUCTION

Modern shipbuilding and development shows a strong demand for highly efficient and powerful propulsion systems. Moreover, tendencies of maximizing the cargo hold lead to decreasing space provided for the propulsion system. On the downside of this progression are highly tip-loaded propellers. This can lead to prominent tip vortex structures and subsequently forwarding to frequent tip vortex cavitation, hull excitation and rudder erosion.

Within a joint research project of MMG Waren GmbH and the University of Rostock an innovative approach has been investigated claiming the possibility of pertubating propeller tip vortices by a roughened propeller tip region.

2 THEORETICAL BACKGROUND

In marine propulsion tip vortices come to mind especially when showing up in its extreme occurrence, forming a cavitating vortex helix. Even though erosion, induced by tip vortex cavitation, in general does not impact on the propeller itself, the harmful effects on installations placed downstream like rudders are quite remarkable [3]. Furthermore, the comfort conditions are affected as well. Hull excitation and underwater noise [10], arising from increased 2^{nd} order pressure fluctuations, are challenges of modern propeller design.

The approach, for delaying or modifying tip vortex structures and cavitation for wing configurations by technical solutions is fairly old. Besides the familiar aspects of classic propeller design, one may know for instance the propeller tip vane by Vatanabe [7], ducted tips or bulbous tips [6], to name but a few. With each solution having its individual benefits, it is obvious that application for retrofit becomes difficult, if cavitation characteristics and customers expectations does not comply.

In lights of this, the investigations of Katz and Galdo [4] pointed out a distinct relation between surface roughness and tip vortex roll-up for a rectangular hydrofoil, demonstrating a shift in detachment point and a substantial reduction in tip vortex strength due to increasing surface roughness. Based on these results, Johnsson and Ruttgerson [1] studied the influence of leading edge roughness on the tip vortex roll-up for different angles of attack. It was shown, that application of roughness on the pressure side near the leading edge has a delaying effect on tip vortex cavitation. On the downside of these results was an increase in drag up to 10% due to the highly exposed roughened area causing a total decrease in efficiency by 2%.

Philipp and Ninnemann [5] suggested, that small scale turbulence pertubation within the boundary layer, caused by surface roughness, may result in a destabilizing of the tip vortex structure. They claimed the back on the suction side of the propeller tip to be the most efficient application area. Cavitation tunnel experiments proved a scattered cavitating vortex structure and a decrease of 2^{nd} order pressure fluctuations of 35% accompanied by a lowering of open water efficiency of 2.5%.

An evidence for the connection between turbulence of the outer flowfield and vortex core dynamics was given by the work of Hussain and Pradeep [2], pointing out that the eigenmodes of the evolving vortex allow resonance effects with the relatively week outer turbulence leading to pertubation amplification by several orders of magnitude.

3 SETUP

3.1 Numerical Setup

A blade model based on the P1380 cavitation tunnel experiments of the Potsdam Model Basin was designed, providing an equal thrust distribution within translational flow as its rotational counterpart. Staying with the chord-, skew- and thickness distribution of the original P1380, the blade sections were straightened into horizontal plane. Using

symmetric sections, the original camber distribution was reset. The pitch distribution was found impressing the calculated thrust distribution $F_{A,des}$ of the original P1380 propeller to the translational model using a panel code for solving the equations

$$\Delta F_{A,j} = \left[F_{A,des,j} - \sum_{i=1}^{N} \left(\frac{\partial F_{A,j}}{\partial \alpha_i} \alpha_i \right) \right] \rightarrow 0 \tag{1}$$

$$\frac{\partial F_{A,i}}{\partial \alpha_i} = \frac{F_{A,i}\left(\alpha_{init} + \Delta\alpha_i\right) - F_{A,i}\left(\alpha_{init}\right)}{\Delta \alpha_i}$$

For optimal validation the blade model was scaled by a factor of 1:7.5, leading to a total span of b=445.5mm and a chord length of c(r/R=0.7)=412.7mm with a maximum thickness of t(r/R=0.7)=17.9mm.

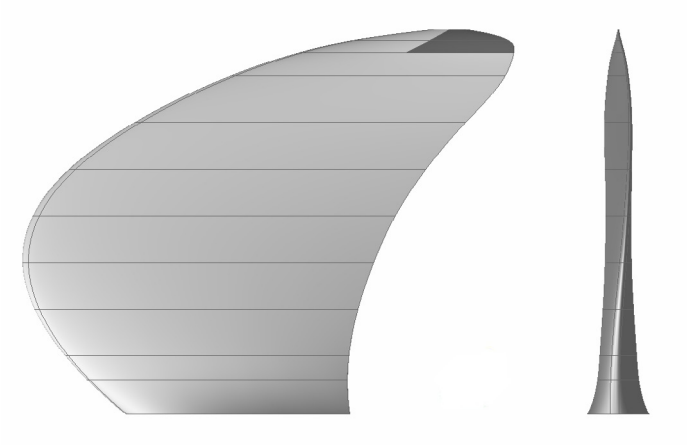


Figure 1: P1380 blade model for translational inflow with tip roughness

The computational domain consists of a block-structured ICEM grid using 19 Mio. as well as 60 Mio. hexahedron cells per blade. To ensure grid independent vortex development, the downstream section of the tip was set up with an equally spaced cartesian grid, resolving the vortex cross section by 56 x 56 and 331 x 331 cells respectively. Calculating the flowfield with the OpenFoam steady state RANS Solver SimpleFoam and a SST turbulence model, the wall function implementation of Tapia [8] was used to model different sizes of sand grain roughness $h_s^+ = h_s u_\tau / \nu$ in the transitional and the fully rough regime. Within the logarithmic profile

$$u^+ = \frac{1}{\kappa} \ln\left(y^+\right) + B - \Delta B \tag{2}$$

the velocity shift for the roughened wall reads

$$\Delta B = \frac{1}{\kappa} \ln\left[\frac{h_s^+ - 2.25}{87.75} + C_s h_s^+ \right]^{\sin\left(0.4258\left(\ln h_s^+ - 0.811\right)\right)} \qquad \text{for } 2.5 \leqslant h_s^+ \leqslant 90 \tag{3}$$

$$\Delta B = \frac{1}{\kappa} \ln\left(1 + C_s h_s^+\right) \qquad \text{for } h_s^+ \geqslant 90$$

The constant C_s, denoting the roughness type, was found in a series of calculation of the Nikuradse wall friction factor for turbulent pipe flows at Re=10^6, showing best overall prediction for C_s=0.35 (fig. 2).

According to [5] sand grain roughness elements of h_s=[0.2, 0.4, 0.6]mm has been considered for suction sided (SS), pressure sided (PS) and suction + pressure sided (SSPS) application areas of $0.95 \leqslant r/R \leqslant 1$ and $0.5 \leqslant c_L \leqslant 1$. The Reynolds-Number was set to Re=10^6 leading to an inlet velocity v_{inlet}=42.3m/s.

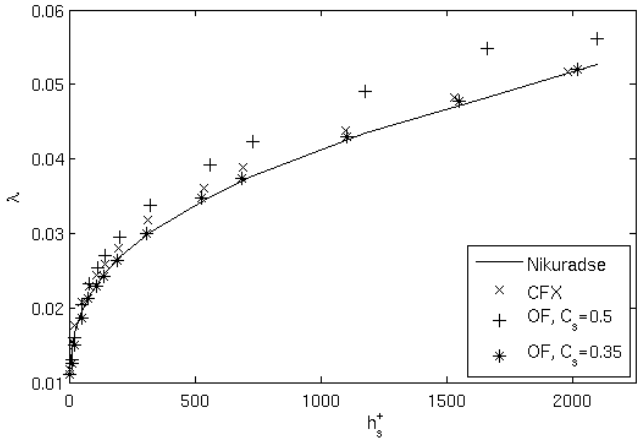


Figure 2: Wall function calculations for wall friction factor in turbulent pipe flows at Re=10^6

3.2 Experimental Setup

For validation purpose the pressure and the velocity field within the tip vortex for a smooth and a roughened wing were measured, showing the same dimensions as in the numerical setup. Two types of roughness structures had been investigated: Unstructured roughness, formed by a single layer of corundum with mean diameters of [0.2, 0.4, 0.6]mm in an adhesive matrix and structured roughness using adhesive stripes with a height of 0.6mm, width of 4.5mm and distance of 4.5mm. The stripes were placed in stream, cross-stream and diagonal direction. Structured roughness types were applied to the suction side of the tip only whereas the unstructured type was used either on suction or pressure side (tab. 1).

The measurement series was carried out at a Goettingen type subsonic wind tunnel, providing a quadratic measurement cross-section of $2m^2$. Integral forces and momentum on the blade model have been recorded by a six-component measurement system. To ensure matching of experimental and simulation data angle of attack and lift of the wing was selected representing the numerical data.

Within a vertical cross section perpendicular to the main inflow direction 0.5m downstream from the generator line with its center at 0.427 m vertical height 3D Hot-Wire as

well as Prandtl Tube measurements were performed. The cross section extended 165 mm x 165 mm being resolved as in the numerical setup by 56 x 56 measurement points.

4 RESULTS

4.1 Numerical Results

The simulations showed a distinct relation between roughness height and area of the tip roughness and specific tip vortex parameters. Applying sand grain roughness to the suction side of the tip, the viscous stresses between tip surfaces and adjacent tip vortex were increased, resulting in a damping of the angular momentum and therefore in an increased vortex pressure. The strong pattern of turbulent kinetic energy, forming above the roughened surface, quantifies the losses of rotational energy within the vortex. Depending on the investigated roughness height, the production rate of turbulent kinetic energy exceeds twice as much as for the smooth configuration. Even though the dissipation rate beeing enhanced as well, leading to an overall reduction of energy contained within the considered system, the turbulent scales dissipate imperfectly. Turbulent fragments tend to roll up into the vortex, shifting the relation between axial and radial cross stresses within the vortex core. For suction sided tip roughness all investigated heights leaded to an increased vortex core pressure compared to the smooth configuration. Due to additional viscous stresses the overall drag of the blade body rises, while the lift decreases.

Applying sand grain roughness to the pressure side, the tip vortex pressure and angular momentum remains nearly constant compared to the smooth wing, as the viscous effects and vortex are physically separated by the propeller blade. Acting on the boundary layer, the roughened region virtually thickens the blade section in the tip area, increasing the lift slightly. The drag of this configuration is larger than for the smooth wing and for the suction sided roughened wing as well.

Suction and pressure sided tip covered with sand grain roughness show a comparable impact on angular momentum and tip vortex pressure as for the suction sided configuration. Drag and lift nearly superposition from the single sided types, leading to the highest drag of all investigated configurations where lift decreases slightly compared to the smooth wing.

Calculating the inverse of the glide ratio ε, one can obtain a decrease in wing efficiency for all setups. These effects become stronger for all configurations as the roughness height increases (fig. 4).

As the wall roughness thickens the boundary layer, the correlation between boundary layer thickness of the wing and tip vortex diameter, like mentioned in [9], was investigated. The tangential vortex velocity at one chordlength downstream of the generator line was compared for the smooth, the suction sided and the pressure sided tip roughness. In addition three more cases were calculated: The complete blade covered with roughness (allrough), providing a thickened boundary layer, the complete blade set up with a no-slip condition (allslip), inhibiting the development of a boundary layer, and a no-slip condition

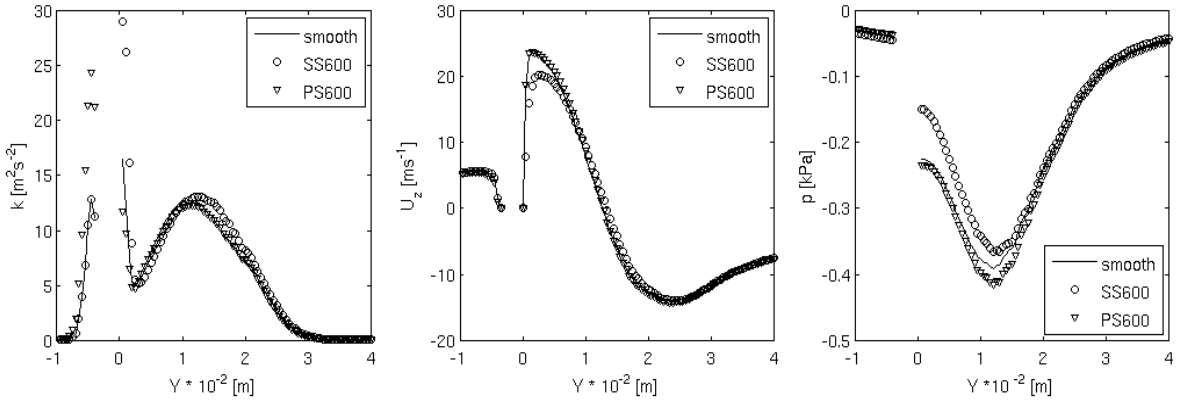


Figure 3: Calculated turbulent kinetic energy (left) tangential velocity (center) and pressure (right) on a horizontal line through the tip vortex adjacent to the roughness patch

for the suction side of the tip only (SSslip), inhibiting the thickening of the boundary layer at the tip.

In the outcome no dependency of the tip vortex diameter on boundary layer thickness was found. Comparing the circumferencal velocities, normed by the lift coefficient, all configurations showed a similar relation between specific lift and vortex circulation, except for two configurations: The suction side roughened blade and the entirely roughened blade as well presented a significant decrease in tangential vortex velocity within a radii of $R \leq 2R_{\text{solid}}$ and subsequently an increase in tip vortex pressure. Even though the entirely covered blade show superior vortex characteristics, it exhibits an essential increase in viscous friction (+85.6%) and therefore reduction of blade efficiency (-73.0%), whereas the suction sided provides nearly the same resistance (+0.4%) and efficiency (-0.9%) as for the smooth blade.

To investigate the effects of turbulent structures, the reynolds stresses, evolving at the roughened patches, were mapped either onto the suction side or the pressure side of the smooth propeller tip. In contrast to the expectations, no influence on the tip vortex pressure has been observed. The turbulent scales roll up into the vortex, traveling downstream within the vortex core.

4.2 Experimental Results

The calculations were assisted by a series of wind tunnel measurements, proving the low-pressure region of the tip vortex being effected by the tip roughness depeding on the applicaton area. Where for the suction sided tip roughness an increase of up to 18.4% was measured, the pressure sided tip roughness seems to have only marginal effect on the vortex vacuum. This is surprising somehow, since the measurements showed a significant decrease of the axial velocity surpression within the vortex core for both roughness

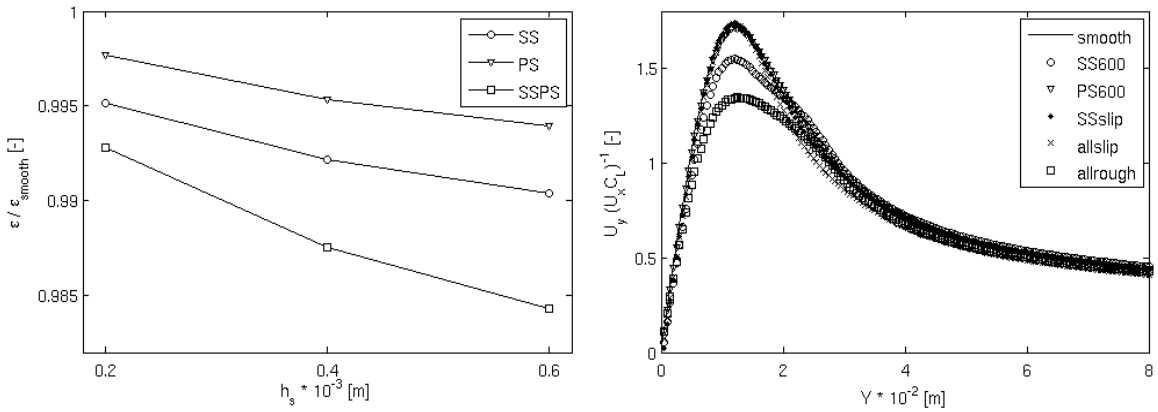


Figure 4: Calculated blade efficiency relative to a smooth wing depending on roughness height and application area (left) and tangential vortex velocity one choordlength downstream of the propeller blade

configurations, with an even stronger effect of the pressure sided tip roughness (SS600: -11.1%/-8.6%; PS600: -31.1%/-23.3% (Prandtl tube/3D Hotwire)). As indicated by the simulation results, the effect of suction side roughness on the tip vortex vacuum correlates with the roughness height. This is true for the unstructured roughness type only, since all structured roughness setups showed to have less impact on the vortex vacuum than the smallest sand grain height, even though this sand grain roughness extends only one third of the structured type. While all structured types provided the same roughness height, their sensitivity regarding the inflow direction became obvious. Whereas the horizontal stripes showed to have the least impact on the tip vortex vacuum from all suction sided measures, the diagonal stripes, aligning perpendicular to the resulting inflow direction of mean flow and vortex rotation, proved to be nearly as effective as the smallest unstructured height.

Table 1: Investigated roughness types

	tip area	type	height	$(p/p_{smooth})_{RANS}$	$(p/p_{smooth})_{Exp}$
SS200	suction side	sand grain	0.2mm	0.974	0.864
SS400	suction side	sand grain	0.4mm	0.939	0.822
SS600	suction side	sand grain	0.6mm	0.905	0.816
PS600	pressure side	sand grain	0.6mm	1.023	0.969
SSHoriz	suction side	horizontal stripe	0.6mm	-	0.903
SSVert	suction side	vertical stripe	0.6mm	-	0.940
SSDiag	suction side	diagonal stripe	0.6mm	-	0.870

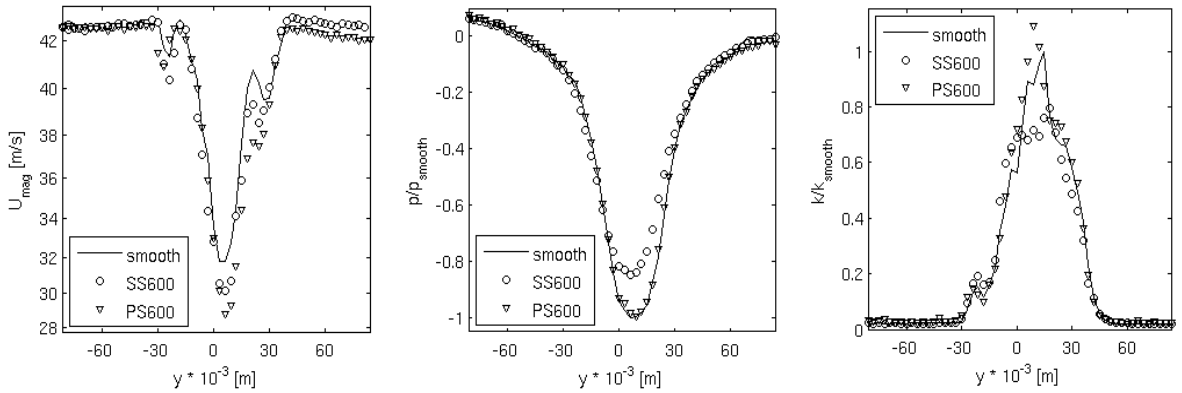


Figure 5: Dynamic pressure (left), static pressure (center) and turbulent kinetic energy (right) for a smooth and a roughened wing (h_s=600μm) on a horizontal line through the vortex core (distance from generator line x=0.35m, z=0.427m)

Comparing the second order moments for the suction side roughness, a diffusion of the turbulent kinetic energy is observed, thickening the turbulent vortex core (fig. 5). By a closer look at the diagonal Reynolds stresses, an amplification of the axial vortex stresses can be noticed, whereas the radial stresses seem to be diminished. Taking into account that for the given configuration the axial stresses averaging at 1/3 of the radial stresses, the vortex diffusion can be divided into two fractions: First, a thickening of the vortex core by an amplification of the axial stresses, and second, the lowering of the total kinetic energy within the core by damping the radial stresses (fig. 6). The shifting relation between axial and radial core stresses is also reflected by the experimental data for the cross-correlations, showing an amplification of the correlations between axial and radial fluctuations in opposite to the damping of the correlations between both components of the radial fluctuations.

As the pressure sided roughness showing a similar amplification of the axial stresses, in this case the radial stresses are amplificated as well, leading to an overall increase of the turbulent kinetic energy within the vortex core. This is in line with the results observed for the radial cross stresses, being enhanced by the pertubation of the vortex roll up in vicinity of the tip, evidencing a more turbulent vortex structure compared to all other configurations.

5 CONCLUSIONS

The effects of propeller tip roughness and application area on the tip vortex pressure had been investigated. It was shown that the tip vortex vacuum can be reduced using suction sided tip roughness. Although the impact on the vortex vacuum was suggested by the calculations, an even stronger influence of the roughened tip on the low-pressure region of the tip vortex was measured. This effect originates from increased viscous wall-friction

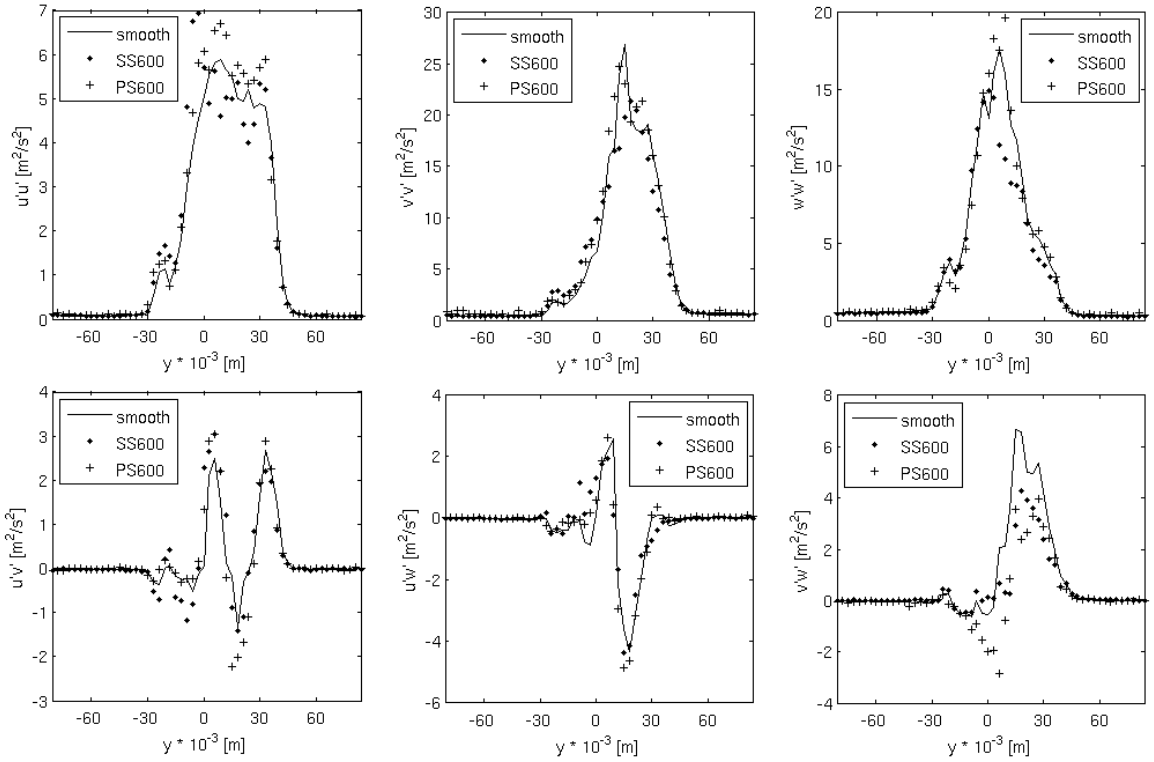


Figure 6: Components of the Reynolds stress tensor for a smooth and a unstructured roughened wing (h_s=600μm) on a horizontal line through the vortex core (distance from generator line x=0.4806m, z=0.427m)

between the vortex and the roughened tip, damping the circumferencal vortex velocity. Considering the suction sided sand grain roughness to be the most effective solution within this investigation, the structured roughness, even though being sensitive regarding the inflow direction, also showed promising potential for vortex pressure modification. Due to the basic design this version seems to be most preferable for practical application. It can be estimated that by minimized reduction of the open water efficiency due to friction induced losses, cavitation safety in the tip vortex can be improved by up to 19%.

As this study is concentrated on the physical effects within one-phase flows in the first, all results are going to be validated during the second phase of the project in cavitation tunnel experiments for the rotational propeller model. At the present state of the investigation it can be expected, that the specific application of discrete roughness structures near the propeller tips offers potential to efficient propulsion systems that meets highest industries demands for cavitation-free operation.

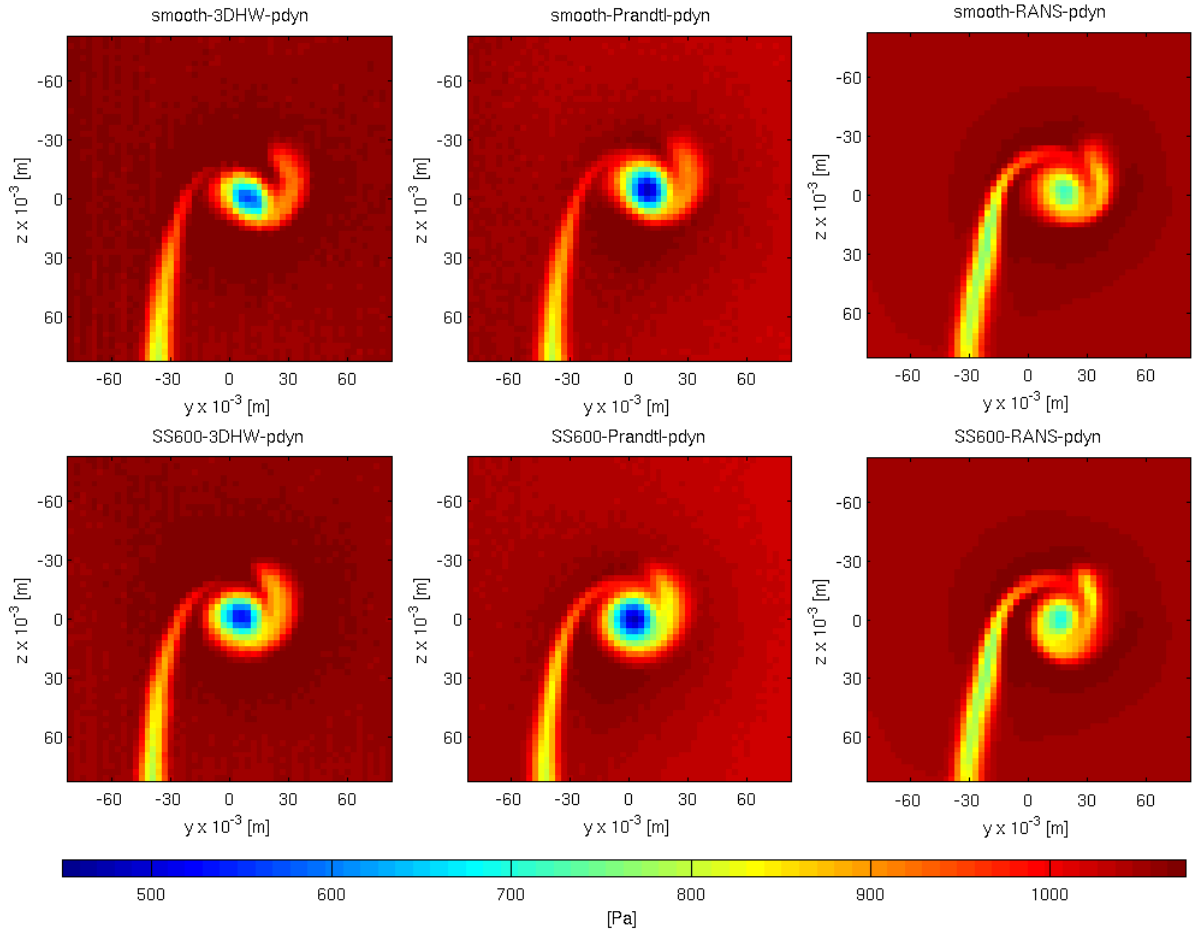


Figure 7: Dynamic pressure from 3D Hot Wire (left), Prandtl Tube (middle) and RANS (right) behind a smooth (top) and a roughened (bottom) propeller tip

REFERENCES

[1] O. Rutgerson C. A. Johnsson. Leading edge roughness - a way to improve propeller tip vortex cavitation. *Propellers and Shafting Symposium*, 1991.

[2] D. S. Pradeep F. Hussain. Mechanism of core pertubation growth in vortex-turbulence interaction. *12th Asian Congress of Fluid Mechanic*, 2008.

[3] A. Junglewitz J. Friesch. Erocav - improved test methods based on full scale investigations and new theoretical approaches for the prediction of erosion damages. *Summer Meeting STG*, 2003.

[4] J. Galdo J. Katz. Effect of roughness on rollup of tip vortices on a rectangular hydrofoil. *Journal of Aircraft*, 26, 1989.

[5] P. Ninnemann O. Philipp. Wirkung von fluegelrauigkeiten auf kavitation und erregung. 2007.

[6] S. Z. Duan S. I. Green. The ducted tip - a hydrofoil tip geometry with superior cavitation performance. *Journal of Fluids Engineering*, 117, 1995.

[7] H. S. Koyama T. Watanabe, H. H. Nigim. The effects of propellertip vane on flow-field behavior. *Experiments in Fluids*, 23, 1997.

[8] X. P. Tapia. Modelling wind flow over complex terrain using openfoam. 2009.

[9] S. I. Liapis G. J. Follin W. J. Devenport, M. C. Rife. The structure and development of a wingtip vortex. *Journal of Fluid Mechanics*, 312, 1996.

[10] D. Wittekind. Current status of underwater noise from shipping and the contribution of the propeller. 2011.

V International Conference on Computational Methods in Marine Engineering
MARINE 2013
B. Brinkmann and P. Wriggers (Eds)

THE DESIGN OF TURBINES FOR HARNESSING MARINE CURRENTS

MARINE 2013

JAIME MOREU†, JESÚS VALLE†, MANUEL MOREU* AND MIGUEL TABOADA*

* Seaplace SL
C/ Bolivia 5, 28016 Madrid, Spain
Email: seaplace@seaplace.es - Web page: http://www.seaplace.es

† ETSIN (Technical School of Naval Architects)
Universidad Politécnica de Madrid, UPM
Av. Arco de la Victoria s/n, 28040 Madrid, Spain

Key words: Hydrokinetic turbine, Nozzle, Diffuser, Lifting line, Actuator disc.

Summary: We have used the lifting-line code OpenProp for modeling a turbine within a nozzle designed to harness marine currents. Corrections based on actuator disc theory have been implemented to consider the accelerating effect of the nozzle. We have also analyzed the effect of the images of the blade vortices caused by the nozzle.

1 INTRODUCTION

The expansion of offshore renewable energies has led to the construction of many prototypes designed to harness marine currents among other sources of energy [1]. These devices frequently use axial-flow turbines to transform kinetic energy into mechanical power. Due to the diversity of designs, trustworthy systematic series cannot be readily drawn to assist in the design which means the most cost-efficient design tool available is based on numerical methods.

For the preliminary analyses blade element and lifting line theories are the preferred methods. They provide great insight into the problem and, as long as the viscous losses are adequately estimated, they help to chose the optimum rotational speed, the number of blades, the chord length distribution and also estimate a reasonable efficiency for medium loaded screws. However, they are not that good at generating the blade geometry because they estimate the section camber and angle of attack distributions considering the foil works in 2D unidirectional flow disregarding the 3D effects, particularly the cascade effect. Therefore potential codes, like the boundary element or lifting surface methods, are required to adjust the blade. Finally, viscous CFD codes must be used to check and validate the design.

The authors have used the lifting line code OpenProp to design a marine turbine within a nozzle. OpenProp is an open source and free code written for MATLAB that handles the design of marine propellers and axial-flow turbines. Professor Kimball led a team of students that have been developing it at MIT since 2007. The code has been slightly modified to include the accelerating effect of nozzles, decoupling the problem by means of an actuator-disc theory that includes the effect of nozzles and diffusers. This allowed us to first optimize the nozzle and later optimize the screw with OpenProp, only requiring one value to model the

effect of the nozzle. The geometry of the turbine has been adjusted to consider three-dimensional effects. OpenProp also gives us the tools to explain how different configurations yield different optimum turbines (i.e. whether or not a duct is included or if in the presence of an exterior ring).

The designed device (nozzle, diffuser and turbine) was called Seaplace-501 Marine Turbine and it was built and tested in 2012 at the CEHIPAR model basin in Madrid, Spain. The results were successful, proving both the capabilities of OpenProp and the efficiency of the prototype.

2 OPENPROP, A LIFTING-LINE CODE FOR THE DESIGN OF TURBINES

There are several lifting-line codes for the preliminary design of propellers. Their theoretical background is explained in references [2], [3] and [4]. OpenProp is among these, being the result of significant research efforts (references [5], [6], [7], [8] and others). On its most recent release (version 2.4, reference [9]) the program was adapted to handle turbines. The code is basically the same, working with negative circulations and thrusts in order to absorb kinetic energy from the flow, but the optimizer is modified to maximize the efficiency, which is differently defined for a turbine than for a propeller.

By the time our research began the current version of OpenProp was v1. The authors changed the code to handle turbines and added some lines to simulate the effect of nozzles. Nozzles not only make an increase of circulation close to the blade tip possible, but also could considerably modify the speed of the flow at the screw plane. This change of speed results from an interaction between duct and screw, although we will appreciably simplify it assuming some results based on actuator disc theory as will be shown in the following paragraphs.

3 ACTUATOR DISC THEORY INCLUDING NOZZLES AND DIFFUSERS

We will apply the actuator disc theory [2], a well known theory in propeller design, to a generator disc surrounded by a nozzle and diffuser (see Figure 1). Successive diffusers could also be added.

Consider an incompressible fluid of constant density ρ in a potential stationary flow of uniform and constant upstream speed V_A. The actuator disc, of radius R, is delimited by the nozzle contour and subtracts a constant pressure Δp from the flow passing through it, being Δp negative for a generating disc. The thrust exerted by the disc onto the flow is $T = \pi R^2 \Delta p$, also negative, and the axial forces produced by the nozzle and diffuser are F_{St} and F_{Sd} respectively, being negative if they are in the same direction than T. The sum of these forces is $F_S = F_{Sd} + F_{St}$. We will use as in reference [10] the coefficient C_S, which is the ratio between the axial force from nozzle and diffuser, and the axial force from the disc (or thrust), this is $C_S = \dfrac{F_S}{T} = \dfrac{F_S}{\frac{\rho}{2}\pi R^2\left[(V_A - u_w)^2 - V_A^2\right]} = \dfrac{F_S}{-\rho\pi R^2 u_w\left(V_A - \frac{u_w}{2}\right)}$. We will later show that in some way this coefficient measures the efficiency of a set of nozzles and diffusers.

The generating disc will subtract kinetic energy from the flow, reducing the speed downstream by $u_w(r)$, where r is the distance to the axis of symmetry. The speed downstream is hence $V_A - u_w(r)$ and the induced downstream speed $u_w(r)$ is positive for a generator. Analogously the speed at the actuator disc will be $V_A - u_a^*(r)$, where $u_a^*(r)$ is the induced speed at the disc and it could be negative for accelerating nozzles.

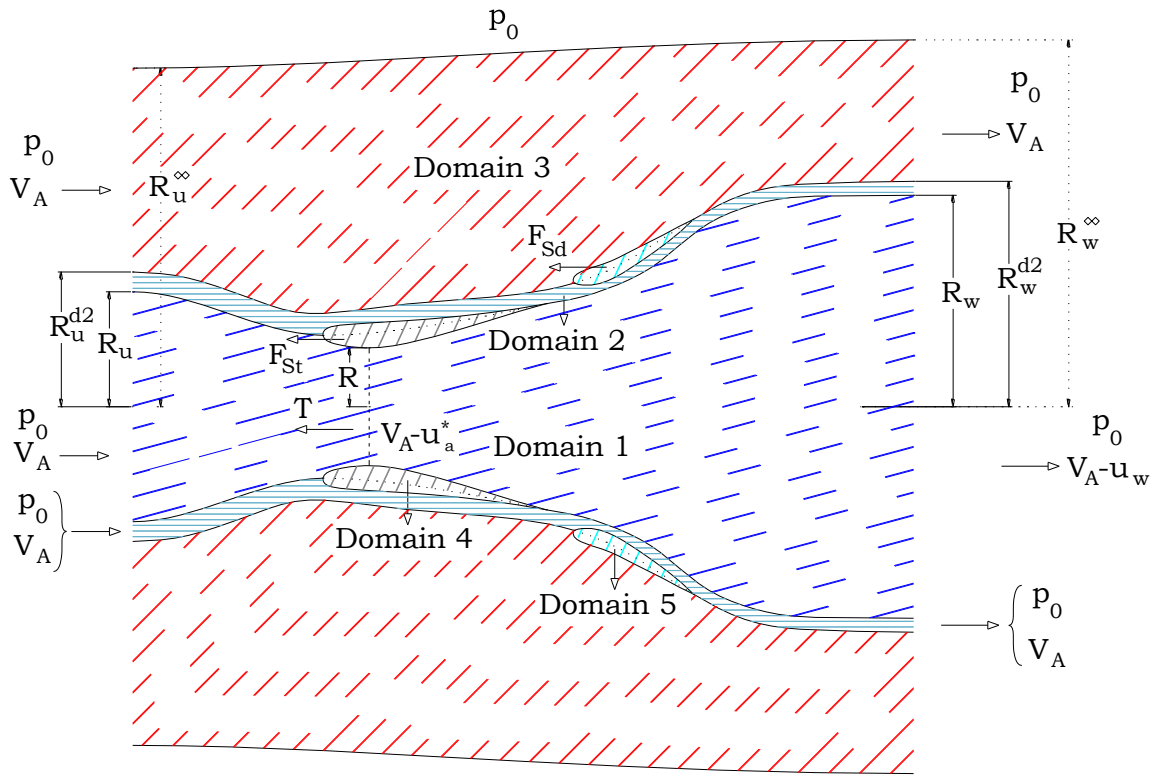


Figure 1 : Actuator disc theory for a general case with nozzle and diffuser

Δp is assumed constant because it gives the optimum efficiency for an actuator disc without nozzle (reference [11]). This fact should be confirmed for an actuator disc within a duct.

We apply Bernoulli's principle to a stream line that passes through the nozzle interior. By comparing a point upstream and a point downstream we get Δp and T as a function of u_w. The pressure in the infinite up and downstream is assumed to be p_0.

$$p_0 + \frac{1}{2}\rho V_A^2 + \Delta p = p_0 + \frac{1}{2}\rho(V_A - u_w)^2 \;\Rightarrow\; \Delta p = -\rho u_w\left(V_A - \frac{u_w}{2}\right)$$
$$T = -\pi R^2 \rho u_w\left(V_A - \frac{u_w}{2}\right) \tag{1}$$

Since we assume Δp is constant u_w will also be constant and will therefore not depend on r.

The next step requires applying the law of conservation of linear momentum on the different domains shown in Figure 1. For a stationary flow and incompressible fluid, this law states:

$$\vec{F} - \iint_S p\vec{n}ds = \rho \iint_S \vec{V}\left(\vec{V}\vec{n}\right)ds \tag{2}$$

where $\vec{n}$ is a unit vector normal to the surface under consideration and pointing outwards of the domain. $\vec{F}$ represents the volume forces on the fluid and $-\iint_S p\vec{n}ds$ the forces on the exterior surfaces of the volume control.

- Domain no. 1: stream tube going through the interior of the nozzle. Conservation of momentum leads to:

$$T = +\iint_{S_1} pn_x ds + \rho \iint_{S_1} \left(V_A - u_a\right)^2 n_x ds \tag{3}$$

  The boundaries of domain no. 1 in the infinite up and down stream are two planes normal to the flow direction. The force due to pressure in these boundaries is $\pi p_0\left(R_u^2 - R_w^2\right)$.

  We will study the other domains before obtaining the pressure forces at the axisymmetric boundary of this control volume.

- Domain no. 2: stream tube going through the exterior of the nozzle and through the interior of the diffuser. The boundaries of domain no. 2 in the infinite up and down stream are two planes normal to the flow direction.

  The application of the conservation of momentum to control volume no. 2, since there are neither volumetric forces nor variations in linear momentum, gives $+\iint_{S_2} pn_x ds = 0$.

  Considering the speed is V_A in both limits up and down stream, the mass conservation then leads to $\left(R_u^{d2}\right)^2 - \left(R_w^{d2}\right)^2 = R_u^2 - R_w^2$. Therefore the resulting pressure force up and down stream of this domain is null. We will study the other domains before obtaining the pressure forces at the axisymmetric boundaries of control volume no. 2.

- Domain no. 3: stream tube surrounding domain no. 2, not passing through the nozzle or the diffuser interiors and whose outer axisymmetric boundary is far away enough to let the pressure be p_0 all around it.

  Because there are no volumetric forces on it and no variation of the momentum flux:

$$-\iint_{S_3} pn_x ds = 0 \tag{4}$$

  Considering the speed is V_A in both limits up and down stream, the mass conservation leads to $\left(R_u^{\infty}\right)^2 - \left(R_w^{\infty}\right)^2 = \left(R_u^{d2}\right)^2 - \left(R_w^{d2}\right)^2$. Therefore the resulting pressure force up and

down stream of this domain is null. Taking into account the mass conservation of volume 2 we obtain $\left(R_u^{\infty}\right)^2-\left(R_w^{\infty}\right)^2=\left(R_u^{d2}\right)^2-\left(R_w^{d2}\right)^2=R_u^2-R_w^2$.

The resulting pressure force on the outer axisymmetric boundary of this control volume is $-\pi p_0\left(\left(R_u^{\infty}\right)^2-\left(R_w^{\infty}\right)^2\right)=-\pi p_0\left(\left(R_u^{d2}\right)^2-\left(R_w^{d2}\right)^2\right)=-\pi p_0\left(R_u^2-R_w^2\right)$. Bearing in mind this and equation (4) the resulting pressure force on the inner axisymmetric boundary of this domain is $\pi p_0\left(\left(R_u^{d2}\right)^2-\left(R_w^{d2}\right)^2\right)=\pi p_0\left(R_u^2-R_w^2\right)$.

- Domain no. 4: this is the nozzle, which is not a fluid domain. The pressure integral around it is the lifting force L_{xt}, which is in the axial direction due to the axisymmetry of the problem. Hence the force exerted by the nozzle on the fluid is $F_{St} = -L_{xt}$. The axial lift would be zero for $\Delta p = 0$, but a $\Delta p < 0$ produces an expansion of the flow downstream that allows the apparition of this axial force.
- Domain no. 5: this is the diffuser, which again is not a fluid domain. The integral of pressure around it is an axial lifting force, L_{xd}, and the force it produces on the fluid is $F_{Sd} = -L_{xd}$.

Knowing the integrals of pressure on the domains 3 and 5 we derive the integral of pressure on the outer tube of the domain no. 2: $-\pi p_0\left(R_u^2-R_w^2\right)+F_{Sd}$. And since in the second volume $\iint_{S_2} p n_x ds = 0$, the axial force on the inner tube of this domain is $+\pi p_0\left(R_u^2-R_w^2\right)-F_{Sd}$.

In a similar manner, considering the forces on domains 4 and 2 we may obtain the integral of pressure on the tube of domain no. 1: $-\pi p_0\left(R_u^2-R_w^2\right)+F_{Sd}+F_{St}$. The sum of forces from the nozzle and diffuser is $F_S = F_{Sd} + F_{St}$, and therefore the integral of pressures on all boundaries of domain 1 gives:

$$-\iint_{S_1} p n_x ds = \pi p_0\left(R_u^2-R_w^2\right)-\pi p_0\left(R_u^2-R_w^2\right)+F_S = F_S \tag{5}$$

The variation of linear momentum on the first control volume is $\rho\iint_{S_1}\left(V_A-u_a\right)^2 n_x ds =$

$= -\rho\pi R^2 u_w\left(V_A-\tilde{u}_a^*\right)$, and thus the conservation of momentum on this volume gives $T = -F_S - \rho\pi R^2 u_w\left(V_A-\tilde{u}_a^*\right)$. This equation compared with equation (1) relates the induced mean speed at the actuator disc with the induced speed downstream:

$$\tilde{u}_a^* = \frac{F_S}{\rho\pi R^2 u_w}+\frac{u_w}{2} \Rightarrow \tilde{u}_a^* = \frac{u_w}{2}\left(1+C_S\right)-C_S V_A \tag{6}$$

The efficiency of the actuator disc when acting as a turbine can be expressed by:

$$\eta = \frac{T\left(V_A-\tilde{u}_a^*\right)}{\frac{1}{2}\rho\pi R^2 V_A^3} = \frac{u_w\left(V_A-\frac{u_w}{2}\right)^2}{\frac{1}{2}V_A^3}\left(1+C_S\right) \tag{7}$$

The maximum efficiency will occur when $\frac{d\eta}{du_w} = 0$, which happens for $u_w|_{opt} = \frac{2}{3}V_A$:

$$\eta_{opt} = \frac{16}{27}(1 + C_S) \tag{8}$$

If the turbine had more diffusers, F_S should include the forces from these diffusers and equation (5) and all subsequent results would still hold true.

If there is no nozzle or diffuser the optimum efficiency is the Betz limit, $\eta_{opt,Betz} = \frac{16}{27}$. Optimum efficiency can grow C_S times when including a duct. The maximum C_S depends on Reynolds number and on the stall characteristics. Increments of efficiency of about 2 to 3 times Betz $(C_S \approx 2 \text{ or } 3)$ can be obtained for well-designed nozzles with no stall. The combination of nozzles and diffusers can increase this value even more, and C_S of about 4 to 5 could be achieved. If stall occurs, bigger values might be possible.

Nozzles and/or diffusers therefore have a significant effect on the efficiency of a specific disc. However, this increment in efficiency has a downside to it: the structure required for the nozzle and diffuser will probably be much heavier than the increase of blades required for harnessing the same amount of energy. Nonetheless in case a duct is advisable for any other reason, using it as an efficiency booster may prove clever.

Note that in the optimum case Δp at the disc does not depend on whether there is a nozzle:

$$\Delta p_{opt} = -\rho u_w|_{opt}\left(V_A - \frac{u_w|_{opt}}{2}\right) = -\frac{4}{9}\rho V_A^2 \tag{9}$$

More complex numerical results suggested us that in fact the optimum induced speed for a turbine within a nozzle is close to $u_w = \frac{2}{3}V_A$. This allowed us to assume that $dC_S/du_w = 0$ when solving for the optimum efficiency in expression (7) in order to derive (8). This approach was good enough for us close to the optimum, and with it we only needed the value of C_S when the pressure drop is that of equation (9). Thus the coefficient C_S can be seen as a function only of the arrangement and shape of the ducts. The main advantage of this is that C_S can be considered constant for the calculation of the propeller at its optimum point, allowing the decoupling of the problem. However we will require computing C_S again if the turbine is not at its operating point.

4 THE ACCELERATING EFFECT OF NOZZLES

On the previous section we obtained the increment of efficiency that a nozzle can produce on a generating disc. Now we want to show the effect nozzles have on the design of a turbine. Two basic data are required to define a turbine: the inlet velocity field and the torque it shall obtain. We will be able to decouple the problem –i.e. study the turbine separately from the nozzle– as long as we determine the effect the nozzle has on these two variables. This will

give us an "equivalent flow", meaning a flow with different inlet speeds and without duct where the designed screw would perform exactly like in the real case with nozzle. Figure 2 illustrates this idea. On its upper half we see the real problem with the screw on the presence of the nozzle. On the lower half we see its behavior with the equivalent flow.

Referring to the equivalent problem with the subscript e, the pressure drop at the disc is Δp_e, the inlet speed is $V_{A,e}(r)$, the flow at the disc is $V_{A,e}(r)-u^*_{a,e}(r)$ and the downstream speed is $V_{A,e}(r)-u_{w,e}(r)$.

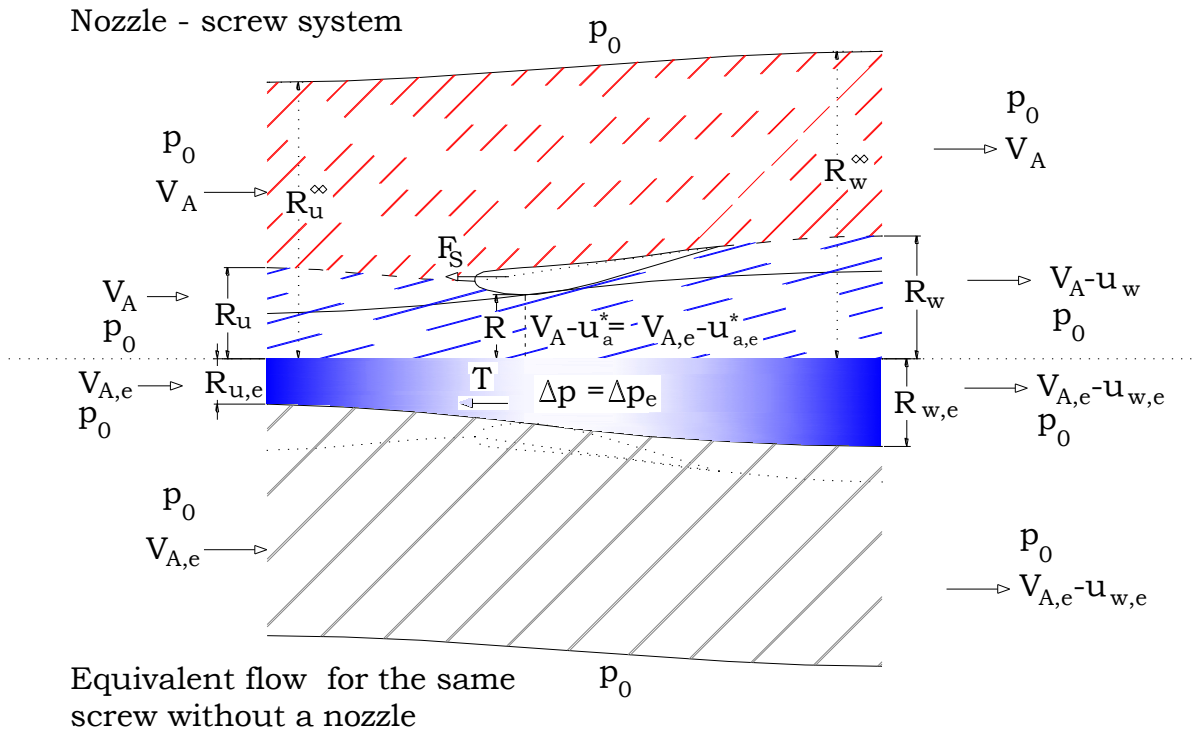


Figure 2 : Representation of the uncoupling between nozzle and turbine

The torque is related to the pressure drop at the actuator disc by equation (1). Besides, expression (9) suggests that the optimum pressure does not depend on whether there is a nozzle. In the equivalent problem the turbine shall provide this same pressure drop than in the real problem in order to subtract the same force from the flow, and thus $\Delta p_e = \Delta p$.

The inlet velocity field is *a priori* not known for the equivalent flow. Nozzles accelerate the flow and thereby the inlet velocity that the screw encounters can be very different from the current speed V_A. Nevertheless we know the speed at the disc shall be equal to that of the real problem; only under this assumption will the lift forces and harnessed energy, among other parameters of the screw, remain equal to the real problem. Therefore we assume:

$$V_{A,e}(r)-u^*_{a,e}(r)=V_A-u^*_a(r) \tag{10}$$

This equality holds for any radius, and thus holds for the average speed at the disc.

Defining the velocity ratio at the disc by $\chi = \frac{V_A - \widetilde{u}_a^*}{V_A}$:

$$\widetilde{V}_{A,e} - \widetilde{u}_{a,e}^* = V_A - \widetilde{u}_a^*(r) = \frac{2\pi}{\pi R^2}\int_0^R r\left(V_A - u_a^*(r)\right)dr = V_A\ \chi \tag{11}$$

If there is no duct and for an optimum disc $\chi = 2/3$, so any value above this implies acceleration. If there is neither disc nor duct χ equals 1, so high values of χ do not necessarily mean high efficiency. Values of χ above 3 can be obtained for optimum discs with nozzle and diffuser.

The disc under the equivalent flow must also comply with Bernoulli's principle, so $\Delta p_e =$ $= -\rho \cdot u_{w,e}(r)\left(V_{A,e}(r) - \frac{u_{w,e}(r)}{2}\right)$. Since we have assumed $\Delta p_e = \Delta p$, considering relation (1):

$$u_{w,e}(r)\left(V_{A,e}(r) - \frac{u_{w,e}(r)}{2}\right) = u_w\left(V_A - \frac{u_w}{2}\right) \tag{12}$$

Substituting this into the newly defined efficiency we obtain:

$$\eta = \frac{T\left(V_A - \widetilde{u}_a^*\right)}{\frac{1}{2}\rho\pi R^2 V_A^3} = \frac{u_w\left(V_A - \frac{u_w}{2}\right)\cdot V_A \cdot \chi}{\frac{1}{2}V_A^3} \tag{13}$$

The efficiency for the equivalent problem (expression (13)) must equal the efficiency for the real case (expression (7)), leading to the following relation between the nozzle coefficient and the velocity ratio:

$$\chi = \left(1 - \frac{u_w}{2V_A}\right)(1 + C_S) \tag{14}$$

For the optimum situation $u_w\big|_{opt} = \frac{2}{3}V_A$ implies that $\chi = \frac{2}{3}(1 + C_S)$ and then the average speed at the disc is $V_A - \widetilde{u}_a^*(r) = V_A\ \chi = V_A(1 + C_S)2/3$. If there is no nozzle $C_S = 0$ and $V_A - \widetilde{u}_a^*(r) = \frac{2}{3}V_A$. But if for instance there is a nozzle and diffuser with $C_S = 4$, the mean speed at the disc is $V_A - \widetilde{u}_a^*(r) \approx 3.3V_A$, 5 times more speed than that with no duct. Since lift forces depend squarely on the speed, 5 times more speed means we need 25 times less chord to obtain the same force with the same lift and advance coefficients $(C_L$ and $J)$, resulting in a significant increase of the aspect ratio $\lambda = s^2/S$, where s is the blade span and S the blade expanded area. This way screws within accelerating ducts can be much slenderer than

turbines with the same diameter under similar working conditions but without a duct, as illustrated by Figure 3, as long as there is no cavitation.

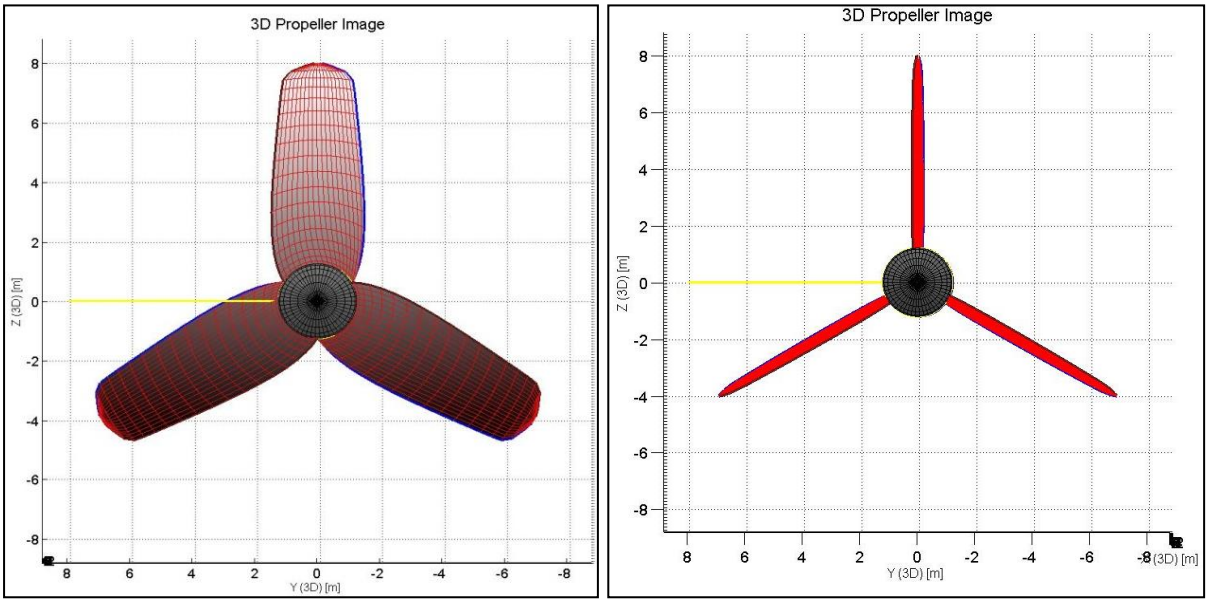


Figure 3 : Front view of two turbines with a diameter of 16 m designed for harnessing a 2 m/s marine current. The left turbine does not have a nozzle, while the right turbine works within a nozzle that doubles the inflow speed. The blades have a linear distribution of C_L along the radius, being C_L = 0.5 at the root and 0.25 at the tip

Regarding the solution of the equivalent speeds note we have three unknowns $\left(V_{A,e}(r),\ u_{w,e}(r),\ u^*_{a,e}(r)\right)$ but two equations (expressions (10) and (12)). We need a third equation, which is why we will suppose that the equivalent induced speed at the disc is half its value downstream:

$$u^*_{a,e}(r) = \frac{u_{w,e}(r)}{2} \tag{15}$$

This assumption follows the approach that Kerwin used for an actuator disc in equation (212) of reference [2]. For the case without nozzle it means the induced speed is constant for a constant pressure drop $\left(u^*_a = u_w/2\right)$, not matching the exact results (reference [11]) but being enough for practical purposes.

Using the variable $f_v(r)$ we can define the speed at a radius r of the disc analogously to relation (11): $V_A - u_a^*(r) = V_{A,e}(r) - u_{a,e}^*(r) = f_v(r) \cdot V_A \cdot \chi$. The function $f_v(r)$ is proportional to the local speed at the disc, and its average is 1 in order to fulfill relation (11) $\left(\frac{2\pi}{\pi R^2} \int_0^R r \cdot f_v(r) \cdot dr = 1 \right)$. Then, considering equations (10), (12) and (15) we get the equivalent speeds:

$$u_{w,e}(r) = \frac{u_w}{f_v(r) \cdot V_A \cdot \chi} \left(V_A - \frac{u_w}{2} \right); \; u_{a,e}^*(r) = \frac{u_{w,e}(r)}{2};$$

$$V_{A,e}(r) = f_v(r) \cdot V_A \cdot \chi + \frac{\frac{u_w}{2}\left(V_A - \frac{u_w}{2} \right)}{f_v(r) \cdot V_A \cdot \chi} \tag{16}$$

From (16) we see the product $f_v(r) \cdot u_{w,e}(r) = \frac{u_w}{\chi V_A}\left(V_A - \frac{u_w}{2} \right)$ is constant for Δp constant. This means the equivalent induced velocities are inversely proportional to the local speed at the actuator disc. Similarly to expression 216 in [2] we develop the following expression: $2\pi \cdot R \cdot V_A \cdot \chi \cdot f_v(r) \cdot u_{a,e}^*(r) = \quad 2\pi R \cdot \left(V_{a,e}(r) + u_{a,e}^*(r) \right) \cdot u_{a,e}^*(r) = \quad Z \cdot \Gamma \cdot \omega \cdot R \quad = constant$, which therefore states that the circulation is constant. Lifting line theory specifies that Γ must be constant for simulating an actuator disc with Δp constant, suggesting that the approach used for the "equivalent" problem is consistent with lifting line theory.

For those screws with no gap between the blade tips and the nozzle –as in an inline screw– we included in the code as in [6] the effect of the image at the duct of the blade vortices.

5 THE IMPLEMENTATION OF AN ACCELERATING DUCT ON A LIFTING LINE CODE

Bearing in mind the previous discussion, we can design a turbine without studying its interaction with the nozzle. We just need to know the coefficient of the duct, C_S, and the distribution of local speed at the turbine plane, $f_v(r)$. The inlet equivalent speed will be $V_{A,e}(r) = f_v(r) \cdot V_A \cdot \chi + \frac{1}{2} u_{w,e}(r)$; and the lifting-line code will derive $u_{w,e}(r)$ and $u_{a,e}^*(r)$. From (16) we know the induced speed downstream of the nozzle will then be $u_w = V_A - \sqrt{V_A{}^2 - 4u_{a,e}^*(r) f_v(r) V_A \cdot \chi}$.

The lifting-line code will iterate in order to maximize the efficiency, which is $\eta = \frac{Q\omega}{\frac{1}{2}\rho V_A^3 \frac{\pi D^2}{4}} = u_w \left(V_A - \frac{u_w}{2} \right) \left(V_A - u_a^*(r) \right) \Big/ \left(\frac{1}{2} V_A^3 \right)$. However the code calculates the

efficiency of a screw via $\eta_e = \dfrac{Q\omega}{\frac{1}{2}\rho \widetilde{V}_{A,e}^3 \frac{\pi D^2}{4}} = C_Q \cdot \dfrac{D}{2} \cdot \dfrac{2\pi N}{60} \Big/ \widetilde{V}_{A,e}$, so we use a variable ψ that makes $\eta(r) = \psi(r) \cdot \eta_e(r)$. Since $\psi(r) = \dfrac{\eta(r)}{\eta_e(r)} = \left(\dfrac{\widetilde{V}_{A,e}}{V_A} \right)^3 = constant$, ψ does not depend on the radius. The lifting-line code calculates the factor ψ in the following way:

$$\psi = \frac{\eta}{\eta_e} = \frac{u_w \left(V_A - \dfrac{u_w}{2} \right) f_v(r)\, \chi}{V_A^2} \frac{\widetilde{V}_{A,e}^3}{u_{w,e}(r) \cdot f_v{}^2(r) \cdot \chi^2 \cdot V_A^2} =$$

$$= \frac{\left[\chi V_A \cdot + \dfrac{\widetilde{f}_v^{-1} \cdot u_w}{2 \cdot \chi V_A} \left(V_A - \dfrac{u_w}{2} \right) \right]^3 \left(V_A - \dfrac{u_w}{2} \right)}{\chi V_A^4} (1 + C_S) = \frac{\left[\left(V_A - \dfrac{u_w}{2} \right)(1 + C_S) + \dfrac{\widetilde{f}_v^{-1} \cdot u_w}{2(1 + C_S)} \right]^3}{V_A^3} \tag{17}$$

Where $\widetilde{f}_v^{-1}(r) = \dfrac{2\pi}{\pi R^2} \displaystyle\int_0^R \frac{r}{f_v(r)} \cdot dr$. Expression (17) allows the appropriate convergence to the optimum $\eta(r)$. ψ somehow represents the loss in efficiency that actually occurs because the flow must decelerate behind the nozzle.

6 EMPIRICAL VALIDATION OF THE THEORY



Figure 4 : Model version of Seaplace-501 turbine for experimental validation at CEHIPAR towing tank

We designed a turbine for harnessing deep currents, the Seaplace-501 Marine Turbine. A

model was built and tested at the CEHIPAR model basin from July 2012 to January 2013 (see Figure 4). The model simulated the behavior of an inline screw and was within a nozzle and diffuser that gave a duct coefficient C_S of 3 when the electric generation was maximum. The prototype was designed for very low Reynolds numbers (*Re* ≈ 200,000) and thus we expect C_S to be above 4 for the full scale prototype.

7 REFERENCES

[1] Manuel Moreu, Miguel Taboada, David Fernández, Alberto Taboada, and Jaime Moreu, "Offshore renewable energy, the experience of a design office," *International Conference on Computational Methods in Marine Engineering*, vol. Marine, 2011.

[2] Justin E. Kerwin, *Hydrofoils and Propellers*., Enero 2001.

[3] H. W. Lerbs, "Moderately loaded propellers with a finite number of blades and an arbitrary distribution of circulation," *SNAME Transactions*, vol. 60, pp. 73-123, 1952.

[4] J. W. Wrench, "The calculation of propeller induction factors," David Taylor Model Basin, Washington DC, Research and development report 1116, 1957.

[5] William Bowles Coney, "A method for the design of a class of optimum marine propulsors," *MIT, PhD thesis*, 1989.

[6] John M. Stubblefield, "Numerically-based ducted propeller design using vortex lattice lifting line theory," *MIT, M.Sc. thesis*, 2008.

[7] Brenden P. Epps, *An impulse framework for hydrodynamic force analysis: fish propulsion, water entry of spheres, and marine propellers*, Massachusetts Institute of Technology, Ed. Boston, Massachusetts, 2010.

[8] Richard W. Kimball and Brenden P. Epps. (2010) OpenProp v2.4 propeller/turbine design code. [Online]. http://openprop.mit.edu

[9] Brenden P. Epps, "OpenProp v2.4 Theory Document," MIT, Department of Mechanical Engineering Technical Report December 2010.

[10] Michael J. Werle and Walter M. Presz, Ducted Wind / Water Turbines and Propellers Revisited.

[11] John T. Conway, "Analytical solutions for the actuator disk with variable radial distribution of load," *Journal of Fluid Mechanics*, vol. 297, pp. 327-355, 1995.

[12] Hermann Glauert, *The elements of aerofoil and airscrew theory*, Second edition ed.: Cambridge University Press, 1983.

V International Conference on Computational Methods in Marine Engineering
MARINE 2013
B. Brinkmann and P. Wriggers (Eds)

THE THESAURUS PROJECT, A LONG RANGE AUV FOR EXTENDED EXPLORATION, SURVEILLANCE AND MONITORING OF ARCHAEOLOGICAL SITES

B.ALLOTTA†, L.PUGI†, F.BARTOLINI†, R.COSTANZI†, A.RIDOLFI†, N.MONNI†, J.GELLI†, G.VETTORI†,L.GUALDESI°, M.NATALINI†

†MDM Lab, Industrial Engineering Department
University of Florence
via Panconi 12, Pistoia, Italy
e-mail: luca.pugi@unifi.it, http://www.unifi.it/mdmlab
°Edgelab SRL www.edgelab.eu

Keywords: Autonomous Underwater Vehicle, Design Optimization, Swarm Control and Navigation

Abstract.

Within the framework of the Thesaurus project (Italian acronym for "TecnicHe per l'Esplorazione Sottomarina Archeologica mediante l'Utilizzo di Robot aUtonomi in Sciami"), the authors have developed a low cost, multirole Autonomous Underwater Vehicle, briefly called Tifone, whose design is the main topic of this paper. According to the expected performances and specifications, the vehicle has to maintain a good autonomy and efficiency, typical features of an AUV (Autonomous Underwater Vehicle), also maintaining high manoeuvrability and hovering capabilities, which are instead more common on ROVs (Remotely Operated Vehicles).Cooperative exploration and surveillance tasks involve the use of swarms of vehicles; the control, the mutual localization and communications among vehicles are fundamental tasks to be optimized. In particular, the optimization of costs with respect to benefits plays a critical role, considering that within the Thesaurus project a first fleet of three vehicles has to be developed. This work mainly deals with the different design phases of the vehicle and with the results of preliminary simulations and tests performed in the MDM laboratories, before the next lake (Roffia basin, between Pisa and Florence, Italy) and sea testing activities (Elba Island, Italy) that will be performed in spring and summer 2013.

1 INTRODUCTION: THESAURUS PROJECT AND VEHICLE SPECIFICATIONS.

Aim of the Thesaurus project is the development of a swarm of AUVs (Autonomous Underwater Vehicles) for the exploration, surveillance and monitoring of archaeological sites. The swarm is composed of 3 identical vehicles, briefly called Tifone, that can be customized to perform different tasks/roles assigned in a cooperative mission profile, including acoustic or visual inspection of the site of interest. In particular, a feasible composition of the swarm

with three different vehicle layouts, corresponding to different mission tasks and instrumentation layouts, is visible in Figure 1:

- Acoustic Explorer: this vehicle is equipped with long/medium range instrumentation, such as Side Scan Sonar (SSS), in order to explore and investigate relatively wide areas, for a large, medium scale reconstruction of the site or a preliminary exploration of a potentially interesting area. The typical distance from a potential target on the sea-bottom is 40 m or more;
- Vision Explorer: this is the vehicle equipped whit short range instrumentation, like cameras, illuminators and/or structured lights, for visual inspection and monitoring of a site. Its applications can be the 3D reconstruction for virtual reality or augmented reality applications, or more ambitiously, a visual based SLAM (Simultaneous Localization And Mapping) of the site. The typical distance from a potential target is about 4 m;
- Swarm Coordinator: the communication and the mutual localization of the swarm AUVs is performed by the Swarm-Coordinator through an USBL (Ultra-Short BaseLine) system. The coordinator is equipped with a transceiver; on the other vehicles the acoustic modems, working as transponders, are installed. The estimation of the absolute position of the coordinator should be periodically fixed using its GPS signal, which implies the periodical emersion of the vehicle. In this way, the swarm coordinator can communicate with the on-board navigation system of each vehicle, to refine the mutual position estimation andto perform the cooperative localization of the whole swarm. Some preliminary simulations concerning possible strategies to be used to perform the mutual localization of the vehicles have been the object of a previous publication [1].

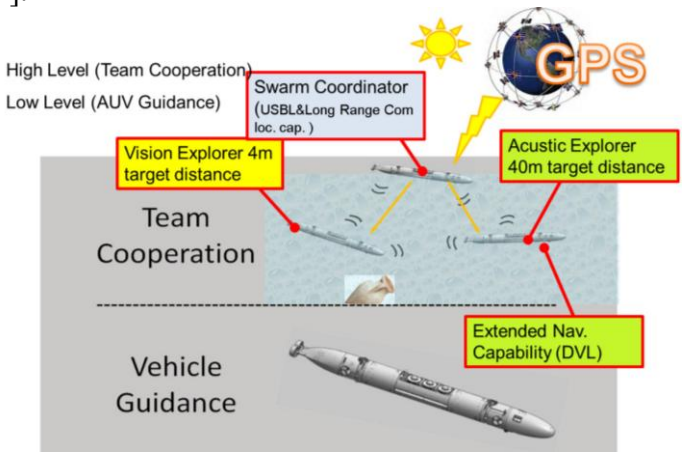


Figure 1: Typical swarm configuration and different vehicle layouts

The vehicle tecnichal specifications were decided considering the performances of existing AUV and in particular with respect to [7], Tifone specifications involve the capability of exploring extended areas, with an autonomy of more than 12 hours with a cruise and a peak speed of respectively 3-4 and 6-7 knots (orresponding to an estimated travelled distance between 150 and 200 km). The maximum operating depth is about 300 m (plus a 20% of safety margin). Good Maneuverability and hovering capabilities are also mandatory specifications, considering the possibility of performing complex cooperative tasks over the

investigated site, including acoustic inspection and visual recognition. An on-board payload of more than 20 kg of instruments have been considered in the design of the vehicle. Optional-future development will consider the feasibility of external payload, such as a manipulating devices, different kind of sensors or, moreover, micro AUV or ROV can be transported on the mission site by Tifone.

2 ON-BOARD EQUIPMENT AND PAYLOAD

Since every vehicle can be customized to manage different payloads and mission profiles the system was designed by dividing the on-board subsystems in two main categories, as shown in Figure 2 and Figure 4:

- Vital Systems: all the navigation, communication and safety related components and functions of the vehicle are controlled by a rugged industrial PC-104 called Vital PC, whose functionality is continuously monitored by a watchdog system. All the components corresponding to vital functions common to all the Tifone vehicles are directly controlled by the Vital PC. Most of the code implemented on the Vital PC, and consequently the corresponding computational load, is quite invariant with respect to the mission profiles and payloads, assuring a high stability of the system also considering the wide variability of operating conditions.
- Customizable Payloads: all the additional functions related to variable payloads are controlled by one or more Data PC to which all the additional sensors and subsystem are connected. In particular, the Data PC also manages the storage on mass memories (conventional hard discs or solid state memories) and the data coming from the connected sensors. In this way, all the processes introduced by additional payloads are implemented on a platform which is also physically separated from the vital one, and also from an electrical point of view the two parts are protected independently through fuses and relays.

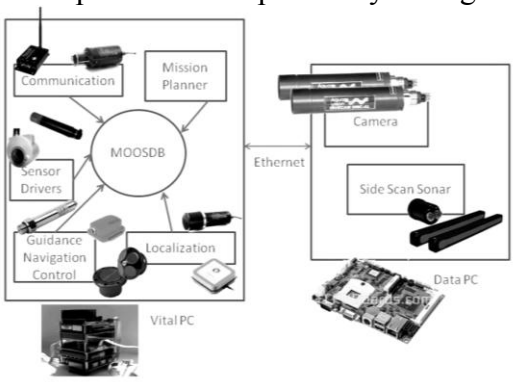


Figure 2: Division between Vital instruments installed on the Vital PC and optional payloads controlled by the Data PC

The on-board integration utilizes MOOS [3] (Mission Oriented Operating Suite) as software infrastructure. MOOS is a publish/subscribe system for inter-process communication (IPC), which supports dynamic, asynchronous, and distributed communication. Its basic functioning, usual in all pub/sub systems, relies on a dispatcher, which is responsible for routing messages from publishers to subscribers. The messages are routed based on their topics, which is an information descriptor contained in the messages themselves. In the case of MOOS the dispatcher is represented by a central database (MOOSDB), which is hence responsible to route the information according to the client registrations, as shown in Figure 3. According to

this paradigm, each process on-board the vehicle will hence be represented by a MOOS client connected to the central database. The main advantage of the chosen software architecture is the easiness of implementing system with distributed intelligence, in which more than one Data PC is used to manage future/optional payloads which have not been taken into account within the original design of the system.

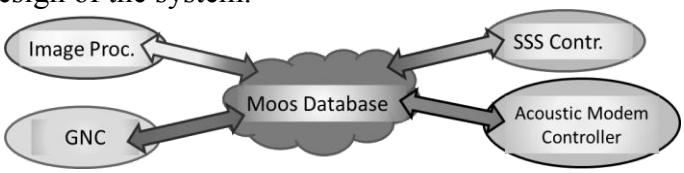


Figure 3: MOOS concept, all the processing (for instance, GNC=Guidance and Navigantion Control) on-board the vehicle connect to the central database which is responsible to route the information according to their registrations

In Figure 4, a simplified scheme of the electric plant is shown: considering the size of the vehicle, including the foreseen propulsion system, a 48V DC bus was chosen for both propulsion and energy storage system. To fed other instruments and sensors 24V DC, 15V DC and 12V DC voltages are provided by suitable DC-DC converters.

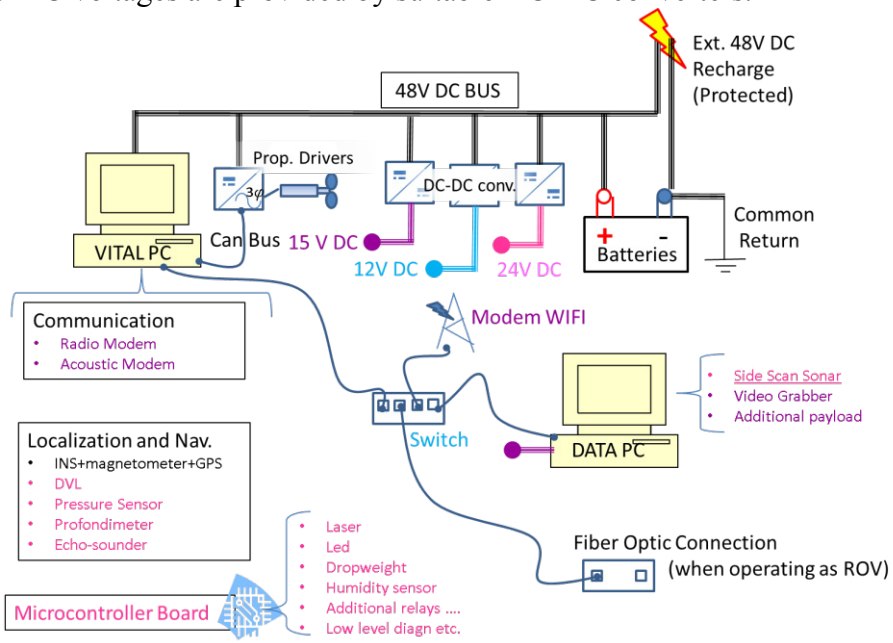


Figure 4: Simplified electric/functional scheme of the plant

2 PRELIMINARY VEHICLE AND SIMULATION MODEL DESCRIPTION

In order to properly size both the propellers and the energy storage system, the dynamical behaviour of the vehicle was reproduced using the approach proposed by [4] which is briefly described by (1):

$$M\dot{\nu} + C(\nu)\nu + D(\nu)\nu + g(\eta) = \tau \tag{1}$$

where vectors τ, η, ν are defined according to Table 1 and the reference system described in Figure 5, matrices *M, C, D* are introduced to model the contributions of the inertial,

Coriolis and viscous effects [8], while vector g represents the combined effects of gravity W and buoyancy B.

Table 1: Reference system (body constrained) and corresponding kinematical/dynamical variables

Degree of freedom	Corresponding Motion	Forces, Torques(τ)	Speed (ν)	Pos.Ang. Coordinates (η)
1	Surge (linear motion along x axis)	X	u	x
2	Sway (linear motion along y axis)	Y	v	y
3	Heave (linear motion along z axis)	Z	w	z
4	Roll (rotation along body x axis)	K	p	ϕ
5	Pitch (rotation along body y axis)	M	q	θ
6	Yaw (rotation along body z axis)	N	r	ψ

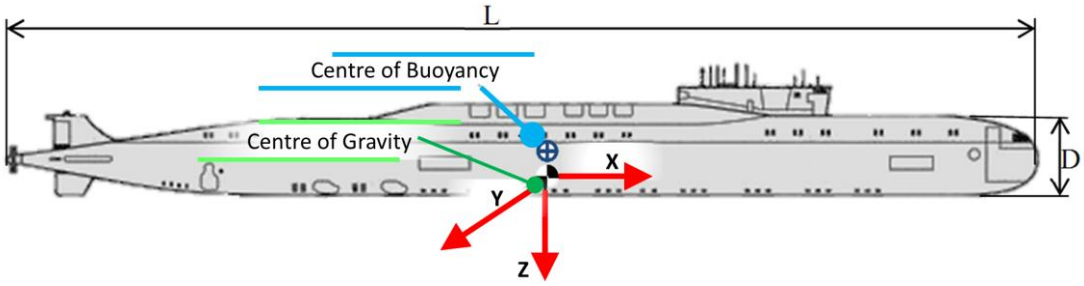


Figure 5: Definition of the body reference system, centres of Buoyancy and Gravity

The values of the coefficients in (1) have been extrapolated considering the results of previous CFD simulations and the know-how available in literature [4],[5],[6],[7].

The calculation of τ is performed considering the layout of the propulsion system which is composed by six actuators: two rear propellers, two lateral and two vertical manoeuvring thrusters (as shown in Figure 6) are used to control 5 DOFs (degrees of freedom) of the vehicle, the three linear translations along x,y,z (surge, sway and heave) and the yaw and pitch rotations. In Table 2 some of the most significant features of the vehicle are also shown.

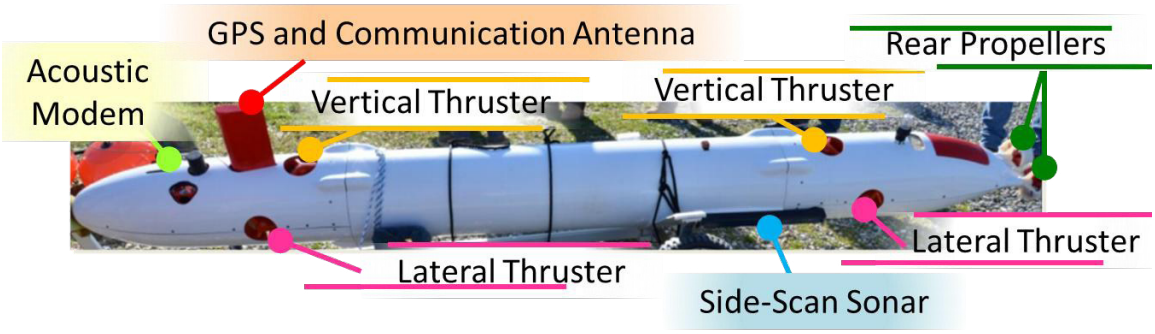


Figure 6: Layout and main components of the Tifone vehicle

Table 2: Main features of Tifone Vehicle

Dimensions (L,D)	Weight in Air /Volume	Speed (cruise, max)	Autonomy (time, trav.distance)	Max Operating Depth
(3.5m, 320mm)	160kg/240dm^3	(2m/s, 3.5-4m/s)	(8-12h, 150-200km)	300m (60m of safety margin)

The propulsion layout, described in Figure 6, is common to some known hybrid glider solutions, such as the italian Folaga [9]. Knowing the six thrusts T_i (i indicates the *i-th* propeller), vector τ is calculated through a constant coefficient matrix R easily evaluated considering static balance considerations (2).

$$\tau = RT; \tag{2}$$

where T is a vector whose scalar components are the efforts T_i exerted by the actuators

The thrust T_i exerted by each actuator is a function of V_{ai}, the relative inlet speed of the fluid and of n_i, the propeller rotational speed. Both rear propellers and thrusters have been assembled in the MDM Lab laboratories: they have been tested and identified in a swimming pool where the bollard thrust of the propeller was evaluated and identified using the experimental layout displayed in Figure 7. Knowing the bollard thrust and the main data of the tested profile, such as the *p/d* ratio between propeller pass *p* and diameter *d*, it is possible to extrapolate for both thrusters and rear propellers a surface, representing the exerted thrust T_i as a tabulated function of the rotation and advance speed n_i and V_{ai} , as reported in Figure 8.

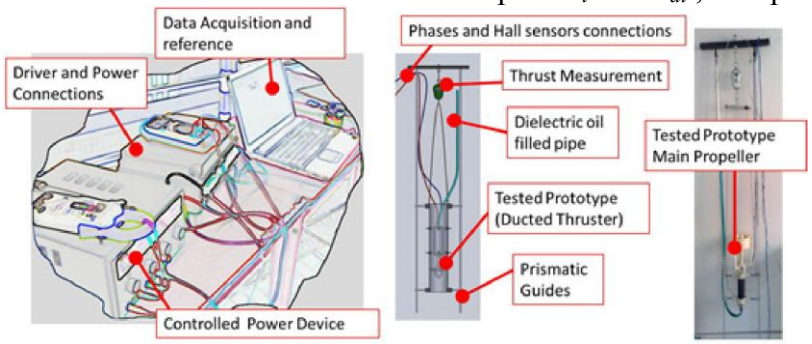


Figure 7: Experimental layout used for the propeller testing

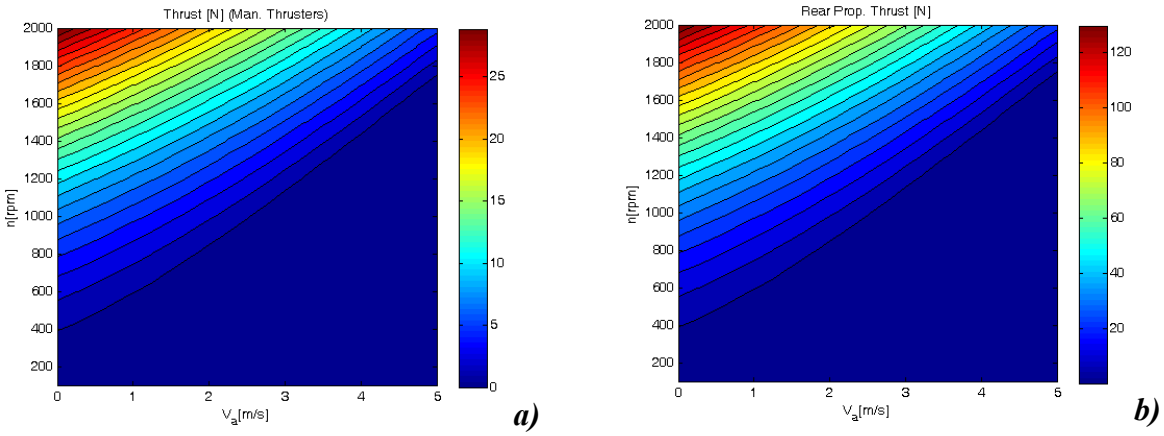


Figure 8: Thruster *a)* and Rear Propeller *b)* thrust as a function of propeller rotational and advance speed (V_a, n), obtained from bollard thrust tests performed in MDM Lab pool of Pistoia (Italy)

The six actuators are supposed to be speed controlled since on Tifone vehicle the chosen PM brushless motors are controlled by a drive which support both current (torque) and speed regulations. A speed loop for motors is chosen mainly for two reasons:

- Both motors and thrusters are sized for maximum performance specifications: during low speed, hovering and precision manoeuvring, the propellers have to exert low efforts at quite low speed with respect to the friction of seals and bearing. In order to avoid a friction influenced cogging behaviour of the thrusters and to avoid parametric uncertainties on low amplitude response of the actuator, speed control was preferred.
- Especially for the rear main propellers an assigned propeller speed roughly corresponds to a known advance speed in steady-state conditions. As consequence, a speed controlled propeller can be more advisable for a precise advance speed control of the vehicle.

To control the vehicle (control the desired vehicle pose η_d starting from the pose estimation η_m) a multi-axis regulator is implemented [8] using five PID type-SISO controllers, each one designed to manage a single DOF of the vehicle, as shown in the scheme of Figure 9. This consideration implies that the extra-diagonal terms of the matrices K_P, K_D and K_I of the PID control law (3) are null, since mutual-cross influences among the controlled axis are neglected.

$$\tau_d = K_P e_r + K_D \dot{e}_r + K_I \int_0^t e dt + g_{rb}(\eta) \tag{3}$$

where $e_r = \eta_d - \eta_m$

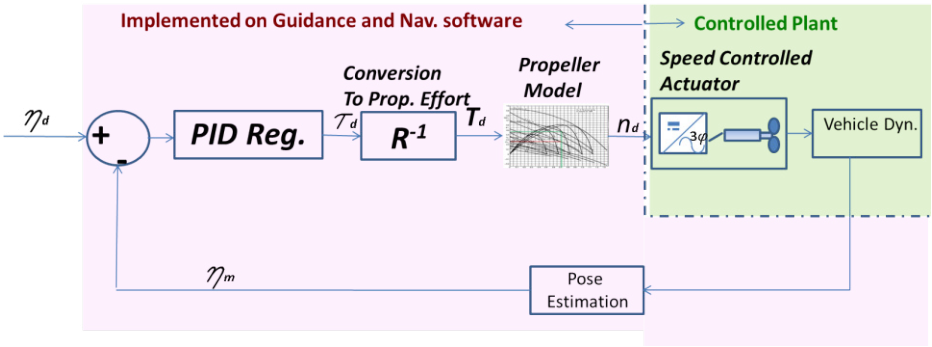


Figure 9: Vehicle control, main components

In (3) it is worth to note the optional feed-forward term $g_{rb}(\eta)$ introduced in order to compensate gravitational and buoyancy contribution.

The output of the regulator is the request of a reference τ_d that have to be converted in reference command for the speed controlled actuators of the propellers. The conversion between the desired effort on the vehicle τ_d and the corresponding speed of propellers is performed using a two stage conversion: first of all, τ_d is converted in the corresponding vector T_d , whose scalar components are the thrust values that have to be exerted by the actuators. Then, from T_d it is possible to evaluate the corresponding desired rotating speeds of each propeller n_d which are used as reference command by the propeller drive system.

Modelling the propeller involves the knowledge of the inlet fluid speed V_a, that, for simulation purposes, was considered as perfectly known/estimated. Since this hypothesis is quite difficult to be verified in real applications, the authors have also considered the case in

which the delivered thrust is roughly estimated as proportional to squared value of propeller speed, through a constant coefficient identified from the bollard thrust experimental tests.
In order to further reduce the energy consumption of the vehicle, in parallel with the regulator described by (3) a static-low bandwidth pitch control is implemented, acting on the longitudinal position of batteries along the hull: the position of vehicle centre of mass can be regulated, limiting the use of manoeuvring thrusters and, consequently, the energy consumption. The related mechanical and implementation schemes are respectively shown in Figure 10 and Figure 11.

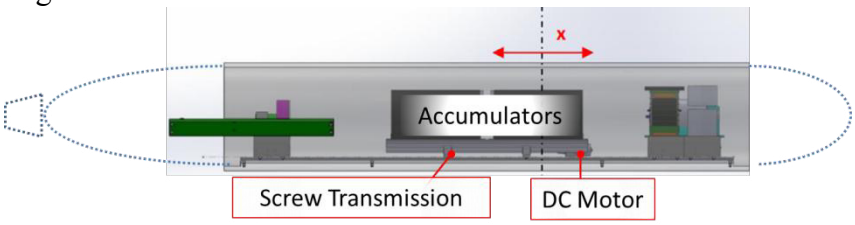


Figure 10: Screw transmission system used to regulate the position of the accumulators and consequently the vehicle center of mass

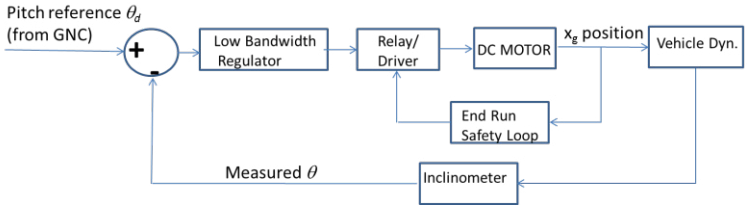


Figure 11: Low frequency pitch control based on the longitudinal translation of batteries

Finally, since one of the main aim of the model was to calculate the energy consumption and conversely to verify the mission autonomy, in the simulation environment the total power consumption W_{tot} is calculated as the sum of elementary contributions W_i of each component, being the i the index corresponding to the *i-th* component or subsystem:

$$W_{tot} = \sum_{i=1}^{n} W_i \tag{4}$$

In particular W_i contributions associated to the propellers are calculated from tabulated functions of the propeller rotation and advance speed which have been extrapolated from experimental activities in the MDM Lab pool. For other components, such as sensors or computers, the related consumptions are evaluated in terms of functional states such as *component switched off*, *idle* or *fully working* to which an energy consumption is assigned according to their technical documentation (and verified through the preliminary laboratory activities).

3 PRELIMINARY SIMULATION AND VERIFICATION OF PROPULSION AND ENERGY STORAGE SYSTEM

Using the previously described model it was possible to simulate close to realistic mission profiles, in which the corresponding energy consumptions have been verified, as in the example of Figure 12, where a simple zig-zag path following is represented.

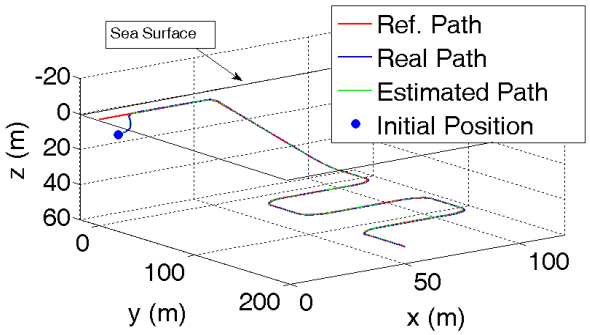
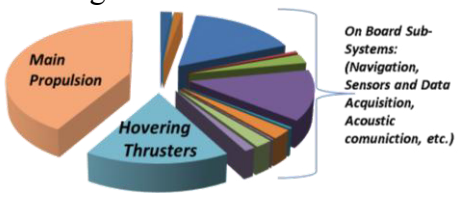
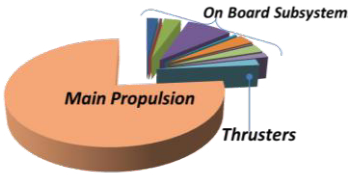


Figure 12 Example of the simulation of a short range mission [8]

Since the simulation of a complete mission of 8-12 hours could be quite heavy in terms of computational resources, the following approach was applied:

- Compiled/not interpreted code: all the simulation code was written in order to support compilation for a generic fast simulation target (e.g. rsim.tlc / matlab rapid simulation target); in this way it is possible to greatly increase the efficiency of the code, also considering simulations of thousands of seconds of equivalent time.
- Assembling of Simple Simulation Scenarios: the simulation of complex operative scenarios was divided in a population of shorter and simple case studies, that were used to calculate the mean consumption profiles associated to each specific task. In this way it is possible to evaluate the mission consumption as a time weighted mean of individual consumption profiles, previously established and calculated. As regards the worst case conditions, related to exceptional power demands, some results are shown in Figure 13.





a) ***b)***

Figure 13: Simulated energy consumptions with worst condition scenarios, such as exploration and hovering on a site with a 1.5 knots current disturbance *(a)* or fast transfer at maximum speed to an interesting site *(b)*

It is also possible to evaluate a penalty map in terms of power demand W_e with respect to the cubic value of the advance speed V_a , useful for many future feasible purposes, e.g. optimization of vehicle control strategies. Moreover, considering pure translations of the vehicle, it is possible to calculate the value of the optimal advance speed v_{opt} with respect to traveling direction, which maximizes the vehicle autonomy to the travelled distance, considering a fixed cautious power consumption of the installed components of about 200 W. The results shown in Figure 14 and Figure 15 have been obtained under the hypothesis that the thrusters have a behaviour which is not dependent from their rotation sense; this

hypothesis is almost true for maneuvering thrusters since they adopt a symmetric blade propellers which were optimized for this purpose during the experimental activities. Concerning the main rear propellers, the behaviour in both sense of rotation was also verified with the experimental tests in the MDM Lab pool confirming their asymmetric behaviour, due to blade profiles and to the applied accelerating nozzle (19-A).
Even considering the asymmetric behaviour of the rear propellers the obtained results are quite symmetric with respect to the ordinate axis, since the shape of the obtained functions seem to be more influenced by the corresponding distribution of the hydrodynamic resistances.

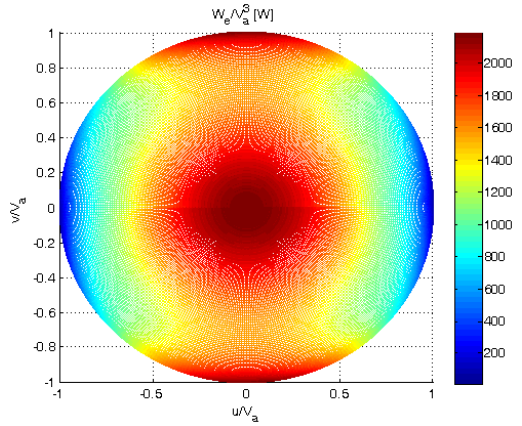


Figure 14: Distribution of the required electric power with respect to the cube of the advance speedconsidering pure translations

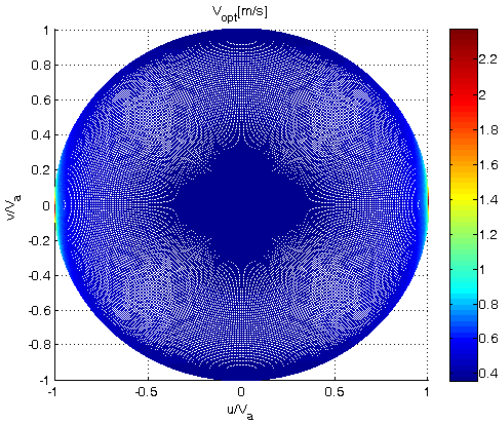


Figure 15: Calculated value of v_{opt} maximizing the vehicle autonomy with respect to travelling direction

From the simulation results it is possible to verify the correct sizing of both the propulsion and energy storage systems, which is composed by two Li-Po accumulators, each one able to deliver 40Ah of DC currents at 48V for a total stored energy of about 4kWh (suitable to largely satisfy the autonomy and speed specifications described in Table 2).

CONCLUSIONS

In this paper some preliminary simulation and testing activities concerning the design of an Autonomous Underwater Vehicle, briefly called Tifone, for the Thesaurus project, are described. Since the vehicle has been successfully assembled, the preliminary testing activities have started at Roffia lake (San Miniato, Pisa, Italy, Figure 16).
The preliminary results are quite encouraging: in particular, the functionality of guidance and navigation systems have been successfully debugged, making possible the execution of simplified mission profiles, including acoustic communication and localization.
The next testing activities will mainly deal with an improved identification of vehicle performances, scheduled forthe month of April 2013.

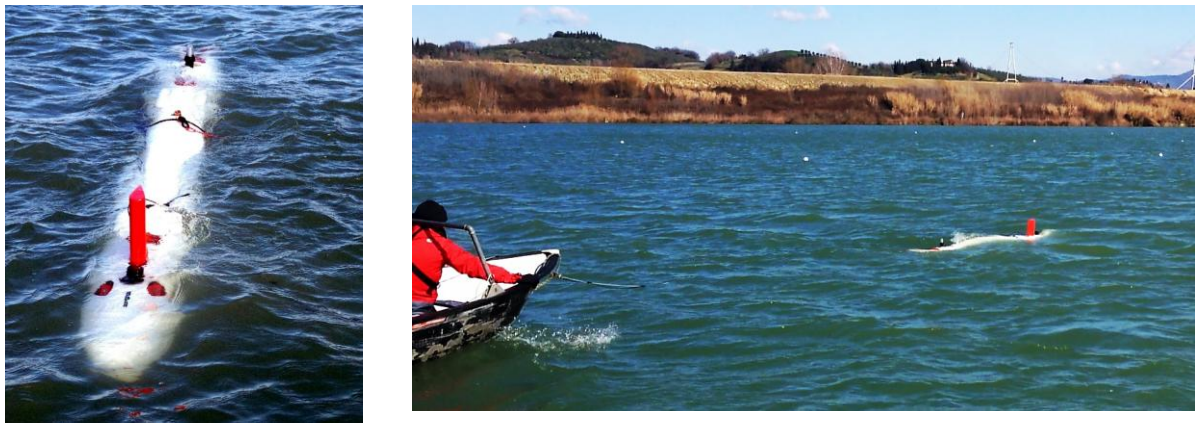


Figure 16: Tifone vehicle during its preliminary testing activities in the basin of Roffia (San Minato, Pisa February 2013) working both as AUV (Autonomous Underwater Vehicle) and ROV (Remotely Operated Vehicle)

ACKNOWLEDGMENTS

The object of this work is within the framework of the Thesaurus Project (http://thesaurus.isti.cnr.it/) which has been financed by Regione Toscana as part of PAR FAS REGIONE TOSCANA Linea di Azione 1.1.a.3.
The authors wish to thank all the partners of the project and in particular Professor Andrea Caiti. Finally for the active support in manufacturing and testing the authors want to remember Vito Balducci (Technowave Srl, the manufacturer of most of the structural parts) and the people of CMRE (Centre for Maritime Research and Experimentation) both sited in la Spezia, Italy.

REFERENCES

[1] Allotta B., Pugi L., Costanzi R., Vettori G., Localization algorithm for a fleet of three AUVs by INS, DVL and Range measurements, The 15th International Conference On Advanced Robotics , Tallinn, June 20-23 2011.
[2] Cairns J., Larnicol E., Ananthakrishnan P., Smith S., Dunn S., Design of AUV propeller based on a blade element method, OCEANS '98 Conference Proceedings , pp. 672-675, vol.2, 1998.
[3] The Oxford robotic group, The Mission Oriented Operating Suite, (doc. available on line).
[4] T.I. Fossen, Guidance and Control of Ocean Vehicles, I° Edition , UK: John Wiley and Sons 1994.
[5] Xianzhao Yu, Yumin Su, Hydrodynamic performance calculation on mini-automatic underwater vehicle, Proceedings of the 2010 IEEE International Conference on Information and Automation June 20 - 23, Harbin, China.
[6] P. Jagadeesh, K. Murali, V.G. Idichandy, Experimental investigation of hydrodynamic force coefficients over AUV hull form, Journal of Ocean Engineering 36, pp. 113–118, 2009.
[7] Peter Michael Ostafichuck, AUV Hydrodynamics and modelling for improved control, PhD Thesis at University of British Coulombia, 1997.

[8] B. Allotta, R. Costanzi, N. Monni, L. Pugi, A. Ridolfi and G. Vettori, Design and Simulation of an Autonomous Underwater Vehicle, European Congress on Computational Methods in Applied Sciences and Engineering, ECCOMAS 2012, Vienna, Austria, September 10-14, 2012.
[9] Caffaz A., Caiti A., Casalino G., Turetta A., The Hybrid Glider-AUV Folaga, Robotics and Automation Magazine IEEE , Vol. 17, Issue 1, March 2010.

V International Conference on Computational Methods in Marine Engineering
MARINE 2013
B. Brinkmann and P. Wriggers (Eds)

NON-STATIONARY PROBABILITY OF PARAMETRIC ROLL OF SHIPS IN RANDOM SEAS

Leo Dostal* **and Edwin Kreuzer***

*Institute of Mechanics and Ocean Engineering
Hamburg University of Technology
Eissendorfer Strasse 42, 21071 Hamburg, Germany
email: dostal@tuhh.de, web page: http://www.mum.tuhh.de

Key words: Random Seas, Ship Dynamics, Parametric Roll

Abstract. We analyze the problem of parametric roll in random seas, where the random wave excitation is modeled by a non-white stationary stochastic process. This process is derived from a spectral description of the random seaway using a traveling effective wave. The method of stochastic averaging is applied, such that the fast oscillatory dynamics of roll is averaged over the roll period. This procedure yields equations for the drift and diffusion of the roll energy. With these equations the non-stationary probability density of roll energy is obtained by solving the corresponding Fokker-Planck equation using a finite difference approach. The results can be used to improve ship hull design as well as for controller design to encounter the occurrence of parametric roll resonance.

1 INTRODUCTION

Modern ships designed towards maximal cargo capacity are endangered by the sudden appearance of large amplitude roll motions as a result of parametric roll resonance. The roll restoring moment of these ships changes oscillatory in head or following waves. This is because the bow and stern areas are submerged deeper and the midship area is less submerged in wave trough compared to wave crest amidships, where the buoyancy is dominated by the midship area. It is a well-known fact, that resonance of roll motion due to parametric excitation is possible, if the wave encounter frequency is about twice the eigenfrequency of roll [1].
In Section 2 we state the underlying equations of motion for the problem of parametric roll in random seas, where the random wave excitation is modeled by a non-white stationary stochastic process. In order to find a lower dimensional description for the parametric roll dynamics, the method of stochastic averaging is applied in Section 3, such that the fast oscillatory dynamics of roll is averaged over the roll period. This procedure results in equations for the drift and diffusion of the roll energy, which have been obtained in [2].

With these equations the probability density of roll energy is obtained in Section 4 by solving the corresponding Fokker-Planck equation. Before we summarize our results, we perform sample calculations of the proposed probabilistic methods for a modern RoRo ferry in Section 5.

2 EQUATIONS OF ROLL MOTION

The roll behavior of a ship can be represented by the following equation if heave and pitch motions are small

$$(I_{xx} + A_{xx})\ddot{\Phi}(t) + b_1\dot{\Phi}(t) + b_3\dot{\Phi}(t)^3 + g\Delta GZ(\Phi, t) = M(t). \tag{1}$$

Here, I_{xx} is the roll moment of inertia, A_{xx} is the hydrodynamic added mass evaluated at the natural frequency ω_n, b_1, and b_3 are linear and cubic damping coefficients, g is the acceleration due to gravity, and Δ is the displacement. In this work we study parametric roll, which occurs when the ship travels in about the same direction as the incident waves. In this case the roll excitation moment M is small and can be well approximated by

$$M_{app}(t) = q_4\xi_t. \tag{2}$$

The Gaussian random process ξ_t is derived from a spectral description of the random seaway using a traveling effective wave [3, 2]. Furthermore, the righting lever GZ is approximated by the nonlinear time variant function

$$GZ_{app}(\Phi, t) = q_1\Phi(t) + q_2\Phi(t)^3 + q_3\xi_t\Phi(t). \tag{3}$$

Considering a moving ship with mean speed U in waves that approach from an angle χ with respect to the ship's forward direction, the frequency of wave encounter ω_e in the ship fixed frame is

$$\omega_e = \omega - \kappa(\omega)U\cos\chi, \tag{4}$$

where $\kappa(\omega)$ is the wave number. The transfer function of the traveling effective wave with length L is

$$f_c(\omega) = \frac{L\kappa(\omega)\sin\left(\frac{L}{2}\kappa(\omega)\right)}{\pi^2 - \left(\frac{L}{2}\kappa(\omega)\right)^2}. \tag{5}$$

From the one sided sea state spectral density $S(\omega)$, we obtain the spectral density $S_{\xi_t\xi_t}(\omega)$ of the random process ξ_t as

$$S_{\xi_t\xi_t}(\omega) = 2S(\omega_e)f_c(\omega)^2. \tag{6}$$

This defines the random process ξ_t owing to excitation by random seas, which is used in equations (2) and (3). We introduce the small parameter $\varepsilon << 1$. After rescaling and transformation of equation (1), with $t = \varepsilon t_\varepsilon$, we obtain the system

$$\begin{aligned} &\frac{d}{dt_\varepsilon}x = y, \\ &\frac{d}{dt_\varepsilon}y = -\alpha_1 x + \alpha_3 x^3 - \varepsilon(\beta_1 y + \beta_3 y^3) + \sqrt{\varepsilon}(\nu_1 + x\nu_2)\xi_{t_\varepsilon}. \end{aligned} \tag{7}$$

Parametric roll has dominant Hamiltonian dynamics due to small hydrodynamic forces compared to the total energy of the dynamical system. Therefore, the fast oscillatory dynamics on constant energy levels can be separated from the slow dynamics of total energy change across the energy levels of the Hamiltonian system. The total energy of roll dynamics is defined by the Hamilton function

$$H(x,y) := \frac{y^2}{2} + \alpha_1 \frac{x^2}{2} - \alpha_3 \frac{x^4}{4}, \tag{8}$$

and the change of the total energy owing to damping and excitation is the time derivative of the Hamilton function

$$\frac{d}{dt_\varepsilon} H = \varepsilon y^2(-\beta_1 - \beta_3 y^2) + \sqrt{\varepsilon} y(\nu_1 + x\nu_2)\xi_{t_\varepsilon}. \tag{9}$$

Now we can reformulate the system of equations (7) in terms of the fast oscillatory variable x and the slowly varying roll energy H

$$\begin{aligned} \frac{d}{dt_\varepsilon} x &= \sqrt{Q(x,H)}, \\ \frac{d}{dt_\varepsilon} H &= \varepsilon Q(x,H)(-\beta_1 - \beta_3 Q(x,H)) + \sqrt{\varepsilon}\sqrt{Q(x,H)}(\nu_1 + x\nu_2)\xi_{t_\varepsilon}, \end{aligned} \tag{10}$$

where the variable y was eliminated by using

$$Q(x,H) := y^2 = 2H - \alpha_1 x^2 + \alpha_3 \frac{x^4}{2}. \tag{11}$$

In the next section the multiple time scale property of the above system is used to further reduce the dimension from two to one.

3 EQUATION FOR ROLL ENERGY

In order to determine a lower dimensional description for the parametric roll dynamics, the method of stochastic averaging is applied, such that the fast oscillatory dynamics of roll is averaged over the roll period. This procedure yields equations for the drift and diffusion of the roll energy. Stochastic averaging of system (10) was proposed in [2]. As a result, the roll energy $H \in [0; H_c]$, converges weakly, as $\varepsilon \to 0$, to the one dimensional Itô equation

$$dH = m(H)dt + \sigma(H)dW_t, \tag{12}$$

with drift

$$\begin{aligned} m(H) =& \frac{4}{Tq} \int_{-\infty}^{0} R_{\xi_t \xi_t}(\tau) \int_0^{K(k)} \left(b^2\nu_2^2 \mathrm{sn}\,\mathrm{sn}_{t+\tau} + \nu_1^2\right) \frac{\mathrm{cn}_{t+\tau}\mathrm{dn}_{t+\tau}}{\mathrm{cn}_t \mathrm{dn}_t} du\, d\tau + \\ &+ \frac{1}{T} \int_0^T Q(x(t),H)(-\beta_1 - \beta_3 Q(x(t),H))dt \end{aligned} \tag{13}$$

and diffusion

$$\sigma^2(H) = \frac{4b^2q}{T} \int_{-\infty}^{\infty} R_{\xi_t\xi_t}(\tau) \int_0^{K(k)} \mathrm{cn}\,\mathrm{dn}\,\mathrm{cn}_{t+\tau}\,\mathrm{dn}_{t+\tau}(\nu_1^2 + b^2\nu_2^2 \mathrm{snsn}_{t+\tau})\,du\,d\tau, \tag{14}$$

where $R_{\xi_t\xi_t}$ is the autocorrelation function of the stochastic process ξ_t. H_c is the energy level corresponding to the roll angle of vanishing stability, which is

$$H_c = \alpha_1^2/4\alpha_3 \tag{15}$$

in our case. For each energy level H the roll period is given by

$$T = \frac{4}{q}K(k), \tag{16}$$

where

$$q = a\sqrt{\frac{\alpha_3}{2}}, \qquad a = \sqrt{\frac{4H}{b^2\alpha_3}}, \tag{17}$$

and b is the roll amplitude for each fixed roll energy H

$$b = \sqrt{\frac{\alpha_1 - \sqrt{\alpha_1^2 - 4\alpha_3 H}}{\alpha_3}}. \tag{18}$$

In equations (13) and (14), we use the abbreviations

$$\mathrm{sn} := \mathrm{sn}(qt,k),\ \mathrm{cn} := \mathrm{cn}(qt,k),\ \mathrm{dn} := \mathrm{dn}(qt,k),\ u := qt. \tag{19}$$

If the subscript τ or $t+\tau$ is used, we refer to the argument $q\tau$ or $q(t+\tau)$, respectively. Furthermore, the function $K(k)$ is the complete elliptic integral of the first kind, and $\mathrm{sn}(\cdot,k)$, $\mathrm{cn}(\cdot,k)$, $\mathrm{dn}(\cdot,k)$ are Jacobian elliptic functions, cf. [4]. The elliptic modulus k is given by

$$k = \frac{b}{a}. \tag{20}$$

Numerical evaluation of $m(H)$ and $\sigma^2(H)$ is possible but not efficient. Therefore, in [2] a closed form solution of equations (13) and (14) in terms of complete elliptic integrals is calculated.

4 PROBABILITY DENSITY OF ROLL ENERGY AND FINITE DIFFERENCE DISCRETIZATION

The roll energy H in the interval $[0; H_c]$ is the solution of the stochastic differential equation (12). Therefore, H is a random variable for each fixed time t. Let us denote the time variant probability density of the roll energy H as $p(H,t)$. Then, $p(H,t)$ is the solution of the following Fokker-Planck equation

$$\frac{\partial}{\partial t}p(H,t) = -\frac{\partial}{\partial H}[m(H)p(H,t)] + \frac{1}{2}\frac{\partial^2}{\partial H^2}[\sigma^2(H)p(H)]. \tag{21}$$

The initial condition at $t = 0$ has to be a scalar function $f_0 : [0; H_c] \mapsto \mathbb{R}^+$ with $\int_0^{H_c} f_0(H)\mathrm{d}H = 1$

$$p(H, 0) = f_0(H). \tag{22}$$

The boundary conditions are a no-flux boundary condition at $H = 0$ and a Dirichlet boundary condition at $H = H_c$. These conditions are

$$p(0,t)\left(-m(0) + \frac{1}{2}\frac{\mathrm{d}}{\mathrm{d}H}\sigma^2(0)\right) + \frac{1}{2}\sigma^2(0)\frac{\partial}{\partial H}p(0,t) = 0, \qquad p(H_c, t) = 0. \tag{23}$$

From the probability density $p(H, t)$ of energy level, we can calculate the probability density $p_b(b, t)$ of roll amplitude b, using the probability density transformation

$$p_b(b,t) = p(H,t)\left(\frac{d}{dH}b\right)^{-1}. \tag{24}$$

We use centered differences in space for the finite difference representation of equation (21). The roll energy interval $[0; H_c]$ is discretized into $N - 1$ equidistant sub-intervals of length $\Delta H := H_c/(N - 1)$. Then the nodes of the finite difference scheme are $H_n = (n - 1)\Delta H$, $n = 1, 2, \ldots, N$. Analogically, the time interval $[0; t_f]$, where $t_f \in \mathbb{R}$ is the final time, is discretized into $M - 1$ equidistant sub-intervals $\Delta t := t_f/(M - 1)$ with nodes $t_j = (j - 1)\Delta t$, $j = 1, 2, \ldots, M$. We have chosen the Cranck-Nicholson method for integration in time, which is stable for arbitrary choices of ΔH and Δt and ensures second order convergence in time. We have a no-flux boundary condition at $H = 0$ and a Dirichlet boundary condition at $H = H_c$. In the no-flux boundary condition at $H = 0$, we approximate $\frac{\partial}{\partial H}p(0, t)$ by a second order forward difference in space.

5 SAMPLE CALCULATIONS FOR A MODERN RORO FERRY

In this section we demonstrate the application of the probabilistic methods from the preceding sections. Our sample calculations are performed for a modern RoRo ferry [5, 6]. The Body plan of this RoRo ferry is shown in Fig. 1. Due to its cargo stowage optimized bulky hull shape with large flare above the still water line, the change in righting lever from wave trough to wave crest condition is significant, see Fig. 2. Thus, this RoRo ferry is expected to be vulnerable to parametric roll resonance. Relevant data of the RoRo ferry are summarized in Tables 1 and 2.

To begin with, we need to identify the excitation process ξ_t due to random seas and determine its autocorrelation function $R_{\xi_t\xi_t}$, which is needed for the calculation of drift $m(H)$ and diffusion $\sigma^2(H)$ in equations (13) and (14). We approximate the effective wave spectrum by

$$S_{\xi_t\xi_t}(\omega) = \frac{1}{2\pi}\frac{b_0^2\omega^2}{a_1^2\omega^2 + (a_2 - \omega^2)^2}, \tag{25}$$

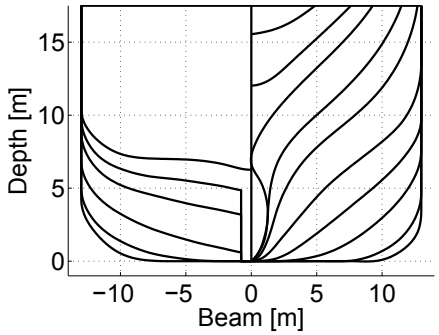


Figure 1: Body plan of the RoRo ferry.

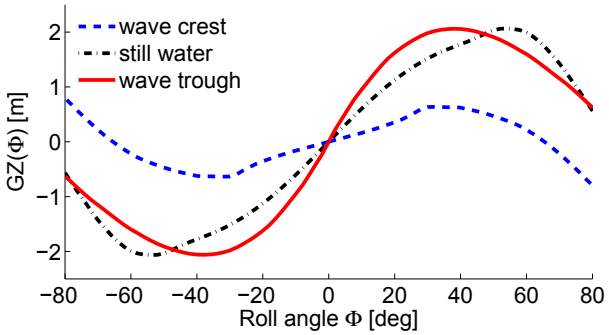


Figure 2: Righting lever GZ of the RoRo ferry.

Table 1: Parameter values of RoRo ferry [6].

Length btw. perpendiculars	L	173.00	m
Displacement	Δ	$16,800$	t
Natural frequency of roll	ω_n	0.515	rad/s
Moment of inertia and added mass	$I_{xx} + A_{xx}(\omega_n)$	$2.20\,10^6$	$\mathrm{t\,m^2}$
Linear damping coefficient	b_1	$1.99\,10^5$	$\mathrm{kN\,m\,s}$
Cubic damping coefficient	b_3	$2.11\,10^6$	$\mathrm{kN\,m\,s^3}$

Table 2: RoRo ship coefficients.

$\varepsilon = .1$	$\alpha_1 = 26.5$	$\alpha_3 = 11.59$	$\beta_1 = 9.046$	$\beta_3 = .959$	$\nu_1 = .8285$	$\nu_2 = 8.285$

Table 3: Parameters of excitation process ξ_t.

Sea state spectrum type	H_s	ω_m	L	U	a_1	a_2	b_0
Pierson-Moskowitz	10 m	0.64 rad/s	170 m	15 kn	0.2874	0.8868	2.0587
JONSWAP	13 m	0.64 rad/s	170 m	9.7 kn	0.1356	0.9292	2.1040

then the autocorrelation function of the Gaussian random process ξ_t is

$$R_{\xi_t\xi_t}(\tau) = -\sum_{i=1}^{2} e^{\mu_i|\tau|}\frac{b_0^2\mu_i^2}{(2\mu_i + a_1)(\mu_i^2 - a_1\mu_i + a_2)}, \quad \mu_{1,2} = -\frac{a_1}{2} \pm \sqrt{\left(\frac{a_1}{2}\right)^2 - a_2}. \tag{26}$$

The coefficients a_1, a_2, and b_0 for two different sea states are given in Table 3.

For the computation of the non-stationary probability density $p(H,t)$ by means of the finite difference scheme from Section 4, we have to use a very fine discretization of the energy interval $[0; H_c]$, since the probability density $p(H,t)$ increases and decreases very fast near $H = 0$. Therefore, we use $N = 640000$ grid points, which leads to a very small $\Delta H = 2.3668 \times 10^{-05}$. We start the finite difference scheme with the following normalized initial condition

$$p(H,0) = \begin{cases} 1 - \cos(2\pi H), & \text{if } 0 \leq H \leq 1, \\ 0, & \text{if } 1 < H \leq H_c. \end{cases}$$

In Fig. 3 the non-stationary probability density $p_b(b,t)$ of roll amplitude is shown for

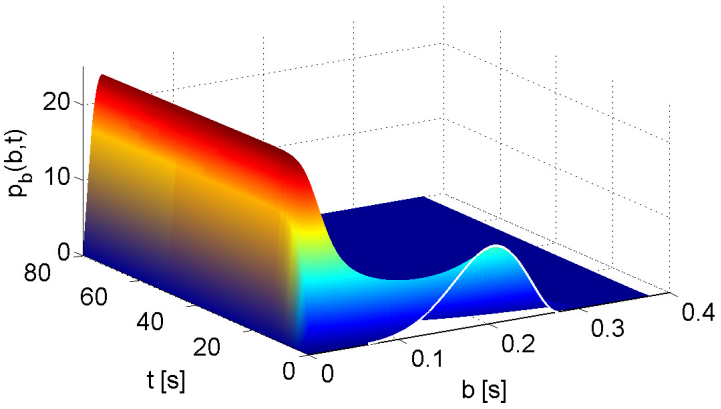


Figure 3: Non-stationary probability density $p_b(b,t)$ for sea state due to the Pierson-Moskowitz spectrum.

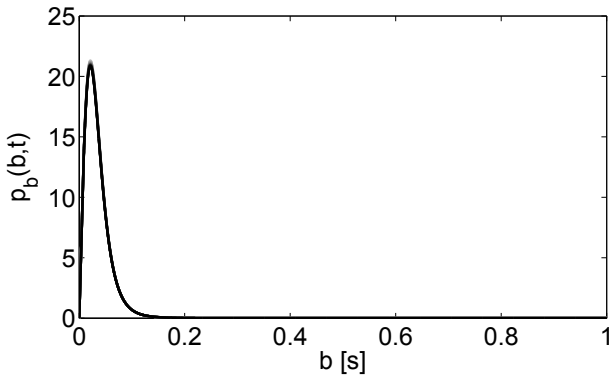


Figure 4: Probability density $p_b(b,t)$ for Pierson-Moskowitz sea state plotted from $t = 25s$ in light gray to $t = 80s$ in black. The gray lines are overlaid by the black lines, since the probability density converges to an almost stationary shape.

the Pierson-Moskowitz sea state from Table 3. After $t = 15s$ the transient change is gone and the probability density converges to an almost stationary shape. The decay of the probability density is almost not visible in Fig. 4, where $p_b(b,t)$ is plotted from $t = 25s$ in light gray to $t = 80s$ in black. We observe significant decay of the non-stationary probability density $p_b(b,t)$ over time for the forcing due to the JONSWAP sea state from Table 3. The reason is, that the probability flux (i.e. probability current) out of the domain $[0; H_c]$ is not small at $H = H_c$. The decay of the probability density for the

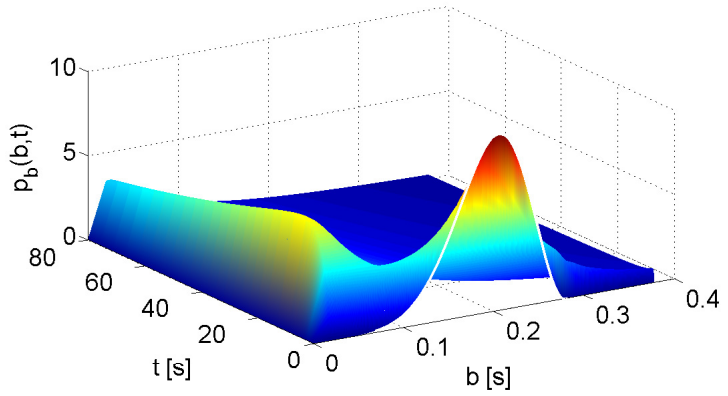


Figure 5: Non-stationary probability density $p_b(b,t)$ for sea state due to the JONSWAP spectrum.

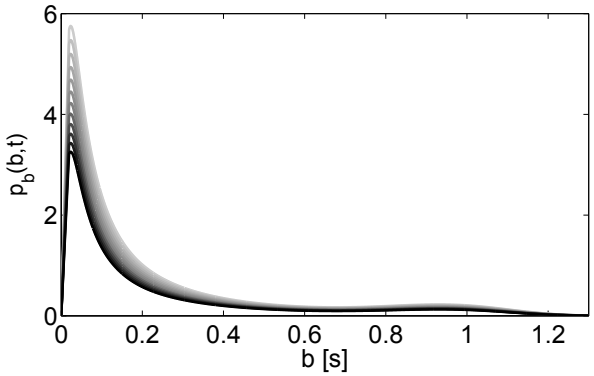


Figure 6: Probability density $p_b(b,t)$ for JONSWAP sea state plotted from $t = 25s$ in light gray to $t = 80s$ in black.

JONSWAP sea state is visualized very well in Fig. 6, where $p_b(b,t)$ is again plotted from $t = 25s$ in light gray to $t = 80s$ in black.

6 SUMMARY AND CONCLUSION

We have calculated the time variant probability densities of roll amplitudes of a RoRo ferry in two different sea states by means of the finite difference Method. The first sea state was given by a Pierson-Moskowitz spectrum with a significant wave height of 10 meters. This sea state led to significant roll oscillations and the corresponding probability density converged to an almost stationary shape. The second analyzed sea state was given by a JONSWAP spectrum with a significant wave height of 13 meters. The non-stationary behavior of probability density of roll amplitude was significant in that case. The probability density decayed very fast with time, due to high probability flux out of the computation domain. We can conclude, that the finite difference method is suitable for the calculation of the non-stationary probability density of roll amplitude, where the drift and diffusion is obtained by means of the stochastic averaging method.

Acknowledgement The authors are indebted to the DFG (Deutsche Forschungsgemeinschaft/German Research Foundation) for funding the project under contract Kr 752/31-1.

References

[1] W. N. France, M. Levadou, T. W. Treakle, J.R. Paulling, R. K. Michel, and C Moore. An investigation of head-sea parametric rolling and its influences on lashing systems. *Mar Technol SNAME N*, 40:1–19, 2003.

[2] L. Dostal, E. Kreuzer, and N. Sri Namachchivaya. Non-standard stochastic averaging of large amplitude ship rolling in random seas. *Proc. R. Soc. A*, 468(2148):4146–4173, 2012.

[3] G. Bulian. On an improved Grim effective wave. *Ocean Engineering*, 35(17–18):1811–1825, 2008.

[4] P. F. Byrd and M. D. Friedman. *Handbook of elliptic integrals for engineers and scientists*. B. G. Teubner, Berlin, 1954.

[5] P. C. Sames, G. K. Kapsenberg, and P. Corrignan. Prediction of bow door loads in extreme wave conditions. In *Design and operation for abnormally conditions*, London, 2001. RINA.

[6] E. Kreuzer and W. Sichermann. Prediction of extreme ship motions in irregular waves. In *5th EUROMECH Nonlinear Dynamics Conference*, Eindhoven, 2005.

V International Conference on Computational Methods in Marine Engineering
MARINE 2013
B. Brinkmann and P. Wriggers (Eds)

NUMERICAL STUDY OF TWO OLYMPIC RACING CANOES IN PRESENCE OF LATERAL WIND

M. HAMDAOUI †, Y. ROUX †, E. JEAN‡, R. DUVIGNEAU #, J.-C. GONNEAUD★ and F. DURING★

† K-Epsilon Company - Espace Antipolis
300 route des crêtes - CS 70116 06902 Sophia Antipolis
Email: yann@k-epsilon.com - Web page: http://www.k-epsilon.com

‡ Jean et Frasca Design, 9,Rue Plan Fourmiguier,
13007 Marseille, France
Email: jfdesign@free.fr - Web page: http://www.jean-et-frasca.com

#INRIA Sophia Antipolis, Opale Project-Team,
Email: regis.duvigneau@inria.fr - Web page: http://team.inria.fr/opale

★ Fédération Française de Canoë-Kayak, 87 quai de la Marne
94340 Joinville le Pont Cedex
Email: ffck@ffck.org - Web page: http://www.ffck.org

ABSTRACT

The objective of this study is to perform a comparative study of the performance of two Olympic racing-canoes in the presence of lateral wind. This collaborative work gathers some experimental measurements of the ship kinematics and geometrical model, numerical simulations for both aerodynamic and hydrodynamic effects and a mechanical analysis of the performance.

A high-fidelity Computational Fluid Dynamics (CFD) solver has been used for steady and unsteady aerodynamic and hydrodynamic simulations, including turbulence and free-surface effects, for different wind conditions. Experimental measures, carried out during real races, allowed to use a realistic kinematic model for the ship movements.

Results are considered to provide a mechanical analysis of the two racing-canoe performances and provide practical advises for different wind conditions.

1 INTRODUCTION

1.1 Presentation of the project

A project consortium composed of the French Canoe Kayak Federation (FFCK), the naval architecture company Jean & Frasca, the K-Epsilon company and INRIA has been set up to compare the performances of two Olympic racing-canoes, denoted here “Plastex” and “Quattro” in the case of unfavourable lateral wind conditions. Jean & Frasca was responsible

for the geometrical analysis of the two racing-canoe hulls, while the K-Epsilon company was in charge of studying the hydrodynamics and aerodynamics of the problem using CFD tools. FFCK provided some experimental measurements of canoe kinematics in real wind conditions. INRIA partner ensured the project coordination.

1.1 Physical description of the problem

We provide hereafter a description of the physics associated with the racing-canoe advancing with a lateral wind. Figure 1 depicts the racing-canoe advancing in straight line. The canoeist exerts a force Fp on his paddle resulting on a propelling force Rp. As the racing-canoe advances at a velocity Vx, a yaw moment MRp appears due to the offset between the force application point and the boat symmetry plane. To keep advancing in straight line, the canoeist has to counter this moment with his paddle while a force Fxhydro is exerted on the racing-canoe at the bow or well forward the bow.

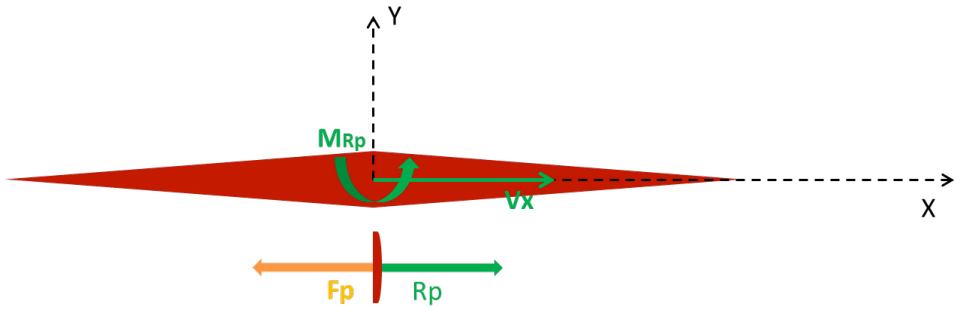


Figure 1 Efforts on the racing-canoe

In windy conditions, the canoeist is submitted to the action of an aerodynamical force Fvent. Its Y-component Fyvent creates a drift velocity Vy that modifies the velocity vector of the racing-canoe that becomes (Vx , Vy) as can be seen on Figure 2. As a result of this drift motion, an hydrodynamical force Fhydro develops on the hull as can be seen on Figure 3.

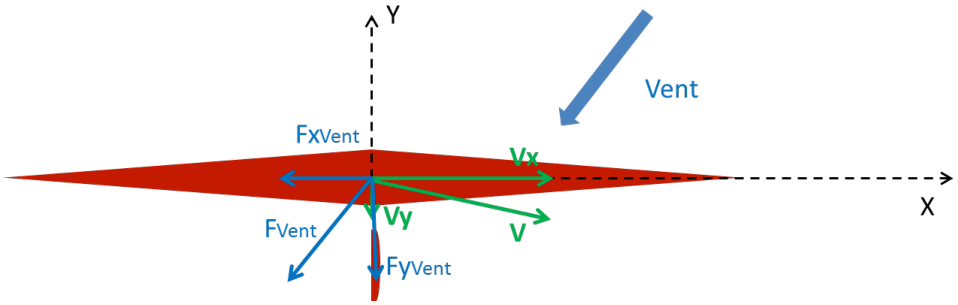


Figure 2 Aerodynamical forces and velocities in portside wind conditions

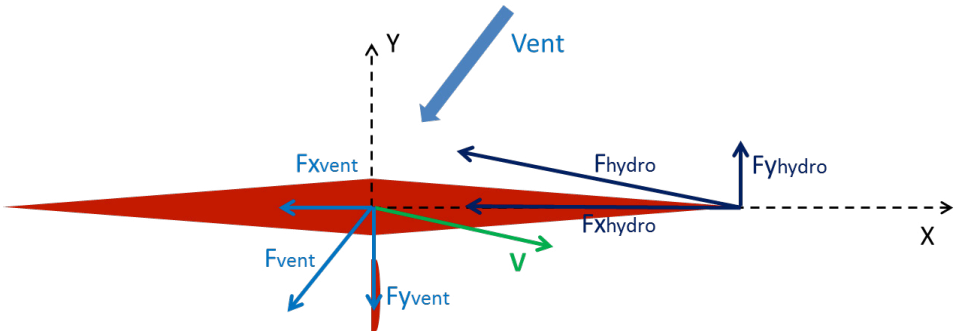


Figure 3 Aerodynamical and hydrodynamical forces and velocities in portside wind conditions

As the forces Fyhydro and Fyvent do not have the same application point, an additional yaw moment is created putting the canoeist in a more difficult position to keep advancing in straight line as can be seen on Figure 4.

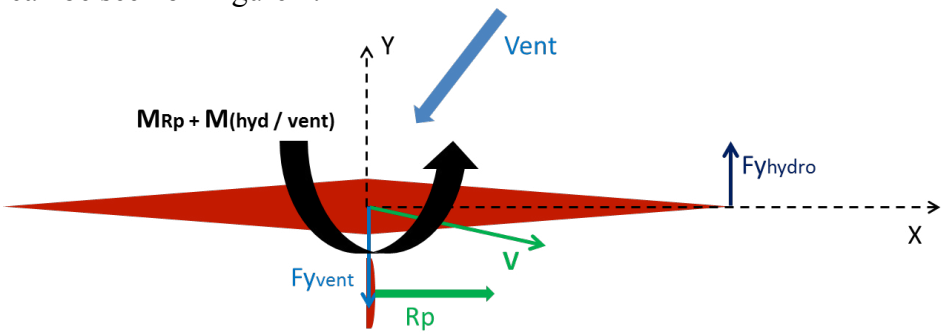


Figure 4 Summary of forces, moments and velocities in portside wind conditions

This unfavourable case will be considered in this study to compare the two racing-canoe hulls. In the case of starboard wind, the moment will cancel each other and the canoeist will be more efficient.

First, the two hulls are compared in terms of drag resistance, using steady CFD computations at different imposed advance velocities Vx (3.5 m/s, 4 m/s , 4.5 m/s). Then, the drift motion that occurs in windy conditions is modelled by imposing a drift velocity Vy = V sin(β), for different drift angles β (2 °, 3 °, 4°) with a constant velocity intensity of V = 4 m/s. The two hulls are compared with respect to the yaw moment MTZ that is developed: the more this moment will be important, the more the canoeist will have to produce an effort to cancel it.

In a second step, unsteady computations using the experimental measurements are considered. Some degrees of freedom (advance velocity Vx, heave position Tz and pitch angle Ry) of the ship motion are imposed and the resulting yaw moment MTZ is used to compare the two hulls. However, the imposed kinematics must be twice differentiable. This is not the case for the heave and pitch signals, for which the kinematics is approximated using sine functions.

2 HYDRODYNAMIC STUDY

2.1 Meshing the computational domain

The computational domain is discretized using unstructured hexahedral cells. The racing-canoe bow is located at X=0, its body is in X<0 and (X,Z) is its symmetry plane.
The fluid domain around the hull has been meshed in order to satisfy the commonly used criteria to get a good description of the boundary layer and to capture the deformation of the free surface:

- The first cell height yp at the wall has been computed using the classical formulas of flat plane boundary layer such that y+ = 40 for a kinematical viscosity ν = 1.0E-6 m²/s resulting in yp = 4.0E-4 m.
- To capture the deformation of the free surface, cells of thickness 0.001 have been used.

The half-mesh counts 1.6 M cells. Steady and unsteady drag resistance computations have been performed on the half-mesh while the computations involving drift have been used the entire mesh (obtained by a (X,Z) symmetry operation). The half-mesh is presented on Figure 5. As can be seen, the cells height is decreased in the region of the fee surface to capture its deformation. On Figure 6, the surface mesh of the hull is shown. One can notice that the mesh is denser at the location of the free surface, at the stern and at the bow.

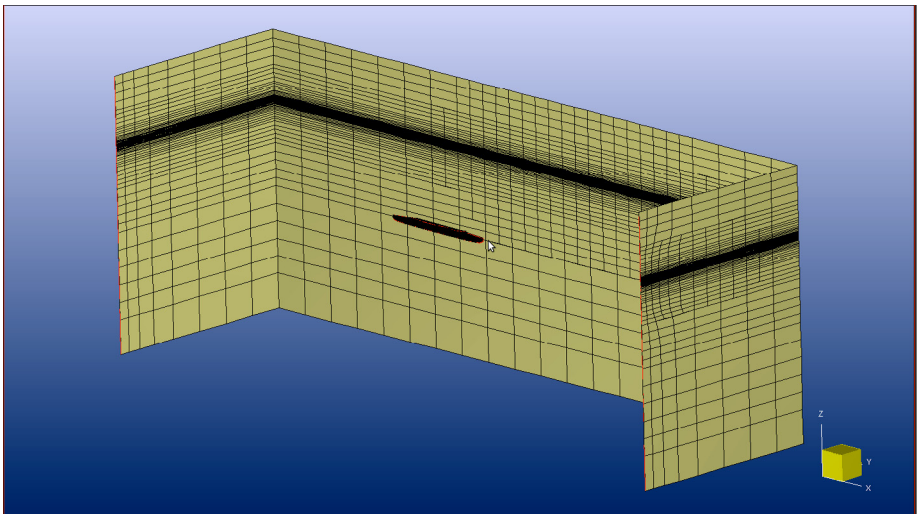


Figure 5 General view of the mesh and the computational domain

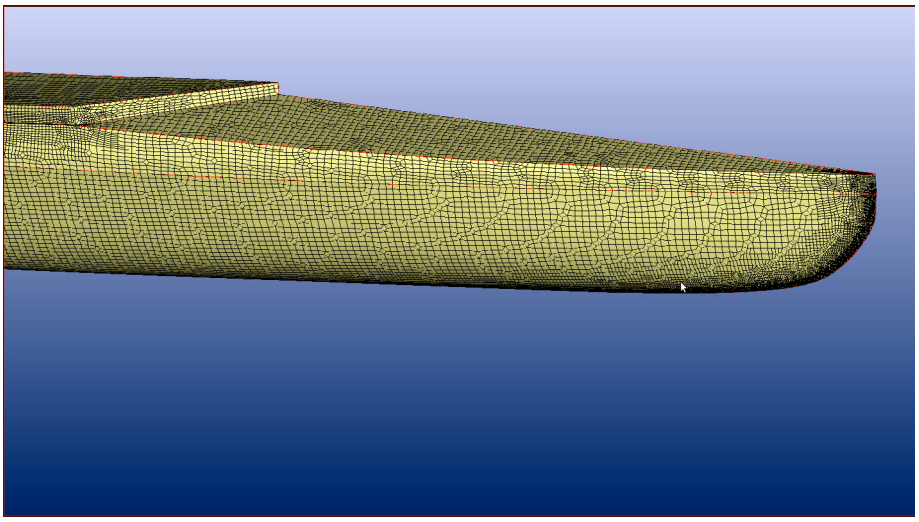


Figure 6 Racing-canoe transom surface mesh

2.2 Numerical simulation

The flow simulation has been performed using the software package FINE/Marine that solves the Reynolds Averaged Navier-Stokes equations with free surface [1]. The half-mesh is enclosed in a parallelepiped and the following boundary conditions are imposed:

- On the planes Xmin, Xmax et Ymax: null velocity,
- On the plane Ymin: symmetry condition,
- On the plane Ymin: null velocity,
- On the hull: boat velocity,
- On the planes Zmin and Zmax: a hydrostatic pressure.

The VOF (Volume Of Fluid) method is used to describe the deformation of the free surface along with a K-Omega turbulence model for the flow. A wall law is used to describe the flow boundary layer.

2.3 Hydrodynamic results

2.3.1 Imposed velocity computations

For steady computations, the nominal boat velocity is imposed using a sine acceleration ramp. For computations involving drift, two ramps are used one along X and another one along Y. A quasi-steady method is used to ease convergence towards a steady state. For unsteady computations, the unsteady signals are damped during their first period.

2.3.2 Hydrodynamics forces and moments

2.3.2.1 Steady drag resistance analysis

The first step is to compare the two hulls using drag resistance computations at prescribed advance X-velocities. The boat's draft is free. The total hydrodynamic forces are reported in Table 1, FTX,Z being the total hydrodynamic forces in X and Z in N.

Table 1 : Steady hydrodynamic total forces.

	Plastex		**Quattro**	
X-Velocity (m/s)	**FTX**	**FTZ**	**FTX**	**FTZ**
3,5	-48	1153	-47	1162
4	-60	1153	-59	1162
4,5	-72	1153	-72	1162

The hydrodynamic forces are decomposed as follows:

- FPX,Z : X and Z components of the pressure forces in N
- FVX,Z : X and Z components of viscous forces in N

Table 2: Steady hydrodynamic total forces decomposition.

	Plastex		**Quattro**	
X-Velocity (m/s)	**FVX**	**FVZ**	**FVX**	**FVZ**
3,5	-32	0	-32	0
4	-41	0	-41	0
4,5	-52	0	-52	0
X-Velocity (m/s)	**FPX**	**FPZ**	**FPX**	**FPZ**
3,5	-15	1153	-14	1162
4	-18	1153	-17	1162
4,5	-20	1153	-20	1162

Quattro canoe is slightly heavier than Plastex, which is corroborated by the values of FTZ that are slightly higher for Quattro than for Plastex. Moreover, the relative difference in drag resistance between the two hulls is inferior to 2.2 % as can be seen from Table 1, which is negligible. The two hulls are then equivalent from drag resistance point of view. Furthermore, Table 2 presents the decomposition of the hydrodynamic forces. One can notice that viscous friction represents 65-70 % of FTX. This points out that the surface finish of the hull can be an important element to consider when dealing with the reduction drag resistance forces.

2.3.2.2 Steady analysis with drift

Steady computations with drift have been achieved to quantify the yaw moment MTZ generated by the portside wind. The norm V of the velocity vector is fixed here at 4 m/s. MTX,Y,Z stands for the total moment in X,Y and Z in N.m calculated at the point (0,0,0). The results are presented in Table 3.

Table 3: Hydrodynamic moments in steady flow with drift.

	Quattro			**Plastex**		
Drift angle β (°)	**MTX**	**MTY**	**MTZ**	**MTX**	**MTY**	**MTZ**
4	0,00	2927,00	37,00	0,00	2805,00	57,00
3	0,00	2925,00	37,00	0,00	2796,00	53,00
2	0,00	2923,00	29,00	0,00	2789,00	39,00

One can see that the yaw moment MTZ is more important in the case of the Plastex than in the case of Quattro. In addition to that, MTZ increases with the drift angle.

2.3.2.3 Unsteady drag resistance analysis

Unsteady signals coming from experimental measurements are imposed. Three cases have been considered:

- *Case 1 : X-Velocity Vx is imposed and the draft Tz is free,*
- *Case 2 : X-Velocity Vx is imposed and the draft Tz is imposed,*
- *Case 3 : X-Velocity Vx is imposed, the draft Tz is imposed and the pitch Ry is imposed.*

The X-Velocity Vx signal is depicted on Figure 7. The signal consists in 6 periods. The first period of the signal is damped. The obtained drag resistance forces for Plastex and Quattro are reproduced on Figure 8 and 9. One can notice that the drag values are close for both racing-canoes, which points out that the two hulls are very close in terms of drag resistance even in unsteady motion.

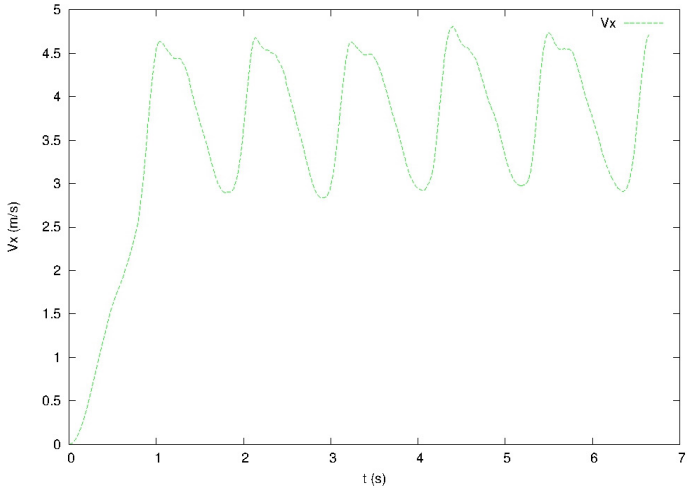


Figure 7 Unsteady imposed X-Velocity

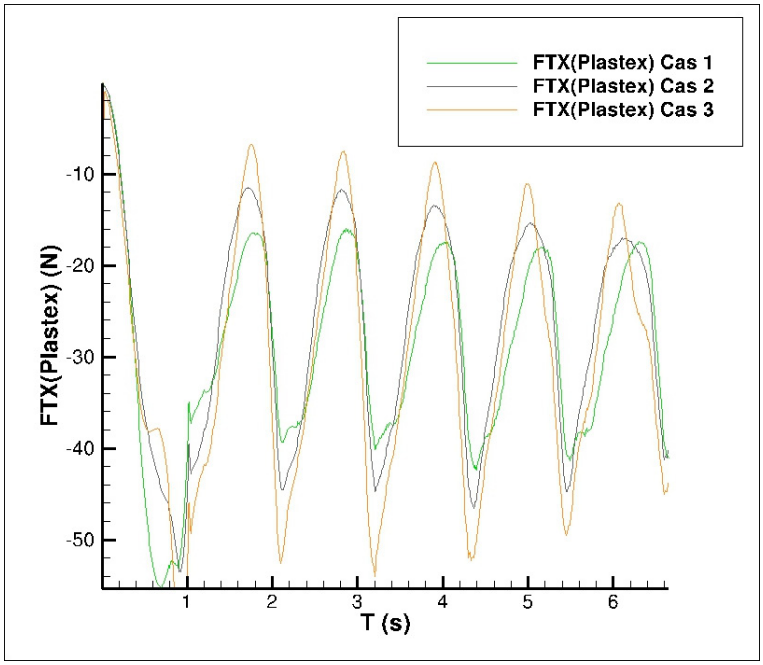


Figure 8 Unsteady FTX for Plastex

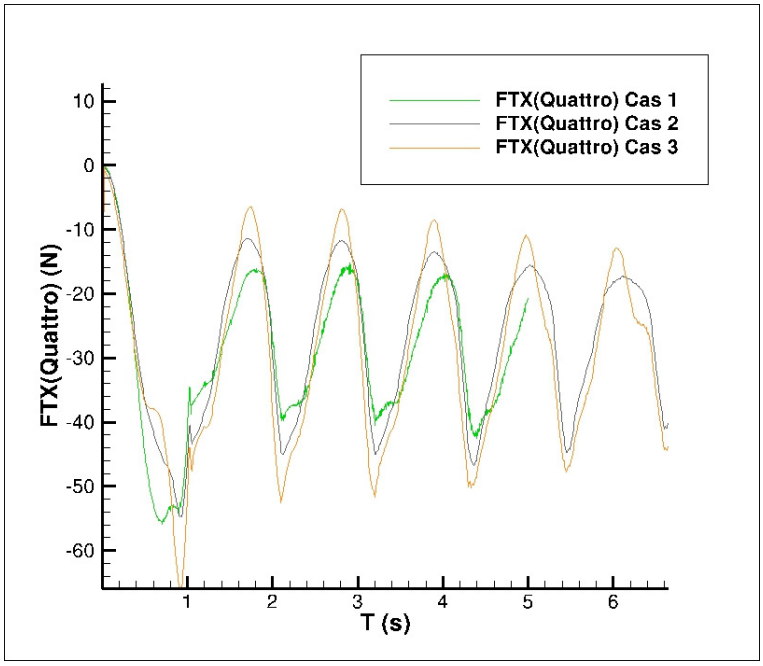


Figure 9 Unsteady FTX for Quattro

2.3.2.3 Unsteady drift analysis

Drift analysis using unsteady experimental signals coming from measurements (Vx is given by a data file, Ry = - 1.5 Sin (5.86 t -4.5) (deg), Tz = 0.03 Sin (5.86 t -2) (m)). Three cases (4, 5 and 6) with have been considered, imposing a drift angle of 2, 3 and 4 degrees.

Unsteady yaw moments MTZ are given in Figure 10, 11 and 12 for Plastex and Quattro showing that MTZ amplitude increases with drift angle. A comparison for each drift angle of the MTZ moments for Plastex and Quattro shows that MTZ is lower for Quattro than for Plastex.

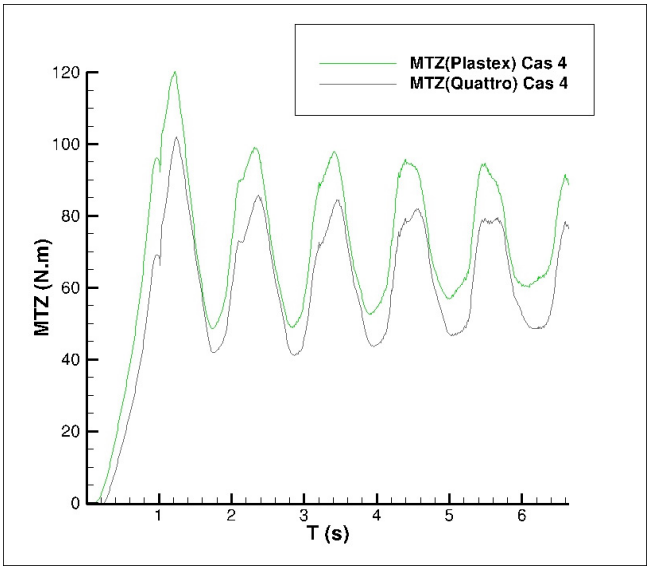


Figure 10 Unsteady MTZ for Plastex and Quattro for Case 4

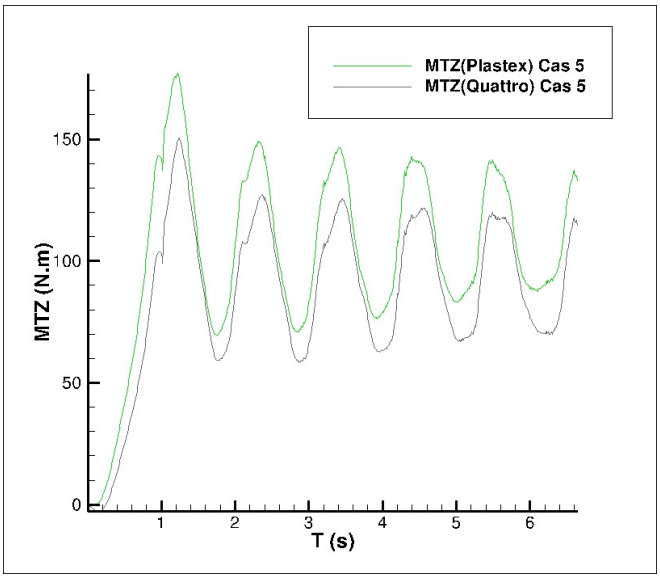


Figure 11 Unsteady MTZ for Plastex and Quattro for Case 5

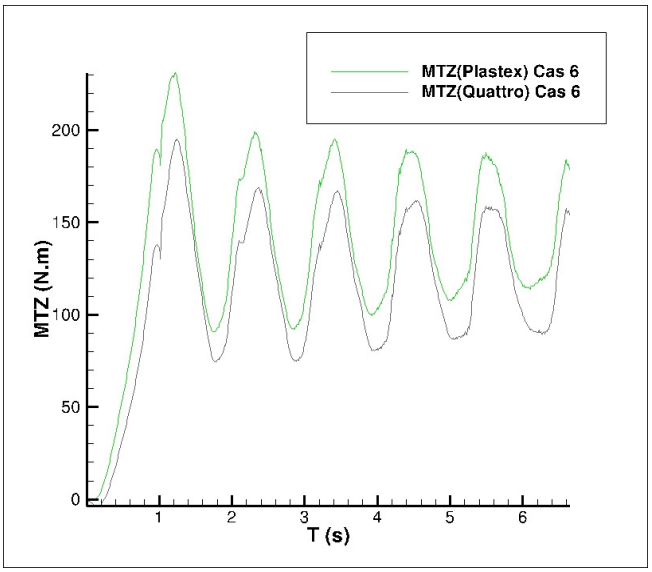


Figure 12 Unsteady MTZ for Plastex and Quattro for Case 6

An additional simulation for a drift angle of 3 degrees (case 7) with X-Velocity Vx imposed, draft Tz imposed and pitch Ry imposed, is considered and the moment MTZ is compared for the two hulls. It is shown that the Quattro experiences a lower yaw moment than the Plastex.

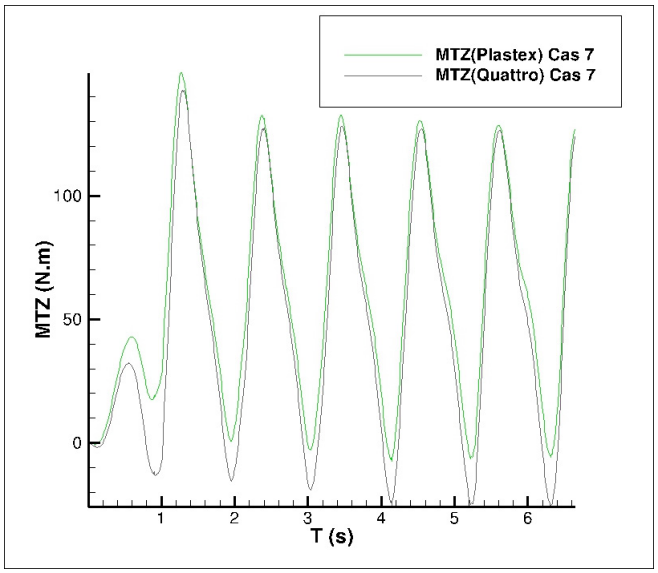


Figure 13 Unsteady MTZ for Plastex and Quattro for Case 7

3 AERODYNAMIC STUDY

The computations in drift, performed for different drift angles gave us the hydrodynamic force FYhydro or FTY that is supposed to be equal to the Y-component FYaero of the aerodynamic force exerted on the canoeist. To determine the real drift angle, aerodynamic computations on the canoeist on the racing-canoe Quattro have been performed for an advance X-velocity Vx of 4m/s and a wind intensity of 4.5 m/s.

3.1 Wind angle

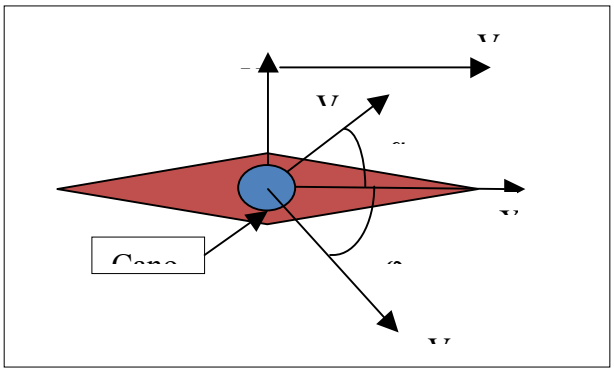


Figure 14 Wind intensity, aerodynamic velocity and racing-canoe X-velocity

The wind angle α has been estimated to maximize the aerodynamical force FYaero. As can be seen on Figure 14, the aerodynamical velocity is Va = Vv-Vx satisfying $Va^2 = Vv^2 + Vx^2 - 2*Vv*Vx*\cos(\alpha)$. The canoeist is modelled by a cylinder of radius r =0.5 m and height h = 1.5 m. It appears that FY is maximized for α = -110 ° resulting in an aerodynamical speed Va whose components are (-2.3941, -6.5778, 0.0).

3.2 Computational domain meshing

A view of the computational domain is presented on Figure 15.

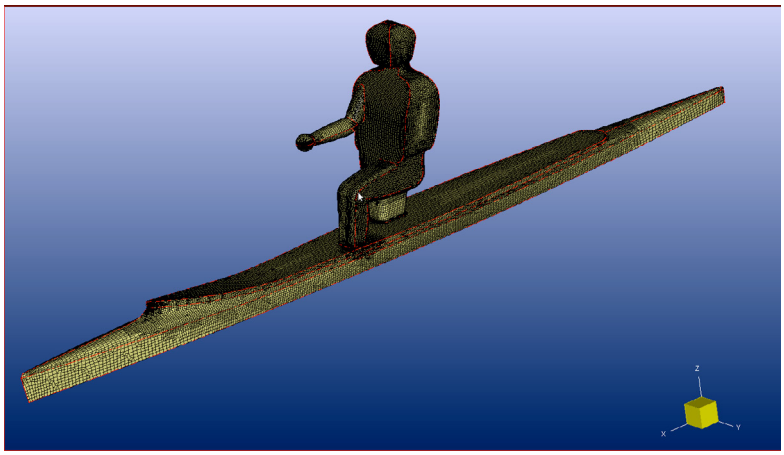


Figure 15 *Portside close view of the surface mesh of the canoeist on the Quattro racing-canoe*

3.3 Numerical simulation

The numerical simulation of the aerodynamics around the canoeist on the racing-canoe Quattro has been performed using the software package FINE/Marine with the following boundary conditions:

- On the planes Xmax, Ymax et Zmax: aerodynamic velocity,
- On the planes Xmin et Ymin: outlet pressure condition,
- On the plan Zmin: a symmetry condition.

Turbulence is modelled using the K-Omega model and wall laws are used to model boundary layers.

3.4 Aerodynamical efforts

The aerodynamic forces exerted on the canoeist are given by FTX,Y,Z in N:

Table 4 Total aerodynamic efforts on the canoeist

FTX	FTY	FTZ
-4	-37	40

The steady hydrodynamic force FTY obtained previously with drift is as follows:

Table 5 Hydrodynamic force FTY on the canoeist versus drift angle.

Drift angle (°)	FTY
4	57,00
3	38,00
2	23,00

One can see that a drift angle of 3 degrees gives a hydrodynamic force of 38 N that is close to the aerodynamic force of 37 N computed on the canoeist.

3.5 Streamlines and pressure field

Streamlines colored by pressure are shown in Figure 24 and y+ values at the walls are shown in Figure 16. One can see that the flow field is highly complex especially around the canoeist and that the y+ values remain reasonable at the walls showing that the mesh is fine enough to capture the physics at the walls.

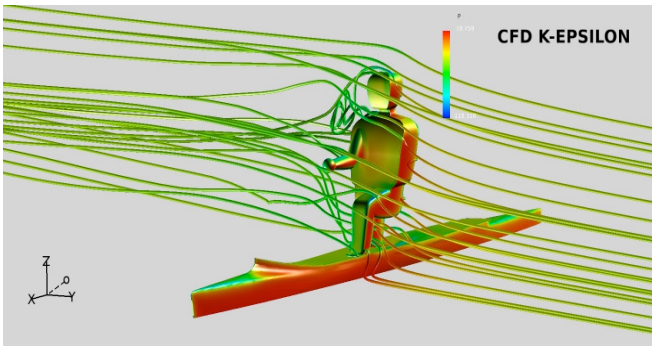


Figure 16 Streamlines colored by pressure around the canoeist.

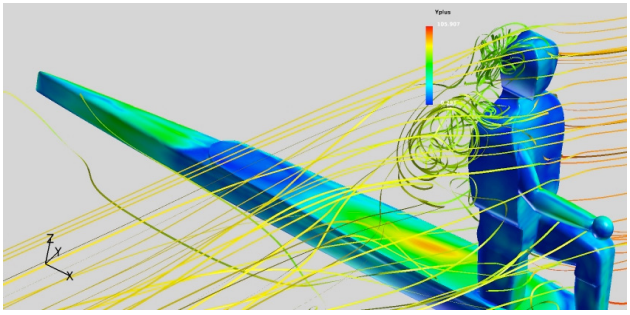


Figure 17 Streamlines colored by pressure and y+ values at the wall.

4 CONCLUSIONS

In conclusion, steady and unsteady CFD hydrodynamic computations, comparing drag resistance and yaw moment in drift, have been considered to compare two racing-canoes in unfavourable portside wind conditions. The results show that, even if the two hulls are equivalent in terms of drag resistance, the racing-canoe Quattro experiences a lower yaw moment in unfavourable portside wind conditions, making it easier to maneuver.

ACKNOLEDGEMENTS

This work has been achieved in the framework of the “OPTICAN” project. Authors gratefully acknowledge the « Ministère des Sports, de la Jeunesse, de l’Education Populaire et de la Vie Associative » and INSEP, which have funded the project.

REFERENCES

[1] QUEUTEY, P.; VISONNEAU, M. (2007), *An interface capturing method for free-surface hydrodynamic flows*, Computers & Fluids 36/9, pp.1481-1510

V International Conference on Computational Methods in Marine Engineering
MARINE 2013
B. Brinkmann and P. Wriggers (Eds)

NUMERICAL SIMULATION OF FLOWS AROUND KVLCC2 HULL FORM WITH SHIP MOTIONS IN REGULAR WAVES

KUNIHIDE OHASHI*, NOBUAKI SAKAMOTO†, TAKANORI HINO††

*National Maritime Research Institute
6-38-1 Shinkawa, Mitaka,Tokyo, Japan
e-mail: k-ohashi@nmri.go.jp

†National Maritime Research Institute
6-38-1 Shinkawa, Mitaka,Tokyo, Japan
e-mail: sakamoto@nmri.go.jp

††Yokohama National University
79-5 Tokiwadai, Hodogaya, Yokohama, Kanagawa, Japan
Email: hino@ynu.ac.jp

Key words: URANS, Regular Wave, Ship Motion

Abstract. Unsteady RANS simulations of flows around a tanker hull form with ship motions in regular waves are carried out. The results of Fourier analysis are similar with the measured results and within the deviation of the results in the workshop. From the analysis of the flows on the propeller plane, the incresing of time averaged nominal coefficient can be derived from the forward speed diffraction case in short wave length. In long wave length, the vortices on the propeller plane are induced by the ship motions and increase of time averaged nominal wake coefficient is affected by the interaction between waves and ship motions, the effect of forward speed diffraction case and forced heave motion are in same order.

1 INTRODUCTION

Recently, Unsteady RANS simulations are progressing, especially in a computation with ship motions and waves[1][2][3]. Forward Speed diffraction case which means without ship motions is set as the CFD verification test case at CFD Workshop 2005[4] and several test cases are employed at Workshop 2010[5] with container, tanker hull forms and DTMB Model 5415 hull form.

Once head waves come, the increase of averaged flows in the propeller diameter, define as nominal wake coefficient, is observed in experiment[1][6]. The difference of the nominal wake coefficient between a calm water condition and a condition with ship motions in

waves affects to the ship performance. Although the estimation of the difference between the calm water case and case with ship motions in waves is important, the analysis for the flows with ship motions in waves are limited few cases due to the difficulty in the experiment.

The analysis of the flows around KVLCC2 hull form with ship motions in waves is carried out by using URANS simulation. The computational conditions are set as the one of the test case at the Workshop 2010[5]. At first,results of ship motions with waves based on Fourier transform analysis are compared with the experimental data. Forward Speed diffraction cases and forced motions cases which are derived from the results of ship motions with waves are carried out to investigate the effect of each components.

2 COMPUTATIONAL METHOD

2.1 Flow solver

The CFD method used is called *SURF* [7, 8], which is under development at National Maritime Research Institute. This solver employs unstructured grids and has capability of handling complex geometry. The governing equations of the present method are 3D Reynolds averaged Navier-Stokes equations for incompressible flows. Artificial compressibility approach is used to velocity-pressure coupling. Spatial discretization is based on a finite-volume method for an unstructured grid. A cell centered layout is adopted in which flow variables are defined at the centroid of each cell and a control volume is a cell itself.

The inviscid fluxes are evaluated by the second-order upwind scheme based on the flux-difference splitting of Roe. The evaluation of viscous fluxes is also second-order accurate. For unsteady flow simulations, a dual time stepping approach is used in order to recover incompressibility at each time step. It consists of the second order two-step backward scheme for the physical time stepping and the first order Euler implicit scheme for the pseudo time. The linear equation system is solved by the symmetric Gauss-Seidel (SGS) method. Multigrid method and local time stepping for the pseudo time are adopted for the fast convergence.

For free surface treatment, an interface capturing method using a single phase level set approach is employed. k-ω SST turbulence model is adopted to Reynolds stresses.

Motion equations are discretized in second order and the motions are strongly coupled with governing equations within the dual time stepping. The computational domain is deformed with the ship motions with the criterion of the distance from the ship hull[9].

2.2 Wave generating method

The velocities and wave height can be derived from eq.(1)-(4) based on the linear wave theory and the transformation to the coordinate translating with velocity U_0.

$$\begin{aligned}\eta(x,y,t) &= asin\{k(-xcos\chi - ysin\chi) \\ &- \omega t + kU_0 tcos\chi\} \end{aligned} \tag{1}$$

$$\begin{aligned}u(x,y,t) &= -\omega a e^{kz} cos\chi sin\{k(-xcos\chi - ysin\chi) \\ &- \omega t + kU_0 tcos\chi\} \end{aligned} \tag{2}$$

$$\begin{aligned}v(x,y,t) &= -\omega a e^{kz} sin\chi sin\{k(-xcos\chi - ysin\chi) \\ &- \omega t + kU_0 tcos\chi\} \end{aligned} \tag{3}$$

$$\begin{aligned}w(x,y,t) &= -\omega a e^{kz} cos\{k(-xcos\chi - ysin\chi) \\ &- \omega t + kU_0 tcos\chi\} \end{aligned} \tag{4}$$

in here, a is wave amplitude, k is wave number, χ is wave direction and ω is wave frequency.

The wave is generated in the zone where is pre-set on a computational domain. The level-set function and the velocities are blending at the zones using the flow variable and the value of eq.(1)-(4).

$$\phi = (1-\alpha)\phi_{in} + \alpha\phi_{wave} \tag{5}$$

$$\boldsymbol{q} = (1-\alpha)\boldsymbol{q}_{in} + \alpha\boldsymbol{q}_{wave} \tag{6}$$

ϕ_{in} and $\boldsymbol{q}_{in}$ are flow variable obtained by solving the governing equations. ϕ_{wave} and $\boldsymbol{q}_{wave}$ is the analysis solution.

The coefficient α is derived by the equations based on the distance from the outer boundary.

$$\alpha_x = \begin{cases} 1.0 & xmin \le x \le xmin1 \\ sin^n(\frac{\pi}{2}\frac{x-xmin2}{xmin1-xmin2}) & xmin1 < x \le xmin2 \end{cases} \tag{7}$$

$$\alpha_x = \begin{cases} 1.0 & xmax1 \le x \le xmax \\ sin^n(\frac{\pi}{2}\frac{x-xmax2}{xmax1-xmax2}) & xmax2 \le x < xmax1 \end{cases} \tag{8}$$

$$\alpha_y = \begin{cases} 1.0 & ymin \le y \le ymin1 \\ sin^n(\frac{\pi}{2}\frac{y-ymin2}{ymin1-ymin2}) & ymin1 < y \le ymin2 \end{cases} \tag{9}$$

$$\alpha_y = \begin{cases} 1.0 & ymax1 \le y \le ymax \\ sin^n(\frac{\pi}{2}\frac{y-ymax2}{ymax1-ymax2}) & ymax2 \le y < ymax1 \end{cases} \tag{10}$$

Variables, xmin2, xmax2, ymin2, ymax2 are the positions of the boundary of wave generating zone in which are the computational domain. Also, xmin1, xmax1, ymin1, ymax1 are arbitrary position between the boundary of wave generating zone and the outer boundary.

The maximum value is selected in lapping region.

$$\alpha = max(\alpha_x, \alpha_y) \tag{11}$$

3 COMPUTATIONAL CONDITIONS

Computational domain is set as $-1.5 \leq x/L \leq 3.5$, $-2.0 \leq y/L \leq 0$, $-2.0 \leq z/L \leq 0.1$ with ship length $L(= 3.2m)$, where FP is located at $x/L = 0$ and the still water level is at z $= 0$. The computation domain consists from 3.1 million refined hexahedral cells, especially the regions near ship hull and free surface are divided into small cells. Reynolds number and Froude number are 2.55×10^6 and 0.142, respectively. Computations with three wave lengths $\lambda/l = 0.6, 1.1, 1.6$ are carried out. The wave height is set as $h/L = 0.01875$.

Fourier transform analysis is carried for the total resistance coefficient, heave motion and pitch angle with three encounter periods. The time $t = 0$ for Fourier transform analysis is when a crest of the coming wave is coincident with FP of the ship hull.

Axial velocities on ship-fixed coordinate system are integrated in the propeller diameter to obtain a nominal wake coefficient. Fourier transform analysis for the nominal wake coefficient is limited to one encounter period.

Forward Speed diffraction case which means without ship motions and forced motions which are derived by the simulation with ship motions with waves are also carried out to examine the effect of each component.

4 RESULTS

Fig.1-3 show the wave elevation contours in three wave lengths. t/T_e is the ratio in encounter period T_e. The regular head waves are propagating in short and long wave length. Once the wave is coming to the ship hull, the interactions are remained in the regions far from the ship hull.

Table 1-3 show the results of Fourier transform analysis and comparisons with measured data. Although almost all the coefficients are smaller than measured results and the numerical test for non-linear turbulence model is remained, the present computational results are within the deviation of the results[5]

Fig.4-6 show axial flow contours and cross flow vectors in ship motions with waves. Fig.7-9 also show the axial flow contours and vectors for the forward speed diffraction case and Fig.10-12 show the case for forced heave motion in calm water condition. In short wave length($\lambda/L = 0.6$), the axial velocity and vectors with ship motions in waves are similar with the results of forward speed diffraction case because the effect of the ship motions are very small.

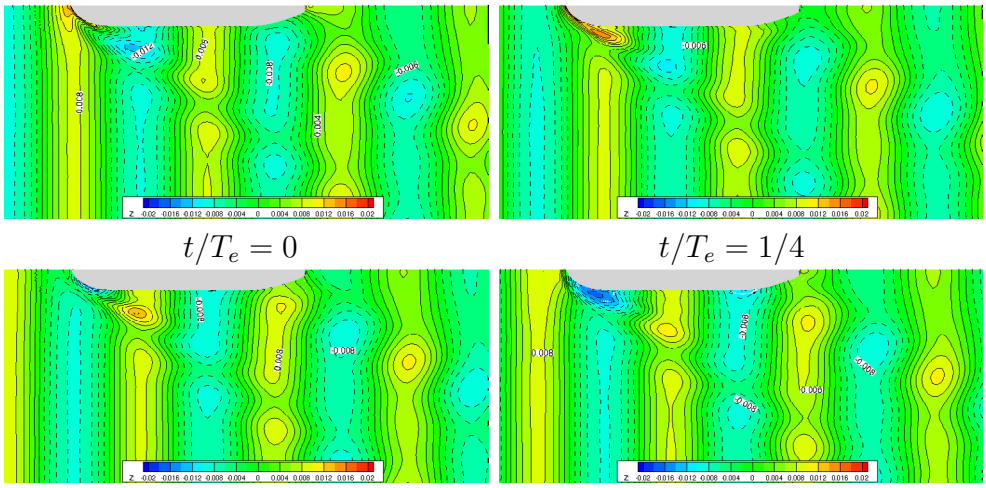


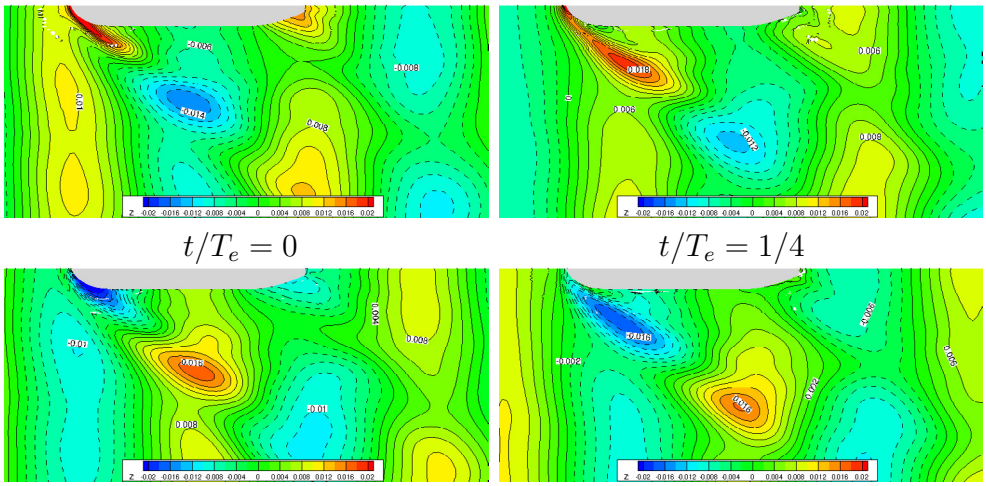
Figure 1: Wave elevation contours[$\lambda/L = 0.6, \Delta z = 0.002$]

The flows are varied largely in larger wave length and can not be superposed from the forward speed diffraction and forced heave motion cases. The vortices are changing with the wave period which are pointed out in the SPIV measurement[1].

In diffraction case, flows are accelerated at the time when the wave crest is staying in the propeller plane, then decreased at the time when the wave trough is staying.

In case of the forced heave motions, the flows are changing in z-direction with the ship heave motions. The lower velocity region is close to ship hull when the ship is sinking, then away from the hull when the ship is floating. The change of vortices position is considered to be induced by the ship motions.

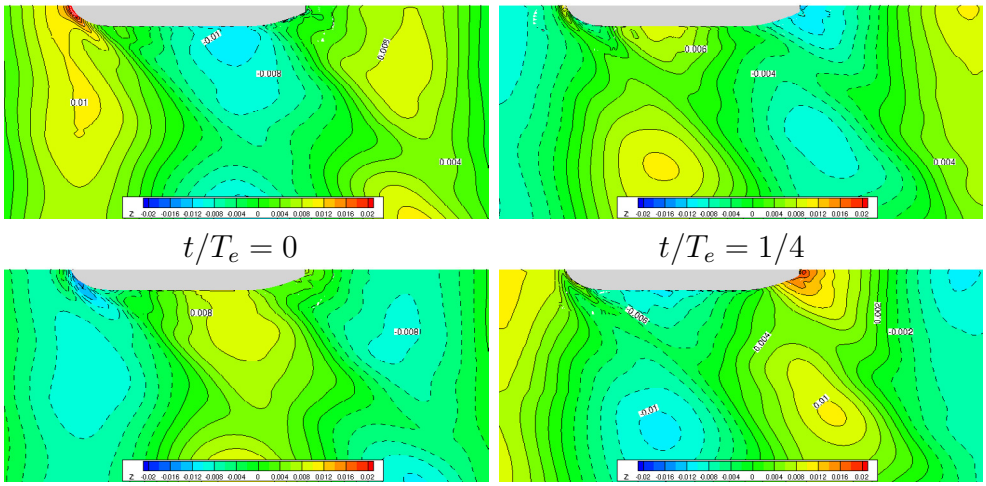
The vortices which are observed in the forward speed diffraction and forced heave motion cases become smaller or are disappeared in the flows with ship motions in waves on $\lambda/L = 1.1$ at the time $t/T_e = 1/2$. The pitch motions affect to the flows, especially $\lambda/L = 1.1, 1.6$, and the simulation of forced pitch motion are in progress.



$t/T_e = 0$ $t/T_e = 1/4$

$t/T_e = 1/2$ $t/T_e = 3/4$

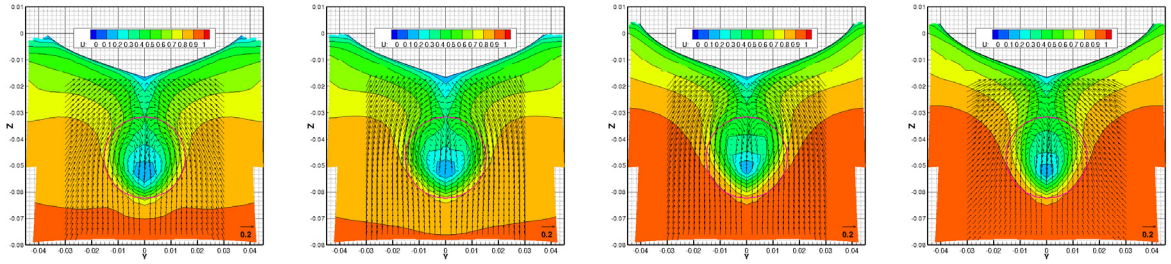
Figure 2: Wave elevation contours$[\lambda/L = 1.1, \Delta z = 0.002]$



$t/T_e = 0$ $t/T_e = 1/4$

$t/T_e = 1/2$ $t/T_e = 3/4$

Figure 3: Wave elevation contours$[\lambda/L = 1.6, \Delta z = 0.002]$



$t/Te = 0$ $t/Te = 1/4$ $t/Te = 1/2$ $t/Te = 3/4$

Figure 4: Axial flow contours and cross flow vectors$[\lambda/L = 0.6, \Delta U = 0.1]$

Table 1: Harmonic amplitudes and phases of total resistance coefficient $C_T \times 10^3$

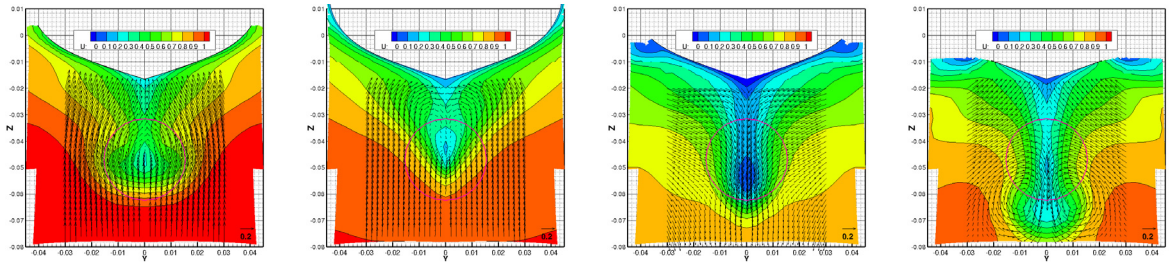
Condition		0th Amplitude	1st Amplitude	1st Phase°
Calm Water	Meas.	5.141	—	—
Calm Water	Comp.	4.429	—	—
$\lambda/L = 0.6$	Meas.	—	—	—
$\lambda/L = 0.6$	Comp.	7.264	40.64	-30.34
$\lambda/L = 1.1$	Meas.	12.480	43.179	118.97
$\lambda/L = 1.1$	Comp.	10.339	28.75	-35.85
$\lambda/L = 1.6$	Meas.	8.256	79.433	58.28
$\lambda/L = 1.6$	Comp.	7.415	54.10	-28.82

Table 2: Harmonic amplitudes and phases of heave motion

Condition		0th Amplitude(mm)	1st Amplitude(mm)	1st Phase°
Calm Water	Meas.	-2.590	—	—
Calm Water	Comp.	-3.328	—	—
$\lambda/L = 0.6$	Meas.	—	—	—
$\lambda/L = 0.6$	Comp.	-4.117	1.43	78.61
$\lambda/L = 1.1$	Meas.	-3.567	19.833	-93.87
$\lambda/L = 1.1$	Comp.	-2.048	22.47	120.75
$\lambda/L = 1.6$	Meas.	-3.593	26.905	-22.98
$\lambda/L = 1.6$	Comp.	-3.562	24.40	-72.26

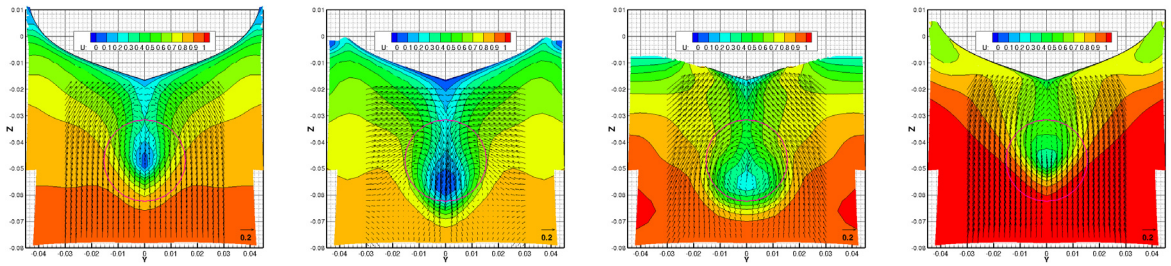
Table 3: Harmonic amplitudes and phases of pitch angle

Condition		0th Amplitude°	1st Amplitude°	1st Phase°
Calm Water	Meas.	-0.142	—	—
Calm Water	Comp.	-0.127	—	—
$\lambda/L = 0.6$	Meas.	—	—	—
$\lambda/L = 0.6$	Comp.	-0.123	0.137	-5.29
$\lambda/L = 1.1$	Meas.	-0.183	1.710	-5.65
$\lambda/L = 1.1$	Comp.	-0.152	1.586	16.81
$\lambda/L = 1.6$	Meas.	-0.155	2.554	39.25
$\lambda/L = 1.6$	Comp.	-0.110	2.308	-46.81



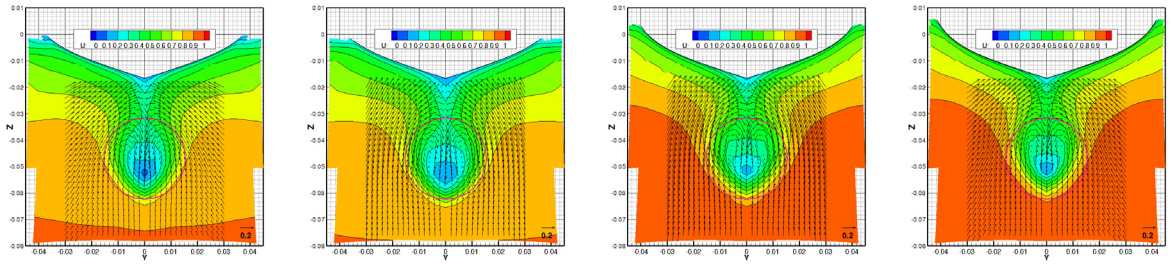
$t/Te = 0$ $t/Te = 1/4$ $t/Te = 1/2$ $t/Te = 3/4$

Figure 5: Axial flow contours and cross flow vectors[$\lambda/L = 1.1, \Delta U = 0.1$]



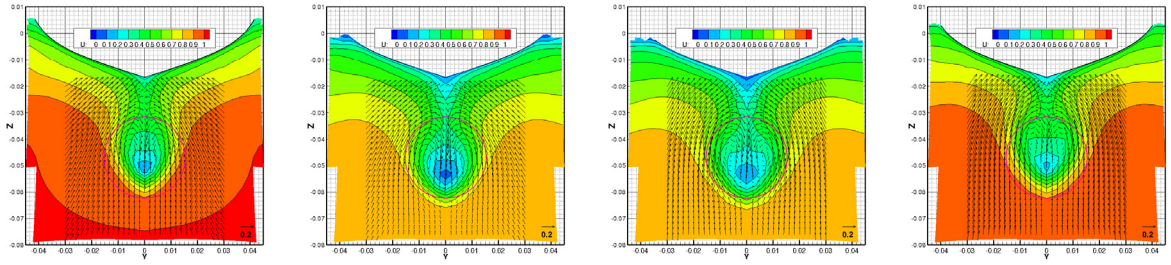
$t/Te = 0$ $t/Te = 1/4$ $t/Te = 1/2$ $t/Te = 3/4$

Figure 6: Axial flow contours and cross flow vectors[$\lambda/L = 1.6, \Delta U = 0.1$]



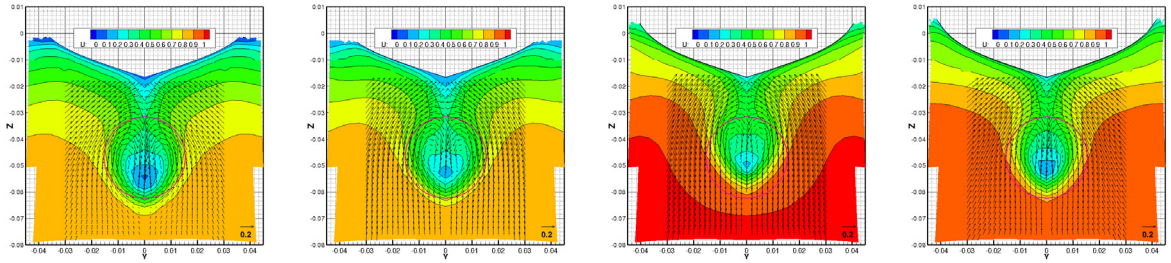
$t/Te = 0$ $t/Te = 1/4$ $t/Te = 1/2$ $t/Te = 3/4$

Figure 7: Axial flow contours and cross flow vectors[Forward Speed diffraction, $\lambda/L = 0.6, \Delta U = 0.1$]



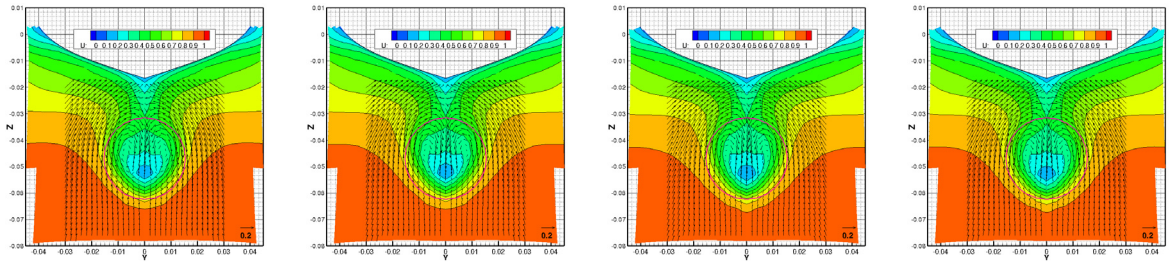
$t/Te = 0$ $t/Te = 1/4$ $t/Te = 1/2$ $t/Te = 3/4$

Figure 8: Axial flow contours and cross flow vectors[Forward Speed diffraction, $\lambda/L = 1.1, \Delta U = 0.1$]



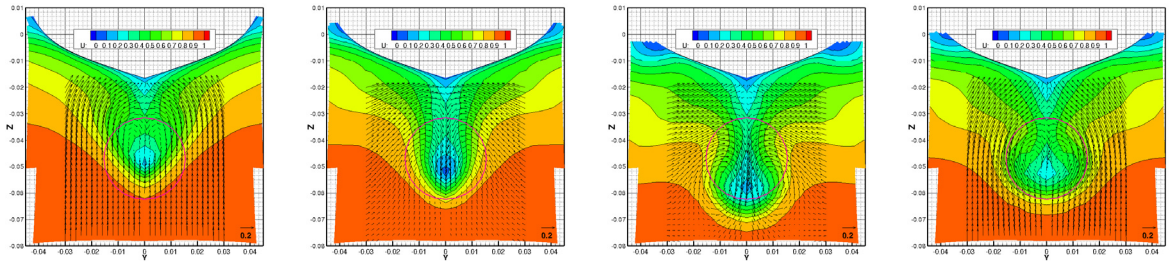
$t/Te = 0$ $t/Te = 1/4$ $t/Te = 1/2$ $t/Te = 3/4$

Figure 9: Axial flow contours and cross flow vectors[Forward Speed diffraction, $\lambda/L = 1.6, \Delta U = 0.1$]



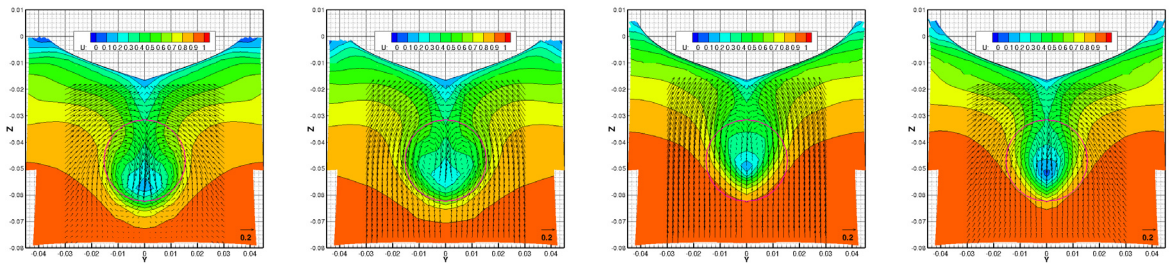
$t/Te = 0$ $t/Te = 1/4$ $t/Te = 1/2$ $t/Te = 3/4$

Figure 10: Axial flow contours and cross flow vectors[Forced heave motion, $\lambda/L = 0.6, \Delta U = 0.1$]



$t/Te = 0$ $t/Te = 1/4$ $t/Te = 1/2$ $t/Te = 3/4$

Figure 11: Axial flow contours and cross flow vectors[Forced heave motion, $\lambda/L = 1.1, \Delta U = 0.1$]



$t/Te = 0$ $t/Te = 1/4$ $t/Te = 1/2$ $t/Te = 3/4$

Figure 12: Axial flow contours and cross flow vectors[Forced heave motion, $\lambda/L = 1.6, \Delta U = 0.1$]

Table 4 shows results of Fourier transform analysis for nominal wake coefficient. Fig 13-15 show the time history of $1 - w_n$, ship motions and wave height at the propeller plane($x/L = 0.9825$). Heave motion is positive in floating and negative in sinking. Pitch angle is positive in bow up condition and negative in bow down condition.

In diffraction case, nominal wave coefficient is varied with the wave motions at all wave length.When the ship is going down in heave motion, nominal wave coefficient increases, then the ship is going up, nominal wave coefficient decreases. Time history of $1 - w_n$ can not be superposed by the results of diffraction and ship motions due to the strong interaction.

Nominal wake coefficient of $\lambda/L = 0.6$ follows the forward speed diffraction case and the increasing for the mean of nominal wake coefficient is derived from the forward speed diffraction case. On the other hand, time history in $\lambda/L = 1.1, 1.6$ of diffraction and forced heave motion cases has the phase difference. Both of forward speed diffraction and forced heave motion cases increase the mean value of nominal wake coefficient.

Table 4: Harmonic amplitudes of nominal wake coefficient $1 - w_n$

Condition	0th Amplitude	1st Amplitude
Calm Water	0.453	—
$\lambda/L = 0.6$ with motions	0.506	0.067
$\lambda/L = 1.1$ with motions	0.527	0.161
$\lambda/L = 1.6$ with motions	0.546	0.160
Diffraction $\lambda/L = 0.6$	0.500	0.087
Diffraction $\lambda/L = 1.1$	0.510	0.128
Diffraction $\lambda/L = 1.6$	0.509	0.124
Forced heave of $\lambda/L = 0.6$	0.456	0.032
Forced heave of $\lambda/L = 1.1$	0.521	0.081
Forced heave of $\lambda/L = 1.6$	0.502	0.093

5 CONCLUSIONS

- The present computational results are compared with the measured data and within the deviation of the results in the workshop.

- The change of vortices positions with ship motions in waves is considered to be induced by the ship motions.

- The increasing of time averaged nominal wake coefficient is derived from the forward speed diffraction case in short wave length because the effect of ship motions are small.

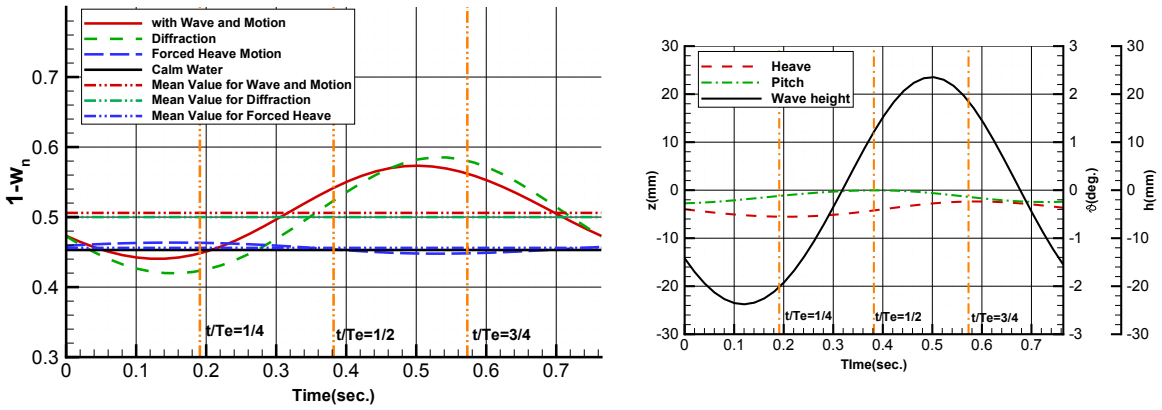


Figure 13: Time history of $1 - w_n$, motions and wave height $[\lambda/L = 0.6]$

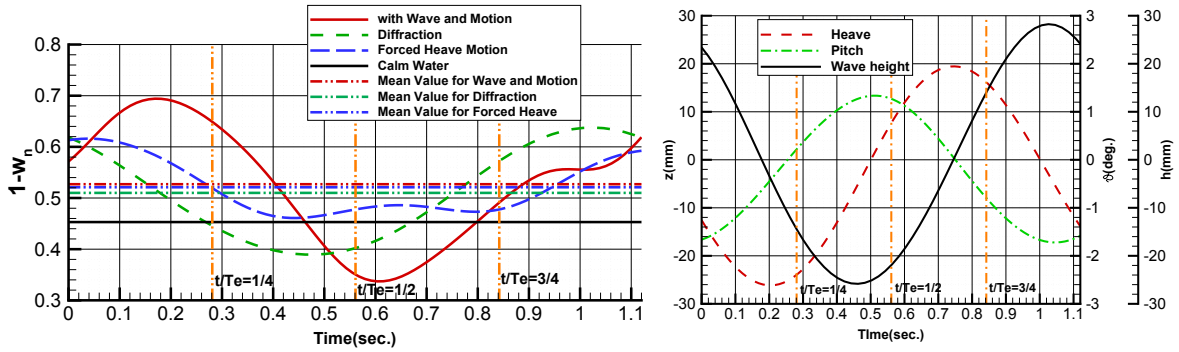


Figure 14: Time history of $1 - w_n$, motions and wave height $[\lambda/L = 1.1]$

- In long wave length, the increasing of time averaged nominal wake coefficient is affected with the interaction between waves and ship motions, the effect of forward speed diffraction case and forced heave motion are in same order.

REFERENCES

[1] Sadat-Hosseini, H., Wu, P.C., Carrica, P.M., Kim, H., Toda, Y., Stern, F., CFD verification and validation of added resistance and motions of KVLCC2 with fixed and free surge in short and long head waves, *Ocean Engineering*, (2013), Vol.59, pp.240-273.

[2] Guo, B.J., Steen, S., Deng, G.B., Seakeeping prediction of KVLCC2 in head waves with RANS, *Ocean Engineering*, (2012), Vol.35, pp.56-67.

[3] Wu, P.C., Kim, H., Hayashi, Y., Oshita, S., Toda, Y., Added resistance and phase averaged wake field of KVLCC2 model ship in waves, *Proc. of EAISS2012*, (2012).

[4] Hino, T., CFD Workshop Tokyo 2005

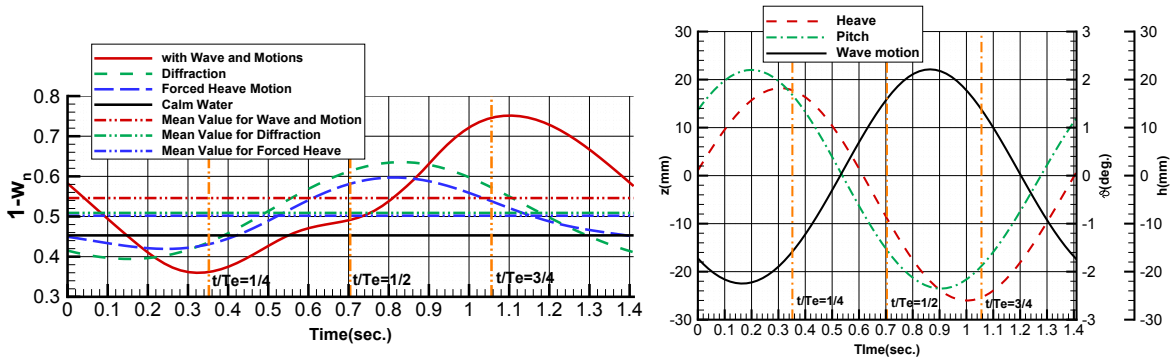


Figure 15: Time history of $1 - w_n$, motions and wave height $[\lambda/L = 1.6]$

[5] Larsson, L., Stern, F., Visonneau, M., A Work- shop on Numerical Ship Hydrodynamics Gothen-burg 2010

[6] Tsukada, Y., Hinatsu, M., Hasegawa, J., ,Measurement of Unsteady Ship Wakes in Waves, *J., Kansai Soc. N.A. Japan*, (1997), No.228, pp.15-20.

[7] Hino, T., A 3D Unstructured Grid Method for Incompressible Viscous Flows, *J. of the Soc. Naval Archit. Japan*, (1997), Vol.182.

[8] Hino, T., An Interface Capturing Method for Free Surface Flow Computations on Unstructured Grids, *J. of the Soc. Naval Archit. Japan* , (1999), Vol.186.

[9] Sakamoto, N., Ohashi, K., Unsteady wake analysis for Series 60 (Cb=0.6) pitching and heaving in regular head seas by URANS, *Proc. 26th CFD Symposium* , (2012).

V International Conference on Computational Methods in Marine Engineering
MARINE 2013
B. Brinkmann and P. Wriggers (Eds)

ANALYSIS AND COMPENSATION OF MAGNETIC ANOMALIES ON VESSEL´S FLIGHT DECKS

ANTONIO VILLALBA MADRID*, ALEJANDRO ÁLVAREZ MELCÓN*

* Electromagnetics and Telecommunications Group
Technical University of Cartagena
Cartagena, Spain
e-mail: anvima@gmail.com, alejandro.alvarez@upct.es

Keywords: Magnetism, Computational Methods, Marine Engineering, Magnetic Compensation.

Abstract. In this paper we propose a novel and effective technique for the study and compensation of local magnetic anomalies, avoiding complex deperming processes. The technique is based on two main steps: Measurement of near-field magnetic maps on the deck of the naval platform, and a post-processing technique to identify the exact location of the main magnetic perturbations and its assessment. After these two steps, the detected magnetic anomalies are effectively compensated with degaussing coils using a genetic algorithm based optimization technique. The new technique has been successfully applied to the detection and compensation of a local magnetic perturbation in a Vessel´s Flight Deck, which was having important operational issues.

1. INTRODUCTION

Vessels´ produce magnetic perturbations in the Earth Magnetic Field. To assure magnetically silent naval platforms two techniques can be used: deperming and degaussing. Deperming is a complex process that consists on installing external coils around the ship. By applying appropriate current cycles permanent magnetic signature can be reduced. On the contrary, the degaussing system [1,2] is a set of coils distributed inside the ship. By selecting the current values circulating across them, the magnetic signature of permanent and induced components can be compensated. The values of the currents and the number of turns of each coil can be optimized with different calibration techniques [3,4,5]. The main principles of magnetic compensations were defined in [6,7]. In these works it is shown that new calibration techniques were able to reduce not only the absolute value of the magnetic field, but also they could reduce the gradient of the associated magnetic anomalies.

If a vessel is compensated by a degaussing system, important local magnetic perturbations may still be present in certain areas of the ship. Generally, it is assumed that available calibration processes cannot eliminate the high local gradients, present in the near field, that can have an influence on some sensitive bearing magnetic sensors, like the bearing sensor of a helicopter over a flight deck. In addition, this local behavior cannot be predicted by the magnetic ship models (theoretical or numerical) used in the design of the degaussing system coils [8,9,10,11]. Therefore, expensive deperming processes must be applied.

In this contribution we propose a novel and effective technique for the study and compensation of local magnetic anomalies, avoiding complex deperming processes. The technique is based on two main steps: Measurement of near-field magnetic maps on the deck of the naval platform, and a post-processing technique to identify the exact location of the main magnetic perturbations and its assessment. With this information, degaussing systems are effectively used for the compensation of the detected local magnetic anomalies.

The new process has been used in the study of a naval platform, using one additional platform for reference. The reference platform is known to be free of magnetic anomalies, and it is used to compute the threshold levels of the different parameters used to detect magnetic anomalies. When the relevant parameters are under the threshold levels, the naval platform operates in a save condition. Results show that compensation of strong local magnetic anomalies is effective when the new procedure is applied. The value and interest of the new approach is that inexpensive degaussing infrastructure can be applied to the effective compensation of local magnetic anomalies, avoiding costly and time consuming deperming processes.

2. MAGNETIC MAPPING SYSTEM

The new system to measure the magnetic map of the deck is a multi-sensor platform. The system is based on the mono-sensor prototype shown in figure 1. For automatizing the acquisition process another semi-automatic system has been developed. It integrates several magnetic triaxial sensors, pitch & roll sensors, distance sensor with an encoder, acquisition card, computer and software to control the whole mapping operations. The acquisition system integrates all these components in a mobile platform with wheels, so that it can be easily displaced along the deck to capture the magnetic field at certain intervals.



Figura 1. Prototype mono-sensor for magnetic mapping.

The measurement process to obtain the magnetic maps with the designed multi-sensor magnetic acquisition system involves the following steps:

- First we have to mount the whole components of the measurement equipment and check the correct operation of all components.
- Calibrating of the measurement equipment. Depending on the size (radius) of the mobile platform wheels, the equivalence between real distance and digital counter pulses of the encoder has to be set in the software. Calibration also involves the definition of the grid width for capturing the data at certain sampling points, and the specification of the sensor height.
- Running steadily the mobile platform along the deck to capture the magnetic field at the specified sampling points within the grid.

After capturing the data we have to make several matrix transformations for correcting pitch and roll angles (deck not perfectly horizontal), change the reference system (magnetic triaxial sensors axis could not be in the same position that the magnetic reference system in the ship), change points sequence of measurement (depending on the tasks of the crew on board, measurements cannot in general be taken consecutively, so they need to be re-mapped with the right order), and finally, mapping the discrete sampling points to meters.

For the study performed in the paper, in a vessel with serious operational problems, the characteristics of the grid used for sampling are the following:

- Measurements taken in the deck area of size: 14.5 meter x 11.5 meter.
- Height: 1 meter. The height of the sensor will be important when we have to calculate the values of the turns and currents needed to compensate the detected magnetic anomaly with a degaussing system.
- Width of the grid: 0.5 meter x 0.5 meter (30 Columns x 24 Rows).
- Ferromagnetic material: naval steel.

As an example, figure 2 shows the *z*-component of the magnetic map of the flight deck studied in this paper. We can see in the stern area (rows 2-3) a high gradient of the magnetic map. In five meters the magnetic field changes from 60.000 nT down to -20.000 nT. This behavior is typical of a transversal magnetic dipole and will be the cause of an existing magnetic anomaly, causing the operational problems in this vessel.

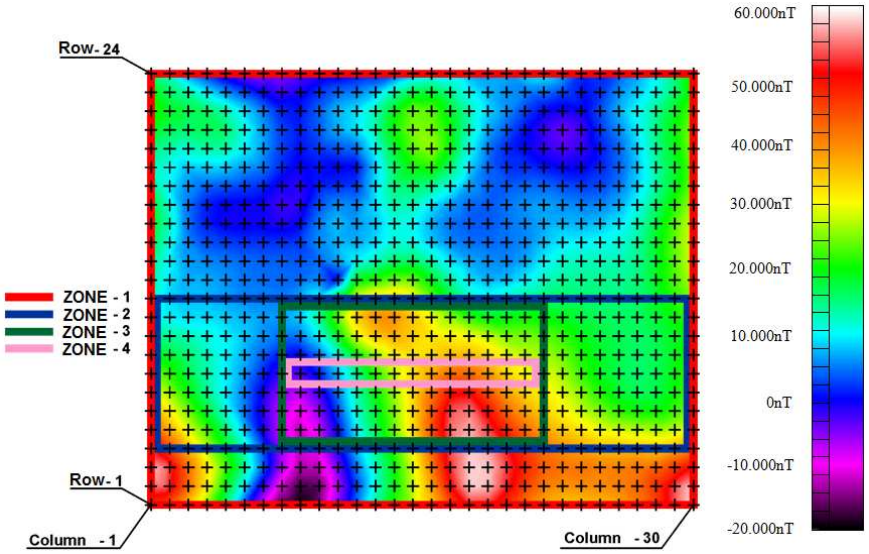


Figura 2. Vertical component of the magnetic field at the height of 1 meter from the deck.

3. POST-PROCESSING MAGNETIC DATA

Once the magnetic map of the deck has been captured, several novel parameters are defined for quantification of the anomalies. This step is based on the study of the data per rows and columns independently for the three components of the measured magnetic field. The six first parameters are: maximum (*VMAX*, eq. 1), minimum (*VMIN*, eq. 2) and average (*VPRO*, eq. 3) of the magnetic flux density, and maximum (VAEmax, eq. 5), minimum (VAEmin, eq. 6) and average (PVAE, eq. 7) of the heading error (V*AE*, eq. 4).

$$V\max = Max(\vec{B}^{H,\theta}_{P(i,j)}(x,y,z))\ \forall\, i,j \in Z_n \tag{1}$$

$$V\min = Min(\vec{B}^{H,\theta}_{P(i,j)}(x,y,z))\ \forall\, i,j \in Z_n \tag{2}$$

$$Vpro = \frac{1}{s \times t} \sum_{i=Z_n(1,j)}^{Z_n(s,j)} \sum_{j=Z_n(i,1)}^{Z_n(i,t)} (\vec{B}^{H,\theta}_{P(i,j)}(x,y,z))\ \forall\, i,j \in Z_n \tag{3}$$

Where, $\vec{B}^{H,\theta}_{P(i,j)}(x,y,z)$ is the measured magnetic flux density in a point *P(i,j)* of the platform, in a given area *H* of the Earth, with heading θ. The symbol Z_n stands for the area of the platform where the magnetic map is studied. In general this area is a sub-set of the whole magnetic map, and comprises *s*-rows and *t*-columns.

$$V_{AE}(i,j) = 180^{o} \times \frac{arctg\left(\dfrac{\vec{B}^{H,\theta}_{P(i,j)}(x)}{\vec{B}^{H,\theta}_{P(i,j)}(y)}\right)}{\pi} + 360^{o} - (RGeo - Dec)\ \forall\, i,j \in Z_n \tag{4}$$

$$V_{AE}\max = Max(V_{AE}(i,j))\ \forall\, i,j \in Z_n \tag{5}$$

$$V_{AE}\min = Min(V_{AE}(i,j)) \forall\, i,j \in Z_n \tag{6}$$

$$PV_{AE} = \frac{1}{s \times t} \sum_{i=Z_n(1,j)}^{Z_n(s,j)} \sum_{j=Z_n(i,1)}^{Z_n(i,t)} V_{AE}(i,j) \forall\, i,j \in Z_n \tag{7}$$

In the definition of the heading error (4), *RGeo* is the geographical heading and *Dec* is the magnetic declination.

The previous parameters are useful in the study of individual Platforms. For comparing the magnetic data with a reference platform, we propose to use the following novel parameters:

- Maximum or minimum variation from the average in nanoTeslas *(DM)* per rows *(DMPR)* and columns *(DMPC)*. These two parameters will be computed for the three components *(X, Y* and *Z)* of the magnetic field leading to the quantities [*DMPR(x,y,z)* and *DMPC(x,y,z)*]. These parameters will show the importance of the magnetic anomaly. The average per rows is computed as:

$$DMPR(x,y,z) = Max(MaPR(x,y,z); MiPR(x,y,z)) \tag{8}$$

Where $MaPR(x,y,z)$, and $MiPR(x,y,z)$ are calculated as:

$$MaPR(x,y,z) = ABS\left(Max\left(PR(i,x,y,z)\big|_{1\le i\le t}\right) - \frac{1}{t}\sum_{i=1}^{t} PR(i,x,y,z) \right)$$

$$MiPR(x,y,z) = ABS\left(\frac{1}{t}\sum_{i=1}^{t} PR(i,x,y,z) - Min\left(PR(i,x,y,z)\big|_{1\le i\le t}\right) \right) \tag{9}$$

$$PR(i,x,y,z) = \frac{1}{t}\sum_{j=Z_n(i,1)}^{Z_n(i,t)} (\vec{B}^{H,\theta}_{P(i,j)}(x,y,z))\Big|_{i,j\in Z_n} = \vec{B}^{H,\theta}_{P(i)}(x,y,z)\Big|_{i\in Z_n} \tag{10}$$

In above equations, *Zn(i,j)* is a specific point inside the area of interest *Zn*, where the magnetic map is studied.

The average per columns is calculated in a similar way, as

$$DMPC(x,y,z) = Max(MaPC(x,y,z); MiPC(x,y,z)) \tag{11}$$

Where $MaPC(x,y,z)$, and $MiPC(x,y,z)$ are calculated as:

$$MaPC(x,y,z) = ABS\left(Max\left(PC(j,x,y,z)\big|_{1\le j\le S}\right) - \frac{1}{s}\sum_{j=1}^{S} PC(j,x,y,z) \right)$$

$$MiPC(x,y,z) = ABS\left(\frac{1}{s}\sum_{j=1}^{S} PC(j,x,y,z) - Min\left(PC(j,x,y,z)\big|_{1\le j\le S}\right) \right) \tag{12}$$

$$PC(j,x,y,z) = \frac{1}{s}\sum_{i=Z_n(1,j)}^{Z_n(s,j)} (\vec{B}^{H,\theta}_{P(i,j)}(x,y,z))\Big|_{i,j\in Z_n} = \vec{B}^{H,\theta}_{P(j)}(x,y,z)\Big|_{j\in Z_n} \tag{13}$$

- Extended Gradient (*GE*): it is extracted from the row and column average, by taking the difference between the maximum and the minimum and dividing by the distance between these two points. It is expressed in nanoTeslas per meter (nT/m). This parameter is also computed per rows and

columns, and for all components (*X,Y,Z*) of the magnetic field, leading to (*GEPR(x,y,z)* and *GEPC(x,y,z)*). This parameter implements a kind of low-pass filter that eliminates normal variations of the magnetic field due to the different components in a ship environment. In this way this parameter will show variations of the magnetic field due to abnormal magnetized elements. The calculation is done similar to the previous parameters as:

$$GEPR(x,y,z) = \frac{1}{\delta_R \times (i_{\max} - i_{\min})}\left[Max\left(\vec{B}^{H,\theta}_{P(i)}(x,y,z)\Big|_{i\in Z_n} \right) - Min\left(\vec{B}^{H,\theta}_{P(i)}(x,y,z)\Big|_{i\in Z_n} \right) \right] =$$

$$= \frac{1}{\delta_R \times (i_{\max} - i_{\min})}\left[\vec{B}^{H,\theta}_{P(i_{\max})}(x,y,z)\Big|_{i_{\max}\in Z_n} - \vec{B}^{H,\theta}_{P(i_{\min})}(x,y,z)\Big|_{i_{\min}\in Z_n} \right] = \quad (14)$$

$$= \frac{1}{\delta_R \times (i_{\max} - i_{\min})}\left[PR(i_{\max},x,y,z)\big|_{Z_n} - PR(i_{\min},x,y,z)\big|_{Z_n} \right]$$

Where, $PR(i_{\max},x,y,z)\big|_{Z_n}$ is the maximum inside the zone of interest Z_n, of the average *PR* as defined in Equation (10), $PR(i_{\min},x,y,z)\big|_{Z_n}$ is the minimum, and i_{max} and i_{min} are the indexes for each component where the maximum or minimum value takes place, respectively. Moreover, δ_R is the distance between rows in meters. The calculation of the parameters per columns follows the same scheme, namely

$$GEPC(x,y,z) = \frac{1}{\delta_C \times (j_{\max} - j_{\min})}\left[Max\left(\vec{B}^{H,\theta}_{P(j)}(x,y,z)\Big|_{j\in Z_n} \right) - Min\left(\vec{B}^{H,\theta}_{P(j)}(x,y,z)\Big|_{j\in Z_n} \right) \right] =$$

$$= \frac{1}{\delta_C \times (j_{\max} - j_{\min})}\left[\vec{B}^{H,\theta}_{P(j_{\max})}(x,y,z)\Big|_{j_{\max}\in Z_n} - \vec{B}^{H,\theta}_{P(j_{\min})}(x,y,z)\Big|_{j_{\min}\in Z_n} \right] = \quad (15)$$

$$= \frac{1}{\delta_C \times (i_{\max} - i_{\min})}\left[PC(j_{\max},x,y,z)\big|_{Z_n} - PC(j_{\min},x,y,z)\big|_{Z_n} \right]$$

Where the average per columns *PC(j,x,y,z)* is defined in Equation (13), and δ_C is the distance between columns in meters.

- Using the average equations per rows of the magnetic field for *x*- and *y*-components, the absolute value of the average of the heading error for the deck of the vessel will be calculated as *GERPR(i)* (16). If we calculate the difference between points of maximum and minimum of *GERPR (i)* and we divide by the distance between these two points we get the variation in grades/meter (º/m) of the rows *GMERPR* (17). The same will be done for columns and *GMERPC* parameter will be calculated (18). These parameters are computed with the following equations:

$$GERPR(i) = ABS\left[\frac{180^{o}}{\pi} \times arctg\left(\frac{PR(i,x)}{PR(i,y)}\right) + 360^{o} - \left(RGeo - Dec\right)\right] \forall\, i \in Z_n \qquad (16)$$

$$GMERPR = \frac{GERPR(i_{\max}) - GERPR(i_{\max})}{\delta_C \cdot (i_{\max} - i_{\min})};\ i_{\max} \in Z_n \qquad (17)$$

Where $GERPR(i_{\max}) = Max(GERPR(i))$ and $GERPR(i_{\min}) = Min(GERPR(i))$ for every i_{max}, $i_{min} \in Z_n$. And if the computation is done per columns,

$$GERPC(j) = ABS\left[\frac{180^{o}}{\pi} \times arctg\left(\frac{PC(j,x)}{PC(j,y)}\right) + 360^{o} - \left(RGeo - Dec\right)\right] \forall\, j \in Z_n \qquad (18)$$

$$GMERPC = \frac{GERPC(j_{\max}) - GERPC(j_{\max})}{\delta_R \cdot (j_{\max} - j_{\min})};\ j_{\max} \in Z_n \qquad (19)$$

Where $GERPC(j_{\max}) = Max(GERPC(j))$ and $GERPC(j_{\min}) = Min(GERPC(j))$ for every *jmax*, *jmin* $\in Z_n$.

In above equations, *PR(i,x)* is the *x*-component .of the average *PR* defined in equation (10), and *PR(i,y)* is the average for the *y*-component. In the same way, *PC(j,x)* is the *x*-component averaged by columns as defined in equation (13), and *PC(j,y)* is the same but for the *y*-component.

3. MAGNETIC ANOMALY ASSESSMENT ON EVALUATION VESSEL

Once the data is captured and conveniently ordered, the parameters defined above are calculated for the detection of possible magnetic anomalies. It is convenient to compute these parameters in several sub-areas within the whole vessel deck. For our naval platform, the whole deck has been divided in four zones, as shown in Figure 2.

The values obtained for *VMAX*, *VMIN*, *VPRO*, *VAEmax*, *VAEmin* y *PVAE* are collected in tables 1 and 2 for all the zones *Z1*, *Z2*, *Z3* y *Z4* . The four zones are defined as:

- Zone 1: the whole magnetic map measured. It´s limited by the points (1,1), (30,1), (30,24) and (1,24). This zone includes the deck´s edge effect in port, starboard and stern.
- Zone 2:It´s limited by the points (1,4), (30,4), (23,12) and (8,12). It´s centered in the most sensitive zone where the heading sensors could be interfered, and includes the deck´s edge effect in port and starboard.
- Zone 3: It´s similar to the Zone 2 but without the edges. It´s limited by indexes (8,4), (23,4), (23,12) and (8,12).
- Zone 4:It´s limited by two points (8,8) and (23,8). It contains only a line of sampling points and it is the smallest region where the anomaly could be.

Tabla 1. Maximum, minimum and average of the magnetic flux density in nanoTeslas.

X,Y,Z	Zone	*VMAX*	*VMIN*	*VPRO*	Zone	*VMAX*	*VMIN*	*VPRO*
X	1	36.600	-4680	13.385	3	36.600	2.880	18.266
	2	36.600	-2.040	12.894	4	31.560	2.880	17.556
Y	1	33.240	3.000	17.715	3	26.160	3.000	15.603
	2	26.160	3.000	14.964	4	25.200	6.000	15.900

X,Y,Z	Zone	*VMAX*	*VMIN*	*VPRO*	Zone	*VMAX*	*VMIN*	*VPRO*
Z	1	85.560	20.520	50.103	3	83.640	27.000	56.141
	2	83.640	27.000	54.422	4	70.680	33.840	55.680

Tabla 2. Maximum, minimum and average of heading error.

Parameter	Zone	*VAEmax*	*VAEmin*	*PVAE*	Zone	*VAEmax*	*VAEmin*	*PVAE*
VAE	1	77º	-11º	36º	3	77º	12º	47º
	2	77º	-7º	38º	4	68º	14º	45º

Results show that Zone *Z3* has, in general, higher values of the parameters investigated than others areas. This could be an indication of a magnetic anomaly. There are two other reasons to discard the others areas. The first one is edge effect (*Z1*, *Z2*) and insufficient area (*Z4*). The second one is that the area *Z3* is where most probably the heading sensors of air-crafts will operate.

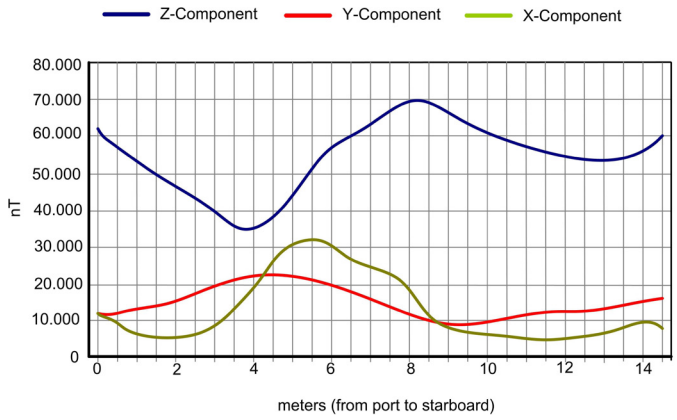


Figure 3: Graphic representation of *PR(i,x,y,z)* (eq. (10)).

In the row average function *PR(i,x,y,z)* (eq. 10) of each component of the magnetic field, shown in Figure 3, we find the influence of a transversal permanent magnetism. This is detected by a maximum or minimum in the *x*-component and a consecutive maximum and minimum in the *z*-component (see figure 3). Figure 3 shows a transversal magnetization between 4 and 8 meters from port to starboard. This magnetization is the cause of the magnetic anomaly presents in the vessel´s deck.

The average of the magnetic field per columns *PC(j,x,y,z)* (eq. 13) is represented in figure 4. It presents an important magnetic vertical component. This does not have, however, influence in the magnetic sensor of heading. Therefore, this is not a serious problem for the operation of the platform. Taking the components *X* and *Y* of average per rows and columns, the error heading is calculated for each average; expressions (16) *GERPR(i)* and (18) *GERPC(j)*, have been used to compute the rows and columns average error, respectively. In figure 5 the heading error for both average values are shown. It can be observed that a maximum error was found in the central area between port and starboard to 6 meters from the stern up to 80º. Between 5 and 8.5 meters from port, the anomaly presented an almost constant value. These values do not impede flight operations over the deck but they may create difficulties during the take-off of air-crafts.

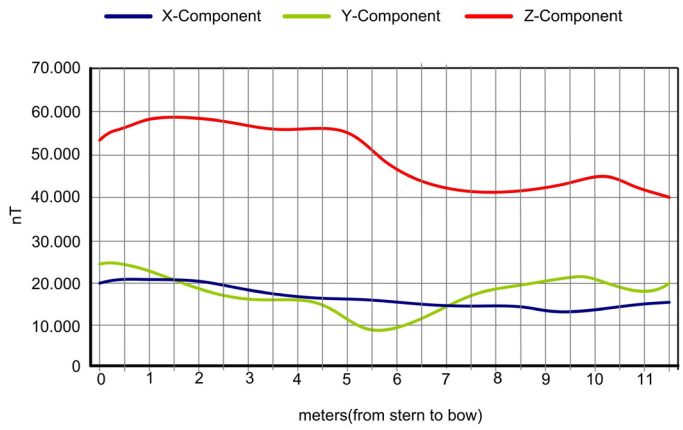


Figure 4: Graphic representation of *PC(j,x,y,z)* (eq. (13)).

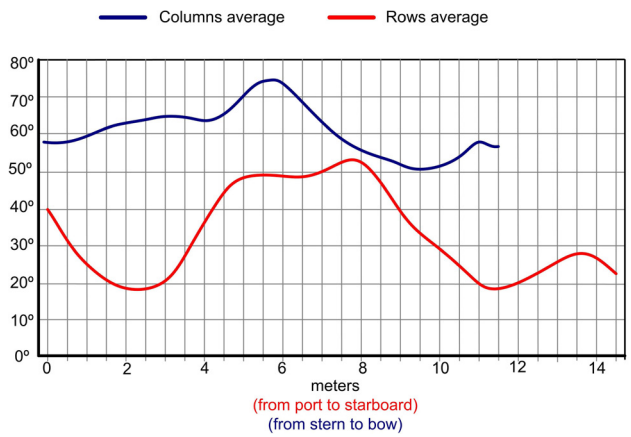


Figure 5: Graphic representation of *GERPR(i)* and *GERPC(j)* (eq. (15)&(17)).

4. COMPARATIVE STUDY WITH REFERENCE VESSEL

After the individual assessment of the platform using the defined parameters, it is now convenient to make a comparison with a reference platform, which is known to be free of any anomaly. The reference platform will serve to define threshold values for the relevant parameters. These thresholds will indicate if an anomaly is present, and the severity of the anomaly.

We use parameters *DM*, *GE* and *GMER* to define the threshold. The threshold for the two first parameters will be defined by using relevant values in the reference platform. For the *GMER* parameter, however, an absolute threshold will be established. The reason for this is that the *GMER* parameter is related to the real heading error, so a reference platform is not needed. These limits are only important for horizontal components of the magnetic field, because a high value of the z-component due to a vertical and strong magnetic dipole does not interfere with the heading sensors of air-crafts (they are horizontal axis sensors).

In Table 3 classification of anomalies according to [12], namely Strong, Weak and Absence of anomaly, is used. The presence of a strong anomaly is connected to magnetic sources well defined. In the case of weak anomaly the precise sources cannot be identified. Sources producing this kind of anomaly will therefore be distributed in several elements of the ship.

Table 3: Classification of the different types of anomalies as a function of parameters *DM*, *GE* and *GMER*

Parameter/ Reference	**ANOMALY**		
	NO	**WEAK**	**STRONG**
DM/REF	<1,1	1,1≤DM/REF<2	≥2
GE/REF	<1,5	1,5≤GE/REF<2,5	≥2,5
GMERPR	0<GMERPR<13	13≤GMERPR<18	GMERPR≥18
GMERPC	0<GMERPC<7	7≤GMERPC<10	GMERPC≥10

Table 4 shows the obtained values for the relevant parameters in the vessel investigated, and in the reference platform. According to the thresholds given in Table 5, we can conclude that a strong anomaly is present in this vessel.

Table 4: Numerical values obtained for DMPRX and GEPRX.

Vessel	DMPRX (nT)	DMPRX/REF	GEPRX (nT/m)	GEPRX/REF	GMEPR/PC(°/m)
Reference	4,642	-	1,245	.	11/4
Investigated	18,479	3.98	4,827	3.88	20/12

5. MAGNETIC ANOMALY COMPENSATION BY GENETIC ALGORITHM

In the case of the vessel investigated it is very clear the presence of a transversal (from bow to stern) permanent magnetic dipole, causing a strong anomaly. This type of anomaly can be compensated either with several transversal coils, or with two vertical coils with currents having opposite phases. The horizontal position of the vertical coils under the deck is more convenient for installation, rather than the vertical position required by the transversal coils. In Figure 6 the average per rows of the *z*-component *PR(i,x,y,z)* of the magnetic field for the vessel investigated is shown. According to the results obtained, the first vertical coil will be mounted between rows 1 and 7 and columns 5 and 10 (rectangular coil). The second coil will be mounted between rows 1 and 7 and columns 14 and 18 (rectangular coil; see figure 6).

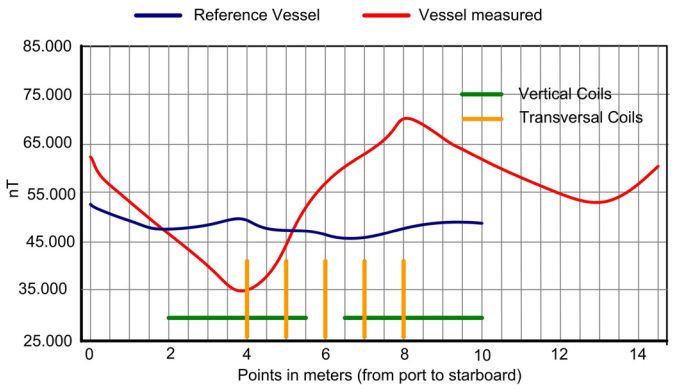


Figure 6. *Z*-component of *PR(i,x,y,z)* and location of the compensation coils.

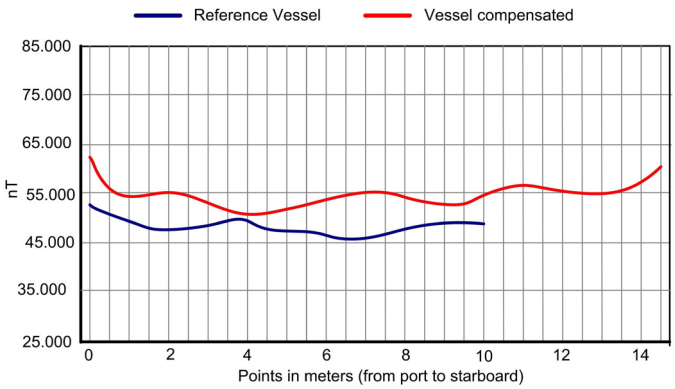


Figure 7. *Z*-component of *PR(i,x,y,z)* after switching on the compensation coils.

Compensation of the anomaly is done using a Genetic Algorithm technique described in [1]. The Genetic Algorithm uses an inverse truncated sigma scaling with tournament selection, and parameter yield of c=3.0. The boundary method is used to calculate the fitness. More details of the technique used can be found in [1].

The expression of the average per rows resultant from the compensation of the magnetic field, after powering the two coils under the deck is the following.

$$PR'(i,x,y,z)=\frac{1}{9}\sum_{j=4}^{12}(\vec{B}^{H,\theta}_{P(i,j)}(x,y,z))\Big|_{1\le i\le 30}+\vec{B}\{B_{M_{Br}}\}(x,y,h_b)+\vec{B}\{B_{M_{Er}}\}(x,y,h_b) \qquad (19)$$

Where $\vec{B}\{B_{M_{Br}}\}(x, y, h_b)$ is the magnetic field produced by the port vertical coil and $\vec{B}\{B_{M_{Er}}\}(x, y, h_b)$ is the same for the starboard vertical coil. Moreover, h_b is the distance from the coils to the plane where the magnetic map has been measured. The new *PR'* function, obtained after the optimization process, can be seen in figure 7, showing that compensation is very effective.

6. CONCLUSIONS

Local magnetic anomalies can still be present in a ship in spite of using degaussing systems for magnetic compensation. In such situations, very costly deperming processes are needed to erase the magnetic signature of vessels. In this work, the authors propose a novel and effective technique for the study and compensation of local magnetic anomalies, avoiding deperming process.

This technique has been applied to a ship's flight deck exhibiting serious operational problems due to the presence of a strong magnetic anomaly. The study shows that the strong anomaly has been detected, and a pair of vertical coils placed under the deck over the identified magnetic sources have successfully minimized the anomaly, putting back the ship into normal operation.

REFERENCES

[1] A. Villalba Madrid, A. Álvarez Melcón, "Using Genetic Algorithms for Compensating the Local Magnetic Perturbation of a Ship in the Earth´s Magnetic Field", *Microwave and Optical Technology Letters, Vol. 47, Nº 3, November 2005*.

[2] F. Le Dorze, J.P. Bongiraud, J.L. Coulomb, P. Labie, X. Brunote, "Modeling of Degaussing Coils Effects in Ships by the Method of Reduced Scalar Potencial Jump", IEEE Transaction On Magnetics, Vol. 34, No. 5, September 1998.

[3] D.S. Weile, E. Michielssen, "Genetic Algorithm Optimization Applied to Electromagnetics: A Review", IEEE Transaction On Antennas And Propagation, Vol. 45, No. 3, March 1997.

[4] D.E. Goldberg, "Genetic Algorithm in Search, Optimization and Machine Learning", Addison-Wesley Professional; 1 edition (January 11, 1989).

[5] Hongda Liu, Zhongli Ma, "Optimization of Warship Degaussing System Based on Poly-population Particle Swarm Algorithm", Ship Engineering, Vol. 2, 2007, pp. 3133-3137.

[6] Potts, W. C., "The Magnetic Field of a Ship and its Neutralization by Coil Degaussing", General Journal of the Institution of Electrical Engineers – Part I, Vol. 93, No. 71, 1946, pp. 488-499.

[7] Yang, Yun-Tao | Shi, Zhi-Yong | Lu, Jian-Gang | Guan, Zhen-Zhen, "A Magnetic Disturbance Compensation Method Based on Magnetic Dipole Magnetic Field Distributing Theory", Journal of China Ordenance. Vol. 5, no. 3, pp. 185-191. Sept. 2009.

[8] X. Brunotte, G. Meunier, "Line Element for Efficient Computation of the Magnetic Field Created by Thin Iron Plates", IEEE Transaction On Magnetics, Vol. 26, No. 5, September 1990.

[9] X. Brunotte, G. Meunier, J.P. Bongiraud, "Ship Magnetization Modeling by the Finite Element Method", *IEEE Transaction On Magnetics, Vol. 29, No. 2, March 1993*.

[10] D. Rogers, P.J. Leonard, H.C. Lai, "Surface Elements For Modelling 3D Fields Around Thin Iron Sheets", *IEEE Transaction On Magnetics, Vol. 29, No.25, March 1993*.

[11] John J. Holmes, "Application of Models in the Design of Underwater Electromagnetic Signature Reduction Systems", Naval Engineers Journal, Volume 119, Issue 4, pages 19–29, November

2007, Article first published online: 22 JAN 2008 DOI: 10.1111/j.1559-3584.2007.00083.x

[12] A. Villalba Madrid, A. Álvarez Melcón,"Process for Compensating Local Magnetic Perturbations on Ferromagnetic Surfaces", Journal of Electromagnetic Analysis and Applications, 2012, 4. Published Online *October 2012 (http://www.SciRP.org/journal/jemaa).*

V International Conference on Computational Methods in Marine Engineering
MARINE 2013
B. Brinkmann and P. Wriggers (Eds)

MEAN LOAD EFFECTS ON THE FATIGUE LIFE OF OFFSHORE WIND TURBINE MONOPILE FOUNDATIONS

J.P. BLASQUES and A. NATARAJAN

Department of Wind Energy. Technical University of Denmark
Frederiksborgvej 399, 4000 Roskilde, Denmark
e-mail: jpbl@dtu.dk, anat@dtu.dk

Key words: fatigue damage, offshore wind turbine, monopile foundation, mean load correction

Abstract. This paper discusses the importance of mean load effects on the estimation of the fatigue damage in offshore wind turbine monopile foundations. The mud line bending moment time series are generated using a fully coupled aero-hydro-elastic model accounting for non-linear water waves and sea current. The fatigue damage is analysed in terms of the lifetime fatigue damage equivalent bending moment. Three different mean value correction techniques are considered, namely, Goodman, Walker, and mean sensitivity factor. An increase in the lifetime fatigue damage equivalent bending moment between 6% (mean sensitivity factor) and 33% (Goodman) is observed when mean load corrections are considered. The lifetime damage equivalent bending moment is further increased by approximately 7% when considering sea current forces. The results indicate that mean load correction techniques should be employed in the analysis of the fatigue life of offshore wind turbine monopile foundations. Moreover, it is shown that a nonlinear hydrodynamic model is required in order to correctly account for the effect of the current.

1 INTRODUCTION

Design load cases on wind turbines comprise of computer simulations that predict the operational, extreme and shutdown loads of a wind turbine in its estimated lifetime. The design load cases are divided into fatigue design and ultimate design cases [1]. The fatigue design loads are to a greater extent determined by simulating turbine operation with normal turbulence wind input from cut-in to cut-out mean wind speeds. The expected value of the wave significant height and peak crossing period at each mean wind speed is used to simulate the hydrodynamic loads. Rainflow counting [2] algorithms process the load time series over all turbine components to determine damage equivalent loads. It is assumed that the limited number of simulations performed is reflective of the total life time of the turbine whereby the resulting accumulated damage can be computed.

Many model uncertainties are present in the computation of fatigue loads on wind turbine structures, which are subject to highly dynamic loads and are also lightly damped. Most model uncertainties [3] that are quantified in literature deal with the aero-hydro-elastic models used in loads simulations, the wind turbulence variations and the methods utilized in quantifying load cycles. Further there are also uncertainties in the S-N curves [4] that are used to predict failure, especially in the presence of grouted or welded joints as in the case of offshore sub structures. However, another key model uncertainty is the inclusion of mean effects in the damage equivalent load determination. Different offshore turbine design standards cite varying recommendations in this regard. For example, the DNV report DNV-RP-C203 [4] neglects the specific use of mean corrections in the damage equivalent load estimation. On the other hand, the GL guidelines [5] recommend considering the mean stress corrections in the determination of damage equivalent loads. The effects of mean stress on fatigue stress limits of steel structures has been classically evaluated using the Goodman method [6]. However, the this method tends to be over conservative and other approaches have been suggested which give superior results. Namely, the Walker [7] formula is shown to be specially suited for cases where the mean stress is relatively low [8]. The material parameter in the Walker model has been calibrated using an extensive database of experimental data. Empirical formulas have been suggested for its determination based on the material ultimate stress [8]. For cases where the mean is relatively large a formulation based on the mean stress sensitivity factor has been put forward [9]. Also here, a material dependent parameter is used based on the ultimate stress of the material. The mean value corrections suggested in the GL guidelines [5] are based on this concept.

Wind turbine support structure dynamics are strongly influenced by the rotor loads, but may also be affected by the marine loads. The marine loads play a greater role as the wind turbine is installed in deeper waters. As wind turbine installations move to moderate water depths of 35m and above, the hydrodynamic models play a significant role in the determination of support structure design loads. Conventional load simulation codes utilize linear irregular wave kinematics or nonlinear regular waves [10] to determine the design loads on offshore turbines, but at these moderate depths the wave kinematics is nonlinear and non Gaussian. Therefore herein a second order nonlinear irregular wave model is utilized to determine the hydrodynamic loads on the monopile structure installed at 35m water depth. The bandwidth of the energy spectra for nonlinear waves is greater than that of linear waves, which implies greater probability of wave excitation of the support structure that influences the fatigue loads. Monopile installations are largely been confined to less than 30m water depths presently, but their potential at water depths near 35m is to be explored.

2 METHODOLOGY

The methodology employed in the determination of the marine loads and analysis of the fatigue loads is presented in this section. Details of the nonlinear wave model including

sea current forces are discussed, following which, the different mean amplitude correction techniques considered in this paper are presented.

2.1 Determination of marine loads

The wave kinematics is modeled using second order irregular nonlinear waves, where the linear part of the wave free surface is derived from the JONSWAP spectrum [1] . The nonlinear wave model depicts a non Gaussian process whereby the first four stochastic moments of the process are utillized to simulate the waves to any time length using a polynomial chaos series expansion [11]. The wave kinematics is developed to predict the wave velocities and accelerations from the soil to the wave crest without utilizing any geometric stretching methods and by satisfying the wave free surface boundary conditions to the second order at each time instant in the time series simulation of waves. The wave acceleration and velocity are formulated as:

$$\begin{aligned} u = &\sum_{i=1}^{N} \frac{gk_i}{\omega_i} A_i \frac{\cosh(k_i(z+h))}{\cosh(k_i h)} \cos(k_i x - \omega_i t + \beta_i) \\ &+ \sum_{i=1}^{N}\sum_{j=1}^{M} B_j B_i \left[P_{ij} \cos(k_{ij}^{-}\chi - \omega_{ij}^{-} t + \beta_i) + Q_{ij} \cos(k_{ij}^{+}\chi - \omega_{ij}^{+} t + \beta_i) \right] \end{aligned} \tag{1}$$

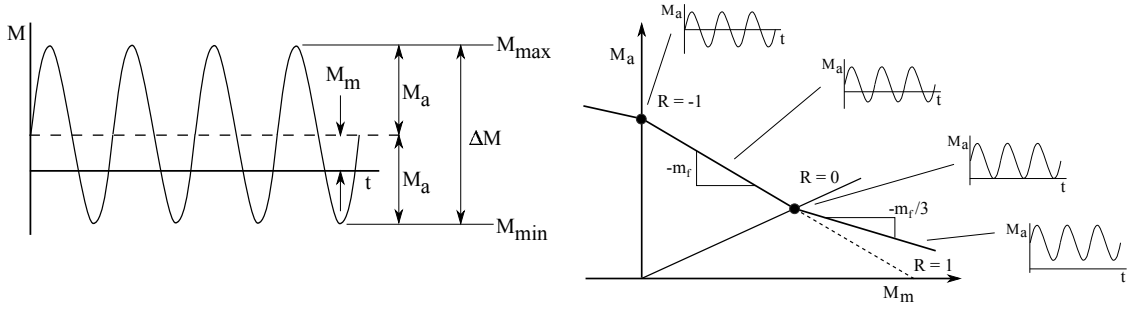
$$\begin{aligned} \dot{u} = &\sum_{i=1}^{N} -gk_i A_i \frac{\cosh(k_i(z+h))}{\cosh(k_i h)} \sin(k_i x - \omega_i t + \beta_i) \\ &+ \sum_{i=1}^{N}\sum_{j=1}^{M} C_j C_i \left[R_{ij} \sin(k_{ij}^{-}\chi - \omega_{ij}^{-} t + \beta_i) + S_{ij} \sin(k_{ij}^{+}\chi - \omega_{ij}^{+} t + \beta_i) \right] \end{aligned} \tag{2}$$

Where B, C, P_{ij}, Q_{ij}, R_{ij}, and S_{ij} are terms dependent on the wave amplitude, frequency and wave number and require a fairly detailed formulation, which is provided in [11]. The superscripts + and − refer to a summation or difference between the frequencies ω_i, ω_j or between the wave numbers k_i, k_j. The forces on the sub-structure are computed using the Morison equation [1], which requires the evaluation of the wave velocity and acceleration normal to the structure. The wave loading at a section of the monopile is given by:

$$dF(z,t) = C_M \rho \frac{\pi}{4} d^2 (\dot{u}_n - a_s) dz + C_d d \frac{1}{2} \rho (u_n - v_s)|u_n - v_s| dz \tag{3}$$

where C_M is the coefficient of inertia, d is the diameter of the monopile, u_n is the normal wave velocity at the section z, a_s is the structural acceleration, v_s is the structural velocity, and C_d is the coefficient of drag.

The presence of currents is common in wind farms, such as tidal currents and they may be in the same direction as the wave or even oppose it. Currents are normally considered



(a) (b)

Figure 1: (a) Description of the cycle amplitude M_a, range ΔM, mean M_m, maximum M_{max}, and minimum M_{min}. (b) Haigh diagram showing magnitude of m_f and the mean and amplitude relation for different ranges of R.

not to impact the fatigue damage equivalent loads [1], but this is due to the assumption of linear wave kinematics, whereby the current only affects the mean drag force. Using the 2-D nonlinear Euler equations of fluid dynamics, Eq. (3) in the presence of currents can be re-written as

$$\begin{aligned} dF(z,t) = C_M \rho \frac{\pi}{4} d^2 \left(\frac{\partial u}{\partial t} + (u+c)\frac{\partial u}{\partial x} + w\frac{\partial u}{\partial z} - a_s \right) dz \\ + C_d d \frac{1}{2} \rho (c + u_n - v_s)|(c + u_n - v_s)|dz \end{aligned} \tag{4}$$

where c is the constant current velocity, $\partial u/\partial x$ and $\partial u/\partial z$ are the derivatives of the normal velocity with displacement and $\partial u/\partial t$ is the local acceleration. From Eq. (4), it can be readily seen that the current velocity, though a constant affects the amplitude of the marine load and not just the mean. As the current velocity enters the inertial forcing term as a multiple of the spatial derivative, the current affects the amplitude of the inertial force, which implies it also affects the damage equivalent load directly. Since the mean of $\partial u/\partial x$ is zero, the mean inertial load is not affected by the current. However the mean drag force is increased due to the presence of the current. Hence using nonlinear waves, the current increases the mean drag force and also increases the amplitude of the inertial loads. The analysis suggested in the next section where the fatigue damage equivalent bending moment includes mean load amplitude corrections, will be able to account for both the mean and amplitude effects.

2.2 Fatigue damage analysis

The damage is assessed based on the mud line bending moment resulting from the wind, wave, and current forces. The fatigue analysis procedure typically based on stresses is herein based on the bending moment. Hence, where one would usually read *stress*, here it is mentioned *moment*.

The analysis of the fatigue damage in the monopile foundation is done in terms of the fatigue damage equivalent bending moment [9]. The fatigue damage D_i resulting from one load cycle of intensity M_i is given by $D_i = 1/N_i$ where N_i is the number of cycles to failure for a bending moment of intensity M_i. The accumulated damage from a varying number of cycles with different stress intensities is given by $D = \sum_{i=1}^{n_c} D_i = \sum_{i=1}^{n_c} n_i/N_i$. In the expression above, n_c is the total number of cycles, and n_i is the number of cycles for which N_i is the limit value at the corresponding bending moment level. The fatigue damage equivalent bending moment is given by

$$M_{eq} = \left(\frac{\sum_{i=1}^{n_b} n_i M_i^m}{N} \right)^{\frac{1}{m}} \tag{5}$$

where n_b is the number of bins used for the cycle counting, n_i and M_i are the number of cycles and moment intensity at bin i, respectively, m is the slope of the SN curve and is material dependent, and N is a predefined number of cycles.

For irregular load signals a cycle counting technique is usually employed to determine the amplitudes and means of the underlying load cycles. The rainflow cycle counting technique has been shown to match experimental results better [12] and an implementation of this algorithm is therefore used in this paper [13]. The rainflow cycle amplitudes are binned in order to determine the values of n_i and M_i which are then used in Eq. (5). The number of cycles counted from the load histories are further scaled by the Weibull hours for each mean wind speed to estimate the lifetime fatigue damage equivalent bending moment.

2.2.1 Mean value correction techniques

The properties of the SN curve are given assuming that the mean of the load cycles is low or negligible with respect to the amplitude. However, in some cases the mean load level may contribute to the fatigue damage. In order to account for mean load effects, different methods have been suggested in which the amplitudes of each cycle are corrected in function of its mean. For a given cycle amplitude and mean – M_a and M_m, respectively – an *equivalent reversed moment amplitude*, M_{ar}, is defined that is expected to cause the same life. Having determined M_{ar} it is possible to determine the mean corrected amplitude histograms and recompute the fatigue damage equivalent bending moments using Eq. (5).

Different mean load amplitude correction techniques with varying degree of accuracy are available in the literature. The accuracy and validity of the different techniques depends, among other, on the magnitude of R, defined here as

$$\begin{cases} R = \frac{M_{min}}{M_{max}}, & \text{iff} \quad M_m \geq 0 \\ R = \frac{M_{max}}{M_{min}}, & \text{iff} \quad M_m < 0 \end{cases} \tag{6}$$

where $M_{max} = M_m + M_a$, $M_{min} = M_m - M_a$. An alternative definition of R can be given in terms of the amplitude and mean of a given cycle as $M_m/M_a = (1+R)/(1-R)$. Different

R values correspond to different relations between cycle amplitude and mean as described in Figure 1(b). Note that the definition of R presented in (6) is different from that typically used for the stresses (see, e.g., Dowling et al [8]). A negative stress corresponds to compression in which case it is to expect that the fatigue life of the component is not increased. In this case it is correct to assume that R is always within the range $-1 \leq R \leq 1$.

Four different mean load correction techniques are considered in this study – Goodman, Walker, mean moment sensitivity factor, and a variation of the latter. The expression proposed by Goodman [6] is

$$M_{ar} = \frac{M_a}{1 - \frac{M_m}{M_u}} \tag{7}$$

where it is assumed that the ultimate bending moment $M_u = 1.5 M_{max}^T$ where M_{max}^T is the maximum bending moment measured throughout the entire time series across all wind speeds. The Goodman expression is characterized by its simplicity and works relatively well for tensile mean stress levels. However, its results maybe be inaccurate and this expression should only be used when none of the material fatigue properties are known [8]. Alternatively, the Walker formula [7] is commonly used for estimating the fatigue life of components and has been shown to give superior results [8]. It is defined as

$$M_{ar} = M_a \left(\frac{2}{1-R} \right)^{1-\gamma}, \text{ where, } \gamma = -0.0002\sigma_u + 0.8818 \tag{8}$$

where $\gamma \in [0, 1]$ is a material dependent parameter and σ_u is the material ultimate stress. The Walker approach is mostly suitable for relatively low mean stresses [9].For relatively large mean stresses an alternative approach has been proposed based on the mean stress sensitivity factor, m_f, or the slope of the line in the Haigh plot [9]. In this case M_{ar} is defined as

$$M_{ar} = M_a + m_f |M_m|, \text{ where, } m_f = 0.00035\sigma_u - 0.1 \tag{9}$$

The material parameter $m_f \in [0, +\infty]$ is determined based on an empirical model. For steel structures the value of m_f can be determined based on the ultimate strength (see, e.g., [9] and [2]). For the cases where $0 \leq R \leq 1$ or $M_m > M_a$, m_f is typically lower by a factor of 3 such that $m_{f,3} \approx m_f/3$ (see Figure 2.2). This is due to the fact that the fatigue damage due to cycles with a high mean and relatively low amplitude is lower than that predicted by m_f. GL [5] suggest the same correction when working with ductile steels. This formulation is henceforth referred to as the R-corrected mean moment sensitivity factor.

3 RESULTS

The analysis of the fatigue damage on the monopile foundation using mean value correction techniques is presented in this section. The setup of the numerical experiments

is described first. The resulting fatigue damage equivalent bending moments are compared and the effect of the amplitude corrections is analysed next. Finally, the effect of the currents is discussed.

3.1 Setup

The mud line bending moment time series acting on the monopile are simulated in HAWC2, an aero-hydro-elastic software [14], using the NREL 5MW wind turbine [15] mounted on a monopile foundation at 35m water depth. The loads are analysed for 18 different mean wind speeds ranging from 8m/s to 25m/s. Three random turbulent seeds are used for each mean wind speed. Each of the time series is 600 s long. The fore-aft (i.e., wind direction) and side-side (i.e., transverse to the wind direction) directions are treated separately. The results are determined with and without sea current which is collinear with the waves and acts in the fore-aft direction. The load time series are filtered using a rainflow cycle counting technique to identify the amplitude and mean of the equivalent load cycles [13]. A number of $n_b = 100$ bins is used for binning the rainflow cycle amplitudes and determine the number of cycles. The Weibull shape parameter is $\kappa = 2$, the mean value $\overline{w}_{wbl} = 10m/s$, and thus the scaling parameter is $\lambda = \overline{w}_{wbl}/\Gamma(1 + 1/\kappa) = 11.28$. The total number of load cycles for each mean wind speed throughout the 20 year lifetime are scaled from the corresponding Weibull hours.

It is assumed that the monopile foundation is built of steel NV-36 for which the stiffness modulus is E=210 Mpa, the shear modulus is G=80 Mpa and the ultimate stress is $\sigma_u = 550$ Mpa. The material dependent parameters used in the Walker Eq. (8) and mean moment sensitivity factor Eq. (9) determined based on the ultimate stress are $\gamma = 0.772$ and $m_f = 0.0925$, respectively. Moreover, for all cases a slope of the SN curve $m = 4$ is chosen. This is within the range between 3 and 5 typically chosen for this type of structures [5].

3.2 Discussion

The fore-aft and side-side lifetime fatigue damage equivalent bending moments with and without current and mean load corrections, are presented in Table 1. Note that the estimated values have an uncertainty associated with it due to the finite number of seeds. This is also the reason for the results in Figure 3 to be non-smooth. The distribution of the counted cycles in an amplitude versus mean histogram for the fore-aft and side-side loads with current is presented in Figures 2 (a) and (b), respectively. The results without current are indistinguishable and are therefore omitted. The mean of the bending moment for each mean wind speed is presented in Figures 2 (c) and (d). The effect of the mean load correction on the fore-aft and side-side lifetime fatigue damage equivalent bending moment with current included is shown in terms of mean wind speed in Figure 3. The results without current are very similar – the magnitudes are slightly lower but the relative differences are the same. The effect of varying m has been studied and is

Table 1: Results for the fore-aft and side-side lifetime fatigue damage equivalent bending moment, M_{eq}. Results with and without current – *Current* and *No current*, respectively. The mean load corrections according to Goodman (GDM), Walker (WLK), mean sensitivity factor (MSF), and R-corrected mean sensitivity factor (MSF/3), are considered. *rel. dif.* and *abs. dif.* refer to relative and absolute differences, respectively. *Orig. vs. Correct.* refers to a comparison between the original and mean corrected values. *Curr. vs. no curr.* refers to a comparison between the results with and without sea current forces.

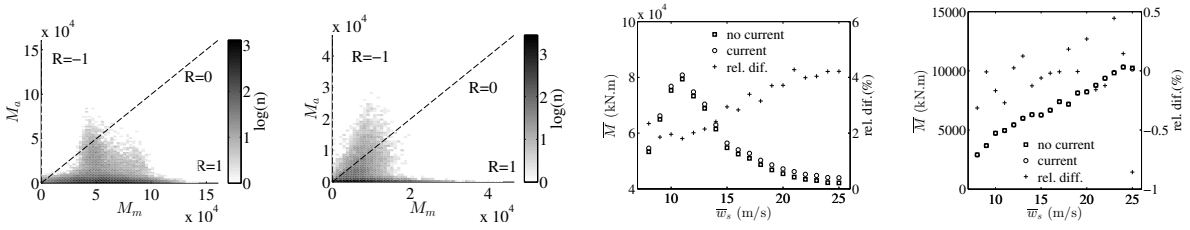
Fore-aft		**Original**	**GDM**	**WLK**	**MSF**	**MSF/3**
No current	$\boldsymbol{M_{eq}}$ **(kNm)**	1.52E5	2.03E5	1.86E5	1.74E5	1.62E5
Orig. vs.	rel. dif. (%)	-	33.6	22.1	14.5	6.2
Correct.	abs. dif. (kNm)	-	5.12E4	3.36E4	2.20E4	9.42E3
Current	$\boldsymbol{M_{eq}}$ **(kNm)**	1.64E5	2.18E5	1.99E5	1.87E5	1.74E5
Orig. vs.	rel. dif. (%)	-	32.8	21.4	13.8	6.0
Correct.	abs. dif. (kNm)	-	5.37E4	3.52E4	2.26E4	9.92E3
Curr. vs.	**rel. dif. (%)**	7.3	6.7	6.8	6.7	7.1
no curr.	**abs. dif. (kNm)**	1.19E4	1.45E4	1.35E4	1.25E4	1.24E4

Side-side		**Original**	**GDM**	**WLK**	**MSF**	**MSF/3**
No current	$\boldsymbol{M_{eq}}$ **(kNm)**	3.76E4	4.24E4	4.26E4	4.03E4	3.96E4
Orig. vs.	rel. dif. (%)	-	12.9	13.3	7.2	5.2
Correct.	abs. dif. (kNm)	-	4.84E3	5.02E3	2.69E3	1.97E3
Current	$\boldsymbol{M_{eq}}$ **(kNm)**	3.78E4	4.26E4	4.28E4	4.05E4	3.98E4
Orig. vs.	rel. dif. (%)	-	12.9	13.3	7.1	5.2
Correct.	abs. dif. (kNm)	-	4.87E3	5.02E3	2.68E3	1.97E3
Curr. vs.	**rel. dif. (%)**	0.5	0.5	0.4	0.4	0.5
no curr.	**abs. dif. (kNm)**	1.84E2	2.16E2	1.87E2	1.75E2	1.86E2

presented in Figure 4 where it is assumed that $\overline{w}_s = 16$ m/s. Finally, the effect of the current on the magnitudes of the lifetime fatigue damage equivalent bending moment is visible in Figure 5.

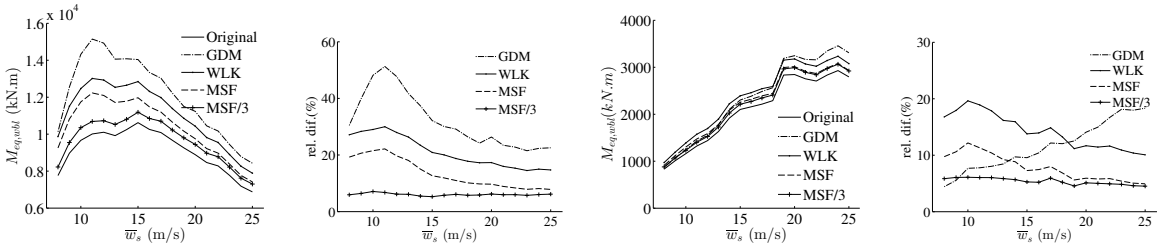
From Table 1 we can see that the effect of the mean load amplitude corrections is more significant in the fore-aft than in the side-side loads. This is in agreement with the results from Figures 2 (c) and (d) which show that the mean of the bending moment of the fore-aft loads is significantly higher. The negative mean values measured in the side-side loads are most probably due to the moment induced by the generator as it counteracts the rotor torque.

In the fore-aft case the R-corrected mean sensitivity factor (MSF/3), mean sensitivity factor (MSF), Walker (WLK), and Goodman (GDM) techniques give increasingly conservative results (see Table 1). The same trend is observed in Figure 3 where it is also clear that the difference between the mean corrected and uncorrected results is larger at lower wind speeds. As can be observed in Figure 2 (a), for most of the load cycles



(a) fore-aft (b) side-side (c) fore-aft (d) side-side

Figure 2: Histogram of amplitude M_a versus mean M_m for the fore-aft (a) and side-side (b) mud line bending moment with sea current included for all wind speeds. Gray scale indicates number of cycles n in each bin (log scale). Fore-aft (c) and side-side (d) mean mud line bending moment, $\overline{M}$, with and without current for different mean wind speeds, $\overline{w}_s$.

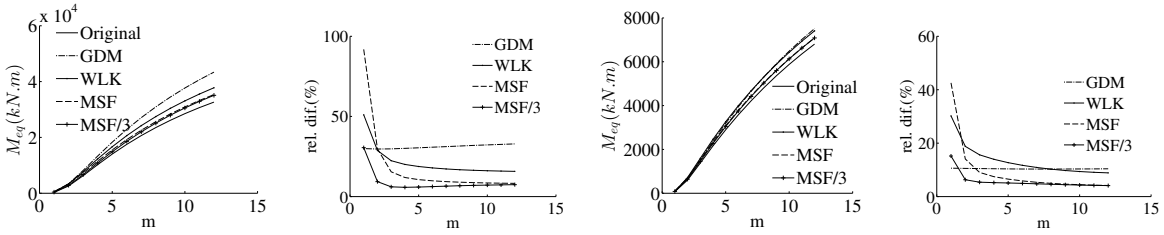


(a) fore-aft (b) fore-aft (c) side-side (d) side-side

Figure 3: Comparison between the fatigue damage equivalent bending moments, M_{eq}, scaled by the Weibull hours for different mean wind speeds, $\overline{w}_s$. Results with and without mean value moment corrections based on Goodman (GDM), Walker (WLK), mean moment sensitivity factor (MSF), and R-corrected mean moment sensitivity factor (MSF/3). Results for $m = 4$ and $N_{eq} = 1 \times 10^6$ cycles. Magnitude (a-c) and relative difference (b-d) of fore-aft and side-side fatigue damage equivalent bending moment.

across all wind speeds the ratio R (from Eq. (6)) is within the range $0 < R < 1$. It is therefore to expect that techniques which are tailored for this type of loads (i.e., MSF and MSF/3) give less conservative results than others developed to work with lower R values (i.e., WLK and GDM). Moreover, the higher values of M_{eq} at lower wind speeds are in agreement with the results from Figure 5 which show that the mean bending moment is higher within this range. Regarding the effect of varying m, there is an asymptotic trend for WLK, MSF, and MSF/3 for which the relative difference remains constant for $m > 5$ (see Figure 4). Below this value and for these three techniques, the error grows rapidly. The relative difference for the GDM case is constant for all mean wind speeds.

The same trend between the different mean correction techniques is observed in the side-side case although here the GDM and WLK results are closer. The variation of the lifetime fatigue damage equivalent bending moment for the different wind speed is also similar except for the GDM case which presents an increasing relative difference with increasing wind speeds (see Figure 3 (d)). Finally the effect of varying m is also very similar although the GDM case is less conservative than the WLK for a wider range of



(a) fore-aft (b) fore-aft (c) side-side (d) side-side

Figure 4: Comparison between the fatigue damage equivalent bending moments, M_{eq}, for different values of m including sea current forces. Results with and without mean value moment corrections based on Goodman (GDM), Walker (WLK), mean moment sensitivity factor (MSF), and R-corrected mean moment sensitivity factor (MSF/3). Results for $\overline{w}_s = 16m/s$ and $N_{eq} = 1 \times 10^6$ cycles. Magnitude (a-c) and relative difference (b-d) of fore-aft and side-side fatigue damage equivalent bending moment.

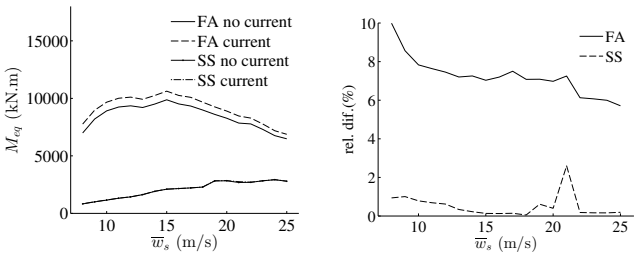
wind speeds.

The effect of the current on the lifetime fatigue damage equivalent bending moment is expected to be null if the current affects only the mean of the loads. However, from Table 1 and Figure 5, it is seen that the results with and without current are different which shows that the amplitudes are also affected by the current. A simple experiment can reveal the effect of the sea current in terms of the amplitude and mean separately. For each mean wind speed the load histories determined without sea current are offset exactly by the mean of the corresponding results with current. This mimics the case where the sea current affects only the mean. As expected, the value of the fatigue damage equivalent bending moment without mean load correction remains the same as the amplitudes remain unchanged. The mean corrected values, on the other hand, present very small differences (approximately 0.5%) independently of the correction technique. These results emphasize the fact that the effect of the sea current in the load cycle amplitudes is the most important contribution to the increase in fatigue damage equivalent bending moment. Most importantly, this effect can only be correctly accounted for if the nonlinear model of the marine loads as in Eq. (4) is used.

Finally, it is noted that the relative difference between the results with and without current is smaller when using mean load amplitude correction techniques. This seems to suggest that the mean correction techniques reduce the effect of the current. However, the absolute differences are larger which is in agreement with the expected trend.

4 CONCLUSIONS

The mud line bending moment acting on the monopile is determined using an aero-hydro-elastic model which accounts for nonlinear wave and sea current effects. The fatigue damage is analysed in terms of the fore-aft and side-side lifetime fatigue damage equivalent bending moment with and without sea current forces. Four different mean load amplitude correction techniques are compared - Goodman (GDM), Walker (WLK), the



(a) magnitude (b) rel. dif.

Figure 5: Magnitude (a) and relative difference (b) of the fore-aft (FA) and side-side (SS) fatigue damage equivalent bending moments, M_{eq}, with and without current for different mean wind speeds, $\overline{w}_s$. Results obtained without mean moment amplitude correction for $m = 4$ and $N_{eq} = 1 \times 10^6$ cycles.

mean moment sensitivity factor (MSF), and the R-corrected mean moment sensitivity factor (MSF/3). Increases in the lifetime fatigue damage equivalent bending moment ranging from approximately 6% (MSF/3) to 30% (GDM) are observed. These results demonstrate the importance of using mean load amplitude correction techniques in the design of monopile foundations. Furthermore, it is also shown that for most of the load cycles the ratio R between the minimum and maximum of each cycle is $0 < R < 1$. This suggests that MSF and MSF/3, which are designed to work in this range of R, are probably the most suitable. Finally, an increase of approximately 7% in the fore-aft lifetime fatigue damage equivalent bending moment due to the sea current is observed. It is shown that this difference is mostly motivated by an increase in the amplitude and not the mean of the load cycles. This result is a clear indication that a nonlinear wave model is required in order to correctly account for the sea current effects.

REFERENCES

[1] IEC International Standard, *Wind Turbines Part 3, Design requirements for offshore wind turbines*, Edition 1, 2009.

[2] Veldkamp, H.F. *Chances in Wind Energy - a Probabilistic approach to wind turbine fatigue design*. Ph.D. Thesis, Delft University, (2006).

[3] Sørensen J.D., Frandsen F., Tarp-Johanssen N.J., Effective turbulence models and fatigue reliability in wind farms, *Journal of Probabilistic Engineering Mechanics*. (2008) **23**(4):531–538.

[4] DNV Recommended Practice, *Fatigue Design of Offshore Steel Structures*, Report number DNV-RP-C203, (2011).

[5] GL Rules and Guidelines, *Guidelines for the certification of wind turbines*. Germainscher Lloyd Industrial Services Gmbh, July 1st, (2010).

[6] Goodman, J. *Mechanics applied to engineering*. Longmans, Green and Co., London, (1919).

[7] Walker, K. The effect of stress ratio during crack propagation and fatigue for 2024-T3 and 7075-T6 aluminum. *Effects of environment and complex load history on fatigue life, ASTM STP 462* (1970) Philadephia, PA, 1–14.

[8] Dowling, N. E. and Calhoun, C. A. and Arcari, A. Mean stress effects in stress-life fatigue and the Walker equation. *Fatigue & Fracture of Engineering Materials & Structures* (2009) **32**(3):163–179.

[9] Lee, Y.L., Pan, J., Hathaway, R., Barkley, M. *Fatigue testing and analysis - theory and practice*. Elsevier, (2005).

[10] De Wries W., Vemula N.K., Passon P., Fischer T., Kaufer D., Matha D., Schmidt B., Vorpahl F. *Support Structure Concepts for Deep Water Sites*. UpWind Project final report D4.2.8, (2011).

[11] Moan T., Zheng X.Y., Quek S.T. Frequency-domain analysis of non-linear wave effects on offshore platform responses. *International Journal of Non-Linear Mechanics* (2007) **42**:555–565.

[12] Dowling, N.E. Fatigue predictions for complicated stress-strain histories. *J. Materials* (1972) **7**:71–87.

[13] WAFO-group, WAFO - A Matlab Toolbox for Analysis of Random Waves and Loads - A Tutorial., Math. Stat., Center for Math. Sci., Lund Univ., Lund, Sweden, (2000).

[14] Larsen, T.J., Hansen, A.M., *How 2 HAWC2, the user's manual*. Technical University of Denmark, (2006).

[15] Jonkman, J., Butterfield, S., Musial, W., Scott, G., *Definition of a 5-MW reference wind turbine for offshore system development*. NREL/TP-500-38060, (2009).

V International Conference on Computational Methods in Marine Engineering
MARINE 2013
B. Brinkmann and P. Wriggers (Eds)

DYNAMIC SIMULATIONS OF AN AIRPLANE-SHAPED UNDERWATER TOWED VEHICLE

MARINE 2013

A. CAMMARATA[*], M. LACAGNINA[#] AND R. SINATRA [†]

[*] Department of Industrial Engineering (DII)
University of Catania
Viale A. Doria n. 6, 95123 , Catania, Italy
e-mail: [*]acamma@dii.unict.it, [#]mlacagnina@dii.unict.it, [†]rsinatra@dii.unict.it.

Key words: Towfish, towed vehicles, tethered vehicles, underwater vehicles, UTV.

Abstract.
This paper discusses the dynamic simulations of a Towfish equipped with three wings, two of which can be moved for a possible stability depth control. The models describing the 3D geometry of both vehicle and towing cable are implemented, their main parameters and the acting forces are evaluated and then simulated using a multibody dynamic software. Numerical values of the hydrodynamic forces and moments, obtained by numerical fluid dynamics analyses, are also added to the vehicle model in order to obtain a more accurate simulation of the open-loop behavior of the system.
As shown in the Fig. 1, the airplane-shaped Towfish has three wings: a main fixed wing, a mobile stern wing and another mobile bow wing, called Canard wing. The vehicle length is 1.8 m, its height is 52.8 cm and its width is 2 m., measured as the wingspan of the main wing.
The system is designed as a not buoyant object, while the airfoil shape of the wings is chosen according to the NACA code. The towing cable has a length of 500 meters, a section diameter of 30 mm and its linear weight in the seawater is 1.27 kg/m. Finally, the connection between the cable and the towfish is reproduced by a spherical joint.

Numerical simulation results show a depth stability of the vehicle associate with a positive pitch angle. The used method can provide some appreciable results to create a stability control system.

1 INTRODUCTION

Underwater Towed Vehicle systems (UTV) are the most commonly used systems for the survey of the seabed. They consist of two main parts: the vehicle, also known as Towfish, and the cable that represents the propulsion system for all the vehicle movements.
The supply system equipped in the majority of the vehicles is the Side-Scan Sonar, it allows to obtain seabed images by sending and receiving sound waves. The most important feature of this kind of system is the pitch stability during the image acquisition time that allows to have high resolution pictures of the seabed using the side-scan sonar [1].

Pioneering works on towfish dynamics can be found in [2], while the cable modelling along with the vehicle's dynamics is described in [3].
The importance of controls and manoeuvre optimization to achieve stability can be found in [4].
In this paper an airplane-shaped Towfish designed at the Department of Industrial Engineering (DII) at the University of Catania is described and its dynamic modelling is formulated.
The dynamic model is well approximated using a two-dimensional approach considering a straight line trajectory of the towing vessel. It provides an useful tool for the understanding of the motion of the vehicle starting from different initial conditions obtained moving the mobile wings orientation. It also could be used for the design and the test of a closed loop control system to maintain the stability.
To develop a complete model needed to understand system's limits and abilities we recur to a multiphysics description in which the rigid body dynamics of the towfish and the flexible dynamics of the cable are coupled and influenced by the hydrodynamic interaction with water.
In Section 2 the system and its subparts are described. Then the cable model is developed by means of two different methods. Section 4 deals with the vehicle's dynamics definition and the determination of hydro-dynamic forces/torques by FEM. Finally, Section 5 reports the numerical results obtained through multibody dynamics software simulations.

2 SYSTEM OVERVIEW

As shown in the Fig. 1, the airplane-shaped Towfish has three wings: a main fixed wing, a mobile stern wing and another mobile bow wing, called Canard wing. The vehicle length is 1.8 m, its height is 52.8 cm and its width is 2 m., measured as the wingspan of the main wing.

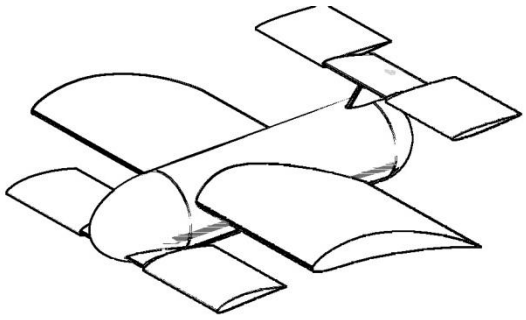


Fig. 1: Towfish

Its volume (V) is 0.3 m^3 and it was designed as a not buoyant object; its buoyancy (I) is equal to 17756 N (this is a force with a positive direction in the used reference system). Its mass in the sea water is 201.4 kg. The airfoil shape of the wings, chosen by the designer, are reported in the following table where every number is referred to the NACA code.

Tab.1: NACA codes of the towfish airfoil wings.

Main wing	8412
Stern wing	0008
Canard wing	4412

Figure 2 shows the fixed coordinate system used to study the motion of the vehicle; the origin is located at the centre of mass, the x axis lies on the vehicle longitudinal axis and directed toward its bow. The y axis is directed to the sea surface.

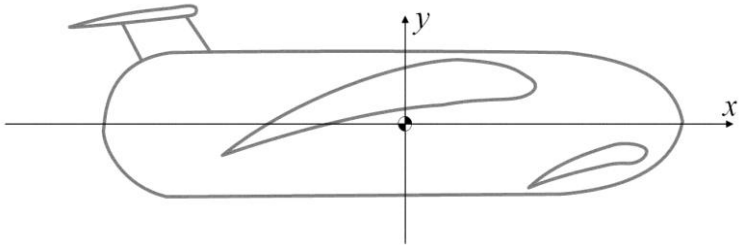


Fig. 2: Towfish reference frame

In Figure 3 the angles of attack of the three wings are indicated. They are evaluated starting from the longitudinal axis of the vehicle where the positive orientation is counterclockwise.

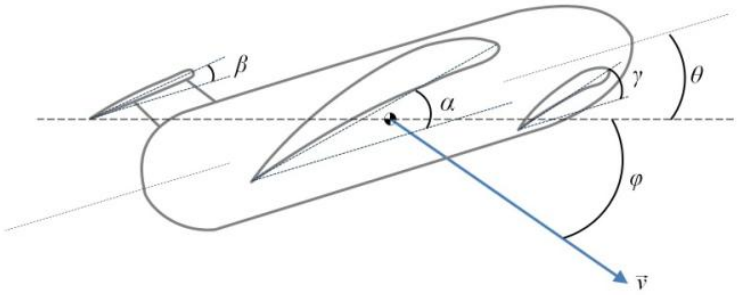


Fig. 3: Towfish angles.

It is important to remember that the angle of attack α of the main wing angle is fixed to the value of 11° and the angles β and γ can be varied between 0° and 10° and between 0° and 20°, respectively.
The same figure also shows the pitch angle θ evaluated starting from the fixed x axis, and the angle φ describing the velocity vector orientation.

The towing cable has a length of 500 meters, a section diameter of 30 mm and its linear weight in the seawater is 11.27 kg/m.

The connection between the cable and the towfish is realized by a spherical joint.

3 CABLE MODELING

Cable modeling for towed underwater vehicle has been investigated in the literature, [6]. Here we recur to two different approaches: a static computation and a dynamic simulation.

The computation approach is a two-dimensional version of a static model [8]. It can simulate the shape of a submerged cable knowing its speed and the force applied to its free end, that, in this case, is equal to the drag supplied by the vehicle during the navigation.

In this model, as shown in Fig. 5, a new coordinate system is used, where the cable orientation at any point is defined by ω, the angle between the cable longitudinal unit vector $\hat{t}$ and the fixed x axis. The second coordinate axis is the unit vector $\hat{n}$, normal to the cable.

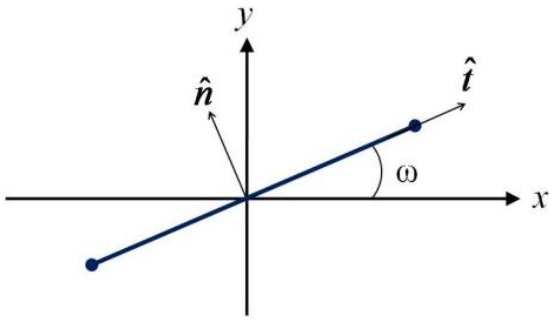


Fig. 5: Cable coordinate system

The equations of the cable are:

$$\begin{cases} \dfrac{\partial T}{\partial s} = W_S \sin\omega \\ \dfrac{\partial \omega}{\partial s} T = C_N \left| U_S \sin\omega \right| U_S \sin\omega + W_S \cos\omega \\ \dfrac{\partial x}{\partial s} = \cos\omega \\ \dfrac{\partial y}{\partial s} = \sin\omega \end{cases} \tag{1}$$

where s is the arc length, T is the tension in the cable, W_S is the linear weight of the material of the cable, C_N is the normal hydrodynamic coefficient, U_S is the speed along the x axis.

Figure 6 shows different curves obtained by modifying the value of the linking angle for a given value of the tension.

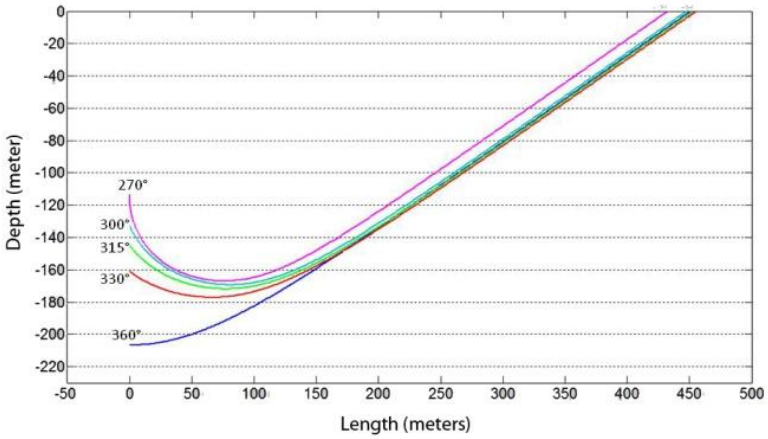


Fig. 6: Shapes of the cable.

For the second approach a pseudo-rigid model is developed. The cable is discretized using 10 cylinder-shaped rigid bodies linked by revolute joints, with a length of 50 meters each. A torsion spring/damper is added to each coupling to simulate the elastic behaviour of the cable. The end links of the cable are attached to the boat and towfish, respectively, via spherical joints.

The stiffness and the damping coefficients are evaluated considering the cable dimension and its material, so their values are respectively: K =2.77 N m/deg and C = 0.05 N m s/deg. The two components of the hydrodynamic force are applied on the centre of mass of each rigid segment of the cable; i.e.

$$H = \tfrac{1}{2} \cdot \rho \cdot S \cdot C_I \cdot v^2 \tag{2}$$

where ρ is the water density, S is the considered surface, v is the speed and C_I is the hydrodynamic coefficient whose value is considered constant and equal to 1.2. Figure 7 compares a dynamic simulation with a vertical force of 800 N applied to the free end to a simulation obtained through the first static approach. It can be observed that the static model shows good accordance to the dynamic one

4 TOWFISH MODELLING

The 3D model of the towfish is realized through CAD software and then imported into a multibody simulation software.

The equations that describes the dynamics of the vehicle are based on the second Newton's law: i.e.

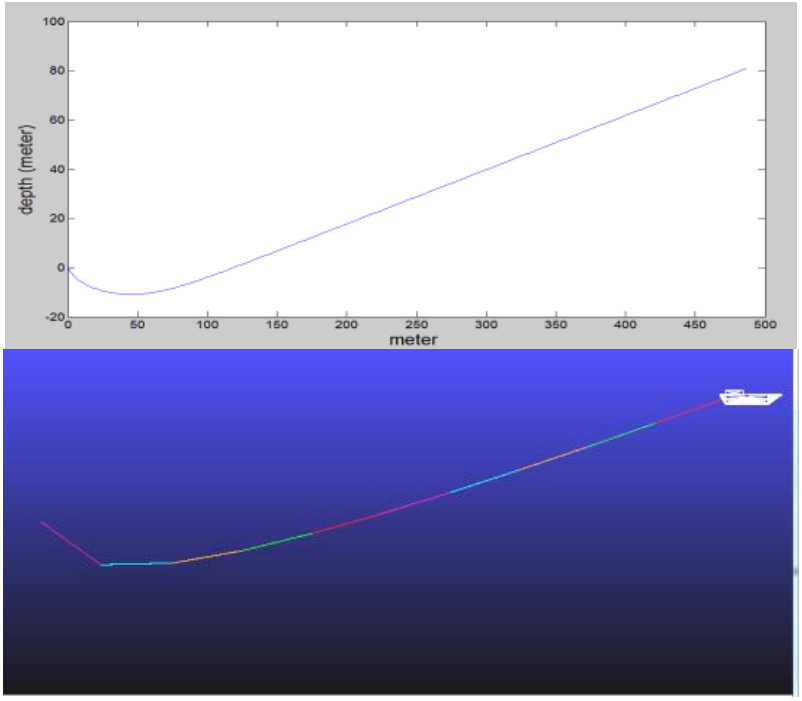


Fig. 7: Comparison between the two cable simulation approaches.

$$\begin{cases} -A_x - B_x - C_x - E_x + T_x = ma_x \\ A_y + B_y + C_y + E_y + (I - G) - T_y = ma_y \\ MA_z + MB_z + MC_z + ME_z + MI_z + MT_z = I_{zz}\ddot{\theta} \end{cases} \tag{3}$$

There are only three equations since a two-dimensional model is taken into account. To have a better comprehension of each term of eq.(3), Fig. 8 represents all the acting forces.

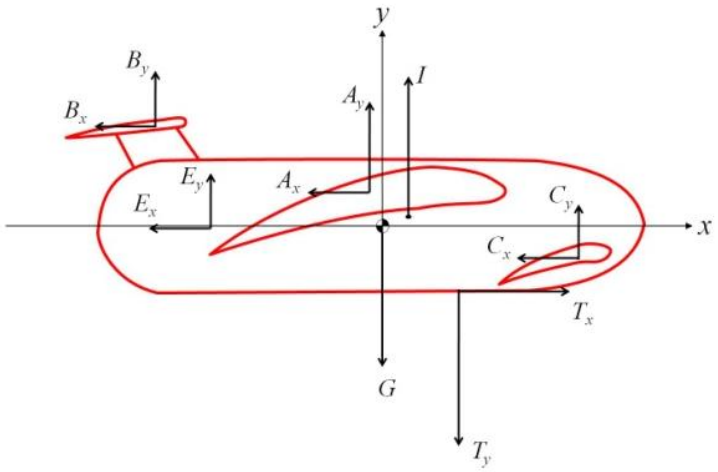


Fig. 8: Forces acting on the towfish.

where I and G are the hydrostatic forces of buoyancy and weight, respectively; A_x, B_x, C_x and E_x are the drag forces of the main wing, the stern wing, the Canard wing and the fuselage, respectively, and A_y, B_y, C_y and E_y are the lift forces of the same parts. T_x and T_y represent the forces of the cable tension that play the same role of the propulsion force in a normal airplane. MA_z, MB_z and the other similar variables indicate the torque acting on every part.

The hydrodynamic forces evaluation, during the vehicle motion, is not easy because of two main reasons: the pressure centre, that is the application point of these forces, changes its position during the motion, being its position not easy to predict. The second reason is that the values of the smaller wings drag forces is difficult to evaluate because the main wing produces vortex due to their small distances. For these reasons, in order to obtain more accurate results of the simulation, the hydrodynamic forces values are obtained using several computational fluid dynamics analyses. The ensuing values of drag, lift forces and torques are then added to the model using *splines*; allowing to obtain the hydrodynamic forces/torques for any given vehicle's speed angle and pitch.

4.1 Computational Fluid Dynamics Analysis

Every simulation has an associated value of the towfish pitch angle and mobile wings angles β and γ. The total amount of the simulations is 32, that is the number of all the combination obtained from all the used parameters values, reported in the following table.

Tab.2: Angle values in degrees used in the CFD simulations.

θ	-15° ; 0° ; 6° ; 15°
β	0° ; 5° ; 10°
γ	0° ; 10° ; 20°

Every simulation has the same phases: the definition of the domains geometry, its discretization using a three-dimensional finite elements mesh, the initial condition parameters setting, the analysis parameter formulation (the maximum STD error is 10^{-4}) and finally the simulation running. From the post-processing phase of every simulation, the hydro dynamics forces and moments are evaluated for all the parts of the towfish. The following picture shows a post-process image of the distribution of the force applied on the Canard wings.

All these values are then elaborated in order to obtain the total hydrodynamic forces and moments acting on the whole towfish for every simulated triad of angles.

Fig. 10 shows the spline for the total lift force, depending on the pitch angle, for the mobile wings position: $\beta = 5$ and $\gamma = 0$.

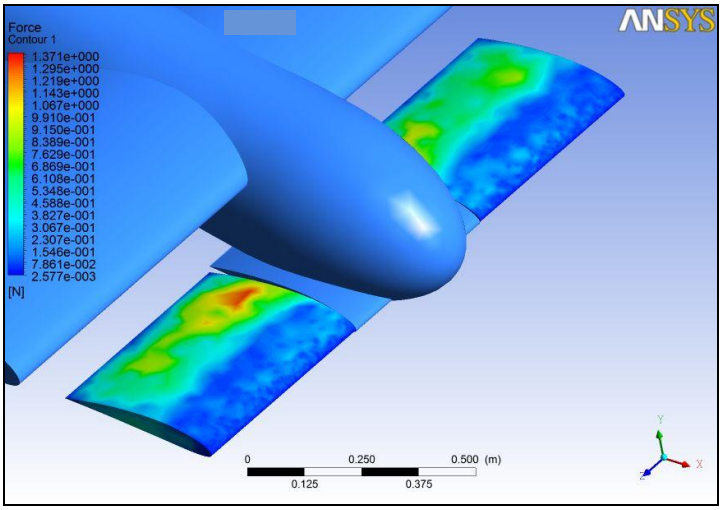


Fig. 9: Force distribution on the Canard wing.

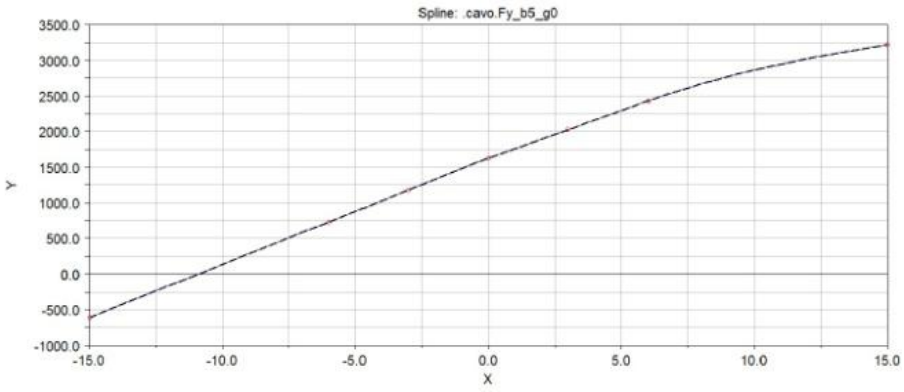


Fig. 10: Curve of the lift force acting on the towfish for a configuration of mobile wings $\beta = 5°$ and $\gamma = 0°$. The X axis represents the independent variable that is set as the θ-φ angle.

This curve is reasonably similar to the typical fluid dynamics coefficient curve plotted versus the angle of attack of a wing. The only difference is that the calculated spline represents the whole lift force, not only the hydro-dynamic coefficient.

5 RESULTS

The first simulation started from the equilibrium condition of the cable, i.e. all its parts was aligned in a vertical position. The boat speed is set as shown in Fig. 11: starting from the static position it reaches the speed of 3 knots (1.543 m/s) in 10 seconds with an initial overshoot. Figure 12 shows the variation of the cable-end depth in two minutes of simulation. It is possible to notice that it reaches a stable depth of 80 meters after 800 seconds.

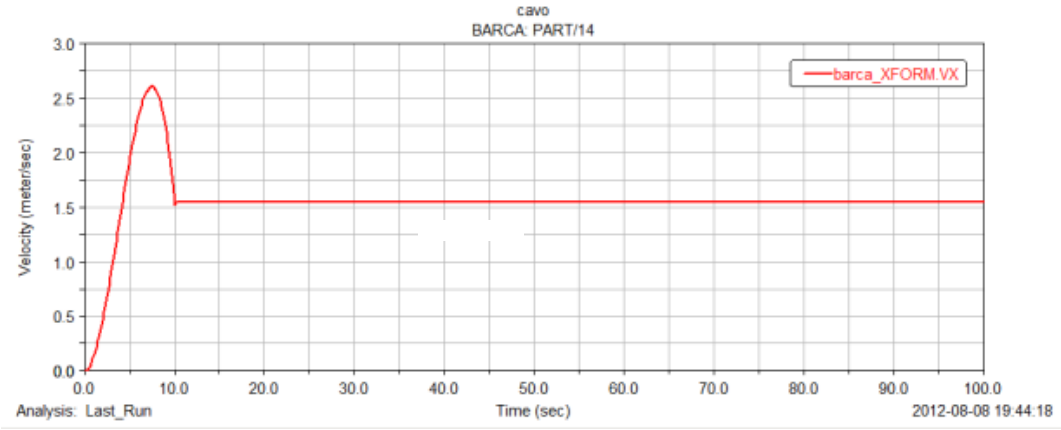


Fig. 11: Boat speed

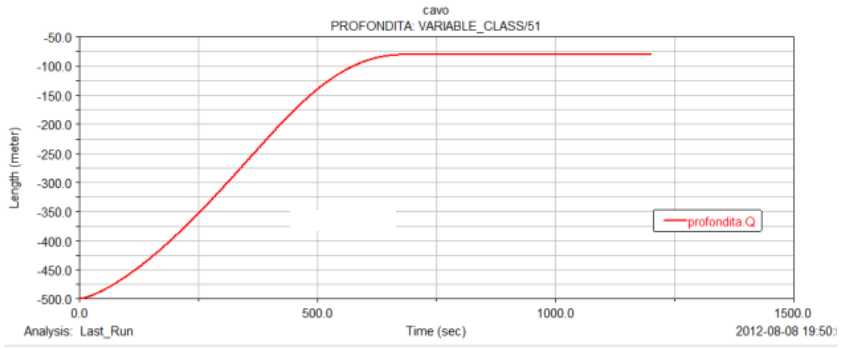


Fig. 12: Free end depth.

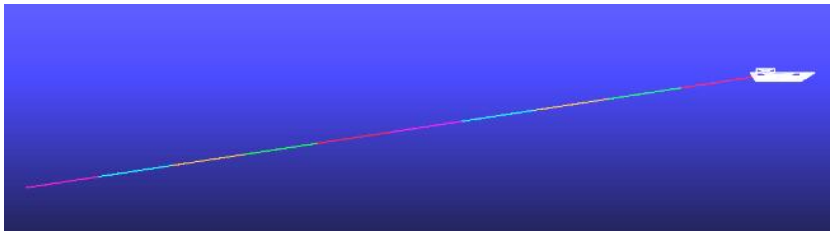


Fig. 12: Shape of the cable during the steady state. The hydrodynamic forces, acting on every segment of the cable, tilts it of an angle ω equal to 11°

Fig. 13 shows the shape of the cable in the moment of the towfish starting simulation.

Most of the simulations cannot provide interesting results because they stops in a very early moment. It happens because the pitch angle value is so high that the forces are not calculated from splines but predicted by the simulator and have values so high that the solver stops the simulation.

The variation of the towfish pitch angle θ of the most interesting simulations is reported in Fig. 13 and Fig. 14. The first one shows a configuration of β = 0°, γ = 0° and the second figure is obtained for a configuration of β = 5° degrees, γ = 0°.

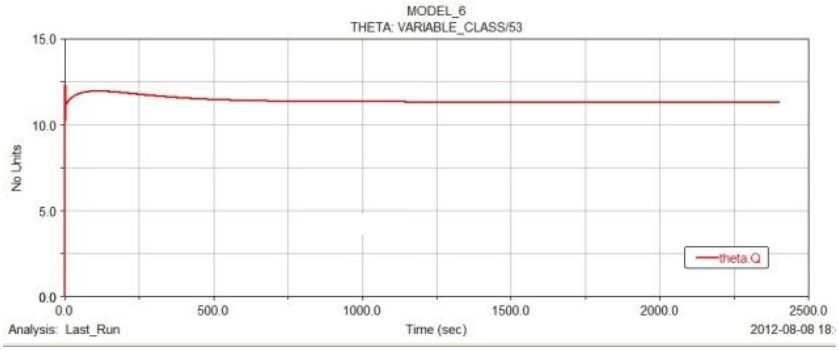


Fig. 13: Towfish pitch variation, configuration β=0°γ= 0°.

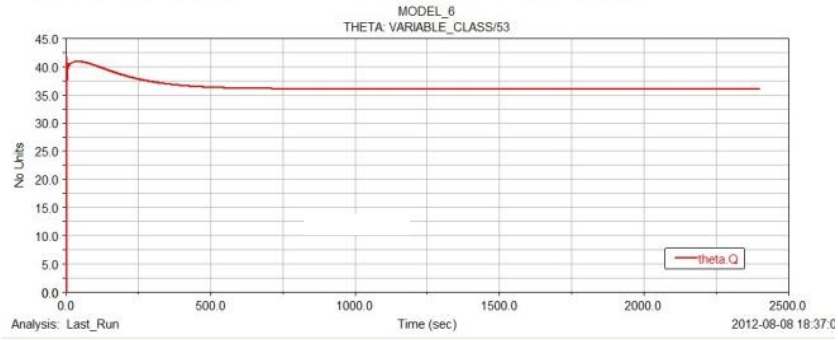


Fig. 14: Towfish pitch variation, configuration β=5°, γ= 0°.

It is possible to understand that, after a small initial oscillation, the vehicle reaches a stable positive pitch angle: 11,3° in the β = 0°, γ = 0° configuration and 36° for the β = 5° , γ = 0° case. The following Fig. 15 shows the towfish in the reached position for the first configuration.

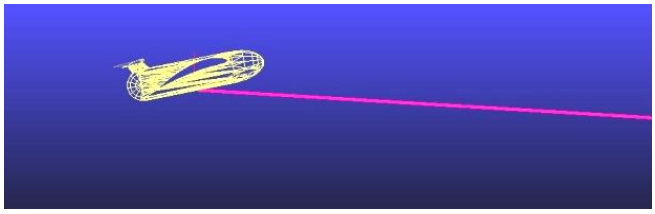


Fig. 15: Towfish pitch angle.

The perfect stability of the towfish, like all the airplanes, is called “level flight” and it means a stable depth and a null pitch angle. This case is not reached during the simulations

but it is possible to obtain it just changing the angle of attack of the mobile wings if the towfish were properly designed.

Figures 16 and 17 show the depth variation during the previous two simulations.

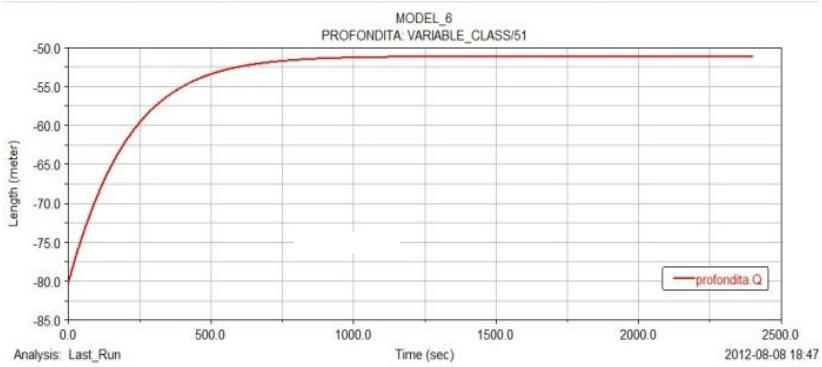


Fig. 16: Towfish depth variation, configuration β=0°γ= 0°.

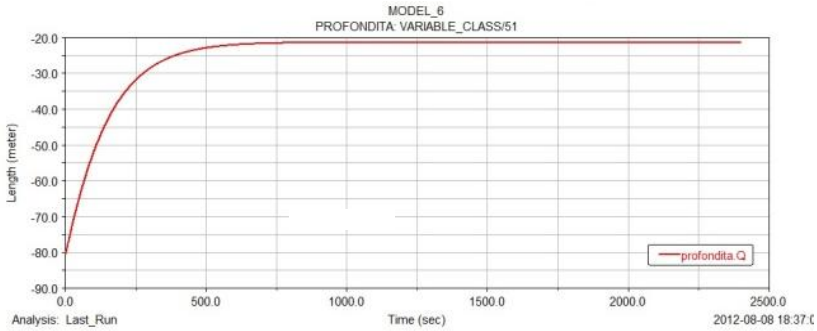


Fig. 17: Towfish depth variation, configuration β=5°γ= 0°.

The configuration β = 0°, γ = 0° allows the towfish to reach the -51 m depth while for the second configuration (β = 5° , γ = 0°) the depth is -21 meters.

6. CONCLUSIONS

In this paper the dynamics of an underwater towed vehicle system has been formulated. The model definition has followed three phases: the flexible cable modeling, the rigid body dynamics formulation and finally the hydro-dynamics forces and torques computation. These phases interact and influence each other. The cable changes its shape according to the depth, coming from the vehicle dynamics, yielding, in turn, a modified traction force on the spherical joint connection tied to the towfish. The fluid-structure interaction is well understood as the drag and lift force components change with the vehicle's orientation, speed direction and moving wings angles. In order to cope with this issue we recurred to splines to model varying fields of forces and torques inside a unique multibody systems simulation package. Results

reveal a span of useful angles providing stability and a good control of the depth. Out of these ranges we observed numerical instabilities due to wings stall producing undisired oscillations and extreme force at the cable connection. Further developments will take this model into account to create a stability control system.

REFERENCES

[1] Preston, J. M. Stability of towfish as sonar platforms and benefits of the two-part tow. *Defence Research Establishment Pacific Technical Memorandum* (1989).

[2] Buckham, B., Nahon, M., Seto, M. Three-dimensional dynamics simulation of a towed underwater vehicle, *In: Proceedings of OMAE '99* (1999).

[3] Bettles, R.W., Chapman, D.A. The experimental verification of a towed body and cable dynamic response theory. *Ocean Engineering* 12 (5), pp. 453–469, (1985).

[4] Buckham, B., Nahon, M., Seto, M., Zhao, X., Lambert, C. Dynamics and control of a towed underwater vehicle system, Part I: Model development. *Ocean Engineering*. Ocean Engineering 30 (4), pp. 453–470, (2003).

[5] Lambert, C., Nahon, M., Buckham, B. and Seto M. Dynamics and control of towed underwater vehicle system, part II: model validation and turn maneuver optimization. *Ocean Engineering* 30 (4), pp. 471–485, (2003).

[6] Delmer, T.M., Stephens, T.C., Coe, J.M. Numerical simulation of towed cables. Ocean Engineering, 10 (2), 119–132, (1983).

[7] Chapman, D.A. Towed cable behaviour during ship turning maneuvers. *Ocean Engineering* 11 (4), pp. 327–361, (1984).

[8] Friswell, M. I. Steady-state analysis of underwater cables, *Journal of waterway, Port, Coastal and Ocean Engineering* 121 (2), pp. 98-104, (1995).

V International Conference on Computational Methods in Marine Engineering
MARINE 2013
B. Brinkmann and P. Wriggers (Eds)

NUMERICAL INVESTIGATION OF SPUDCAN FOOTING PENETRATION IN LAYERED SOIL

P. GÜTZ[*], P. PERALTA[†], K. ABDEL-RAHMAN[*], M. ACHMUS[*]

[*] Institute for Geotechnical Engineering,
Leibniz University of Hannover, Hannover, Germany
e-mail: khalid@igth.uni-hannover.de, www.igth.uni-hannover.de

[†] Fugro GeoConsulting, Belgium
e-mail: pperalta@fugro.be, www.fugro.com

Key words: Spudcan, Layered Soil, Coupled Eulerian-Lagrangian, Soil-Structure-Interaction.

Abstract. Spudcans are a type of foundation for mobile jack-up rigs and are connected to each of the three or four independent legs of a rig. These rigs are widely operating in the offshore industries such as oil and gas exploration and offshore wind park constructions. The diameter of a spudcan is typically between 10 and 16 m, but has steadily increased in recent years with some exceeding 20 m.

An accurate prediction of the leg or spudcan penetration is required to assess the minimum leg length of a jack-up rig and to predict any hazards such as risk of rapid leg penetration that can destabilize the rig and lead to catastrophic accidents. Rapid and sudden leg penetration can occur in layered soils where a strong layer overlies a weak layer. This type of failure mechanism in soil is called “punch through”.

The current state-of-practice to assess the penetration depth of a spudcan is to evaluate the bearing capacity of the footing applying analytical methods at discrete depths. Analytical bearing capacity methods strongly simplify the penetration process and rely on empirical factors. Continued investigation of the spudcan penetration process by means of physical or numerical models can reduce the amount of empiricism in applied methods in practice, thereby increase accuracy in penetration predictions and reduce risk of rig instability.

The results of a finite element numerical model to investigate the spudcan penetration process in layered soils are presented in this paper. The numerical model combines conventional Lagrangian elements, which represent the spudcan, with Eulerian elements that idealize the soil. The utilization of this so-called Coupled Eulerian-Lagrangian finite element method enables the numerical simulation of large deformation processes such as the spudcan footing penetration. Preliminary results are presented and compared with state-of-practice analytical solutions.

1 INTRODUCTION

Spudcans are used as footing foundations for offshore mobile jack-up rigs to allow the easy installation and extraction of the legs while providing temporary stability during the operation of such rigs. The legs of the rig are jacked into the seafloor to hold the rig in its position and ensure stability against horizontal and vertical forces during the operational phase. These rigs are widely used in the offshore industries such as oil and gas exploration for drilling wells, maintenance work or temporary production, as well as for the installation of offshore wind energy plants.

Spudcans generally have a polygonal shape but can be approximated to be circular and mostly have a conical underside (about 15° to 30° to the horizontal). Additionally, a spudcan can incorporate an acute tip, called a spigot, centered on the bottom, which improves its sliding resistance. The top face also exhibits a conical shape with angle to the horizontal similar to the one of the underside. Figure 1 depicts a typical shape of a spudcan-footing.

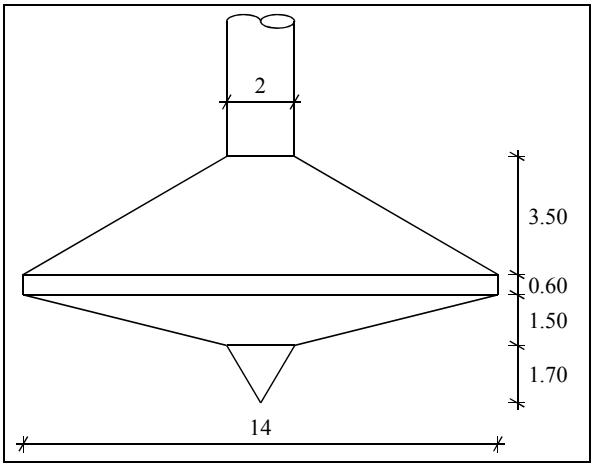


Figure 1: Typical geometry (dimensions in [m]) of a spudcan [14]

Guidelines on the site specific assessment of jack-up rigs and its components are provided in the International Standard ISO 19905 [10] and in the Technical and Research Bulletin 5-5A of the Society of Naval Architects and Marine Engineers (SNAME) [18]. Further guidelines on geotechnical assessments including foundation design can be found in ISO 19901 [9] .

2 OVERVIEW OF METHODS

During deep penetration of a spudcan footing, several failure mechanisms can occur within the soil. In homogenous soil, general shear failure occurs, similar to conventional shear failure of shallow foundations for which well-known bearing capacity equations have been developed. In layered soils, squeezing of soft soil between harder layers and/or punch through of the spudcan through a hard layer to a weaker or soft soil layer can occur. Of the different mechanisms, the latter presents a significant risk to the stability of a mobile jack-up rig since sudden and rapid leg penetrations can occur.

The current state-of-practice to assess the depth of spudcan penetration is to determine the vertical bearing capacity of the spudcan at discrete depths below the seabed and plot the

bearing capacity versus footing penetration. The maximum expected load (or pre-load) is compared to the bearing capacity graph to predict final penetration and any hazards such as risk of rapid and sudden leg penetration or "punch through" risk. Closed-form, analytical bearing capacity solutions are applied based on theories developed for shallow foundations. These solutions have been modified through the use of factors to account for backflow (during deep penetration), conical spudcan shapes, spudcan-soil interface roughness and mobilized soil strength among others. Thus, these analytical methods for spudcan penetration assessment may have significant limitations, especially when encountering complex soil conditions, such as highly layered soil profiles [11].

In homogeneous clay, standard practice [10], [18] is to apply bearing capacity and depth factors from Skempton [17] as suggested by Young et al. [22] for an average of the undrained shear strength to a depth 0.5 diameters below the level where maximum spudcan diameter is in contact with the soil. Other bearing capacity factors that take into account the cone angle, spudcan roughness, embedment depth and shear strength increase, such as those from Houlsby [8] are also recommended. The international standard [10] presents the bearing capacity factors proposed by Martin [12] to evaluate the bearing capacity of a spudcan in homogeneous sand. These bearing capacity factors are derived for flat, rough circular footings and for friction angles between 20° and 40° [1], [2].

If the soil is layered, other failure mechanisms can occur. This paper focuses on the case of a hard sand layer overlying a soft clay layer where "punch-through" mechanism may be likely to happen. For sand overlying clay, common methods applied are those by Hanna & Meyerhof [5] and the load-spread method, both adopted in ISO 19905 [10] and SNAME [18]. The punch-through bearing capacity developed by Hannah and Meyerhof considers forces on the assumed vertical failure surfaces in the upper sand layer, which is taken as the total passive earth pressure inclined at an average angle and acting upwards.

An alternative method recommended by Young et al. [22], is the load-spread method. The method is empirical and idealizes the punch-through failure mechanism by simply projecting the bearing capacity of the footing on to the lower layer. This allows a variation of load-spread gradients 1:n to be considered. Values of load-spread gradients between 1:3 and 1:5 are recommended in [10] and [18]. It is noted in [10] and [18] that both methods for punch-through capacity of sand over clay can significantly underestimate the actual bearing capacity.

In recent years, the assessment of spudcan penetration has been investigated applying numerical methods. Classic Finite Element Analysis (FEA) methods using Lagrangian elements have been used to model a spudcan [13]. However, such analyses are limited to small-deformation problems. As the spudcan penetrates further into the soil, large deformations of model elements occur leading to numerical and convergence problems, as well as the distortion of the elements affects the accuracy of the simulation. The large deformations in the model cause significant distortions of the mesh and its elements as well as contact problems between the spudcan and the soil [3], [7], [14].

More recently, using Coupled Eulerian-Lagrangian (CEL) elements in ABAQUS has been shown to be able to model large-deformation problems. [20] first applied the CEL method for the assessment of spudcan penetrations. This approach has been benchmarked and validated for application in other large-deformation, geotechnical problems. There are several other recent publications documenting the applicability of the CEL method for spudcan penetration assessments [13],[14],[15], [19], [21].

3 FINITE ELEMENT MODELING

The CEL method in ABAQUS combines the advantages of Eulerian and Lagrangian elements to analyze problems involving both small and large deformations, which is generally not feasible with conventional Lagrangian FEA methods. In geotechnical applications, the CEL method allows the soil, which may undergo large deformations, to be modeled using Eulerian elements while solid structures with little deformations can be modeled using Lagrangian elements. Numerical convergence problems associated with stress and strain concentrations at the edge of a solid structure are overcome since the Eulerian soil element is able to move freely.

The interface between the two elements defines the boundary of the Lagrangian body. The Lagrangian body occupies a region in the Eulerian mesh, while it pushes the Eulerian material out of the elements since there is no material flow of Eulerian material in the Lagrangian body [19]. The CEL method is particularly advantageous in simulating installation processes in geotechnical engineering, which typically involve large soil deformations. The installation of foundations, such as piles and/or footings, can be simulated realistically beginning at the ground surface in contrast to modeling pre-embedded foundations.

3.1 Development of CEL Model

The spudcan penetration analysis under purely vertical loading is an axisymmetric process, which could, in principle, be analyzed as a two-dimensional problem. However, ABAQUS provides only one Eulerian element type that is a 3D element requiring eight nodes [16]. Therefore, a 3D model of the spudcan and soil mass was created in this study; however, the model was optimized by utilizing symmetry conditions. Two planes of symmetry were established and only one-fourth of the spudcan and soil domain was modeled (see Figure 2). Boundary conditions were applied to the planes of symmetry, which inhibit material movement normal to the planes of symmetry. The type of boundary condition in the ABAQUS model was set to “no-flow-boundaries”. This type of boundary condition enforces zero velocity in the boundary, in the direction of the given boundary condition.

The model contains a spudcan with radius 7 m (Diameter (B) = 14.0m) and a soil domain with radius 28 m, which is equal to four times the spudcan radius (Figure 2). The dimensions of the numerical model are thus expected to be large enough to avoid any boundary effects. The height of the numerical model in case of homogenous soil (model a) was defined to 56 m, which is equal to four times the diameter of the spudcan. This allows penetration of the spudcan up to a multiple of its diameter without boundary effects. In addition, an initial void region above the soil mass provides enough space for the soil heave.

In case of layered soil analyses (model b), the height of the numerical model was equal to the thickness of the upper sandy layer (T) which was varied according to the spudcan diameter (B), plus the depth of the underlying clay layer which was defined to 46.0 m beneath the upper sandy layer. Also an initial void region above the soil mass provides enough space for the soil heave during the analysis (see Figure 2).

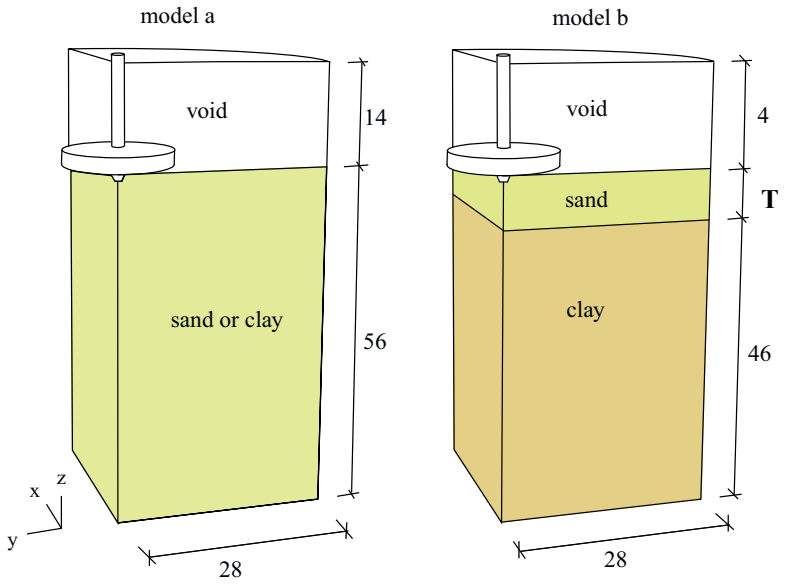


Figure 2: Dimensions and geometry of spudcan penetration model

In the CEL model, the soil mass and initial void regions above the soil were assigned with Eulerian elements while the spudcan itself was assigned with Lagrangian elements. A fine mesh was applied in proximity to the spudcan while a coarser mesh was applied to the model parts close to the boundaries. This allowed an optimization of total number of elements in the model without compromising on accuracy of calculated soil movements in proximity to the spudcan. The linear elastic-plastic with Mohr-Coulomb criterion constitutive law was chosen to represent the behavior of different soil layers. Table 1 & 2 contain the required soil properties for the Mohr-Coulomb constitutive law which were applied in the numerical model. For the sand layers, a negligible value of cohesion was assumed to overcome numerical instabilities.

Table 1: Applied soil properties for sand layers

Parameter	Sand (S1)	Sand (S2)
Unit weight	9 kN/m^3	11 kN/m^3
Young's modulus	30.0 MPa	50.0 MPa
Poisson's ratio	0.25	0.25
Friction angle	30.0°	38.0°
Dilatation angle	0.0°	8.0°
Cohesion	0.01 kPa	0.01 kPa

Table 2: Applied soil properties for clay layers (undraind)

Parameter	Clay (C1)	Clay (C2)
Unit weight	7 kN/m^3	8 kN/m^3
Young's modulus	2.0 MPa	10.0 MPa
Poisson's ratio	0.49	0.49
Friction angle	0.01°	0.01°
Dilatation angle	0.01°	0.01°
Cohesion (c_u)	10.0 kPa	50.0 kPa

ABAQUS provides the general contact method to define the interaction between the Lagrangian and Eulerian material, which allows finite sliding of two separated surfaces. This aspect is essential for the spudcan penetration analysis, where the soil continuously moves along the spudcan surface. The definition of a friction coefficient represents the roughness of the spudcan surface. The interaction property is stated as a penalty contact with assumed friction coefficient of 0.5 (interface friction angle δ=26.57°).

The numerical analysis is generally performed in two steps. The initial step defines the geostatic stress field, which is induced by self-weight of the soil under gravity. The second step applies loads in the model to initiate the analysis and includes the spudcan penetration process. The latter step is a dynamic, explicit type analysis. The time period of the step was defined in relation to the penetration rate of the spudcan and penetration depth to be reached (with penetration depth/time period = penetration rate).

3.2 Validation of the Numerical Model

The numerical results of the spudcan penetration analysis were compared to results from analytical methods. Analytical methods to estimate the spudcan penetration depth were applied using Fugro in-house software, which calculates spudcan penetration in accordance with latest state-of-practice standards, i.e. ISO 19905 [10] and SNAME [18] .

Two models considering homogeneous sand (S1 properties) and homogeneous clay (C1 properties) were initially investigated.

Figure 3 depicts the comparison of numerical and analytical results in terms of spudcan reaction versus penetration depth in homogeneous sandy soil (S1). The penetration depth D is defined as the depth of the spudcan's widest bearing area below the seafloor.

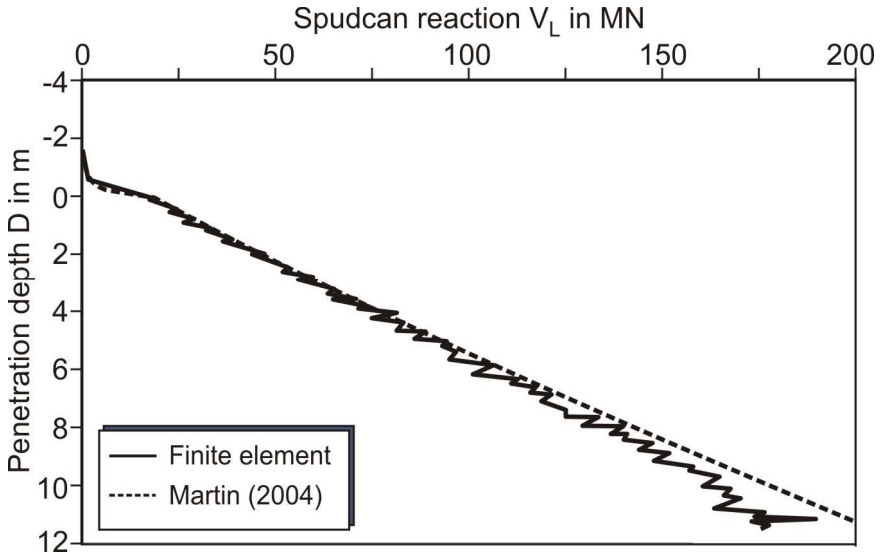


Figure 3: Comparison of finite element and analytical results (Sand S1)

For the spudcan at ground surface, the method of Martin [12] results in similar spudcan reactions, which are in good agreement with the FE results. The bearing capacity reaction determined with Martin's method is almost identical with FE results up to penetration D = 4 m (during partial spudcan embedment or penetration). At penetration depth D > 4 m (at deeper penetration), the bearing capacity results of the FE analysis still matches very well the results applying Martin's method..

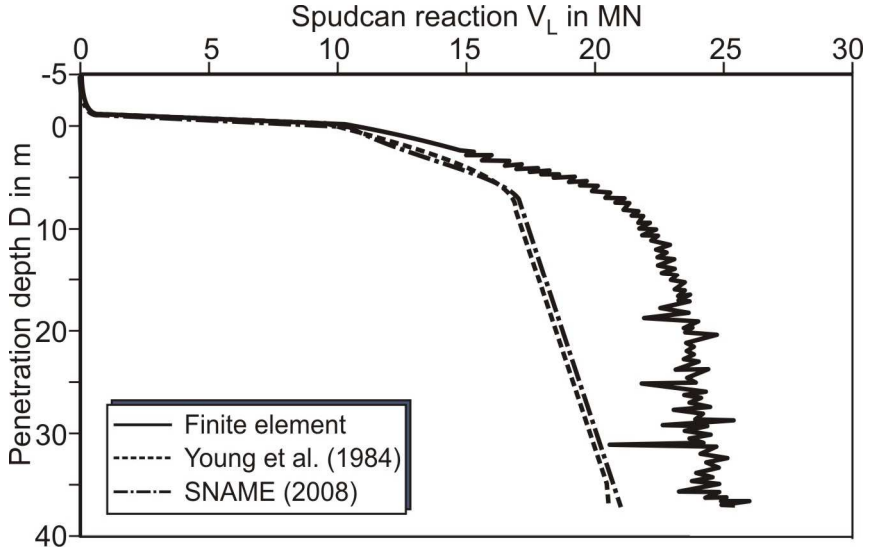


Figure 4: Comparison of finite element and analytical results (Clay C1)

Figure 4 shows the results of the spudcan reaction versus penetration depth of finite element and analytical analysis for the clay C1 (c_u = 10 kPa). The analytical results increase strongly at partial penetration, because the bearing capacity is mobilised due to a growing bearing area. The further increase of the spudcan reaction is due to the backflow of soft clay, which causes surcharge on top of the spudcan. After this transition, the spudcan reaction grows steadily with penetration depth.

Generally, the analytical methods exhibit a lower spudcan reaction than the results of the finite element method, which is less significant at shallow embedment, than at deep penetration (penetration deeper than eight metres). However, both of the analytical and finite element results show the same tendency regarding the behavior of spudcan in clay.

Based on the validation of the model, a convergence study on the mesh density as well as the penetration rate was performed. Different meshes with varying number of elements as well as the minimum element size were investigated. The comparison reveals no substantial differences in the calculated resistance of the spudcan due to the mesh densities used. However, bearing pressure graphs are much smoother (without excessive instabilities) as the number of elements in the model is increased. Since there were no significant differences between the different meshes, a final mesh with total element number of 100,536 was chosen for all subsequent analyses to optimize accuracy and computational time. The penetration rate of 0.5 m/s to the spudcan was adopted in the modeling. For more details on the numerical modeling, pl. refer to [4].

4 NUMERICAL RESULTS

The spudcan penetration in sand (S2) overlying clay (C1) has been modelled and compared with the analytical methods. Figure 5 shows the results of case S2-C1 using both analytical and finite element analyses, whereas the analytical calculation considers the method of Martin [12] for sand and the method of Young et al. [22] for clay. The method of Hanna & Meyerhof [5] and the load spread method are taken into account to determine the bearing capacity for punching through the sand.

Directly after penetration the spudcan reaction rapidly decreases in the case of load spread ratio method, where the reduction for the lower load spread ratio is more significant. Finally, both graphs show the same spudcan reaction in clay layer ($D > 21$ m), since the bearing capacity is calculated with the same approach for uniform clay. The method of Hanna & Meyerhof shows a high increase of bearing capacity up to $D = 0$ m. While the spudcan penetrates deeper, the assumed shear planes in the overlying sand layer become smaller and the reduction of bearing capacity increases with advancing penetration depth. The reason for this progress is that the amount of bearing capacity due to general shear in the clay underneath becomes more relevant in comparison to the shearing at the vertical planes in the sandy layer.

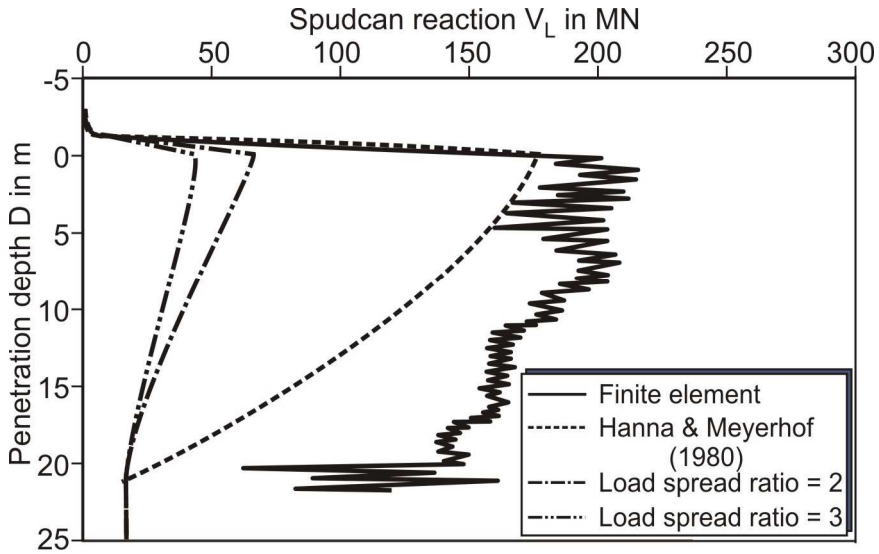


Figure 5: Comparison of finite element and analytical results; soil S2-C1 with T/B = 1.5

The results of the finite element simulation show a high increase of spudcan reaction up to $D = 0$ m. However, the spudcan reaction remains approximately constant up to $D = 7$ m, followed by a progressive reduction with advancing penetration depth of the spudcan. The graph in figure 5 indicates significant numerical instabilities for penetration depth $D > 19$ m, which is verified in the visualisation of the simulation, where unrealistic soil movements can be observed.

In terms of the spudcan reaction at ground surface, the method of Hanna & Meyerhof provides the best approximation of the finite element result. However, the analytical

approaches generally underestimate the spudcan reaction up to D = 19 m. Considering the slope of the graph at punch through failure mechanism (0 m < D < 19 m), the load spread method with a ratio of two gives the best match, although it significantly underestimates the spudcan reaction.

To investigate the influence of the soil strength of the underlying soil on the punch through mechanism the results of sandy layer (S2) overlying clay (C2) are depicted in Figure 6. The analytical calculations are based on the same methods and parameters as in the previous case. Generally, the spudcan reaction at ground surface is significantly higher, which can be associated to the higher undrained shear strength of the underlying clay (see Table 2).

In case of the analytical methods, the projected footing on the interface mobilizes a higher bearing capacity. This aspect highly affects the load spread method (larger bearing area on soil with higher strength). In contrast, the higher undrained shear strength has a lower effect on the method of Hanna & Meyerhof, which considers a projected footing of the same size and the shearing in the sand layer that does not change to the case S2-C1.

Hence, the spudcan reaction at ground surface calculated with the load spread method ($n_s = 2$) exceeds the one determined with the method of Hanna & Meyerhof. For spudcan penetration deeper than D = 21 m, the predicted spudcan reaction with analytical methods is the same in every approach, but on a higher magnitude than in the case S2-C1 (general shearing failure in clay with higher undrained shear strength).

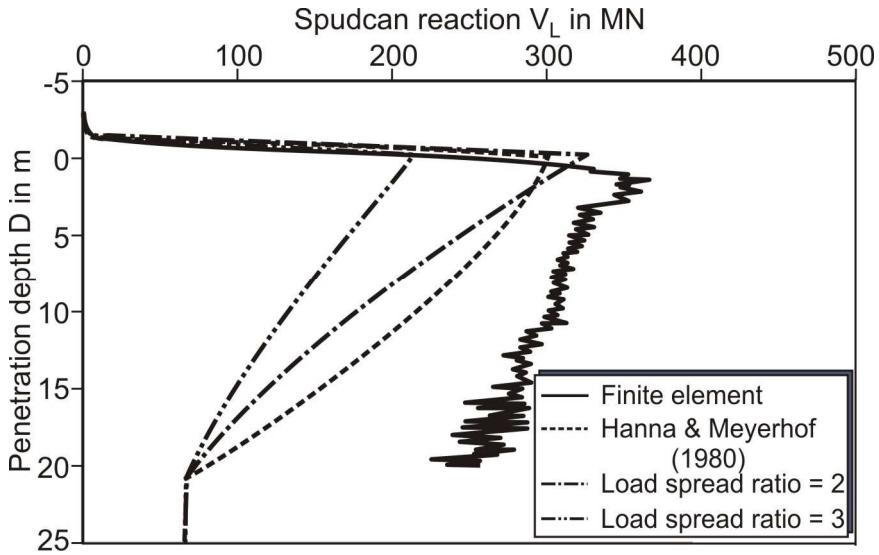


Figure 6: Comparison of finite element and analytical results; soil S2-C2 with T/B = 1.5

The finite element results, depicted in Figure 6, exhibit a high increase of spudcan reaction up to D = 1.50 m, which remains approximately constant up to D = 3 m. As the spudcan penetration exceeds this depth, the underlying clay becomes progressively more affected by the penetration process and thus, the spudcan reaction reduces as the sand is forced downwards instead of mobilising resistance against the penetrating spudcan. Subsequent to this rapid decrease, the spudcan reaction reduces steadily with advancing penetration depth.

Comparing the results of the finite element method with the ones of the analytical calculations shows that the approach of Hanna & Meyerhof as well as the load spread method ($n_s = 2$) give a good approximation of the highest spudcan reaction of the finite element result. The slope of the graph during punch through calculated with the method of Hanna & Meyerhof matches well with the finite element graph up to D ≈ 10 m, whereas the load spread ratio of $n_s = 2$ owes a too high decrease of spudcan reaction with depth. The load spread ratio of $n_s = 3$ represents a similar slope like the finite element graph, but significantly underestimates the spudcan reaction at ground surface and in the underlying soil.

Figure 7 provides a comparison of multiple thicknesses of the sand layer S2 above clay C2, which are represented for depth (D) normalised by the diameter of the spudcan (B). The penetration depths (D) is normalised by the layer thickness (T). The graph of T/B 1.5 is depicted up to D/T = 0.71 to exclude the numerical instabilities that occur for penetration depth D > 15 m. Figure 6 shows that the thicker the overlying layer, the higher is the initial spudcan reaction at ground surface, because a thicker sand layer is able to resist a higher load and thus prevents effects of the underlying clay. For T/B ≥ 1, the clay becomes affected after the resistance of the sand layer is exceeded (peak value) and the sand is forced downwards. For a normalised layer thickness of T/B < 1, no punch through failure is observed. Nevertheless, an increase of the layer thickness causes a higher spudcan reaction.

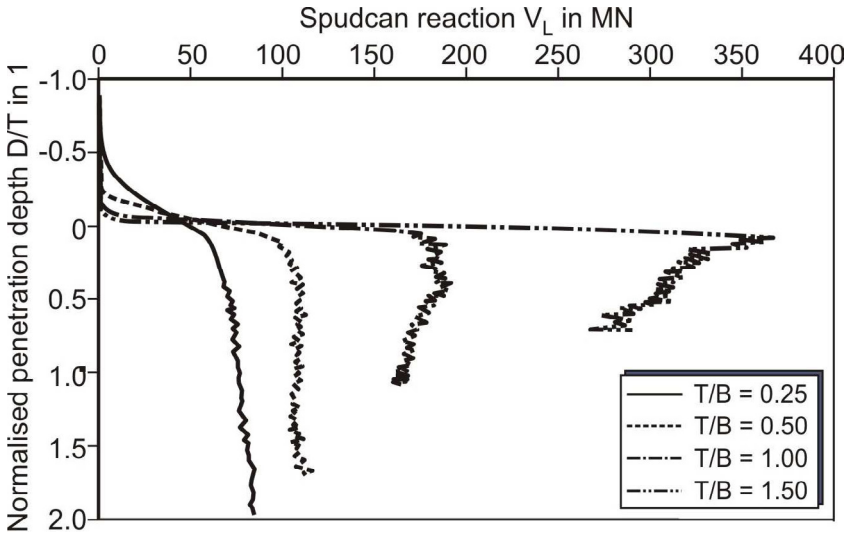


Figure 7: Effect of the layer thickness on the punch through of sand; soil S2-C2

For T/B < 1, the underlying soil is almost immediately affected by the spudcan penetration and thus the spudcan reaction results mainly of the underlying clay augmented by the resistance of the sand surrounding the penetrating spudcan. While the spudcan penetrates in the sand, a soil plug is formed beneath and moves progressively downwards together with the spudcan. The most typical punch through failure is represented in T/B = 1.5, where a high spudcan reaction is followed by a major reduction of spudcan reaction. A residual spudcan reaction subsequent to the punch through cannot be observed, but is expected to occur at a deeper penetration.

5 CONCLUSIONS

A numerical study was performed that aimed at comparing analytical and finite element results for multiple cases and investigated the effects or mechanisms that occur as the spudcan penetrates in layered soil. An essential aspect is the application of the Coupled Eulerian-Lagrangian method in the numerical model, which is suitable for analysis of large deformation problems.

In case of homogeneous sandy soil the analytical methods applied in practice to estimate the spudcan penetration depth generally match well with finite element results and it was observed that the analytical results mostly underestimated the results from the FE model by homogeneous clay.

If the soil is layered, it was observed that the results of the applied analytical methods mostly underestimated the results from the FE model. Hanna & Meyerhof method gives the best estimate of spudcan penetration resistance compared to FE-analyses. Load spread ratio results depend on the shear strength of the underlaying clay layer, so it gives better results for the max. penetration force in case of underlying clay layer with high cohesion value beneath the upper sandy layer.

To improve the reliability of the relatively novel CEL method for use in geotechnical applications, further studies comparing model tests and in-situ data with such simulation are highly useful. The continual verification of FE results with model tests, as well as a better understanding and consequently prevention of numerical instabilities will greatly improve the applicability of finite element methods to investigate and analyze the spudcan penetration process.

REFERENCES

[1] Cassidy, M. J. & Houlsby, G. T., 2002. Vertical bearing capacity factors for conical footings on sand. *Géotechnique,* 52(9), pp. 687-692.

[2] Craig, W. H. & Chua, K., 1990. Deep penetration of spud-can foundations on sand and clay.*Géotechnique,* 40(4), pp. 541-556.

[3] Gao, W., Yu, L. & Hu, Y., 2012. Large deformation FE analysis of large diameter spudcan penetration into two-layer of uniform clays. *International Journal of Geotechnical Engineering,* 6(2), pp. 171-177.

[4] Gütz, P, 2012 . Finite Element Analysis of Spudcan Footing Penetration, Diploma thesis, Leibniz University of Hannover (unpublished).

[5] Hanna, A. M. & Meyerhof, G. G., 1980. Design charts for bearing capacity of foundations on sand overlying soft clay. *Canadian Geotechnical Journal,* 17(2), pp. 300-303.

[6] Hossain, M. S., Hu, Y., Randolph, M. F. & White, D. J., 2005. Limiting cavity depth for spudcan foundations penetrating clay. *Géotechnique,* 55(9), pp. 679-690.

[7] Hossain, M. S. & Randolph, M. F., 2010b. Deep-penetrating spudcan foundations on layered clays: numerical analysis. *Géotechnigque,* 60(3), pp. 171-184.

[8] Houlsby, G. T. & Cassidy, M. J., 2011. A simplified mechanically based model for predicting partially drained behavior of penetrometers and shallow foundations. *Géotechnique Letters,* 1(3), pp. 65-69.
[9] ISO 19901-4:2003, 2003. *Petroleum and natural gas industries — Specific requirements for offshore structures — Part 4: Geotechnical and foundation design considerations,* s.l.: International Organization for Standardization.
[10] ISO 19905-1:2011, 2011. *Petroleum and natural gas industries — Site-specific assessment of mobile offshore units — Part 1: Jack-ups,* s.l.: International Organization for Standardization.
[11] Kellezi, L. & Stromann, H., 2003. *FEM analysis of jack-up spudcan penetration for multi-layered critical soil conditions.* Dundee, BGA International Conference on Foundations, pp. 411-420.
[12] Martin, C. M., 2004. *User Guide for ABC – Analysis of Bearing Capacity,* University of Oxford: Department of Engineering Science.
[13] Qiu, G. & Henke, S., 2011. Controlled installation of spudcan foundations on loose sand overlying weak clay. *Marine Structures,* Band 24, pp. 528-550.
[14] Qiu, G., Henke, S. & Grabe, J., 2011a. *3D FE analysis of the installation process of spudcan foundations.* London, 2nd International Symposium on Frontiers in Offshore Geotechnics.
[15] Qiu, G., Henke, S. & Grabe, J., 2011b. Application of a Coupled Eulerian–Lagrangian approach on geomechanical problems involving large deformations. *Computers and Geotechnics,* 38(1), pp. 30-39.
[16] Simulia, 2012. Abaqus 6.12.
[17] Skempton, A. W., 1951. *The Bearing Capacity of Clays.* London, Building Research Congress.
[18] SNAME, 2008. *Guidelines for Site Specific Assessment of Mobile Jack-Up Units. Technical and Research Bulletin 5-5A,* New Jersey: The Society of Naval Architects and Marine Engineers (SNAME).
[19] Tho, K. K., Leung, C. F., Chow, Y. K. & Swaddiwudhipong, S., 2012. Eulerian Finite-Element Technique for Analysis of Jack-Up Spudcan Penetration. *International Journal of Geomechanics,* 12(1), pp. 64-73.
[20] Tho, K. K., Leung, C. F. & Swaddiwudhipong, S., 2009. *Application of eulerian finite element technique for analysis of spudcan and pipeline penetration into the seabed.* London, 12th International Jack-up Conference
[21] Yi, J. T. et al., 2012. Eulerian finite element analysis of excess pore pressure generated by spudcan installation into soft clay. *Computers and Geotechnics,* Band 42, pp. 157-170.
[22] Young, A. G., Remmes, B. D. & Meyer, B. J., 1984. Foundation Performance of Offshore Jack-Up Drilling Rigs. *Journal of Geotechnical Engineering,* Vol. 110, No. (7,), pp. 841-859.

V International Conference on Computational Methods in Marine Engineering
MARINE 2013
B. Brinkmann and P. Wriggers (Eds)

DEFORMATION BEHAVIOUR OF REINFORCED CONCRETE SHELLS FOR OFFSHORE STRCTURES

MARINE 2013

Waldemar Krakowski, Martin Empelmann, Lars Eckfeldt

iBMB – Concrete Construction Department
Technische Universität Braunschweig
Beethovenstraße 52, 38106 Braunschweig, Germany
e-mail: massivbau@ibmb.tu-bs.de, www.ibmb.tu-braunschweig.de

Key words: GBS, reinforced concrete, shell structures, testing, material modelling

1 INTRODUCTION

Gravity base structures (GBS) are shell structures made of reinforced concrete (RC). After past few years with little development activity, interest in robust structures for the arctic environment, as for liquefied natural gas terminals and for special floating barges is growing again (Figure 1) [3]. For the design of GBS extensive knowledge about the material and deformation behaviour is needed.



Figure 1: Gravity base structure “Sakhalin II” in the arctic region (source: *http://gazprom-sh.nl*)

Modelling of the nonlinear deformation behaviour and the cracking process has been examined for reinforced concrete structures as plates, panels and shells in detail. However, the object of investigation was limited to elements with reinforcement parallel to the tension direction. For GBS loads from waves, wind or filling operations vary [8], [14]. The principal stress and strain directions therefore may change. That is why reinforcement in tension will not be stressed ideally, but in a certain skewed angle. Experimental data shows for those cases larger crack widths and deformations as in cases of tension stresses parallel to the

reinforcement [2], [11], [16].

Based on own tests and those from literature a new approach for predicting the deformation behaviour of reinforced concrete structures with arbitrary reinforcement orientation has been formulated.

2 GENERAL CONSIDERATIONS

The deformation behaviour of RC structures in compression is dominated by concrete. In case of tension, cracking of concrete occurs at a very low stress level. Within cracks the steel transfers the whole tension force. Beyond cracks the tension force is transmitted via bond into the concrete again. Therefore, the behaviour in tension as well for steel as for concrete has to be considered adequate in order to achieve a realistic material modelling. The deformation behaviour in compression and tension may be idealized as strut and tie model. This allows a separate consideration in tension and compression. A typical simple application for a beam in bending is shown in Figure 2.

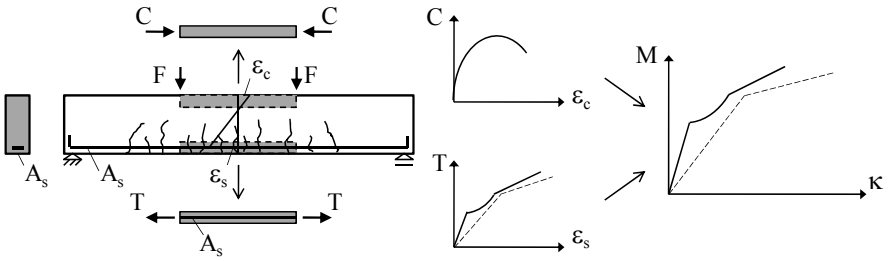


Figure 2: Strut and tie modelling for a beam

The same principles of strut and tie modelling as for beams are applicable to shell structures. However, modelling of shell structures is more complex due to the changing path of tensile stress but fixed position of rebars. Therefore, extended calculation methods have been established, documented in reference [2] and [15]. They allow a very accurate determination of the real load-deformation behaviour for concrete shell structures with arbitrary reinforcement direction. However, these methods include iterative calculation algorithms. The complex algorithms do not allow fast nonlinear calculations in extensive structures modelled by the finite element method (FEM). Therefore, a new approach in closed form is needed, which allows a highly accurate but non-iterative material modelling.

3 FULL SCALE TESTS ON PANELS

3.1 Testing program

Due to the lack of test data from panels under biaxial tension, a new full scale testing facility for concrete members with arbitrary reinforcement orientation has been developed (Figure 3) [7]. One of the requirements to this testing facility has been the free elongation in each loading directions without any restraint due to transverse cracking. Therefore single steel plates have been bolted to the specimen with prestress about 400 Nm (Figure 4). The steel plates have been connected to a cantilever via 50 mm round bars. The round bars have been greased and were enabled to glide on a high strength steel interlayer, which has been placed

between the round bar and the cantilever. Hence, every round bar was able to transfer in-plane forces in the loading direction, but no in-plane force in the transverse direction. In order to avoid bending forces from unwanted eccentricity, a ball nut has been placed on each end of the cantilever. The horizontal and the vertical bearings have been fixed to the floor via prestressed bars for the reason to limiting deformations of the test setup.

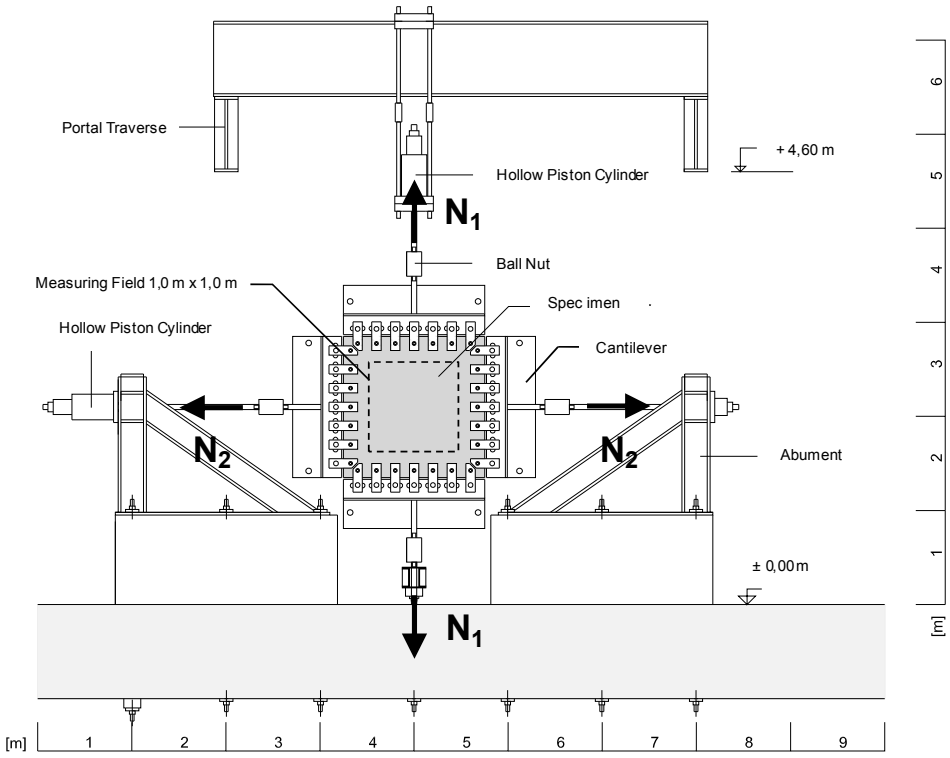


Figure 3: Test setup

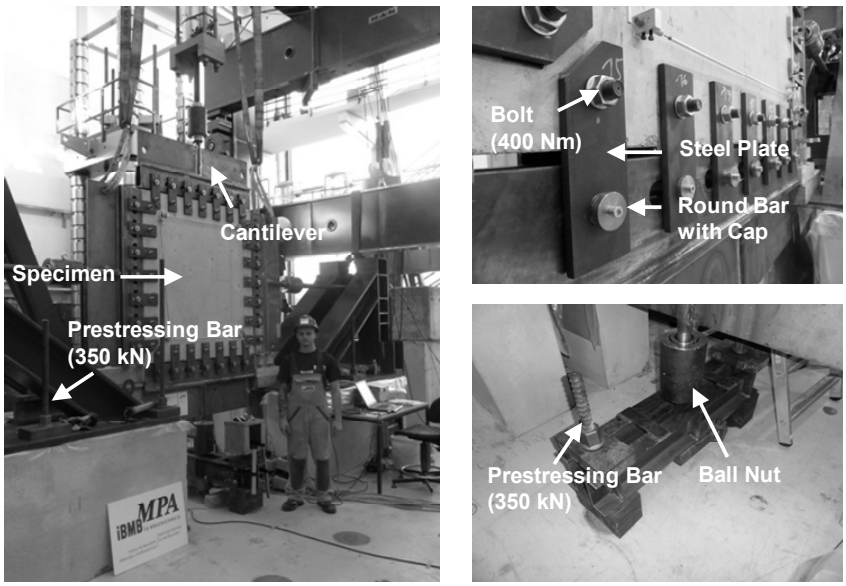


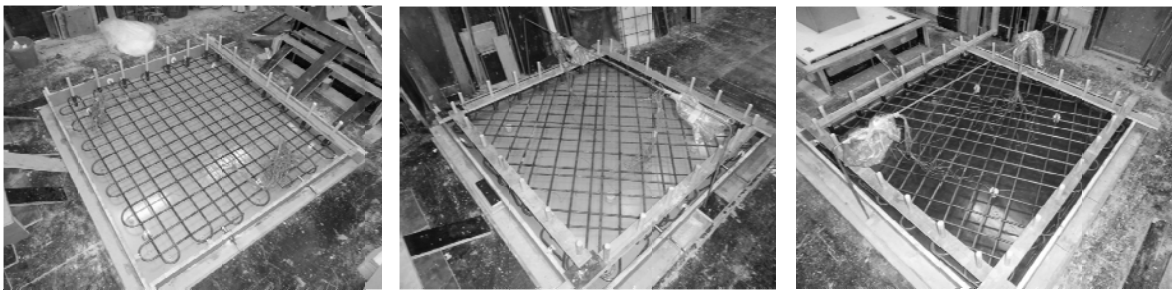
Figure 4: Details of test setup

The specification of every specimen are summarised in Table 1. The bar diameter have been chosen to be 10 mm, except specimen Z3 where bar diameter of 8 mm in the x-direction has been applied ($\lambda = A_{s,x}/A_{s,y} = 0{,}6$). The bar spacing s_x and s_y was constant for all specimen.

Table 1: Specimen specifications

	Θ [°]	$d_{s,x}$ [mm]	$d_{s,y}$ [mm]	s_x [mm]	s_y [mm]	λ [-]	k [-]	$f_{ct,sp}$ [N/mm²]	$f_{c,cyl}$ [N/mm²]
Z1	0	10	10	100	100	1,0	1,0	2,9	31,0
Z2	45	10	10	100	100	1,0	0,0	2,3	25,2
Z3	45	8	10	100	100	0,6	0,5	2,7	30,4
Z4	22,5	10	10	100	100	1,0	0,0	2,9	37,8
Z5	22,5	10	10	100	100	1,0	0,7	3,4	38,8
Z6	22,5	10	10	100	100	1,0	0,5	3,0	30,8

To ensure a certain loading level, the reinforcement was anchored with loops and hooks around a steel bush as shown in Figure 5. The steel bush has been set in position before casting for a later bolting. Each reinforcement direction consisted of one layer, which has been placed at the centre of the specimen. The ribbed reinforcing steel consisted of B500 S with a yield strength $f_{yk} = 500$ N/mm². The main influencing parameters have been chosen to be the reinforcement orientation related to the tension direction with $\Theta = 0°$, 22,5°, 45°, and loading ratio $k = N_2/N_1$.



(a) (b) (c)

Figure 5: Formwork and reinforcement: (a) Specimen Z1, (b) specimen Z2 and (c) specimen Z4

The measuring program consisted of longitudinal displacement transducers (LDT) in the loading directions at both sides of the specimen and LDT which have been applied diagonal at one side. Steel strains have been measured via strain gauges, which were glued to the reinforcement before casting. Crack widths have been measured by a special digital camera system with high resolution. Crack formation and crack spacing have been documented too.

3.2 Test results

For increasing loading ratio $k = N_2/N_1$ a decreasing concrete tensile strength σ_{1cr} has been established from the conducted research program, as shown in Figure 6. Herein the concrete tensile strength from specimen has been related to material testing strength (5%-quantile), which shows good accordance for k = 0. The difference between Z2 with k = 0 and Z1 with k = 1 is about 25%. This outcome is confirmed by reference [2].

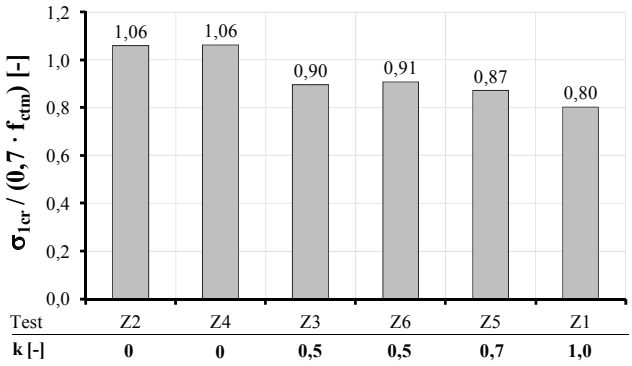


Figure 6: Concrete tensile strength from tests related to the material testing depending on k

It has to be stated, for $k \leq 0,7$ cracking occurred almost perpendicular to N_1 only [7]. For in-plane hydrostatic loading with $k = 1$ the crack pattern of specimen Z1 showed hardly any kind of orientation. Cracking for Z1 was neither oriented on rebars nor on loading directions, whereas for the rest of the series the crack pattern was mostly oriented at the loading direction (Figure 7). Closing of existing cracks and forming of new cracks with severe different orientation has not been noticed during loading for k = const. In reference [9], [11] the crack orientation related to the loading direction has been examined for test series on plates and panels under uniaxial tension. Within the elastic steel strains the crack orientation can be assumed to be perpendicular to the tension direction in uniaxial as well as in biaxial tension with $k \leq 0,7$ (Figure 7). For $k > 0,7$ there is no significant cracking direction. However, for hydrostatic in-plane loading the measured stiffness was the same as in uniaxial tension parallel to reinforcement with σ_0.

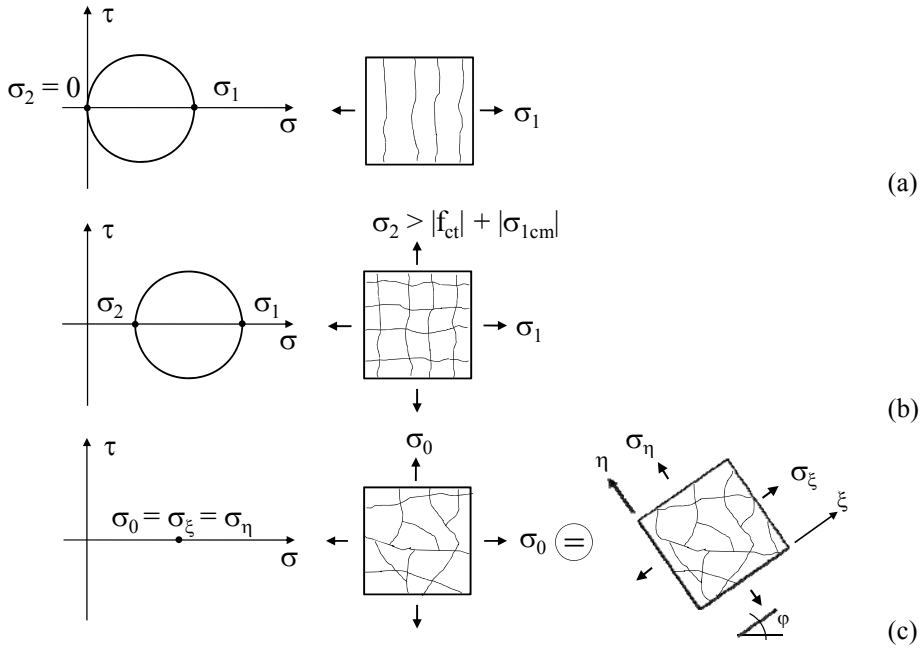


Figure 7: Mohrs cycle: (a) uniaxial tension and crack pattern, (b) biaxial tension and crack pattern, (c) hydrostatic loading and crack pattern

4 MODELLING THE MATERIAL BEHAVIOUR FOR RC STUCTURES

4.1 Concrete in compression

The nonlinear stress-strain relationship of concrete in compression may be expressed trough

$$\frac{\sigma_c}{f_c} = \left(\frac{k \cdot \eta - \eta^2}{1 + (k-2) \cdot \eta} \right) \tag{1}$$

according to EC2 [5] or MC 2010 [3]. When calculation of concrete strains ε_c in the descending brand with Eq. (1) is not needed, the parabola formulation according to EC2 [5] can be rearranged with

$$\frac{\sigma_c}{f_c} = -\left(1 - \left(1 - \frac{\varepsilon_c}{\varepsilon_{c1}}\right)^2\right) \tag{2}$$

and gives comparative results for normal strength concrete in the ascending branch as shown in Figure 8.

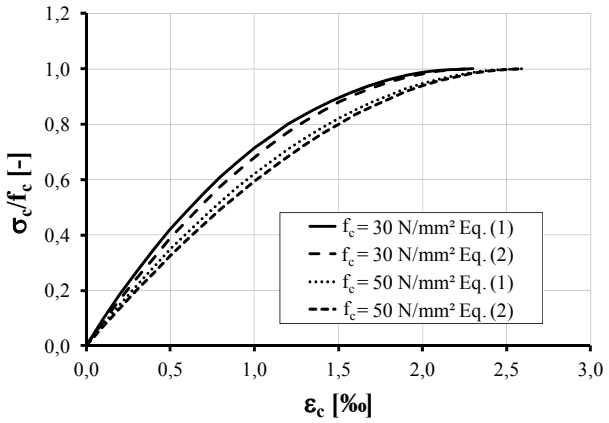


Figure 8: Comparing different formulations for concrete in compression

4.2 Reinforcement steel

Reinforcement steel in compression as well as in tension is characterised trough a constant modulus of elasticity with E_s = 200.000 N/mm². After yielding strain hardening is possible. Strain hardening makes up to 10 % of the yielding stress according to the German provisions for steel class B500 [5]. For sake of simplicity strain hardening can be neglected.

4.3 Reinforced concrete in shear

Shear stress capacity of cracked concrete is limited to a certain value. The mathematical formulation for shear capacity, as proposed in MC 2010 [3], needs an iterative procedure and is applicable to local friction, known as aggregate interlock, only. In reference [11] a formulation for shear capacity of cracked concrete has been established, which can be expressed with

$$\tau_{c,max} = \left(\frac{\rho_x}{0{,}006}\right)^{0,4} \cdot C \cdot \sqrt{f_{c,cyl}}. \tag{3}$$

Herein is

$\tau_{c,max}$ shear capacity of the crack surface,

ρ_x reinforcement ratio in x-direction with $\rho_x = \frac{A_{s,x}}{A_c}$,
the reinforcement cross section $A_{s,x,}$ the concrete cross section A_c,

C factor with $C = \left(\cos^2(\Theta + 15°) + \frac{1}{\lambda} \cdot \sin^2(\Theta)\right)$, $\lambda = \frac{A_{s,x}}{A_{s,y}}$,

$f_{c,cyl}$ concrete cylinder strength in N/mm².

The above mentioned formulation is applicable to uniaxial tension with one way and orthogonal two way reinforcement. It has been verified against test results from reference [12] and [17] (Figure 9) and shows good agreement with experimental values.

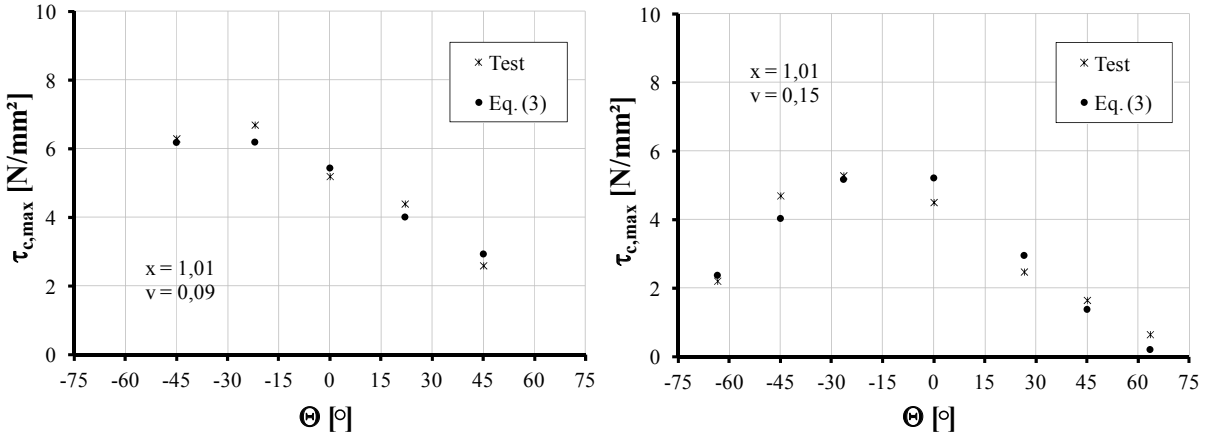


Figure 9: Comparison between test results and Eq. (3) for (a) specimen from [17] and (b) specimen from [12]

5 MODELLING THE DEFORMATION BEHAVIOUR FOR RC STRUCTURES

5.1 Mathematical formulation for pure tension

As mentioned in [2], [9], [16] the orientation of yield lines may deviate from crack orientation in the elastic state of steel strains. Aoyagi [1] compared different calculation methods with fixed and rotating crack angles. He stated for the ultimate loading capacity the crack orientation is not relevant, as all applied methods lead to very similar results. In the following for plastic steel strains the same crack angle as for the elastic strains will be assumed. According to Vecchio & Collins [15], for practical use the relatively small deviation between principal strain direction and principal stress direction will be neglected.

Following failure modes are relevant for shell elements:

- Failure of reinforcement of one or both directions, when ε_{su} is exceeded.
- Failure of concrete, when ε_c exceeds $\varepsilon_{c1.}$

For in-plane loading as for panels, the following failure mode has to be considered too:

- Failure of crack plane when the maximum shear capacity is reached with $|\tau_{c,xy}| = \tau_{c,max}$.

The steel stress may be calculated as proposed in reference [10] with:

$$\sigma_{1s,x} = \frac{\sigma_1 \cdot \cos^2\Theta \cdot A_c}{\left(A_{s,x} \cdot \cos^4\Theta + A_{s,y} \cdot \sin^4\Theta\right)} \leq f_{yk}$$
$$\sigma_{1s,y} = \frac{\sigma_1 \cdot \sin^2\Theta \cdot A_c}{\left(A_{s,x} \cdot \cos^4\Theta + A_{s,y} \cdot \sin^4\Theta\right)} \leq f_{yk} \quad (4)$$

From equilibrium in the crack plane the shear stress follows with:

$$\tau_{1c,xy} = \frac{\left(\sigma_{1s,x} \cdot A_{s,x} - \sigma_{1s,y} \cdot A_{s,y}\right)}{A_c} \cdot \sin\Theta \cdot \cos\Theta \leq \tau_{c,max} \quad (5)$$

On basis of own tests (Figure 6) and tests from reference [2] it has to be stated, the tensile strength of concrete depends not only on the material parameter f_{ct}, but on the interaction of the principal tension stress too. This interaction from biaxial tension can be determined via reduction factor k_t for first cracking with the following expression:

$$k_t = 1 - 0{,}30 \cdot \frac{\sigma_2}{\sigma_1} \leq 1{,}0 \quad (6)$$

According to Figure 2 the tension zone may by expressed on behalf of a modified steel stress-strain-relationship, which has been applied in principal tensile direction (Figure 10).

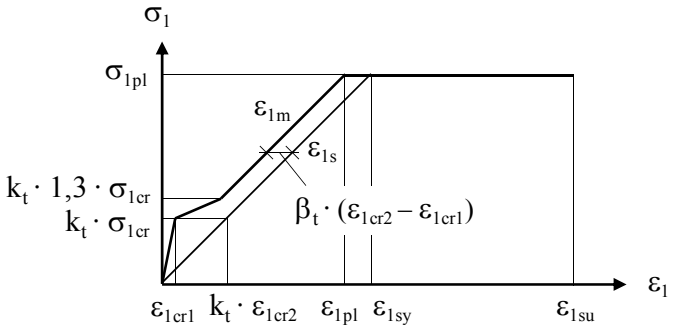


Figure 10: Modified tensile stress-strain-relationship in principal direction

For uncracked concrete ($0 < \varepsilon_{1m} \leq k_t \cdot \varepsilon_{cr1}$) the following formulation of the average strain ε_{1m} has to be applied in the first principal tensile direction:

$$\varepsilon_{1m} = \varepsilon_{1c} \quad (7)$$

For the phase of initial cracking ($k_t \cdot \varepsilon_{1cr1} < \varepsilon_{1m} < k_t \cdot 1{,}3 \cdot \varepsilon_{1cr1}$) the average strain is:

$$\varepsilon_{1m} = \varepsilon_{1s} - \frac{\beta_t \cdot (\sigma_1 - k_t \cdot \sigma_{1cr}) + k_t \cdot (k_t \cdot 1{,}3 \cdot \sigma_{1cr} - \sigma_1)}{k_t \cdot 0{,}3 \cdot \sigma_{1cr}} \cdot (\varepsilon_{1cr2} - \varepsilon_{1cr1}) \quad (8)$$

The average strain within the stabilized cracking stage ($k_t \cdot 1{,}3 \cdot \varepsilon_{1cr1} < \varepsilon_{1m} < \varepsilon_{1pl}$) may be expressed trough:

$$\varepsilon_{1m} = \varepsilon_{1s} - \beta_t \cdot (\varepsilon_{1cr2} - \varepsilon_{1cr1}) \quad (9)$$

Herein is

σ_1 first principal tensile stress,

ε_{1m} first average tensile strain,

ε_{1c} concrete strain before cracking in the first principal tensile direction,

ε_{1cr1} principal tensile strain for uncracked concrete when tensile strength of concrete is reached with $\varepsilon_{1cr1} = \frac{f_{ctm}}{E_c}$,

σ_{1cr} cracking stress $\sigma_{1cr} = f_{ctm} \cdot (1 + \alpha_e \cdot \text{eff}\rho_1^*)$,

ε_{1cr2} principal tensile strain in the crack plane when concrete tensile strength is reached with $\varepsilon_{1cr2} = \frac{f_{ctm} \cdot (1+\alpha_e \cdot \text{eff}\rho_1^*)}{E_s \cdot \text{eff}\rho_1^*}$,

ε_{1s} principal tensile strain in the crack plane with $\varepsilon_{1s} = \frac{\sigma_1 - \sigma_{2cm}}{E_s \cdot \text{eff}\rho_1^*} \geq 0$,

σ_{2cm} average concrete compression stress with $\sigma_{2cm} = \beta_t \cdot \sigma_2 \cdot \frac{\Theta}{45^\circ}$ for $\sigma_2 \geq k_t \cdot 1{,}3 \cdot \sigma_{2cr}$, else $\sigma_{2cm} = 0$,

ε_{1pl} maximum principal tensile strain in the crack plane when yielding is reached with $\varepsilon_{1pl} = \frac{f_{yk} \cdot A_c}{E_s \cdot (A_{s,x} \cdot \cos^4\Theta + A_{s,y} \cdot \sin^4\Theta)}$ and $A_c = h \cdot b$,

$\text{eff}\rho_1^*$ effective reinforcement ratio with $\text{eff}\rho_1^* = \frac{A_{s,x} \cdot \cos^4\Theta + A_{s,y} \cdot \sin^4\Theta}{A_{c,eff}}$,

β_t coefficient for short term loading ($\beta_t = 0{,}4$) and long term loading ($\beta_t = 0{,}25$),

k_t coefficient for interaction between σ_1 and σ_2 according to Eq (6).

In most cases the second principal tensile direction will remain either uncracked or under compression stress. For the special case of additional cracking in the second principal direction, it is referred to reference [11].

5.2 Mathematical formulation for combined in-plane loading

On basis of the material behaviour as defined in the previous sections and the fundamental mechanical principles for in-plane loading, a new approach for combined loads will be derived. The following expressions are based on the definitions as shown in Figure 11.

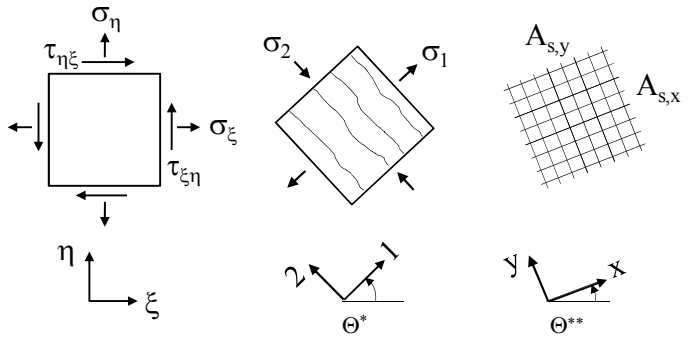


Figure 11: Definition of coordinate system: (a) general loading direction, (b) direction of principal stresses with crack pattern and (c) direction of reinforcement

Between the general loading and the principal stress directions the following geometric definition holds:

$$\tan 2\Theta^* = \frac{2 \cdot \tau_{\xi\eta}}{\sigma_\xi - \sigma_\eta} \tag{10}$$

Herein is

Θ^* angle between the $\xi\eta$-coordinates and principal stress coordinates,
$\tau_{\xi\eta}$, σ_ξ, σ_η loading stress.

On basis of Mohrs cycle the principal stresses are:

$$\sigma_{1,2} = \frac{(\sigma_\xi + \sigma_\eta)}{2} \pm \sqrt{\left(\frac{\sigma_\xi - \sigma_\eta}{2}\right)^2 + {\tau_{\xi\eta}}^2} \tag{11}$$

The reinforcement stresses are determined as defined in Eq (4). The average strain ε_{1m} is calculated as proposed in section 5.1. As stated by Veccio & Collins [15] compressive strength of concrete decreases as the average strain ε_{1m} in the first principal direction increases. Therefore, a modification of the expression for Eq. (2) according to [15] has been adopted. Rearanging Eq. (2) and consideration of a decreasing compressive strength can be expressed in closed form with:

$$\varepsilon_{2m} = \varepsilon_{c1} \cdot \left(1 - \sqrt{\frac{\sigma_2}{f_c^*} + 1}\right) \leq \varepsilon_{c1} \tag{12}$$

Herein is

ε_{2m} second principal compressive strain,
ε_{c1} maximum compressive concrete strain
(ε_{c1} for normal strength concrete with 2,0 ‰),
f_c^* reduced compressive strength due to transversal strain.

For the reduced compressive concrete strength the following expression holds:

$$\frac{f_c}{f_c^*} = \frac{1}{0{,}8 + 0{,}34 \cdot \frac{\varepsilon_{1m}}{\varepsilon_{c1}}} \tag{13}$$

Herein is

f_c uniaxial compressive concrete strength,
ε_{1m} average tensile strain ε_{1m}.

Deformations of the $\xi\eta$-system are calculated with back transformation from the principal strains as following:

$$\begin{aligned} \varepsilon_{\xi m} &= \varepsilon_{1m} \cdot \cos^2\Theta^* + \varepsilon_{2m} \cdot \sin^2\Theta^* \\ \varepsilon_{\eta m} &= \varepsilon_{1m} \cdot \sin^2\Theta^* + \varepsilon_{2m} \cdot \cos^2\Theta^* \\ \gamma_{\xi\eta m} &= 2 \cdot (\varepsilon_{1m} - \varepsilon_{2m}) \cdot \sin\Theta^* \cdot \cos\Theta^* \end{aligned} \tag{14}$$

6 MODEL VERIFICATION

Panel tests performed by Peter [13] show a load-deformation behaviour depending on the reinforcement orientation Θ. In Figure 12 for S 2r 0 with Θ = 0° as well as for S 2r 40 with Θ = 40° good accordance between calculated values and values from tests has been achieved. Influence of skew reinforcement has been considered accurately within calculations by the new approach.

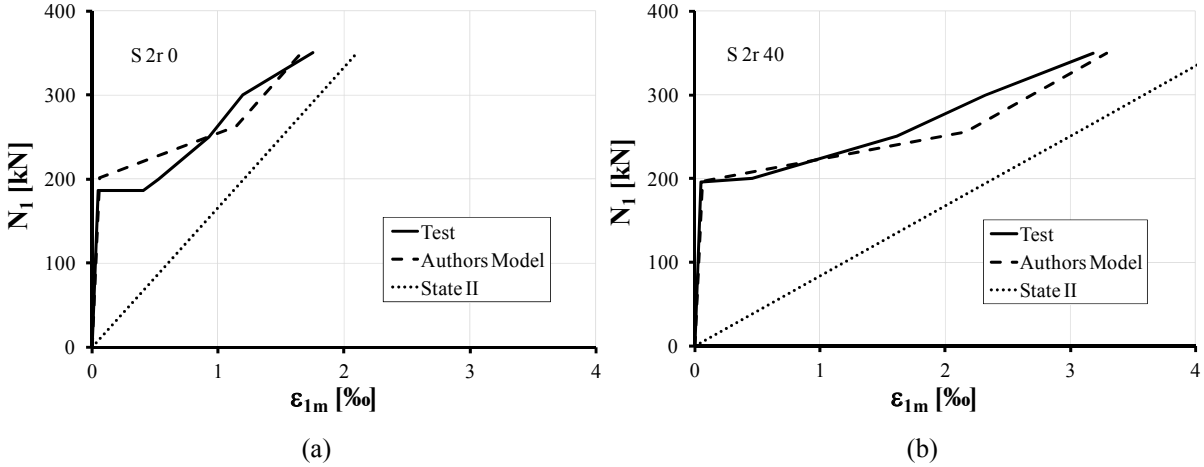


Figure 12: Comparison between authors model and test results (a) specimen S 2r 0 and (b) S 2r 40 from [9]

Own tests performed with biaxial loading show in Figure 13 a loading-deformation behaviour depending on the angle Θ and the interaction k =σ_2/σ_1. For Specimen Z1 with k = 1,0 and Θ = 0° the calculated values show only good accordance, when interaction of principal stresses has been considered. For Z3 the deformation behaviour is strongly influenced by biaxial tension with k = 0,5 and skew reinforcement with Θ = 45°. The calculated values from the proposed model agree very well with test results.

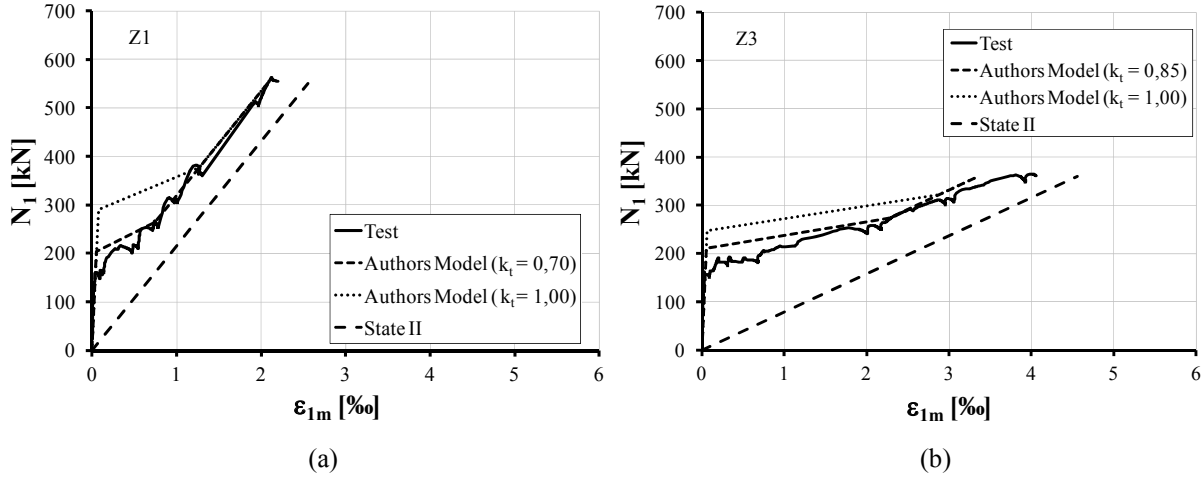
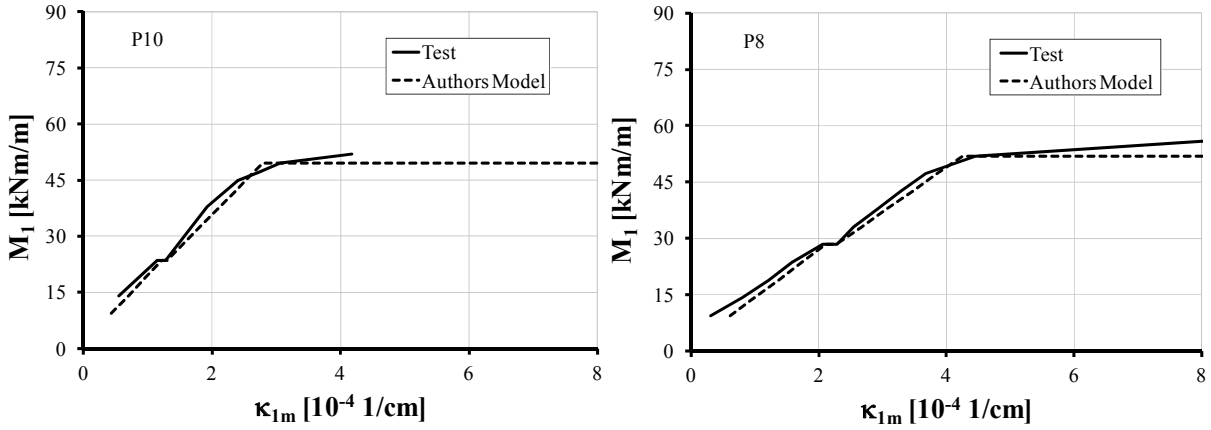


Figure 13: Comparison between authors model and own test results (a) specimen Z1 and (b) Z3

Uniaxial bending tests performed by Iványi & Lardi [9] have been compared to the proposed model as well for the elastic steel strains as for the ultimate loading (Figure 14). The prediction of the ultimate bending capacity for any kind of reinforcement orientation shows for all specimen good agreement with the test results (Table 2). Within calculations the inner lever arm has been supposed to be $z = 0{,}9 \cdot d$ and therefore $M_1 = N_1 \cdot z$. After first loading all specimen have been reloaded with cyclic steel stress (upper steel strains about 1 ‰) and 10^4 load cycles. In calculation for the first loading β_t has been supposed to be 0,4 and while cyclic loading $\beta_t = 0{,}25$. The increasing deformation due to cyclic loading has been considered through modification of the E-modulus of concrete depending on performed load cycles according to MC 2010 [3], see reference [11].



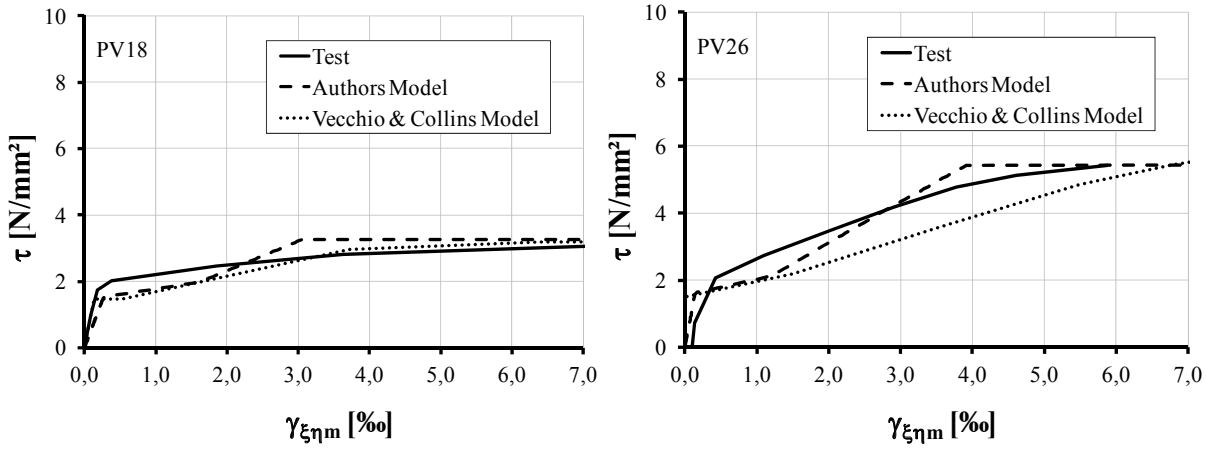
(a) (b)

Figure 14: Comparison between authors model and test results (a) specimen P10 and (b) P8 from [9]

Table 2: Load-carrying-capacity from tests of Iványi & Lardi [9] and authors model

No. [-]	Θ [°]	$f_{sy,x}$ [N/mm²]	$f_{sy,y}$ [N/mm²]	$f_{c,prism}$ [N/mm²]	$f_{ct,sp}$ [N/mm²]	$M_{1Rd,test}$ [kNm/m]	$M_{1Rd,cal}$ [kNm/m]	$M_{1Rd,test}$ / $M_{1Rd,cal}$ [-]
P5	60	429	501	20,8	2,2	16,9	16,1	1,05
P8	30	550	486	22,2	2,5	56,7	51,9	1,09
P10	0	525	495	29,0	2,2	51,9	49,6	1,05
P11	30	535	495	27,6	2,7	23,6	26,0	0,91
P12	30	540	538	31,5	2,5	42,5	33,1	1,28
P13	30	489	449	27,4	2,5	49,1	44,4	1,11
P15	30	469	469	27,0	2,3	80,3	73,7	1,09
							MW	1,08
							s	0,11
							v	0,10

The proposed model has been compared with values from combined in-plane loading tests performed by Vecchio & Collins [16]. The new model is able to predict the deformation behaviour for any in-plane action as well as the ultimate load carrying capacity (Figure 15). Beside good agreement in calculating the deformations with the new method, accordance of predicting the correct failure mode for every specimen has been achieved and documented in Table 3.



(a) (b)

Figure 15: Comparison between authors model and test results (a) specimen PV18 and (b) PV26 from [16]

Table 3: Load-carrying-capacity from tests of Vecchio & Collins [9] and authors model

								Authors Model			Vecchio & Collins Model	
No.	Θ	$f_{sy,x}$	$f_{sy,y}$	λ	$f_{c,cyl}$	f_{ct}	$\tau_{Rd,test}$	$\tau_{Rd,cal}$	$\tau_{Rd,test}$ / $\tau_{Rd,cal}$	failure	$\tau_{Rd,cal}$	$\tau_{Rd,test}$ / $\tau_{Rd,cal}$
[-]	[°]	[N/mm²]	[N/mm²]	[-]	[N/mm²]	[N/mm²]	[N/mm²]	[N/mm²]	[-]	[-]	[N/mm²]	[-]
PV2	45	428	428	1,0	23,5	1,7	1,16	1,20	0,97	S	1,61	0,72
PV3	45	662	662	1,0	26,6	1,9	3,07	3,19	0,96	S	3,20	0,96
PV4	45	242	242	1,0	26,6	1,9	2,89	2,57	1,12	S	2,59	1,12
PV6	45	226	226	1,0	29,8	2,0	4,55	4,65	0,98	S	4,76	0,96
PV10	45	276	276	1,8	14,5	1,2	3,97	3,86	1,03	S	3,68	1,08
PV11	45	235	235	1,4	15,6	1,3	3,56	3,56	1,00	S	3,59	0,99
PV12	45	469	269	4,0	16,0	1,3	3,13	3,07	1,02	S + R	2,94	1,06
PV13	45	248	-	∞	18,2	1,5	2,01	1,68	1,20	R	1,42	1,42
PV16	45	255	255	1,0	21,7	1,6	2,14	1,88	1,14	S	1,90	1,13
PV18	45	431	412	5,7	19,5	1,5	3,04	3,27	0,93	R	3,22	0,94
PV19	45	458	299	2,5	19,0	1,5	3,95	3,76	1,05	S + R	4,05	0,98
PV20	45	460	297	2,0	19,6	1,5	4,26	3,96	1,08	S	4,46	0,96
PV21	45	458	302	1,4	19,5	1,5	5,03	4,65	1,08	S	5,30	0,95
PV26	45	456	463	1,8	21,3	1,6	5,41	5,48	0,99	S	5,99	0,90

S = steel failure	MW	1,04	MW	1,01
R = crack plane failure	s	0,08	s	0,15
R + S = combined failure	v	0,07	v	0,15

f_{ct} from $f_{c,cyl}$ with k_s = 0,7 (loss of concrete tensile strength due to shrinkage)

7 CONCLUSIONS

Reinforced concrete is suitable to withstand the strong environment exposure in offshore structures. To fulfil the high requirements for the designing of these structures, adequate models are required. Today calculation methods show good accordance with experimental results, but have the disadvantage to be very extensive. The new approach has been developed in order to reduce the complex algorithms for shell structures to a possible limit and lead to highly accurate results. Its easy handling and programming are benefits of the new approach.

ACKNOWLEDGEMENT

The research work has been achieved with the financial support of the "German Research Foundation" (DFG) within the research project EM 203/3-1. All support is gratefully acknowledged.

REFERENCES

[1] Aoyagi, Y. “Analytical Approach to the Design of Orthogonally Reinforced Concrete Shell Elements to in-Plane Shear”, Proc. of JCI Colloq. on Shear Analysis of RC Structures, (1982).

[2] Aoyagi, Y. and Yamada, K. “An Experimental Approach to the Design of Network Reinforcement Against in-Plane Shear in Reinforced Concrete Containments”, 5th SMiRT Conference J4/7, (1979).

[3] CEB FIP “Model Code 2010”, First Complete Draft, Lausanne, (2010).

[4] CEB FIP “Concrete Structures for Oil and Gas Fields in Hostile Marine Environments”, State-of-the-Art Report (Bulletin 50), Task Group 1.5, Lausanne, (2009).

[5] EC 2: Design of Concrete Structures – Part 1-1: General Rules for Buildings, (2011).

[6] Empelmann, M. and Krakowski, W. “Crack Width Control of Construction Elements with Skew Reinforcement”, fib Symposium Prague, Long Edition, (2011).

[7] Empelmann, M. and Krakowski, W. “Experimentelle Untersuchungen zum Rissverhalten von Stahlbetonscheiben bei schiefwinkliger Bewehrung (Experimental Study to the Cracking Behaviour of Concrete Panels with Arbitrary Reinforcement Orientation, Paper in German)”, Festschrift Prof. M. Keuser, Universität der Bundeswehr München, (2012).

[8] FIP ”Recommendations for the Design of Concrete Sea Structures“, London, (1973).

[9] Iványi, G. and Lardi, R. “Trag- und Verformungsverhalten von netzbewehrten Stahlbetonplatten“, Forschungsberichte aus dem Fachbereich Bauwesen (No. 19). Universität Essen Gesamthochschule, (1982).

[10] Krakowski, W. and Henke, V. and Empelmann, M. “Rissbreitenberechnung bei schiefwinkliger Bewehrung (Abstract in English)”, Final Report: IRB T 3237, (2010).

[11] Krakowski, W. “Rissverhalten von Flächentragwerken aus Stahlbeton mit beliebig orientierter Bewehrung (Abstract in English)”, Submitted and Accepted Dissertation, Technische Universität Braunschweig, (2013).

[12] Mattock, A. “Shear Transfer in Concrete Having Reinforcement at an Angle to the Shear Plane”, ACI SP 42-2, 17–42, (1974).

[13] Peter, J. “Zur Bewehrung von Scheiben und Schalen für Hauptspannungen schiefwinklig zur Bewehrungsrichtung“, Dissertation, TH Stuttgart, (1964).

[14] Reddy, D. and Arockiasamy, M. “Offshore Structures”, Volume 1 & 2, Krieger Publishing Company, (1991).

[15] Vecchio, F. and Collins, M, “The Modified Compression-Field Theory for Reinforced Concrete Elements Subjected to Shear”, ACI Journal, 219–231, (1986).

[16] Vecchio, F. and Collins, M. “The Response of Reinforced Concrete to in-Plane Shear and Normal Stresses“, Publication No. 82-03, University of Toronto, (1982).

[17] Walraven, J. “Aggregate Interlock; A Theoretical and Experimental Analysis”. Dissertation. Delft University, (1980).

V International Conference on Computational Methods in Marine Engineering
MARINE 2013
B. Brinkmann and P. Wriggers (Eds)

PROGRAMMING METHODS FOR PRE-DESIGN OF COASTAL STRUCTURES

MÁRCIA LIMA[*,†], CARLOS B. COELHO[*,†] AND PAULO B. CACHIM[*,‡]

[*] Civil Engineering Department – University of Aveiro (DEC-UA)
Campus Universitário de Santiago 3810-193 Aveiro, Portugal
E-mail: marcia.lima@ua.pt, ccoelho@ua.pt, pcachim@ua.pt
Web page: www.ua.pt, www.ua.pt/decivil, civilxd.web.ua.pt

† Centre for Environmental and Marine Studies (CESAM)
Campus Universitário de Santiago 3810-193 Aveiro, Portugal
Web page: www.cesam.ua.pt

‡ Laboratory for the Concrete Technology and Structural Behaviour (LABEST)
Rua Dr. Roberto Frias 4200-465 Porto, Portugal
Web page: www.fe.up.pt/labest

Key words: Coastal Structures, Block Weight, Cross-Section Geometry, Sensitivity Analysis, C# language.

Abstract. The coastal areas are facing serious erosion problems and, consequently, an increasing investment to build and maintain shore protection structures is expected. Coastal works involve very high costs, being important to search for optimal solutions. Furthermore, the existence of numerous pre-design formulations amplifies the need to understand the influence of the represented parameters in the final results. So, the main purpose of this work was the development of a software (XD-Coast Xpress Design of COAstal STructures), using C# language, which the main goal is the calculation of armour layer blocks unit weight, for different formulations and types of structures. The XD-Coast was developed in order to facilitate calculation processes, allowing a quick comparison between several alternative solutions, and to allow sensitivity analysis about variables involved in the calculations. Therefore, it was intended that the model was resourceful, with an intuitive and easy graphical interface. In addition, it allows not only isolated calculations, but also repeated calculations with increment of several calculation steps for some variables, generating tables of results, exportable to Excel files. These tables allow understanding the influence of each parameter in armour layer blocks unit weight. A sensitivity analysis was performed and is presented, for all formulations and various parameters. Finally, XD-Coast model purpose is to be a good tool to obtain optimized solutions during the pre-design phase of a structure.

1 INTRODUCTION

The increasing urban pressure on coastal areas and the continuous shoreline retreat, allows anticipating significant investments in order to build and maintain shore protection structures along the coast. Coastal works involve high costs and so, improving the knowledge related to conception and pre-design of coastal structures can helps on searching optimized solutions. Previous considerations justify the need to develop automatic tools for comparison of

different solutions and thus, the main purpose of this work was to develop a software to calculate armour layer blocks unit weight, for different formulations and types of structures.

The cross-section of shore protection structures are usually composed by a bedding layer and a core of quarry-run stone covered by one or more layers of larger stone, and an exterior layer or layers of large quarrystone or concrete armour units [1]. In this work, only rock and tetrapod armour layers were considered. Respecting to the armour stability, it is common to distinguish the structures between: non-overtopped or marginally structures; low-crested, *i.e.*, overtopped structures but with crest level above sea water level; and submerged structures, *i.e.*, the crest level is below sea water level.

The software developed in this work uses three different formulations for calculations related to non-overtopped structures (Hudson [5], van der Meer for rocks [7] and van der Meer and Jong for tetrapods [3, 8], and one formulation for low-crested and submerged structures (van der Meer for rocks [9]). The coastal structures are exposed to several energetic loads as waves, currents and tides. The developed software only considers the load represented by wave height (the most important and conditional load). It is important to note that more formulations can be found in literature [1, 2].

With the aim to understand the influence of each parameter in the pre-design results, a sensitivity analysis was performed, encompassing all formulations and types of structures previously referred.

2 PRE-DESIGN OF CROSS-SECTION

To conceive and design a coastal work four fundamental steps must be followed. Firstly it is very important to define a correct load setting, represented by wave height. Then, the structure pre-design is developed, based in empirical formulations. Thereafter, a physical model at reduced scale should be built and tested in laboratory, in order to understand the real performance of the structure. Finally, the design of structure is carried out, taking into account the pre-design and the laboratory tests results.

This work presents a program (XD-Coast: Xpress Design of COAstal Structures) which aims to help designers in the pre-design phase. Thus, the purpose of this chapter is to describe all pre-design assumptions and formulations considered in XD-Coast. XD-Coast is a program to evaluate the cross-section characteristics of coastal structures that allows the calculation of armour layer blocks unit weight (W) and the determination of the main geometric cross-section characteristics. The armour layer pre-design formulations are presented in section 2.1 and the other geometric cross-section characteristics formulations are described in section 2.2.

2.1 Armour Layer

The pre-design methodologies are essentially based in formulations that allow the calculation of armour layer blocks unit weight able to resist to wave loads. There are numerous formulations for armour layer pre-design and their application depends essentially of the structure (non-overtopped, overtopped or submerged structures) and the armour layer material adopted. Hudson and van der Meer are the most used formulations for armour layer pre-design [3], allowing estimating the weight of the block (W), or the equivalent cube length of median rock (D_{n50}), related between each other by $W = \gamma_s D_{n50}$, where γ_s represents the specific weight of armour layer. Five formulations were considered which encompass the three kinds of structure and two different materials for the blocks.

2.1.1 Non-overtopped (marginally) structures

Non-overtopped or marginally overtopped structures are structures with a high crest elevation only overtopped under severe wave conditions [2]. The wave attack on the seaward slope is higher than for low-crested structures. For non-overtopped structures, three formulations are presented: Hudson, for any material; van der Meer, for rocks; and van der Meer and Jong, for tetrapods.

Hudson (generic)

Hudson formula [5] is based on model tests with regular waves on non-overtopped structures with a permeable core. The main advantage of this formula is its simplicity and the wide range of armour units and configurations for which K_D values have been derived. However, it has limitations such as: the use of regular waves only; no account of the wave period and the storm duration; no description of the damage level; and the use of non-overtopped and permeable structures only [2]. For rock structures, Hudson formula is shown in Equation 1 [1, 2, 4]:

$$\frac{H}{\Delta D_{n50}} = (K_D cot\ \alpha)^{1/3} \quad (1)$$

where H is the wave height, Δ corresponds to relative density ($\Delta = \rho_s/\rho_w - 1$, where ρ_s and ρ_w are, respectively, mass density of rocks and water), K_D is a stability coefficient and α corresponds to the slope angle. For concrete armour layer blocks, the Equation 1 is also applied, but with D_n rather than D_{n50}, where D_n represents the equivalent cube length, *i.e.*, the length of a cube with the same volume as the block. For concrete blocks, K_D takes higher values (*e.g.* approximately 3-4 for rocks and 6-8 for tetrapods).

Van der Meer (rocks)

Van der Meer stability formula is more complex than Hudson, but as a great advantage, do include the effects of storm duration, wave period, the structure's permeability and a clearly defined damage level. The formula allows to distinguish between surging waves and plunging waves, given by, respectively, Equation 2 and 3 [1, 2, 4]:

$$\frac{H}{\Delta D_{n50}} = 1.0\ S^{0.2} P^{-0.13} N_z^{-0.1} (\cot\alpha)^{0.5} \xi_m^P \quad \text{for} \quad \xi_m > \xi_{mc} \quad (2)$$

$$\frac{H}{\Delta D_{n50}} = 6.2\ S^{0.2} P^{0.18} N_z^{-0.1} \xi_m^{-0.5} \quad \text{for} \quad \xi_m < \xi_{mc} \quad (3)$$

where S represents the relative eroded area or damage level (S values can be consulted in [1]), P corresponds to notational permeability of the structure ($0.1 \leq P \leq 0.6$, more information about permeability can be found in [1]) and N_z is the number of incident waves at the toe of the structure (which depends on the duration of the wave conditions, $N_z \leq 7500$). ξ_m is the Iribarren number for mean wave period T_m ($\xi_m = s_{om}^{-0.5} \tan\alpha$), where s_{om} represents the wave steepness ($s_{om} = H/L_{om}$, L_{om} is the deepwater wavelength and $0.005 \leq s_{om} \leq 0.06$). The transition from plunging to surging waves is derived from the structure slope and can be calculated with Equation 4, using a critical value ξ_{mc}.

$$\xi_{mc} = (6.2 P^{0.31} (\tan\alpha)^{0.5})^{1/(P+0.5)} \quad (4)$$

Van der Meer (tetrapods)

The design of concrete armour layers generally follows the overall approach for rock armouring [2]. Van der Meer [8] developed Equation 5, for non-overtopped concrete blocks structures (specifically for tetrapods) based in rock formulations [1][2]:

$$\frac{H}{\Delta D_n} = \left(3.75\left(\frac{N_{od}}{\sqrt{N_z}}\right)^{0.5} + 0.85\right) s_{om}^{-0.2} \quad (5)$$

where N_{od} represents the number of units displaced out of the armour layer within a strip width of one cube length D_n (N_{od} value depends of damage level). For tetrapods, N_{od} takes the value ranging 0.2-0.5, for start of damage, 1 for intermediate damage, and 1-5 for failure [2]. Equation 5 is only valid for two layer of tetrapods on H/V = 3/2 (≈34º) slope and P = 0.4. According to some authors [2], this formula is only valid for surging waves. Then, de Jong [3] analysed more data on tetrapods and proposed Equation 6 for plunging waves [2].

$$\frac{H}{\Delta D_n} = \left(8.6\left(\frac{N_{od}}{\sqrt{N_z}}\right)^{0.5} + 3.94\right) s_{om}^{-0.2} \quad (6)$$

2.1.2 Low-crested (overtopped) structures

Low-crested structures or overtopped structures are structures with a low crest elevation, where significant wave overtopping occurs. This wave overtopping reduces the required size of the armourstone on the seaward slope because part of the wave energy can pass over the structure [2]. For overtopped structures, the pre-design formulation proposed by van der Meer for rocks is presented.

Van der Meer (rocks)

Van der Meer [9] suggested that the van der Meer stability formulae for non-overtopped rock slope (Equation 2 and 3), could be used with $D_{n50,overtopped}$ ($D_{n50,overtopped} = f_i D_{n50}$) substituted by D_{n50}. The reduction factor f_i is given by Equation 7 and it is valid only in the range $0.8 < f_i < 1.0$ [1, 2].

$$f_i = \left(1.25 - 4.8\frac{R_c}{H}\sqrt{\frac{s_{op}}{2\pi}}\right)^{-1} \qquad \text{valid when} \qquad 0 < \frac{R_c}{H}\sqrt{\frac{s_{op}}{2\pi}} < 0.052 \quad (7)$$

where R_c is the crest freeboard (distance between crest elevation and sea water level), s_{op} represents deepwater wave steepness corresponding to the peak of the wave spectrum.

2.1.3 Submerged structures

Submerged structures have their crest below sea water surface level but the depth of submergence of these structures is sufficiently small that wave breaking processes affect the stability. Submerged structures are overtopped by all waves and the stability increases significantly as the crest height decreases [2]. As was adopted for overtopped structures, for submerged structures only van der Meer formulation for rocks is presented.

Van der Meer (rocks)

For irregular waves and H/V = 2/1 (≈27º) slope angle, van der Meer [9] developed Equation 8 for rock submerged structures [1].

$$\frac{h'_c}{d} = (2.1 + 0.1S)\, exp(-0.14N_s^*) \quad (8)$$

where d represents the water depth, h'_c is the height of the structure over seabed level ($d - h'_c$ is the water depth over the structure crest) and N_s^* is the spectral stability number (Equation 9). The s_p parameter represents the local wave steepness, which depends of L_p value (local wavelength associated with the peak spectral period, T_p).

$$N_s^* = \frac{H}{\Delta D_{n50}} s_p^{-1/3} \quad (9)$$

2.2 Cross-section

After the armour layer blocks unit weight definition (obtained with expressions presented in section 2.1), it is possible to describe the main geometric characteristics of the cross-section. Pre-design equations for crest width, thickness of armour layer and placing density, are described below. The first underlayer, second underlayer and core blocks unit weight are function of the blocks unit weight obtained to primary cover layer W, according to [1].

Crest width

Crest width (B) greatly depends on the degree of allowable overtopping. However, this dependency has not been quantified into general design guidance. The general rule of thumb for overtopping conditions is that minimum crest width should equal the combined widths of three armour units (n_b = 3) as determined by the Equation 10 [1].

$$B = n_b\, k_\Delta \left(\frac{W}{\gamma_s}\right)^{1/3} \quad (10)$$

where n_b is the number of stones (n_b = 3 is recommended minimum), k_Δ represents the layer coefficient (correspondent values can be consulted in [1]), and the other variables have the previously defined meaning.

Thickness of armour layer

The thickness of the cover layer and underlayers I is calculated through Equation 11, similar to Equation 10. In this case, n is the number of quarrystone or concrete armour units in thickness, typically equal to 2 [1].

$$r = n\, k_\Delta \left(\frac{W}{\gamma_s}\right)^{1/3} \quad (11)$$

Placing density

The placing density, *i.e.*, the number of armour units per unit area (N_a/A), is estimated by Equation 12. N_a/A value is dependent on cover layer average porosity (P', see correspondents values in [1]) and it is also dependent on all the parameters mentioned in the two previous equations [1].

$$\frac{N_a}{A} = n\, k_\Delta \left(1 - \frac{P'}{100}\right) \left(\frac{\gamma_s}{W}\right)^{2/3} \quad (12)$$

3 XD-COAST PROGRAM

The main purpose of this work was the development of a computational tool, which allows the pre-design of armour layer of coastal structures that was intended to be simple to use, with an intuitive and easy graphical interface. XD-Coast software (Xpress Design of COAstal Structures) was developed in Microsoft Visual C# language, which main objective is the calculation of armour layer blocks unit weight, for different formulations and types of structures. Furthermore, the program also allows the calculation of the main parameters of cross-section, in function of the value of armour layer blocks unit weight. The download of XD-Coast is available for free in www.civilxd.web.ua.pt.

3.1 XD-Coast description

XD-Coast was developed in order to facilitate calculation processes, allowing quick comparisons between several alternative solutions, and to carry out sensitivity analysis about variables involved in calculations. Figure 1 shows the features and the organization of the program. The XD-Coast is divided into two main parts: estimative of the armour layer blocks unit weight; cross-shore geometric characteristics definition, based on the previous results.

In the first part, the process begins by choosing the kind of structure and formulation required. Then, the user defines the type of calculation (isolated calculation or sensitivity analysis) and fills the frame with all the parameters required. Then, the user obtains a single value for armour layer unit weight (isolated calculation) or obtains a table of results (sensitivity analysis). Afterward, in the second part, the other characteristics and a schematization of the cross-section (in the case of isolated calculations) or a table of results (in the case of a sensitivity analysis), can be obtained. It is important to emphasize that the second part results are dependent upon the first part results.

In order to facilitate the analysis, XD-Coast allows exporting results tables into an Excel® data sheet, enabling the use of tools provided by this software (charting, numerical analysis, etc.). XD-Coast windows also contain some help icons () which aims to clarify the user. However, the users' knowledge about the calculations concepts (section 2 and general state of the art) is essential for a correct use of the software.

3.2 XD-Coast application

As an example, a cross-section of a detached breakwater is considered. Three different crest elevation (C) situations are taken into account for a constant water depth (d = 4m). In the first scenario the structure is considered non-overtopped (C = 8m), in the second scenario the structure is low-crested (C = 5m and R_c = 1m) and in the third scenario the crest is below sea water level (C = 3m), *i.e*, it is a submerged structure. The armour layer was pre-designed for the three previous scenarios. For Hudson formula, two different materials were considered: rock armour layer and concrete armour layer (tetrapod). In this work, only the results obtained by van der Meer formula (scenario 2, low-crested structure) are presented in detail (Figure 2). Regarding to the remaining formulations, only the armour layer blocks unit weight are exposed (Table 1). The common parameters were considered the same in the all the formulations. The remaining considerations may be consulted in [6].

It is not possible a direct comparison between these results, because each formula has different considerations and assumptions. However, it is possible to verify that armour layer blocks unit weight corresponding to non-overtopping structure is higher than low-crested

structure (about 57% for van der Meer formula). For the submerged structures, the armour layer blocks unit weight required is much lower that non-overtopping and low-crested structures. Comparing armour layer material, it was possible to verify that rock implies higher values than tetrapods (more 45% and 107%, respectively for Hudson and van der Meer formulae). Generically, van der Meer formulation is more conservative (88% and 32% more weight, respectively for rock and tetrapod armour layer).

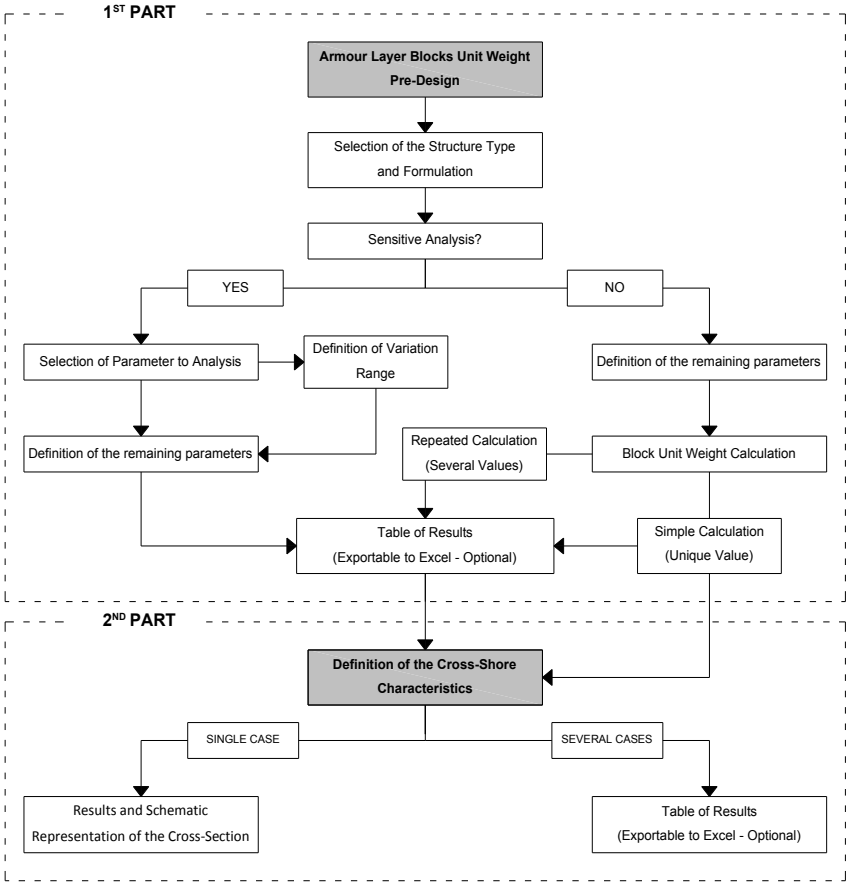


Figure 1: XD-Coast organizational chart.

The pre-design tables provide the armour layer blocks unit weight for different combinations of the involved parameters. With XD-Coast, it is simple and intuitive to obtain this kind of tables. In the pre-design step, the use of these tables can be an advantage for designers, allowing a quick comparison between different solutions. The tables cover all the parameters with influence in the results (except γ_w), with multiple hypotheses for each of them. An example for Hudson formulation is shown in Table 2. Pre-design tables for other formulations can be easily generated by XD-Coast, or can be consulted in Lima [6].

4 SENSITIVITY ANALYSIS

The pre-design of the armour layer blocks unit weight is based on empirical formulations, which is dependent of several parameters. It is very important to understand each parameter influence in the final results, in order to achieve optimized solutions. In this chapter, sensitivity analyses were performed using XD-Coast, encompassing all the considered formulations.

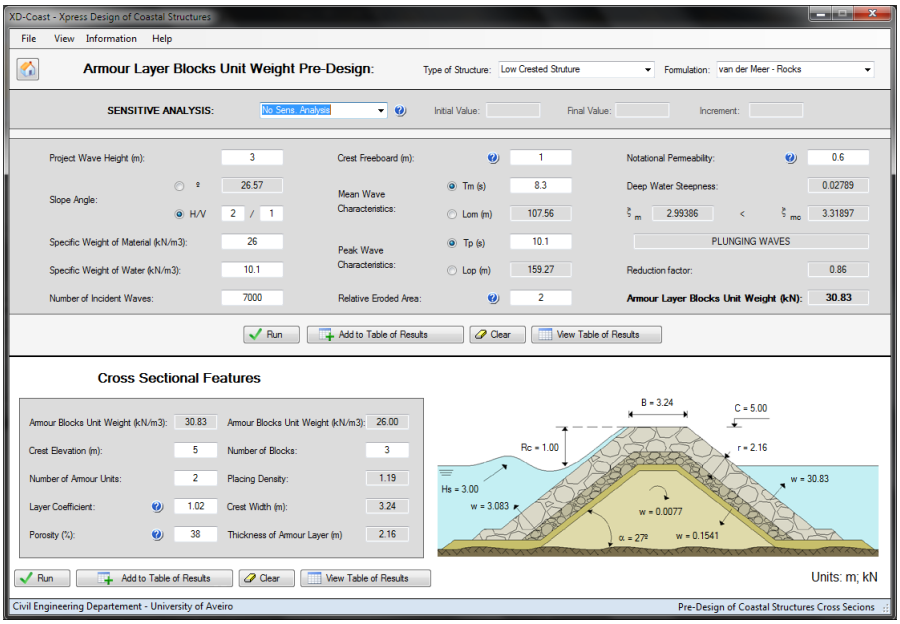


Figure 2: XD-Coast window results, for van der Meer formula (low-crested structure)

Table 1: Armour layer blocks unit weight obtained by XD-Coast, for all formulae.

ARMOUR LAYER BLOCKS UNIT WEIGHT (kN)			
SCENARIO 1 Non-Overtopping Structure	Hudson	Rock	25.70
		Tetrapod	17.76
	Van der Meer	Rock	48.42
	Van der Meer and Jong	Tetrapod	23.42
SCENARIO 2 Low-Crested Structure	Van der Meer	Rock	30.83
SCENARIO 3 Submerged Structure	Van der Meer	Rock	7.20

Table 2: Pre-design of armour layer blocks unit weight (kN) according to Hudson formulation

		K_D = 3 (≈ rock)			K_D = 7 (≈ tetrapods)		
		H/V = 1/1	H/V = 2/1	H/V = 3/1	H/V = 1/1	H/V = 2/1	H/V = 3/1
γ_s = 20 kN/m^3	H = 2 m	56.6	28.3	18.9	24.3	12.1	8.1
	H = 4 m	453.1	226.5	151.0	194.2	97.1	64.7
	H = 6 m	1529.0	764.5	509.7	655.3	327.7	218.4
γ_s = 26 kN/m^3	H = 2 m	17.8	8.9	5.9	7.6	3.8	2.5
	H = 4 m	142.2	71.1	47.4	60.9	30.5	20.3
	H = 6 m	479.8	239.9	159.9	205.6	102.8	68.6
γ_s = 32 kN/m^3	H = 2 m	8.4	4.2	2.8	3.6	1.8	1.2
	H = 4 m	67.0	33.5	22.3	28.7	14.4	9.6
	H = 6 m	226.0	113.0	75.3	96.9	48.4	32.3

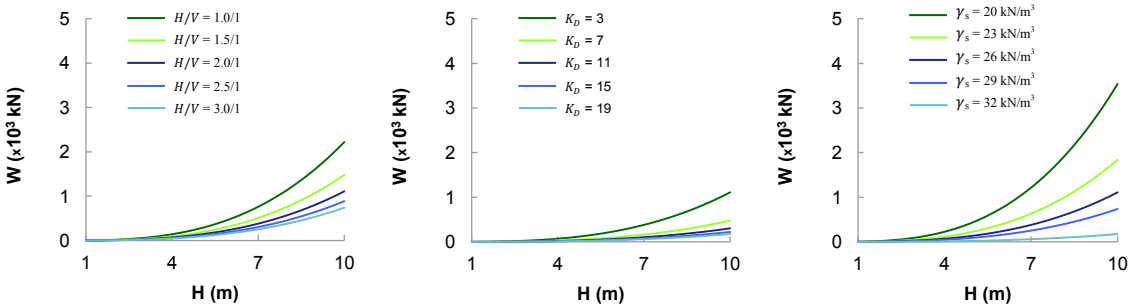
The wave height (H) is very important in the pre-design of coastal structures, because a wrong setting can lead to the structure collapse (if undersized) or to high costs (if oversized). For the following analyses, the armour layer blocks unit weight is considered as a function of H (ranging between 1 and 10m). Beside the wave height, the specific weight of the armour layer material and of the water (γ_s and γ_w respectively) are also common to all the studied

formulations. Generically the wave height increase implies a great increase in the blocks weight, being more important for lower wave heights. As an example, for H values of 7-10m, an increase of 1m in wave height implies an increase around 40% in armour layer blocks unit weight, but if H is ranging between 1-4m, this increase is about 300%. It can be also observed that an increase of γ_w implies higher blocks weight and an increase of S led to lower blocks weight. The influence of S parameter is similar on non-overtopping and low-crested structures and it is less significant on submerged structures.

4.1 Hudson formula (non-overtopping structures)

According to Equation 1, the armour layer blocks unit weight value depends also of the slope angle (α) and the stability coefficient (K_D). Then, the influence of this two parameters and the specific weight of armour layer material (γ_s) were analysed using Hudson formulation, considering five different values for each (Figure 3).

An increase of the armour layer blocks unit weight it was verified when the slope angle is greater and when the stability coefficient and the specific weight of armour layer material are lower. A cross-section with H/V = 1/1 needs a block weight about 100% higher than with H/V = 2/1. Stability coefficient influence is more important to lower values, *i.e.*, the consideration of K_D = 3 instead of K_D = 7 implies an increase of about 133% in the armour layer blocks unit weight. On the other hand, considering K_D = 15 as an alternative to K_D = 19, represents an increases around 27%. Specific weight armour layer material behaviour is similar, *i.e.*, the increase of results is greatest for lower specific weight values (an armour layer material with γ_s = 20kN/m^3 lead to results about 92% higher than γ_s = 23N/m^3 and when it is considered γ_s = 29kN/m^3 instead of γ_s = 32kN/m^3, the increase is only about 41%).



a) Different values for H/V (K_D = 3 and γ_s = 26 kN/m^3).

b) Different values for K_D (H/V = 2/1 and γ_s = 26 kN/m^3).

c) Different values for γ_s (H/V = 2/1 and K_D = 3).

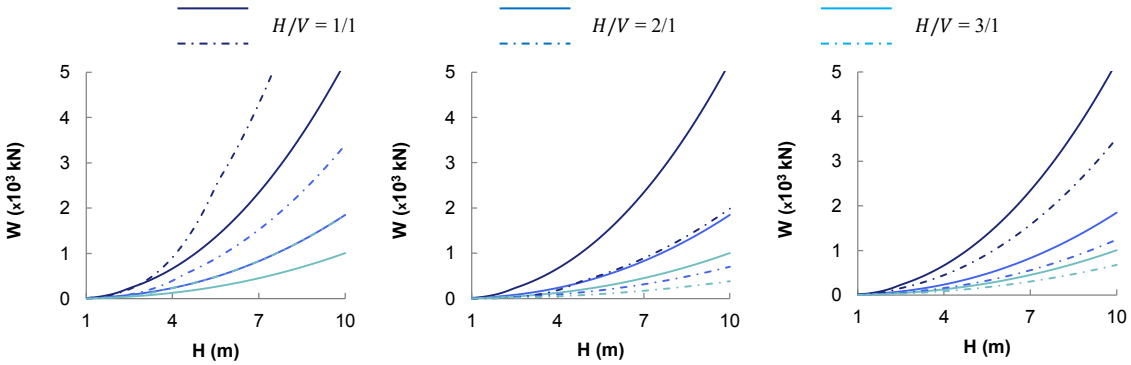
Figure 3: Armour layer weight for Hudson formula (non-overtopping structures)

4.2 Van der Meer formula (non-overtopping structures)

Van der Meer proposed two formulations for the pre-design of the armour layer blocks unit weight, distinguishing surging and plunging waves (Equation 2 and 3 respectively). According with this author, the results are influenced by the mean wave period (T_m), slope angle (α), permeability (P), eroded relative area (S) and the number of incident waves (N_z), in addition to the common parameters (H, γ_s and γ_w). Figure 4 shows the influence of the slope angle for three different situations. The influence of specific weight of armour layer was not analysed.

The influence of the slope angle is similar for the three situations, but different for surging and plunging waves. Considering slope angles of H/V = 1/1 instead of H/V = 2/1, increases

the blocks weight is 130% and 183%, for surging and plunging waves, respectively. The specific weight of the material has the same behaviour for the three situations, also without differences for surging and plunging waves. The behaviour of wave period is significantly influenced by the breaking wave type. It was verified that an increase of T_m of surging waves (lower wave heights) implies a decrease in armour layer blocks unit weight and the behaviour is contrary for plunging waves (T_m = 12s instead of T_m = 8s implies a decrease of about 11% for surging waves and an increase of about 84% for plunging waves). The armour layer blocks unit weight corresponding to impermeable slopes (P = 0.1) is higher than for permeable slopes (P = 0.6). The correspondent surging waves increases are higher, being over than 160% for both type of waves. The influence of the number of incident waves is similar for surging and plunging waves (N_z = 7500 instead of N_z = 2000 implies an increase of about 50% in the bocks weight).



a) P = 0.1 and N_z = 7500 (continous line for T = 8s and doted line for T = 12s).

b) T = 8s and N_z = 7500 (continous line for P = 0,1 and doted line for P = 0,6).

c) T = 8s and P = 0.1 (continous line for N_z = 7500 and doted line for N_z = 2000).

Figure 4: Armour layer weight, for different slope angles (van der Meer, non-overtopping structures)

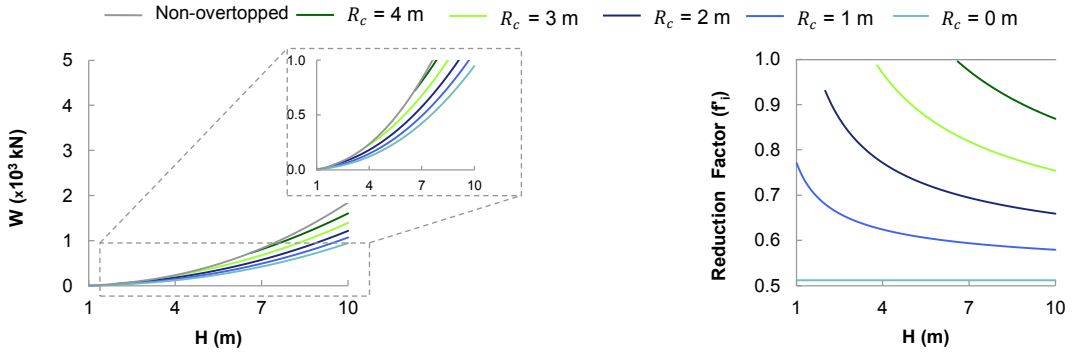
4.3 Van der Meer and Jong formula (non-overtopping structures)

The results related to concrete armour layers (tetrapods) are not presented, because it was found that the behaviour was similar to previous formulation. However, Concerning to the analysis of the number of incident waves, the increases are different for surging and plunging waves (50% and 29% respectively). An initial damage level of N_{od} = 0.0 implies an armour layer blocks unit weight to increase 295% and 113%, when compared to a damage level near to failure (N_{od} = 1.5), for surging and plunging waves respectively.

4.4 Van der Meer formula (low-crested structures)

For low-crested structures, Van der Meer proposed an expression for the armour layer blocks unit weight obtained by non-overtopped formulae (Equation 2 and 3) affected by a reduction factor f_i, given by Equation 7 (equivalent to $W_{overtopped} = f_i^3 W_{non-overtopped}$, because $W = \gamma_s {D_{n,50}}^3$ and, consequently, $0.512 < f_i^3 = f'_i < 1$). The reduction factor is mainly influenced by the crest freeboard (R_c). Then, there were considered five different values for R_c parameter (from 0 to 4m) in order to analyse the armour layer blocks unit weight (Figure 5a) and reduction factor (Figure 5b) behaviour. In this analysis, T_m = 8s, P = 0.1, N_z = 7500, H/V = 2/1, γ_s = 26kN/m^3, S = 2 and T_p = 9.8s (considering T_m = 0.82 T_p) were considered.

The armour layer blocks unit weight obtained for each R_c value and the same results for non-overtopped structures were compared. Generically, a decrease of R_c implies lower reduction factors and consequently, a smaller blocks weight. The influence of R_c depends of the wave height considered. For H = 7m, R_c = 4m implies a reduction of 3% in armour layer results and R_c = 0m implies a reduction of 49% (maximum reduction possible).



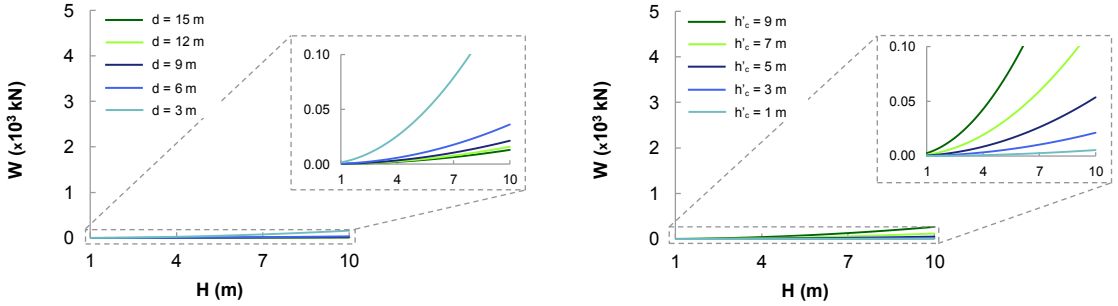
a) Armour layer bocks unit weight b) Reduction factor

Figure 5: Evaluation of crest freeboard influence, according to van der Meer formula (low-crested structures)

4.5 Van der Meer formula (submerged structures)

Van der Meer proposed Equation 8 for the pre-design of submerged structures. In this formulation, the armour layer blocks unit weight depends mainly of the water depth (d) and of the height of the structure (h'_c). The sensitivity of these two parameters in armour layer blocks unit weight was analysed (Figure 6).

A decrease of water depth value and an increase of structure height lead to higher values of armour layer blocks unit weight. For the first parameter, the higher increase was related to the lower depth water (d = 12m instead of d = 15m implies results 22% higher and d = 3m instead of d = 6m return results over than 300% higher). Relatively to the structure's height, the increase corresponding to h'_c = 3m instead to h'_c = 1m is about 286% and is about 121%, when considering h'_c = 9m instead of h'_c = 7m.



a) h'_c = 3 m b) d = 9 m

Figure 6: Evaluation of water depth and structure height (van der Meer formula - submerged structures)

5 CONCLUSIONS

This work aimed the development of an automatic tool (XD-Coast: Xpress Design of COAstal STructures), which the main goal was the calculation of armour layer blocks unit weight. XD-Coast was intended resourceful, with an intuitive and easy graphical interface.

Aiming to understand the influence of each parameter involved in block weight calculations, XD-Coast allows not only isolated calculations, but also repeated ones. Thus, tables with several results can be generated and exported to Excel files. XD-Coast allows quick comparison of different options, in order to achieve optimized solutions.

XD-Coast encompasses non-overtopping structures, low-crested structures and submerged structures. In the first case, three different formulations are considered (Hudson, van der Meer for rocks and van der Meer and Jong for tetrapods), and for the others two types of structures only a formulation was considered (van der Meer for rocks).

Sensitivity analyses were performed for all the formulations, aiming to understand the influence of each parameter in armour layer blocks unit weight. Wave heights have great importance, because its increase implies significant increases in armour layer blocks unit weights. In addition to wave height, specific weight of armour layer material and water are common parameters to all the formulations. The influence of some other parameters (mean wave period, permeability, etc.) depends on wave breaking type (surging or plunging waves). Generically, the blocks unit weight corresponding to non-overtopping structures is higher than for low-crested structures (about 60%, in the considered example) and much higher than submerged structure (over 300%).

This software tool was programmed to help on the pre-design step of coastal structures. It is important to note that this is not enough for a costal structure conception and the construction of physical models at reduced scale are crucial to understand the real performance of these structures.

REFERENCES

[1] Burcharth, H. F., Hughes, S. A. *Fundamentals of Design*. Coastal Engineering Manual, Part VI: Design of Coastal Project Elements, Chapter 5, U.S. Army Corps of Engineers, Washington, DC, 312p (2006).

[2] CIRIA, C. C. *The Rock Manual. The Use of Rock in Hydraulic Engineering (2nd Edition)*. Chapter V - Physical Processes and Design Tools, C683, CIRIA, London, pp 487-756 (2007).

[3] De Jong, T. J. *Stability of Tetrapods at Front Crest and Rear of a Low-Crested Breakwater*. Delft Hydraulics Publication No. 453, Delft Hydraulics Laboratory, The Netherlands (1996).

[4] Fleming, C. A., Allsop, N. W. H., Lerming, M. B., Sharp, B. N., Slater, D., Williams, A. J., Titman, P. *Concrete in Coastal Structures*. Thomas Telford, London, 301 p (1998).

[5] Hudson, R. Y. *Concrete Armor Units for Protection Against Wave Attack*. Miscellaneous, Paper H-74-2, U. S. Army Engineer Waterways Experiment Station, Vicksburg, MS (1974).

[6] Lima, M. *Programação de Métodos de Pré-Dimensionamento de Obras Costeiras*. Master Thesis, Aveiro University, 131p (2011).

[7] van der Meer, J. W. *Rock Slopes and Gravel Beaches Under Wave Attack*. Ph.D. diss, Delft University of Technology, The Netherlands, 214 p (1988a).

[8] van der Meer, J. W. *Stability of Cubes, Tetrapods and Accropode*. Proceedings of the Breakwaters '88 Conference, Design of Breakwaters, Institution of Civil Engineers, Thomas Telford, London, UK, pp 71-80 (1988b).

[9] van der Meer, J. W. *Stability and Transmission at Low-Crested Structures*. Delft Hydraulics Publication No. 453, Delft Hydraulics Laboratory, The Netherlands (1991).

V International Conference on Computational Methods in Marine Engineering
MARINE 2013
B. Brinkmann and P. Wriggers (Eds)

MODELING FLAT SHIP PLATES USING EQUIVALENT SINGLE LAYER THEORY

JANI ROMANOFF[*], JASMIN JELOVICA[*], EERO AVI[†] AND ARI NIEMELÄ[†]

[*] Department of Applied Mechanics, Marine Technology
Aalto University
P.O.Box 15300, 00076 Aalto, Finland
e-mail: jani.romanoff@aalto.fi, www.aalto.fi

[†] STX Finland
Telakkakatu 1, 20101 Turku, Finland
email: eero.avi@stxeurope.com, www.stxeurope.com

Key words: Equivalent Single Layer Theory, Marine Engineering

Abstract. The present paper discusses on the modeling of ship deck panels at concept design stage using Equivalent Single Layer (ESL) plate theory. First order shear deformation theory is utilized that enables modeling of one-side stiffened plates used traditionally in shipbuilding, but also double-skinned structures such as sandwich plates and composite structures. Interaction between the plate element and supporting girders is modeled using offset beams. The static, vibration, bifurcation buckling and post-buckling response are considered. The validation is done with fine mesh FE-analyses based on modeling the actual 3D topology with shell elements. The paper shows that ESL is very efficient way to model and optimize the ship structure where differences of scale, as well as the complexity of the geometry, cause difficulties for the Finite Element discretization as well as to the solution. The benefit of the method is that FE-mesh needs to be created only once. This enables optimization during the design by changing only the equivalent stiffness properties of the beams and plates leaving the mesh unchanged.

1 INTRODUCTION

Ship structural design has challenges due to small series and structural complexity of the final product. Small series limits the amount of design hours, while the complexity of the structures increases the need of direct strength analyses. These facts are highlighted in passenger ships, see Fig. 1, where safety of the vessel is of high importance while there is high economical risk associated with the delay of the design and construction. The structural design is nowadays, from very early stages, carried out using the Finite Element Method (FEM) [1-4]. In concept design stage, where large changes in general arrangement are possible, the use of FEM is challenging due to the fact that it requires creation of the mesh, solving the large system of linear or non-linear equations and finally analysing the results. Numerous techniques have been developed to speed up the process, i.e. sub-modelling [3-6], parametric modelling [7, 8] and using dimension reduction methods such as equivalent beams and shells [9-13]. The use of equivalent beams and plates is the most beneficial in concept design stage since it reduces computational efforts in all stages of FE-analysis. In ship

structural design the static analysis is used to define the stresses and deformations for given load cases. The aim is to check that the stress levels are not excessive resulting in yielding, buckling or fatigue. Typically nominal stress levels are checked against predefined closed form design equations given by Classification Society rules, e.g. [14, 15].

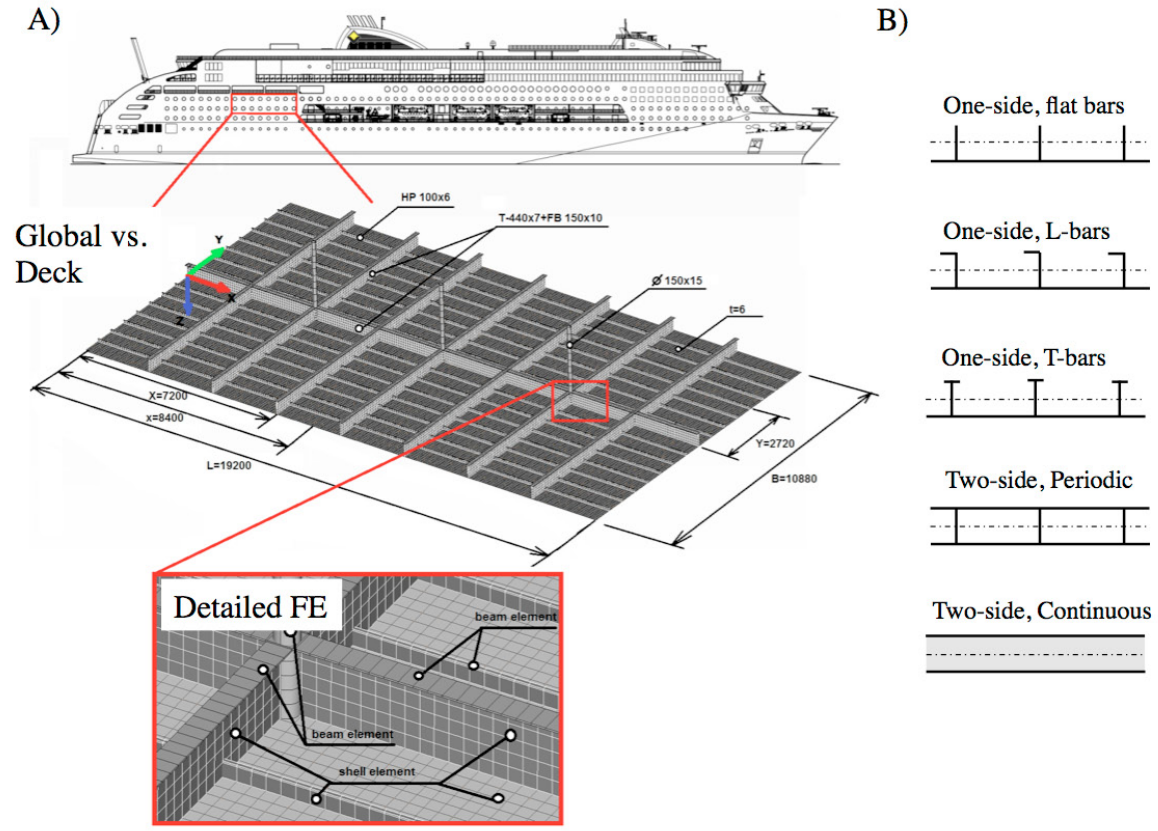


Figure 1: A) Stiffened deck with fine mesh in passenger ship and B) different deck plate configurations.

Use of *Equivalent Single Layer (ESL)* plate theory [16-18] is often applied in ship structural design [3, 15] when global hull-girder strength analysis is carried out, while detailed FE-analyses are carried out at the local, panel, stiffener or plate, levels using different mesh. In Refs. [3, 19] the use of ESL has been applied for one-sided stiffened plates used commonly in ship structures. However, these works neglect the effect of out-of-plane shear deformations and the fact that the process of homogenization needed to create the ESL element omits any local deformations occurring within the unit cell; that is only the change of different physical quantities at unit cell edges are considered. Thus, the theory is limited to slender structures, which do not have significant shear deformations and to cases where local stresses between the stiffeners are not significant. In Refs. [10-13] the theory has been extended to cover one-side stiffened plates and also other structural configurations such as hollow steel sandwich panels where the out-of-plane shear deformations are significant. In addition, the problem of local stress calculation has been solved giving a possibility to use the same element for global and local strength analysis of ship structures. The interaction between the ESL element and offset beams has been discussed in Refs. [13, 20] and the use of the element in global strength

analysis in Refs. [13, 21]; see Fig. 2. These works show that the same element can be used very accurately to predict stresses and deformations of the ship structure. The vibration analysis of ship structures has been increasing its importance during last few decades due to comfort requirements. In Refs. [13, 22-24] free and forced vibrations have been investigated at local and global scales. These works show that the ESL technique works well for the vibration assessment. The buckling and post-buckling strength of the structure needs to be checked as well in structural analysis. In Ref. [25] the bifurcation buckling of sandwich panels using the ESL has been shown to lead to very good accuracy. In Ref. [26] the post-buckling region, have been shown to be predicted very accurately as well.

This process explained above applies to any structural design at concept design stage. Thus, the process can be easily automatized making it very attractive approach for structural design and optimization [27]. This paper present the structural design framework based on the ESL and reviews it through examples given in open literature. In the end a short summary of the future developments is given.

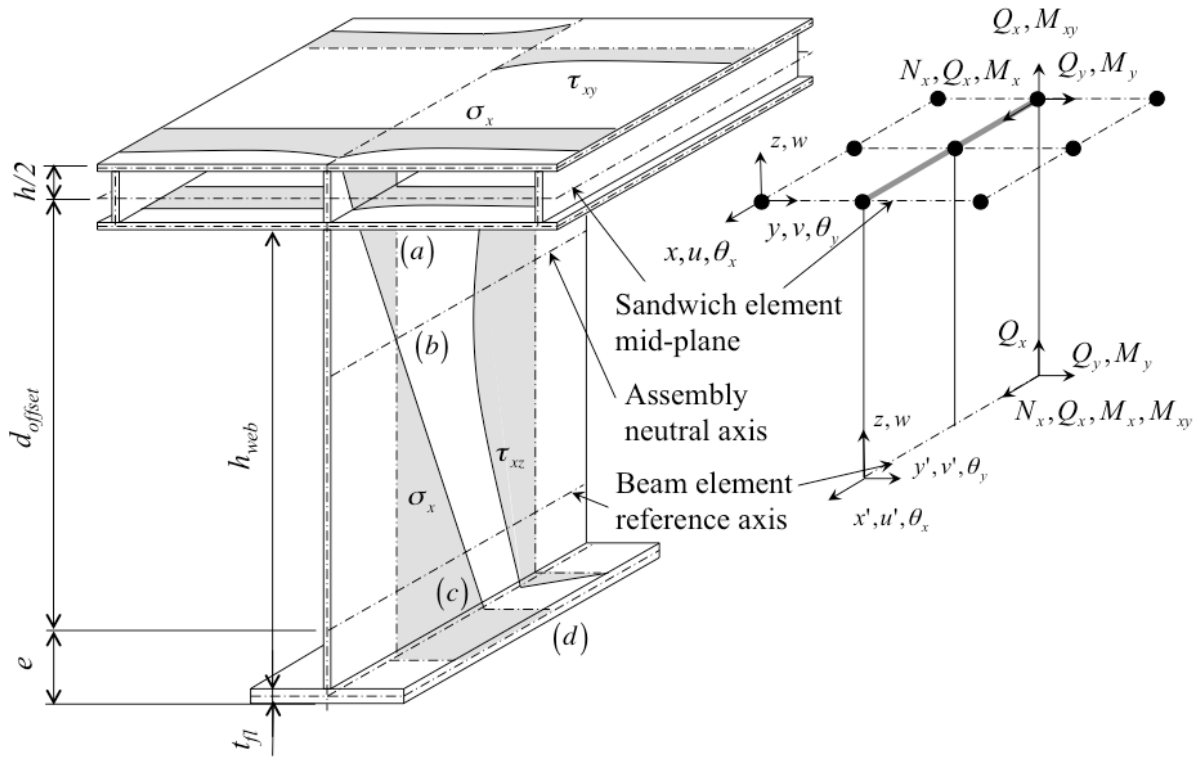


Figure 2: Equivalent shell element with offset beam.

2 THEORY

2.1 Equivalent Single Layer Theory for Plates

The basic idea is that the actual 3D structure is described mathematically using only shell elements, which do not have physical thickness; see [11-13, 16-18]. Similarly the girders are modeled using offset beams. The kinematics of the plate and beam elements is presented in Fig. 2. The linear relation between stress resultants and strains and curvatures is based on first

order shear deformation theory and is given as [16]:

$$\begin{Bmatrix} \{N\} \\ \{M\} \\ \{Q\} \end{Bmatrix} = \begin{bmatrix} [A] & [B] & [0] \\ [B] & [D] & [0] \\ [0] & [0] & [D_Q] \end{bmatrix} \begin{Bmatrix} \{\varepsilon_0\} \\ \{\kappa\} \\ \{\gamma\} \end{Bmatrix}. \tag{1}$$

where N, M, and Q are the normal force, moment and shear force of the cross-section. A is the extension, B is the coupling, D bending and D_Q the shear stiffness; the calculation of these is given for stiffened plates in Ref. [13, 19] and various sandwich panels in Refs. [10-12, 19]. Eq. (1) can be easily extended to include non-linear von Karman strains; e.g. [16], which enables the post-buckling analysis of plates.

2.2 Use of Offset beams

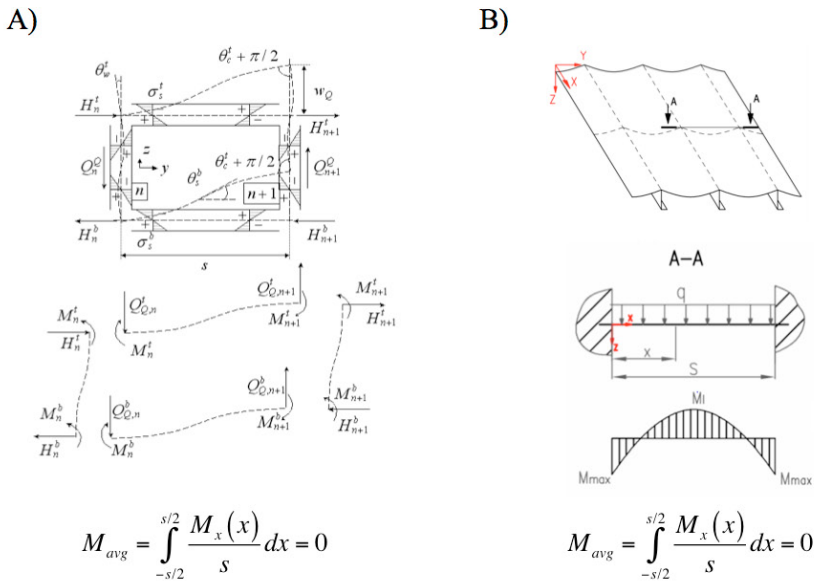
For beams Eq. (1) simplify to the first terms only since extension and bending happen only in x-direction. The beam element reference axis does not coincide in general with the neutral axis of the beam, so beam element offset is defined through

$$\begin{Bmatrix} du_0/dx^* \\ d^2w^*/dx^2 \end{Bmatrix} = \begin{bmatrix} 1 & d_{offset} \\ 0 & 1 \end{bmatrix} \begin{Bmatrix} du_0/dx \\ d^2w/dx^2 \end{Bmatrix} = [T] \begin{Bmatrix} du_0/dx \\ d^2w/dx^2 \end{Bmatrix}, \tag{2}$$

which alters also the beam bending stiffness matrix by $[ABD^*]=[T]^T[ABD][T]$; for details see Ref. [20].

2.3 Calculation of the Periodic Response

The homogenization assumes that the length of unit cell is infinitely small in comparison to the characteristic length of the structure or deformation, e.g. $s/B \to 0$. This means that the differential equations inside the unit cell contain only the incremental change of each physical quantity at the unit cell border, but within it. In practice this means that the response is averaged over the unit cell and averaging any odd function over unit cell lead to zero average; see Ref. [10]. This means that for example, the shear-induced secondary normal stress in the unit cell disappears due to homogenization; see Figure 3. In practice, the ratio s/B has finite value, so the error introduced by this homogenization process might become significant in terms of assessing the response. The same averaging process applies to local pressure loads. Both of these effect can be corrected by considering local unit cell response and reconsidering the periodic response after the homogenized solution has been obtained.



$$M_{avg} = \int_{-s/2}^{s/2} \frac{M_x(x)}{s} dx = 0 \qquad M_{avg} = \int_{-s/2}^{s/2} \frac{M_x(x)}{s} dx = 0$$

Figure 3: Calculation of the A) shear-induced secondary response [10] and B) response due to local loads; uniform pressure load [13].

3 EXAMPLES

3.1 Static Response

The static response is demonstrated by two examples given in Refs. [10, 13]. The first case demonstrates how homogenization without reconsideration of the periodic response leads to serious underestimation of stresses; see Figure 4A. In this case the unit cell to breadth ratio is *s/B*=8 and the influence of shear induced secondary oscillating stress dominates the total stress response. It is evident that reconsideration of the periodic response after homogenized solution has been obtained, leads to very accurate stress estimation. In Fig. 4B the approach is demonstrated for the deck plate given in Fig. 1. Again very good correspondence between 3D FEM and the ESL approach is obtained.

3.3 Bifurcation and Post Buckling

The bifurcation and post buckling of a panel is demonstrated with web-core sandwich panel, which is loaded in the stiffener direction; see Fig. 5. It is seen that the response is captured with very good accuracy until the point local buckling happens, which the ESL approach cannot capture.

3.2 Vibration Response

The vibration response is demonstrated by example of the deck plate given in Fig. 1 [13]. Fig. 6 shows the comparison of the eigenmodes and corresponding frequencies obtained by the ESL and 3D-FEM. It can be seen that the global modes involving mainly panel deformation modes are captured with good accuracy, while some deviations are seen for the higher modes where the plate between the stiffeners starts to vibrate.

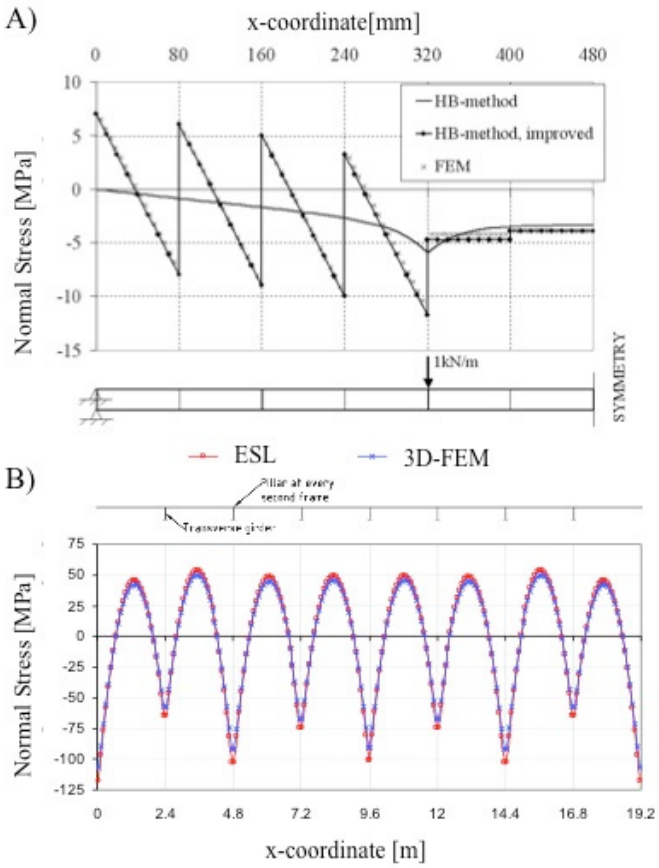


Figure 4: Comparison of the periodic normal stresses by ESL and 3D-FEM. A) web-core sandwich beam in four-point-bending (t=4mm, h=28mm, s=80mm, stress at top face plate) and B) deck plate from Fig. 1 (stress at stiffener flange at y=2.72 m).

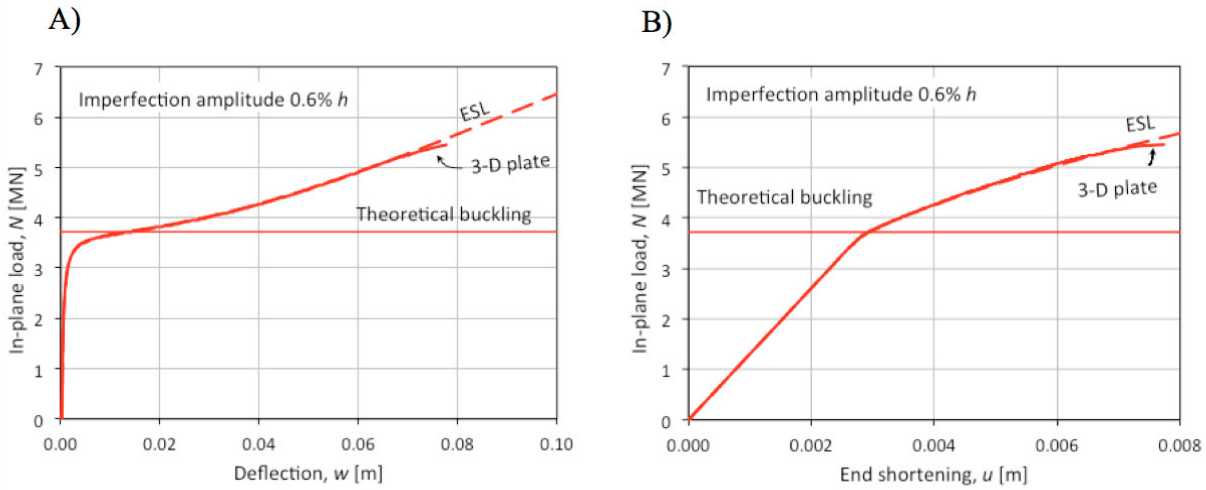


Figure 5: Comparison of the A) load-deflection and B) load-end-shortening by ESL and 3D-FEM [26].

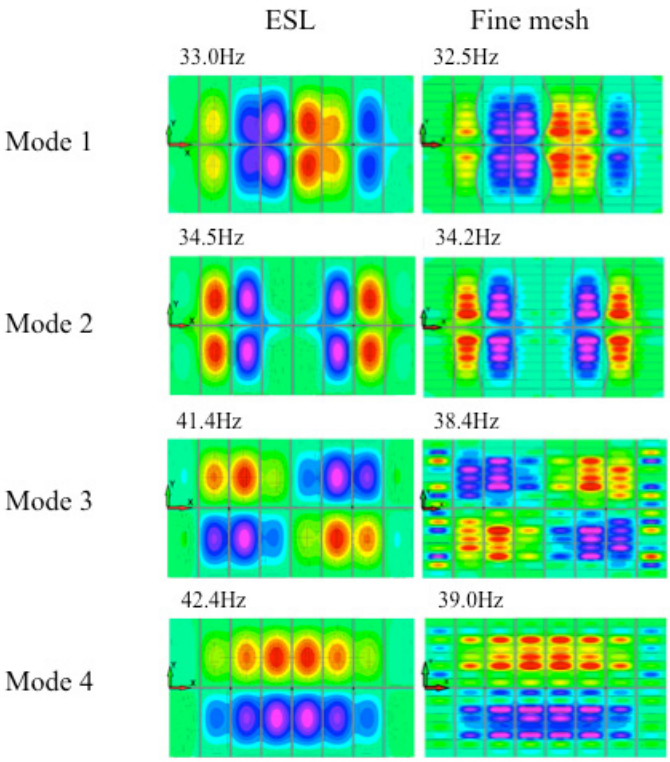


Figure 6: Comparison of the eigenmodes and frequencies by ESL and 3D-FEM (deck plate from Fig. 1).

4 CONCLUSIONS AND FUTURE WORK

The present paper reviewed the recent developments on the use of equivalent single layer (ESL) theory and offset beams in strength assessment of ship hull girder. Using the approach both the traditional one-side stiffened plates and more advanced plates such as composite laminates and sandwich structures can be presented using the same FE-mesh. This gives benefits for the structural design, since the mesh for large complex structure need to be created only once. Thus, the technique is suitable especially to conceptual design stage where the general arrangement might change, affecting the mesh, and for each design alternative the FE-analysis needs to be carried out to find the optimum structural and material configuration. As the structural assessment is carried out many limit states need to be assessed, i.e. static response to check the nominal stress levels in the structure, vibratory response to obtain the eigen frequencies and bifurcation and post buckling analysis to check the capacity of the structure.

The static response has been developed to the stage where the stress and displacement prediction can be carried out with good confidence at conceptual design stage. The essential issue is to realize that the often used mathematical assumption of unit cell size being very small in comparison to the characteristic length of deformation, $s/B=0$, does not hold for realistic ship structures. Due to this, secondary effects such as shear-induced normal stress become significant. In order to correct this, periodic response needs to be considered in the

post-processing of the results of the homogenized solution. The same effect can be seen when vibratory response, buckling and ultimate strength is assessed. In case of vibrations the homogenized ESL solution starts to deviate from the 3D-FE solution when local modes become active. Analogously to the static case, correcting this is seen to be straightforward. In buckling and post-buckling assessment the deviation between ESL and 3D-FEM is also seen when local modes start to occur. In ultimate strength assessment the stiffness, i.e. *ABD*- and D_Q-matrix, of the ESL plate need to be modified in increments as the load increases and local buckling occurs. In Refs. [28-29] these modifications are presented using analytical formulae for stiffened plate. Using the same ideas, the extension to the ultimate strength assessment, that includes local buckling, is seen to be straightforward as well. However, these items are left for future work.

REFERENCES

[1] ISSC, *Committee II.1 – Quasi-Static Response*, Proceedings of the 13th International Ship and Offshore Structure Congress, 18-22 August 1997, Trondheim, Norway, Editors Moan, T. and Berge, S., Pergamon (1998), **1**:158-165.

[2] ISSC, *Committee II.1 – Quasi-Static Response*, Proceedings of the 18th International Ship and Offshore Structures Congress, 10-13 September 2012, Rostock, Germany, Editors, Fricke, W. and Bronsart, R., (2012), **1**:151-212.

[3] Hughes O.; Mistree, F; Zanic, V. 1980. A practical method for the rational design of ship structures. *Journal of Ship Research*, **24/2**:101–13.

[4] Andric, J. and Zanic, V., The Global Structural Response Model for Multi-Deck Ships in Concept Design Stage, *Ocean Engineering*, (2010), **37**:688-704.

[5] Cook RD, Malkus DS, Plesha ME., *The concepts and applications of finite element analysis: 3rd edition*, John Wiley & Sons, (1989).

[6] Mobasher Amini, A., Dureisseix, D., Cartraud, P. and Buannic, N., A domain decomposition method for problems with structural heterogeneities on the interface: Application to a passenger ship, *Computer Methods in Applied Mechanics and Engineering*, (2009) **198**: 3452-3463.

[7] Ehlers, S., A Procedure to Optimize Ship Side Structures for Crashworthiness, *Journal of Engineering for the Maritime Environment*, 2010, **224**:1-11.

[8] Jang, B.S., Suh, Y.S., Kim, E.K. and Lee, T.H., Automatic FE modeller using stiffener-based mesh generation algorithm for ship structural analysis, *Marine Structures* (2008) **21**:294-325.

[9] Hughes, O. F., *Ship Structural Design: A Rationally-Based, Computer-Aided, Optimization Approach*, John Wiley & Sons, Inc., (1983).

[10] Romanoff, J., Varsta, P. and Klanac, A., Stress Analysis of Homogenized Web-Core Sandwich Beams, *Composite Structures*, (2007), **79**:411-422.

[11] Romanoff, J. and Varsta, P., Bending response of web-core sandwich plates, *Composite Structures*, (2007), **81**: 292–302.

[12] Romanoff, J., Varsta, P. And Remes, H., Laser-Welded Web-Core Sandwich Plates under Patch-Loading, *Marine Structures*, (2007), **20**:25–48.

[13] Avi, E., Niemelä, A., Lillemäe, I. and Romanoff, J., Equivalent shell element for ship structural design, *Proceedings of the 4th International Conference on Marine*

Structures, March 25th – 27th 2013, Helsinki, Finland.
[14] Det Norske Veritas (DNV), *Rules for Classification of Steel Ships*, (1991).
[15] DNV Classification notes No. 21.8: *Direct Strength Analysis of Hull Structures in Passenger*, Ships, (2007).
[16] Reddy, J.N., *Mechanics of Laminated Composite Plates and Shells; 2nd Edition*, CRC Press, (2004).
[17] Carrera E., Historical review of zig-zag theories for multilayered plates and shells, *Applied Mechanics Reviews,* (2003), **56/3**:287–308.
[18] Carrera E.A., Unified formulation to assess theories of multilayered plates for various bending problems, *Composite Structures*, (2005), **69**:271–93.
[19] Buannic N., Cartraud P. and Quesnel T., Homogenization of corrugated core sandwich panels, *Composite Structures,* (2003), **59**:299–312.
[20] Romanoff, J., Interaction between laser-welded web-core sandwich plate and girder under bending loads, *Thin-Walled Structures*, (2011), **49**:772-781.
[21] Romanoff, J., Naar, H. and Varsta, P., Interaction between Web-core Sandwich Deck and Hull Girder of Passenger Ship, *Journal Marine Systems & Ocean Technology*, (2011), **6/1**:39-45.
[22] Lok, T.S., and Cheng, Q.H., Free vibration of clamped orthotropic sandwich panel, *Journal of Sound and Vibration* (2000) **229**:311-327.
[23] Lok, T.S., and Cheng, Q.H., Free and forced vibration of simply supported, of orthotropic sandwich panel, *Computers and Structures* (2001) **79**:301-312.
[24] Lok, T.S., and Cheng, Q.H., Bending and forced vibration response of clamped orthotropic thick plate and sandwich panel, *Journal of Sound and Vibration* (2001), **245**:63-78.
[25] Jelovica , J., Romanoff, J., Ehlers, S. and Varsta, P., Influence of Weld Stiffness on the Buckling Strength of Laser-Welded Web-core Sandwich Plates, *Journal of Constructional Steel Research* (2012), **77**:12–18.
[26] Jelovica, J. and Romanoff, J., Load-carrying behaviour of web-core sandwich plates in compresssion, submitted to *Thin-Walled Structures* (2012).
[27] Romanoff, J. and Klanac, A., Design Optimization of Steel Sandwich Hoistable Car Decks Applying Homogenized Plate Theory, *Journal of Ship Production*, (2008), **24/2**:108-115.
[28] Byklum, E., Steen, E., and Amdahl, J., A semi-analytical model for global buckling and postbuckling analysis of stiffened panels, *Thin-Walled Structures*, (2004), **42/5**:701-717.
[29] Byklum, E. and Amdahl, J., A simplified method for elastic large deflection analysis of plates and stiffened panels due to local buckling, *Thin-Walled Structures*, (2002), **40/11**:925-953.

V International Conference on Computational Methods in Marine Engineering
MARINE 2013
B. Brinkmann and P. Wriggers (Eds)

A SEMI-ANALYTICAL MODEL FOR STRUCTURAL RESPONSE CALCULATIONS OF SUBSEA PIPELINES IN INTERACTING FREE SPANS

HÅVAR SOLLUND[*†] AND KNUT VEDELD[†]

[*†]Mechanics Division,
Department of Mathematics, University of Oslo,
Moltke Moes vei 35, Pb. 1053 Blindern,
0316 Oslo, Norway
E-mail: haavaras@math.uio.no - Web page: http: // www.math.uio.no

Key words: Modal analysis, Rayleigh-Ritz, Pipeline, Free span, Multi-span

1 INTRODUCTION

Pipeline free spans may be caused by uneven seabed, by surrounding subsea infrastructure such as pipeline crossings or by erosion processes like seabed scouring. On the seabed, the pipeline is subject to wave and current loading, and in free spans the surrounding flow may give rise to vortex shedding. The vortex shedding generates oscillations in the drag and lift forces acting on the pipe [1]. If the frequencies of the force oscillations are close to one of the eigenfrequencies of the free spanning pipeline, the pipeline may experience large-amplitude vibrations. Such vibrations are termed vortex-induced vibrations (VIV), and fatigue failure due to VIV in free spans is a major risk factor for offshore pipelines [2,3]. Moreover, the natural frequency of a free span decreases quickly with increasing span length, making long spans more prone to VIV-induced fatigue damage. Since the cost of seabed intervention in order to reduce span lengths is high, modern design codes, like Det Norske Veritas' recommended practice provisions, DNV-RP-F105 “Free Spanning Pipelines” [4], allow for the occurrence of VIV as long as the accumulated fatigue damage is accounted for.

It is essential for reliable free span design to estimate eigenfrequencies and associated modal stresses with a high degree of accuracy. For multi-span configurations and complicated single-span configurations, the structural analyses are normally performed by means of detailed non-linear finite element analysis (FEA). However, such analyses are time-consuming, and since the number of free spans along a pipeline route may be substantial, fast and reliable methods for identifying critical span configurations are attractive for the pipeline engineering community. A simplified method for calculation of eigenfrequencies and associated stresses was therefore presented by Fyrileiv and Mørk in 2002 [3], and later included in DNV-RP-F105. The method developed by Fyrileiv and Mørk has a limited range of application with regard to span length and static deflection into the span [3,5]. Furthermore, the simplified method can only be applied on single-span scenarios. A semi-analytical method for static and dynamic free span analyses was recently developed by Sollund and Vedeld [5]. The semi-analytical method has no practical limitations on span length and mid-span deflections, while still being ~600 times faster than FEA for typical span configurations [5].

The present paper describes an extension of the semi-analytical method, making the

method applicable for multi-span configurations. With regard to computational time, the multi-span model operates equally fast as the single-span model, thereby addressing the need in the pipeline industry for a screening tool for interacting free spans, and making the method highly suitable for implementation in engineering software programs.

2 PROBLEM DEFINITION

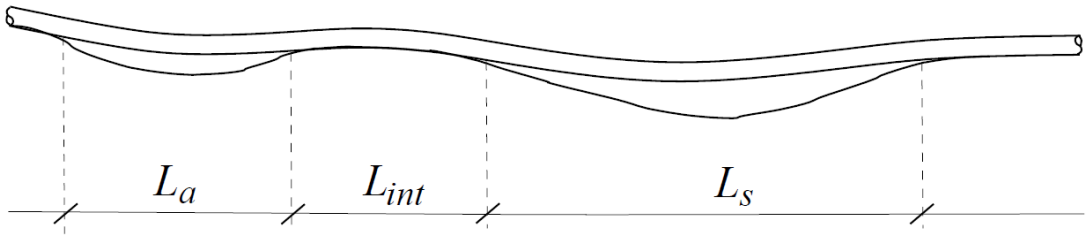


Figure 1: Multi-span scenario of a pipeline, indicating free span length L_s, adjacent span length L_a and intermediate shoulder length L_{int}.

Figure 1 displays a free span scenario with two adjacent spans. In the figure, the main span length is L_s, the adjacent span length is L_a and the shoulder length in-between the span is L_{int}, which in the following will be termed the intermediate shoulder length. The combined length $L_{sa} = L_a + L_{int} + L_s$ will be called the span area length. The regions where the pipe touches down on the seabed on either side of the span area are labeled span shoulders.

In DNV-RP-F105 [4], some guidance is given on how to determine whether free spans are influenced by other neighboring free spans or not. The guidance for span classification consists of a single set of curves (with each curve representing a particular soil type) separating between interacting and isolated spans, and these curves are replotted in Figure 2.

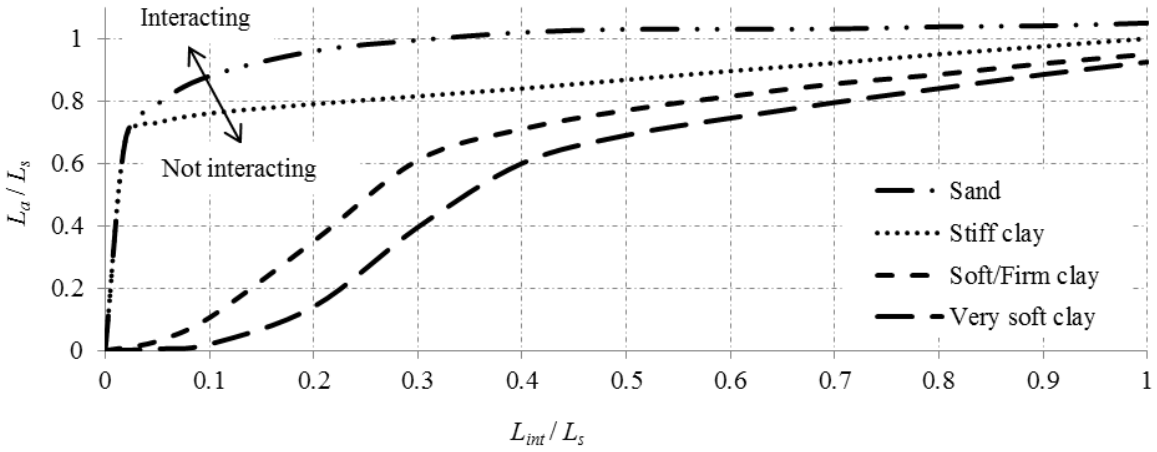


Figure 2: Span interaction curves, as defined in DNV-RP-F105 [4].

For a given free span length with a specified intermediate shoulder length, the curves in Figure 2 indicate that there is a limit adjacent span length for which longer adjacent spans result in interaction between the two spans, and shorter adjacent spans result in no interaction

between the two spans. A main objective in the following text is to evaluate the curves and assess whether the dimensionless parameter representation in Figure 2 is sufficient for a classification of interacting and isolated spans.

Traditionally, indication of directions in VIV analyses is defined based on the direction of flow rather than the axis of the excited cylinder. Hence, in the following the horizontal direction will be termed in-line and the vertical direction will be termed cross-flow.

The geometry and boundary conditions of the model are idealized as shown in Figure 3. The shoulders are considered to be horizontal and straight, and the pipeline ends are assumed to be simply supported, allowing no axial or transversal displacements. This assumption is physically motivated, either by span shoulders that are sufficiently long to provide approximate axial fixity as a result of axial pipe-soil friction, or that other effects from the seabed induces axial fixation (such as neighboring spans, rock dumps, pipe crossings, etc.).

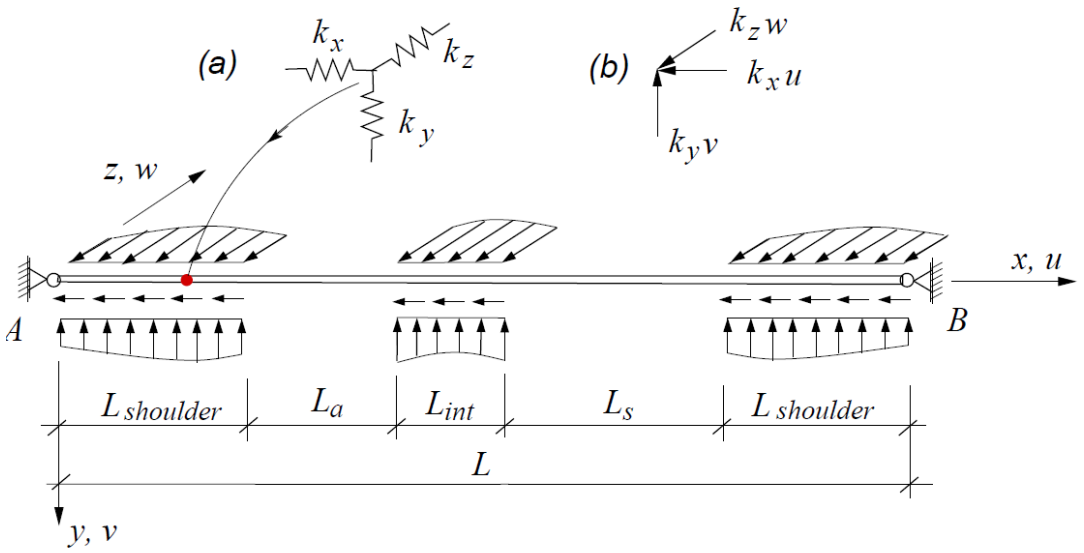


Figure 3: Definition of pipeline model and Cartesian coordinate system. (a) Static and dynamic soil springs are applied axially, laterally and vertically at the span shoulders. (b) Directions of spring forces.

The modeled pipe has a dry mass including mass of fluid content per unit length m_d and a submerged weight q. For dynamic response calculations, one also has to include the effect of the added mass m_a due to acceleration of the surrounding water. The effective mass m_e, given by the sum of m_d and m_a, is taken as an input parameter to the dynamic response calculations. The pipe-soil interaction will be modeled according to the recommendations in DNV-RP-F105 [4], distinguishing between stiffness coefficients for vertical static, vertical dynamic, lateral dynamic, axial static and axial dynamic displacements. The static and dynamic soil stiffnesses are termed K_{VS}, K_V, K_L, K_{AXS} and K_{AX}, respectively. In the numerical computation, the shoulder lengths are taken as three times the length of the span area L_{sa}. The axial friction is ignored when determining the deflected geometry due to the static loading, but dynamic axial soil stiffness is included in the modal analyses. However, the semi-analytical model presented below is equally applicable for other choices of span shoulder lengths and axial

friction behavior. The effective axial force concept [6] will be applied for calculation of geometric stiffness effects.

In the semi-analytical method presented in the next section, three solutions to the problem defined by Figure 3 will be required:

1. A solution for the static equilibrium case, where the pipe is subject to its submerged weight q and effective axial force S_{eff}.
2. A solution to determine the eigenfrequencies and associated mode shapes for the linearized harmonic eigenvalue problem in the in-line direction subject to pipe effective mass m_e and effective axial force S_{eff}.
3. A solution, dependent on the static vertical configuration, to determine eigen-frequencies and mode shapes for the linearized harmonic eigenvalue problem in the cross-flow direction, accounting for the stiffening effect of the vertical static displacement, effective mass m_e and effective axial force S_{eff}.

3 THE SEMI-ANALYTICAL METHOD

To include the effects of the static vertical deflections of the model defined in Figure 3 a curvilinear coordinate system is chosen. The coordinate system is defined in Figure 4, where $\mathbf{e}_n$ is the direction normal to the pipe axis and $\mathbf{e}_s$ is the direction tangential to the pipe axis. Unlike the x,y-coordinate system, the $\mathbf{e}_s$,$\mathbf{e}_n$-system is not fixed in space, but will rotate along the pipe length ensuring that the $\mathbf{e}_s$ direction is always tangential to the pipe axis. The curvilinear coordinate (or arc length coordinate) s denotes the position along the pipe length. The coordinate directed from the pipe centroidal axis towards the outer circumference is denoted n. Depending upon the analysis type, this direction will either be in the horizontal plane (in-line analyses) or the vertical plane (cross-flow analyses). At each position s the displacement in tangential direction is u_s while the displacement in normal direction is u_n. The radius of curvature $R(s)$ will vary along the pipe length.

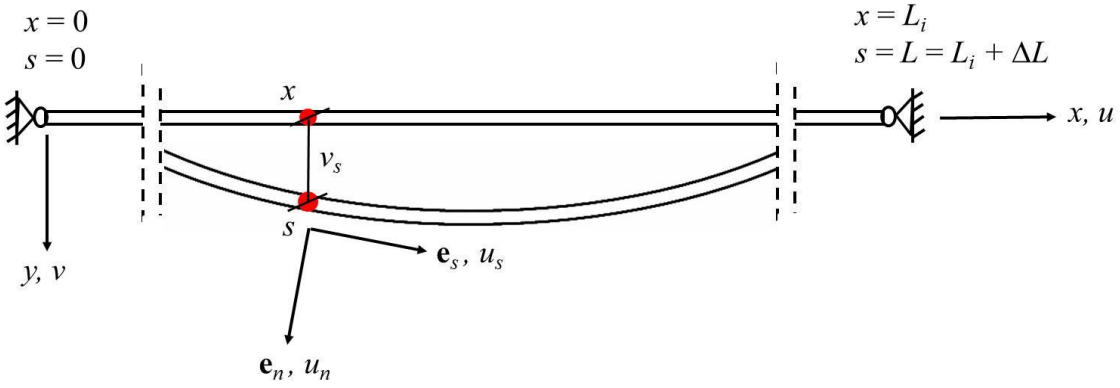


Figure 4: Curvilinear coordinate system with unit vectors $\mathbf{e}_s$ in the tangential direction and $\mathbf{e}_n$ in the normal direction. The static deflection v_s and the Cartesian coordinate system oriented along the undeformed pipe axis are also shown.

Consistent with the Euler-Bernoulli beam theory, the only non-zero component of the strain tensor is ε_{ss}. The following expression, as derived by Sollund and Vedeld [5], applies:

$$\varepsilon_{ss} = \frac{1}{1-\kappa n}\left(\frac{\partial u_s}{\partial s} - \kappa u_n\right) = \frac{1}{1-\kappa n}\left[\frac{\partial u_0}{\partial s} - \kappa v_0 - n\frac{\partial}{\partial s}\left(\frac{\partial v_0}{\partial s} + \kappa u_0\right)\right] \tag{1}$$

The displacements u_0 and v_0 of a point on the pipe centroidal axis are the unknown displacements for which we must solve. The boundary conditions require that u_0 and v_0 must be zero at positions $s = 0$ and $s = L$. Note that for the static analysis and the in-line modal analysis, this corresponds to the positions $x = 0$ and $x = L_i$, where L_i is the initial pipe length before deflection into the span. Thus, the following Fourier sine approximation can be applied for u_0 and v_0

$$\left.\begin{aligned} u_0(s,t) &= \sum_{i=1}^{\infty} D_{u,i}\sin\left(\frac{i\pi s}{L}\right)\sin(\omega t) = \mathbf{N}_u\mathbf{D}_u\sin(\omega t) \\ v_0(s,t) &= \sum_{i=1}^{\infty} D_{v,i}\sin\left(\frac{i\pi s}{L}\right)\sin(\omega t) = \mathbf{N}_v\mathbf{D}_v\sin(\omega t) \end{aligned}\right\} \Rightarrow \mathbf{u} = \begin{bmatrix} \mathbf{N}_u & \mathbf{0} \\ \mathbf{0} & \mathbf{N}_v \end{bmatrix}\begin{bmatrix} \mathbf{D}_u \\ \mathbf{D}_v \end{bmatrix} = \mathbf{ND} \tag{2}$$

Based on the strain expression in Eq. (1), a differential operator may be defined as

$$\mathbf{d} = \begin{bmatrix} d_{u_0} & d_{v_0} \end{bmatrix} = \frac{1}{1-\kappa(s)n}\left[\frac{\partial}{\partial s} - n\frac{\partial}{\partial s}\kappa(s) \quad -\kappa(s) - n\frac{\partial^2}{\partial s^2}\right] \tag{3}$$

The static analysis may thus be performed by solving

$$\mathbf{KD} = \mathbf{R} \tag{4}$$

where the stiffness matrix is obtained from

$$\mathbf{K} = \mathbf{K}_{struc} + \mathbf{K}_g + \mathbf{K}_{soil} \tag{5}$$

and $\mathbf{K}_{struc}$, $\mathbf{K}_g$ and $\mathbf{K}_{soil}$ denotes the structural stiffness matrix, the geometric stiffness matrix and the soil stiffness matrix, respectively.

The structural stiffness matrix is given by

$$\mathbf{K}_{struc} = E\int_V (\mathbf{dN})^T(\mathbf{dN})dV \tag{6}$$

The geometric stiffness matrix is dependent on the effective axial force S_{eff} and is obtained in the usual manner [5,7]. In the single-span model previously presented by Sollund and Vedeld [5], a non-linear static analysis which included the build-up of tension in the pipe due to pipe lengthening, was incorporated. However, it is often convenient to determine the distribution of effective axial forces in a global analysis, and taking the relevant value of effective axial force as an input to the local model of the span area. Therefore, the effective axial force has been kept constant during the static analysis in the present study.

The soil stiffness matrix can be found by

$$\mathbf{K}_{soil} = \int_0^L \begin{bmatrix} k_{soil,A}\mathbf{N}_u^T\mathbf{N}_u & \mathbf{0} \\ \mathbf{0} & k_{soil}\mathbf{N}_v^T\mathbf{N}_v \end{bmatrix} ds \tag{7}$$

where the axial soil stiffness $k_{soil,A}$ is replaced by K_{AXS} or K_{AX}, and the transverse soil stiffness k_{soil} is replaced by K_{VS}, K_V, or K_L depending on the analysis type (cross-flow/in-line, static/dynamic). The soil stiffnesses are set to zero in the spans L_a and L_s.

The load vector **R** is given by

$$\mathbf{R} = \int_0^L \mathbf{N}^T \begin{bmatrix} \mathbf{0} \\ q\mathbf{1} \end{bmatrix} ds \tag{8}$$

where **1** is a vector with unit value in all its entries.

The eigenfrequencies and mode shapes are obtained from the static configuration by solving the equations for free vibration of the pipe

$$\mathbf{M}\ddot{\mathbf{D}} + \mathbf{K}\mathbf{D} = \mathbf{0} \quad \Rightarrow \quad \left(\mathbf{K} - \omega^2 \mathbf{M}\right)\mathbf{D} = \mathbf{0} \tag{9}$$

where **M** is the mass matrix and the eigenvalues ω are the natural circular frequencies of the pipe. An attractive feature of the Fourier sine expansions applied for expressing the displacements, Eq. (2), is that the mass matrix **M** is diagonal.

4 FINITE ELEMENT ANALYSES

The commercially available finite element solution software ABAQUS [8] was used for finite element (FE) analyses. The FE analyses were performed in order to provide benchmarks for evaluation of the semi-analytical multi-span model. The beam element PIPE31 was used for the FE modeling of the pipe. This is a first order shear deformable linear beam element. Linear springs were used to model the soil stiffness. The model was generated according to Figure 3, with vertical, lateral and axial springs at each node. Shoulder lengths and span lengths were set to be equally long in the finite element and corresponding semi-analytical models. The effective axial force was kept constant during the static analysis, by introducing a roller support on the right side of the model. The axial displacement due to the introduction of the roller support was negligible (~0.1 pipe diameter compared to a total model length of ~1000 pipe diameters) and did not affect the outcome of the analysis.

The recommendation for maximum element lengths in DNV-RP-F105 [4] is one outer pipeline diameter, i.e., the ratio of the element length to the outer pipeline diameter should be less than 1. Based on convergence studies, an element length equal to 10% of the outer pipe diameter was chosen throughout in the analyses, ensuring highly accurate estimates of modal frequencies and associated stresses.

5 RESULTS AND DISCUSSION

5.1 Validation of the semi-analytical method

Detailed FE analyses, as described in the preceding section, were performed in order to assess the accuracy of the semi-analytical multi-span model. Three different pipe cross-sections were applied for the comparisons. The three configurations are described by the parameters listed in Table 1. Pipe 1 is a small-diameter (4-inch internal diameter), thick-walled oil pipeline with steel diameter-to-thickness (D_s/t_s) ratio as small as 7.4, without external coating. The second pipe cross-section has a 9-inch internal diameter, a D_s/t_s ratio of

19.8 and a 50-mm thermal insulation coating. The final pipe configuration is a large-diameter gas pipeline with D_s/t_s equal to 35.8 and a 60-mm concrete coating. The effective masses of the pipes range from 80 kg/m to more than 1300 kg/m. Thus, the three cases span a wide diameter and mass range, as seen from Table 1.

Table 1: Input parameters for pipe cross-sections.

Input parameter	Symbol	Unit	Pipe 1	Pipe 2	Pipe 3
Outer steel diameter	D_s	mm	140.7	254.3	720.2
Steel thickness	t_s	mm	19.1	12.85	20.1
Coating thickness	t_{coat}	mm	0	50	5.0
Concrete thickness	t_{conc}	mm	0	0	60
Density of steel	ρ_{steel}	kg/m^3	7850	7850	7850
Density of coating	ρ_{coat}	kg/m^3	-	793	1300
Density of concrete	ρ_{conc}	kg/m^3	-	-	2250
Density of content	ρ_{cont}	kg/m^3	821	821	150
Young's modulus	E	GPa	207	207	207
Submerged weight	q	N/m	471.71	459.75	1652.11
Effective mass	m_e	kg/m	80.02	249.37	1334.50

Six FE analyses were performed for each of the three pipe cross-sections. Each set of six analyses comprised two analyses on very soft clay, two analyses on stiff clay and two analyses on dense sand. Relevant values of soil stiffnesses were taken from DNV-RPF105 [4]. For each soil type, analyses were performed for two values of relative intermediate shoulder length L_{int}/L_s (see Figure 1 for definitions). The first of these intermediate shoulder lengths would represent a very short shoulder with L_{int}/L_s of either 0.1 or 0.2, while a longer intermediate shoulder would be applied for the second analysis, covering L_{int}/L_s values from 0.3 to 0.8. Based on Figure 2 and on preliminary analyses with the semi-analytical method, the value of the relative adjacent span length L_a/L_s was always adjusted in such a manner that interaction in the first mode would occur, either in the in-line direction or in the cross-flow direction or both. This resulted in a variation of L_a/L_s from 0.6 to 0.9. The results of the semi-analytical multi-span model coincided with the results of the semi-analytical single-span model when the spans were not interacting. Hence, smaller values of L_a/L_s were not of interest for the present study, since the accuracy of the single-span model has been evaluated previously [5]. The 18 validation cases also covered relative span lengths L_s/D_s of the dominant span ranging from 60 to 160.

The results of the validation study are displayed in Figure 5. The figure shows the ratios of the fundamental frequencies predicted by the semi-analytical method to the corresponding frequencies obtained by FEA, as well as the ratios of predicted modal stresses to modal stresses from FEA. Results are shown for both the in-line and the cross-flow direction. It is seen that the accuracies of frequency calculations are within 3-4% for the in-line direction and within ±1% for the cross-flow direction. The accuracy of the modal stress results is within ±5% as compared to the FE results. The results reveal that there is a small, but consistent stiff bias in the in-line direction, i.e., the frequencies and stresses are slightly overestimated

compared to the results obtained by FEA. The stiff bias appears to be most pronounced for cases with a short intermediate shoulder length L_{int}/L_s and a short relative length of the dominant span L_s/D_s. A similar consistent, but less pronounced, stiff bias in in-line direction could be observed for short relative span lengths in the assessment of the single-span model [5]. However, in an engineering context, the semi-analytical method performs excellently and well within the accuracy that was deemed acceptable for the approximate response calculation method previously presented by Fyrileiv and Mørk [3], and later incorporated in DNV-RP-F105 [4]. In fact, also the method developed by Fyrileiv and Mørk exhibited a stiff bias for short spans, and it is likely that this bias is caused by shear deformations which have been included in the FE modeling, but ignored in the semi-analytical method as well as in the method by Fyrileiv and Mørk [3,5].

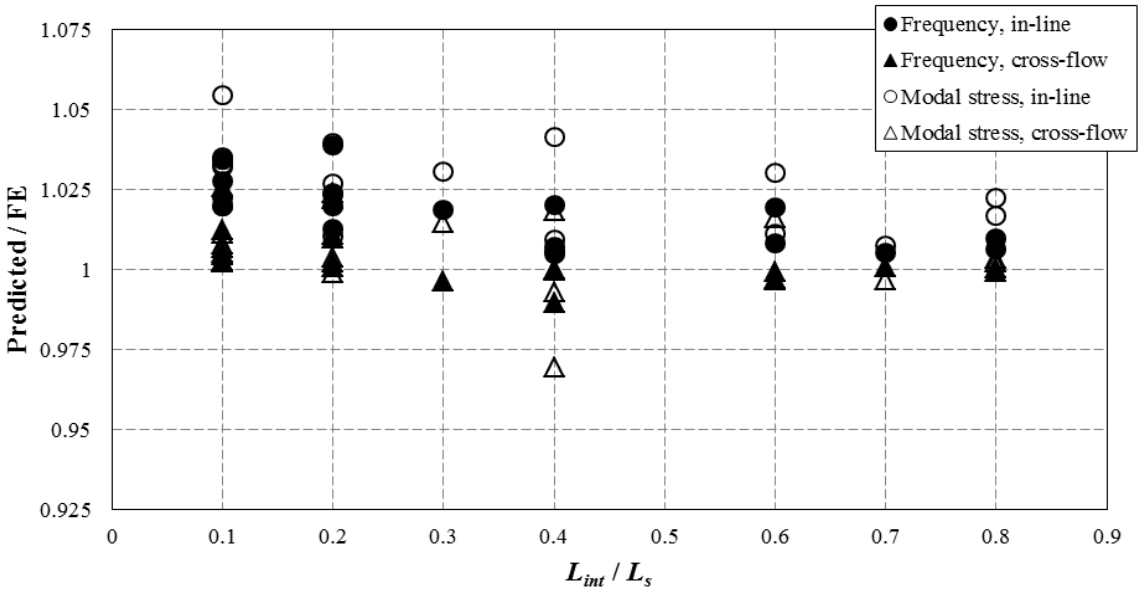


Figure 5: Ratios of predicted fundamental frequencies and associated stresses to FE results for both the in-line and the cross-flow direction.

5.2 Assessment of multi-span classification curves

Prior to determining whether two neighboring free spans interact or not, a criterion for interaction has to be established. A reasonable engineering approach is to classify two spans as interacting if the presence of an adjacent span influences the frequency or modal stress of the main span above a certain limit. The limit should be aligned with the accuracy of dynamic response calculations using FE analysis or approximate calculation methods, like the semi-analytical method or the single-span method outlined in DNV-RP-F105. Minor inaccuracies will then be covered by the calibrated safety factors (e.g., 1.1 on natural frequencies and 1.3 on modal stresses for well-defined spans subject to normal safety requirements [4]) in leading design codes such as DNV-RP-F105 [4]. Based on this reasoning the following definition has been proposed and applied for the present study:

Two free spans are interacting if the presence of an adjacent span changes the fundamental frequency, either in-line or cross-flow, of the main span by more than 5% or the

associated first-mode dynamic stress of the main span by more than 10%.

While the introduction of an adjacent span may be regarded as a softening of the main-span shoulder, and consequently, will result in a consistent drop in the natural frequencies, the effect on the modal stresses is less certain and more dependent on local geometry and possibly on intermediate shoulder lengths. The 10% limit on modal stresses in the definition above will account for such variation in stresses.

Based on the proposed span interaction definition, classification curves like illustrated in Figure 2 were determined with the semi-analytical method for the three pipe configurations described in Table 1. Four different soil types were applied; very soft clay, stiff clay, loose sand and dense sand, respectively. For each combination of pipe and soil type, classification curves were established for ten values of relative length L_s/D_s of the main span, ranging from 30 to 160. Each individual classification curve was constructed from 15 classification points, i.e., 15 values of required adjacent span length L_a/L_s, each corresponding to a given intermediate shoulder length L_{int}/L_s. The algorithm for identifying the classification points is illustrated by the flow chart shown in Figure 6. As displayed in Figure 6, the accuracy by which the classification points are obtained is controlled by the tolerance T. For the purpose of the present study, T was set to $0.005 \cdot L_s$. Large numbers of analyses are necessary in order to establish the classification curves with such high precision. However, due to its computational efficiency, the semi-analytical method is highly suited for this type of large-scale parameter studies.

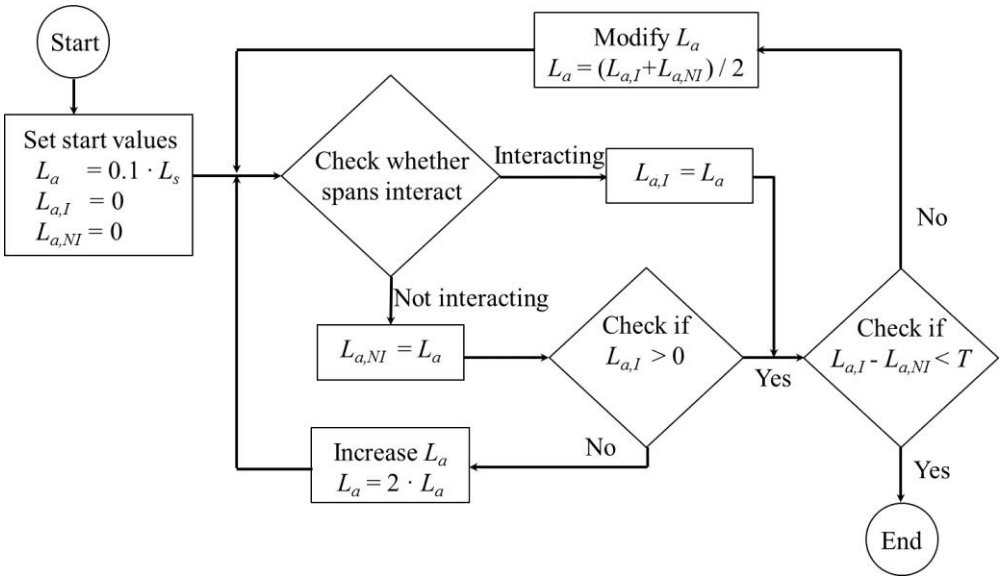


Figure 6: Algorithm for determining the length of the adjacent span L_a that is required for span interaction.

The results obtained for pipe 1 (see Table 1) on dense sand are displayed in Figure 7. Results are shown for all the selected values of L_s/D_s. It is observed that the classification points follow the curve from DNV-RP-F105 for L_{int}/L_s above 0.4. For intermediate shoulder lengths above this limit the spans behave as isolated spans independently of the length of the adjacent span. For values of L_a/L_s slightly larger than one, the adjacent span will be longer than the main span, and soon have a fundamental frequency that is 5% smaller than the main

span frequency. Hence, the interaction criterion will be fulfilled. The fact that the obtained classification points coincides with the RP-curve in this region indicates that the definition of interacting spans applied in the present study is well aligned with the approach previously applied for establishing the classification curves in [4]. For values of L_{int}/L_s below 0.4, the calculated classification points are scattered around the RP-curve, thereby clearly demonstrating that onset of span interaction will depend on the length of the main span. Interestingly, the results for the shortest (denoted L1) and the longest (denoted L10) main spans in the study are both well below the RP-curve, that is, on the "isolated span" side of the curve. However, while the required adjacent span length for interaction increases smoothly for the shortest main span length, the required value of L_a/L_s for the longest main span stabilizes around 0.8 and then experiences an abrupt jump when L_{int}/L_s reaches the threshold value of 0.4. This behavior, with an L_a/L_s plateau followed by an abrupt change to values of L_a/L_s above one for a threshold intermediate shoulder length, was observed many times in this study and was most pronounced for large values of the main span length. The results for loose sand (not shown) resembled the results for dense sand, but the threshold value of L_{int}/L_s increased to ~0.6 for the longest main span.

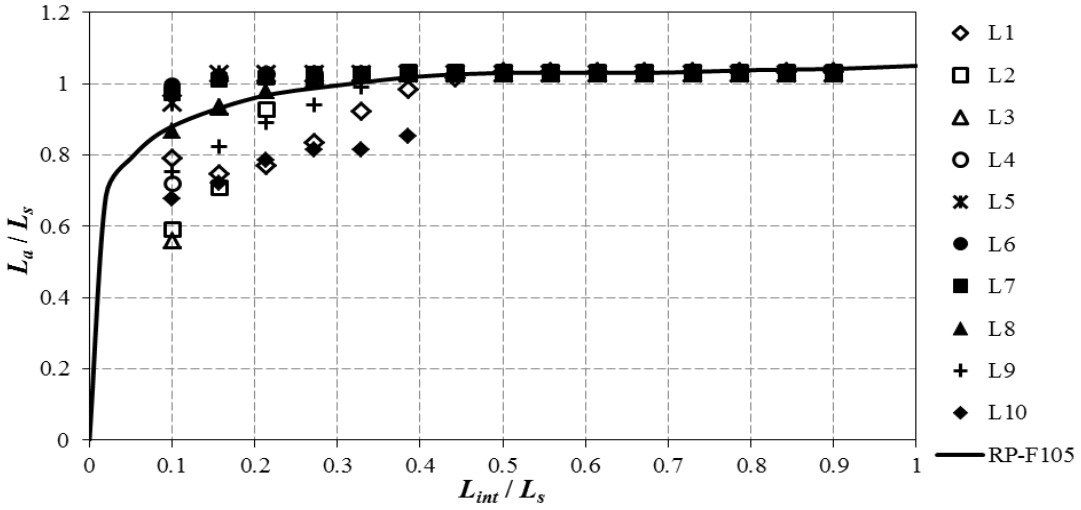


Figure 7: Multi-span classification points for pipe 1 on dense sand. Results are shown for 10 values of relative main span length L_s/D_s ranging from 30 to 160, where L1 corresponds to 30 and L10 to 160.

Figure 8 shows the results obtained for the large-diameter gas pipeline, pipe 3, on very soft clay. This time the scatter around the RP-curve is significant, and it is clearly demonstrated by the amount of scatter in Figure 8, that a dimensionless parameter representation based only on the quantities L_{int}/L_s and L_a/L_s will not be able to accurately predict whether two neighboring free spans interact. It should be noted, however, that Figure 8 exhibits the worst visual fit to the RP-curve of the cases investigated in this study. For pipe 1 and 2 on very soft clay (results not shown) only the results for the two longest main spans fell below the RP-curve, and the results for the shortest main spans followed the slope of the RP-curve quite closely for small intermediate shoulder lengths. Thus, it appears that the RP-curve may have been established as a lower bound for L_a/L_s based on results generated for shorter main span lengths than L_s/D_s equal to ~130 (corresponding to L8 in Figure 8). In fact, L_s/D_s equal to 130 is the upper limit

of the application range for the approximate response calculation method in DNV-RP-F105, and it may have been implicitly assumed that FE analyses are required for all spans exceeding this limit. However, no validity range is explicitly stated for the multi-span interaction curves. On the other hand, the RP does emphasize that the curves are provided for indicative purposes only, and are meant to be used in lieu of detailed data, thereby recognizing the inherent limitations in the validity of the curves.

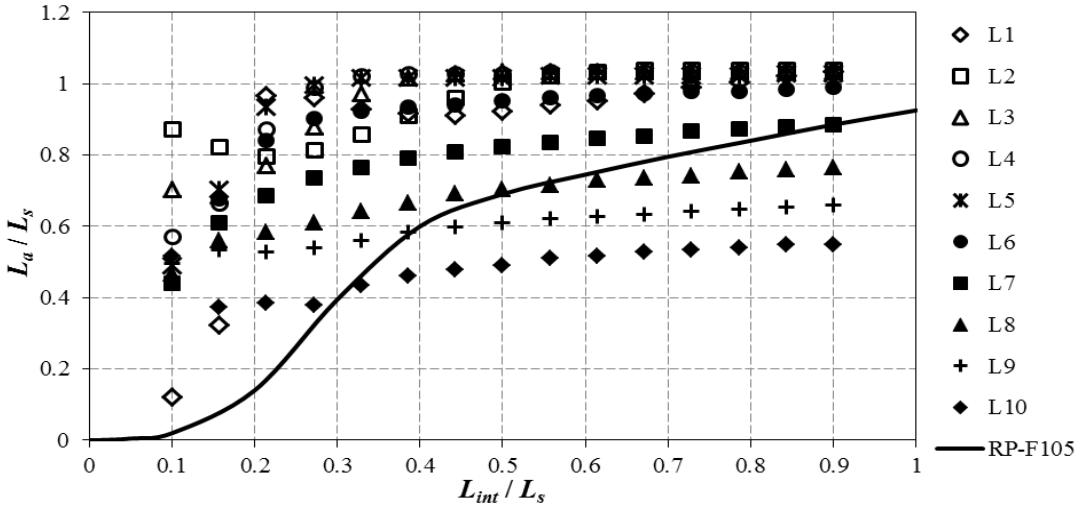


Figure 8: Multi-span classification points for pipe 3 on very soft clay. Results are shown for 10 values of relative main span length L_s/D_s ranging from 30 to 160, where L1 corresponds to 30 and L10 to 160.

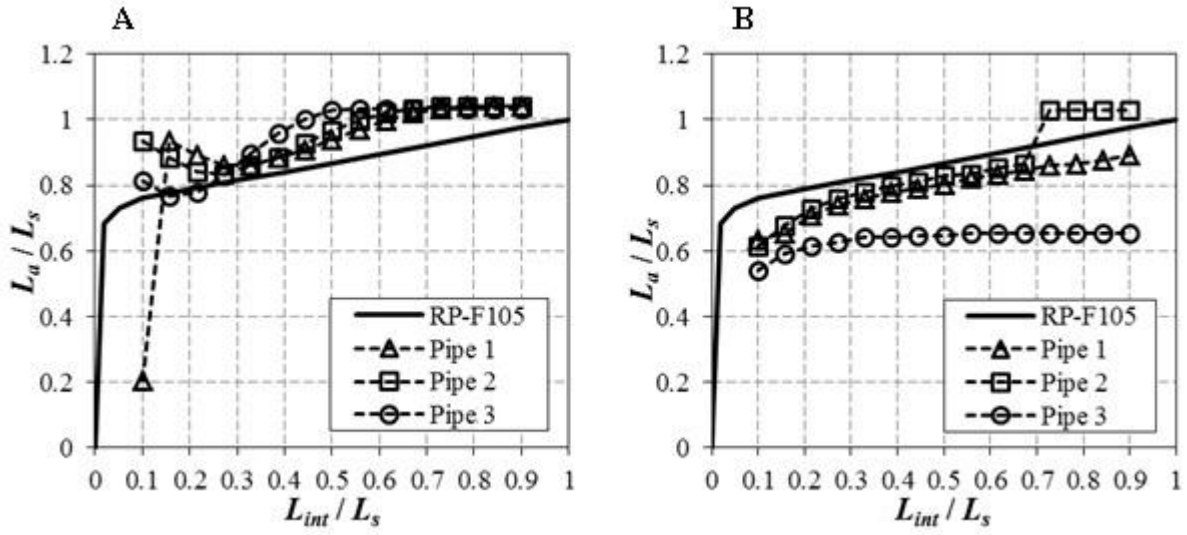


Figure 9: Multi-span classification curves for the three selected pipe configurations on stiff clay. Panel A shows results for L_s/D_s = 30. Panel B shows results for L_s/D_s = 160.

In Figure 9 above, results are compared for the three different pipe cross-sections on stiff clay. Panel A displays the results for a relative main span length of 30, while panel B displays the results for a relative main span length of 160. All the curves in Figure 9, with the

exception of the curve for pipe 3 in panel B, follow the RP-curve quite closely. However, as seen previously, the curves for the shortest main span length lie above the RP-curve, i.e., on the "interacting spans" side, while the curves for the longest main span length fall below the RP-curve. The classification point for pipe 1 at L_{int}/L_s equal to 0.1 in panel A, may appear as an outlier, but this behavior was not untypical for the shortest main span length. Indeed a similar trend is seen for the shortest main span series in Figure 8, but it is obscured by the large amount of data points in that plot. Based on Figure 9, one may conclude that also the characteristics of the pipe cross-section, such as diameter and specific gravity, will influence whether two neighboring free spans interact for a given intermediate shoulder length.

6 CONCLUSIONS

- A semi-analytical method for the dynamics analysis of pipelines with interacting multi-spans has been developed, and comparisons have been made with FE analyses.
- The semi-analytical method is accurate to within 5% deviation for calculation of fundamental frequencies and associated modal stresses compared to detailed FE analyses.
- The curves given in DNV-RP-F105 [4] for classification of free spans into isolated and interacting spans have been evaluated by performing several thousand analyses with the semi-analytical method.
- It has been shown that span interaction is a complex issue which depends on more parameters than the relative length of the adjacent span and the relative length of the intermediate span shoulder. A strong dependence on the relative length of the main span has been demonstrated, as well as a dependence on the characteristics of the pipe cross-section.

REFERENCES

[1] Sumer, B.M. and Fredsøe, J. *Hydrodynamics around cylindrical structures*. Adv. Series on Ocean Eng., Vol. 12, World Scientific, (2006)

[2] Fyrileiv, O., Mørk, K. and Chezhian, M. Experiences using DNV-RP-F105 in assessment of free spanning pipelines. *Proc. of 24th Int. Conf. on Offshore Mechanics and Arctic Engineering, OMAE 2005*, Halkidiki, Greece, June 12-17 (2005)

[3] Fyrileiv, O. and Mørk, K. Structural response of pipeline free spans based on beam theory. *Proc. of 21st Int. Conf. on Offshore Mechanics and Arctic Engineering, OMAE 2002*. Oslo, Norway, June 23-28 (2002)

[4] DNV-RP-F105. *Free Spanning Pipelines*. Det Norske Veritas, Norway (2006)

[5] Sollund, H. and Vedeld, K. A semi-analytical model for free vibrations of free spanning offshore pipelines. *Research Report in Mechanics, No. 12-2, Mechanics Division, Department of Mathematics, University of Oslo, Norway* (2012)

[6] Fyrileiv, O. and Collberg, L. Influence of pressure in pipeline design – effective axial force. *Proc. of 24th Int. Conf. on Offshore Mechanics and Arctic Engineering, OMAE 2005*, Halkidiki, Greece, June 12-17 (2005)

[7] Cook, R.D., Malkus, D.S, Plesha, M. E. and Witt, R. J. *Concepts and applications of finite element analysis*. Wiley, 4th ed., (2002)

[8] ABAQUS, v. 6.12, Dassault Systèmes Simulia Corp., Providence, RI, USA (2012)

V International Conference on Computational Methods in Marine Engineering
MARINE 2013
B. Brinkmann and P. Wriggers (Eds)

STRUCTURAL DESIN OF A BULBOUS BOW WITH REGARD TO COLLISION SAFETY

I. Tautz*, M. Schöttelndreyer*, J. Gauerke*, E. Lehmann* and W. Fricke*

* Hamburg University of Technology (TUHH)
Schwarzenbergstrasse 95c, 21073 Hamburg, Germany
e-mail: tautz@tuhh.de, web page: http://www.tuhh.de/skf

Key words: Structural Design, Crashworthiness, Ship Collision, Bulbous Bow, Buffer Bow

Abstract. Dimensioning of bulbous bows is based on conservative and usually empirically developed Classification Rules. Furthermore their structural design is subordinate to manufacturing aspects. Thus bulbous bow structures are mostly overdimensioned and could be regarded as rigid in case of a ship collision. Weakening bulbous bows stiffness results in noticeable influence on absorbable collision energies. Anyhow this approach is limited because usual operating loads like hydrostatic pressure or slamming loads are still to be considered. The paper describes a design approach for bulbous bows that aims at the best compromise between preferably weak regarding collision load on the one hand and preferably stiff under operating load on the other hand. Linear and nonlinear FEM-calculations based on ultimate load theory are combined in order to estimate stability of weakened designs. Examinations are accompanied by nonlinear explicit FEM-calculation of a ship collision scenario taking into account stiffness of striking and struck ship.

1 INTRODUCTION

In the overwhelming majority of cases, ship-ship collisions lead to damages that are more severe at the struck than at the striking ship. At worst this leads to the loss of the struck ship with all well-known hazards for crew, passengers and environment. Compared to that damage at the striking ship is of minor relevance or even negligible. This issue leads to considerations regarding alternative design of bow structures comparable to the development of crumple zones in automotive industry.

A first proposal was made by Cheung [1]. He introduced a so-called soft bow design of a forecastle structure being stiffened with systems of tubes arranged in parallel rows. Although he estimated energy absorption of his design with quite rough assumptions, he described the essential principle of function already applicable. If the strength of the soft bow is less than the struck ship side strength, the soft bow will be crushed. In the contact area of the collision soft bow flattens to a certain extend. By that collision process will be less sharp and more kinetic energy can be absorbed until fracture of the side of the struck ship.

In order to gain detailed understanding of this principle, highly nonlinear problems like large deformation, contact, plasticity and failure have to be solved. Hence, extensive research on the field of soft bow design was carried out not before a high development status of the finite element method was reached. In this context two consecutive research projects are to be highlighted that have been carried out in Japan from 1991-2006. Results have been published

amongst others by Kitamura [3], Yamada [8] and Endo [2] with promising results. They describe a so-called buffer bow design for a bulbous bow which is transversally stiffened and optimized with special regard to minimized plate thicknesses and minimized inner supporting structure. Design of the buffer bow is in line with Classification Rules. Thus bow hooks in comparably close distance are mandatory in the bulb tip. That means reducing axial crushing resistance of the bulbous bow is limited especially in the area where first contact occurs. Thus flattening of the bulb tip is not improved. However this is one helpful effect to increase energy absorption capabilities of struck and striking ship as well. Detailed research regarding that issue was carried out by the authors since 2008 and published in [6] - [8].

This paper presents a procedure to find a structural design that leads to a flattening of the tip and that is acceptable for Classification Societies as well. The basic idea is to replace the conventional bulb tip by a kind of cap, fitted on a watertight tank boundary about one or two frame spaces aft of the bow tip. The scantlings of this unstiffened cap are proposed to be developed on basis of a comparison design study independent from existing rules. The cap may be regarded as an appendix to the ship hull not being relevant for the vessel's strength integrity. Anyhow, the strength reduction of the cap is limited because usual operating loads still have to be considered. Unfortunately Classification Rules do not provide explicit design loads on bulbous bows for direct calculations. Thus, in cooperation with Lloyd's Register (LR), four explicit load cases were proposed representing most important operational conditions. Additionally one collision load case was defined according to the rules of Germanischer Lloyd (GL). All load cases were applied to a conventional bulbous bow design of a ship new building that was approved by LR as a reference. In order to compare the results all calculations have been repeated using bulbous bow designs with a less strengthened cap as described above. Results have been evaluated by comparison of stresses and deformations to the reference structure.

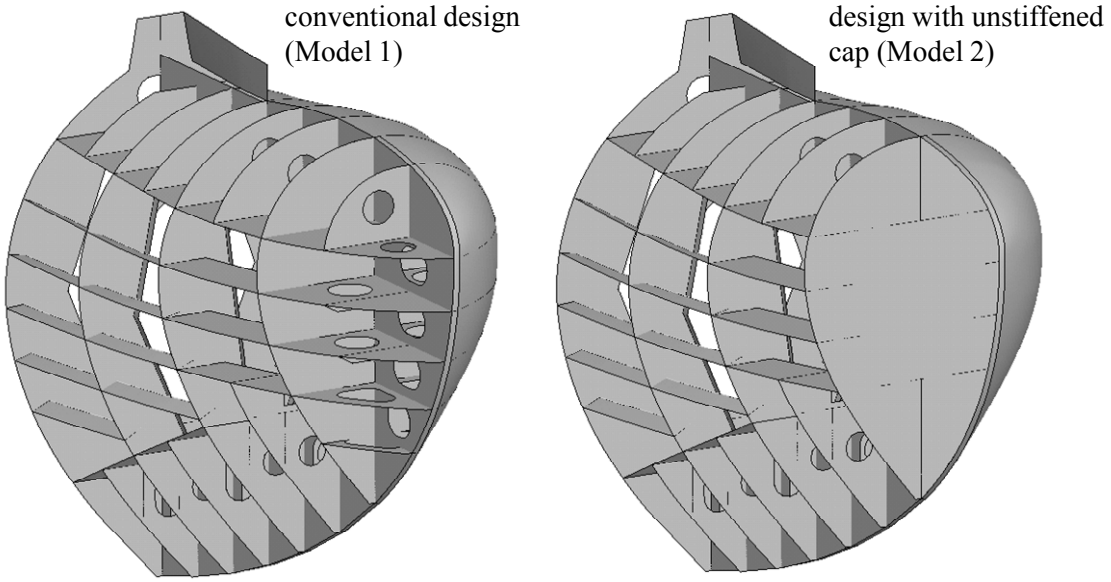


Figure 1: Investigated design variants, outer shell blanked on starboard side

2 COLLISION SIMULATION

In order to determine scantlings of the unstiffened cap, that lead to the desired flattening of the bulb tip, several collision simulations have been carried out for a rectangular, central impact. Struck and striking ship are identical, with same displacement and draught. These assumptions follow rules of GL in parts. Both vessels are modelled according to design drawings of ship class ConRo **2**0 built by Flensburger Schiffbau-Gesellschaft mbH, Germany.

Simulation model considers the bulbous bow of the striking ship and the double hull of the lower hold of the struck ship according to Fig. 2. Remaining ship mass of striking ship is assigned to all nodes at the aft boundary of the bulbous bow. These nodes are coupled for motion in x-direction, all other degrees of freedom have been fixed. An initial velocity of 5 m/s is given to all nodes of the bulbous bow. Model boundaries of the struck ship have been fixed in translational degrees of freedom as shown in Fig. 2. No rotations have been fixed. Model of the struck ship exhibits a web frame spacing of 2400 mm, five web frame spacings have been considered. Aft and fore end of the struck ship model are fixed in y-translational-degree of freedom. Penetration occurs in the middle of struck ship model. Calculations have been carried out with LS-DYNA, Version 971/ R6.1.0.

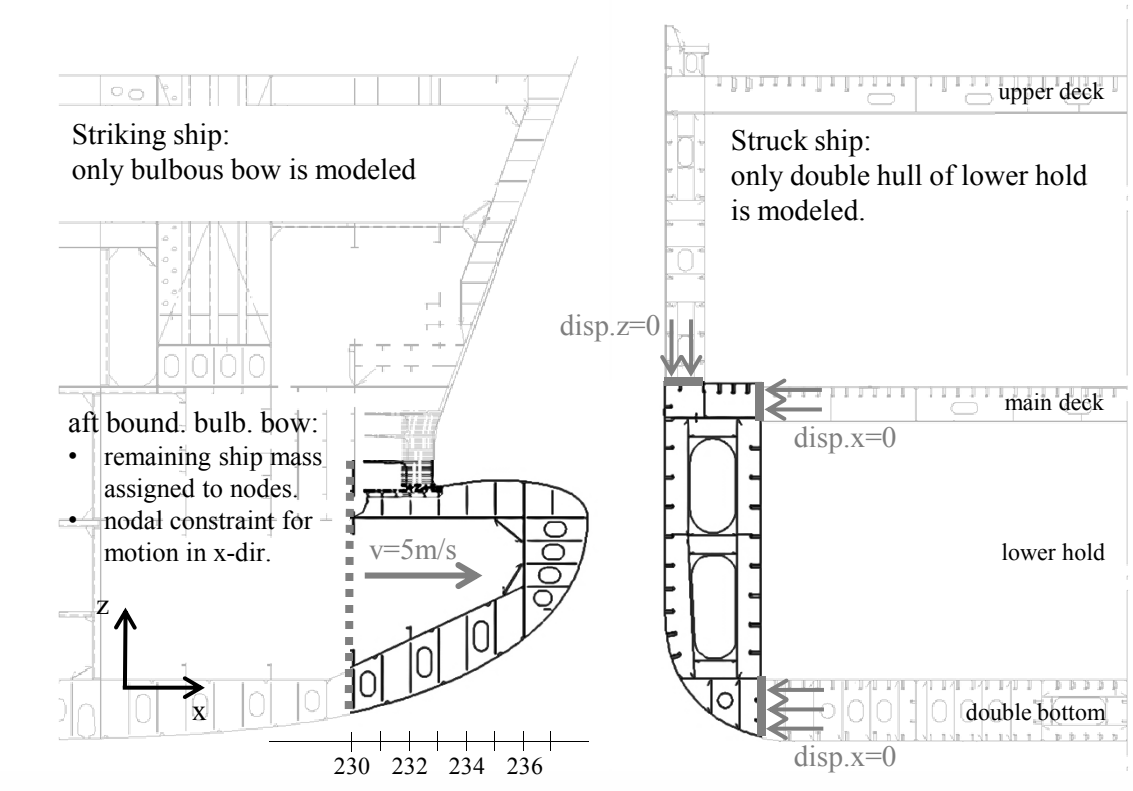


Figure 2: Collision scenario and model boundaries

For both vessels shell elements are used - four noded quadrilateral Belytschko-Lin-Tsay formulation with five integration points through their thickness. Reduced integration was used for most parts (Type 2) except the outer shell of the bulbous bow where fully integrated elements were used (Type 16). HP-profiles are represented as L-Profiles with appropriate

moment of inertia (struck ship) or as flat bars with added beam-elements for the bulb (striking ship). Mean shell element edge length is about 80 mm for the bulbous bow and 100 mm for the struck ship, aspect ratio is almost equal to unity. LS-DYNA contact type "automatic single surface" and "automatic surface to surface" is used. Nonlinear material behaviour is considered by LS-DYNA material type *MAT 123 (modified piecewise linear plasticity) with standard parameters for mild steel. A true stress strain relationship for mild steel, determined from tensile tests as described in [7], is used. Failure is represented with an equivalent plastic failure strain criteria being dependent from element edge length l and thickness t that was proposed by Peschmann [4] for shell elements with a thickness less than 12 mm as follows:

$$\varepsilon_f = 0.1 + 0.8\frac{t}{l} \tag{1}$$

And for shell elements with a thickness greater than 12 mm as follows:

$$\varepsilon_f = 0.08 + 0.65\frac{t}{l} \tag{2}$$

Failure is considered just for the struck ship. As experiments show [6], [8] failure is negligible for bulbous bow structures collapsing in progressive folding mode. Thus no failure criteria is applied for the striking ship model.

Calculations have been carried out with a striking ship consisting of model 1 and model 2 shown in Fig. 1. Model 2 was calculated with varying shell thickness. Results have been evaluated regarding the degree of deformation just before rupture of outer shell (Fig. 3).

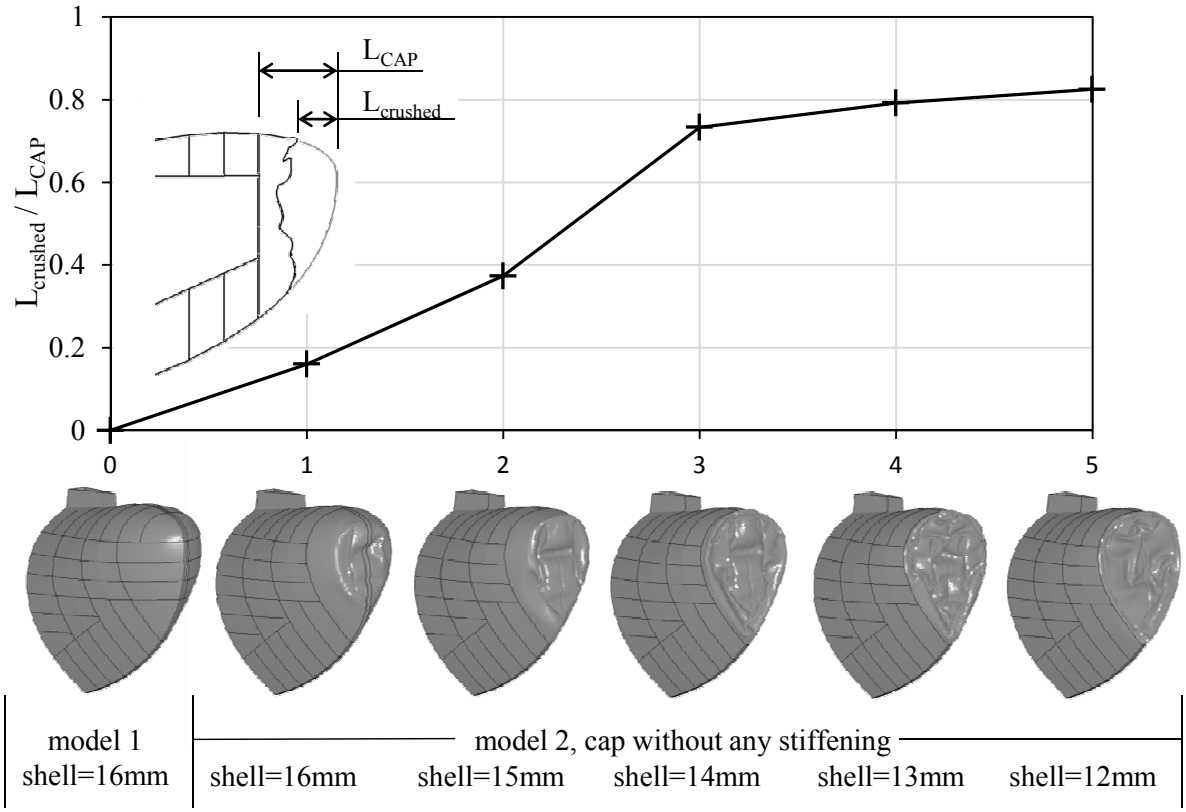


Figure 3: Degree of deformation just before rupture of outer shell for all calculated variants

As a result of the collision simulations it can be stated that the maximum crushed length $L_{crushed}$ is about 80% of the length of the unstiffened cap L_{CAP}. A design with unstiffened cap but with shell thickness equal to the conventional design leads to minor degree of deformation before rupture of outer shell. Although deformation will increase during subsequent collision process, further decrease of shell thickness was examined because this study aims the best possible flattening of the tip at a preferably early stage. A shell thickness of 14 mm seems to meet this target quite well and will therefore be taken for further investigations under operating loads.

3 PRESSURE LOADS (LC 1-3)

The design of a bulbous bow with unstiffened cap can be accepted from a structural point of view in general if it is added as an appendix to the ship hull. Integrity of the remaining bulbous bow can be provided by Classification Rules. In principle the cap could then be even left away although this is not a realistic option because of hydrodynamic requirements.

Although requirements of the cap can be formally detached from existing rules, its strength has to be evaluated in an adequate manner. Thus operating loads have been proposed in collaboration with Lloyd's Register as load cases for direct calculations. This chapter describes hydrostatic and hydrodynamic load assumptions.

Calculations have been carried out with ANSYS Mechanical APDL Release 14.0. Bulbous bow is discretized as described in Chapter 2. ANSYS Shell Element Type 63 is used (fully integrated, four nodes), bulbs of stiffeners are represented by Type 8 (truss). Linear elastic material behaviour with standard values for mild steel is used. Aft boundary of the bulbous bow is fixed in all degrees of freedom.

3.1 Hydrostatic Pressure (LC 1)

Bulbous bow is exposed to hydrostatic pressure dependent from draught and from a possible increase due to wave crest. According to rules of LR wave-crest-amplitude can be calculated based on the given rule length L=184,51 m as follows

$$C_w = 7{,}71 \cdot 10^{-2} \cdot L \cdot e^{-0{,}0044L} = 6{,}32m \tag{3}$$

Assuming the increase due to wave crest to be constant over the draught T, hydrostatic pressure for each shell element is calculated according to its vertical coordinate z as follows

$$p_{hs} = \rho \cdot g \cdot [(T - z) + C_w] \tag{4}$$

3.2 Slamming (LC 2)

Rules of Lloyd's Register provide a quite detailed description of bow flare wave impact pressure and wave impact pressure on other parts of the side shell plating close to and above the design waterline (Part 4, Chapter 2, Section 4.2.1). Definition is dependent on x- and z-position and angle of slope α_p, β_p and γ_p described in Fig. 4.

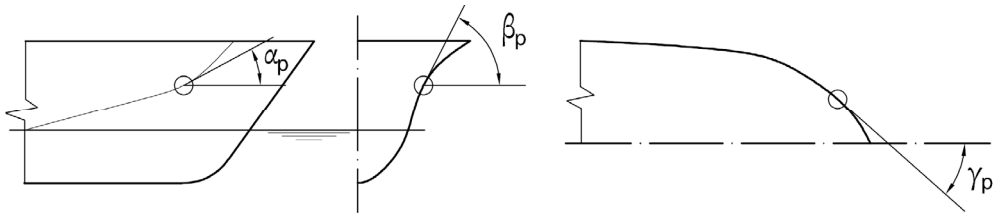


Figure 4: Notation for angle of slope α_p, β_p and γ_p

Based on the input of these geometric parameters slamming pressure can be determined as

$$P_{bf} = 0{,}5\left(K_{bf} \cdot V_{bf}^2 + K_{rv} \cdot H_{rv} \cdot V_{rv}^2\right) \tag{5}$$

where K_{bf} is a hull form shape coefficient for wave impacts (dependent from β_p), V_{bf} is the wave impact velocity (dependent from α_p, x- and z-position), K_{rv} is a hull form shape coefficient for impact due to forward speed (dependent from α_p), H_{rv} is a relative wave heading coefficient (dependent from γ_p) and V_{rv} is the relative forward speed (dependent from γ_p). Described dependencies from z-position find indirect expression by determining a probability of a wave impact. Z-position is measured from waterline and has direct influence only on this probability in a squared form. Thus it can be assumed, that formula (5) can also be applied for slamming loads affecting the bulbous bow, although it is underneath the waterline.

The described geometric parameters have been determined for each shell element of the outer shell and an element specific pressure was calculated according to formula (5). Figure 5 gives an impression of the resulting pressure distribution in comparison with the calculated hydrostatic pressure.

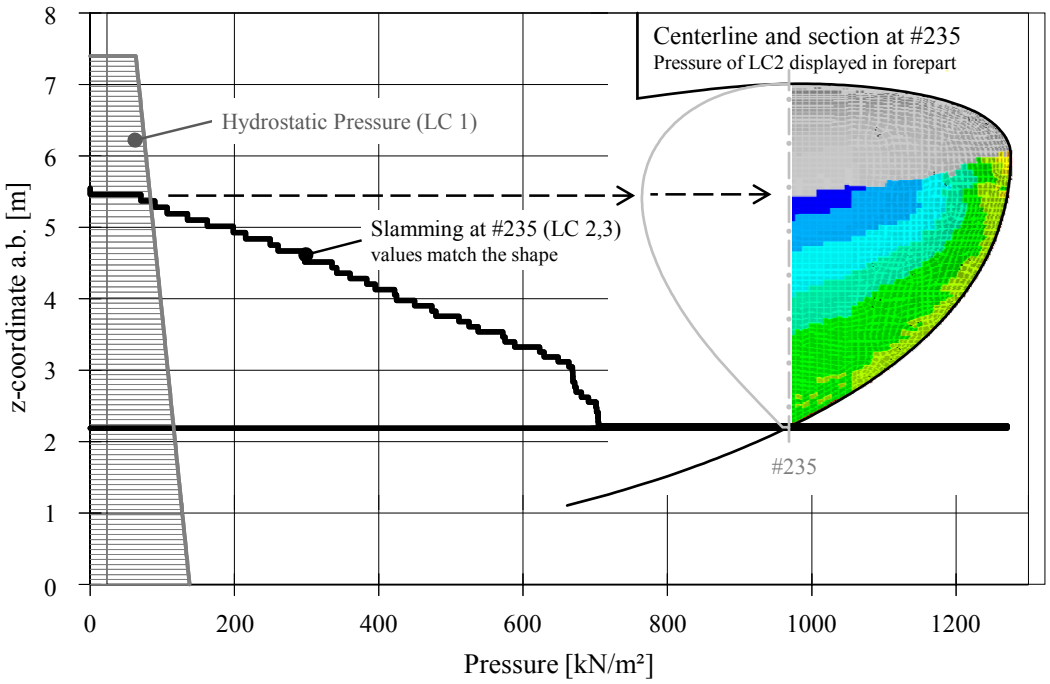


Figure 5: Pressure distribution for load cases 1-3, slamming displayed exemplarily at #235

3.3 Unilateral pressure (LC 3)

The bulbous bow can be exposed to unilateral pressure e.g. when rolling and/or pitching in heavy seas. That kind of condition is considered by applying LC 2 described in Chapter 3.2 unilaterally. Rules of GL (Part I, Section 9, A 5.3.3) propose a formula for a constant unilateral pressure which could be an alternative but is not investigated in this paper.

3.4 Results

In general results of model 2 (unstiffened cap) are evaluated focusing the relation to values of model 1 (conventional). In some extent evaluation of the differences is more meaningful than evaluation of absolute values.

Results have been plotted and evaluated for bottom, middle and top layer for all principal stresses separately for outer shell and inner stiffening system. Inner stiffening and global bending behaviour of the bulbous bow is not affected in a problematic manner by changes between model 1 and 2. Thus results are just displayed for a part of the model in front of #234. Stresses are shown according to LR's common practice without nodal average, integration point results have been transferred to nodes without any extrapolation. Main effects are discussed as follows according to results shown in Fig. 6.

For model 1 it can be seen that stress level in the bulb tip is quite low compared to panels located behind #236. Stress level in model 2 only increases in the lower part of the cap where curvature is less. In average it reaches values comparable to the panels behind #236. Regarding local maxima, values are higher. In the upper part, where curvature is high, stress increase is somehow surprisingly moderate or even negligible. This can be explained with regard to theory of curved shells.

Stress level for hydrostatic pressure is moderate. Slamming and unilateral pressure leads to somehow confusing high stresses for an elastic analysis. Hence model 1 is in line with rules, evaluation is still possible. However focus has to be limited to the relation between model 1 and 2.

By classifying described effects as local ones, permissible stresses according to Rules of LR are $\sigma_{perm} = 120$ N/mm² for bending stress and $\sigma_{perm} = 150$ N/mm² for equivalent stress. Detailed stress evaluation with regard to permissible stresses was carried out at positions shown in Fig. 7 for model 2. Equivalent positions behind #236 for model 1 have been used as an appropriate reference. Calculated stress is normalized with permissible stress.

For hydrostatic pressure (LC1) model 2 fulfils the requirements although significantly higher values can be observed compared to model 1. Results of LC2 and LC3 are just comparable when introducing a load-dependent scaling factor found to be $f_{scale} = 6.2$ for the permissible stress. This approach is only valid for comparison purpose of course. Nevertheless some statements regarding the evaluation of LC2 and LC3 are possible.

Stress increase at LC2 and LC3 comparing model 1 with model 2 is in the range of the increase at LC1. Thus – in some degree - it can be drawn the conclusion that LC2 and LC3 do not account for additional effects that could not be evaluated with LC1. This conclusion is only valid if/because the changes in design from model 1 to model 2 are limited to a comparably small area at the bulb tip. Even with this limitation it is not of general validity. LC2 and LC3 might lead to additional effects when analysing bulbous bows of significantly differing shape.

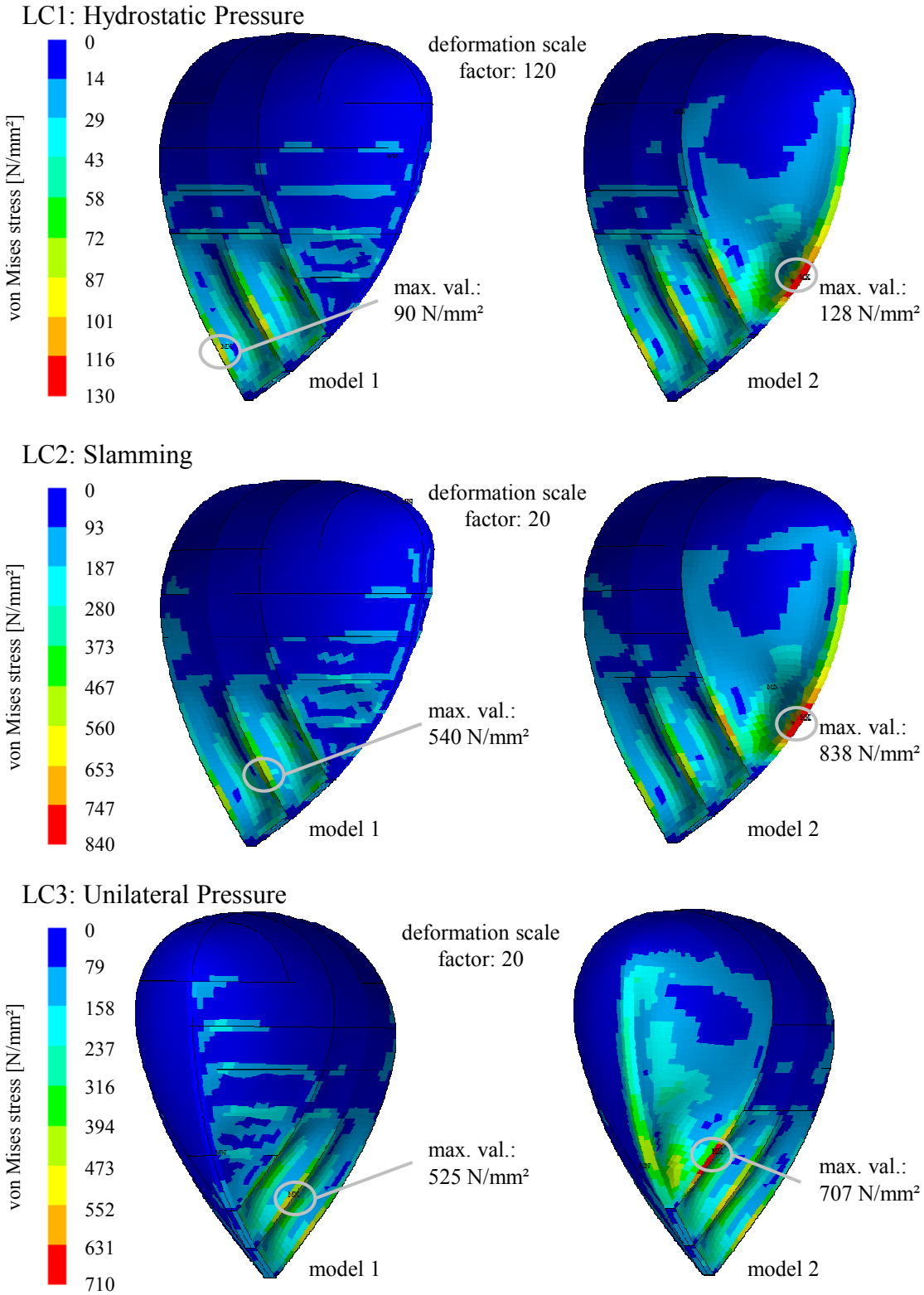


Figure 6: Stress contours for calculated variants and models, displayed in front of #234 only

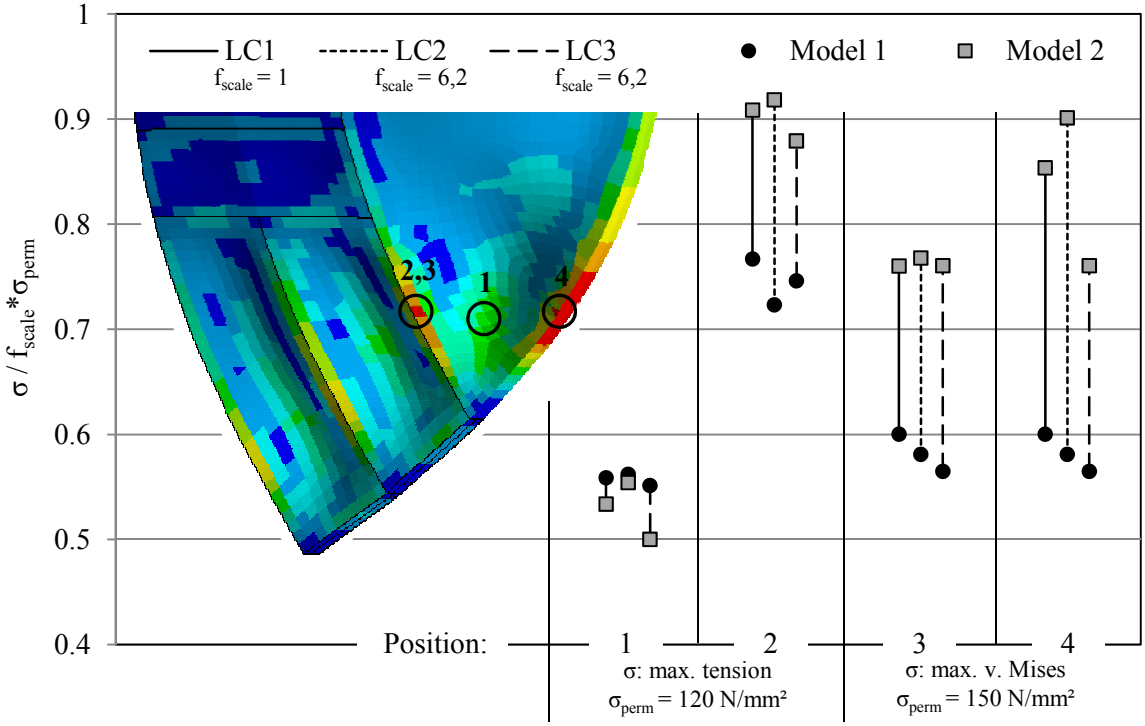


Figure 7: Detailed stress evaluation at certain points normalized to permissible values

4 IMPACT LOADS

Impact loads consider certain peak loads that could act on the bulbous bow e.g. caused by contact to the anchor, its chain or floating objects. These kinds of loads are high but narrow bounded contact loads that might lead to a certain plastic deformation. This might be acceptable when load bearing reserves are considered in appropriate manner. Thus additional FE-calculations have been carried out using models described in Chapter 3 with following changes. Nonlinear material behaviour is considered with bilinear behaviour being ideal plastic after reaching yield stress. ANSYS Shell Element Type 181 is used (reduced integration, four nodes). Aft boundary - fixed in all degrees of freedom - is at #234. Thus the model is four frames shorter than for all other investigations.

Impact loads are considered as area loads on four shell elements resulting in nine loaded nodes shown in Fig. 8. According area of impact is almost equal to 160x160 mm². Positioning of impact loads was carried out aiming to cover almost all possible draught conditions and aiming to hit the bulb in the middle

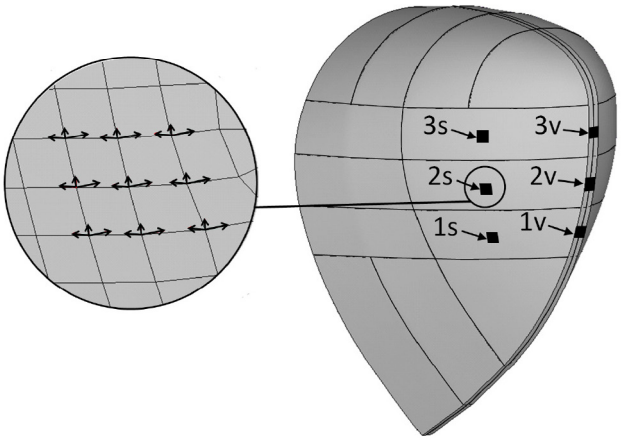


Figure 8: Impact load positions for ultimate load evaluation

of a stiffened panel (model 1) and at the bulb tip. In order to get a clear evaluation of results calculations have been limited to a total number of six positions. Evaluation was carried out by plotting applied load against displacement normal to the loaded areas. Reaching yield stress at top- / bottom layer is depicted with a circle (F_{el}). Ultimate load is marked with a rhomb and is defined in accordance to a beam with rectangular cross section as

$$F_{pl} = 1{,}5 \cdot F_{el} \tag{6}$$

All results are compared with the load-displacement curve of a supported flat panel 1600mm x 620mm x 16,5mm as a reference. Chosen dimensions are typically in the area of the bulbous bow. It is assumed that no larger ultimate load capacity is required than provided by the reference field.

Results are shown for positions on the side of the bulbous bow in Fig. 9. For all positions, ultimate load of model 1 is greater than provided by the reference panel. Model 2 leads to significant decrease of ultimate load which is acceptable for positions 2s and 3s. Ultimate load of model 2 at position 1s is about 25% less than the reference. Positions at the front are significantly greater for all positions and both models. Thus position 1s at model 2 is the only result where ultimate load decrease reaches a significant undercut compared to the reference. According to this background this might be acceptable. The fact that position 1s is located quite low with regard to possible impacts supports this conclusion.

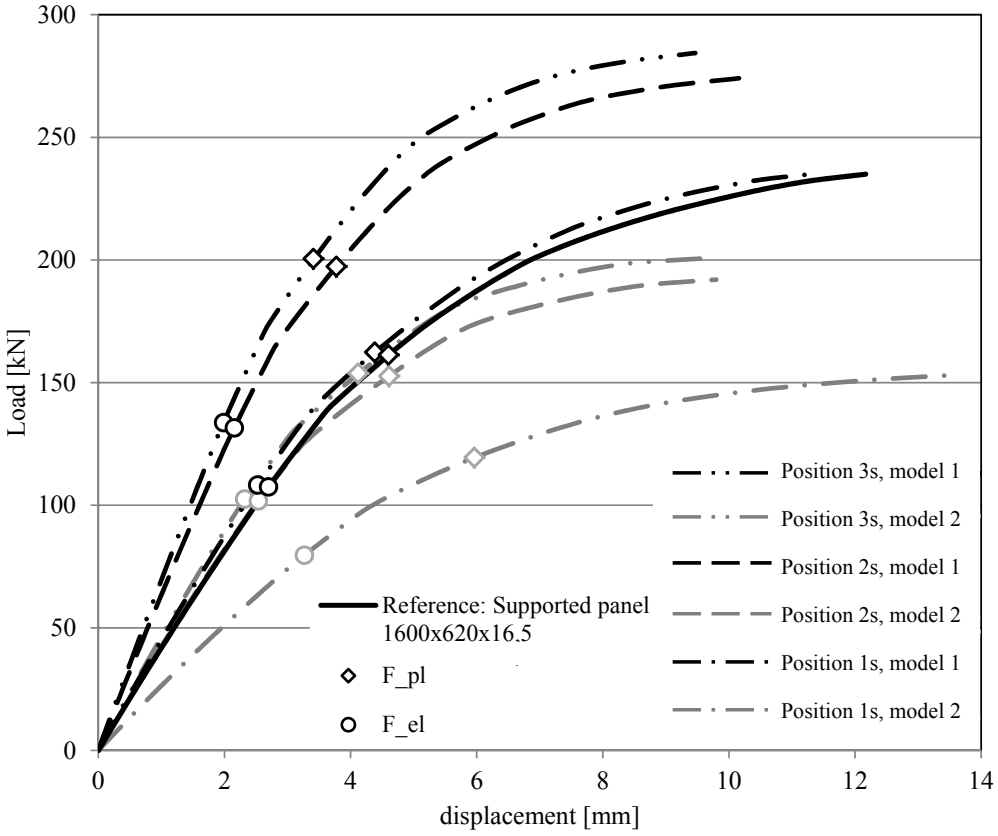


Figure 9: Load-displacement curves for positions shown in Fig. 8

5 CONCLUSION

An alternative bulbous bow design providing good crushing behavior in case of a ship collision is presented. Dimensioning of the alternative design is a challenge because it is formally separated from Classification Rules. Thus a procedure for dimensioning is proposed that has been harmonized with comments of Lloyd's Register. Three pressure load cases and one impact load case are proposed for direct calculations. Results confirm the fact that conventional design of the bulbous bow used as a reference is quite conservative. Thus softening of parts of the structure as described in the paper is permissible in a certain manner. It was shown that for hydrostatic pressure, acceptance of the softening was verified with absolute values. For all other load cases comparative evaluation with the conventional design was carried out with promising results.

5 ACKNOLEDGEMENT

The work presented in this paper was performed within the research Project ELKOS, funded by German Federal Ministry of Economics and Technology (BMWi) under project no. 03SX284B. The authors are responsible for the content of this paper and wish to thank for supporting this project. The authors' gratitude is also addressed to German shipyard Flensburger Schiffbau-Gesellschaft that provided the FE-model of the struck ship and drawings of the bulbous bow.

REFERENCES

[1] Cheung L.: A soft bow for ships, *European Shipbuilding* No. 3, 52-53, 1969

[2] Endo H, Yamada Y. Performance of Buffer Bow Structure against Collision - On the Effect in Preventing Oil Outflow. *Marine Technology*, Vol. 45, No.1, January 2008

[3] Kitamura 0.: *Buffer Bow Design for the Improved Safety of Ships*, IMO, MEPC45/INF.5, Annex, 2000

[4] Peschmann J. 2001. Berechnung der Energieabsorption der Stahlstruktur von Schiffen bei Kollision und Grundberührung. Dissertation, Hamburg University of Technology: Hamburg.

[5] Schöttelndreyer, M.; Tautz, I.; Kubiczek J.M.; Fricke, W. & Lehmann, E. 2011. Influence of bulbous bow structures on their collision behaviour. In C. Guedes Soares, W. Fricke, *Advances in Marine Structures*: pp.381-390, London: CRC Press Taylor & Francis Group

[6] Tautz I, Schöttelndreyer M, Fricke W, Lehmann E. 2010. Experimental Investigations on Collision Behaviour of Bow Structures. In: Ehlers S, Romanoff J. *Proc. of 5th International Conference on Collision and Grounding of Ships*; June 14-16; Espoo, Finland. 179-183

[7] Tautz I, Schöttelndreyer M, Fricke W, Lehmann E. 2013. Collision tests with rigid and deformable bulbous bows driven against double hull side structures. To be published in: *Proc. of 6th International Conference on Collision and Grounding of Ships*; June 17-19; Trondheim, Norway.

[8] Yamada Y. 2006. *Bulbous Buffer Bows: A Measure to Reduce Oil Spill in Tanker Collisions*. Dissertation, Technical University of Denmark: Lyngby (Denmark)

V International Conference on Computational Methods in Marine Engineering
MARINE 2013
B. Brinkmann and P. Wriggers (Eds)

A NEW COMPOSITE MATERIAL FOR FIBERGLASS BOAT CONSTRUCTION

HENRIQUE JOSÉ CARIBÉ RIBEIRO*, ALEXANDRE DE M. WAHRHAFTIG†, AND ADEMAR NOGUEIRA NASCIMENTO†

*Federal Institute of Technologichal Education of Bahia (IFBa) – Campus Salvador
Emidio dos Santos Street, Barbalho, Salvador – BA, Brazil, CEP 40.301-015
e-mail: hcaribe@ifba.edu.br - web page: http://www.ifba.edu.br

† Federal University of Bahia (UFBa), Polytechnic School
Aristides Novís Street, number 02, 5th floor, Federação, Salvador – BA, Brazil, CEP: 40210-910
emails: alixa@ufba.br, annas@ufba.br - Web page: http://www.ufba.br

Key words: Fiberglass, Marine Structures, Composite Material, Computational Analysis, Structural Engineering.

Abstract. The present paper investigates the properties of an alternative material to be used in marine engineering field. It is a composite material based on a sandwich configuration, which is both rigid and light, made of expanded *polystyrene* and fiberglass. This material has several atractives as section modulus improver, besides technical and economical advantages, like low price and weight, commercially available, various dimensions, and easy to manipulate. Mathematical simulations are used to analyze the behavior of the proposed material based on finite element method. Ultimately, this paper aims to contribute with a unique study which will motivate future investigations regarding to extend the application of this material to construction of ships, boats and serve as an academic guide for future references in the naval architecture field.

1 INTRODUCTION

Since the middle of last century fibreglass has been widely used in construction of boats. Advantages and disadvantages are also well known in boat construction industry and the material has proved its applicability as a good option in the marine field.

Fiberglass is resistant to marine environment and chemically inert, composes light weight high strength structures, can mould complex shapes and has competitive costs when used in boat construction. On the other hand, potential problems like low modulus of elasticity and low fatigue strength, when compared to steel and aluminium, are still important to be considered, although fibreglass is in fact the most used material when building small boats.

So, the aim of this paper is to study the possibility of gathering advantages of fibreglass and improve its lacks by creating a new composite material.

Traditionally fiberglass structures have been used worldwide in single skin and sandwich panels. Sandwich panels, for example, improve section modulus and the thickness of the panel without increasing its weight. But this configuration has still a low stiffness and may,

therefore, need framing, what could also increase weight and reduce space inside the boat. Weight has been an important factor in high speed boats, while total internal volume available is important when operating cargo transport ships and boats.

The overall cost of a fiberglass boat is usually slightly higher than the equivalent wood or steel boat being built. As size becomes greater, the need to shift to a sandwich structure is certain, what makes the cost to become also higher. Sandwich panels made of divinycell® and polyurethane are not only expensive options but also not available in a wide range of different thicknesses.

This paper investigates a composite material which solves the major part of these problems, once it forms, together with fibreglass, a light, cheap and widely available composite material. The main objective of this work is to show that this material is a good and cheap choice when compared to others. So, in the next sections a comparison between basic core materials and the one here used is made, while structural concepts and design aspects assist the conclusions of the paper.

2 BASIC CORE MATERIALS

One understands that the core does not subsist alone, and it needs the resin and the glass reinforcements, and they will work altogether in order to make a usable material in boat and also in some ships construction. So, in this section of the paper it will be briefly mentioned the main core materials used in boat construction, and further analyzed the possible combinations formed with resins and glass reinforcements.

There are about three or four types of core among the most used: foamed plastics, honeycomb and woods like balsa wood. According to reference [1], a good core material should have good shear strength and rigidity, ability to bond adequately to the facings with a minimum of difficulty, light weight, resistance to deterioration due to water and sufficient crushing strength to withstand loading.

Among the foamed plastics is expanded polystyrene. Though expanded polystyrene is attacked by polyester resins, it is hoped to show that even the price compensates when used together with epoxy resins.

The most used foamed plastic today is PVC foam. One of the greatest advantages of PVC foam is its ability to soften when heated, and then be draped over the curved surfaces of the boat. Returning to normal environment temperature it recovers the hardness. This tendency to soften with temperature makes this core not usable in decks and other places on board, wherever submitted to temperature. The need to reduce this problem made available a cross linked foam containing both PVC and polyurethane, but with some reduced properties, when compared to original PVC foam.

Honeycomb is available in different sizes, weights and materials like aluminum, fiberglass laminates and waterproof paper. Good characteristics are light weight and good rigidity. On the other hand it has poor resistance to concentrated loads and requires special abilities to produce good bonding between core and the faces of the laminate. Thus, the use of honeycombs in boat constructions is restricted to interiors like bulkheads and other places not submitted to high loads.

Woods can also be used as core materials, and soft woods are mostly used. Hard woods are avoided as they can swell and crack the laminate. Hard woods do not bond well to fiber, what

makes them avoidable in boat construction. Soft woods bond better to FRP, but can sometimes cause swelling problems. Though soft woods can drape very well over the curved surfaces of the boat, they have been avoided below the waterline because of possible rotting, swelling and degradation.

At the center of this discussion is expanded polystyrene (EPS). EPS has special attractives as very light weight, be very cheap and resistant to fungi and water. On the other hand, like most very light materials, low mechanical properties are expected as low shear and compressive strength. This makes them susceptible to delamination and damage, but this can be satisfactorily solved with the increase of the core thickness or the use of shear webs.

Also, polystyrene is not recommended because polyester resin attacks it, but it is possible to use some thin PVC cover, bonded to the central polystyrene core to avoid the use of epoxy resin to bond the faces. If shear webs are used, epoxy resin mixed to glass strands can compose the webs.

To make objective comparison between the mentioned cores the properties are listed in table 1, as follows:

Table 1: Comparison between mechanical properties of different core materials

Propriedade	Renicell 240 (PVC)	Balsa LD7	Honeycomb PP30-5	EPS 3	EPS 3 with shear webs
Specific Gravity (kg/m³)	240	90	100	14	38
Compression Strength (psi)	580	783	235	9	26000
Compression Modulus(ksi)	19	268	10.5	- -	22000
Tensile Strength (psi)	479	1015	175	18	30000
Shear Strength (psi)	363	232	75	9	11000
Shear Modulus (ksi)	14	14	2	0,48	- -

3 STRUCTURAL CONCEPTS

Figure 1 shows the structural arrangement in simplified top and side views of present proposal in this paper. Though of the low values mentioned in table 1 for mechanical properties of expanded polystyrene (EPS), shear webs overcome more than satisfactorily this lack of strength and rigidity.

In order to uniform all the aspects to be showed, a comparison is made on the basis of a thickness of the core of 10 mm, but it is good to remember that EPS is available in all thicknesses. This makes the proposal applicable in many different circumstances. For instance, if a thicker EPS core is used, shear webs may become an efficient framing system. As the webs are present in both longitudinal and transverse directions, the webs dispense the formal framing system, freeing space inside the boat, providing a light and rigid composite material.

If the thickness of the core increases, it is possible to use thinner faces and webs. It is important to observe that in this case, the faces that cover the core act like the flanges of an

"I" beam. As the shear, compressive and tensile strength of faces and webs are far higher than those of the EPS core, the voids between the webs provide a mold surface for the whole assembly and prevent the buckling of the webs.

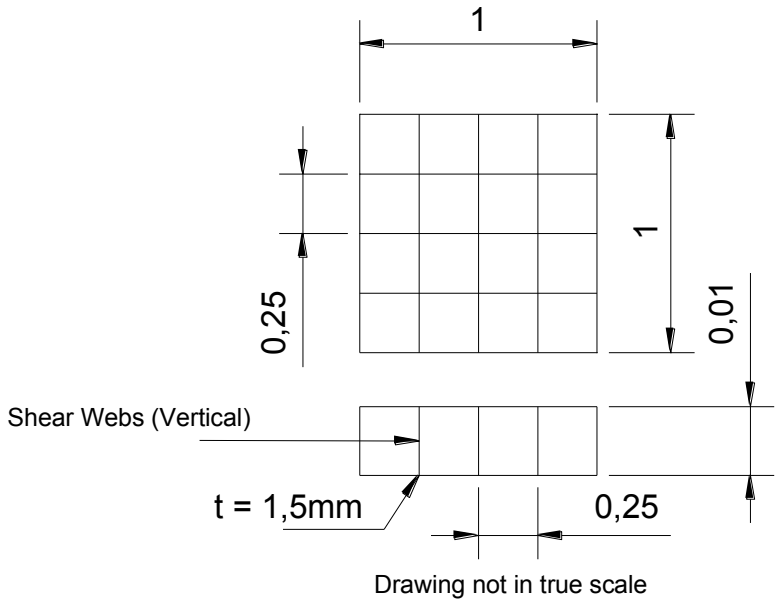


Figure 1: Structural Arrangement of New Composite

The option presented here considers an EPS core with vertical shear webs. As EPS is attacked by polyester resins, it is needed to use epoxy resins in the construction of the webs. In order to make the sandwich to drape even better to the boat surface, the material can be provided already bonded to a thin surface in one side only. To make the dimensions of the webs uniform, the blocks of the cores that forms the void between the webs can be easily delivered in this arrangement. Figure 2 shows this possibility.

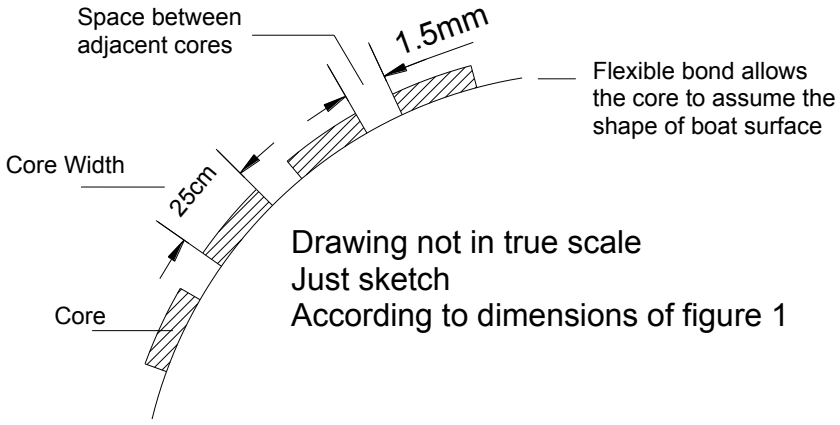


Figure 2: Basic structural arrangement. At the space between cores should be laminated shear webs

It should also be observed that, besides all the mentioned and forthcomming advantages of using epoxy resins in this case, there is the fact that polyester resins elongate less than the reinforcement. This means that the failure should occur before the strength of the reinforcement is reached. So, by using epoxy resin, the strength of the whole assembly is optimized, what constitutes a very important characteristic of this composite.

4 DESIGN AND CONSTRUCTION ASPECTS

Though overall and local loads acting on small boat hulls seem not to be very well defined, making the designer of such boats to work strongly based on experience, it is seen that this material is not only restricted to small recreational boats. It is intended to apply also to medium sized ships and boats, where these loads can be better known. So, it is admitted that overall and local loads defining the structural design problem are well defined.

Even facing the possibility of using a thin cover of PVC bonded to the main EPS core, in order to make possible to use polyester resins, it seems that the best option is to use epoxy resin all around, wherever needed. This makes important to observe the special difficulties of laying up manually with epoxy resins and the need of well trained people only.

Design techniques are as usual as the ones used in any material for boat and ship construction, but it is good to make a simple comparison between the tensions and displacements developed in each of the panels identified in figure 3. Divinycell is very used in sandwich constructions of fiberglass boats, and was thus chosen for comparison. The structural loads are defined as follows in the computational simulation.

4.1 Computational Simulation

The numerical computational modeling of the structure was performed using the Finite Element Method (FEM) and followed linear criteria to geometric and material point of view. In Figure 3 can be seen the Finite Element Model and the mesh used. The model is presented in three-dimensional view with the discretization of the structure, containing solid elements and its contour condition. In figure 4 and figure 5 one can see details of corner and middle for both models. The More details about Finite Element Method are presented by Clough [2], Bucalem [3] and Cook [4].

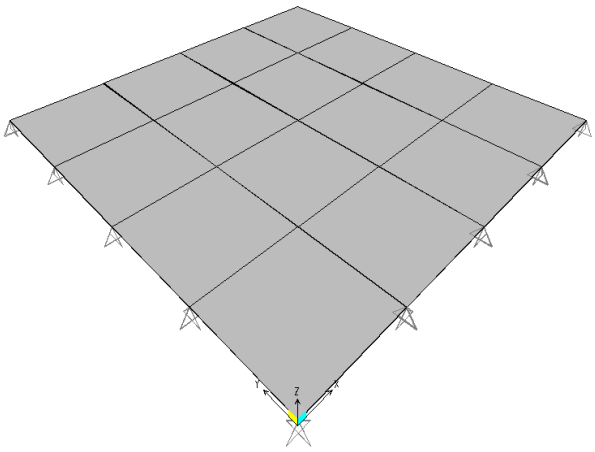


Figure 3: – 3D Model in FEM

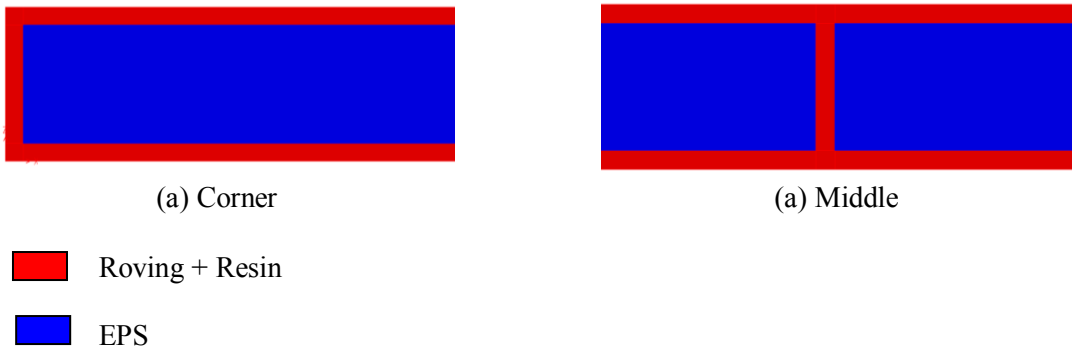


Figure 4: XZ Lateral view in FEM – Model with EPS

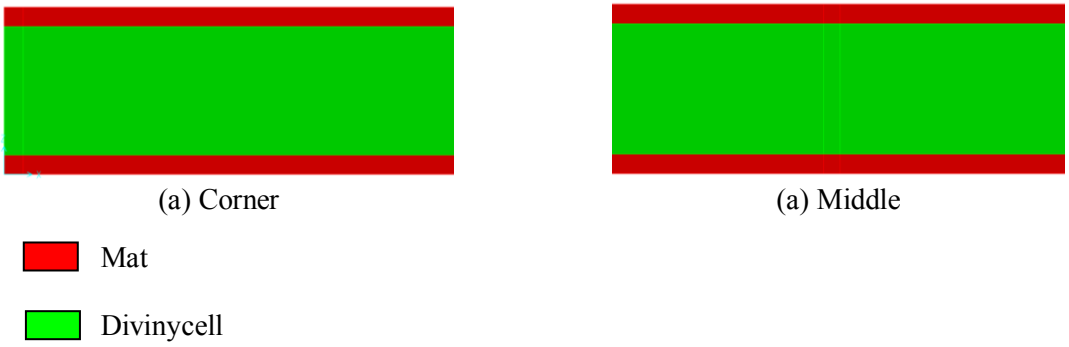


Figure 5: XZ Lateral view in FEM – Model with Divinycell

Simulations were conducted for the compositions and dimensions seen in figure 9. The applied pressure corresponds to a water column of 2 m height and the boundary condition imposed is on the pinned support. The results in terms of stress (Maximal Tension – Principal Stress), in mentioned position, and displacement in the central point of the plate are in table 2, figures 6, 7 and 8. In order to calculate the admissible stresses were used a safety coefficient equal to 2, applied in relation to rupture stress.

Table 2: Results from FEM Analysis

Parameter		Unit	Roving + resin (EPS Model)	Mat (Divinycell Model)
Analysis Results from FEM	Max Tension Stress	N/mm^2	11.48	10.29
	Max Compression Stress	N/mm^2	15.11	14.66
	Max Shear Stress	N/mm^2	3.21	1.72
	Max Displacement	mm	14.84	14.00
Strength Resistances	Admissible Tension Stress	N/mm^2	103.42	34.47
	Admissible Compression Stress	N/mm^2	89.63	68.95
	Admissible Shear Stress	N/mm^2	37.92	37.92

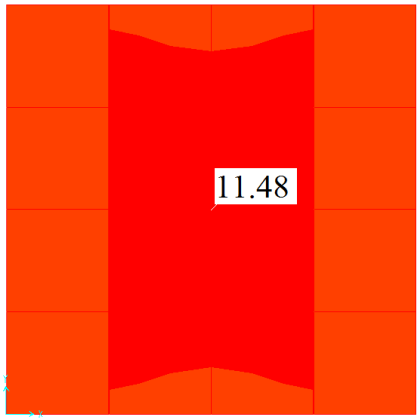


Figure 6: Max Tension (N/mm^2) in FEM Analysis– Model with EPS

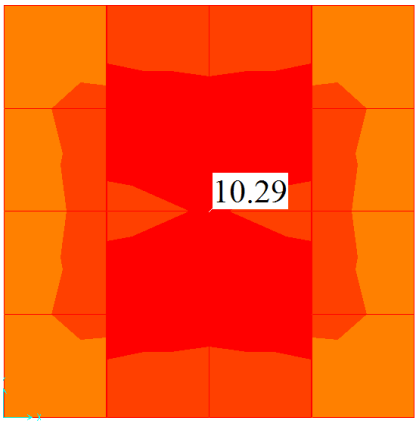


Figure 7: Max Tension (N/mm^2) in FEM Analysis– Model with Divinycell

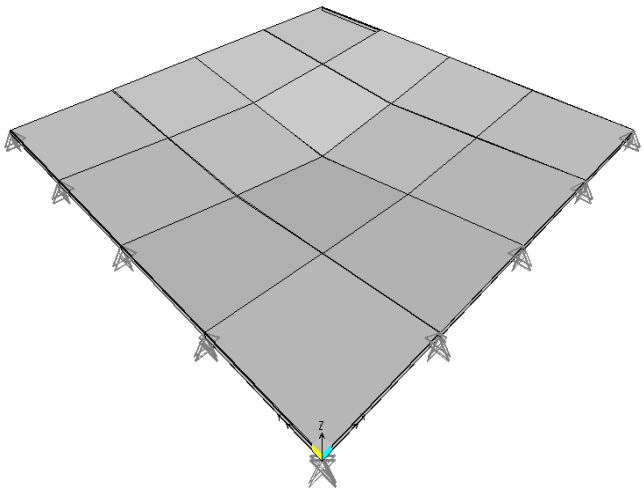


Figure 8: Deformed Configuration (mm) in FEM Analysis – Similar for Both Models

5 ECONOMICS

Now it must be considered economic aspects in order to make sure that the use of EPS cores is viable and worthy. Prices of the pieces were taken in Brazilian Real (BRL), just to make easier the comparison between Divinycell and EPS as cores. The basic structural arrangements of EPS and Divinycell are showed below, in figure 9. The dimensions of each panel are as showed in figure 1.

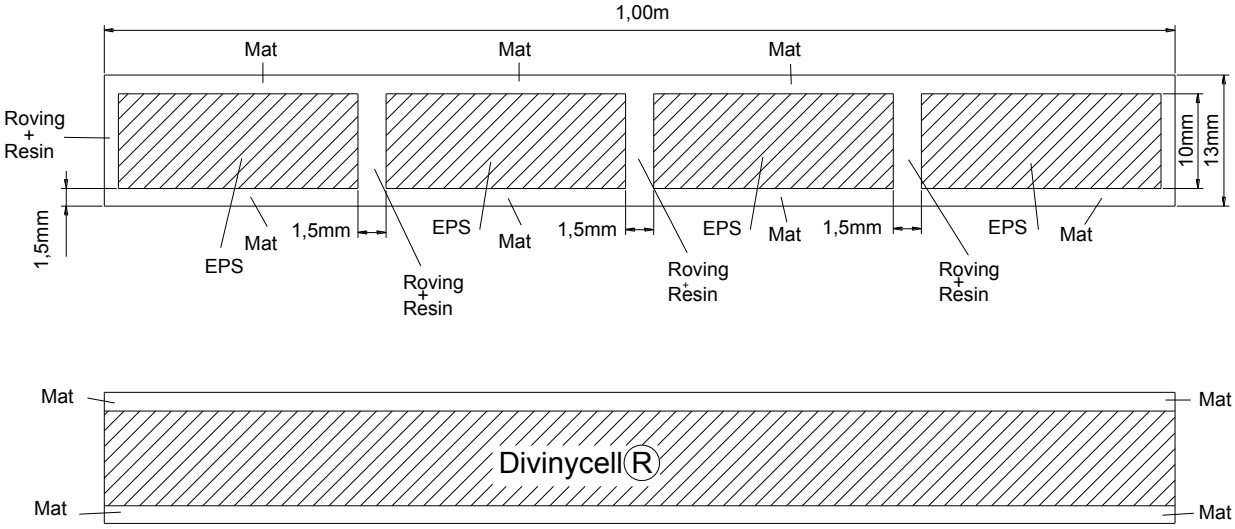


Figure 9: Structural arrangement of the two cores considered to economic comparison

Composition of prices is as shown in table 3.

Table 3: Price composition of panels using EPS and Divinycell as cores:

Item	Panel with EPS core	Panel with Divinycell
Mat 300g/m²	15,00	15,00
Roving Wire	2,80	0,00
Epoxy Resin	168,5	0,00
Polyester Resin	0,00	70,00
EPS (1m²)	2,00	0,00
Divinycell (1m²)	0,00	150,00
Total Price (BRL):	188,30	235,00

7 CONCLUSIONS

Simulations and comparisons made have showed that this composite material is fully feasible and competitive. Even considering its low mechanical properties, its use as a

simple core makes possible to use shear webs made with epoxy resin, improving the strength of the material, making it similar to the sandwich made with Divinycell, which has much higher mechanical properties than the EPS properties. It is good to observe that EPS is a very much lighter material than Divinycell. If it is remembered that weight is a very important factor in boat construction, mainly in speed boats, this makes EPS an agreeable option. Also, table 3 has shown that the composite material made with EPS is about 20 % cheaper than the panel made with Divinycell.

REFERENCES

[1] Robert J. Scott, "Fiberglass Boat Design and Construction", Second Edition, SNAME, USA, NJ (1996).

[2] R.W, Clough, J. Penzien, Dynamic of Structures, McGraw Hill International Editions, Second Edition, Taiwan, 1993.

[3] M. L. Bucalem, K. J. Bathe: The Mechanics of Solids and Structures – Hierarchical Modeling and the Finite Element Solution. Springer, German, (2011).

[4] Cook, R. D. Concepts and Applications of Finite Element Analysis. John Wiley and Sons, Inc., NJ, USA, (1974).

V International Conference on Computational Methods in Marine Engineering
MARINE 2013
B. Brinkmann and P. Wriggers (Eds)

THE PULL-OUT CAPACITY OF MOBILE PLATFORM LEGS FROM SATURATED SILT

X.W. ZHANG*, R. UZUOKA† AND X.W. TANG‡

*Dalian University of Technology; The University of Tokushima
No.2 Linggong Road, Ganjingzi District, 116024 Dalian, CHINA
e-mail: zhangxw_11@163.com, Web page: http://www.dlut.edu.cn/en/

† The University of Tokushima
2-1 Minamijyousanjima-cho, 770-8506 Tokushima, JAPAN
e-mail: uzuoka@ce.tokushima-u.ac.jp, Web page: http://www.tokushima-u.ac.jp/english/

‡ Dalian University of Technology
No.2 Linggong Road, Ganjingzi District, 116024 Dalian, CHINA
e-mail: tangxw@dlut.edu.cn, Web page: http://www.dlut.edu.cn/en/

Key words: Mobile Platform, Pullout, Suction Force

Abstract. Many new types of structures are extensively used in offshore engineering in recent few decades. Such as the mobile platforms, suction caissons, anchors, spudcans, and so on. The capacities of these structures during penetration, operation and remove are crucial issues for engineers. In this paper, the model test and numerical simulation are conducted to estimate the pullout capacity of the mobile platform's leg submerged in saturated silt. The platform's leg is simplified as a square shape with a dimension of 30cm×30cm, while the buried depths are 1cm, 3cm, 5cm, respectively. The modified Cam-Clay model and finite deformation theory are applied in numerical simulation.
We did the short-time pullout in experiment and numerical simulation. The peak pullout force is about 1-4 times larger than the model's weight. The pullout resistance is influenced by the object buried depth, soil property and so on. It is shown that during uplift, the negative pore water pressure under the object provides the main role to the resistance capacity. As the increase of negative pore water pressure and decrease of the soil confining pressure, the soil failure and large deformation happens, then the structure extricates itself from the silt. The numerical result is acceptable to predict the breakout although couldn't simulate the separation of object and soil.

1 INTRODUCTION

There are many types of offshore platforms which are extensively used for oil and natural gas extraction. Now, many special platforms are used for turbine installation, sunken ship salvage and so on. For the offshore structures, there are many challenges in geotechnical engineering, such as site investigation, the interaction between the structure and the seabed soil and so on [1]. In this paper, we will focus on a special marine platform, Jack-up platform. Figure 1 shows the Jack-up wind turbine installation platform which works in Nantong City of China.



Figure 1: Jack-up wind turbine installation platform (Nantong City, China)

Jack-up platform is a new type and most popular mobile platform in the world. It consists of a buoyant hull and a number of movable legs. The buoyant hull enable the platform to float on the water, while the legs can penetrate into the seabed soil to support the upper platform. This kind of platform can only be placed in relatively shallow water, about less than 100m of water. It can be used as exploratory drilling platform or wind farm service platform.

Jack-up platform has three working process. The first one is penetration. When the jack-up platform arrivals at the working location, the legs will penetrate into the seabed soil by the platform's selfweight and additional water, while the jacking system raises the hull above the water surface with a certain height. Many researchers did research on the penetration process and the capacity of the seabed to support the platform in complicated marine enviroment. Then second one is working. After installation and preloading, the platform can work for construction or salvage. The third one is remove. The jacking system will put down the hull to the water surface and pullout the legs. In this process the pullout force always larger than the legs weight because of the suction force between the seabed and the legs. We will investigate the pullout resistance during the remove of Jack-up platform.

The suction force F_s is defined as the difference between vertical pull force F and the self-weight of leg G. $F_s = F - G$. The suction force is consisted of structure bottom adhesion force, the side friction force and the negative porewater pressure, among which negative porewater pressure is the main factor to the suction force [2]. And the suction force is influenced by many factors such as the shape of the structure, the embedded depth and the seabed soil characteristics. So that, the calculation and the prediction is difficult and complex. Many researchers have done a lot of work in model tests, theory and empirical prediction and numerical simulations (Finn [3], Sawiciki [4], Purwana [5], Zhou [6]). And published literature is still relatively scarce.

These suction force should be overcome in order to pullout the platform's legs. Sometimes, the legs are difficult to pullout, or the large impulse force will induce huge damage to the platform and the equipments. This phenomenon is called breakout phenomenon [7, 4]. Chen [8] did a series of centrifuge tests to test the pullout resistance of offshore structure. He found that during remove the structure, the suction force infuence the uplift process. The breakout phenomenon can be divided into short time breakout and long time breakout. As its name suggests, in short time breakout, the vertical force is applied quickly, the object will be pulled out in a short time. In long time breakout, a constant force is applied, as the migration of around water, the object will get extrication in the last, but it will need a longer time. In this paper, the model test and numerical simulation were conducted to predict the peak pullout force and peak suction force in the case of short time pullout. The mechanism of the short time breakout will be discussed.

2 EXPERIMENT AND NUMERICAL MODEL

The experiment equipments and numerical model are shown in Figure 2. The platform leg's bottom is simplified as a square with a dimension of 30cm×30cm.

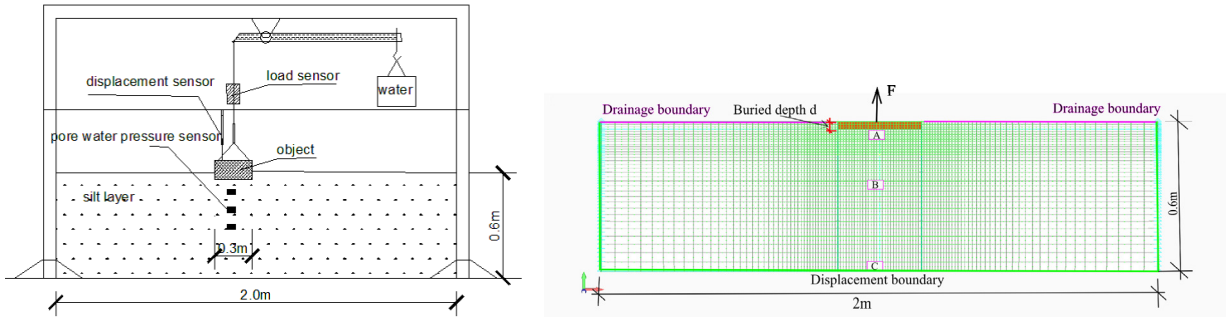


Figure 2: (a) Experiment equipment ; (b) Finite element model

2.1 Basic condition

The weight of the leg is 103N, while the buried depths are 1cm, 3cm, 5cm respectively. In the experiment, the soil is silt which was excavated from the seabed near Dafeng city

of China. The properties of the silt are shown in Table 1. During the pullout, the displacement, pullout force and the porewater pressure were recorded by the sensors and computer. In numerical simulation, the leg is a rigid body, leg's two sides are free while the bottom is tied with the soil elements. A vertical force with a loading rate of 12N/s is applied on the center of the leg.

Table 1: soil property

Porosity	Intrinsic density	Compression index	Swelling index	Critical stress ratio
0.42	2.73 t/m^3	0.047	0.0043	1.578

In numerical analysis, Al-Shamrani [9] used finite element method to calculate the breakout force with the assumption that no separation of the object and the surrounding soil. Sawiciki [4] and Zhou [6] suggested that the breakout process could be consist of two stages (no gape stage and with gape stage) or three stage (no gape stage,transition stage and with-gap stage). In our experiments, a short time pullout is conducted, which means the leg will be pulled out in a short time. In this case, the pullout time is about dozens of seconds or several minutes, the water and soil migration are not considered. What's more, in our experiment, we found that the stage before the gape emergence is very important. In this stage, the bottom porewater pressure will change form postive to negative, the soil effective stress will decrease and near to zero. After the gape emergence, plenty of water will flow into the gape, the leg will be pulled out in a short time.
As we know, the bubble or the gape is generated in saturated soil when the negative pore water pressure is less than -100kPa (one atmos). Actually, the negative pore water pressure is larger than that value in our experiment. So that, a no gape model is assumed in this paper. To simulate the soil property, the modified cam-clay model is applied to simulate the elasto-plastic behavious in the numerical analysis.

2.2 Governing equations

According to Uzuoka [10] porous media theory and finite strain analysis, we used quasi-static analyses and established mass and momentum balance equations for the saturated soil. The momentum balance equation for total mixture is obtained as:

$$\mathrm{div}\,(\boldsymbol{\sigma}' - p^{\mathrm{w}}\boldsymbol{I}) + \rho\boldsymbol{b} = 0 \tag{1}$$

Where, $\boldsymbol{\sigma}'$ is Cauchy effective stress tensor, p^{w} is pore water pressure, $\boldsymbol{I}$ is the second-order identity tensor (Kronecker delta function), ρ is density of the mixture, $\boldsymbol{b}$ is the body force vector. The mass and momentum balance equation for pore water is obtained as:

$$\frac{n\rho^{\mathrm{wR}}}{K^{\mathrm{w}}}\frac{D^{\mathrm{s}}p^{\mathrm{w}}}{Dt} + \rho^{\mathrm{wR}}\mathrm{div}\,\boldsymbol{v}^{\mathrm{s}} + \mathrm{div}\left\{\frac{k^{\mathrm{ws}}}{g}(-\mathrm{grad}\,p^{\mathrm{w}} + \rho^{\mathrm{wR}}\boldsymbol{b})\right\} = 0 \tag{2}$$

Where, n is the porosity, ρ^{wR} is intrinsic density of fluid, K^{w} is water bulk modulus, $\boldsymbol{v}^{\mathrm{s}}$ is velocity of soil skeleton, k^{ws} is permeability coefficients of pore water, g is gravity acceleration.
Then, the finite element method is used for the spatial discretization. Using conventional Galerkin method, the weak form of equation (1) is obtained as

$$\delta w^{\mathrm{s}} = \int_{B^{\mathrm{s}}} \delta \boldsymbol{d}^{\mathrm{s}} : \boldsymbol{\sigma}' dv - \int_{B^{\mathrm{s}}} p^{\mathrm{w}} \mathrm{div}\, \delta \boldsymbol{v}^{\mathrm{s}} dv - \int_{B^{\mathrm{s}}} \rho \delta \boldsymbol{v}^{\mathrm{s}} \cdot \boldsymbol{b} dv - \int_{\partial B^{\mathrm{s}}_{\mathrm{t}}} \delta \boldsymbol{v}^{\mathrm{s}} \cdot \bar{\boldsymbol{t}} da = 0. \tag{3}$$

The weak form of equation (2) is

$$\begin{aligned} \delta w^{\mathrm{w}} = & \int_{B^{\mathrm{s}}} \delta p^{\mathrm{w}} \frac{n s^{\mathrm{w}} \rho^{\mathrm{wR}}}{K^{\mathrm{w}}} \frac{D^{\mathrm{s}} p^{\mathrm{w}}}{Dt} dv + \int_{B^{\mathrm{s}}} \delta p^{\mathrm{w}} \rho^{\mathrm{wR}} \mathrm{div}\, \boldsymbol{v}^{\mathrm{s}} dv \\ & - \int_{B^{\mathrm{s}}} \mathrm{grad}\, \delta p^{\mathrm{w}} \cdot \left\{ \frac{k^{\mathrm{ws}}}{g} (-\mathrm{grad}\, p^{\mathrm{w}} + \rho^{\mathrm{wR}} \boldsymbol{b}) \right\} dv \\ & + \int_{\partial B^{\mathrm{s}}_{\mathrm{wq}}} \delta p^{\mathrm{w}} \bar{q}^{\mathrm{w}} da = 0. \end{aligned} \tag{4}$$

Where, B^{s} is body area, $\partial B^{\mathrm{s}}_{\mathrm{t}}$ and $\partial B^{\mathrm{s}}_{\mathrm{wp}}$ are natural boundary, $\bar{\boldsymbol{t}}$ is the prescribed traction vector at $\partial B^{\mathrm{s}}_{\mathrm{t}}$, $\bar{q}^{\mathrm{w}}$ is the prescribed mass flux on a unit at $\partial B^{\mathrm{s}}_{\mathrm{wp}}$. The following equation (5) shows the linearized formulations of the weak forms in Newton-Raphson scheme.

$$\begin{aligned} D\delta w^{\mathrm{s}}[\Delta \boldsymbol{v}^{\mathrm{s}}] + D\delta w^{\mathrm{s}}[\Delta \dot{p}^{\mathrm{w}}] &= -\delta w^{\mathrm{s}}_k \\ D\delta w^{\mathrm{w}}[\Delta \boldsymbol{v}^{\mathrm{s}}] + D\delta w^{\mathrm{w}}[\Delta \dot{p}^{\mathrm{w}}] &= -\delta w^{\mathrm{w}}_k \end{aligned} \tag{5}$$

Where, $\Delta \boldsymbol{v}^{\mathrm{s}}$ and $\Delta \dot{p}^{\mathrm{w}}$ are the variations at the current iterative step $k+1$. δw^{s}_k and δw^{w}_k are the weak form of equation (1) and equation (2) at the previous iterative step k. $D\square[\Delta\bullet]$ denotes the directional derivative of $\square$ with respect to $\bullet$. The solutions at the current iterative step $k+1$ are obtained as

$$\begin{aligned} \boldsymbol{v}^{\mathrm{s}}_{k+1} &= \boldsymbol{v}^{\mathrm{s}}_k + \Delta \boldsymbol{v}^{\mathrm{s}} \\ \dot{p}^{\mathrm{w}}_{k+1} &= \dot{p}^{\mathrm{w}}_k + \Delta \dot{p}^{\mathrm{w}} \end{aligned} \tag{6}$$

The iteration continues until the norms of the residual vectors of δw^{s}_k and δw^{w}_k are smaller than a specified error tolerance. In quasi-static analyses, only the velocity components are considered. The displacement of the soil skeleton and the pore water pressure of element are expressed as:

$$\boldsymbol{u}^{\mathrm{s}} = \boldsymbol{u}^{\mathrm{s}}_t + (1-\gamma)\Delta t\, \boldsymbol{v}^{\mathrm{s}}_t + \gamma \Delta t\, \boldsymbol{v}^{\mathrm{s}} \tag{7}$$

$$p^{\mathrm{w}} = p^{\mathrm{w}}_t + (1-\gamma)\Delta t\, \dot{p}^{\mathrm{w}}_t + \gamma \Delta t\, \dot{p}^{\mathrm{w}} \tag{8}$$

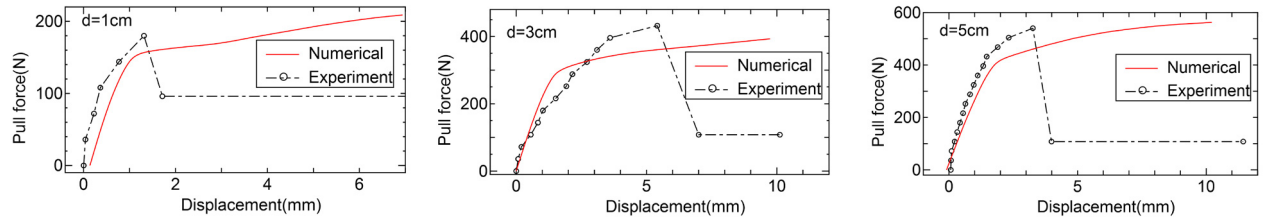
Here, γ is the parameter in quasi-static analysis.

3 RESULTS OF EXPERIMENT AND NUMERICAL SIMULATION

In short time pullout, we will apply a linear loading with a rate of 12N/s, In this case, the pullout time is about dozens of seconds, the soil can be considered as in undrained condition. We will discuss the results about relationship between displacement and vertical force. Then, the transformation of pore water pressure and suction force will be presented.

3.1 Displacement-force relationship

Figure 3 shows the relationship between vertical pull force and leg's vertical displacemetn in different buried depth. From this figure, we can see that in different buried depth, the pullout force is different. As increase of buried depth d, the pullout force becomes larger. At the beginning, the vertical displacement increase slowly, while the vertical force has to overcome the object's weight and the suction force. Then, the displacement increase rapidly which is induced by the large soil deformation and partial soil failure.



(a) (b) (c)

Figure 3: The relationship of displacement and pull force (a)buried deppth d=1cm ; (b) buried deppth d=3cm ; (c) buried deppth d=5cm

In experiment, the pull force decrease rapidly after reach the peak pullout force, that because of the disappear of resistance after the separation between object and the soil, the load sensor can only record the inertial force of the object in the last. In numerical simulation, we can see the obvious turning point. After that point, the soil became weak, which means small force increment will induce large deformation. So, we get the similar phenomenon both from experiment and numerical simulation, that the object has large and rapid displacement in the last. For practical engineering, in the moment of separation, a large impulse force will be generated and it will cause unimaginable damage to the platform.

3.2 The suction force

To pull out the object from the seabed soil, the pullout force should be larger than the object's weight. In table 2, it shows the peak pullout force and peak suction force.

Table 2: Suction force

Buried depth	selfweight	Peak pullout force		Peak suction force	
		Experiment	Numerical	Experiment	Numerical
1cm	103N	180N	209N	77N	106N
3cm	103N	432N	392N	329N	289N
5cm	103N	540N	560N	437N	455N

We define the suction force F_s equals to the difference between vertical force F and the effective selfweight G. $F_s = F - G$. Clearly, the peak pullout force is larger than the object's weight. The experiment results and the numerical simulation have the same trend although a little difference exist.

3.3 Pore water pressure response

From the model test and numerical simulation, the time history of pore water pressure and the effective stress under the bottom of the object are shown in figure 4.

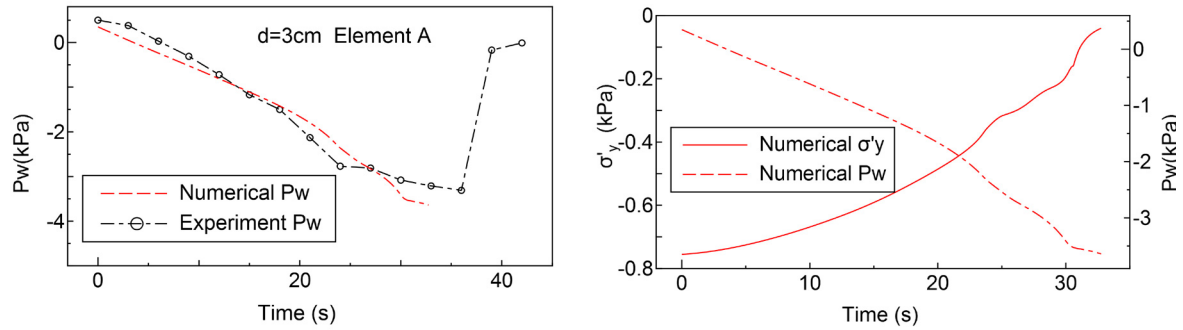


Figure 4: (a)The time history of pore water pressure $\boldsymbol{P_w}$; (b)The time history of effective stress $\boldsymbol{\sigma'}$

It is found that, as time goes on, the external vertical force will be transfered and transmited to the base pore water and soil skeleton. As soil effective stress is very small, the pore water pressure becomes the main receiver. But soil effective stress also have to be unloaded, until the moment losing its strength.
In the experiment, the pore water pressure will increase back towards the hydrostatic pressure at the moment of breakout, that beacuse the object will seperate from the soil, the around water will flow into the bottom suddenly, the negative pore water pressure will disappear in a short time. As we know, soil effective stress is difficult to get accurately in model test. But, in numerical simulation, the element effective stress response can be easily presented. So that, from figure 4, we can predict the object will have large displacement by the status of soil skeleton. Not only that, the numerical method also can

describe developing trend of pore water pressure and other variables.

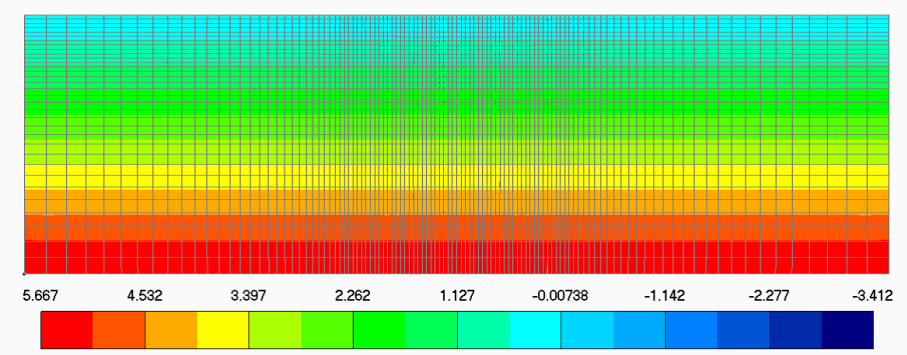


Figure 5: The distribution of initial $\boldsymbol{P}_{\mathbf{w}}$

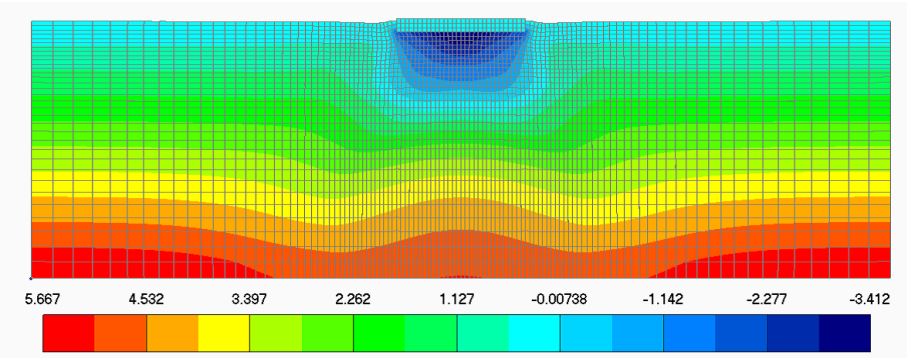


Figure 6: The distribution of $\boldsymbol{P}_{\mathbf{w}}$ when(d=3cm,t=30s)

Figure 5 and figure 6 show the distribution of initial pore water pressure and the pore water pressure when t=30s. The initial pore water pressure equals to the hydrostatic pressure. When t=30s, the area under the object has negative pore water pressure, while the area near the boundary has postive pore water pressure and near the hydrostatic pressure. It can clearly infer that during the pullout process, the vertical pull force induce the negative pore water pressure generated around the object and diffuse to the distance.

3.4 Soil deformation

From figure 4, the soil effective stress increase and near to 0 kPa. In figure 7, it shows the ditribution of deviatoric strain in the whole domain when buried depth d=3cm, time t=30s. The deviatoric strain around the object has large value. That means the large soil deformation will happen. In the model test, the soil around the object also has obvious failure area which is shown in figure 8. The numerical simulation and the experiment have the similar phenomenon that the soil around the object has large deformation and the object will has rapid increase in displacement at the beginning of the breakout.

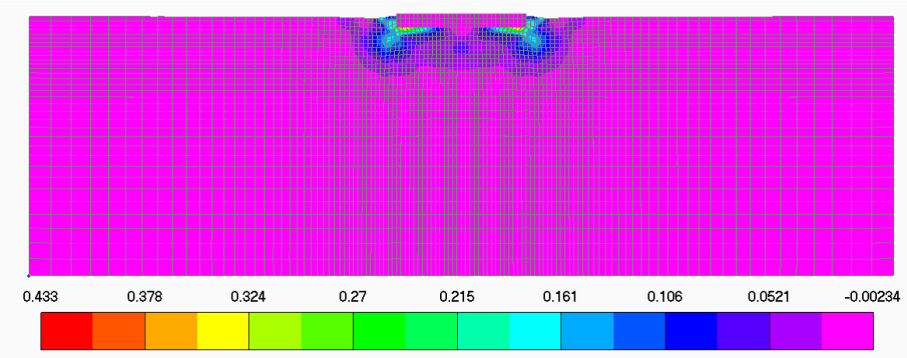


Figure 7: The distribution of deviatoric strain (d=3cm,t=30s)

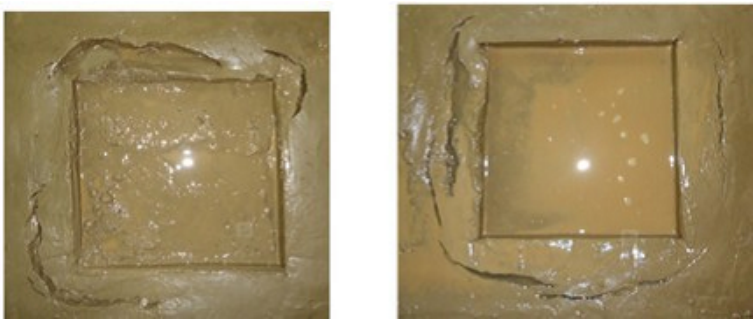


Figure 8: The soil around the object after breakout

4 CONCLUSIONS

- In this paper, the model tests and numerical simulations are conducted to verify the pullout capacity of the platform legs from saturated silt. The influence and the mechanism of suction force under the legs are explained. From this research, the suction force is mainly composed of negative pore water pressure, to pullout the object, the suction force provide the great mass of resistance.

- During pullout process, the vertical force firstly overcome the object's self weight, then the difference force between vertical force and object effective weight induce the pore water pressure form positive to negative, the effective soil stress will increase near to zero. The partial soil failure around the object occurs, which will lead to large soil deformation and rapid increase of object displacement. In the last, the object will be pulled out.

- In numerical simulation, the porous media theory and finite strain method are used. The time history of the pore water pressure and the displacement are reappeared. It shows the soil large deformation and the rapid increase of displacement very clearly. The model test and numerical simulation have similar phenomenon and results.

The numerical method can be used to predict the pullout resistance in the practical engineering.

REFERENCES

[1] Randolph, M. , Cassidy, M. and Gourvenec, S. Challenges of offshore geotechnical engineering. *Proceedings of The 16th International Conference on Soil Mechanics and Geotechnical Engineering*. Vol. 1: 123-176, (2005).

[2] Foda, M.A. , On the extrication of large objects from the ocean bottom (the breakout phenomenon). *Journal of Fluid Mechanics*. Vol. 117: 211-231, (1982).

[3] Finn, W.D. , and Byrne, P.M. The evaluation of the breakout force for a submerged ocean platform. *Proceedings, Fourth Annual Offshore Technology Conference, Houston, Texas.*. Vol. 1: 863-868, (1972).

[4] Sawicki, A. , Mierczynski, J. Mechanics of the breakout phenomenon. *Computers and Geotechnics*. Vol. 30: 231-243, (2003).

[5] Purwana, O.A. , Leung, C.F. , Chow, Y.K , and Foo, K.S. Influence of base suction on extraction of jack-up spudcans. *Geotechnique*. Vol. 55(10): 741-753, (2005).

[6] Zhou, X.X. , Chow, Y.K. and Leung, C.F. Numerical modeling of breakout process of objects lying on the seabed surface. *Computers and Geotechnics*. Vol. 35: 686-702, (2008).

[7] Mei, C.C. , Yeung, R.W. and Liu K.F. Lifting of a large object from a porous seabed. *Journal of Fluid Mechanics*. Vol. 152: 203-215, (1985).

[8] Chen, R. ,Gaudin. C. and Cassidy, M.J. Investigation of the vertical uplift capacity of deep water mudmats in clay. *Canadian Geotechnical Journal*. Vol. 49(7): 853-865, (2012).

[9] Al-Shamrani, M. A. Finite Element Analysis of Breakout Force of Objects Embedded in Sea Bottom. *Civil Engineering Research Magazine, Al-Azhar University, Cairo, Egypt*. Vol. 19(2): 288-304, (1997).

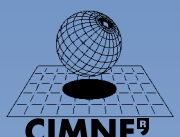
[10] Uzuoka, R. and Borja, R.I. Dynamics of unsaturated poroelastic solids at finite strain. *Internal Journal for Numerical and Analytical Methods in Geomechanics*. Vol. 36: 1535—1573, (2012).

INDEX AUTHORS

Abdel-Maksoud, M. 512
Abdel-Rahman, K. 842
Achmus, M. 842
Allotta, B. 760
Altosole, M. 400
Álvarez, A. 806
Avi, E. 880
Bagaev, D.V. 699
Bartminn, D. 58
Bartolini, F. 760
Baso, S. 376
Bauer, C. 424, 433
Becchi, P. 723
Beck, F. 479
Belibassakis, K. 144
Bergdahl, L. 455
Berger, S. 512
Berrini, E. 412
Bertram, V. 81
Bi, C. 190
Bigay, P. 365
Birken, P. 202
Blanchard, L. 412
Blasques, J. 818
Bletzinger, K.-U. 289
Borsboom, M. 599
Brenner, M. 69
Breuer, M. 241
Broglia, R. 711
Brubak, L. 320
Brunner, D. 213
Cabos, C. 21
Cachim, P. 868
Cammarata, A. 830
Caribe Ribeiro, H.J. 912
Cazuguel, M. 611
Celikkol, B. 168, 178
Cerfontaine, B. 587
Chandras, P. 113
Charlier, R. 587
Chatterjee, D. 113
Chen, J.J. 689
Coelho, C. 868
Conti, F. 723
Coraddu, A. 530
Costa, C. 552
Costanzi, R. 760
Croft, T.N. 137
De Nayer, G. 241
DeCew, J. 168, 178
Delaitre, M. 491
Deng, G. 541
Didier, E. 388
Diez, M. 89
Doi, Y. 376
Dong, G. 190
Dorez, L. 491
Dostal, L. 772
Drach, A. 168, 178
Druckenbrod, M. 512
Dubbioso, G. 711
Dunigneau, R. 144
Durand, M. 491
Durante, D. 711
During, F. 781
Duvigneau, R. 412, 781
Duz, B. 599
Dymarski, C. 444
Dymarski, P. 444
D'Alvise, L. 611
Eberhard, P. 479
Eckfeldt, L. 854
Empelmann, M. 854
Erdem, C. 622
Eskilsson, C. 455
Esteve Perez, J.A. 309
Fernandes, J. 467
Fernandez, H. 125
Figari, M. 400, 530
Fischer, C. 660
Fleissner, F. 479
Foeth, E.J. 101
Fonseca, N. 344
Fortes, C. 467
Francois, A. 611
Fricke, W. 660, 901
Fyrileiv, O. 677
Gaggero, S. 723
García-Espinosa, J. 309
Gauerke, J. 901
Gaul, L. 213
Gelli, J. 760

Gerostathis, T. 144
Ginnis, A. 144
Gleim, T. 202
Gonneau, J.C. 781
Gualdesi, L. 760
Gui, F. 190
Guilcher, P.M. 365
Gutiérrez Romero, J.E. 309
Gütz, P. 842
Hamdaoui, M. 781
Hareide, O.J. 320
Harries, S. 69
Heimann, J. 81
Heitmann, K. 634
Hellesland, J. 320
Hino, T. 794
Hochkirch, K. 81
Huijsmans, R. 599
Hurtado, C. 178
Iglesias, G. 125
Jahn, C. 652
Jakobi, G. 255
Janßen, C. 229
Jean, E. 412, 781
Jelovica, J. 880
Jeon, H. 642
Junge, M. 213
Kaklis, P.D. 144
Kalmbach, A. 241
Kim, K.D. 642
Kornev, N. 255, 737
Kostas, K. 144
Krakowski, W. 854
Kreuzer, E. 772
Kroemer, M. 21
Krueger, C. 737
Kuhl, D. 202
Kurch, M. 156
Lacagnina, M. 830
Lake, T. 137
Le Touzé, D. 365
Lefebvre, J.P. 611
Lehmann, E. 901
Leroy, C. 365
Leroyer, A. 491
Levasseur, S. 587
Li, Y. 190
Lima, M. 868
Lippert, S. 634
Lippert, T. 634
Lobachev, M.P. 699
Lochte-Holtgreven, S. 35
Lombardi, M. 266
Lopez, I. 125
Lothode, C. 491
Luppes, R. 356, 502
M. Paredes, G. 455
Manovachirasan, A. 642
Mao, W. 332
Marinacci, C. 564
Marinich, N. 575
Martelli, M. 400
Masala, R. 564
Masters, I. 137
Matthies, H.G. 278
Meister, A. 202
Meneghetti, G. 660
Monni, N. 760
Moreu, J. 748
Moreu, M. 748
Mourrain, B. 412
Muensterberg, T. 652
Mutsuda, H. 376
Nagrelli, H. 229
Nascimento, A. 912
Nascimento, M.F. 344
Nataletti, M. 400
Natalini, M. 760
Natarajan, A. 818
Neves, C.F. 344
Neves, D.R.C.B. 388
Neves, M.G. 388
Niemelä, A. 880
Ogeman, V. 332
Oger, G. 365
Ohashi, K. 794
Osienski, M. 168
Ovchinnikov, N.A. 699
Palm, J. 455
Parolini, N. 266
Paschen, M. 737
Peralta, P. 842
Pergande, M. 512
Peri, D. 89
Pinheiro, L. 467
Poletz, N. 611
Politis, C. 144
Pugi, L. 760
Queutey, P. 541
Quintana, D.J. 58
Rang, J. 278
Rauer, R. 652
Ribakov, Y. 670
Ricci, G. 552
Ricci, S. 564
Ridolfi, A. 760

Ringsberg, J. 332
Rizzo, C.M. 660
Rodrigues, S. 344
Romanoff, J. 880
Rosenloecher, T. 433
Rosenlöcher, T. 47, 424
Roux, Y. 412, 491, 781
Ruhnau, M. 634
Rung, T. 229
Sakamoto, N. 794
Salvatore, F. 541
Santos, J.A. 344, 467
Satta, A. 552
Savio, S. 530
Schaumann, P. 35
Schimmels, S. 125
Schlecht, B. 47, 424, 433
Schulze, T. 47
Schöttelndreyer, M. 901
Semlow, C. 737
Senyushkina, A. 575
Shah, A. 670
Sharma, L. 113
Sicklinger, S. 289
Sinatra, R. 830
Sollund, H. 889
Sollund, H.A. 677
Stein, T. 69
Swift, M.R. 178
Taboada, M. 748
Tamm, C. 156
Tang, X.W. 921
Tani, G. 723
Taranov, A.E. 699
Tautz, I. 901
Tavera Pinto, F. 455
Teixeira, P.R.F. 388
Tieri, A. 564
Tsukrov, I. 168, 178
Tutar, M. 622
Uzuoka, R. 921
Valdenazzi, F. 723
Valle, J. 748
van der Heiden, H. 502
van der Heiden, H.J.L. 356
van der Plas, P. 356, 502
van der Ploeg, A. 101
Vedeld, K. 677, 889
Veldman, A. 502, 599
Veldman, A.E.P. 356
Verstappen, R.W.C.P. 356
Vettori, G. 760
Vignolo, S. 400
Villalba, A. 806
Visonneau, M. 491, 541
Viviani, M. 400, 723
von Estorff, O. 634
Wahrhaftig, A. 912
Wang, J.H. 689
Wang, T. 289
Warmowska, M. 299
Wellens, P. 599
Wyart, E. 611
Wüchner, R. 289
Xia, X.H. 689
Xu, Y.F. 689
Yakovlev, A. 575
Zagkas, V. 69
Zamora Parra, B. 309
Zhang, C. 670
Zhang, X.W. 921
Zhao, Y. 190



CIMNE

International Center
for Numerical Methods in Engineering